Second Edition

PHOSPHOR HANDBOOK

The CRC Press
Laser and Optical Science and Technology Series

Editor-in-Chief: Marvin J. Weber

Alexander A. Kaminskii
Crystalline Lasers:
Physical Processes and Operating Schemes

A.V. Dotsenko, L.B. Glebov, and V.A. Tsekhomsky
Valentina F. Kokorina
Glasses for Infrared Optics
Physics and Chemistry of Photochromic Glasses

Marvin J. Weber
Handbook of Laser Wavelengths

Marvin J. Weber
Handbook of Lasers

Marvin J. Weber
Handbook of Optical Materials

Michael C. Roggemann and Byron M. Welsh
Imaging Through Turbulence

Andrei M. Efimov
Optical Constants of Inorganic Glasses

Piotr A. Rodnyi
Physical Processes in Inorganic Scintillators

William M. Yen, Shigeo Shionoya, and Hajime Yamamoto
Phosphor Handbook, Second Edition

Hiroyuki Yokoyama and Kikuo Ujihara
Spontaneous Emission and Laser Oscillation in Microcavities

Sergei V. Nemilov
Thermodynamic and Kinetic Aspects of the Vitreous State

Second Edition

PHOSPHOR HANDBOOK

Edited by

William M. Yen

Shigeo Shionoya (Deceased)

Hajime Yamamoto

CRC Press
Taylor & Francis Group
Boca Raton London New York

CRC Press is an imprint of the
Taylor & Francis Group, an informa business

CRC Press
Taylor & Francis Group
6000 Broken Sound Parkway NW, Suite 300
Boca Raton, FL 33487-2742

© 2007 by Taylor & Francis Group, LLC
CRC Press is an imprint of Taylor & Francis Group, an Informa business

No claim to original U.S. Government works
Printed in the United States of America on acid-free paper
10 9 8 7 6 5 4 3 2 1

International Standard Book Number-10: 0-8493-3564-7 (Hardcover)
International Standard Book Number-13: 978-0-8493-3564-8 (Hardcover)

This book contains information obtained from authentic and highly regarded sources. Reprinted material is quoted with permission, and sources are indicated. A wide variety of references are listed. Reasonable efforts have been made to publish reliable data and information, but the author and the publisher cannot assume responsibility for the validity of all materials or for the consequences of their use.

No part of this book may be reprinted, reproduced, transmitted, or utilized in any form by any electronic, mechanical, or other means, now known or hereafter invented, including photocopying, microfilming, and recording, or in any information storage or retrieval system, without written permission from the publishers.

For permission to photocopy or use material electronically from this work, please access www.copyright.com (http://www.copyright.com/) or contact the Copyright Clearance Center, Inc. (CCC) 222 Rosewood Drive, Danvers, MA 01923, 978-750-8400. CCC is a not-for-profit organization that provides licenses and registration for a variety of users. For organizations that have been granted a photocopy license by the CCC, a separate system of payment has been arranged.

Trademark Notice: Product or corporate names may be trademarks or registered trademarks, and are used only for identification and explanation without intent to infringe.

Library of Congress Cataloging-in-Publication Data

Phosphor handbook. -- 2nd ed. / edited by William M. Yen, Shigeo Shionoya, Hajime Yamamoto.
p. cm. -- (CRC Press laser and optical science and technology series ; 21)
Includes bibliographical references and index.
ISBN 0-8493-3564-7
1. Phosphors--Handbooks, manuals, etc. 2. Phosphors--Industrial applications--Handbooks, manuals, etc. I. Yen, W. M. (William M.) II. Shionoya, Shigeo, 1923-2001. III. Yamamoto, Hajime, 1940 Feb. 5- IV. Title. V. Series.

QC467.7.P48 2006
620.1'1295--dc22 2006050242

Visit the Taylor & Francis Web site at
http://www.taylorandfrancis.com

and the CRC Press Web site at
http://www.crcpress.com

Dedication

Dr. Shigeo Shionoya 1923–2001

This handbook is a testament to the many contributions Dr. Shionoya made to phosphor art. The revised volume is dedicated to his memory.

In Memoriam

Kenzo Awazu
Formerly of Mitsubishi
Electric Corp.
Amagasaki, Japan

Kiyoshi Morimoto
Formerly of Futaba Corp.
Chiba, Japan

Shigeharu Nakajima
Formerly of Nichia Chemical
Industries, Ltd.
Tokashima, Japan

Shigeo Shionoya
Formerly of the University of Tokyo
The Institute for Solid State Physics
Tokyo, Japan

Shosaku Tanaka
Tottori University
Department of Electrical & Electronic
Engineering
Tottori, Japan

Akira Tomonaga
Formerly of Mitsubishi Electric Corp.
Amagasaki, Japan

The Editors

William M. Yen obtained his B.S. degree from the University of Redlands, Redlands, California in 1956 and his Ph.D. (physics) from Washington University in St. Louis in 1962. He served from 1962–65 as a Research Associate at Stanford University under the tutelage of Professor A.L. Schawlow, following which he accepted an assistant professorship at the University of Wisconsin-Madison. He was promoted to full professorship in 1972 and retired from this position in 1990 to assume the Graham Perdue Chair in Physics at the University of Georgia-Athens.

Dr. Yen has been the recipient of a J.S. Guggenheim Fellowship (1979–80), of an A. von Humboldt Senior U.S. Scientist Award (1985, 1990), and of a Senior Fulbright to Australia (1995). He was recently awarded the Lamar Dodd Creative Research Award by the University of Georgia Research Foundation. He is the recipient of the ICL Prize for Luminescence Research awarded in Beijing in August 2005. He has been appointed to visiting professorships at numerous institutions including the University of Tokyo, the University of Paris (Orsay), and the Australian National University. He was named the first Edwin T. Jaynes Visiting Professor by Washington University in 2004 and has been appointed to an affiliated research professorship at the University of Hawaii (Manoa). He is also an honorary professor at the University San Antonio de Abad in Cusco, Peru and of the Northern Jiatong University, Beijing, China. He has been on the technical staff of Bell Labs (1966) and of the Livermore Laser Fusion Effort (1974–76).

Dr. Yen has been elected to fellowship in the American Physical Society, the Optical Society of America, the American Association for the Advancement of Science and by the U.S. Electrochemical Society.

Professor Shionoya was born on April 30, 1923, in the Hongo area of Tokyo, Japan and passed away in October 2001. He received his baccalaureate in applied chemistry from the faculty of engineering, University of Tokyo, in 1945. He served as a research associate at the University of Tokyo until he moved to the department of electrochemistry, Yokohama National University as an associate professor in 1951. From 1957 to 1959, he was appointed to a visiting position in Professor H.P. Kallman's group in the physics department of New York University. While there, he was awarded a doctorate in engineering from the University of Tokyo in 1958 for work related to the industrial development of solid-state inorganic phosphor materials. In 1959, he joined the Institute for Solid State Physics (ISSP, Busseiken) of the University of Tokyo as an associate professor; he was promoted to full professorship in the Optical Properties Division of the ISSP in 1967. Following a reorganization of ISSP in 1980, he was named head of the High Power Laser Group of the Division of Solid State under Extreme Conditions. He retired from the post in 1984 with the title of emeritus professor. He helped in the establishment of the Tokyo Engineering University in 1986 and served in the administration and as a professor of Physics. On his retirement from the Tokyo Engineering University in 1994, he was also named emeritus professor in that institution.

During his career, he published more than two hundred scientific papers and authored or edited a number of books—the *Handbook on Optical Properties of Solids* (in Japanese, 1984) and the *Phosphor Handbook* (1998).

Professor Shionoya has been recognized for his many contributions to phosphor art. In 1977, he won the Nishina Award for his research on high-density excitation effects in semiconductors using picosecond spectroscopy. He was recognized by the Electrochemical Society in 1979 for his contributions to advances in phosphor research. Finally, in 1984 he was the first recipient of the ICL Prize for Luminescence Research.

Hajime Yamamoto received his B.S. and Ph.D. degrees in applied chemistry from the University of Tokyo in 1962 and 1967. His Ph.D. work was performed at the Institute for Solid State Physics under late Professors Shohji Makishima and Shigeo Shionoya on spectroscopy of rare earth ions in solids. Soon after graduation he joined Central Research Laboratory, Hitachi Ltd., where he worked mainly on phosphors and p-type ZnSe thin films. From 1971 to 1972, he was a visiting fellow at Professor Donald S. McClure's laboratory, Department of Chemistry, Princeton University. In 1991, he retired from Hitachi Ltd. and moved to Tokyo University of Technology as a professor of the faculty of engineering. Since 2003, he has been a professor at the School of Bionics of the same university.

Dr. Yamamoto serves as a chairperson of the Phosphor Research Society and is an organizing committee member of the Workshop on EL Displays, LEDs and Phosphors, International Display Workshops. He was one of the recipients of Tanahashi Memorial Award of the Japanese Electrochemical Society in 1988, and the Phosphor Award of the Phosphor Research Society in 2000 and 2005.

Preface to the Second Edition

We, the editors as well as the contributors, have been gratefully pleased by the reception accorded to the *Phosphor Handbook* by the technical community since its publication in 1998. This has resulted in the decision to reissue an updated version of the *Handbook*. As we had predicted, the development and the deployment of phosphor materials in an ever increasing range of applications in lighting and display have continued its explosive growth in the past decade. It is our hope that an updated version of the *Handbook* will continue to serve as the initial and preferred reference source for all those interested in the properties and applications of phosphor materials.

For this new edition, we have asked all the authors we could contact to provide corrections and updates to their original contributions. The majority of these responded and their revisions have been properly incorporated in the present volume. It is fortunate that the great majority of the material appearing in the first edition, particularly those sections summarizing the fundamentals of luminescence and describing the principal classes of light-emitting solids, maintains its currency and hence its utility as a reference source.

Several notable advances have occurred in the past decade, which necessitated their inclusion in the second edition. For example, the wide dissemination of nitride-based LEDs opens the possibility of white light solid-state lighting sources that have economic advantages. New phosphors showing the property of "quantum cutting" have been intensively investigated in the past decade and the properties of nanophosphors have also attracted considerable attention. We have made an effort, in this new edition, to incorporate tutorial reviews in all of these emerging areas of phosphor development.

As noted in the preface of the first edition, the *Handbook* traces its origin to one first compiled by the Phosphor Research Society (Japan). The society membership supported the idea of translating the contents and provided considerable assistance in bringing the first edition to fruition. We continue to enjoy the cooperation of the Phosphor Research Society and value the advice and counsel of the membership in seeking improvements in this second edition.

We have been, however, permanently saddened by the demise of one of the principals of the society and the driving force behind the *Handbook* itself. Professor Shigeo Shionoya was a teacher, a mentor, and a valued colleague who will be sorely missed. We wish then to dedicate this edition to his memory as a small and inadequate expression of our joint appreciation.

We also wish to express our thanks and appreciation of the editorial work carried out flawlessly by Helena Redshaw of Taylor & Francis.

William M. Yen
Athens, GA, USA

Hajime Yamamoto
Tokyo, Japan

Preface to the First Edition

This volume is the English version of a revised edition of the *Phosphor Handbook* (*Keikotai Handobukku*) which was first published in Japanese in December, 1987. The original *Handbook* was organized and edited under the auspices of the Phosphor Research Society (in Japan) and issued to celebrate the 200th Scientific Meeting of the Society which occurred in April, 1984.

The Phosphor Research Society is an organization of scientists and engineers engaged in the research and development of phosphors in Japan which was established in 1941. For more than half a century, the Society has promoted interaction between those interested in phosphor research and has served as a forum for discussion of the most recent developments. The Society sponsors five annual meetings; in each meeting four or five papers are presented reflecting new cutting edge developments in phosphor research in Japan and elsewhere. A technical digest with extended abstracts of the presentations is distributed during these meetings and serve as a record of the proceedings of these meetings.

This *Handbook* is designed to serve as a general reference for all those who might have an interest in the properties and/or applications of phosphors. This volume begins with a concise summary of the fundamentals of luminescence and then summarizes the principal classes of phosphors and their light emitting properties. Detailed descriptions of the procedures for synthesis and manufacture of practical phosphors appear in later chapters and in the manner in which these materials are used in technical applications. The majority of the authors of the various chapters are important members of the Phosphor Research Society and they have all made significant contributions to the advancement of the phosphor field. Many of the contributors have played central roles in the evolution and remarkable development of lighting and display industries of Japan. The contributors to the original Japanese version of the *Handbook* have provided English translations of their articles; in addition, they have all updated their contributions by including the newest developments in their respective fields. A number of new sections have been added in this volume to reflect the most recent advances in phosphor technology.

As we approach the new millennium and the dawning of a radical new era of display and information exchange, we believe that the need for more efficient and targeted phosphors will continue to increase and that these materials will continue to play a central role in technological developments. We, the co-editors, are pleased to have engaged in this effort. It is our earnest hope that this *Handbook* becomes a useful tool to all scientists and engineers engaged in research in phosphors and related fields and that the community will use this volume as a daily and routine reference, so that the aims of the Phosphor Research Society in promoting progress and development in phosphors is fully attained.

Co-Editors:
Shigeo Shionoya
Tokyo, Japan

William M. Yen
Athens, GA, USA
May, 1998

Contributors

Chihaya Adachi
Kyushu University
Fukuoka, Japan

Pieter Dorenbos
Delft University of Technology
Delft, The Netherlands

Takashi Hase
Formerly of Kasei Optonix, Ltd.
Odawara, Japan

Noritsuna Hashimoto
Mitsubishi Electric Corp.
Kyoto, Japan

Gen-ichi Hatakoshi
Toshiba Research
Consulting Corp.
Kawasaki, Japan

Sohachiro Hayakawa
Formerly of The Polytechnic University
Kanagawa, Japan

Naoto Hirosaki
National Institute of Materials Science
Tsukuba, Japan

Takayuki Hisamune
Kasei Optonix, Ltd.
Odawara, Japan

Sumiaki Ibuki
Formerly of Mitsubishi Electric Corp.
Amagasaki, Japan

Kenichi Iga
Formerly of Tokyo Institute of Technology
Yokohama, Japan

Shuji Inaho
Formerly of Kasei Optonix, Ltd.
Kanagawa, Japan

Toshio Inoguchi
Formerly of Sharp Corp.
Nara, Japan

Mitsuru Ishii
Formerly of Shonan Institute of Technology
Kanagawa, Japan

Shigeo Itoh
Futaba Corporation
Chiba, Japan

Yuji Itsuki
Nichia Chemical Industries, Ltd.
Tokushima, Japan

Dongdong Jia
Lock Haven University
Lock Haven, Pennsylvania

Weiyi Jia
University of Puerto Rico
Mayaguez, Puerto Rico

Shigeru Kamiya
Formerly of Matsushita Electronics Corp.
Osaka, Japan

Sueko Kanaya
Kanazawa Institute of Technology
Ishikawa, Japan

Tsuyoshi Kano
Formerly of Hitachi, Ltd.
Tokyo, Japan

Hiroshi Kobayashi
Tokushima Bunri University
Kagawa, Japan

Masaaki Kobayashi
KEK
High Energy Accelerator Research Org.
Ibaraki, Japan

Kohtaro Kohmoto
Formerly of Toshiba Lighting
& Technology Corp.
Kanagawa, Japan

Takehiro Kojima
Formerly of Dai Nippon Printing Co., Ltd.
Tokyo, Japan

Yoshiharu Komine
Formerly of Mitsubishi Electric Corp.
Amagasaki, Japan

Hiroshi Kukimoto
Toppan Printing Co., Ltd.
Tokyo, Japan

Yasuaki Masumoto
University of Tsukuba
Ibaraki, Japan

Hiroyuki Matsunami
Kyoto University
Kyoto, Japan

Richard S. Meltzer
University of Georgia
Athens, Georgia

Akiyoshi Mikami
Kanazawa Institute of Technology
Ishikawa, Japan

Yoh Mita
Formerly of Tokyo University of
Technology
Tokyo, Japan

Mamoru Mitomo
National Institute of Materials Science
Tsukuba, Japan

Noboru Miura
Meiji University
Kawasaki, Japan

Norio Miura
Kasei Optonix, Ltd.
Kanagawa, Japan

Sadayasu Miyahara
Sinloihi Co., Ltd.
Kanagawa, Japan

Hideo Mizuno
Formerly of Matsushita
Electronics Corp.
Osaka, Japan

Makoto Morita
Formerly of Seikei University
Tokyo, Japan

Katsuo Murakami
Osram-Melco Co., Ltd.
Shizuoka, Japan

Yoshihiko Murayama
Nemoto & Co., Ltd.
Tokyo, Japan

Yoshinori Murazaki
Nichia Chemical Industries, Ltd.
Tokushima, Japan

Shuji Nakamura
University of California
Santa Barbara, California

Eiichiro Nakazawa
Formerly of Kogakuin University
Tokyo, Japan

Shigetoshi Nara
Hiroshima University
Hiroshima, Japan

Kohei Narisada
Formerly of Matsushita Electric
Ind. Co., Ltd.
Osaka, Japan

Kazuo Narita
Formerly of Toshiba Research Consulting
Corp.
Kawasaki, Japan

Masataka Ogawa
Sony Electronics Inc.
San Jose, California

Katsutoshi Ohno
Formerly of Sony Corp.
Display Co.
Kanagawa, Japan

R. P. Rao
Authentix, Inc.
Douglassville, Pennsylvania

Hiroshi Sasakura
Formerly of Tottori University
Tottori, Japan

Atsushi Suzuki
Formerly of Hitachi, Ltd.
Tokyo, Japan

Takeshi Takahara
Nemato & Co., Ltd.
Kanagawa, Japan

Kenji Takahashi
Fuji Photo Film Co., Ltd.
Kanagawa, Japan

Hiroto Tamaki
Nichia Chemical Industries, Ltd.
Tokushima, Japan

Masaaki Tamatani
Toshiba Research Consulting Corporation
Kawasaki, Japan

Shinkichi Tanimizu
Formerly of Hitachi, Ltd.
Tokyo, Japan

Brian M. Tissue
Virginia Institute of Technology
Blacksburg, Virginia

Yoshifumi Tomita
Formerly of Hitachi, Ltd.
Chiba, Japan

Tetsuo Tsutsui
Kyushu University
Fukuoka, Japan

Koichi Urabe
Formerly of Hitachi, Ltd.
Tokyo, Japan

Xiaojun Wang
Georgia Southern University
Statesboro, Georgia

Rong-Jun Xie
Advanced Materials Laboratory, National
Institute of Materials Science
Tsukuba, Japan

Hajime Yamamoto
Tokyo University of Technology
Tokyo, Japan

William M. Yen
University of Georgia
Athens, Georgia

Toshiya Yokogawa
Matsushita Electric Ind. Co., Ltd.
Kyoto, Japan

Masaru Yoshida
Sharp Corp.
Nara, Japan

Taisuke Yoshioka
Formerly of Aiwa Co., Ltd.
Tokyo, Japan

Contents

Part I: Introduction

Chapter 1 Introduction to the handbook
- 1.1 Terminology
- 1.2 Past and present phosphor research
- 1.3 Applications of phosphors
- 1.4 Contents of the handbook

Part II: Fundamentals of phosphors

Chapter 2 Fundamentals of luminescence
- 2.1 Absorption and emission of light
- 2.2 Electronic states and optical transition of solid crystals
- 2.3 Luminescence of a localized center
- 2.4 Impurities and luminescence in semiconductors
- 2.5 Luminescence of organic compounds
- 2.6 Luminescence of low-dimensional systems
- 2.7 Transient characteristics of luminescence
- 2.8 Excitation energy transfer and cooperative optical phenomena
- 2.9 Excitation mechanism of luminescence by cathode-ray and ionizing radiation
- 2.10 Inorganic electroluminescence
- 2.11 Lanthanide level locations and its impact on phosphor performance

Chapter 3 Principal phosphor materials and their optical properties
- 3.1 Luminescence centers of ns^2-type ions
- 3.2 Luminescence centers of transition metal ions
- 3.3 Luminescence centers of rare-earth ions
- 3.4 Luminescence centers of complex ions
- 3.5 Ia-VIIb compounds
- 3.6 IIa-VIb compounds
- 3.7 IIb-VIb compounds
- 3.8 ZnSe and related luminescent materials

3.9 IIIb-Vb compounds
3.10 (Al,Ga,In)(P,As) alloys emitting visible luminescence
3.11 (Al,Ga,In)(P,As) alloys emitting infrared luminescence
3.12 GaN and related luminescence materials
3.13 Silicon carbide (SiC) as a luminescence material
3.14 Oxynitride phosphors

Part III: Practical phosphors

Chapter 4 Methods of phosphor synthesis and related technology
4.1 General technology of synthesis
4.2 Inorganic nanoparticles and nanostructures for phosphor applications
4.3 Preparation of phosphors by the sol–gel technology
4.4 Surface treatment
4.5 Coating methods
4.6 Fluorescent lamps
4.7 Mercury lamps
4.8 Intensifying screens (Doctor Blade Method)
4.9 Dispersive properties and adhesion strength

Chapter 5 Phosphors for lamps
5.1 Construction and energy conversion principle of various lamps
5.2 Classification of fluorescent lamps by chromaticity and color rendering properties
5.3 High-pressure mercury lamps
5.4 Other lamps using phosphors
5.5 Characteristics required for lamp phosphors
5.6 Practical lamp phosphors
5.7 Phosphors for high-pressure mercury lamps
5.8 Quantum-cutting phosphors
5.9 Phosphors for white light-emitting diodes

Chapter 6 Phosphors for cathode-ray tubes
6.1 Cathode-ray tubes
6.2 Phosphors for picture and display tubes
6.3 Phosphors for projection and beam index tubes
6.4 Phosphors for observation tubes
6.5 Phosphors for special tubes
6.6 Listing of practical phosphors for cathode-ray tubes

Chapter 7 Phosphors for X-ray and ionizing radiation
- 7.1 Phosphors for X-ray intensifying screens and X-ray fluorescent screens
- 7.2 Phosphors for thermoluminescent dosimetry
- 7.3 Scintillators
- 7.4 Phosphors for X-ray image intensifiers
- 7.5 Photostimulable phosphors for radiographic imaging

Chapter 8 Phosphors for vacuum fluorescent displays and field emission displays
- 8.1 Vacuum fluorescent displays
- 8.2 Field emission displays

Chapter 9 Electroluminescence materials
- 9.1 Inorganic electroluminescence materials
- 9.2 Inorganic electroluminescence
- 9.3 Organic electroluminescence

Chapter 10 Phosphors for plasma display
- 10.1 Plasma display panels
- 10.2 Discharge gases
- 10.3 Vacuum-ultraviolet phosphors and their characteristics
- 10.4 Characteristics of full-color plasma displays
- 10.5 Plasma displays and phosphors

Chapter 11 Organic fluorescent pigments
- 11.1 Daylight fluorescence and fluorescent pigments
- 11.2 Manufacturing methods of fluorescent pigments
- 11.3 Use of fluorescent pigments

Chapter 12 Other phosphors
- 12.1 Infrared up-conversion phosphors
- 12.2 Luminous paints
- 12.3 Long persistent phosphors
- 12.4 Phosphors for marking
- 12.5 Stamps printed with phosphor-containing ink
- 12.6 Application of near-infrared phosphors for marking

Chapter 13 Solid-state laser materials
- 13.1 Introduction
- 13.2 Basic laser principles
- 13.3 Operational schemes

13.4 Materials requirements for solid-state lasers
13.5 Activator ions and centers
13.6 Host lattices
13.7 Conclusions

Part IV: Measurements of phosphor properties

Chapter 14 Measurements of luminescence properties of phosphors
14.1 Luminescence and excitation spectra
14.2 Reflection and absorption spectra
14.3 Transient characteristics of luminescence
14.4 Luminescence efficiency
14.5 Data processing
14.6 Measurements in the vacuum-ultraviolet region

Chapter 15 Measurements of powder characteristics
15.1 Particle size and its measurements
15.2 Methods for measuring particle size
15.3 Measurements of packing and flow

Part V: Related important items

Chapter 16 Optical properties of powder layers
16.1 Kubelka-Munk's theory
16.2 Johnson's theory
16.3 Monte Carlo method

Chapter 17 Color vision
17.1 Color vision and the eye
17.2 Light and color
17.3 Models of color vision
17.4 Specification of colors and the color systems
17.5 The color of light and color temperature
17.6 Color rendering
17.7 Other chromatic phenomena

Part VI: History

Chapter 18 History of phosphor technology and industry
18.1 Introduction
18.2 Phosphors for fluorescent lamps
18.3 Phosphors for high-pressure mercury vapor lamps
18.4 Photoluminescent devices from 1995 to 2005
18.5 Phosphors for black-and-white picture tubes

18.6 Phosphors for color picture tubes
18.7 Cathodoluminescent displays from 1995 to 2005
18.8 Phosphors for X-ray
18.9 Medical devices using radioluminescence from 1995 to 2005
18.10 A short note on the history of phosphors
18.11 Production of luminescent devices utilizing phosphors
18.12 Production of phosphors

part one

Introduction

chapter one

Introduction to the handbook

Shigeo Shionoya

Contents

1.1 Terminology 3
1.2 Past and present phosphor research 4
1.3 Applications of phosphors 5
1.4 Contents of the handbook 6
References 8

This Handbook is a comprehensive description of phosphors with an emphasis on practical phosphors and their uses in various kinds of technological applications. Following this introduction, Part II deals with the fundamentals of phosphors: namely, the basic principles of luminescence and the principal phosphor materials and their optical properties. Part III describes practical phosphors: phosphors used in lamps, cathode-ray tubes, X-ray and ionizing radiation detection, etc. Part IV describes the common measurement methodology used to characterize phosphor properties, while Part V discusses a number of related important items. Finally, Part VI details some of the history of phosphor technology and industry.

1.1 Terminology

The origin and meaning of the terminology related to phosphors must first be explained. The word *phosphor* was invented in the early 17th century and its meaning remains unchanged. It is said that an alchemist, Vincentinus Casciarolo of Bologna, Italy, found a heavy crystalline stone with a gloss at the foot of a volcano, and fired it in a charcoal oven intending to convert it to a noble metal. Casciarolo obtained no metals but found that the sintered stone emitted red light in the dark after exposure to sunlight. This stone was called the "Bolognian stone." From the knowledge now known, the stone found appears to have been barite ($BaSO_4$), with the fired product being BaS, which is now known to be a host for phosphor materials.

After this discovery, similar findings were reported from many places in Europe, and these light-emitting stones were named *phosphors*. This word means "light bearer" in Greek, and appears in Greek myths as the personification of the morning star Venus. The word *phosphorescence*, which means persisting light emission from a substance after the exciting radiation has ceased, was derived from the word *phosphor*.

Prior to the discovery of Bolognian stone, the Japanese were reported to have prepared phosphorescent paint from seashells. This fact is described in a 10th century Chinese document (Song dynasty) (see 18.7 for details). It is very interesting to learn that the credit for preparing phosphors for the first time should fall to the Japanese.

The word *fluorescence* was introduced to denote the imperceptible short after-glow of the mineral fluorite (CaF_2) following excitation. This is to distinguish the emission from *phosphorescence*, which is used to denote a long after-glow of a few hours.

The word *luminescence*, which includes both fluorescence and phosphorescence, was first used by Eilhardt Wiedemann, a German physicist, in 1888. This word originates from the Latin word *lumen*, which means light.

Presently, the word *luminescence* is defined as a phenomenon in which the electronic state of a substance is excited by some kind of external energy and the excitation energy is given off as light. Here, the word *light* includes not only electromagnetic waves in the visible region of 400 to 700 nm, but also those in the neighboring regions on both ends, i.e., the near-ultraviolet and the near-infrared regions.

During the first half of this century, the difference between fluorescence and phosphorescence was a subject actively discussed. Controversy centered on the duration of the after-glow after excitation ceased and on the temperature dependence of the after-glow. However, according to present knowledge, these discussions are now meaningless.

In modern usage, light emission from a substance during the time when it is exposed to exciting radiation is called *fluorescence*, while the after-glow if detectable by the human eye after the cessation of excitation is called *phosphorescence*. However, it should be noted that these definitions are applied only to inorganic materials; for organic molecules, different terminology is used. For organics, light emission from a singlet excited state is called *fluorescence*, while that from a triplet excited state is defined as *phosphorescence* (see 2.5 for details).

The definition of the word *phosphor* itself is not clearly defined and is dependent on the user. In a narrow sense, the word is used to mean inorganic phosphors, usually those in powder form and synthesized for the purpose of practical applications. Single crystals, thin films, and organic molecules that exhibit luminescence are rarely called phosphors. In a broader sense, the word phosphor is equivalent to "solid luminescent material."

1.2 *Past and present phosphor research*

The scientific research on phosphors has a long history going back more than 100 years. A prototype of the ZnS-type phosphors, an important class of phosphors for television tubes, was first prepared by Théodore Sidot, a young French chemist, in 1866 rather accidentally (see 3.7.1 for details). It seems that this marked the beginning of scientific research and synthesis of phosphors.

From the late 19th century to the early 20th century, Philip E.A. Lenard and co-workers in Germany performed active and extensive research on phosphors, and achieved impressive results. They prepared various kinds of phosphors based on alkaline earth chalcogenides (sulfides and selenides) and zinc sulfide, and investigated the luminescence properties.

They established the principle that phosphors of these compounds are synthesized by introducing metallic impurities into the materials by firing. The metallic impurities, called luminescence activators, form luminescence centers in the host. Lenard and co-workers tested not only heavy metal ions but various rare-earth ions as potential activators. Alkaline chalcogenide phosphors developed by this research group are called Lenard phosphors, and their achievements are summarized in their book.[1]

P. W. Pohl and co-workers in Germany investigated Tl^+-activated alkali halide phosphors in detail in the late 1920s and 1930s. They grew single-crystal phosphors and performed extensive spectroscopic studies. They introduced the configurational coordinate model of luminescence centers in cooperation with F. Seitz in the U.S. and established the basis of present-day luminescence physics.

Humbolt Leverenz and co-workers at Radio Corporation of America (U.S.) also investigated many practical phosphors with the purpose of obtaining materials with desirable characteristics to be used in television tubes. Detailed studies were performed on ZnS-type phosphors. Their achievements are compiled in Leverenz's book.[2] Data on emission spectra in the book still remain useful today (see 6.2).

Since the end of World War II, research on phosphors and solid-state luminescence has evolved dramatically. This has been supported by progress in solid-state physics, especially semiconductor and lattice defect physics; advances in the understanding of the optical spectroscopy of solids, especially that of transition metals ions and rare-earth ions, have also helped in these developments. The important achievements obtained along the way are briefly discussed below.

The concept of the configurational coordinate model of luminescence centers was established theoretically. Spectral shapes of luminescence bands were explained on the basis of this model. The theory of excitation energy transfer successfully interpreted the phenomenon of sensitized luminescence. Optical spectroscopy of transition metal ions in crystals clarified their energy levels and luminescence transition on the basis of crystal field theory. In the case of trivalent rare-earth ions in crystals, precise optical spectroscopy measurements made possible the assignment of complicated energy levels and various luminescence transitions.

Advances in studies of band structures and excitons in semiconductors and ionic crystals contributed much to the understanding of luminescence properties of various phosphors using these materials as hosts. The concept of direct and indirect transition types of semiconductors helped not only to find efficient luminescence routes in indirect type semiconductors, but also to design efficient materials for light-emitting diodes and semiconductors lasers. The concept of donor-acceptor pair luminescence in semiconductors was proposed and found to produce efficient luminescence in semiconductor phosphors.

Turning to the applications of phosphors, one notes the more recent appearance of various new kinds of electronic displays using phosphors, such as electroluminescent displays, vacuum fluorescent displays, plasma displays, and field emission displays; this is, of course, in addition to the classical applications such as fluorescent lamps, television tubes, X-ray screens, etc. These applications will be described in Section 1.3 below.

Research on phosphors and their applications requires the use of a number of fields in science and technology. Synthesis and preparation of inorganic phosphors are based on physical and inorganic chemistry. Luminescence mechanisms are interpreted and elucidated on the basis of solid-state physics. The major and important applications of phosphors are in light sources, display devices, and detector systems. Research and development of these applications belong to the fields of illuminating engineering, electronics, and image engineering. Therefore, research and technology in phosphors require a unique combination of interdisciplinary methods and techniques, and form a fusion of the above-mentioned fields.

1.3 *Applications of phosphors*

The applications of phosphors can be classified as: (1) light sources represented by fluorescent lamps; (2) display devices represented by cathode-ray tubes; (3) detector systems represented by X-ray screens and scintillators; and (4) other simple applications, such as luminous paint with long persistent phosphorescence.

Another method to classify the applications is according to the excitation source for the phosphors. Table 1 lists various kinds of phosphor devices according to the method used to excite the phosphor. It gives a summary of phosphor devices by the manner in which the phosphors are applied. No further explanation of the table is necessary.

1.4 *Contents of the handbook*

This Handbook is organized as follows. Part II deals with the fundamentals of phosphors and is composed of two chapters. Chapter 2 describes the fundamentals of luminescence, while Chapter 3 describes principal phosphor materials and their optical properties. In Chapter 2, the physics necessary to understand the luminescence mechanisms in solids is explained, and then various luminescence phenomena in inorganic and organic materials are interpreted on the basis of this physics. The luminescence of recently developed low-dimensional systems, such as quantum wells and dots, is also interpreted. Further, the excitation mechanisms for luminescence by cathode-ray and ionizing radiation and by electric fields to produce electroluminescence are also discussed in this chapter.

In Chapter 3, phosphor materials are classified according to the class of luminescence centers employed or the class of host materials used. The optical properties of these materials, including their luminescence characteristics and mechanisms, are interpreted. Emphasis is placed on those materials that are important from a practical point of view. Those possessing no possibility for practical use but being important from a basic point of view are also included.

Part III deals with practical phosphors, and is a most important and unique part of this Handbook. In Chapter 4, a general explanation of the methods used for phosphor synthesis and related technologies is given. In Chapters 5 through 12, practical phosphors are classified according to usage and explained. First, the operating principle and structure of phosphor devices are described; the phosphor characteristics required for a given device are specified. Then, manufacturing processes and characteristics of the phosphors currently in use are described. Discussions are presented on the research and development currently under way on phosphors with potential for practical usage. A narration is also given of phosphors that have played a historical role, but are no longer of practical use.

Chapters 5 and 6 describe phosphors for lamps and cathode-ray tubes, respectively. These two classes of phosphors are extremely important in the phosphor industry, so that a comprehensive treatment is given in these two chapters. Chapter 7 deals with phosphors for X-ray and ionizing radiation. Chapter 8 concerns phosphors for vacuum fluorescent and field emission displays, while Chapter 9 describes inorganic and organic electroluminescence materials. Chapter 10 treats phosphors for plasma displays. Chapter 11 deals with organic fluorescent pigments, while Chapter 12 treats phosphors used in a variety of other practical applications. Finally, in Chapter 13, solid-state laser materials are taken up and interpreted; this inclusion is made because the optical and luminescence properties of laser materials are essentially the same as those of phosphors and knowledge of them is useful for phosphor research.

Part IV deals with measurements of phosphor properties, and is composed of Chapter 14 describing measurements of luminescence properties and Chapter 15 dealing with powder characteristics. Part V treats miscellanies and contains Chapter 16, which details the optical properties of powder layers, and Chapter 17, which describes the properties of color vision. In Part VI, Chapter 18 offers a detailed history of phosphor technology and industry.

Table 1 Phosphor Devices

- Phosphor Devices
  - Electron beam (5-30 kV)
    - CRT for TV
      - Color
      - Black & White
      - Projection
      - View finder
    - CRT for display
      - Color
      - monochrome
    - CRT for measurements
      - Oscilloscope
      - Storage tube
    - Other CRT
      - Flying spot scanner
      - Radar
      - Image intensifier (output screen)
  - (10 V–10 kV)
    - Large sized outdoor display
    - Field emission display
    - Vacuum fluorescent display
  - Light (UV-Vis-IR)
    - White LED
    - Luminous paint, Fluorescent pigment, Fluorescent marking
    - IR-Vis up-conversion
    - Solid-state laser material, Laser dye
  - (250-400 nm)
    - High pressure mercury lamp
  - (254 nm)
    - Fluorescent lamp
      - General illumination
        - Wide band type
        - Narrow 3-band type
      - High color rendering
      - Special uses
        - LCD back light
        - Outdoor display
        - Copying machine
        - Black light, Viewer
        - Medical use
        - Agricultural use
  - (Vacuum UV)
    - Plasma display
    - Neon sign, Neon tubing
  - High energy radiation (X-rays and others)
    - Fluoroscopic screen
    - Intensifying screen
    - Scintillators
    - Image intensifier (input screen)
    - Radiographic imaging plate
    - Dosimeter
  - Electric field (Electroluminescence)
    - Inorganic EL
      - High field EL
        - Thin film type
        - Powder phosphor type
      - Injection EL
        - Light emitting diode
        - Semiconductor laser
    - Organic EL
      - EL panel

As mentioned, this Handbook covers all the important items on phosphors—from the fundamentals to their applications. It presents comprehensive descriptions of the preparation methods and the characteristics of phosphors important to phosphor technology and industry. Every effort has been made to include the most recent results in research and technological development of phosphors in the various chapters.

The Handbook contains two indices: Subject Index and Chemical Formula Index. The latter index is a unique and very useful feature; this index contains all the chemical formulae of the phosphors described in this Handbook. The chemical formula of a phosphor is expressed in terms of the host plus activator(s). For example, the white-emitting halophosphate phosphor used extensively in fluorescent lamps appears as $Ca_5(PO_4)_3(F,Cl){:}Sb^{3+},Mn^{2+}$. Additionally, the Chemical Formula Index indexes all the activators utilized in the phosphors listed. For example: for Mn^{2+} as an activator, all the Mn^{2+}-activated phosphors, including halophosphate phosphors, are cross-referenced in this index.

References

1. Lenard, P.E.A., Schmidt, F., and Tomaschek, R., "Phosphoreszenz und Fluoreszenz," in *Handbuch der Experimentalphysik*, Bd. 23, 1. u. 2. Teil, Akademie Verlagsgesellschaft, Leipzig, 1928.
2. Leverenz, H.W., *An Introduction to Luminescence of Solids*, John Wiley & Sons, New York, 1950.

part two

Fundamentals of phosphors

chapter two — section one

Fundamentals of luminescence

Eiichiro Nakazawa

Contents

2.1 Absorption and emission of light 11
  2.1.1 Absorption and reflection of light in crystals 12
    2.1.1.1 Optical constant and complex dielectric constant 12
    2.1.1.2 Absorption coefficient 13
    2.1.1.3 Reflectivity and transmissivity 13
  2.1.2 Absorption and emission of light by impurity atoms 14
    2.1.2.1 Classical harmonic oscillator model of optical centers 14
    2.1.2.2 Electronic transition in an atom 15
    2.1.2.3 Electric dipole transition probability 16
    2.1.2.4 Intensity of light emission and absorption 17
    2.1.2.5 Oscillator strength 18
    2.1.2.6 Impurity atoms in crystals 19
    2.1.2.7 Forbidden transition 19
    2.1.2.8 Selection rule 19

2.1 Absorption and emission of light

Most phosphors are composed of a transparent microcrystalline host (or a matrix) and an activator, i.e., a small amount of intentionally added impurity atoms distributed in the host crystal. Therefore, the luminescence processes of a phosphor can be divided into two parts: the processes mainly related to the host, and those that occur around and within the activator.

Processes related to optical absorption, reflection, and transmission by the host crystal are discussed, from a macroscopic point of view, in 2.1.1. Other host processes (e.g., excitation by electron bombardment and the migration and transfer of the excitation energy in the host) are discussed in a later section. 2.1.2 deals with phenomena related to the activator atom based on the theory of atomic spectra.

The interaction between the host and the activator is not explicitly discussed in this section; in this sense, the host is treated only as a medium for the activator. The interaction processes such as the transfer of the host excitation energy to the activator will be discussed in detail for each phosphor in Part III.

2.1.1 Absorption and reflection of light in crystals

Since a large number of phosphor host materials are transparent and nonmagnetic, their optical properties can be represented by the optical constants or by a complex dielectric constant.

2.1.1.1 Optical constant and complex dielectric constant

The electric and magnetic fields of a light wave, propagating in a uniform matrix with an angular frequency ω (= 2πν, ν:frequency) and velocity v = ω/k are:

$$E = E_0 \exp\left[i\left(\tilde{\boldsymbol{k}} \cdot \boldsymbol{r} - \omega t\right)\right] \tag{1}$$

$$H = H_0 \exp\left[i\left(\tilde{\boldsymbol{k}} \cdot \boldsymbol{r} - \omega t\right)\right], \tag{2}$$

where $\boldsymbol{r}$ is the position vector and $\tilde{\boldsymbol{k}}$ is the complex wave vector.

E and H in a nonmagnetic dielectric material, with a magnetic permeability that is nearly equal to that in a vacuum ($\mu \approx \mu_0$) and with uniform dielectric constant ε and electric conductivity σ, satisfy the next two equations derived from Maxwell's equations.

$$\nabla^2 E = \sigma\mu_0 \frac{\partial E}{\partial t} + \varepsilon\mu_0 \frac{\partial^2 E}{\partial t^2} \tag{3}$$

$$\nabla^2 H = \sigma\mu_0 \frac{\partial H}{\partial t} + \varepsilon\mu_0 \frac{\partial^2 H}{\partial t^2} \tag{4}$$

In order that Eqs. 1 and 2 satisfy Eqs. 3 and 4, the $\tilde{\boldsymbol{k}}$-vector and its length $\tilde{k}$, which is a complex number, should satisfy the following relation:

$$\tilde{\boldsymbol{k}} \cdot \tilde{\boldsymbol{k}} = \tilde{k}^2 = \left(\varepsilon + \frac{i\sigma}{\omega}\right)\mu_0\omega^2 = \tilde{\varepsilon}\mu_0\omega^2 \tag{5}$$

where $\tilde{\varepsilon}$ is the complex dielectric constant defined by:

$$\tilde{\varepsilon} = \varepsilon' + i\varepsilon'' \equiv \varepsilon + i\frac{\sigma}{\omega} \tag{6}$$

Therefore, the refractive index, which is a real number defined as $n \equiv c/v = ck/w$ in a transparent media, is also a complex number:

$$\tilde{n} = n + i\kappa \equiv c\tilde{k}/\omega = \left(\frac{\tilde{\varepsilon}}{\varepsilon_0}\right)^{1/2} \tag{7}$$

where c is the velocity of light in vacuum and is equal to $(\varepsilon_0\mu_0)^{-1/2}$ from Eq. 5. The last term in Eq. 7 is also derived from Eq. 5.

The real and imaginary parts of the complex refractive index, i.e., the real refractive index n and the extinction index κ, are called optical constants, and are the representative constants of the macroscopic optical properties of the material. The optical constants in a nonmagnetic material are related to each other using Eqs. 6 and 7,

$$\frac{e'}{\varepsilon_0} = n^2 - \kappa^2 \tag{8}$$

$$\frac{\varepsilon''}{\varepsilon_0} = 2n\kappa \tag{9}$$

Both of the optical constants, n and κ, are functions of angular frequency ω and, hence, are referred to as dispersion relations. The dispersion relations for a material are obtained by measuring and analyzing the reflection or transmission spectrum of the material over a wide spectral region.

2.1.1.2 *Absorption coefficient*

The intensity of the light propagating in a media a distance x from the incident surface having been decreased by the optical absorption is given by Lambert's law.

$$I = I_0 \exp(-\alpha x) \tag{10}$$

where I_0 is the incident light intensity minus reflection losses at the surface, and $\alpha(\mathrm{cm}^{-1})$ is the absorption coefficient of the media.

Using Eqs. 5 and 7, Eq. 1 may be rewritten as:

$$E = E_0 \exp(-\omega\kappa x/c)\exp[-i\omega(t + nx/c)] \tag{11}$$

and, since the intensity of light is proportional to the square of its electric field strength E, the absorption coefficient may be identified as:

$$\alpha = 2\omega\kappa/c \tag{12}$$

Therefore, κ is a factor that represents the extinction of light due to the absorption by the media.

There are several ways to represent the absorption of light by a medium, as described below.

1. Absorption coefficient, $\alpha(\mathrm{cm}^{-1})$: $I/I_0 = e^{-\alpha x}$
2. Absorption cross-section, α/N (cm^2). Here, N is the number of absorption centers per unit volume.
3. Optical density, absorbance, $D = -\log_{10}(I/I_0)$
4. Absorptivity, $(I_0 - I)/I_0 \times 100$, (%)
5. Molar extinction coefficient, $\varepsilon = \alpha \log_{10} e/C$. Here, $C(\mathrm{mol}/l)$ is the molar concentration of absorption centers in a solution or gas.

2.1.1.3 *Reflectivity and transmissivity*

When a light beam is incident normally on an optically smooth crystal surface, the ratio of the intensities of the reflected light to the incident light, i.e., normal surface reflectivity R_0, can be written in terms of the optical constants, n and κ, by

$$R_0 = \frac{(n-1)^2 + \kappa^2}{(n+1)^2 + \kappa^2} \tag{13}$$

Then, for a sample with an absorption coefficient α and thickness d that is large enough to neglect interference effects, the overall normal reflectivity and transmissivity, i.e., the ratio of the transmitted light to the incident, are; respectively:

$$\bar{R} = R_0\left(1 + \bar{T}\exp(-\alpha d)\right) \tag{14}$$

$$\bar{T} = \frac{(1-R_0)^2\left(1+\kappa^2/n^2\right)\exp(-\alpha d)}{1 - R_0^2\exp(-2\alpha d)} \simeq \frac{(1-R_0)^2\exp(-\alpha d)}{1 - R_0^2\exp(-2\alpha d)} \tag{15}$$

If absorption is zero ($\alpha = 0$), then,

$$\bar{R} = \frac{(n-1)^2}{\left(n^2+1\right)} \tag{16}$$

2.1.2 Absorption and emission of light by impurity atoms

The emission of light from a material originates from two types of mechanisms: thermal emission and luminescence. While all the atoms composing the solid participate in the light emission in the thermal process, in the luminescence process a very small number of atoms (impurities in most cases or crystal defects) are excited and take part in the emission of light. The impurity atom or defect and its surrounding atoms form a luminescent or an emitting center. In most phosphors, the luminescence center is formed by intentionally incorporated impurity atoms called activators.

This section treats the absorption and emission of light by these impurity atoms or local defects.

2.1.2.1 Classical harmonic oscillator model of optical centers

The absorption and emission of light by an atom can be described in the most simplified scheme by a linear harmonic oscillator, as shown in Figure 1, composed of a positive charge ($+e$) fixed at $z = 0$ and an electron bound and oscillating around it along the z-axis. The electric dipole moment of the oscillator with a characteristic angular frequency ω_0 is given by:

$$M = ez = M_o \exp(i\omega_o t) \tag{17}$$

and its energy, the sum of the kinetic and potential energies, is $\left(m_e\omega_o^2/2e^2\right)M_o^2$, where m_e is the mass of the electron. Such a vibrating electric dipole transfers energy to electromagnetic radiation at an average rate of $\left(\omega_o^4/12\pi\varepsilon_0 c^3\right)M_0^2$ per second, and therefore has a total energy decay rate given by:

$$A_0 = \frac{e^2\omega_o^2}{6\pi\varepsilon_0 m_e c^3} \tag{18}$$

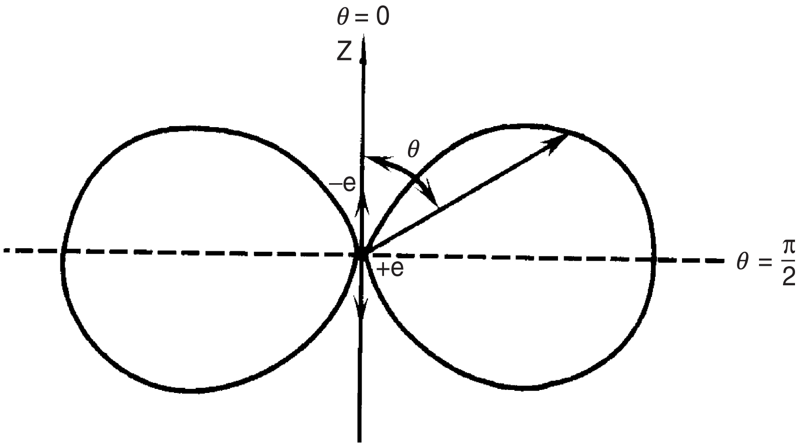

Figure 1 Electromagnetic radiation from an electric dipole oscillator. The length of the arrow gives the intensity of the radiation to the direction.

When the change of the energy of this oscillator is expressed as an exponential function e^{-t/τ_0}, its time constant τ_o is equal to A_0^{-1}, which is the radiative lifetime of the oscillator, i.e., the time it takes for the oscillator to lose its energy to e^{-1} of the initial energy. From Eq. 8, the radiative lifetime of an oscillator with a 600-nm ($\omega_0 = 3 \times 10^{15}$ s^{-1}) wavelength is $\tau_0 \approx 10^{-8}$ s. The intensity of the emission from an electric dipole oscillator depends on the direction of the propagation, as shown in Figure 1.

A more detailed analysis of absorption and emission processes of light by an atom will be discussed using quantum mechanics in the following subsection.

2.1.2.2 *Electronic transition in an atom*

In quantum mechanics, the energy of the electrons localized in an atom or a molecule have discrete values as shown in Figure 2. The absorption and emission of light by an

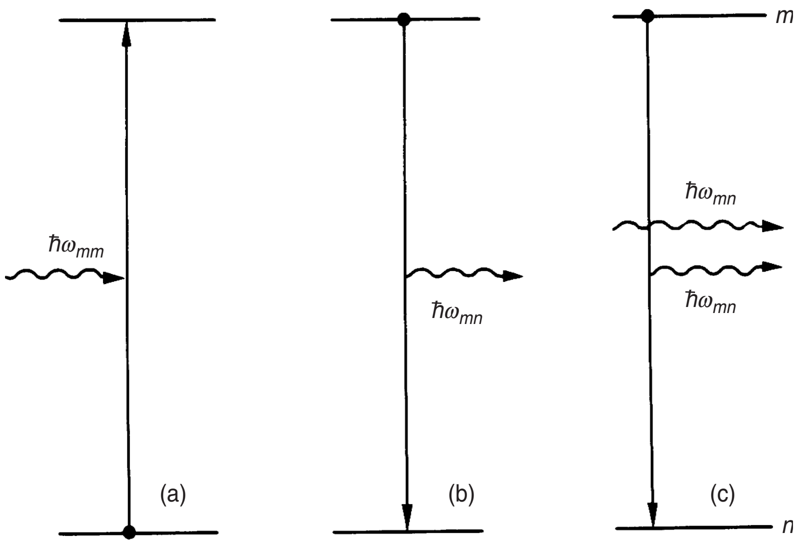

Figure 2 Absorption (a), spontaneous emission (b), and induced emission (c) of a photon by a two-level system.

atom, therefore, is not a gradual and continuous process as discussed in the above section using a classical dipole oscillator, but is an instantaneous transition between two discrete energy levels (states), m and n in Figure 2, and should be treated statistically.

The energy of the photon absorbed or emitted at the transition $m \leftrightarrow n$ is:

$$\hbar\omega_{mn} = E_m - E_n, \qquad (E_m > E_n) \tag{19}$$

where E_n and E_m are the energies of the initial and final states of the transition, respectively, and $\omega_{mn}(=2\pi\nu_{mn})$ is the angular frequency of light.

There are two possible emission processes, as shown in Figure 2; one is called spontaneous emission (b), and the other is stimulated emission (c). The stimulated emission is induced by an incident photon, as is the case with the absorption process (a). Laser action is based on this type of emission process.

The intensity of the absorption and emission of photons can be enumerated by a transition probability per atom per second. The probability for an atom in a radiation field of energy density $\rho(\omega_{mn})$ to absorb a photon, making the transition from n to m, is given by

$$W_{mn} = B_{n\to m}\rho(\omega_{mn}) \tag{20}$$

where $B_{n\to m}$ is the transition probability or Einstein's B-coefficient of optical absorption, and $\rho(\omega)$ is equal to $I(\omega)/c$ in which $I(\omega)$ is the light intensity, i.e., the energy per second per unit area perpendicular to the direction of light.

On the other hand, the probability of the emission of light is the sum of the spontaneous emission probability $A_{m\to n}$ (Einstein's A-coefficient) and the stimulated emission probability $B_{m\to n}\rho(\omega_{mn})$. The stimulated emission probability coefficient $B_{m\to n}$ is equal to $B_{n\to m}$.

The equilibrium of optical absorption and emission between the atoms in the states m and n is expressed by the following equation.

$$N_n B_{n\to m}\rho(\omega_{mn}) = N_m\left\{A_{m\to n} + B_{m\to n}(\omega_{mn})\rho(\omega_{mn})\right\}, \tag{21}$$

where N_m and N_n are the number of atoms in the states m and n, respectively. Taking into account the Boltzmann distribution of the system and Plank's equation of radiation in thermodynamic equilibrium, the following equation is obtained from Eq. 21 for the spontaneous mission probability.

$$A_{m\to n} = \frac{\hbar\omega_{mn}^3}{\pi^2 c^3} B_{m\to n} \tag{22}$$

Therefore, the probabilities of optical absorption, and the spontaneous and induced emissions between m and n are related to one another.

2.1.2.3 *Electric dipole transition probability*

In a quantum mechanical treatment, optical transitions of an atom are induced by perturbing the energy of the system by $\Sigma_i(-e\boldsymbol{r}_i)\cdot\boldsymbol{E}$, in which $\boldsymbol{r}_i$ is the position vector of the electron from the atom center and, therefore, $\Sigma_i(-e\boldsymbol{r}_i)$ is the electric dipole moment of the atom (see Eq. 17). In this electric dipole approximation, the transition probability of optical absorption is given by:

$$W_{mn} = \frac{\pi}{3\varepsilon_0 c\hbar^2} I(\omega_{mn})\left|M_{mn}\right|^2 \tag{23}$$

Here, the dipole moment, M_{mn} is defined by:

$$M_{mn} = \int \psi_m^* \left(\sum_i e\mathbf{r}_i \right) \psi_n d\tau \tag{24}$$

where ψ_m and ψ_n are the wavefunctions of the states m and n, respectively. The direction of this dipole moment determines the polarization of the light absorbed or emitted. In Eq. 23, however, it is assumed that the optical center is isotropic and then $|(M_{mn})_z|^2 = |M_{mn}|^2/3$ for light polarized in the z-direction.

Equating the right-hand side of Eq. 23 to that of Eq. 20, the absorption transition probability coefficient $B_{n\rightarrow m}$ and then, from Eq. 22, the spontaneous emission probability coefficient $A_{m\rightarrow n}$ can be obtained as follows:

$$\begin{aligned} B_{n\rightarrow m} &= \frac{\pi}{3\varepsilon_0 \hbar^2} |M_{mn}|^2 \\ A_{m\rightarrow n} &= \frac{\omega_{mn}^3}{3\pi\varepsilon_0 \hbar c^3} |M_{mn}|^2 \end{aligned} \tag{25}$$

2.1.2.4 *Intensity of light emission and absorption*

The intensity of light is generally defined as the energy transmitted per second through a unit area perpendicular to the direction of light. The spontaneous emission intensity of an atom is proportional to the energy of the emitted photon, multiplied by the transition probability per second given by Eq. 25.

$$I(\omega_{mn}) \propto \hbar\omega_{mn} A_{m\rightarrow n} = \frac{\omega_{mn}^4}{3\pi\varepsilon_0 c^3} |M_{mn}|^2 \tag{26}$$

Likewise, the amount of light with intensity $I_0(\omega_{mn})$ to be absorbed by an atom per second is equal to the photon energy ω_{mn} multiplied by the absorption probability coefficient and the energy density I_0/c.

It is more convenient, however, to use a radiative lifetime and absorption cross-section to express the ability of an atom to make an optical transition than to use the amount of light energy absorbed or emitted by the transition.

The radiative lifetime τ_{mn} is defined as the inverse of the spontaneous emission probability $A_{m\rightarrow n}$.

$$\tau_{mn}{}^{-1} = A_{m\rightarrow n} \tag{27}$$

If there are several terminal states of the transition and the relaxation is controlled only by spontaneous emission processes, the decay rate of the emitting level is determined by the sum of the transition probabilities to all final states:

$$A_m = \sum_n A_{m\rightarrow n} \tag{28}$$

and the number of the excited atoms decreases exponentially, $\propto \exp(-t/\tau)$, with time a constant $\tau = A_m^{-1}$, called the natural lifetime. In general, however, the real lifetime of the excited state m is controlled not only by radiative processes, but also by nonradiative ones (see 2.7).

The absorption cross-section σ represents the probability of an atom to absorb a photon incident on a unit area. (If there are N absorptive atoms per unit volume, the absorption coefficient α in Eq. 10 is equal to σN. Therefore, since the intensity of the light with a photon per second per unit area is $I_0 = \ \ \omega_{mn}$ in Eq. 23, the absorption cross-section is given by:

$$\sigma_{nm} = \frac{\pi\omega_{mn}}{3\varepsilon_0 c\hbar}\left|M_{mn}\right|^2 \tag{29}$$

2.1.2.5 *Oscillator strength*

The oscillator strength of an optical center is often used in order to represent the strength of light absorption and emission of the center. It is defined by the following equation as a dimensionless quantity.

$$f_{mn} = \frac{2m_e\omega_{mn}}{\hbar e^2}\left|\left(M_{mn}\right)_z\right|^2 = \frac{2m_e\omega_{mn}}{3\hbar e^2}\left|M_{mn}\right|^2 \tag{30}$$

The third term of this equation is given by assuming that the transition is isotropic, as it is the case with Eq. 24.

The radiative lifetime and absorption cross-section are expressed by using the oscillator strength as:

$$\tau_{mn}^{-1} = A_{m\to n} = \frac{e^2\omega_{mn}^2}{2\pi\varepsilon_0 mc^3} f_{mn} \tag{31}$$

$$\sigma_{nm} = \frac{\pi e^2}{2\varepsilon_0 mc} f_{mn} \tag{32}$$

Now one can estimate the oscillator strength of a harmonic oscillator with the electric dipole moment $\boldsymbol{M} = -e\boldsymbol{r}$ in a quantum mechanical manner. The result is that only one electric dipole transition between the ground state ($n = 0$) and the first excited state ($m = 1$) is allowed, and the oscillator strength of this transition is $f_{10} = 1$. Therefore, the summation of all the oscillator strengths of the transition from the state $n = 0$ is also $\Sigma_m f_{m0} = 1$ ($m \neq 0$). This relation is true for any one electron system; for N-electron systems, the following f-sum rule should be satisfied; that is,

$$\sum_{m\neq n} f_{mn} = N \tag{33}$$

At the beginning of this section, the emission rate of a linear harmonic oscillator was classically obtained as A_0 in Eq. 18. Then, the total transition probability given by Eq. 32 with $f = 1$ in a quantum mechanical scheme coincides with the emission rate of the classical linear oscillator A_0, multiplied by a factor of 3, corresponding to the three degrees of freedom of the motion of the electron in the present system.

2.1.2.6 *Impurity atoms in crystals*

Since the electric field acting on an impurity atom or optical center in a crystal is different from that in vacuum due to the effect of the polarization of the surrounding atoms, and the light velocity is reduced to c/n (see Eq. 7), the radiative lifetime and the absorption cross-section are changed from those in vacuum. In a cubic crystal, for example, Eqs. 31 and 32 are changed, by the internal local field, to:

$$\tau_{mn}^{-1} = \frac{n\left(n^2+2\right)^2}{9} \cdot \frac{e^2\omega_{mn}^2}{2\pi\varepsilon_0 mc^3} f_{nm} \tag{34}$$

$$\sigma_{nm} = \frac{\left(n^2+2\right)^2}{9n} \cdot \frac{\pi e^2}{2\pi\varepsilon_0 mc} f_{nm} \tag{35}$$

2.1.2.7 *Forbidden transition*

In the case that the electric dipole moment of a transition M_{nm} of Eq. 25 becomes zero, the probability of the electric dipole (E1) transition in Eq. 25 and 26 is also zero. Since the electric dipole transition generally has the largest transition probability, this situation is usually expressed by the term forbidden transition. Since the electric dipole moment operator in the integral of Eq. 24 is an odd function (odd parity), the electric dipole moment is zero if the initial and final states of the transition have the same parity; that is, both of the wavefunctions of these states are either an even or odd function, and the transition is said to be parity forbidden. Likewise, since the electric dipole moment operator in the integral of Eq. 24 has no spin operator, transitions between initial and final states with different spin multiplicities are spin forbidden.

In Eq. 24 for the dipole moment, the effects of the higher-order perturbations are neglected. If the neglected terms are included, the transition moment is written as follows:

$$\left|M_{mn}\right|^2 = \left|(e\boldsymbol{r})_{mn}\right|^2 + \left|\left(\frac{e}{2mc}\boldsymbol{r}\times\boldsymbol{p}\right)_{mn}\right|^2 + \frac{3\pi\omega_{mn}^2}{40c^2}\left|(e\boldsymbol{r}\cdot\boldsymbol{r})_{mn}\right|^2 \tag{36}$$

where the first term on the right-hand side is the contribution of the electric dipole (E1) term previously given in Eq. 24; the second term, in which $\boldsymbol{p}$ denotes the momentum of an electron, is that of magnetic dipole (M1); and the third term is that of an electric quadrupole transition (E2). Provided that $(\boldsymbol{r})_{mn}$ is about the radius of a hydrogen atom (0.5 Å) and ω_{mn} is 10^{15} rad/s for visible light, radiative lifetimes estimated from Eq. 26 and 36 are ~10^{-8} s for E1, ~10^{-3} s for M1, and ~10^{-1} s for E2.

E1-transitions are forbidden (parity forbidden) for *f-f* and *d-d* transitions of free rare-earth ions and transition-metal ions because the electron configurations, and hence the parities of the initial and final states, are the same. In crystals, however, the E1 transition is partially allowed by the odd component of the crystal field, and this partially allowed or forced E1 transition has the radiative lifetime of ~10^{-3} s. (See 3.2).

2.1.2.8 *Selection rule*

The selection rule governing whether a dipole transition is allowed between the states m and n is determined by the transition matrix elements $(e\boldsymbol{r})_{mn}$ and $(\boldsymbol{r} \times p)_{mn}$ in Eq. 36. However, a group theoretical inspection of the symmetries of the wavefunctions of these states and the operators $e\boldsymbol{r}$ and $\boldsymbol{r}\times p$ enables the determination of the selection rules without calculating the matrix elements.

When an atom is free or in a spherical symmetry field, its electronic states are denoted by a set of the quantum numbers S, L, and J in the LS-coupling scheme. Here, S, L, and J denote the quantum number of the spin, orbital, and total angular momentum, respectively, and ΔS, for example, denotes the difference in S between the states *m* and *n*. Then the selection rules for E1 and M1 transitions in the LS-coupling scheme are given by:

$$\Delta S = 0, \quad \Delta L = 0 \quad \text{or} \quad \pm 1 \tag{37}$$

$$\Delta J = 0 \quad \text{or} \quad \pm 1 \quad \left(J = 0 \rightarrow J = 0, \quad \text{not allowed}\right) \tag{38}$$

If the spin-orbit interaction is too large to use the **LS**-coupling scheme, the **JJ**-coupling scheme might be used, in which many (**S**, **L**)-terms are mixed into a **J**-state. In the **JJ**-coupling scheme, therefore, the ΔS and ΔL selection rules in Eqs. 37 ad 38 are less strict, and only the ΔJ selection rule applies.

While the E1 transitions between the states with the same parity are forbidden, as in the case of the *f*-*f* transitions of free rare-earth ions, they become partially allowed for ions in crystals due to the effects of crystal fields of odd parity. The selection rule for the partially allowed E1 *f*-*f* transition is $|\Delta J| \leq 6$ ($J = 0 - 0, 1, 3, 5$ are forbidden). M1 transitions are always parity allowed because of the even parity of the magnetic dipole operator $\boldsymbol{r} \times \boldsymbol{p}$ in Eq. 36.

chapter two — section two

Fundamentals of luminescence

Shigetoshi Nara and Sumiaki Ibuki

Contents

2.2 Electronic states and optical transition of solid crystals 21
  2.2.1 Outline of band theory 21
  2.2.2 Fundamental absorption, direct transition, and indirect transition 28
  2.2.3 Exciton 32
References 34

2.2 Electronic states and optical transition of solid crystals

2.2.1 Outline of band theory

First, a brief description of crystal properties is given. As is well known, a crystal consists of a periodic configuration of atoms, which is called a *crystal lattice*. There are many different kinds of crystal lattices and they are classified, in general, according to their symmetries, which specify invariant properties for translational and rotational operations. Figure 3 shows a few, typical examples of crystal structures, i.e., a rock-salt (belonging to one of the cubic groups) structure, a zinc-blende (also a cubic group) structure, and a wurtzeite (a hexagonal group) structure, respectively.

Second, consider the electronic states in these crystals. In an isolated state, each atom has electrons that exist in discrete electronic energy levels, and the states of these bound electrons are characterized by atomic wavefunctions. Their discrete energy levels, however, will have finite spectral width in the condensed state because of the overlaps between electronic wavefunctions belonging to different atoms. This is because electrons can become itinerant between atoms, until finally they fall into delocalized electronic states called *electronic energy bands*, which also obey the symmetries of crystals. In these energy bands, the states with lower energies are occupied by electrons originating from bound electrons of atoms and are called *valence bands*. The energy bands having higher energies are not occupied by electrons and are called *conduction bands*. Usually, in materials having crystal symmetries such as rock-salt, zinc-blende, or wurtzeite structures, there is no electronic state between the top of the valence band (the highest state of occupied bands) and the bottom of the conduction band (the lowest state of unoccupied bands); this region is called the *bandgap*. The reason why unoccupied states are called

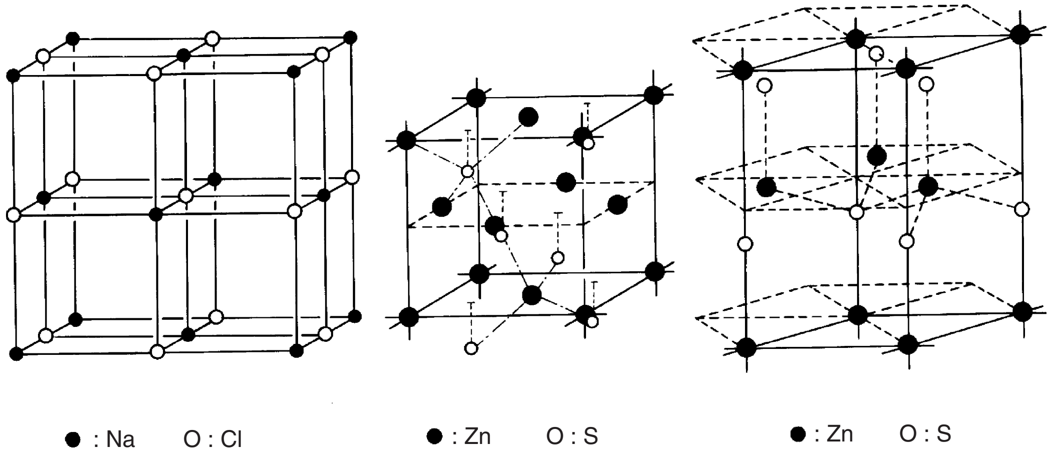

Figure 3 The configuration of the atoms in three important kinds of crystal structures. (a) rock-salt type, (b) zinc-blende type, and (c) wurtzeite type, respectively.

conduction bands is due to the fact that an electron in a conduction band is almost freely mobile if it is excited from a valence band by some method: for example, by absorption of light quanta. In contrast, electrons in valence bands cannot be mobile because of a fundamental property of electrons; as *fermions*, only two electrons (spin up and down) can occupy an electronic state. Thus, it is necessary for electrons in the valence band to have empty states in order for them to move freely when an electric field is applied. After an electron is excited to the conduction band, a hole that remains in the valence band behaves as if it were a mobile particle with a positive charge. This hypothetical particle is called a *positive hole*. The schematic description of these excitations are shown in Figure 4. As noted above, bandgaps are strongly related to the optical properties and the electric conductivity of crystals.

A method to evaluate these electronic band structures in a quantitative way using quantum mechanics is briefly described. The motion of electrons under the influence of electric fields generated by atoms that take some definite space configuration specified by the symmetry of the crystal lattice, can be described by the following Schrödinger equation.

$$-\frac{\hbar^2}{2m}\nabla^2\psi(\mathbf{r}) + V(\mathbf{r})\psi(\mathbf{r}) = E\psi(\mathbf{r}) \tag{39}$$

where $V(\mathbf{r})$ is an effective potential applied to each electron and has the property of:

$$V(\mathbf{r}+\mathbf{R}_n) = V(\mathbf{r}) \tag{40}$$

due to the translational symmetry of a given crystal lattice. $\mathbf{R}_n$ is a lattice vector indicating the n^{th} position of atoms in the lattice. In the Fourier representation, the potential $V(\mathbf{r})$ can be written as:

$$V(\mathbf{r}) = \sum_n V_n e^{iG_n\cdot\mathbf{r}} \tag{41}$$

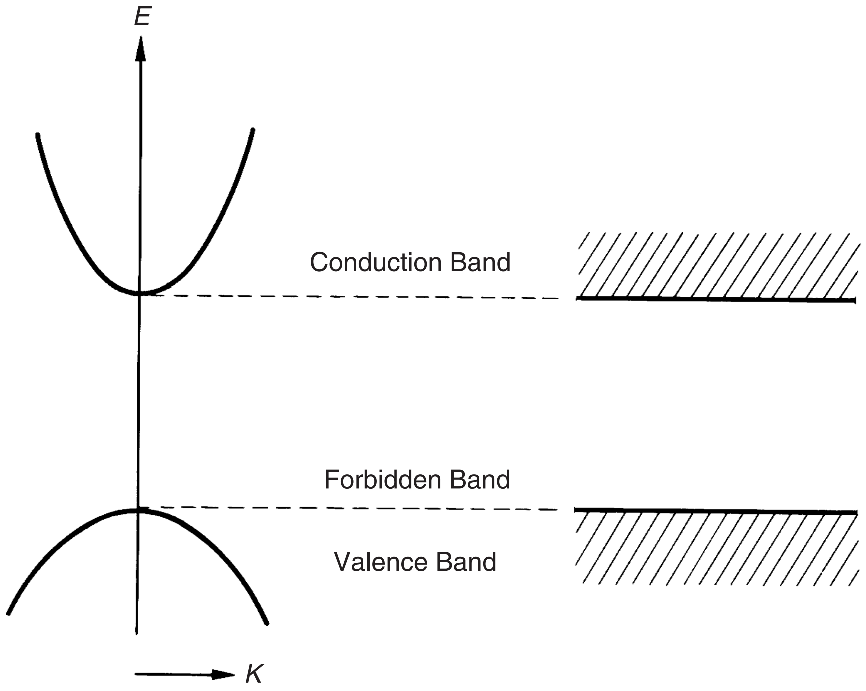

Figure 4 The typical band dispersion near the minimum band gap in a semiconductor or an insulator with a direct bandgap in the Brillouin zone.

where $\mathbf{G}_n$ is a reciprocal lattice vector. (See any elementary book of solid-state physics for the definition of $\mathbf{G}_n$)

It is difficult to solve Eq. 39 in general, but with the help of the translational and rotational symmetries inherent in the equation, it is possible to predict a general functional form of solutions. The solution was first found by Bloch and is called *Bloch's theorem*. The solution $\psi(\mathbf{r})$ should be of the form:

$$\psi(\mathbf{r}) = e^{i\mathbf{k}\cdot\mathbf{r}} u_{\mathbf{k}}(\mathbf{r}) \tag{42}$$

and is called a *Bloch function*. $\mathbf{k}$ is the wave vector and $u_{\mathbf{k}}(\mathbf{r})$ is the periodic function of lattice translations, such as:

$$u_{\mathbf{k}}(\mathbf{r} + \mathbf{R}_n) = u_{\mathbf{k}}(\mathbf{r}) \tag{43}$$

As one can see in Eq. 40, $u_{\mathbf{k}}(\mathbf{r})$ can also be expanded in a Fourier series as:

$$u_{\mathbf{k}}(\mathbf{r}) = \sum_n C_n(\mathbf{k}) e^{iG_n\cdot\mathbf{r}} \tag{44}$$

where $C_n(\mathbf{k})$ is a Fourier coefficient. The form of the solution represented by Eq. 42 shows that the wave vectors $\mathbf{k}$ are well-defined quantum numbers of the electronic states in a given crystal. Putting Eq. 44 into Eq. 42 and using Eq. 41, one can rewrite Eq. 39 in the following form:

$$\left\{\frac{\hbar^2}{2m}\left(\mathbf{k}+\mathbf{G}_l\right)^2 - E\right\}C_l + \sum_n C_n V_{l-n} = 0 \tag{45}$$

where E eigenvalues determined by:

$$\left|\left\{\frac{\hbar^2}{2m}\left(\mathbf{k}+\mathbf{G}_l\right)^2 - E\right\}\delta_{\mathbf{G}_l\mathbf{G}_n} + V_{\mathbf{G}_l-\mathbf{G}_n}\right| = 0 \tag{46}$$

Henceforth, the **k**-dependence of the Fourier components $C_n(\mathbf{k})$ are neglected. These formulas are in the form of infinite dimensional determinant equations. For finite dimensions by considering amplitudes of $V_{G_l-G_n}$ in a given crystal, one can solve Eq. 46 approximately. Then the energy eigenvalues $E(\mathbf{k})$ (energy band) may be obtained as a function of wave vector **k** and the Fourier coefficients C_n.

In order to obtain qualitative interpretation of energy band and properties of a wavefunction, one can start with the 0th order approximation of Eq. 46 by taking

$$C_0 = 1, \qquad C_n = 0 \quad (n \neq 0) \tag{47}$$

in Eq. 44 or 45; this is equivalent to taking $V_n = 0$ for all n (a vanishing or constant crystal potential model). Then, Eq. 46 gives:

$$E = \frac{\hbar^2}{2m}\mathbf{k}^2 = E_0(\mathbf{k}) \tag{48}$$

This corresponds to the free electron model.

As the next approximation, consider the case that the nonvanishing components of V_n are only for n = 0, 1. Eq. 46 becomes:

$$\begin{vmatrix} \frac{\hbar^2}{2m}\mathbf{k}^2 - E & V_{G_1} \\ V_{-G_1} & \frac{\hbar^2}{2m}\left(\mathbf{k}+\mathbf{G}_1\right)^2 - E \end{vmatrix} = 0 \tag{49}$$

This means that, in **k**-space, the two free electrons having $E(\mathbf{k})$ and $E(\mathbf{k} + \mathbf{G})$ are in independent states in the absence of the *crystal potential* even when $\|\mathbf{k}\| = \|\mathbf{k}+\mathbf{G}\|$; this energy degeneracy is lifted under the existence of nonvanishing $V_{\mathbf{G}}$. In the above case, the eigenvalue equation can be solved easily and the solution gives

$$E = \frac{1}{2}\left\{E(\mathbf{k}) + E(\mathbf{k}+\mathbf{G})\right\} \pm \sqrt{\left\{\frac{E(\mathbf{k}) - E(\mathbf{k}+\mathbf{G})}{2}\right\}^2 + V_{\mathbf{G}}^2} \tag{50}$$

Figure 5 shows the global profile of E as a function of **k** in one dimension. One can see the existence of energy gap at the wave vector that satisfies:

$$\mathbf{k}^2 = \left(\mathbf{k}+\mathbf{G}_1\right)^2 \tag{51}$$

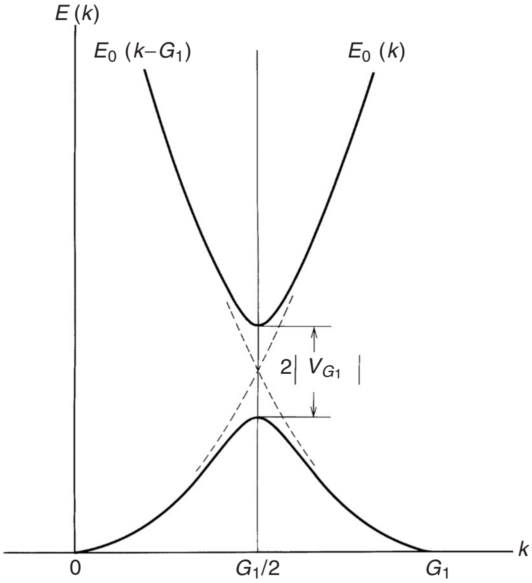

Figure 5 The emergence of a bandgap resulting from the interference between two plane waves satisfying the Bragg condition, in a one-dimensional model.

This is called the *Bragg condition*. In the three-dimensional case, the wave vectors that satisfy Eq. 51 form closed polyhedrons in **k** space and are called the 1st, 2nd, or 3rd, …, *n*th Brillouin zone.

As stated so far, the electronic energy band structure is determined by the symmetry and Fourier amplitudes of the crystal potential $V(\mathbf{r})$. Thus, one needs to take a more realistic model of them to get a more accurate description of the electronic properties. There are now many procedures that allow for the calculation of the energy band and to get the wavefunction of electrons in crystals. Two representative methods, the *Pseudopotential method* and the *LCAO method* (Linar Combination of Atomic Orbital Method), which are frequently applied to outer-shell valence electrons in semiconductors, are briefly introduced here.

First, consider the pseudopotential method. Eq. 46 is the fundamental equation to get band structures of electrons in crystals, but the size of the determinant equation will become very large if one wishes to solve the equation with sufficient accuracy, because, in general, the Fourier components $V_{\mathbf{G}_n}$ do not decrease slowly due to the Coulomb potential of each atom. This corresponds to the fact that the wave functions of valence electrons are free-electron like (plane-wave like) in the intermediate region between atoms and give rapid oscillations (atomic like) near the ion cores.

Therefore, to avoid this difficulty, one can take an effective potential in which the Coulomb potential is canceled by the rapid oscillations of wavefunctions. The rapid oscillation of wavefunctions originates from the orthogonalization between atomic-like properties of wavefunctions near ion cores. It means that one introduces new wavefunctions and a weak effective potential instead of plane waves and a Coulombic potential to represent the electronic states. This effective potential gives a small number of reciprocal wave vectors (**G**) that can reproduce band structures with a corresponding small number of Fourier components. This potential is called the *pseudopotential*. The pseudopotential method necessarily results in some arbitrariness with respect to the choice of these effective potentials, depending on the selection of effective wavefunctions. It is even possible to parametrize a small number of components in $V_{\mathbf{G}_n}$ and to determine them empirically.

For example, taking several $V_{\mathbf{G}_n}$ values in high symmetry points in the Brillouin zone and, after adjusting them so as to reproduce the bandgaps obtained with experimental measurements, one calculates the band dispersion $E(\mathbf{k})$ over the entire region.

In contrast, the LCAO method approximates the Bloch states of valence electrons by using a linear combination of bound atomic wavefunctions. For example,

$$\psi_k(\mathbf{r}) = \sum_n e^{i\mathbf{k}\cdot\mathbf{R}_n}\phi(\mathbf{r}-\mathbf{R}_n) \tag{52}$$

satisfies the Bloch condition stated in Eq. 42, where $\phi(\mathbf{r})$ is one of the bound atomic wavefunctions. In order to show a simple example, assume a one-dimensional crystal consisting of atoms having one electron per atom bound in the *s*-orbital. The Hamiltonian of this crystal can be written as:

$$H = -\frac{\hbar^2}{2m}\nabla^2 + V(\mathbf{r}) = H_0 + \delta V(\mathbf{r}) \tag{53}$$

where H_0 is the Hamiltonian of each free atom, and $\delta V(\mathbf{r})$ is the term that represents the effect of periodic potential in the crystal. Using Eq. 53 and the wavefunctions expressed in Eq. 52, the expectation value obtained by multiplying with $\phi^*(\mathbf{r})$ yields:

$$E(\mathbf{k}) = E_0 + \frac{E_1 + \Sigma_{n\neq 0} e^{i\mathbf{k}\cdot\mathbf{R}_n} S_1(\mathbf{R}_n)}{1 + \Sigma_{n\neq 0} e^{i\mathbf{k}\cdot\mathbf{R}_n} S_0(\mathbf{R}_n)} \tag{54}$$

where E_0 is the energy level of *s*-orbital satisfying $H_0\phi(\mathbf{r}) = E_0\phi(\mathbf{r})$, and E_1 is the energy shift of E_0 due to δV given by $\int\phi^*(\mathbf{r})\delta \mathrm{V}(\mathbf{r})\phi(\mathbf{r})d\mathbf{r}$. $S_0(\mathbf{R}_n)$ is called the overlap integral and is defined by:

$$S_0(\mathbf{R}_n) = \int \phi^*(\mathbf{r})\phi(\mathbf{r}-\mathbf{R}_n)d\mathbf{r} \tag{55}$$

Similarly, $S_1(\mathbf{R}_n)$ is defined as:

$$S_1(\mathbf{R}_n) = \int \phi^*(\mathbf{r})\delta V(\mathbf{r})\phi(\mathbf{r}-\mathbf{R}_n)d\mathbf{r} \tag{56}$$

Typically speaking, these quantities are regarded as parameters, and they are fitted so as to best reproduce experimentally observed results. As a matter of fact, other orbitals such as *p*-, *d*-orbitals etc. can also be used in LCAO. It is even possible to combine this method with that of pseudopotentials. As an example, Figure 6 reveals two band structure calculations due to Chadi[1]; one is for Si and the other is for GaAs.

In Figure 6, energy = 0 in the ordinate corresponds to the top of the valence band. In both Si and GaAs, it is located at the Γ point (**k** = (000) point). The bottom of the conduction band is also located at the Γ point in GaAs, while in Si it is located near the X point (**k** = (100) point).

It is difficult and rare that the energy bands can be calculated accurately all through the Brillouin zone with use of a small number of parameters determined at high symmetry points. In that sense, it is quite convenient if one has a simple perturbational method to

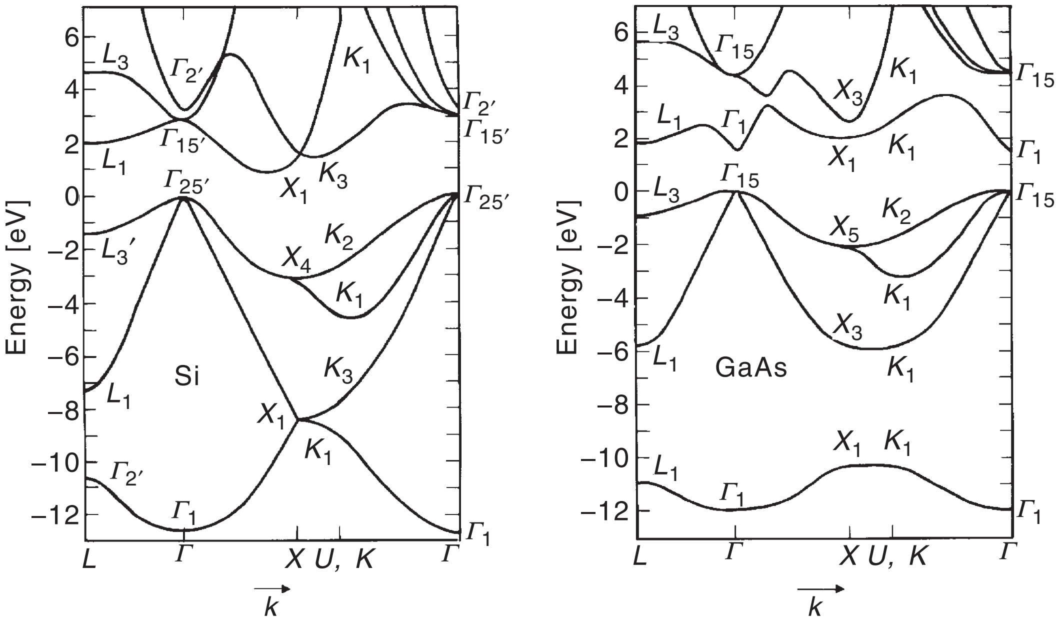

Figure 6 Calculated band structures of (a) Si and (b) GaAs using a combined pseudopotential and LCAO method. (From Chadi, D.J., Phys. Rev., B16, 3572, 1977. With permission.)

calculate band structures approximately at or near specific points in the Brillouin zone (e.g., the top of the valence band or a conduction band minimum). In particular, such procedures are quite useful when the bands are degenerate at some point in the Brillouin zone of interest.

Now, assume that the Bloch function is known at $\mathbf{k} = \mathbf{k}_0$ and is expressed as $\psi_{n\mathbf{k}_0}(\mathbf{r})$. Define a new wavefunction as:

$$\eta_{n\mathbf{k}}(\mathbf{r}) = e^{i\mathbf{k}\cdot\mathbf{r}}\psi_{n\mathbf{k}_0}(\mathbf{r}) \tag{57}$$

and expand the Bloch function in terms of $\eta_{n\mathbf{k}}(\mathbf{r})$ as:

$$\zeta_{n\mathbf{k}} = \sum_{n'} C_{n'}\eta_{n'\mathbf{k}}(\mathbf{r}) \tag{58}$$

Introducing these wavefunctions into Eq. 39 obtains the energy dispersion $E(\mathbf{k}_0 + \mathbf{k})$ in the vicinity of $\mathbf{k}_0$. In particular, near the high symmetry points of the Brillouin zone, the energy dispersion takes the following form:

$$E_n(\mathbf{k}_0 + \mathbf{k}) = E_n(\mathbf{k}_0) + \sum_{ij} \frac{\hbar^2}{2}\left(\frac{1}{m^*}\right)_{ij} k_i k_j \tag{59}$$

where $(1/m^*)_{ij}$ is called the *effective mass tensor.* From Eq. 59, the effective mass tensor is given as:

$$\left(\frac{1}{m^*}\right)_{ij} = \frac{1}{\hbar^2} \cdot \frac{\partial^2 E}{\partial k_i \partial k_j} \qquad (i, j = x,\ y,\ z) \tag{60}$$

For the isotropic case, Eq. 60 gives the scalar effective mass m^* as:

$$\frac{1}{m^*} = \frac{1}{\hbar^2} \cdot \frac{d^2 E}{dk^2} \tag{61}$$

Eq. 61 indicates that m^* is proportional to the inverse of curvature near the extremal points of the dispersion relation, E vs. $\mathbf{k}$. Furthermore, Figure 5 illustrates the two typical cases that occur near the bandgap, that is, a positive effective mass at the bottom of the conduction band and a negative effective mass at the top of the valence band, depending on the sign of $\mathrm{d}^2E/\mathrm{d}k^2$ at each extremal point. Hence, under an applied electric field $\mathbf{E}$, the specific charge e/m^* of an electron becomes negative, while it becomes positive for a hole. This is the reason why a hole looks like a particle with a positive charge.

In the actual calculation of physical properties, the following quantity is also important:

$$N(E)dE = \frac{1}{3\pi\hbar^2}\left(2m^*\right)^{3/2} E^{1/2} dE \tag{62}$$

This is called the *density of states* and represents the number of states between E and $E + dE$. We assume in Eq. 62 that space is isotropic and m^* can be used.

The band structures of semiconductors have been intensively investigated experimentally using optical absorption and/or reflection spectra. As shown in Figure 7, in many compound semiconductors (most of III-V and II-VI combination in the periodic table), conduction bands consist mainly of *s*-orbitals of the cation, and valence bands consist principally of *p*-orbitals of the anion. Many compound semiconductors have a direct bandgap, which means that the conduction band minimum and the valence band maximum are both at the Γ point ($\mathbf{k} = 0$). It should be noted that the states just near the maximum of the valence band in zinc-blende type semiconductors consist of two orbitals, namely Γ_8 which is twofold degenerate and Γ_7 without degeneracy; these originate from the *spin-orbit interaction*. It is known that the twofold degeneracy of Γ_8 is lifted in the $\mathbf{k} \neq 0$ region corresponding to a light and a heavy hole, respectively. On the other hand, in wurzite-type crystals, the valence band top is split by both the spin-orbit interaction and the crystalline field effect; the band maximum then consists of three orbitals: Γ_9, Γ_9, and Γ_7 without degeneracy. In GaP, the conduction band minimum is at the X point ($\mathbf{k}$ = [100]), and this compound has an indirect bandgap, as described in the next section.

2.2.2 Fundamental absorption, direct transition, and indirect transition

When solid crystals are irradiated by light, various optical phenomena occur: for example, transmission, reflection, and absorption. In particular, absorption is the annihilation of light (photon) resulting from the creation of an electronic excitation or lattice excitation in crystals. Once electrons obtain energy from light, the electrons are excited to higher states. In such quantum mechanical phenomena, one can only calculate the probability of excitation. The probability depends on the distribution of microscopic energy levels of

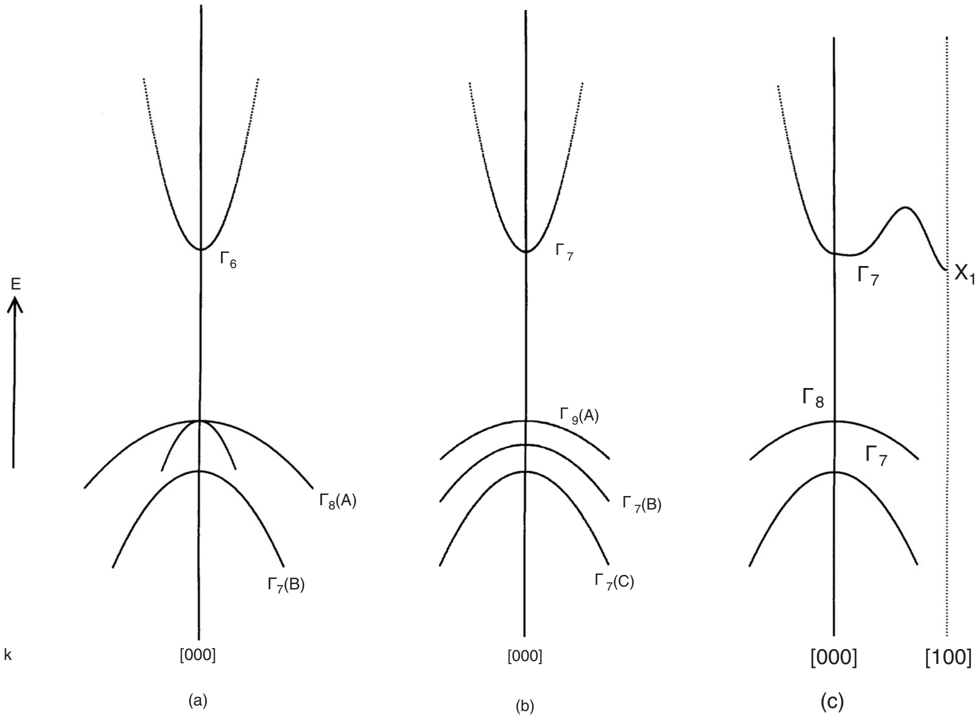

Figure 7 The typical band dispersion near Γ-point (**k** = 0) for II-VI or III-V semiconductor compounds. (a) a direct type in zinc-blende structure; (b) a direct type in wurzeite structure; and (c) an indirect type in zinc-blende structure (GaP).

electrons in that system. The excited electrons will come back to their initial states after they release the excitation energy in the form of light emission or through lattice vibrations.

Absorption of light by electrons from valence bands to conduction bands results in the fundamental absorption of the crystal. Crystals are transparent when the energy of the incident light is below the energy gaps of crystals; excitation of electrons to the conduction band becomes possible at a light energy equal to, or larger than the bandgap. The intensity of absorption can be calculated using the absorption coefficient $\alpha(h\nu)$ given by the following formula:

$$\alpha(h\nu) = A\sum p_{if} n_i n_f \tag{63}$$

where n_i and n_f are the number density of electronic states in an initial state (occupied by electron) and in a final state (unoccupied by electron), respectively, and p_{if} is the transition probability between them.

In the calculation of Eq. 63, quantum mechanics requires that two conditions are satisfied. The first is *energy conservation* and the second is *momentum conservation*. The former means that the energy difference between the initial state and the final state should be equal to the energy of the incident photon, and the latter means that the momentum difference between the two states should be equal to the momentum of the incident light. It is quite important to note that the momentum of light is three or four orders of magnitude smaller than that of the electrons. These conditions can be written as $(\hbar^2/2m^*)k_f^2 = (\hbar^2/2m^*)k_i^2 + h\nu$ (energy conservation); $\hbar k_f = \hbar(k_i + q)$ (momentum

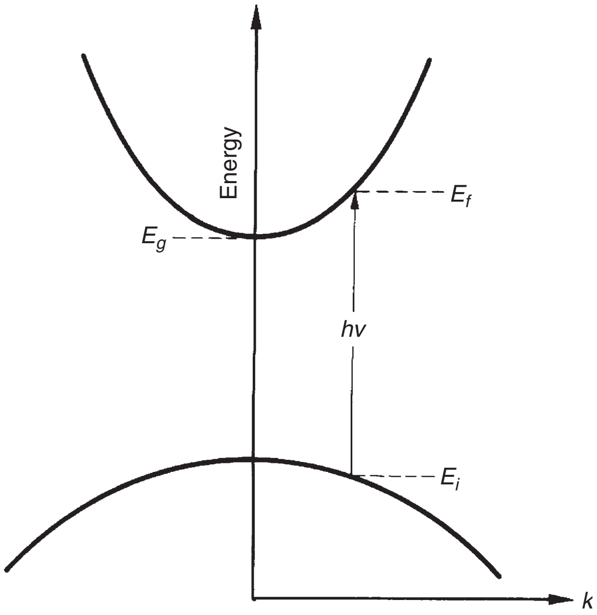

Figure 8 The optical absorption due to a direct transition from a valence band state to a conduction band state.

conservation); and $\nu = cq$ if one assumes a free-electron-like dispersion for band structure $E(\mathbf{k})$, where k_f and k_i are the final and initial wave vectors, respectively, c is the light velocity, and q is the photon momentum. One can neglect the momentum of absorbed photons compared to those of electrons or lattice vibrations. It results in optical transitions occurring almost vertically on the energy dispersion curve in the Brillouin zone. This rule is called the *momentum selection rule* or **k**-*selection rule*.

As shown in Figure 8, consider first the case that the minimum bandgap occurs at the top of valence band and at the bottom of conduction band; in such a case, the electrons of the valence band are excited to the conduction band with the same momentum. This case is called a *direct transition*, and the materials having this type of band structure are called *direct gap materials*. The absorption coefficient, Eq. 63, is written as:

$$\alpha(h\nu) = A^*\left(h\nu - E_g\right)^{1/2} \tag{64}$$

with the use of Eqs. 63 and 64. A^* is a constant related to the effective masses of electrons and holes. Thus, one can experimentally measure the bandgap E_g, because the absorption coefficient increases steeply from the edge of the bandgap. In actual measurements, the absorption increases exponentially because of the existence of impurities near E_g. In some materials, it can occur that the transition at $\mathbf{k} = 0$ is forbidden by some selection rule; the transition probability is then proportional to $(h\nu - E_g)$ in the $\mathbf{k} \neq 0$ region and the absorption coefficient becomes:

$$\alpha(h\nu) = A'\left(h\nu - E_g\right)^{3/2} \tag{65}$$

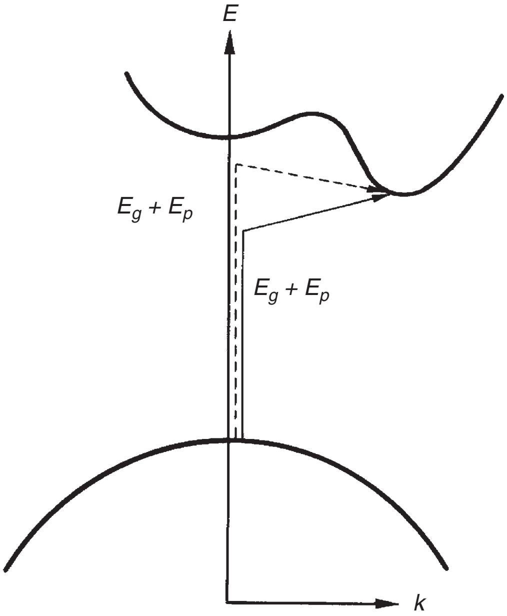

Figure 9 The optical absorption due to an indirect transition from a valence band state to a conduction band state. The momentum of electron changes due to a simultaneous absorption or emission of a phonon.

In contrast to the direct transition, in the case shown in Figure 9, both the energy and the momentum of electrons are changed in the process; excitation of this type is called an *indirect transition*. This transition corresponds to cases in which the minimum bandgap occurs between two states with different **k**-values in the Brillouin zone. In this case, conservation of momentum cannot be provided by the *photon*, and the transition necessarily must be associated with the excitation or absorption of *phonons* (lattice vibrations). This leads to a decrease in transition probability due to a higher-order stochastic process. The materials having such band structure are called *indirect gap materials*. An expression for the absorption coefficient accompanied by *phonon absorption* is:

$$\alpha(h\nu) = A\left(h\nu - E_g + E_p\right)^2 \left(\exp\left(\frac{E_p}{k_B T}\right) - 1\right)^{-1} \tag{66}$$

while the coefficient accompanied by *phonon emission* is:

$$\alpha(h\nu) = A\left(h\nu - E_g - E_p\right)^2 \left(1 - \exp\left(\frac{-E_p}{k_B T}\right)\right)^{-1} \tag{67}$$

where, in both formulas, E_p is the phonon energy.

In closing this section, the light emission process is briefly discussed. The intensity of light emission R can be written as:

$$R = B\sum p_{ul} n_u n_l \tag{68}$$

where n_u is the number density of electrons existing in upper energy states and n_l is the number density of *empty states* with lower energy. The large difference from absorption is in the fact that, usually speaking, at a given temperature electrons are found only in the vicinity of conduction band minimum and light emission is observed only from these electrons. Then, Eq. 68 can be written as:

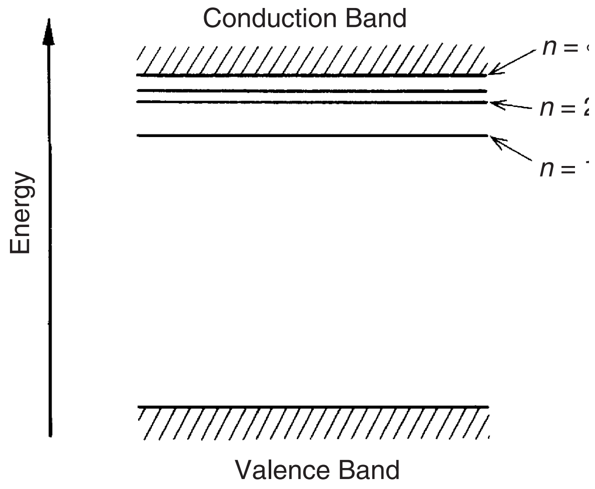

Figure 10 Energy levels of a free exciton.

$$L = B'\left(h\nu - E_g + E_p\right)^{1/2} \exp\left(-\frac{h\nu - E_g}{k_B T}\right) \tag{69}$$

confirming that emission is only observed in the vicinity of E_g. In the case of indirect transitions, light emission occurs from electronic transitions accompanied by phonon emission (cold band); light emission at higher energy corresponding to phonon absorption (hot band) has a relatively small probability since it requires the presence of thermal phonons. Hot-band emission vanishes completely at low temperatures.

2.2.3 Exciton

Although all electrons in crystals are specified by the energy band states they occupy, a characteristic excited state called the *exciton*, which is not derived from the band theory, exists in almost all semiconductors or ionic crystals. Consider the case where one electron is excited in the conduction band and a hole is left in the valence band. An attractive Coulomb potential exists between them and can result in a bound state analogous to a hydrogen atom. This configuration is called an *exciton*. The binding energy of an exciton is calculated, by analogy, to a hydrogen atom as:

$$G_{ex} = -\frac{m_r^* e^4}{32\pi^2 \hbar^2 \epsilon^2} \cdot \frac{1}{n^2} \tag{70}$$

where n (= 1, 2, 3, …) is a quantum number specifying the states, ϵ is the dielectric constant of crystals, and m_r^* is the reduced mass of an exciton.

An exciton can move freely through the crystal. The energy levels of the free exciton are shown in Figure 10. The state corresponding to the limit of $n \to \infty$ is the minimum of the conduction band, as shown in the figure. The energy of the lowest exciton state obtained by putting $n = 1$ is:

$$E_{ex}(n=1) = E_g - |G_{ex}| \tag{71}$$

Two or three kinds of excitons can be generated, depending on the splitting of the valence band, as was shown in Figure 7. They are named, from the top of the valence band, as A- and B-excitons in zinc-blende type crystals; and A, B, and C-excitons in wurzite-type crystals. There are two kinds of A-excitons in zinc-blende materials originating from the existence of a light and heavy hole, as has already been noted.

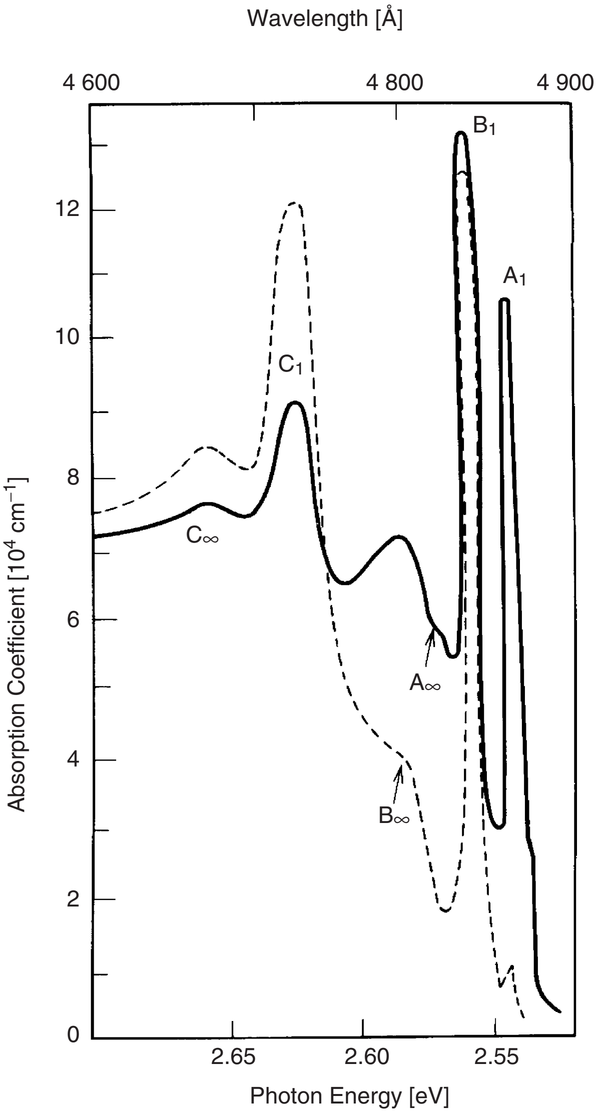

Figure 11 The exciton absorption spectrum of CdS (at 77K). The solid line and the broken line correspond to the cases that the polarization vector of incident light are parallel and perpendicular to the *c*-axis of the crystal, respectively. (From Mitsuhashi, H. and Fujishiro, Y., personal communication. With permission.)

Excitons create several sharp absorption lines in the energy region just below E_g. Figure 11 shows the absorption spectra of excitons in CdS.[2] One can easily recognize the absorption peaks due to A-, B-, and C-excitons with $n = 1$, and the beginning of the inter-band absorption transition corresponding to $n \rightarrow \infty$ (E_g). The order of magnitude of absorption coefficient reaches 10^5 cm^{-1} beyond E_g, as seen from the figure. As noted previously, the absorption coefficient in the neighborhood of E_g in a material with indirect transition, like GaP, is three to four orders of magnitude smaller than the case of direct transition.

An exciton in the $n = 1$ state of a direct-gap material can be annihilated by the recombination of the electron-hole pair; this produces a sharp emission line. The emission from the states corresponding to the larger n states is usually very weak because such states relax rapidly to the $n = 1$ state and emission generally occurs from there.

With intense excitation, excitons of very high concentrations can be produced; excitonic molecules (also called biexcitons) analogous to hydrogen molecules are formed from two single excitons by means of covalent binding. The exciton concentration necessary for the formation of excitonic molecules is usually of the order of magnitude of about 10^{16} cm^{-3}. The energy of the excitonic molecule is given by:

$$E_m = 2E_{ex} - G_m \tag{72}$$

where G_m is the binding energy of the molecule. The ratio of G_m to G_{ex} depends on the ratio of electron effective mass to hole effective mass, and lies in the range of 0.03 to 0.3. An excitonic molecule emits a photon of energy $E_{ex} - G_m$, leaving a single exciton behind.

If the exciton concentration is further increased by more intense excitation, the exciton system undergoes the insulator-metal transition, the so-called Mott transition, because the Coulomb force between the electron and hole in an exciton is screened by other electrons and holes. This results in the appearance of the high-density electron-hole plasma state. This state emits light with broad-band spectra.

References

1. Chadi, D.J., *Phys. Rev.*, B16, 3572, 1977.
2. Mitsuhashi, H. and Fujishiro, Y., unpublished data.

chapter two — section three

Fundamentals of luminescence

Hajime Yamamoto

Contents

2.3 Luminescence of a localized center....35
  2.3.1 Classification of localized centers....35
  2.3.2 Configurational coordinate model....36
    2.3.2.1 Description by a classical model....36
    2.3.2.2 Quantum mechanical description....38
  2.3.3 Spectral shapes....40
    2.3.3.1 Line broadening by time-dependent perturbation....44
    2.3.3.2 Line broadening by time-independent perturbation....46
  2.3.4 Nonradiative transitions....46
References....47

2.3 *Luminescence of a localized center*

2.3.1 *Classification of localized centers*

When considering optical absorption or emission within a single ion or a group of ions in a solid, it is appropriate to treat an optical transition with a localized model rather than the band model described in Section 2.2. Actually, most phosphors have localized luminescent centers and contain a far larger variety of ions than delocalized centers. The principal localized centers can be classified by their electronic transitions as follows (below, an arrow to the right indicates optical absorption and to the left, emission):

1. $1s \rightleftharpoons 2p$; an example is an F center.
2. $ns^2 \rightleftharpoons nsnp$. This group includes Tl^+-type ions; i.e., Ga^+, In^+, Tl^+, Ge^{2+}, Sn^{2+}, Pb^{2+}, Sb^{3+}, Bi^{3+}, Cu^-, Ag^-, Au^-, etc.
3. $3d^{10} \rightleftharpoons 3d^9 4s$. Examples are Ag^+, Cu^+, and Au^+. Acceptors in IIb-VIb compounds are not included in this group.
4. $3d^n \rightleftharpoons 3d^n$, $4d^n \rightleftharpoons 4d^n$. The first and second row transition-metal ions form this group.
5. $4f^n \rightleftharpoons 4f^n$, $5f^n \rightleftharpoons 5f^n$; rare-earth and actinide ions.

6. $4f^n \rightleftharpoons 4f^{n-1}5d$. Examples are Ce^{3+}, Pr^{3+}, Sm^{2+}, Eu^{2+}, Tm^{2+}, and Yb^{2+}. Only absorption transitions are observed for Tb^{3+}.
7. A charge-transfer transition or a transition between an anion p electron and an empty cation orbital. Examples are intramolecular transitions in complexes such as VO_4^{3-}, WO_4^{2-}, and MoO_4^{2-}. More specifically, typical examples are a transition from the $2p$ orbital of O^{2-} to the $3d$ orbital of V^{5+} in VO_4^{3-}, and transitions from $O^{2-}(2p)$ or $S^{2-}(3p)$ to $Yb^{3+}(4f)$. Transitions from anion p orbitals to Eu^{3+} or transition metal ions are observed only as absorption processes.
8. $\pi \rightleftharpoons \pi^*$ and $n \rightleftharpoons \pi^*$. Organic molecules having π electrons make up this group. The notation n indicates a nonbonding electron of a heteroatom in an organic molecule.

2.3.2 *Configurational coordinate model*[1–5]

2.3.2.1 *Description by a classical model*

The configurational coordinate model is often used to explain optical properties, particularly the effect of lattice vibrations, of a localized center. In this model, a luminescent ion and the ions at its nearest neighbor sites are selected for simplicity. In most cases, one can regard these ions as an isolated molecule by neglecting the effects of other distant ions. In this way, the huge number of actual vibrational modes of the lattice can be approximated by a small number or a combination of specific normal coordinates. These normal coordinates are called the *configurational coordinates*. The *configurational coordinate model* explains optical properties of a localized center on the basis of potential curves, each of which represents the total energy of the molecule in its ground or excited state as a function of the configurational coordinate (Figure 12). Here, the total energy means the sum of the electron energy and ion energy.

To understand how the configurational coordinate model is built, one is first reminded of the adiabatic potential of a diatomic molecule, in which the variable on the abscissa is simply the interatomic distance. In contrast, the adiabatic potential of a polyatomic molecule requires a multidimensional space, but it is approximated by a single configurational coordinate in the one-dimensional configurational coordinate model. In this model, the totally symmetric vibrational mode or the "breathing mode" is usually employed. Such a simple model can explain a number of facts qualitatively, such as:

1. Stokes' law; i.e., the fact that the energy of absorption is higher than that of emission in most cases. The energy difference between the two is called the Stokes' shift.
2. The widths of absorption or emission bands and their temperature dependence.
3. Thermal quenching of luminescence. It must be remarked, however, that the one-dimensional model gives only a qualitative explanation of thermal quenching. A quantitatively valid explanation can be obtained only by a multidimensional model.[6]

Following the path of the optical transition illustrated in Figure 12, presume that the bonding force between the luminescent ion and a nearest-neighbor ion is expressed by Hooke's law. The deviation from the equilibrium position of the ions is taken as the configurational coordinate denoted as Q. The total energy of the ground state, U_g, and that of the excited state, U_e, are given by the following relations.

$$U_g = K_g \frac{Q^2}{2} \tag{73a}$$

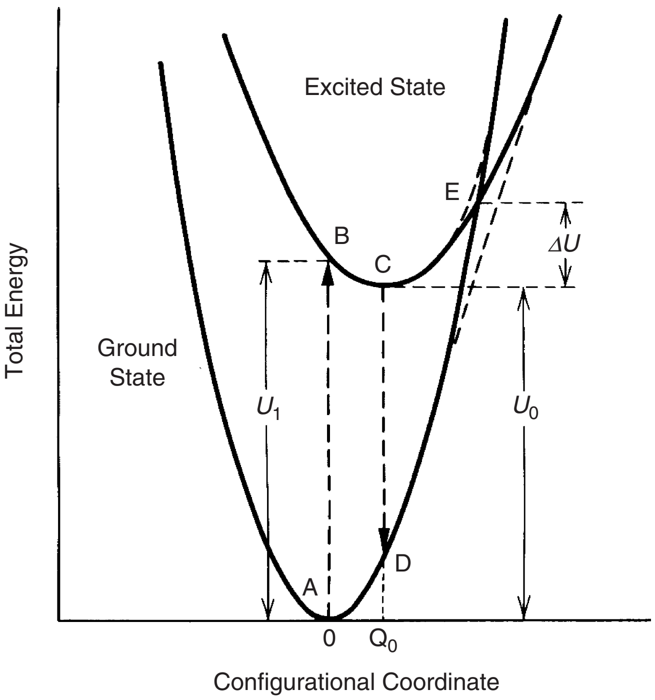

Figure 12 A schematic illustration of a configurational coordinate model. The two curves are modified by repulsion near the intersection (broken lines). The vertical broken lines A $\rightleftharpoons$ B and C $\rightleftharpoons$ D indicate the absorption and emission of light, respectively.

$$U_e = K_e \frac{(Q - Q_0)^2}{2} + U_0 \tag{73b}$$

where K_g and K_e are the force constants of the chemical bond, Q_0 is the interatomic distance at the equilibrium of the ground state, and U_0 is the total energy at $Q = Q_0$.

The spatial distribution of an electron orbital is different between the ground and excited states, giving rise to a difference in the electron wavefunction overlap with neighboring ions. This difference further induces a change in the equilibrium position and the force constant of the ground and excited states, and is the origin of the Stokes' shift. In the excited state, the orbital is more spread out, so that the energy of such an electron orbital depends less on the configuration coordinate; in other words, the potential curve has less curvature.

In Figure 12, optical absorption and emission processes are indicated by vertical broken arrows. As this illustration shows, the nucleus of an emitting ion stays approximately at the same position throughout the optical processes. This is called the Franck-Condon principle. This approximation is quite reasonable since an atomic nucleus is heavier than an electron by 10^3 to 10^5 times. At 0K, the optical absorption proceeds from the equilibrium position of the ground state, as indicated by the arrow A → B. The probability for an excited electron to lose energy by generating lattice vibration is 10^{12} to 10^{13} s^{-1}, while the probability for light emission is at most 10^9 s^{-1}. Consequently, state B relaxes to the equilibrium position C before it emits luminescence. This is followed by the emission process C → D and the relaxation process D → A, completing the cycle. At finite temperature, the electron state oscillates around the equilibrium position along the configurational coordinate curve up to the thermal energy of kT. The amplitude of this oscillation causes the spectral width of the absorption transition.

When two configurational coordinate curves intersect with each other as shown in Figure 12, an electron in the excited state can cross the intersection E assisted by thermal energy and can reach the ground state nonradiatively. In other words, one can assume a nonradiative relaxation process with the activation energy ΔU, and with the transition probability per unit time N given by:

$$N = s \exp \frac{-\Delta U}{kT} \tag{74}$$

where s is a product of the transition probability between the ground and excited states and a frequency, with which the excited state reaches the intersection E. This quantity s can be treated as a constant, since it is only weakly dependent on temperature. It is called the *frequency factor* and is typically of the order of 10^{13} s^{-1}.

By employing Eq. 74 and letting W be the luminescence probability, the luminescence efficiency η can be expressed as:

$$\eta = \frac{W}{W+N} = \left[1 + \frac{s}{W} \exp \frac{-\Delta U}{kT}\right]^{-1} \tag{75}$$

If the equilibrium position of the excited state C is located outside the configurational coordinate curve of the ground state, the excited state intersects the ground state in relaxing from B to C, leading to a nonradiative process.

It can be shown by quantum mechanics that the configurational coordinate curves can actually intersect each other only when the two states belong to different irreducible representations. Otherwise, the two curves behave in a repulsive way to each other, giving rise to an energy gap at the expected intersection of the potentials. It is, however, possible for either state to cross over with high probability, because the wavefunctions of the two states are admixed near the intersection. In contrast to the above case, the intersection of two configurational coordinate curves is generally allowed in a multidimensional model.

2.3.2.2 *Quantum mechanical description*

The classical description discussed above cannot satisfactorily explain observed phenomena, e.g., spectral shapes and nonradiative transition probabilities. It is thus necessary to discuss the configurational coordinate model based on quantum mechanics.

Suppose that the energy state of a localized center involved in luminescence processes is described by a wavefunction Ψ. It is a function of both electronic coordinates $\mathbf{r}$ and nuclear coordinates $\mathbf{R}$, but can be separated into the electronic part and the nuclear part by the *adiabatic approximation*:

$$\psi_{nk}(\mathbf{r},\mathbf{R}) = \psi_k(\mathbf{r},\mathbf{R})\chi_{nk}(\mathbf{R}) \tag{76}$$

where n and k are the quantum numbers indicating the energy states of the electron and the nucleus, respectively. For the nuclear wavefunction $\chi_{nk}(\mathbf{R})$, the time-independent Schrödinger equation can be written as follows:

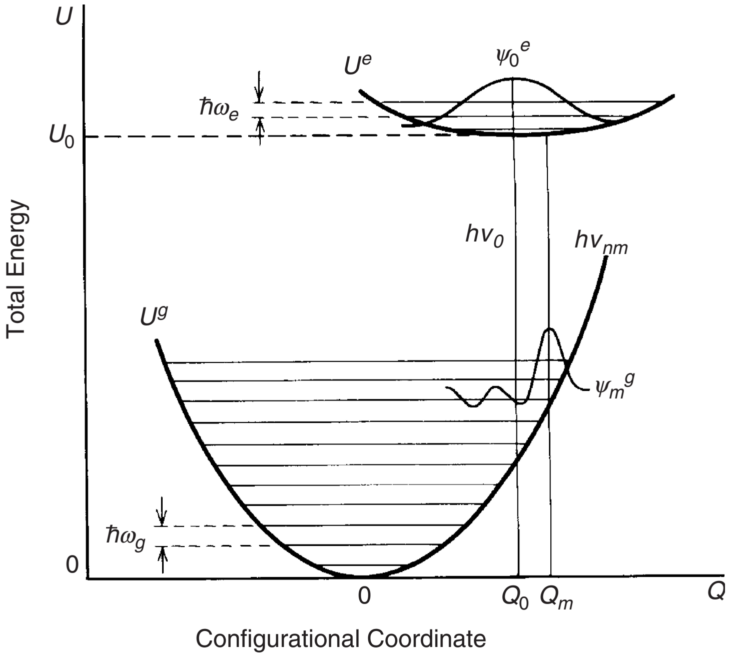

Figure 13 Discrete energy levels due to lattice vibration, each with the energy of $\hbar\omega$ and the wavefunctions ψ_0^e and ψ_m^g of harmonic oscillators representing the two states. The notation ν_0 means the frequency at the emission peak. A luminescent transition can occur at ν_{nm}.

$$\left\{-\sum_{\alpha}\left(\hbar^2/2M_\alpha\right)\Delta\mathbf{R}_\alpha + U_k(\mathbf{R})\right\}\chi_{nk}(\mathbf{R}) = E_{nk}\chi_{nk}(\mathbf{R}) \tag{77}$$

with α being the nuclear number, M_α the mass of the α^{th} nucleus, $\Delta\mathbf{R}_\alpha$ the Laplacian of $\mathbf{R}_\alpha$, and E_{nk} the total energy of the localized center. The energy term $U_{\text{k}}(\mathbf{R})$ is composed of two parts: the energy of the electrons and the energy of the electrostatic interaction between the nuclei around the localized center. Considering Eq. 77, one finds that $U_{\text{k}}(\mathbf{R})$ plays the role of the potential energy of the nuclear wavefunction χ_{nk}. (Recall that the electron energy also depends on **R**.) Thus, $U_{\text{k}}(\mathbf{R})$ is an adiabatic potential and it forms the configurational coordinate curve when one takes the coordinate Q as **R**. When $U_{\text{k}}(\mathbf{R})$ is expanded in a Taylor series up to second order around the equilibrium position of the ground state, the potentials are expressed by Eq. 73. For a harmonic oscillation, the second term is the first nonvanishing term, while the first term is non-zero only when the equilibrium position is displaced from the original position. In the latter case, the first term is related to the Jahn-Teller effect. Sometimes, the fourth term in the expansion may also be present, signaling anharmonic effects. In the following, consider for simplicity only a single coordinate or a two-dimensional model.

Consider a harmonic oscillator in a potential shown by Eq. 73. This oscillator gives discrete energy levels inside the configurational coordinate curves, as illustrated in Figure 13.

$$E_m = \left(m + 1/2\right)\hbar\omega \tag{78}$$

where ω is the proper angular frequency of the harmonic oscillator.

The electric dipole transition probability, W_{nm}, between the two vibrational states n and m is given by:

$$W_{nm} = \left| \iint \psi_e \chi_{en}^* er \psi_g \chi_{gm} dr dQ \right|^2 = \left| \int \chi_{en}^* \chi_{gm} M_{eg}(Q) dQ \right|^2 \tag{79}$$

Here,

$$M_{eg}(Q) \equiv \int \psi_e^*(r,Q) er \psi_g(r,Q) dr \tag{80}$$

When the transition is allowed, M_{eg} can be placed outside the integral, because it depends weakly on Q. This is called the Condon approximation and it makes Eq. 79 easier to understand as:

$$W_{nm} = \left| M_{eg}(Q) \right|^2 \cdot \left| \int \chi_{en}^* \chi_{gm} dQ \right|^2 \tag{81}$$

The wavefunction of a harmonic oscillator has the shape illustrated in Figure 13. For m (or n) = 0, it has a Gaussian shape; while for m (or n) ≠ 0, it has maximum amplitude at both ends and oscillates m times with a smaller amplitude between the maxima. As a consequence, the integral $\left| \int \chi_{en}^* \chi_{gm} dQ \right|$ takes the largest value along a vertical direction on the configurational coordinate model. This explains the Franck-Condon principle in terms of the shapes of wavefunctions. One can also state that this is the condition for which $W_{nm} \propto \left| \int \chi_{en}^* \chi_{gm} dQ \right|^2$ holds. The square of the overlap integral $\left| \int \chi_{en}^* \chi_{gm} dQ \right|^2$ is an important quantity that determines the strength of the optical transition and is often called the Franck-Condon factor.

2.3.3 *Spectral shapes*

As described above, the shape of an optical absorption or emission spectrum is decided by the Franck-Condon factor and also by the electronic population in the vibrational levels at thermal equilibrium. For the special case where both ground and excited states have the same angular frequency ω, the absorption probability can be calculated with harmonic oscillator wavefunctions in a relatively simple form:

$$W_{nm} = e^{-S} \left[\frac{m!}{n!} \right] S^{n-m} \left[L_m^{n-m}(S) \right]^2 \tag{82}$$

Here $L_\beta^\alpha(z)$ are Laguerre's polynomial functions. The quantity S can be expressed as shown below, with K being the force constant of a harmonic oscillator and Q_0 the coordinate of the equilibrium position of the excited state.

$$S = {}^1\!/_2 \frac{K}{\hbar\omega} (Q - Q_0)^2 \tag{83}$$

As can be seen in Figure 14, S is the number of emitted phonons accompanying the optical transition. It is commonly used as a measure of electron-phonon interaction and is called the *Huang-Rhys-Pekar factor.* At 0K or $m = 0$, the transition probability is given by the simple relation:

$$W_{no} = S^n \frac{e^{-S}}{n!} \tag{84}$$

A plot of W_{n0} against n gives an absorption spectrum consisting of many sharp lines. This result is for a very special case, but it is a convenient tool to demonstrate how a spectrum varies as a function of the intensity of electron-phonon interaction or the displacement of the equilibrium position in the excited state. The results calculated for S = 20 and 2.0 are shown in Figures 14 (a) and (b),[7] respectively. The peak is located at $n \cong S$. For $S \cong 0$ or weak electron-phonon interaction, the spectrum consists only of a single line at $n = 0$. This line (a zero-phonon line) becomes prominent when S is relatively small. For luminescence, transitions accompanied by phonon emission show up on the low-energy side of the zero-phonon line in contrast to absorption shown in Figure 14(b). If the energy of the phonon, $\hbar\omega$, is equal both for the ground and excited states, the absorption and emission spectra form a mirror image about the zero-phonon line. Typical examples of this case are the spectra of $\text{YPO:}_4\text{Ce}^{3+}$ shown in Figure 15,[8] and that of ZnTe:O shown in Figure 16.[9]

Examples of other S values are described. For the A emission of KCl:Tl^+ having a very broad band width, S for the ground state is found to be 67, while for the corresponding A absorption band, S of the excited state is about 41.[10] Meanwhile, in $\text{Al}_2\text{O}_3\text{:Cr}^{3+}$ (ruby), $S = 3$ for the narrow ${}^4A_2 \rightarrow {}^4T_2$ absorption band, and $S \approx 10^{-1}$ for the sharp R lines (${}^4A_2 \leftrightarrow {}^4T_2$) were reported.[11] A very small value similar to that of R lines is expected for sharp lines due to $4f^n$ intraconfigurational transitions. The spectra of $\text{YPO}_4\text{:Ce}^{3+}$ in Figure 15, which is due to $4f \leftrightarrow 5d$ transition, show $S \approx 1$.[8]

The above discussion has treated the ideal case of a transition between a pair of vibrational levels (gm) and (en) resulting in a single line. The fact is, however, that each line has a finite width even at 0K as a result of zero-point vibration.

Next, consider a spectral shape at finite temperature T. In this case, many vibrational levels at thermal equilibrium can act as the initial state, each level contributing to the transition with a probability proportional to its population density. The total transition probability is the sum of such weighted probabilities from these vibrational levels. At sufficiently high temperature, one can treat the final state classically and assume the wavefunction of the final state is a δ-function and the population density of the vibrational levels obeys a Boltzmann distribution. By this approximation, the absorption spectrum has a Gaussian shape given by:

$$W(\hbar\omega) = \frac{1}{\sqrt{2\pi\sigma_a}} \exp\left[\frac{-(\hbar\omega - U_1)^2}{2\sigma_a^2}\right] \tag{85}$$

Here,

$$U_1 \equiv U_0 + \frac{K_e}{2Q_0^2} \tag{86}$$

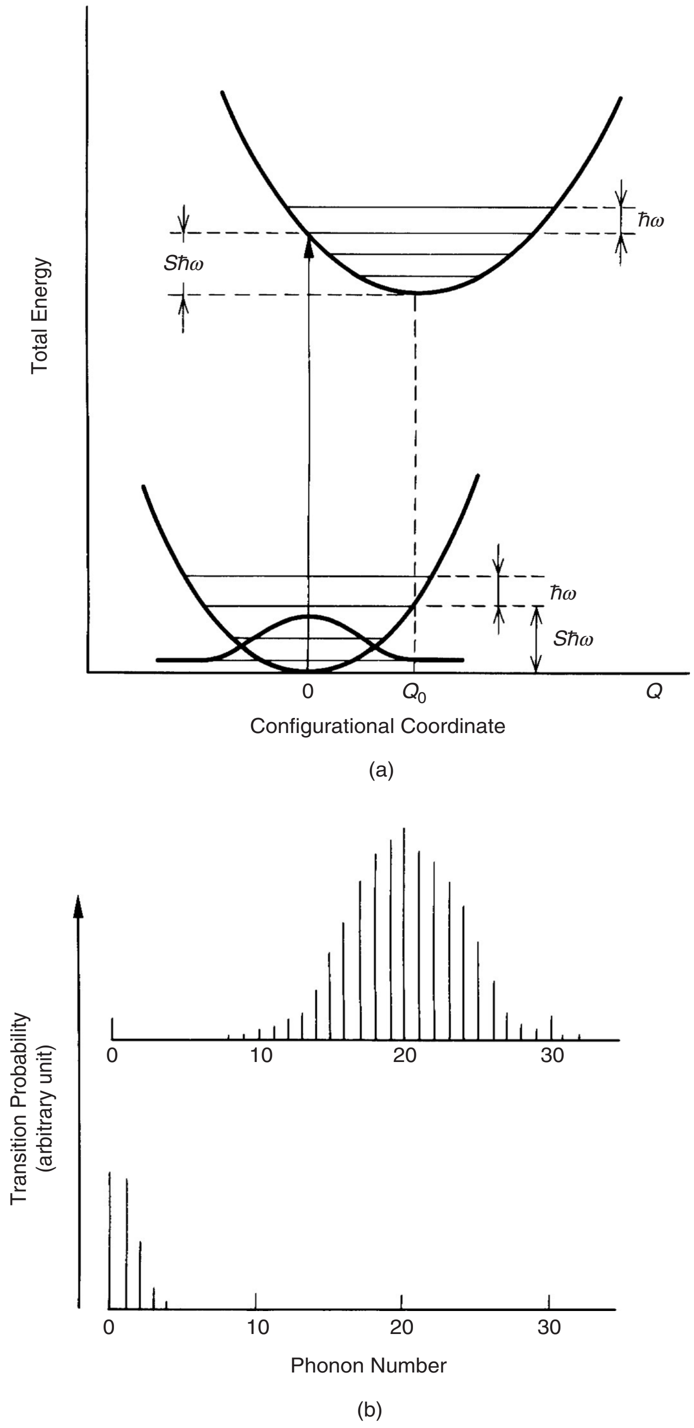
Total Energy
Sħω
ħω
ħω
Sħω
0
Q0
Q
Configurational Coordinate
(a)
Transition Probability (arbitrary unit)
0
10
20
30
0
10
20
30
Phonon Number
(b)

Figure 14 (b) shows the spectral shape calculated for the configurational coordinate model, in which the vibrational frequency is identical in the ground and excited states shown in (a). The upper figure in (b) shows a result for $S = 20$, while the lower figure is for $S = 2.0$. The ordinate shows the number of phonons n accompanying the optical transition. The transition for $n = 0$ is the zero-phonon line.

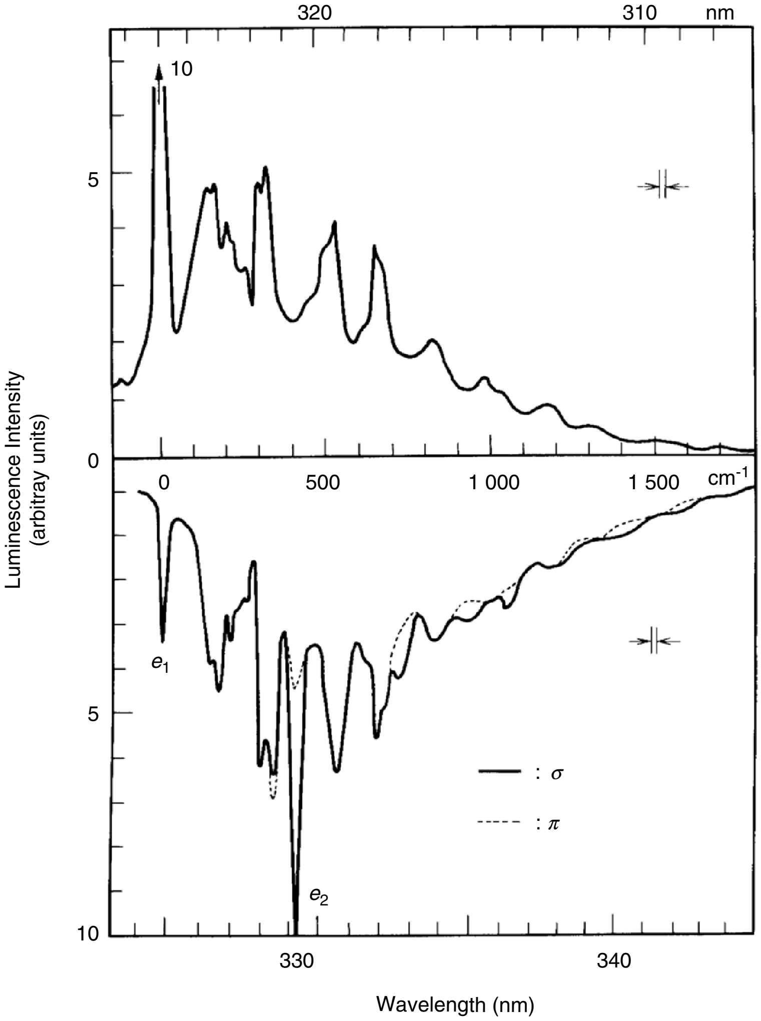

Figure 15 Optical spectra of $5d \rightleftharpoons 4f(^2F_{3/2})$ transition of Ce^{3+} doped in a YPO_4 single crystal. The upper figure is an excitation spectrum, with the lower luminescence spectrum at 4.2K. The two spectra are positioned symmetrically on both sides of the zero-phonon line at 325.0 nm. Vibronic lines are observed for both spectra. The notations π and σ indicate that the polarization of luminescence is parallel or perpendicular to the crystal *c*-axis, respectively.

$$\{\sigma_a(T)\}^2 \equiv S_e \frac{(\hbar\omega_e)^3}{\hbar\omega_g} \coth \frac{\hbar\omega_g}{2kT} \tag{87}$$

$$\approx 2S_e \cdot kT \cdot \frac{(\hbar\omega_e)^3}{(\hbar\omega_g)^2} \tag{88}$$

where $\hbar\omega$ is the energy of an absorbed phonon, and S_e denotes S of the excited state. The coefficient on the right-hand side of Eq. 85 is a normalization factor defined to give $\int W(\hbar\omega)d\omega = 1$. By defining w as the spectral width, which satisfies the condition $W(U_1 + w) = W(U_1)/e$, one finds:

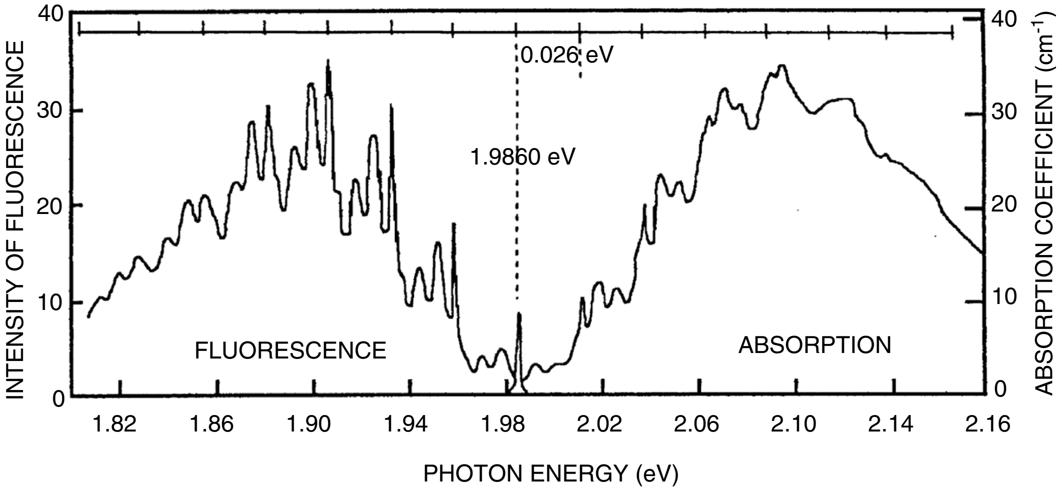

Figure 16 Absorption and luminescence spectra of ZnTe:O at 20K. (From Merz, J.L., *Phys. Rev.*, 176, 961, 1968. With permission.)

$$w = \sqrt{2\sigma_a} \tag{89}$$

At sufficiently high temperature, the spectral width w is proportional to $\sqrt{T}$ and the peak height is inversely proportional to $\sqrt{T}$. The relations for the luminescence process are found simply by exchanging the suffixes e and g of the above equations.

In experiments, a Gaussian shape is most commonly observed. It appears, however, only when certain conditions are satisfied, as is evident from the above discussion. In fact, more complicated spectral shapes are also observed. A well-known example is the structured band shape of a transition observed for Tl^+-type ions in alkali halides.[6] It has been shown that this shape is induced by the Jahn-Teller effect and can be described by a configurational coordinate model based on six vibrational modes around a Tl^+-type ion. Another example is the asymmetric luminescence band of Zn_2SiO_4:Mn^{2+}. To explain this shape, a configurational coordinate model with a small difference between the excited- and ground-state potential minima ($S = 1.2$) has been proposed.[12]

In summarizing the discussion of the spectral shape based on the configurational coordinate model, one can review the experimental results on luminescence bandwidths. In Figure 17,[13] the halfwidth of the luminescence band of typical activators in phosphors is plotted against the peak wavelength.[13] The activators are classified by the type of optical transition described in the Section 2.3.1. When the $d \rightleftharpoons d$ (Mn^{2+}), $f \rightleftharpoons d$ (Eu^{2+}), and $s^2 \rightleftharpoons sp$ transitions (Sn^{2+}, Pb^{2+}, and Sb^{3+}) are sequentially compared, one finds that the halfwidth increases in the same order. This is apparently because the overlap of the electron wavefunctions between the excited and ground states increases in the above order. The difference in the wavefunction overlap increases the shift of the equilibrium position of the excited state, Q_0, and consequently the Stokes' shift and the halfwidth increase as well.

Weak electron-phonon interactions give line spectra. The line width in this case results from factors other than those involved in the configurational coordinate model. Such factors are briefly reviewed below.

2.3.3.1 *Line broadening by time-dependent perturbation*

The most fundamental origin of the line width is the energy fluctuation of the initial and final states of an optical transition caused by the uncertainty principle. With τ being the

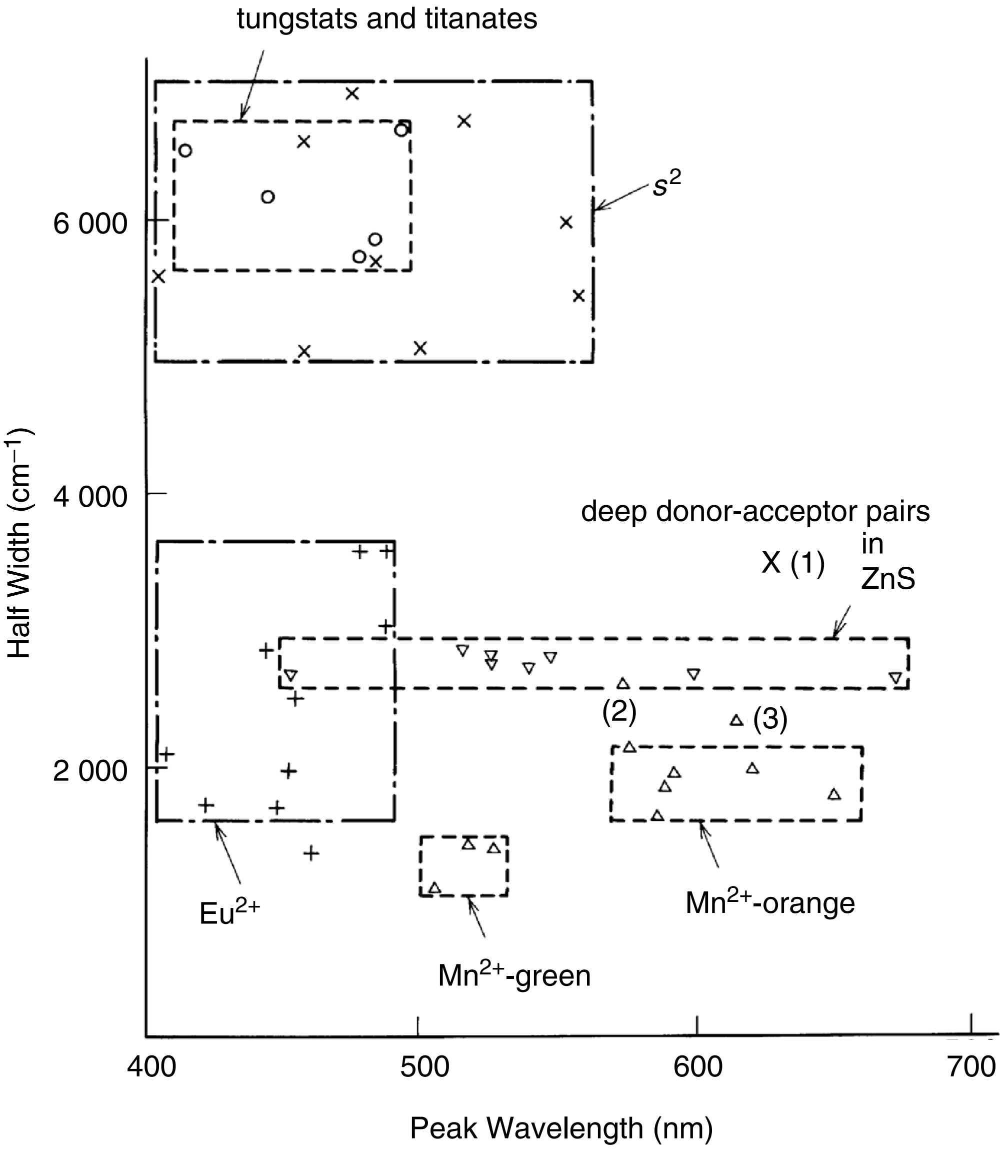

Figure 17 A plot of peak wavelength and half-width of various phosphors. The points (1)-(3) indicate the following materials. The luminescence of (2) and (3) originates from Mn^{2+} principally. (1) $(Sr,Mg)_3(PO_4)_2:Sn^{2+}$; (2) $Sr_5(PO_4)_3F:Sb^{3+},Mn^{2+}$ (3) $CaSiO_3:Pb^{2+}$, Mn^{2+}. (From Narita, K., Tech. Digest Phosphor Res. Soc. 196th Meeting, 1983 (in Japanese). With permission.)

harmonic mean of the lifetimes of the initial and final states, the spectral line width is given by $\hbar/\tau$ and the spectral shape takes a Lorentzian form:

$$I(\nu) = \frac{1}{\pi} \cdot \frac{1/\nu_L}{1 + (\nu - \nu_0)^2 / \nu_L^2} \tag{90}$$

where $\nu_L \equiv (\tau_i^{-1} + \tau_f^{-1})/4\pi c$, ν is the frequency of light, ν_0 the frequency at the line center, and τ_i and τ_f are the lifetimes of the initial and final states, respectively.

In addition to the spectral width given by Eq. 89, there are other kinds of time-dependent perturbation contributing to the width. They are absorption and emission of a photon, which makes "the natural width," and absorption and emission of phonons. The fluorescent lifetime of a transition-metal ion or a rare-earth ion is of the order of 10^{-6} s at the shortest, which corresponds to 10^{-6} cm^{-1} in spectral width. This is much sharper than the actually observed widths of about 10 cm^{-1}; the latter arise from other sources, as discussed below.

At high temperatures, a significant contribution to the width is the Raman scattering of phonons. This process does not have any effect on the lifetime, but does make a Lorentzian contribution to the width. The spectral width due to the Raman scattering of phonons, ΔE, depends strongly on temperature, as can be seen below:

$$\Delta E = \alpha\left(\frac{T}{T_D}\right)^7 \int_0^{X_0} \frac{x^6 e^x}{\left(e^x - 1\right)^2}\,dx, \quad X_0 = \frac{\hbar\omega_a}{KT} \tag{91}$$

where T_D is Debye temperature and α is a constant that includes the scattering probability of phonons.

2.3.3.2 *Line broadening by time-independent perturbation*

When the crystal field around a fluorescent ion has statistical distribution, it produces a Gaussian spectral shape.

$$I(\nu) = \frac{1}{\sqrt{2\pi}\sigma} \exp\left\{-\frac{\left(\nu - \nu_0\right)}{2\sigma^2}\right\} \tag{92}$$

with σ being the standard deviation.

Line broadening by an inhomogeneously distributed crystal field is called *inhomogeneous broadening*, while the processes described in Section 2.3.3.1 result in *homogeneous broadening*.

2.3.4 *Nonradiative transitions*

The classical theory describes a *nonradiative transition* as a process in which an excited state relaxes to the ground state by crossing over the intersection of the configurational coordinate curve through thermal excitation or other means (refer to Section 2.3.2). It is often observed, however, that the experimentally determined activation energy of a nonradiative process depends upon temperature.

This problem has a quantum mechanical explanation: that is, an optical transition accompanied by absorption or emission of $m - n$ phonons can take place when an n^{th} vibrational level of the excited state and an m^{th} vibrational level of the ground state are located at the same energy. The probability of such a transition is also proportional to a product of the Franck-Condon coefficient and thermal distribution of population in the ground state, giving the required temperature-dependent probability. When the phonon energy is the same both at the ground and excited states, as shown in Figure 14, the nonradiative relaxation probability is given by:

$$N_p = N_{eg} \cdot \exp\left\{-S\left(2\langle n\rangle + 1\right)\right\} \sum_{j=0}^{\infty} \frac{\left(S\langle n\rangle\right)^j \left\{S\left(1 + \langle n\rangle\right)\right\}^{p+j}}{j!\left(p + j\right)!} \tag{93}$$

Here, let $p \equiv m - n$, and $\langle n \rangle$ denotes the mean number of the vibrational quanta n at temperature T expressed by $\langle n \rangle = \left\{ \exp\left(\hbar\omega / kT \right) - 1 \right\}^{-1}$. The notation N_{eg} implies the overlap integral of the electron wavefunctions.

The temperature dependence of N_p is implicitly included in $\langle n \rangle$. Obviously, Eq. 93 does not have a form characterized by a single activation energy. If written in a form such as $N_p \propto \exp\left(-E_p / kT \right)$, one obtains:

$$E_p = \left(\langle n \rangle_p - \langle n \rangle \right) \hbar\omega \tag{94}$$

where $\langle n \rangle_p \hbar\omega$ is the mean energy of the excited state subject to the nonradiative process. The energy E_p increases with temperature and one obtains $E_p < \Delta U$ at sufficiently low temperature.

If $S < 1/4$ or if electron-phonon interaction is small enough, Eq. 93 can be simplified by leaving only the term for $j = 0$.

$$N_p = N_{eg} \cdot \exp\left\{ -S\left(1 + 2\langle n \rangle \right) \right\} \left\{ -S\left(1 + \langle n \rangle \right) \right\}^p / p! \tag{95}$$

In a material that shows line spectra, such as rare-earth ions, the dominating nonradiative relaxation process is due to multiphonon emission. If E_{gap} is the energy separation between two levels, the nonradiative relaxation probability between these levels is given by an equation derived by Kiel:[25]

$$N_p = A_K \epsilon^p \left(1 + \langle n \rangle \right)^p \tag{96}$$

$$p\hbar\omega = E_{gap} \tag{97}$$

where A_K is a rate constant and ϵ is a coupling constant.

Eq. 95 can be transformed to the same form as Eq. 96 using the conditions $S \approx 0$, $\exp\left\{ -S\left(1 + 2\langle n \rangle \right) \right\} \approx 1$, $S^p / p! \approx \epsilon^p$ and $A_K = N_{eg}$, although Eq. 95 was derived independently of the configurational coordinate model. If two configurational coordinate curves have the same curvature and the same equilibrium position, the curves will never cross and there is no relaxation process by thermal activation between the two in the framework of the classical theory. However, thermal quenching of luminescence can be explained for such a case by taking phonon-emission relaxation into account, as predicted by Kiel's equation.

References

1. Klick, C.C. and Schulman, J.H., *Solid State Physics*, Vol. 5, Seitz, F. and Turnbull, D., Eds., Academic Press, 1957, pp. 97-116.
2. Curie, D., *Luminescence in Crystals*, Methuen & Co., 1963, pp. 31-68.
3. Maeda, K., *Luminescence*, Maki Shoten, 1963, pp. 6-10 and 37-48 (in Japanese).
4. DiBartolo, B., *Optical Interactions in Solids*, John Wiley & Sons, 1968, pp. 420-427.
5. Kamimura, A., Sugano, S., and Tanabe, Y., *Ligand Field Theory and Its Applications*, First Edition, Shokabo, 1969, pp. 269-321 (in Japanese).
6. Fukuda, A., *Bussei*, 4, 13, 1969 (in Japanese).
7. Keil, T., *Phys. Rev.*, 140, A601, 1965.

8. Nakazawa, E. and Shionoya, S., *J. Phys. Soc. Jpn.*, 36, 504, 1974.
9. Merz, J.L., *Phys. Rev.*, 176, 961, 1968.
10. Williams, F.E., *J. Chem. Phys.*, 19, 457, 1951.
11. Fonger, W.H. and Struck, C.W., *Phys. Rev.*, B111, 3251, 1975.
12. Klick, C.C. and Schulman, J.H., J. Opt. Soc. Am., 42, 910, 1952.
13. Narita, K., *Tech. Digest Phosphor Res. Soc. 196th Meeting*, 1983 (in Japanese).
14. Struck, C.W. and Fonger, W.H., *J. Luminesc.*, B111, 3251, 1975.
15. Kiel, A., *Third Int. Conf. Quantum Electronics*, Paris, Grivet, P. and Bloembergen, N., Eds., Columbia University Press, p. 765, 1964.

chapter two — section four

Fundamentals of luminescence

Sumiaki Ibuki

Contents

2.4 Impurities and luminescence in semiconductors 49
  2.4.1 Impurities in semiconductors 49
  2.4.2 Luminescence of excitons bound to impurities 50
  2.4.3 Luminescence of isoelectronic traps 53
  2.4.4 Luminescence of donor-acceptor pairs 53
  2.4.5 Deep levels 56
References 59

2.4 *Impurities and luminescence in semiconductors*

2.4.1 *Impurities in semiconductors*

As is well known, when semiconductors are doped with impurities, the lattices of the semiconductors are distorted and the energy level structures of the semiconductors are also affected. For example, when in Si an As atom (Group V) is substituted for a Si atom (Group IV), one electron in the outermost electronic orbit in the N shell of the As atom is easily released and moves freely in the Si lattice, because the number of electrons in the N shell of As (5) is one more than that in the M shell of Si (4). Thus, impurities that supply electrons to be freed easily are called *donors*.

On the contrary, when a Ga atom (Group III) is substituted for a Si atom, one electron is attracted from a Si atom, forming a hole that moves freely in the Si lattice; this is because the number of electrons in the N shell of Ga (3) is one less than that in the M shell of Si (4). Thus, impurities that supply free holes easily are called *acceptors*. In compound semiconductors, it is easily understood in a similar way what kinds of impurities play the role of donors and acceptors.

Usually, in compound semiconductors such as ZnS and GaAs, the stoichiometry does not hold strictly. Therefore, when more positive ions exit, negative ion vacancies are created and work as donors. Similarly, when more negative ions exit, positive ion vacancies work as acceptors.

In a donor, one excess electron orbits around the positively charged nucleus, as in a hydrogen atom. This electron moves around in a semiconductor crystal (which usually has a large dielectric constant) so that the Coulomb interaction between the nucleus and

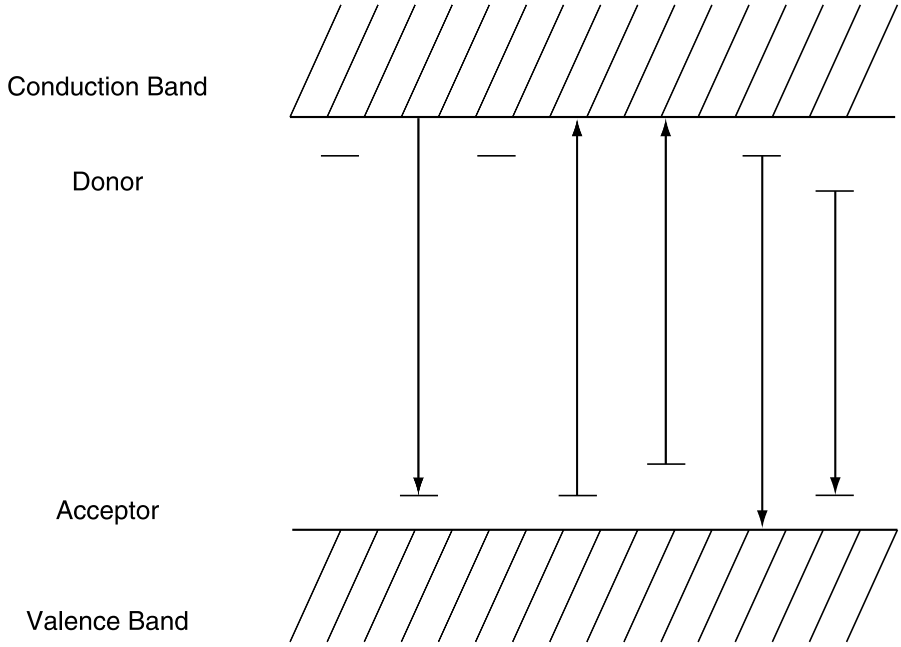

Figure 18 Shallow impurity levels in a semiconductor.

the electron is weakened. The radius of the electron orbit becomes large under these conditions and the electron is greatly affected by the periodic potential of the crystal. For example, when the effective mass of the electron is 0.5 and the dielectric constant of the crystal is 20, the Bohr radius of the electron becomes 40 times larger than that in the hydrogen atom. Therefore, the excess electron of the donor can be released from its binding to the nucleus by an excitation of small energy. This means that the donor level is located very close to the bottom of the conduction band, as shown in Figure 18. Similarly, the acceptor level is located very close to the top of the valence bond. Impurity levels with small ionization energies are called *shallow* impurity levels. Other impurity levels can also be located at *deep* positions in the forbidden land.

Light absorption takes place between the valence band and impurity levels, or between impurity levels and the conduction band. When a large quantity of impurities exists, the band shape can be observed in absorption.

Luminescence takes place through these impurity levels with wavelengths longer than the bandgap wavelength. When the dopant impurity is changed, the luminescent wavelength and efficiency also change. It is usually found that in *n*-type semiconductors, luminescence between the conduction band and acceptor levels is strong; whereas in *p*-type semiconductors, luminescence between donor levels and the valence band is strong.

2.4.2 Luminescence of excitons bound to impurities

The number of impurities included in semiconductors is of the order of magnitude of 10^{14} to 10^{16} cm^{-3}, even in so-called pure semiconductors. Therefore, excitons moving in a crystal are generally captured by these impurities and *bound exciton* states are created. Luminescence from such bound excitons is, in ordinary crystals, stronger than that from *free excitons*. Excitons bound to donors or acceptors create H_2 molecule-type complexes. Those bound to ionized donors or acceptors create H_2^+ molecular ion-type complexes. Binding energies of excitons in these complexes depend on the effective mass ratio of electron to hole, and

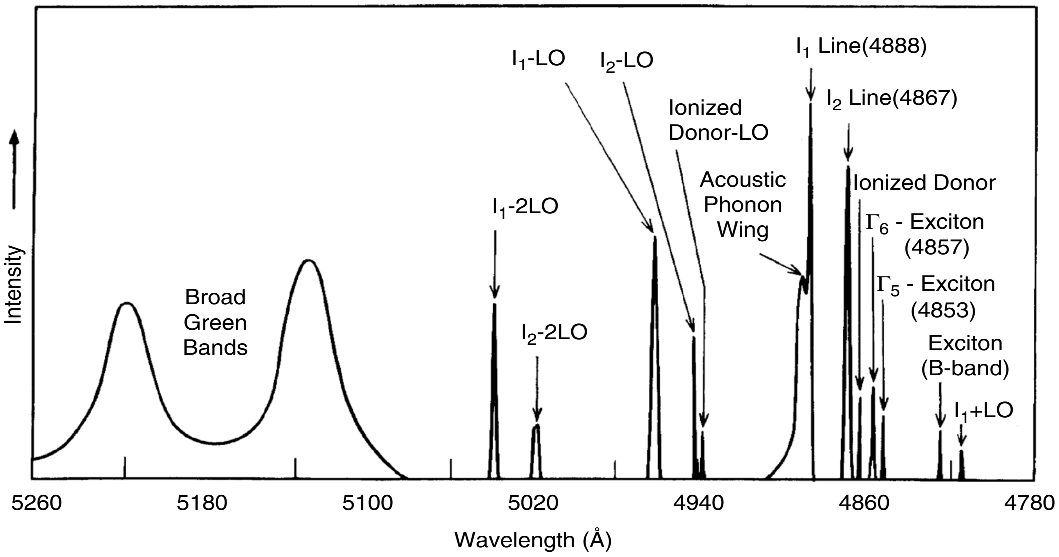

Figure 19 Luminescence spectrum near the band gap of CdS (1.2K). (From Litton, C.W., Reynolds, D.C., Collins, T.C., and Park, Y.S., *Phys. Rev. Lett.*, 25, 1619, 1970. With permission.)

are about 0.1 to 0.3 of ionization energies of the donor or acceptor impurities. The radiative recombination of bound excitons takes place efficiently with energy less than that of free excitons. The halfwidths of luminescence lines are very narrow.

As an example, a luminescence spectrum of CdS, a II-VI compound of the *direct transition type*, near the band edge is shown in Figure 19.[1] In the figure, the I_1, I_2, and I_3 lines correspond to the luminescence of excitons bound to neutral acceptors, neutral donors, and ionized donors, respectively. They were identified by measurements of their Zeeman effect. The binding energies of these bound excitons are 19, 8, and 5 meV, respectively. The halfwidths of the luminescence line are very narrow, about 2–3 cm^{-1}, and are much less than those of the free exciton lines shown as Γ_5 and Γ_6 excitons. In II-VI compounds like CdS, excitons couple strongly with the longitudinal optical (LO) phonons that generate a polarized electric field. As a result, exciton luminescence lines accompanied by simultaneous emission of one, two, or more LO phonons are observed strongly, as shown in the figure.

The oscillator strength of the I_2 bound exciton was obtained from the area of the absorption spectrum and found to be very large, about 9.[2] The oscillator strength of the free exciton is 3×10^{-3}, so that of the bound exciton is enhanced by $\sim 10^3$. This enhancement effect is called the giant oscillator strength effect. From a theoretical point of view, the ratio of the oscillator strength of the bound exciton to the free exciton is given by the ratio of the volume in which the bound exciton moves around, to that of the unit cell. In CdS, this ratio is $\sim 10^3$, so that the very large value observed for the I_2 bound exciton is reasonable. This value gives a calculated lifetime of 0.4 ns for I_2. The lifetimes of excitons are determined from luminescence decay measurement.[3] For the I_2 bound exciton, a value of 0.5 ± 0.1 ns was obtained, which agrees well with the calculated value. This also indicates that the luminescence quantum efficiency of the I_2 bound exciton is close to 1.

In the case of *indirect transition-type* semiconductors, on the other hand, the luminescence efficiency of bound excitons is very low. A typical example is the case of S donors in GaP. The luminescence quantum efficiency has been estimated to be $1/(700 \pm 200)$.[4] The reason for the low efficiency is ascribed to the Auger effect. The state in which an exciton

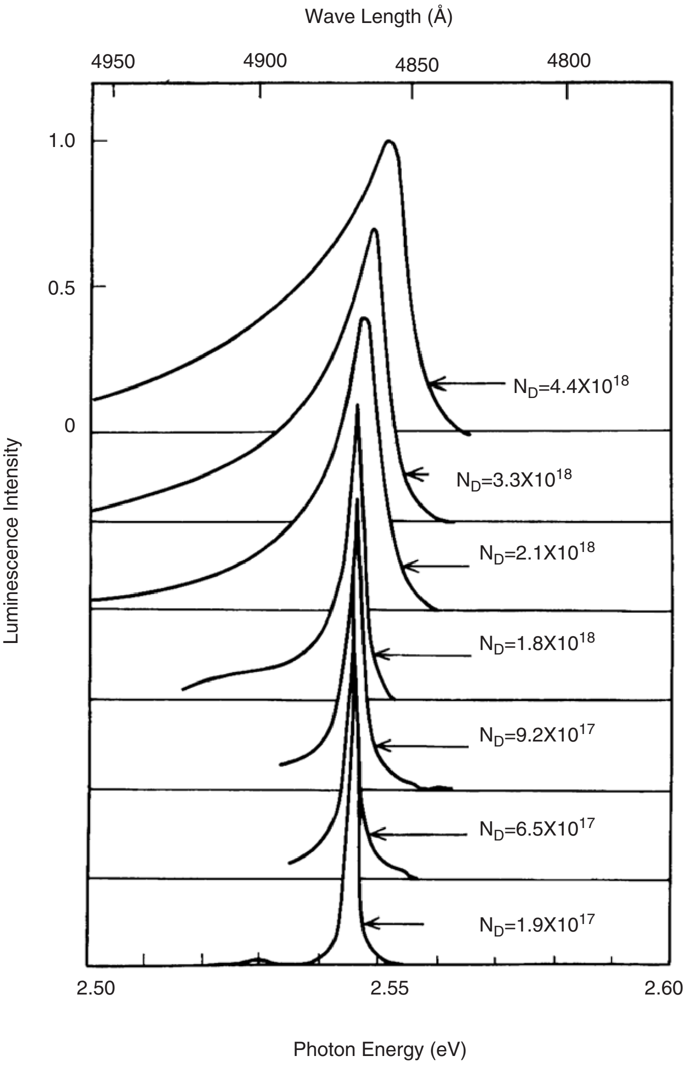

Figure 20 Changes of luminescence spectra of excitons bound to Cl donors in CdS (1.8K) with the Cl concentration. N_D:Cl donor concentration (cm^{-3}). (From Kukimoto, H., Shionoya, S., Toyotomi, S., and Morigaki, K., J. Phys. Soc. Japan, 28, 110, 1970. With permission.)

is bound to a neutral donor includes two electrons and one hole, so when one electron and one hole recombine, the recombination energy does not result in light emission, but is instead transferred to the remaining electron to raise it into the conduction band.

Next, the effect of high concentrations of impurities on the bound exciton luminescence is discussed. As an example, consider the case of an I_2 bound exciton in CdS:Cl as shown in Figure 20.[5] With increasing Cl donor concentration N_D, the spectral width broadens. Beyond $N_D \sim 2 \times 10^{18}$ cm^{-3}, the emission peak shifts toward the high-energy side with further increases of N_D. Simultaneously, the spectral width broadens more and the shape becomes asymmetric, having long tails toward the low-energy side.

These facts can be interpreted theoretically.[6] At higher N_D, an exciton bound to a donor collides with other donors. Donor electrons can thus be virtually excited and can exert the screening effect on the bound excitons through changes of the dielectric constant. This brings about the high-energy shift of the emission peak. The asymmetry of the spectral shape with long tails is interpreted as being caused by the Stark effect due to ionized impurities, i.e., compensated donors and acceptors.

2.4.3 *Luminescence of isoelectronic traps*

In semiconductor crystals, if an isoelectronic element, (i.e., an element belonging to the same column in the periodic table as a constituent element) is substituted for a constituent element, either a free electron or a hole in the semiconductor is attracted to the isoelectronic element. This is because of the differences in electronegativity between the isoelectronic element and the mother element. Such isoelectronic elements are called *isoelectronic traps*.

When an electron is trapped in an isoelectonic trap, a hole is attracted to the top trap by the Coulomb force, and an exciton bound to an isoelectronic trap is created. This state produces luminescence that is quite different from that due to an exciton bound to a donor or acceptor. In such cases, an electron or hole is attracted to the donor or acceptor by a long-range Coulomb force. On the other hand, the isoelectric trap attracts an electron or a hole by the short-range type force that comes from the difference in the electronegativity. Therefore, the wavefunctions of the electron or hole trapped at the isoelectronic trap is very much localized in real space and, instead, is greatly extended in **k**-space. This plays an important role in the case of indirect transition-type semiconductors.

Figure 21 shows the wavefunction of the electron bound to an N isoelectronic trap in GaP.[7] The bottom of the conduction band of GaP is located at the X point in **k**-space, and the electron has a relatively large amplitude, even at the Γ point. Therefore, the electron can recombine with a hole at the Γ point with a high probability for conditions applicable to direct transitions. The emission spectrum is shown in Figure 22.[8] The recombination probability is 100 times larger than that of an exciton bound to a neutral S donor, for which only the indirect transition is possible. Moreover, in the GaP:N system, there is no third particle (electron or hole), so the Auger nonradiative recombination does not occur, and the recombination probability is actually close to 1. When the concentration of N traps is high, luminescence of an exciton strongly bound to a pair of N traps closely located to each other is also observed at a slightly longer wavelength. Other isoelectric traps in GaP, Zn-O, and Cd-O centers, in which two elements are located in the nearest neighbor sites, are known. These centers also produce efficient luminescence, as do isoelectric traps in direct transition-type semiconductors, of which CdS:Te[9] and ZnTe:O[10] have been identified.

2.4.4 *Luminescence of donor-acceptor pairs*

When the wavefunction of an electron trapped at a donor overlaps to some extent with the wavefunction of a hole located at an acceptor, both particles can recombine radiatively. The luminescence thus produced has some interesting characteristics because the electron and the hole in this pair are located in lattice sites apart from each other. As explained below, the luminescence wavelength and probability will depend on the electron-hole distance in a pair.

As shown in Figure 23, at the start of luminescence, the electron is located at the donor D and the hole at the acceptor A. The energy of this initial stage is expressed, taking the origin of the energy axis to be the acceptor level A, as $E_i = E_g - (E_D + E_A)$, where E_g, E_D, and E_A are the bandgap energy, ionization energy of a neutral donor, and that of a neutral acceptor, respectively. After the recombination, a positive effective charge is left in the donor and a negative effective charge in the acceptor. The final state is determined by the Coulomb interaction between them, giving the final state energy to be $E_f = -\varepsilon^2/4\pi\varepsilon r$, where ε is the static dielectric constant of the crystal, and r is the

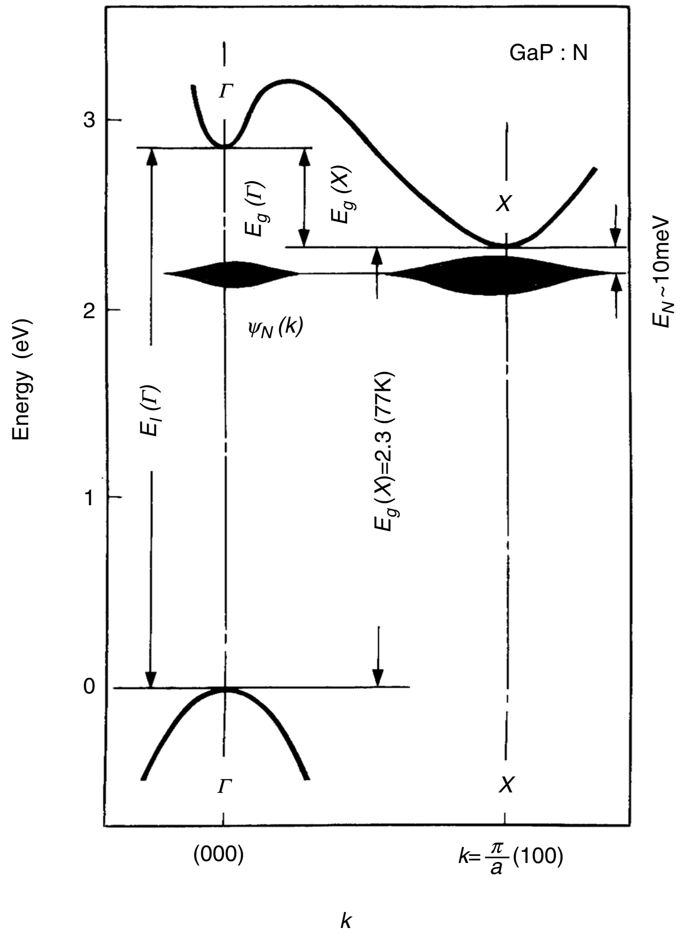

Figure 21 Energy level and wavefunction of N isoelectronic trap in GaP in the **k**-space. (From Holonyak, N., Campbell, J.C., Lee, M.H., et al., *J. Appl. Phys.*, 44, 5517, 1973. With permission.)

distance between the donor and acceptor in the pair. Therefore, the recombination energy E_r is given by:

$$\begin{aligned} E_r &= E_i - E_f \\ &= E_g - \left(E_D + E_A\right) + e^2/4\pi\varepsilon r \end{aligned} \tag{98}$$

In this formula, r takes discrete values. For smaller r values, each D-A pair emission line should be separated, so that a series of sharp emission lines should be observed. For larger r values, on the other hand, intervals among each emission line are small, so that they will not be resolved and a broad emission band will be observed.

The transition probability should be proportional to the square of the overlap of the electron and hole wavefunctions. Usually, the wavefunction of a donor electron is more widely spread than that of an acceptor hole. The electron wavefunction of a hydrogen-like donor is assumed to decrease exponentially with r. Therefore, the transition probability W(r) is expressed as:

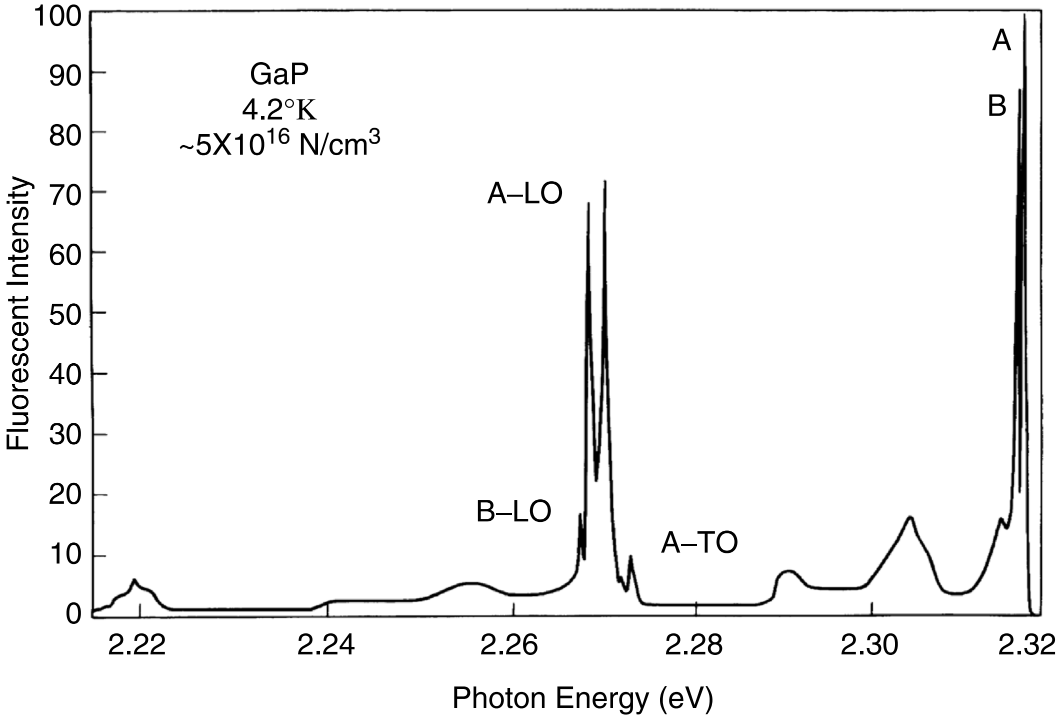

Figure 22 Luminescence spectrum of GaP:N (4.2K). (From Thomas, D.G. and Hopfield, J.J., *Phys. Rev.*, 150, 680, 1966. With permission.)

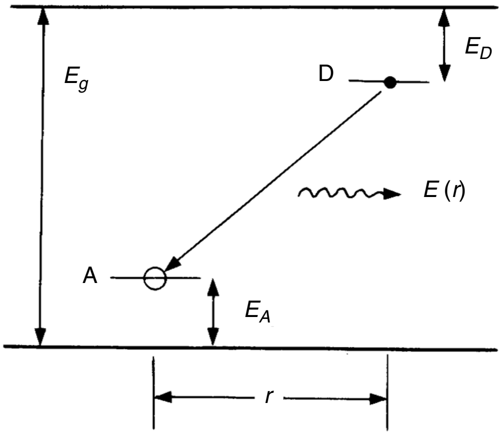

Figure 23 Energy levels of a donor-acceptor pair.

$$W(r) = W_0 \exp(-2r/r_B), \tag{99}$$

where r_B is the Bohr radius of the donor electron and W_0 is a constant related to the D-A pairs.

As a typical example of D-A pair luminescence, a spectrum of S donor and Si acceptor pairs in GaP is shown in Figure 24.[11] Both S and Si substitute for P. The P site, in other words the site of one of the two elements constituting GaP, composes a face-centered cubic lattice. In this lattice, r is given by $\{(1/2)m\}^{1/2}a$, where m is the shell number and a is the lattice constant. For the shell numbers m = 1, 2, … 12, 13, 15, 16, …, there exists atoms;

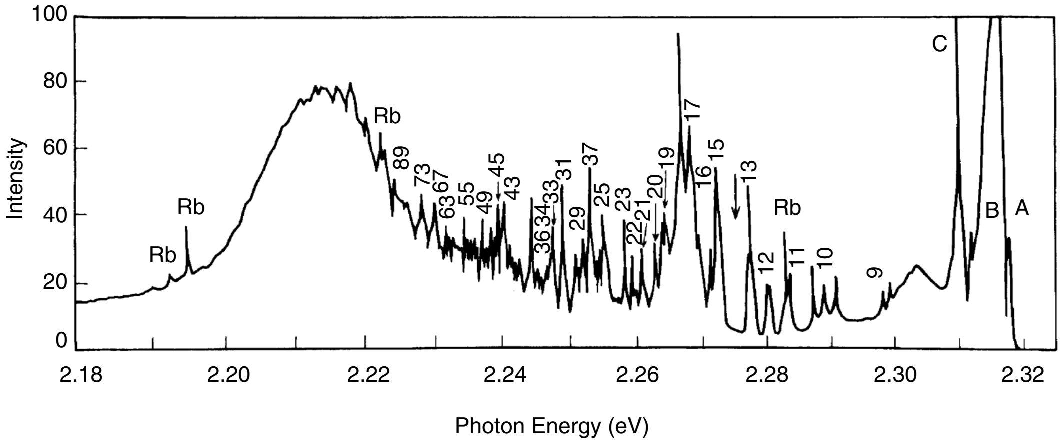

Figure 24 Luminescence spectrum of D-A pairs in GaP:Si,S (1.6K). (From Thomas, D.G., Gershenzon, M., and Trumbore, F.A., *Phys. Rev.*, 133, A269, 1964. With permission.)

but for m = 14, 30, 46, …, atoms do not exist. Assuming that the position of each emission line is given by Eq. 98 with r given in this way and $E_D + E_A = 0.14$ eV ($E_g = 2.35$ eV), it is possible to determine the shell number for each line, as shown in Figure 24. As expected, lines for m = 14, 30, … do not appear as seen in the figure. Agreement between experiment and theory is surprisingly good.

As understood from Eqs. 98 and 99, the smaller the r value is, the shorter the luminescence wavelength emitted and the higher the transition probability becomes; in other words, the shorter the decay time. Therefore, if one observes a time-resolved emission spectrum for a broad band composed of many unresolved pair lines, the emission peak of the broad band should shift to longer wavelengths with the lapse of time. The broad band peaking at 2.21 eV in Figure 24 is the ensemble of many unresolved pair lines. Figure 25[12] shows time-resolved luminescence spectra of this band. It is clearly seen that the peak shifts to longer wavelengths with time, as expected. Similar time shifts in D-A pair luminescence have been observed in II-VI compounds such as ZnSe and CdS. (See 3.7.)

2.4.5 *Deep levels*

As the final stage of this section, luminescence and related phenomena caused by deep levels in semiconductors are discussed. Certain defects and impurities create deep localized levels with large ionization energies. In these deep levels, electron-lattice interactions are generally strong, so that the nonradiative recombination takes place via these levels, thus lowering the luminescence efficiencies of emitting centers. Further, these deep centers sometimes move and multiply by themselves in crystals, and cause the deterioration of luminescence devices because of the local heating by multiphonon emission.

Changes of the states of deep levels caused by photoexcitation are studied from measurements of conductivity, capacitance, and magnetic properties. In this way, the structure, density, position of energy levels, and capture and release probabilities for carriers have been determine for various deep levels. Calculations of binding energies of deep levels using wavefunctions of the conduction and valence bands have also been performed. In this way, binding energies of O in GaP and GaAs and those of Ga and As vacancies in GaAs are obtained. Calculations are further made for complex defects including O, for example, a complex of O and Si or Ge vacancy, and atoms occupying antisites.[13]

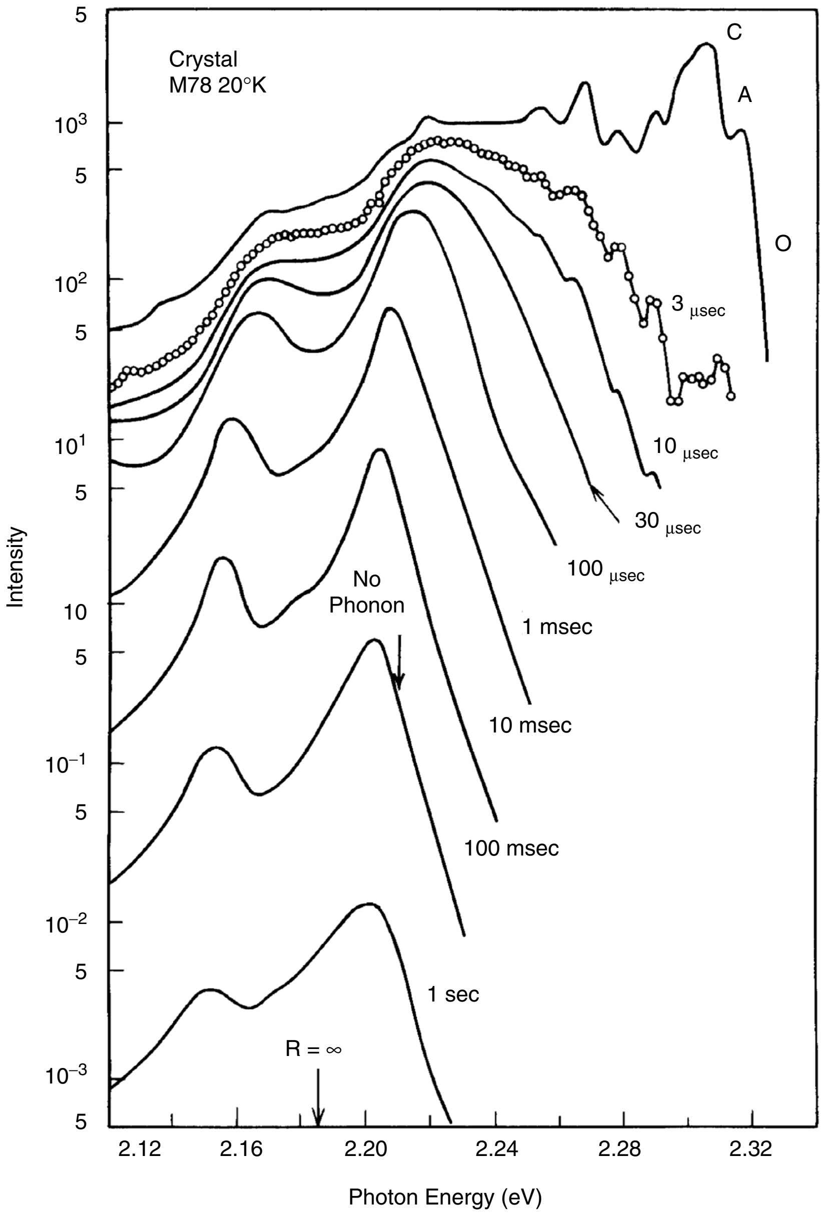

Figure 25 Time-resolved luminescence spectra of D-A pairs in GaP:Si,S (20K). (From Thomas, D.G., Hopfield, J.J., and Augustniak, W.M., *Phys. Rev.*, 140, A202, 1965. With permission.)

Transition metals incorporated in semiconductors usually create deep levels and exhibit luminescence. Since electron-lattice interactions are strong, broad-band spectra with relatively weak zero-phonon lines are usually observed. Figure 26 shows luminescence spectra of Cr^{3+} in GaAs[14] as an example. Coupling with phonons results in the phonon sidebands shown in Figure 26.

As for the nonradiative recombination through defects, not only the Auger recombination process but also many phonon emission process are observed. The transition probabilities of the latter increase when related levels are deep and crystal temperatures are high. In certain cases, the energy level of a localized trap is shallow before trapping

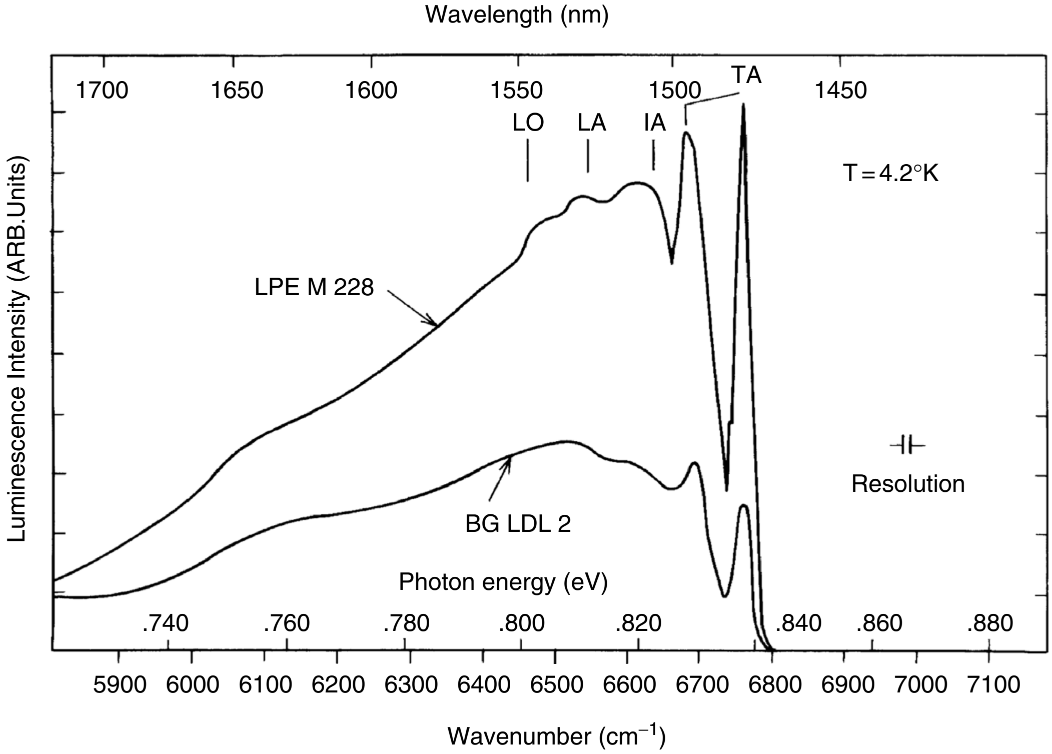

Figure 26 Luminescence spectrum of Cr^{3+} in GaAs (4.2K). (From Stocker, H.J. and Schmidt, M., *J. Appl. Phys.*, 47, 2450, 1976. With permission.)

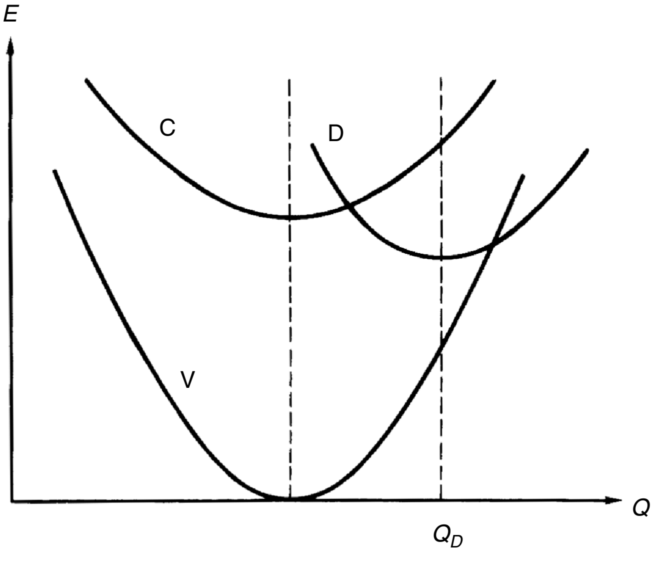

Figure 27 Configurational coordinate model of deep defect level. (C: conduction band, V: valence band, D: deep defect.)

an electron; but after trapping, lattice relaxation and the rearrangement of surrounding atoms take place and the energy level is made deep, as shown by the configurational coordinate model (2.3.2) in Figure 27. In this state, the difference between the optical activation energy and thermal activation energy is large, and nonradiative recombination through the emission of many phonons occurs with high probability.[15]

References

1. Litton, C.W., Reynolds, D.C., Collins, T.C., and Park, Y.S., *Phys. Rev. Lett.*, 25, 1619, 1970.
2. Thomas, D.G. and Hopfield, J.J., *Phys. Rev.*, 175, 1021, 1968.
3. Henry, C.H. and Nassau, K., *Phys. Rev.*, B1, 1628, 1970.
4. Nelson, D.F., Cuthbert, J.D., Dean, P.J., and Thomas, D.G., *Phys. Rev. Lett.*, 17, 1262, 1966.
5. Kukimoto, H., Shionoya, S., Toyotomi, S., and Morigaki, K., *J. Phys. Soc. Jpn.*, 28, 110, 1970.
6. Hanamura, E., *J. Phys. Soc. Jpn.*, 28, 120, 1970.
7. Holonyak, Jr., N., Campbell, J.C., Lee, M.H., Verdeyen, J.T., Johnson, W.L., Craford, M.G., and Finn, D., *J. Appl. Phys.*, 5517, 1973.
8. Thomas, D.G. and Hopfield, J.J., *Phys. Rev.*, 150, 680, 1966.
9. Aften, A.C. and Haaustra, J.H., *Phys. Lett.*, 11, 97, 1964.
10. Merz, J.L., *Phys. Rev.*, 176, 961, 1968.
11. Thomas, D.G., Gershenzon, M., and Trumbore, F.A., *Phys. Rev.*, 133, A269, 1964.
12. Thomas, D.G., Hopfield, J.J., and Augustyniak, W.M., *Phys. Rev.*, 140, A202, 1965.
13. Alt, H.Ch., *Materials Science Forum*, 143-147, 283, 1994.
14. Stocker, H.J. and Schmidt, M., *J. Appl. Phys.*, 47, 2450, 1976.
15. Kukimoto, H., *Solid State Phys.*, 17, 79, 1982 (in Japanese).

chapter two — section five

Fundamentals of luminescence

Chihaya Adachi and Tetsuo Tsutsui

Contents

2.5 Luminescence of organic compounds 61
 2.5.1 Origin of luminescence in organic compounds 61
 2.5.2 Electronically excited states of organic molecules and their photoluminescence 62
 2.5.3 Fluorescence of organic molecules in a solid state 64
 2.5.4 Quantum yield of fluorescence 66
 2.5.5 Organic fluorescent and phosphorescence compounds with high quantum yields 66
References 69

2.5 Luminescence of organic compounds

2.5.1 Origin of luminescence in organic compounds

The luminescence of organic compounds is essentially based on localized π-electron systems within individual organic molecules[1]. This is in clear contrast to inorganic phosphors where luminescence is determined by their lattice structures, and thus their luminescence is altered or disappears altogether when the crystals melt or decompose. In organic luminescent compounds, in contrast, it is the π-electron systems of individual molecules that are responsible for luminescence. Therefore, even when organic crystals melt into amorphous aggregates, luminescence still persists. Further, when molecules are in vapor phase or in solution, they basically demonstrate similar luminescence spectrum as in solid films.

Luminescence from organic compounds can be classified into two categories: luminescence from electronically excited singlet (S_1) or triplet (T_1) states. Emission from singlet excited states, called “fluorescence,” is commonly observed in conventional organic compounds. Emission from triplet excited states, called “phosphorescence,” is rarely observed in conventional organic compounds at ambient temperatures due to the small radiative decay rate of phosphorescence.

Electronically excited states of organic compounds are easily produced not only via photoexcitation but also by other excitation methods (such as chemical reactions, electrochemical reactions, mechanical forces, heat, and electric charge recombination) capable of producing electronically excited states in organic molecules, as depicted in Figure 28.

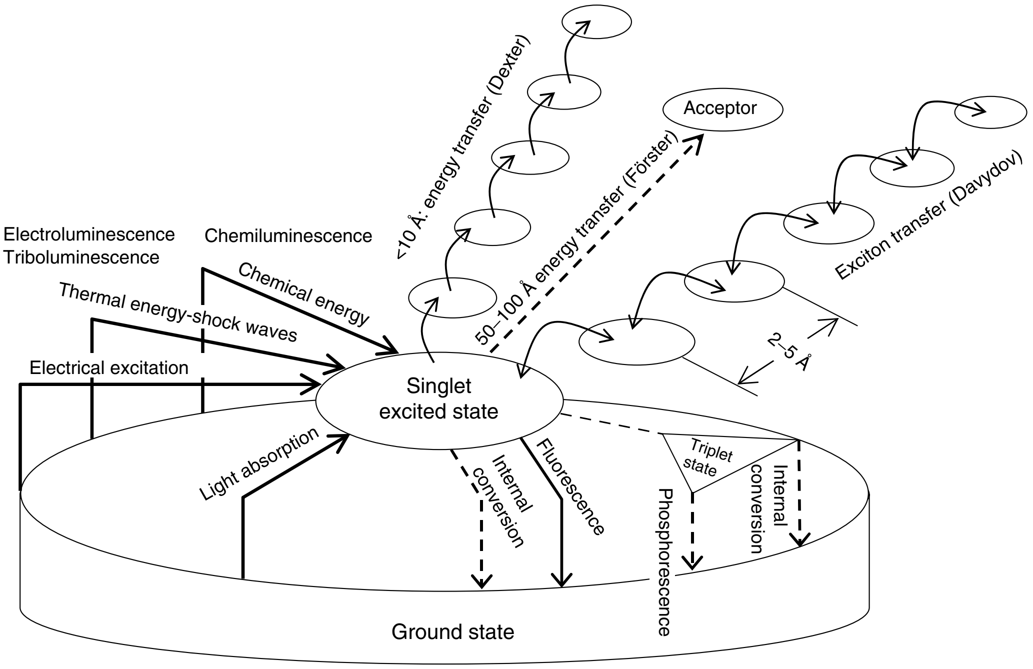
Electroluminescence
Triboluminescence
Chemiluminescence
Chemical energy
Thermal energy-shock waves
Electrical excitation
Light absorption
<10 Å: energy transfer (Dexter)
50–100 Å energy transfer (Förster)
Acceptor
Exciton transfer (Davydov)
2–5 Å
Singlet excited state
Internal conversion
Fluorescence
Triplet state
Phosphorescence
Internal conversion
Ground state

Figure 28 The various excitation methods, i.e., light absorption, thermal, chemical and charged-particle, and decay processes, i.e., photoluminescence, thermal deactivation, and energy transfer and migration, in organic molecules.

It should be emphasized that any kind of luminescence in organic compounds is due to well-defined electronically neutral singlet or triplet excited states in the organic molecules, even though luminescence can be produced by a variety of excitation methods having different names like photoluminescence, chemiluminescence, electrochemiluminescence, triboluminescence, thermoluminescence, and electroluminescence. In addition to radiative decay, the excited molecules also decay nonradiatively through thermal deactivation and energy transfer and migration.

2.5.2 *Electronically excited states of organic molecules and their photoluminescence*

Electronic transitions in organic molecules are described by the molecular orbitals of σ-electrons and π-electrons. Each molecular orbital can accept two electrons with antiparallel spins according to Pauli's exclusion principle, and both σ and π-electrons participate in chemical bonding. Here, π-electrons demonstrate a variety of photo- and electronic activities compared with σ-electrons, since σ-electrons become located at deeper energy levels compared with those of π-electrons (Figure 29). The ground state is characterized by the π-electrons in the highest occupied molecular orbital (HOMO). In order to produce an electronically excited state, a molecule must absorb energy equal to or greater than the energy difference between the HOMO and the lowest unoccupied molecular orbital (LUMO) levels

$$\Delta E = E_{LUMO} - E_{HOMO}. \tag{100}$$

With absorption of energy, an electron is promoted from HOMO to LUMO, and this constitutes an electronic transition from the ground state (S_0) to an electronically excited state (S_1). Here, the energy level diagrams (Jablonski diagram) for molecular orbitals for the ground

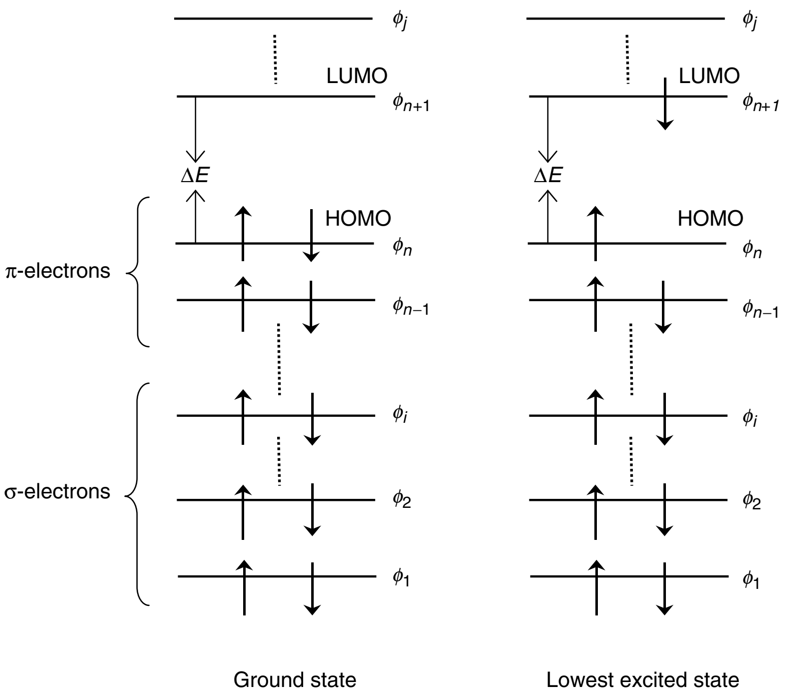

Figure 29 Energy level diagrams of molecular orbitals and electron configurations for ground and singlet excited states.

and excited states are commonly used for the description of electronic transitions in organic molecules (Figure 30). In Figure 30, the transition of an electron from HOMO to LUMO is expressed in terms of its spin states. The electronic transitions are expressed in terms of the difference in energy between the ground and excited states in the electronic-state diagram. The spin multiplicity of the states is implicitly indicated by the notations of S (singlet) or T (triplet). The ground state, S_0, and lowest singlet and triplet states, S_1 and T_1, are composed of multiple vibrational states, due to vibronic and rotation energy levels of the molecules.

When an energy larger than the HOMO–LUMO energy difference is absorbed by a molecule, either higher vibronic states within the S_1 states or higher singlet excited states S_2 and S_3 are produced. The higher vibronic states of S_1 relax to the lowest vibronic state of S_1 within a timescale of ~10^{-12} s. The higher energy singlet states such as S_2 and S_3 relax to the S_1 state via nonradiative, internal conversion (IC) processes. Triplet excited states are usually produced via an intersystem crossing (ISC) process from $S_1 \rightarrow T_1$, since the transition probability of direct excitation from S_0 into T_1 is very small. Also, the higher energy triplet states such as T_2 and T_3 relax to the T_1 state via nonradiative processes. Thus, radiative transitions take place as an electronic transition from the lowest excited states of S_1 or T_1 to the ground state S_0. The radiative transition from $S_1 \rightarrow S_0$ is classified as a spin-allowed transition and therefore the timescale of the transition is of the order of ~10^{-9} s. On the other hand, the timescale of the $T_1 \rightarrow S_0$ transition is much longer, ranging from micro- to milliseconds because the process is intrinsically spin-forbidden. The emission spectra of organic molecules often exhibit a vibronic structure because the ground state also contains vibronic and rotational fine structures.

Figure 31 shows schematically the relation between absorption and emission spectra. An emission spectrum looks like the mirror image of the electronic absorption spectrum of a molecule due to the presence of vibrational levels in each energy level. The emission wavelength for the radiative transition from the lowest S_1 state to the lowest S_0 state, the 0–0

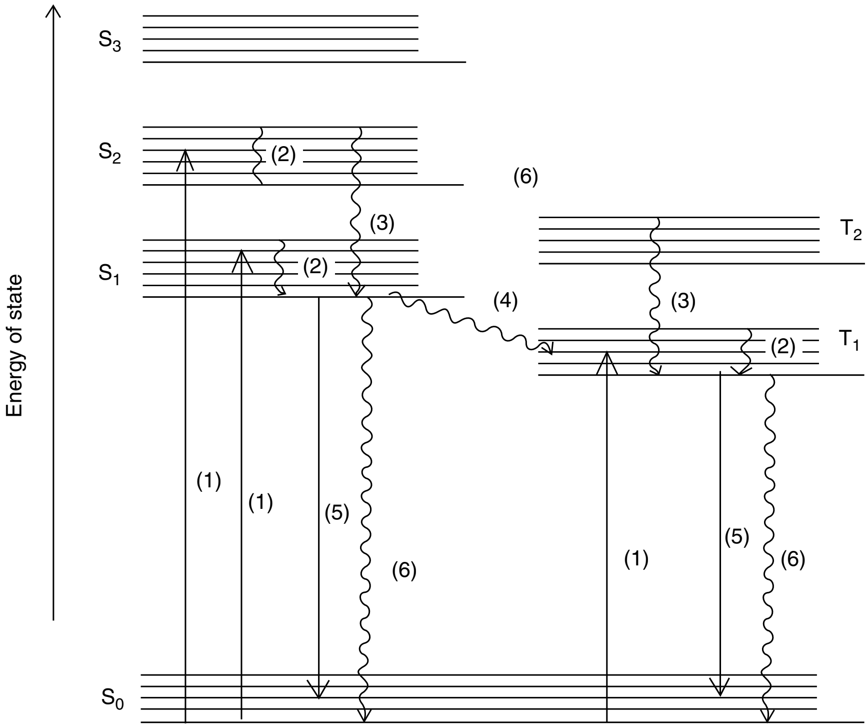

Figure 30 The Jablonski diagram, which explains photophysical processes in molecular systems: (1) light absorption, (2) vibrational relaxation, (3) internal conversion (IC), (4) intersystem crossing (ISC), (5) radiative transition, and (6) nonradiative transition.

emission, corresponds to the wavelength for the electronic transition from the lowest S_0 state to the lowest S_1 state, the 0–0 absorption. However, in the actual absorption and emission spectra, the peaks of the 0–0 transitions do not coincide with each other because of Stokes' shift.

2.5.3 Fluorescence of organic molecules in a solid state

Fluorescence in organic solids is essentially the same as that from the individual molecules of the solid. This is because molecular orbitals assumed for isolated molecules are only weakly perturbed in the solid state by the presence of weak van der Waals interactions among the molecules. However, one has to note that drastic changes of fluorescence can appear in solids because of the formation of intermolecular complexes and due to energy migration and transfer among the molecules.

Intermolecular complexes that are formed in their excited states, called excimers and exciplexes, give characteristic emissions at wavelengths different from those of the component molecules. An excimer is an excited-state complex formed between two same molecules. Aromatic hydrocarbons such as anthracene and perylene, for example, show a characteristic broad, featureless excimer fluorescence. On the other hand, exciplexes are excited-state complexes made of two different molecules. Further, charge–transfer interactions between donor and acceptor molecules sometimes cause the formation of CT-complexes, which have broad and redshifted weak fluorescence spectra. Such intermolecular complexes formed in their ground states also show changes in their absorption spectra. The absorption spectra of molecular aggregates with parallel arrangements are shifted significantly to shorter wavelengths compared with those of isolated component molecules, and their fluorescence spectra are also different. Molecular aggregates called

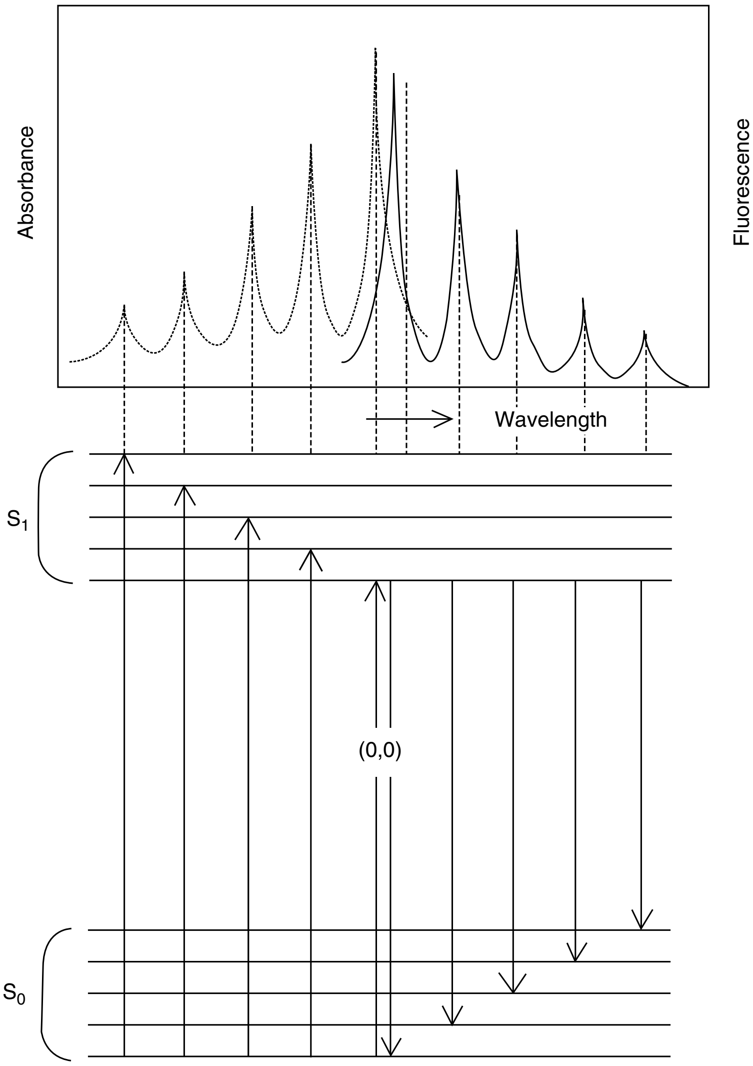

Figure 31 Explanation for the relationship between absorption and emission spectra based on the energy state diagram.

J-aggregates in which molecules are arranged in a head-to-tail fashion, in particular, show very sharp, redshifted absorption and fluorescence.

Very rapid and efficient migration or transfer of excitation energy among molecules occurs in a solid state, and these mechanisms induce drastic changes in fluorescence spectra. Anthracene crystals doped with a trace amount of tetracene, for example, never give characteristic anthracene emission, but yield the tetracene emission spectrum instead, although the absorption spectrum still looks the same as that of anthracene. The excited states produced in anthracene molecules by photoexcitation are efficiently transferred from anthracene to tetracene molecules. Therefore, the effects of trace amounts of impurities incorporated in organic solids should be carefully considered. In some cases, impurities act as effective exciton-quenching centers, reducing the intrinsically high fluorescence yields of organic solids. Here, we make a distinction between energy migration and energy transfer. Energy migration implies coherent energy transfer between like molecules, where energy is transferred as an exciton. Therefore, it is the dominant mechanism in single crystals where identical molecules are regularly aligned. On the other hand, energy transfer involving dipole–dipole interaction via the near-field electromagnetic interaction, i.e., the Förster mechanism, dominantly occurs in donor–acceptor molecular combinations where the emission spectrum of the donor and the absorption spectrum of the acceptor overlap. Therefore, the Förster mechanism occurs between singlet–singlet energy transfers where spin conservation is maintained. Further, the Dexter mechanism involving direct electron exchange between adjacent molecules dominates in the case of triplet–triplet energy transfer.

2.5.4 *Quantum yield of fluorescence*

The fluorescence "quantum yield" is given as the ratio of the emitted and absorbed photons and is normally determined experimentally through careful photoluminescence measurements using an integrated sphere. A more general definition of quantum yield of fluorescence is the ratio of the radiative transition rate, k_{r}, and total (radiative and non-radiative) transition rate, $k_{\mathrm{r}} + k_{\mathrm{nr}}$, from a singlet excited state to the ground state.

$$\phi_f = \frac{k_{\mathrm{r}}}{k_{\mathrm{r}} + k_{\mathrm{nr}}} \tag{101}$$

Here, nonradiative processes include the direct radiation-less transition from S_1 to S_0 and the ISC from S_1 to T_1. In a solid state, energy migration and energy transfer processes also need to be included. The experimentally determined quantum efficiency values of isolated molecules are not always useful for the evaluation of the efficiency of organic solids, because molecular aggregation occurs. For example, coumarins are laser dyes with high quantum yields of ~90% in dilute solutions, but they yield weak fluorescence in bulk solid states. Deactivation processes intrinsic to solid states, called concentration-quenching processes, occur in many compounds, although some aromatic hydrocarbons such as anthracene and pyrene show high quantum yields both as single molecules and crystals. The quantum yields of fluorescence are strongly dependent on temperature because thermal nonradiative decay processes are highly dependent on temperature. At temperatures lower than the liquid nitrogen temperature, almost all rotational and vibrational motions of pendant groups are frozen and quantum yields tend to be high.

2.5.5 *Organic fluorescent and phosphorescence compounds with high quantum yields*

Organic molecules with well-developed π-conjugated systems usually show intense electronic absorption in the ultraviolet to visible wavelength regions due to a transition from the bonding π^* orbital into the antibonding π^* orbital (i.e., a transition from S_0 to S_1 states). The absorption maxima shift to longer wavelengths as the length of the π-conjugated systems increases. Incorporation of heteroatoms such as nitrogen, oxygen, and sulfur within the π-conjugated systems usually causes a redshift in the absorption peaks. Attachment of electron-donating groups such as $-NH_2$, $-CH_3$, and $-OCH_3$ or electron-accepting groups such as $-CN$ and $-NO_2$ also causes redshifts in the absorption spectra. Organic compounds with strong absorptions in the near ultraviolet to visible regions usually exhibit visible fluorescence. The highest bonding π orbital and the lowest antibonding π^* orbital mainly govern the quantum yields of fluorescence, as well as do the emission peak wavelengths. However, it should be noted that nonbonding π orbitals play a role in determining quantum yields in some cases.[2] Organic fluorescent molecules can be classified into the following categories:[3]

1. Aromatic hydrocarbons and their derivatives. This category includes polyphenyl hydrocarbons, hydrocarbons with fused aromatic nuclei, and hydrocarbons with arylethylene and arylacetylene groups

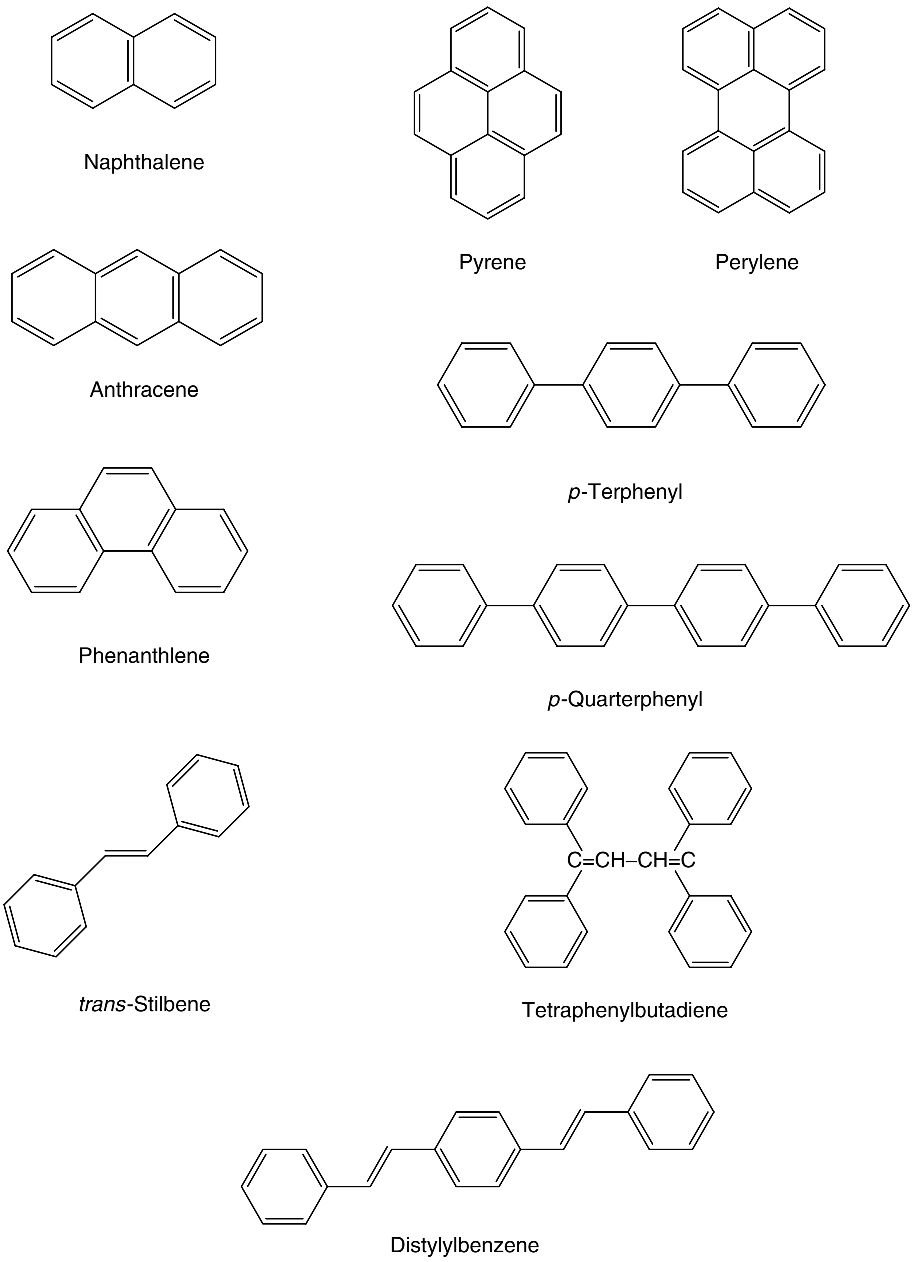

Naphthalene

Pyrene

Perylene

Anthracene

p-Terphenyl

Phenanthlene

p-Quarterphenyl

trans-Stilbene

Tetraphenylbutadiene

Distylylbenzene

Figure 32 Examples of aromatic hydrocarbons with intense fluorescence.

2. Compounds with five- and six-membered heterocycles
3. Compounds with carbonyl groups
4. Complexes of metals with organic ligands

Aromatic hydrocarbons form one of the most important groups among fluorescent compounds, which emit light in the violet to blue regions, and their quantum yields are fairly high even in crystalline states as well as in solutions[4]. Introduction of substituents can shift the fluorescence toward longer wavelengths. Naphthalene, anthracene, phenanthlene, pyrene, perylene, *p*-terphenyl, and *p*-quarterphenyl are typical examples of this class of compounds (Figure 32). Some polyphenyl hydrocarbons and hydrocarbons with fused aromatic nuclei show poor solubility in conventional organic solvents, which may limit their practical applications. Polyphenyl hydrocarbons with arylethylene and arylacetylene groups, such as *trans*-stilbenes, tetraphenylbutadiene, and distylylbenzenes, show very similar optical characteristics with polyphenyl hydrocarbons. Syntheses of these molecules are relatively easy, and therefore, these compounds are useful in various applications.

One of the most popular classes of fluorescent compounds comprises derivatives of five- and six-membered heterocycles. Intense fluorescence is observed, simply when heterocycles are incorporated in developed π-conjugated systems. Almost all the compounds of this group show this property, both in solution and in the crystalline state, with spectral ranges spanning the violet to the red. 2,5-Diphynyloxazole, 2-pheny-5-(4-biphenyl)-1,3,4-oxadiazole, and 1,3,5-triphenyl-2-pyrazoline, shown in Figure 32, are typical fluorescent compounds with five-membered heterocycles.

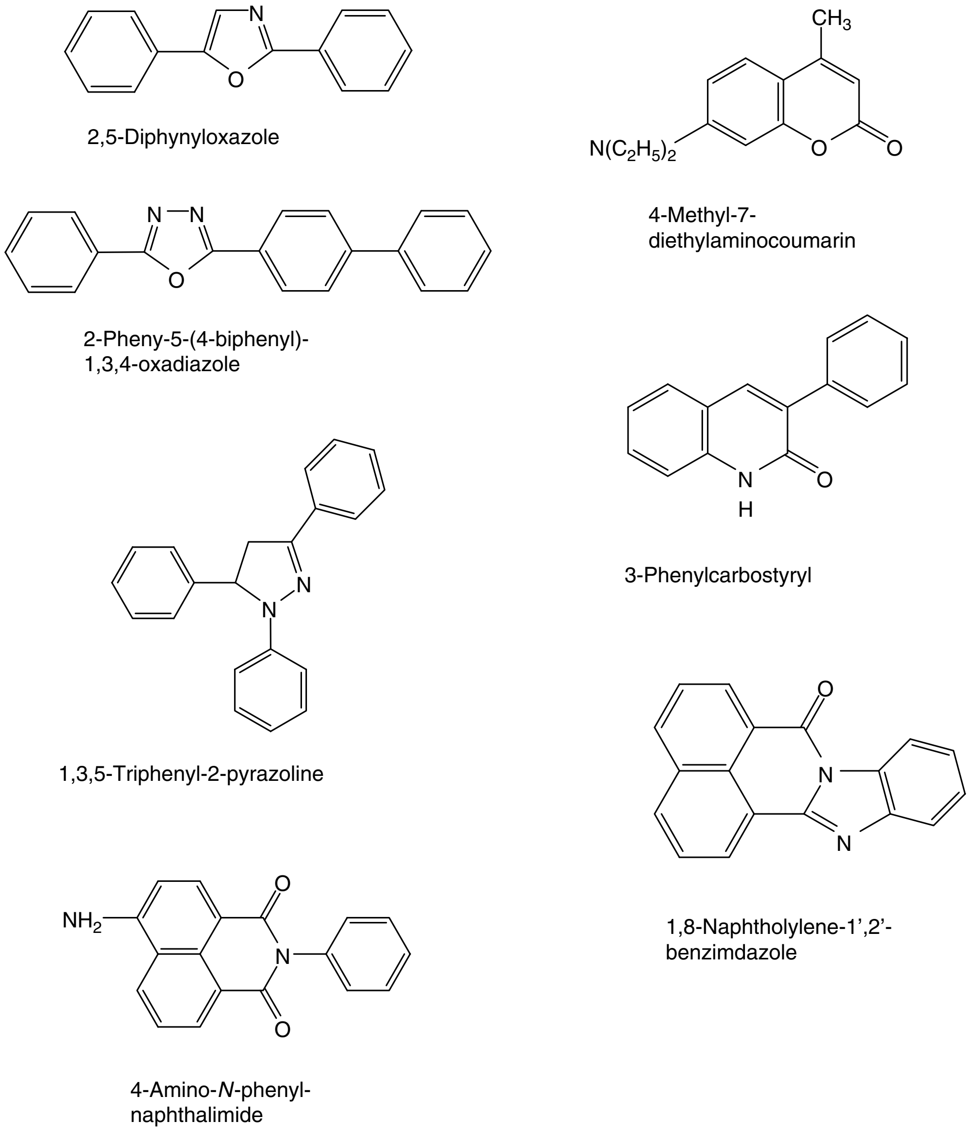
2,5-Diphynyloxazole
4-Methyl-7-diethylaminocoumarin
2-Pheny-5-(4-biphenyl)-1,3,4-oxadiazole
3-Phenylcarbostyryl
1,3,5-Triphenyl-2-pyrazoline
1,8-Naphtholylene-1’,2’-benzimdazole
4-Amino-*N*-phenyl-naphthalimide

Figure 33 Examples of fluorescence molecules containing heteroatoms.

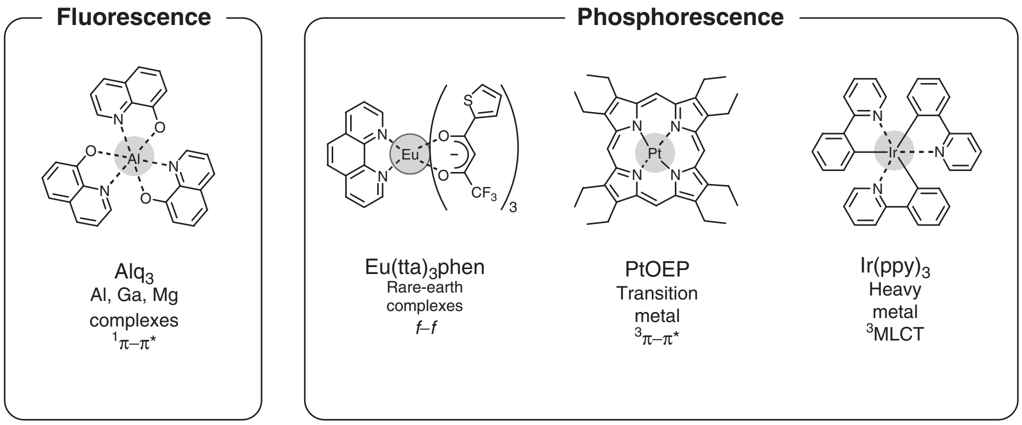

Figure 34 Examples of metal complexes demonstrating intense photoluminescence.

It is more difficult to describe the fluorescence behavior of aromatic compounds containing carbonyl groups, because a delicate balance exists between the π–π^* transition of π-conjugated systems, and the π–π^* transitions related to the carbonyl groups govern the transition from singlet excited states to the ground states. One finds a variety of useful compounds with intense fluorescence among carbonyl-containing molecules, for example, coumarins, carbostyryls, naphthalimides, and naphtholylene benzimdazoles. Typical carbonyl-containing compounds are depicted in Figure 33.

Metal complexes with organic ligands are another important class of fluorescent compounds (Figure 34).[5] Some of these compounds exhibit rather broad fluorescence spectra similar to those of organic ligands. One such compound is (8-hydroxyquinolino)aluminum, which has been used for organic thin-film electroluminescent devices. Metal complexes, such as some europium and terbium complexes, that exhibit narrow-band luminescence specific to incorporated metal ions are also known. Further, heavy metal complexes such as Ir, Pt, Ru, and Au complexes were recently revealed to have intense phosphorescence based on the transition of the metal-to-ligand charge transfer (MLCT) complex triplet state. Since the MLCT has a nature of mixing singlet and triplet excited states, radiative decays are allowed, leading to intense phosphorescence. In particular, Ir complexes have been widely developed in recent years, and iridium tris(phenypyridine), in particular, shows almost 100% phosphorescence efficiency.[6]

References

1. Pope, M. and Swenberg, C.E., *Electronic Processes in Organic Crystals*, Oxford University Press, New York, 1982, chap. 1.
2. Krasovitskii, B.M. and Bolotin, B.M., *Organic Luminescent Materials*, VCH Publishers, New York, 1988, chap. 7.
3. Krasovitskii, B.M. and Bolotin, B.M., *Organic Luminescent Materials*, VCH Publishers, New York, 1988, chap. 18.
4. Becker, R.S., *Theory and Interpretation of Fluorescence and Phosphorescence*, John Wiley & Sons, New York, 1969, chap. 13.
5. Yersin, H., Transition Metal and Rare Earth Compounds: Excited States, Transitions, Interactions I (Topics in Current Chemistry), Springer Verlag.
6. C. Adachi, Baldo, M.A., and Forrest, S.R., Nearly 100% internal quantum efficiency in an organic light-emitting device, *J. Appl. Phys.*, 90, 5048, 2001.

chapter two — section six

Fundamentals of luminescence

Yasuaki Masumoto

2.6 Luminescence of low-dimensional systems 71
References 82

2.6 Luminescence of low-dimensional systems

Low-dimensional systems discussed in this section are two-dimensional (2D) systems, one-dimensional (1D) systems, and zero-dimensional (0D) systems. 2D systems include layered materials and quantum wells; 1D systems include linear chain-like materials and quantum wires; and 0D systems include small microcrystallites and quantum dots. Optical properties of low-dimensional systems are substantially different from those of three-dimensional (3D) systems. The most remarkable modification comes from different distributions of energy levels and densities of states originating from the spatial confinement of electrons and holes.

Different distributions of energy levels in low-dimensional systems arise from the quantum confinement of electrons and holes. The simplest model for 2D systems is that of a particle in a box with an infinitely deep well potential, as is shown in Figure 35. The wavefunctions and energy levels in the well are known from basic quantum mechanics and are described by:

$$\psi_n(z) = \left(2/L_z\right)^{1/2} \cos\left(n\pi z/L_z\right) \tag{102}$$

$$E_n = \frac{\hbar^2}{2m}\left(\frac{\pi n}{L_z}\right)^2, \qquad n = 1,\ 2,\ 3,\ \ldots \tag{103}$$

In type-I semiconductor quantum wells, both electrons and holes are confined in the same wells. The energy levels for electrons and holes are described by:

$$E_e = E_g + \frac{\hbar^2}{2m_e^*}\left(\frac{\pi n_e}{L_z}\right)^2 + \frac{\hbar^2}{2m_e^*}\left(k_x^2 + k_y^2\right) \tag{104}$$

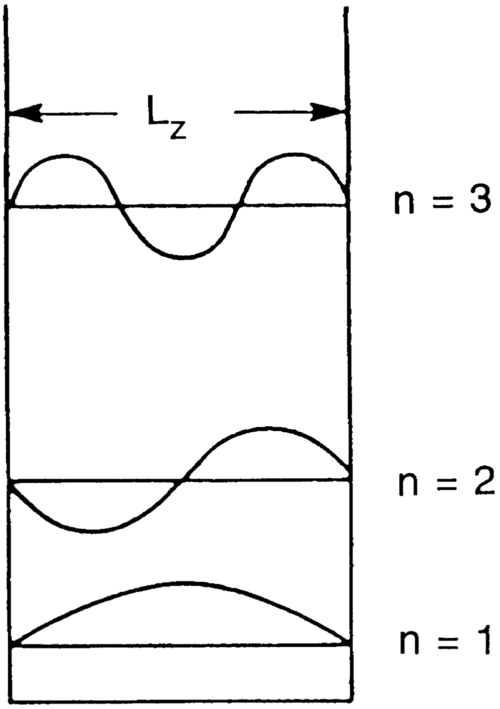

Figure 35 A particle in a box made of infinitely tall potential barriers.

$$E_h + \frac{\hbar^2}{2m_h^*}\left(\frac{\pi n_h}{L_z}\right)^2 + \frac{\hbar^2}{2m_h^*}\left(k_x^2 + k_y^2\right) \tag{105}$$

where m_e^* and m_h^* are the effective masses of electron and hole, respectively.

If electric dipole transitions are allowed from the valence band to the conduction band, the optical transition occurs from the state described by n_h, k_x, and k_y to the state described by n_e, k_x, and k_y. Therefore, the optical transition takes place at an energy:

$$E = E_e + E_h = E_g + \frac{\hbar^2}{2\mu}\left(\frac{\pi n}{L_z}\right)^2 + \frac{\hbar^2}{2\mu}\left(k_x^2 + k_y^2\right) \tag{106}$$

where μ is the reduced mass given by $\mu^{-1} = m_e^{*-1} + m_h^{*-1}$

It is well known that the joint density of states ρ_{3D} for the 3D for an allowed and direct transition in semiconductors is represented by:

$$\rho_{3D}(E) = \frac{1}{2\pi^2}\left(\frac{2\mu}{\hbar^2}\right)^{3/2}\left(E - E_g\right)^{1/2} \tag{107}$$

Here, E_g is the bandgap energy and μ is the reduced mass as above. The joint densities of states for 2D, 1D, and 0D systems are given, respectively, by the expressions

$$\rho_{2D}(E) = \frac{\mu}{\pi\hbar^2}\sum_n \theta\left(E - E_n - E_g\right) \tag{108}$$

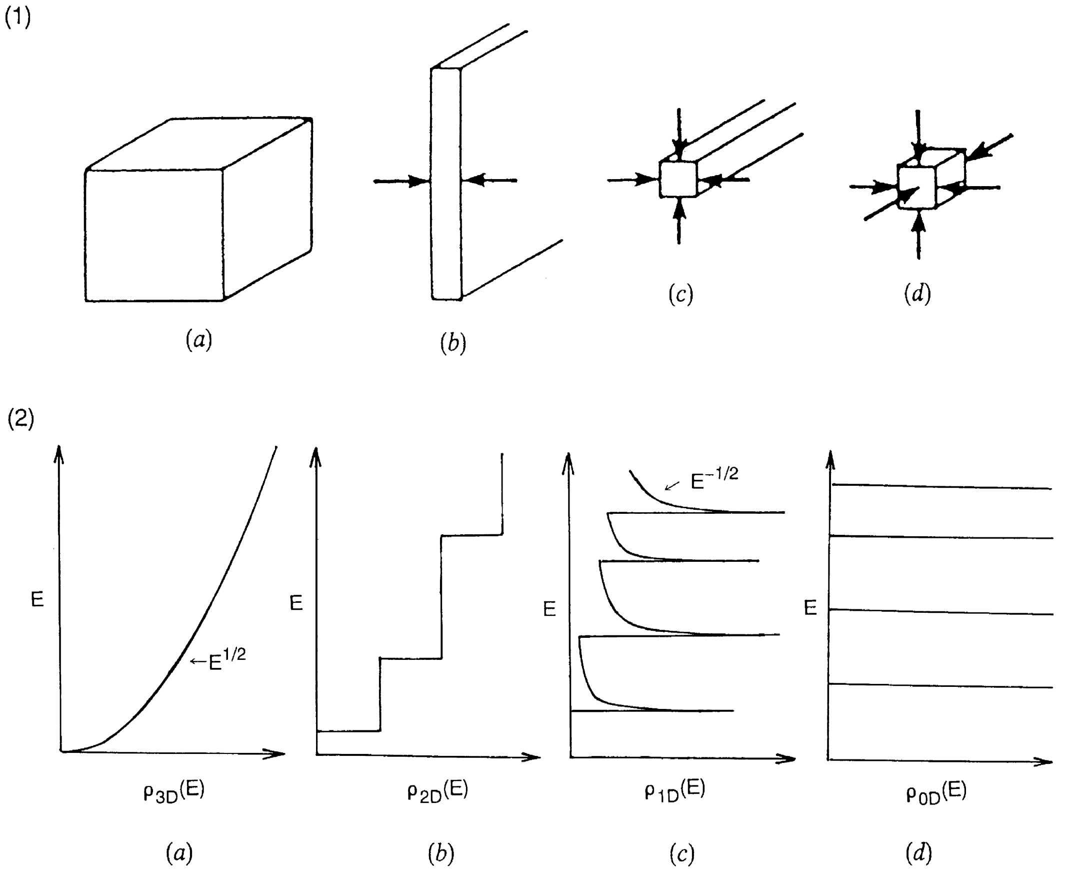

Figure 36 (1) Schematic illustrations of (a) 3D, (b) 2D, (c) 1D, and (d) 0D systems. (2) Densities of states for (a) 3D, (b) 2D, (c) 1D, and (d) 0D systems are shown.

$$\rho_{1D}(E) = \frac{(2\mu)^{1/2}}{\pi\hbar} \sum_{m,n} \frac{1}{\left(E - E_m - E_n - E_g\right)^{1/2}} \tag{109}$$

$$\rho_{0D}(E) = 2\sum_{l,m,n} \delta\left(E - E_l - E_m - E_n - E_g\right) \tag{110}$$

where θ is a step function and δ is a delta function. The sum of quantum confinement energies of electrons and holes are represented by E_l, E_m, and E_n, where E_l, E_m, and E_n refer to the three directions of spatial confinement. Figure 36 shows schematically the joint densities of states for 3D, 2D, 1D, and 0D systems given by Eqs. 107-110.

The optical absorption spectrum α(E) is proportional to the joint density of states, if the energy dependence of the optical matrix element and the other slowly varying energy dependence are neglected. As a result, the absorption spectral shapes of 3D, 2D, 1D, and 0D systems are well described by the joint density of states as shown in Figure 36.

Although the exciton effect has been neglected thus far, it dominates the absorption spectrum around the bandgap. The exciton is a composite of an electron and a hole due to the Coulomb attraction. As in the hydrogen atom, the Coulomb attraction forms bound levels of the exciton. The lowest-energy bound state is characterized by the effective

Rydberg energy Ry^* and the effective Bohr radius a_B^*. The lowest exciton state is lower than the unbound continuum state by Ry^*, and its radius is given by a_B^*. In the 3D case, the effective Rydberg energy and the effective Bohr radius are given by:

$$Ry^* = \frac{\mu}{\varepsilon^2 m_0} Ry \tag{111}$$

$$a_B^* = \frac{\varepsilon m_0}{\mu} a_B \tag{112}$$

where ε is the dielectric constant, m_0 is the electron mass, and Ry = 13.6 eV and a_B = 52.9 pm are the Rydberg energy and Bohr radius of the hydrogen atom, respectively. The exciton energy levels are described by:

$$E_n = E_g - \frac{Ry^*}{n^2}, \qquad (n = 1,\ 2,\ 3,\ \ldots) \tag{113}$$

and the absorption spectrum is modified as shown in Figure 37.[1]

In the 2D case, the binding energy of the lowest-energy exciton is enhanced to be $4Ry^*$, because the exciton energy levels are described by:

$$E_{n,m} = E_g + E_n - \frac{Ry^*}{\left(m + \frac{1}{2}\right)^2}, \qquad (m = 0,\ 1,\ 2,\ \ldots) \tag{114}$$

where *n* is the quantum number for electrons and holes, and *m* is the quantum number for their relative motion. The wavefunction of a 2D exciton shrinks in the 2D plane and its radius becomes $(\sqrt{3/4})\ a_B^*$. This means that the overlap between the electron wavefunction and hole wavefunction is enhanced compared with the 3D case. As a result, the oscillator strength of a 2D exciton is larger than that of a 3D exciton. The oscillator strength of a 2D nth exciton per unit layer f_n^{2D} is written as:

$$f_n^{2D} = \frac{n^3}{\left(n + \frac{1}{2}\right)^3} a_B^* f_n^{3D} \tag{115}$$

where f_n^{3D} is the oscillator strength of the nth 3D exciton. The enhancement of the exciton binding energy and the oscillator strength lead to the stability of the 2D exciton at room temperature. Figure 38 shows an example of the observation of a 2D exciton in the optical absorption spectrum of GaAs quantum wells at room temperature.[2]

The binding energy and the oscillator strength of an exciton increase with a decrease in size and dimension.[3] Figure 39 shows the increase of the binding energy of 2D, 1D, and 0D excitons with the decrease in size and dimensionality. Here, the 1D exciton is confined in a square parallelepiped and the 0D exciton is confined in a cube, where the side-length of the square or the cube is L. Since the radiative lifetime is inversely proportional to the oscillator strength, it decreases with a decrease in size and dimensionality. Shortening of the radiative lifetime of the exciton with decreasing size is observed in GaAs quantum wells.[4]

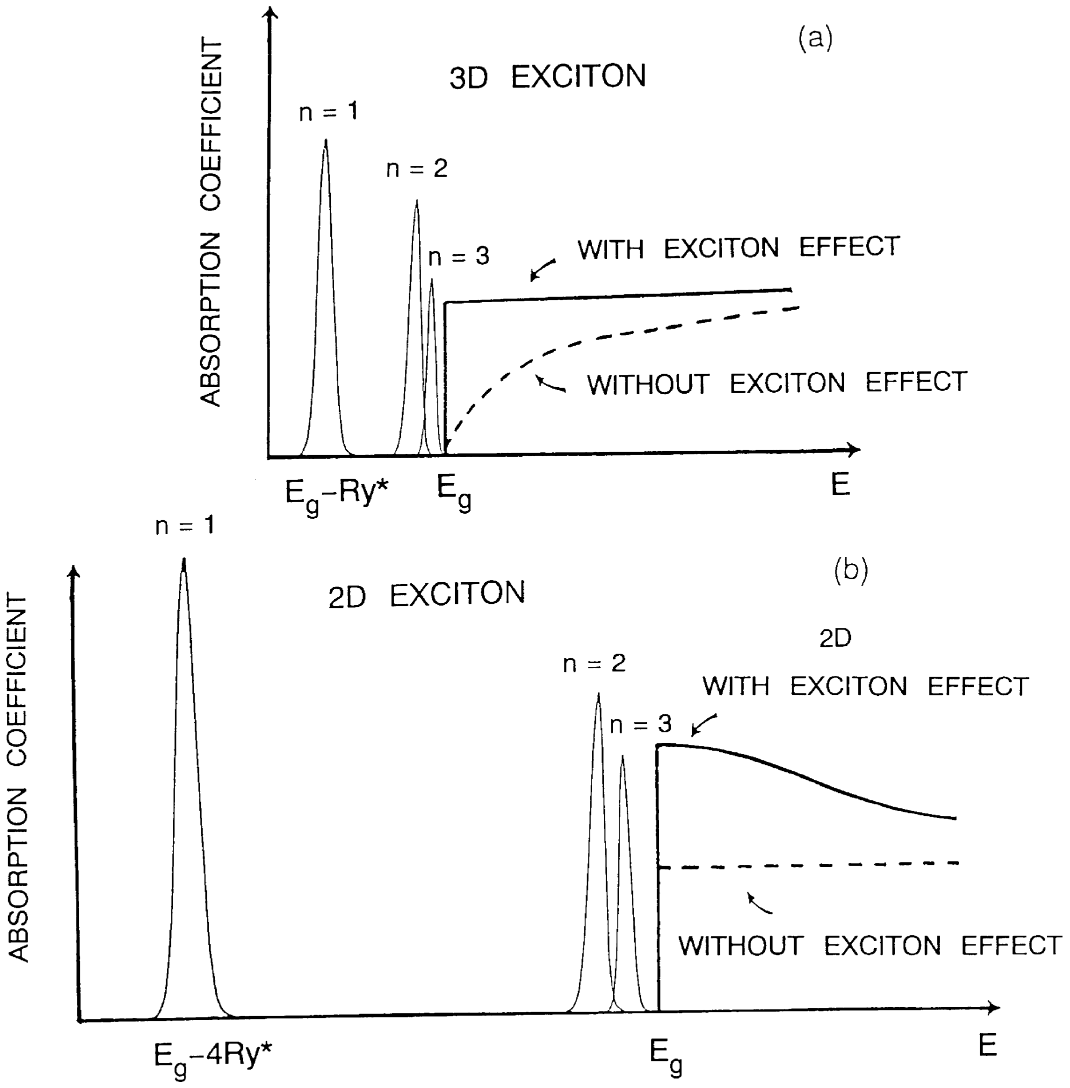

Figure 37 Absorption spectra for (a) 3D or (b) 2D excitons. Above the energy gap E_g, the absorption coefficient is enhanced from its value by the Sommerfeld factor, as a result of the Coulomb interaction between electrons and holds. (From Weisbuch, C. and Vinter, B., *Quantum Semiconductor Structures*, Academic Press, Boston, 1991. With permission.)

Discussion thus far has focused on the optical properties of low-dimensional systems, with special emphasis on semiconductor quantum wells. However, in phosphors, the more important low-dimensional systems are small semiconductor microcrystallites and quantum dots. Many kinds of nanometer-size microcrystallites made by various means behave as quantum dots. For example, microcrystallites of II-VI and I-VII compounds can be chemically grown in polymers, solutions, and zeolites. Porous Si, made by means of electrochemical etching, is regarded as an ensemble of quantum dots and quantum wires. III-V semiconductors GaAs and GaInAs microcrystallites can be epitaxially grown on the oriented GaAs crystal surface.

The above-mentioned, nanometer-size semiconductor microcrystallites can be regarded as quantum dots in the sense that they show the quantum size effect. That is with a decrease in size, the absorption bands show a blue-shift due to this effect, because

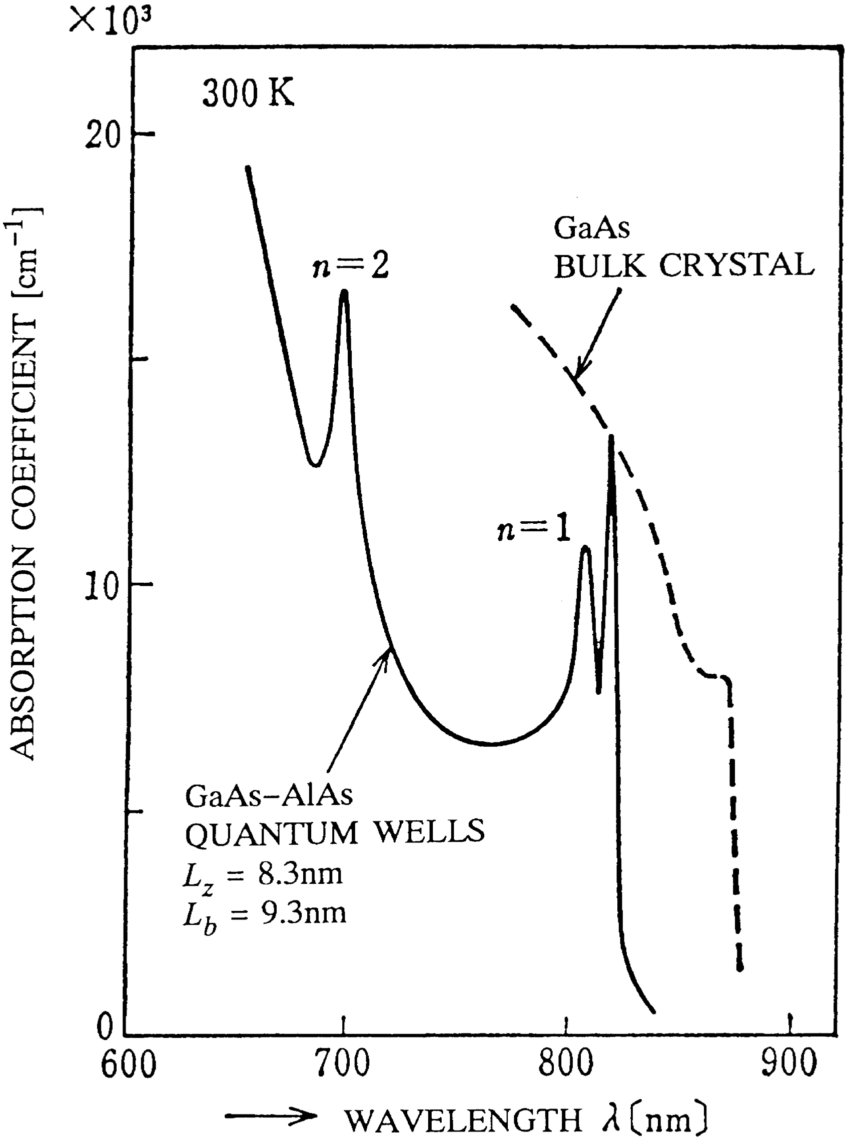

Figure 38 Absorption spectra of GaAs-AlAs quantum well structures and a bulk GaAs crystal at 300K. (From Ishibashi, T., Tarucha, S., and Okamoto, H., *Inst. Phys. Conf. Ser. No. 63*, 1982, chap. 12, 587. With permission.)

the spatial confinement of electrons, holes, and excitons increases the kinetic energy of these particles. Simultaneously, the same spatial confinement increases the Coulomb interaction between electrons and holes. The quantum confinement effect can be classified into three categories[5]: the weak confinement, the intermediate confinement, and the strong confinement regimes, depending on the relative size of the radius of microcrystallites R compared to an electron a_e^*, a hole a_h^*, and an exciton Bohr radius a_B^*, respectively. Here, the microcrystallites are assumed to be spheres, and a_e^* and a_h^* are defined, respectively, by:

$$a_e^* = \frac{\hbar^2 \varepsilon}{m_e^* e^2} \quad \text{and} \quad a_h^* = \frac{\hbar^2 \varepsilon}{m_h^* e^2} \tag{116}$$

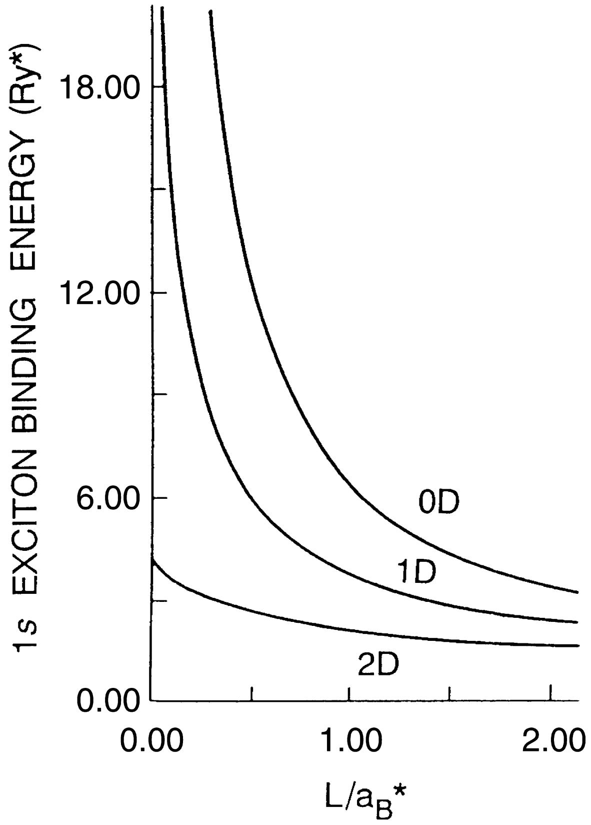

Figure 39 Binding energies of 1*s* excitons in a plane L thick, a square parallelepiped, and a cube of a side L. (From Matsuura, M. and Kamizato, T., *Surf. Sci.*, 174, 183, 1986. With permission.)

The exciton Bohr radius a_B^* is given by:

$$a_B^* = \frac{\hbar^2 \varepsilon}{\mu e^2} \tag{117}$$

and an inequality a_e^*, $a_h^* < a_B^*$ holds.

- *Strong confinement* ($R << a_e^*$, $a_h^* < a_B^*$). The individual motion of electrons and holes is quantized and the Coulomb interaction energy is much smaller than the quantized kinetic energy. Nanometer-size GaAs, CdS, CdSe, and CdTe microcrystallites are good examples of the strong confinement regime. The ground-state energy is:

$$E(R) = E_g + \frac{\hbar^2 \pi^2}{2\mu R^2} - \frac{1.786 e^2}{\varepsilon R} - 0.248 Ry^* \tag{118}$$

where the second term is the kinetic energy of electrons and holes, the third term is the Coulomb energy, and the last term is the correlation energy.

- *Intermediate confinement* ($a_h^* < R < a_e^*$). In this case, the electron motion is quantized, while the hole is bound to the electron by their Coulombic attraction. Many II-VI microcrystallites belong to the intermediate confinement regime.

- *Weak confinement* ($R >> a_B^* > a_e^*, a_h^*$). In this case, the center-of-mass motion of excitons is quantized. Nanometer-size CuCl microcrystallites are typical examples of the weak confinement regime; the ground-state energy is written as:

$$E = E_g - Ry^* + \frac{\hbar^2\pi^2}{2MR^2} \tag{119}$$

where $M = m_e^* + m_h^*$ is the translational mass of the exciton.

Typical experimental data for three categories are shown in Figure 40.[6] CdS, CuBr, and CuCl microcrystallites belong to strong, intermediate, and weak confinement regimes, respectively. With a decrease in microcrystallite size, the continuous band changes into a series of discrete levels in CdS, although the levels are broadened because of the size distribution. In the case of CuCl, the exciton absorption bands show blue-shifts with a decrease in size.

The luminescence of semiconductor microcrystallites not only depends on the microcrystallites themselves, but also on their surfaces and their surroundings since the surface:volume ratio in these systems is large. The luminescence spectrum then depends on the preparation conditions of microcrystallites. Thus it is that some samples show donor-acceptor pair recombination, but other samples do not; in others, the edge luminescence at low temperature consists of exciton and bound exciton luminescence. The exciton luminescence spectrum of many samples shows Stokes shift from the absorption spectrum, indicating the presence of localized excitons. Typical examples of the luminescence spectra of CdSe microcrystallites and CuCl microcrystallites are shown in Figures 41 and 42.[7,8]

Impurities or defects in insulating crystals often dominate their luminescence spectra; this is also the case with semiconductor microcrystallites, but additional effects occur in the latter. Nanometer-size semiconductor microcrystallites can be composed of as few as 10^3–10^6 atoms; if the concentration of centers is less than ppm, considerable amounts of the microcrystallites are free from impurities or defects. This conjecture is verified in AgBr microcrystallites, which are indirect transition materials.[9] Figure 43 shows luminescence spectra of AgBr microcrystallites with average radii of 11.9, 9.4, 6.8, and 4.2 nm. The higher-energy band observed at 2.7 eV is the indirect exciton luminescence, and the lower-energy band observed at 2.5 eV is the bound exciton luminescence of iodine impurities. In contrast to AgBr bulk crystals, the indirect exciton luminescence is strong compared with the bound exciton luminescence at iodine impurities. The ratio of the indirect exciton luminescence to the bound exciton luminescence at iodine impurities increases with the decrease in size of AgBr microcrystallites. This increase in ratio shows that the number of impurity-free microcrystallites increases with the decrease in size. Simultaneously, the decay of the indirect exciton luminescence approaches single exponential decay approximating the radiative lifetime of the free indirect exciton. The blue-shift of the indirect exciton luminescence shown in Figure 43 is due to the exciton quantum confinement effect, as discussed previously.

Nanometer-size semiconductor microcrystallites can be used as a laser medium.[10] Figure 44 shows the lasing spectrum of CuCl microcrystallites. When the microcrystallites embedded in a NaCl crystal are placed in a cavity and excited by a nitrogen laser, lasing occurs at a certain threshold. The emission spectrum below the threshold, shown in Figure 44, arises from excitonic molecule (biexciton) luminescence. Above the threshold, the broad excitonic molecule emission band is converted to a sharp emission spectrum having a maximum peak at 391.4 nm. In this case, the lasing spectrum is composed of a few longitudinal modes of the laser cavity consisting of mirrors separated by 0.07 nm. The optical gain of the CuCl microcrystallites compared with that in a bulk CuCl sample is found to be much larger. The high optical gain of CuCl microcrystallites comes from the spatial confinement of excitons, resulting in the enhanced formation efficiency of excitonic molecules.

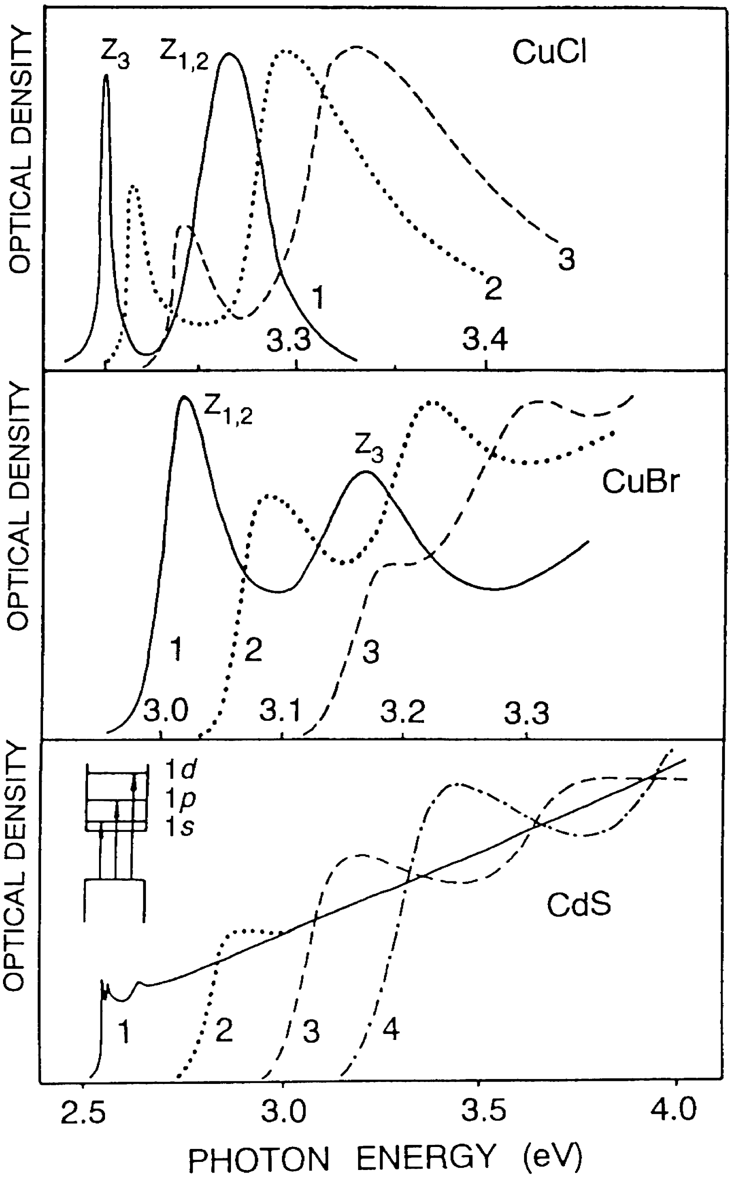

Figure 40 Absorption spectra at 4.2K for CuCl, CuBr, and CdS microcrystallites. For CuCl, the average radius R = 31 nm (1), 2.9 nm (2), and 2.0 nm (3); for CuBr, R = 24 nm (1), 3.6 nm (2), and 2.3 nm (3); for CdS, R = 33 nm (1), 2.3 nm (2), 1.5 nm (3), and 1.2 nm (4). (From Ekimov, A.I., *Phyica Scripta T*, 39, 217, 1991. With permission.)

After the initial report of visible photoluminescence from porous Si,[11] much effort has been devoted to clarify the mechanism of the photoluminescence. Figure 45 shows a typical example of a luminescence spectrum from porous Si. As the first approximation, porous Si made by electrochemical etching of Si wafers can be treated as an ensemble of quantum dots and quantum wires. However, real porous Si is a much more complicated system, consisting of amorphous Si, SiO_2, Si-oxygen-hydrogen compounds, Si microcrystallites, and Si wires. This complexity obscures the quantum size effect with other effects, and the physical origin of the visible luminescence from porous Si remains a puzzle. Depending on the sample preparation method, porous Si shows red, green, or blue luminescence. The

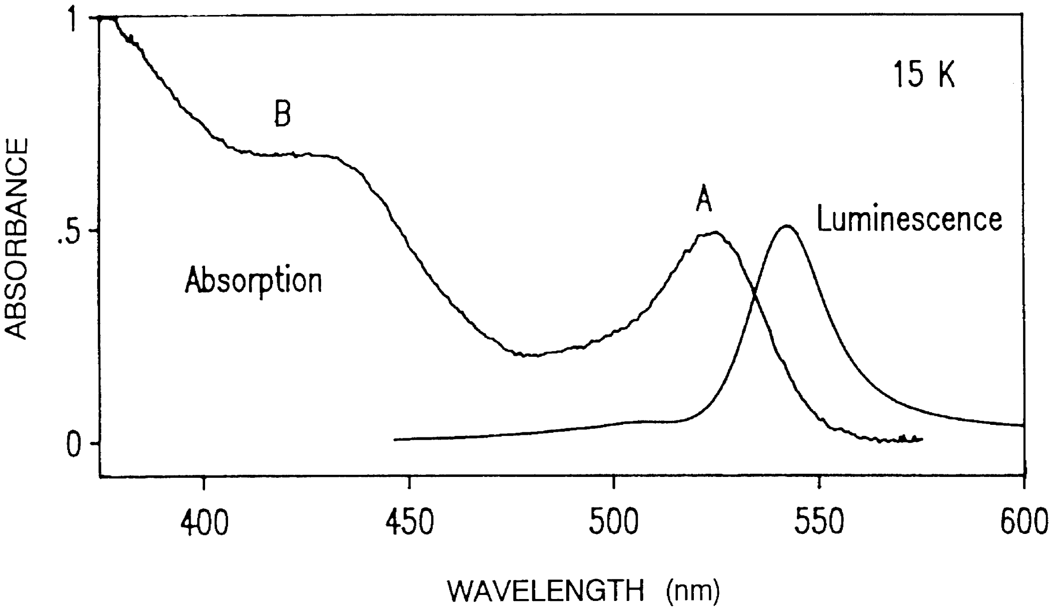

Figure 41 Absorption and luminescence spectra of wurtzite CdSe microcrystallites (R = 1.6 nm). (From Bawendi, M.G., Wilson, W.L., Rothberg, L., et al., *Phys. Rev. Lett.*, 65, 1623, 1990. With permission.)

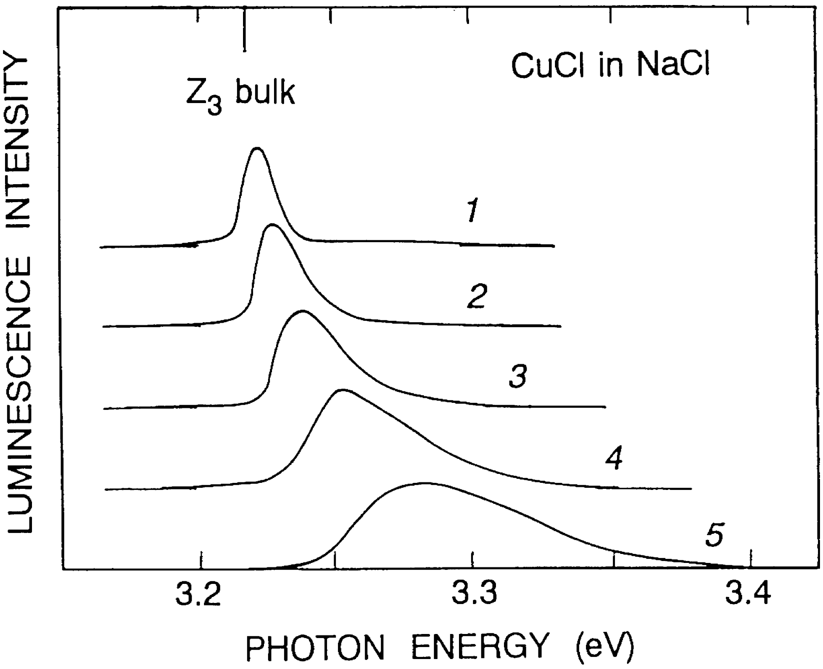

Figure 42 Exciton luminescence spectra of CuCl microcrystallites at 77K. The average radius R is 5.7 nm (1), 4.9 nm (2), 3.4 nm (3), 2.7 nm (4), and 2.2 nm (5). The energy of Z_3 exciton for bulk CuCl crystals at 77K is indicated by a vertical bar. (From Itoh, T., Iwabuchi, Y., and Kataoka, M., *Phys. Stat. Solidi (b)*, 145, 567, 1988. With permission.)

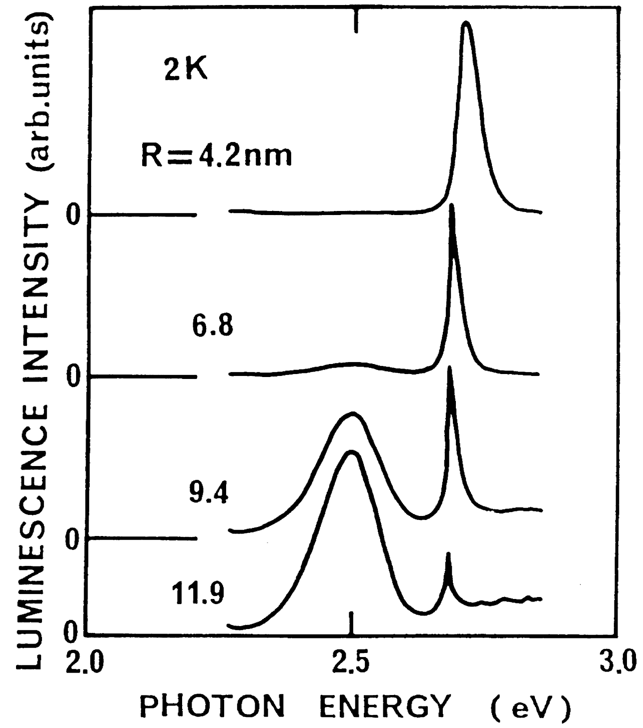

Figure 43 Photoluminescence spectra of AgBr microcrystallites at 2K. The average radius R of microcrystallites is 11.9, 9.4, 6.8, and 4.2 nm. The luminescence spectra are normalized by their respective peak intensities. The 2.7-eV band is indirect exciton luminescence, and the 2.5-eV band is bound exciton luminescence at iodine impurities. (From Masumoto, Y., Kawamura, T., Ohzeki, T., and Urabe, S., *Phys. Rev.*, B446, 1827, 1992. With permission.)

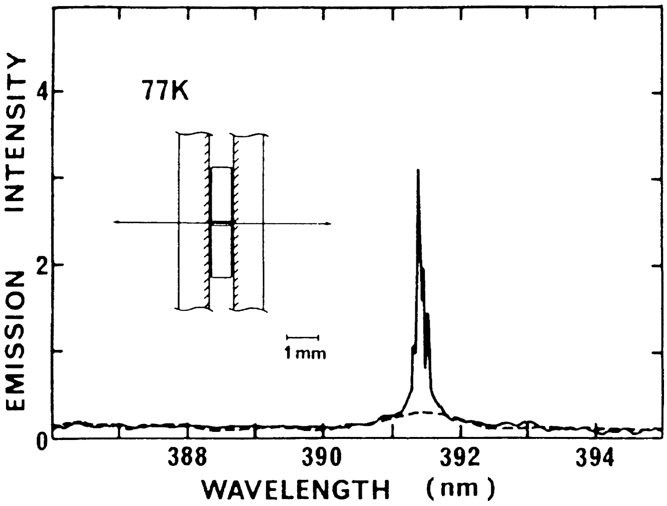

Figure 44 Emission spectra of the laser device made of CuCl microcrystallites at 77K below and above the lasing threshold. The threshold I_{th} is about 2.1 MW cm^{-2}. The solid line shows the spectrum under the excitation of 1.08 I_{th}. The dashed line shows the spectrum under the excitation of 0.86 I_{th}. (From Matsumoto, Y., Kawamura, T., and Era, K., *Appl. Phys. Lett.*, 62, 225, 1993. With permission.)

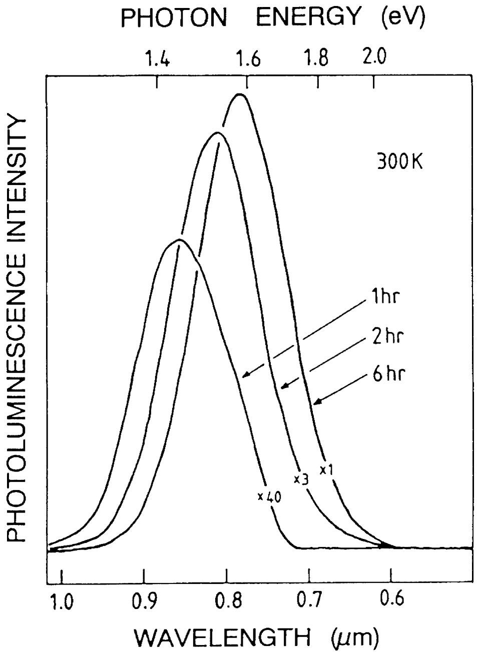

Figure 45 Room-temperature photoluminescence from the porous Si. Anodization times are indicated. (From Canham, L.T., *Appl. Phys. Lett.*, 57, 1046, 1990. With permission.)

photoluminescence quantum efficiency of porous Si exhibiting red luminescence is as high as 35%, but its electroluminescence quantum efficiency is 0.2% Light-emitting diodes made of porous Si have also been demonstrated but the quantum efficiency is too low for practical application. If the electroluminescence quantum efficiency is improved substantially, porous Si will be used in light-emitting devices because Si is the dominant material in the semiconductor industry.

References

1. Weisbuch, C. and Vinter, B., *Quantum Semiconductor Structures*, Academic Press, Boston, 1991.
2. Ishibashi, T., Tarucha, S., and Okamoto, H., Int. Symp. GaAs and Related Compounds, Oiso, 1981, Inst. Phys. Conf. Ser. No. 63, 1982, chap. 12, 587.
3. Matsuura, M. and Kamizato, T., *Surf. Sci.*, 174, 183, 1986; Masumoto, Y. and Matsuura, M., *Solid State Phys. (Kotai Butsuri)*, 21, 493, 1986 (in Japanese).
4. Feldmann, J., Peter, G., Göbel, E.O., Dawson, P., Moore, K., Foxon, C., and Elliott, R.J., *Phys. Rev. Lett.*, 59, 2337, 1987.
5. Yoffe, A.D., *Adv. Phys.*, 42, 173, 1993.
6. Ekimov, A.I., *Phyica Scripta T*, 39, 217, 1991.
7. Bawendi, M.G., Wilson, W.L., Rothberg, L., Carroll, P.J., Jedju, T.M., Steigerwald, M.L., and Brus, L.E., *Phys. Rev. Lett.*, 65, 1623, 1990.
8. Itoh, T., Iwabuchi, Y., and Kataoka, M., *Phys. Stat. Solidi (b)*, 145, 567, 1988.
9. Matsumoto, Y., Kawamura, T., Ohzeki, T., and Urabe, S., *Phys. Rev.*, B446, 1827, 1992.
10. Masumoto, Y., Kawamura, T., and Era, K., *Appl. Phys. Lett.*, 62, 225, 1993.
11. Canham, L.T., *Appl. Phys. Lett.*, 57, 1046, 1990.
12. *Properties of Porous Silicon*, Canham, L., ed., The Institute of Electrical Engineers, 1997.

Note: a). An updated discussion on the size affect on radiative properties alluded to in Reference 10 above appears in Chapter 4.
b). A recent reference on the optical properties of porous silicon is *Properties of Porous Silicon*, Canham, L., Ed., Institute of Electrical Engineers, 2005.

chapter two — section seven

Fundamentals of luminescence

Eiichiro Nakazawa

Contents

2.7 Transient characteristics of luminescence 83
  2.7.1 Decay of luminescence 83
    2.7.1.1 Decay of fluorescence 84
    2.7.1.2 Quasistable state and phosphorescence 86
    2.7.1.3 Traps and phosphorescence 87
  2.7.2 Thermoluminescence 90
  2.7.3 Photostimulation and photoquenching 95
References 97

2.7 Transient characteristics of luminescence

This section focuses on transient luminescent phenomena, that is, time-dependent emission processes such as luminescence after-glow (phosphorescence), thermally stimulated emission (thermal glow), photo (infrared)-stimulated emission, and photoquenching. All of these phenomena are related to a quasistable state in a luminescent center or an electron or hole trap.

2.7.1 Decay of luminescence

Light emission that persists after the cessation of excitation is called *after-glow.* Following the terminology born in the old days, luminescence is divided into fluorescence and phosphorescence according to the duration time of the after-glow. The length of the duration time required to distinguish the two is not clearly defined. In luminescence phenomena in inorganic materials, the after-glow that can be perceived by the human eye, namely that persisting for longer than 0.1 s after cessation of excitation, is usually called phosphorescence. Fluorescence implies light emission during excitation. Therefore, fluorescence is the process in which the emission decay is ruled by the lifetime (<10 ms) of the emitting state of a luminescence center, while the phosphorescence process is ruled by a quasistable state of a center or a trap.

In organic molecules, fluorescence and phosphorescence are distinguished by a quite different definition. The two are distinguished by whether the transition to emit light is allowed or forbidden by spin selection rules. Light emission due to an allowed transition is called *fluorescence*, while that due to a forbidden transition, usually showing a long after-glow, is called *phosphorescence* (see 2.5).

2.7.1.1 Decay of fluorescence

The decay process of the luminescence intensity $I(t)$ after the termination of excitation at $t = 0$ is generally represented by an exponential function of the elapsed time after the excitation.

$$I(t) = I_0 \exp(-t/\tau) \tag{120}$$

where τ is the decay time constant of the emission. It should be noted that the emission decay curve of nonlocalized centers, donor-acceptor pairs for example, is not always represented in the exponential form of Eq. 120. (See 2.4.)

If one denotes the number of excited luminescence centers in a unit volume by n^*, and the radiative and nonradiative transition probabilities by W_R and W_{NR}, respectively, then the rate equation for n^* is:

$$\frac{dn^*}{dt} = -(W_R + W_{NR})n^* \tag{121}$$

and the solution of this equation is:

$$n^*(t) = n_0^* \exp\left[-(W_R + W_{NR})t\right] \tag{122}$$

Here, n_0^* is the value at $t = 0$, that is, at the end-point of excitation or, in other words, at the start point of the after-glow.

Therefore, the lifetime of the center, which corresponds to the elapsed time for n^* to be decreased by the factor of e^{-1} of n_0^*, is $(W_R + W_{NR})^{-1}$. Since the emission intensity is proportional to n^*, the decay time of the after-glow in Eq. 120 is equal to the lifetime of the center:

$$\tau = (W_R + W_{NR})^{-1} \tag{123}$$

and the luminescence efficiency of the center is given by:

$$\eta = \frac{W_R}{W_R + W_{NR}} \tag{124}$$

The radiative transition probability W_R of an emitting state is the summation of the spontaneous emission probability $A_{m\to n}$ from the state m to all the final states n, (see Eq. 29)

$$W_R = \sum_n A_{m\to n} = \sum_n \frac{1}{\tau_{mn}} \tag{125}$$

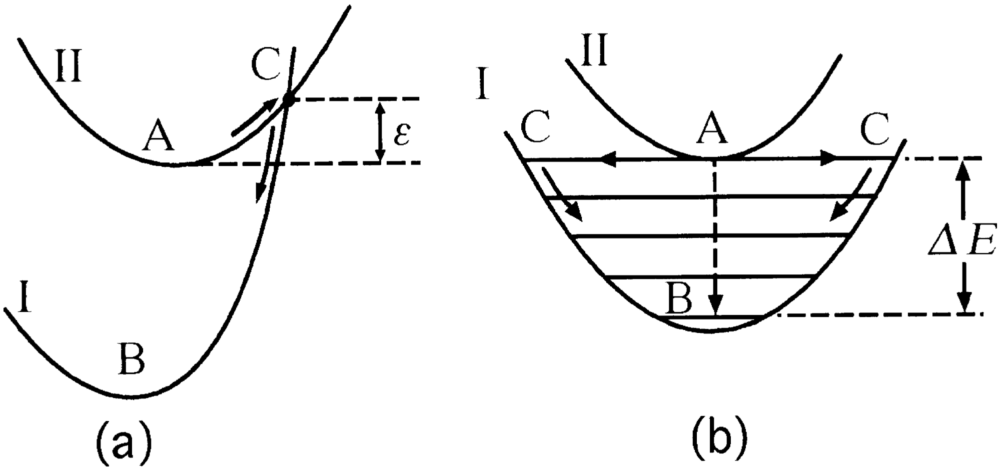

Figure 46 Configurational coordinate models of nonradiative relaxation processes: thermal activation type (a), and multiphonon type (b).

where τ_{mn} is given by Eqs. 32 or 35. The ratio of the transition probability to a particular final state n to W_R, $A_{m\to n}/W_R$, is called the *branching ratio*.

While the nonradiative transition probability W_{NR} is generally ruled by thermal relaxation processes (i.e., the emission of energy into lattice vibrations), it is also increased by the effect of resonant energy transfer between optical centers. (See 2.8.1.)

The thermal relaxation in a luminescence center can be divided into two types of mechanisms as shown by the two configurational coordinate diagrams (a) and (b) in Figure 46. In the first type (a), the center is thermally activated from point A, the point of the lowest energy on the exited state II, to the crossing point C where the electronic states of the excited and ground states are intermixed, and then thermally released from C to B on the ground state I. The energy ε necessary to excite the center from A to C is called the *thermal activation energy*. The probability that the center will make the transition from state II to state I by thermal activation via point C is generally given by:

$$a = s\exp\left(\frac{-\varepsilon}{kT}\right) \tag{126}$$

Therefore, the nonradiative transition probability by thermal activation is given by:

$$W_{NR} = a_{II\to I} = s\exp\left(\frac{-\varepsilon}{kT}\right) \tag{127}$$

where k is the Boltzmann constant and s is the frequency factor. This type of nonradiative transition is strongly dependent on temperature, resulting in thermal quenching, that is, the decrease of emission efficiency and shortening of the emission decay time at high temperature (see Eqs. 123 and 124).

An example of the thermal quenching effect is shown in Figure 47 for $Y_2O_2S:Yb^{3+}$.[1] The emission from the charge-transfer state (CTS) of Yb^{3+} ions at 530 nm is strongly reduced by thermal quenching at high temperature. The 4*f* emission under CTS excitation (313 nm), however, is increased at high temperature due to the increased amount of excitation transfer from the CTS. The Figure also shows that, as expected, the emission from the

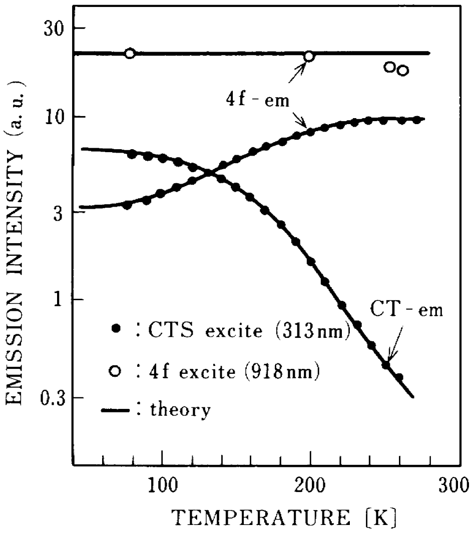

Figure 47 Temperature dependence of two types of the emission in Y_2O_2S:Yb^{3+}, from the CTS (charge-transfer state) and from a 4*f*-emitting level of Yb^{3+} ions. (From Nakazawa, E., *J. Luminesc.*, 18/19, 272, 1979. With permission.)

4*f* level at 930 nm is not so thermally quenched under direct 4*f* excitation into the emitting level (918 nm).

The second type of nonradiative transition is a multiphonon process shown in Figure 46b. This type is often observed in the relaxation between the 4*f* excited levels of rare-earth ions, where no cross-point exists between curves I and II in the configuration coordinate diagram because of the similarity of the electronic states. The transition between states I and II occurs at point A, where an energy gap ΔE exists between the states: namely, the transition from the pure electronic state of II to the electron-phonon-coupled state of I with n phonons takes place at A, which is followed by the instantaneous transfer to point C and relaxation to B. The nonradiative transition probability is, therefore, dependent on ΔE or n, the number of phonons necessary to fill the energy gap, since $\Delta E = n \ \omega_p$, where ω_p is the largest phonon energy. The nonradiative multiphonon transition probability is then given by:[2]

$$W_{NR}(\Delta E) = W_{NR}(0)e^{-\alpha \Delta E} \tag{128}$$

where α depends on the character of the phonon (lattice vibration). Since the process is mainly due to the spontaneous emission of phonons, the temperature dependence of the probability is small. An experimental result[2] showing the applicability of Eq. 128 is shown in Figure 48.

2.7.1.2 *Quasistable state and phosphorescence*

If one of the excited states of a luminescent center is a quasistable state (i.e., an excited state with very long lifetime), a percentage of the centers will be stabilized in that state during excitation. After excitation has ceased, after-glow is caused by the thermal activation of the state. This situation is illustrated using the configurational coordinate diagram in Figure 49, where state III is a quasistable state and state II is an emitting state with a radiative transition probability W_R. The center, once stabilized at A', transfers from state III to state II by thermal activation via point C. The probability of this activation, $a_{III \to II}$, is given by Eq. 126. Then, if $W_R \gg a_{III \to II}$, the decay time constant of the emission becomes

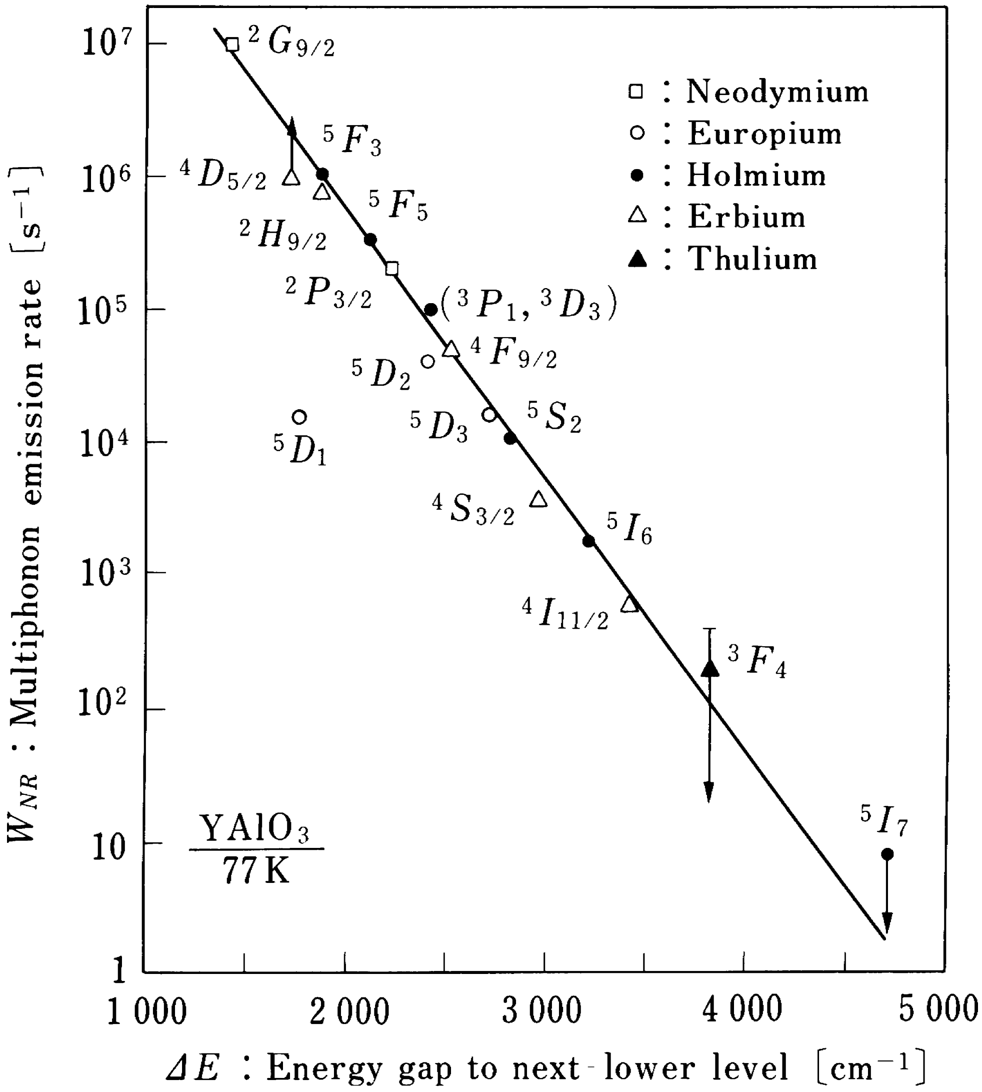

Figure 48 Energy gap law of nonradiative relaxation due to multiphonon processes. (From Weber, M.J., *Phys. Rev.*, B8, 54, 1993. With permission.)

almost equal to $1/a_{III \to II}$, that is, the lifetime of the quasistable state. The decay curve of the after-glow is represented by an exponential function that is similar to Eq. 120, and is strongly temperature dependent. The decay time constant of an emitting center with quasistable states is not usually longer than a second.

2.7.1.3 *Traps and phosphorescence*

Excited electrons and holes in the conduction and valence bands of a phosphor can often be captured by impurity centers or crystal defects before they are captured by an emitting center. When the probability for the electron (hole) captured by an impurity or defect center to recombine with a hole (electron) or to be reactivated into the conduction band (valence band) is negligibly small, the center or defect is called a *trap*.

The electrons (holes) captured by traps may cause phosphorescence (i.e., long after-glow) when they are thermally reactivated into the conduction band (valence band) and then radiatively recombined at an emitting center. The decay time of phosphorescence

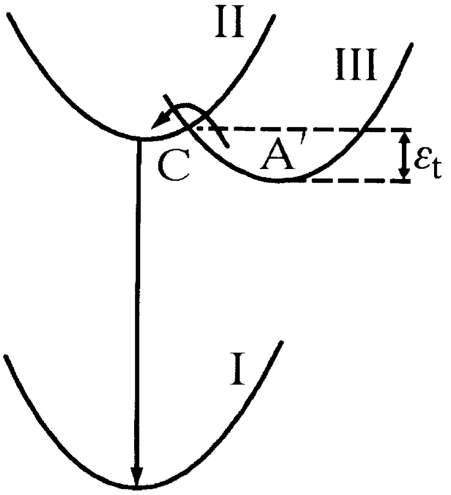

Figure 49 Configurational coordinate model of the luminescence after-glow (phosphorescence) via a quasistable state.

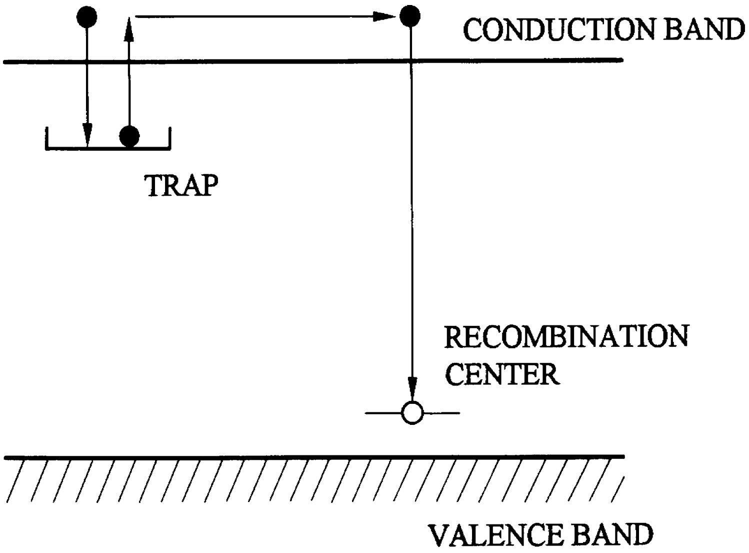

Figure 50 Luminescence after-glow process via a trap in an energy band scheme.

due to traps can be as long as several hours and is often accompanied by photoconductive phenomena.

The decay curve of the after-glow due to traps is not generally represented by a simple exponential function. The form of the curve is dependent on the concentration of the traps and on the electron capture cross-sections of the trap and the emitting center. Furthermore, it also depends on the excitation intensity level.

While several kinds of traps usually exist in practical phosphors, only one kind of electron trap is presumed to exist in the simple model shown in Figure 50. Let N be the trap concentration, and n_c and n_t the number of electrons per unit volume in the conduction band and trap states, respectively. The number of holes denoted by p is equal to $n_c + n_t$. The rate equation representing the decaying processes of the concentration of electrons and holes after the termination of excitation is:

$$\begin{aligned}\frac{dn_t}{dt} &= -an_t + b(N-n_t)n_c \\ \frac{dp}{dt} &= -rpn_c\end{aligned} \tag{129}$$

where a is the probability per second for a trapped electron to be thermally excited into the conduction band and is given by the same form as Eq. 126 with the density of states in the conduction band included in s. The probabilities that a free electron in the conduction band will be captured by a trap or to recombine with a hole are given by b and r, respectively. It is supposed that the number of the electrons n_c in the conduction band in the after-glow process is so small that $p \simeq n_t$ and $dp/dt \simeq dn_t/dt$. Then, the above two equations give:

$$\frac{dn_t}{dt} = \frac{-an_t^2}{n_t + (b/r)(N-n_t)} \tag{130}$$

This equation can be solved analytically for two cases: $b \ll r$ and $b \simeq r$.

First, the case of $b \ll r$, which presumes that the electrons once released from traps are not retrapped in the after-glow process. Eq. 130 then simplifies to:

$$\frac{dn_t}{dt} = -an_t \tag{131}$$

Since the emission intensity is given by $I(t) \propto dp/dt$, and $dp/dt \simeq dn_t/dt$ as mentioned above, then

$$I(t) = I_o \exp(-at) \tag{132}$$

This simple exponential decay of after-glow is the same as the one due to the quasistable state mentioned previously and is called a first-order or monomolecular reaction type in the field of chemical reaction kinetics.

In the case $b \simeq r$, which means that the traps and emitting centers have nearly equal capturing cross-sections, Eq. 130 can be simplified to:

$$\frac{dn_t}{dt} = -\frac{a}{N} n_t^2 \tag{133}$$

and then the number of trapped electrons per unit volume is given by:

$$n_t = \frac{n_{t0}}{1 + (N/an_{t0})t} \tag{134}$$

Approximating $I(t) \propto dn_t/dt$ as before, the decay curve of the after-glow is obtained as:

$$I(t) = \frac{I_o}{(1+\gamma t)^2}, \qquad (\gamma = N/an_t) \tag{135}$$

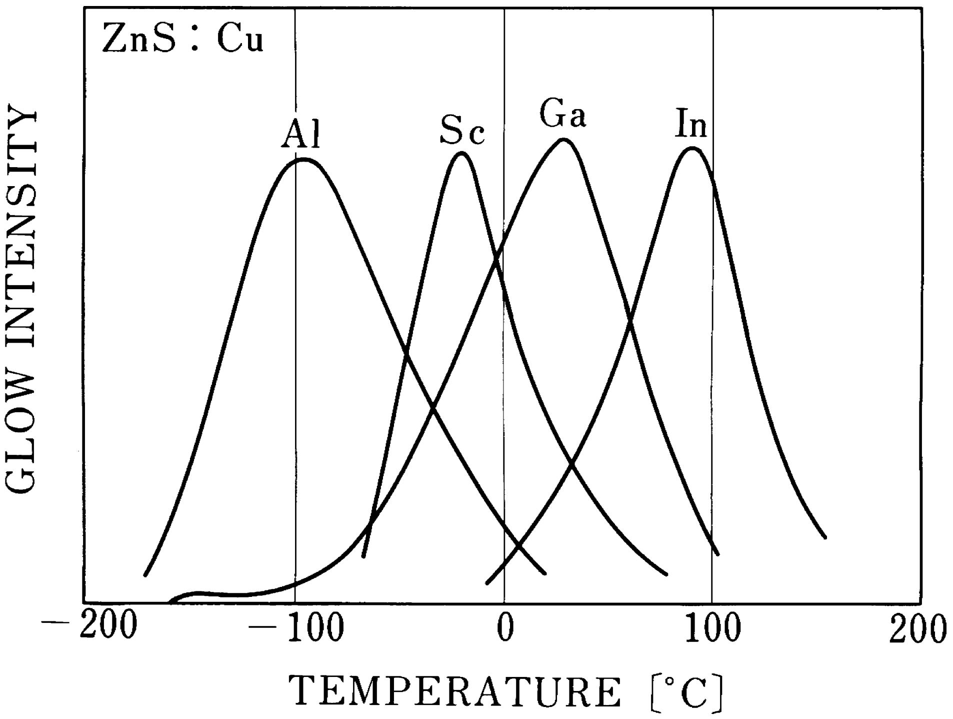

Figure 51 Glow curves of ZnS:Cu phosphors co-activated with Al, Sc, Ga, and In. (From Hoogenstraaten, W., *Philips Res. Rept.*, 13, 515, 1958. With permission.)

This form is called the second-order or bimolecular reaction type, where the decay curve is changed by excitation intensity as well as by temperature.

While the treatise mentioned above is a simple model presuming a single kind of trap, the real phosphors may have several kinds of traps of different depths. In many real cases, therefore, the after-glow decay curve is not represented simply by a monomolecular or bimolecular reaction curve. It often fits into the following equation.

$$I(t) = \frac{I_o}{(1+\gamma t)^n} \tag{136}$$

where n is around 0.5–2. If $t \gg 1/\gamma$, this decay curve can be approximated by $I(t) \propto t^{-n}$. The decay time constant of an after-glow is therefore denoted either by the $1/e$ decay time or the 10% decay time.

2.7.2 *Thermoluminescence*

When a phosphor with deep traps is excited for a while at rather low temperatures and then heated, it shows an increased after-glow called thermally stimulated luminescence due to the recombination of electrons thermally reactivated from the deep traps. This emission is also called thermoluminescence, and the temperature dependence of the emission intensity is called the glow curve, which is a good means to measure the depth (i.e., the activation energy of traps). Figure 51 shows the glow curves of ZnS:Cu phosphors with various co-activators.[3]

The measurement of a glow curve of a phosphor sample proceeds as follows.

1. The sample is cooled to a low temperature (liquid nitrogen is often used as coolant).
2. The sample is excited by UV light until the traps are filled with electrons or holes.
3. The excitation is terminated, and the temperature of the sample is raised at a constant rate, $dT/dt \equiv \beta$, while the intensity is recorded.
4. The temperature dependence of fluorescence is then measured under a constant UV excitation, which is used to calibrate the effect of temperature quenching on the thermoluminescence intensity.

The glow curve thus obtained is analyzed with the following theory. Assume that (1) a single kind of trap exists; (2) the decay of after-glow is of the first-order type given by Eq. 132, and (3) the probability for the trapped electrons to be thermally released into the conduction band is given by Eq. 126. Since the retrapping of the released electrons is neglected in the first-order kinetics, the change in the number of trapped electrons is:

$$\frac{dn_t}{dt} = -n_t s \exp(-\varepsilon/kT) \tag{137}$$

Integrated from a temperature T_0 to T with the relation $dT/dt = \beta$, this equation gives the number of residual electrons in the traps at T as:

$$n_t(T) = n_{t0} \exp\left(-\int_{t_0}^{t} s \exp\left(\frac{-\varepsilon}{kT}\right) \cdot \frac{dT}{\beta} \right) \tag{138}$$

where n_{t_0} is the number of the trapped electrons at the initial temperature T_o. Therefore, the emission intensity at T, approximated by $I \propto dn_t/dt$ as mentioned in the previous section, is given by:

$$I(T) \propto n_{t0} s \exp\left(\frac{-\varepsilon}{kT}\right) \exp\left(-\int_{T_0}^{T} s \exp\left(\frac{-\varepsilon}{kT}\right) \cdot \frac{dT}{\beta} \right) \tag{139}$$

Based on this equation, the following techniques have been proposed for obtaining the trap depth (activation energy ε) from a glow curve.

(a) In the initial rising part of the glow peak on the low-temperature side where the number of trapped electrons is nearly constant, Eq. 139 is approximated by

$$I(T) \propto s \exp \frac{-\varepsilon}{kT} \tag{140}$$

Then the slope of the Arrhenius plot ($1/T$ vs. ln I) of the curve in this region gives the trap depth ε. In fact, however, it is not easy to determine the depth with this method because of the uncertainty in fixing the initial rising portion.

(b) Let the peak position of a glow curve be T_m. Then, the following equation derived from $dI/dT = 0$ should be valid.

$$\frac{\beta\varepsilon}{kT_m^2} = s \exp\left(\frac{-\varepsilon}{kT_m}\right) \tag{141}$$

Table 1

β/s [K]	K [K/eV]	T_n [K]
10^{-4}	833	35
10^{-5}	725	28
10^{-6}	642	22
10^{-7}	577	17
10^{-8}	524	13
10^{-9}	480	10
10^{-10}	441	7
10^{-11}	408	6
10^{-12}	379	6
10^{-13}	353	5
10^{-14}	331	5
10^{-15}	312	4

From Curie, D., Luminescence in Crystals, John Wiley & Sons, 1963, chap. VI. With permission.

If the frequency factor s is obtained in some manner, ε can be estimated by this relation from the observed value of T_m. Note that the temperature rise rate β should be kept constant throughout the measurement for this analysis. Randall and Wilkins[4] performed a numerical calculation based on this theory and obtained the following equation, which approximates the trap depth ε with 1% error.

$$\varepsilon = \frac{T_m - T_o(\beta/s)}{K(\beta/s)} \tag{142}$$

Here, $T_o(\beta/s)$ and $K(\beta/s)$ are the parameters determined by β/s as listed in Table 1.

For ZnS:Cu, $s = 10^9$ s^{-1} is assumed and the following estimations have been proposed for various values of β.[5]

$$\varepsilon|eV| = T_m/500 \qquad (\beta = 1K/s)$$

$$\varepsilon|eV| \approx T_m/400 \qquad (\beta = 0.01K/s)$$

$$\varepsilon|eV| = (T_m - 7)/433 \qquad (\beta = 0.06K/s)$$

(c) If the glow curve is measured with two different rise rates, β_1 and β_2, it is apparent that one can obtain the value of ε without assuming the value of s in Eqs. 141 or 142, using the following equation.

$$\frac{\varepsilon}{k}\left(\frac{1}{T_{m2}} - \frac{1}{T_{m1}}\right) = \ln\left(\frac{\beta_1}{\beta_2} \cdot \frac{T_{m2}^2}{T_{m1}^2}\right) \tag{143}$$

Hoogenstraaten[3] extended this method for many raising rates β_i, and, by plotting the curves ($1/T_{mi}$ vs. $\ln(T_{mi}^2/\beta_i)$), obtained the trap depth from the slope ε/k of the straight line connecting the plotted points as shown in Figure 52.[6] A numerical analysis[7] has shown that Hoogenstraaten's method gives the best result among several methods for obtaining trap depths from glow curves.

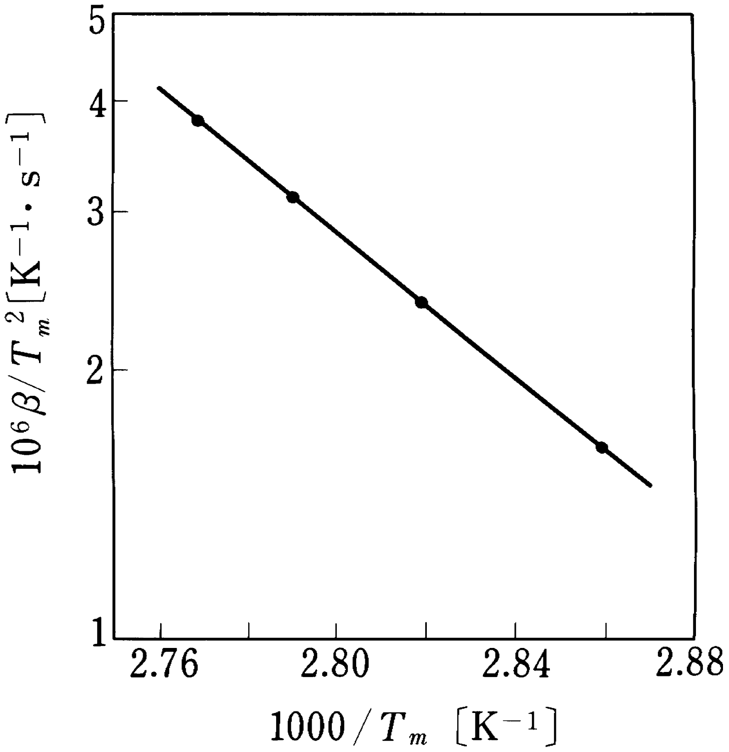

Figure 52 Hoogenstraaten plot showing the dependence of the peak temperature (T_m) of a glow curve on the temperature-raising rate (β). The slope of this line gives the depth (activation energy) of the trap. (From Avouris, P. and Morgan, T.N., *J. Chem. Phys.*, 74, 4347, 1981. With permission.)

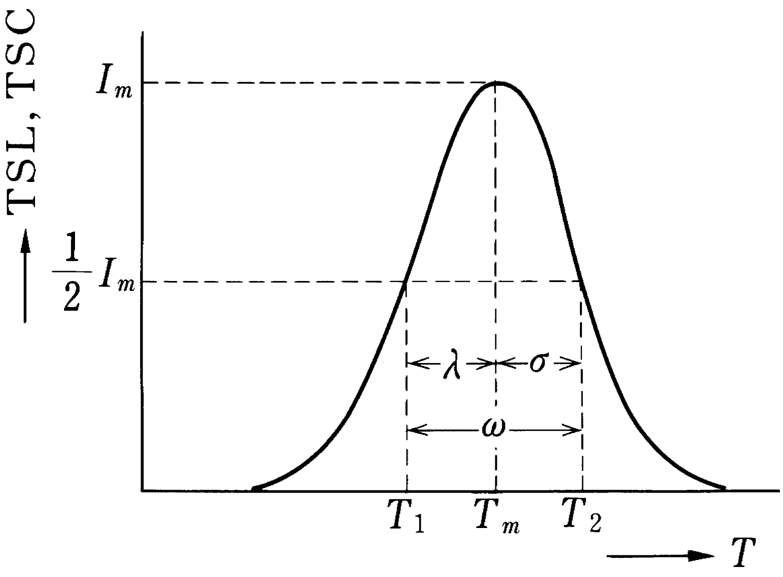

Figure 53 Predicted shape of a glow curve.

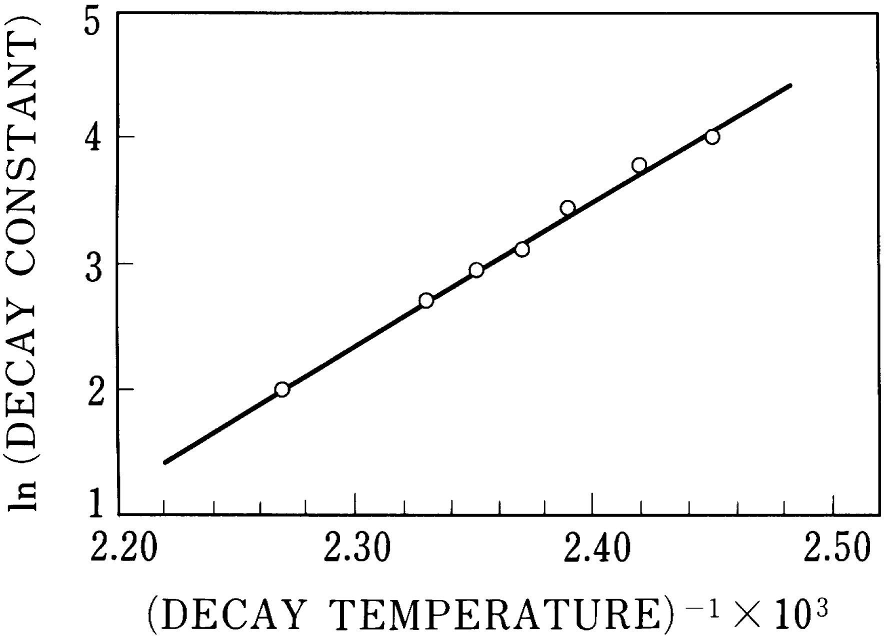

Figure 54 Temperature dependence of the decay time constant of ZnS:Cu. (From Bube, R.H., *Phys. Rev.*, 80, 655, 1950. With permission.)

(d) Many methods for obtaining the depth ε from the width of the peak of a glow curve have been proposed.[5] The results are listed below, where the width for a peak is defined in various ways, as shown in Figure 53.

1. $\varepsilon = kT_m^2\sigma$
2. $\varepsilon = 2kT_m(1.25T_m/\omega - 1)$
3. $\varepsilon = 1.52\,kT_m^2/\lambda - 3.16\,kT_m$
4. $\varepsilon = (1 + \omega/\lambda)kT_m^2/\sigma$

Note that these methods are usable under certain restricted conditions.[5]

There is a method to obtain trap depth other than the glow-curve method described above. It is to use the temperature dependence of the decay time of after-glow, that is, phosphorescence. As mentioned in relation to Eq. 132, the decay time constant of the exponential after-glow due to the first-order reaction kinetics is equal to the inverse of the thermal detrapping probability, a^{-1}, and its temperature dependence is given by:

$$\tau_{1/e} = s^{-1}\exp\left(\frac{\varepsilon}{kT}\right) \tag{144}$$

Therefore, the trap depth ε can be obtained from the measurements of the phosphorescence decay time $\tau_{1/e}$ at several different temperatures (T_i). An example is shown in Figure 54, in which the depth is obtained from the slope of the straight line connecting the Arrhenius plots of the observed values[8] for τ_i and T_i.

A usable method with which trap depths and relative trap densities are obtained more easily and accurately was recently proposed.[9] In this method, the sample is excited periodically under a slowly varying temperature and the after-glow (phosphorescence) intensity is measured at several delay times (t_d) after the termination of excitation in each cycle.

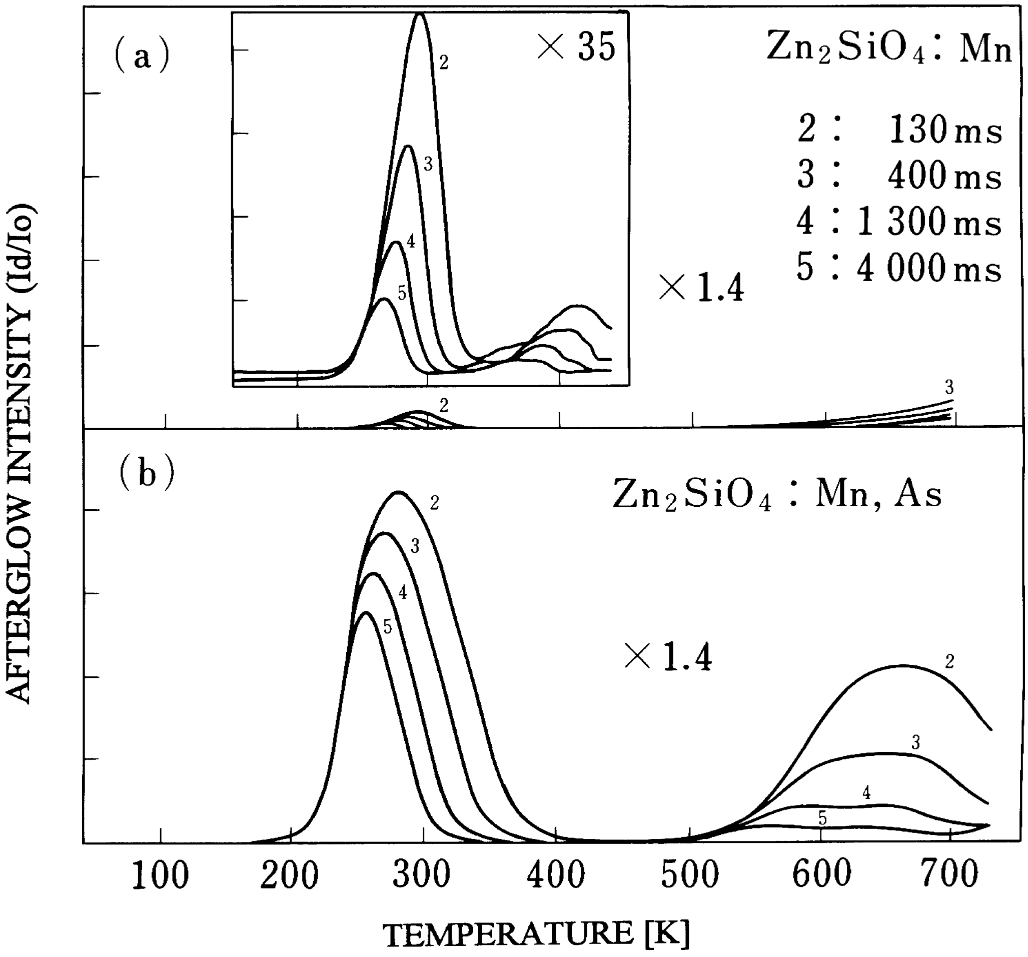

Figure 55 Temperature dependencies of the after-glow intensity of (a) $Zn_2SiO_4:Mn^{2+}$ and (b) $Zn_2SiO_4:Mn^{2+}$, As. The delay time (t_d) is 0.13, 0.4, 1.3, and 4.0 s, respectively, for the curves numbered from 2 through 5 in the figures. (From Nakazawa, E., *Jpn. J. Appl. Phys.*, 23(9), L755, 1984. With permission.)

The temperature dependence of the after-glow intensity at each delay time makes a peak at a certain temperature T_m. From the equation $dI/dT = 0$ and using either Eq. 132 or Eqs. 135 and 136, the following relation is obtained between the peak temperature T_m and the delay time t_d.

$$t_d = s^{-1} \exp\left(\frac{\varepsilon}{kT_m}\right) \tag{145}$$

Since Eq. 145 is similar to Eq. 144 (i.e., the decay time method), the method used there for obtaining the trap depth ε can be applied hereby, substituting t_d for τ, and T_m for T_i. An example of the measured after-glow intensity curves is shown in Figure 55.

2.7.3 *Photostimulation and photoquenching*

When a phosphor with deep traps is once excited and then irradiated by infrared (IR) or red light during the decay of its phosphorescence, it sometimes shows photostimulation

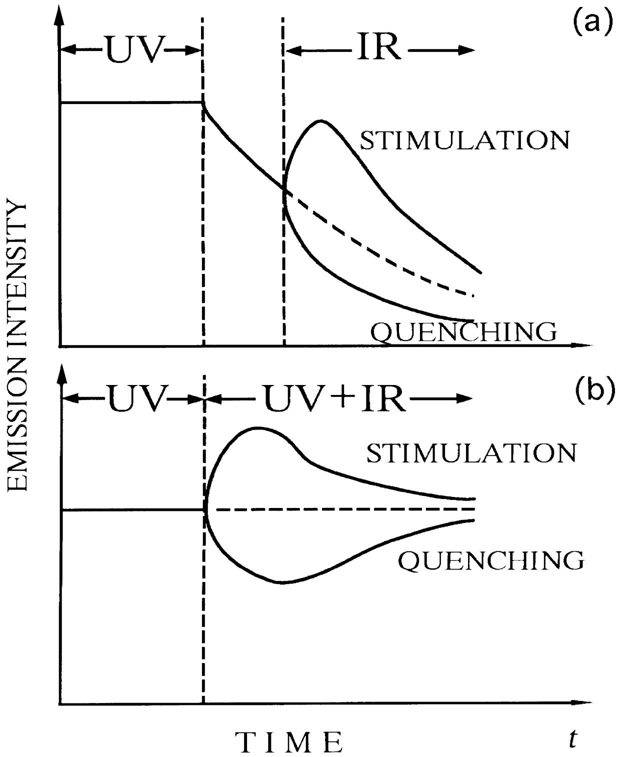

Figure 56 Photostimulation and photoquenching simulation for the case (b) under a constant excitation and (a) in the after-glow process after the termination of excitation.

or photoquenching of luminescence; that is, an increase or decrease of the emission intensity as schematically shown in Figure 56(a). Under a stationary excitation shown in Figure 56(b), the stimulation enhances and the quenching reduces the emission intensity temporarily.

These phenomena are utilized for IR detection and radiographic imaging, in which the intensity of the stimulated emission is used to measure the intensity of IR light or X-rays (see 7.4).

Photostimulation is caused by the radiative recombination of the electrons (holes) released by photoactivation from deep trap levels, as shown in Figure 57(a). On the other hand, photoquenching is caused by the nonradiative recombination of holes (electrons) photoactivated from luminescent centers as shown in Figure 57(b). Figure 58 depicts the configuration coordinate model of photostimulation. The activation energy ε_0 of photostimulation is not generally equal to the thermal activation energy ε_t of trapped electrons discussed before with reference to Figure 49. Since the optical absorption process takes place in a very short time period without changing the configuration of the atoms in the center at that moment, the process is represented by the straight vertical transition in Figure 58 from state III (a trap or the quasi-stable state of emitting centers) to state II (the conduction band or emitting centers). On the other hand, the thermal activation needs energy ε_t to overcome at least the lowest barrier between states II and III in Figure 58; hence, the activation energy ε_t is generally smaller than ε_0. Photostimulation spectra (i.e., excitation spectra for IR stimulation) can be used to measure the optical activation energy ε_0.

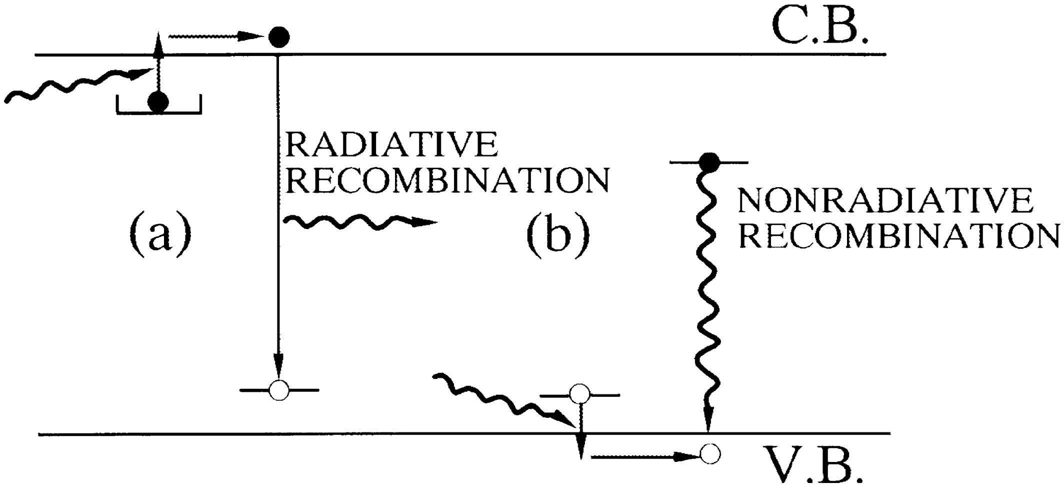
C.B.
RADIATIVE
RECOMBINATION
(a)
(b)
NONRADIATIVE
RECOMBINATION
V.B.

Figure 57 Photostimulation process (a), and photoquenching process (b) in an energy band scheme. C.B. and V.B. indicate the conduction band and the valence band of the host crystal, respectively.

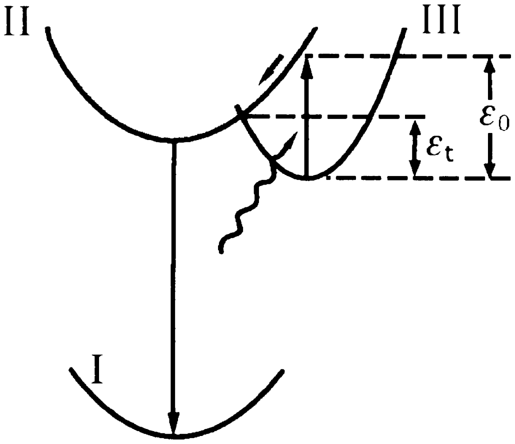
II
III
ε_0
ε_t
I

Figure 58 Photostimulation in configurational coordinate models.

References

1. Nakazawa, E., *J. Luminesc.*, 18/19, 272, 1979.
2. Weber, M.J., *Phys. Rev.*, B8, 54, 1973.
3. Hoogenstraaten, W., *Philips Res. Rept.*, 13, 515, 1958.
4. Randall, J.T. and Wilkins, M.H.F., *Proc. Roy. Soc.*, A184, 366, 1945.
5. Curie, D., *Luminescence in Crystals*, John Wiley & Sons, 1963, chap. VI.
6. Avouris, P. and Morgan, T.N., *J. Chem. Phys.*, 74, 4347, 1981.
7. Kivits, P. and Hagebeuk, H.J.L., *J. Luminesc.*, 15, 1, 1977.
8. Bube, R.H., *Phys. Rev.*, 80, 655, 1950.
9. Nakazawa, E., *Jpn. J. Appl. Phys.*, 23(9), L755, 1984.
10. Nakazawa, E., *Oyo Buturi*, 55(2), 145, 1986 (in Japanese).

chapter two — section eight

Fundamentals of luminescence

Eiichiro Nakazawa

2.8 Excitation energy transfer and cooperative optical phenomena 99
  2.8.1 Excitation energy transfer 99
    2.8.1.1 Theory of resonant energy transfer 100
    2.8.1.2 Diffusion of excitation 104
    2.8.1.3 Sensitization of luminescence 105
    2.8.1.4 Concentration quenching of luminescence 106
  2.8.2 Cooperative optical phenomena 107
References 110

2.8 Excitation energy transfer and cooperative optical phenomena

2.8.1 Excitation energy transfer

The process of excitation energy transfer from an excited point in a crystal to a luminescent center can be classified into the following two types.

1. Migration of free electrons (holes), electron-hole pairs, or quasi-particles such as excitons and plasmons conveys the excitation energy to luminescent centers. This type of transfer seems to be active especially in such semiconductor-like hosts as ZnS and CdS, which are widely used as cathode-ray tube (CRT) phosphors. In the initial excitation process of CRT phosphors, the local excitation by a high-energy electron produces several hundreds of these particles, and they are dispersed in the crystal by this type of transfer. (See 2.9.)
2. Excitation energy is transferred from an excited center (energy donor) to an unexcited center (energy acceptor) by means of quantum mechanical resonance.[1,2] This type of transfer is practically utilized for the sensitization of luminescence in lamp phosphors, which are mostly oxides or oxoacid salts with less-mobile electrons and holes than in CRT phosphor materials.

In this section, the resonant energy transfer process and related phenomena, such as the sensitization and quenching of luminescence, will be discussed. More recent experimental studies on this topic are referred to in the reference list.[3]

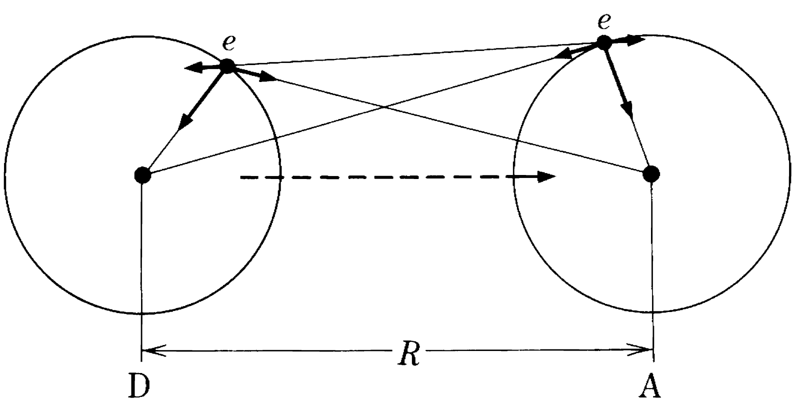

Figure 59 Coulomb interaction in a resonant energy transfer process.

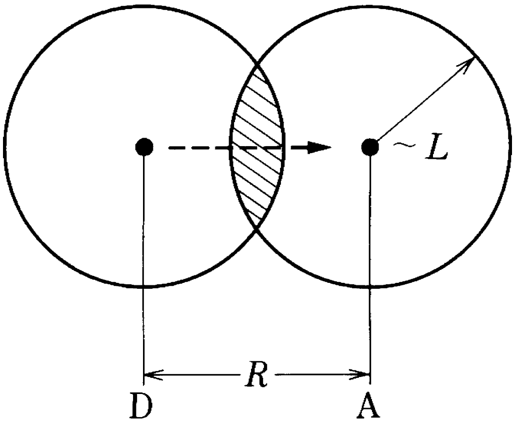

Figure 60 Resonant energy transfer by the exchange interaction, in which the overlapping of the wavefunctions of D and A (shaded region) is necessary.

2.8.1.1 Theory of resonant energy transfer

Dexter's theory of resonant energy transfer[2] has elucidated that two optical centers within a certain distance may be in resonance and transfer the excitation energy from one (donor) to the other (acceptor). The close proximity of the centers enables them to be connected by the electrostatic interaction shown in Figure 59 or by the quantum mechanical exchange interaction shown in Figure 60. The energy donor, which is called a *sensitizer* in practical usage, is denoted hereafter by D and the acceptor by A. For resonant energy transfer to take place, it is necessary that the transition energies of D and A be equal.

(a) Multipolar Interaction. The mechanisms of resonant energy transfer can be classified into several types based on the character of the transitions in D and A. When both transitions in D and A are of electric dipole character (dipole-dipole interaction), the probability per second of energy transfer from D to A is given by:

$$P_{dd}(R) = \frac{3c^4\hbar^4\sigma_A}{4\pi n^4\tau_D R^6}\int \frac{f_D(E)F_A(E)}{E^4}dE \tag{146}$$

Here, R is the separation between D and A, n is the refractive index of the crystal, σ_A is the absorption cross-section of A, and τ_D is the radiative lifetime of D. Likewise, the transfer probability due to the dipole-quadrupole interaction is:

$$P_{dq}(R) = \frac{135\pi\alpha c^8\hbar^9}{4n^6\tau_D\tau_A R^8}\int\frac{f_D(E)F_A(E)}{E^8}dE \qquad (\alpha = 1.266) \tag{147}$$

In these equations, $f_D(E)$ and $F_A(E)$ represent the shape of the D emission and A absorption spectra, respectively, which are normalized (i.e., $\int f_D(E)dE = 1$ and $\int F_A(E)dE = 1$. The integrals in Eqs. 146 and 147 are, therefore, the overlapping ratios of these two spectra, which is a measure of the resonance condition. The transfer probabilities due to all multipolar interactions—i.e., dipole-dipole (d-d) in Eq. 146, dipole-quadrupole (d-q) in Eq. 147, and quadrupole-quadrupole (q-q), are summarized in Eq. 148 with their R dependence being noticed.

$$P_s(R) = \frac{\alpha_{dd}}{R^6} + \frac{\alpha_{dq}}{R^8} + \frac{\alpha_{qq}}{R^{10}} + \ldots = \sum_{s=6,8,10}\frac{\alpha_s}{R^s} \tag{148}$$

Here, s in the third term is 6, 8, and 10 for (dd), (dq), and (qq), respectively.

If the dipole transition is allowed for both D and A, the magnitudes of α_s are $\alpha_{dd} > \alpha_{dq} > \alpha_{qq}$, and the dipole-dipole interaction has the highest transfer probability. However, if the dipole transition is not completely allowed for D and/or A, as is the case with the f-f transition of rare-earth ions, it is probable that the higher-order interaction, d-q or q-q, may have the larger transfer probability for small distance pairs due to the higher-order exponent of R in Eq. 148.[4,5]

Since the emission intensity and the radiative lifetime of D are decreased by energy transfer, the mechanism of the transfer can be analyzed using the dependence of the transfer probability on the pair distance given by Eq. 148, and hence the dominant mechanism among (dd), (dq), and (qq) can be determined.

When the acceptors are randomly distributed with various distances from a donor D in a crystal, the emission decay curve of D is not an exponential one. It is given by the following equation for the multipolar interactions.[6]

$$\phi(t) = \exp\left[-\frac{t}{\tau_D} - \Gamma\left(1-\frac{3}{s}\right)\frac{C}{C_0}\left(\frac{t}{\tau_D}\right)^{3/s}\right], \qquad (s = 6,\ 8,\ 10) \tag{149}$$

Here, $\Gamma()$ is the gamma function, and C and C_0 are, respectively, the concentration of A and its critical concentration at which the transfer probability is equal to the radiative probability $(1/\tau_D)$ of D.

Thus, the emission efficiency η and the emission decay time constant τ_m can be estimated using Eq. 149 and the following equations:

$$\frac{\eta}{\eta_0} = \frac{\int_0^\infty \phi(t)dt}{\tau_D} \tag{150}$$

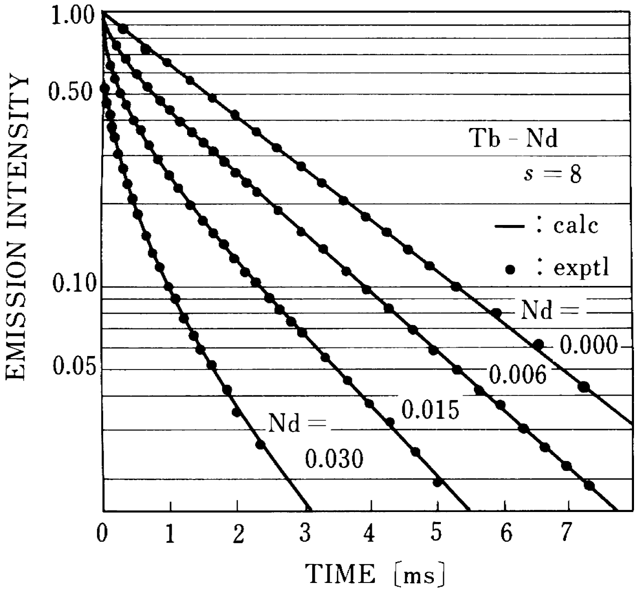

Figure 61 Decay curves of Tb^{3+} emission ($^5D_4 - 7F_j$) affected by the energy transfer to Nd^{3+} ions in $Ca(PO_3)_2$. (From Nakazawa, E. and Shionoya, S., *J. Chem. Phys.*, 47, 3211, 1967. With permission.)

$$\tau_m = \frac{\int_0^\infty t\phi(t)dt}{\int_0^\infty \phi(t)dt} \tag{151}$$

Figure 61 shows the decay curves of Tb^{3+} emission ($^5D_4 - {}^7F_j$) in $Ca(PO_3)_2$, which are affected, due to energy transfer,[4] by the concentration of the co-activated Nd^{3+} ions. The dependence of the emission intensity and decay time of the donor Tb^{3+} ion on the concentration of the acceptor Nd^{3+} ion in the same system are shown in Figure 62. Theoretical curves in these figures are calculated using Eqs. 150 and 151 with $s = 8$ (quadrupole-dipole interaction).

(b) Exchange Interaction. When an energy donor D and an acceptor A are located so close that their electronic wavefunctions overlap each other as shown in Figure 60, the excitation energy of D could be transferred to A due to a quantum mechanical exchange interaction between the two. If the overlap of wavefunctions varies as $\exp(-R/L)$ with R, the transfer probability due to this interaction becomes:[2]

$$P_{ex}(R) = (2\pi/\hbar)K^2 \exp(-2R/L)\int f_D(E)F_A(E)dE \tag{152}$$

where K^2 is a constant with dimension of energy squared and L is an effective Bohr radius; that is, an average of the radii of D in an excited state and A in the ground state.

The emission decay curve of D, taking into account a randomly distributed A interacting through the exchange mechanism, is given (similar to Eq. 149) by:[6]

$$\phi(t) = \phi_0 \exp\left[-\frac{t}{\tau_D} - \gamma^{-3}\frac{C}{C_0}g\left(\frac{e^{\gamma t}}{\tau_D}\right)\right] \qquad (\gamma = 2R_0/L) \tag{153}$$

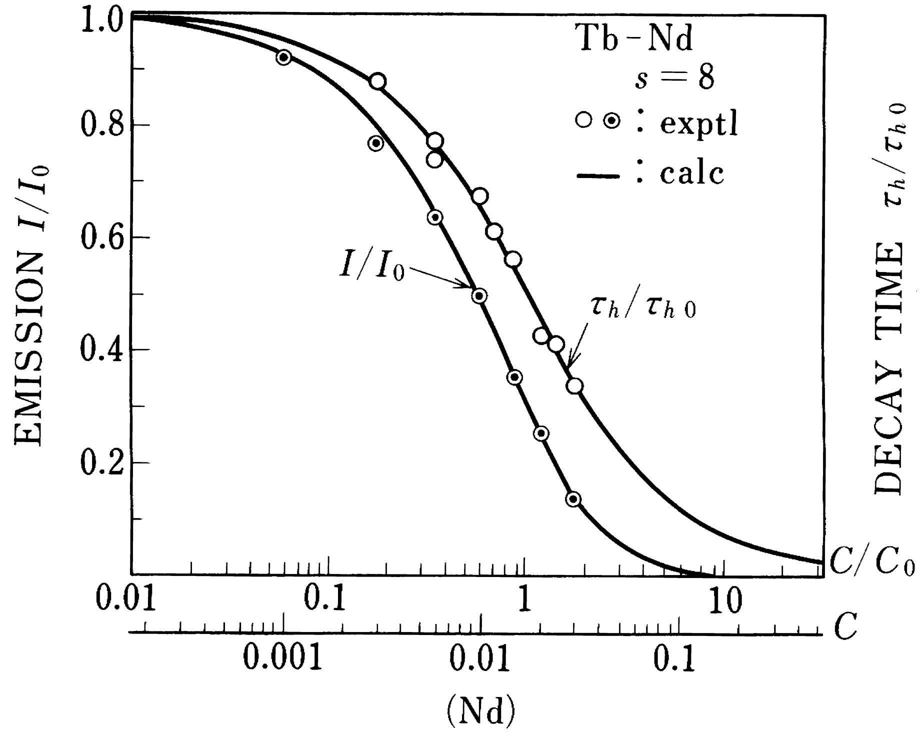

Figure 62 Intensity and decay time of Tb^{3+} emission in the same system as that in Figure 61. Solid curves are theoretical ones for quadrupole-dipole interaction (s = 8). (From Nakazawa, E. and Shionoya, S., *J. Chem. Phys.*, 47, 3211, 1967. With permission.)

The emission efficiency and the averaged emission decay time τ_m can be estimated using Eqs. 150, 151, and 153.

Since the exchange interaction requires the overlapping of the electron clouds of D and A (see Figure 60), the ion can be no further away than the second nearest site in the host crystal.

Note that while Eq. 152 requires the spectral overlap for the resonance condition, it is irrelevant to the spectral intensities. Therefore, if A is located next to D, and if the transitions are not completely electric dipole allowed, the transfer probability by exchange interaction can be larger than for multipolar interactions.

As described later in reference to Figures 64 and 65, the emission of Mn^{2+} in the halophosphate phosphor, the most general lamp phosphor, is excited by the energy transfer from Sb^{3+} due to the exchange interaction since the corresponding transition in the Mn^{2+} ion is a forbidden d-d transition.[7]

Perrin's model[8] treats the emission decay of D under general energy transfer in a simple manner. In this model, it is assumed that the transfer probability is a constant if A exists within some critical distance and is zero outside the range. This model, therefore, is thought to be most applicable to the short-range exchange interaction.

(c) Phonon-Assisted Energy Transfer. Phonon-assisted energy transfer occurs when the resonance condition is not well satisfied between D and A, resulting in the spectral overlap in Eqs. 148 and 149 being small. In this case, the difference δE between the transition energies of D and A is compensated by phonon emission or absorption. The transfer probability[9] is given by:

$$P_{as}(\Delta E) = P_{as}(0)e^{-\beta\Delta E} \tag{154}$$

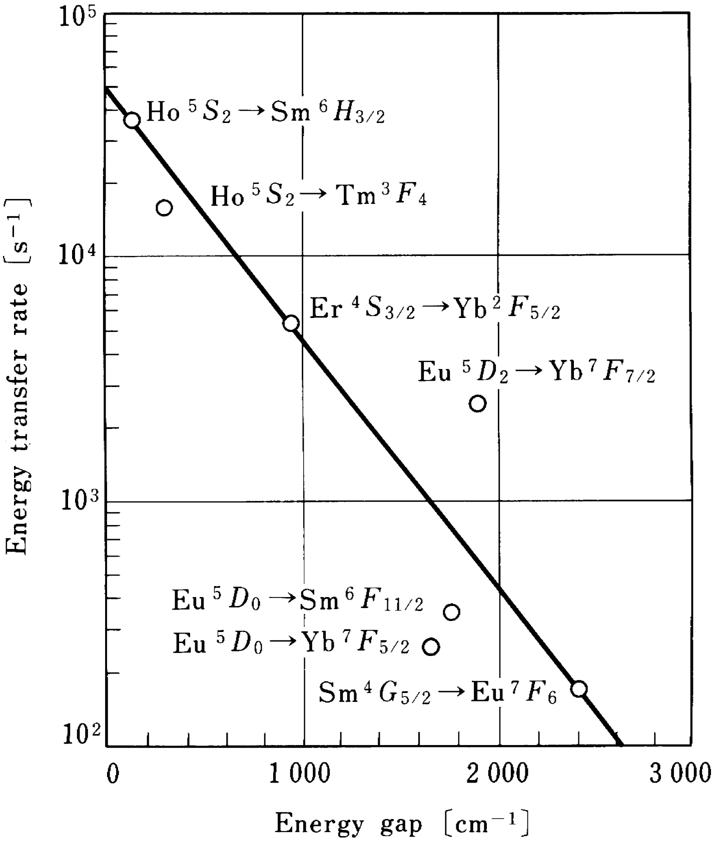

Figure 63 Relation between the nonresonant phonon-assisted energy transfer rate and the energy mismatch δ in Y_2O_3:R^{3+} (R = rare earth ions). (From Yamada, N., Shionoya, S., and Kushida, T., *J. Phys. Soc. Japan*, 32, 1577, 1972. With permission.)

where $P_{as}(0)$ is equal to the resonant transfer probability given by Eqs. 148 or 149, and β is a parameter that depends on the energy and occupation number of participating phonons. The energy gap ΔE is equal to $n \quad \omega_p$ with n and ω_p being the number and energy, respectively, of the largest energy phonon in the host. Figure 63 shows the energy transfer rates for various D-A systems of rare-earth ions in Y_2O_3 host[10]; these are in excellent agreement with Eq. 154.

2.8.1.2 Diffusion of excitation

Energy transfer to the same type of ion is called excitation migration or energy migration. While the effect of energy migration among donors (D → D) prior to D → A transfer is neglected in the above discussion, it must be taken into account in the emission decay of sensitized phosphors. The effect of D → D migration on D → A systems is theoretically expressed by the following equation.[11,12]

$$\phi(t) = \exp-\left(\frac{1}{\tau_D} + \frac{1}{\tau_M}\right)t \tag{155}$$

where migration rate is defined as $\tau_M^{-1} = 0.51 \cdot 4\pi N_A \alpha^{1/4} D^{3/4}$, in which D is a diffusion constant, typically 5×10^{-9} cm^2s^{-1} for the Pr^{3+}-Pr^{3+} pair in $La_{0.8}Pr_{0.2}Cl_3$:Nd and 6×10^{-10} cm^2s^{-1} for the Eu^{3+}-Eu^{3+} pair in $Eu(PO_3)$ glass.[12,13]

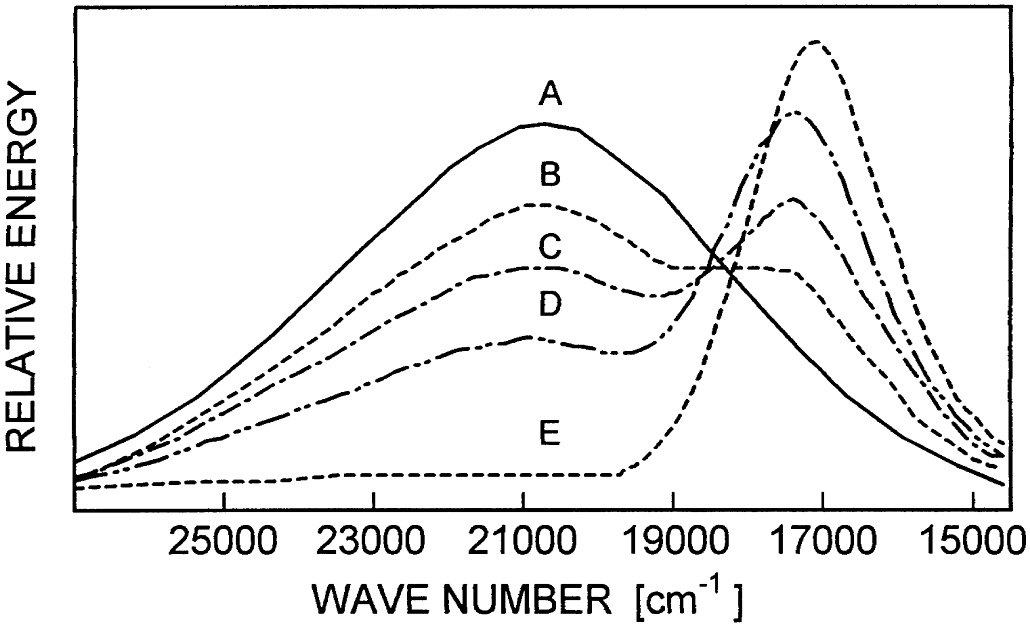

Figure 64 Emission spectra of a lamp phosphor, $Ca_5(PO_4)_3(F,Cl):Sb^{3+}$, Mn^{2+}, in which the Sb^{3+} ions sensitize the emission of Mn^{2+} ions by an energy transfer process. The Sb^{3+} concentration is fixed to be 0.01 mol/mol Ca. The Mn^{2+} concentration is changed, A:0, B:0.005, C:0.010, D:0.020 and E:0.080 mol/mol Ca. (From Batler, K.H. and Jerome, C.W., *J. Electrochem. Soc.*, 97, 265, 1950. With permission.)

2.8.1.3 Sensitization of luminescence

Energy transfer processes are often used in practical phosphors in order to enhance the emission efficiency. The process is called *sensitization of luminescence*, and the energy donor is called a sensitizer. The emission intensity of Mn^{2+}-activated silicate, phosphate, and sulfide phosphors, for example, is sensitized by Pb^{2+}, Sb^{3+}, and Ce^{3+}. In the halophosphate phosphor widely used in fluorescent lamps ($3Ca_3(PO_4)_2Ca(F,Cl)_2:Sb^{3+},Mn^{2+}$), Sb^{3+} ions play the role of a sensitizer as well as the role of an activator. As shown in Figure 64,[14] the intensity of the blue component of the emission spectra due to the Sb^{3+} activator of this lamp phosphor decreases with the concentration of Mn^{2+} ions because of the excitation energy transfer from Sb^{3+} to Mn^{2+}. Figure 65 shows the excitation spectra for the blue Sb^{3+} emission of this phosphor and for the red emission component due to Mn^{2+} activator.[15] The similarities between the two spectra are evidence of energy transfer (see also 5.1.1).

The emission of Tb^{3+} is sensitized by Ce^{3+} ions in many oxide and double oxide, green-emitting phosphors.[16,17]

While the energy transfer from a donor to an emitting center causes sensitization of luminescence, the transfer from an emitting center to a nonradiative center causes the quenching of luminescence. A very small amount (~10ppm) of Fe, Co, and Ni in ZnS phosphors, for example, appreciably quenches the original emission as a result of this type of energy transfer (see 3.7.4.1).[18] They are called *killer* or *quencher* ions. In some phosphors, however, these killers are intentionally added for the purpose of reducing the emission decay time, thereby obtaining a fast-decay phosphor at the expense of emission intensity[19] (see Eq. 151).

Two-step or tandem energy transfer from Yb^{3+} donors to Er^{3+} or Tm^{3+} acceptors is used in infrared-to-visible up-conversion phosphors (see 12.1).

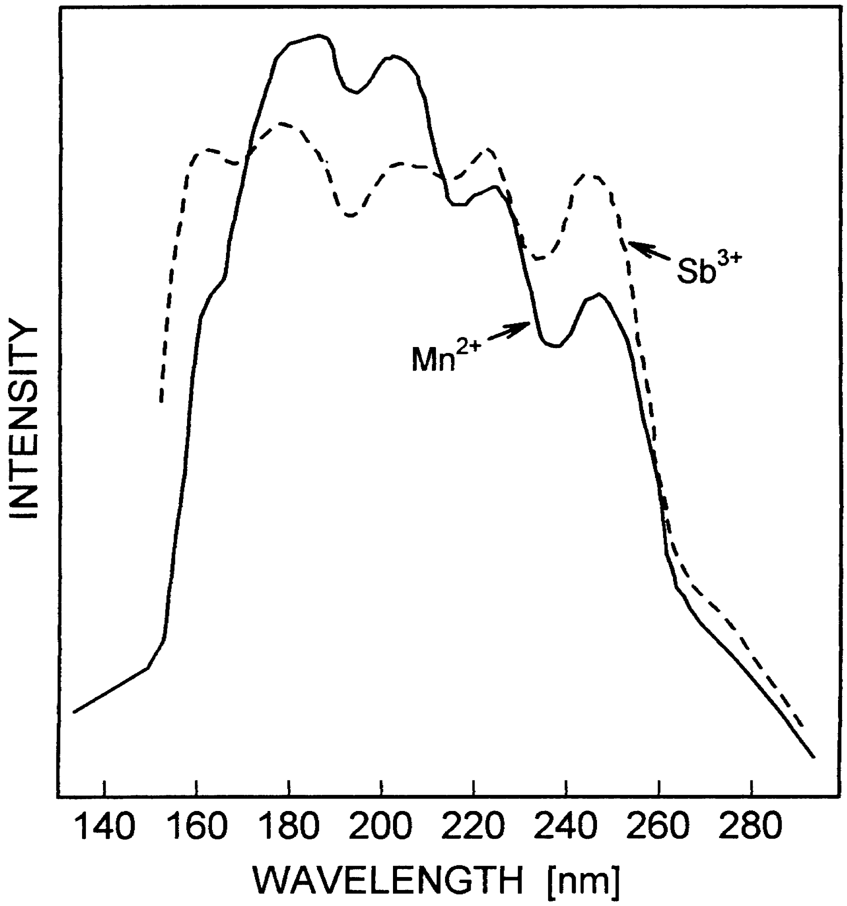

Figure 65 Excitation spectra for the blue Sb^{3+} emission and the red Mn^{2+} emission in the same system as that in Figure 64. (From Johnson, P.D., *J. Electrochem. Soc.*, 108, 159, 1961. With permission.)

2.8.1.4 Concentration quenching of luminescence

If the concentration of an activator is higher than an appropriate value (usually several wt %), the emission of the phosphor is usually lowered, as shown in Figure 66. This effect is called *concentration quenching*. The origin of this effect is thought to be one of the following:

1. Excitation energy is lost from the emitting state due to cross-relaxation (described later) between the activators.
2. Excitation migration due to the resonance between the activators is increased with the concentration (see 2.1.2), so that the energy reaches remote killers or the crystal surface acting as quenching centers.[20,21]
3. The activator ions are paired or coagulated, and are changed to a quenching center.

In some rare-earth activated phosphors, the effect of concentration quenching is so small that even stoichiometric phosphors, in which all (100%) of the host constituent cations are substituted by the activator ions, have been developed. Figure 67 shows the concentration dependence of the emission intensity of the Tb^{3+} activator in $Tb_xLa_{1-x}P_5O_{14}$, a stoichiometric phosphor, in which the emission intensity from the $^5D_4$ emitting level (see the energy level diagram of Tb^{3+} in 3.3) attains the maximum at $x = 1$.[22] This phosphor has the same crystal

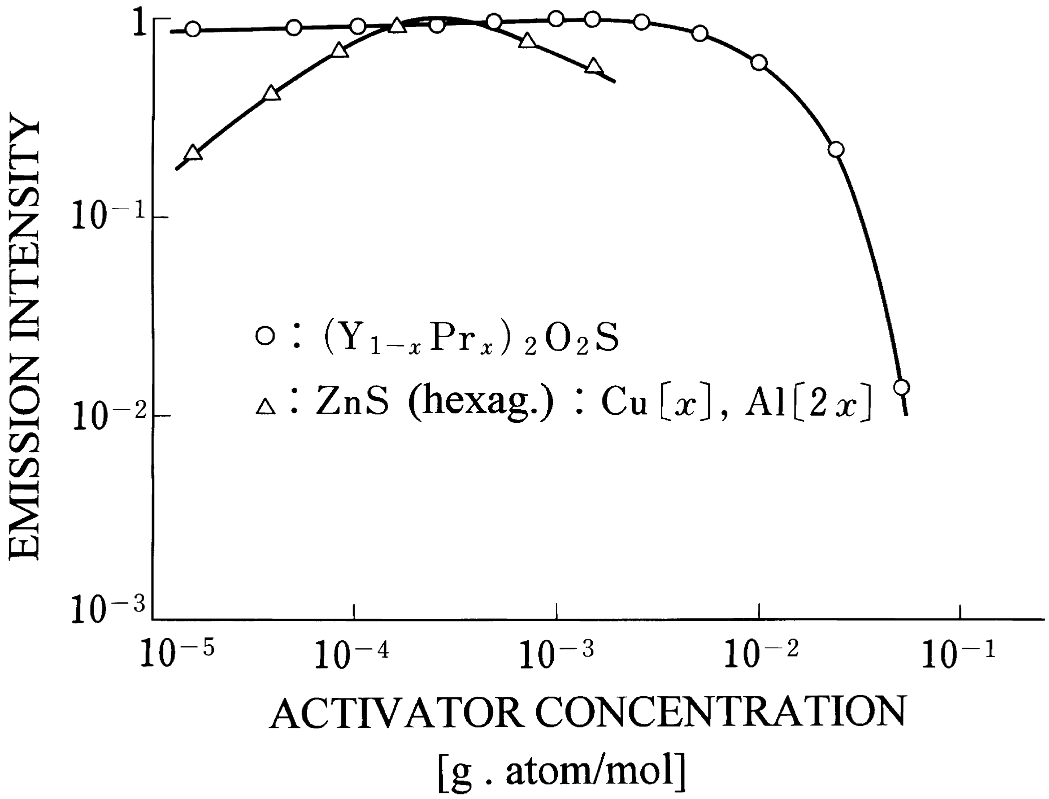

Figure 66 Activator concentration dependence of the cathode-luminescence intensities of Y_2O_2S:Eu^{3+} and ZnS:Cu. (From Kuboniwa, S., Kawai, H., and Hoshina, T., *Jpn. J. Appl. Phys.*, 19, 1647, 1980. With permission.)

structure as NdP_5O_{14}, a typical stoichiometric phosphor, in which each Nd^{3+} ion is isolated by the surrounding PO_4 groups.[23]

When the concentration quenching due to cross-relaxation (relaxation due to resonant energy transfer between the same element atoms or ions [see the insertion in Figure 68]) occurs on a particular level among several emitting levels, the emission color of the phosphor changes with the activator concentration. For example, while the emission color of Tb^{3+}-activated phosphors is blue-white due to mixing of blue emission from the $^5D_3$ emitting level and green emission from the $^5D_4$ level at concentrations below 0.1%, the color changes to green at the higher concentrations. The change is caused by cross-relaxation, as shown in Figure 68,[24] between the $^5D_3$ and $^5D_4$ emitting levels, thereby diminishing the population of Tb^{3+} ions in $^5D_3$ state and increasing the one in the $^5D_4$ state.

2.8.2 *Cooperative optical phenomena*

In emission and absorption spectra of crystals highly doped with two types of rare-earth ions, labeled *A* and *B*, sometimes show weak additional lines other than the inherent spectral lines specific to the *A* and *B* ions. These additional lines are due to the cooperative optical processes induced in an *AB* ion-pair coupled by electrostatic or exchange interactions. The cooperative optical process can be divided into three types as shown in Figure 69. They are: (a) cooperative absorption ($AB + \omega_{A+B} \rightarrow A^*B^*$); (b) Raman luminescence ($A^*B \rightarrow AB^* + \omega_{A-B}$); and (c) cooperative luminescence ($A^*B^* \rightarrow AB + \omega_{A+B}$). The observed intensities of all these cooperative spectra are very weak (10^{-5} of the normal f-f

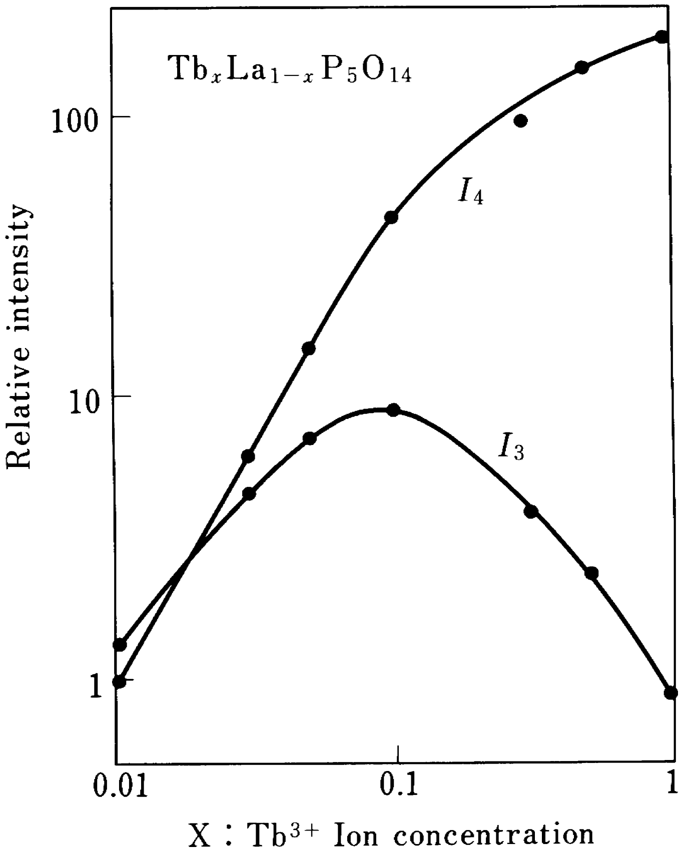

Figure 67 Activator concentration dependence of photoluminescence intensity of a "stoichiometric" phosphor, $Tb_xLa_{1-x}P_5O_{14}$, whose emission reaches the maximum intensity at the complete substitution of host La^{3+} ions by the activator Tb^{3+} ions ($x = 1$). (From Tanaka, S., Nakamura, A., Kobayashi, H., and Sasakura, H.,*Tech. Digest Phosphor Res. Soc., 166th Meeting*, 1977 (in Japanese). With permission.)

transition). Cooperative absorption has been observed for Pr^{3+}-Pr^{3+}, Pr^{3+}-Ce^{3+}, and Pr^{3+}-Ho^{3+} pairs,[25,26] Raman luminescence for Gd^{3+}-Yb^{3+} and Tm^{3+}-Tm^{2+} pairs[27,28], and cooperative luminescence for Yb^{3+}-Yb^{3+} and Pr^{3+}-Pr^{3+} pairs.[29,30]

The cooperative absorption transition $AB + \hbar\omega \rightarrow A^*B^*$ proceeds via an intermediate state A^i or B^i in a manner $AB \rightarrow A^iB^* \rightarrow A^*B^*$.[31] These three states are combined by the multipolar or exchange interaction operator H_{AB}, which is also operative in energy transfer processes described in 2.8.1, and the perturbation P by the radiation field given by $-e\boldsymbol{r}\cdot\boldsymbol{E}$ for electric dipole transitions as described in 2.1.

Then, the moment of the transition (see 2.1) is given by:

$$M_{AB} = \sum_i \left[\frac{-\langle A^*|P|A^i\rangle\langle A^iB^*|H_{AB}|AB\rangle}{E_A^i + E_B} + \frac{\langle A^*B^*|H_{AB}|A^iB\rangle\langle A^i|P|A\rangle}{E_A^i - E_A - E_B} \right] \tag{156}$$

The cooperative absorption intensity of the Pr^{3+}-Pr^{3+} ion pair in PrCl$_3$ crystals, estimated by this equation, agrees well with that of observed cooperative spectra.[32,33] The estimation indicates that the dq or higher-order multipolar interaction is effective in this pair.[33]

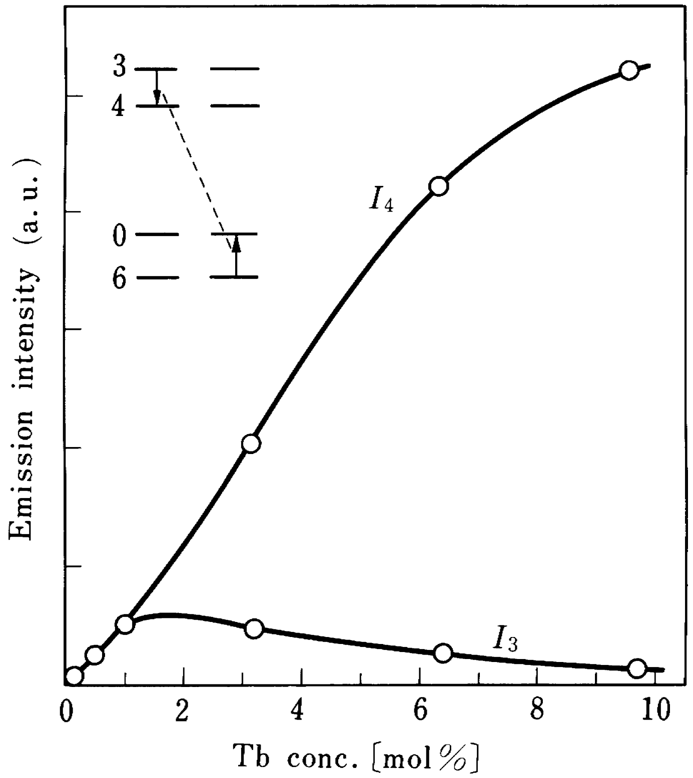

Figure 68 Activator concentration dependence of the emission intensities of the two emitting levels of Tb^{3+},$I_3(^5D_3)$, and $I_4(^5D_4)$. The relative intensity between the two and therefore the emission color is changed from blue-white to green with the increase of the activator concentration due to cross-relaxation between $^5D_3$-$^5D_4$ and $^7F_6$-$^7F_0$. (From Nakazawa, E. and Shionoya, S., *J. Phys. Soc. Japan*, 28, 1260, 1970. With permission.)

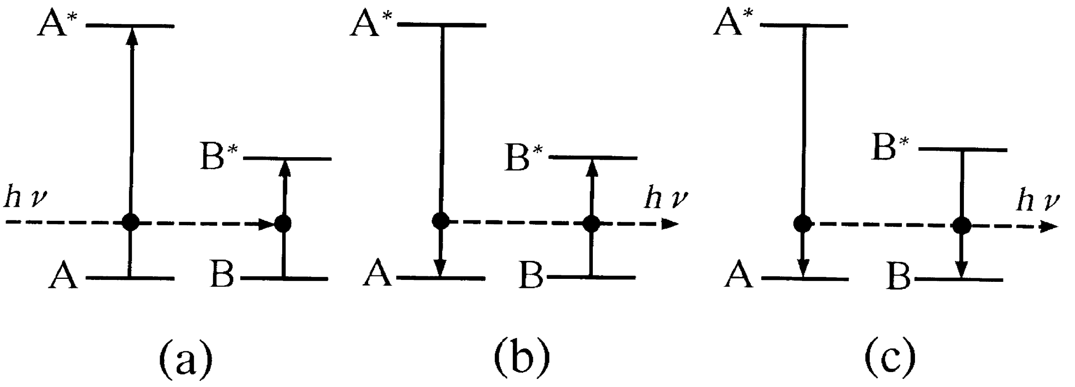

Figure 69 Transition in cooperative optical processes: (a) cooperative absorption, (b) Raman luminescence and (c) cooperative luminescence.

References

1. Foerster, Th., *Ann. Phys.*, 2, 55, 1948.
2. Dexter, D.L., *J. Chem. Phys.*, 21, 836, 1953.
3. Yen, W.M., *Modern Problems in Condensed Matter Science*, Vol. 21, Elsevier, Amsterdam, 1989, pp. 185-249.
4. Nakazawa, E. and Shionoya, S., *J. Chem. Phys.*, 47, 3211, 1967.
5. Kushida, T., *J. Phys. Soc. Japan*, 34, 1313; 1327; 1334; 1983.
6. Inokuti, M. and Hirayama, F., *J. Chem. Phys.*, 43, 1978, 1965.
7. Soules, T.H., Bateman, R.L., Hews, R.A., and Kreidler, E.H., *Phys. Rev.*, B7, 1657, 1973.
8. Perrin, F., *Compt. Rend.*, 178, 1978, 1924.
9. Miyakawa, T. and Dexter, D.L., *Phys. Rev.*, B1, 2961, 1970.
10. Yamada, N., Shionoya, S., and Kushida, T., *J. Phys. Soc. Japan*, 32, 1577, 1972.
11. Yokota, M. and Tanimoto, O., *J. Phys. Soc. Japan*, 22, 779, 1967.
12. Weber, M.J., *Phys. Rev.*, B4, 2934, 1971.
13. Krasutky, N. and Moose, H.W., *Phys. Rev.*, B8, 1010, 1973.
14. Batler, K.H. and Jerome, C.W., *J. Electrochem. Soc.*, 97, 265, 1950.
15. Johnson, P.D., *J. Electrochem. Soc.*, 108, 159, 1961.
16. Shionoya, S. and Nakazawa, E., *Appl. Phys. Lett.*, 6, 118, 1965.
17. Blasse, G. and Bril, A., *J. Chem. Phys.*, 51, 3252, 1969.
18. Tabei, M. and Shionoya, S., *Jpn. J. App. Phys.*, 14, 240, 1975.
19. Suzuki, A., Yamada, H., Uchida, Y., Kohno, H., and Yoshida, M., *Tech. Digest Phosphor Res. Soc. 197th Meeting*, 1983 (in Japanese).
20. Ozawa, L. and Hersh, H.N., *Tech. Digest Phosphor Res. Soc. 155th Meeting*, 1974 (in Japanese).
21. Kuboniwa, S., Kawai, H., and Hoshina, T., *Jpn. J. Appl. Phys.*, 19, 1647, 1980.
22. Tanaka, S., Nakamura, A., Kobayashi, H., and Sasakura, H., *Tech. Digest Phosphor Res. Soc. 166th Meeting*, 1977 (in Japanese).
23. Danielmeyer, H. G., *J. Luminesc.*, 12/13, 179, 1976.
24. Nakazawa, E. and Shionoya, S., *J. Phys. Soc. Japan*, 28, 1260, 1970.
25. Varsani, F. and Dieke, G.H, *Phys. Rev. Lett.*, 7, 442, 1961.
26. Dorman, E., *J. Chem. Phys.*, 44, 2910, 1966.
27. Feofilov, P.P. and Trifimov, A.K., *Opt. Spect.*, 27, 538, 1969.
28. Nakazawa, E., *J. Luminesc.*, 12, 675, 1976.
29. Nakazawa, E. and Shionoya, S., *Phys. Rev. Lett.*, 25, 1710, 1982.
30. Rand, S.C., Lee, L. S., and Schawlow, A.L., *Opt. Commun.*, 42, 179, 1982.
31. Dexter, D.L., *Phys. Rev.*, 126, 1962, 1962.
32. Shinagawa, K., *J. Phys. Soc. Japan*, 23, 1057, 1967.
33. Kushida, T., *J. Phys. Soc. Japan*, 34, 1318, 1973; 34, 1327, 1973; 34, 1334, 1973.

chapter two — section nine

Fundamentals of luminescence

Hajime Yamamoto

Contents

2.9 Excitation mechanism of luminescence by cathode-ray and ionizing radiation 111
- 2.9.1 Introduction 111
- 2.9.2 Collision of primary electrons with solid surfaces 111
- 2.9.3 Penetration of primary electrons into a solid 113
- 2.9.4 Ionization processes 115
- 2.9.5 Energy transfer to luminescence centers 117
- 2.9.6 Luminescence efficiency 117

References 118

2.9 *Excitation mechanism of luminescence by cathode-ray and ionizing radiation*

2.9.1 *Introduction*

Luminescence excited by an electron beam is called *cathodoluminescence* and luminescence excited by energetic particles, i.e., α-ray, β-ray or a neutron beam, or by γ-ray, is called either *radioluminescence* or *scintillation*.*

The excitation mechanism of cathodoluminescence and of radioluminescence can be discussed jointly because these two kinds of luminescence have a similar origin. In solids, both the electron beam and the high-energy radiation induce ionization processes, which in turn generate highly energetic electrons. These energetic electrons can be further multiplied in number through collisions, creating "secondary" electrons, which can then migrate in the solid with high kinetic energy, exciting the light-emitting centers. The excitation mechanism primarily relevant to cathodoluminescence is discussed here.

2.9.2 *Collision of primary electrons with solid surfaces*

Energetic electrons incident on a solid surface in vacuum are called *primary electrons* and are distinct from the secondary electrons mentioned above. A small fraction of the electrons is scattered and reflected back to the vacuum, while most of the electrons penetrate into

---

* The word originally means flash, as is observed under particle beam excitation.

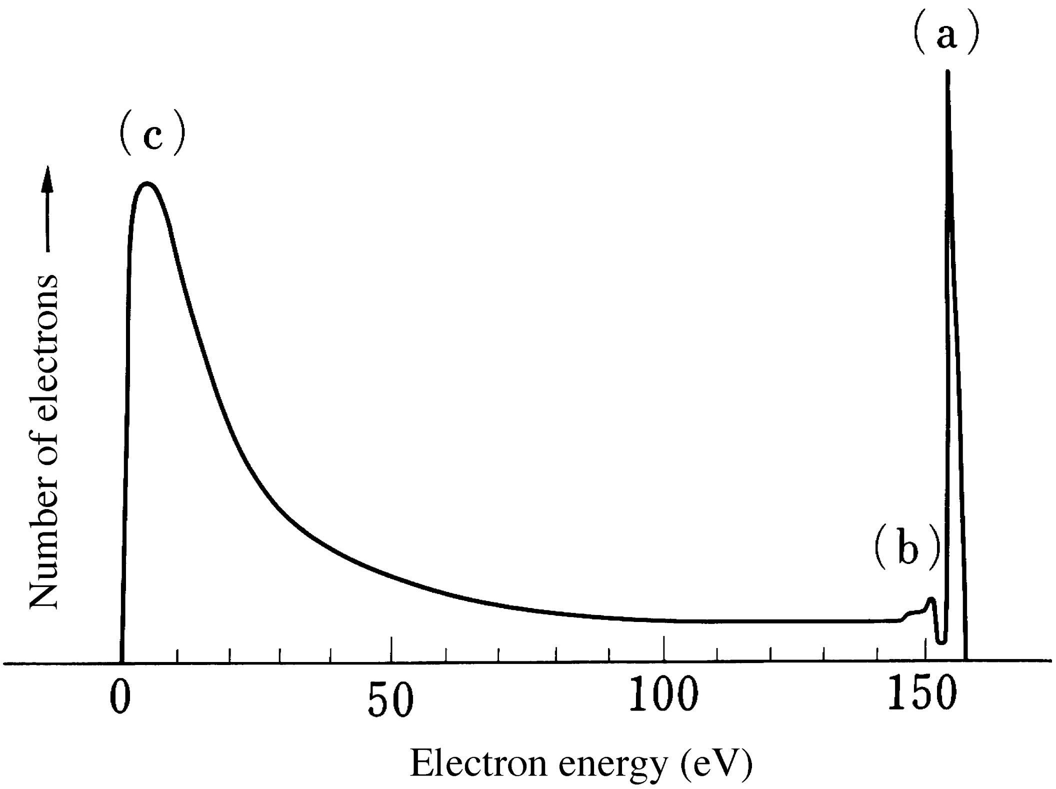

Figure 70 The energy distribution of electrons emitted from the Ag surface exposed by the primary electrons of 153 eV: (a)electrons emitted by elastic scattering, (b) electrons by inelastic scattering and (c) secondary electrons. (From Dekker, A.J., *Solid State Physics*, Prentice-Hall, Tokyo, 1960, 418-420. With permission.)

the solid. The reflected electrons can be classified into three types: (a) elastically scattered primary electrons, (b) inelastically scattered primary electrons, and (c) secondary electrons.[1] The secondary electrons mentioned here are those electrons generated by the primary electrons in the solid and are energetic enough to overcome the work function of the solid surface. This phenomenon, i.e., the escape of secondary electrons from the solid, is similar to the photoelectric effect. The relative numbers of the three types of scattered electrons observed for the Ag surface are shown in Figure 70.[1,2] As shown in this figure, the inelastically scattered primary electrons are much smaller in number than the other two types.

The ratio of the number of the emitted electrons to the number of the incident electrons is called the *secondary yield* and usually denoted as δ. With this terminology, δ should be defined only in terms of the secondary electrons (c), excluding (a) and (b). However, in most cases, δ is stated for all the scattered electrons—(a), (b), and (c)—for practical reasons.

For an insulator, δ depends on the surface potential relative to the cathode as is schematically shown in Figure 71. For $\delta < 1$, the insulator surface is negatively charged; as a consequence, the potential of a phosphor surface is not raised above V_{II} shown in Figure 71, even for an accelerating voltage higher than V_{II}. In other words, the surface potential stays at V_{II} and is called the sticking potential. To prevent electrical charging of surface, an aluminizing technique is employed in cathode-ray tubes (CRTs). Negative charging of a phosphor is also a problem for vacuum fluorescent tubes and some of field emission displays, which use low-energy electrons at a voltage below V_I. The aluminizing technique cannot be used in these cases, however, because the low-energy primary

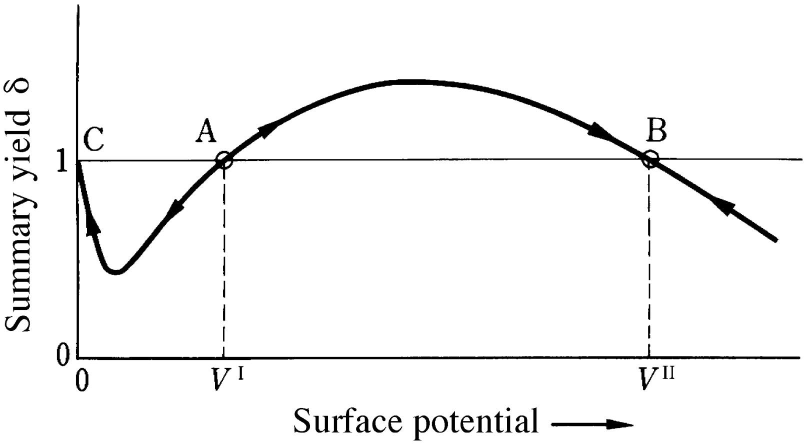

Figure 71 A schematic illustration of secondary yield as a function of the surface potential of an insulator. The secondary yield δ is unstable at point A, while it is stable at B and C. At these points, the state shifts toward the direction of the given arrows with a change in the potential. Near point C, where the potential is in a region of a few to several tens of volts, the yield approaches 1 because the incident primary electrons are reflected. (From Kazan, B. and Knoll, M., *Electron Image Storage*, Academic, New York, 1968, 22. With permission.)

electrons, for example a few ten or hundred eV, cannot go through an aluminum film, even if it is as thin as 100 nm, which is practically the minimum thickness required to provide sufficient electrical conductivity and optical reflectivity. It is, therefore, required to make the phosphor surface electrically conductive (see Chapter 8).

To evaluate a cathodoluminescence efficiency, one must exclude the scattered primary electrons (a) and (b) in Figure 70. The ratio of the electrons (a) and (b) to the number of the incident electrons is called *back-scattering factor,* denoted by η_0. Actually, the electrons (b) are negligible compared with the electrons (a) as shown in Figure 70. The value of η_0 depends weakly on the primary electron energy but increases with the atomic number of a solid. η_0 obeys an empirical formula, with the atomic number or the number of electrons per molecule being $Z_m{}^3$; that is:

$$\eta_0 = (1/6)\ln Z_m - (1/4) \tag{157}$$

The value calculated by this formula agrees well with experimental results obtained for single-crystal samples. For example, the calculated values for ZnS with Z_m of 23 is 0.25 and for YVO_4 with Z_m of 15.7 is 0.21, while the observed values for single crystals of these compounds are 0.25 and 0.20, respectively.[4] In contrast, a smaller value of η_0 is found for a powder layer because some of the reflected electrons are absorbed by the powder through multiple-scattering. The observed values of η_0 are 0.14,[4] both for ZnS and YVO_4 in powder form. It has also been reported that η_0 varies by several percent depending on the packing density of a powder layer.[6]

2.9.3 *Penetration of primary electrons into a solid*

The penetration path of an electron in a solid has been directly observed with an optical microscope by using a fine electron beam of 0.75 μm diameter (Figure 72). This experiment shows a narrow channel leading to a nearly spherical region for electron energy higher than 40 keV, while it shows a semispherical luminescent region for lower electron energies.

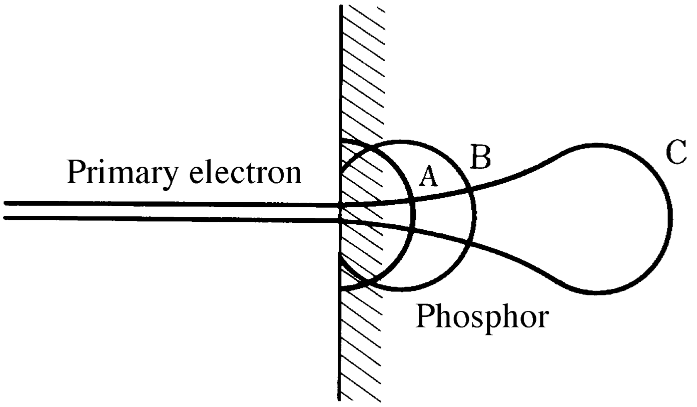

Figure 72 A schematic illustration of a region excited by an electron beam. This region can be visualized as the luminescent profile of the solid phosphor particle as seen through a microscope. The energy of the primary electrons increases in the order of A, B, and C. For A, the energy is several keV and for C, 40 keV or higher. (From Ehrenberg, W. and Franks, J., *Proc. Phys. Soc.*, B66, 1057, 1953; Garlick, G.F.J., *Br. J. Appl. Phys.*, 13, 541, 1962. With permission.)

The former feature is found also for high-energy particle excitation, i.e., the excitation volume is confined to a narrow channel until the energy is dissipated by ionization processes. This result indicates that the scattering cross-section of an electron or a particle in a solid is larger for lower electron energy. The energy lost by a charged particle passing through a solid is expressed by Bethe's formula[9]:

$$dE/dx = \left(2\pi N Z_m e^4 / E\right) \ln\left(E/E_i\right) \tag{158}$$

where E denotes the energy of a primary electron at distance x from the solid surface, N the electron density (cm^{-3}) of the solid, Z_m the mean atomic number of the solid, and E_i the mean ionization potential averaged over all the electrons of the constituent atoms.

Various formulas have been proposed to give the relation between E and x. Among them, the most frequently used is Thomson-Whiddington's formula,[10] which we can derive from Eq. 158 simply by putting $\ln(E/E_i)$ = constant.

$$E = E_0\left(1 - x/R\right)^{1/2} \tag{159}$$

Here, E_0 is the primary electron energy at the surface and R is a constant called as the range, i.e., the penetration depth at $E = 0$*. It is to be noted that an incremental energy loss, $-dE/dx$, increases with x according to Eq. 159.

In a range of E_0 = 1–10 keV, the dependence of R on E_0 is given by[11]:

$$R = 250\left(A/\rho\right)\left(E_0 / Z_m^{1/2}\right)^n \tag{160}$$

where $n = 1.2/(1-0.29\log Z_m)$, ρ is the bulk density, A the atomic or molecular weight, Z_m the atomic number per molecule, and E_0 and R are expressed in units of keV and Å, respectively. When E_0 = 10 keV, Eq. 160 gives R = 1.5 μm for ZnS and R = 0.97 μm for $CaWO_4$. The experimental values agree well with the calculated values.

---

* Other formulas define the range as the penetration depth at $E = E_0/e$.

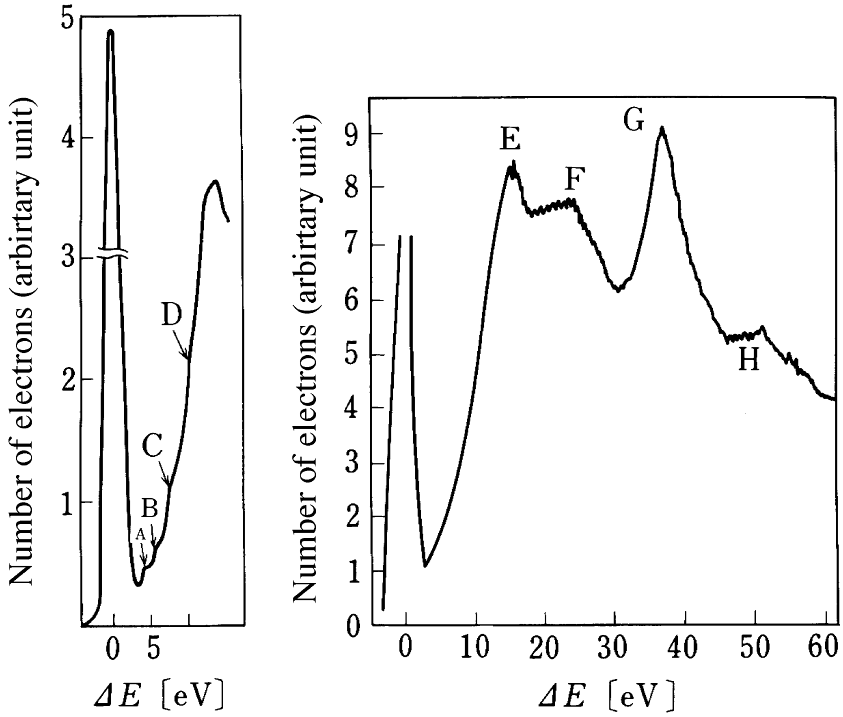

Figure 73 Electron energy loss spectra of YVO_4: (a) peaks A to D originate in the electronic transitions of the VO_4^{-3} complex; (b) peak E can be assigned to plasmon excitation. Peak G is due to a transition from Y 4*p* orbital to the conduction band and, peak H from V 3*p* to the conduction band. The origin of peak F is not identified. The strong peak at 0 eV indicates the incident electrons with no energy loss. (From Tonomura, A., Endoh, J., Yamamoto, H., and Usami, K., *J. Phys. Soc. Japan*, 45, 1654, 1978. With permission.)

When E_0 is decreased at a fixed electron beam current, luminescence vanishes at a certain positive voltage, called the dead voltage. One of the explanations of the dead voltage is that, at shallow R, the primary electron energy is dissipated within a dead layer near the surface, where nonradiative processes dominate as a result of a high concentration of lattice defects.[12] It is also known, however, that the dead voltage decreases with an increase in electrical conductivity, indicating that the dead voltage is affected by electrical charging as well.

2.9.4 Ionization processes

A charged particle, such as an electron, loses its kinetic energy through various modes of electrostatic interaction with constituent atoms when it passes through a solid. Elementary processes leading to energy dissipation can be observed experimentally by the electron energy loss spectroscopy, which measures the energy lost by a primary electron due to inelastic scattering (corresponding to the electrons (b) in Figure 70). Main loss processes observed by this method are core-electron excitations and creation of plasmons, which are a collective excitation mode of the valence electrons. Core-electron excitation is observed in the range of 10 to 50 eV for materials having elements of a large atomic number, i.e., rare-earth compounds or heavy metal oxides such as vanadates or tungstates.[13] The plasmon energy is found in the region of 15 to 30 eV. Compared with these excitation modes, the contribution of the band-to-band transition is small. As an example exhibiting various modes of excitation, the electron energy loss spectrum of YVO_4 is shown in Figure 73.[14]

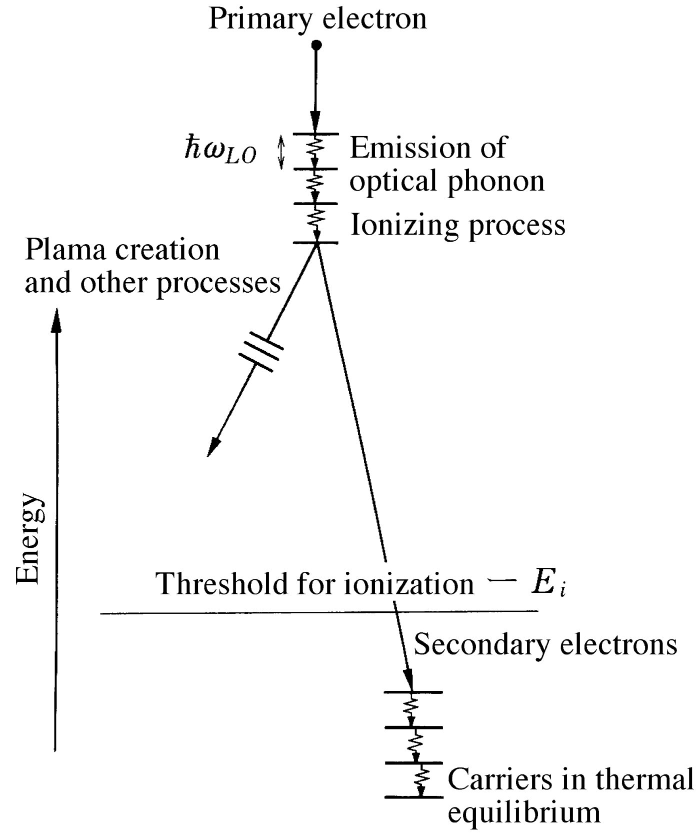
Primary electron
$\hbar\omega_{LO}$
Emission of optical phonon
Ionizing process
Plama creation and other processes
Energy
Threshold for ionization
E_i
Secondary electrons
Carriers in thermal equilibrium

Figure 74 A schematic illustration of excitation processes by a high-energy electron, which penetrates into a solid. (From Robbins, D.J., *J. Electrochem. Soc.*, 127, 2694, 1980. With permission.)

Plasmons are converted to single-electron excitations in an extremely short period of time, ~10^{-15} s. As a consequence, electrons with energies of 10 to 50 eV are created every time an energetic primary electron is scattered in a solid as a result of core-electron excitation or plasmon creation. This results in a series of ionization processes in a solid. Most of the electrons generated by the scattering events, or the secondary electrons, are still energetic enough to create other hot carriers by Auger processes. Secondary electron multiplication can last until the energy of the electron falls below the threshold to create free carriers. All through this electron energy loss process, scattering is accompanied by phonon creation, as schematically shown in Figure 74.[15] Secondary electron multiplication is essentially the same as the photoexcitation process in the vacuum ultraviolet region.

The average energy required to create an electron-hole pair near the band edges, E_{av}, is given by the following empirical formula.[16]

$$E_{av} = 2.67E_g + 0.87\ [\text{eV}] \tag{161}$$

where E_g is the bandgap energy either for the direct or the indirect gap. This formula was originally obtained for elements or binary compounds with tetrahedral bonding, but it is applied often to phosphors with more complex chemical compositions and crystal structures. It is not, however, straightforward to define the bandgap energy for a material having low-lying energy levels characteristic of a molecular group, e.g., vanadates or tungstates. Therefore, one must be careful in applying the above formula to some phosphors.

As described above, the average creation energy of an electron-hole pair is closely related to the cathodoluminescence efficiency (see also Section 2.9.6). There is, however, another way to consider the luminescence efficiency; it focuses on phonon emission,[16] which competes with the electron-hole pair creation in the ionization processes. The phonon emission probability, denoted as R_p here, is proportional to the interaction of an electron with an optical phonon, and is expressed as:

$$R_p \propto \left(\hbar\omega_{LO}\right)^{1/2}\left(1/\varepsilon_\infty - 1/\varepsilon_0\right) \tag{162}$$

where ω_{LO} is the energy of a longitudinal optical phonon interacting with an electron, and ε_∞ and ε_0 are high-frequency and static dielectric constants, respectively. When multiplied with the phonon energy, the probability R_p contributes to the pair creation energy E_{av} as a term independent of E_g, e.g., the second term 0.87 eV in Eq. 161.

The luminescence excited by energetic particles is radioluminescence.[17] The excitation mechanism of radioluminescence has its own characteristic processes, though it involves ionization processes similar to the cathodoluminescence processes.

For example, the energy of γ-rays can be dissipated by three processes: (1) the Compton effect, (2) the photoelectric effect directly followed by X-ray emission and Auger effect, and (3) the creation of electron-positron pairs. Subsequent to these processes, highly energetic secondary electrons are created, followed by the excitation of luminescence centers, as is the case with cathodoluminescence.

A characteristic energy loss process of neutrons, which has no electric charges but much larger mass than an electron, is due to the recoil of hydrogen atoms. If the neutron energy is large enough, a recoiled hydrogen is ionized and creates secondary electrons. It must be added, however, that hydrogen atoms are not contained intentionally in inorganic phosphors.

2.9.5 *Energy transfer to luminescence centers*

The final products of the secondary-electron multiplication are free electrons and free holes near the band edge, i.e., so-called *thermalized* electrons and holes. They recombine with each other, and a part of the recombination energy may be converted to luminescence light emission.

The process in which either a thermalized electron-hole pair or the energy released by their recombination is transferred to a luminescence center is called *host sensitization* because the luminescence is sensitized by the optical absorption of the host lattice. This process is analogous to the optical excitation near the band edge. Detailed studies were made on the optical excitation of luminescence in IIb-VIb and IIIb-Vb compounds, as described in 3.7 and 3.8. Luminescence of rare-earth ions and Mn^{2+} ions arises because these ions capture electrons and holes by acting as isoelectronic traps.[18,19] In inorganic compounds having complex ions and organic compounds, the excitation energy is transferred to the luminescence centers through the molecular energy levels.

2.9.6 *Luminescence efficiency*

The cathodoluminescence energy efficiency η, for all the processes described above can be expressed by[20]:

Table 2 Examples of Cathodoluminescence Efficiency

Chemical composition	WTDS designation	Energy efficiency (%)	Peak wavelength (nm)	Luminescence color
$Zn_2SiO_4:Mn^{2+}$	GJ	8	525	Green
$CaWO_4:Pb$	BJ	3.4	425	Blue
ZnS:Ag,Cl	X	21	450	Blue
ZnS:Cu,Al	X	23, 17	530	Green
$Y_2O_2S:Eu^{3+}$	X	13	626	Red
$Y_2O_3:Eu^{3+}$	RF	8.7	611	Red
$Gd_2O_2S:Tb^{3+}$	GY	15	544	Yellowish green
$CsI:Tl^{+}$	—	11	—	Green
$CaS:Ce^{3+}$	—	22	—	Yellowish green
$LaOBr:Tb^{3+}$	—	20	544	Yellowish green

Note: The phosphor screen designation by WTDS (Worldwide Phosphor Type Designation System) is presented (See 6.3).

Many data are collected in Alig, R.C. and Bloom, S., *J. Electrochem. Soc.*, 124, 1136, 1977.

$$\eta = (1-\eta_0)\eta_x (E_{em}/E_g) q \tag{163}$$

where η_0 is the back-scattering factor given by Eq. 157, η_x the mean energy efficiency to create thermalized electrons and holes by the primary electrons or E_g/E_{av}, q the quantum efficiency of the luminescence excited by thermalized electron-hole pairs, and E_{em} the mean energy of the emitted photons. Thus,

$$\eta < \eta_x (E_{em}/E_g) \tag{164}$$

and also $\eta_x < 1/3$ according to Eq. 161.

The energy efficiency, luminescence peak wavelength and color are shown in Table 2 for some efficient phosphors. For the commercial phosphors, ZnS:Ag,Cl; ZnS:Cu,Al; $Y_2O_2S:Eu^{3+}$; and $Y_2O_3:Eu^{3+}$, we find $\eta_x \simeq 1/3$ from Eq. 163 by assuming that $\eta_0 = 0.1$ and $q = 0.9$–1.0. This value of η_x suggests that the energy efficiency is close to the limit predicted by Eq. 163 for these phosphors. It is to be emphasized, however, that this estimate does not exclude a possibility for further improvement in the efficiency of these phosphors, for example by 10 or 20%, since the calculated values are based on a number of approximations and simplifying assumptions. It should also be noted that the bandgap energy is not known accurately for the phosphors given in Table 2, except for ZnS, CsI, and CaS. For the other phosphors, the optical absorption edge must be used instead of the bandgap energy, leaving the estimation of η approximate. For CaS, the indirect bandgap, 4.4 eV, gives $\eta_x = 0.21$, while the direct bandgap, 5.3 eV, gives the value exceeding the limit predicted by Eq. 163.

References

1. Dekker, A.J., *Solid State Physics*, Prentice-Hall, Maruzen, Tokyo, 1960, 418-420.
2. Rudberg, E., *Proc. Roy. Soc. (London)*, A127, 111, 1930.
3. Tomlin, S.G., *Proc. Roy. Soc. (London)*, 82, 465, 1963.
4. Meyer, V.G., *J. Appl. Phys.*, 41, 4059, 1970.
5. Kazan, B. and Knoll, M., *Electron Image Storage*, Academic Press, New York, 1968, 22.
6. Kano, T. and Uchida, Y., *Jpn. J. Appl. Phys.*, 22, 1842, 1983.
7. Ehrenberg, W. and Franks, J., *Proc. Phys. Soc.*, B66, 1057, 1953.

8. Garlick, G.F.J., *Br. J. Appl. Phys.*, 13, 541, 1962.
9. Bethe, H.A., *Ann. Physik*, 13, 541, 1930.
10. Whiddington, R., *Proc. Roy. Soc. (London)*, A89, 554, 1914.
11. Feldman, C., *Phys. Rev.*, 117, 455, 1960.
12. Gergley, Gy., *J. Phys. Chem. Solids*, 17, 112, 1960.
13. Yamamoto, H. and Tonomura, A., *J. Luminesc.*, 12/13, 947, 1976.
14. Tonomura, A., Endoh, J., Yamamoto, H., and Usami, K., *J. Phys. Soc. Japan*, 45, 1654, 1978.
15. Robbins, D.J., *J. Electrochem. Soc.*, 127, 2694, 1980.
16. Klein, C.A., *J. Appl. Phys.*, 39, 2029, 1968.
17. For example, Brixner, L.H., *Materials Chemistry and Physics*, 14, 253, 1987; Derenzo, S.E., Moses, W.W., Cahoon, J.L., Perera, R.L.C., and Litton, J.E., *IEEE Trans. Nucl. Sci.*, 37, 203, 1990.
18. Robbins, D.J. and Dean, P.J., *Adv. Phys.*, 27, 499, 1978.
19. Yamamoto, H. and Kano, T., *J. Electrochem. Soc.*, 126, 305, 1979.
20. Garlick, G.F.J., *Cathodo- and Radioluminescence in Luminescence of Inorganic Solids*, Goldberg, P., Ed., Academic Press, New York, 1966, 385-417.
21. Alig, R.C. and Bloom, S., *J. Electrochem. Soc.*, 124, 1136, 1977.

chapter two — section ten

Fundamentals of luminescence

Shosaku Tanaka, Hiroshi Kobayashi, Hiroshi Sasakura, and Noboru Miura

Contents

2.10 Inorganic electroluminescence 121
  2.10.1 Introduction 121
  2.10.2 Injection EL 122
  2.10.3 High-field EL 123
    2.10.3.1 Injection of carriers 124
    2.10.3.2 Electron energy distribution in high electric field 128
    2.10.3.3 Excitation mechanism of luminescence centers 132
References 137

2.10 Inorganic electroluminescence

2.10.1 Introduction

Electroluminescence (EL) is the generation of light by the application of an electric field to crystalline materials, or resulting from a current flow through semiconductors. The EL of inorganic materials is classified into the two groups: injection EL and high electric field EL. The high- field EL is further divided into two types: powder phosphor EL and thin-film EL. The classification of EL with regard to typical device applications is summarized as follows:

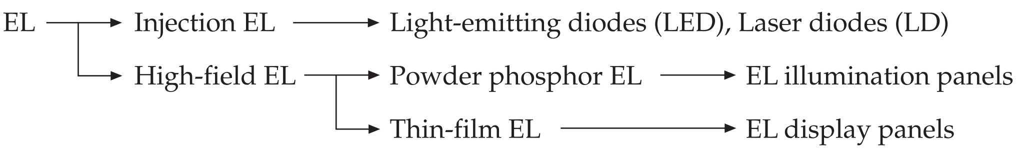

Historically, the EL phenomenon was first observed by Destriau[1,2] in 1936, who observed luminescence produced from ZnS powder phosphors suspended in castor oil when a strong electric field was applied. This type of EL is, today, classified as powder phosphor EL. Later on, in the early 1960s, polycrystalline ZnS thin films were prepared and used as EL materials. This type of EL is typical of thin-film EL.

On the other hand, in 1952 Haynes and Briggs[3] reported infrared EL from forward-biased *p-n* junctions in Ge and Si diodes. This type of EL is classified as injection EL. Visible EL is observed in diodes made of wide bandgap semiconductors, such as GaP. These diodes are called light-emitting diodes (LEDs) and have been widely used since the late 1960s. Semiconductor lasers, first demonstrated in 1962 using GaAs diodes, operate by stimulating injection EL light in an appropriate optical cavity. As will be described below, the mechanisms of light generation in injection EL and high-field EL are quite different from each other. In addition, the applications of these EL phenomena to electronic devices are different.

Usually, the term EL is used, in a narrow sense, to mean high-field EL. In this section, therefore, the description will focus on the basic processes of the high-field EL, in particular on the excitation mechanisms in thin-film EL. The mechanisms of injection EL are described only briefly.

2.10.2 *Injection EL*

The term "injection EL" is used to explain the phenomenon of luminescence produced by the injection of minority carriers. Energy band diagrams for p-n junction at thermal equilibrium and under forward biased conditions (p-type side:positive) are shown in Figures 75(a) and (b), respectively. At thermal equilibrium, a depletion layer is formed and a diffusion potential V_d across the junction is produced. When the p-n junction is forward-biased, the diffusion potential V_d decreases to $(V_d - V)$, and electrons are injected from the n-region into the p-region while holes are injected from the p-region into the n-region; that is, minority carrier injection takes place. Subsequently, the minority carriers diffuse and recombine with majority carriers directly or through trapping at various kinds of recombination centers, producing injection EL. The total diffusion current on p-n junction is given by:

$$\begin{aligned} J &= J_p + J_n = J_s\left(\exp\left(\frac{qV}{nkT}\right) - 1\right) \\ J_s &= q\left(\frac{D_p p_{n0}}{L_p} + \frac{D_n n_{p0}}{L_n}\right) \end{aligned} \tag{165}$$

where D_p and D_n are diffusion coefficients for holes and electrons, p_{no} and n_{po} are the concentrations of holes and electrons as minority carriers at thermal equilibrium, and L_p and L_n are diffusion lengths given by $\sqrt{D\tau}$, where τ is the lifetime of the minority carriers.

The LEDs that became commercially available in the late 1960s were the green-emitting GaP:N and the red-emitting GaP:Zn,O diodes. GaP is a semiconductor having an indirect bandgap; the N and (Zn,O) centers in GaP are isoelectronic traps that provide efficient recombination routes for electrons and holes to produce luminescence in this material (See 3.8.2). Very bright LEDs used for outdoor displays were developed using III-V compound alloys in the late 1980s to early 1990s; these alloys all have a direct bandgap. Green-, yellow-, orange-, and red-emitting LEDs with high brightness are fabricated using InGaAlP, GaAsP, or GaAlAs (See 3.8.3). In 1993 to 1994, GaInN (another alloy with a direct bandgap) was developed, leading to very bright blue and green LEDs (See 3.8.5). Thus, LEDs covering the entire visible range with high brightness are now commercially available.

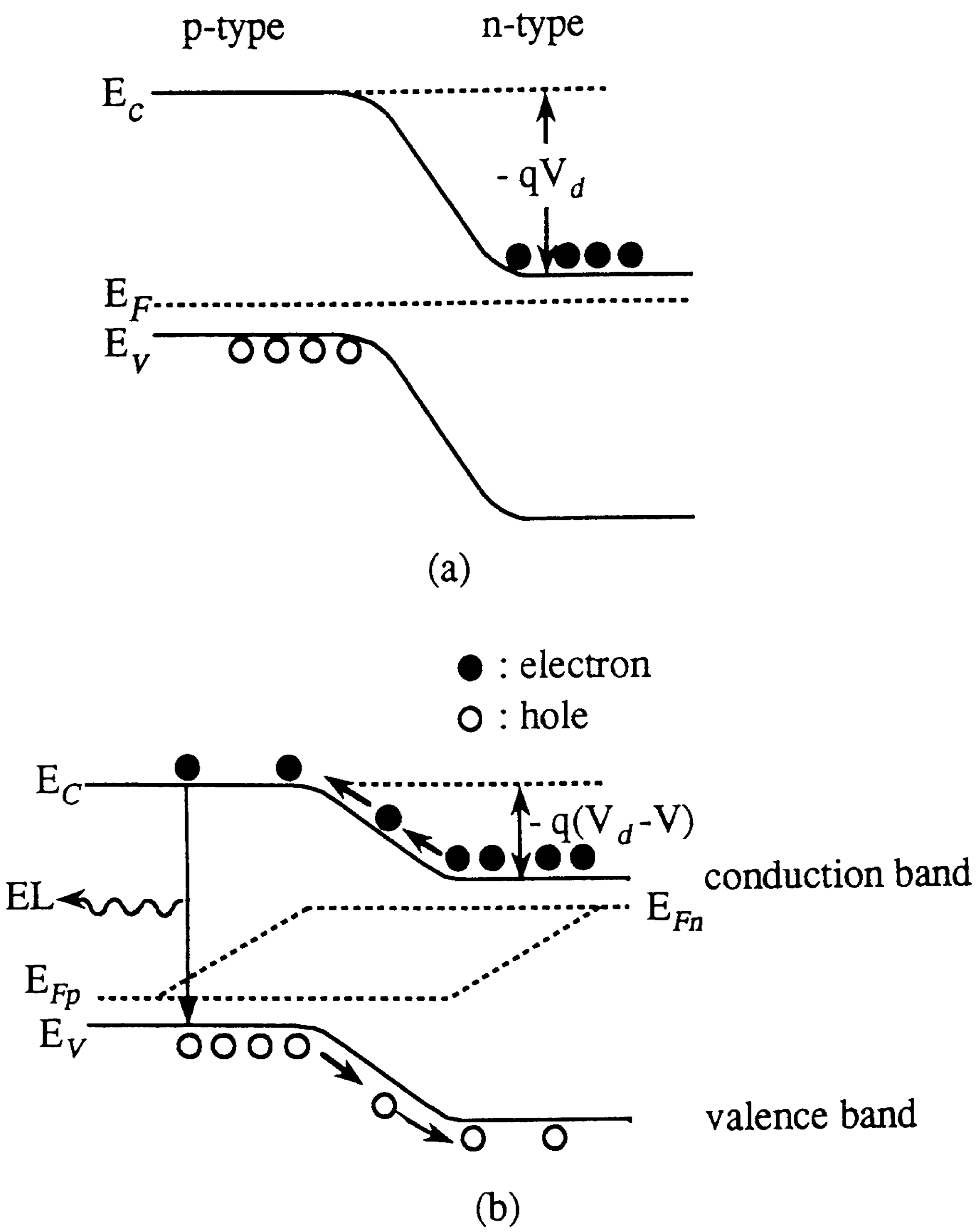
p-type
n-type
E_C
$-qV_d$
E_F
E_V
(a)
● : electron
o : hole
E_C
$-q(V_d-V)$
conduction band
EL
E_{Fn}
E_{Fp}
E_V
valence band
(b)

Figure 75 Energy band diagrams for the p-n junction under (a) thermal equilibrium and under (b) forward-biased conditions.

2.10.3 *High-field EL*

In the case of thin-film EL used for display panels, a high electric field of the order of 10^6 V cm^{-1} is applied to the EL materials. Electrons, which are the majority carriers in this case, are injected into the EL emitting layers. These electrons are accelerated by the electric field until some of them reach energies sufficient to cause impact excitation of luminescent centers generating EL light. The most common luminescent centers in ZnS and other EL hosts are Mn^{2+} and the rare-earth ions; these activators offer a wide variety of emission colors. As noted above, the mechanism of high-field thin-film EL is quite different from that of injection EL. Here, the basic processes of high-field EL—that is, (1) the injection of carriers, (2) the carrier energy distribution in the high electric field region, and (3) the excitation mechanism of the luminescence centers—are discussed.

In the case of high-field, powder phosphor EL, electrons and holes are injected by tunnel emission (field emission) induced by high electric field (10^6 V cm^{-1}) applied to a conductor-phosphor interface (see 9.1.3). The excitation mechanism is similar to that of thin-film EL, and is also discussed in this section.

2.10.3.1 *Injection of carriers*

Injection of majority carriers through a Schottky barrier.[4] When a semiconductor is in contact with metal, a potential barrier, called the Schottky barrier, is formed in the contact region. Before interpreting the Schottky effect in the metal-semiconductor system, one can consider this effect in a metal-vacuum system, which will then be extended to the metal-semiconductor barrier.

The minimum energy necessary for an electron to escape into vacuum from its position within the Fermi distribution is defined as the work function $q\phi_m$, as shown in Figure 76. When an electron is located at a distance x from the metal, a positive charge will be induced on the metal surface. The force of attraction between the electron and the induced positive charge is equivalent to the force that would exist between the electron and the positive image charge located at a distance of –x. The attractive force is called the image force, and is given by: $F = -q^2/16\pi\varepsilon_0 x^2$, where ε_0 is a permittivity in vacuum. The potential

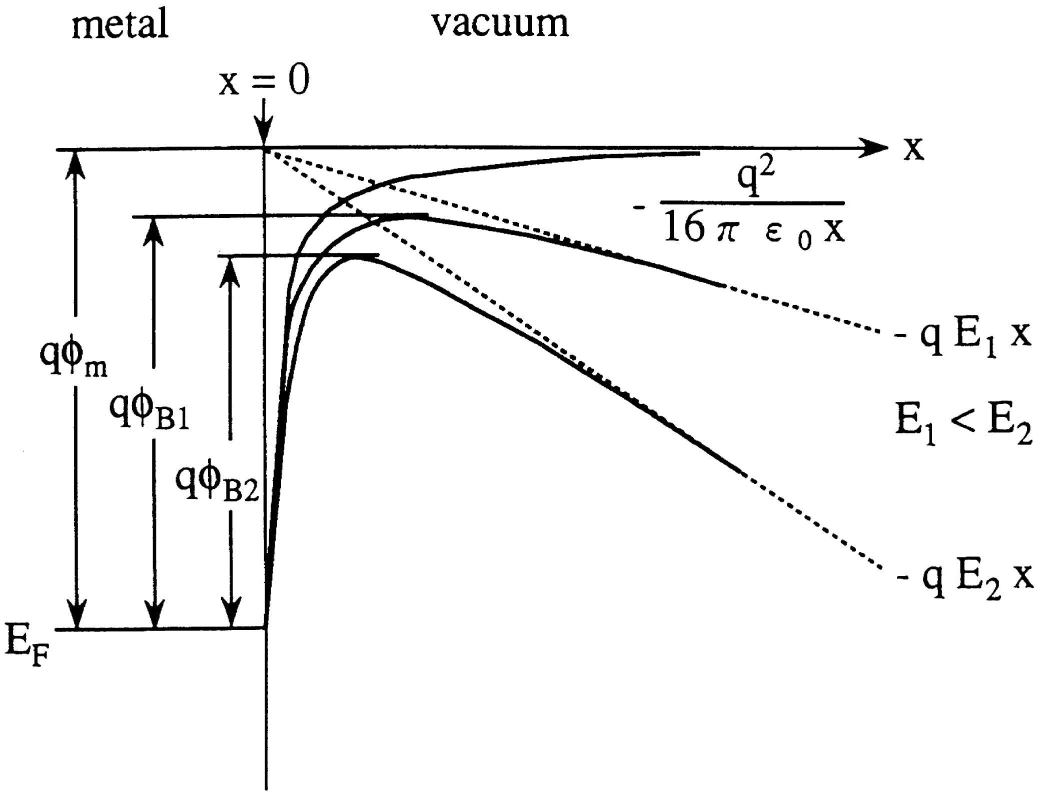

Figure 76 Energy band diagram representing the Schottky effect between metal surface and vacuum. The barrier lowering under reverse bias is $q(\phi_m - \phi_B)$.

is given by $U = q^2/16\pi\varepsilon_0 x$. When an external field E is applied, the total potential energy is given by: $U_T = q^2/16\pi\varepsilon_0 x + qEx$, as shown in the figure. Thus, at high fields, the potential barrier is lowered considerably, and the effective metal work function for thermoionic emission $q\phi_B$ is reduced. This lowering of the potential barrier induced by the image charge is known as the Schottky effect.

The energy band diagrams for an *n*-type semiconductor in contact with a metal are shown for the case of thermal equilibrium and under reverse-biased conditions (semiconductor side: positive) in Figures 77(a) and (b), respectively. When an electric field is applied to the metal-semiconductor contact region, the potential energy is lowered in the semiconductor by the image force or Schottky effect. The barrier height $q\Phi_B$ is lowered as discussed and electrons can be thermally injected into the semiconductor. The current density for this process is expressed as:

$$\begin{aligned} J &= AT^2 \exp\left(\frac{-q\Phi_B - \left(qE/4\pi\varepsilon_s\right)^{1/2}}{kT}\right) \\ &\sim T^2 \exp\left(\frac{aV^{1/2}}{T} - \frac{q\Phi_B}{kT}\right) \end{aligned} \tag{166}$$

where the permittivity in the semiconductor ε_s is used instead of that in vacuum, ε_0. The injected electrons are then accelerated by the electric field and excite the luminescent centers by impact.

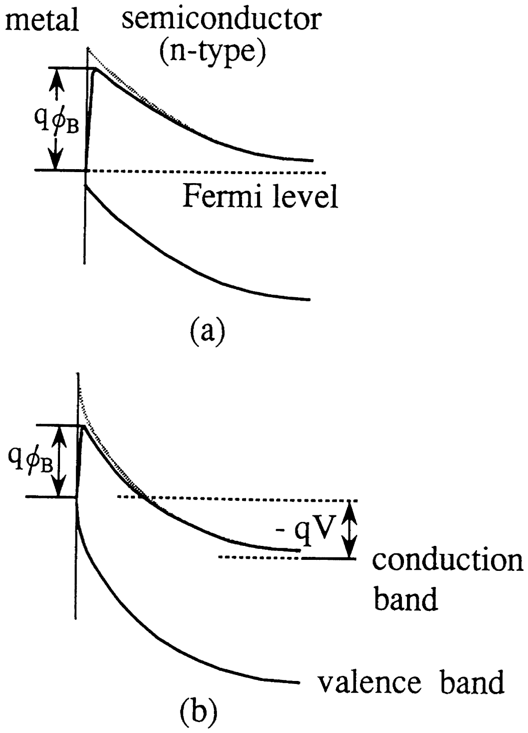

Figure 77 Energy band diagrams for the *n*-type semiconductor in contact with metal (a) under thermal equilibrium and (b) under reverse-biased conditions.

In the case of ZnS:Cu EL powder phosphors, a Schottky barrier is thought to be formed between the *n*-ZnS semiconductor and the Cu metal or the conducting Cu_xS microparticles found in the phosphors (see 9.1.3). In the latter, electron injection occurs from the conductive phase through the Schottky barrier and causes the electroluminescence.

Injection of carriers due to Poole-Frenkel emission.[4] Semiconductors with fairly wide gaps of 3.5 to 4.5 eV (such as ZnS, CaS, and SrS) are used as EL materials. In these compounds, a large number of electrons are usually trapped in traps caused by lattice defects. When an electric field is applied, trapped electrons are released into the conduction band, as shown in Figure 78. This process is known as the Poole-Frenkel emission process and is due to field-enhanced thermal excitation of trapped electrons into the conduction band. For an electron trapped by a Coulomb-like potential $U \propto 1/r^n$, the expression for this process is identical to that for Schottky emission. With the barrier height $q\phi_B$ reduced by the electric field as shown in the figure, the current density due to Poole-Frenkel emission is expressed as:

$$J \simeq E \exp\left(\frac{-q\Phi_B - \left(qE/\pi\varepsilon_s \right)^{1/2}}{kT} \right) \tag{167}$$

In the case of thin-film EL devices, a fraction of the initial electrons is injected by this process.

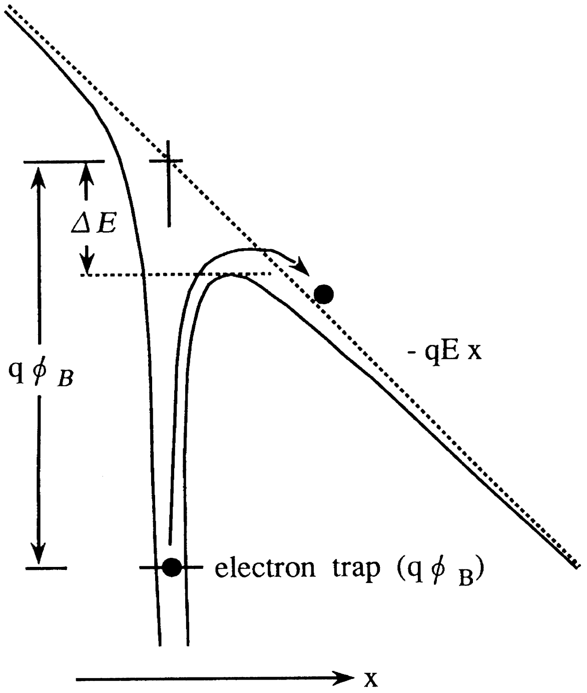

Figure 78 Energy band diagram for deep electron traps under high electric field. Electron injection due to Poole-Frenkel effect is illustrated.

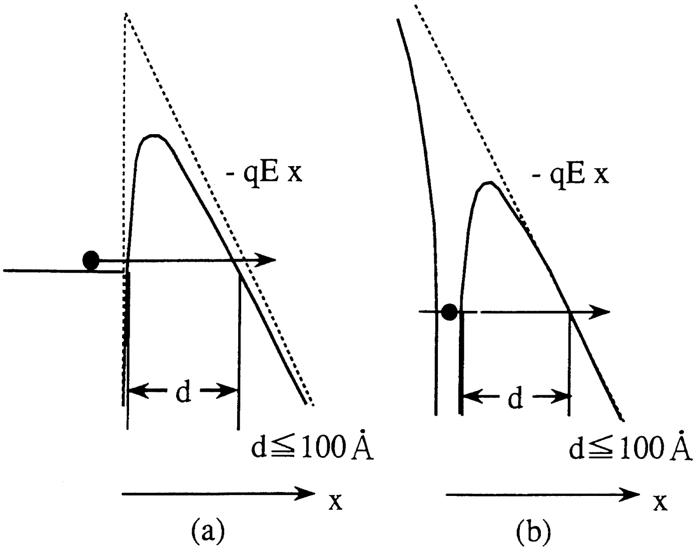

Figure 79 Energy band diagram for (a) Schottky barrier and for (b) deep electron traps under high electric field. Electron injection due to the tunneling effect is illustrated.

Injection of carriers due to tunnel emission (field emission).[4] When an extremely high electric field of over 10^6 V cm^{-1} is applied to a Schottky barrier or to electron traps, the barrier width d becomes very thin, with a thickness in the neighborhood of 100 Å. In this case, electrons tunnel directly into the conduction band, as illustrated in Figure 79. The current density due to this process depends only on the electric field and does not depend on temperature, and is described by:

$$\begin{aligned} J &\simeq E^2 \exp\left(\frac{-4\left(2m^*\right)^{1/2}\left(q\Phi_B\right)^{3/2}}{3q\hbar E}\right) \\ &\simeq V^2 \exp\left(-\frac{b}{V}\right) \end{aligned} \tag{168}$$

where m* is the effective electron mass.

Since the average electric field within thin phosphor films used in EL panels is nearly 10^6 V cm^{-1}, it is possible to conclude that electron injection due to tunneling takes place in addition to Schottky and Poole-Frenkel emission, with tunneling emission becoming predominant at high electric field conditions.

For powder-type EL devices, it is known that thin embedded Cu_xS conducting needles are formed in the ZnS microcrystals. Although the average applied electric field in the devices is about 10^4–10^5 V cm^{-1}, the electric field is concentrated at the tips of these microcrystals and the local electric field can be 10^6 V cm^{-1} or more. Electrons are injected by tunneling from one end of the needle and holes from the other end. This mechanism is known as the bipolar field-emission model. The injected electrons recombine with holes, which were injected by the same process and were trapped at centers previously, thus producing EL. This mechanism is described in 9.1.3 in detail.

Injection of carriers from interfacial state.[5] When semiconductors are in contact with insulators (dielectric materials), states are formed at the interface having energy levels

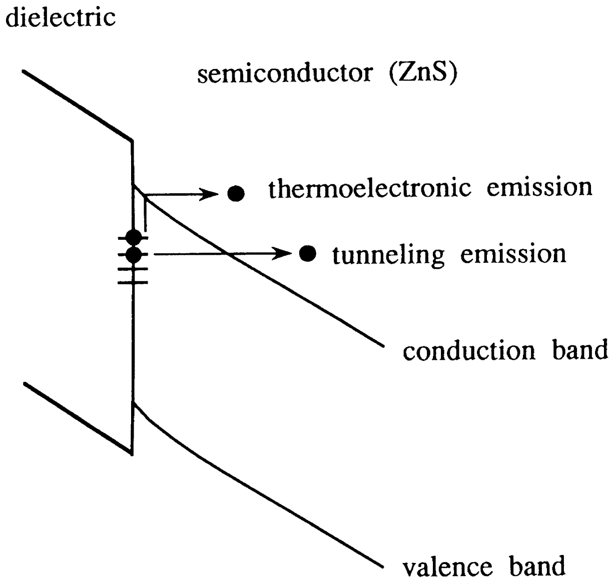

Figure 80 Energy band diagram of a dielectric material and a semiconductor in contact. Electron injection from interfacial states under high electric field is illustrated.

distributed in the forbidden bandgap of the semiconductors, as illustrated in Figure 80. The density of the interfacial states is of the order of 10^{12}–10^{13} cm^{-2}. When an electric field is applied, electrons trapped in these states are injected into the conduction band due to tunneling and/or Poole-Frenkel emission. A typical ac-thin-film EL panel has a doubly insulating structure consisting of glass substrate/ITO (indium-tin oxide) transparent electrodes/insulating layer/EL phosphor layer/insulating layer/metal electrodes. For this type of EL device, the dominant electron injection mechanism into the EL phosphor layer is field emission from the insulator/EL phosphor interfacial states.

2.10.3.2 *Electron energy distribution in high electric field*

At thermal equilibrium, electrons in semiconductors emit and absorb phonons, but the net rate of energy exchange between the electrons and the lattice is zero. The energy distribution of electrons at thermal equilibrium is expressed by the Maxwell-Boltzmann distribution function as:

$$f(\varepsilon) = \exp\left(-\frac{\varepsilon}{kT}\right), \qquad \varepsilon = \frac{m^* v^2}{2} \tag{169}$$

This distribution function is spherical in momentum space, as illustrated in Figure 81(a).

In the presence of an electric field, the electrons acquire energy from the field and lose it to the lattice by emitting more phonons. Simultaneously, the electrons move with the drift velocity v_d, proportional to and in the direction of the electric field. In this case, the energy distribution of the electrons changes to a displaced Maxwell-Boltzmann distribution function (see Figure 81(b)) given by:

$$f(\varepsilon) = \exp\left(-\frac{\varepsilon}{kT}\right), \qquad \varepsilon = \frac{m^* (v - v_d)^2}{2} \tag{170}$$

At moderately high electric field (~10^3 V cm^{-1}), the most frequent scattering event is the emission of optical phonons. The electrons acquire on the average more energy than

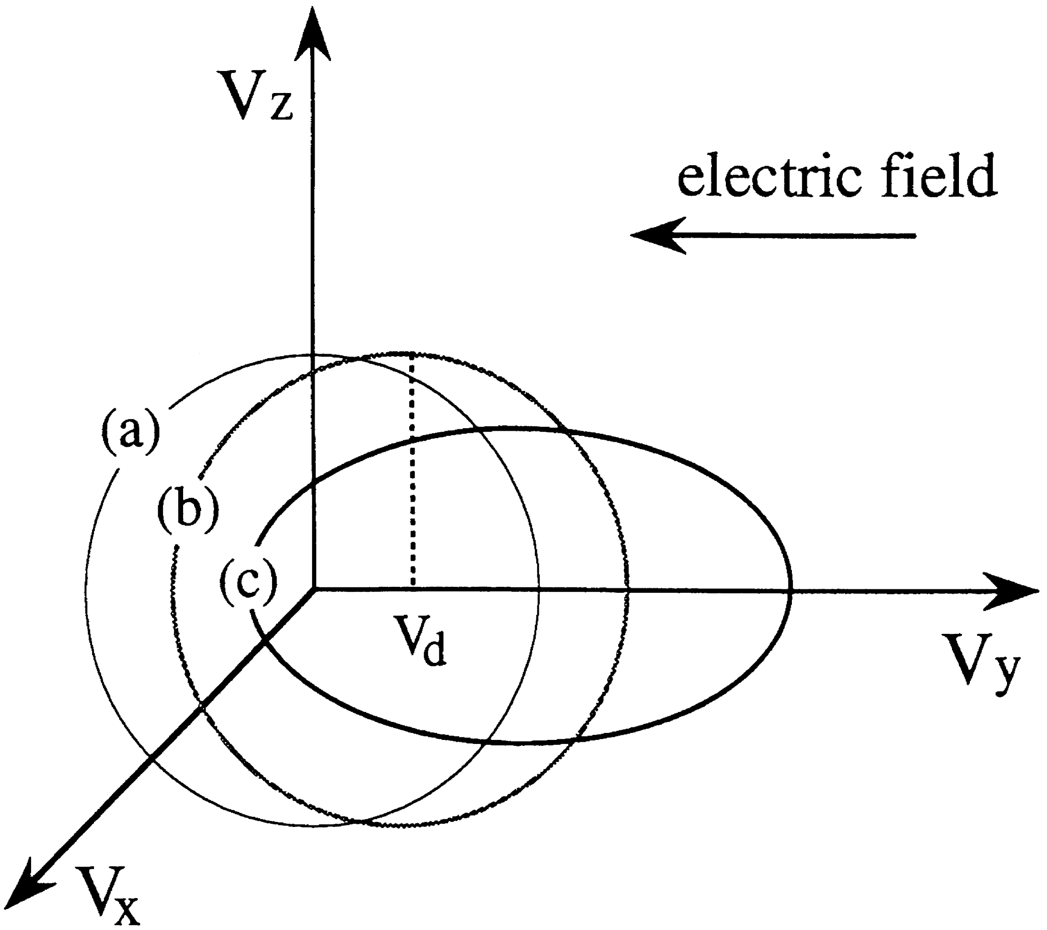

Figure 81 Electron energy distributions is in the momentum space as a function of electron velocity: (a) Maxwell-Boltzmann, (b) displaced Maxwell-Boltzmann, and (c) Baraff's distribution function.

they have at thermal equilibrium describable by an effective temperature T_e higher than the lattice temperature T_L. These electrons, therefore, are called *hot electrons*. However, the energy of hot electrons is still too low to excite luminescent centers or to ionize the lattice; the thermal energy of hot electrons is only 0.05 eV, even at T_e = 600K, while an energy of at least 2 to 3 eV is required for the impact excitation of luminescent centers.

When the electric field in semiconductors is increased above 10^5 V cm^{-1}, electrons gain enough energy to excite luminescent centers by impact excitation and also to create electron-hole pairs by impact ionization of the lattice. The energy distribution of these hot electrons can be expressed by Baraff's distribution function[6] (see Figure 81(c)), given by:

$$
\begin{aligned}
f(\varepsilon) &= \varepsilon^{-a+0.5}\exp(-b\varepsilon) \\
a &= \frac{E_O - qE\lambda}{2E_O + qE\lambda} \\
b^{-1} &= \frac{3}{2}qE\lambda + \frac{1}{3}\frac{(qE\lambda)^2}{E_O}
\end{aligned}
\tag{171}
$$

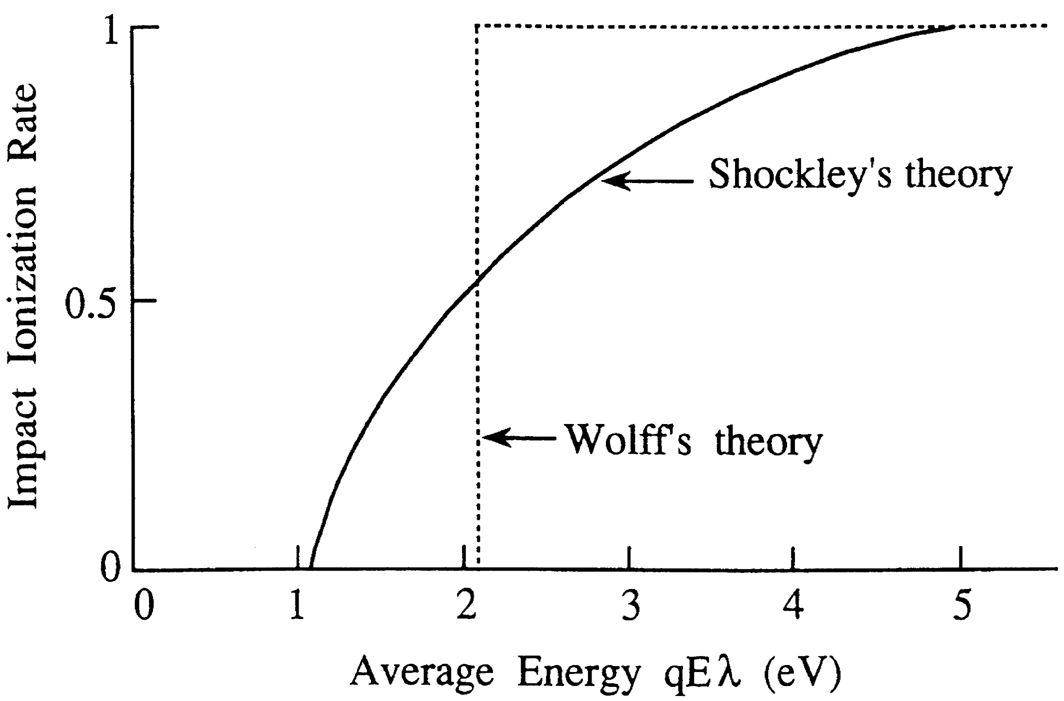

Figure 82 Dependence of impact ionization rate on the average electron energy calculated from Shockley's and Wolff's theories.

where E_O is the optical phonon energy and λ is the mean free path of electrons.

In the case of moderately high electric field ($qE\lambda < E_o$). When the electric field is moderately high, and the average electron energy, qEλ, is smaller than the optical phonon energy E_o, Eq. 171 can be reduced to the following form:

$$f(\varepsilon) \propto \varepsilon^{-1} \exp\left(-\frac{\varepsilon}{qE\lambda}\right) \tag{172}$$

This function agrees with Shockley's distribution function,[7] and implies that some electrons with very high energy can exist, even in the case of relatively low electric fields. This model is, therefore, called the lucky electron model. The impact ionization rate increases when the average electron energy is increased, as illustrated by the solid curve in Figure 82. The threshold energy—in other words, the threshold field—for impact ionization is relatively low in this model.

In the case of extremely high electric field ($qE\lambda \gg E_O$). When the electric field is extremely high, and the average electron energy, qEλ, is larger than the optical phonon energy E_O, Eq. 171 can be rearranged into the following form:

$$f(\varepsilon) \propto \exp\left(-\frac{3\varepsilon E_0}{(qE\lambda)^2}\right) \tag{173}$$

This function agrees with Wolff's distribution function derived using the diffusion approximation[8]; Eq. 173 gives a threshold energy for the impact ionization that is higher than that for the lucky electron model, as shown in Figure 82.

Recently, Bringuier[9,10] investigated electron transport in ZnS-type, thin-film EL. Two basic transport modes in the lucky-drift theory are considered. First, the ballistic regime, which is defined in terms of the optical-phonon mean free path λ and the electron-phonon collision rate $1/\tau_m$. This regime implies a collision-free (ballistic) mode. Second is the drift regime, which is characterized by the length λ_e and the rate $1/\tau_e$ of the energy relaxation. This mode predominates after the electron has suffered one collision since, once it has collided, it is deflected and the probability of other collisions is greatly increased. In the ballistic mode, an electron travels with a group velocity $v_g(\varepsilon)$, so that $\lambda = v_g\tau_m$; while in the drift mode, the motion is governed by a field-dependent drift velocity $v_d(\varepsilon)$ and $\lambda = v_d\tau_e$. The lucky-drift model may be applied to the case where $\tau_e \gg \tau_m$ and $\lambda_e \gg \lambda$, which should hold true for wide-gap semiconductors in the high-field regime. When these two inequalities are fulfilled, each collision results in an appreciable momentum loss for the electron, with little energy loss. Over the energy relaxation length, an electron drifting in the field loses its momentum and direction, but conserves much of its energy.

The energy exchange between electrons and phonons is described by the electron-phonon interaction Hamiltonian, where electrons can emit or absorb one phonon at a time. Because a phonon is a boson, the probability of the phonon occupation number changing from n to (n+1) is proportional to (n+1), while a change from n to (n–1) is proportional to n. Therefore, the ratio of the phonon emission $r_e(n \rightarrow n+1)$ to the phonon absorption $r_a(n \rightarrow n-1)$ rates is given by (n+1)/n. Because $r_e > r_a$, an electron experiences a net energy loss to the lattice, tending to stabilize the electron drift. Hot electrons in high electric field lose energy mostly to optical phonons and also to zone-edge acoustic phonons, though somewhat less effectively. At temperature T, the phonon occupation number $n(\omega)$ is given as $n(\omega) = 1/(\exp(\ \omega/kT)-1)$. For ZnS, the optical phone energy ω is 44 meV. Thus, one obtains an occupation number, $n(\omega) = 0.223$ at 300K. The analytical expression for the saturated drift velocity v_s in the lucky-drift theory is given by:

$$v_s = \left(\frac{\hbar\omega}{(2n+1)m^*}\right)^{1/2} \tag{174}$$

which yields 1.38×10^7 cm s^{-1} at 300K for electrons in the energy minimum Γ point at k = (000) of the conduction band.

In order to assess the electron-phonon coupling, the electron-phonon scattering rate $1/\tau$ ($= r_e + r_a$, $r_e/r_a = (n+1)/n$) needs to be determined. From these rates, the average energy loss per unit time of an electron can be derived; in the steady state, this loss offsets the energy gained by drifting in the field, yielding:

$$\hbar\omega\left(r_e - r_a\right) = \frac{\hbar\omega}{(2n+1)\tau} = qEv_s \simeq 10^{13}\ \text{eV s}^{-1} \tag{175}$$

By substituting n = 0.223 and $\omega = 44$ meV into Eq. 175, one obtains $1/\tau \simeq 3.2 \times 10^{14}$ s^{-1}, or an electron mean free time of $\tau \simeq 3$ fs. The competition between heating by the field and cooling by a lattice scattering determines not only the average energy ε_{av} but also the nonequilibrium energy distribution function. The energy balance condition is obtained by setting the following equation to zero.

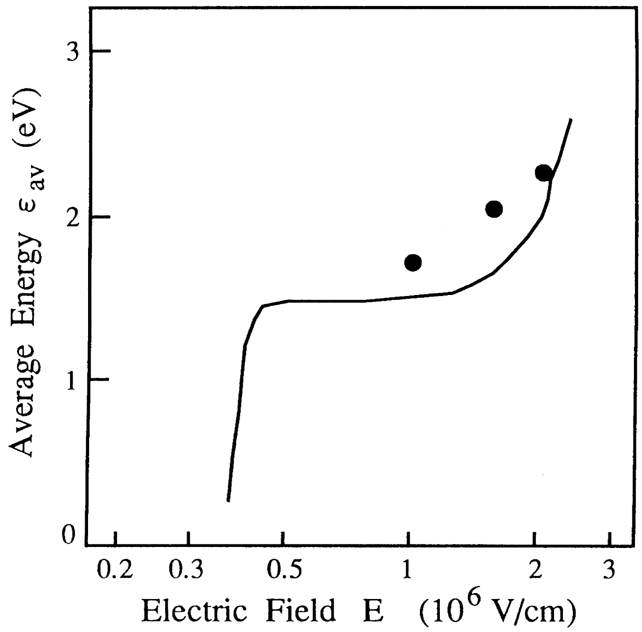

Figure 83 Solid line shows average electron energy ε_{av} as a function of electric field E in ZnS at 300K obtained from the energy balance condition. Solid circles are the Monte-Carlo calculated ε_{av}. (From Bringuier, E., *J. Appl. Phys.*, 75, 4291, 1994; Bhattacharyya, K., Goodnick, S.M., and Wager, J.F., *J. Appl. Phys.*, 73, 3390, 1993. With permission.)

$$\frac{d\varepsilon}{dt} = qEv_d - \frac{\hbar\omega}{(2n+1)\tau(\varepsilon)} \tag{176}$$

where $1/\tau(\varepsilon)$ is the energy-dependent scattering rate. The average electron energies ε_{av} obtained from this equation are plotted in Figure 83 as a function of the electric field E. It can be seen that the average electron energy ε_{av} increases sharply when the electric field exceeds 2×10^6 V cm^{-1}. An average electron energy ε_{av} exceeding 2 eV is sufficient for the impact excitation of luminescent centers, as described in the next section.

Recently, an ensemble Monte-Carlo simulation of electron transport in ZnS bulk at high electric fields was performed.[11] Scattering mechanisms associated with polar optical phonons, acoustic phonons, inter-valley scattering in the conduction band, and impurities were included into a nonparabolic multi-valley model. The average electron energy ε_{av} calculated in this way is also shown in Figure 83. Close agreement was obtained between the ε_{av} values calculated by the Monte-Carlo method and those obtained by the lucky-drift theory. Simulated results of the electron energy distribution are shown in Figure 84, together with the impact excitation cross-section for the Mn^{2+} center discussed in the next section. The results show that energetic electrons are available at field strengths exceeding 10^6 V cm^{-1} to cause impact excitation, and that transient effects such as ballistic transport can be disregarded in explaining the excitation mechanism of thin-film EL.

2.10.3.3 Excitation mechanism of luminescence centers

In EL phosphors presently used, there are two types of luminescent centers. One is the donor-acceptor pair type, and the other is the localized center type. For the latter, Mn^{2+} ions producing luminescence due to $3d^5$ intra-shell transitions are the most efficient centers used in ZnS thin-film EL devices. Some divalent and trivalent rare-earth ions emitting

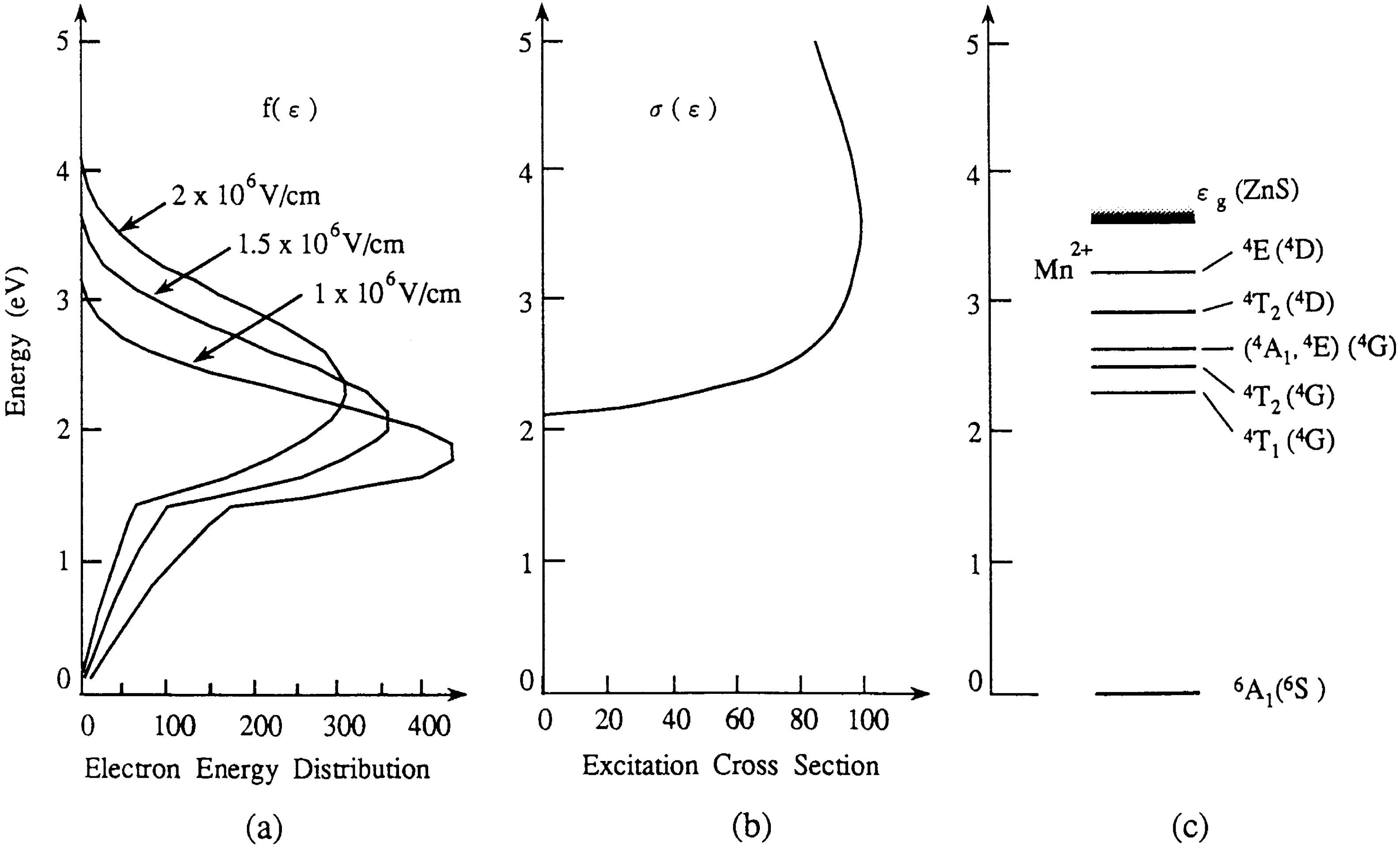

Figure 84 (a) Electron energy distribution f(ε), (b) Mn^{2+} impact excitation cross-section σ(ε) as a function of energy, and (c) energy levels of Mn^{2+}. (From Bhattacharyya, K., Goodnick, S.M., and Wager, J.F., *J. Appl. Phys.*, 73, 3390, 1993. With permission.)

luminescence due to $4d^{n-1}5d \rightarrow 4f^n$ or $4f^n$ intra-shell transitions are also efficient luminescent centers; these ions are potential candidates for color EL. The excitation processes of these luminescent centers are described in this section.[12]

Electron-hole pair generation by hot electron impact ionization. In the ZnS host lattice, a high electric field of 2×10^6 V cm^{-1} is enough to produce hot electrons. Consequently, these hot electrons ionize the ZnS lattice by collision, and by creating electron-hole pairs. This process is called impact ionization of the lattice. If impurities, donor and/or acceptor exist, they will also be ionized. The electron-hole pairs are recaptured by these ionized donors and acceptors, and luminescence is produced as a result of the recombination of electrons and holes. These processes are illustrated in Figure 85(a).

The ionization rate P_{ion} of the lattice is calculated using the following equation:

$$P_{ion} \propto \int_{\varepsilon_g}^{\infty} \sigma(\varepsilon)\, f(\varepsilon)\, d\varepsilon \tag{177}$$

where $\sigma(\varepsilon)$ is the ionization cross-section of the lattice, ε_g is the bandgap energy, and $f(\varepsilon)$ is the electron energy distribution function. $\sigma(\varepsilon)$ is proportional to the product of the density of states of the valence and conduction bands.

In cathode-ray tubes, luminescence due to donor-acceptor pair recombination is very efficient, and ZnS:Ag,Cl and ZnS:Cu,Al(Cl) phosphors are widely and commonly used as blue and green phosphors, respectively. ZnS:Cu,Al(Cl) phosphors are also used for powder-type EL. However, these phosphors are not efficient when used in thin-film EL devices. This is understood in terms of the reionization of the captured electrons and holes by the applied electric field prior to their recombination.

Direct impact excitation of luminescent centers by hot electrons. If hot electrons in the host lattice collide directly with localized luminescent centers, the ground-state electrons of the centers are excited to higher levels, so that luminescence is produced, as illustrated in Figure 85(b). EL of ZnS:Mn^{2+} is due to the impact excitation of the $3d^5$ intra-shell configuration of Mn^{2+} centers. Similarly, EL of trivalent rare-earth (RE)-doped ZnS is based on the impact excitation of the $4f^n$ intra-shell configurations. This excitation mechanism is thought to be dominant in thin-film EL device operation.

Assuming direct impact excitation, the excitation rate P of centers can be expressed by:

$$P \propto \int_{\varepsilon_0}^{\infty} \sigma(\varepsilon, \gamma)\, f(\varepsilon)\, d\varepsilon \tag{178}$$

where $\sigma(\varepsilon,\gamma)$ is the impact excitation cross-section to the excited state γ of the centers, $f(\varepsilon)$ is the energy distribution of hot electrons discussed above, and ε_0 is the threshold energy for the excitation.

Although calculations of impact excitation and ionization cross-sections in free atoms or ions are very sophisticated and accurate, they are still crude in solids. Allen[13] has pointed out that the problems lie in the form of the wavefunctions of the luminescent centers to be used, especially when covalent bonding with the host crystal is included. There is also a problem of dielectric screening. This screening should be properly taken as dependent on the energy and wave vector of carriers, or be taken approximately as a function of distance r using the screened Coulomb potential expressed by $\phi(r) = (-A/r)\exp(-r/\lambda_D)$, where λ_D is the potential decay coefficient. In addition, the carrier velocity is not a simple

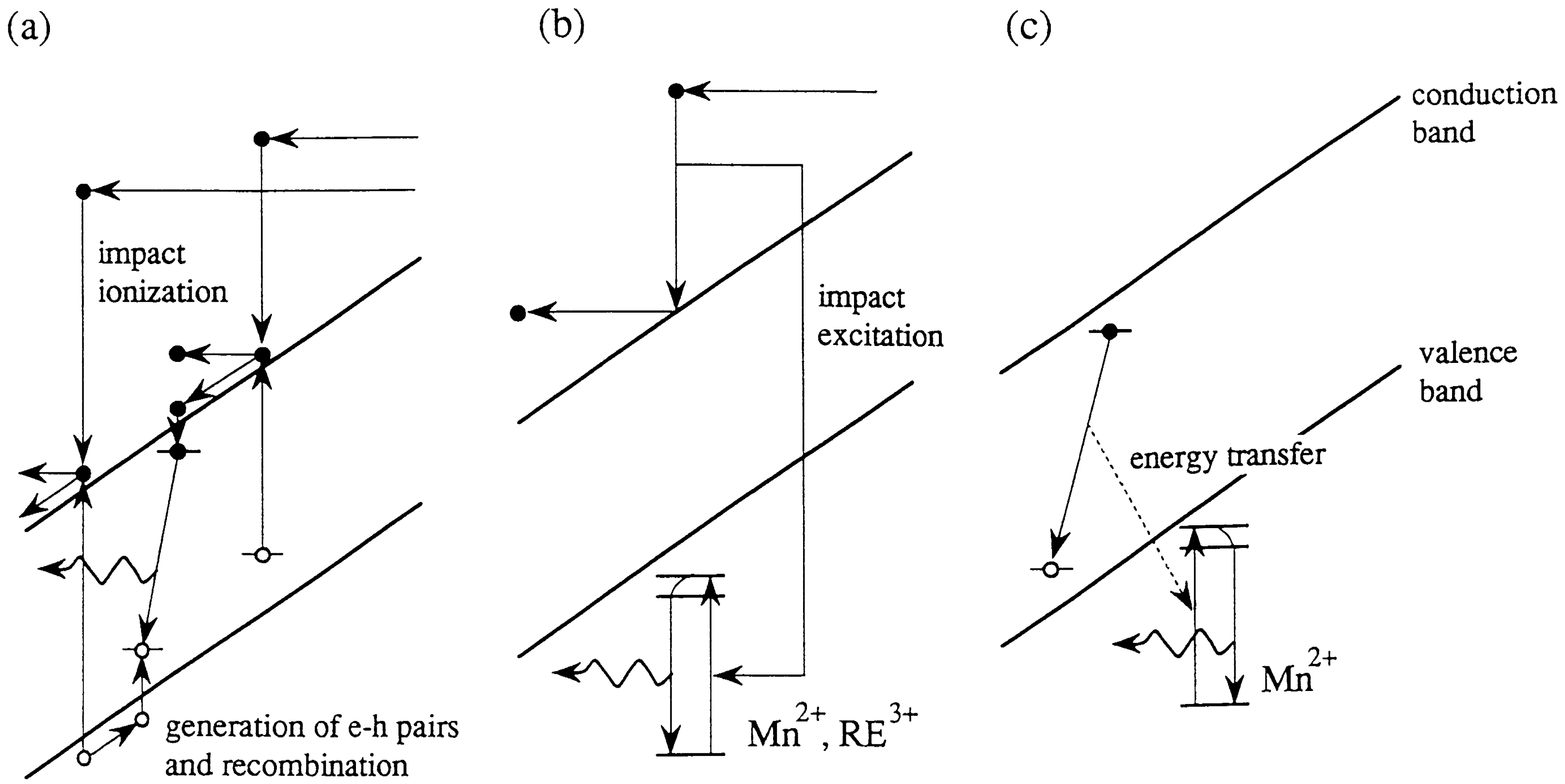
(a)
impact
ionization
generation of e-h pairs
and recombination
(b)
impact
excitation
Mn2+, RE3+
(c)
conduction
band
valence
band
energy transfer
Mn2+

Figure 85 Three excitation processes of luminescent centers in thin-film EL devices: (a) impact ionization and recombination, (b) direct impact excitation, and (c) energy transfer.

function of its energy. Allen[13] calculated a cross-section σ for impact excitation using a simple Born-Bethe treatment of the direct Coulomb term and obtained the following expression.

$$\sigma = \frac{1}{\varepsilon^2 n_r \left(\frac{\varepsilon_{eff}}{\varepsilon_0}\right)} \times \frac{2\pi m_1^{*} e^2 \hbar c^3 S_{1u}^2}{v_u E_{ge}^2 K_u} \ln\left(\frac{k_u + k_1}{k_u - k_1}\right) \times \left(\frac{1}{\tau_{e-d}}\right) \tag{179}$$

Here, σ is explicitly written as the product of three terms. The first term describes the screening effect, where ε is the dielectric constant, n_r is the refractive index, and $(\varepsilon_{eff}/\varepsilon_0)$ is an effective field ratio. The second term is a function of the properties of the electron when the incident excited electron with the initial velocity v_u and with wave vector k_u in the conduction band is scattered to a lower state l with wave vector k_1, the electron loses kinetic energy E_{ge} corresponding to the energy difference between the ground and excited states of the center. In the second term, m_1^* is an electron effective mass, and S_{1u} represents the value of the overlap integral of the Bloch function for the electron with wave vector k_1 and that for the electron with k_u. The third term is the electric dipole radiative transition rate of the center. For centers with radiative lifetimes in the range of 10 μs to 1 ms, the cross-section is estimated to be 10^{-18} to 10^{-20} cm^2, which is too small to be useful.

There is an apparent difference between the nature of the electrons in vacuum and in a solid like ZnS. ZnS is a direct-bandgap semiconductor having both the bottom of the conduction band and the top of the valence band at the Γ point k = (000). In vacuum, the velocity of electrons increases monotonically with the increase in its energy; whereas, in ZnS, it is possible to have electrons with high energy but low velocity in the upper minima of the conduction band at the L [k = (111)] and X [k = (001)] valleys (see 3.7.2.3). As seen in Eq. 179, if the velocity of the incident electron v_u is low when it has sufficient energy E_{ge} for impact excitation, the excitation cross-section is considerably enhanced. Such a situation is realized in ZnS:Mn^{2+} when incident electrons in the X or L valley collide with Mn^{2+} centers and are scattered to the Γ valley; simultaneously, $3d^5$ electrons of Mn^{2+} are excited from the ground to the excited state.

Exchange effects are expected to dominate because of a resonance between the energy spacings of Mn^{2+} centers and those within the conduction band. The Born-Bethe treatment—i.e., the use of the Fermi Golden Rule—is not appropriate for exchange processes. Although there is no simple approximation to calculate rates of exchange processes, some qualitative conclusions can be drawn from our knowledge of what happens in the impact excitation of free atoms. The long-range part of the interaction is no longer dominant; so instead of the perturbing Hamiltonian in the dipole approximation, one must use the full Coulomb term. The exchange interaction is predominantly at the short range. Hence, in a crystal of high dielectric constant, the direct interaction is screened much more effectively than the exchange interaction. This is likely to be the cause for the large cross-section.

In ZnS:Mn^{2+}, the cross-section for the impact excitation is then doubly enhanced. One can, therefore, conclude that ZnS:Mn^{2+} is a suitable combination of host and center that produces efficient EL by the impact excitation. This is because ZnS satisfies the need for a host in which hot carriers have a suitable energy distribution, and Mn^{2+} has an unusually large cross-section near the threshold.

In Figures 84(a) and (b), the electron energy distribution f(ε) and excitation cross-section of Mn^{+} centers σ(ε) are illustrated.[11] The energy levels of Mn^{2+} centers are also shown in Figure 84(c). The peak in f(ε) near 2 eV implies that a large electron population exists in the X and L valleys, where electrons have sufficient energy to excite Mn^{2+} centers, but have relatively low velocities. The threshold energy for the excitation is a little smaller than the lowest excited state $^4T_1$ of Mn^{2+}. This results from the broadening due to the uncertainty principle. As seen from the Figures 84(a) and (b), at electric fields of the order of 1×10^6 V cm^{-1} and larger, a significant fraction of the total electron population exists at energies exceeding the threshold excitation energy of 2.1 eV for Mn^{2+}. A good match of the hot electron distribution with the Mn^{2+} excitation energy brings about the relatively high EL efficiencies in this system; the efficiencies are of the order of 4 to 6 lm W^{-1}.

It was demonstrated[14] that $ZnS{:}Tb^{3+}O^{2-}F^{-}$ thin-film EL devices show efficient green EL with an efficiency of the order of 1 to 2 lm W^{-1}. It has been shown that in TbOF complex centers, Tb^{3+} substitutes into the Zn^{2+} site, O^{2-} substitutes into the S^{2-} site, and F^{-} is located at an interstitial site to compensate for the charge difference. Therefore, TbOF centers seem to form centers isoelectronic with ZnS. $ZnS{:}Tb^{3+}F^{-}$ EL films with a Tb:F ratio of unity, with Tb^{3+} at Zn^{2+} sites and interstitial F^{-} ions, also form isoelectric centers that show efficient EL. It is believed that these isoelectronic centers have larger cross-sections for impact excitation than those for isolated rare-earth ions, so that high EL efficiencies result.

Energy transfer to luminescent centers. In AC powder EL phosphors such as ZnS:Cu,Cl, donor (Cl)–acceptor (Cu) (D-A) pairs are efficient luminescent centers (see 3.7.4), and the EL emission is caused by the radiative recombination of electron-hole pairs through D-A pairs. Electrons and holes are injected into the ZnS lattice by bipolar field emission described in 9.1.3. By further incorporating Mn^{2+} centers in ZnS:Cu,Cl, yellow emission due to Mn^{2+} is observed. In this case, the excitation of Mn^{2+} centers is due to the non-radiative resonant energy transfer from D-A pairs to Mn^{2+}, as illustrated in Figure 85(c).

Ionization of centers and recapture of electrons to produce luminescence. In thin-film EL of rare-earth-doped IIa-VIb compounds such as blue/green-emitting $SrS{:}Ce^{3+}$ and red-emitting $CaS{:}Eu^{2+}$, the transient behavior of the EL emission peaks under pulse excitation exhibits emission peaks when the pulsed voltage is turned on and turned off; in other words, the second peak appears when the electric field is reversed in the direction due to polarization charge trapped in the phosphor-insulator interfaces.[15] The luminescence of these phosphors is due to the $4f^{n-1}5d \rightarrow 4f^{n}$ transition. It is probable that the $4f^{n}$ ground-state level is located in the forbidden gap, while the $4f^{n-1}5d$ excited state is close to the bottom of the conduction band. The EL excitation mechanism is as follows: the luminescence centers are excited by the impact of the electron accelerated by the pulsed voltage and then ionized by the applied pulsed field. Electrons released to the conduction band are captured by traps. This process has been experimentally confirmed by measurements of the excitation spectra of the photoinduced conductivities.[15] When the voltage is turned back to zero, the trapped electrons are raised by the reversed field to the conduction band again and are recaptured by the ionized centers to produce luminescence.

References

1. Destriau, G., *J. Chim. Phys.*, 33, 620, 1936.
2. Destriau, G., *Phil. Mag.*, 38, 700, 1947; 38, 774, 1947; 38, 880, 1947.
3. Haynes, J.R. and Briggs, H.B., *Phys. Rev.*, 99, 1892, 1952.
4. Sze, S.M., *Physics of Semiconductor Devices*, 2nd edition, John Wiley & Sons, New York, 1981, chap. 5 and 6.
5. Kobayashi, H., *Optoelectronic Materials and Devices, Proc. 3rd Int. School*, Cetniewo, 1981, PWN-Polish Scientific Publishers, Warszawa, 1983, chap. 13.
6. Baraff, G.A., *Phys. Rev.*, 133, A26, 1964.

7. Shockley, W., *Solid State Electron.*, 2, 35, 1961.
8. Wolff, P.A., *Phys. Rev.*, 95, 1415, 1954.
9. Bringuier, E., *J. Appl. Phys.*, 66, 1314, 1989.
10. Bringuier, E., *J. Appl. Phys.*, 75, 4291, 1994.
11. Bhattacharyya, K., Goodnick, S.M., and Wager, J.F., *J. Appl. Phys.*, 73, 3390, 1993.
12. Kobayashi, H., *Proc. SPIE*, 1910, 15, 1993.
13. Allen, J.W., *Springer Proc. in Physics 38, Proc. 4th Int. Workshop on Electroluminescence*, Springer-Verlag, Heidelberg, 1989, p. 10.
14. Okamoto, K., Yoshimi, T., and Miura, S., *Springer Proc. in Physics 38, Proc. 4th Int. Workshop on Electroluminescence*, Springer-Verlag, Heidelberg, 1989, p. 139.
15. Tanaka, S., *J. Crystal Growth*, 101, 958, 1990.

chapter two — section eleven

Fundamentals of luminescence

Pieter Dorenbos

Contents

2.11 Lanthanide level locations and its impact on phosphor performance 139
  2.11.1 Introduction 139
  2.11.2 Level position and phosphor performance 140
  2.11.3 The free (gaseous) lanthanide ions 143
  2.11.4 4f–5d energy differences of lanthanide ions in compounds 144
  2.11.5 Methods to determine absolute level locations 147
  2.11.6 Systematic variation in absolute level locations 147
  2.11.7 Future prospects and pretailoring phosphor properties 152
References 152

2.11 *Lanthanide level locations and its impact on phosphor performance*

2.11.1 *Introduction*

The lanthanide ions either in their divalent or trivalent charge state form a very important class of luminescence activators in phosphors and single crystals.[1] The fast 15–60 ns 5d–4f emission of Ce^{3+} in compounds like $LaCl_3$, $LaBr_3$, Lu_2SiO_5, and Gd_2SiO_5 is utilized in scintillators for γ-ray detection.[2] The same emission is utilized in cathode ray tubes and electroluminescence phosphors. The photon cascade emission involving the $4f^2$ levels of Pr^{3+} has been investigated for developing high quantum efficiency phosphors excited by means of a Xe discharge in the vacuum-UV.[3] The narrow-line $4f^3$ transitions in Nd^{3+} are used in laser crystals like $Y_3Al_5O_{12}$:Nd^{3+}. Sm^{3+} is utilized as an efficient electron trap and much research has been devoted to its information storage properties. For example, MgS:Ce^{3+};Sm^{3+} and MgS:Eu^{2+};Sm^{3+} were studied for optical memory phosphor applications,[4] Y_2SiO_5:Ce^{3+};Sm^{3+} was studied for X-ray imaging phosphor applications,[5] and $LiYSiO_4$:Ce^{3+};Sm^{3+} for thermal neutron imaging phosphor applications.[6] The famous $^5D_0 \rightarrow {}^7F_J$ $4f^6$ redline emissions of Eu^{3+} and the blue to red 5d–4f emission of Eu^{2+} are both used in display and lighting phosphors.[1] The $4f^8$ line emission of Tb^{3+} is often responsible for the green component in tricolor tube lighting.[1] Dy^{3+} plays an important role in the persistent luminescence phosphor $SrAl_2O_4$:Eu^{2+};Dy^{3+}.[7,8] Er^{3+} and Tm^{3+} are, like Pr^{3+}, investigated for possible photon cascade emission phosphor applications.

This brief and still incomplete summary illustrates the diversity of applications involving the luminescence of lanthanide ions. It also illustrates that we can distinguish two types of lanthanide luminescent transitions. (1) Transitions between levels of the $4f^n$ configuration. In this chapter, the energy of each $4f^n$ excited state relative to the lowest $4f^n$ state will be regarded as invariant with the type of compound. One may then use the Dieke diagram with the extension provided by Wegh et al.[9] to identify the many possible luminescence emission and optical absorption lines. (2) Transitions between the $4f^{n-1}$ 5d and the $4f^n$ configurations. The energy of 5d levels, contrary to the 4f levels, depends very strongly on the type of compound. For example, the wavelength of the 5d–4f emission of Ce^{3+} may range from the ultraviolet region in fluorides like that of $KMgF_3$ to the red region in sulfides like that of Lu_2S_3.[10]

In all phosphor applications the color of emission and the quantum efficiency of the luminescence process are of crucial importance as is the thermal stability of the emission in some applications. These three aspects are related to the relative and absolute location of the lanthanide energy levels. For example, the position of the host-sensitive lowest 5d state relative to the host-invariant 4f states is important for the quenching behavior of both 5d–4f and 4f–4f emissions by multiphonon relaxation. The absolute position of the 4f and 5d states relative to valence band and conduction band states also affects luminescence quenching and charge-trapping phenomena. Although it was realized long ago that absolute location is crucial for phosphor performance, the experimental and theoretical understanding of the placement of energy levels relative to the intrinsic bands of the host has been lacking.

In this section, first, a survey is provided on how relative and absolute locations of lanthanide energy levels affect phosphor performance. Next, methods and models to determine relative and absolute locations are treated. After discussing the energy levels of the free (or gaseous) lanthanide ions, the influence of the host compound on the location of the 5d levels relative to the 4f levels is presented. Next, the influence of the host compound on the absolute location of the lowest $4f^n$ state above the top of the valence band is explained. This forms the basis for drawing schemes for the absolute placement of both the 4f and 5d states of all the divalent and trivalent lanthanide ions.

2.11.2 Level position and phosphor performance

The importance of the relative and absolute positions of the energy levels of lanthanide ions is illustrated in Figure 86. We distinguish occupied states that can donate electrons and empty states that can accept electrons. Let us start with the "occupied states." Figure 86(a) illustrates the downward shift of the lowest-energy 5d level when a lanthanide is brought from the gaseous state (free ion) into the crystalline environment of a compound (A). Due to the interaction with the neighboring anion ligands (the crystal field interaction), the degenerate 5d levels of the free ion split (crystal field splitting), depending on the site symmetry. In addition, the whole 5d configuration shifts (centroid shift) toward lower energy. The crystal field splitting combined with the centroid shift lowers the lowest 5d level with an amount known as the redshift or depression D. Clearly the value of D determines the color of emission and wavelength of absorption of the 4f–5d transitions.

Figure 86(b) illustrates the importance of lowest-energy 5d level location relative to $4f^2$ levels in Pr^{3+}. With the 5d level above the $^1S_0$ level of Pr^{3+}, multiphonon relaxation from the lowest 5d state to the lower lying $^1S_0$ level takes place. A cascade emission of two photons may result, which leads to quantum efficiency larger than 100%. However, with the lowest 5d state below $^1S_0$, broad-band 5d–4f emission is observed. Much research is devoted toward the search for Pr^{3+} quantum-splitting phosphors and for finding efficient 5d–4f-emitting Pr^{3+}-doped materials for scintillator applications. Depending on the precise

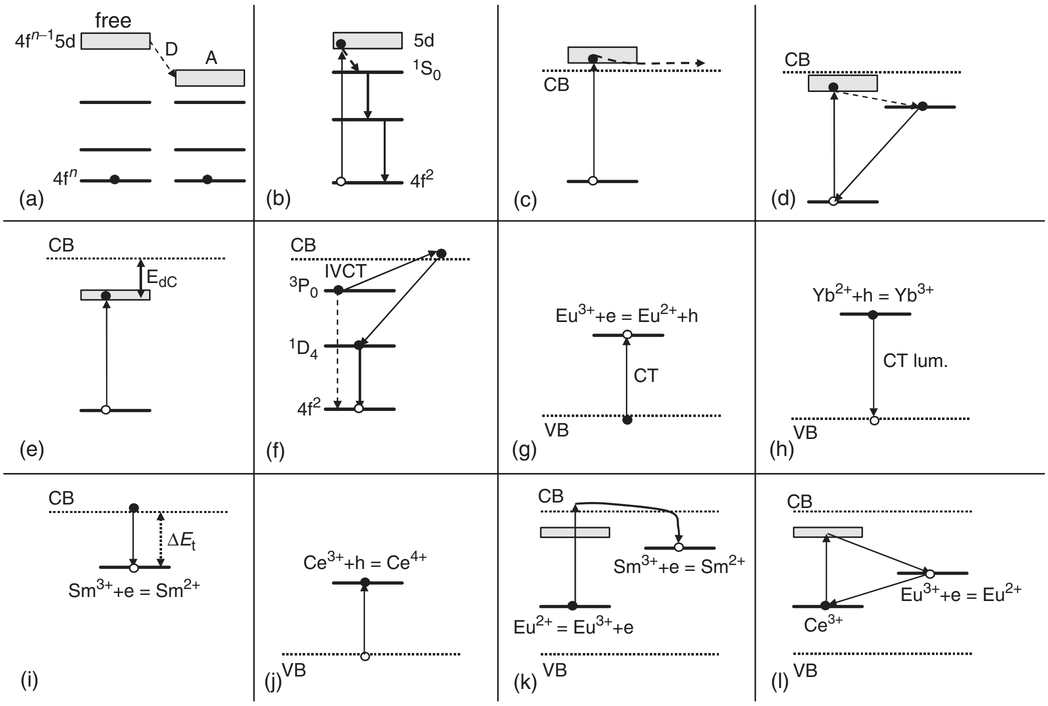

Figure 86 Illustration of influence of level location on phosphor properties: (a) the redshift *D* of the 5d state, (b) photon cascade emission in Pr^{3+}, (c) 5d–4f emission quenching by autoionization, (d) anomalous 5d emission, (e) thermal quenching by ionization, (f) quenching by intervalence charge transfer, (g) valence band charge transfer, (h) charge transfer luminescence, (i) electron trapping by Sm^{3+}, (j) hole trapping by Ce^{3+}, (k) electron transfer from Eu^{2+} to Sm^{3+}, (l) luminescence quenching by lanthanide to lanthanide charge transfer.

location of the lowest 5d state in Nd^{3+}, Eu^{2+}, and Sm^{2+}, either broad-band 5d–4f or narrow-line 4f–4f emissions can be observed.[11]

Figure 86(c), (d), and (e) show the interplay between the localized 5d electron and the delocalized conduction band states. If the lowest 5d state is above the bottom of the conduction band as in Figure 86(c), autoionization occurs spontaneously and no 5d–4f emission is observed. This is the case for $LaAlO_3$:Ce^{3+}, rare-earth sesquioxides Ln_2O_3:Ce^{3+},[1] and also for Eu^{2+} on trivalent rare-earth sites in oxide compounds.[12] Figure 86(d) illustrates the situation with 5d just below the conduction band. The 5d electron delocalizes but remains in the vicinity of the hole left behind. The true nature of the state, which is sometimes called an impurity trapped exciton state, is not precisely known. The recombination of the electron with the hole leads to the so-called anomalous emission characterized by a very large Stokes shift.[13,14] Finally, Figure 86(e) shows the situation with the 5d state well below the conduction band, leading to 5d–4f emission. The thermal quenching of this emission by means of ionization to conduction band states is controlled by the energy E_{dC} between the 5d state (d) and the bottom of the conduction band (C).[15,16] A review on the relationship between E_{dC} for Eu^{2+} and thermal quenching of its 5d–4f emission recently appeared.[16] Knowledge on such relationships is important for developing temperature-stable Eu^{2+}-doped light-emitting diode (LED) phosphors or temperature-stable Ce^{3+}-doped scintillators. For electroluminescence applications, E_{dC} is an important parameter to discriminate the mechanism of impact ionization against the mechanism of field ionization.[17]

Figure 86(f) shows a typical situation for Pr^{3+} in a transition metal complex compound like $CaTiO_3$. The undesired blue emission from the Pr^{3+} $^3P_0$ level is quenched by intervalence charge transfer (IVCT).[18] The electron transfers from the $^3P_0$ level to the transition metal (Ti^{4+}). The electron is transferred back to the red emitting Pr^{3+} $^1D_4$ level. The position of the $^3P_0$ level relative to the transition metal-derived conduction band controls the quenching process, and thereby the color of emission.

So far we have discussed examples of absolute location of "occupied states." However, a trivalent lanthanide ion may accept an electron to form a divalent lanthanide ion. The location of the occupied ground-state level of a divalent lanthanide ion is therefore the same as the unoccupied electron-accepting state of the corresponding trivalent lanthanide ion. The accepted electron may originate from the valence band, the conduction band, or another lanthanide ion. Figure 86(g) pertains to a Eu^{3+}-doped compound. Eu^{3+} introduces an unoccupied Eu^{2+} state in the forbidden gap. The excitation of an electron from the valence band to the unoccupied state creates the ground state of Eu^{2+}. This is a dipole-allowed transition that is used, for example, to sensitize $Y_2O_3:Eu^{3+}$ phosphors to the 254 nm Hg emission in tube lighting.[1] Recombination of the electron with the valence band hole leaves the Eu^{3+} ion in the $^5D_0$ excited state resulting in red $4f^6$–$4f^6$ emission. Figure 86(h) shows a similar situation for Yb^{3+}. In the case of Yb^{3+} the recombination with the hole in the valence band produces a strong Stokes-shifted charge transfer (CT) luminescence. This type of luminescence gained considerable interest for developing scintillators for neutrino detection.[19] Clearly, the absolute location of the divalent lanthanide ground state is important for CT excitation and CT luminescence energies.

Figure 86(i) shows the trapping of an electron from the conduction band by Sm^{3+} to form the ground state of Sm^{2+}. The absolute location of an "unoccupied" divalent lanthanide ground state determines the electron trapping depth provided by the corresponding trivalent lanthanide ion. On the other hand, the absolute location of an "occupied" lanthanide ground state determines the valence band hole trapping depth provided by that lanthanide ion. Figure 86(j) illustrates trapping of a hole from the valence band by Ce^{3+}. This hole trapping is an important aspect of the scintillation mechanism in Ce^{3+}-doped scintillators. Similarly, Eu^{2+} is an efficient hole trap of importance for the X-ray storage phosphor $BaFBr:Eu^{2+}$.

Phosphor properties become more complicated when we deal with "double lanthanide-doped systems." Figure 86(k) shows the situation in Eu^{2+} and Sm^{3+} double-doped compounds like SrS and MgS that were studied for optical data storage applications.[4,11] The ultraviolet write pulse excites an electron from Eu^{2+} to the conduction band, which is then trapped by Sm^{3+}. Eu^{3+} and Sm^{2+} are created in the process. An infrared read pulse liberates the electron again from Sm^{2+}, resulting, eventually, in Eu^{2+} 5d–4f emission. Similar mechanisms apply for $Y_2SiO_5:Ce^{3+};Sm^{3+}$ and $LiYSiO_4:Ce^{3+};Sm^{3+}$ compounds that were developed for X-ray and thermal neutron storage phosphor applications, respectively.[5,6] The true mechanism in the persistent luminescence phosphor $SrAl_2O_4:Eu^{2+};Dy^{3+}$ is still disputed. One needs to know the absolute level energy locations to arrive at plausible mechanisms or to discard implausible ones.[8]

As a last example, Figure 86(l) shows quenching of emission in Ce^{3+} and Eu^{3+} co-doped systems. The Ce^{3+} electron excited to the lowest 5d state can jump to Eu^{3+} when the unoccupied Eu^{2+} ground state is located at a lower energy than the occupied lowest Ce^{3+} 5d excited state. After the jump, Eu^{2+} and Ce^{4+} are formed. The Eu^{2+} electron can jump back to Ce^{4+} if the unoccupied Ce^{3+} ground state is located below the occupied Eu^{2+} ground state. The original situation is restored without emission of a photon. Similar quenching routes pertain to Ce^{3+} in Yb-based compounds, and with appropriate level schemes, other "killing" combinations can be found as well.

The above set of examples shows the importance of energy level locations for the performance of phosphors. This importance was realized long ago, but not until recently methods and models became available that allow the determination of these absolute positions. In the following sections, the historic developments and current status of absolute level positioning are briefly reviewed. For detailed information, original literature should be consulted.

2.11.3 The free (gaseous) lanthanide ions

The previous section illustrated the importance of lanthanide level locations for phosphor performance. To understand and predict these locations we first need to understand the properties of the free (gaseous) lanthanide ions. Figure 87 shows the data available on the energy (E_{fd}) needed to excite an electron from the lowest level of the $4f^n5d^06s^m$ configuration to the lowest level of the $4f^{n-1}5d^16s^m$ configuration in the gaseous free lanthanide ions or atoms. The data are from Brewer[20] and Martin[21] together with later updates.[11] Data are most complete for the neutral atoms ($m = 2$, curve c), the monovalent lanthanides ($m = 1$, curve b), and the divalent lanthanides ($m = 0$, curve a). A universal curve, curve a in Figure 87, can be constructed. By shifting the energy of this universal curve, the 4f–5d energies as a function of n can be reproduced irrespective of the charge of the lanthanide ion (0, +1, +2, or +3) or the number, m, of electrons in 6s ($m = 0$, 1, or 2). This remarkable phenomenon is due to the inner-shell nature of the 4f orbital. Apparently, the occupation number of electrons in the 6s shell has no influence on the universal behavior. The main features of this universal variation have been known for a long time and understood in terms of Jörgensens spin pairing theory for the binding of 4f electrons.[22] The energy is large when the 4f configuration is half- ($n = 7$) or completely ($n = 14$) filled, and the energy is small when it is occupied by one or eight electrons.

Figure 88 shows the binding energy (or ionization energy) of the 4f and 5d electrons in the free divalent and free trivalent lanthanide ions with $m = 0$. When we add the corresponding energies, E_{fd}, from Figure 87 to curves b and d in Figure 88, we obtain the binding energies for the 5d electron (see curves a and c). The stronger binding of the 4f and 5d electrons in the trivalent lanthanides than in the divalent ones is due to a stronger Coulomb attraction. Clearly, the binding of the 4f electron is responsible for the universal behavior in the 4f–5d transitions. The binding energy of the 5d electron is rather constant with n which indicates that the nature of the 5d state is relatively invariant with the type of lanthanide ion.

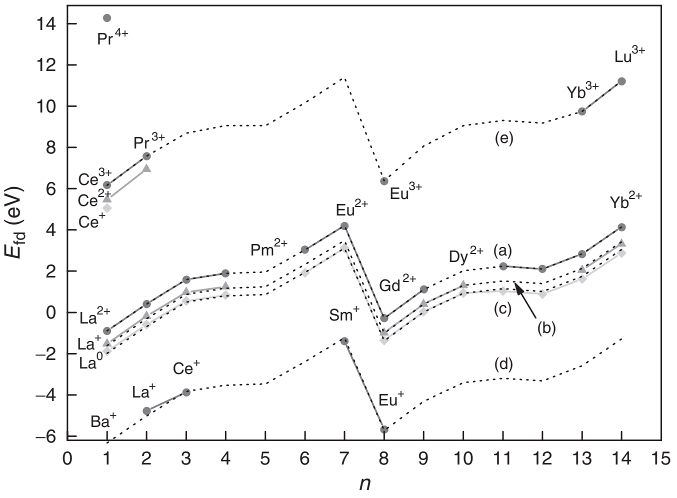

Figure 87 Experimentally observed energies E_{fd} for the transition between the lowest $4f^n5d^06s^m$ and the lowest $4f^{n-1}5d^16s^m$ states of free (gaseous) lanthanide ions and atoms. A shift of the dashed curve (a) by −0.71 eV, −1.09 eV, −5.42 eV, and +7.00 eV gives curves (b), (c), (d), and (e), respectively.

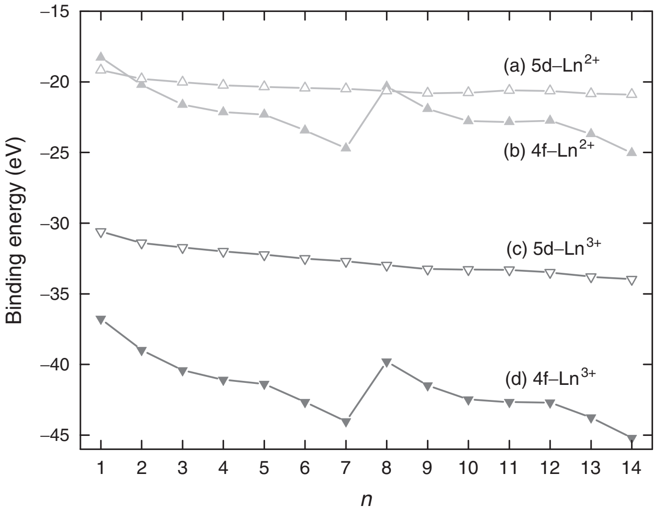

Figure 88 The binding energy in eV of the 5d (curves a and c) and 4f electron (curves b and d) in the free divalent (curves a and b) and free trivalent lanthanide ions (curves c and d).

2.11.4 4f–5d energy differences of lanthanide ions in compounds

Figure 87 indicates that the variation of E_{fd} with n does not depend on the charge of the lanthanide ion or on the number of electrons in the 6s orbital. It is also well established that the Dieke diagram of 4f energy levels is almost invariant with the type of compound.

The situation is completely different for the 5d states. Their energies are influenced 50 times stronger by the host compound than those of 4f states. Due to crystal field splitting of the 5d states and a shift (centroid shift) of the average energy of the 5d configuration, the lowest level of the 5d configuration decreases in energy as illustrated in Figure 89 for Ce^{3+} in $LiLuF_4$ (see also Figure 86(a)). The decrease is known as the redshift or depression $D(n,Q,\mathrm{A}) \approx D(Q,\mathrm{A})$ where n, Q, and A stand for the number of electrons in the $4f^n$ ground state, the charge of the lanthanide ion, and the name of the compound, respectively. The redshift depends very strongly on A but appears, to good first approximation, independent of n, i.e., the type of lanthanide ion. This implies that both the crystal field splitting and the centroid shift of the 5d levels depend on the type of compound but to a good first approximation are the same for each lanthanide ion.

Figure 90 shows this principle. It is an inverted Dieke diagram where the zero of energy is at the lowest 5d state of the free trivalent lanthanide ion. When the lanthanide ions are present in a compound, one simply needs to shift the 5d levels down by the redshift $D(3+,\mathrm{A})$ to find the appropriate diagram for that compound. Figure 90 illustrates this for $LiLuF_4$. The 4f–5d transition energy of each lanthanide ion can be read from the diagram. In equation form this is written as:

$$E_{\mathrm{fd}}(n,3+,\mathrm{A}) = E_{\mathrm{fd}}(n,3+,\mathrm{free}) - D(3+,\mathrm{A}) \tag{180}$$

where $E_{\mathrm{fd}}(n,3+,\mathrm{free})$ is the energy for the first $4f^n$–$4f^{n-1}5d$ transition in the trivalent (3+) free lanthanide ion.[23] In addition to 4f–5d energies in $LiLuF_4$, the diagram also predicts that the lowest 5d state of Pr^{3+} is below the $^1S_0$ state, and broad-band 5d–4f emission and

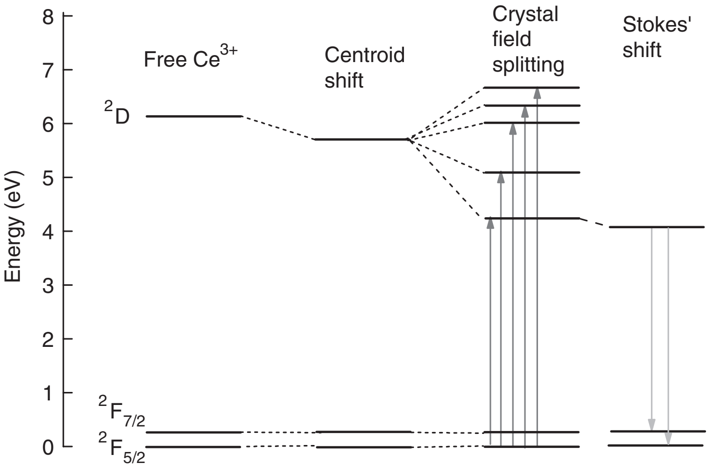

Figure 89 The effect of the crystal field interaction on the (degenerate) free Ce^{3+} energy states in $LiLuF_4$. The combination of centroid shift and crystal field splitting decreases the lowest 5d state with a total energy *D*. On the far right the Stokes shifted 5d–4f emission transitions are shown.

not narrow-band $^1S_0$ line emission will be observed (see Figure 86(b)). The lowest-energy Nd^{3+} 5d state in $LiLuF_4$ is predicted to be stable enough against multiphonon relaxation to the $^2G_{7/2}$ level. Indeed Nd^{3+} 5d–4f emission has been observed.

Redshift values are known for many hundreds of different compounds.[10] Figure 91 summarizes the redshift values $D(3+,A)$ for the trivalent lanthanide ions.[10] It is by definition zero for the free ions, and for the halides it increases from F to I in the sequence F, Cl, Br, I. For the chalcogenides, an increase in the sequence O, S, Se, and presumably Te is observed. This is directly connected with the properties of the anions that affect the centroid shift. The origin of the centroid shift is very complicated and related with covalency and polarizability of the anions in the compound.[24–26] The crystal field splitting is

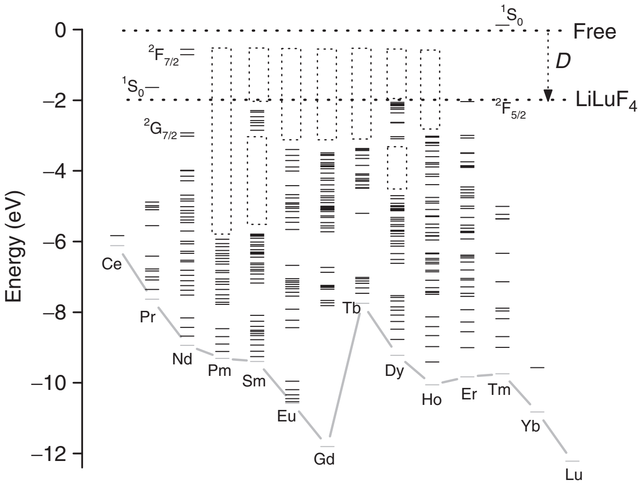

Figure 90 The inverted Dieke diagram where the energy of the lowest 5d level of the free trivalent lanthanide ions are defined as the zero of energy. A downward shift of the 5d levels with the redshift value $D = 1.9$ eV provides the relative position of the lowest 5d level for the trivalent lanthanides in $LiLuF_4$.

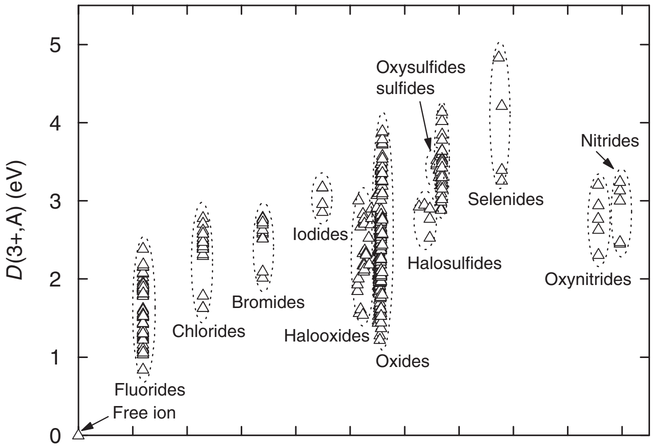

Figure 91 The redshift $D(3+,A)$ for trivalent lanthanide ions in compounds. The parameter along the horizontal axis groups the data depending on the type of compound.

related with the shape and size of the first anion coordination polyhedron.[26,27] The small fluorine and oxygen anions provide the largest values for the crystal field splitting and this is the main reason for the large spread in redshift values for these two types of compounds.[26] With the compiled redshift values, one may predict the 4f–5d transition energies for each of the 13 trivalent lanthanide ions in several hundreds of different compounds using the very simple relationship of Eq. 180. Eq. 180 equally well applies for the 5d–4f emission because the Stokes shift between absorption and emission is to first approximation also independent of the lanthanide ion.

For the divalent lanthanide ions in compounds the story is analogous.[11,12] Again one can introduce a redshift $D(2+,A)$ with a similar relationship

$$E_{\mathrm{fd}}(n,2+,\mathrm{A}) = E_{\mathrm{fd}}(n,2+,\mathrm{free}) - D(2+,\mathrm{A}) \tag{181}$$

and construct figures like Figure 90 and Figure 91.

With all data available on $D(3+,A)$ and $D(2+,A)$, the redshift in divalent lanthanides can be compared with that in the trivalent ones; a roughly linear relationship is found.[28]

$$D(2+,\mathrm{A}) = 0.64D(3+,\mathrm{A}) - 0.233\,\mathrm{eV} \tag{182}$$

Investigations also show a linear relationship between crystal field splitting, centroid shift, and Stokes' shift.[28]

Combining Eqs. 180, 181, and 182 with the available data on $D(2+,A)$ and $D(3+,A)$, it is now possible to predict 4f–5d energy differences for all 13 divalent and all 13 trivalent lanthanides in about 500 different compounds, i.e., about 13000 different combinations! Usually, the accuracy is a few 0.1 eV but deviations occur. The work by van Pieterson et al.[29,30] on the trivalent lanthanides in $LiYF_4$, YPO_4, and CaF_2 shows that the crystal field splitting decreases slightly with the smaller size of the lanthanide ion. In these cases the redshift may not be the same for all lanthanide ions. A study on the crystal field splitting in Ce^{3+} and Tb^{3+} also revealed deviations of the order of a few tenths of eV from the idealized situation expressed by Eqs. 180, 181, and 182.[31]

2.11.5 *Methods to determine absolute level locations*

The experimental basis for the results in the previous sections are from the 4f–5d energy differences, which are easily measured by means of luminescence, luminescence excitation, or optical absorption techniques. We deal with a dipole-allowed transition from a localized ground state to a localized excited state involving one and the same lanthanide ion. Both states have a well-defined energy.

To determine the location of energy levels relative to the valence band or to the conduction band is not straightforward. Again one may use information from optical spectroscopy. Figure 86(g) shows the transition of an electron from the top of the valence band (an anion) to Eu^{3+}. The final state is the $4f^7$ ground state of Eu^{2+}. The energy needed for this CT provides then a measure for the energy difference between the valence band and the Eu^{2+} ground state. Wong et al.[32] and Happek et al.[33] assume that the CT energy provides the location of the ground state of the electron-accepting lanthanide relative to the top of the valence band directly. However, this is not so trivial. The transferred electron and the hole left behind are still Coulomb attracted to each other, and this reduces the transition energy by perhaps as much as 0.5 eV. On the other hand Eu^{2+} is about 18 pm larger than Eu^{3+}, and the optical transition ends in a configuration of neighboring anions that is not yet in its lowest-energy state. Both these effects tend to compensate each other, and fortuitously the original assumption by Wong et al., and later by Happek et al., appears quite plausible.[34] The location of occupied 4f states relative to the occupied valence band states can also be probed by X-ray or UV photoelectron spectroscopy (XPS or UPS).[35]

With the techniques mentioned in the preceding paragraph, the localized level positions of lanthanide ions relative to the valence band states can be probed. The level locations relative to the conduction band can be determined with other techniques. Various methods rely on the ionization of 5d electrons to conduction band states. The thermal quenching of 5d–4f emission in Ce^{3+} or Eu^{2+} is often due to such ionization processes.[15,16] By studying the quenching of intensity or the shortening of decay time with temperature, the energy difference, E_{dC}, between the (lattice relaxed) lowest 5d state and the bottom of the conduction band can be deduced from their Arrhenius behavior.[15] Such studies were done by Lizzo et al.[36] for Yb^{2+} in $CaSO_4$ and SrB_4O_7, by Bessière et al.[17] for Ce^{3+} in $CaGa_2S_4$, and by Lyu and Hamilton.[15] Also, the absence of Ce^{3+} emission due to a situation sketched in Figure 86(c) or the presence of anomalous emission as in Figure 86(d) provides qualitative information on 5d level locations.[14] One may also interpret the absence or presence of vibronic structures in 5d excitation bands as indicative of 5d states contained within the conduction band.[29] One- or two-step photoconductivity provides information on the location of 4f ground states relative to the bottom of the conduction band.[37–40] Another related technique is the microwave conductivity method developed by Joubert and coworkers that was applied to Lu_2SiO_5:Ce^{3+}.[41]

2.11.6 *Systematic variation in absolute level locations*

The previous section provides an explanation on the techniques that have been used to obtain information on level positions. But often these techniques were applied to a specific lanthanide ion in a specific compound with the aim of understanding properties of that combination. Furthermore, each of these techniques provides its own source of unknown systematic errors. These individual studies do not provide us with a broad overview on how level energies change with the type of lanthanide ion and the type of compound. Such an overview is needed to predict phosphor properties and to guide the researcher in the quest for new and better materials.

One of the first systematic approaches was by Pedrini et al. who undertook photoconductivity measurements to determine the location of the 4f ground state of divalent lanthanides in the fluorite compounds CaF_2, SrF_2, and BaF_2 relative to the bottom of the conduction band.[39] They also provide a model to explain the observed variation in 4f ground-state energy with n.

The first systematic approach to determine the levels of trivalent lanthanides was undertaken by Thiel and coworkers using XPS.[42,43] They studied the trivalent lanthanides in $Y_3Al_5O_{12}$ and determined the 4f ground-state energies relative to the valence band of the host crystal. They also combined their findings with the systematic in 4f–5d energy difference found in Ref. 23 to locate the 5d states in the band gap. The absolute energy of the lowest 5d state appears relatively constant with the type of lanthanide ion.

Both XPS and photoconductivity experiments have drawbacks. The oscillator strength for the transition of the localized 4f ground state to the delocalized conduction band states is very small and photoconductivity is rarely observed due to such direct transitions. Two-step photoconductivity is observed more frequently. After a dipole-allowed excitation to the 5d state, it is either followed by autoionization (see Figure 86(c)) or thermally assisted ionization (see Figure 86(e)). For the XPS experiments, high Ln^{3+}-concentrated samples are needed,[42,44] and one has to deal with uncertain final state effects to obtain reliable data.[45] At this moment the amount of information obtained with these two methods is scarce. Although they provide us with very valuable ideas and insight on how level energies change with the type of lanthanide ion, there is not enough information to obtain detailed insights into the effect of type of compound.

Another method to obtain the systematic variation in level position with the type of lanthanide is CT spectroscopy. It appears that the energy of CT to Sm^{3+} is always (at least in oxide compounds) a fixed amount higher than that for the CT to Eu^{3+}. The same applies for Tm^{3+} and Yb^{3+}. This was noticed long ago[22,46,47] and reconfirmed by more recent studies.[48–50] An elaborate analysis of data on CT retrieved from the literature revealed that the systematic behavior in CT energies holds for all lanthanides in all types of different compounds.[34]

Figure 92 illustrates the method to construct diagrams with absolute level location of the divalent lanthanide in $CaGa_2S_4$. The top of the valence band is defined as zero of energy. The arrows numbered 1 through 6 show the observed energies for CT to trivalent lanthanide ions, and they provide us with the location of the ground state of the corresponding divalent lanthanides (see Figure 86(g)). Using these data we can construct precisely the same universal curve, but in an inverted form, as found for the energy E_{fd} of 4f–5d transitions in the free lanthanide ions and atoms of Figure 87. Arrow 7 shows the energy of the first 4f–5d transition in Eu^{2+}. Using Eq. 181, the absolute location of the lowest 5d state for each divalent lanthanide ion can be drawn in the scheme. It appears constant with n.

The universal behavior in the energy of the lowest 4f state with n is determined by the binding of 4f electrons, similar to that depicted in Figure 88, but modified by the Madelung potential at the lanthanide site in the compound. This Madelung potential increases with smaller size of the lanthanide ion due to the inward relaxation of the neighboring negatively charged anions.[14,34,39,43] The increase in 5d electron binding energy by 1–2 eV, as observed for the free divalent lanthanides in Figure 88, is absent in $CaGa_2S_4$ where the binding of the 5d electron is found independent of n. This fortuitous situation for $CaGa_2S_4$, which is also expected for other sulfide compounds, does not apply to oxides and fluorides. For these compounds it was found that from Eu^{2+} to Yb^{2+} the binding of the levels gradually decrease by about 0.5 eV.[14,34] In other words, the 5d state of Yb^{2+} is found 0.5 eV closer to the bottom of the conduction band than that of Eu^{2+}, which is

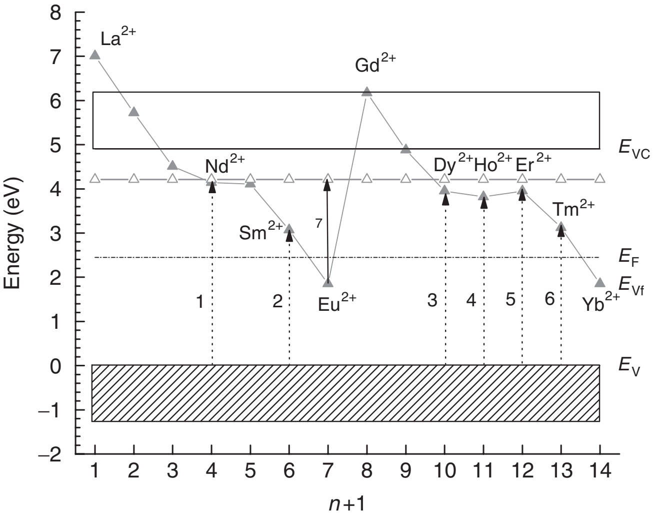

Figure 92 The location of the lowest 4f and lowest 5d states of the divalent lanthanide ions in $CaGa_2S_4$. Arrows 1 through 6 show observed energies of charge transfer to Ln^{3+}. Arrow 7 shows the observed energy for the first 4f–5d transition in Eu^{2+}.

consistent with the observation that Yb^{2+} in oxides and fluorides is more susceptible to anomalous emission than Eu^{2+} in these compounds.[14]

The universal behavior in both 4f–5d energy differences and CT energies forms the basis for a construction method of the diagrams as seen in Figure 92. Only three host-dependent parameters, i.e., E^{CT} (6,3+,A), D(2+,A), and the energy E_{VC} (A) between the top of the valence band (V) and the bottom of the conduction band, are needed. These parameters are available for many different compounds.[51] Figure 93 shows the energy E^{CT} (6,3+,A) of CT to Eu^{3+} (with $n = 6$) in compound (A), and Figure 94 shows the energy of the first excitonic absorption maximum. The mobility band gap, i.e., the energy of the bottom of the conduction band at E_{VC}, is assumed to be 8% higher in energy.[51]

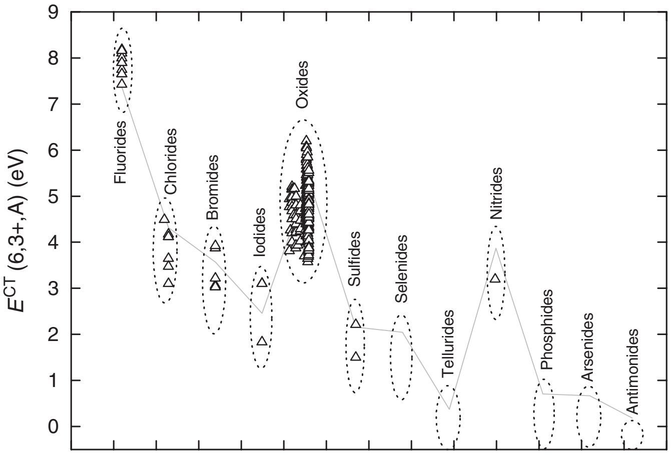

Figure 93 The energy E^{CT} (6,3+,A) of charge transfer to Eu^{3+} in inorganic crystalline compounds. The parameter along the horizontal axis groups the data depending on the type of compound. The solid curve is given by $E^{CT} = 3.72\eta(X) - 2.00$ eV where η(X) is the Pauling electronegativity of the anion.

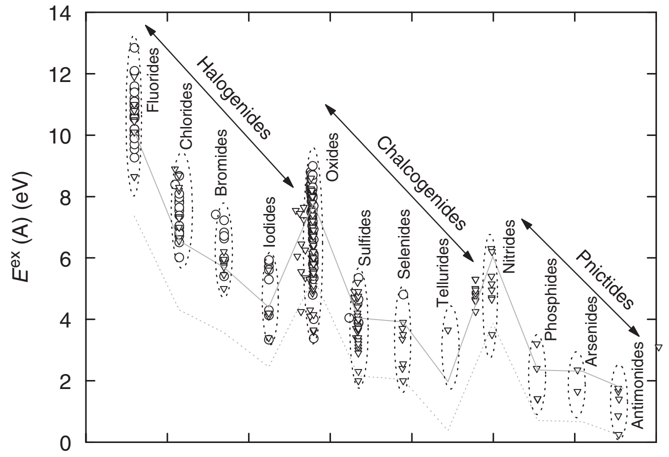

Figure 94 The optical band gap E^{ex} of inorganic compounds. The parameter along the horizontal axis groups the data depending on the type of compound. The solid curve is given by $E^{ex} = 4.34\eta - 7.15$ eV where η is the Pauling electronegativity of the anion. The dashed curve is the same as in Figure 93.

With the richness of data on E^{CT} (6,3+,A), D(2+,A), D(3+,A), and E_{VC} (A) pertaining to hundreds of different compounds, one may now study the relationship between level location and type of compound in detail. Figure 93 shows already the effect of the type of anion on the position of the Eu^{2+} ground state above the top of the valence band. The location is at around 8 eV in fluorides and a clear pattern emerges when the type of anion varies. The energy decreases for the halides from F to I in the sequence F, Cl, Br, I, and for the chalcogenides from O to Se in the sequence O, S, Se, and presumably Te. This pattern is not new and has been interpreted with the Jörgensen model of optical electronegativity.[52]

$$E^{CT} = 3.72\left(\eta(X) - \eta_{opt}(Eu)\right) \tag{183}$$

where η(X) is the Pauling electronegativity of the anion X and η_{opt}(Eu) is the optical electronegativity of Eu, a value that must be determined empirically from observed CT energies. With $\eta_{opt}(Eu) = 2$ the curve through the data in Figure 93 was constructed.[51] The curve reproduces the main trend with the type of anion. It also predicts where we can expect the Eu^{2+} ground state in the pnictides; a decrease in the sequence N, O, As, Sb is expected. However, the wide variation of CT energies within, for example, the oxide compounds is not accounted for by the Jörgensen model. Parameters like lanthanide site size and anion coordination number are also important and need to be considered for a refined interpretation of CT data.[51]

An equation similar to Eq. 183 can be introduced for E^{ex} to illustrate the main trend in the band gap with the type of anion.[51] The band gap follows the same pattern as the energy of CT with changing the type of anion. Interestingly, one may also notice a similar behavior in the values for the redshift in Figure 91 with changing the type of anion. This shows that the parameter values of our model (E^{CT} (6,3+,A), D(2+,A), D(3+,A), and E_{VC} (A)) are not entirely independent from one another.

Analogous to the systematic behavior of the lowest 4f energies for divalent lanthanides with changing n, a systematic behavior of the lowest 4f energies for trivalent lanthanides has been proposed.[34] One may then use, in principle, the same method as used for the divalent lanthanides to construct absolute level diagrams for trivalent lanthanide ions.

For the divalent lanthanides, the “anchor point” of construction is the CT energy to Eu^{3+} (see Figure 93). The CT to Ce^{4+} might play the role of such an anchor point for the trivalent lanthanide level positions. However, information on CT to the Ce^{4+} ion is only sparsely available, insufficient to routinely construct level diagrams. We, therefore, need another anchor point. The energy difference E_{dC} (1,3+,A) between the lowest 5d state of Ce^{3+} and the bottom of the conduction band may serve as the required anchor point. Its value (see Figure 86(d)) can be obtained from two-step photoconductivity experiments or from luminescence-quenching data.

Figure 95 demonstrates the level positions of both divalent and trivalent lanthanides in the same compound YPO_4. The scheme can be compared with that of the free ions in Figure 88. Note that the binding energy difference of more than 10 eV between the free trivalent and free divalent 5d levels is drastically reduced to about 0.8 eV in YPO_4. Energy differences of 0.5–1.0 eV are commonly observed when constructing diagrams for other compounds. The binding energy difference of almost 20 eV between the 4f states of the free ions is reduced to about 7.5 eV in YPO_4. This value also appears fairly constant for different host materials.

The full potential of schemes, similar to those for YPO_4, is demonstrated by comparing Figure 95 with the situations sketched in Figure 86. Actually, each of the 12 situations in Figure 86 can be found in the scheme of YPO_4. The arrows marked 86g, 86h, 86i, 86j, and 86l show the same type of transitions as in Figure 86(g), (h), (i), (j), and (l), respectively. Various other types of transitions, quenching routes, and charge-trapping depths can be read directly from the diagram. To name a few: (1) The lowest 5d states of all the divalent lanthanide ions are between E^{ex} and the bottom of the conduction band. In this situation, the 5d–4f emission is always quenched due to autoionization processes (see Figure 86(c) and (d)). (2) The 5d states of the trivalent lanthanides are well below E^{ex}, and for Ce^{3+}, Pr^{3+}, Nd^{3+}, Er^{3+}, and Tm^{3+} 5d–4f emissions are observed.[29,30] (3) Apart from Eu^{3+}, Gd^{3+}, Yb^{3+}, and Lu^{3+}, all the trivalent lanthanides form valence band hole traps. The trap is

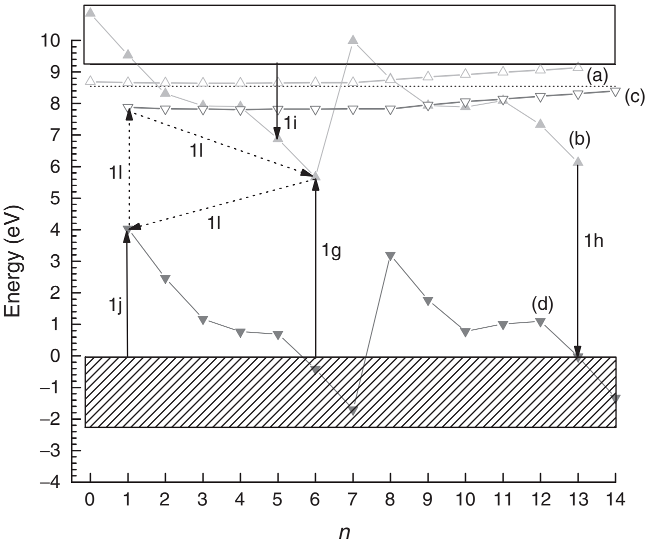

Figure 95 The location of the lowest 4f (curves b and d) and lowest 5d states (curves a and c) of the divalent (curves a and b) and trivalent (curves c and d) lanthanide ions in YPO_4. n and $n + 1$ are the number of electrons in the 4f shell of the trivalent and divalent lanthanide ion, respectively. Arrows indicate specific transitions that were also discussed in Figure 86. The horizontal dashed line at 8.55 eV is E^{ex}.

deepest for Ce^{3+} followed by Tb^{3+}. (4) The ground-state energies for the divalent lanthanides are high above the top of the valence band. In practice this means that even for Eu and Yb it is not possible to stabilize the divalent state during synthesis. (5) The trivalent lanthanides create stable electron traps because the ground states of the corresponding divalent lanthanides are well below the conduction band. (6) The ground states of Sm^{2+}, Eu^{2+}, Tm^{2+}, and Yb^{2+} are below the 5d state of the trivalent lanthanides. This means that Sm^{3+}, Eu^{3+}, Tm^{3+}, and Yb^{3+} can quench the 5d emission of trivalent lanthanide ions.

2.11.7 Future prospects and pretailoring phosphor properties

With the methods described in this section one can construct level schemes for all the lanthanide ions with few parameters. These parameters are available for hundreds of different compounds. At this stage, the schemes still contain systematic errors. Often the bottom of the conduction band is not well defined or known or levels may change due to charge-compensating defects and lattice relaxation which may result in (systematic) errors that are estimated at around 0.5 eV. Such errors are still very important for phosphor performance because a few tenths of eV shift of absolute energy level position may change the performance of a phosphor from very good to useless. The level schemes are, however, already very powerful in predicting 4f–5d and CT transition energies.

We may deduce trends in the energy difference between the lowest 5d state and the bottom of the conduction band, and then use these trends to guide the search for finding better temperature stable phosphors.[16] We may deduce trends in the absolute location of the lanthanide ground state that determines its susceptibility to oxidization or reduction.[53] For example, oxidation of Eu^{2+} is believed to play an important role in the degradation of $BaMgAl_{10}O_{17}:Eu^{2+}$ phosphors,[54] and knowledge on level energies may provide us ideas to further stabilize Eu^{2+}. The level schemes are particularly useful when more than one lanthanide ion is present in the same compound. CT reactions and pathways from one lanthanide to the other can be read from the level schemes. For permanent information storage deep charge traps are required and for persistent luminescence shallow traps are needed. The level schemes provide very clear ideas on what combination of lanthanide ions are needed to obtain the desired properties. Perhaps even more importantly at this stage is that the level schemes provide very clear ideas on what combination not to choose for a specific application.

This chapter has surveyed where we are today with our knowledge and experimental techniques on the prediction and determination of absolute location of lanthanide ion energy levels in phosphors. Currently we have a basic model, but it needs to be more accurate. Aspects like lattice relaxation, charge-compensating defects, intrinsic defects, the nature of the bottom of the conduction band, dynamic properties involved in charge localization and delocalization processes, and theoretical modeling all need to be considered to improve our knowledge further. It will be the next step on the route for the tailoring of phosphor properties beforehand.

References

1. Blasse, G., and Grabmaier, B.C., *Luminescent Materials*, Springer-Verlag, Berlin, 1994.
2. Weber, M.J., Inorganic scintillators: Today and tomorrow, *J. Lumin.*, 100, 35, 2002.
3. van der Kolk, E., et al., Vacuum ultraviolet excitation and emission properties of Pr^{3+} and Ce^{3+} in MSO_4 (M = Ba, Sr, and Ca) and predicting quantum splitting by Pr^{3+} in oxides and fluorides, *Phys. Rev.*, B64, 195129, 2001.
4. Chakrabarti, K., Mathur, V.K., Rhodes, J.F., and Abbundi, R.J., Stimulated luminescence in rare-earth-doped MgS, *J. Appl. Phys.*, 64, 1362, 1988.

5. Meijerink, A., Schipper, W.J., and Blasse, G., Photostimulated luminescence and thermally stimulated luminescence of Y_2SiO_5-Ce,Sm, *J. Phys. D: Appl. Phys.*, 24, 997, 1991.
6. Sidorenko, A.V., et al., Storage effect in $LiLnSiO_4$:Ce^{3+},Sm^{3+},Ln = Y,Lu phosphor, *Nucl. Instrum. Methods*, 537, 81, 2005.
7. Matsuzawa, T., Aoki, Y., Takeuchi, N., and Murayama, Y., A new long phosphorescent phosphor with high brightness, $SrAl_2O_4$:Eu^{2+},Dy^{3+}, *J. Electrochem. Soc.*, 143, 2670, 1996.
8. Dorenbos, P., Mechanism of persistent luminescence in Eu^{2+} and Dy^{3+} co-doped aluminate and silicate compounds, *J. Electrochem. Soc.*, 152, H107, 2005.
9. Wegh, R.T., Meijerink, A., Lamminmäki, R.-J., and Hölsä, J., Extending Dieke's diagram, *J. Lumin.*, 87–89, 1002, 2000.
10. Dorenbos, P., The 5d level positions of the trivalent lanthanides in inorganic compounds, *J. Lumin.*, 91, 155, 2000.
11. Dorenbos, P., f → d transition energies of divalent lanthanides in inorganic compounds, *J. Phys.: Condens. Matter*, 15, 575, 2003.
12. Dorenbos, P., Energy of the first $4f^7 \rightarrow 4f^6 5d$ transition in Eu^{2+}-doped compounds, *J. Lumin.*, 104, 239, 2003.
13. McClure, D.S. and Pedrini, C., Excitons trapped at impurity centers in highly ionic crystals, *Phys. Rev.*, B32, 8465, 1985.
14. Dorenbos, P., Anomalous luminescence of Eu^{2+} and Yb^{2+} in inorganic compounds, *J. Phys.: Condens. Matter*, 15 2645, 2003.
15. Lyu, L.-J. and Hamilton, D.S., Radiative and nonradiative relaxation measurements in Ce^{3+}-doped crystals, *J. Lumin.*, 48&49, 251, 1991.
16. Dorenbos, P., Thermal quenching of Eu^{2+} 5d–4f luminescence in inorganic compounds, *J. Phys.: Condens. Matter*, 17, 8103, 2005.
17. Bessière, A., et al., Spectroscopy and lanthanide impurity level locations in $CaGa_2S_4$:Ln (Ln = Ce, Pr, Tb, Er, Sm), *J. Electrochem. Soc.*, 151, H254, 2004.
18. Boutinaud, P., et al., Making red emitting phosphors with Pr^{3+}, *Opt. Mater.*, 28, 9, 2006.
19. Guerassimova, N., et al., X-ray excited charge transfer luminescence of ytterbium-containing aluminium garnets. *Chem. Phys. Lett.*, 339, 197, 2001.
20. Brewer, L., *Systematics and the Properties of the Lanthanides*, edited by S.P. Sinha, D. Reidel Publishing Company, Dordrecht, The Netherlands, 1983, 17.
21. Martin, W.C., Energy differences between two spectroscopic systems in neutral, singly ionized, and doubly ionized lanthanide atoms, *J. Opt. Soc. Am.*, 61, 1682, 1971.
22. Jörgensen, C.K., Energy transfer spectra of lanthanide complexes, *Mol. Phys.*, 5, 271, 1962.
23. Dorenbos, P., The $4f^n \leftrightarrow 4f^{n-1}5d$ transitions of the trivalent lanthanides in halogenides and chalcogenides, *J. Lumin.*, 91, 91, 2000.
24. Andriessen, J., Dorenbos, P., and van Eijk, C.W.E., Ab initio calculation of the contribution from anion dipole polarization and dynamic correlation to 4f–5d excitations of Ce^{3+} in ionic compounds, *Phys. Rev.*, B72, 045129, 2005.
25. Dorenbos, P., 5d-level energies of Ce^{3+} and the crystalline environment. I. Fluoride compounds, *Phys. Rev.*, B62, 15640, 2000.
26. Dorenbos, P., 5d-level energies of Ce^{3+} and the crystalline environment. IV. Aluminates and simple oxides, *J. Lumin.*, 99, 283, 2002.
27. Dorenbos, P., 5d-level energies of Ce^{3+} and the crystalline environment. II. Chloride, bromide, and iodide compounds, *Phys. Rev.*, B62, 15650, 2000.
28. Dorenbos, P., Relation between Eu^{2+} and Ce^{3+} f→d transition energies in inorganic compounds, *J. Phys.: Condens. Matter*, 15, 4797, 2003.
29. van Pieterson, L., et al., $4f^n \rightarrow 4f^{n-1}5d$ transitions of the light lanthanides: Experiment and theory, *Phys. Rev.*, B6, 045113, 2002.
30. van Pieterson, L., Reid, M.F., Burdick, G.W., and Meijerink, A., $4f^n \rightarrow 4f^{n-1}5d$ transitions of the heavy lanthanides: Experiment and theory, *Phys. Rev.*, B65, 045114, 2002.
31. Dorenbos, P., Exchange and crystal field effects on the $4f^{n-1}5d$ levels of Tb^{3+}, *J. Phys.: Condens. Matter*, 15, 6249, 2003.

32. Wong, W.C., McClure, D.S., Basun, S.A., and Kokta, M.R., Charge-exchange processes in titanium-doped sapphire crystals. I. Charge-exchange energies and titanium-bound excitons, *Phys. Rev.*, B51, 5682, 1995.
33. Happek, U., Choi, J., and Srivastava, A.M., Observation of cross-ionization in $Gd_3Sc_2Al_3O_{12}$:Ce^{3+}, *J. Lumin.*, 94–95, 7, 2001.
34. Dorenbos, P., Systematic behaviour in trivalent lanthandie charge transfer energies, *J. Phys.: Condens. Matter*, 15, 8417, 2003.
35. Sato, S., Optical absorption and X-ray photoemission spectra of lanthanum and cerium halides, *J. Phys. Soc. Jpn.*, 41, 913, 1976.
36. Lizzo, S., Meijerink, A., and Blasse, G., Luminescence of divalent ytterbium in alkaline earth sulphates, *J. Lumin.*, 59, 185, 1994.
37. Jia, D., Meltzer, R.S., and Yen, W.M., Location of the ground state of Er^{3+} in doped Y_2O_3 from two-step photoconductivity, *Phys. Rev.*, B65, 235116, 2002.
38. van der Kolk, E., et al., 5d electron delocalization of Ce^{3+} and Pr^{3+} in Y_2SiO_5 and Lu_2SiO_5, *Phys. Rev.*, B71, 165120, 2005.
39. Pedrini, C., Rogemond, F., and McClure, D.S., Photoionization thresholds of rare-earth impurity ions. Eu^{2+}:CaF_2, Ce^{3+};YAG, and Sm^{3+}:CaF_2, *J. Appl. Phys.*, 59, 1196, 1986.
40. Fuller, R.L. and McClure, D.S., Photoionization yields in the doubly doped SrF_2:Eu,Sm system, *Phys. Rev.*, B43, 27, 1991.
41. Joubert, M.F., et al., A new microwave resonant technique for studying rare earth photoionization thresholds in dielectric crystals under laser irradiation, *Opt. Mater.*, 24, 137, 2003.
42. Thiel, C.W., Systematics of 4f electron energies relative to host bands by resonant photoemission of rare-earth ions in aluminum garnets, *Phys. Rev.*, B64, 085107, 2001.
43. Thiel, C.W., Sun, Y., and Cone, R.L., Progress in relating rare-earth ion 4f and 5d energy levels to host bands in optical materials for hole burning, quantum information and phosphors, *J. Mod. Opt.*, 49, 2399, 2002.
44. Pidol, L., Viana, B., Galtayries, A., and Dorenbos, P., Energy levels of lanthanide ions in a $Lu_2Si_2O_7$:Ln^{3+} host, *Phys. Rev.*, B72, 125110, 2005.
45. Poole, R.T., Leckey, R.C.G., Jenkin, J.G., and Liesegang, J., Electronic structure of the alkaline-earth fluorides studied by photoelectron spectroscopy, *Phys. Rev.*, B12, 5872, 1975.
46. Barnes, J.C. and Pincott, H., Electron transfer spectra of some lanthanide (III) complexes, *J. Chem. Soc.* (a), 842, 1966.
47. Blasse, G. and Bril, A., Broad-band UV excitation of Sm^{3+}-activated phosphors, *Phys. Lett.*, 23, 440, 1966.
48. Krupa, J.C., Optical excitations in lanthanide and actinide compounds, *J. of Alloys and Compounds*, 225, 1, 1995.
49. Nakazawa, E., The lowest 4f-to-5d and charge-transfer transitions of rare earth ions in YPO_4 hosts, *J. Lumin.*, 100, 89, 2002.
50. Krupa, J.C., High-energy optical absorption in f-compounds, *J. Solid State Chem.*, 178, 483, 2005.
51. Dorenbos, P., The Eu^{3+} charge transfer energy and the relation with the band gap of compounds, *J. Lumin.*, 111, 89, 2004.
52. Jörgensen, C.K., *Modern Aspects of ligand Field Theory*, North-Holland Publishing Company, Amsterdam, 1971.
53. Dorenbos, P., Valence stability of lanthanide ions in inorganic compounds, *Chem. Mater.*, 17, 2005, 6452.
54. Howe, B., and Diaz, A.L., Characterization of host-lattice emission and energy transfer in $BaMgAl_{10}O_{17}$:Eu^{2+}, *J. Lumin.*, 109, 51, 2004.

chapter three — section one

Principal phosphor materials and their optical properties

Shinkichi Tanimizu

Contents

3.1 Luminescence centers of ns^2-type ions 155
  3.1.1 Optical spectra of s^2 ions in alkali halides 155
    3.1.1.1 Absorption spectra 155
    3.1.1.2 Structure of the A and C absorption bands 159
    3.1.1.3 Temperature dependence of the A, B, and C absorption bands 161
    3.1.1.4 Emission spectra 162
  3.1.2 s^2-Type ion centers in practical phosphors 162
References 165

3.1 *Luminescence centers of* ns^2*-type ions*

Ions with the electronic configuration ns^2 for the ground state and n*snp* for the first excited state (n = 4, 5, 6) are called ns^2-type ions. Table 1 shows 15 ions with the outer electronic configuration s^2. Luminescence from most of these ions incorporated in *alkali halides* and other crystals has been observed. Among these ions, luminescence and related optical properties of Tl^+ in KCl and other similar crystals have been most precisely studied,[1–5] so s^2 ions are also called Tl^+-like ions. As for powder phosphors, excitation and emission spectra of Sn^{2+}, Sb^{3+}, Tl^+, Pb^{2+}, and Bi^{3+} ions introduced into various oxygen-dominated host lattices have been reported,[6,7] though the analyses of these spectra have not yet been completed due to structureless broad-band spectra and unknown site symmetries. In this section, therefore, experimental and theoretical works on s^2 ions mainly in alkali halides will be summarized.

3.1.1 *Optical spectra of* s^2 *ions in alkali halides*

3.1.1.1 *Absorption spectra*

The intrinsic absorption edge of a pure KCl crystal is located at about 7.51 eV (165 nm) at room temperature. When Tl^+ is incorporated as a substitutional impurity in the crystal with concentrations below 0.01 mol%, four absorption bands appear below 7.51 eV, as shown in Figure 1(a). They have been labeled A, B, C, and D bands in order of increasing energy. Similar bands are observed by the incorporation of Pb^{2+} or Ag^- ions, as shown in Figures 1(b), (c).[8–10] One or two D bands lying near the absorption edge are due to charge-transfer transitions from Cl^- to s^2 ions or to perturbed excitons, and are not due to $s^2 \rightarrow sp$ transitions. The following discussion will, therefore, be restricted to the A, B, and C bands.

First, a model based on free Tl^+ ions following the original work of Seitz[1] will be discussed. The $6s^2$ ground state is expressed by $^1S_0$. The $6s6p$ first excited state consists of a triplet ^3P_J and a singlet $^1P_1$. The order of these states is $^3P_0$, $^3P_1$, $^3P_2$, and $^1P_1$ from the low-energy side. When a Tl^+ ion is introduced into an alkali halide host and occupies a cation site, it is placed in an octahedral (O_h) crystal field. The energy levels of the Tl^+ ion are labeled by the irreducible representation of the O_h point group. The labeling is made as follows: for the ground state $^1S_0 \rightarrow {}^1A_{1g}$, and for the excited state $^3P_0 \rightarrow {}^3A_{1u}$, $^3P_1 \rightarrow {}^3T_{1u}$, $^3P_2 \rightarrow {}^3E_u + {}^3T_{2u}$, and $^1P_1 \rightarrow {}^1T_{1u}$.

The $^1A_{1g} \rightarrow {}^1T_{1u}$ transition is dipole- and spin-allowed, while the $^1A_{1g} \rightarrow {}^3A_{1u}$ transition is strictly forbidden. The $^1A_{1g} \rightarrow {}^1T_{1u}$ transition is partially allowed by singlet-triplet spin-orbit mixing, and $^1A_{1g} \rightarrow ({}^3E_u + {}^3T_{2u})$ is also allowed due to vibronic mixing of ^3E_u and $^3T_{2u}$ with $^3T_{1u}$.

Then, the observed absorption bands shown in Figure 1 can be assigned as follows:

$$\begin{aligned} &\text{A bands}: {}^1A_{1g} \rightarrow {}^3T_{1u} && ({}^1S_0 \rightarrow {}^3P_1) \\ &\text{B bands}: {}^1A_{1g} \rightarrow {}^3E_u + {}^3T_{2u} && ({}^1S_0 \rightarrow {}^3P_2) \\ &\text{C bands}: {}^1A_{1g} \rightarrow {}^1T_{1u} && ({}^1S_0 \rightarrow {}^1P_1) \end{aligned}$$

Focusing on the characteristics of the A, B, and C absorption bands, the centers of the gravity of the energies of these bands are given by[11]:

$$\begin{aligned} \overline{E}_A &= F - \zeta/4 - \sqrt{(G+\zeta/4)^2 + (\lambda\zeta)^2/2} \\ \overline{E}_B &= F - G + \zeta/2 \\ \overline{E}_C &= F - \zeta/4 + \sqrt{(G+\zeta/4)^2 + (\lambda\zeta)^2/2} \end{aligned}$$

Here, F and G are the parameters of Coulomb and exchange energies as defined by Condon and Shortley.[11] ζ is the spin-orbit coupling constant. λ for the A and C bands is called the King-Van Vleck factor,[12] and is a parameter expressing the spatial difference between the $^1T_{1u}$ and $^3T_{1u}$ wavefunctions. The values of ζ and λ can be obtained from the values of $\overline{E}_A$ and $\overline{E}_C$ extrapolated to T = 0K, as shown in Figure 2.[13] The oscillator strength ratio of the C to A bands is given by[14]:

$$f_C/f_A = (\overline{E}_C/\overline{E}_A)\cdot R(\lambda, x)$$

where

$$R(\lambda, x) = \frac{1+\lambda^2(1-x)+\sqrt{1+2\lambda^2 x(1-x)}}{1+\lambda^2 x-\sqrt{1+2\lambda^2 x(1-x)}} \tag{1a}$$

Table 1 Ions with the ns^2 Configuration in the Ground State

Atomic No.	Element	(ns)(np)	Ion species
29	Cu	$(4s)^1$	Cu^-
30	Zn	$(4s)^2$	Zn^0
31	Ga	$(4s)^2(4p)^1$	Ga^+
32	Ge	$(4s)^2(4p)^2$	Ge^{2+}
33	As	$(4s)^2(4p)^3$	As^{3+}
47	Ag	$(5s)^1$	Ag^-
48	Cd	$(5s)^2$	Cd^0
49	In	$(5s)^2(5p)^1$	In^+
50	Sn	$(5s)^2(5p)^2$	$^*Sn^{2+}$
51	Sb	$(5s)^2(5p)^3$	$^*Sb^{3+}$
79	Au	$(6s)^1$	Au^-
80	Hg	$(6s)^2$	Hg^0
81	Tl	$(6s)^2(6p)^1$	$^*Tl^+$
82	Pb	$(6s)^2(6p)^2$	$^*Pb^{2+}$
83	Bi	$(6s)^2(6p)^3$	$^*Bi^{3+}$

* Luminescence is observed also in powder phosphors. (See 3.1.2)

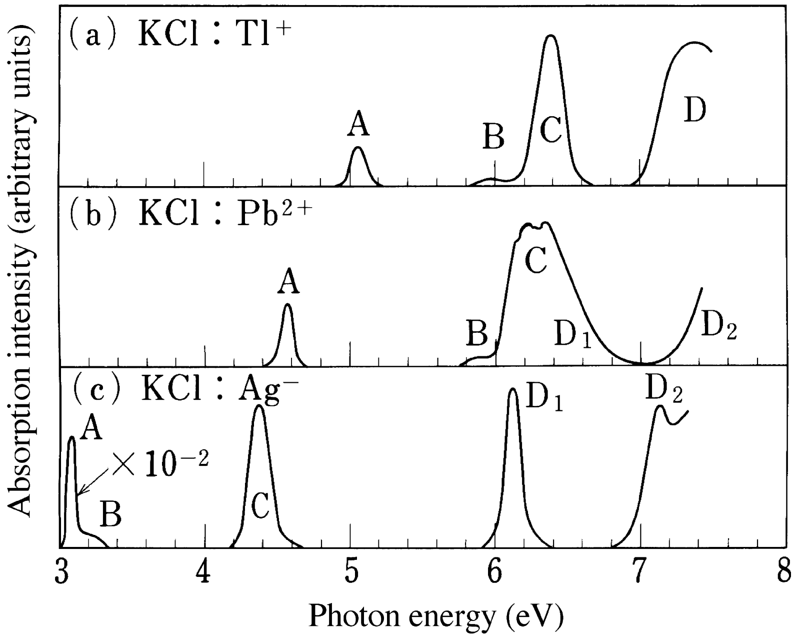

Figure 1 Absorption spectra of (a) Tl^+, (b) Pb^{2+}, and (c) Ag^- ions introduced in KCl crystals at 77K. (From Fukuda, A., *Science of Light (Japan)*, 13, 64, 1964; Kleeman, W., *Z. Physik*, 234, 362, 1970; Kojima, K., Shimanuki, S., and Kojima, T., *J. Phys. Soc. Japan*, 30, 1380, 1971. With permission.)

and

$$x = \left(\overline{E}_B - \overline{E}_A\right)/\left(\overline{E}_C - \overline{E}_A\right) \tag{1b}$$

Values of important parameters mentioned above are listed in Table 2[9] for various ns^2-type ions.

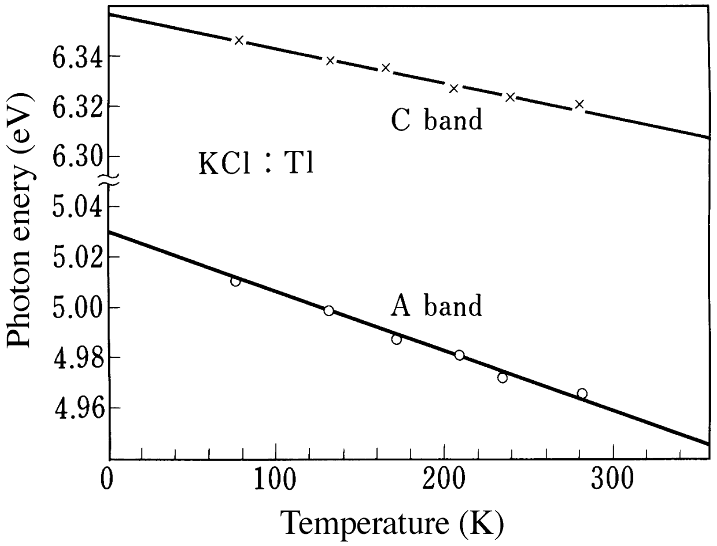

Figure 2 Temperature dependence of $\overline{E}_A$ and $\overline{E}_C$ for the A and C absorption bands in KCl:Tl$^+$. (From Homma, A., *Science of Light (Japan)*, 17, 34, 1968. With permission.)

Table 2 Various Parameters Related to the A, B, and C Absorption Bands of ns^2-Type Ions in Alkali Halide Crystals

ns^2	Phosphors	R	$\overline{E}_A$ (eV)	$\overline{E}_B$ (eV)	$\overline{E}_C$ (eV)	λ	ζ (eV)	G (eV)	F (eV)
	KCl:Sn^{2+}	18	4.36	4.94	5.36	0.599	0.527	0.316	4.992
	KCl:In$^+$	54	4.343	4.630	5.409	0.754	0.268	0.447	4.943
	CsI:Ag$^-$	360	2.780	2.865	3.770	0.897	0.082	0.472	3.296
5 s^2	KCl:Ag$^-$	435	3.100	3.250	4.349	0.575	0.147	0.585	3.762
	Cd^0	478	3.80	3.87	5.41	0.762	0.142	0.769	4.643
	KI:Ag$^-$	525	2.878	2.981	3.985	0.663	0.101	0.516	3.457
	KBr:Ag$^-$	570	3.005	3.132	4.180	0.556	0.125	0.554	3.624
	KCl:Pb^{2+}	4.2	4.57	5.86	6.33	1.03	0.951	0.304	5.688
6 s^2	KCl:Tl$^+$	5.4	5.031	5.930	6.357	0.984	0.692	0.283	5.867
	KCl:Au$^-$	14.0	4.08	4.37	5.44	2.412	0.199	0.540	5.258
	Hg^0	34.2	4.89	5.11	6.70	0.758	0.529	0.731	5.92

Note: R: see text, $\overline{E}_A$, $\overline{E}_B$, $\overline{E}_C$: The centers of gravity of the energies of A, B, and C absorption bands, λ: King-Van Vleck factor, ζ: Spin-orbit coupling constant, G: Exchange energy, F: Coulomb energy.

From Kleeman, W., *Z. Physik*, 234, 362, 1970. With permission.

If the $^1T_{1u}$ and $^3T_{1u}$ wavefunctions are identical, λ becomes 1. Assuming that $\lambda = 1$, Eq. 1a becomes:

$$R(x) = \frac{4 - 2x + \sqrt{6 - 2(2x-1)^2}}{2 + 2x - \sqrt{6 - 2(2x-1)^2}} \tag{2}$$

This equation is known as Sugano's formula.[14] Figure 3[9] shows a plot of Eq. 2 and the experimental data obtained for various ns^2-type ions in alkali halide crystals. Deviations

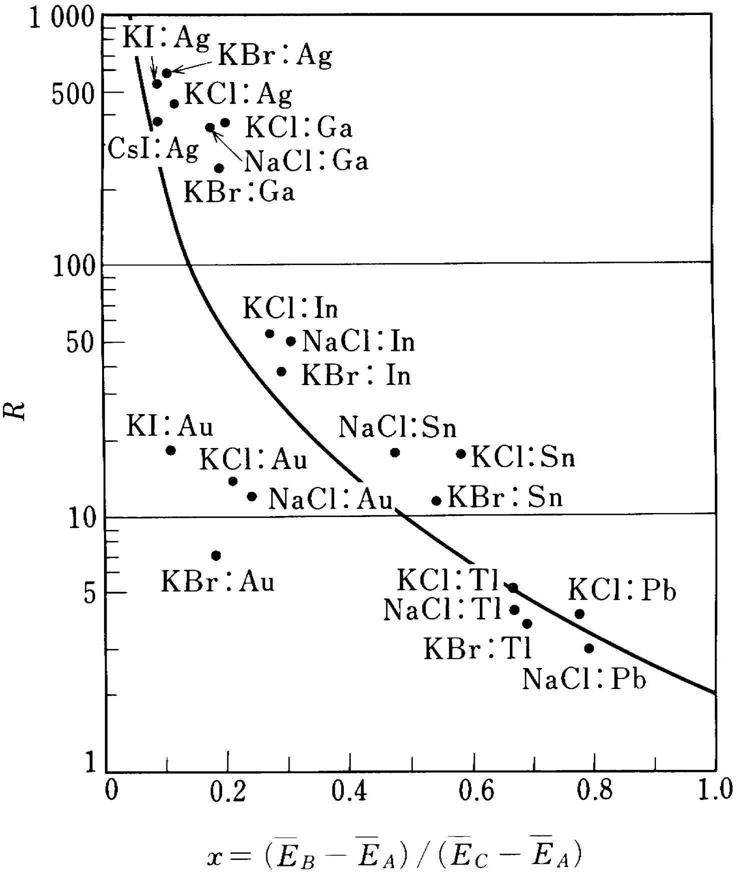

Figure 3 Experimentally obtained R values plotted against x for various ns^2-type ions in alkali halide crystals. The drawn curve is Sugano's formula, Eq. 2. (From Kleeman, W., *Z. Physik*, 234, 362, 1970. With permission.)

from the curve reflect the deviation of λ from 1. Figure 3 and Table 2 show that the observed R values for the same s^2-type ions are nearly the same magnitude for different alkali halide hosts, whereas the values for cationic s^2-type ions and for anionic s^2-type ions differ markedly for the same hosts; for example, R is 5.4 for KCl:Tl$^+$, and 435 for KCl:Ag$^-$. In the case of anionic Ag$^-$, the energy separation between the A and B absorption bands is as small as 0.15 eV, and their intensities are about one-hundredth of that of the C band because of the weak spin-orbit interaction of Ag$^-$.

It may be worth mentioning at this point that Sugano's formula was derived from molecular orbital approximation, but it uses the experimentally determined values for both G and ζ. The formula should, therefore, be considered as a special case of the atomic orbital approximation.

3.1.1.2 *Structure of the A and C absorption bands*

The C absorption band of KCl:Pb^{2+} has a triplet structure as shown in Figure 1(b). This structure is explained as a result of the splitting of the excited states due to the interaction with lattice vibrations, i.e., due to the dynamical Jahn-Teller effect.[15] The lattice vibrational modes interacting with the excited states of s^2 ions in O_h symmetry consist of A_{1g}, E_g, and T_{2g}. The symmetric triplet structure of the C band appears when the potential curves of the ground and excited states in the configurational coordinate model have the same

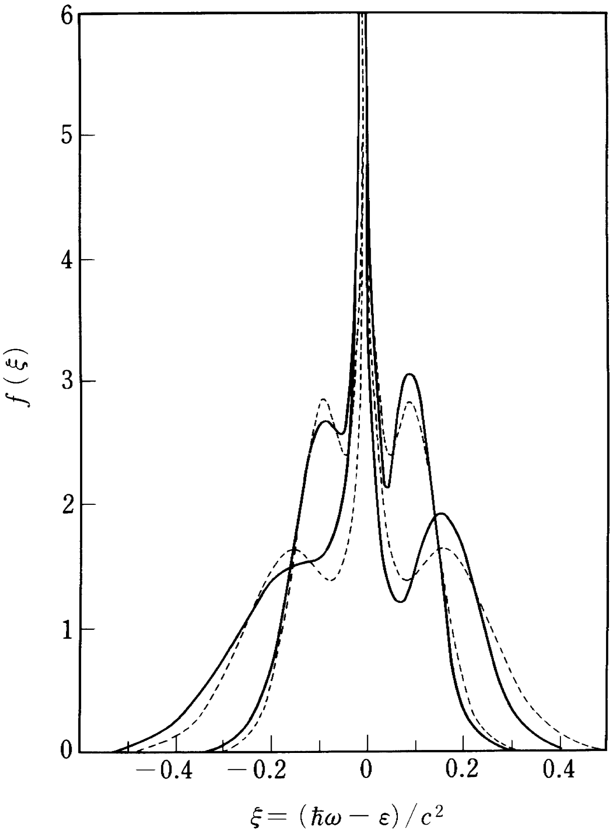

Figure 4 Calculated spectra of the C absorption band (${}^1A_{1g} \to {}^1T_{1u}$) for two different (high and low) temperatures. Dotted curves represent symmetric cases. Solid curves represent the case that the ${}^1T_{1u}$ excited state has the curvature that is half as small as that of the ${}^1A_{1g}$ ground state. (From Fukuda, A., *J. Phys. Soc. Japan*, 27, 96, 1969. With permission.)

curvature within the framework of the Franck-Condon approximation, while the asymmetric triplet structure of the C band appears when they have different curvatures.

Figure 4 shows examples of calculated spectra of the C band for two different temperatures by taking account of the T_{2g} interaction mode.[15,16] The parameter c^2 appearing in the horizontal axis is that representing the coupling constant between s^2-type ions and lattice vibrational modes. The value of c^2 becomes smaller as the host lattice constant becomes larger, and becomes larger if the charge number of the ion becomes larger in the same host lattices. For example, the values of c^2 are 1.2 eV for NaCl:Tl$^+$, 0.82 eV for KCl:Tl$^+$, and 1.82 eV for KCl:Pb^{2+}.[15]

The A band, on the other hand, theoretically has a doublet structure, because two components consisting of the above-mentioned triplet structure have coalesced together due to the interaction between the A and B bands. Figure 5 shows an example of the calculated A absorption bands for two different temperatures θ. However, it is noted that the observed A bands shown in Figure 1 have no clear-cut doublet structure, in disagreement with the calculated bands in Figure 5, and appear as structureless bands. It is also noted that the doublet structure can be observed for KCl:Sn^{2+} and KCl:In$^+$ (see p. 836 -837 in Reference 4).

Define the calculated splitting energy of the A doublet band as δ_A and that of the C triplet band as δ_C. The ratio of the two is given by[15]:

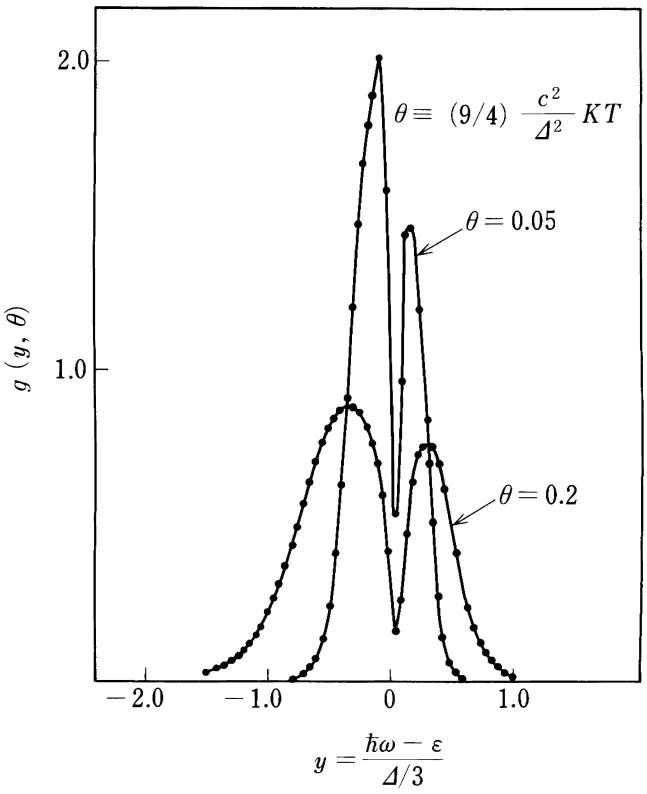

Figure 5 Calculated spectra of the A absorption band ($^1A_{1g} \rightarrow {}^3T_{1u}$) for two different (high and low) temperatures. Δ is a normalized energy parameter of the adiabatic potentials for $^3T_{1u}$ interacting with the T_{2g} mode. (From Toyozawa, Y. and Inoue, M., *J. Phys. Soc. Japan*, 21, 1663, 1966. With permission.)

$$\delta_A/\delta_C = 0.85 \cdot (R-2)/(R-1/2) \tag{3}$$

where R is the parameter of Eq. 2. It is understood that the values of δ_A are smaller than those of δ_C for heavy ions such as Tl^+ and Pb^{2+} because of their smaller R values, as shown in Table 2. This is considered as one reason that the doublet structure of the A band is not observed experimentally.

3.1.1.3 Temperature dependence of the A, B, and C absorption bands

The intensity of the C band is rather constant up to about 150K, and then slightly increases between 150 and 300K. The triplet structure of this band has a tendency to be prominent at higher temperatures. As for the B band, the intensity increases as temperature increases, because the band originates from vibration-allowed transitions. In some cases, temperature-dependent structure is observed in this band, but it is not precisely studied because of the small intensity of this band. The intensity of the A band varies with temperature similar to the C band. In KCl:Tl^+, however, the increase of the B band intensity is counterbalanced by the decrease of the A band intensity, which suggests a mixing of the excited states of the A and B bands.

The above-mentioned characteristics of the A, B, and C absorption bands are prominent features of s^2 ions in alkali halide host lattices. In hosts other than alkali halides, these features are also observed. The appearance of these features is useful for the identification of observed absorption and excitation bands.

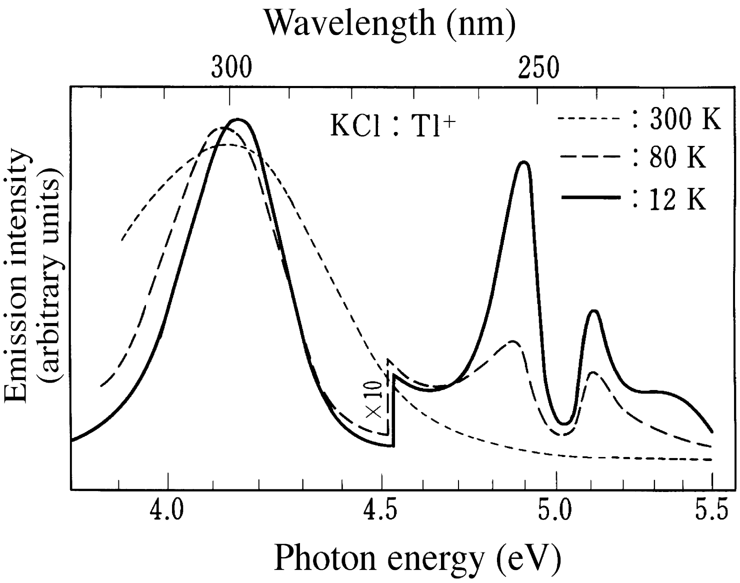

Figure 6 Emission spectra for KCl:Tl$^+$ at 300, 80, and 12K. (From Edgerton, R. and Teegarden, K., *Phys. Rev.*, 129, 169, 1963. With permission.)

3.1.1.4 Emission spectra

Figure 6 shows emission spectra of KCl:Tl$^+$ (0.01 mol%) as an example.[17] At 300K (dotted curve), excitation in any of the A, B, or C bands produces the same emission spectrum, i.e., the A emission band peaking at 4.12 eV (300 nm) and having a width at half-maximum of 0.56 eV (40 nm). At low temperatures, excitation in the A absorption band produces the emission at 4.13–4.17 eV, similar to the case at 300K; whereas excitation in the B or C bands produces another emission band located at about 5 eV in addition to the A band. This emission band has a large dip at 5 eV because of the overlap with the A absorption band. The 5-eV emission observed below 80K is assigned to the C emission ($^1P_1 \rightarrow {}^1S_0$).

Although the A emission band in KCl:Tl$^+$ has a simple structure, the A band in most other cases of s^2-type ion luminescence is composed of two bands: the high-energy band labeled A_T and the low-energy band labeled A_X. Table 3[18] shows energy positions of the A_T and A_X bands for various monovalent s^2-type ions at temperatures in the range of 4.2 to 20K. In Group I, A_T is much stronger than A_X at 4.2K. With increasing temperature, the A_T intensity decreases while the A_X intensity increases, maintaining the sum of both intensities as constant. Above 60K, only A_X is observed. In Group II, there is no temperature region in which A_X is mainly observed. In Group III, the only band observed is assigned to A_T.

The mechanism that the A emission band is composed of two bands is ascribed to the spin-orbit interaction between the A band emitting state (i.e., the triplet $^3T_{1u}$ state) and the upper singlet $^1T_{1u}$ state.[18] This is explained by the configurational coordinate model as shown in Figure 7.[3–5] If the spin-orbit interaction is strong enough, the $^3T_{1u}$ state and $^1T_{1u}$ states repel each other, so that the lower triplet state is deformed to a relaxed excited state with two minima as shown in Figure 7(b). Thus, the two emission bands are produced from the two minima T and X.

As for decay kinetics of the A emission in KCl:Tl$^+$, readers are referred to Reference 19.

3.1.2 s^2-Type ion centers in practical phosphors

Some of the ns^2-type ions listed in Table 1 have long been known as luminescence centers of fluorescent lamp phosphors. In oxygen-dominated host lattices, the emissions

Table 3 Classification of the Observed A Emission Peaks at 4.2–20K and Their Assignments

Group	Phosphor	A_T (eV)	A_X (eV)
I	KI:Ga^+	2.47	2.04
	KBr:Ga^+	2.74	2.24
	KCl:Ga^+	2.85	2.35
	NaCl:Ga^+	3.10	2.45
	KI:In^+	2.81	2.20
	KI:Tl^+	3.70	2.89
II	KBr:In^+	2.94	2.46
	KBr:Tl^+	4.02	3.50
III	KCl:In^+	2.95	—
	NaCl:In^+	3.05	—
	KCl:Tl^+	4.17	—

From Fakuda, A., *Phys. Rev.*, B1, 4161, 1970. With permission.

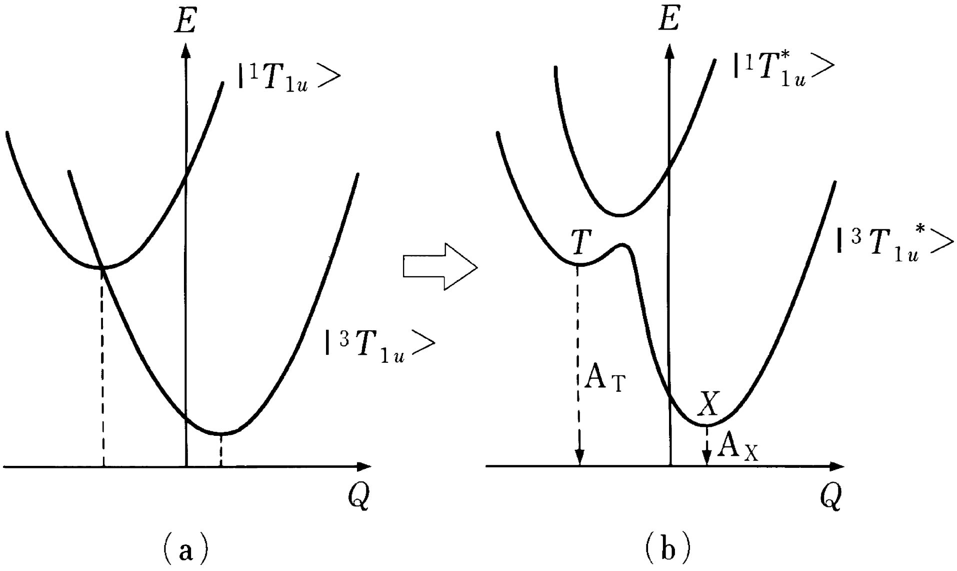

Figure 7 Configurational coordinate model to account for the A_T and A_X emission bands: (a) without spin-orbit interaction, (b) with spin-orbit interaction. (From Farge, Y. and Fontana, Y.P., *Electronic and Vibrational Properties of Point Defects in Ionic Crystals*, North-Holland Publishing, Amsterdam, 1974, 193; Ranfagni, A., Magnai, D., and Bacci, M., *Adv. Phys.*, 32, 823, 1983; Jacobs, P.W.M., *J. Phys. Chem. Solids*, 52, 35, 1991. With permission.)

from Sn^{2+}, Sb^{3+}, Tl^+, Pb^{2+}, and Bi^{3+} are reported. These ions are marked with asteriks in the table.

Luminescence features of the above five ions are as follows.

1. The luminescence is due to the A band transition ($^3P_1 \rightarrow {}^1S_0$).
2. The luminescence is usually associated with a large Stokes' shift, and the spectra are considerably broad, especially in case of Sn^{2+} and Sb^{3+}.
3. The luminescence decay is not very fast and of the order of microseconds. This is because the luminescence transition is spin-forbidden.

Spectral data[20] and 1/e decay times of practical phosphors activated with s^2-type ions at room temperature under 230–260 nm excitation are given below.

$Sr_2P_2O_7$:Sn^{2+} (Ref. 21,22)
Excitation bands: 210, 233, and 250 nm.
Emission band: 464 nm with halfwidth 105 nm.

SrB_6O_{10}:Sn^{2+} (Ref. 23)
Excitation bands: 260 and 325 nm.
Emission band: 420 nm with halfwidth 68 nm.
Decay time: 5 μs.

$Ca_5(PO_4)_3F$:Sb^{3+} (Ref. 24, 25)

Excitation bands:
- 175,[26] 202, 226, 235, 250, and 281 nm for O_2-compensated samples.
- 190, 200, 225, 246, and 267 nm for Na-compensated samples.

Emission bands:
- 480 nm with halfwidth 140 nm.
- 400 nm with halfwidth 96 nm.

Decay times:
- 7.7 μs for 480 nm emission.
- 1.95 μs for 400 nm emission.

The behavior of Sb^{3+} in fluorapatite [$Ca_5(PO_4)_3F$] host lattice is not so simple, because of the existence of two different Ca sites and charge compensation. The low-lying excited states of Sb^{3+} with and without O_2 compensation were calculated by a molecular orbital model.[25] However, the reason why the decay times for 480 and 400 nm emission bands differ noticeably has not yet been elucidated.

YPO_4:Sb^{3+} (Ref. 27, 28)
Excitation bands: 155 nm, 177–202 nm, 230 nm, and 244 nm.
Emission bands: 295 nm with halfwidth 46 nm, and 395 nm with halfwidth 143 nm.
Decay time: Below 1 μs.

$(Ca,Zn)_3(PO_4)_2$:Tl^+ (Ref. 29)
Excitation bands: 200 and 240 nm.
Emission band: 310 nm with halfwidth 41 nm.

The emission peaks vary with Zn contents.

$BaMg_2Al_{16}O_{27}$:Tl^+ (Ref. 30)

Excitation bands:
- 200 nm and 245 nm for 1% Tl.
- Unknown for 3 and 10% Tl.

Emission bands:
- 1% Tl: 295 nm with halfwidth 30 nm.
- 3% Tl: 420 nm with halfwidth 115 nm.
- 10% Tl: 460 nm with halfwidth 115 nm.

Decay times:
- 0.2 μs for 295 nm emission.
- 0.6 μs for 460 nm emission.

$BaSi_2O_5$:Pb^{2+} (Ref. 31, 32)
Excitation bands: 187 and 238 nm.
Emission band: 350 nm with halfwidth 39 nm.

In BaO-SiO_2 systems, Ba_2SiO_4, $BaSiO_3$, and $BaSi_3O_8$, are also known. Ba_2SiO_4:Pb^{2+} reveals two emissions peaked at 317 and 370 nm. The excitation bands lie at 180, 202, and 260 nm.

Pb^{2+} in another host; $SrAl_{12}O_{19}$:Pb^{2+} (Ref. 30)

Excitation bands: Below 200 nm, and 250 nm for 1% Pb.
- Unknown for 25 and 75% Pb.

Emission bands:
- 1% Pb: 307 nm with halfwidth 40 nm.
- 25% Pb: 307 nm with halfwidth 46 nm, and 385 nm with halfwidth 75 nm.
- 75% Pb: 405 nm with halfwidth 80 nm.

Decay time:
- 0.4 μs for 307 nm emission.

As for the spectral data and decay times of Bi^{3+} activated phosphors, readers are referred to References 33, 34, 35, and 36.

YPO_4:Bi^{3+} (Ref. 33, 36)

Excitation bands: 156, 169, 180, 220, 230, and 325 nm (for a Bi-Bi pair)
Emission bands: 241 nm
Decay time: 0.7 s

References

1. Seitz, F., *J. Chem. Phys.*, 6, 150, 1938.
2. Fowler, W.B., Electronic States and Optical Transitions of Color Centers, in *Physics of Color Centers*, Fowler, W.B., Ed., Academic Press, New York, 1968, 133.
3. Farge, Y. and Fontana, M.P., *Electronic and Vibrational Properties of Point Defects in Ionic Crystals*, North-Holland Publishing Co., Amsterdam, 1974, 193.
4. Ranfagni, A., Magnai, D., and Bacci, M., *Adv. Phys.*, 32, 823, 1983.
5. Jacobs, P.W.M., *J. Phys. Chem. Solids*, 52, 35, 1991.
6. Butler, K.H., *Fluorescent Lamp Phosphors*, Pennsylvania State University Press, 1980, 161.
7. Blasse, G. and Grabmaier, B.C., *Luminescent Materials*, Springer Verlag, Berlin, 1994, 28.
8. Fukuda, A., *Science of Light (Japan)*, 13, 64, 1964.
9. Kleemann, W., *Z. Physik*, 234, 362, 1970.
10. Kojima, K., Shimanuki, S., and Kojima, T., *J. Phys. Soc. Japan*, 30, 1380, 1971.
11. Condon, E.U. and Shortley, G.H., *The Theory of Atomic Spectra*, Cambridge University Press, London, 1935.
12. King, G.W. and Van Vleck, J.H., *Phys. Rev.*, 56, 464, 1939.
13. Homma, A., *Science of Light (Japan)*, 17, 34, 1968.
14. Sugano, S., *J. Chem. Phys.*, 36, 122, 1962.
15. Toyozawa, Y. and Inoue, M., *J. Phys. Soc. Japan*, 21, 1663, 1966; Toyozawa, Y., *Optical Processes in Solids*, Cambridge University Press, London, 53, 2003.
16. Fukuda, A., *J. Phys. Soc. Japan*, 27, 96, 1969.
17. Edgerton, R. and Teegarden, K., *Phys. Rev.*, 129, 169, 1963.
18. Fukuda, A., *Phys. Rev.*, B1, 4161, 1970.
19. Hlinka, J., Mihokova, E., and Nikl, M., *Phys. Stat. Sol.*, 166(b), 503, 1991.
20. See Table 10 and 10a in 5.6.2.
21. Ropp, R.C. and Mooney, R.W., *J. Electrochem. Soc.*, 107, 15 1960.
22. Ranby, P.W., Mash, D.H., and Henderson, S.T, *Br. J. Appl. Phys.*, Suppl. 4, S18, 1955.
23. Leskela, M., Koskentalo, T., and Blasse, G., *J. Solid State Chem.*, 59, 272, 1985.
24. Davis, T.S., Kreidler, E.R., Parodi, J.A., and Soules, T.F., *J. Luminesc.*, 4, 48, 1971.
25. Soules, T.F., Davis, T.S., and Kreidler, E.R., *J. Chem. Phys.*, 55, 1056, 1971; Soules, T.F., Bateman, R.L., Hewes, R.A., and Kreidler, E.R., *Phys. Rev.*, B7, 1657, 1973.

26. Tanimizu, S. and Suzuki, T., *Electrochem. Soc.*, Extended Abstr., 74-1, No. 96, 236, 1974.
27. Grafmeyer, J., Bourcet, J.C., and Janin, J., *J. Luminesc.*, 11, 369, 1976.
28. Omen, E.W.J.L., Smit, W.M.A., and Blasse, G., *Phys. Rev.*, B37, 18, 1988.
29. Nagy, R., Wollentin, R.W., and Lui, C.K., *J. Electrochem. Soc.*, 97, 29, 1950.
30. Sommerdijk, J.L., Verstegen, J.M.P.J., and Bril, A., *Philips Res. Repts.*, 29, 517, 1974.
31. Clapp, R.H. and Ginther, R.J., *J. Opt. Soc. Am.*, 37, 355, 1947.
32. Butler, K.H., *Trans. Electrochem. Soc.*, 91, 265, 1947.
33. Blasse, G. and Bril, A., *J. Chem. Phys.*, 48, 217, 1968.
34. Boulon, G., *J. Physique*, 32, 333, 1971.
35. Blasse, G., *Prog. Solid State Chem.*, 18, 79, 1988.
36. J-Stel, T., Huppertz, P., Mayr, W., Wiechert, D.U. *J. Lumin.*, 106, 225, 2004.

chapter three — section two

Principal phosphor materials and their optical properties

Masaaki Tamatani

Contents

3.2 Luminescence centers of transition metal ions 167
- 3.2.1 Crystal field theory 167
  - 3.2.1.1 The simplest case: $3d^1$ electron configuration 168
  - 3.2.1.2 The cases of more than one d electron 171
  - 3.2.1.3 Tanabe-Sugano diagrams 173
  - 3.2.1.4 Spin-orbit interaction 174
  - 3.2.1.5 Intensities of emission and absorption bands 174
- 3.2.2 Effects of electron cloud expansion 177
  - 3.2.2.1 Nephelauxetic effect 177
  - 3.2.2.2 Charge-transfer band 178
- 3.2.3 Cr^{3+} Phosphors ($3d^3$) 178
- 3.2.4 Mn^{4+} Phosphors ($3d^3$) 182
- 3.2.5 Mn^{2+} Phosphors ($3d^5$) 183
  - 3.2.5.1 Crystal field 183
  - 3.2.5.2 Different Mn^{2+} sites in crystals 185
  - 3.2.5.3 UV absorption 186
  - 3.2.5.4 Luminescence decay time 187
- 3.2.6 Fe^{3+} Phosphors ($3d^5$) 187

References 188

3.2 Luminescence centers of transition metal ions

3.2.1 Crystal field theory[1–7]

The $3d$ transition metal ions utilized in commercial powder phosphors have three electrons (in the case of Cr^{3+} and Mn^{4+}) or five electrons (Mn^{2+} and Fe^{3+}) occupying the outermost $3d$ electron orbitals of the ions. When the $3d$ ions are incorporated into liquids or solids, spectroscopic properties (such as spectral positions, widths, and intensities of luminescence and absorption bands) are considerably changed from those of gaseous free ions.

These changes are explained in terms of *crystal field theory*, which assumes anions (ligands) surrounding the metal ion as point electric charges. When the theory is extended to take into consideration the overlap of electron orbitals of the metal ion and ligands, it is called *ligand field theory*. In the following, these theories will be described briefly. For more details, the reader is referred to Reference 1.

3.2.1.1 *The simplest case:* $3\mathrm{d}^1$ *electron configuration*

First, take the case of an ion that has the $3d^1$ electron configuration, such as Ti^{3+}. Table 4 shows the wavefunctions for the five $3d$ electron orbitals, and Figure 8 the electron distributions for these orbitals. For a free ion, the energies of the five $3d$ orbitals are identical, and are determined by an electron kinetic energy and a central field potential caused by the inner electron shell.* In cases where different orbitals have the same energy, the orbitals are said to be degenerate.

When this ion is incorporated in a crystal, surrounding anions affect it. Consider the case where there are six anions (negative point charges) at a distance R from a central cation nucleus located at $\pm x$, $\pm y$, and $\pm z$ as shown by open circles in Figure 8. This ligand arrangement is called the octahedral coordination. These anions induce an electrostatic potential V on a $3d$ electron of the central cation, which is expressed by

$$V = \sum_{i}^{i=6} \frac{Ze^2}{|\boldsymbol{R}_i - \boldsymbol{r}|} \tag{4}$$

Here, $\boldsymbol{R}_i$ represents a position of the i^{th} anion, $\boldsymbol{r}$ a position of the $3d$ electron (coordinates x, y, z), Z a valency of an anion, and e an electron charge.

When $|\boldsymbol{R}_i| \gg |\boldsymbol{r}|$, the following equation is obtained from Eq. 4 by the expansion on $\boldsymbol{r}$ up to 4th order.

$$V = \frac{6Ze^2}{R} + \frac{35Ze^2}{4R^5}\left(x^4 + y^4 + z^4 - \frac{3}{5}r^4\right) \tag{5}$$

The effect of the potential V on the $3d$ electron orbital energy is expressed by the following integration.

$$\int \psi(3d)V\psi(3d)d\tau = \langle 3d|V|3d\rangle \tag{6}$$

The first term of Eq. 5 increases the energy of all five orbitals by the same amount. It may be neglected in the field of optical spectroscopy, where only energy differences among electron states are meaningful. From the second term in Eq. 5, the following orbital energies are obtained.

$$\langle\xi|V|\xi\rangle = \langle\eta|V|\eta\rangle = \langle\varsigma|V|\varsigma\rangle = -4Dq \tag{7}$$

$$\langle u|V|u\rangle = \langle v|V|v\rangle = 6Dq \tag{8}$$

---

* Here, the spin-orbit interaction of an electron is neglected.

Table 4 Wavefunctions for a 3*d* Electron

$$\varphi_u = \sqrt{5/16\pi}\, R_{3d}(r)\left(1/r^2\right)\left(3z^2 - r^2\right)$$

$$\varphi_v = \sqrt{5/16\pi}\, R_{3d}(r)\left(1/r^2\right)\left(x^2 - y^2\right)$$

$$\varphi_\xi = \sqrt{15/4\pi}\, R_{3d}(r)\left(1/r^2\right)yz$$

$$\varphi_\eta = \sqrt{15/4\pi}\, R_{3d}(r)\left(1/r^2\right)zx$$

$$\varphi_\zeta = \sqrt{15/4\pi}\, R_{3d}(r)\left(1/r^2\right)xy$$

Note: $R_{3d}(r)$ means the radial wavefunction of a 3*d* electron. There are many ways to construct five wavefunctions for a 3*d* electron. Here, they are constructed so as to diagonalize the matrix for the cubic crystal field *V*; that is, nondiagonal elements of the seqular equation (e.g., $\langle u|V|v\rangle$) are equal to zero.

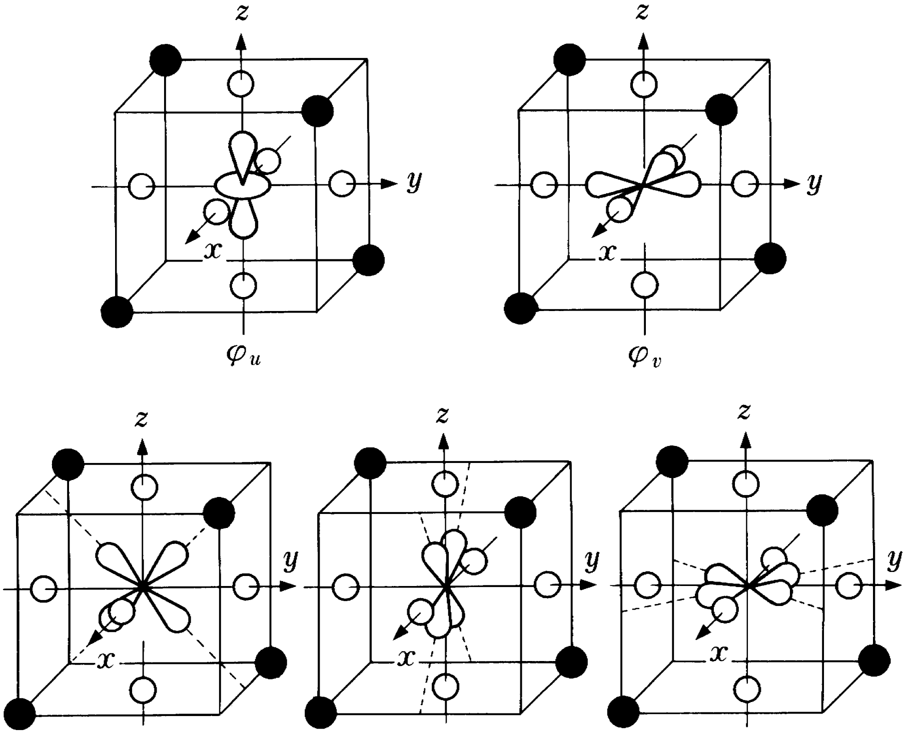

Figure 8 Shapes of *d* orbitals and ligand positions. ○: Ligands for octahedral symmetry. ●: Ligands for tetrahedral symmetry.

Here,

$$D = \frac{35Ze}{4R^5} \tag{9}$$

$$q = \frac{2e}{105}\int \left|R_{3d}(r)\right|^2 r^4 dr \tag{10}$$

Therefore, the fivefold degenerate 3*d* orbitals split into triply degenerate orbitals (ξ,η,ζ) and doubly degenerate orbitals (u,v). The former are called t_2 orbitals, and the latter *e* orbitals.* The energy difference between the t_2 and *e* orbitals is 10*Dq*.** The splitting originates from the fact that *u* and *v* orbitals pointing toward anions in the *x*, *y*, and *z* directions suffer a larger electrostatic repulsion than ξ, η, and ζ orbitals, which point in directions in which the anions are absent.

Next, consider the case where four anions at a distance *R* from the central cation form a regular tetrahedron (tetrahedral coordination). The electrostatic potential caused by these anions at a 3*d* electron of the cation, V_t, is expressed as follows.

$$V_t = \frac{4Ze^2}{R} + eTxyz + eD_t\left(x^4 + y^4 + z^4 - \frac{3}{5}r^4\right) \tag{11}$$

Here,

$$T = \frac{10\sqrt{3}\,Ze}{3R^4} \tag{12}$$

$$D_t = -\frac{4}{9}D \tag{13}$$

The sign of the second term in Eq. 11 changes when the electron coordinates are inverted as $x \to -x$, $y \to -y$, and $z \to -z$, (that is, the term has "odd parity"), and the integrated value of Eq. 6 is zero. Since the third term of Eq. 11 has the same form as the second term in Eq. 5, values similar to Eqs. 7 and 8 are obtained for the 3*d* electrons, lifting the degeneration. However, as shown by Eq. 13, a t_2 orbital has a higher energy than an *e* orbital, and the splitting is smaller than that in octahedral coordination. These results reflect the facts that the t_2 orbitals point toward the anion positions and that the number of the ligands is smaller than that in the octahedral case.

In most crystals, each metal ion is surrounded by four or six ligands. So, the electrostatic effect from the ligands on the central cation (the crystal field) may be approximated by Eqs. 5 or 11, where all ligands are assumed to be located at an equal distance from the central cation, and to have a geometric symmetry of O_h or T_d in notation of the crystal point group. The crystal field with a slightly lower symmetry than the O_h or T_d may be treated by a perturbation method applied to Eq. 5 or 11. The energy levels split further in this case.

For the above procedures, group theory may be utilized based on the symmetry of the geometric arrangement of the central ion and ligands. This is based on the fact that a crystal field having a certain symmetry is invariant when the coordinates are transformed by elemental symmetry operations that belong to a point group associated with the symmetry; all terms other than the crystal field in the Hamiltonian for electrons are also not changed in form by the elemental symmetry operations. In addition, electron wavefunctions can be used as the basis of a representative matrix for the symmetry operations, and the eigenvalues (energies) of the Hamiltonian can be characterized by the reduced representations. Particularly when the Hamiltonian includes the inter-electron electrostatic and spin-orbit interactions in a multi-electron system, group theory is useful for obtaining

---

* They are sometimes called $d\varepsilon$ and $d\gamma$ orbitals in crystal field theory. Notation of t_2 and *e* is generally used more in ligand field theory.

** The energy difference of 10*Dq*, a measure of the crystal field, is sometimes represented as Δ.

Table 5 Correlation of Reduced Representations

Point group	O_h	T_d	D_{4h}	C_{2v}	C_{3v}
Representation	A_{1g}	A_1	A_{1g}	A_1	A_1
	A_{2g}	A_2	B_{1g}	A_2	A_2
	E_g	E	A_{1g}, B_{1g}	A_1, A_2	E
	T_{1g}	T_1	A_{2g}, E_g	A_2, B_1, B_2	A_2, E
	T_{2g}	T_2	B_{2g}, E_g	A_1, B_1, B_2	A_1, E

Note: Subscript g means even parity. Odd parity representations, A_{1u}, A_{2u}, ..., T_{2u}, are not shown.

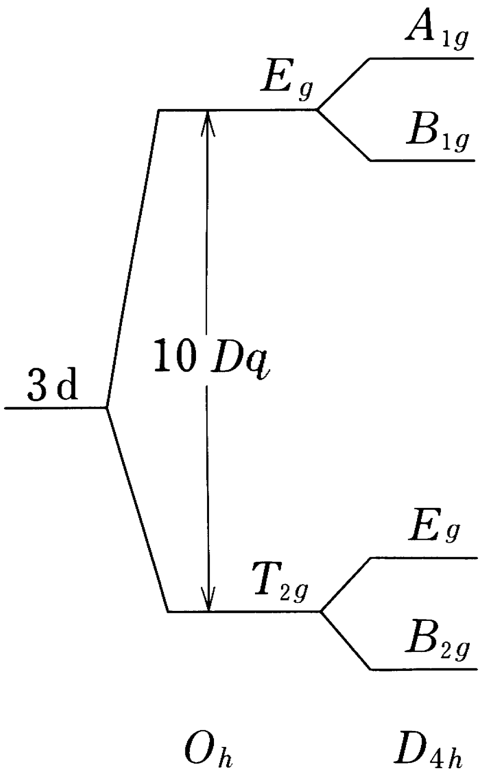

Figure 9 3d level splitting caused by the crystal field.

energy level splitting and wavefunctions, calculating level energies, and predicting the selection rule for transitions between energy levels. Wavefunctions for the t_2 and e orbitals are the basis for the reduced representations T_{2g} and E_g, respectively, in the O_h group.

When the symmetry of the crystal site is lowered from O_h to D_{4h}, one obtains representations in the lower symmetry group contained in the original (higher) symmetry representations from a correlation table of group representations.[8] Table 5 shows an example. From this table, the number (splitting) and representations of energy levels in the lower symmetry can be seen. Figure 9 shows the energy level splitting due to symmetry lowering.

3.2.1.2 The cases of more than one d *electron*

Strong crystal field. When there are more than one electron, the electrons affect each other electrostatically through a potential of $\sum_{i,j} e^2/r_{ij}$, where r_{ij} represents the distance between the two electrons. When the contribution of the crystal field is so large that the electrostatic interaction can be neglected, energies of the states for the d^N electron configuration are determined by the number of electrons occupying the t_2 and e orbitals only. That is, (N + 1) energy levels of e^N, t_2e^{N-1}, …, t_2^N configurations are produced with energies for $t_2^n e^{N-n}$ given by:

$$E(\mathrm{n},\ \mathrm{N}-\mathrm{n}) = \left(-4\mathrm{n} + 6(\mathrm{N}-\mathrm{n})\right)Dq \tag{14}$$

The energy difference between the neighboring two levels is $10Dq$.

When the electrostatic interaction is taken into consideration as a small perturbation, the lower symmetry levels split from the levels of these electron configurations. They are derived from the group theoretical concept of products of representations, applied together with the *Pauli principle*. The latter states that only one electron can occupy each electron orbital, inclusive of spin state. For example, in the case of d^2 (V^{3+} ion), the following levels can be derived:

$$t_2^{\ 2} \to {}^3T_1,\ {}^1A_1,\ {}^1E,\ {}^1T_2$$

$$t_2e \to {}^3T_1,\ {}^3T_2,\ {}^1T_1,\ {}^1T_2$$

$$e^2 \to {}^3A_2,\ {}^1A_1,\ {}^1E$$

Here, each level of ${}^{2S+1}\Gamma$, which is $(2S+1)(\Gamma)$ degenerate, is called a multiplet. S stands for the total spin angular momentum of the electrons. (Γ) represents the degeneracy of the reduced representation Γ; it is 1 for A_1, A_2, B_1, and B_2, 2 for E, and 3 for T_1 and T_2. The energy for a multiplet is obtained as the sum given by Eq. 14 and the expectation value of e^2/r_{12} (e.g., $\left\langle t_2^{\ 2}\ {}^3T_1 \middle| e^2/r_{12} \middle| t_2^{\ 2}\ {}^3T_1 \right\rangle$). To distinguish the parent electron configuration, each multiplet is usually expressed in the form of ${}^{2S+1}\Gamma(t_2^n e^{N-n})$.

Medium crystal field. When the crystal field strength decreases, one cannot neglect the interaction between levels having the same reduced representation but different electron configurations; for example, $\left\langle t_2^{\ 2}\ {}^3T_1 \middle| e^2/r_{12} \middle| t_2e\ {}^3T_1 \right\rangle$. This interaction is called the configuration interaction. The level energies of the reduced representation are derived from the eigenvalues of a determinant or a secular equation that contains the configuration interaction.

Weak crystal field. When the crystal field energy is very small compared with that of the configuration interaction, total angular quantum numbers of L and S for orbitals and spins, respectively, determine the energy. In the case of $Dq = 0$, a level is expressed by ${}^{2S+1}L$, with degeneracy of $(2S+1)(2L+1)$. Symbols S, P, D, F, G, H, … have been used historically, corresponding to $L = 0, 1, 2, 3, 4, 5, \ldots$. For the d^2 configuration, there exist ${}^1S$, ${}^1G$, ${}^3P$, ${}^1D$, and ${}^3F$ levels. Levels split from these levels by a small crystal field perturbation are represented by ${}^{2S+1}\Gamma({}^{2S+1}L)$.

In all three cases described above, integral values for e^2/r_{12} can be shown as linear combinations of a set of parameters: A, B, and C introduced by Racah (Racah parameters). Parameter A makes a common contribution to energies of all levels. Therefore, level energies are functions of Dq, B, and C for spectroscopic purposes, where the energy difference between the levels is the meaningful quantity.

3.2.1.3 *Tanabe-Sugano diagrams*[2]

Each crystal field and electron configuration interaction affects the level energies of the 3*d* transition metal ions by about 10^4 cm^{-1}. Tanabe and Sugano[2a] calculated the determinants of the electron configuration interaction described in Section 3.2.1.2 for the d^2 to d^8 configurations in an octahedral crystal field. They presented the solutions of the determinants in so-called Tanabe-Sugano diagrams.[2b] Figures 10 to 16 show the diagrams for the d^2 to d^8 configurations. These diagrams were prepared for the analysis of optical spectra.* The level energies (E) from the ground level are plotted against the crystal field energy (Dq), both in units of B. For $C/B = \gamma$, values of 4.2 to 4.9 obtained from the experimental spectra in free ions are used. Note that one can treat the configuration interaction for n electrons occupying 10 *d* orbitals in the same manner as that for (10–n) holes; the diagram for d^n is the same as that for d^{10-n} for $Dq = 0$. In addition, the sign of the Dq value for electrons becomes opposite for holes, so that the diagram for d^{10-n} in the octahedral field is also used for d^n in the tetrahedral field.

Optical absorption spectra for $[M(H_2O)_6]^{n+}$ complex ions of 3*d* metals can be well explained by the Tanabe-Sugano diagrams containing the two empirical parameters of Dq and B (about 1000 cm^{-1}).[3] The Dq values for metal ions are in the order:

$$Mn^{2+} < Ni^{2+} < Co^{2+} < Fe^{2+} < V^{2+} < Fe^{3+} < Cr^{3+} < V^{3+} < Co^{3+} < Mn^{4+} \tag{15}$$

They are about 1000 cm^{-1} for divalent metals, and about 2000 cm^{-1} for trivalent metals. For a metal ion, Dq is known to depend on ligand species in the order:

$$I^- < Br^- < Cl^- \sim SCN^- < F^- < H_2O < NH_3 < NO_2^- < CN^- \tag{16}$$

This ordering is called the *spectrochemical series*.[7] Dq values in liquid are not so different from those in crystal, but are governed by the ligand ion species directly bound to the central metal ion. Thus, the spectrochemical series may be rewritten as[7]:

$$I < Br < Cl < S < F < O < N < C \tag{17}$$

Tanabe-Sugano diagrams demonstrate that those configurations in which the lowest excited levels (light-emitting levels) are located in the visible spectral region are d^3 and d^5. For d^3 (Figure 11), the light-emitting levels are ${}^2E({}^2G)$ and ${}^4T_2({}^4F)$ above and below the crossover value of $Dq/B \sim 2.2$, respectively. As will be described later, luminescence bands from these two levels are observed for Cr^{3+} depending on the crystal field strength of host materials. For d^5 (Figure 13), ${}^4T_1({}^4G)$ is the lowest excited level, which is located in the visible region at weak crystal field of $Dq/B < 1.5$. Mn^{2+} of this configuration, having the smallest Dq value among transition metal ions in Eq. 15, is a suitable activator for green- to red-emitting phosphors. The dependence of the ${}^2E({}^2G)$ states for d^3 on Dq is almost parallel to that of the ground level. This suggests that the wavelength of the emitted light does not depend significantly on the crystal field strength of different host materials or on the temperature. Lattice vibrations also lead to instantaneous Dq variation, but the emitting level energy is insensitive to these variations and, consequently, the spectral band may be a sharp line. On the other hand, the curves of the ${}^4T_2({}^4F)$ for d^3 and ${}^4T_1({}^4G)$ for d^5 have steep slopes when plotted against Dq, suggesting that the position of

---

* Orgel[3] also presented diagrams of energy levels as a function of Dq for some transition metal ions such as $V^{3+}(d^2)$, $Ni^{2+}(d^8)$, $Cr^{3+}(d^3)$, $Co^{2+}(d^7)$, and $Mn^{2+}(d^5)$.

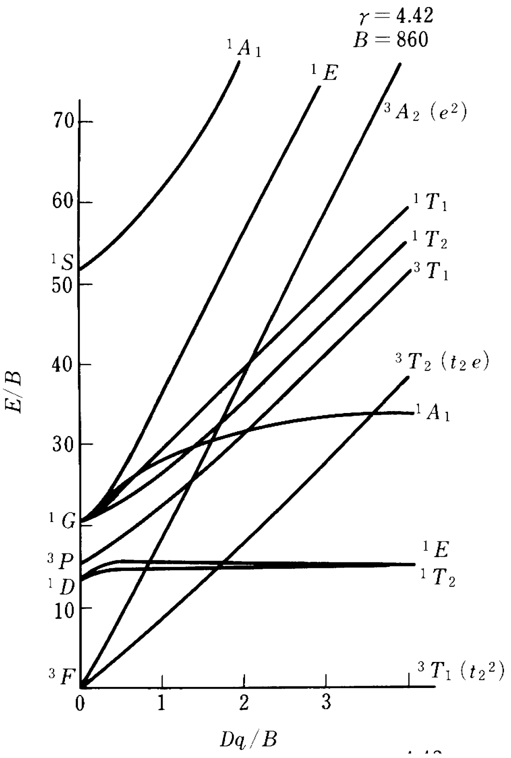

Figure 10 Energy level diagram for the d^2 configuration. (From Kamimura, H., Sugano, S., and Tanabe, Y., *Ligand Field Theory and its Applications*, Syokabo, Tokyo, 1969 (in Japanese). With permission.)

the emitting bands will depend strongly on host materials and that their bandwidths may be broad.

There have been extensive studies on solid-state laser materials doped with transition metal ions. In particular, for tunable lasers working in the far-red to infrared regions, the optical properties of various ions—d^1 (Ti^{3+}, V^{4+}); d^2 (V^{3+}, Cr^{4+}, Mn^{5+}, Fe^{6+}); d^3 (V^{2+}, Cr^{3+}, Mn^{4+}); d^4 (Mn^{3+}); d^5 (Mn^{2+}, Fe^{3+}); d^7 (Co^{2+}); and d^8 (Ni^{2+})—have been investigated in terms of Tanabe-Sugano diagrams with considerable success. (See 13.)

In the diagrams for d^4, d^5, d^6, and d^7 configurations, the ground levels are replaced by those of the lower spin quantum numbers when Dq/B exceeds 2 to 3. This gives an apparent violation of Hund's rule, which states that the ground state is the multiplet having the maximum orbital angular quantum number among those having the highest spin quantum number. It is known that the ion valency is unstable around the Dq/B values at which Hund's rule starts to break down.[4,5]

3.2.1.4 *Spin-orbit interaction*

For 3*d* transition metal ions, the contribution from the spin-orbit interaction in electrons ($\sum_i \xi l_i \cdot s_i$) is as small as 100 cm^{-1}, compared with that due to the crystal field (~10^4 cm^{-1}). Hitherto, this interaction has been neglected. Spin-orbit plays a role, however, in determining the splitting of sharp spectral lines and the transition probability between the levels.

3.2.1.5 *Intensities of emission and absorption bands*

The interaction between an oscillating electromagnetic field of light and an electron brings about a transition between different electronic states. Since the electric dipole (***P***)

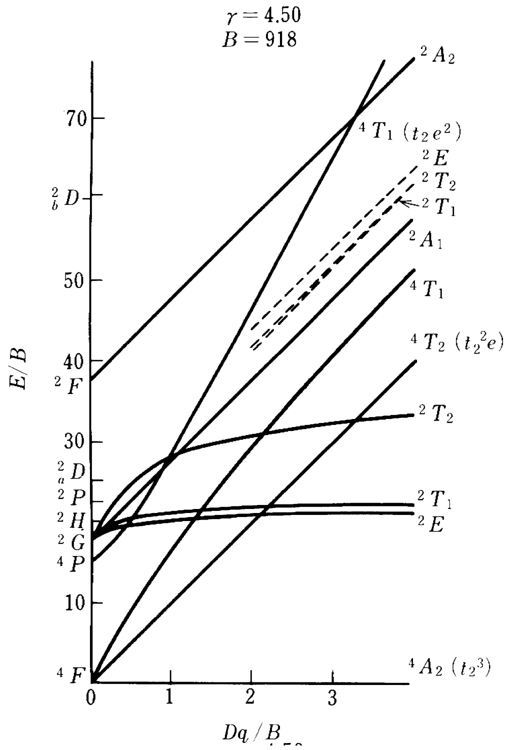

Figure 11 Energy level diagram for the d^3 configuration. (From Kamimura, H., Sugano, S., and Tanabe, Y., *Ligand Field Theory and its Applications*, Syokabo, Tokyo, 1969 (in Japanese). With permission.)

component of the electric field of light has odd parity, and since all wavefunctions of pure d^n states have even parity, one obtains

$$\left\langle 3d^n\, f \middle| \boldsymbol{P} \middle| 3d^n\, i \right\rangle = 0 \tag{18}$$

This means that a transition between the states *i* and *f* having the same parity is forbidden (Laporte's rule). When a crystal field V_{odd} has no inversion symmetry, however, this expression may have small finite value, since wavefunctions having odd parity may be admixed with the $3d^n$ wavefunctions according to the following expression.

$$\psi = \psi_{3d^n} + \sum_u \frac{\psi_u \left\langle u \middle| V_{odd} \middle| 3d^n \right\rangle}{\Delta E_u} \tag{19}$$

Here, ψ_u is a wavefunction for an odd parity state lying at higher energies; these could be $(3d)^{n-1}4p$ states and/or charge-transfer states which will be described later. ΔE_u is the energy difference between the ψ_{3d^n} and ψ_u states.

Even in the case of O_h having the inversion symmetry, V_{odd} may be produced instantaneously by lattice vibrations having odd parity, resulting in a slight violation of Laporte's rule. On the other hand, a magnetic dipole produced by the oscillating magnetic field of light has even parity, and transitions between d^n levels are allowed via this mechanism. In the above, it is assumed that multiplets involved in the transition have a same spin quantum number. Transitions between different spin states are forbidden by orthogonality

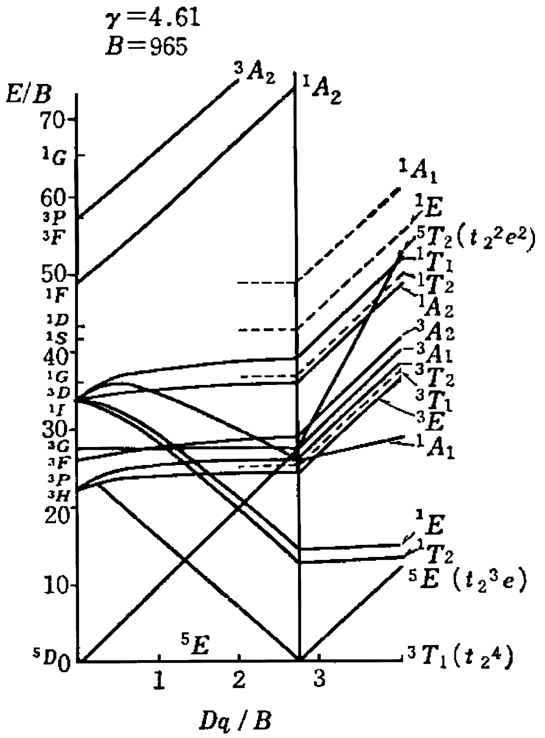

Figure 12 Energy level diagram for the d^4 configuration. (From Kamimura, H., Sugano, S., and Tanabe, Y., *Ligand Field Theory and its Applications*, Syokabo, Tokyo, 1969 (in Japanese). With permission.)

of the spin wavefunctions (spin selection rule). However, in this case also, they can be partly allowed, since different spin wavefunctions may be slightly mixed by means of the spin-orbit interaction. Based on the above considerations, intensities of absorption bands in the visible region for metal complexes have been evaluated in terms of their oscillator strength f. Table 6 shows the results.*

The luminescence decay time, i.e., the time required for an emission from a level to reach $1/e$ of its initial intensity value after excitation cessation, τ (seconds), and the oscillator strength, f, have the following relations.[9] For electric dipole transitions,

$$f\tau = \frac{1.51\left(E_c/E_{eff}\right)^2 \lambda_0^{\,2}}{n} \tag{20}$$

and for magnetic dipole transitions,

$$f\tau = \frac{1.51\lambda_0}{n^3} \tag{21}$$

Here, E_c is the average electric field strength in a crystal, E_{eff} is the electric field strength at the ion position, λ_0 is the wavelength in vacuum (cm), and n is the refraction index. In Table 6, τ values estimated from these equations are also shown.

---

* Note that oscillator strength f for transitions allowed by odd lattice vibrations depends on temperature as $\coth(\hbar\omega/2kT)\cdot$ *Here*, $\hbar\omega$ means phonon energy.

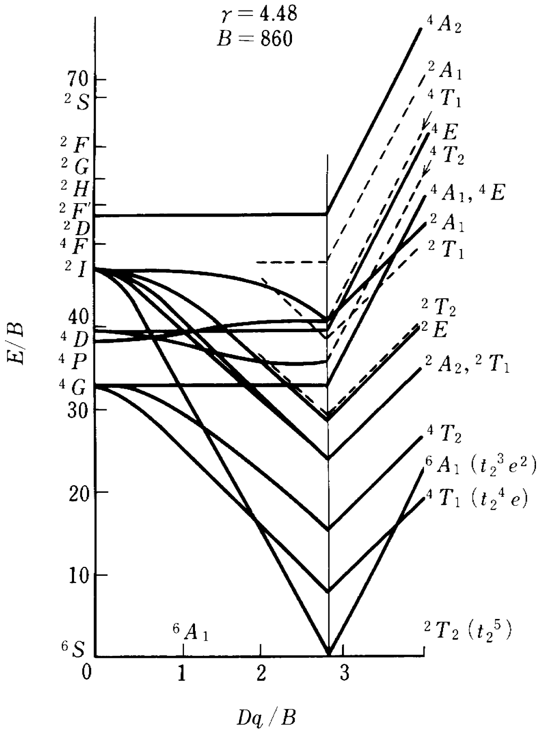

Figure 13 Energy level diagram for the d^5 configuration. (From Kamimura, H., Sugano, S., and Tanabe, Y., *Ligand Field Theory and its Applications*, Syokabo, Tokyo, 1969 (in Japanese). With permission.)

3.2.2 Effects of electron cloud expansion

3.2.2.1 Nephelauxetic effect[7]

The Racah parameters, *B* and *C*, in a crystal are considerably smaller than those for a free ion, as shown in Tables 7, 8, 10, and 11. The reason is as follows. Some electrons of the ligands move into the orbitals of the central ion and reduce the cationic valency. Due to this reduction, the *d*-electron wavefunctions expand toward the ligands to increase the distances between electrons, reducing the interaction between them. This effect is called the *nephelauxetic effect*. In fact, some 3*d* electrons are known to exist even at the positions of the nuclei of the ligands as determined by ESR and NMR experiments. Therefore, the assumption in crystal field theory that expansion of the 3*d* orbitals may be negligibly small does not strictly hold. The reduction of *B* and *C* for various ligands is in the order:

$$\mathrm{F} < \mathrm{O} \sim \mathrm{N} < \mathrm{Cl} \sim \mathrm{C} < \mathrm{Br} < \mathrm{I} \sim \mathrm{S} \tag{22}$$

For central cations, it is:

$$\mathrm{Mn}^{2+} < \mathrm{Ni}^{2+} < \mathrm{Cr}^{3+} < \mathrm{Fe}^{3+} < \mathrm{Co}^{3+} \tag{23}$$

This effect may be considered to increase with covalency between the cation and ligands. Note that the relation in Eq. 22 corresponds to a decreasing order in the electronegativity of elements.

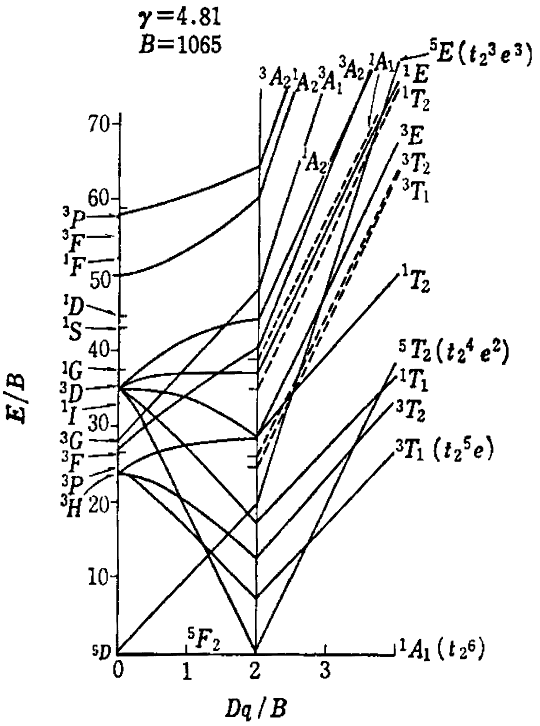

Figure 14 Energy level diagram for the d^6 configuration. (From Kamimura, H., Sugano, S., and Tanabe, Y., *Ligand Field Theory and its Applications*, Syokabo, Tokyo, 1969 (in Japanese). With permission.)

3.2.2.2 Charge-transfer band

In crystal field theory, transitions with higher energies than those within the d^n configuration entail $d^n \rightarrow d^{n-1}s$ or $d^n \rightarrow d^{n-1}p$ processes. However, in energy regions (e.g., 200 to 300 nm for oxides) lower than these interconfigurational transitions, strong absorption bands ($f \sim 10^{-1}$), called charge-transfer (CT) (or electron-transfer) bands, are sometimes observed.[4,7,9] These absorption bands are ascribed classically to electron transfers from the ligands to a central cation. It is argued that (1) the band energy is lower as the electronegativity of the ligands decreases, and (2) it is reduced as the valency increases for cations having the same number of electrons.[4,7] Charge-transfer states for 3*d* ions, however, are not fully understood, unlike those for 4*d* and 5*d* ion complexes.*

3.2.3 Cr^{3+} phosphors (3d^3)

Luminescence due to Cr^{3+} is observed in the far-red to infrared region, and only limited applications have been proposed for Cr^{3+} phosphors.[12] This ion has attracted, however, the attention of spectroscopists since the 1930s, because Cr^{3+} brings about luminescence with an interesting line structure in the 680- to 720-nm spectral region in various host materials. In particular, the optical spectra of ruby (Al_2O_3:Cr^{3+}) were fully explained for the first time by applying crystal field theory (1958)[13]; ruby was utilized for the first solid-state laser (1960).[14]

Figures 17 and 18 show the luminescence[15] and absorption[1] spectra of ruby crystals, respectively. The two strong luminescence lines at 694.3 nm (= 14399 cm^{-1}) and 692.9

---

* See 3.4. For rare-earth phosphors, the effect of the charge-transfer bands is investigated in considerable detail with respect to the fluorescence properties of *f*-*f* transitions.[11]

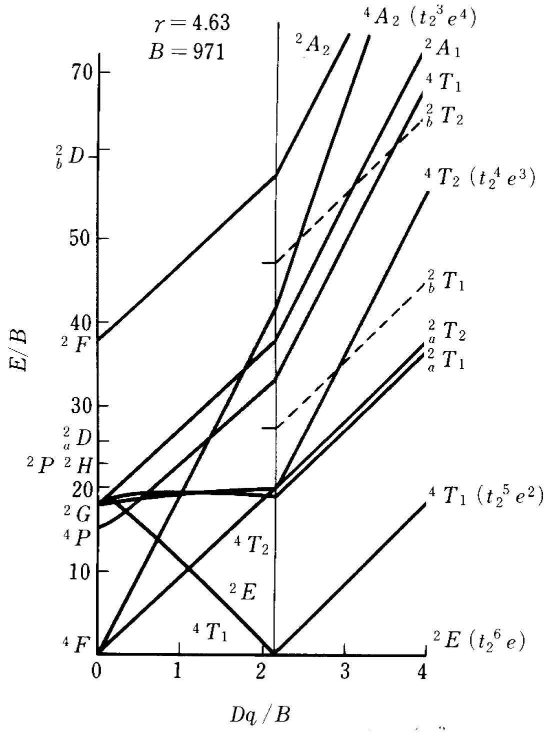

Figure 15 Energy level diagram for the d^7 configuration. (From Kamimura, H., Sugano, S., and Tanabe, Y., *Ligand Field Theory and its Applications*, Syokabo, Tokyo, 1969 (in Japanese). With permission.)

nm (= 14428 cm^{-1}) with width of ~10 cm^{-1} and decay time of 3.4 ms at room temperature are called R_1 and R_2 lines. They lie at the same wavelengths as lines observed in the absorption spectrum (zero-phonon lines). These lines correspond to the transition from ${}^2E(t_2^3) \rightarrow {}^4A_2(t_2^3)$ in Figure 11. The ${}^2E$ level splits into two levels due to a combination of the spin-orbit interaction and symmetry reduction in the crystal field from cubic to trigonal.[1] Two strong absorption bands at ~18000 cm^{-1} and ~25000 cm^{-1} correspond to the spin-allowed transitions from the ground level (${}^4A_2(t_2^3)$) to the ${}^4T_2(t_2^2e)$ and ${}^4T_1(t_2^2e)$ levels, respectively. The spectral band shape differs, depending on the electric field direction of the incident light due to the axial symmetry in the crystal field (dichroism).

Many spin doublets originate from the t_2^2e configuration of Cr^{3+} in addition to the above two spin quartets.* Transitions from the ground level (${}^4A_2$) to those spin doublets are spin-forbidden, the corresponding absorption bands being very weak to observe.** Strong spin-allowed absorption bands to those spin doublets, however, are observable from ${}^2E(t_2^3)$, when a number of Cr^{3+} ions are produced by an intense light excitation into this excited state (excited-state absorption).[16] For 11 multiplet levels, including those obtained through excited-state absorption studies, all the properties of the absorption bands—such as spectral position, absorption intensity, and dependence on the polarized light—have been found to agree very well with those predicted from crystal (ligand) field theory.[1,16]

As shown in Figure 17, with the increase in Cr^{3+} concentration, additional luminescence lines begin to appear at the longer wavelength side of the R lines, and grow up to be broad bands that become stronger than R lines; this is accompanied by the reduction

---

* In Figure 11, positions for these doublets are not shown clearly.

** In a strong crystal field, two-electron transitions such as $t_2^3 \rightarrow t_2e^2$ are forbidden.

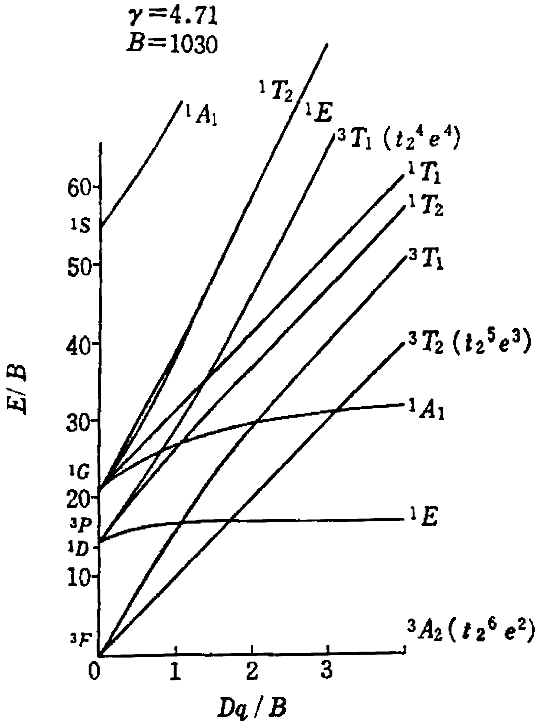

Figure 16 Energy level diagram for the d^8 configuration. (From Kamimura, H., Sugano, S., and Tanabe, Y., *Ligand Field Theory and its Applications*, Syokabo, Tokyo, 1969 (in Japanese). With permission.)

Table 6 Oscillator Strength and Luminescence Decay Time

		Laporte's rule allowed		Laporte's rule forbidden Electric dipole	
		Electric dipole	Magnetic dipole	V_{odd} allowed	Lattice vibration allowed
Spin-allowed	f	~1	~10^{-6}	~10^{-4}	~10^{-4}
	τ	~5 ns	~1 ms	~50 μs	~50 μs
Spin-forbidden	f	10^{-2}–10^{-3}	10^{-8}–10^{-9}	10^{-6}–10^{-7}	10^{-6}–10^{-7}
	τ	0.5–5 μs	10^2–10^3 ms	5–50 ms	5–50 ms

Note: 1. f values for the case of spin-allowed are estimated in Reference 1. f values for the case of spin-forbidden are assumed to be 10^{-2}–10^{-3} of those for spin-allowed.

2. Decay times are calculated from Eqs. 22 and 23, assuming $E_c/E_{eff} = (n^2 + 2)/3$ (Lorenz field), $n = 1.6$, and $\lambda_0 = 500$ nm.

in the luminescence decay time of R lines, in the case of Figure 17, from 3.5 ms to 0.8 ms at room temperature.[15] Additional lines are attributed to magnetically coupled Cr^{3+}-Cr^{3+} pairs and clusters. Luminescence lines are assigned to such pairs up to the fourth nearest neighbor; for example, the N_1 line is assigned to pairing to the third nearest neighbor, and N_2 to the fourth nearest.[17]

In compounds such as various gallium garnets in which Cr^{3+} ions are located in weak crystal fields, $^4T_2(^4F)$, instead of $^2E(^2G)$, is the emitting level.[18] As expected from Figure 11, the luminescence spectrum consists of a broad band in the near-infrared region, i.e., at a longer wavelength region than that in the ^2E case. The decay time is as short as ~0.1 ms because the transition is spin-allowed. These properties make them promising candidates

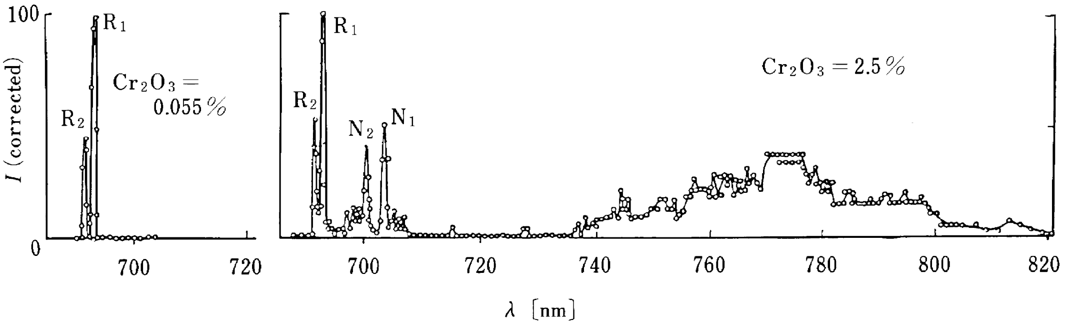

Figure 17 Luminescence spectra in rubies (at 77K). (Figure 1 in the source shows luminescence spectra and decay times for rubies containing 0.4, 0.86, 1.5, and 8% concentrations of Cr_2O_3, in addition to the above two examples.) (From Tolstoi, N.A., Liu, S., and Lapidus, M.E., *Opt. Spectrosc.*, 13, 133, 1962. With permission.)

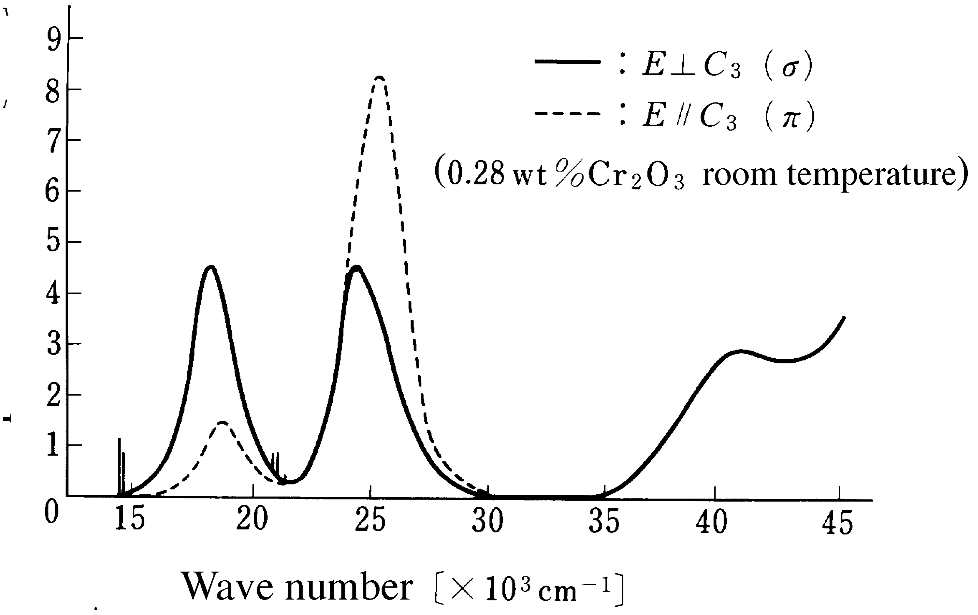

Figure 18 Absorption spectra of a ruby. (Courtesy of A. Misu, unpublished.) *E* represents the electric field direction of an incident light, and C_3 does a three-fold axis direction of the crystal. Spectrum at higher energies than 35000 cm^{-1} is for natural light. Absorption lines around 15000 and 20000 cm^{-1} are shown only in the case of the σ spectrum, qualitatively with respect to intensity and linewidth. (From Kamimura, H., Sugano, S., and Tanabe, Y., *Ligand Field Theory and its Applications*, Syokabo, Tokyo, 1969 (in Japanese). With permission.)

for tunable solid-state laser materials.[19,20] The change of the emitting state depending on the host materials is a good example of the importance of the crystal field in determining the optical properties of the transition-metal-doped compounds.

Table 7 shows the crystal field parameters obtained from absorption spectra and luminescence decay times for Cr^{3+} in several hosts. Most luminescence bands in 3*d* ions are caused by electric dipole transitions. In such materials as $MgAl_2O_4$ and MgO, in which a metal ion lies in the crystal field with the inversion symmetry, however, the *R* lines occur via a magnetic dipole process[21,22]; consequently, the decay times are long.

Table 7 Crystal Field Parameters for Cr^{3+}

Host	λ (nm)		Dq (cm^{-1})	B (cm^{-1})	C (cm^{-1})	τ (ms)		Ref.
α-Al_2O_3 (ruby)	694.3	692.9[14]	1630	640	3300	3	(R)	23
$Be_3Al_2Si_6O_{18}$ (Emerald)	682.1	679.2[26]	1630	780	2960			23
$MgAl_2O_4$	682.2	681.9	1825	700	3200	36.5	(N)	21
MgO	698[27]		1660	650	3200	12	(N)	22
$LiAl_5O_8$ [a]	715.8	701.6	1750	800	2900	3.7		24
$Y_3Al_5O_{12}$	688.7	687.7	1725	640	3200	1.5		28
$Gd_3Ga_5O_{12}$	745 (broad)[b]		1471	645		0.16		18
$Y_3Ga_5O_{12}$	730 (broad)[b]		1508	656		0.24		18
$Cr(H_2O)_6^{3+}$	Abs.		1720	765				3
Free ion	684.2	(^2G)[25]		918				3

Note: λ: peak wavelength of luminescence; τ: $1/e$ decay time; (R), room temperature; (N), 77K.

[a] Ordered type

[b] $^4T_2 \to {}^4A_2$ transition, otherwise $^2E \to {}^4A_2$ transition.

3.2.4 Mn^{4+} phosphors ($3d^3$)

Only $3.5MgO{\cdot}0.5MgF_2{\cdot}GeO_2{:}Mn^{4+}$ is now in practical use among the Mn^{4+} phosphors, though $6MgO{\cdot}As_2O_5{:}Mn^{4+}$, which has a performance almost equal to that of $3.5MgO{\cdot}0.5MgF_2{\cdot}GeO_2{:}Mn^{4+}$, was used previously,[29] and a number of titanate phosphors were developed between 1940 and 1950.[30]

Luminescence bands due to Mn^{4+} exist at 620 to 700 nm in most host materials. The spectrum has a structure consisting of several broad lines originating from transitions aided by lattice vibration. In Al_2O_3 and Mg_2TiO_4, it resembles the R lines of Cr^{3+}, and is assigned to the $^2E(t_2^3) \to {}^4A_2(t_2^3)$ transition.

Figure 19 shows the luminescence spectra for $3.5MgO{\cdot}0.5MgF_2{\cdot}GeO_2{:}Mn^{4+}$. It consists of more than six lines at room temperature; the intensity of the lines at the shorter wavelength side decreases at low temperatures. This behavior is explained by assuming that thermal equilibrium exists between two levels in the emitting state, and that there are more than two levels in the ground state.[31] As for the origin of the emitting and ground states, different assignments have been proposed.

Kemeny and Haake assigned the bands to the $^4T_2(t_2^2e) \to {}^4A_2(t_2^3)$ transition in Figure 11, assuming the Mn^{4+} site has octahedral coordination.[31] They propose that the $^4T_2$ level splits into two levels due to the low symmetry field, and that more than two vibronic levels accompany the ground state. Butler insisted that a $(MnO_4)^{4-}$ complex replaced $(GeO_4)^{4-}$, which is tetrahedrally coordinated.[32] In this case, the appropriate energy diagram is Figure 15 instead of Figure 11, and the luminescence originates from the $^2E(e^3) \to {}^4T_1(e^2t_2)$ transition.* The ^2E and $^4T_1$ levels split into two and three due to the low symmetry field, respectively. These proposals, however, could not account for such facts as the luminescence has a decay time of the order of milliseconds; in addition, no visible luminescence has been observed due to Mn^{4+} in solid-state materials in which the metal ions are tetrahedrally coordinated.

Ibuki's group assigned the lines to transitions from two excited levels of $^2E(t_2^3)$ and $^2T_1(t_2^3)$ to the ground state $^4A_2(t_2^3)$ in Figure 11, assuming Mn^{4+} has an octahedral coordination.[33] The main peak structure in the range 640 to 680 nm at room temperature originates from the lattice vibration associated with the $^2E \to {}^4A_2$ zero-phonon transition at 640 nm.

Blasse explained the spectral characteristics by assuming only one electronic transition of $^2E \to {}^4A_2$ in octahedrally coordinated Mn^{4+}.[34] Both the ground and excited states are

---

* See 3.2.1.3. The transition corresponds to $^2E(t_2^6e) \to {}^4T_1(t_2^5e^2)$ in Figure 15.

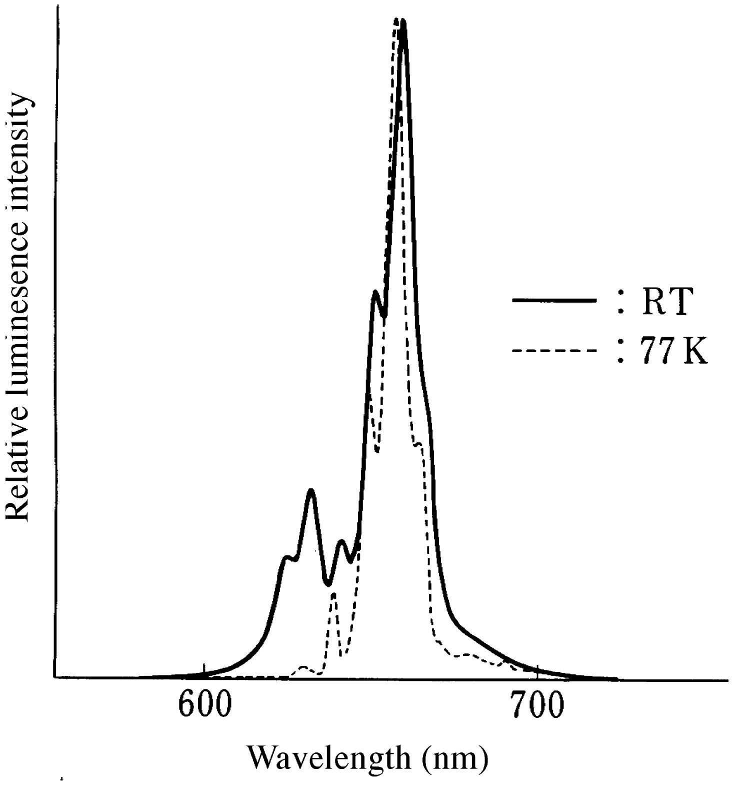

Figure 19 Luminescence spectra of $3.5MgO{\cdot}0.5MgF_2.GeO_2{:}Mn^{4+}$. (Observed by the author.)

coupled with special vibration modes. The shorter wavelength peaks, which disappear at low temperatures, are ascribed to transitions from an excited vibronic level (anti-Stokes vibronic transitions).

Strong absorption bands due to Mn^{4+} exist, corresponding to the spin-allowed transitions of $^4A_2(t_2^3) \rightarrow {}^4T_1, {}^4T_2(t_2^2e)$ in the visible to near-UV region, and the body color of the phosphor is usually yellow. Table 8 shows the crystal field parameters and luminescence decay times for Mn^{4+} in several hosts. The larger valency leads to Dq/B values as large as 3, compared with those for Cr^{3+} (~2.5), and this, in turn, to the absorption bands at shorter wavelengths as expected from Figure 11. The charge-transfer band, on the other hand, lies at longer wavelength (~285 nm in Al_2O_3), resulting from the larger valency of Mn^{4+}.[10,35] (See 3.2.2.2.)

3.2.5 *Mn^{2+} phosphors (3d^5)*

3.2.5.1 *Crystal field*

Luminescence due to Mn^{2+} is known to occur in more than 500 inorganic compounds.[40] Of these, several are being used widely for fluorescent lamps and CRTs. The luminescence spectrum consists of a structureless band with a halfwidth of 1000 to 2500 cm^{-1} at peak wavelengths of 490 to 750 nm. (See also 2.3 and 5.6.) Figure 20 shows the luminescence and excitation spectra due to Mn^{2+} in $La_2O_3{\cdot}11Al_2O_3$ as an example.[41] The energy level diagram for Mn^{2+} in both octahedral and tetrahedral coordinations is represented by Figure 13. In phosphors, Mn^{2+} ions are located in the weak crystal field of $Dq/B \simeq 1$, and the luminescence corresponds to the $^4T_1(^4G) \rightarrow {}^6A_1(^6S)$ transition.

When a metal ion occupies a certain position in a crystal, the crystal field strength that affects the ion increases as the space containing the ion becomes smaller, as expected

Table 8 Crystal Field Parameters for Mn^{4+}

Host	λ (nm)		Dq (cm^{-1})	B (cm^{-1})	C (cm^{-1})	τ (ms)		Ref.
α-Al_2O_3	676.3	672.6[39]	2170	700	2800	0.8	(N)	35
Mg_2TiO_4	655.6	653.2 vib	2096	848	3300	0.5[38]	(R)	36
$LiAl_5O_8$ [a]	716	702 vib	2014	725	2900	0.2	(N)	37
$3.5MgO{\cdot}0.5MgF_2{\cdot}GeO_2$	623–664 str.		2375	709	3080	3.3[31]	(R)	33
$Mg_6As_2O_{11}$	620–665 str.		(2375)	(709)	(3080)	2.8[27]	(R)	33
Free ion	576.4 (^2G)[25]			1065	4919			3

Note: λ: peak wavelength of luminescence; τ: 1/e decay time; (R): room temperature; (N): 77K; vib: vibration structure, str: structured band.

[a] Ordered type.

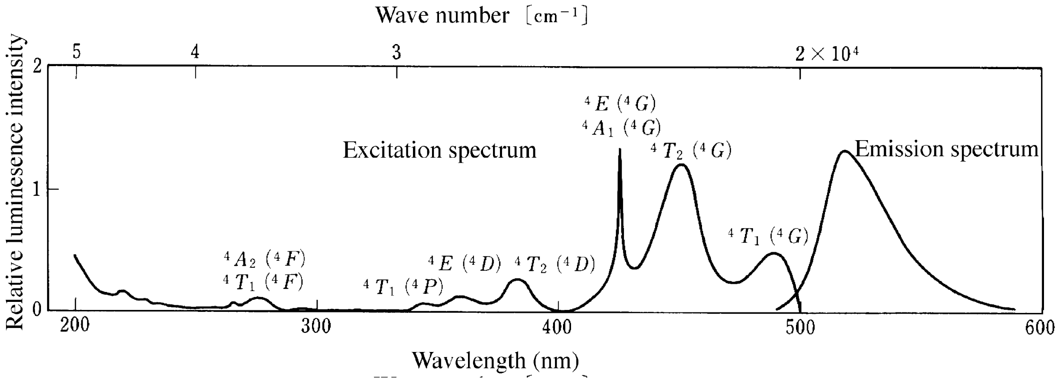

Figure 20 Luminescence and excitation spectra of $La_2O_3{\cdot}11Al_2O_3{:}Mn^{2+}$. (From Tamatani, M., *Jpn. J. Appl. Phys.*, 13, 950, 1974. With permission.)

from Eq. 9. For increases in the field, the transition energy between the $^4T_1$ and $^6A_1$ levels is predicted to decrease (shift to longer wavelengths). (See Figure 13.) In fact, the peak wavelength of the Mn^{2+} luminescence band is known to vary linearly to longer wavelength (547 to 602 nm) with a decrease in Mn-F distance (2.26 to 1.99Å) in a group of fluorides already studied, including 10 perovskite lattices of the type $A^IB^{II}F_3$, ZnF_2, and MgF_2.[42] A similar relationship also holds for each group of oxo-acid salt phosphors having an analogous crystal structure; the wavelength is longer when Mn^{2+} replaces a smaller cation in each group, as seen in Table 9. On the other hand, a larger anion complex makes the cation space shrink, leading to longer-wavelength luminescence. For $Ca_{10}(PO_4)_6F_2{:}Mn^{2+}$, the crystal field at a Mn^{2+} ion produced by ions in eight unit cells around it was calculated theoretically. The result was consistent with the observed luminescence peak shift (100 cm^{-1}) to longer wavelength due to a lattice constant decrease (0.14%) when one Ca in each $Ca_{10}(PO_4)_6F_2$ is replaced by Cd.[43]

In spite of the fact that the ionic radius for Zn^{2+} (0.72 Å) is smaller than that for Ca^{2+} (0.99 Å), the luminescence wavelength in $Zn_2SiO_4{:}Mn^{2+}$ is shorter than in $CaSiO_3{:}Mn^{2+}$. This is attributed to a smaller coordination number (4) in the former as compared with that (6) in the latter. (See Eq. 13.) In materials containing a spinel structure, Mn^{2+} can occupy either octahedral or tetrahedral sites. From the fact that the luminescence occurs in the shorter-wavelength (green) region, the tetrahedral site is expected to be occupied preferentially by Mn^{2+}. This is confirmed by ESR[44] and ion-exchange[45] studies for β-aluminas and supported by thermodynamic data.[45]

Table 9 Mn^{2+} Sites and Luminescence Properties

Host	Crystal symmetry	Site	Coordination number	Inversion symmetry	λ (nm)	τ (ms)
CaF_2	O_h	Ca	8	g	495	83[46]
ZnF_2	D_{4h}	Zn	6	g	587	100
$KMgF_3$	(O_h)	Mg	6	g	602[42]	104[62]
$ZnGa_2O_4$	O_h	(A site)	(4)	u	506	4
$ZnAl_2O_4$	O_h	(A site)	(4)	u	513	5
Zn_2SiO_4	C_{3i}	2Zn	4	u	525	12
Zn_2GeO_4	C_{3i}	2Zn	4	u	537	10
$Ca_5(PO_4)_3F$	C_{6h}	2Ca	6[63]	u	570[a]	14[66]
$Sr_5(PO_4)_3F$	C_{6h}	2Sr	6	u	558	
monocl-$CaSiO_3$	C_2	3Ca[64]	6	u	550 620	30
monocl-$MgSiO_3$	C_{2h}	2Mg[65]	6	u	660 740	
CaS	O_h	Ca	6	g	588	2.2–4.8[67]
hex–ZnS	T_d	Zn	4	u	591	0.25

Note: 1. 2Ca in the site column means existence of two different Ca sites. (A site) means larger probability for existence in A sites than for octahedral B sites.

2. Except for those referred, crystal symmetries follow those in Reference 61, and luminescence wavelengths and decay times in Reference 51.

3. In the inversion symmetry column, g and u correspond to existence and nonexistence of a center of symmetry, respectively.

[a] A value obtained in an Sb-Mn co-doped sample.

In CaF_2:Mn^{2+}, though Mn^{2+} occupies a cubic site with high coordination number, *Dq* is not so large because the anion valency of F^- is smaller than that of O^{2-}. In addition, *B* is large because of the smaller nephelauxetic effect.[46] Consequently, this compound yields the shortest luminescence wavelength (~495 nm) observed among Mn^{2+}-doped phosphors.*

Since every excited level of d^5 is either a spin quartet or a doublet, all transitions from the ground sextet to them are spin-forbidden. Optical absorption intensity is weak, and the phosphors are not colored (i.e., the powder body color is white). The $^4A_1$ and $^4E(^4G)$ levels have the same energy and are parallel to the ground level $^6A_1$ in Figure 13. The absorption band corresponding to $^6A_1 \rightarrow {}^4A_1,{}^4E(^4G)$ therefore has a narrow bandwidth, lying at ~425 nm, irrespective of the kind of host material.[48,49] One notices that this band splits into more than one line when carefully investigated. The splitting is considered to reflect the reduction of the crystal field symmetry.[48,49]

Table 10 shows the crystal field parameters for Mn^{2+} in representative phosphors. Note that Dq/B for the tetrahedral coordination is smaller (<1) than that (>1) for the octahedral one.

3.2.5.2 *Different Mn^{2+} sites in crystals*

Since the luminescence wavelength due to Mn^{2+} is sensitive to the magnitude of the crystal field, several emission bands are observed when different types of Mn^{2+} sites exist in a host crystal. In $SrAl_{12}O_{19}$, the bands at 515, 560, and 590 nm are considered to originate from Mn^{2+} ions replacing tetrahedrally coordinated Al^{3+}, fivefold coordinated Al^{3+}, and 12-fold coordinated Sr^{2+}, respectively.[45] In lanthanum aluminate, which has a layer structure of spinel blocks, a 680-nm band is observed due to Mn^{2+} in octahedral coordination, in addition to a green-emitting band due to tetrahedral coordination.[50] Two emission

---

* The other shortest peak wavelength is at 460 to 470 nm, observed in $SrSb_2O_6$,[47] in which Mn^{2+} is considered to be located in an extraordinary weak crystal field (Sr–O distance is as large as 2.5 Å).

Table 10 Crystal Field Parameters for Mn^{2+}

Host	λ (nm)	*Dq* (cm^{-1})	*B* (cm^{-1})	*C* (cm^{-1})	Coordination	Ref.
$MgGa_2O_4$	504	520	624	3468	(4)	48
$LaAl_{11}O_{18}$	517	543	572	3455	4	41
Zn_2SiO_4	525	540	(624)	(3468)	4	48
$Ca_5(PO_4)_3F$	572	760	691	3841	6	68
$Mg_4Ta_2O_9$	659	425	(698)	(3678)	6	55
CaF_2	495	(2375)	770	3449	8	46
hex·ZnS	591[51]	520	630	3040	4	69
$Mn(H_2O)_6^{2+}$	Abs.	1230	860	3850	6	3
Free ion	372.5 (^{4}G)[25]		860	3850		3

Note: *B* and *C* values in parenthesis, which were obtained from other phosphors, are used for calculating *Dq* values.

bands separated by about 50 nm were recognized long ago in Mn^{2+}-doped alkaline earth silicates.[51]

Even in the case of the same coordination number, different luminescence bands may come from Mn^{2+} ions occupying crystallographically different sites. In $Ca_5(PO_4)_3F$, there are principally Ca(I) and Ca(II) sites having different crystallographic symmetries; several additional sites accompany these two main calcium sites. The correspondence between the luminescence bands and the various sites has been investigated by means of polarized light,[52] ESR,[53] and excitation[52] spectral studies. In the case of the commercially available phosphor $Ca_5(PO_4)_3(F,Cl){:}Sb^{3+},Mn^{2+}$ (for Cool White fluorescent lamps), the Mn^{2+} band consists of three bands at 585, 584, and 596 nm, originating from Mn^{2+} ions replacing Ca(I), Ca(II), and Cl, respectively.[54] (See 5.6.2.)

Figure 21 shows the spectra in $Zn_2SiO_4{:}Mn^{2+}$, where two zero-phonon lines are observed at very low temperatures (504.6 and 515.3 nm at 4.2K).[55] These lines are assigned to two types of Mn^{2+} differing in their distance to the nearest oxygen; one is 1.90 Å and the other is 1.93 Å. Since the *Dq* value depends on the fifth power of the distance (Eqs. 9 and 13), a 7% difference in the *Dq* value is expected between the two types of Mn^{2+} sites; this is consistent with the difference estimated by crystal field theory from the observed line positions (2% difference).[55] The polarization of the luminescence light observed in a single crystal is also related to the site symmetry of Mn^{2+}.[56] The zero-phonon lines are accompanied by broad bands in the longer wavelength side; these originate from lattice-electron interactions and are known as vibronic sidebands (See Section 2.3.) Multi zero-phonon lines resulting from different Mn^{2+} sites are also observed in $Mg_4Ta_2O_9$ [55] and $LiAl_5O_8$.[37]

In ZnS doped with high concentrations of Mn^{2+}, although there is only one cation site crystallographically, two zero-phonon lines appear at 558.9 and 562.8 nm at low temperatures. These are ascribed to a single Mn^{2+} ion (τ = 1.65 ms) and a Mn^{2+}-Mn^{2+} pair (τ = 0.33 ms).[57] In this material, the luminescence band shifts to longer wavelength and is accompanied by a decrease in decay time with increasing Mn^{2+} concentration; this is also observed in such hosts as Zn_2SiO_4,[51] $MgGa_2O_4$,[58] $ZnAl_2O_4$,[51] $CdSiO_3$,[51] and ZnF_2.[51] Most of these effects are attributed to Mn^{2+}-Mn^{2+} interactions.

3.2.5.3 UV absorption

Lamp phosphors must absorb the mercury ultraviolet (UV) line at 254 nm. In most cases, Mn^{2+} does not have strong absorption bands in this region. To counter the problem, energy-

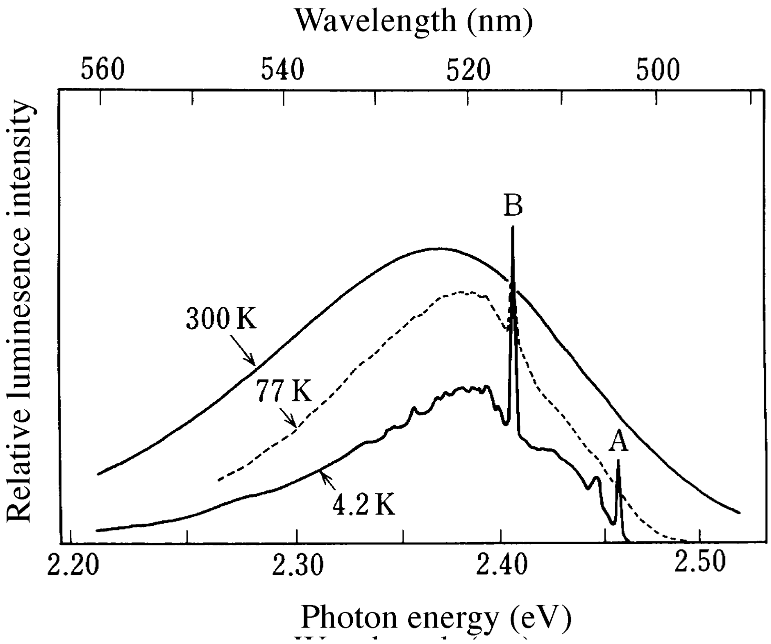

Figure 21 Luminescence spectra of Zn_2SiO_4:Mn^{2+}. (From Stevels, A.L.N. and Vink, A.T., *J. Luminesc.*, 8, 443, 1974. With permission.)

transfer mechanisms are utilized to sensitize Mn^{2+}; transfers are effected through the host* or via such ions as Sb^{3+}, Pb^{2+}, Sn^{2+}, Ce^{3+}, and Eu^{2+}, which absorb the UV efficiently through allowed transitions. These ions are called sensitizers for the Mn^{2+} luminescence. (See also 2.8 and 5.6.2) In Zn_2SiO_4, a strong absorption band appears at wavelengths shorter than 280 nm when doped with Mn^{2+}.[30] This band is ascribed to $Mn^{2+} \rightarrow Mn^{3+}$ ionization[59] or to a $d^5 \rightarrow d^4s$ transition.[32,60]

3.2.5.4 *Luminescence decay time*

The decay time of Mn^{2+} luminescence is usually in the millisecond range (Table 9). A shorter decay time is expected in the tetrahedral coordination because it has no center of inversion symmetry. In most practical phosphors, the Mn^{2+} sites are surrounded by six oxygen ions, but the symmetry is lower than octahedral and the sites do not have a center of inversion. (See Table 9.) It follows that the difference in the decay time between the phosphors having Mn^{2+} with four and six coordination numbers is not actually so large. Decay times in the fluoride phosphors are one order of magnitude longer than those in the oxo-acid salt phosphors. This is thought to be due to the fact that Laporte's rule holds more strictly in the fluorides, since odd states do not mix into the *d* states easily because: (1) Mn^{2+} ions in the fluorides are located at a center of inversion symmetry, and (2) the smaller nephelauxetic effect makes the odd states lie at higher energies than those in oxo-acid salts.

3.2.6 *Fe^{3+} Phosphors ($3d^5$)*

Luminescence due to Fe^{3+} lies in the wavelength region longer than 680 nm, and only $LiAlO_2$:Fe^{3+} and $LiGaO_2$:Fe^{3+} are used for special fluorescent lamp applications.[70] It is easily understood from Figure 13 why the luminescence wavelengths due to Fe^{3+} are so much

---

* The host-absorption wavelength does not always correspond to the bandgap energy of the host material.

Table 11 Crystal Field Parameters for Fe^{3+}

Host	λ (nm)	Dq (cm^{-1})	B (cm^{-1})	C (cm^{-1})	Coordination	Ref.
$LiAl_5O_8$ [a]	680	800	644	2960	4	72
β-$LiAlO_2$	735	883	630	3000	4	73
$Ca(PO_3)_2$	830	1250			6	75
γ-AlF_3	735	1220	895	3000	6	71
$Fe(H_2O)_6^{2+}$	Abs.	1350	820	3878	6	3
Free ion	312 (^{4}G)[25]		1015	4800		3

[a] Ordered structure, $\tau = 7.1$ ms.

longer than those due to Mn^{2+}, which has the same electronic configuration of $3d^5$. That is, the larger valency of Fe^{3+} brings about the stronger crystal field, reducing the transition energy of $^4T_1(^4G) \rightarrow {}^6A_1(^6S)$. In fact, as shown in Table 11, Dq/B for Fe^{3+} is ~1.2, even at tetrahedral sites, and larger than that (<1) for Mn^{2+}. The reason for the emission wavelength being as short as 735 nm despite the octahedral coordination in AlF_3 is attributable to the large B value resulting from the small nephelauxetic effect.[71]

The absorption (or excitation) spectrum in the visible region due to Fe^{3+} resembles the shape of that of Mn^{2+}. Zero-phonon lines are also observed in $LiAl_5O_8$ [72] and $LiAlO_2$.[73] In the UV region, contrary to the Mn^{2+} case, however, a strong absorption band supposedly caused by charge transfer appears,[10,72,74] and the Fe^{3+} phosphors can be excited directly by 254-nm light irradiation without the need of sensitization through other ions.

References

1. Kamimura, H., Sugano, S., and Tanabe, Y., *Ligand Field Theory and Its Applications*, Syokabo, Tokyo, 1969 (in Japanese); Sugano, S., Tanabe, Y., and Kamimura, H., *Multiplets of Transition-Metal Ions in Crystals*, Academic Press, 1970.
2. a) Tanabe, Y. and Sugano, S., *J. Phys. Soc. Jpn.*, 9, 753, 1954; b). *ibid.*, 766.
3. Orgel, L.E., *J. Chem. Phys.*, 23, 1004, 1955.
4. McClure, D.S., *Electronic spectra of molecules and ions in crystals. Part II. Spectra of ions in crystals*, in *Solid State Physics*, Seitz, F. and Turnbull, D., Eds., 9, 399, Academic Press, 1959.
5. Griffith, J.S., *The Theory of Transition Metal Ions*, Cambridge Univ. Press, 1964.
6. Ballhausen, C.J., *Introduction to Ligand Field Theory*, McGraw-Hill, 1962.
7. Jørgensen, C.K., *Absorption Specta and Chemical Bonding in Complexes*, Pergamon Press, Elmsford, NY, 1962.
8. Prather, J.L., *National Bureau of Standards Monogr.*, 19, 1, 1961.
9. Di Bartolo, B., *Optical Interactions in Solids*, John Wiley & Sons, 1968.
10. Tippins, H.H., *Phys. Rev.*, B1, 126, 1970.
11. Hoshina, T., Imanaga, S., and Yokono, S., *J. Luminesc.*, 15, 455, 1977.
12. Sluzky, E., Lemoine, M., and Hesse, K., *J. Electrochem. Soc.*, 141, 3172, 1994.
13. Sugano, S. and Tsujikawa, I., *J. Phys. Soc. Jpn.*, 13, 899, 1958; Sugano, S. and Tanabe, Y., *ibid.*, 880.
14. Maiman, T.H., *Nature*, 187, 493, 1960.
15. Tolstoi, N.A., Liu, S., and Lapidus, M.E., *Opt. Spectrosc.*, 13, 133, 1962.
16. Kushida, T., *J. Phys. Soc. Jpn.*, 21, 1331, 1966; Shinada, M., Sugano, S., and Kushida, T., *ibid.*, 1342.
17. Powell, R.C. and Di Bartolo, B., *Phys. Status Solidi (a)*, 10, 315, 1972.
18. Petermann, K. and Huber, G., *J. Luminesc.*, 31&32, 71, 1984.
19. Walling, J.C., Tunable paramagnetic-ion solid-state lasers, in *Tunable Lasers*, Mollenauer, L.F. and White, J.C., Eds., Springer-Verlag, 1987.
20. Moulton, P.F., Tunable paramagnetic-ion lasers, in *Laser Handbook*, Vol. 5, Bass, M. and Stitch, M.L., Eds., Elseviers Science, B. V., 1985.

21. Wood, D.L., Imbusch, G.F., Macfarlane, R.M., Kisliuk, P., and Larkin, D.M., *J. Chem. Phys.*, 48, 5255, 1968.
22. Macfarlane, R.M., *Phys. Rev.*, B1, 989, 1970.
23. Wood, D.L., Ferguson, J., Knox, K., and Dillon, Jr., J.F., *J. Chem. Phys.*, 39, 890, 1963.
24. Pott, G.T. and McNicol, B.D., *J. Solid State Chem.*, 7, 132, 1973.
25. Moore, C.E., *Atomic Energy Levels*, Vol. II, NBS Circular, 1952, 467.
26. Wood, D.L., *J. Chem. Phys.*, 42, 3404, 1965.
27. Imbusch, G.F., Experimental spectroscopic techniques for transition metal ions in solids, in *Luminescence of Inorganic Solids*, Di Bartolo, B., Ed., Plenum Press, 1978, 135.
28. Sevast'yanov, V.P., Sviridov, D.T., Orekhova, V.P., Pasternak, L.B., Sviridova, R.K., and Veremeichik, T.F., *Sov. J. Quant. Electron.*, 2, 339, 1973.
29. Ouweltjes, J.L., Elenbaas, W., and Labberte, K.R., *Philips Tech. Rev.*, 13, 109, 1951.
30. Kröger, F.A., *Some Aspects of Luminescence of Solids*, Elsevier, 1948.
31. Kemeny, G. and Haake, C.H., *J. Chem. Phys.*, 33, 783, 1960.
32. Butler, K.H., *Proc. Int. Conf. Luminesc.*, Budapest, 1966, 1313.
33. Ibuki, S., Awazu, K., and Hata, T., *Proc. Int. Conf. Luminesc.*, Budapest, 1966, 1465.
34. Blasse, G. and Grabmaier, B.C., *Luminescent Materials*, Springer-Verlag, 1994, 128.
35. Geschwind, S., Kisliuk, P., Klein, M.P., Remeika, J.P., and Wood, D.L., *Phys. Rev.*, 126, 1684, 1962.
36. Stade, J., Hahn, D., and Dittmann, R., *J. Luminesc.*, 8, 318, 1974.
37. McNicol, B.D. and Pott, G.T., *J. Luminesc.*, 6, 320, 1973.
38. Dittmann, R. and Hahn, D., *Z. Phys.*, 207, 484, 1967.
39. Travniçek, M. Kröger, F.A., Botden, Th.P.J., and Zahm, P., *Physica*, 18, 33, 1952.
40. Data obtained from Chemical Abstracts in 1948 to 1971, and References 30 and 51.
41. Tamatani, M., *Jpn. J. Appl. Phys.*, 13, 950, 1974.
42. Klasens, H.A., Zahm, P., and Huysman, F.O., *Philips Res. Repts.*, 8, 441, 1953.
43. Narita, K., *J. Phys. Soc. Jpn.*, 16, 99, 1961; *ibid.*, 18, 79, 1963.
44. Antoine, J., Vivien, D., Livage, J., Thery, J., and Collongues, R., *Mat. Res. Bull.*, 10, 865, 1975.
45. Bergstein, A. and White, W.B., *J. Electrochem. Soc.*, 118, 1166, 1971.
46. Alonso, P.J. and Alcalá, *J. Luminesc.*, 22, 321, 1981.
47. Yamada, H., Matsukiyo, H., Suzuki, T., Yamamoto, H., Okamura, T., Imai, T., and Morita, M., *Electrochem. Soc. Fall Meeting*, Abstr. No. 564, 1988.
48. Palumbo, D.T. and Brown, Jr., J.J., *J. Electrochem. Soc.*, 117, 1184, 1970.
49. Palumbo, D.T. and Brown, Jr., J.J., *J. Electrochem. Soc.*, 118, 1159, 1971.
50. Stevels, A.L.N., *J. Luminesc.*, 20, 99, 1979.
51. Leverenz, H.W., *An Introduction to Luminescence of Solids*, John Wiley & Sons, New York, 1950; Recent publications for Zn_2SiO_4:Mn are Barthou, C., Benoit, J., Benalloul, P., and Morell, A., *J. Electrochem. Soc.*, 141, 524, 1994; Ronda, C.R., *Proc. 2nd Int. Display Workshops*, Vol. 1, 1995, 69.
52. Ryan, F.M., Ohlman, R.C., and Murphy, J., *Phys. Rev.*, B2, 2341, 1970.
53. Kasai, P.H., *J. Phys. Chem.*, 66, 674, 1962.
54. Ryan, F.M. and Vodoklys, F.M., *J. Electrochem. Soc.*, 118, 1814, 1971.
55. Stevels, A.L.N. and Vink, A.T., *J. Luminesc.*, 8, 443, 1974.
56. Bhalla, R.J.R.S. and White, E.W., *J. Electrochem. Soc.*, 119, 740, 1972.
57. Busse, W., Gumlich, H.E., Meissmer, B., and Theis, D., *J. Luminesc.*, 12/13, 693, 1976.
58. Brown, Jr., J.J., *J. Electrochem. Soc.*, 114, 245, 1967.
59. Robbins, D.J., Avouris, P., Chang, I.F., Dove, D.B., Giess, E.A., and Mendez, E.E., *Electrochem. Soc. Spring Meeting*, Abstr. No. 513, 1982.
60. Butler, K.H., *Fluorescent Lamp Phosphors*, Pennsylvania State University Press, 1980.
61. Wyckoff, R.W.G., *Crystal Structures*, Interscience Publishers, 1965.
62. Van Noy, B.W. and Mikus, F.F., *Proc. Int. Conf. Luminesc.*, Budapest, 1966, 794.
63. Náray-Szabó, S., *Z. Krist.*, 75, 387, 1930.
64. Tolliday, J., *Nature*, 182, 1012, 1958.
65. Morimoto, N., Appleman, D.E., and Evans, Jr., E.T., *Z. Krist.*, 114, 120, 1960.
66. Soules, T.F., Bateman, R.L., Hewes, R.A., and Kreidler, E.R., *Phys. Rev.*, B7, 1657, 1973.
67. Yamamoto, H., Megumi, K., Kasano, H., Suzuki, T., Ueno, Y., Morita, Y., and Ishigaki, T., *Tech. Digest, Phosphor Res. Soc. 198th Meeting*, 1983 (in Japanese).

68. Uehara, Y., *Toshiba Rev.*, 24, 1090, 1969 (in Japanese).
69. Kushida, T., Tanaka, Y., and Oka, Y., *Solid State Commun.*, 14, 617, 1974.
70. Van Broekhoven, J., *J. Illum. Eng. Soc.*, 3, 234, 1974.
71. Telfer, D.J. and Walker, G., *J. Luminesc.*, 11, 315, 1976.
72. Pott, G.T. and McNicol, B.D., *J. Chem. Phys.*, 56, 5246, 1972.
73. Stork, W.H.J. and Pott, G.T., *J. Phys. Chem.*, 78, 2496, 1974.
74. Tamatani, M. and Tsuda, N., *Tech. Digest, Phosphor Res. Soc. 157th Meeting*, 1970 (in Japanese).
75. Fox, K.E., Furukawa, T., and White, W.B., *J. Am. Cer. Soc.*, 64, C-42, 1981.

chapter three — section three

Principal phosphor materials and their optical properties

Tsuyoshi Kano

Contents

3.3 Luminescence centers of rare-earth ions 192
  3.3.1 Electronic configuration 192
  3.3.2 Electronic processes leading to luminescence 193
    3.3.2.1 $4f$ Energy levels and relaxation 193
    3.3.2.2 $4f^{n-1}\,5d^1$ states and charge-transfer states (CTS) 198
    3.3.2.3 Divalent and tetravalent cations 199
    3.3.2.4 Energy transfer 199
  3.3.3 Luminescence of specific ions 200
    3.3.3.1 Ce^{3+} 200
    3.3.3.2 Pr^{3+} 201
    3.3.3.3 Nd^{3+} 203
    3.3.3.4 Nd^{4+} 203
    3.3.3.5 Sm^{3+} 203
    3.3.3.6 Sm^{2+} 203
    3.3.3.7 Eu^{3+} 204
    3.3.3.8 Eu^{2+} 206
    3.3.3.9 Gd^{3+} 207
    3.3.3.10 Tb^{3+} 208
    3.3.3.11 Dy^{3+} 209
    3.3.3.12 Dy^{2+} 210
    3.3.3.13 Dy^{4+} 210
    3.3.3.14 Ho^{3+} 210
    3.3.3.15 Ho^{2+} 211
    3.3.3.16 Er^{3+} 211
    3.3.3.17 Tm^{3+} 211
    3.3.3.18 Yb^{3+} 211
    3.3.3.19 Yb^{2+} 211
References 211

3.3 *Luminescence of rare earth ions*[1–3]

3.3.1 *Electronic configuration*

The rare-earth elements usually comprise 17 elements consisting of the 15 lanthanides from La (atomic number 57) to Lu (atomic number 71), of Sc (atomic number 21), and of Y (atomic number 39). The electronic configurations of trivalent rare-earth ions in the ground states are shown in Table 12. As shown in the table, Sc^{3+} is equivalent to Ar, Y^{3+} to Kr, and La^{3+} to Xe in electronic configuration. The lanthanides from Ce^{3+} to Lu^{3+} have one to fourteen 4*f* electrons added to their inner shell configuration, which is equivalent to Xe. Ions with no 4*f* electrons, i.e., Sc^{3+}, Y^{3+}, La^{3+}, and Lu^{3+}, have no electronic energy levels that can induce excitation and luminescence processes in or near the visible region. In contrast, the ions from Ce^{3+} to Yb^{3+}, which have partially filled 4f orbitals, have energy levels characteristic of each ion and show a variety of luminescence properties around the visible region.[1–3] Many of these ions can be used as luminescent ions in phosphors, mostly by replacing Y^{3+}, Gd^{3+}, La^{3+}, and Lu^{3+} in various compound crystals.

The azimutal quantum number (l) of 4*f* orbitals is 3, giving rise to 7 (= 2l + 1) orbitals, each of which can accommodate two electrons. In the ground state, electrons are distributed so as to provide the maximum combined spin angular momentum (S). The spin angular momentum S is further combined with the orbital angular momentum (L) to give the total angular momentum (J) as follows;

$J = L - S$, when the number of 4*f* electrons is smaller than 7

$J = L + S$, when the number of 4*f* electrons is lager than 7

An electronic state is indicated by notation $^{2S+1}L_J$, where L represents *S*, *P*, *D*, *F*, *G*, *H*, *I*, *K*, *L*, *M*, …, corresponding to L = 0, 1, 2, 3, 4, 5, 6, 7, 8, 9, …, respectively. More accurately, an actual electronic state is expressed as an intermediate coupling state, which can be described as a mixed state of several $^{2S+1}L_J$ states[2,4] combined by spin-orbit interaction. For qualitative discussions, however, the principal L state can be taken to represent the actual

Table 12 Electronic Configurations of Trivalent Rare-Earth Ions in the Ground State

Atomic number	Ions	Corresponding element	4*f* electrons							S Σs	L Σl	J Σ(L+S)
21	Sc^{3+}	Ar								0	0	0
39	Y^{3+}	Kr								0	0	0
57	La^{3+}									0	0	0
58	Ce^{3+}	Xe	↑							1/2	3	5/2
59	Pr^{3+}	Xe	↑	↑						1	5	4
60	Nd^{3+}	Xe	↑	↑	↑					3/2	6	9/2
61	Pm^{3+}	Xe	↑	↑	↑	↑				2	6	4
62	Sm^{3+}	Xe	↑	↑	↑	↑	↑			5/2	5	5/2
63	Eu^{3+}	Xe	↑	↑	↑	↑	↑	↑		3	3	0
64	Gd^{3+}	Xe	↑	↑	↑	↑	↑	↑	↑	7/2	0	7/2
65	Tb^{3+}	Xe	↑↓	↑	↑	↑	↑	↑	↑	3	3	6
66	Dy^{3+}	Xe	↑↓	↑↓	↑	↑	↑	↑	↑	5/2	5	15/2
67	Ho^{3+}	Xe	↑↓	↑↓	↑↓	↑	↑	↑	↑	2	6	8
68	Er^{3+}	Xe	↑↓	↑↓	↑↓	↑↓	↑	↑	↑	3/2	6	15/2
69	Tm^{3+}	Xe	↑↓	↑↓	↑↓	↑↓	↑↓	↑	↑	1	5	6
70	Yb^{3+}	Xe	↑↓	↑↓	↑↓	↑↓	↑↓	↑↓	↑	1/2	3	7/2
71	Lu^{3+}	Xe	↑↓	↑↓	↑↓	↑↓	↑↓	↑↓	↑↓	0	0	0

state. The mixing due to spin-orbit interaction is small for the levels near ground states, while it is considerable for excited states that have neighboring states with similar *J* numbers. The effect of mixing is relatively small on the energy of levels, but can be large on their optical transition probabilities.

3.3.2 Electronic processes leading to luminescence

3.3.2.1 4f energy levels and relaxation

The 4*f* electronic energy levels of lanthanide ions are characteristic of each ion. The levels are not affected much by the environment because 4*f* electrons are shielded from external electric fields by the outer $5s^2$ and $5p^6$ electrons. This feature is in strong contrast with transition metal ions, whose 3*d* electrons, located in an outer orbit, are heavily affected by the environmental or crystal electric field. The characteristic energy levels of 4*f* electrons of trivalent lanthanide ions have been precisely investigated by Dieke and co-workers.[5] The results are shown in Figure 22, which is known as a Dieke diagram.[5] The levels were determined experimentally by considering the optical spectra of individual ions incorporated in $LaCl_3$ crystals; this diagram is applicable to ions in almost any environment because the maximum variation of the energy levels is, at most, of the order of several hundred cm^{-1}.

Each level designated by the number J in Figure 22 is split into a number of sublevels by the Stark effect due to the crystal field. The number of split sublevels is, at most, (2J + 1) or (J + 1/2) for J of integer or J of half-integer, respectively. The number of levels is determined by the symmetry of the crystal field surrounding the rare-earth ion. The width of each level shown in Figure 22 indicates the range of splittings within each component.

Light-emitting levels are indicated by semicircles below the energy levels. Most of the emitting levels are separated from the next lower level by at least 2×10^3 cm^{-1} or more. This is because the excited states relax via two competitive paths: one is by light emission and the other by phonon emission. The rate of phonon emission, *w*, depends on the number of phonons emitted simultaneously to bridge the energy gap and is expressed as:

$$w \propto \exp\left(-k\Delta E/h\nu_{\max}\right), \tag{24}$$

where ΔE is the energy gap to the nearest lower level and $h\nu_{\max}$ is the maximum energy of phonons coupled to the emitting states. The phonon emission rate, *w*, decreases rapidly with an increase in ΔE, so that the competitive light emission or radiative process becomes dominant.[6] Thus, the well-known high luminescence efficiencies for $^5D_0$ of Eu^{3+} and $^5D_4$ of Tb^{3+} are based on the large energy gap of more than 10^4 cm^{-1} that needs to be bridged to the next lower level of these ions. The above formula implies that large values of $h\nu_{\max}$ also quench light emission. This is demonstrated by the fact that luminescence of Eu^{3+} in aqueous solution is almost quenched, but begins to appear if H_2O is replaced by D_2O.[7]

Luminescence originating from electronic transitions between 4*f* levels is predominantly due to electric dipole or magnetic dipole interactions. Electric dipole *f-f* transitions in free 4*f* ions are parity-forbidden, but become partially allowed by mixing with orbitals having different parity because of an odd crystal field component. The selection rule in this case is $|\Delta J|$ ð 6, (except for 0→0, 0→1, 0→3, 0→5). Typical examples of this mechanism are demonstrated by the luminescence from the ^5D_J states of Eu^{3+}; the intensity of these transitions depends strongly on the site symmetry in a host crystal (See Section 3.3.3.7 Eu^{3+}). Magnetic dipole *f-f* transitions are not affected much by the site symmetry because they are parity-allowed. The *J* selection rule in this case is $\Delta J = 0, \pm 1$ (except for 0→0).

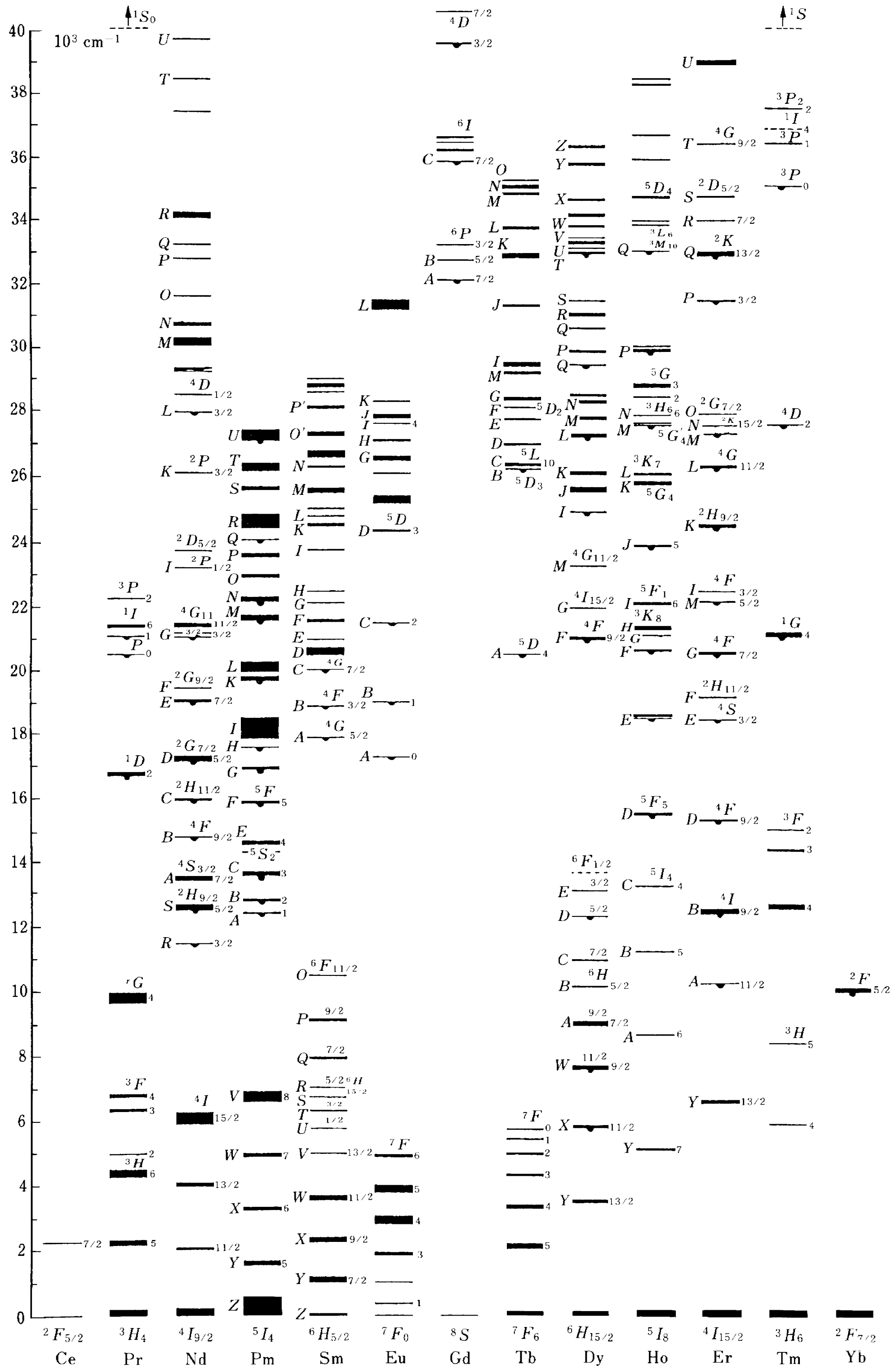

Figure 22 Energy levels of trivalent lanthanide ions. (From Dieke, G.H., *Spectra and Energy Levels of Rare Earth Ions in Crystals*, Interscience, 1968; *American Institute of Physics Handbook*, 3rd edition, McGraw-Hill, 1972, 7-25. With permission.)

Oscillator strengths are of the order of 10^{-5} to 10^{-8} for partially allowed electric dipole transitions, and 10^{-8} for magnetic dipole transitions.

The electric dipole transition probability between $4f$ levels can be calculated using the Judd-Ofelt theory.[8,9] This theory assumes closure of the wavefunctions mixed to a $4f$ orbital and takes an average for the energy separation between the allowed states and the $4f$ levels. In spite of such approximations, the theory gives satisfactory agreement with observed values in many cases. The points of the calculation are sketched out as follows.

The absorption coefficient, $k(\lambda)$, is experimentally determined; here, $k(\lambda) = \ln(I/I_0)/a$, where I_0 is intensity of incident light, I is intensity of transmitted light, and a is sample thickness. By using the value of $k(\lambda)$, the line strength S is given by the following formula.

$$\int k(\lambda)d\lambda = \frac{8\pi^3 e^2 \lambda \rho}{3ch(2J+1)} \cdot \frac{1}{n} \cdot \frac{(n^2+2)^2}{9} \cdot s \tag{25}$$

where ρ is the density of the lanthanide ion and n is the refractive index. The parameters Ω_2, Ω_4, and Ω_6, giving the light emission probability, are included in S and are determined by a least square fit of:

$$s = \sum_{t=2,4,6} \Omega_t \left| <(S,L)J \left\| U^{(t)} \right\| (S',L')J'> \right|^2 \tag{26}$$

Here, $<(S,L)J \| U^{(t)} \| (S',L')J'>$ (t = 2, 4, 6) are reduced matrix elements characteristic of individual ions and available as a table.[8] Using the parameters Ω_2, Ω_4, and Ω_6 for specific host material, the light emission probability, A, between the levels of interest is calculated as follows:

$$\begin{aligned} A &= \frac{64\pi^4 e^2}{3h(2J'+1)\lambda^3} \cdot n \cdot \frac{(n^2+2)^2}{9} \cdot s' \\ S' &= \Omega_2\left[U^{(2)}\right]^2 + \Omega_4\left[U^{(4)}\right]^2 + \Omega_6\left[U^{(6)}\right]^2 \end{aligned} \tag{27}$$

The theory contains some assumptions not strictly valid in actual cases, but still provides useful theoretical explanations for the nature of the luminescence spectra, as well as the excited-state lifetime, of lanthanide ions.[2,10]

Luminescence spectra of various trivalent lanthanide ions in YVO_4 (or YPO_4) are shown in Figure 23.[12] The luminescence and excitation spectra in Y_2O_3 are shown in Figure 24.[13] The luminescence spectra are composed of groups of several sharp lines. Each group corresponds to a transition between an excited and ground state designated by the total angular momentum, J. The assignment of the transition corresponding to each group of lines can be made on the basis of the energy level diagram shown in Figure 22. The excitation spectra generally consist of sharp lines due to the $4f$-$4f$ transition and of broad bands due to the $4f$-$5d$ transition and/or charge-transfer processes. Excited states giving rise to these broad excitation bands will be discussed in the next subsection.

The lifetimes of the luminescence due to $4f \rightarrow 4f$ transitions are mostly in the range of milliseconds because of the forbidden character of the luminescence transition.[11] For luminescence due to a spin-allowed transition between levels having equal spin multiplicity (e.g., ${}^3P_0 \rightarrow {}^3H_J$ of Pr^{3+}), a relatively short lifetime of $\sim 10^{-5}$ s is observed.

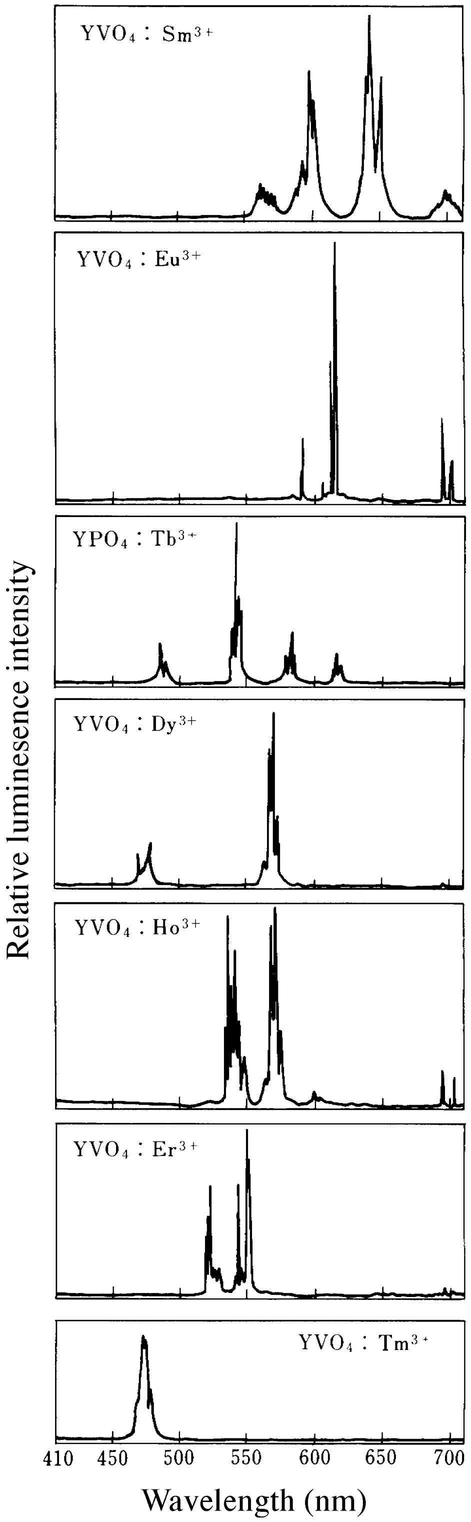

Figure 23 Emission spectra of various trivalent rare-earth ions in YVO_4 or YPO_4 hosts under cathode-ray excitation. (From Pallila, F.C., *Electrochem. Technol.*, 6, 39, 1968. With permission.)

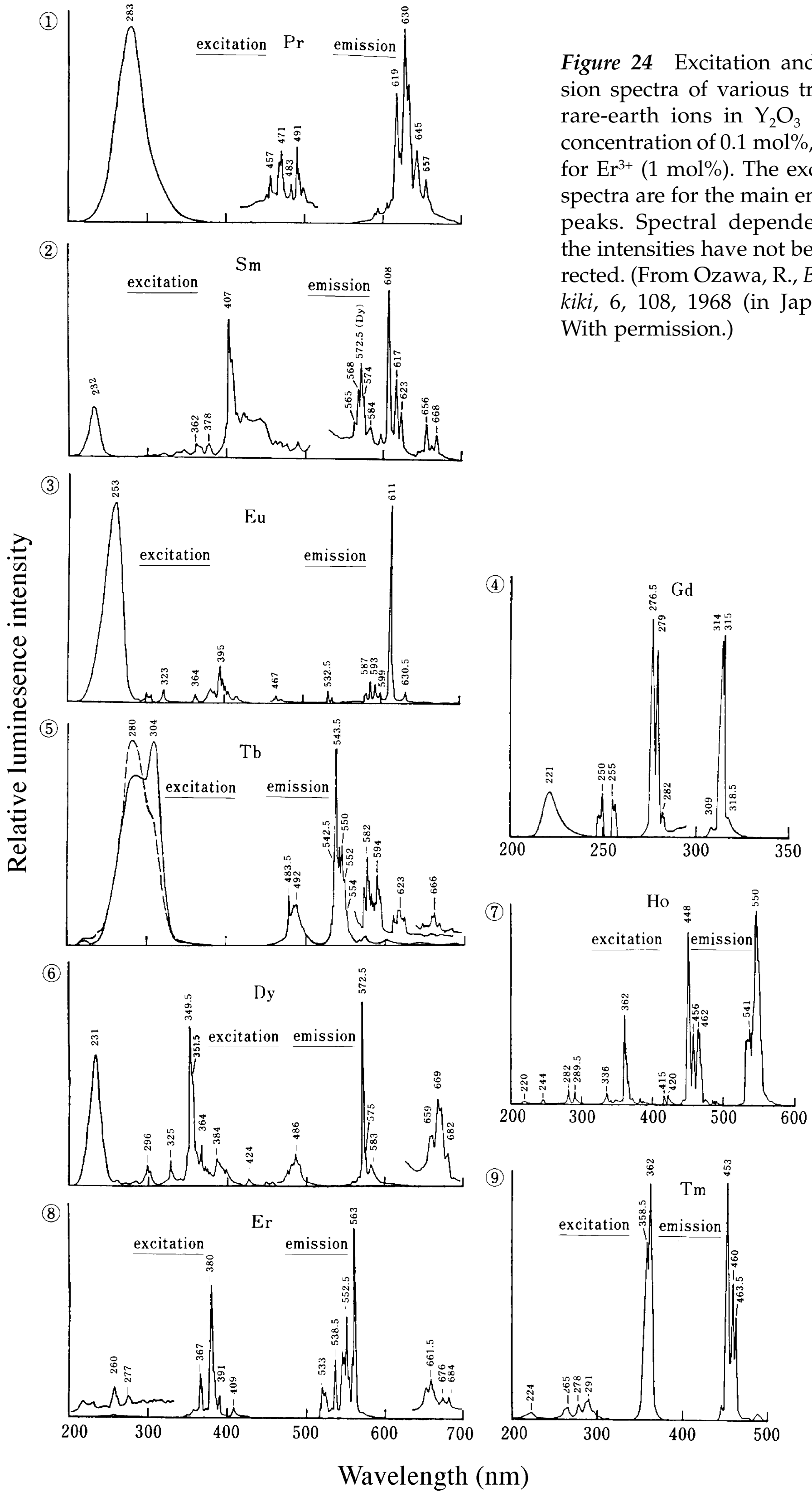

Figure 24 Excitation and emission spectra of various trivalent rare-earth ions in Y_2O_3 with a concentration of 0.1 mol%, except for Er^{3+} (1 mol%). The excitation spectra are for the main emission peaks. Spectral dependence of the intensities have not been corrected. (From Ozawa, R., *Bunseki-kiki*, 6, 108, 1968 (in Japanese). With permission.)

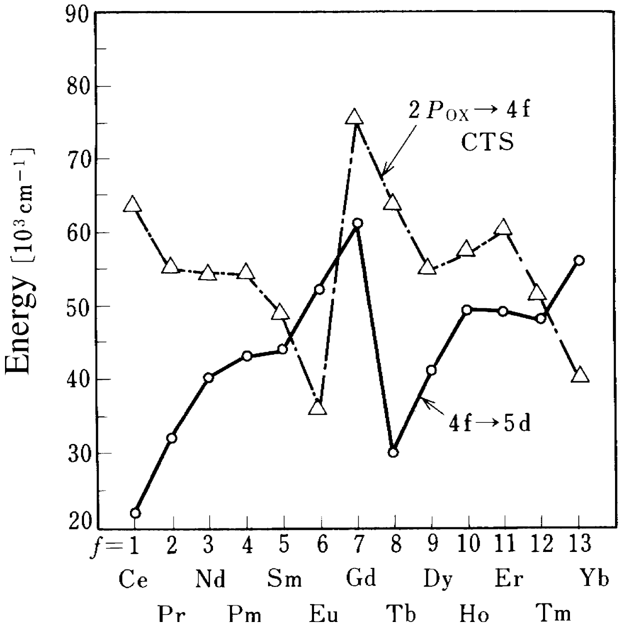

Figure 25 Energies for $4f \rightarrow 5d$ and CTS transitions of trivalent rare-earth ions. (From Hoshina, T., *Luminescence of Rare Earth Ions*, Sony Research Center Rep., 1983 (in Japanese). With permission.)

3.3.2.2 $4f^{n-1}$ $5d^1$ states and charge-transfer states (CTS)

In the energy region spanned by 4*f* levels, one finds two additional kinds of electronic states with different characters from those levels. They are the $4f^{n-1}5d^1$ states and the charge-transfer states (CTS). In the former, one of the 4*f* electron(s) is transferred to a 5*d* orbital and, in the latter case, electrons in the neighboring anions are transferred to a 4*f* orbital. Both of these processes are allowed and result in strong optical absorptions. They are observed as broadband excitation spectra around 300 nm, as is shown in Figure 24. Optical absorptions due to *f-d* transitions are found for Pr^{3+} and Tb^{3+}; those due to a charge-transfer transition are found in Eu^{3+}. The broad-band excitation spectra around 230 nm for Sm^{3+}, Dy^{3+}, and Gd^{3+} are due to host absorptions.

The energies of the $4f^{n-1}5d^1$ and CTSs are more dependent on their environments than the energies of 4*f* states, but the relative order of energies of these states are found to be the same for the whole series of rare-earth ions in any host materials. The transition energies from the ground states to these states are shown in Figure 25.[2,14] These energies are obtained by determining the values of parameters so as to agree with absorption spectra of trivalent rare-earth oxides. As shown in the figure, 4*f*-5*d* transitions in Ce^{3+}, Pr^{3+}, Tb^{3+}, and CTS absorptions in Eu^{3+} and Yb^{3+} have energies less than ca. 40×10^3 cm^{-1}. They can, therefore, interact with 4*f* levels, leading to $f \rightarrow f$ emissions. In case the energy levels of these states are lower than those of 4*f* levels, direct luminescence transitions from these levels are found, such as $5d \rightarrow 4f$ transitions in Ce^{3+}, Pr^{3+}, and Eu^{2+}. Spectra of this luminescence vary as a result of crystal field splitting in host crystals (Section 3.3.3). Luminescence due to the transition from CTS has also been reported for Yb^{3+} (See Section 3.3.3.18).

By comparing chemical properties of trivalent rare-earth ions with Figure 25, one can conclude that those ions that are easily oxidized to the tetravalent state have lower $4f \rightarrow 5d$ transition energies, while those that are easily reducible to the divalent state have lower CTS transition energies. It has also been confirmed that $4f^0$, $4f^7$, and $4f^{14}$ electronic configurations are relatively stable.

3.3.2.3 *Divalent and tetravalent cations*

In appropriate host crystals with divalent constituent ions such as Ca^{2+}, Sr^{2+}, or Ba^{2+}, Sm^{2+}, Eu^{2+}, and Yb^{2+} are stable and can luminesce. The electronic configurations of these ions are the same as those of Eu^{3+}, Gd^{3+}, and Lu^{3+}, respectively. The excited states of the divalent ions, however, are lowered compared with those of the corresponding trivalent ions, because the divalent ions have smaller nuclear charges. The lower 4*f*-5*d* transition energy reflects their chemical property of being easily ionized into the trivalent state. All trivalent ions, from La^{3+} to Yb^{3+}, can be reduced to the divalent state by γ-ray irradiation when doped in CaF_2.[15]

The electronic configurations of the tetravalent cations, Ce^{4+}, Pr^{4+}, and Tb^{4+} are the same as those of trivalent ions La^{3+}, Ce^{3+}, and Gd^{3+}, respectively. Their CTS energy is low, in accordance with the fact that they are easily reduced. When Ce, Pr, or Tb ions are doped in compound oxide crystals of Zr, Ce, Hf, or Th, the resulting powders show a variety of body colors, probably due to the CTS absorption band.[16] Luminescence from these CTSs has not been reported.

3.3.2.4 *Energy transfer*

The excitation residing in an ion can migrate to another ion of the same species that is in the ground state as a result of resonant energy transfer when they are located close to each other. The ionic separation where the luminescence and energy transfer probabilities become comparable is in the vicinity of several Angstroms. Energy migration processes increase the probability that the optical excitation is trapped at defects or impurity sites, enhancing nonradiative relaxation. This causes concentration quenching, because an increase in the activator concentration encourages such nonradiative processes. As a result, that excitation energy diffuses from ion to ion before it is trapped and leads to emission. On the other hand, a decrease in the activator concentration decreases the energy stored by the ions. Consequently, there is an optimum in the activator concentration, typically 1 to 5 mol% for trivalent rare-earth ions, resulting from the trade-off of the above two factors. In some compounds such as NdP_5O_{14}, the lattice sites occupied by Nd are separated from each other by a relatively large distance (5.6 Å), and a high luminescence efficiency is achieved even when all the sites are occupied by activator ions (Nd). Such phosphors are called *stoichiometric phosphors*.

The energy transfer between different ion species can take place when they have closely matched energy levels. The energy transfer results either in the enhancement (e.g., $Ce^{3+} \rightarrow Tb^{3+}$) or in the quenching (e.g., $Eu^{3+} \rightarrow Nd^{3+}$) of emission. The effects of impurities on the luminescence intensities of lanthanide ions in Y_2O_3 are shown in Figure 26. Energy transfer between 4*f* levels has been shown to originate from the electric dipole-electric quadrupole interaction using glass samples.[17]

The luminescence spectra of Eu^{3+}, as well as that of Tb^{3+}, have strong dependence on the concentration. This is because at higher concentrations, the higher emitting levels, $^5D_1$ of Eu^{3+} and $^5D_3$ of Tb^{3+}, transfer their energies to neighboring ions of the same species by the following cross-relaxations; that is:

$$^5D_1\left(\mathrm{Eu}^{3+}\right)+{}^7F_0\left(\mathrm{Eu}^{3+}\right)\rightarrow{}^5D_0\left(\mathrm{Eu}^{3+}\right)+{}^7F_6\left(\mathrm{Eu}^{3+}\right)$$

$$^5D_3\left(\mathrm{Tb}^{3+}\right)+{}^7F_6\left(\mathrm{Tb}^{3+}\right)\rightarrow{}^5D_4\left(\mathrm{Tb}^{3+}\right)+{}^7F_0\left(\mathrm{Tb}^{3+}\right)$$

The energy transfer from a host crystal to activators leads to host-excited luminescence. The type of charge carriers to be captured by the doped ions, either electrons or holes, determines the nature of the valence changes in the ions. For a Y_2O_2S host, Tb^{3+} and Pr^{3+}

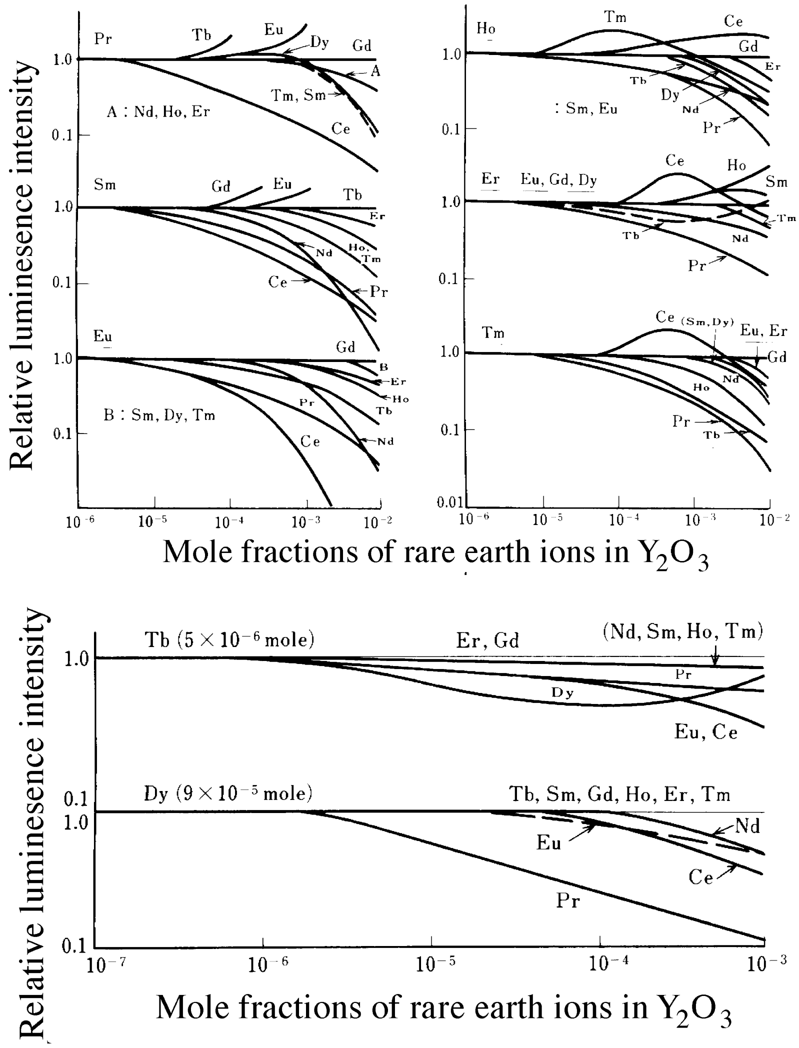

Figure 26 Decrease of luminescence intensities of trivalent rare-earth ions in Y_2O_3 due to the addition of other rare-earth ions. The concentration of ions is 10^{-3} mol% except for Tb and Dy (see the figure). (From Ozawa, R., *Bunseki-kiki*, 6, 108, 1968 (in Japanese). With permission.)

will act as hole traps, while Eu^{3+} will act as an electron trap at the initial stage of host excitation. In the next stage, these ions will capture an opposite charge and produce excitation of 4*f* levels.[18–20] A similar model has also been applied to $Y_3Al_5O_{12}$:Ce^{3+},Eu^{3+},Tb^{3+}.[21] Energy transfer from an excited oxy-anion complex to lanthanide ions is responsible for the luminescence observed in $CaWO_4$:Sm^{3+},[22] YVO_4:Eu^{3+},[23,24] and Y_2WO_6:Eu^{3+}.[25]

3.3.3 *Luminescence of specific ions*

3.3.3.1 *Ce^{3+}*

Among the lanthanide ions, the $4f \rightarrow 5d$ transition energy is the lowest in Ce^{3+}, but the energy gap from the $5d^1$ states to the nearest level ($^2F_{7/2}$) below is so large that the 5*d* level serves as an efficient light-emitting state. The luminescence photon energy depends strongly on the structure of the host crystal through the crystal-field splitting of the 5*d* state, as shown in Figure 27[26] (see also Reference 27 and the discussion in Section 3.3.3.8

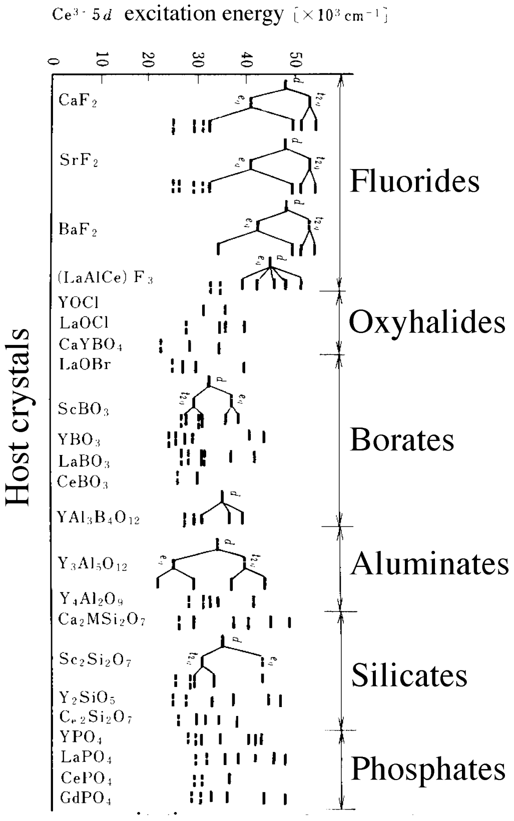

Figure 27 Energies of 5*d* excited levels of Ce^{3+} in various host crystals. (From Narita, K. and Taya, A., *Tech. Digest, Phosphor Res. Soc. 147th Meeting*, 1979 (in Japanese). With permission.)

on Eu^{2+} described below) and varies from near-ultraviolet to the green region. Typical luminescence spectra of some Ce^{3+}-activated phosphors are shown in Figure 28.[28] The two emission peaks are due to the two terminating levels, $^2F_{5/2}$ and $^2F_{7/2}$, of the 4*f* configuration of Ce^{3+}.

The decay time of the Ce^{3+} emission is 10^{-7} to 10^{-8} s, the shortest in observed lanthanide ions. This is due to two reasons: the $d \rightarrow f$ transition is both parity-allowed and spin-allowed since $5d^1$ and $4f^1$ states are spin doublets.[29] By virtue of the short decay time, Y_2SiO_5:Ce^{3+} and $YAlO_3$:Ce^{3+} are used for flying spot scanners or beam-index type cathode-ray tubes. (See Sections III.6.2.3.3 and 6.2.1.6.) Also, Ce^{3+} is often used for the sensitization of Tb^{3+} luminescence in such hosts as $CeMgAl_{11}O_{19}$[30] (See Section III.5.3.1).

3.3.3.2 Pr^{3+}

Luminescence of Pr^{3+} consists of many multiplets, as follows: ~515 nm ($^3P_0 \rightarrow {}^3H_4$), ~670 nm ($^3P_0 \rightarrow {}^3F_2$), ~770 nm ($^3P_0 \rightarrow {}^3F_4$), ~630 nm ($^1D_2 \rightarrow {}^3H_6$), ~410 nm ($^1S_0 \rightarrow {}^1I_6$), and ultraviolet ($5d \rightarrow 4f$) transitions. The relative intensities of the peaks depend on the host crystals. As an example, the emission spectrum of Y_2O_2S:Pr^{3+} is shown in Figure 29. The radiative decay time of the $^3P_0 \rightarrow {}^3H_J$ or ^3F_J emission is ~10^{-5} s, which is the shortest lifetime observed in $4f \rightarrow 4f$ transitions. For example, in Y_2O_2S host, decay times until 1/10 initial intensity are 6.7 μs for Pr^{3+}, 2.7 ms for Tb^{3+}, and 0.86 ms for Eu^{3+}.[2] The short decay time of Pr^{3+} is ascribed to the spin-allowed character of the transition. Since the short decay time is fit for fast information processing, $Gd_2O_2S(F)$:Pr^{3+},Ce^{3+} ceramic has been developed for an X-ray detector in X-ray computed tomography.[31]

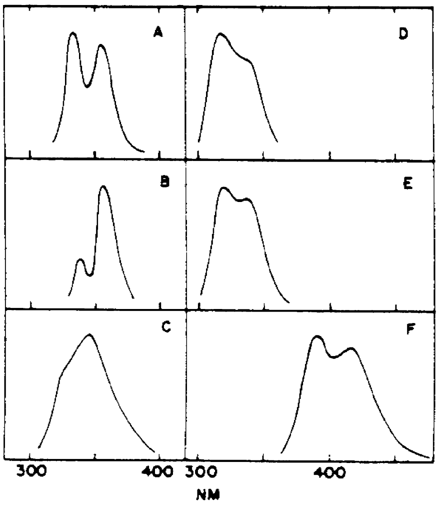

Figure 28 Emission spectra and excitation wavelengths of Ce^{3+} in various hosts. (A) YPO_4, 254-nm excitation; (B) YPO_4, 324-nm excitation; (C) $GdPO_4$, 280-nm excitation; (D) $LaPO_4$, 254-nm excitation; (E)$LaPO_4$, 280-nm excitation; (F) YBO_3, 254-nm excitation. (From Butler, K.H., *Fluorescent Lamp Phosphors, Technology and Theory,* The Pennsylvania State University Press, 1980, 261. With permission.)

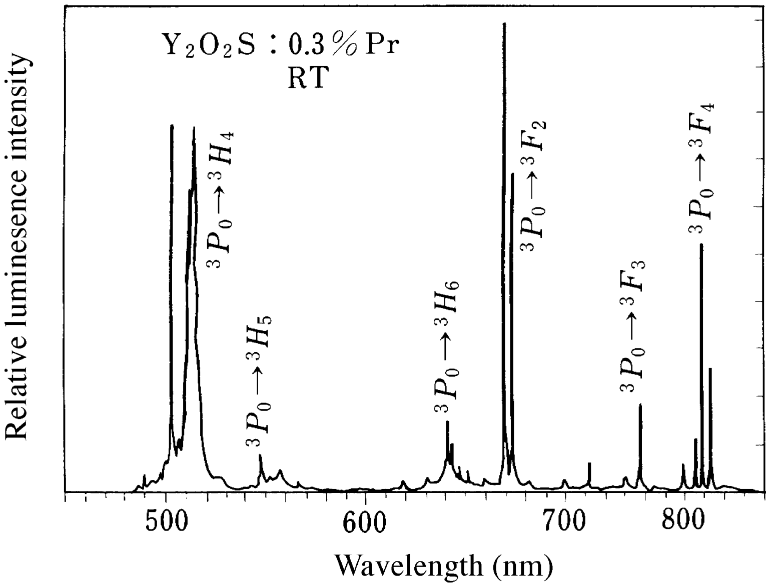

Figure 29 Emission spectrum of $Y_2O_2S:Pr^{3+}$ (0.3%) at room temperature. (From Hoshina, T., *Luminescence of Rare Earth Ions*, Sony Research Center Rep., 1983 (in Japanese). With permission.)

The quantum efficiency of more than 1 was reported for Pr^{3+} luminescence when excited by 185-nm light.[32,33] The excitation-relaxation process takes the following paths: $^3H_4 \rightarrow {}^1S_0$ (excitation by 185 nm), $^1S_0 \rightarrow {}^1I_6$ (405-nm emission), $^1I_6 \rightarrow {}^3P_0$ (phonon emission), $^3P_0 \rightarrow {}^3H_4$ (484.3-nm emission), $^3P_0 \rightarrow {}^3H_5$ (531.9 nm emission), $^3P_0 \rightarrow {}^3H_6$, $^3F_2$ (610.3-nm emission), and $^3P_0 \rightarrow {}^3F_3$, $^3F_4$ (704 nm emission). The sum of the visible light emissions in the above processes was estimated to have a quantum efficiency of 1.4.[33] In some fluoride crystals, the $4f^15d^1$ state was found to be lower than $^1S_0$, resulting in broad-band UV luminescence (see Figure 30).

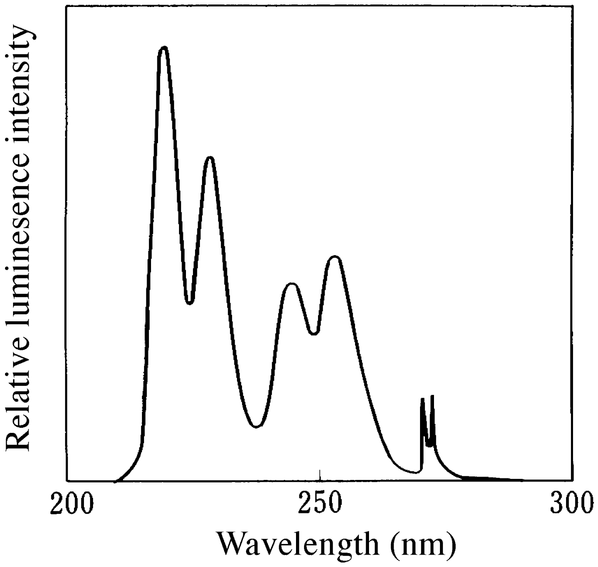

Figure 30 Emission spectrum of $LiYF_4$:Pr^{3+} (1%) using 185-nm excitation. (From Piper, W.W., Deluca, J.A., and Ham, F.S., *J. Luminesc.*, 8, 344, 1974. With permission.)

3.3.3.3 Nd^{3+}

The four lower-lying levels of Nd^{3+} provide a condition favorable to the formation of population inversion. For this reason, Nd^{3+} is used as the active ion in many high-power, solid-state lasers (at 1.06 μm wavelength); the most common hosts are $Y_3Al_5O_{12}$ single crystals (yttrium aluminum garnet, YAG) or glass. The relative emission intensity of Nd^{3+} in $Y_3Al_5O_{12}$ has been found to be as follows[34];

$^4F_{3/2} \rightarrow {}^4I_{9/2}$	$(0.87-0.95\ \mu\text{m})$	$:0.25$
$^4F_{3/2} \rightarrow {}^4I_{11/2}$	$(1.05-1.12\ \mu\text{m})$	$:0.60$
$^4F_{3/2} \rightarrow {}^4I_{13/2}$	$(\sim 1.34\ \mu\text{m})$	$:0.15$
$^4F5_{3/2} \rightarrow {}^4I_{9/2}$	and others $(\tau = 230\ \mu\text{s})$	$:\sim 0.010$

3.3.3.4 Nd^{4+}

Luminescence in the regions ~415, 515, 550, and ~705 nm has been reported in Cs_3NdF_7:Nd^{4+}.[35]

3.3.3.5 Sm^{3+}

Red luminescence at ~610 nm ($^4G_{5/2} \rightarrow {}^6H_{7/2}$) and ~650 nm ($^4G_{5/2} \rightarrow {}^6H_{9/2}$) is observed in Sm.$^{3+}$ High luminescence efficiency in Sm^{3+}, however, has not been reported. Sm^{3+} acts as an auxiliary activator in photostimulable SrS:Eu^{2+} (Mn^{2+} or Ce^{3+}) phosphors. Under excitation, Sm^{3+} captures an electron, changing to Sm^{2+}, which in turn produces an excitation band peaking at 1.0 μm.[36,37] (See 3.6.)

3.3.3.6 Sm^{2+}

The $4f^55d^1$ level of Sm^{2+} is located below its $4f$ levels in CaF_2, resulting in band luminescence due to the $5d \rightarrow 4f$ transition (728.6 nm, τ ~ μs). In SrF_2 and BaF_2, on the other hand, a line spectrum due to the $4f \rightarrow 4f^5\ D_0 \rightarrow {}^7F_1$ transition has been observed (696 nm, τ ~ μs).[38]

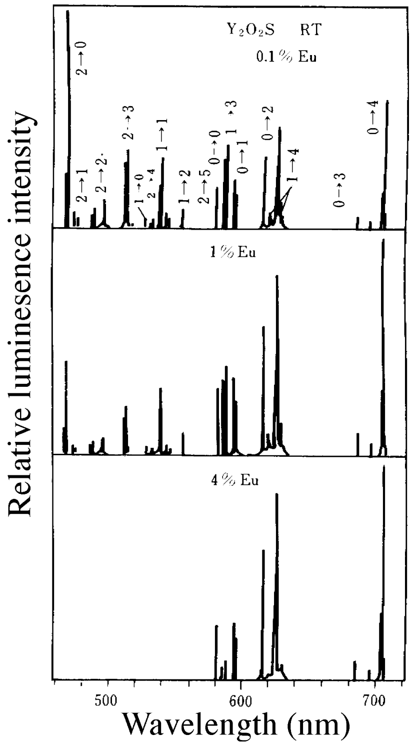

Figure 31 Eu^{3+} concentration dependence of the emission spectrum of Y_2O_2S:Eu^{3+}. (From Hoshina, T., *Luminescence of Rare Earth Ions*, Sony Research Center Rep., 1983 (in Japanese). With permission.)

Also, in BaFCl, line emission at 550 to 850 nm due again to $^5D_{0,1} \rightarrow {}^7F_{0\sim4}$ transitions has been reported.[39]

3.3.3.7 Eu^{3+}

A number of luminescence lines due to $^5D_J \rightarrow {}^7F_{J'}$ of Eu^{3+} in Y_2O_2S are shown in Figure 31. As can be seen, the emissions from $^5D_2$ and $^5D_1$ are quenched, with an increase in the Eu^{3+} concentration due to a cross-relaxation process, $({}^5D_J \rightarrow {}^5D_0) \rightarrow ({}^7F_0 \rightarrow {}^7F_{J'})$, as discussed in Section 3.3.2.4. The emission in the vicinity of 600 nm is due to the magnetic dipole transition $^5D_0 \rightarrow {}^7F_1$, which is insensitive to the site symmetry. The emission around 610–630 nm is due to the electric dipole transition of $^5D_0 \rightarrow {}^7F_2$, induced by the lack of inversion symmetry at the Eu^{3+} site, and is much stronger than that of the transition to the $^7F_1$ state. Luminescent Eu^{3+} ions in commercial red phosphors such as YVO_4, Y_2O_3 and Y_2O_2S, occupy the sites that have no inversion symmetry. The strong emission due to the electric dipole transition is utilized for practical applications. (See 5.3.2 and 6.2.1.) If the Eu^{3+} site has inversion symmetry, as in Ba_2GdNbO_5, $NaLuO_2$,[40] and $InBO_3$,[41] the electric dipole emission is weak, and the magnetic dipole transition becomes relatively stronger and dominates, as is shown in Figure 32.

The spectral luminous efficacy as sensed by the eye has its maximum at 555 nm. In the red region, this sensitivity drops rapidly as one moves toward longer wavelengths. Therefore, red luminescence composed of narrow spectra appear brighter to the human eye than various broad red luminescences having the same red chromaticity and emission energy. For the red emission of color TV to be used in the NTSC system, the red chromaticity standard has been fixed at the coordinates x = 0.67, y = 0.33; in 1955, the ideal emission spectra were proposed as a narrow band around 610 nm, before the development of Eu^{3+}

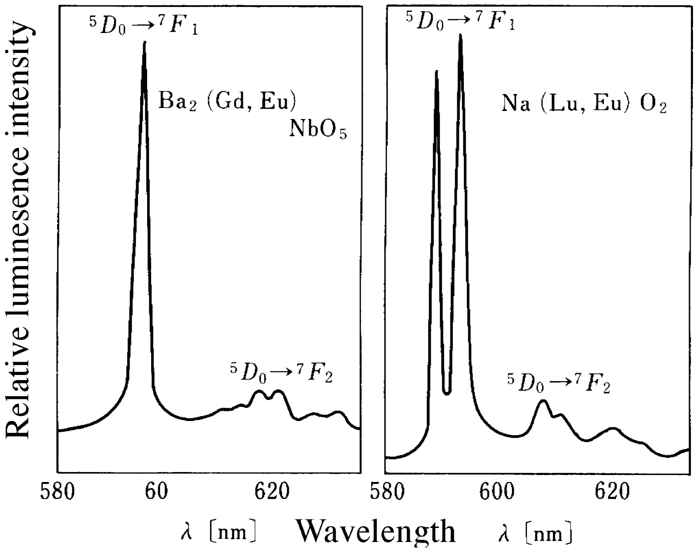

Figure 32 Emission spectra of Eu^{3+} from the sites having the inversion symmetry. (From Blasse, G. and Bril, A., *Philips Tech. Rev.*, 31, 304, 1970. With permission.)

phosphors.[42] This proposal was dramatically fulfilled for the first time in 1964 by newly developed YVO_4:Eu^{3+}.[43] Since then, Eu^{3+} phosphors have completely replaced broad-band emitting Mn^{2+} phosphors or (Zn,Cd)S;Ag, which were predominantly in use at that time. Just after the introduction of YVO_4:Eu^{3+}, another Eu^{3+}-activated phosphor, Y_2O_2S;Eu^{3+}, was developed[44] and is in current use due to its better energy efficiency as well as its stability during recycling in the screening process of CRT production. The possibility of further improvement can occur in materials with single-line emission, as in $Y_2(WO_4)_3$:Eu^{3+}.[45] Use of narrow-band luminescence is also advantageous in three-band fluorescent lamp applications, where both brightness and color reproducibility are required. For high color rendering lamps, Y_2O_3:Eu^{3+} has been used as the red-emitting component.

The sequence of excitation, relaxation, and emission processes in Y_2O_2S;Eu^{3+} is explained by the configurational coordinate model shown in Figure 33.[46] The excitation of Eu^{3+} takes place from the bottom of the $^7F_0$ curve, rising along the straight vertical line, until it crosses the charge-transfer state (CTS). Relaxation occurs along the CTS curve. Near the bottom of the CTS curve, the excitation is transferred to ^5D_J states. Relaxation to the bottom of the ^5D_J states is followed by light emission downward to ^7F_J states. This model can explain the following experimental findings. (1) No luminescence is found from $^5D_3$ in Y_2O_2S:Eu^{3+}. (2) The luminescence efficiency is higher for phosphors with higher CTS energy.[47] (3) The quenching temperature of the luminescence from ^5D_J is higher as J (0,1,2,3) decreases. The excited 4f states may dissociate into an electron-hole pair. This model is supported by the observation that the excitation through the $^7F_0 \rightarrow {}^5D_2$ transition of La_2O_2S:Eu^{3+} causes energy storage that can be converted to luminescence by heating. The luminescence is the result of the recombination of a thermally released hole with an Eu^{2+} ion.[48,49]

By taking a model where CTS is a combination of $4f^7$ electrons plus a hole, one finds that the resulting spin multiplicities should be 7 and 9. It is the former state that affects optical properties related to the ^7F_J state by spin-restricted covalency.[50] The intensity ratio of the luminescence from $^5D_0 \rightarrow {}^7F_2$ and from $^5D_0 \rightarrow {}^7F_1$ decreases with increasing CTS energy sequentially as $ScVO_4$, YVO_4, $ScPO_4$, and YPO_4, all of which have the same type of zircon structure.[51] The above intensity ratio is small in YF_3:Eu^{3+}, even though Eu^{3+} occupies a site without inversion symmetry.[52] It is to be noted that CTSs in fluorides have

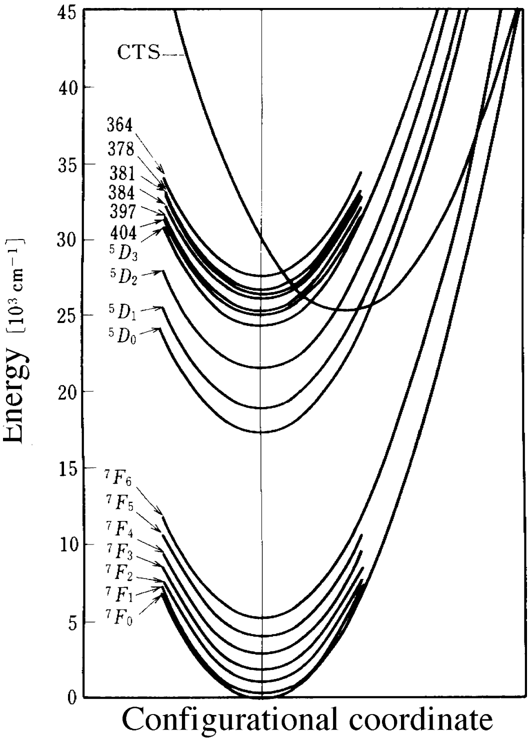

Figure 33 Configurational coordinate model of Y_2O_2S:Eu^{3+}. (From Struck, C.W. and Fonger, W.H., *J. Luminesc.*, 1/2, 456, 1970. With permission.)

higher energies than those in oxides. These results suggest that higher CTS energies reduce the strength of the electric dipole transition $^5D_0 \rightarrow {}^7F_2$ in Eu^{3+}.

3.3.3.8 Eu^{2+}

The electronic configuration of Eu^{2+} is $4f^7$ and is identical to that of Gd^{3+}. The lowest excited state of 4f levels is located at about 28×10^3 cm^{-1} and is higher than the $4f^6 5d^1$ level in most crystals, so that Eu^{2+} usually gives broad-band emission due to *f-d* transitions The wavelength positions of the emission bands depend very much on hosts, changing from the near-UV to the red. This dependence is interpreted as due to the crystal field splitting of the 5*d* level, as shown schematically in Figure 34.[53] With increasing crystal field strength, the emission bands shift to longer wavelength. The luminescence peak energy of the 5*d*-4*f* transitions of Eu^{2+} and Ce^{3+} are affected most by crystal parameters denoting electron-electron repulsion; on this basis, a good fit of the energies can be obtained.[27]

The near-UV luminescence of Eu^{2+} in $(Sr,Mg)_2P_2O_7$ is used for lamps in copying machines using photosensitive diazo dyes. The blue luminescence in $BaMgAl_{10}O_{17}$ is used for three-band fluorescent lamps. (See Figure 35.)[54] Ba(F,Br): Eu^{2+} showing violet luminescence is used for X-ray detection through photostimulation[55] (see 7.5). Red luminescence is observed in Eu^{2+}-activated CaS[36]; the crystal field is stronger in sulfides than in fluorides and oxides.

The lifetime of the Eu^{2+} luminescence is 10^{-5}–10^{-6} s, which is relatively long for an allowed transition. This can be explained as follows. The ground state of $4f^7$ is ^8S, and the multiplicity of the excited state $4f^6 5d^1$ is 6 or 8; the sextet portion of the excited state contributes to the spin-forbidden character of the transition.[29]

Sharp-line luminescence at ~360 nm due to an *f-f* transition and having a lifetime of milliseconds is observed when the crystal field is weak so that the lowest excited state of

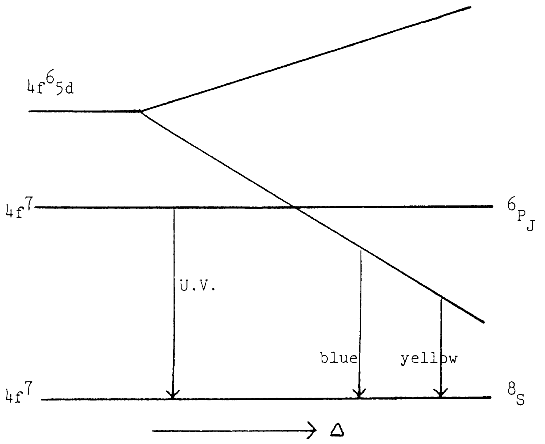

Figure 34 Schematic diagram of the energies of $4f^7$ and $4f^65d^1$ levels in Eu^{2+} influenced by crystal field Δ. (From Blasse, G., Material science of the luminescence of inorganic solids, in *Luminescence of Inorganic Solids*, DiBartolo, B., Plenum Press, 1978, 457. With permission.)

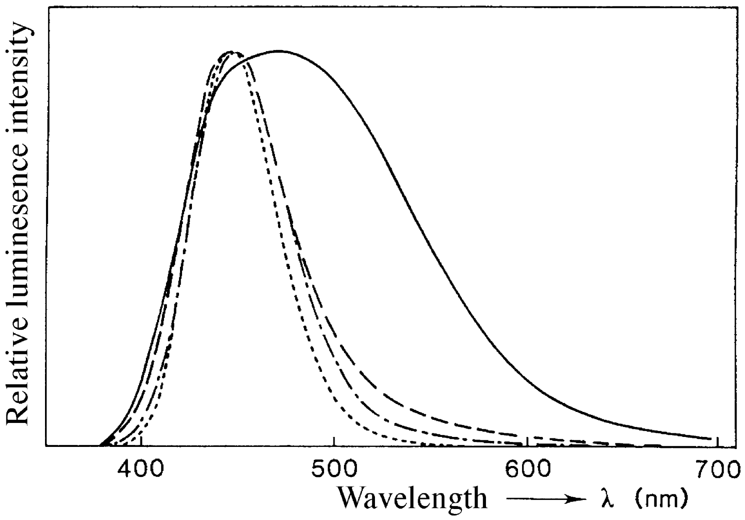

Figure 35 Emission spectra of Eu^{2+} in $BaMgAl_{10}O_{17}$ and related compounds using 254-nm excitation at 300K. ----: $Ba_{0.95}Eu_{0.05}MgAl_{10}O_{17}$, —·—·—: $Ba_{0.825}Eu_{0.05}Mg_{0.5}Al_{10.5}O_{17.125}$, — — —: $Ba_{0.75}Eu_{0.05}Mg_{0.2}Al_{10.8}O_{17.2}$, ———: $Ba_{0.70}Eu_{0.05}Al_{11}O_{17.25}$. (From Smets, B.M.J. and Verlijsdonk, J.G., *Mater. Res. Bull.*, 21, 1305, 1986. With permission.)

$4f^7(^6P_J)$ is lower than the $4f^65d^1$ state, as illustrated in Figure 34. The host crystals reported to produce UV luminescence are $BaAlF_5$, $SrAlF_5$ [56] (see Figure 36), $BaMg(SO_4)_2$,[57] $SrBe_2Si_2O_7$,[58] and Sr(F,Cl).[59]

3.3.3.9 Gd^{3+}

The lowest excited 4*f* level of Gd^{3+} ($^6P_{7/2}$) gives rise to sharp-line luminescence at ~315 nm[60] and can sensitize the luminescence of other rare-earth ions.[61] The energy levels of the CTS and the $4f^65d^1$ states are the highest among rare-earth ions, so that Gd^{3+} causes no quenching in other rare-earth ions. As a consequence, Gd^{3+} serves, as Y^{3+} does, as a good constituent cation in host crystals to be substituted by luminescent rare-earth ions. For X-ray phosphors, Gd^{3+} is better suited as a constituent than Y^{3+} since it has a higher absorption cross-section due to its larger atomic number.

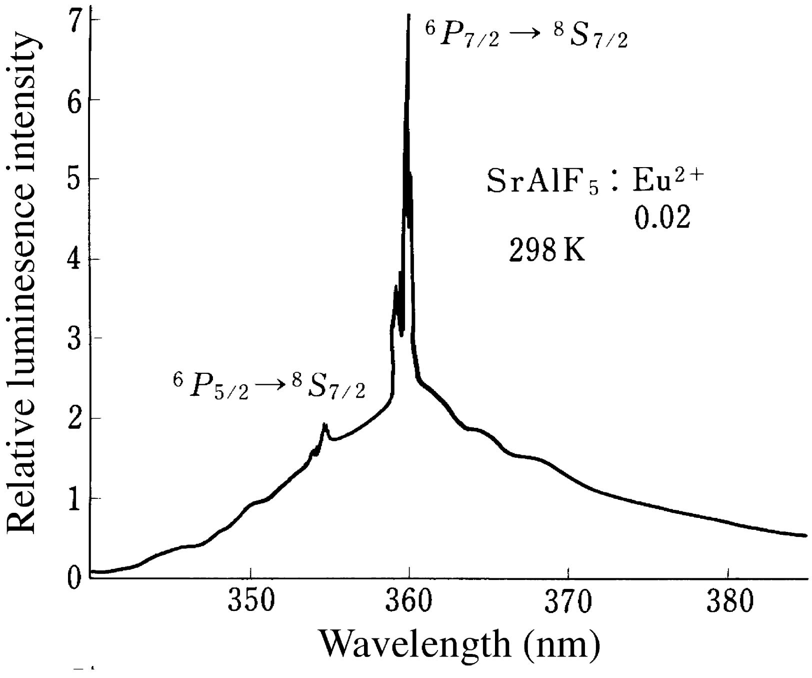

Figure 36 Emission spectrum at 298K of SrAlF$_5$:Eu^{2+} using 254-nm excitation. (From Hews, R.A. and Hoffman, M.V., *J. Luminesc.*, 3, 261, 1970. With permission.)

3.3.3.10 Tb^{3+}

Luminescence spectra consisting of many lines due to $^5D_J \rightarrow {}^7F_{J'}$ are observed for Tb^{3+}. As an example, the spectra of Y$_2$O$_2$S:Tb^{3+} are shown in Figure 37, in which the Tb^{3+} concentration varies over a wide range. The intensity of the emissions from $^5D_3$ decreases with increasing Tb^{3+} concentration due to cross-relaxation, as discussed in Section 3.3.2.4. Among the emission lines from the $^5D_4$ state, the $^5D_4 \rightarrow {}^7F_5$ emission line at approximately 550 nm is the strongest in nearly all host crystals when the Tb^{3+} concentration is a few mol% or higher. The reason is that this transition has the largest probability for both electric-dipole and magnetic-dipole induced transitions.[2] The Tb^{3+} emission has a broad excitation band in the wavelength region 220 to 300 nm originating from the $4f^8 \rightarrow 4f^75d^1$ transition.

The chromaticity due to the Tb^{3+} emission has been estimated by calculation of the various transition probabilities.[62] The spectral region around 550 nm is nearly at the peak in the spectral luminous efficacy; in this region, therefore, the brightness depends only slightly on the wavelength and the spectral width. Thus, the narrow spectral width of the Tb^{3+} emission is not so advantageous in cathode-ray tube applications as compared with the case of red Eu^{3+} emission previously described.

The intensity ratio of the emission from $^5D_3$ to that from $^5D_4$ depends not only on the Tb^{3+} concentration, but also on the host material. In borate hosts such as ScBO$_3$, InBO$_3$, and LuBO$_3$, the relative intensity of $^5D_3$ emission is much weaker than in other hosts, such as phosphates, silicates, and aluminates.[2] Figure 38 shows emission spectra of a series of Ln$_2$O$_2$S:Tb^{3+}(0.1%) (Ln = La, Gd, Y, and Lu) materials having the same crystal structure.[2] It is seen that the relative intensity of the $^5D_3$ emission increases dramatically as one progresses from La → Gd → Y → Lu, with the ionic radii becoming smaller.

In addition to the Tb^{3+} concentration, one needs to consider two additional factors that help determine the ratio of $^5D_3$ to $^5D_4$ intensity. One is the maximum energy of phonons that causes phonon-induced relaxation, as discussed in Section 3.3.2.1; if the maximum phonon

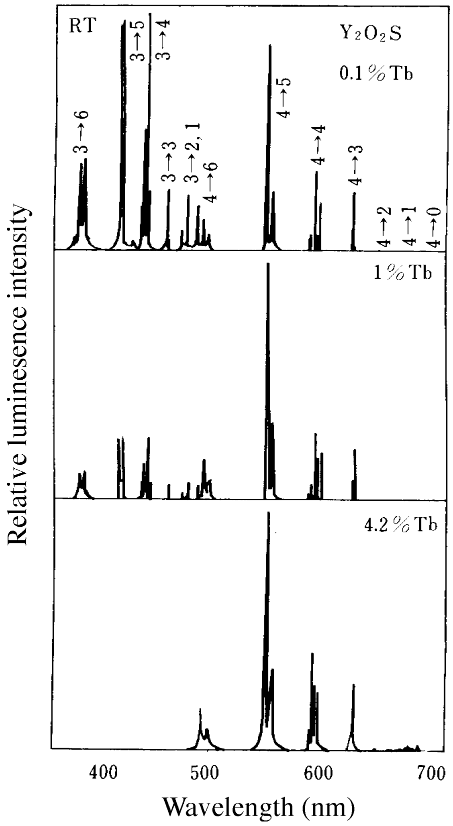

Figure 37 Tb^{3+} concentration dependence of emission spectra of $Y_2O_2S:Tb^{3+}$ at room temperature. (From Hoshina, T., *Luminescence of Rare Earth Ions*, Sony Research Center Rep., 1983 (in Japanese). With permission.)

energy is large, the ratio of $^5D_3$ to $^5D_4$ intensity becomes small. The luminescence of Tb^{3+} in borate hosts is explained by this factor. The other factor is the energy position of the $4f^75d^1$ level relative to $4f^8$ levels, which can be discussed in terms of the configurational coordinate model. In this model, the potential curve of $4f^75d^1$ can be drawn just like the CTS in Figure 33. If the minimum of the $4f^75d^1$ curve is fairly low in energy and the Frank-Condon shift is fairly large, there is a possibility that an electron excited to the $4f^75d^1$ level can relax directly to the $^5D_4$, bypassing the $^5D_3$ and thus producing only $^5D_4$ luminescence.[2] The net effect of these two factors on the spectra of $Ln_2O_2S:Tb^{3+}$ in Figure 38 is not known quantitatively.

YVO_4 is a good host material for various Ln^{3+} ions, as shown in Figure 23. However, Tb^{3+} does not luminesce in this host. A nonradiative transition via a charge-transfer state of Tb^{4+}-O^{2-}-V^{4+} has been proposed as a cause.[63] The transition energy to this proposed state is considered to be relatively low because both the energies of conversion from Tb^{3+} to Tb^{4+} and that from V^{5+} to V^{4+} are low. The Frank-Condon shift in the transition would be so large that the proposed state would provide a nonradiative relaxation path from excited Tb^{3+} to the ground state.

Tb^{3+}-activated green phosphors are used in practice in three-band fluorescent lamps (see 5.3.2), projection TV tubes (6.2.1.5), and X-ray intensifying screens (7.1).

3.3.3.11 Dy^{3+} [64,65]

The luminescence lines of Dy^{3+} are in the 470 to 500-nm region due to the $^4F_{9/2} \rightarrow {}^6H_{15/2}$ transition, and in the 570 to 600-nm region due to the $^6F_{15/2} \rightarrow {}^6F_{11/2}$ transition. The color

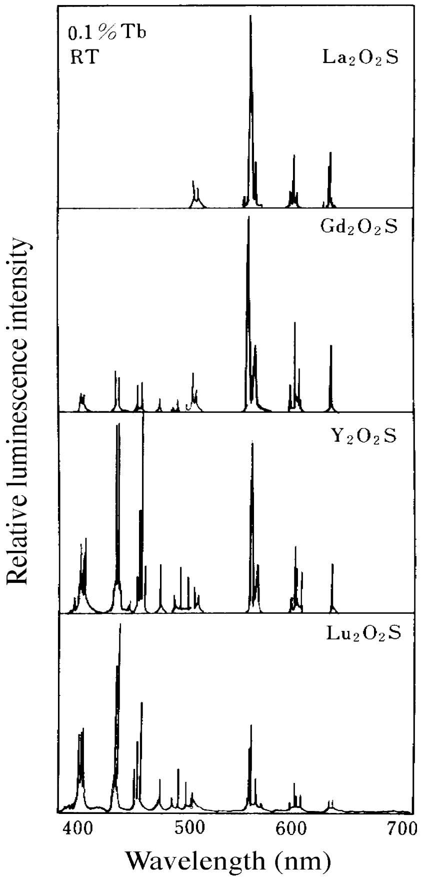

Figure 38 Emission spectra of Ln_2O_2S:Tb^{3+} (0.1%) (Ln = La, Gd, Y, and Lu) at room temperature. (From Hoshina, T., *Luminescence of Rare Earth Ions*, Sony Research Center Rep., 1983 (in Japanese). With permission.)

of the luminescence is close to white. In Y(P,V)O_4, the relative intensity of the latter decreases with increasing P concentration. This can be understood if one considers that the $\Delta J = 2$ transition probability decreases with a decrease in the polarity of the neighboring ions as in the case of the $^5D_0 \rightarrow {}^7F_2$ transition of Eu^{3+}. The energy of the CTS and $4f^85d^1$ is relatively large so that direct UV excitation of Dy^{3+} is not effective. The excitation via host complex ions by energy transfer can however be effective. The quantum efficiency of UV-excited (250–270 nm) luminescence of YVO_4:Dy^{3+} has been reported to be as high as 65%.

3.3.3.12 Dy^{2+} [66]

Luminescence of Dy^{2+} has been reported to consist of line spectra at 2.3–2.7 μm at 77K and 4.2K in CaF_2, SrF_2, and BaF_2. Dy^{2+} in these hosts was prepared by the reduction of Dy^{3+} through γ-ray irradiation.

3.3.3.13 Dy^{4+} [67]

Luminescence lines of Cs_3DyF_7:Dy^{4+} at 525 nm due to $^5D_4 \rightarrow {}^7F_5$ transition and at 630 nm due to $^5D_4 \rightarrow {}^7F_3$ transition have been reported.

3.3.3.14 Ho^{3+}

Efficient luminescence of Ho^{3+} has rarely been found due to the crowded energy level diagram of this ion. In $LaCl_3$, cross-relaxation between ($^5S_2 \rightarrow {}^5I_4$) ↔ ($^5I_8 \rightarrow {}^5I_7$) at an interioninc distance of 7.5 Å has been reported.[68] A green luminescence due to the $^5F_4$, $^5S_2 \rightarrow {}^5I_8$ transition has been reported in an infrared-to-visible up-conversion phosphor, $LiYF_4:Yb^{3+},Ho^{3+}$.[69]

3.3.3.15 Ho^{2+}

Infrared luminescence of Ho^{2+} in CaF_2 appearing around 1.8 µm at 77K has been reported.[70]

3.3.3.16 Er^{3+}

Green luminescence due to the $^4S_{3/2} \rightarrow {}^4I_{15/2}$ transition of Er^{3+} has been reported in infrared-to-visible up-conversion phosphors, such as $LaF_3:Yb^{3+},Er^{3+}$,[71] and $NaYF_4:Yb^{3+},Er^{3+}$.[72] (See 12.1). This luminescence was also reported in ZnS,[73] Y_2O_3,[74] and Y_2O_2S.[75] The emission color is a well-saturated green.

Er^{3+} ions embedded in an optical fiber (several hundreds ppm) function as an optical amplifier for 1.55-µm semiconductor laser light. Population inversion is realized between lower sublevels of $^4I_{13/2}$ and upper sublevels of $^4I_{15/2}$. This technology has been developed for optical amplification in the long-distance optical fiber communication systems.[76]

3.3.3.17 Tm^{3+}

The blue luminescence of Tm^{3+} due to the $^1G_4 \rightarrow {}^3H_6$ transition has been reported in ZnS,[77] as well as in infrared-to-visible up-conversion phosphors sensitized by Yb^{3+} such as $YF_3:Tm^{3+},Yb^{3+}$.[78] Electroluminescent $ZnS:TmF_3$ has also been investigated as the blue component of multicolor displays.[79] The efficiency of the blue luminescence of Tm^{3+} is low, and is limited by the competitive infrared luminescence, which has a high efficiency.

3.3.3.18 Yb^{3+}

The infrared absorption band of Yb^{3+} at about 1 µm due to the $^5F_{5/2} \rightarrow {}^5F_{7/2}$ transition is utilized for Er^{3+}-doped infrared-to-visible up-conversion phosphors as a sensitizer (See 12.1).[71,72] The CTS energy of Yb^{3+} ions is low next to the lowest of Eu^{3+} among the trivalent lanthanide ions (see Figure 25). Yb^{3+} has no 4*f* energy levels interacting with CTS, so that luminescence due to the direct transition from CTS to the 4*f* levels can occur. This luminescence has been observed in phosphate[80] and oxysulfide hosts.[81] Figure 39 shows the excitation and emission spectra of $Y_2O_2S:Yb^{3+}$ and $La_2O_2S:Yb^{3+}$.[81] As seen in Figure 33, CTS is characterized by a fairly large Frank-Condon shift. As a result, the emission spectra are composed of two fairly broad bands terminating in $^2F_{5/2}$ and $^2F_{7/2}$, as shown in Figure 39.

3.3.3.19 Yb^{2+}

The emission and absorption of Yb^{2+} due to the $4f^{14} \leftrightarrow 4f^{13}5d^1$ transition have been reported.[82] Emission peaks are at 432 nm in $Sr_3(PO_4)_2$ (see Figure 40), 505 nm in Ca_2PO_4Cl, 560 nm in $Sr_5(PO_4)_3Cl$, and 624 nm in $Ba_5(PO_4)_3Cl$. The lifetimes of the emissions are between $1–6 \times 10^{-5}$ s.

References

1. Blasse, G., *Handbook on the Physics and Chemistry of Rare Earths*, ed. by Gschneidner, Jr., K.A. and Eyring, L., Vol. 4, North-Holland Pub. 1979, 237.
2. Hoshina, T., *Luminescence of Rare Earth Ions*, Sony Research Center Rep. (Suppl.) 1983 (in Japanese).
3. Adachi, G., *Rare Earths—Their Properties and Applications*, ed. by Kano, T. and Yanagida, H., Gihodo Pub. 1980, 1 (in Japanese). Kano, T., *ibid*, 173.
4. Ofelt, G.S., *J. Chem. Phys.*, 38, 2171,1963.
5. Dieke, G.H., *Spectra and Energy Levels of Rare Earth Ions in Crystals*, Interscience, 1968; *American Institute of Physics Handbook*, 3rd edition, McGraw-Hill, 1972, 7-25.
6. Riseberg, L.A. and Moos, H.W., *Phys. Rev.*, 174, 429, 1968.

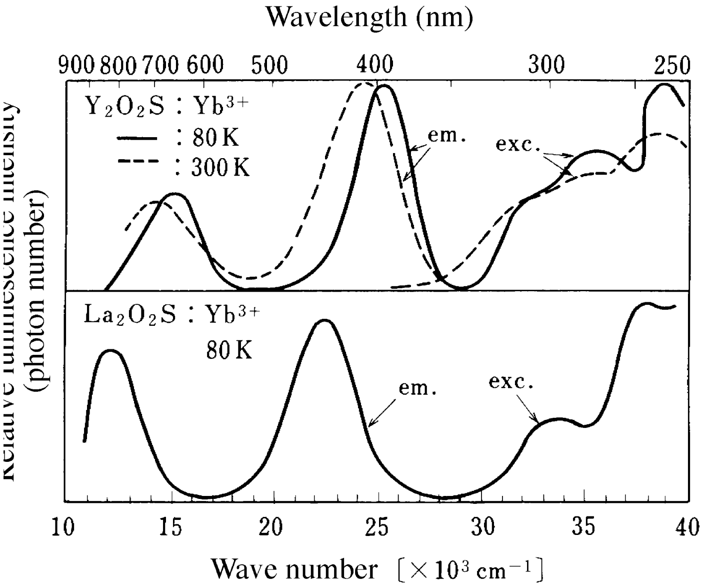

Figure 39 Excitation and emission spectra of $Y_2O_2S:Yb^{3+}$ and $La_2O_2S:Yb^{3+}$. (From Nakazawa, E., *J. Luminesc.*, 18/19, 272, 1979. With permission.)

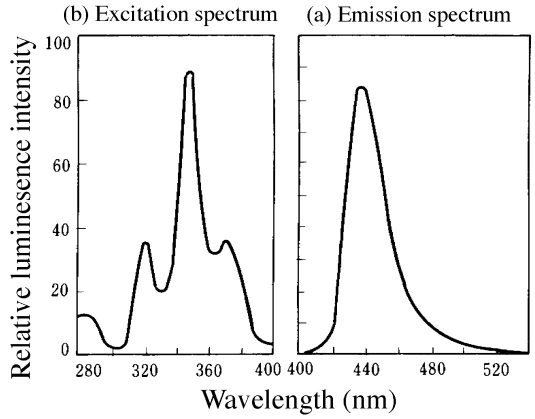

Figure 40 Emission (a) and excitation (b) spectra of $Sr_3(PO_4)_2:Yb^{2+}$ at liquid nitrogen temperature. (From Palilla, F.C., O'Reilly, R.E., and Abbruscato, V.J., *J. Electrochem. Soc.*, 117, 87, 1970. With permission.)

7. Kropp, J.L. and Windsor, M.W., *J. Chem. Phys.*, 42, 1599, 1965.
8. Judd, B.R., *Phys. Rev.*, 127, 750, 1962.
9. Ofelt, G.S., *J. Chem. Phys.*, 37, 511, 1962.
10. Hirao, K., *Rev. Laser Eng.*, 21, 618, 1993 (in Japanese).
11. Barasch, G.E. and Dieke, G.H., *J. Chem. Phys.*, 43, 988, 1965.
12. Pallila, F.C., *Electrochem. Technol.*, 6, 39, 1968.
13. Ozawa, R., *Bunseki-kiki*, 6, 108, 1968 (in Japanese).
14. Joergensen, C.K., Papalardo, R., and Rittershaus, E., *Z. Naturforschg.*, 20-a, 54, 1964.
15. McClure, D.S. and Kiss, Z., *J. Chem. Phys.*, 39, 3251, 1963.
16. Hoefdraad, H.E., *J. Inorg. Nucl. Chem.*, 37, 1917, 1975.
17. Nakazawa, E. and Shionoya, S., *J. Chem. Phys.*, 47, 3211, 1967.
18. McClure, D.S., *The Electrochem. Soc., Extended Abstr.*, 77-1, 365, 1977.

19. Ozawa, L., *The Electrochem. Soc., Extended Abstr.*, 78-1, 850, 1978.
20. Yamamoto, H. and Kano, T., *J. Electrochem. Soc.*, 126, 305, 1979.
21. Robins, D.J., Cockayne, B., Glasper, J.L., and Lent, B., *J. Electrochem. Soc.*, 126, 1221, 1979.
22. Botden, Th.P., *Philips Res. Rpts.*, 6, 425, 1951.
23. Van Uitert, L.G., Soden, R.R., and Linares, R.C., *J. Chem. Phys.*, 36, 1793, 1962.
24. Pallila, F.C., Levin, A.K., and Rinkevics, M., *J. Electrochem. Soc.*, 112, 776, 1965.
25. Blasse, G. and Bril, A., *J. Chem. Phys.*, 51, 3252, 1969.
26. Narita, K. and Taya, A., *Tech. Digest, Phosphor Res. Soc. 147th Meeting*, 1979 (in Japanese).
27. Van Uitert, L.G., *J. Luminesc.*, 29, 1, 1984.
28. Butler, K.H., *Fluorescent Lamp Phosphors, Technology and Theory*, The Pennsylvania State University Press, 1980, 261. Copyright 1996 by The Pennsylvania State University.
29. Blasse, G., Wanmaker, W.L., Tervrugt, J.W., and Bril, A., *Philips Res. Rept.*, 23, 189, 1968.
30. Sommerdijk, J.L. and Verstegen, J.M.P.J., *J. Luminesc.*, 9, 415, 1974.
31. Yamada, H., Suzuki, A., Uchida, Y., Yoshida, M., Yamamoto, H., and Tsukuda, Y., *J. Electrochem. Soc.*, 136, 2713, 1989.
32. Sommerdijk, J.L., Bril, A., and de Jager, A.W., *J. Luminesc.*, 8, 341, 1974.
33. Piper, W.W., Deluca, J.A., and Ham, F.S., *J. Luminesc.*, 8, 344, 1974.
34. Kushida, T., Marcos, H.M., and Geusic, J.E., *Phys. Rev.*, 167, 289, 1968.
35. Vaga, L.P., *J. Chem. Phys.*, 49, 4674, 1968.
36. Urbach, F., Pearlman, D., and Hemmendinger, H., *J. Opt. Soc. Am.*, 36, 372, 1946.
37. Keller, S.P., Mapes, J.E., and Cheroff, G., *Phys. Rev.*, 111, 1533, 1958.
38. Feofilof, P.D. and Kaplyanskii, A.A., *Opt. Spectrosc.*, 12, 272, 1962.
39. Mahbub'ul Alam, A.S. and Baldassare Di Bartolo, B., *J. Chem. Phys.*, 47, 3790, 1967.
40. Blasse, G. and Bril, A., *Philips Tech. Rev.*, 31, 304, 1970.
41. Avella, F.J., Sovers, O.J., and Wiggins, C.S., *J. Electrochem. Soc.*, 114, 613, 1967.
42. Bril, A. and Klassens, H.A., *Philips Res. Rept.*, 10, 305, 1955.
43. Levine, A.K. and Pallila, F.C., *Appl. Phys. Lett.*, 5, 118, 1964.
44. Royce, M.R. and Smith, A.L., *The Electrochem. Soc., Extended Abstr.*, 34, 94, 1968.
45. Kano, T., Kinameri, K., and Seki, S., *J. Electrochem. Soc.*, 129, 2296, 1982.
46. Struck, C.W. and Fonger, W.H., *J. Luminesc.*, 1&2, 456, 1970.
47. Blasse, G., *J. Chem. Phys.*, 45, 2356, 1966.
48. Forest, H., Cocco, A., and Hersh, H., *J. Luminesc.*, 3, 25, 1970.
49. Struck, C.W. and Fonger, W.H., *Phys. Rev.*, B4, 22, 1971.
50. Hoshina, T., Imanaga, S., and Yokono, S., *J. Luminesc.*, 15, 455, 1977.
51. Blasse, G. and Bril, A., *J. Chem. Phys.*, 50, 2974, 1969.
52. Blasse, G. and Bril, A., *Philips Res. Rept.*, 22, 481, 1967.
53. Blasse, G., Material science of the luminescence of inorganic solids, in *Luminescence of Inorganic Solids*, DiBartolo, B., Ed., Plenum Press, 1978, 457.
54. Smets, B.M.J. and Verlijsdonk, J.G., *Mater. Res. Bull.*, 21, 1305, 1986.
55. Takahashi, K., Kohda, K., Miyahara, J., Kanemitsu, Y., Amitani, K., and Shionoya, S., *J. Luminesc.*, 31&32, 266, 1984.
56. Hews, R.A. and Hoffman, M.V., *J. Luminesc.*, 3, 261, 1970.
57. Ryan, F.M., Lehmann, W., Feldman, D.W., and Murphy, J., *J. Electrochem. Soc.*, 121, 1475, 1974.
58. Verstegen, J.M.P.J. and Sommerdijk, J.L., *J. Luminesc.*, 9, 297, 1974.
59. Sommerdijk, J.L., Verstegen, J.M.P.J., and Bril, A., *J. Luminesc.*, 8, 502, 1974.
60. Wickerscheim, K.A. and Lefever, R.A., *J. Electrochem. Soc.*, 111, 47, 1964.
61. D'Silva, A.P. and Fassel, V.A., *J. Luminesc.*, 8, 375, 1974.
62. Hoshina, T., *Jpn. J. Appl. Phys.*, 6, 1203, 1967.
63. DeLosh, R.G., Tien, T.Y., Gibbon, F.F., Zacmanidis, P.J., and Stadler, H.L., *J. Chem. Phys.*, 53, 681, 1970.
64. Sommerdijik, J.L. and Bril, A., *J. Electrochem. Soc.*, 122, 952, 1975.
65. Sommerdijik, J.L., Bril, A., and Hoex-Strik, F.M.J.H., *Philips Res. Rept.*, 32, 149, 1977.
66. Kiss, Z.J., *Phys. Rev.*, 137, A1749, 1965.
67. Varga, L.P., *J. Chem. Phys.*, 53, 3552, 1970.
68. Porter, Jr., J.F., *Phys. Rev.*, 152, 300, 1966.

69. Watts, R.K., *J. Chem. Phys.*, 53, 3552, 1970.
70. Weakliem, H.A. and Kiss, Z.J., *Phys. Rev.*, 157, 277, 1967.
71. Hews, R.A. and Sarver, J.F., *Phys. Rev.*, 182, 427, 1969.
72. Kano, T., Yamamoto, H., and Otomo, Y., *J. Electrochem. Soc.*, 119, 1561, 1972.
73. Larach, S., Shrader, R.E., and Yocom, P.N., *J. Electrochem. Soc.*, 116, 47, 1969.
74. Kisliuk, P. and Krupke, W.F., *J. Chem. Phys.*, 40, 3606, 1964.
75. Shrader, R.E. and Yocom, P.N., *J. Luminesc.*, 1&2, 814, 1970.
76. Hagimoto, K. Iwatsuki, K., Takada, A., Nakagawa, M., Saruwatari, M., Aida, K., Hakagawa, K., and Horiguchi, M., *OFC'89 PD-15*, 1989.
77. Shrader, R.E., Larach, S., and Yocom, P.N., *J. Appl. Phys.*, 42, 4529, 1971. (Erratum: *J. Appl. Phys.*, 43, 2021, 1972.)
78. Geusic, J.E., Ostermayer, F.W., Marcos, H.M., Van Uitert, L.G., and Van der Ziel, J.P., *J. Appl. Phys.*, 42, 1958, 1971.
79. Kobayashi, H., Tanaka, S., Shanker, V., Shiiki, M., Kunou, T., Mita, J., and Sasakura, H., *Physi. Stat. Sol. (a)*, 88, 713, 1985.
80. Nakazawa, E., *Chem. Phys. Lett.*, 56, 161, 1978.
81. Nakazawa, E., *J. Luminesc.*, 18/19, 272, 1979.
82. Palilla, F.C., O'Reilly, R.E., and Abbruscato, V.J., *J. Electrochem. Soc.*, 117, 87, 1970.

chapter three — section four

Principal phosphor materials and their optical properties

Makoto Morita

Contents

3.4 Luminescence centers of complex ions 215
  3.4.1 Introduction 215
  3.4.2 Scheelite-type compounds 216
    3.4.2.1 Scheelite compounds and their general properties 216
    3.4.2.2 Electronic structures of closed-shell molecular complex centers 216
    3.4.2.3 Luminescence centers of VO_4^{3-} ion type 217
    3.4.2.4 Luminescence centers of MoO_4^{2-} ion type 218
    3.4.2.5 Luminescence centers of WO_4^{2-} ion type 219
    3.4.2.6 Other closed-shell transition metal complex centers 220
  3.4.3 Uranyl complex centers 220
    3.4.3.1 Electronic structure 220
    3.4.3.2 Luminescence spectra 220
  3.4.4 Platinum complex centers 221
    3.4.4.1 $[Pt(CN)_4]^{2-}$ Complex ions 222
    3.4.4.2 Other platinum complex ions 223
  3.4.5 Other complex ion centers 224
    3.4.5.1 WO_6^{6-} Ion 224
    3.4.5.2 Perspective of other interesting centers 224
References 225

3.4 *Luminescence centers of complex ions*

3.4.1 *Introduction*

Phosphors containing luminescence centers made up of complex ions have been well known since 1900s. The specific electronic structures are reflected in the spectral band shapes and transition energies. These phosphors have been widely used in practical applications. However, in spite of their common usage, it is only in the last three decades that the electronic structures of the complex ions have been explained in terms of the crystal field theory (See 3.2.1); because of this understanding, new phosphors have been prepared with a variety of colors and with high quantum yields.[1] This section will first focus on the luminescence from complex ions with closed-shell electronic structures such as the scheelite compounds and others and describe a variety of applications for these phosphors. Other interesting luminescence centers such as uranyl(II), platinum(II), mixed-valence, and other complexes are discussed subsequently.

3.4.2 *Scheelite-type compounds*

3.4.2.1 *Scheelite compounds and their general properties*

Calcium tungstate ($CaWO_4$) has long been known as a practical phosphor, and it is a representative scheelite compound. The luminescence center is the WO_4^{2-} complex ion in which the central W metal ion is coordinated by four O^{2-} ions in tetrahedral symmetry (T_d). Other analogous T_d complexes are *molybdate* (MoO_4^{2-}) and vanadate (VO_4^{3-}). In these three complex ions, the electronic configuration of the outer-shell is [Xe]$4f^{14}$, [Kr], and [Ar] for WO_4^{2-}, MoO_4^{2-}, and VO_4^{3-}, respectively. In general, scheelite phosphors take the form of A_pBO_4 with A standing for a monovalent alkaline, divalent alkaline earth, or trivalent lanthanide metal ion, p for the number of ions, and B for W, Mo, V, or P. Bright luminescence in the blue to green spectral regions was observed in the early 20th century. An introduction to the electronic configurations common to these complex ions is followed by a discussion of the results of investigations, referring to a number of recent review articles on this subject.[1,2]

3.4.2.2 *Electronic structures of closed-shell molecular complex centers*

As a typical complex ion center, consider the electronic structure of the MnO_4^- ion. In this case, the Mn^{7+} ion has a closed-shell structure with no *d* electrons. Using a one-electron transition scheme, consider a one-electron charge transfer process from the oxygen 2*p* orbital (t_1 symmetry in T_d) to the 3*d* orbital (*e* and t_2 symmetry) of the Mn^{7+} ion. A molecular orbital calculation[3] leads to e^* and a t_1 states for the lowest unoccupied molecular orbital (LUMO) and the highest occupied molecular orbital (HOMO), respectively. By taking the $e \rightarrow t_1$ transition into account, the excited electronic states of t_1^5e electronic configuration in T_d symmetry are found to consist of $^3T_1 \leqq {}^3T_2 < {}^1T_1 < {}^1T_2$ in order of increasing energies, the ground state being a $^1A_1$ state. The orbital triplets ($^3T_1$, $^3T_2$) have degenerate levels in the spectral region of 250 to 500 nm. By employing more advanced calculations (the Xα method), similar results for the $e \leftarrow t_1$ transition have been calculated for the VO_4^{3-} ion.[4]

Electronic structures of the scheelite compounds have in common closed-shell electronic configurations as explained for the MnO_4^- ion, and their luminescence and absorption processes are exemplified in the model scheme of the MO_4^{n-} complex. Generally speaking, the luminescence of MO_4^{n-} ion is due to the spin-forbidden $^3T_1 \rightarrow {}^1A_1$ transition that is made allowed by the spin-orbit interaction. The corresponding $^3T_1 \leftarrow {}^1A_1$ absorption transition is not easily observed in the excitation spectrum due to the strong spin selection rule, and the first strong absorption band is assigned to the spin-allowed $^1T_1 \leftarrow {}^1A_1$ transition. Electronic levels and their assignments are given schematically in Figure 41 for the MO_4^{n-} ion.[2] In this model, assume an energy level scheme for the MO_4^{n-} complex in a tetrahedral environment. The energy separation between $^3T_1$ and $^3T_2$ has been estimated to be about 500 cm^{-1} for the VO_4^{3-} complex from luminescence experiments.[2] The splitting of $^3T_1$, shown in the figure, amounts to several tens of cm^{-1} and is due to the lowering of the crystal field symmetry from T_d and to the inclusion of the spin-orbit interaction. We want to understand changes of spectral properties and decay times of the luminescence from these complexes at temperatures between room temperature and 77K. Then, the

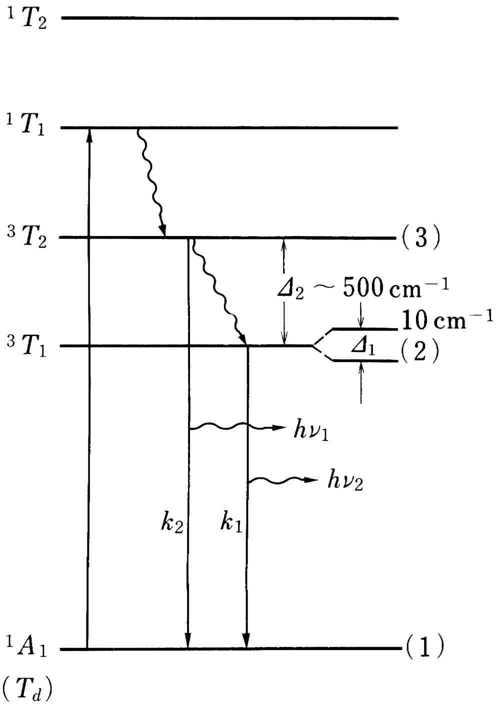

Figure 41 Three-level energy scheme for luminescence processes of MO_4^{n-} ion in scheelite compounds. It is necessary to take into account of the splittings of the $^3T_1$ state to analyze changes of emission decay times at very low temperatures. (From Blasse, G., *Structure and Bonding*, 42, 1, 1980. With permission.)

simplified three-level model based on the two excited states ($^3T_1$, $^3T_2$) and the ground state $^1A_1$ is quite satisfactory.

Figure 41 illustrates a simple but useful model for the energy levels of ions in scheelite compounds. If the species of the central metal ion M are changed, the position of the higher excited states and the splitting of these levels will change considerably .[4] However, the ordering of the states is rigorously observed. Higher excited states due to the $t_1^5\ t_2$ configuration have also been examined theoretically.[5] Excited-state absorption from the t_1^5e to the $t_1^5\ t_2$ have been investigated in $CaWO_4$ crystals.[6]

3.4.2.3 *Luminescence centers of VO_4^{3-} ion type*

Yttrium vanadate (YVO_4) is a very useful phosphor in use for a long time. This compound does not show luminescence at room temperature; but at temperatures below 200K, it shows blue emission centered at 420 nm, as shown in Figure 42.[7] The broad band has a full width at half maximum (FWHM) of about 5000 cm^{-1}, with a decay time of several milliseconds. Even at 4K, no vibronic structure is seen. The first excitation band is located at about 330 nm, separated by 6000 cm^{-1} from the emission band. The emission and excitation are due to the $^3T_1 \leftrightarrow {}^1A_1$ transition, and the large Stokes' shift is due to the displacement between the excited- and the ground-state potential minima in the configurational coordinate model. In YVO_4, energy migration tends to favor nonradiative transition processes; because of this thermal quenching, luminescence is not observed at room temperature. However, room-temperature luminescence is observed in YPO_4:VO_4^{3-} mixed crystals. Bright luminescence from VO_4^{3-} ions is commonly observed in other vanadate complexes such as $Mg_3(VO_4)_2$, $LiZnVO_4$, $LiMgPO_4$:VO_4^{3-}, and $NaCaVO_4$. If trivalent rare-earth ions such as Eu^{3+} and Dy^{3+} are incorporated into the YVO_4 host, bright luminescence

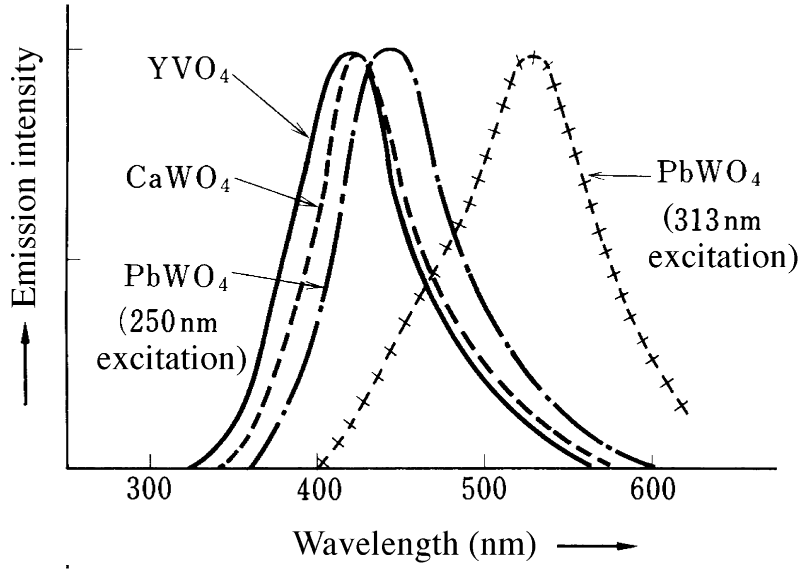

Figure 42 Emission spectra of YVO$_4$ (——), CaWO$_4$ (------), and PbWO$_4$ (—·—·—, +++++) under 250-nm excitation at 77K. Two emission bands of blue and green colors are seen in PbWO$_4$ under 313-nm excitation. (From Blasse, G., *Radiationless Processes*, DiBartolo, B., Ed., Plenum Press, New York, 1980, 287. With permission.)

due to the dopant ions is observed because of efficient energy transfer processes from the vanadate ions (See 5.3.2 and 6.2.1).

3.4.2.4 Luminescence centers of MoO_4^{2-} ion type

Many molybdate phosphors containing MoO_4^{2-} centers are known with a general chemical formula $MMoO_4$ (where $M^{2+} = Ca^{2+}$, Sr^{2+}, Cd^{2+}, Zn^{2+}, Ba^{2+}, Pb^{2+}, etc.). Luminescence properties do not depend significantly on the ion M. In $PbMoO_4$, a green emission band due to the $^3T_1 \rightarrow {}^1A_1$ transition is observed at around 520 nm at low temperatures (77K), as shown in Figure 43.[8] The FWHM of this broad band is about 3300 cm^{-1}. The lifetime is 0.1 ms, shorter than that of VO_4^{3-} compounds. The degree of polarization in luminescence has been measured in some molybdate single crystals as a function of temperatures in the low-temperature region.[9] From these studies, the upper triplet state $^3T_2$ separation has been determined to be $\Delta_2 \approx 550$ cm^{-1}, with the triplet $^3T_1$ being lowest. The decay time from $^3T_2$ to $^1A_1$ is in the 1 to 0.1 μs range.

Orange-to-red luminescence is also observed in some molybdate complexes in addition to the green luminescence. In $CaMoO_4$,[10] for example, green emission appears under UV-light excitation (250–310 nm), but the orange emission at 580 nm is observable only if the excitation light of wavelengths longer than 320 nm is used. Orange emission was thus observed under excitation just below the optical bandgap. The intensity of the orange emission decreases or increases when $CaMoO_4$ is doped with Y^{3+} or Na^+ ions.[2] Therefore, this orange emission is ascribed to lattice defects. In the case of $PbMoO_4$,[8] red emission (centered at 620 nm) is also observed under photoexcitation at 360 nm at room temperature, as shown in Figure 43. Deep-red emission can be seen under 410-nm excitation at 77K. These bands are thought to be due to defect centers of MoO_4^{2-} ions coupled to O^{2-} ion vacancies.

Thermoluminescence of MoO_4^{2-} salts[11] has been investigated to clarify the electronic structure of the defect centers and impurities in these materials. Studies of the luminescence of molybdate compounds containing trivalent rare-earth ions as activators, such as $Gd_2(MoO_4)_3$:Er^{3+} (abbreviated as GMO:Er^{3+}),[12] $Na_5Eu(MoO_4)_4$, and $KLa(MoO_4)_2$:Er^{3+}, have been

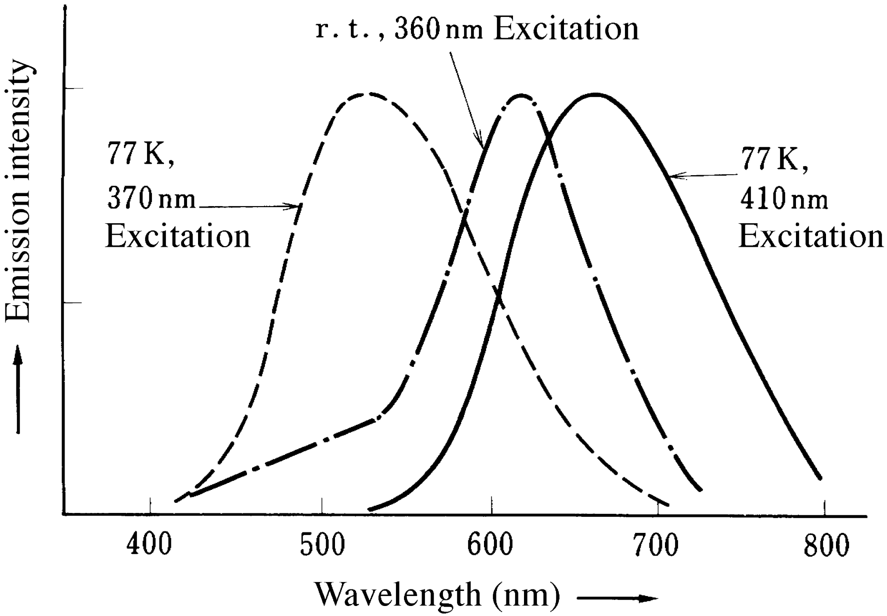

Figure 43 Spectral features of emission from $PbMoO_4$. Orange-to-red emission (—·—·—) is observed at room temperature under photoexcitation at 360 nm. This emission is compared with the deep-red one (——) at 77K under 410-nm excitation and the green one (------) under 370-nm excitation also at 77K. (From Bernhardt, H.J., *Phys. Stat. Sol. (a)*, 91, 643, 1985. With permission.)

reported. Strong, sharp luminescence due to rare-earth ions has been reported in the visible and the near-infrared spectral regions due to efficient energy transfer from the MoO_4^{2-} ion.

3.4.2.5 Luminescence centers of WO_4^{2-} ion type

There are many blue phosphors of interest in the metal tungstate series of complexes having the chemical formula MWO_4 (M^{2+} = alkaline earth metal ion). The splitting Δ_1 of the $^3T_1$ state, shown in Figure 41, is about 20 cm^{-1} for the WO_4^{2-} ion center. The spin-orbit interaction in the MO_4^{n-} ion becomes stronger with increasing atomic numbers of the metal; thus, $VO_4^{3-} < MoO_4^{2-} < WO_4^{2-}$. In order of increasing L-S coupling, the spin-forbidden $^3T_1 \leftrightarrow {}^1A_1$ transition probability is enhanced and the emission lifetime decreases correspondingly. The lifetime of the blue emission from the WO_4^{2-} ion is as short as 10 μs; this is 100 times shorter than that of the VO_4^{3-} ion.

A representative tungstate phosphor is $CaWO_4$; this material emits a bright blue emission in a broad band (centered at 420 nm) with FWHM of about 5000 cm^{-1} (See 5.3.2). The mixed crystal $(Ca,Pb)WO_4$ produces a very strong green emission with high quantum yields reaching 75%.[7] The blue emission spectra of $CaWO_4$ and $PbWO_4$ under 250-nm excitation are shown in Figure 42. In $CaWO_4$, there is a weak emission band at Ý530 nm superimposed on the longer wavelength tail of the blue emission. $PbWO_4$ manifests the presence of the orange band under 313-nm excitation. The orange luminescence was interpreted as being due to impurity ions or to Schottky defects. In decay time measurements of $CaWO_4$,[13] the fast decay component of about 30 μs was found at temperatures between 1.5 and 5.0K, which cannot be explained as being due to the crystal field splitting of the emitting level $^3T_1$. It has also been confirmed by studies of the emission and excitation spectra that only a single, broad blue emission band exists in pure single crystals of $CdWO_4$ and $ZnWO_4$.[14]

$Ba_2WO_3F_4$ has a crystal structure similar to $MgWO_4$ and this structure is considered to be most favorable to realize a high quantum efficiency. This is because a substitution of the F^- ion for O^{2-} seems to reduce the magnitude of the phonon energy and this in turn quenches nonradiative transition processes in the $[WO_3F]^-$ tetrahedron. The emission process was analyzed using the configurational coordinate diagram,[15] and quantum yields of 75% have been reported in this material.[16]

3.4.2.6 Other closed-shell transition metal complex centers

There are other interesting emission centers with closed-shell configurations besides VO_4^{3-}, MoO_4^{2-}, and WO_4^{2-} ions.[2] They form a series of phosphors of the $[MO_4^{n-}]$ type, where $M = Ti^{4+}$, Cr^{6+}, Zr^{4+}, Nb^{5+}, Hf^{4+}, and Ta^{5+}. These complexes have been investigated extensively as possible new media for solid-state lasers.[17] The luminescence spectra from $KVOF_4$, K_2NbOF_5,[18] and SiO_2 glass:Cr^{6+} [19,20] have been reported recently as new complex centers possessing this electronic configuration.

3.4.3 Uranyl complex centers

3.4.3.1 Electronic structure

The uranyl ion is a linear triatomic ion with a chemical formula $[O{=}U{=}O]^{2+}$ ($D_{\infty h}$ symmetry). The strong, sharp line luminescence from this center has been known for more than half a century. Jørgensen and Reisfeld[21] have thoroughly discussed the historical background and theoretical aspects of the luminescence of these centers. The electronic structure of uranyl ions is particularly interesting.

As for the excited states of uranyl ions, first consider the charge-transfer process of an electron from O_2^{4-} to U^{6+}. The resulting U^{5+} ($5f^1$) ion has the following atomic orbitals: σ_u ($5f_0$), π_u ($5f_{\pm 1}$), δ_u ($5f_{\pm 2}$), ϕ_u ($5f_{\pm 3}$). The electronic levels, $^2F_{7/2}$ and $^2F_{5/2}$, consist of several states having total angular momentum $\Omega_1 = 1/2, 3/2, 5/2, 7/2$ in $D_{\infty h}$ symmetry. On the other hand, O_2^{3-} has molecular orbital configurations, ($\pi_u^4\ \sigma_u$) and ($\pi_u^3\ \sigma_u^2$). A combination of these states gives total angular momentum $\Omega_2 = 1/2, 3/2$. From vector coupling of Ω_1 and Ω_2,[21,22] the UO_2^{2+} ion can be expressed as possessing total angular momentum of $\Omega = 0, 1, 2, 3, 4, 5$.[21,22] On the basis of investigations of the polarized absorption and the isotope effects, Denning et al.[23] have determined that the lowest excited state is $\Omega = 1$ ($^1\Pi_g$, $\sigma_u\delta_u$) (σ_u and δ_u stand for the electronic states of O_2^{3-} and the $5f^1$ ion, respectively), as shown in Figure 44. The luminescence of UO_2^{2+} corresponds to a $^1\Pi_g \rightarrow {}^1\Sigma_g^+$ ($D_{\infty h}$) magnetic dipole-allowed transition. More precise molecular orbital calculations[24] and absorption experiments in $Cs_2UO_2Cl_{4-x}Br_x$ mixed crystals[25] confirm the ($\sigma_u\delta_u$) state as the lowest excited state. The states arising from the ($\pi_u^3\ \delta_u$) configuration must be taken into account to consider the higher electronic excited states. Until the nature of the excited electronic state of $\Omega = 1$ ($^1\Pi_g$, $\sigma_u\delta_u$) was finally clarified in 1976, the odd parity state $^1\Gamma_u$ was thought to be the lowest excited state. Therefore, reports on uranyl ions published before 1976 must be read with this reservation in mind. Figure 44 shows assignments and positions (in units of cm^{-1}) of electronic levels of uranyl ions as determined from the absorption spectra of $Cs_2UO_2Cl_4$.[23]

3.4.3.2 Luminescence spectra

A luminescence spectrum from a $Cs_2UO_2Cl_4$ single crystal at 13K, accompanied by vibronic structure due to Morita and Shoki,[26] is shown in Figure 45. The Frank-Condon pattern shows vibronic progressions of the fundamental vibrations, $\nu_s = 837\ cm^{-1}$ and $\nu_{as} = 916\ cm^{-1}$, of the UO_2^{2+} ion. By applying the configurational coordinate model to $Cs_2UO_2Cl_4$, the nuclear displacement ΔQ is estimated to be 0.094 Å for the two potential minima of the $^1E_g(^1\Pi_g)$ excited state and the $^1A_{1g}(^1\Sigma_g^+)$ ground state in D_{4h} ($D_{\infty h}$) symmetry.[26] Emission peaks with symbol * in the figure are due to traps, and these peaks disappear above 20K. The fine structures seen in the vibronic progressions are electric dipole-allowed transitions due to coupling with odd-parity lattice vibrations.

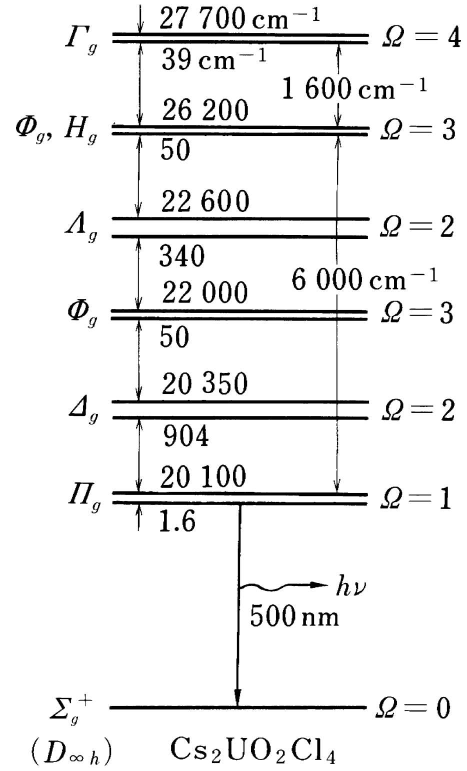

Figure 44 Energy levels and their assignments of UO_2^{2+} ion in $D_{\infty h}$ symmetry. Emission is due to the magnetic dipole-allowed $^1\Pi_g \rightarrow {}^1\Sigma_g^+$ $(D_{\infty h})$ transition. (From Denning, R.G., Snellgrove, T.R., and Woodwark, D.R., *Molec. Phys.*, 32, 419, 1976. With permission.)

Flint and Tanner[27] have investigated the luminescence of various other uranyl complexes, of the series $A_2UO_2Cl_4{\cdot}nH_2O$ (A = Rb^+, Cs^+, K^+, $(CH_3)_4N^+$). They found good agreement between the molecular vibrations observed in the luminescence spectra and those reported in infrared and Raman spectra. Dynamic aspects of luminescence of $[UO_2Cl_4]^{2-}$ phosphors have also proved to be of interest. Krol[28] has investigated the decay of the luminescence of $Cs_2UO_2Cl_4$ at 1.5K under strong laser irradiation and obtained nonexponential decays; these decays are thought to be due to the presence of biexcitons associated with interionic interactions. Localization of excitons has also been reported in $CsUO_2(NO_3)_3$.[29] Excitation energy transfer to traps has been studied in $Cs_2UO_2Br_4$[30] in the temperature range between 1.5 and 25K and compared with a diffusion-limited transfer model. There are additional spectral features in uranyl compounds. For example, optically active single crystals of $NaUO_2(CH_3COO)_3$ exhibit[31] a series of complicated vibronic lines due to the presence of two emission centers, which are resolved by the difference of the degree of circular polarization in luminescence. Decay times of the luminescence of uranyl β-diketonato complexes[32] in liquid solvents have been found to be in the 1 to 500-ns range; the drastic variations are understood in terms of changes in the nonradiative rate constants correlated to the energy position of the zero-phonon emission line.

3.4.4 *Platinum complex ion centers*

Platinum(II) and mixed-valence platinum(II, IV) complex ions have also been investigated extensively. The best known platinum(II) complex is a yellow-green compound, barium tetracynoplatinate (II) $Ba[Pt(CN)_4]{\cdot}4H_2O$ (abbreviated BCP), which possesses a linear chain

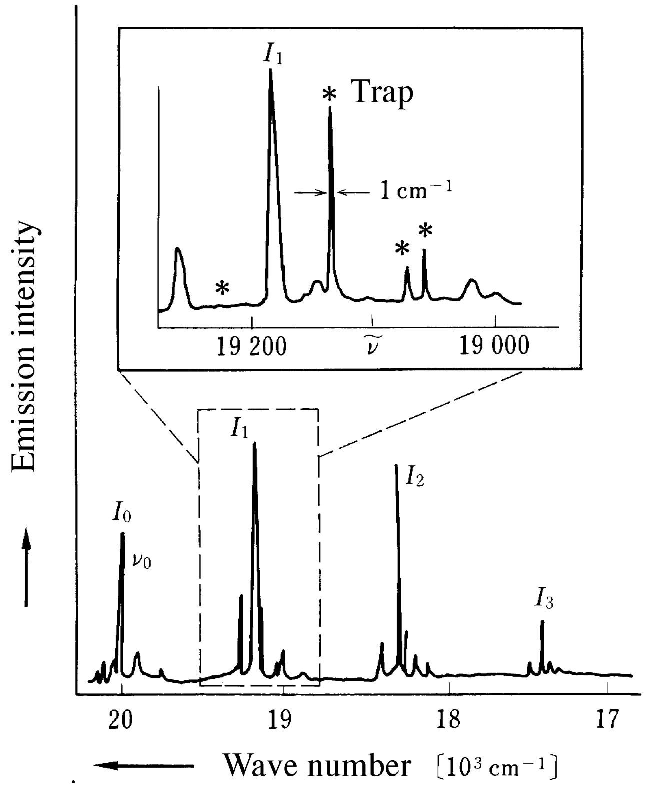

Figure 45 Emission spectra of $Cs_2UO_2Cl_4$ at 13K, showing the vibronic progressions. Inserted figure shows details of vibronic structures and trap centers are denoted by the symbol *. (From Morita, M. and Shoki, T., *J. Luminesc.*, 38/39, 678, 1987 and unpublished results. With permission.)

structure. Mixed-valence complexes such as the bromide-doped potassium tetracyanoplatinate $K_2[Pt(CN)_4]$ $Br_{0.3}\cdot 3H_2O$ (KCP:Br) and Wolfram's red salt (WRS salt), i.e., $[Pt(II)L_4]$ $[Pt(IV)L_4X_2]X_4\cdot 2H_2O$ (L = ethylamine $C_2H_5NH_2$; X = Cl, Br) have also been studied comprehensively. With reference to earlier review articles,[1,33] the electronic structure of one-dimensional platinum(II) complexes is described below and along with the unique spectroscopic character of these complexes.

3.4.4.1 $[Pt(CN)_4]^{2-}$ Complex ions

The very strong green luminescence of the anisotropic platinum(II) complex BCP has been known for more than 65 years. The $[Pt(CN)_4]^{2-}$ ion forms a flat tetragonal plane, with the Pt^{2+} being located in the center; in BCP, the Pt^{2+} forms a linear chain as shown in Figure 46. X-ray diffraction analysis[34] confirms a linear chain structure of planar $[Pt(CN)_4]^{2-}$ along the *c*-axis. Since the Pt^{2+}-to-Pt^{2+} distance in BCP is as short as 0.327 nm, the direct overlap of the $5d_z{}^2$ orbitals is possible. Monreau-Colin[35] has tabulated optical properties of these materials obtained from studies of the reflection, absorption, and emission spectra for a series of platinum complexes of the general form: $M[Pt(CN)_4]\cdot nH_2O$ (where M = Mg^{2+}, Ba^{2+}, Ca^{2+}, $Li_2{}^{2+}$ and $K_2{}^{2+}$). Large spectral shifts of the emission bands are observed with changes in the M ion. It has been established that these shifts are correlated to the Pt^{2+}-to-Pt^{2+} interaction along the one-dimensional platinum(II) chain.

From molecular orbital calculations,[36] 5*d* and 6*p* orbitals of Pt(II) can couple with the π^* orbital of the CN^- ion to form a_{1g} ($5d_z{}^2$) HOMO and $a_{2u}{}^*(6p_z)$ LUMO orbitals. The emission in BCP is due to the $a_{2u}{}^* \rightarrow a_{1g}$ transition in D_{4h} symmetry and shows a strong polarization

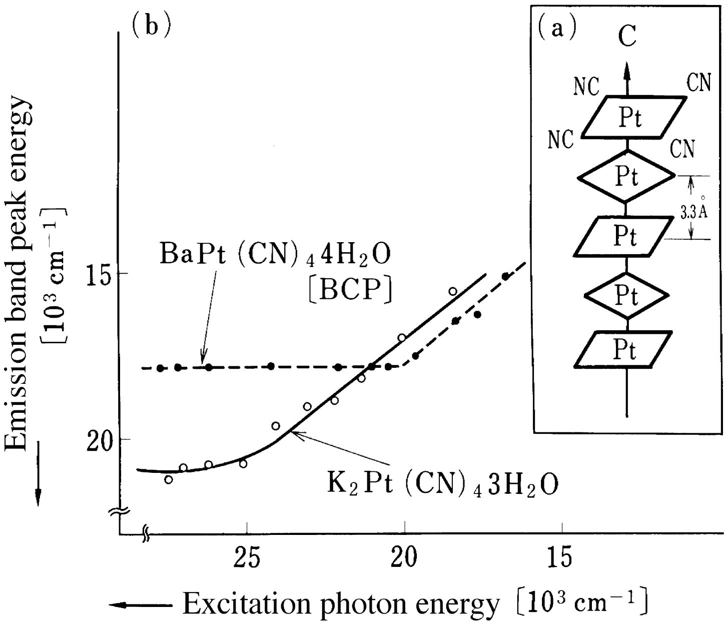

Figure 46 (a) Schematic structure of the one-dimensional platinum(II) complex Ba$[Pt(CN)_4]\cdot 4H_2O$ (BCP). (b) Abnormal shifts of emission band peeks of platinum(II) complexes, BCP (dotted line) and $K_2[Pt(CN)_4]\cdot 3H_2O$ (solid line), with changing excitation photon energy at 4.2K. (From Murata, K. and Morita, M., *Tech. Rep. Seikei Univ.*, 18, 1383, 1974 and unpublished results. With permission.)

dependence along the *c*-axis (Pt^{2+}-Pt^{2+} chain). The room-temperature emission of BCP is centered at 520 nm; the emission shows a large blue shift to 440 nm when Ba^{2+} is replaced by K^+. The emission process is interpreted as being due to Frenkel excitons.[37] This is because the position of the emission band shows a red shift proportional to R^{-3}, where R is the Pt-Pt distance and is a function of ionic radius of the M ion. The emission band position of BCP at 4.2K shifts continuously to lower energies as the wavelength of the excitation light is varied from the ultraviolet to visible spectral region.[38] Figure 46 shows this phenomenon, one that cannot be interpreted by present theoretical understanding. This effect is likely related to the dynamic relaxation of excitons in one-dimensional platinum(II) chains.

3.4.4.2 *Other platinum complex ions*

There are many additional luminescent materials containing $[Pt(CN)_4]^{2-}$ complexes besides those mentioned above. Luminescence of $[Pt(CN)_4]^{2-}$ is observed in mixed crystals[39] of $K_2[Pt(CN)]_6$:$K_2[Pt(CN)_4]$ (1:1) under nitrogen laser excitation arising from intervalence transitions between Pt(IV) and Pt(II) ions. When the Ba ion in BCP is replaced by rare-earth(III) ions, new complexes $Ln_2[Pt(CN)_4]_3\cdot nH_2O$ (Ln = Eu^{3+}, Sm^{3+}, Er^{3+}, etc.) can be formed.[33] Sharp line luminescence of Ln(III) ions is normally observed in these materials due to energy transfer from the $[Pt(CN)_4]^{2-}$ complex. Extensive investigations have been conducted at low temperature using high pressure and strong magnetic fields.[33,40]

A mixed-valence platinum complex is KCP:Br, with a valency equal to 2.3. This compound is metallic in appearance and does not fluoresce. A typical example of a luminescent mixed complex is the WRS salt mentioned previously; it contains Pt(II) and Pt(IV) ions. The structure of the WRS salt consists of an alternative stack of a tetragonal plane unit $[Pt(II)L_4]$ and an octahedral unit with six coordination atoms $[Pt(IV)L_4X_2]$. These units form a quasi-one-dimensional linear chain of [X-Pt(IV)-X--Pt(II)--X] bridged by halogens. The

WRS complex has been known since the late 19th century; it was determined by Day[37] to be a typical low-dimensional compound. Tanino and Kobayashi[41] first reported resonance Raman scattering and NIR luminescence at about 1 μm in WRS salts at 4.2K. A similar mixed-valence complex, $[Pt(en)_2][Pt(en)_2I_2](ClO_4)_4$ (en = $NH_2CH_2CH_2NH_2$), was found to show a luminescence band at 1 μm, with a lifetime of about 200 ps at 2K.[42] The origin of this luminescence band is ascribed to self-trapped-excitonic (STE) states.[42]

3.4.5 *Other complex ion centers*

3.4.5.1 *WO_6^{6-} Ion*

In Bi_2WO_6,[43] the emission center is identifiable as WO_6^{6-} in a cubic crystal field. Red emission is observed at 4.2K, with a peak at 600 nm and a FWHM of about 1500 cm^{-1}. The excitation spectrum consists of a band at 390 nm with an apparent Stokes' shift of 9000 cm^{-1}. According to self-consistent field molecular orbital calculations,[44] the emitting levels in WO_6^{6-} are due to two $^3T_{1u}$ states. By employing Figure 41, the emission and absorption can be assigned to $^3T_{1u} \rightarrow A_{1g}$ and $^1T_{1u} \leftrightarrow {}^1A_{1g}$ transitions, respectively. Emission centers of the WO_6^{6-} ion were also reported in many compounds with the perovskite structure A_2BWO_6 (A = Ca^{2+}, Sr^{2+}, Ba^{2+}; B = Mg^{2+}, Ca^{2+}, Sr^{2+}, Ba^{2+}). Wolf and Kammler-Sack[45] reported infrared emission of rare-earth ions incorporated into a very complicated compound 18R-$Ba_6Bi_2W_3O_{18}$. In this case, there are three WO_6^{6-} ion sites in the compound with an hexagonal closed-packed polymorphic structure. The emission spectra consist of two bands at 21700 and 17000 cm^{-1} due to two 6c sites and one 3a site, respectively. The corresponding excitation bands are at 36000 cm^{-1} (6c) and 29000 cm^{-1} (3a), respectively. The luminescence of WO_6^{6-} ions can also be seen in other materials such as Li_6WO_6, 12R-$Ba_2La_2MgW_2O_{12}$, and $Ca_3La_2W_2O_{12}$.

3.4.5.2 *Perspective of other interesting centers*

The above-mentioned WO_6^{6-} luminescence center is one of the closed-shell transition metal complex ions, generally expressed as $[MO_6]^{n-}$ (where M = Ti, Mo, Nb, Zr, Ta, and W). Two papers[2,46] on the luminescence properties of MoO_4^{2-} and MoO_6^{6-} complexes have been published. Recently, luminescence from a europium octamolybdate polymer, $Eu_2(H_2O)_{12}[Mo_8O_{27}]$ $6H_2O$[47] and the picosecond decay of the transient absorbance of $[W_{10}O_{32}]^{4-}$ in acetonitrile[48] have been reported. The luminescence of uranate (UO_6^{6-}) centers in solids have been reviewed by Bleijenberg.[49]

Thus far, this discussion of luminescence centers of complex ions focused on practical phosphors. However, under the category of complex ions, a more general survey is possible. Complex compounds consist of a central metal ion and surrounding anions or organic ligands. In these compounds, there are—in principle—four possible luminescence processes that originate from the central metal ion, from the ligand, from ligand-to-metal charge-transfer (LMCT), and from metal-to-ligand charge-transfer (MLCT) transitions. Due to these different transition processes, the luminescence from complex ions can either be sharp or broad, and can occur in a broad spectral region. Uranyl complexes luminescing of green-yellow color are examples of central metal ion transitions. Eu(III) β-diketonato complex, a typical NMR shift reagent, also shows bright and sharp red luminescence due to the central Eu(III) ion. For more than half a century, the luminescence of the Zinc(II) 8-hydroxyquinolinato complex has been shown to be due to the aromatic organic ligands. Emission transitions due to the LMCT scheme is found in scheelite compounds. Phosphorescence due to MLCT transitions is predominant in complexes such as ruthenium(II) tris-bipyridyl ($[Ru(bpy)_3]^{2+}$), metal-phthalocyanines (e.g., Cu-Pc, a famous pigment), and metalloporphyrins (e.g., Mg-TPP). The latter two complexes are usually considered as organic phosphors because of 16-membered π-ring structures.

In the future, one will be able to design new phosphors of complex ion types that can be excited by various excitation sources such as high electron beams, X-ray lasers, and NIR-laser diodes. Phosphors of complex ions will continue to play a useful role in luminescence applications.

References

1. Morita, M., MoO_4^{2-}, WO_4^{2-} compounds, and one-dimensional compounds, in *Hikaribussei Handbook (Handbook of Optical Properties of Solids)*, Shionoya, S., Toyozawa, Y., Koda, T., and Kukimoto, H., Eds., Asakura Shoten, Tokyo, 1984, chap. 2. 12. 6 and 2. 19. 2. (in Japanese).
2. Blasse, G., *Structure and Bonding*, 42, 1, 1980.
3. Ballhausen, C.J. and Liehr, A.D., *J. Mol. Spectrosc.*, 4, 190, 1960.
4. Ziegler, T., Rank, A., and Baerends, E.J., *Chem. Phys.*, 16, 209, 1976.
5. Kebabcioglu, R. and Mueller, A., *Chem. Phys. Lett.*, 8, 59, 1971.
6. Koepke, C., Wojtowica, A.J., and Lempicki, A., *J. Luminesc.*, 54, 345, 1993.
7. Blasse, G., Radiationless processes in luminescent materials, in *Radiationless Processes*, DiBartolo, B., Ed., Plenum Press, New York, 1980, 287.
8. Bernhardt, H.J., *Phys. Stat. Sol.(a)*, 91, 643, 1985.
9. Rent, E.G., *Opt. Spectrosc. (USSR)*, 57, 90, 1985.
10. Groenink, J.A., Hakfoort, C., and Blasse, G., *Phys. Stat. Sol.(a)*, 54, 329, 1979.
11. Böhm, M., Erb, O., and Scharman, A., *J. Luminesc.*, 33, 315, 1985.
12. Herren, M. and Morita, M., *J. Luminesc.*, 66/67, 268, 1996.
13. Blasse, G. and Bokkers, G., *J. Solid. State. Chem.*, 49, 126, 1983.
14. Shirakawa, Y., Takahara, T., and Nishimura, T., *Tech. Digest, Phosphor Res. Soc. Meeting*, 206, 15, 1985.
15. Tews, W., Herzog, G., and Roth, I., *Z. Phys. Chem. Leipzig*, 266, 989, 1985.
16. Blasse, G., Verhaar, H.C.G., Lammers, M.J.J., Wingelfeld, G., Hoppe, R., and De Maayer, P., *J. Luminesc.*, 29, 497, 1984.
17. Koepke, C., Wojtowicz, A.J., and Lempicki, A., *IEEE J. Quant. Elec.*, 31, 1554, 1995.
18. Hazenkamp, M.F., Strijbosch, A.W.P.M., and Blasse, G., *J. Solid State Chem.*, 97, 115, 1992.
19. Herren, M., Nishiuchi, H., and Morita, M., *J. Chem. Phys.*, 101, 4461, 1994.
20. Herren, M., Yamanaka, K., and Morita, M., *Tech. Rep. Seikei Univ.*, 32, 61, 1995.
21. Jørgensen, C.K. and Reisfeld, R., *Structure and Bonding*, 50, 122, 1982.
22. Denning, R.G., Foster, D.N.P., Snellgrove, T.R., and Woodwark, D.R., *Molec. Phys.*, 37, 1089 and 1109, 1979.
23. Denning, R.G., Snellgrove, T.R., and Woodwark, D.R., *Molec. Phys.*, 32, 419, 1976.
24. Dekock, R.L., Baerends, E.J., Boerrigter, P.M., and Snijders, J.G., *Chem. Phys. Lett.*, 105, 308, 1984.
25. Denning, R.G., Norris, J.O.W., and Laing, P.J., *Molec. Phys.*, 54, 713, 1985.
26. Morita, M. and Shoki, T., *J. Luminesc.*, 38/39, 678, 1987 and unpublished results.
27. Flint, S.D. and Tanner, P.A., *Molec. Phys.*, 44, 411, 1981.
28. Krol, D.M., *Chem. Phys. Lett.*, 74, 515, 1980.
29. Thorne, J.R.G. and Denning, R.G., *Molec. Phys.*, 54, 701, 1985.
30. Krol, D.M. and Roos, A., *Phys. Rev.*, 23, 2135, 1981.
31. Murata, K. and Morita, M., *J. Luminesc.*, 29, 381, 1984.
32. Yayamura, T., Iwata, S., Iwamura, S., and Tomiyasu, H., *J. Chem. Soc. Faraday Trans.*, 90, 3253, 1994.
33. Gliemann, G. and Yersin, H., *Structure and Bonding*, 62, 89, 1985.
34. Krogmann, K., *Angew. Chem.*, 81, 10, 1969.
35. Monreau-Colin, M.L., *Structure and Bonding*, 10, 167, 1972.
36. Moncuit, S. and Poulet, H., *J. Phys. Radium*, 23, 353, 1962.
37. Day, P., Collective states in single and mixed valence metal chain compounds, in *Chemistry and Physics of One-Dimensional Metals*, Keller, H.J., Ed., NATO-ASI Series B25, Plenum Press, New York, 1976, 197.
38. Murata, K. and Morita, M., *Tech. Rep. Seikei Univ.*, 18, 1383, 1974 and unpublished results.

39. Wiswarath, A.K., Smith, W.L., and Patterson, H.H., *Chem. Phys. Lett.*, 87, 612, 1982.
40. Yersin, H. and Stock, M., *J. Chem. Phys.*, 76, 2136, 1982.
41. Tanino, H. and Kobayashi, K., *J. Phys. Soc. Japan*, 52, 1446, 1983.
42. Wada, Y., Lemmer, U., Göbel, E.O., Yamashita, N., and Toriumi, K., *Phys. Rev.*, 55, 8276, 1995.
43. Blasse, G. and Dirkson, G.J., *Chem. Phys. Lett.*, 85, 150, 1982.
44. Van Oosternhout, A.B., *J. Chem. Phys.*, 67, 2412, 1977.
45. Wolf, D. and Kemmler-Sack, S., *Phys. Stat. Sol. (a)*, 86, 685, 1984.
46. Wiegel, K. and Blasse, G., *J. Solid State Chem.*, 99, 388, 1992.
47. Yamase, T. and Naruke, H., *J. Chem. Soc. Dalton Trans.*, 1991, 285.
48. Duncan, D.C., Netzel, T.L., and Hill, C.L., *Inorg. Chem.*, 34, 4640, 1995.
49. Bleijenberg, K.C., *Structure and Bonding*, 50, 97, 1983.

chapter three — section five

Principal phosphor materials and their optical properties

Shigeo Shionoya

Contents

3.5 Ia-VIIb compounds 227
  3.5.1 Introduction 227
  3.5.2 Intrinsic optical properties 228
    3.5.2.1 Band structure and exciton 228
    3.5.2.2 Self-trapping of excitons and intrinsic luminescence 228
  3.5.3 Color centers 228
  3.5.4 Luminescence centers of ns^2-type ions 229
  3.5.5 Luminescence of isoelectronic traps 230
References 230

3.5 Ia-VIIb compounds

3.5.1 Introduction

Ia-VIIb compounds—that is, alkali halides—are prototypical colorless ionic crystals. Their crystal structure is of the rock-salt type except for three compounds (CsCl, CsBr, and CsI) that possess the cesium chloride structure. Melting points are generally in the 620–990°C range, which is relatively low.

Research on the luminescence of alkali halides has a long history. Since the 1920s, luminescence studies on ns^2-type (Tl^+-type) ions incorporated in alkali halides have been actively pursued (See 3.1). In the basic studies of those early days, alkali halides were used as hosts for various luminescence centers, because as nearly ideal ionic crystals theoretical treatments of the observations were possible. Since the 1940s, the optical spectroscopy, including luminescence of color centers, has become an active area of study. It was discovered in the late 1950s that excitons in pure alkali halides are self-trapped and can themselves produce luminescence.

Although alkali halides are important from the point of view of basic research as mentioned above, their luminescence is rarely utilized in practical applications. This is because alkali halides are water soluble and have low melting points, so that they are unsuitable as hosts of practical phosphors. Alkali halide phosphors presently in common use include NaI:Tl$^+$ and CsI:Na$^+$ only as discussed below.

3.5.2 *Intrinsic optical properties*

3.5.2.1 *Band structure and exciton*

All alkali halides have band structures of the direct transition type. Both the bottom of the conduction band and the top of the valence band are located at the k = 0 point (Γ point) in **k**-space. The bandgap energies E_g are as follows. The largest is 13.6 eV for LiF, and the smallest is 6.30 eV for KI, with RbI and CsI having almost the same value. For NaCl, a representative alkali halide, E_g is 8.77 eV. E_g decreases with increasing atomic number of the cations or anions making up the alkali halides.

A little below the fundamental absorption edge, sharp absorption lines due to excitons are observed. The valence band is composed of *p* electrons of the halogen ions, and it is split into two compounds, with the inner quantum numbers representing total angular momentum j = 3/2 and 1/2. Corresponding to this splitting, two sharp exciton absorption lines are observed. The binding energy of excitons is 1.5 eV (NaF) at its largest and 0.28 eV (NaI) at its smallest; it is 0.81 eV in NaCl.

3.5.2.2 *Self-trapping of excitons and intrinsic luminescence*[1]

Excitons in all alkali halides except iodides do not move around in the crystal, unlike excitons in IIb-VIb and IIIb-Vb compounds; these excitons are self-trapped immediately after their creation as a result of very strong electron-lattice coupling. Self-trapped excitons emit luminescence called *intrinsic luminescence*. In iodides, excitons can move freely for some distance before becoming self-trapped and emitting their intrinsic luminescence.

Before discussing the self-trapping of excitons, let us consider the self-trapping of positive holes. In alkali halides, holes do not move freely, but are self-trapped and form V_K centers. As shown in Figure 47, the V_K center is a state in which two nearest-neighbor anions are attracted to each other by trapping a positive hole between them, so that it takes the form of a molecular ion denoted as X_2^-. The self-trapped exciton is a state in which an additional electron is trapped by the V_K center.

The spectral position of the intrinsic luminescence is shifted considerably toward lower energies from the exciton absorption. This is because an exciton undergoes a large lattice relaxation, emitting phonons to reach a self-trapped state. Emission spectra are composed of two broad bands in most cases. The luminescence of the short-wavelength band, called σ-luminescence, is polarized parallel, while that of the long-wavelength band, called π-luminescence, is polarized perpendicular to the molecular axis of V_K centers. In NaCl, the peaks of these two types of luminescence are σ: 5.47 eV and π: 3.47 eV. σ-luminescence is due to an allowed transition from the singlet excited state, while π-luminescence is due to a forbidden transition from the triplet excited state. As a result, the decay time of the former is short (about 10 ns), while that of the latter is relatively long (about 100 μs).

3.5.3 *Color centers*[2]

In alkali halides, lattice defects that trap an electron or a hole have absorption bands in the visible region, and hence color the host crystals. Therefore, such defects are called *color centers*. Figure 47(a) illustrates the principal electron-trapping centers F, F_A, F′, M, and M′. Principal hole-trapping centers V_K, V_{KA}, H, and H_A are illustrated in Figure 47(b). Most of color centers emit luminescence. The F center has an electronic energy structure analogous to the hydrogen atom. It shows strong absorption and emission due to the *s* ↔ *p* transition.

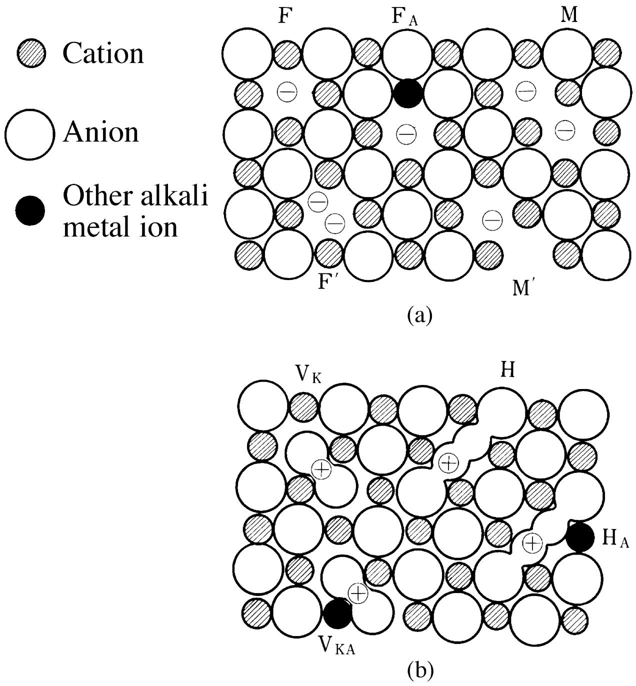

Figure 47 (a) Principal electron trapping centers and (b) principal positive hole trapping centers in alkali halides.

In NaCl, the absorption is at 2.75 eV and the emission at 0.98 eV. Alkali halide crystals containing some kind of color centers, typically an F_A center, are used as materials for tunable solid-state lasers operating in the near-infrared region (See 13).

3.5.4 *Luminescence centers of ns^2-type ions*

For some time, n*s*^{2}-type (Tl^+-type) ion centers in alkali halides have been investigated in detail from both experimental and theoretical points of view as being a typical example of an impurity center in ionic crystals (See 3.1). Almost all n*s*^{2}-type ions, i.e., Ga^+, In^+, Sn^{2+}, Pb^{2+}, Sb^{3+}, Bi^{3+}, Cu^-, Ag^-, and Au^-, have been studied; Tl^+ has been studied in significant detail. For these ion centers, the absorption and emission due to the $s^2 \leftrightarrow sp$ transition, their spectral shapes, the polarization correlation between the absorption and the emission, and the dynamical Jahn-Teller effect in excited states due to electron-lattice interactions have been investigated thoroughly. The range of phenomena have been well elucidated in the literature and are an example of the remarkable contributions that optical spectroscopic studies have made to our understanding of impurity centers.

However, the luminescence in alkali halides is almost worthless from a practical point of view of application, so that further detailed description will not be provided here. The only example of practical use of these materials is $NaI:Tl^+$ and $CsI:Tl^+$ single-crystal phosphors (near-ultraviolet to blue emitting), which have been used as scintillators (See 7.3). For alkali halides such as NaI and CsI, it is easy to grow large single crystals so that they are suitable for these applications in particle and high-energy radiation detection.

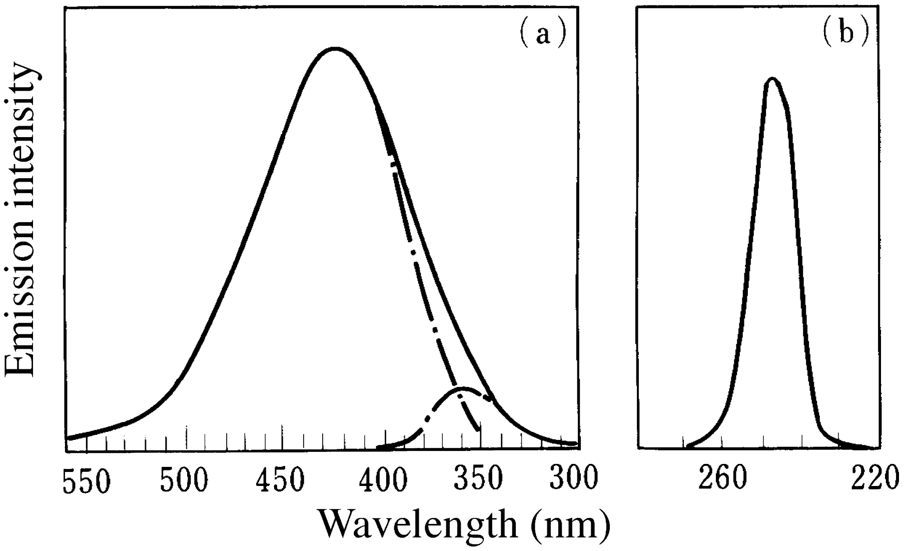

Figure 48 (a) Emission spectrum (300K) and (b) excitation spectrum of CsI:Na$^+$. (From Hsu, O.L. and Bates, C.W., *Phys. Rev.*, B15, 5821, 1977. With permission.)

3.5.5 Luminescence of isoelectronic traps

An example of an isoelectronic trap (See 2.4.4) showing luminescence is CsI:Na$^+$. It emits blue luminescence with high efficiency when excited by high-energy radiation.[3] Presently, CsI:Na$^+$ films prepared by a vapor deposition method are used for X-ray image intensifiers (See 7.4). The concentration of Na$^+$ is very low, 6 ppm being the optimum value.

Emission and excitation spectra of CsI:Na$^+$ are shown in Figure 48.[4] The peak of the excitation spectrum agrees well with the calculated value of an exciton bound to an isoelectronic trap Na$^+$. The luminescence is considered to arise from the relaxed exciton state of this bound exciton, which is assumed to be a V_{KA} center trapping an electron. If so, the luminescence should be polarized parallel or perpendicular to the molecular axis of the V_{KA} center. However, no polarization was observed in experiments, leaving the structure of the emitting state undetermined as yet.

References

1. Review articles:
   (a) Song, K.S. and Williams, R.T., *Self-Trapped Excitons*, (Springer Series in Solid-State Sciences 105), Springer-Verlag, Berlin, 1993.
   (b) Kan'no K., Tanaka, K., and Hayashi, T., *Rev. Solid State Sci.*, 4(2/3), 383, 1990.
2. Review articles:
   (a) Schulman, J.H. and Compton, W.D., *Color Centers in Solids*, Pergamon Press, Oxford, 1963.
   (b) Fowler, W.B., Ed., *Physics of Color Centers*, Academic Press, New York, 1968.
3. Brinckmann, P., *Phys. Lett.*, 15, 305, 1965.
4. Hsu, O.L. and Bates, C.W., *Phys. Rev.*, B15, 5821, 1977.

chapter three — section six

Principal phosphor materials and their optical properties

Hajime Yamamoto

Contents

3.6 IIa-VIb compounds 231
- 3.6.1 Introduction 231
- 3.6.2 Fundamental physical properties 232
  - 3.6.2.1 Crystal structures 232
  - 3.6.2.2 Band structures 233
  - 3.6.2.3 Phonon energies and dielectric constants 234
- 3.6.3 Overview of activators 234
- 3.6.4 Typical examples of applications 238
  - 3.6.4.1 Storage and stimulation 238
  - 3.6.4.2 Cathode-ray tubes 239
  - 3.6.4.3 Electroluminescence (EL) 240
- 3.6.5 Host excitation process of luminescence 241
- 3.6.6 Preparation methods of phosphors 242
  - 3.6.6.1 Sulfides 242
  - 3.6.6.2. Selenides 244

References 244

3.6 IIa-VIb compounds

3.6.1 Introduction

Phosphors based on alkaline earth chalcogenides, mostly sulfides or selenides, are one of the oldest classes of phosphors. Many investigations were made on these phosphors from the end of 19th century to the beginning of 20th century, particularly by Lenard and co-workers as can be seen in Reference 1. For this reason, these phosphors are still called *Lenard phosphors*.

Even with their long history, progress in understanding the fundamental physical properties for these phosphors has been quite slow. There are good reasons for this: these materials are hygroscopic and produce toxic H_2S or H_2Se when placed in contact

Table 13 The Lattice Constant, Dielectric Constants, and Phonon Frequencies of IIa-VIb Compounds[17]

Compounds	Lattice constant (nm)	Dielectric constants		Phonon frequency (cm^{-1})	
		ε_0	ε_∞	ω_{TO}	ω_{LO}
MgO[a]	0.4204	9.64	2.94[d]	401	725
CaO	0.4812	11.1[b], 11.6[c]	3.33[b], 3.27[c]	295[b], 311[c]	577[b], 585[c]
CaS	0.5697	9.3	4.15[d]	229	342
CaSe	0.5927	7.8	4.52[d]	168	220
SrO	0.5160	13.1[b], 14.7[c]	3.46[d]	231[b], 229[c]	487[b], 472[c]
SrS	0.6019	9.4	4.06[d]	185	282
SrSe	0.6237	8.5	4.24[d]	141	201
BaO	0.5524	32.8[c]	3.61[b], 3.56[d]	146[c]	440[c]
BaS	0.6384	11.3	4.21[d]	150	246
BaSe	0.6600	10.7	4.41[d]	100	156

Note: The notation ε_0 and ε_∞ indicate static and optical dielectric constant, and ω_{TO} and ω_{LO} the frequency of the transverse and longitudinal optical phonon, respectively.

[a] From Reference 18.

[b] From Reference 19.

[c] From Reference 20.

[d] From Reference 21.

with moisture. Further, their luminescence properties are sensitive to impurities and nonstoichiometry. Such problems make it difficult to obtain controlled reproducibility in performance when technologies for ambiance control and material purification were insufficient.

In the 1930s and 1940s, research on this family of materials was carried out actively to meet demands for military uses, mostly for the detection of infrared light by the photostimulation effect. After this period, these materials were ignored for many years, until around 1970 when Lehmann[2–6] demonstrated that the alkaline earth chalcogenides could be synthesized reproducibly. He also showed that an exceptionally large number of activators can be introduced into CaS, many of which exhibit high luminescence efficiency. He showed that these features of CaS phosphors were attractive to applications and seem to compensate for the drawback caused by their hygroscopic nature. Accordingly, Lehmann's work revived research interest in these materials and this activity has continued through the years.

In the 1980s, some attempts were made to apply CaS phosphors to CRTs.[7–10] Also in this period, single crystals were grown for many of the IIa-VIb compounds.[11–12] The band structure was investigated and the basic optical parameters were obtained in these single crystals.[11–14,17]

3.6.2 Fundamental physical properties

3.6.2.1 Crystal structures

Most of the IIa-VIb family have NaCl-type structures, except for MgTe, which crystallizes in the zinc-blende structure, and BeO, which favors the wurtzite lattice.[15] The lattice parameters are shown in Table 13.

The compounds in the NaCl-type structure can form solid solutions in a wide range of composition. As a consequence, the emission color can be varied by changing the host composition as well as the activator species and concentration. Such diversity is one of the advantageous features of the IIa-VIb compounds.

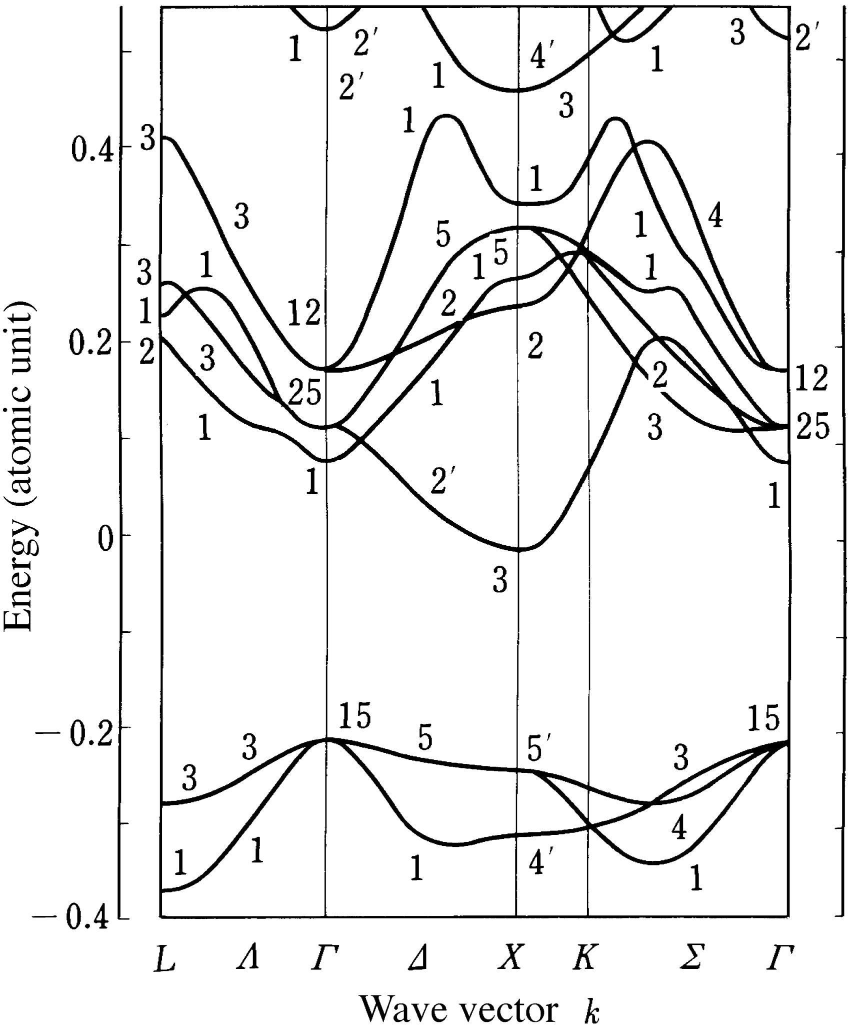

Figure 49 The band structure of SrS calculated by the self-consistent APW (augmented plane wave) method. The energy scale is shown by the atomic unit (= Rydberg constant × 2 = 13.6 × 2 eV). Note that energy values obtained in the figure (e.g., bandgap energies) do not necessarily agree with experimentally obtained values. (From Hasegawa, A. and Yanase, A., *J. Phys. C*, 13, 1995, 1980. With permission.)

3.6.2.2 Band structure

The band structure calculated for SrS is shown by Figure 49.[16] The first thing one should notice is that the absorption edge is of the indirect transition type,[13,16] with the valence band maximum at the *Γ* point (**k** = 000), and the conduction band minimum at the *X* point (**k** = 100). However, the optical transition corresponding to this edge is forbidden because phonons having the momentum and parity required to induce a phonon-assisted direct transition are not available in the NaCl-type structure. The lowest direct transition occurs at the *X* point of the valence band and not at the *Γ* point.

In SrS, the conduction band is composed mainly of 5*s* and 4*d* orbitals of the Sr atom, and the *Γ* point has mainly 5*s* character while the *X* point possesses 4*d* character. The 5*s* and 4*d* orbitals are close to each other in energy, allowing the *X* point to be located at lower energy than the *Γ* point when the SrS crystal is formed. The same feature is also

Table 14 The Observed Bandgap Energies of IIa-VIb Compounds (in eV)

Compound	Bandgap energies at 2K[a]			Absorption edge at 300K[c]
	$E_g(X_c - \Gamma_v)$[b]	Gap at X point	Gap at Γ point	
CaO	—	6.875	—	—
CaS	4.434	5.343	5.80	4.20
CaSe	3.85	4.898	—	—
SrO	—	5.793	6.08	—
SrS	4.32	4.831	5.387	4.12
SrSe	3.813	4.475	4.570	3.73
BaO	—	3.985	8.3	—
BaS	3.806	3.941	5.229	3.49
BaSe	3.421	3.658	4.556	3.20

[a] Data from Kaneko, Y. and Koda, T., *J. Crystal Growth*, 86, 72, 1988.

[b] The gap between X point in the conduction band and Γ point in the valence band.

[c] Data from Morimoto, K., Masters Thesis, The University of Tokyo, 1982 (in Japanese).

found in Ca and Ba chalcogenides. In contrast to this, Mg atoms have $3d$ orbitals that lie some 40 eV higher than $3s$; as a consequence, MgO has a direct bandgap. The bandgap energies measured at 2K[13] and the absorption edge energies at 300K[17] for IIa-VIb compounds are shown in Table 14. The exciton binding energies of about 40 to 70 meV are obtained at Γ point.[13]

The spectral shape of optical absorption near the edge follows Urbach's rule quite well.[13,22] That is, the absorption coefficient α is expressed as a function of photon energy E by the following formula.

$$\alpha(E) = \alpha_0 \exp\left\{-\sigma(E_0 - E)/kT\right\} \tag{28}$$

where α_0, σ, and E_0 are material constants. For SrS, $\alpha_0 = 4 \times 10^7$ cm^{-1}, $\sigma = 1.07$, and $E_0 = 4.6$ eV, which is nearly equal to the lowest exciton energy at the X point.[12] This fact indicates that the absorption tail at room temperature appears as a result of interaction between excitons and phonons at the X point. The absorption edge due to the forbidden indirect transition is masked by the absorption tail of the direct transition. At sufficiently low temperatures, however, the indirect absorption appears and reveals a spectral shape characterized by $\alpha \propto (E_0 - E)^2$.

3.6.2.3 *Phonon energies and dielectric constants*

The dielectric constants and optical phonon energies obtained from infrared reflection spectra of single crystals[11] are given in Table 13.

3.6.3 *Overview of activators*

Activators that can be introduced into CaS and their main luminescence properties are summarized in Tables 15 and 16.[4] Elements not appearing in these tables were found to be nonluminescent.[4] However, radioactive elements except for U and Th, the platinum-group elements, and Hg and Tl have not been examined. As for the description of luminescence properties, it is noted that the tables present only typical examples since the luminescence spectra and decay characteristics depend on the activator concentration.

As an example of the activators listed in Table 15, the luminescence and absorption spectra of Bi^{3+} in CaS due to $6s^2 \rightarrow 6s6p$ transitions are shown in Figure 50.[6]

Table 15 Activators and Coactivators in CaS and Luminescence Properties

Activators	Coactivators[a]	Luminescence color	Luminescence spectrum[b]	Peak (eV)	Type of decay curve	Decay time constant[c]
O	Nothing	Bluish-green	Band	2.53	Exponential	6.5 µs
P	**Cl**, Br	Yellow	Band	2.13	Hyperbolic	~500 µs
Sc	**Cl**, Br, Li	Yellowish-green	Band	2.18	—	—
Mn	Nothing	Yellow	Narrow band	2.10	Exponential	4 ms
Ni	Cu, Ag	Red to IR	Broad band	—	—	—
Cu	**F**, **Li**, **Na**, Rb, P, Y, As	Violet to blue	Two bands	2.10	Hyperbolic	50 µs
Ga	Nothing, or Cu, Ag	Orange, red, and yellow	Broad band	—	—	—
As	F, Cl, Br	Yellowish-orange	Band	2.00	—	—
Y	F, **Cl**, Br	Bluish-white	Broad band	2.8	Hyperbolic	~200 µs
Ag	Cl, Br, Li, Na	Violet	Band	—	Hyperbolic	~1 ms
Cd	Nothing	UV to IR	Very broad band	—	—	—
In	Na, K	Orange	Broad band	—	—	—
Sn	**F**, Cl, Br	Green	Band	2.3	Hyperbolic	~500 µs
Sb	Nothing, or **Li**, **Na**, K	Yellowish-green	Band	2.27	Exponential	0.8 µs
La	Cl, Br, I	Bluish-white	Broad band	2.55	Hyperbolic	~200 µs
Au	Li, K, Cl, I	Blue to bluish-green	Two bands	—	Hyperbolic	~10 µs
Pb	**F**, **Cl**, **Br**, I, P, As, Li	UV	Narrow band	3.40	Hyperbolic	~1 µs
Bi	**Li**, **Na**, **K**, Rb	Blue	Narrow band	2.77	Hyperbolic	~1 µs

Note: The rare-earth elements are listed in Table 16.

[a] Efficient co-activators are shown in bold letters.

[b] A spectrum changes depending on a co-activator.

[c] The period when the luminescence intensity falls to 1/e times the initial value.

From Lehmann, W., *J. Luminesc.*, 5, 87, 1972. With permission.

Table 16 Rare Earth Activators in CaS and Luminescence Properties

Ion	Luminescence color	Luminescence spectrum	Type of decay curve	Decay time constant[b]
Ce^{3+}	Green	Two bands, peaked at 2.10, 2.37 eV	Hyperbolic	~1 μs
Pr^{3+}	Pink to green	Lines, green, red, and IR	Green: exponential	260 μs
(Nd^{3+})[a]	—		—	—
Sm^{3+}	Yellow	Lines, yellow, red, and IR	Yellow: exponential	5 μs
Sm^{2+}	Deep red (low temperature)	Lines, green, red, and IR	—	—
Eu^{2+}	Red	Narrow band, peaked at 1.90 eV	Hyperbolic	~1 μs
Gd^{3+}	—	Lines, UV	Exponential	1.5 ms
Tb^{3+}	Green	Lines, UV to red	Green: exponential	1.8 ms
Dy^{3+}	Yellow & bluish-green	Lines, yellow, bluish-green, and IR	Yellow: $(1+t/\tau)^{-1}$	150 μs
Ho^{3+}	Greenish-white	Lines, blue to IR	Green: $(1+t/\tau)^{-1}$	150 μs
Er^{3+}	Green	Lines, UV, green, and IR	Green: $(1+t/\tau)^{-1}$	370 μs
Tm^{3+}	Blue with some red	Lines, blue and red	Blue: exponential	1.05 ms
Yb^{3+}	—	Lines, IR	—	—
Yb^{2+}	Deep red	Band, peaked at 1.66 eV	Hyperbolic	~10 μs

[a] Luminescence of Nd^{3+} is not identified.

[b] The period when the luminescence intensity falls to 1/e times the initial value. For the type expressed by $(1+t/\tau)^{-1}$, the time constant means τ.

From Lehmann, W., *J. Luminesc.*, 5, 87, 1972. With permission.

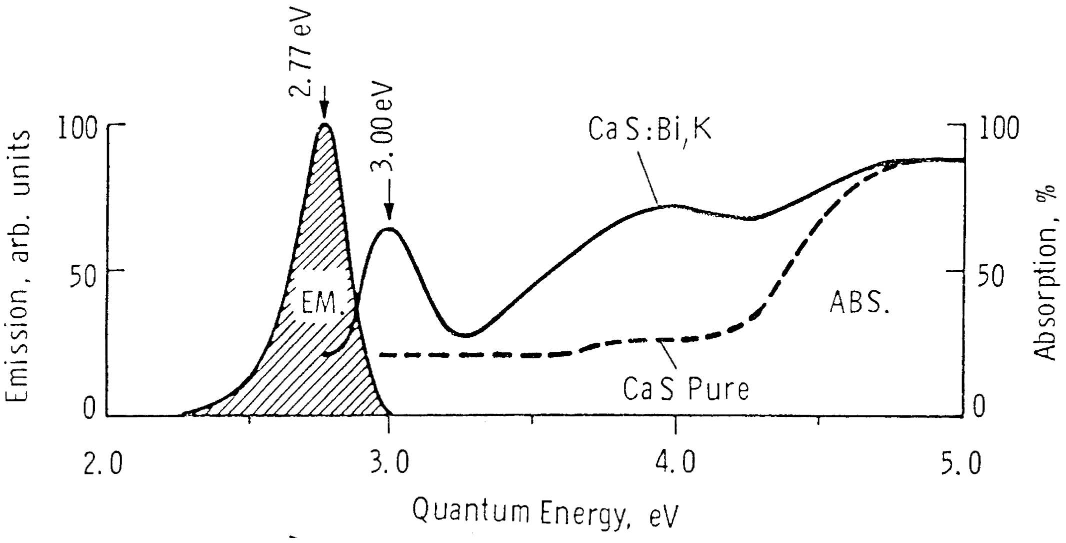

Figure 50 Luminescence and absorption spectra of CaS:Bi^{3+} (0.01%),K^+ at room temperature. The hatched zone indicates the luminescence spectrum. The solid line shows the absorption spectrum of CaS:Bi^{3+},K^+, and the broken line that of pure CaS. (From Lehmann, W., *Gordon Research Conference Report*, July 1971. With permission.)

One significant difference between IIa-VIb compounds and IIb-VIb compounds is that the concept of the donor or acceptor in the latter is not applicable in the former. For example, donor-acceptor pair luminescence is not observed for IIa-VIb compounds doped with (Cu^+, Cl^-) or (Cu^+, Al^{3+}) pairs. Another example is that alkali ions act as "co-activators" of Ag or Au activators, just as halogen ions do. As this example indicates, many activator/co-activator combinations violate the charge compensation rule in an ionic crystal. In fact, the co-activators do not play a donor role similar to that of halogen ions in IIb-VIb compounds; instead, these ions help the activator diffuse into the host lattice by creating lattice defects. These observations are presumably related to the stronger ionicity of IIa-VIb compounds compared to IIb-VIb compounds. As is the case with alkali halides, luminescence centers are localized in IIa-VIb compounds.

As described previously, many materials of this group have high luminescence efficiency. Cathodoluminescence efficiencies for various phosphors are shown in Table 17.[5,7] Above all, CaS:Ce^{3+} shows an efficiency nearly as high as ZnS:Ag,Cl or ZnS:Cu,Al, which are the most efficient cathode-ray phosphors. The efficiencies of CaS:Eu^{2+},Ce^{3+} and MgS:Eu^{2+} are much higher than the efficiency of Y_2O_2S:Eu^{3+} (about 13% in energy efficiency) and very good red-emitting phosphors. (Here, Ce^{3+} acts as a sensitizer of Eu^{2+} luminescence.) Luminance of CaS:Eu^{2+},Ce^{3+} is, however, only 80% that of Y_2O_2S:Eu^{3+}, because the emission peak of CaS:Eu^{2+},Ce^{3+} is at 650 nm, while that of Y_2O_2S:Eu^{3+} is at 627 nm.

It should be noted that the data listed in Table 17 were measured at low electron-beam current density. It was found that for the Eu^{2+}, Mn^{2+}, and Ce^{3+} emissions, the efficiency decreases with increasing current density. This saturation in luminescence intensity can be reduced by increasing the activator concentration, but not eliminated; the reason for the saturation is not clear as yet.

As shown in Table 18, the luminescence peak shifts to shorter wavelengths in Eu^{2+} and Ce^{3+} (*f-d* transitions) and in Mn^{2+} (*d-d* transition) when the host lattice is varied from CaS to SrS to BaS. This shift is reasonable from theoretical points of view because the

Table 17 Cathodoluminescence Efficiency of Alkali Earth Chalcogenide Phosphors

Phosphors	Energy efficiency (%)	Luminescence color
$MgS:Eu^{2+}$	16	Orange-red
$CaS:Mn^{2+}$	16	Yellow
CaS:Cu	18	Blue-violet
CaS:Sb	18	Yellow-green
$CaS:Ce^{3+}$	22	Green
$CaS:Eu^{2+}$	10	Red
$CaS:Eu^{2+},Ce^{3+}$	16	Red
$CaS:Sm^{3+}$	12 (+IR)	Yellow
$CaS:Pb^{2+}$	17	UV
$CaO:Mn^{2+}$	5	Yellow
$CaO:Pb^{2+}$	10	UV

Note: The efficiency was measured at room temperature relative to a standard material. For $MgS:Eu^{2+}$, excitation was made at an accelerating voltage of 18 kV and a current density of 10^{-7} A/cm^2. The standard was $Y_2O_2S:Eu^{3+}$. For other phosphors, excitation was made at 8 kV and 10^{-6} A/cm^2 or less. The standard was P-1, P-22, or $MgWO_4$. The measurement error is ±10%.

From Lehmann, W., *J. Electrochem. Soc.*, 118, 1164, 1971; Lehmann, W., *Gordon Research Conference Report*, July 1971; Kasano, H., Megumi, K., and Yamamoto, H., *Abstr. Jpn. Soc. Appl. Phys. 42nd Meeting*, No. 8P-Q-11, 1981. With permission.

Table 18 Spectral Peak Shift by a Host Material for Eu^{2+}, Ce^{3+}, and Mn^{2+} Activation

	Peak wavelength (nm)			Distance between the nearest neighbor ions
	Eu^{2+}	Ce^{3+}	Mn^{2+}	
Host	0.1%	0.04%	0.2%	(nm)
CaS	651	520	585	0.285
SrS	616	503	~550	0.301
BaS	572	482	~541	0.319

From Kasano, H., Megumi, K., and Yamamoto, H., *Abstr. Jpn. Soc. Appl. Phys. 42nd Meeting*, No. 8P-Q-11, 1981. With permission.

crystal field parameter (10*Dq*) (see 3.2.1) decreases in the above order. See also 3.2.5 for Mn^{2+} luminescence and 3.3.3 for Eu^{2+} and Ce^{3+} luminescence.

3.6.4 *Typical examples of applications*

3.6.4.1 *Storage and stimulation*

It is another remarkable feature of the IIa-VIb compounds that they show various phenomena related to traps, e.g., storage, photostimulation (infrared stimulation), and photoquenching (see 2.7).

$Ca_{0.7}Sr_{0.3}S:Bi^{3+},Cu$ was developed as a particularly efficient storage material.[24] This material doped with Bi^{3+} shows bluish-violet emission due to the $6s6p \rightarrow 6p^2$ transition of Bi^{3+}; the addition of Cu shifts the emission toward longer wavelengths and improves its luminance (see 12.2).

$CaS:Bi^{3+}$, reported as early as in 1928 by Lenard,[1] is one of the best known of all CaS phosphors. This phosphor requires the Bi^{3+} luminescent centers to be co-activated by an

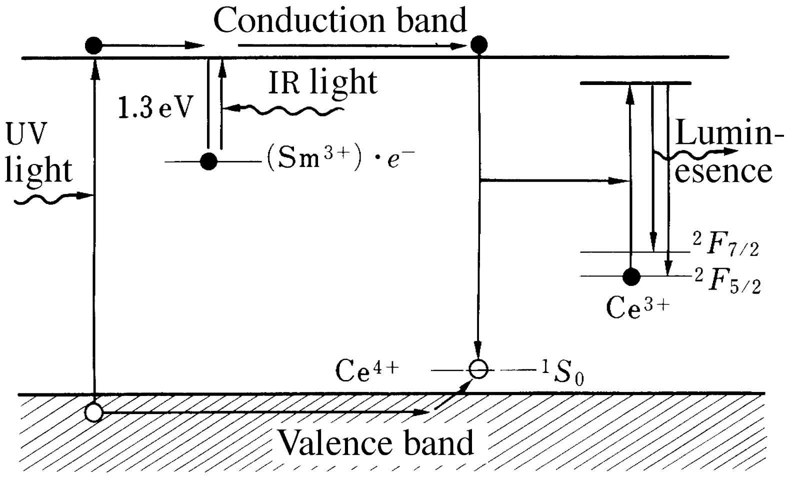

Figure 51 Schematic diagram of infrared stimulation mechanism of SrS:Ce^{3+},Sm^{3+}. The original figure has been simplified. (From Keller, S.P. and Pettit, G.D., *Phys. Rev.*, 111, 1533, 1958. With permission.)

alkali metal ion. The luminescence and absorption spectra of CaS:Bi^{3+},K^+ are shown in Figure 50.[4]

Photostimulation attracted attention as a means to detect infrared light. During World War II, an enormous volume of research was carried out on this phenomenon in Japan[23] and the U.S. for military purposes. Some of the materials developed in this period includes (Ca,Sr)S:Ce^{3+},Bi^{3+},[23] SrS:Eu^{2+},Sm^{3+} and SrS:Ce^{3+},Sm^{3+}.[24] In these compositions, the primary activator (i.e., Ce^{3+} or Eu^{2+}) determines the luminescence spectrum, while the auxiliary activator (i.e., Bi^{3+} or Sm^{3+}) forms the necessary traps that determine the stimulable wavelength in the infrared. These wavelengths range from 0.8 to 1.4 μm for Sm^{3+} and 0.5 to 1.0 μm for Bi^{3+}.

The stimulation mechanism proposed for SrS:Ce^{3+},Sm^{3+} is schematically shown in Figure 51.[25] Here, one assumes that Sm^{3+} forms electron traps and Ce^{3+} forms hole traps. Electrons trapped by Sm^{3+} ions are released to the conduction band by absorption of infrared light of energy corresponding to the trap depth. After migration through the lattice, some of the electrons are retrapped by Ce^{3+}, which already has trapped holes. The electron and the hole recombine in Ce^{3+}, releasing energy characteristic of the Ce^{3+} luminescence. In SrS:Eu^{2+},Sm^{3+}, it is thought that Eu^{2+} plays a similar role as Ce^{3+}. The concept of an activator ion working either as an electron or a hole trap is also applicable to other materials with localized luminescence centers.

3.6.4.2 Cathode-ray tubes

Application of CaS phosphors applied to CRTs have attracted attention because of their high efficiency and diversity in emission colors.[26] Green-emitting CaS:Ce^{3+} with weak temperature quenching has been tested for application in heavily loaded projection tubes.[8,9] However, CaS:Ce^{3+} was found to be not satisfactory for projection tube uses because it shows serious luminance saturation at high current density. Amber-emitting (Ca,Mg)S:Mn^{2+} has been tested in terminal display tubes.[10] The commercial application of this phosphor was also abandoned because its efficiency and persistence were found to be unsatisfactory. Screening technology for this family of phosphors has improved, but evolution of toxic H_2S gas in the manufacturing and reclaiming processes remains a serious impediment for the widespread application of these phosphors.

Table 19 (a) Color and Luminance of DC Electroluminescence of CaS and SrS Powder Phosphors

Phosphors	Luminescence color	Luminance (cd/m^2) (Applied voltage is shown in parenthesis) Continuous drive	Pulse drive[a]
$CaS:Ce^{3+}$	Green	1700 (70 V)	600 (110 V)
$CaS:Er^{3+}$	Green	300 (80 V)	85 (120 V)
$CaS:Tb^{3+}$	Green	17 (80 V)	50 (120 V)
$CaS:Eu^{3+}$	Red	100 (50 V)	17 (120 V)
$SrS:Ce^{3+}$	Bluish-green	400 (70 V)	200 (110 V)
$SrS:Mn^{2+}$	Green	270 (120 V)	—
SrS:Cu,Na	Green	270 (80 V)	17 (120 V)

[a] Pulse width is 10–20 μs. Duty is 1–1¼ %.

From Vecht, A., *J. Crystal Growth*, 59, 81, 1982. With permission.

Table 19 (b) Properties of Thin-Film AC Electroluminescence Devices Using CaS or SrS Phosphors

Chemical composition	Maximum luminance (cd/m^2)	Maximum efficiency (lm/W)	Luminescence color
$CaS:Eu^{2+}$	200	0.05	Red
$CaS:Ce^{3+}$	150	0.1	Green
$SrS:Ce^{3+}$	900	0.44	Greenish-blue

Note: The driving voltage has a frequency of 1 kHz.

From Ono, Y.A., *Electroluminescence Displays*, Series for Information Display, Vol. 1, World Scientific Publishing, Singapore, p. 84, 1995. With permission.

3.6.4.3 Electroluminescence (EL)

Phosphors based on CaS and other IIa-VIb compounds are important electroluminescent materials because they can provide colors other than the orange color provided by $ZnS:Mn^{2+}$ (See 2.10 and 9.1). Table 19(a) shows the properties of the EL cells made of fine phosphor particles manufactured by Phosphor Products Co.[27] (See also [Sections 3.6.6.1). Among the materials listed in this table, $CaS:Ce^{3+}$ is nearly as bright as $ZnS:Mn^{2+}$. Although the degradation has been improved, the lifetime of this material is still at an impractical level.

In thin-film electroluminescent devices, CaS and SrS phosphors provide luminances that are higher than ZnS phosphors in the red and green-blue regions. The luminance and luminous efficiency of the three primary colors obtained by IIa-VIb compounds are shown in Table 19(b).[28]

As SrS:Ce EL was developed in 1984[29], formation process of SrS:Ce thin-films has been investigated by various techniques, e.g., electron-beam deposition, sputtering, hot-wall deposition, and molecular beam epitaxy. A recent study has shown that thin-film formation in excess sulfur promotes introduction of Ce^{3+} ions in SrS lattice by creating Sr vacancies[30]. By this optimization, luminous efficiency higher than 1 lm/W was achieved at 1 KHz driving frequency[30]. However, the emission color of SrS:Ce is not saturated blue, but greenish-blue with color coordinates x=0.30 and y=0.52 in the above case[30]. Luminescence of more saturated blue with x=0.18 and y=0.34 can be achieved either by codoping of Rb as a charge compensator[31] or by supplying H_2O vapor during SrS:Ce film deposition[32].

A thin-film of SrS:Cu shows better performance of blue EL[33]. Moderately high luminous efficiency of 0.22 lm/W was obtained at 60 Hz driving with saturated blue of color coordinates, x=0.15 and y=0.23.

Addition of Ag to Cu further improves color coordinates to x=0.17 and y=0.13, which is close to the primary blue in CRTs. Luminous efficiency of SrS:Cu, Ag was reported to be 0.15 lm/W at 60 Hz driving.

Photoluminescence studies have shown that a SrS:Cu thin film has the emission peak at around 480 nm, while CaS:Cu shows the peak at around 420 nm. Accordingly, the emission peak can be tuned by the formation of the solid solution (Sr, Ca):Cu[34]. However, EL by the solid solution has not been obtained yet, though EL of CaS:Cu thin films was reported recently[35].

3.6.5 Host excitation process of luminescence

Figure 52 shows a luminescence spectrum of SrSe containing trace amounts of Ba^{2+}.[13] The line at 3.74 eV can be assigned to a free exciton at the indirect bandgap (i.e., an indirect exciton), while the broad band at lower energy arises from the recombination of a localized indirect exciton trapped by the short-range potential of Ba^{2+} acting as an isoelectronic impurity. Presumably, the localized indirect excitons also produce luminescence by other types of activators.

It was observed that the excitation spectrum of CaS:Eu^{2+} in the vacuum-UV region shows that the luminescence efficiency increases with a step-like shape at the energy position twice that of the direct exciton transition (Figure 53).[22] This fact shows that an excited electron can efficiently create two direct excitons through an Auger process. Direct excitons thus created are scattered and transformed to indirect excitons, which eventually transfer energy to an impurity producing luminescence. These experimental results provide evidence that excitation energy given by the band-to-band transition is efficiently transferred to activators via excitons in alkali earth sulfides and selenides.

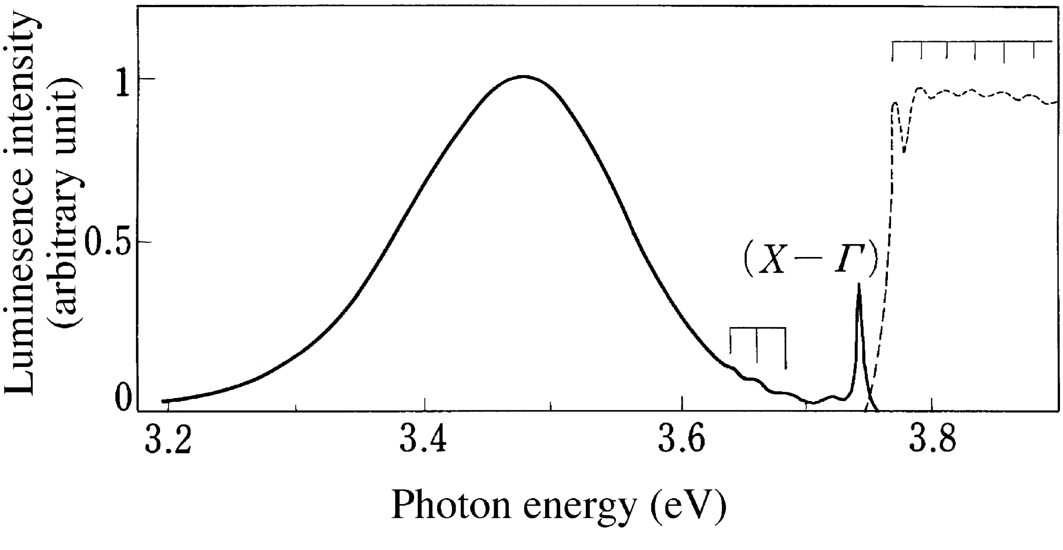

Figure 52 A luminescence (a solid line) and an excitation spectrum (a broken line) of SrSe containing a trace of Ba^{2+} at 2K. The notation (X-Γ) indicates a recombination transition of an exciton from the X point of the conduction band to the Γ point of the valence band. The vertical lines above the spectra show phonon structures. The broad emission band is due to localized excitons at the isoelectronic Ba center. (From Kaneko, Y. and Koda, T., *J. Crystal Growth*, 86, 72, 1988. With permission.)

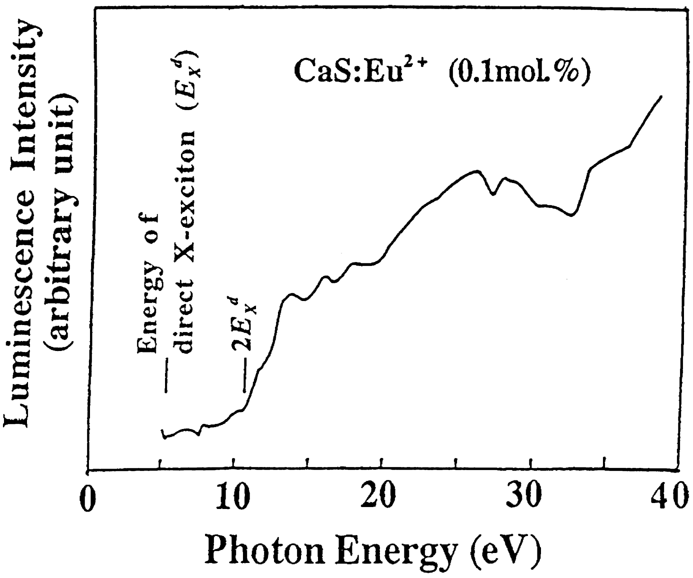

Figure 53 An excitation spectrum of CaS:Eu^{2+} (0.1 mol%) in the vacuum UV region at 77K. (From Kaneko, Y., Ph.D. Thesis, The University of Tokyo, 1984 (in Japanese). With permission.

3.6.6 Preparation methods of phosphors

3.6.6.1 Sulfides

The preparation of sulfide phosphors can be classified into two methods; one entails the sulfurization of alkaline earth oxides or carbonates and the other involves the reduction of sulfates. The following agents are known to sulfurize or reduce the starting materials; the sulfurizing agents are H_2S, CS_2, S+C (in many cases, starch or sucrose are used as the source of carbon), and Na_2CO_3+S (or Na_2S), and the reducing agents are H_2 and C.

In addition to these agents, fluxes are often added to the starting materials at the level of several to 10 wt%. Typical fluxes are alkali carbonates, alkali sulfates, and NH_4Cl. Lithium compounds are particularly effective in promoting crystal growth and diffusion of activator ions into the sulfide lattice. This is probably because Li^+, which has a small ionic radius, enters interstitial sites and generates cation vacancies; ionic diffusion is accelerated through these means. Fluxes that promote crystal growth and ion diffusion effects remarkably, however, may have a side effect to degrade luminescence efficiency because the constituent ions of the fluxes (e.g., Li^+ F^-) are likely to remain in the phosphor lattice as impurities. The material and the quantity of a flux are selected by considering these two kinds of effect.

Typical preparation methods are shown below for CaS:Ce^{3+}.[36]

$$\begin{gathered}\mathrm{CaSO_4} \xrightarrow{\mathrm{H_2+H_2S}} \mathrm{CaS} \\ \mathrm{CaS + Ce_2S_3 + NH_4Cl + S} \xrightarrow[\text{2 hr}]{1200^\circ\mathrm{C}} \mathrm{CaS : Ce^{3+}}\end{gathered} \qquad (29)^3$$

$$CaSO_4 + Ce(NO_3)_3 \cdot 6H_2O + Na_2SO_4 + C \xrightarrow[2\ hr]{900°C} CaS:Ce^{3+} \qquad (30)^{37}$$

$$CaCO_3 + Ce_2(SO_4)_3 \cdot 8H_2O + Na_2CO_3 + S \xrightarrow[1-72\ hr]{800-1100°C} CaS:Ce^{3+} \qquad (31)^{38,39}$$

$$\begin{aligned} &CaCO_3 + CeO_2 \xrightarrow[2\ hr]{1300°C} CaO:Ce^{3+} \\ &CaO:Ce^{3+} \xrightarrow[1200°C,\ 2\ hr]{H_2S + PCl_3} CaS:Ce^{3+} \end{aligned} \qquad (32)^{40}$$

$$\begin{aligned} &Ca(CH_2O)_2 + 2H_2S \xrightarrow[2\ hr]{} Ca(HS)_2 + 2CH_3OH \\ &Ca(HS)_2 + Ce_2S_3 \xrightarrow[1000°C,\ 2\ hr]{N_2} CaS:Ce^{3+} + H_2S \end{aligned} \qquad (33)$$

When the sulfurizing or reducing agents are in the solid or liquid state, the reaction can be performed in an encapsulated crucible. When the agents are in the gas phase, however, the reaction must be done in a quartz tube that allows a gas flow. In this review, the former will be called the *crucible method* and the latter the *gas-flow method*. These two methods are described below.

The crucible method. Examples of this method are given in the second reaction of Eq. 29, and Eqs. 30 and 31. By selecting an appropriate flux, this method provides particles of fairly large size and good dispersion characteristics. On the other hand, contact with the flux can introduce impurities into the phosphor, resulting in degraded efficiency. Insufficient sulfurization or partial oxidation may also occur by exposure to oxygen, since quantities of a flux generally used are insufficient to cover all the particle surfaces. When firing must be carried out for many hours at high temperature, a double-crucible configuration is used; one crucible nestles in the other with carbon between, thus preventing phosphors from oxidation.

The gas-flow method. Examples are given in the first reaction of Eq. 29, and Eqs. 32 and 33. Alkali compounds, which are used as fluxes in the crucible method, cannot be used in this case because they can vaporize and react with the quartz tube during the firing. As a result, this method provides smaller particles with poor dispersion characteristics. Improvement is obtained in some cases if a small amount of PCl_3 gas is supplied for a period of time, as in the method for Eq. 32.

On the other hand, the gas-flow method can give high luminescence efficiency because contamination of phosphors with impurities are less probable than in the crucible method and also because stoichiometry may be controlled through adjustment of the compositions and flow rates of the gases. In this case, firing may be repeated and different preparation methods can be experimented with and/or combined, if necessary. The method in Eq. 33 is used to obtain fine particles for electroluminescent powder phosphors.

Preparation methods can have considerable effects on luminescence properties. The luminescence peak positions of CaS:Ce^{3+} prepared by the flux method show a peak that is blue-shifted by about 600 cm^{-1} relative to the positions obtained in phosphors prepared by the gas-flow method. Differences are also observed in the excitation spectra and temperature dependencies of the luminescence intensity.[41]

Sulfides other than CaS can essentially be obtained by the same process. However, polysulfides are formed more easily from sulfides of the heavier cation elements. In other words, the sulfurizing reaction proceeds more slowly for the sulfides of lighter elements. It has been reported that the reduction of sulfates is a better way for the synthesis of SrS and BaS. For example, the following reactions have been employed:[23]

$$\mathrm{SrSO_4 + S + starch\ (or\ sucrose)} \longrightarrow \mathrm{SrS + (CO_2,\ CO,\ H_2O,\ SO_2)} \tag{34}$$

The synthesis of MgS by reduction of MgO or $MgSO_4$ requires repeated reactions to complete sulfurization.[7] Another method for MgS synthesis starting with Mg metal and employing CS_2, a more powerful sufurizing agent, has also been used. This latter method is reported to be particularly effective in producing MgS.[23]

$$\begin{aligned} &\mathrm{Mg\ powder + S} \longrightarrow \mathrm{MgS\ (an\ explosive\ reaction)} \\ &\mathrm{2MgO + CS_2} \longrightarrow \mathrm{2MgS + CO_2} \end{aligned} \tag{35}$$

3.6.6.2 *Selenides*[23]

Selenides are synthesized by methods similar to those to form sulfides using elemental Se or H_2Se instead. The following reaction can be used to prepare CaSe:

$$\mathrm{CaO + amidol\ (a\ weak\ organic\ base)} \longrightarrow \mathrm{CaSe + (CO_2,\ CO,\ NH_3,\ H_2O,\ SeO_2)} \tag{36}$$

SrSe and BaSe are obtained by firing Sr or Ba nitrates with Se and starch. The fired products include Se and polyselenides, which are then vaporized by annealing in vacuum at about 600°C. After annealing, a single phase of SrSe or BaSe is obtained.

References

1. Lenard, P., Schmidt, F., and Tomascheck, R., *Handb. Exp. Phys.*, Vol. 23, Akadem. Verlagsges, Leipzig, 1928.
2. Lehmann, W., *J. Electrochem. Soc.*, 117, 1389, 1970.
3. Lehmann, W. and Ryan, F.M., *J. Electrochem. Soc.*, 118, 477, 1971.
4. Lehmann, W., *J. Luminesc.*, 5, 87, 1972.
5. Lehmann, W., *J. Electrochem. Soc.*, 118, 1164, 1971.
6. Lehmann, W., *Gordon Research Conference Report*, July 1971.
7. Kasano, H., Megumi, K., and Yamamoto, H., *J. Electrochem. Soc.*, 131, 1953, 1984.
8. Kanehisa, O., Megumi, K., Kasano, H., and Yamamoto, H., *Abstr. Jpn. Soc. Appl. Phys. 42nd Meeting*, No. 8P-Q-11, 1981.
9. Tsuda, N., Tamatani, M., and Sato, T., *Tech. Digest, Phosphor Res. Soc. 199th Meeting*, 1984 (in Japanese).
10. Yamamoto, H., Megumi, K., Kasano, H., Kanehisa, O., Uehara, Y., and Morita, Y., *J. Electrochem. Soc.*, 134, 2620, 1987.

11. Kaneko, Y., Morimoto, K., and Koda, T., *J. Phys. Soc. Japan*, 51, 2247, 1982.
12. Kaneko, Y., Morimoto, K., and Koda, T., *J. Phys. Soc. Japan*, 52, 4385, 1983.
13. Kaneko, Y. and Koda, T., *J. Crystal Growth*, 86, 72, 1988.
14. Kaneko, Y., Morimoto, K., and Koda, T., *Oyo Buturi*, 50, 289, 1981 (in Japanese).
15. Krebs, H., *Fundamentals of Inorganic Crystal Chemistry*, McGraw-Hill, London, 1968, 159 and 163.
16. Hasegawa, A. and Yanase, A., *J. Phys. C*, 13, 1995, 1980.
17. Morimoto, K., Masters Thesis, The University of Tokyo, 1982 (in Japanese).
18. Jasperse, J.R., Kahan, A., Plendel, J.N., and Mitra, S.S., *Phys. Rev.*, 146, 526, 1966.
19. Jacobsen, J.L. and Nixon, E.R., *J. Phys. Chem. Solids*, 29, 967, 1968.
20. Galtier, M., Montaner, A., and Vidal, G., *J. Phys. Chem. Solids*, 33, 2295, 1972.
21. Boswarva, I.M., *Phys. Rev. B1*, 1698, 1970.
22. Kaneko, Y., Ph.D. Thesis, The University of Tokyo, 1984 (in Japanese).
23. Kameyama, N., *Theory and Applications of Phosphors*, Maruzen, Tokyo, 1960 (in Japanese).
24. Keller, S.P., Mapes, J.F., and Cheroff, G., *Phys. Rev.*, 108, 663, 1958.
25. Keller, S.P. and Pettit, G.D., *Phys. Rev.*, 111, 1533, 1958.
26. *Japanese Patent Publication (Kokoku)* 47-38747, 1972.
27. Vecht, A., *J. Crystal Growth*, 59, 81, 1982.
28. Ono, Y.A., *Electroluminescent Displays*, Series for Information Displays, Vol. 1, World Scientific Publishing, Singapore, 1995, 84.
29. Barrow W.A., Coovert R.E., and King, C.N., *Digest of Technical Papers, 1984 SID Intl. Symp*. 249, 1984.
30. Ohmi, K., Fukuda, H., Tokuda, N., Sakurai, D., Kimura, T., Tanaka, S., and Kobayashi, H., *Proc. 21st Intl. Display Research Conf., (Nogoya)*, 1131, 2001.
31. Fukada, H., Sasakura, A., Sugio, Y., Kimura, T., Ohmi, K., Tanaka, S. and Kobayashi, H., *Jpn. J. Appl. Phys*., 41 L941, 2002.
32. Takasu, K., Usui, S., Oka, H., Ohmi, K., Tanaka, S., and Kobayashi, H, *Proc. 10th Intl. Display Workshop, (Hiroshima)*, 1117, 2003.
33. Sun, S.S., Dickey, E., Kane, J., and Yocom, P.N., *Proc. 17th Intl. Display Research Conf., (Toronto)*, 301, 1997.
34. Ehara, M., Hakamata, S., Fukada, H., Ohmi, K., Kominami, H., Nakanish, Y., and Hatanaka, Y, *Jpn. Appl. J. Phys.* 43, 7120-7124, 2004.
35. Hakamata, S., Ehara, M., Fukuda, H., Kominami, H., Nakanishi, Y., and Hatanaka, Y., *Appl. Phys. Lett*., 85, 3729-3730, 2004.
36. Okamoto, F. and Kato, K., *Tech. Digest, Phosphor Res. Soc. 196th Meeting*, 1983 (in Japanese).
37. Vij, D.R. and Mathur, V.K., *Ind. J. Pure Appl. Phys.*, 6, 67, 1968a.
38. Okamoto, F. and Kato, K., *J. Electrochem. Soc.*, 130, 432, 1983.
39. Kato, K. and Okamoto, F., *Jpn. J. Appl. Phys.*, 22, 76, 1983.
40. Yamamoto, H., Manabe, T., Kasano, H., Suzuki, T., Kanehisa, O., Uehara, Y., Morita, Y., and Watanabe, N., *Electrochem. Soc. Meeting, Extended Abstracts*, No. 496, 1982.
41. Kanehisa, O., Yamamoto, H., Okamura, T., and Morita, M., *J. Electrochem. Soc.*, 141, 3188, 1994.

chapter three — section seven

Principal phosphor materials and their optical properties

Shigeo Shionoya

Contents

3.7 IIb-VIb compounds 247
  3.7.1 Introduction 247
  3.7.2 Fundamental intrinsic properties 248
    3.7.2.1 Crystal structure 248
    3.7.2.2 Melting point and crystal growth 248
    3.7.2.3 Band structure 248
    3.7.2.4 Exciton 251
    3.7.2.5 Type of conductivity and its control 252
  3.7.3 Luminescence of shallow donors and acceptors 252
  3.7.4 ZnS-type phosphors 254
    3.7.4.1 Luminescence of deep donors and acceptors 254
    3.7.4.2 Luminescence of transition metal ions 268
    3.7.4.3 Luminescence of rare-earth ions 270
  3.7.5 ZnO Phosphors 270
References 271

3.7 IIb-VIb compounds

3.7.1 Introduction

IIb-VIb compounds include the oxides, sulfides, selenides, and tellurides of zinc, cadmium, and mercury. Among these compounds, those with bandgap energies (E_g) larger than 2 eV (i.e., ZnO, ZnS, ZnSe, ZnTe, and CdS) are candidate materials for phosphors that emit visible luminescence; ZnS is the most important in this sense. In this section, the fundamental optical properties and luminescence characteristics and mechanisms of this class of phosphors will be explained.[1] The term IIb-VIb compounds used below will be limited to the above-mentioned compounds.

ZnS-type phosphors are presently very important as cathode-ray tube (CRT) phosphors (see 6.2). These phosphors have a long history, dating back about 130 years. At the

International Conference on Luminescence held in 1966 in Budapest, a presentation titled "The Century of the Discovery of Luminescent Zinc Sulfide" was given,[2] in which the history of luminescent ZnS was discussed. In 1866, a young French chemist, Théodore Sidot, succeeded in growing tiny ZnS crystals by a sublimation method. Although his original purpose was to study crystal growth, the crystals grown exhibited phosphorescence in the dark. The experiments were repeated, the observations confirmed, and a note to the Academy of Sciences of Paris was presented. This note was published by Becquerel.[3] These phosphorescent ZnS (zinc-blende) crystals were thereafter called Sidot's blende. From present knowledge, one can conclude that Sidot's blende contained a small quantity of copper as an impurity responsible for the phosphorescence. The historical processes of the evolution of Sidot's blende to the present ZnS phosphors are described in 3.7.4.

3.7.2 Fundamental intrinsic properties

Important physical properties of IIb-VIb compounds related to luminescence are shown in Table 20.

3.7.2.1 Crystal structure

IIb-VIb compounds crystallize either in the cubic zinc blende (ZB) structure or in the hexagonal wurtzite (W) structure; ZnO, CdS, and CdSe crystallize in the W structure, while ZnSe, ZnTe, and CdTe in the ZB structure. ZnS crystallizes into both the W type (traditionally called α-ZnS) and the ZB type (β-ZnS). The ZB structure corresponds to the low-temperature phase; the ZB → W transition temperature is known to be about 1020°C.

3.7.2.2 Melting point and crystal growth

In IIb-VI compounds, the sublimation pressure is very high. As a result, the compounds, with the exception of the tellurides, do not melt at atmospheric pressure. They do melt at pressures of several tens of atmospheres of argon, but the melting points are pretty high: 1975°C for ZnO, 1830 ± 20°C for ZnS, and about 1600°C for ZnSe. ZnS powder phosphors are prepared by firing ZnS powders at 900 to 1200°C. Phosphor particles fired at relatively low temperature (below about 1000°C) are of the ZB structure, while those fired at temperatures above 1000°C are of the W structure.

In the past, single crystals of IIb-VIb compounds with high sublimation pressure were grown by the sublimation-recrystallization method, the vapor phase reaction method, the vapor phase chemical transport method, or by the high-pressure melt growth method. Recently, various epitaxial growth methods, such as molecular beam epitaxy (MBE), metalorganic chemical vapor deposition (MOCVD), and atomic layer epitaxy (ALE), have been actively developed, especially for ZnSe and ZnS (see 3.7.6). As a result, thin single-crystal films with very high purity and high crystallinity are presently available for these two compounds.

3.7.2.3 Band structure

In the IIb-VIb compounds treated in this section, the conduction band has the character of the *s* orbital of the cations, while the valence band has the character of the *p* orbital of the anions. These compounds are all direct-transition type semiconductors, and both the bottom of the conduction band and the top of the valence band are located at the Γ point [$k = (000)$] in **k**-space. This is simply shown in Figures 7(a) and (b) in 2.2 for the ZB and W structure. The band structure of ZnSe of the ZB structure obtained by nonlocal pseudopotential calculations is shown in Figure 54.[4]

Table 20 Important Physical Properties of IIb-VIb Compounds Related to Luminescence

	Crystal structure	Lattice constant (Å)	Static dielectric constant	Bandgap energy (eV)		Exciton energy, 4K (eV)	Exciton binding energy (meV)	Effective mass m^*/m_0	
				4K	RT			Electron	Hole
ZnO	W	a = 3.2403 c = 5.1955	c ∥ 8.8 c ⊥ 8.5	3.436	3.2	3.375	59	0.28	0.59
ZnS	W	a = 3.820 c = 6.260	8.6	3.911	3.8	3.871	40	0.28	c ∥ 1.4 c ⊥ 0.49
	ZB	5.4093	8.3	3.84	3.7	3.799	36	0.39	
ZnSe	ZB	5.6687	8.1	2.819	2.72	2.802	17	0.16	0.75
ZnTe	ZB	6.1037	10.1	2.391	2.25	2.381	11	0.09	Heavy: 0.6 Light: 0.16
CdS	W	a = 4.1368 c = 6.7163	c ∥ 10.3 c ⊥ 9.35	2.582	2.53	2.552	28	0.2	c ∥ 5.0 c ⊥ 0.7
CdSe	W	a = 4.30 c = 7.02	c ∥ 10.65 c ⊥ 9.70	1.840	1.74	1.823	15	0.112	c ∥ 2.5 c ⊥ 0.45
CdTe	ZB	6.4818	10.2	1.606	1.53	1.596	10	0.096	Heavy: 1.0 Light: 0.1

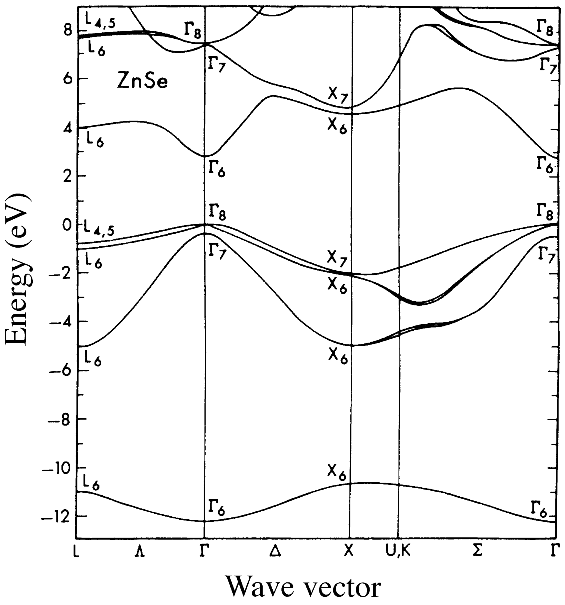

Figure 54 Band structure of ZnSe. (From Chelikowsky, J.R. and Cohen, M.L., *Phys. Rev.*, B14, 556, 1976. With permission.)

As shown in Figure 7(a) of 2.2, the valence band in the ZB structure is split by the spin-orbit interaction into a higher lying Γ_8(A) state (in which the orbital state is doubly degenerate) and a nondegenerate Γ_7(B) state. In the W structure as shown in Figure 7(b), on the other hand, all the orbital degeneracy is lifted by the spin-orbit interaction and the aniosotropy of crystal field, and the split states are Γ_9(A), Γ_7(B), and Γ_7(C) in descending order of energy. The case of ZnO is an exception: Γ_9(A) and Γ_7(B) are reversed, so that the order is Γ_7(A), Γ_9(B), and Γ_7(C) instead. This originates from the fact that in ZnO the splitting by the spin-orbit interaction is negative and smaller than that due to the crystal field anisotropy, unlike other IIb-VIb compounds. The negative spin-orbit splitting arises because of mixing of the *d* orbitals of Zn with the valence band.

In MX-type compound semiconductors, the bandgap energy E_g usually increases if M or X is replaced by a heavier element. Looking at E_g values in Table 20, it can be noted that this general rule is usually observed, except in the case of ZnO, where the E_g value is smaller than that of ZnS. This is also caused by the mixing of the Zn *d* orbital with the valence band.

It is seen in the band structure of ZnSe, shown in Figure 54, that in the conduction band there are two minima in upper energy regions at the L [k = (111)] and the X [k = (100)] points with energies of 1.2 and 1.8 eV above the bottom of the conduction band, respectively. The conduction band structure of ZnS is very similar, having the two upper minima at the same points. The existence of these two upper minima plays an important role in the excitation process of high-field, thin-film electroluminescence in ZnS (See 2.10).

The fact that IIb-VIb compounds are direct-gap semiconductors means that they are appropriate host materials for phosphors. If one compares the radiative recombination coefficient of electrons and holes for direct and indirect transitions, the value for the former is four orders of magnitude larger. In practical phosphors, the radiative emission is not caused by direct recombination, but by transitions taking place via energy levels of activators introduced as impurities. For impurities as donors or acceptors, their energy levels

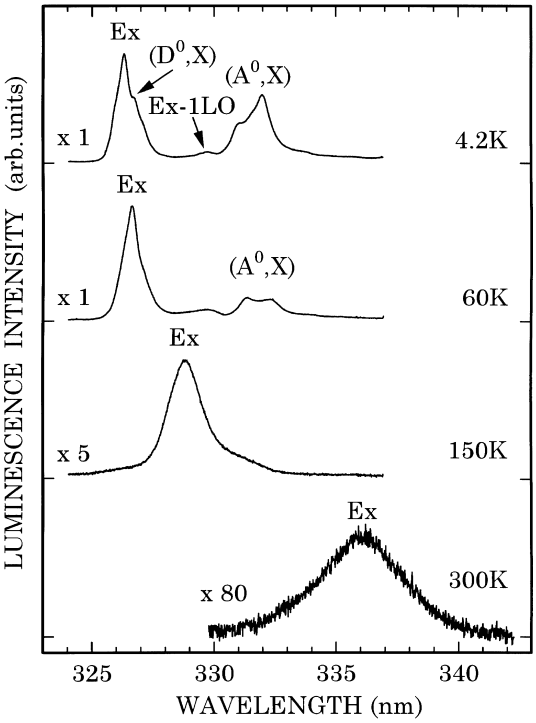

Figure 55 Exciton luminescence spectra of ZnS (ZB type) at various temperatures. (From Nakamura, S., Sakashita, T., Yoshimura, K., Yamada, Y., and Taguchi, *Jpn. J. Appl. Phys.*, 36, L491, 1997. With permission.)

are generated by perturbation on the conduction or valence band. Therefore, the impurity energy levels take on the same character as their parent bands, and the radiative recombination processes and rates in these levels are similar to those in the pure host material. ZnS:Cu,Al and ZnS:Ag,Cl phosphors, which are very important as phosphors for cathode ray tubes (CRT), are typical examples of this type of phosphor, as will be explained in 3.7.4. This is the reason why direct-gap type materials are most favorable as phosphor hosts.

3.7.2.4 Exciton

In IIb-VIb compounds, the exciton structure is clearly observed at low temperature in absorption and reflection spectra near the fundamental absorption edge. Absorption spectra of CdS shown in Figure 11 of 2.2 are a typical example. The exciton energy and its binding energy are shown in Table 20.

An exciton is annihilated, emitting a photon by the recombination of the constituent electron and hole pair. Figure 55 shows exciton luminescence spectra from a high-quality epitaxial layer of ZB-type ZnS grown by MOCVD at various temperatures.[5] At 4.2K, the Ex line from intrinsic free excitons at 326.27 nm is the strongest. The line Ex-1LO is the free exciton line accompanied by the simultaneous emission of one longitudinal optical (LO) phonon.

Even in very pure crystals of IIb-VIb compounds, a trace amount of impurities, at concentration levels of 10^{14} to 10^{15} cm^{-3}, are found. Excitons are bound to these impurities, and luminescence from these bound excitons is also observed at low temperature. Lines (D^0, X) and (A^0, X) are from excitons bound to neutral donors (D^0) and neutral acceptors (A^0). These bound exciton lines are customarily denoted as I_2 and I_1, respectively. Frequently,

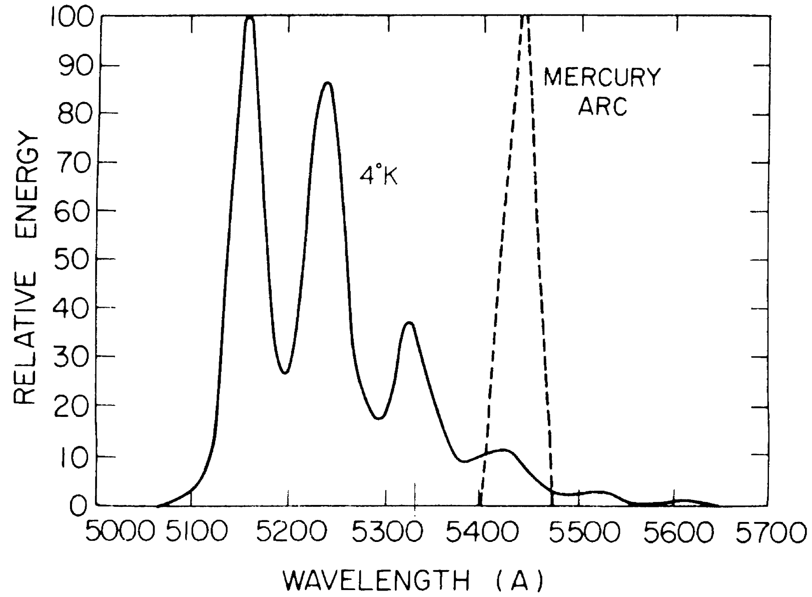

Figure 56 Spectrum of the edge emission of CdS at 4K; dashed line represents spectrometer window. (From Klick, C.C., *J. Opt. Soc. Am.*, 37, 939, 1947. With permission.)

an I_3 line due to excitons bound to ionized donors is observed at wavelength a little shorter than I_2. With increasing temperature from 4.2K, bound excitons are released from impurities, so that only the luminescence line due to free excitons is observed as can be seen in the figure. The binding energy of the exciton in ZB-type ZnS is 36 meV, so that exciton luminescence is observed up to room temperature.

The exciton binding energy in ZnO is as large as 59 meV and is the largest among IIb-VIb compounds. Luminescence of free excitons is observed at 385 nm at room temperature in pure ZnO. This ultraviolet luminescence was found as early as the 1940s,[6] but it was not recognized at that time that this luminescence originates from excitons. This luminescence persists up to fairly high temperatures; it is still observed at temperatures as high as 770K.[7]

3.7.2.5 *Type of conductivity and its control*

As-grown single crystals of ZnO, ZnS, ZnSe, and CdS are usually *n*-type in conductivity, while those of ZnTe are *p*-type. The conductivity control of IIb-VIb compounds, especially for ZnSe, has made remarkable progress recently. This progress is due to the demand to develop blue and blue-green light-emitting diodes and semiconductor lasers. The preparation of *p*-type ZnSe with high conductivity has been a fundamental problem, which was solved recently by introducing nitrogen acceptors using nitrogen plasma (See 3.7.6). Presently, it is possible to control the type of conductivity in most IIb-VIb compounds.

3.7.3 *Luminescence of shallow donors and acceptors*

Since the 1940s, it has been known that pure CdS crystals show luminescence at low room temperature with a characteristic spectral structure on the low-energy side of the fundamental absorption edge. This luminescence was called *edge emission*. Its spectrum is shown in Figure 56.[8] It has been established that the characteristic edge emission is observed in all IIb-VIb compounds except for ZnO.

The lines in Figure 56 are equally spaced, with an interval of about 40 meV, which is equal to the energy of longitudinal optical (LO) phonons in CdS. The halfwidth of the lines is approximately 5 meV. The relative intensities of the lines in the figure (numbered n = 0, 1, 2, … from the short wavelength side) decrease toward longer wavelengths with ratios of 1.00:0.87:0.38:0.12:0.030:0.015. This ratio exactly obeys the Poisson distribution $I_n = e^{-S}S^n/n!$ with S = 0.87. The n = 0 line is known as the zero-phonon line, while lines of n = 1, 2, … are caused by simultaneous emission of 1, 2, … LO phonons.

It has been established that the characteristics of the edge emission are satisfactorily interpreted in terms of donor(D)-acceptor(A) pair luminescence (see 2.4.4). The transition energy E of this luminescence is a function of the distance r between D and A in a pair, and is given by:

$$E(r) = E_g - (E_D + E_A) + e^2/4\pi\varepsilon r \tag{37}$$

where E_D and E_A are the ionization energies of a neutral donor and acceptor, respectively, and ε is the static dielectric constant. The transition probability W also depends on r and is expressed by

$$W(r) = W_0 \exp(-2r/r_B) \tag{38}$$

where r_B is Bohr radius of the donor electron and W_0 is a constant related to the D-A pair.

The mechanism for donor-acceptor pair luminescence was first verified in the edge emission in GaP doped with S donors and Si acceptors (see 2.4.4 and 3.8).[9] The intra-pair distance r is distributed discretely, so that a spectrum consisting of discrete lines is expected. In GaP:Si,S, a great number of sharp lines were observed adjacent to the high-energy tail of the n = 0 line, and the value of r for each line was determined. On this basis, the main part of the n = 0 line is thought to be composed of a large number of unresolved pair lines for pairs with relatively large r values.

A great number of sharp lines were also observed in the edge emission of CdS[10,11] and ZnSe.[12,13] These facts present clear evidence as to the origin of the edge emission. In ZnSe, the identification of each line has been made in analogy to the GaP case; in CdS, the analysis is not easy to make since the spectra are much more complicated because of the W structure.

Eqs. 37 and 38 indicate that the pair emission energy shifts to lower energies and the decay time becomes longer with increasing r values. Then one expects that in the time-resolved spectra of the edge emission, the peaks of the lines composed of unresolved pair lines should shift to lower energies as a function of time after pulse excitation. This has been observed in CdS,[14] and presents further evidence for the pair emission mechanism in the edge emission.

The fact that the relative intensity ratio of the edge emission lines obeys a Poisson distribution indicates that the configurational coordinate model (see 2.3.2) is applicable to each pair center with a different r value. The donors and acceptors participating in the edge emission are shallow. In these cases, the constant S appearing in the Poisson distribution, which is called the Huang-Rhys-Pekar factor and a measure of the strength of the electron-phonon interaction, is small, of the order of 1 or less; the phonon coupled to the center is the LO phonon of the entire lattice, but not a local mode phonon.

The depths of donor and acceptor levels (E_D and E_A) in IIb-VIb compounds are determined from bound exciton emission lines, edge emission spectra, or absorption spectra between a donor or acceptor level and the band. The available data on levels are

Table 21 Depths of Donor and Acceptor Levels, E_D and E_A (meV) in IIb-VIb Compounds

(a) Donor	$E_{D,\,calc}$	B	Al	Ga	In	F	Cl	Br	I	Li[a]
ZnS	110		100							
ZnSe	29±2	25.6	25.6	27.2	28.2	28.2	26.2			21
ZnTe			18.5				20.1			
CdS	33.9			33.1	33.8	35.1	32.7	32.5	32.1	28
CdSe	20±2									

[a] Interstitial Li.

(b) Acceptor	$E_{A,\,calc}$	Li	Na	Cu	Ag	Au	N	P	As
ZnS		150	190	1250	720	1200			
ZnSe	108	114	102	650	430	550	110	85,500	110
ZnTe	62	60.5	62.8	148	121	277		63.5	79
CdS		165	169	1100	260			120,600	750
CdSe		109							

Note: Calculated values by the effective mass approximation[15], $E_{D,\,calc}$ and $E_{A,\,calc}$, are also shown.

shown in Table 21. Calculated values of E_D E_A by the effective mass approximation are also shown.[15]

3.7.4 *ZnS-type phosphors*

3.7.4.1 *Luminescence of deep donors and acceptors*

ZnS type phosphors such as the green-emitting ZnS:Cu,Al and the blue-emitting ZnS:Ag,Cl are very important from a practical point of view, especially as phosphors for cathode-ray tubes. Luminescence centers in these phosphors are formed from deep donors or deep acceptors, or by their association at the nearest-neighbor sites. In this subsection, a brief history of the development of these phosphors will be given first, and then the characteristics and the mechanisms of their luminescence will be explained.

(a) History. After the research by Sidot described in 3.7.1, it became gradually clear that when ZnS powders are fired with the addition of a small amount of metallic salt, luminescence characteristic of that metal is produced. In the 1920s, it was established that a small amount of copper produces green luminescence, while silver produces blue luminescence. In this sense, copper and silver were called *activators* of luminescence. The firing is made at 900 to 1200°C with the addition of halides (such as NaCl) with low melting points as fluxes. It was found that if the firing is made without the addition of activators but with a halide flux, blue luminescence is produced. Thus, this type of blue luminescence was called *self-activated luminescence*.

In the 1930s and 1940s, research on ZnS-type phosphors was very active. Results of the research are described in detail in a book by Leverenz[16] published in 1950. In this book, the emission spectra of a great number of phosphors in ZnS, (Zn,Cd)S, or Zn(S,Se) hosts activated with Cu or Ag are shown. The spectral data shown in the book are still very useful (see 6.2.1). It should be noted that this book was written before the concept of the co-activator was conceived, so that chemical formulas of some phosphors given in the book are always not appropriate, and care must be exercised. For example, a phosphor written as ZnS:Ag[NaCl] should be written as ZnS:Ag,Cl according to the rule in use today. The ZnS self-activate phosphor is shown as ZnS:[Zn] in the book, but should be ZnS:Cl(orAl) instead, as will be explained.

In the late 1940s, Kröger and co-workers[17,18] demonstrated that halide flux added in the firing process to ZnS phosphors not only promotes crystal growth, but introduces halide ions (VIIb group anions) into the ZnS lattice, and that these halide ions participate in the formation of luminescence centers. Kröger et al. assumed that the copper or silver activators are in the monovalent state and substitute for Zn^{2+} ions, and that charge compensation for the monovalent activators is accomplished by introducing VIIb group anions substituting for S^{2-} ions. It was supposed that charge compensation should occur not only with VII group anions, but also with IIIb group cations, such as Al^{3+}, substituting for Zn^{2+} ions. Kröger's group[19] clearly showed that if Al^{3+} ions are introduced without using halide fluxes, similar kinds of luminescence are produced, and thus evidenced the above assumption. The VIIb or IIIb ions were called co-activators. These ions are indispensable for the formation of luminescence centers, but the luminescence spectrum is determined only by the kind of Ib ion activators and is almost independent of the kind of co-activators. This is the reason for the naming of co-activators.

In those days, the nature of the electronic transitions responsible for the luminescence in ZnS phosphors was actively discussed. The so-called Schön-Klasens model, first proposed by Schön and then discussed in detail by Klasens,[20] gained general acceptance. This model assumes that the luminescence is caused by the recombination of an electron in the conduction band, with a hole located in a level a little above the valence band.

Prencer and Williams[21] pointed out that Ib group activators and VIIb or IIIb group co-activators should be recognized, respectively, as the acceptors and the donors. It was assumed that donors and acceptors are spatially associated in some way; then it was proposed that the luminescence takes place in centers of pairs of donors (co-activators) and acceptors (activators) associated at the second and third nearest-neighbor site, and that the luminescence transition occurs from the excited state of donors to the ground state of acceptors. This was the first proposal for the donor-acceptor pair luminescence concept, which was later recognized as a basis for understanding semiconductor luminescence as mentioned in 3.7.3.

The above narration touches upon the essential points of the progress in research in this area up until the 1950s. This research was actively pursued in the 1960s. As a result, the luminescence mechanism of ZnS-type phosphors using activators of Ib elements has been elucidated quite thoroughly. This will be described below.

(b) Classification and emission spectra. The luminescence of ZnS-type phosphors using Ib group activators (Cu, Ag) and IIIb (Al, Ga, In) or VIIb (Cl, Br, I) group co-activators can be classified into five kinds, depending on the relative ratio of the concentrations of activators (X) and co-activators (Y). This condition is shown in Figure 57.[22] The range of concentrations for X and Y is 10^{-6} to 10^{-4} mol/mol. The labels of the luminescence in the figure originate from the emission color in the case that the activator is Cu; that is, G = green, B = blue, and R = red. R-Cu,In appears only when the co-activator is a IIIb group element. SA means the self-activated blue luminescence.

Figure 58 depicts the emission spectra of these five kinds of phosphors at room temperature and at 4.2K.[23] As shown in Table 20, the bandgap energy E_g of ZnS is 0.08 eV larger for the W structure than for the ZB structure. Corresponding to this, the emission peaks of phosphors with the W structure are shifted by almost this amount toward shorter wavelength. In general, phosphors prepared by firing above 1000°C have the W structure, while those below this have the ZB structure. Emission peaks at room temperature are located at longer wavelengths than those at 4.2K, except in the case of the SA luminescence. The long wavelength shift is almost proportional to that of E_g. The SA luminescence shows the inverse behavior; that is, the peak at room temperature is located at shorter

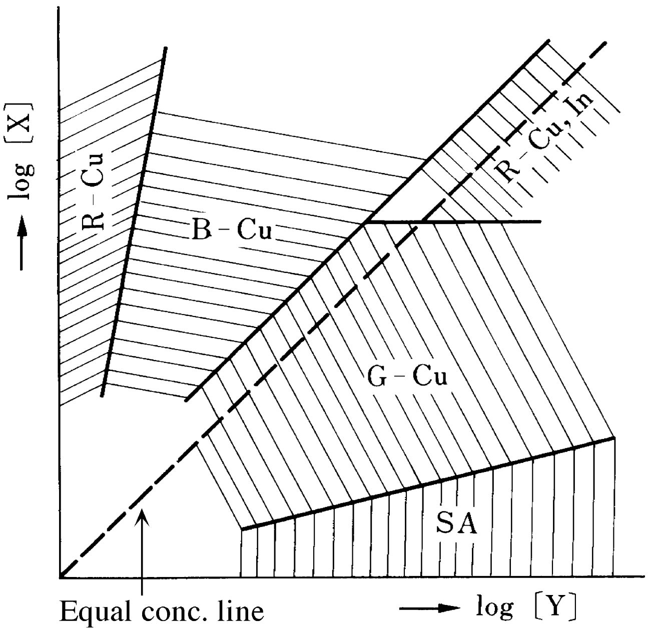

Figure 57 Five kinds of luminescence in ZnS phosphors classified from the point of view of the relative ratio of the concentrations of activators (X) and co-activators (Y). G-Cu: green Cu, B-Cu: blue Cu, R-Cu: red Cu, R-Cu, In: red Cu, In, SA: self-activated blue. (From van Gool, W., *Philips Res. Rept. Suppl.*, 3, 1, 1961. With permission.)

wavelengths. These emission spectra are almost independent of the kind of co-activators, except for the case of the SA luminescence. The G-Cu emission spectra of ZnS:Cu,Al shown in Figure 58 are almost the same as those of ZnS:Cu,Cl. In the case of the SA luminescence, the spectra of ZnS:Cl and ZnS:Al are a little different. The spectrum of ZnS:Al is slightly shifted to longer wavelengths.

If the activator is changed from Cu to Ag, the emission peaks are shifted by 0.4 to 0.5 eV to shorter wavelengths. The blue luminescence of ZnS:Ag,Cl (peak at 45 nm, W type) corresponds to the G-Cu luminescence. Au, a Ib group element, also acts as an activator. The luminescence of ZnS:Au,Al corresponding to the G-Cu luminescence has its peak at 550 nm in the ZB structure, which is shifted slightly to longer wavelengths relative to ZnS:Cu,Al.

ZnS and CdS, and also ZnS and ZnSe, form binary alloys (solid solutions) with relatively simple properties. E_g changes almost in proportion to the composition. For example, E_g in (Zn,Cd)S (W) changes from 3.91 eV for ZnS to 2.58 eV in CdS, almost in proportion to the ratio of Cd. The five kinds of luminescence discussed above also appear in the alloyed materials and have similar properties. In $Zn_xCd_{1-x}S$:Ag,Cl (W), the emission peak changes almost proportionally to E_g, i.e., changes from 435 nm for $x = 1$ to 635 nm for $x = 0.4$ continuously. It is possible to obtain a desired luminescence color from blue to red by simply adjusting the composition. In ZnS_xSe_{1-x}:Ag,Cl, the situation is similar, but the change of the emission peak is not always proportional to E_g and sometimes a weak subband appears.

Among the five kinds of luminescence discussed above, the important one for practical use is the G-Cu luminescence, which is produced when the concentrations of the activator and co-activator are nearly equal; in this case, charge compensation is readily and simply attained. ZnS:Cu,Al (green-emitting) and ZnS:Ag,Cl (blue-emitting) phosphors are

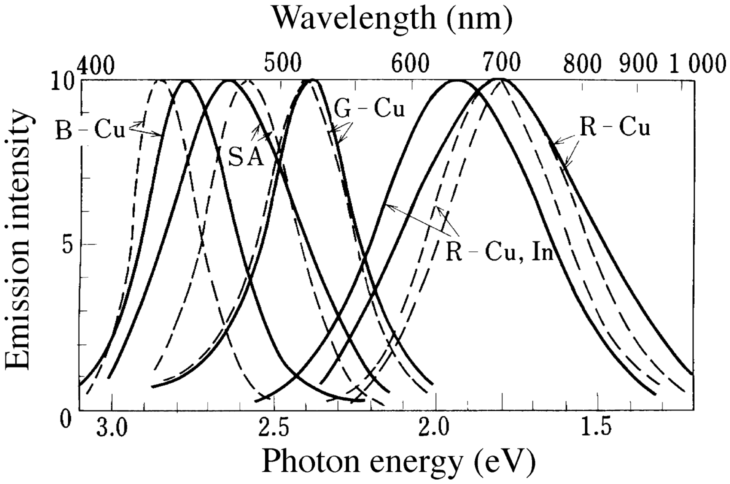

Figure 58 Spectra of the five kinds of luminescence in ZnS phosphors at room temperature (solid line) and 4.2K (dotted line). Activators and co-activators of these phosphors and the crystal structure are shown below. (Shionoya, S., Koda, T., Era, K., and Jujiwara, H., *J. Phys. Soc. Japan*, 19, 1157, 1964. With permission.)

Luminescence	Activator	Co-activator	Crystal structure
G-Cu	Cu	Al	W
B-Cu	Cu	I	ZB
SA	—	Cl	ZB
R-Cu	Cu	—	W
R-Cu,In	Cu	In	ZB

extremely important in CRT applications. ZnS:Cu,Au,Al (green-emitting) phosphors in which both Cu and Au are used as activators also find usage in this area.

The excitation spectra for these five kinds of luminescence consist of two bands in all cases. The first one, having the peak at 325 to 340 nm, corresponds to the fundamental absorption edge (or the exciton position) of the ZnS host crystal, and is called the host excitation band. The second, having the peak at 360 to 400 nm in the longer wavelength region, is characteristic of the luminescence center, and is called the characteristic excitation band. This band is produced by the transition from the ground state of the center (corresponding to the acceptor level) to the excited state of the center (corresponding to the donor level) or to the conduction band. As an example, the excitation spectra for the SA luminescence in a ZnS:Cl single crystal (ZB) are shown in Figure 59(a).[1a,24] An absorption spectrum of the crystal and the absorption band of the SA center are shown in Figure 59(b) for comparison.

(c) Atomic structure of luminescence centers and luminescence transitions. The atomic structure of the luminescence centers and the nature of luminescence transitions for the five kinds of luminescence mentioned above were elucidated in 1960s, mostly by the research of Shionoya and co-workers, as will be described below. Experimental tools that played important roles in clarifying these subjects included measurements of the polarization of luminescence light using phosphor single crystals grown by melting powder phosphors under high argon pressure[25] and measurements of time-resolved emission spectra. The essential characteristics derived from the results of these measurements, as well as the

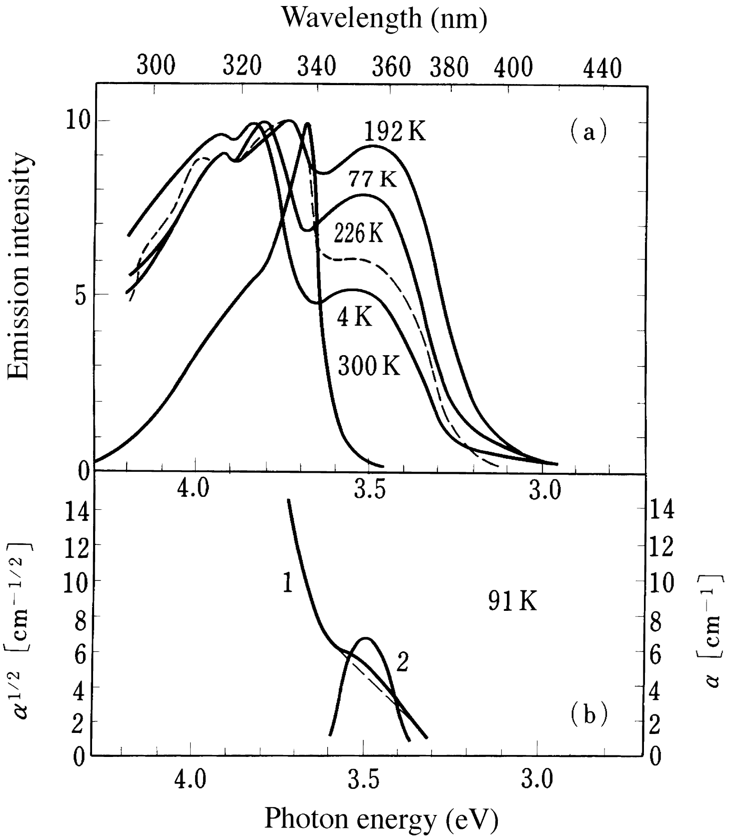

Figure 59 Excitation spectra (a) for the SA luminescence at various temperatures and an absorption spectrum (b) at 91K in a ZnS:Cl single crystal. In (b), curve 1 is the absorption spectrum plotted as $\alpha^{1/2}$ vs. E (α = absorption coefficient, E = photon energy), and curve 2 is the absorption band of the SA center obtained from curve 1 and plotted as α vs. E. (From Koda, T. and Shionoya, S., *Phys. Rev. Lett.*, 11, 77, 1963; Koda, T. and Shionoya, S., *Phys. Rev.*, 136, A541, 1964; Shionoya, S., in *Luminescence of Inorganic Solids*, Goldberg, P., Ed., Academic Press, New York, 1966, chap. 4. With permission.)

atomic structure of the luminescence centers and the nature of the luminescence transitions obtained from these results, are summarized in Table 22.

(i) Polarization of luminescence. Luminescence light from centers located within the host crystals with uniaxial symmetry, like the wurtzite structure crystals, shows polarization due to the anisotropic crystal fields. In the case of isotropic crystals, if the luminescence center is a spatially associated center, including an activator and/or a co-activator with the site symmetry which is characteristic of the center and is lower than the symmetry of the host crystal, then the polarization of luminescence light results when polarized excitation light is used. Therefore, one can determine the nature of the site symmetry of the luminescence center by observing the difference in the polarization of luminescence light when polarized and unpolarized light are used for excitation.

Among the five kinds of luminescence of ZnS phosphors, polarization measurements were first conducted for the SA luminescence of a ZnS:Cl single crystal.[24] This crystal had the cubic ZB structure, but contained a considerable amount of stacking disorder, leading to small volumes in which hexagonal structure occurred. The hexagonal regions have the *c*-axis defined by the $[111]_c$ axis of the ZB structure. In polarization

Table 22 Characteristics of the Five Kinds of Luminescence in ZnS-type Phosphors

Luminescence	Phosphor	Polarization of luminescence	Symmetry of center	Shift of emission peak	Type of luminescence transition	Structure of center
G-Cu	ZnS:Cu,Al(Cl)	ZB:no pol. W :pol. ⊥ c	No charact. symm.	Observed	D-A pair	Cu^{+}_{sub} and $Al^{+}_{sub}(Cl^{-}_{sub})$ (random distrib.)
SA	ZnS:Cl(Al)	Charact. pol.	Charact. symm. ZnS:Cl, C_{3v} ZnS:Al, C_s	Observed (ZnS:Cl)	D-A pair	$V(Zn^{2+})$-Cl^{-}_{sub} (Al^{3+}_{sub}) (associated)
B-Cu	ZnS:Cu,I(Cl)	Charact. pol.	Charact. symm. C_{3v}	No shift	Intra-center	Cu^{+}_{sub}-Cl^{+}_{int} (associated)
R-Cu	ZnS:Cu	Charact. pol.	Charact. symm. C_{3v}	No shift	Intra-center	$V(S^{2-})$-Cu^{+}_{sub} (associated)
R-Cu,In	ZnS:Cu,In	Charact. pol.	Charact. symm. C_s	No shift	Intra-center	Cu^{+}_{sub}-In^{3+}_{sub} (associated)

Note: The polarization of luminescence, the symmetry of the luminescence center obtained from the characteristics of the polarization, the spectral shift of emission peak in time-resolved emission spectra, the type of luminescence transition inferred from the spectral shift, and the atomic structure of the center. (V = vacancy; sub = substitutional; int = interstitial).

measurements, one of the crystal surfaces was irradiated perpendicularly by polarized excitation light, and the polarization was measured for the luminescence light emitted from the opposite surfaces.

The measurements were made for (110), (112), and (111) planes. Excitation was made with 340-nm light belonging to the host excitation band (H) and with 365-nm light belonging to the characteristic excitation band (C). Both polarized and unpolarized light was used. The results were expressed in terms of the degree of polarization observed, i.e., $P(\theta) = [(I_{\parallel} - I_{\perp})/(I_{\parallel} + I_{\perp})]_{\theta}$, where $I_{\parallel}$ and $I_{\perp}$ are the emission intensities measured with the analyzer parallel and perpendicular, respectively, to the polarizer, and θ is the angle between the optical axis of the polarizer and a particular crystal axis. In the case of unpolarized excitation, θ is the angle between the optical axis of the analyzer and a particular crystal axis.

The $P(\theta)$ curves measured at 77K are shown in Figure 60.[24] In the case of the characteristic (C) excitation, the $P(\theta)$ curves depend critically on whether the excitation light is polarized or unpolarized; under polarized excitation, $P(\theta)$ shows specific angular dependencies that vary for different crystal planes. In the case of host (H) excitation, on the other hand, the $P(\theta)$ curves are quite independent of the polarization of excitation light, and are the same as those obtained under the unpolarized C excitation.

The results observed under the polarized characteristic excitation clearly indicate that the center has the characteristic symmetry, which is lower than that of the host lattice. Prener and Williams[26] proposed a model for the structure of the SA center, which assumes that the center consists of a Zn^{2+} vacancy $[V(Zn^{2+})]$ and one of the charge-compensating co-activators associated at one of the nearest substitutional sites, i.e., a Cl^- co-activator at the nearest S^{2-} site or an Al^{3+} co-activator at the nearest Zn^{2+} site. Figure 61 shows a model of the SA center in ZnS:Cl. The results of polarization measurements were analyzed assuming this model.

According to this model, the SA center in ZnS:Cl has C_{3v} symmetry (in the case of ZnS:Al, C_s symmetry). Dipole transitions that are allowed in a C_{3v} center are those due to a σ-dipole perpendicular to and a π-dipole parallel to the symmetry axis. The angular dependence of the polarization of luminescence due to a σ- or a π-dipole was calculated assuming that the symmetry axes of the centers are distributed uniformly along the various directions of the Zn-S bonding axes.

The results of the calculation are represented in Figure 60 by the thin solid lines. Comparing the experimentally observed $P(\theta)$ curves under polarized C excitation with those calculated, it can be concluded that the observed anisotropy of the luminescence results from the σ-dipole. Thus, the Prener and Williams model for the atomic structure of the SA center was confirmed by these observations. The polarization of the luminescence perpendicular to the *c*-axis observed under unpolarized C excitation and under polarized and unpolarized H excitation is ascribed to the crystal structure inclusive of the hexagonal domains arising from the stacking disorder.

Measurements of the polarization of luminescence were also made for the SA luminescence in a ZnS:Al crystal.[27] The observed $P(\theta)$ curves showed characteristic angular dependencies under polarized C excitation similar to the SA luminescence in ZnS:Cl. The results were analyzed assuming C_s symmetry for the center as in the Prener and Williams model, and were well explained by ascribing the luminescence to a dipole lying in the mirror plane of the center (∥ dipole).

Results of measurements of the polarization for the five kinds of luminescence are summarized in Table 22. B-Cu,[28] R-Cu,[29] and R-Cu,In[30] luminescence showed characteristic polarizations under C excitation, indicating that the luminescence centers are some kinds of spatially associated centers. The symmetries of the centers determined by analysis are also shown in the table.

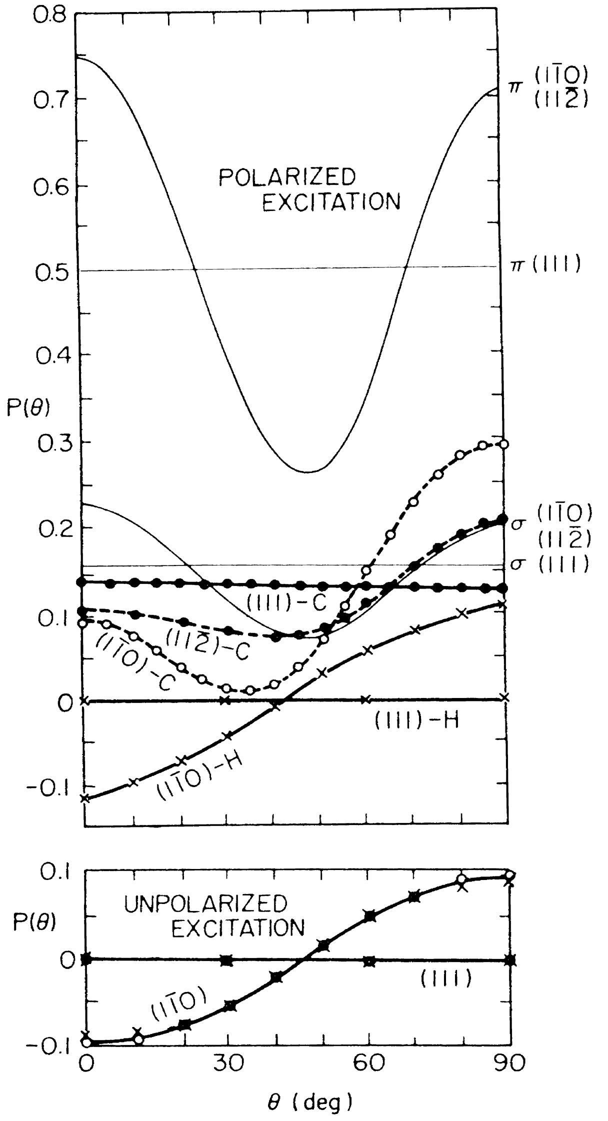

Figure 60 The degree of polarization P(θ) for the SA luminescence in a ZnS:Cl single crystal at 77K under polarized and unpolarized excitation. C and H denote, respectively, the characteristic and host excitation. θ is the angle between the optical axis of the polarizer (or the analyzer in the case of unpolarized excitation) and particular crystal axis [111]c for the surface (110) and (112), and [112] for the surface $(111)_C$. Open circles, closed circles, and crosses show experimental results. The curves drawn with thin solid lines are P(θ) curves calculated assuming σ- or π-dipole. (From Koda, T. and Shionoya, S., *Phys. Rev. Lett.*, 11, 77, 1963; *Phys. Rev.*, 136, A541, 1964. With permission.)

The G-Cu luminescence does not show characteristic polarization differently from the other four kinds of luminescence.[31] In a ZnS:Cu,Al crystal of the W structure, the polarization of luminescence perpendicular to the *c*-axis was observed independently of whether the excitation was due to the C or H band and was also independent of whether the excitation was polarized or unpolarized. In the case of a crystal of the ZB structure, no polarization was observed. These facts indicate that activators and co-activators forming the G-Cu centers are not associated with each other spatially, but are randomly distributed in a crystal occupying respective lattice sites.

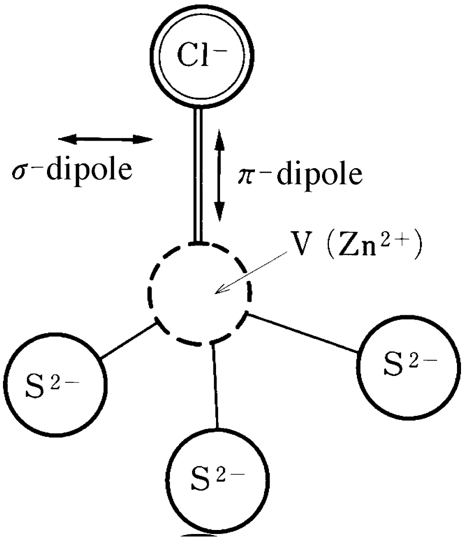

Figure 61 Model of the SA luminescence center in ZnS:Cl phosphors.

(ii) Time-resolved emission spectra. In D-A pair luminescence, spectral lines or bands are composed of a large number of unresolved pair lines. In time resolved emission spectra, as explained in 3.7.3, the peak of the lines or bands should shift to lower energies with the lapse of time. Figure 62 shows time-resolved spectra of the green luminescence of ZnS:Cu,Al.[32] It is clearly seen that the peak shifts dramatically to lower energies as a function of time.

If the excitation intensity is increased over a wide range, the D-A pair luminescence peak should shift to higher energies under certain conditions. With sufficient intensity, the lines that originate from pairs with larger intra-pair distances, and hence have long lifetimes, can be saturated, thus leading to the shift. Figure 63 shows changes in the green luminescence spectra of ZnS:Cu,Al observed with changing excitation intensity over a range of five orders of magnitude.[32] The peak is seen to shift to higher energies with excitation intensity. Also for the blue luminescence of ZnS:Ag,Al, very similar spectral peak shifts were observed, both as a function of time and with increasing excitation intensity.[32] In Table 22, shifts of emission peaks observed in the time-resolved spectra are listed for the five kinds of luminescence.

(iii) Atomic structure of various centers and luminescence transitions. The atomic structure of luminescence centers and the nature of luminescence transitions deduced from above-mentioned experimental observations and their analysis are summarized in Table 22 for the five kinds of luminescence. The luminescence for which peak shifts are observed is thought to be caused by D-A pair type transitions, while the luminescence not showing peak shifts is surely due to intra-center transitions.

G-Cu center—This center is formed by activators (A) (Cu, Ag, or Au) and co-activators (D) (Al or Cl, Br) introduced with nearly equal concentrations and distributed randomly in the lattice occupying the appropriate lattice sites. Luminescence transition takes place from the D level to the A level in various D-A pairs having different intra-pair distances. Emission spectra consist of broad bands that are quite different from those of the edge emission. In the G-Cu luminescence, the A level is much deeper than those levels involved in the edge emission. The electron-phonon interaction for the acceptors is much stronger, resulting in a Huang-Rhys-Pekar factor

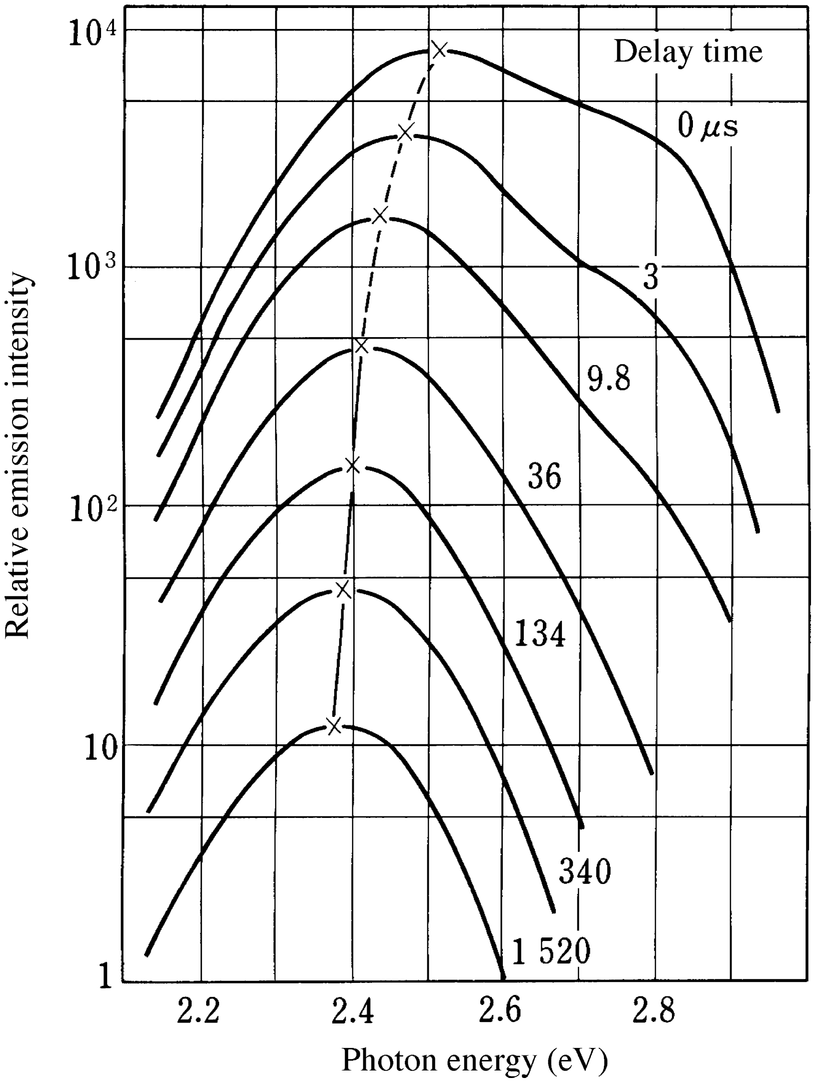

Figure 62 Time-resolved spectra of the green luminescence of ZnS:Cu,Al phosphor at 4.2K. (From Era, K., Shionoya, S., and Washizawa, T., *J. Phys. Chem. Solids*, 29, 1827, 1968; Era, K., Shionoya, S., Washizawa, Y., and Ohmatsu, H., *J. Phys. Chem. Solids*, 29, 1843, 1968. With permission.)

S much larger than 1 in the configurational coordinate model. Spectra for S = 20 are broad Gaussians (see Section II.2.3). The spectra of the G-Cu luminescence can be interpreted in this way.

The energy levels of ZnS:Cu,Al are shown in Figure 64.[33] Before excitation, Cu is monovalent (1+), while Al is trivalent (3+), so that charge compensation is realized in the lattice. Absorption A of the figure located at about 400 nm gives the characteristic excitation band of the center. When excited, Cu and Al become divalent (2+). The levels of Cu^{2+} ($3d^9$ configuration) are split by the crystal field into $^2T_2$ and ^2E states, with $^2T_2$ lying higher in the ZB structure. Under excitation, three induced absorption bands B, C, and D are observed, as shown in Figure 65.[34] The C absorption taking place inside Cu^{2+} states has a sharp zero-phonon line at 1.44 μm. Luminescence of Cu^{2+} due to the downward transition of C is observed.

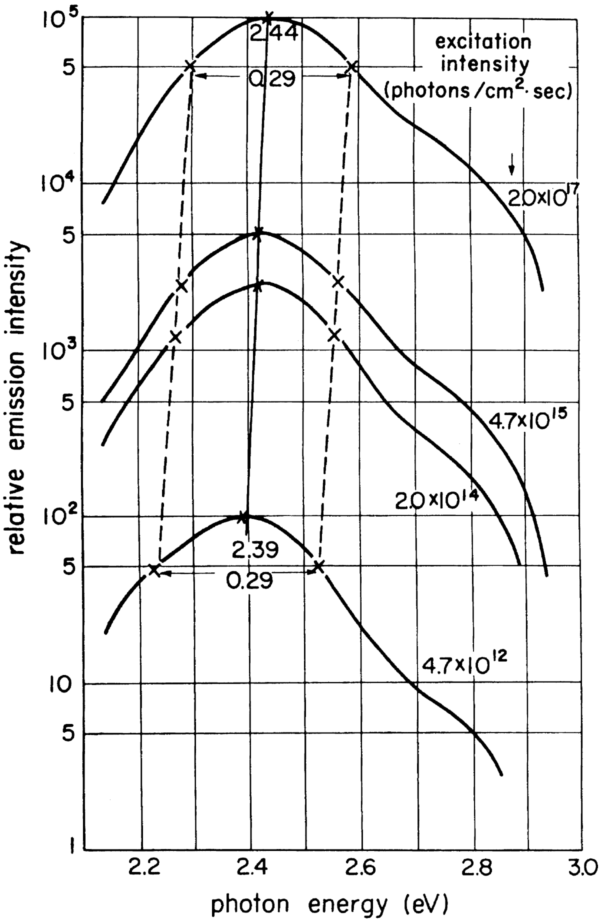

Figure 63 Changes of green luminescence spectra of ZnS:Cu,Al phosphor observed with changing excitation intensity in a wide range at 4.2K. (From Era, K., Shionoya, S., and Washizawa, T., *J. Phys. Chem. Solids*, 29, 1827, 1968; Era, K., Shionoya, S., Washizawa, Y., and Ohmatsu, H., *J. Phys. Chem. Solids*, 29, 1843, 1968. With permission.)

Utilizing the induced absorption bands due to Cu^{2+} (C band) and to Al^{2+} (B band), direct evidence for the D-A pair emission mechanism of the G-Cu luminescence can be obtained.[33] If the green luminescence of ZnS:Cu,Al originates from Cu-Al pairs, the decay rate of the luminescence R_{lum} must be correlated with the decay rates of the intensities of the Cu- and Al-induced absorption, R_{Cu} and R_{Al}. Results of studies of the luminescence decay and the decays of Cu and Al absorption intensities are shown in Figure 66.[33] It is seen in the figure that R_{Cu} and R_{Al} are equal to each other, and both are always equal to the half value of R_{lum} during decay, namely $R_{lum} = R_{Cu} + R_{Al}$. This experimentally observed relation presents very clear and direct evidence for the Cu-Al pair mechanism.

SA center—This center is formed by the spatial association of a Zn^{2+} vacancy with a co-activator Cl^- (or Al^{3+}) at the nearest-neighbor site. An emission peak shift is observed as shown in Tables 22, so that the initial state of this emission is not a level in the associated center, but is considered to be the level of an isolated Cl (Al) donor. A Zn^{2+} vacancy needs two Cl^- ions for charge compensation; one of the two Cl^- ions forms the associated center, while the other is isolated and is responsible for the initial state of the emission. The polarization of luminescence is determined by the symmetry of the surroundings of the hole at a Zn^{2+} vacancy.

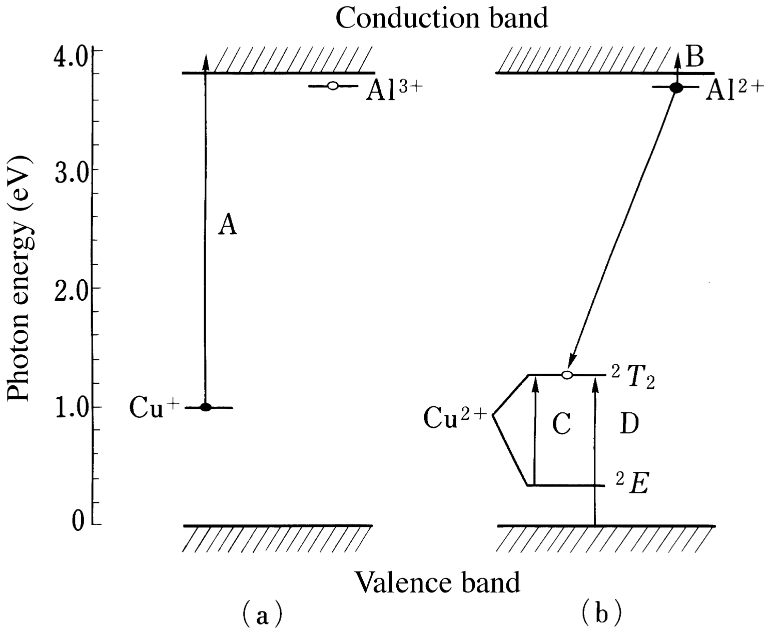

Figure 64 Energy levels and absorption transitions of ZnS:Cu,Al phosphor before excitation (a) and during excitation (b). (From Suzuki, A. and Shionoya, S., *J. Phys. Soc. Japan*, 31, 1455, 1971. With permission.)

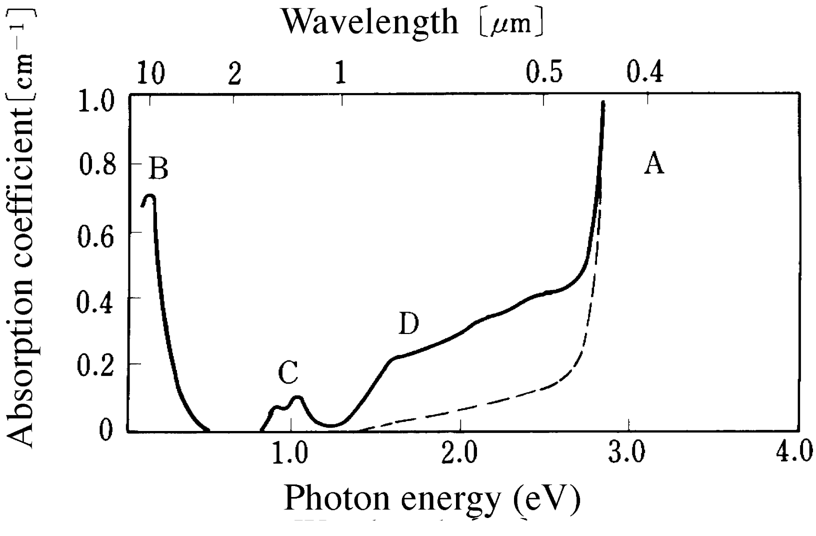

Figure 65 Spectrum of induced absorption (solid line) of a ZnS:Cu,Al single crystal under excitation at 77K, and absorption spectrum before excitation (dashed line). (From Suzuki, A. and Shionoya, S., *J. Phys. Soc. Japan*, 31, 1455, 1971. With permission.)

R-Cu center—The polarization characteristics of this luminescence can be interpreted by assuming C_{3v} symmetry and by taking into account the crystal field splitting of the Cu^{2+} 3*d* orbital in this symmetry.[29] It has been concluded that this center is formed by the spatial association of a substitutional Cu^+ and a S^{2-} vacancy at the nearest-neighbor sites. Therefore, this center is one in which the relation between activator and co-activator is just reversed from that of the SA center. In this sense, this center can be also called the self-coactivated

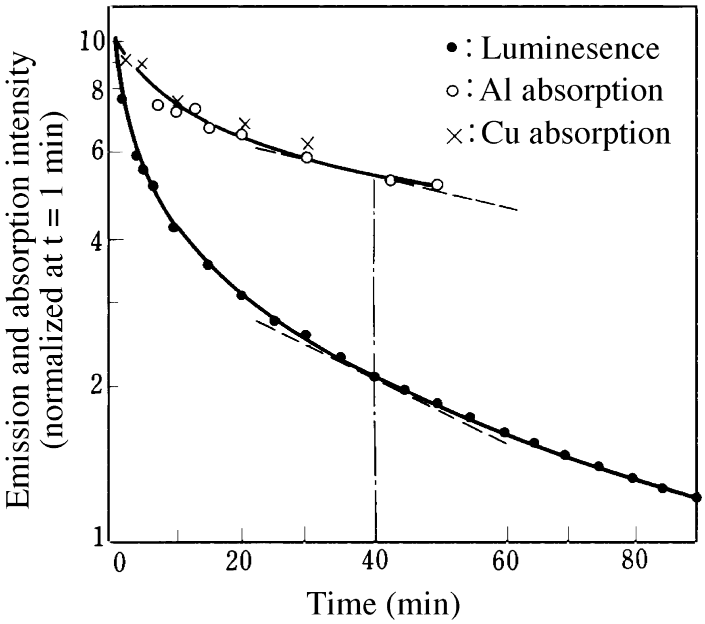

Figure 66 Decay curves of green luminescence and induced absorption intensities due to Cu and Al in a ZnS:Cu,Al single crystal at about 10K. (From Suzuki, A. and Shionoya, S., *J. Phys. Soc. Japan*, 31, 1455, 1971. With permission.)

center. No spectral shift is observed, so that this luminescence is due to intra-center transitions and the initial state is the level of the S^{2-} vacancy.

R-Cu,In center—The polarization characteristics of this luminescence can be interpreted by assuming C_s symmetry and by taking into account the splitting of the Cu^{2+} 3*d* orbital.[30] There is no spectral shift. Therefore, this center is formed by the spatial association of a substitutional Cu^+ and In^{3+} at the nearest neighbor sites, and the luminescence is due to intra-center transitions from the In donor level to the Cu acceptor level.

B-Cu center—The polarization characteristics of this luminescence can be explained if one assumes either C_{3v} or C_s symmetry for the center.[28] A model of this center has been proposed, which suggests that the center is formed by the spatial association of a substitutional Cu^+ and an interstitial Cu^+.[35] Such a proposed center would have C_{3v} symmetry.

In ZnSe, the center corresponding to the B-Cu center in ZnS shows green luminescence. Measurements of optically detected electron spin resonance indicates that the center has the structure of a pair composed of a substitutional Cu^+ and an interstitial Cu^+.[36] It is clear that the B-Cu center in ZnS has the same type of structure and has C_{3v} symmetry. The B-Cu luminescence shows no spectral shift, indicating that it is due to an intra-center transitions. However, the nature of the initial state of the transition is not clear.

(d) Other luminescence characteristics

(i) Stimulation and quenching. It has been known since the beginning of this century that Cu-activated green ZnS phosphors show distinct stimulation or quenching of the luminescence if irradiated by red or near-infrared (NIR) light while under ultraviolet excitation or during the luminescent decay following excitation. Whether stimulation or quenching occurs depends on the conditions of observation, i.e., the ratio of the intensity of the excitation light to the red or NIR light and on the temperature. Exposure with red or NIR light during decay usually results in stimulation first, changing to quenching as time

progresses. The spectra of the light producing stimulation and quenching have two peaks at 0.6–0.8 and 1.3 μm. It is seen from Figures 64 and 65 that these two peaks correspond to the induced absorption bands C and D, indicating that absorption by excited Cu activators (Cu^{2+} ions) is responsible for these phenomena.

By measuring time-resolved emission spectra and photoconductivity under irradiation with red to NIR light, the mechanisms for stimulation and quenching have been established.[37] Holes are created in the valence band by induced absorption of the C and D bands (in the case of the C band, only at room temperature). These holes move in the valence band and are trapped by unexcited Cu activators. If Al (or Cl) co-activators exist in the vicinity and have trapped electrons, green luminescence is produced immediately. In D-A type luminescence, the transition probability is larger when the intra-pair distance is smaller, so that this immediate luminescence process occurs. Under the stimulation irradiation of red to NIR light with ultraviolet excitation, the average value of the intra-pair distance for excited Cu-Al pairs becomes shorter, increasing the average transition probability and producing stimulated luminescence. On the other hand, quenching is caused by a process where holes created in the valence band are trapped by various nonradiative recombination centers, thus decreasing the effective number of holes.

(ii) Killer effect. It has also been known since the 1920s that the luminescence intensity of ZnS phosphors is greatly reduced by contamination with very small amounts of the iron group elements Fe, Ni, and Co. Because of it, the iron group elements were called *killers* of luminescence. It follows that it is very important to remove iron group elements in the manufacturing processes of ZnS phosphors.

Figure 67 shows how contamination by Fe^{2+}, Ni^{2+}, and Co^{2+} reduces the intensity of the green luminescence in ZnS:Cu,Al.[38] The results for Mn^{2+}, which also belongs to the iron group, are also shown. In this case, an orange luminescence of Mn^{2+} is produced, as will be described in 3.7.4.2; the Mn^{2+} intensity is also shown in the figure.

The iron group ions have absorption bands in the visible region, and their spectra overlap the G-Cu luminescence spectrum. It is thought that resonance energy transfer from excited G-Cu centers to iron group ions takes place, reducing the G-Cu luminescence intensity and causing the killer effect. The overlap between the luminescence and the absorption spectra of iron group ions obtained using single crystals, and the decrease in the green luminescence intensity caused by energy transfer were calculated. The results are shown in Figure 67(b) by the dotted lines. The decrease of the luminescence intensity in Mn^{2+} is well described by this energy transfer effect. In the case of Fe^{2+}, Ni^{2+}, and Co^{2+}, the actual intensity decrease is considerably more than that which was calculated. As the reason for this disagreement, it is suggested that iron group ions create deep levels, and electrons and holes recombine nonradiatively via these levels.

(iii) Concentration quenching and luminescence saturation. In ZnS:Cu,Al phosphors, if the concentration of activators and co-activators is increased to obtain brighter phosphors, concentration quenching results. The optimum concentration is Cu: 1.2×10^{-4} mol/mol and Al: 2×10^{-4}. These phosphors show, when used in CRTs, the phenomenon of luminescence intensity saturation when the current density is raised, as shown in Figure 68.[39] A very similar phenomenon occurs in ZnS:Ag,Al.[40] Luminescence saturation phenomena present serious problems in the practical use of these phosphors for CRT purposes.

The cause of the concentration quenching and luminescence saturation is not well understood, but the nonradiative Auger effect is thought to play an important role.[38] In this effect, excited Cu-Al pairs are annihilated nonradiatively, their energy is transferred

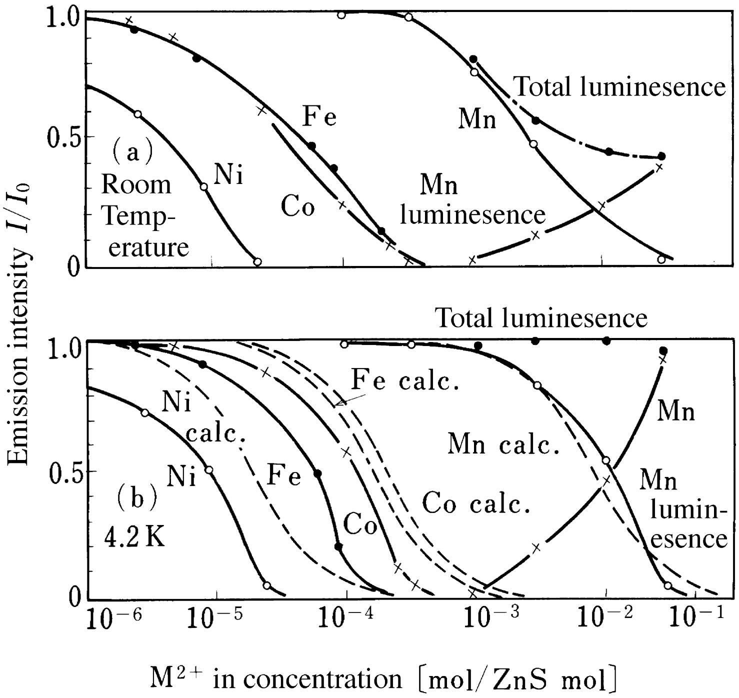

Figure 67 Dependence of the G-Cu luminescence intensity (solid curves) in ZnS:Cu,Al(M) phosphors on the concentration of Mn^{2+} (Mn^{2+}, Fe^{2+}, Ni^{2+}, and Co^{2+}) at (a) room temperature and (b) 4.2K. In the case of Mn^{2+}, the intensity of the Mn^{2+} orange luminescence and the total of the intensities of the G-Cu and Mn^{2+} luminescence are also shown. Dotted curves in (b) are calculated assuming the killer effect due to resonance energy transfer. (From Tabei, M., Shionoya, S., and Ohmatsu, H., *Jpn. J. Appl. Phys.*, 14, 240, 1975. With permission.)

to unexcited Cu activators, and electrons are raised into the conduction band. In this way, the excitation energy migrates in the lattice, and is dissipated in nonradiative recombination traps.

3.7.4.2 Luminescence of transition metal ions

Divalent transition metal ions with a $3d^n$ electron configurations have ionic radii close to those of the cations of IIb-VIb compounds. Therefore, these transition metal ions can be easily introduced into IIb-VIb compounds; the optical properties of such ions have been investigated in detail. Optical transitions taking place within the ions can be interpreted by crystal field theory (see 3.2), assuming T_d symmetry in ZB lattices. Besides intra-ion absorption, various charge-transfer absorptions, such as the valence band → ion and ion → the conduction band, are observed. Luminescence from charge-transfer transitions is also observed in some cases. The absorption band A of ZnS:Cu,Al in Figure 64 is an example of this kind of absorption.

$\underline{Mn}^{2+}$—The orange luminescence of ZnS:Mn^{2+} has been known since early days, and is important in applications in electroluminescence (see 2.10 and 9.1). The emission spectrum has a peak at 585 nm at room temperature with a halfwidth of 0.2 eV.

Absorption spectra of a ZnS:Mn^{2+} single crystal are shown in Figure 69.[41] The ground state of Mn^{2+} is $^6A_1$ (originating from the free ion state ^6S). Absorption bands at 535, 495, 460, 425, and 385 nm correspond to transitions from the ground state to $^4T_1(^4G)$, $^4T_2(^4G)$, $(^4A_1,^4E)(^4G)$, $^4T_2(^4D)$, and $^4E(^4D)$ excited states, respectively. Luminescence is produced from

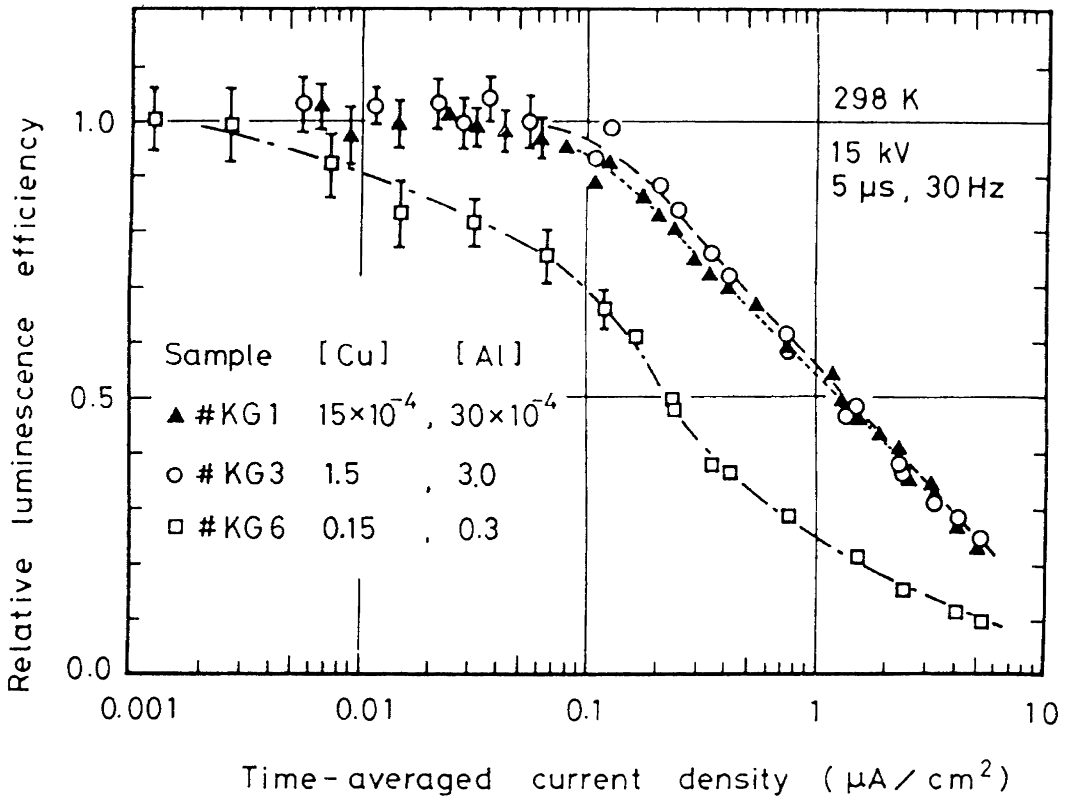

Figure 68 Current density dependence of the green luminescence of three kinds of ZnS:Cu,Al (W type) phosphors at room temperature. Excitation was made by a pulsed 15-kV electron beam with 5-μs duration and a repetition frequency of 30 Hz. (From Kawai, H., Kuboniwa, S., and Hoshina, T., *Jpn. J. Appl. Phys.*, 13, 1593, 1974. With permission.)

the lowest excited state $^4T_1(^4G)$, and a sharp zero-phonon line common to the absorption and the emission is observed at 558.94 nm.[42]

The location of the Mn^{2+} energy levels in relation to the energy bands of the ZnS host is important in discussing the excitation mechanism for Mn^{2+}. From measurements of X-ray photoelectron spectroscopy, it has been found that the Mn^{2+} ground state is located 3 eV below the top of the ZnS valence band.[43] In more recent measurements using resonant synchrotron radiation, the locations of the Mn^{2+} ground state in ZnS, ZnSe, and ZnTe are 3.5, 3.6, and 3.8 eV, respectively, below the top of the valence band.[44]

Fe^{2+} and Fe^{3+} — Iron in ZnS is usually divalent. Two kinds of infrared luminescence due to intra-ion transitions of Fe^{2+} are known. One appears at 3.3 to 4.2 μm and is due to the transition from the lowest excited state $^5T_2(^5D)$ to the ground state $^5E(^5D)$ of Fe^{2+}.[45] The other is composed of two bands at 971 nm and 1.43 μm, which are due to transitions from a higher excited state $^3T_1(^3H)$ to the ground state ^5E and the lowest excited state $^5T_2$, respectively.[46] In the killer effect of Fe^{2+} mentioned in Section 3.7.4.1, excitation energy is transferred from the G-Cu center to Fe^{2+} and is down-converted to infrared luminescence or is dissipated nonradiatively.

It has also been known since early days that iron in ZnS emits red luminescence at 660 nm. This luminescence is due to a pair-type transition, and is considered to be caused by a transition from a Cl^{2-} state (Cl^- donor trapping and electron) to an Fe^{3+} state

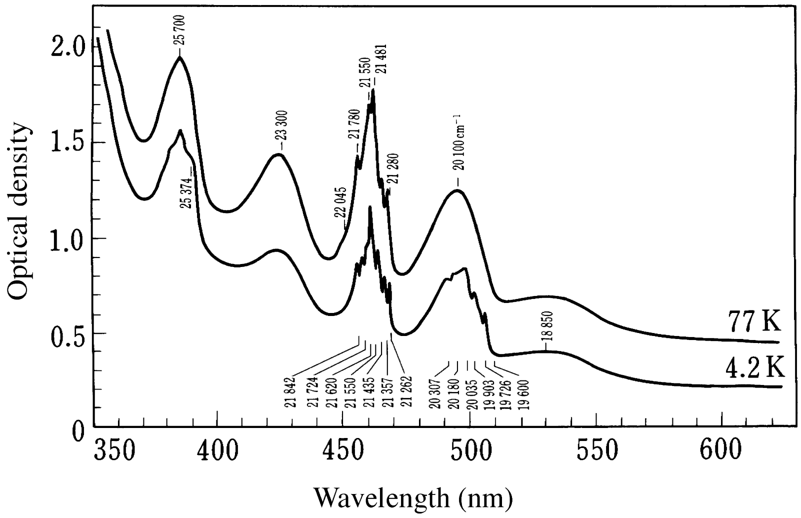

Figure 69 Absorption spectra of a ZnS:Mn^{2+} (4.02 mol%) (ZB type) single crystal with 1.34-mm thickness at 4.2 and 77K. (From McClure, D.S., *J. Chem. Phys.*, 39, 2850, 1963. With permission.)

(photoionized Fe^{2+}).[47] In this process, luminescence at 980 nm is also produced from intra-ion transitions in Fe^{3+}.[48]

Cu^{2+}—Copper in ZnS is usually monovalent. As mentioned in 3.7.4.1(c)(iii), when ZnS:Cu,Al phosphors are excited, an ionization process $Cu^+ \rightarrow Cu^{2+}$ takes place and luminescence at 1.44 μm, due to an intra-ion transition from $^2T_2(^2D)$ to $^2E(^2D)$ of Cu^{2+}, is produced (see Figure 64).

ZnO:Cu exhibits green luminescence in a band spectrum with the peak at 510 nm and a broad halfwidth of 0.4 eV. The zero-phonon line was observed at 2.8590 eV.[49] In ZnO the Cu^{2+} level is located 0.2 eV below the bottom of the conduction band, which is different from the case of ZnS. Luminescence is considered to be produced by the recombination of an electron trapped at the Cu^{2+} level (Cu^+ state) with a hole in the valence band.

3.7.4.3 *Luminescence of rare-earth ions*

The luminescence of trivalent rare-earth ions in IIb-VIb compounds has also been investigated in fair detail. The introduction of trivalent rare-earth ions with high concentrations into IIb-VIb compounds is difficult, because the valence is different from the host cations and the chemical properties are also quite different. This is one of the reasons that bright luminescence from trivalent rare-earth ions in ZnS is rather difficult to obtain.

Exceptionally bright and highly efficient luminescence has been observed in ZnS:Tm^{3+}.[50] This phosphor shows bright blue luminescence under cathode-ray excitation. The spectrum is shown in Figure 70; the strongest line at 487 nm is due to the $^1G_4 \rightarrow {}^3H_6$ transition (see 3.3).[51] Beside this line, there are weak lines at 645 nm ($^1G_4 \rightarrow {}^3F_4$) and 775–800 nm ($^1G_4 \rightarrow {}^3H_5$). In the figure, the spectra of commercial ZnS:Ag,Cl phosphors (P22 and P11) used in color CRTs (see 6.3) are also shown for comparison. The energy efficiency of ZnS:Tm^{3+} under cathode-ray excitation is 0.216 W/W and is very high; this value should be compared with 0.23 W/W obtained in ZnS:Ag,Cl (P22).

3.7.5 *ZnO phosphors*

It has been known since the 1940s that by firing pure ZnO powders in a reducing atmosphere, a phosphor showing bright white-green luminescence can be prepared.[6] The

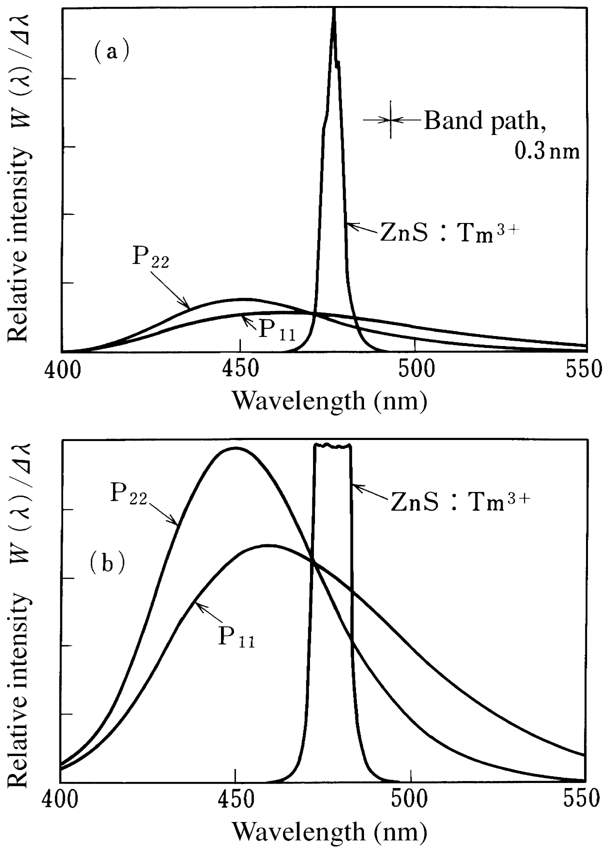

Figure 70 Emission spectra of a ZnS:Tm^{3+} phosphor under cathode-ray excitation. Spectra of ZnS:Ag,Cl phosphors (P22, P11) are also shown for comparison. (From Shrader, R.E., Larach, S., and Yocom, P.N., *J. Appl. Phys.*, 42, 4529, 1971. With permission.)

chemical formula of this phosphor is written customarily as ZnO:Zn because it is obtained in a reducing atmosphere without adding activators. The emission spectrum has a peak at 495 nm and is very broad, having a halfwidth of 0.4 eV. This phosphor shows conductivity, and hence is an exceedingly valuable phosphor for applications to vacuum fluorescent displays and field emission displays (see Chapter 8).

The origin of the luminescence center and the luminescence mechanism of ZnO:Zn phosphors are barely understood. Due to firing in reducing atmospheres, these phosphors contain excess zinc; its amount can be determined by colorimetric analysis and has been found to be in the 5–15 ppm range. This amount of excess zinc is almost proportional to the intensity of the white-green luminescence of these phosphors.[52] Therefore, it is clear that intertitial zinc or oxygen vacancy participates in the formation of the luminescence center, but nothing has been established with certainty. The decay constant of the emission is about 1 μs; the decay becomes faster with increased excitation intensity.[53] From this, the luminescence is thought to be due to a bimolecular type recombination.

References

1. Review of luminescence of IIb-VIb compounds:
   a. Shionoya, S., Luminescence of lattices of the ZnS type, in *Luminescence of Inorganic Solids*, Goldberg, P., Ed., Academic Press, New York, 1966, chap. 4.

    b. Shionoya, S., *II–VI Semiconducting Compounds, 1967 International Conference*, Thomas, D.G., Ed., W. A. Benjamin, Inc., 1967, 1.
    c. Shionoya, S., *J. Luminesc.*, 1/2, 17, 1970.
    d. Curie, D. and Prener, J.S., Deep Center Luminescence, in *Physics and Cemistryn of II-VI Compounds*, Aven, M. and Prener, J.S., Ed., North-Holland Pub. Co., Amsterdam, 1967, chap. 4.
2. Arpiarian, N., *Proc. Int. Conf. Luminesc.*, Budapest, 1966, Szigeti, G., Ed., Akadémiai Kiadó, Budapest, 1968, 903.
3. Becquerel, E., *Compt. Rend. Acad. Sci.*, LXIII, 188, 1866.
4. Chelikowsky, J.R. and Cohen, M.L., *Phys. Rev.*, B14, 556, 1976.
5. Nakamura, S., Sakashita, T., Yoshimura, K., Yamada, Y., and Taguchi, T., *Jpn. J. Appl. Phys.*, 36, L491, 1997.
6. Shrader, R.E. and Leverenz, H.W., *J. Opt. Soc. Am.*, 37, 939, 1947.
7. Miyamoto, S., *Jpn. J. Appl. Phys.*, 17, 1129, 1978.
8. Klick, C.C., *J. Opt. Soc. Am.*, 37, 939, 1947.
9. Thomas, D.G., Gershenzon, M., and Trumbore, F.A., *Phys. Rev.*, 133, A269, 1964.
10. Henry, C.H., Faulkner, R.A., and Nassau, K., *Phys. Rev.*, 183, 708, 1968.
11. Reynolds, D.C. and Collins, T.C., *Phys. Rev.*, 188, 1267, 1969.
12. Dean, P.J. and Merz, J.L., *Phys. Rev.*, 178, 1310, 1969.
13. Merz, J.L., Nassau, K., and Siever, J.W., *Phys. Rev.*, B8, 1444, 1973.
14. Colbow, K., *Phys. Rev.*, 141, 742, 1966.
15. Bhargava, R.N., *J. Cryst. Growth*, 59, 15, 1982.
16. Leverenz, H.W., *An Introduction to Luminescence of Solids*, John Wiley & Sons, New York, 1950.
17. Kröger, F.A. and Hellingman, J.E., *Trans. Electrochem. Soc.*, 95, 68, 1949.
18. Kröger, F.A., Hellingman, J.E., and Smit, N.W., *Physica*, 15, 990, 1949.
19. Kröger, F.A. and Dikhoff, J.A.M., *Physica*, 16, 297, 1950.
20. Klasens, H.A., *J. Electrochem. Soc.*, 100, 72, 1953.
21. Prener, J.S. and Williams, F.E., *J. Electrochem. Soc.*, 103, 342, 1956.
22. van Gool, W., *Philips Res. Rept. Suppl.*, 3, 1, 1961.
23. Shionoya, S., Koda, T., Era, K., and Fujiwara, H., *J. Phys. Soc. Japan*, 19, 1157, 1964.
24. Koda, T. and Shionoya, S., *Phys. Rev. Lett.*, 11, 77, 1963; *Phys. Rev.*, 136, A541, 1964.
25. Kukimoto, H., Shionoya, S., Koda, T., and Hioki, R., *J. Phys. Chem. Solids*, 29, 935, 1968.
26. Prener, J.S. and Williams, F.E., *J. Chem. Phys.*, 25, 361, 1956.
27. Urabe, K. and Shionoya, S., *J. Phys. Soc. Japan*, 24, 543, 1968.
28. Urabe, K., Shionoya, S., and Suzuki, A., *J. Phys. Soc. Japan*, 25, 1611, 1968.
29. Shionoya, S., Urabe, K., Koda, T., Era, K., and Fujiwara, H., *J. Phys. Chem. Solids*, 27, 865, 1966.
30. Suzuki, A. and Shionoya, S., *J. Phys. Soc. Japan*, 31, 1719, 1971.
31. Shionoya, S., Kobayashi, Y., and Koda, T., *J. Phys. Soc. Japan*, 20, 2046, 1965; Suzuki, A. and Shionoya, S., *J. Phys. Soc. Japan*, 31, 1462, 1971.
32. Era, K., Shionoya, S., and Washizawa, Y., *J. Phys. Chem. Solids*, 29, 1827, 1968; Era, K., Shionoya, S., Washizawa, Y., and Ohmatsu, H., *J. Phys. Chem. Solids*, 29, 1843, 1968.
33. Suzuki, A. and Shionoya, S., *J. Phys. Soc. Japan*, 31, 1455, 1971.
34. Broser, I., Maier, H. and Schultz, H.J., *Phys. Rev.*, 140, A2135, 1965.
35. Blicks, H., Riehl, N., and Sizmann, R., *Z. Phys.*, 163, 594, 1961.
36. Patel, J.L., Davies, J.J., and Nicholls, J.E., *J. Phys.*, C14, 5545, 1981.
37. Tabei, M. and Shionoya, S., *J. Luminesc.*, 15, 201, 1977.
38. Tabei, M., Shionoya, S., and Ohmatsu, H., *Jpn. J. Appl. Phys.*, 14, 240, 1975.
39. Kawai, H., Kuboniwa, S., and Hoshina, T., *Jpn. J. Appl. Phys.*, 13, 1593, 1974.
40. Raue, R., Shiiki, M., Matsukiyo, H., Toyama, H., and Yamamoto, H., *J. Appl. Phys.*, 75, 481, 1994.
41. McClure, D.S., *J. Chem. Phys.*, 39, 2850, 1963.
42. Langer, D. and Ibuki, S., *Phys. Rev.*, 138, A809, 1965.
43. Langer, D., Helmer, J.C., and Weichert, N.H., *J. Luminesc.*, 1/2, 341, 1970.
44. Weidemann, R., Gumlich, H.-E., Kupsch, M., and Middelmann, H.-U., *Phys. Rev.*, B45, 1172, 1992.

45. Slack, G.A. and O'Meara, B.M., *Phys. Rev.*, 163, 335, 1967.
46. Skowrónski, M. and Lire, D., *J. Luminesc.*, 24/25, 253, 1981.
47. Jaszczyn-Kopec, P. and Lambert, B., *J. Luminesc.*, 10, 243, 1975.
48. Nelkowski, H., Pfützenreuter, O. and Schrittenlacher, W., *J. Luminesc.*, 20, 403, 1979.
49. Dingle, R., *Phys. Rev. Lett.*, 23, 579, 1969.
50. Shrader, R.E., Larach, S., and Yocom, P.N., *J. Appl. Phys.*, 42, 4529, 1971.
51. Charreire, Y. and Parche, P., *J. Electrochem. Soc.*, 130, 175, 1983.
52. Harada, T. and Shionoya, S., *Tech. Digest, Phosphor Res. Soc., 174th Meeting*, February 1979 (in Japanese).
53. Pfanel, A., *J. Electrochem. Soc.*, 109, 502, 1962.

chapter three — section eight

Principal phosphor materials and their optical properties

Toshiya Yokogawa

Contents

3.8 ZnSe and related luminescent materials 275
  3.8.1 MOVPE 275
  3.8.2 MBE 276
  3.8.3 *n*-Type doping 277
  3.8.4 *p*-Type doping 278
  3.8.5 ZnSe-based blue-green laser diodes 278
  3.8.6 ZnSe-based light-emitting diodes 280
References 281

3.8 ZnSe and related luminescent materials

The wide-bandgap ZnSe and related luminescent materials have attracted considerable recent attention because of the advent of blue-green lasers and light emitting diodes (LEDs). Since ZnSe is nearly lattice matched to GaAs (which is a high-quality substrate material), high-quality ZnSe can be grown. Furthermore, addition of S, Mg, or Cd to ZnSe leads to a ternary or quaternary alloy with a higher or lower bandgap, a property which is needed to fabricate heterostructure devices. Advanced crystal growth techniques such as metal organic vapor phase epitaxy (MOVPE) and molecular beam epitaxy (MBE) have made it possible to grow not only high-quality ZnSe but also lattice-matched ternary and quaternary alloys on (100) GaAs substrates. The success of these growth techniques at low temperatures has resulted in limiting the concentration of background impurities. The reduction of background impurities has allowed us to control the conductivity by the incorporation of shallow acceptors and donors. In this section, crystal growth techniques for ZnSe and related luminescent materials will be described first, and then application for ZnSe-based laser diodes will be discussed.

3.8.1 MOVPE

MOVPE growth of ZnSe involves the pyrolysis of a vapor-phase mixture of H_2Se and, most commonly, dimethylzinc (DMZn) or diethylzinc (DEZn). Free Zn atoms and Se molecules are formed and these species recombine on the hot substrate surface in an irreversible reaction to form ZnSe. Growth is carried out in a cold-wall reactor in flowing H_2 at atmospheric or low pressure. The substrate is heated to temperatures of 300 to 400°C, typically by radio frequency (RF) heating. Transport of the metal-organics to the growth zone is achieved by bubbling H_2 through the liquid sources, which are held in temperature-controlled containers.

When DMZn and H_2Se are used for the MOVPE growth, a premature reaction takes place, resulting in poor uniformity and poor surface morphology of the ZnSe epitaxial layers. This has been solved by using dialkyl zincs and dialkyl selenides (DMSe or DESe).[1] With these source materials, uniform growth of ZnSe epitaxial layers with smooth surface morphology has been achieved. However, the growth temperature has to be increased above 500°C for ZnSe.

Recently, it has been established that the growth at relatively lower temperature and the use of high-purity source materials are required to obtain high-quality ZnSe films. It has also been reported that photo-assisted MOVPE growth dramatically enhances the growth rate of ZnSe at temperatures as low as 350°C, reducing the optimum growth temperature.[2]

It was generally thought that the source materials of DMZn or DEZn typically contain 10 to 100 ppm chlorine impurity. The ZnSe epitaxial layers grown using such sources show strong bound-exciton emission due to chlorine donor impurities. On the other hand, ZnSe layers grown using high-purity DMZn showed dominant free-exciton emission in the low-temperature photoluminescence spectrum, as shown in Figure 71.[2] The DMZn used was purified so that the chlorine content was below the detection limit of 5 ppm.

Numerous attempts have been made to grow *p*-type ZnSe crystals using group I and V elements as acceptor dopants. However, there have been only a few attempts for the MOVPE growth of *p*-type ZnSe. With Li doping by MOVPE, high *p*-type conductivity ($50\ \Omega^{-1}\ \mathrm{cm}^{-1}$) materials with carrier concentrations up to $10^{18}\ \mathrm{cm}^{-3}$ have been demonstrated, although the very fast diffusion rate of Li dopants in ZnSe crystal results in poor controllability of carrier concentrations.[3] Nitrogen is thought to be a stable acceptor impurity. However, nitrogen doping in the MOVPE resulted in highly resistive ZnSe films. The nitrogen doping in MOVPE still experiences a problem with the low activation efficiency of acceptors due to hydrogen passivation.[4,5]

n-type doping elements for the MOVPE growth also has been investigated using Al and Ga to substitute for the Zn site and Cl, Br, and I for the Se site in the ZnSe lattice. It has been reported that iodine doping with ethyliodide or n-butyliodide results in a good controllability of carrier concentrations, which range from 10^{15} to $10^{19}\ \mathrm{cm}^{-3}$.[6,7]

3.8.2 MBE

Molecular beam epitaxy (MBE) is the growth of semiconductor films such as ZnSe by the impingement of directed atomic or molecular beams on a crystalline surface under ultra-high-vacuum (UHV) condition. Molecular beams of Zn and Se are generated in a resistively heated Knudsen cell within the growth chamber. GaAs substrates are usually used for the ZnSe growth. Modern II-VI MBE systems are generally a multichamber apparatus comprising a fast entry load-lock, a preparation chamber, and two growth chambers for II-VI and III-V films. Systems are of stainless steel construction pumped to UHV conditions. Base pressures of 10^{-11} to 10^{-10} Torr are normally attained. A major attraction of MBE is that the use of UHV conditions enables the incorporation of high-vacuum-based surface analytical and diagnostic techniques. Reflection high-energy electron diffraction (RHEED) is commonly employed to examine the substrate and the actual epitaxial film during

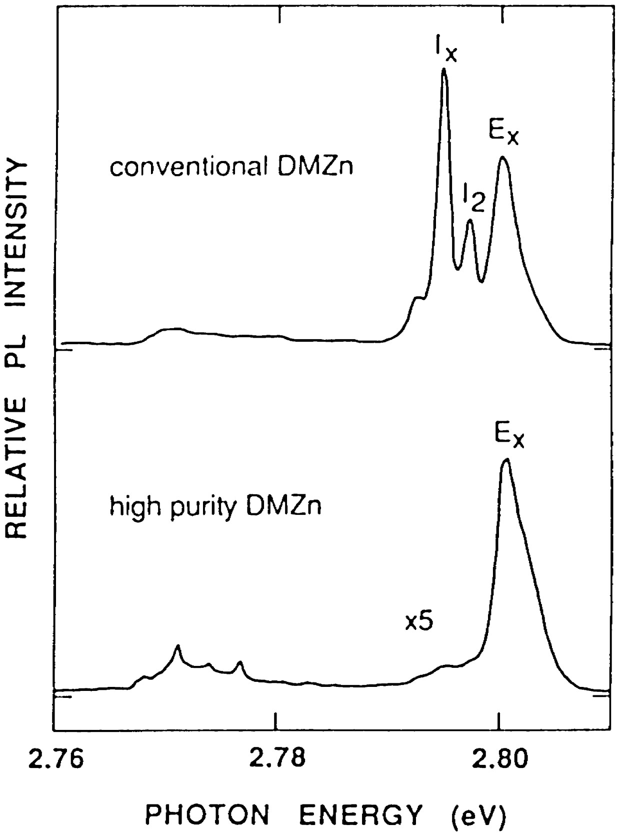

Figure 71 Photoluminescence spectra at 10K of ZnSe films grown using a conventional DMZn source in which about 15 ppm chlorine impurities are involved (upper trace), and using a purified source for which the chlorine content is below the detection limit of 5 ppm. The emission line labeled E_x is due to free excitons, and emission lines I_2 and I_x are due to excitons bound to neutral acceptors. (From Kukimoto, H., *J. Crystal Growth*, 101, 953, 1990. With permission.)

growth. A (quadrupole) mass spectrometer is essential for monitoring the gas composition in the MBE growth chamber.

Early ZnSe-based laser diodes show room-temperature and continuous wave (RTCW) lifetimes of the order of a minute because of degradation caused by extended crystalline defects such as stacking faults. Transmission electron microscopy (TEM) imaging indicates that the degradation originates from dislocation networks that developed in the quantum well region during lasing. The dislocation networks were produced by the stacking faults nucleated at the II-VI/GaAs interface and extending into the II-VI layer. To reduce the stacking fault density, incorporation of GaAs and ZnSe buffer layers and Zn treatment of the II-VI/GaAs interface were employed.[8] The lowest defect density films were reported to be obtained when the (2X4) As-stabilized GaAs surface was exposed to a Zn flux, which resulted in (2X4) to (1X4) surface reconstructions. This was then followed by the epitaxial growth of ZnSe. Stacking fault densities of 10^3 cm^{-2} or less were achieved under this growth condition.

3.8.3 *n-Type doping*

Group III atoms such as Al and Ga substituting in Zn sites and Group VII atoms such as Cl and I in Se sites are typical impurities producing *n*-type carriers in ZnSe crystals.

n-Type doping in ZnSe during MBE growth has been extensively studied. Ga impurities have often been used as a donor dopant although maximum carrier concentrations are limited to approximately 10^{17} cm^{-3}. The photoluminescence (PL) properties of Al- or Ga-doped layers shows a remarkable degradation of the band-edge emission when the carrier concentration exceeds 10^{17} cm^{-3}.[9] Cl impurities were also studied as a donor dopant at the Se site.[10] In Cl doping, *n*-type carrier concentration increases with the temperature of the $ZnCl_2$ cell. The maximum carrier concentration has been estimated to be 10^{19} cm^{-3}, resulting in a small resistivity of 10^{-3} Ωcm. Lately, Cl impurities have been used to fabricate blue-green laser diodes and light-emitting diodes because of advantages presented by controllability and crystalline quality.

3.8.4 p-*Type doping*

Group I atoms such as Li and Na at Zn sites and group V atoms such as N, P, and As at Se sites are typical impurities used to produce *p*-type carriers in ZnSe crystals. Net acceptor concentrations (N_A–N_D) of 10^{17} cm^{-3} have been achieved using Li doping at a growth temperature of 300°C.[11] Capacitance-voltage (C-V) profiling is usually used to measure N_A–N_D, which implies uncompensated acceptor concentration. When the Li impurity concentration (N_A) exceeds 10^{17} cm^{-3}, N_A–N_D decreases due to increased compensation. This compensation is thought to originate from increased concentration (N_D) of Li interstitial donors in heavily doped ZnSe. Lithium doping is also problematic in that lithium atoms can easily diffuse within the epitaxial layer.

Highly resistive ZnSe films have been grown with As and P doping. A first principles total energy calculation suggests that two neutral acceptors combine to form a new deep state that results in the high resistivity of As- and P-doped ZnSe.[12] Experimental results, which show *p*-type conduction is difficult in As- or P-doped ZnSe, are consistent with this proposed model.

An important breakthrough came with the development of a N_2 plasma source for MBE.[13,14] This technique employs a small helical-coil RF plasma chamber replacing the Knudsen cell in the MBE chamber. The active nitrogen species is thought to be either neutral, monoatomic N free radicals, or neutral, excited N_2 molecules. This technique has been used to achieve N_A–N_D = 3.4×10^{17} cm^{-3} and blue emission in LEDs. This advance was rapidly followed by the first ZnSe-based laser. Maximum net acceptor concentration has been limited to around 1×10^{18} cm^{-3} in ZnSe. At present, however, the nitrogen-plasma doping is the best way available to achieve *p*-type ZnSe and has been most frequently used to grow *p-n* junctions by MBE and to fabricate ZnSe-based laser diodes. N incorporation depends on the growth temperature and the plasma power. Increased N incorporation is found with low growth temperature and high RF power.

Photoluminescence (PL) spectra in lightly N-doped ZnSe layers with concentrations less than 10^{17} cm^{-3} show a neutral acceptor bound-exciton emission and a weak emission due to donor-acceptor pair (DAP) recombination. With increasing N concentration, up to 10^{18} cm^{-3}, DAP emission became dominant in the PL spectrum. This highly N-doped ZnSe shows a *p*-type conduction as confirmed by capacitance-voltage and Van der Pau measurements. From PL analyses of the excitonic and DAP emissions, the N-acceptor ionization energy was estimated to be about 100 meV, which is in good agreement with the result calculated with an effective mass approximation.

3.8.5 *ZnSe-based blue-green laser diodes*

ZnSe-based blue-green laser diodes have been studied intensively to be applied in next-generation, high-density optical disk memories and laser printers. Since the first demonstration of II-VI blue-green laser diodes,[15] further improvements in materials quality coupled with the use of wide bandgap ZnMgSSe quaternary alloys for improved electrical as well as optical confinement and the development of ohmic contacts to *p*-type layers have led to room-temperature (RT) CW operation of ZnSe-based laser diodes with very reduced threshold currents and voltages has been achieved.[16]

The first electrically injected ZnSe-based laser was obtained using ZnSSe cladding layers lattice-matched to the GaAs substrate and a ZnCdSe single quantum well surrounded by ZnSe waveguide layers. The band structure in the strained-layer $Zn_{0.82}Cd_{0.18}Se/ZnSe$ system was thought to be a type I quantum well structure with conduction and valence band offsets of $\Delta E_c = 230$ meV and $\Delta E_v = 50$ meV, respectively. According to a common anion rule, the conduction band offset is relatively larger than that of the valence band in this system. Optical and electrical confinement in this prototypical laser structure is quite weak due to the constraint in the device design by the large lattice mismatch between ZnSe and CdSe. The use of the lattice-matched quaternary ZnMgSSe allows greater refractive index and bandgap differences to be realized. The incorporation of Mg into the cladding layer improves the confinement factor, resulting in the RTCW operation of the II-VI lasers. Shorter-wavelength lasers with a ZnSe active layer have also been made possible.

A typical structure of the ZnCdSe/ZnSSe/ZnMgSSe separate-confinement heterostructure (SCH) laser is shown schematically in Figure 72.[16] The incorporation of GaAs:Si and ZnSe:Cl buffer layers and the Zn beam exposure on an As-stabilized surface of the GaAs buffer layer were employed to reduce stacking fault density. The stacking fault density of the laser structure was estimated to be 3×10^3 cm^{-2}. For the *p*- and *n*-$Zn_{1-x}Mg_xS_ySe_{1-y}$ cladding layers, designed for optical confinement, the Mg concentration was nominally $x = 0.1$ and the sulfur concentration $y = 0.15$. The Cd composition of 0.35 in the ZnCdSe active layer results in lasing wavelength $\lambda = 514.7$ nm. Low-resistance quasi-ohmic contact to *p*-ZnSe:N is usually achieved using heavily *p*-doped ZnTe:N and ZnSe/ZnTe multiquantum wells as an intermediate layer. The threshold current under CW operation was found to be 32 mA, corresponding to a threshold current density of 533 A cm^{-2}, for a laser diode with a stripe area of 600 µm × 10 µm and 70/95% high reflective coating. The threshold voltage was 11 V. Currently, the lifetime of laser diodes operating at a temperature of 20°C has been reported to be 101.5 hours, the longest for ZnSe-based laser diodes.[17]

The spectacular progress in edge-emitting lasers has stimulated exploration of more advanced designs such as the vertical-cavity surface-emitting lasers (VCSELs) operating in the blue-green region. VCSELs have recently attracted much attention because of their surface-normal operation, potential for extremely low threshold currents, and the ease with which they may be fabricated in closely spaced and two-dimensional arrays. These lasers are ideal for integration with other devices such as transistors for photonic switching applications. Output characteristics such as narrow divergence beams and operation in a single longitudinal mode, due to the large mode spacing of a short cavity, are additional advantages.

Blue-green VCSELs have experienced significant progress recently. For example, electrical pumped operation has been demonstrated at 77K.[18] The VCSEL structures used were consistent with a CdZnSe/ZnSe multiquantum-well (MQW) active layer, *n*- and *p*-ZnSe cladding layers, and two SiO_2/TiO_2 distributed Bragg reflectors (DBRs), as shown in Figure 73. The reflectivity of the SiO_2/TiO_2 dielectric mirrors was greater than 99%. The VCSEL devices were characterized at 77K under pulsed operation. A very low threshold current of 3 mA was obtained in the VCSEL. Single longitudinal mode operation was obtained at the lasing wavelength of 484 nm. Above the threshold, the far-field radiation angle was as narrow as 7°, which indicated the spatial coherence expected for VCSEL

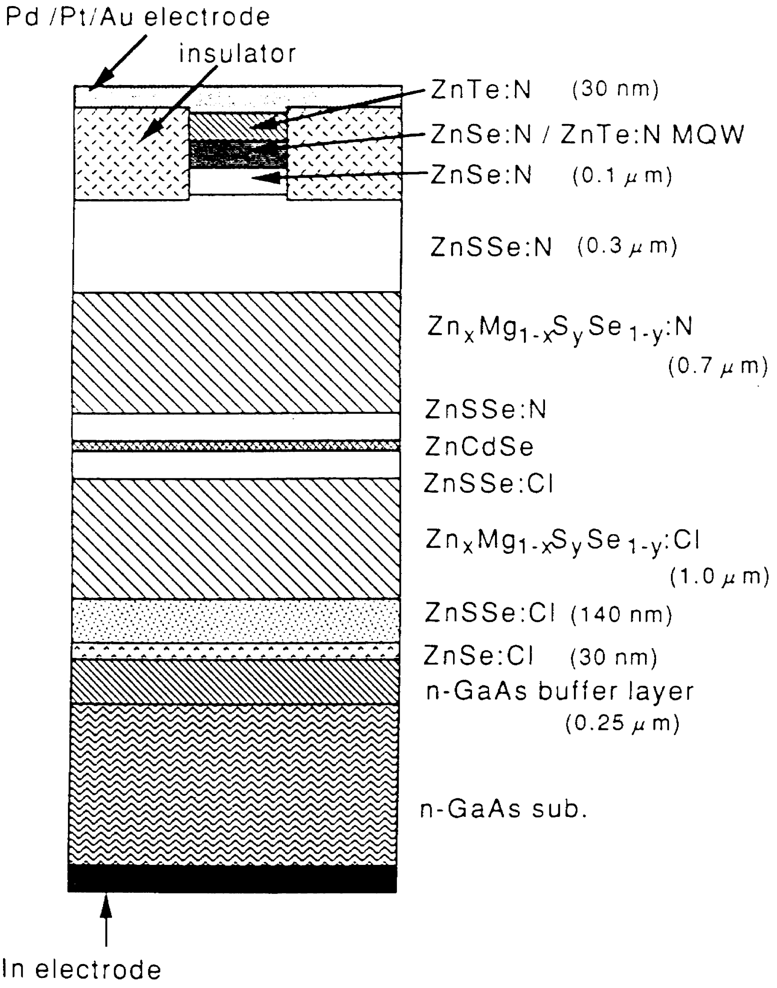
Pd /Pt/Au electrode
insulator
ZnTe:N (30 nm)
ZnSe:N / ZnTe:N MQW
ZnSe:N (0.1 μm)
ZnSSe:N (0.3 μm)
$Zn_xMg_{1-x}S_ySe_{1-y}$:N (0.7 μm)
ZnSSe:N
ZnCdSe
ZnSSe:Cl
$Zn_xMg_{1-x}S_ySe_{1-y}$:Cl (1.0 μm)
ZnSSe:Cl (140 nm)
ZnSe:Cl (30 nm)
n-GaAs buffer layer (0.25 μm)
n-GaAs sub.
In electrode

***Figure** 72* Schematic structure of ZnCdSe/ZnSSe/ZnMgSSe SCH lasers. (From Itoh, S., Nakayama, N., Matsumoto, S., et al., *Jpn. J. Appl. Phys.*, 33, L938, 1994. With permission.)

emission. This blue VCSEL opens the door for a broad range of new device applications for II-VI materials.

3.8.6 ZnSe-based light-emitting diodes

Further improved performance of ZnSe-based light-emitting diodes (LEDs) has also been demonstrated since the first demonstration of II-VI blue-green laser diodes. Recently, high-brightness ZnSe-based LEDs operating at peak wavelengths in the 489- to 514-nm range have been reported.[19] The LED consisted of a 3-μm thick *n*-type ZnSe:Cl layer, a 50- to 100-nm green-emitting active region of $ZnTe_{0.1}Se_{0.9}$, and a 1-μm thick *p*-type ZnSe:N layer grown by MBE on the ZnSe substrates. The devices produced 1.3 mW (10 mA, 3.2 V), peaking at 512 nm with an external efficiency of 5.3%. The emission spectrum of the LED was relatively broad (50 nm) due to emission from the ZnTeSe active region. The luminous performance of the device was 17 lm W^{-1} at 10 mA, which is comparable to the performance of super-bright red LEDs (650 nm) based on AlGaAs double heterostructures. The lifetime of the LEDs at RT has been reported to exceed 2000 hours, which is the longest lifetime of any ZnSe-LED device.

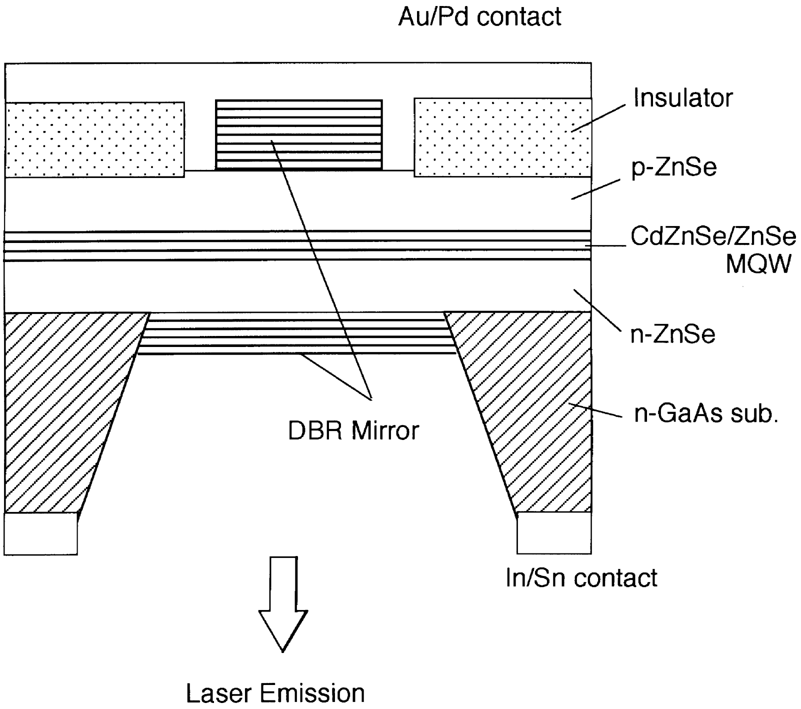

Figure 73 Schematic structure of CdZnSe/ZnSe blue-green vertical cavity surface emitting lasers. (From Yokogawa, T., Yoshii, S., Tsujimura, A., Sasai, Y., and Merz, J.L., *Jpn. J. Appl. Phys.*, 34, L751, 1995. With permission.)

High-brightness LEDs with a ZnCdSe quantum well have been demonstrated.[20] The LED consists of a ZnCdSe/ZnSSe multiquantum well and ZnMgSSe cladding layers grown on GaAs substrates. The devices produced 2.1 mW (20 mA, 3.9 V), and peaked at 512 nm with an external efficiency of 4.3%. A narrow spectral output of 10 nm has been obtained in the devices.

References

1. Mitsuhashi, H., Mitsuishi, I., Mizuta, M., and Kukimoto, H., *Jpn. J. Appl. Phys.*, 24, L578, 1985.
2. Kukimoto, H., *J. Cryst. Growth*, 101, 953, 1990.
3. Yasuda, T., Mitsuishi, I., and Kukimoto, H., *Appl. Phys. Lett.*, 52, 57, 1988.
4. Kamata, A., Mitsuhashi, H., and Fujita, H., *Appl. Phys. Lett.*, 63, 3353, 1993.
5. Wolk, J.A., Ager, III, J.W., Duxstad, K., Haller, J.E.E., Tasker, N.R., Dorman, D.R., and Olego, D.J., *Appl. Phys. Lett.*, 63, 2756, 1993.
6. Shibata, N., Ohki, A., and Katsui, A., *J. Cryst. Growth*, 93, 703, 1988.
7. Yasuda, T., Mitsuishi, I., and Kukimoto, H., *Appl. Phys. Lett.*, 52, 57, 1988.
8. Gunshor, R.L., Kolodziejski, L.A., Melloch, M.R., Vaziri, M., Choi, C., and Otsuka, N., *Appl. Phys. Lett.*, 50, 200, 1987.
9. Niina, T., Minato, T., and Yoneda, K., *Jpn. J. Appl. Phys.*, 21, L387, 1982.
10. Ohkawa, K., Mitsuyu, T., and Yamazaki, O., *J. Appl. Phys.*, 62, 3216, 1987.
11. DePuydt, J.M., Hasse, M.A, Cheng, H., and Potts, J.E., *Appl. Phys. Lett.*, 55, 1103, 1989.
12. Chadi, D.J. and Chang, K.L., *Appl. Phys. Lett.*, 55, 575, 1989.
13. Park, R.M., Troffer, M.B., Rouleau, C.M., DePuydt, J.M., and Haase, M.A., *Appl. Phys. Lett.*, 57, 2127, 1990.
14. Ohkawa, K., Karasawa, T., and Mitsuyu, T., *Jpn. J. Appl. Phys.*, 30, L152, 1991.
15. Hasse, M.A., Qiu, J., DePuydt, J.M., and Cheng, H., *Appl. Phys. Lett.*, 59, 1272, 1991.

16. Itoh, S., Nakayama, N., Matsumoto, S., Nagai, M., Nakano, K., Ozawa, M., Okuyama, H., Tomiya, S., Ohata, T., Ikeda, M., Ishibashi, A., and Mori, Y., *Jpn. J. Appl. Phys.*, 33, L938, 1994.
17. Taniguchi, S., Hino, T., Itoh, S., Nakano, K., Nakayama, N., Ishibashi, A., and Ikeda, M., *Electron. Lett.*, 32, 552, 1996.
18. Yokogawa, T., Yoshii, S., Tsujimura, A., Sasai, Y., and Merz, J.L., *Jpn. J. Appl. Phys.*, 34, L751, 1995.
19. Eason, D.B., Yu, Z., Hughes, W.C., Roland, W.H., Boney, C., Cook, Jr., J.W., Schetzina, J.F., Cantwell, G., and Harsch, W.C., *Appl. Phys. Lett.*, 66, 115, 1995.
20. *Nikkei Electronics*, 614, 20, 1994 (in Japanese).

chapter three — section nine

Principal phosphor materials and their optical properties

Hiroshi Kukimoto

Contents

3.9 IIIb-Vb compounds 283
  3.9.1 General overview 283
  3.9.2 GaP as luminescence material 286
    3.9.2.1 Energy band structure 286
    3.9.2.2 Isoelectronic traps 286
    3.9.2.3 Donor-acceptor pair emission 288
    3.9.2.4 Application for light-emitting diodes 290
References 291

3.9 IIIb-Vb compounds

3.9.1 General overview

IIIb-Vb compounds, which consist of the group IIIb and Vb elements of the periodic table, include many important semiconductors such as GaP, GaAs, GaN, and InP. These materials are not used for phosphors in a polycrystalline form as is the case of IIb-VIb compounds, but they are utilized for many optoelectronic devices such as light-emitting diodes, semiconductor lasers, and photodiodes in a single crystalline form of thin films. IIIb-Vb compounds are to some extent similar to IIb-VIb compounds in terms of the nature of the atomic bond; more precisely, from a viewpoint of the nature of their ionic and covalent bonding, they are well situated between group IV elemental semiconductors and IIb-VIb compound semiconductors. Therefore, many similarities in the optical properties can be seen between these classes of compounds. In some cases, the optical properties due to impurities can be more clearly observed in IIIb-Vb compounds than in IIb-VIb compounds. Before moving on to the optical properties of typical IIIb-Vb compounds, an overview of the composition of this group is presented.

Typical characteristics of IIIb-Vb compounds are shown in Table 23. The materials composed of lighter elements tend to be more ionic than those composed of heavier elements. This trend is reflected in their crystal structure and energy gap; the wurtzite

Table 23 Properties of IIIb-Vb Compounds

		Lattice const. (Å)			Melting			Effective mass[d]		Mobility (cm^2 V^{-1} s^{-1})		Dielectric constant		
Material	Crystal structure[a]	*a*	*c*	Density (g cm^{-3})	point (°C)	Band structure[b]	Bandgap[c] (eV)	Electron	Hole	Electron	Hole	Static ε_0	Optical ε_∞	Refractive index[e]
BN	ZB	3.615	—	3.49		ID	7.2					7.1	4.5	2.12 (0.589)
	H	2.51	6.69	2.26		D	3.8					6.85 (⊥c), 5.09 (∥c)	4.95 (⊥c), 4.10 (∥c)	2.20 (0.05)
BP	ZB	4.538	—	2.97	>2000	ID	2.0					11	8.2	3.0~3.5
BAs	ZB	4.777	—	5.22		ID	1.6	1.2	0.51 (h), 0.2 (l)				10.2	
BSb	ZB		—											
AlN	W	3.111	4.980	3.26		D	6.20	0.29				8.5	4.8	2.25 (0.4)
AlP	ZB	5.467	—	2.40	1525	ID	2.45		0.63 (h), 0.20 (l)	80		9.8	7.5	2.99 (0.5)
AlAs	ZB	5.662	—	3.60	1740	ID	2.15	0.5 1.56 (∥), 0.19 (⊥)	0.5 (h), 0.26 (l)	180	290	10.1	8.2	3.2 (0.56)
AlSb	ZB	6.136	—	4.26	1080	ID	1.63	0.39 1.64 (∥), 0.23 (⊥)	0.5 (h), 0.11 (l)	200	400	12.0	10.2	3.45 (1.1)
GaN	W	3.189	5.185	6.10		D	3.39	0.22	0.8	1200		9.5 (⊥c), 10.4 (∥c)	5.4	2.00 (0.58)
GaP	ZB	5.451	—	4.13	1465	ID	2.27	0.25	0.67 (h), 0.17 (l)	300	100	11.0	9.1	5.19 (0.344)
GaAs	ZB	5.653	—	5.32	1238	D	1.43	0.0665	0.475 (h), 0.087 (l)	8500	400	12.9	10.9	3.66 (0.8)
GaSb	ZB	6.096	—	5.61	712	D	0.70	0.042	0.32 (h), 0.045 (l)	4000	1400	15.7	14.4	3.82 (1.8)
InN	W	3.533	5.693	6.88	~1200	D	0.6~0.7	0.04		4000		15.0	6.3	
InP	ZB	5.869	—	4.79	1070	D	1.34	0.079	0.45 (h), 0.12 (l)	4600	650	12.6	9.6	3.33 (1.0)
InAs	ZB	6.058	—	5.67	943	D	0.35	0.023	0.41 (h), 0.025 (l)	33000	460	15.2	12.3	3.52 (3.74)

Table 23 Properties of IIIb-Vb Compounds (continued)

Material	Crystal structure[a]	Lattice const. (Å)		Density (g cm^{-3})	Melting point (°C)	Band structure[b]	Bandgap[c] (eV)	Effective mass[d]		Mobility (cm^2 V^{-1} s^{-1})		Dielectric constant		Refractive index[e]
		a	*c*					Electron	Hole	Electron	Hole	Static ε_0	Optical ε_∞	
InSb	ZB	6.479	—	5.78	525	D	0.18	0.014	0.40 (h), 0.016 (l)	78000	750	16.8	15.7	4.00 (7.87)

[a] ZB: zinc-blende, H: hexagonal, W: wurtzite.

[b] D: direct type, ID: indirect type.

[c] At 300K.

[d] ∥, ⊥: parallel and perpendicular to the principal axis; h and l: heavy and light holes.

[e] Wavelength µm in parenthesis.

structure and wider gaps are prevalent in lighter materials, while the zinc-blende structure and narrower bandgaps occur in heavier materials. Furthermore, one should note that optical properties of these materials largely depend on the type of energy band structure, direct (D) or indirect (ID).

Light materials, including BN, BP, AlN, and GaN, have high melting points and wide bandgaps. In general, conductivity control of these materials has not been so easy. Recently, GaN and related alloys have become important materials for blue light emission as is described in Section 3.8.5. In contrast, heavy materials including AlSb, GaSb, InSb, and InAs have low melting points and narrow bandgaps. In addition, they features high mobility. These properties are suited for light-emitting devices and photodetectors operating in the infrared region.

AlP, AlAs, GaP, GaAs, and InP are located between the above two extremes. Their bandgaps range from the near-infrared to the visible light region, and these materials and related alloys of AlGaAs, GaPAs, GaInP, GaInAs, and GaAlPAs are key materials for the optoelectronic applications, which are described in Section 3.8.3.

3.9.2 GaP as luminescence material

3.9.2.1 Energy band structure

GaP is an indirect gap semiconductor with an energy band structure similar to that of Si, as illustrated in Figure 74. The bottom of the conduction band is located near the X point in momentum or wave vector ($\boldsymbol{k}$) space, while the top of the valence band is found at the Γ point. Before and after the event of optical transition, momentum must be conserved for light and electron alike. Because the momentum of light is negligibly small, direct electron transitions must take place between bands at the same $\mathbf{k}$ values. Therefore, the probability of an intrinsic optical transition across the bandgap in GaP, i.e., between the X and Γ points, is inherently very low unless phonons participate in the transition. For the same reason, the optical transition probability associated with *shallow* donors and acceptors is also small. Nevertheless, GaP is an important material for practical light-emitting diodes. The reason for this is to be found in the following section.

3.9.2.2 Isoelectronic traps

The description of isoelectronic traps given in this section can also be found in 2.4 dealing with the fundamentals of luminescence in semiconductors. Considering nitrogen-doped GaP, the nitrogen (N) atom enters at the phosphorous (P) site of the GaP lattice. N and P atoms are isoelectronic with each other since they belong to the same Vb column of the periodic table and have the same number of valence electrons. Therefore, the N impurity in GaP would appear to be unable to bind electrons or holes to itself as do other common donor or acceptor impurities in semiconductors. Yet, the N atom in GaP does bind an electron because N is more attractive to electrons than P, owing to the nuclear charge of N being more exposed, i.e., due to large difference of electron negativity between N and P. Similarly, a Bi atom in GaP can bind a hole. These impurities in GaP are called *isoelectronic traps* (or centers).[2]

Since the trapped electron is localized around the N atom in real space, its wavefunction is spread considerably in momentum space. Such a situation is shown in Figure 75, where the electron density of an isoelectronic trap with a binding energy of 10 meV is compared to that of a shallow donor with a binding energy of 100 meV. One can clearly see that the amplitude of the electron wavefunction at the Γ point for the isoelectronic trap is about three orders of magnitude larger than that for the shallow donor.

Once an electron is bound to N by a short range potential, a hole can also be bound to the negatively charged center by the Coulombic potential, resulting in the formation

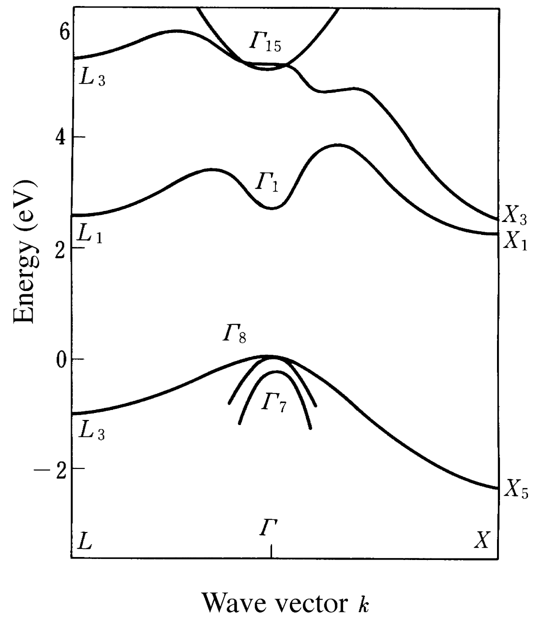

Figure 74 Energy band structure of GaP. Energies at 0K are: $X_1 - \Gamma_8 = (2.339 + 0.002)$ eV, $\Gamma_1 - \Gamma_8 = (2.878 + 0.002)$ eV. (From Cohen, M.L. and Bergstresser, T.K., *Phys. Rev.*, 141, 789, 1966. With permission.)

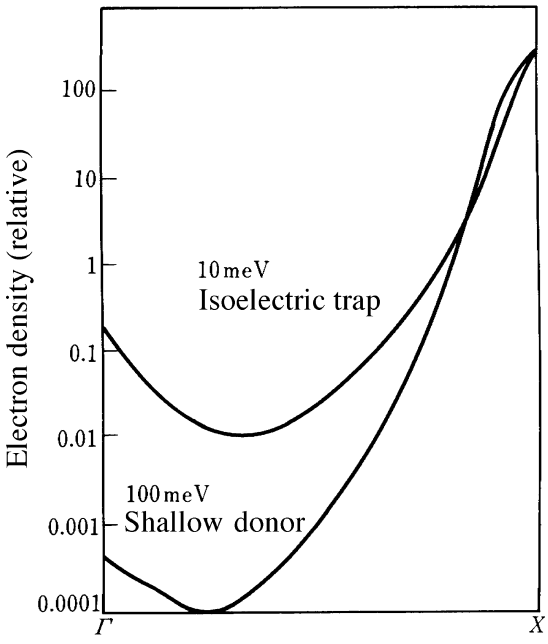

Figure 75 Electron density distributions for a 10-meV isoelectronic trap and a 100-meV shallow donor in GaP. (From Dean, P.J., *J. Luminesc.*, 1/2, 398, 1970. With permission.)

of an exciton bound to N. Thus, the radiative recombination of excitons bound to N in GaP takes place with high probability. The high efficiency of bound exciton recombination at N centers is further promoted by the fact that Auger recombination due to a third particle (electron or hole) cannot take place as it does in the case of exciton recombination at neutral donors or acceptors. Thus, N is responsible for the efficient luminescence observed in green GaP light-emitting diodes.

At high N concentrations, the luminescence due to excitons preferably bound to N-N pairs is observed.[4] The pair distribution in GaP occurs with different distances and leads to the spectrum shown in Figure 76. This type of luminescence is used for yellow-green GaP light-emitting diodes.

Slightly more complicated isoelectronic traps in GaP consist of nearest-neighbor donor-acceptor complexes of Zn-O, Cd-O, or Mg-O, and a triplex of Li-O-Li.[5,6] Each of these complexes can be regarded as being isoelectronic with one GaP molecule where eight valence electrons reside. Because of the highly localized nature of the O potential, these complexes can bind electrons and form bound excitons as is the case of N. The luminescence due to excitons bound to Zn-O is utilized for red GaP light-emitting diodes.

3.9.2.3 Donor-acceptor pair emission

A general concept and nature of donor-acceptor pair emission is described in 2.4. The important equations for the emission are repeated here. The transition energy $E(R)$ of a discrete pair with separation R is given by:

$$E(R) = E_g - \left(E_D + E_A\right) + e^2/4\pi\varepsilon R \tag{39}$$

where E_g is bandgap energy, E_D and E_A are the donor and acceptor binding energies, respectively, e is the electronic charge, and ε is the static dielectric constant. On the other hand, the transition probability $W(R)$ between a tightly bound electron (or hole) and a loosely bound hole (or electron) is approximately given by:

$$W(R) = W_0 \exp\left(-2R/R_B\right) \tag{40}$$

where W_0 is a constant and R_B is the Bohr radius of a loosely bound electron (or hole).

Since GaP is an indirect gap semiconductor with a low transition probability, emission from the remote pair can be easily saturated under high excitation conditions. This situation results in the observation of well-resolved, fine line structure in the luminescence spectra corresponding to various donor-acceptor pairs with discrete values of R. The spectrum as shown in Figure 24 in 2.4 is for the emission taking place between S donors substituting into the P sites and Si acceptors substituting into the Ga sites. For this type of emission (type I) in a zinc-blende structure, R can be expressed in terms of a shell number m as $R = (m/2)^{1/2}a_0$, where $m \neq 14, 30, 46, \ldots$. From this relation, it is possible to assign specific lines with corresponding R values. Once the value of R is determined, the observed energy can be plotted against R. Then, with extrapolation to $R = \infty$, $E_g - (E_D + E_A)$ can be determined. Fits of the simple expression Eq. 39 to some observed values are shown in Figure 77 as examples.

If either E_D or E_A is known through other experiments, the other is determined. The results obtained in this manner for emission spectra arising from various pair combinations of donors and acceptors in GaP are shown in Table 24.

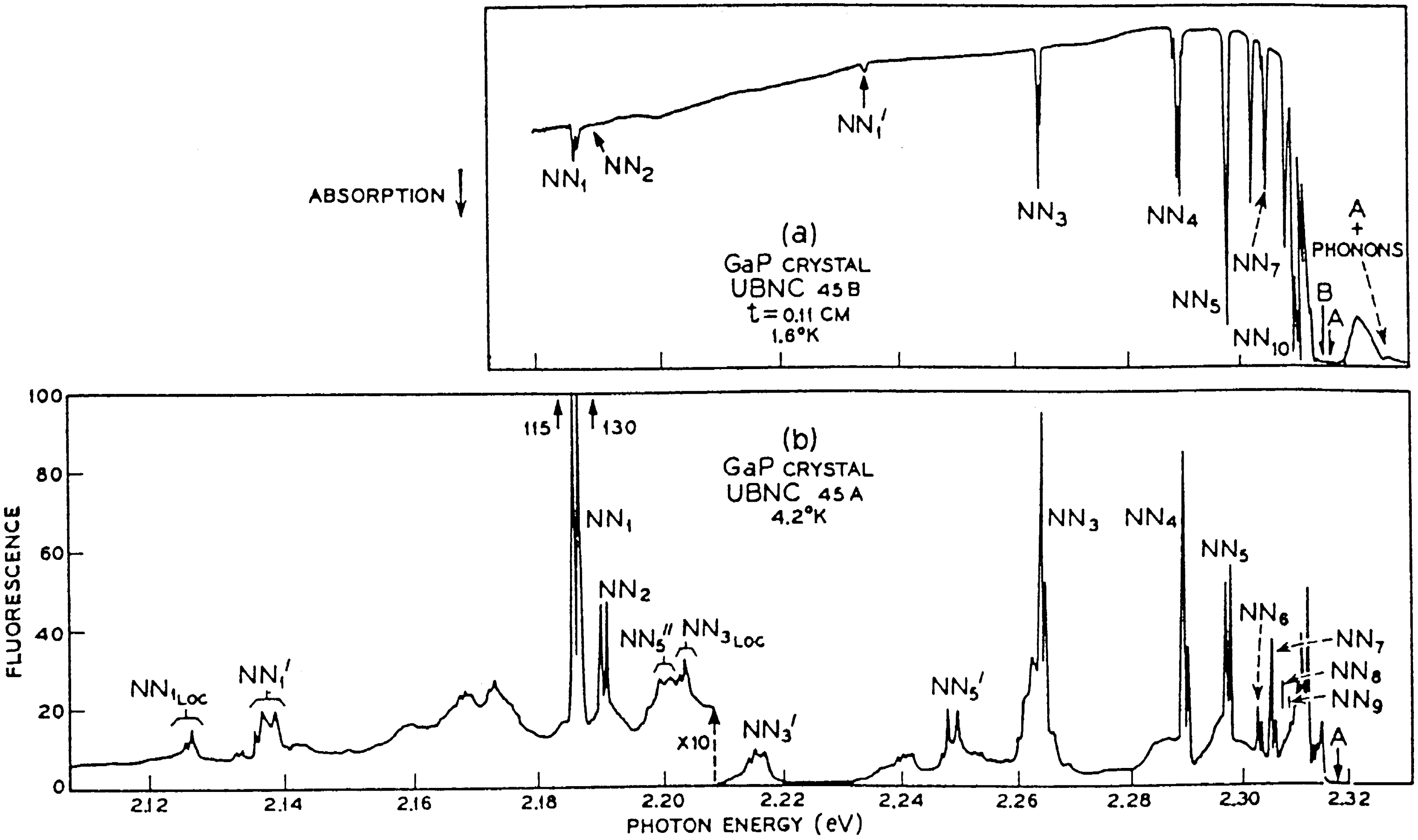

Figure 76 Absorption and emission spectra of heavily N-doped GaP at low temperature. (From Thomas, D.G. et al., *Phys. Rev. Lett.*, 15, 857, 1965. With permission.)

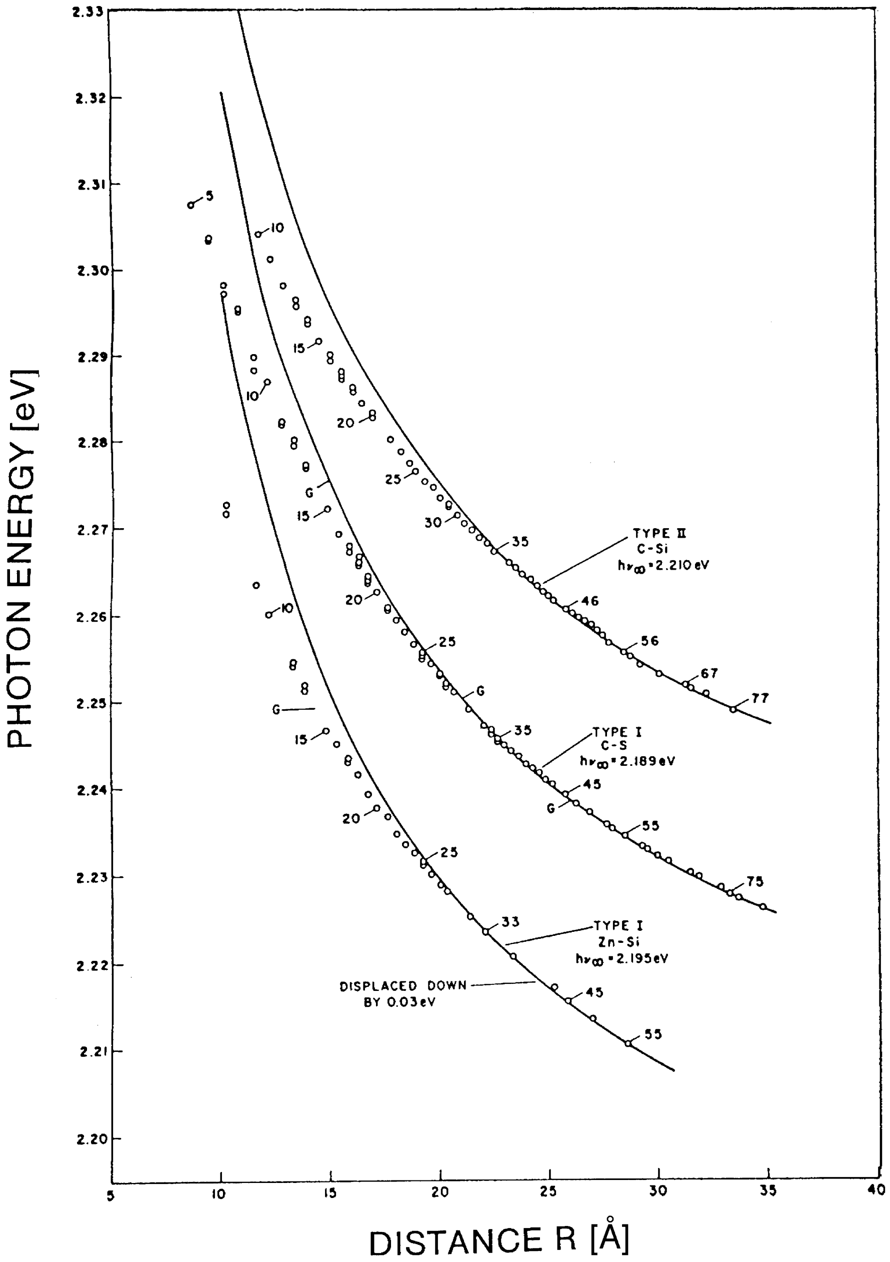

Figure 77 The fitting of type-I C-S and Zn-Si and of type-II C-Si pair spectra in GaP to Eq. 39. (From Dean, P.J., Frosch, C.J., and Henry, C.H., *J. Appl. Phys.*, 39, 5631, 1968. With permission.)

3.9.2.4 Application for light-emitting diodes

The characteristics of practical GaP light-emitting diodes are summarized in Table 25. One should note again that isoelectronic impurities of N, N-N pairs, and Zn-O are utilized for green, yellow, and red light-emitting diodes, respectively. Another thing to be noted is that pure-green diodes have also become available, where GaP without isoelectronic impurities is used. This has become possible by improving crystal quality in terms of decreasing the defects that act as nonradiative recombination centers. The emission is ascribed to the transition associated with free holes and donor bound electrons.

Table 24 Energy Depths of Donors and Acceptors in GaP

Donor	E_D (meV)	Acceptor	E_A (meV)
Li(int. A)	58	C(P)	46.4
Sn(Ga)	69	Be(Ga)	48.7
Si(Ga)	82.1	Mg(Ga)	52.0
Li(int. B)	88.3	Zn(Ga)	61.7
Te(P)	89.8	Cd(Ga)	94.3
Se(P)	102.6	Si(P)	202
S(P)	104.2	Ge(P)	257
Ge(Ga)	201.5		
O(P)	896.0		

Note: P or Ga in parentheses indicates the lattice sites to be substituted. Li occupies two different interstitial sites A and B.

Table 25 Properties of GaP Light-Emitting Diodes

Materials	Emission color	Peak wavelength (nm)	Ext. quantum efficiency (%)	Luminous efficiency (lm/W)
GaP:Zn,O	Red	700	4	0.8
GaP:NN	Yellow	590	0.2	0.9
GaP:N	Green	565	0.3	1.8
GaP	Pure green	555	0.2	1.4

References

1. Cohen, M.L. and Bergstresser, T.K., *Phys. Rev.*, 141, 789, 1966.
2. Thomas, D.G. and Hopfield, J.J., *Phys. Rev.*, 150, 680, 1966.
3. Dean, P.J., *J. Luminesc.*, 1/2, 398, 1970.
4. Thomas, D.G. et al., *Phys. Rev. Lett.*, 15, 857, 1965.
5. Henry, C.H., Dean, P.J., and Cuthbert, J.D., *Phys. Rev.*, 166, 754, 1968.
6. Dean, P.J. and Illegems, M., *J. Luminesc.*, 4, 201, 1971.
7. Dean, P.J., Frosch, C.J., and Henry, C.H., *J. Appl. Phys.*, 39, 5631, 1968.

chapter three — section ten

Principal phosphor materials and their optical properties

Gen-ichi Hatakoshi

Contents

3.10 (Al,Ga,In)(P,As) alloys emitting visible luminescence 293
  3.10.1 Bandgap energy 293
  3.10.2 Crystal growth....294
  3.10.3 Characteristics of InGaAlP crystals grown by MOCVD....295
  3.10.4 Light-emitting devices....298
References....300

3.10 *(Al,Ga,In)(P,As) alloys emitting visible luminescence*

3.10.1 *Bandgap energy*

GaAlAs, GaAsP, InGaAsP, and InGaAlP are IIIb-Vb compound semiconductor materials used for devices in the visible wavelength region. Table 26 shows the compositional dependence of the bandgap energy E_g,[1–11] where E_g^Γ, E_g^X and E_g^L correspond to the distance between valence-band edge and conduction-band edge for Γ, X, and L valleys, respectively. Emission by direct transition occurs in a composition region, where the E_g^Γ value is smaller than that for E_g^X and E_g^L.

Lattice constants of alloys are determined by their composition and generally vary depending on the composition ratio. Therefore, the lattice constant of ternary alloys such as GaAlAs and GaAsP is determined uniquely by the bandgap energy value. In the case of GaAlAs, the compositional dependence of the lattice constant a is very small: for example, a = 5.653 Å for GaAs and a = 5.661 Å for AlAs.[1,2] Therefore, epitaxial layers of GaAlAs can be grown using a GaAs substrate. The change in the lattice constant of GaAsP is comparatively large; in this case, GaAs or GaP is used as a substrate, depending on the composition of the epitaxial layer.

In quaternary alloys such as InGaAsP and InGaAlP, the bandgap energy can be varied without altering the value of the lattice constant. The E_g value for InGaAlP[9–11] in Table 26 corresponds to the case where the alloy is lattice-matched to GaAs. This means that GaAs can be used as a substrate for crystal growth of InGaAlP alloys. InGaAsP can also be lattice-matched to GaAs, and visible light emission is obtained for this case. Such lattice

Table 26 Compositional Dependence of the Bandgap Energy

Material system	Bandgap energy (eV)	Direct-indirect transition point[a]	Ref.
$Ga_{1-x}Al_xAs$	$E_g^{\Gamma} = 1.425 + 1.155x + 0.370x^2$	$x_c = 0.4–0.45$	3
	$E_g^{X} = 1.911 + 0.005x + 0.245x^2$	$E_g(x = 0.4) \sim 1.95$ eV	
	$E_g^{L} = 1.734 + 0.574x + 0.055x^2$		
$GaAs_{1-x}P_x$	$E_g^{\Gamma} = 1.424 + 1.150x + 0.176x^2$	$x_c = 0.45–0.49$	2,4,5
	$E_g^{X} = 1.907 + 0.144x + 0.211x^2$	$E_g(x = 0.49) \sim 2.03$ eV	
	$E_g^{\Gamma} = 1.514 + 1.174x + 0.186x^2$ (77K)		5,6
	$E_g^{X} = 1.977 + 0.144x + 0.211x^2$ (77K)		
	$E_g^{L} = 1.802 + 0.770x + 0.160x^2$ (77K)		
$In_{1-x}Ga_xAs_yP_{1-y}$	$E_g^{\Gamma} = 1.35 + 0.668x–1.068y$		7
	$+ 0.758x^2 + 0.078y^2 - 0.069xy$		
	$- 0.322x^2y + 0.03xy^2$		
$In_{0.5}(Ga_{1-x}Al_x)_{0.5}P$	$E_g^{\Gamma} = 1.91 + 0.59x$	$x_c = 0.6–0.7$	9–11
	$E_g^{X} = 2.26 + 0.09x$	$E_g(x = 0.7) \sim 2.32$ eV	

Note: Values at room temperature except as indicated.

[a] There is some discrepancy in the value for x_c and several values are reported.

matching with GaAs can be realized by selecting the composition ratio according to $y \sim 0.5$ for the $In_{1-y}(Ga_{1-x}Al_x)_yP$ system and $x \sim (1 + y)/2.08$ for the $In_{1-x}Ga_xAs_yP_{1-y}$ system,[8] respectively.

All materials described here have the zinc-blende structure. Band structures for $Ga_{1-x}Al_xAs$, $In_{0.5}(Ga_{1-x}Al_x)_{0.5}P$, and $GaAs_{1-x}P_x$ vary between direct transition and indirect transition types. In general, direct transition-type crystals have the advantages of high radiative efficiency and narrow emission spectrum.

3.10.2 Crystal growth

Thin-film crystals for optical devices using the aforementioned compound semiconductors are grown by liquid phase epitaxy (LPE), vapor phase epitaxy (VPE), and molecular beam epitaxy (MBE). LPE utilizes the recrystallization of the solute from a supersaturated solution. Conventional halogen-transport VPE is classified into hydride VPE and chloride VPE. Metalorganic chemical vapor deposition (MOCVD), another VPE method, uses metal organic compounds, such as trimethylgallium (TMGa) and trimethylindium (TMIn), as source gases for Group III materials. MBE is a type of ultra-high-vacuum deposition, where molecules or atoms of the constituent elements are supplied from solid sources or gas sources.

Attainable device structures for light-emitting diodes (LEDs) and semiconductor lasers depend on the method of crystal growth. For example, the growth aspect on a stepped or grooved substrate varies, depending on the method. In the LPE method, crystal growth proceeds so as to embed and level the groove. Such a characteristic feature has been utilized to obtain various structures of GaAlAs semiconductor lasers for practical use.[12,13] InGaAsP crystal can also grown by LPE. Transverse-mode stabilized structures for InGaAsP/GaAlAs semiconductor lasers oscillating in the 0.6-μm wavelength range have been grown by the LPE method.[14]

The problems with the LPE method arise from the difficulty to grow ultra-thin layers and to control the composition of epitaxial layers for some material systems. For example, the segregation coefficient (defined as the ratio of atoms incorporated from the liquid solution to those in the solid crystal) of Al is relatively large in the case of LPE growth for GaAlAs. This causes a gradual decrease in the Al amount in the solution, resulting in a graded composition structure for thick GaAlAs growth. The problem of segregation is even more serious for InGaAlP growth. It was very difficult to obtain high-quality InGaAlP crystals by the LPE methods because of the extremely large segregation coefficient of Al.[15]

The development of MBE and MOCVD techniques has enabled the production of high-quality, thin-film crystals for the InGaAlP systems.[9,16–18] The MBE and MOCVD methods have an advantage in that controlled ultra-thin layers, which can be applied to form multiquantum well (MQW) structures for light-emitting devices, can easily be obtained.

In order to realize a double heterostructure for semiconductor lasers and LEDs, *p*-type and *n*-type semiconductor crystals are required. In general, Group VI elements, such as Se and S, act as donors for the III-V system and thus are used as *n*-type dopants. Group II elements such as Zn, Mg, and Be behave as acceptors and are used as *p*-type dopants. Group IV dopants such as Si and Ge are amphoteric impurities. For example, when Si is substituted for a Group III site atom, it acts as a donor. On the contrary, it acts as an acceptor when substituted for a Group V site atom. The substitution site depends on the growth condition.

3.10.3 Characteristics of InGaAlP crystals grown by MOCVD

An attractive technique for MOCVD growth of InGaAlP material systems is growth on an off-angle substrate. This process is related to the formation of a natural superlattice.[19–21] In the InGaAlP system, the bandgap energy value depends on the growth condition, for example, on the growth temperature. This is attributed to the dependence of atomic ordering on the growth temperature. An ordered structure of an InGaAlP alloy is produced by the formation of a natural superlattice, where the Group III atoms are arranged systematically. It is known that a disordered alloy has a larger bandgap energy than that of an ordered

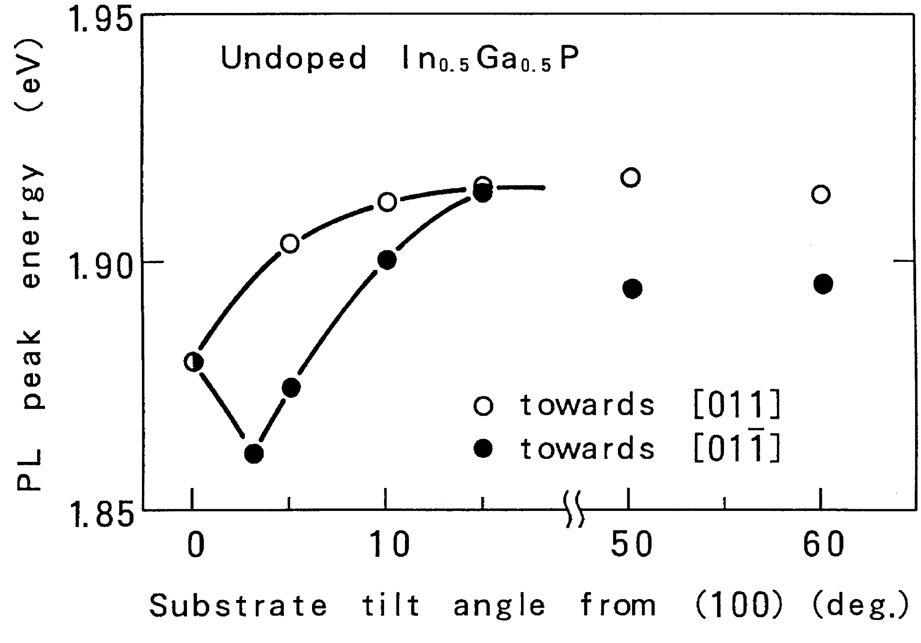

Figure 78 Photoluminescence (PL) peak energy of InGaP vs. substrate orientation. (From Suzuki, M., Nishikawa, Y., Ishikawa, M., and Kokubun, Y., *J. Crystal Growth*, 113, 127, 1991. With permission.)

alloy, and that the disordered state is enhanced by using an intentionally misoriented substrate. It follows that the bandgap energy of the InGaAlP crystal grown on a misoriented substrate has a larger bandgap energy than that grown on a (100)-oriented substrate.

Figure 78 shows the dependence of the bandgap energy, obtained by photoluminescence measurement, of InGaAlP alloys on the substrate orientation.[22] As shown in the figure, the bandgap energy increases with increasing substrate tilt angle away from the (100) plane toward the [011] direction.* This is considered to be due to the suppression of crystal ordering.

The off-angle substrate technique is utilized to fabricate short-wavelength InGaAlP lasers. In general, shortening of the oscillating wavelength or, equivalently, an increase in the bandgap energy is obtained by increasing the Al composition of the alloy as shown in Table 26. Introduction of off-angle substrates has the advantage of wavelength shortening while using a smaller Al content in the active layer. This is preferable because formation of undesirable nonradiative recombination centers arising from incorporation of oxygen impurities (which increase with increasing Al composition) is reduced. The

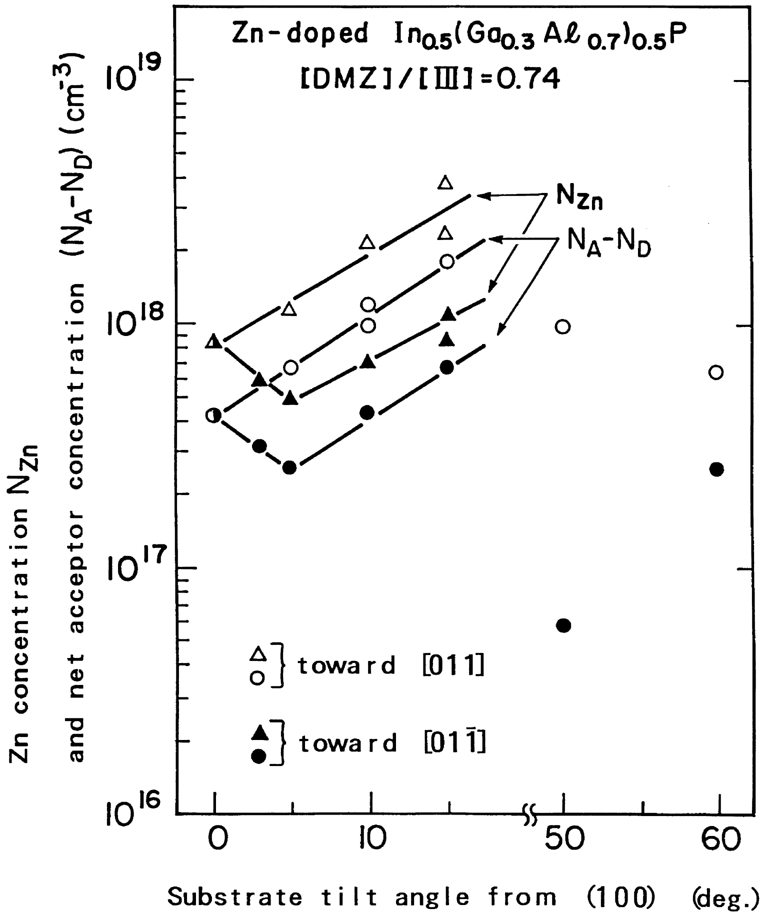

Figure 79 Net acceptor concentration and Zn concentration vs. substrate orientation. (From Suzuki, M., Nishikawa, Y., Ishikawa, M., and Kokubun, Y., *J. Crystal Growth*, 113, 127, 1991. With permission.)

---

* Conventionally, (*hkl*) and [*hkl*] represent a crystal plane and a crystal direction, respectively: e.g., (100) denotes a crystal plane normal to the [100] direction.

bandgap of the cladding layers can also be increased by using off-angle substrates. Thus, electron overflow can be effectively suppressed by creating a larger bandgap difference between the active and cladding layers in this way.

Another effect of off-angle substrates is to increase acceptor concentration in *p*-type layers. As shown in Figure 79, Zn incorporation and the net acceptor concentration strongly depend on the tilt angle of the substrate.[22] This dependence is similar to that for the PL peak energy shown in Figure 78. Both the Zn concentration and the net acceptor concentration increase with increasing tilt angle from (100) toward the [011] direction. High acceptor concentrations are preferable for *p*-type cladding layers because of their effect in reducing electron overflow from the active layer to the *p*-cladding layer,[23,24] due to the increase in the conduction-band heterobarrier height at the interface between the active and the *p*-cladding layers.

Electrical activity of *p*-type dopants depends on the effects of residual impurities such as hydrogen and oxygen and also upon growth conditions. Oxygen incorporation into InGaAlP crystals results in the electrical compensation of Zn acceptors. It also causes a nonradiative center due to the formation of deep levels. These phenomena are serious problems for light-emitting devices. Oxygen incorporation can be reduced by increasing the V:III ratio in MOCVD growth[25] and by the utilization of the off-angle technique.[26] An example of experimental results is shown in Figure 80.[26] The effect on oxygen reduction in off-angle substrate is remarkable, especially for high Al composition crystals, and is very useful for producing highly doped *p*-type cladding layers. High acceptor concentrations exceeding 1×10^{18} cm^{-3} have been reported for InAlP crystals fabricated by MOCVD growth on off-angle substrates.[27]

Experimental results showing improvements in the hetero-interface properties of quantum wells grown on misoriented substrates have been reported.[28] Full width at half maximum (FWHM) value of the PL spectra for InGaP/InGaAlP single quantum wells shows a strong dependence on the substrate misorientation. The FWHM value is found

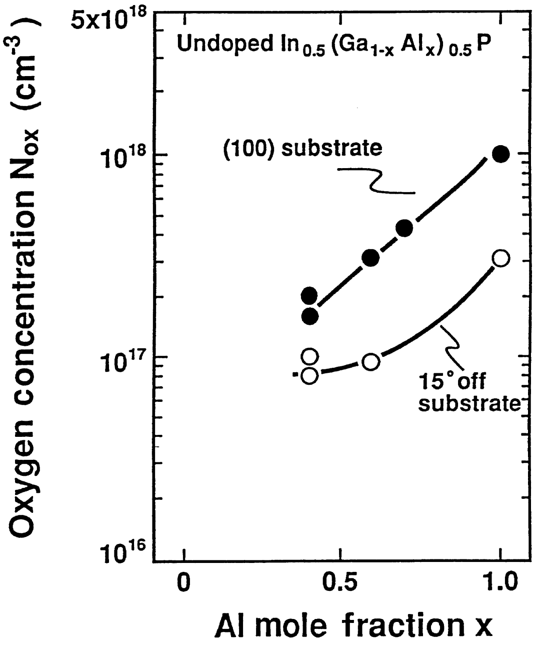

Figure 80 Oxygen concentration vs. Al mole fraction. (From Suzuki, M., Itaya, K., Nishikawa, Y., Sugawara, H., and Okajima, M., *J. Crystal Growth*, 133, 303, 1993. With permission.)

to decrease with increasing misorientation from the (100) toward the [011] direction. This result indicates that the interface smoothness and abruptness are improved by employing off-angle substrates.

A remarkable improvement in the temperature characteristics of InGaAlP lasers has been achieved by employing an off-angle technique. Short-wavelength and high-temperature operation have been reported for InGaAlP lasers grown on misoriented substrates.

3.10.4 *Light-emitting devices*

Semiconductor lasers and LEDs in the visible wavelength region are obtained using GaAlAs, GaAsP, InGaAsP, and InGaAlP systems. Figure 81 shows the available wave-

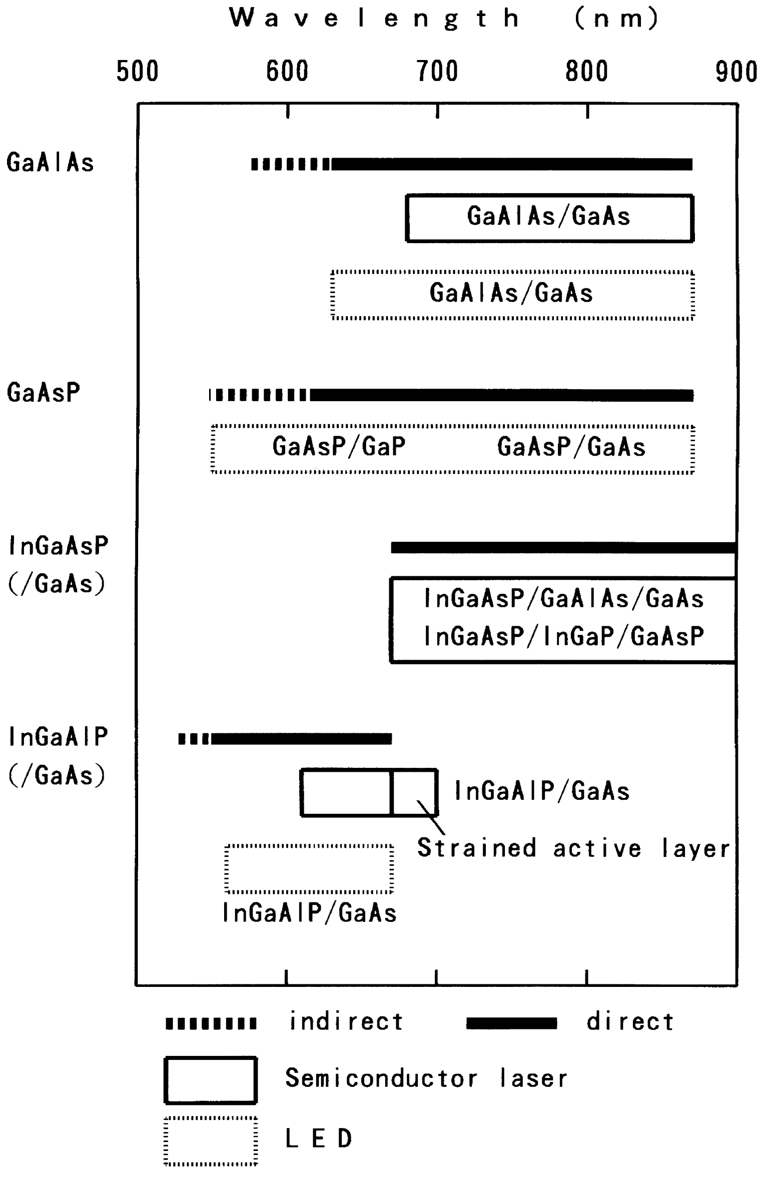

Figure 81 Available wavelength range for semiconductor lasers and LEDs. Constituent alloy systems are indicated by D/B or A/C/B, where D, A, C, and B denote the material systems for the double heterostructure, the active layer, the cladding layer, and the substrate, respectively.

length range for semiconductor lasers and LEDs. The wavelength range is restricted in the case of semiconductor lasers because the active layer is required to have a direct-transition-type band structure; here also, cladding layers with bandgap energies greater than that of the active layer are required in order to confine the injected carrier within the active layer. It is difficult, in general, to obtain shorter wavelength semiconductor lasers for a given material system because the bandgap difference between the active and the cladding layers decreases with shortening oscillation wavelength, resulting in a significant carrier overflow from the active layer. Visible-light oscillations in the 0.6-μm wavelength region have been realized for InGaAlP/GaAs,[16–18] GaAlAs/GaAs,[29] InGaAsP/GaAlAs/GaAs,[14] and InGaAsP/InGaP/GaAsP[30] systems.

As for LEDs, indirect-transition-type alloys can also be used for emission layers, and cladding layers are not necessarily required. Therefore, the possible wavelength range for LEDs is larger than that for semiconductor lasers. In general, high-brightness characteristics are obtained by using direct-transition alloys and by introducing a double heterostructure. The isoelectronic trap technique, which is effective in improving the emission efficiency of GaP LEDs, is also applicable to the GaAsP systems[5,6,31] in the indirect transition region. Nitrogen is used as the isoelectronic impurity. GaAsP:N LEDs show electroluminescence efficiencies of an order of magnitude higher than those without nitrogen doping.[31]

Examples of emission spectra for visible-light LEDs are shown in Figure 82. GaAlAs[32] and InGaAlP[33] alloys have direct transition band structures and thus the LEDs with these alloys have higher brightness and narrower emission spectra, as shown in the figure.

Light-extraction efficiency of LEDs is affected by various factors, which can be controlled by device design.[34,35] Remarkable enhancement of light-extraction efficiency has been reported for InGaAlP LEDs by introducing current-spreading and current-blocking layers.[33,34] Introduction of DBR mirror[36] is effective for LEDs with absorbing substrates. High-power InGaAlP/Gap LEDs with chip reshaping[37] have also been reported. Other

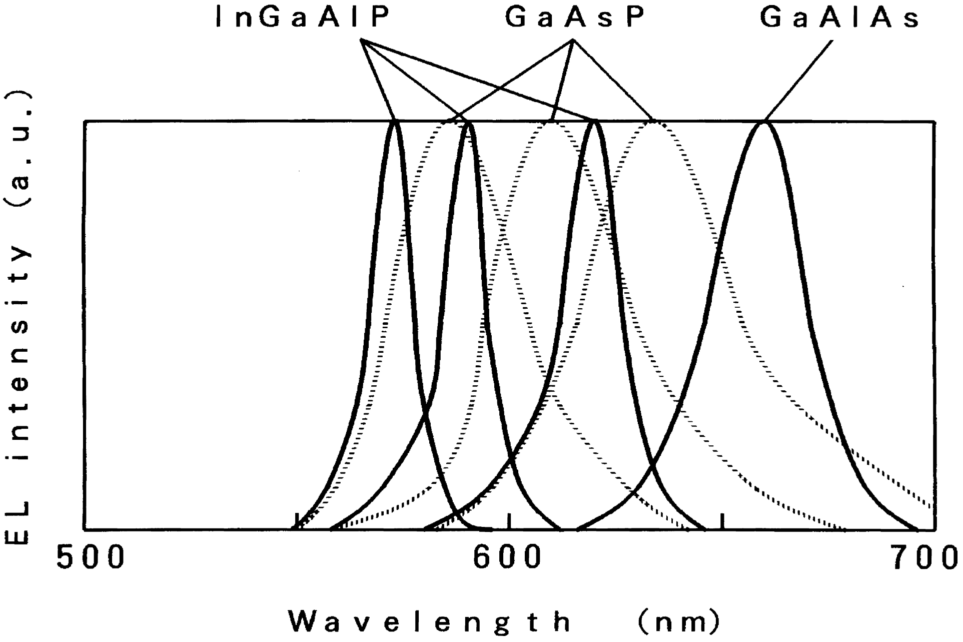

Figure 82 Electroluminescence spectra for visible-light LEDs.

approaches such as surface texture, resonant cavity structure, and photonic crystals have been investigated for improving the LED efficiency.[38]

References

1. Madelung, O., Ed., *Landolt-Börnstein, Numerical Data and Functional Relationships in Science and Technology*, III, 17 and 22a, Springer-Verlag, Berlin, 1982.
2. Casey, H.C., Jr. and Panish, M.B., *Heterostructure Lasers*, Academic Press, New York, 1978.
3. Lee, H.J., Juravel, L.Y., Woolley, J.C., and SpringThorpe, A.J., *Phys. Rev. B*, 21, 659, 1980.
4. Thompson, A.G., Cardona, M., Shaklee, K.L., and Woolley, J.C., *Phys. Rev.*, 146, 601, 1966.
5. Craford, M.G., Shaw, R.W., Herzog, A.H., and Groves, W.O., *J. Appl. Phys.*, 43, 4075, 1972.
6. Holonyak, N., Jr., Nelson, R.J., Coleman, J.J., Wright, P.D., Fin, D., Groves, W.O., and Keune, D.L., *J. Appl. Phys.*, 48, 1963, 1977.
7. Kuphal, E., *J. Cryst. Growth*, 67, 441, 1984.
8. Adachi, S., *J. Appl. Phys.*, 53, 8775, 1982.
9. Asahi, H., Kawamura, Y., and Nagai, H., *J. Appl. Phys.*, 53, 4928, 1982.
10. Honda, M., Ikeda, M., Mori, Y., Kaneko, K., and Watanabe, N., *Jpn. J. Appl. Phys.*, 24, L187, 1985.
11. Watanabe, M.O. and Ohba, Y., *Appl. Phys. Lett.*, 50, 906, 1987.
12. Aiki, K., Nakamura, M., Kuroda, T., Umeda, J., Ito, R., Chinone, N., and Maeda, M., *IEEE J. Quantum Electron.*, QE-14, 89, 1978.
13. Yamamoto, S., Hayashi, H., Yano, S., Sakurai, T., and Hijikata, T., *Appl. Phys. Lett.*, 40, 372, 1982.
14. Chong, T. and Kishino, K., *IEEE Photonics Tech. Lett.*, 2, 91, 1990.
15. Kazumura, M., Ohta, I., and Teramoto, I., *Jpn. J. Appl. Phys.*, 22, 654, 1983.
16. Kobayashi, K., Kawata, S., Gomyo, A., Hino, I., and Suzuki, T., *Electron. Lett.*, 21, 931, 1985.
17. Ikeda, M., Mori, Y., Sato, H., Kaneko, K., and Watanabe, N., *Appl. Phys. Lett.*, 47, 1027, 1985.
18. Ishikawa, M., Ohba, Y., Sugawara, H., Yamamoto, M., and Nakanisi, T., *Appl. Phys. Lett.*, 48, 207, 1986.
19. Suzuki, T., Gomyo, A., Iijima, S., Kobayashi, K., Kawata, S., Hino, I., and Yuasa, T., *Jpn. J. Appl. Phys.*, 27, 2098, 1988.
20. Nozaki, C., Ohba, Y., Sugawara, H., Yasuami, S., and Nakanisi, T., *J. Crystal Growth*, 93, 406, 1988.
21. Ueda, O., Takechi, M., and Komeno, J., *Appl. Phys. Lett.*, 54, 2312, 1989.
22. Suzuki, M., Nishikawa, Y., Ishikawa, M., and Kokubun, Y., *J. Crystal Growth*, 113, 127, 1991.
23. Hatakoshi, G., Itaya, K., Ishikawa, M., Okajima, M., and Uematsu, Y., *IEEE J. Quantum Electron.*, 27, 1476, 1991.
24. Hatakoshi, G., Nitta, K., Itaya, K., Nishikawa, Y., Ishikawa, M., and Okajima, M., *Jpn. J. Appl. Phys.*, 31, 501, 1992.
25. Nishikawa, Y., Suzuki, M., and Okajima, M., *Jpn. J. Appl. Phys.*, 32, 498, 1993.
26. Suzuki, M., Itaya, K., Nishikawa, Y., Sugawara, H., and Okajima, M., *J. Crystal Growth*, 133, 303, 1993.
27. Suzuki, M., Itaya, K., and Okajima, M., *Jpn. J. Appl. Phys.*, 33, 749, 1994.
28. Watanabe, M., Rennie, J., Okajima, M., and Hatakoshi, G., *Electron. Lett.*, 29, 250, 1993.
29. Yamamoto, S., Hayashi, H., Hayakawa, T., Miyauchi, N., Yano, S., and Hijikata, T., *Appl. Phys. Lett.*, 41, 796, 1982.
30. Usui, A., Matsumoto, T., Inai, M., Mito, I., Kobayashi, K., and Watanabe, H., *Jpn. J. Appl. Phys.*, 24, L163, 1985.
31. Craford, M.G. and Groves, W.O., *Proc. IEEE*, 61, 862, 1973.
32. Ishiguro, H., Sawa, K., Nagao, S., Yamanaka, H., and Koike, S., *Appl. Phys. Lett.*, 43, 1034, 1983.
33. Sugawara, H., Itaya, K., Nozaki, H., and Hatakoshi, G., *Appl. Phys. Lett.*, 61, 1775, 1992.
34. Hatakoshi, G. and Sugawara, H., *Display and Imaging*, 5, 101, 1997.
35. Hatakoshi, G., *10th Int. Display Workshop (IDW'03), Fukuoka*, 1125, 2003.
36. Sugawara, H., Itaya, K., and Hatakoshi, G., *J. Appl. Phys.*, 74, 3189, 1993.
37. Krames, M.R., Ochiai-Holcomb, M., Hofler, G.E., Carter-Coman, C., Chen, E.I., Tan, I.-H., Grillot, P., Gardner, N.F., Chui, H.C., Huang, J.-W., Stockman, S.A., Kish, F.A., and Craford, M.G., *Appl. Phys. Lett.*, 75, 2365, 1999.
38. Issue on High-Efficiency Light-Emitting Diodes, *IEEE J. Sel. Top. Quantum Electron.*, 8, No. 2, 2002.

chapter three — section eleven

Principal phosphor materials and their optical properties

Kenichi Iga

Contents

3.11 (Al,Ga,In)(P,As) alloys emitting infrared luminescence 301
  3.11.1 Compound semiconductors based on InP 301
  3.11.2 Determination of GaInAsP/InP solid compositions........303
  3.11.3 Crystal growth........304
  3.11.4 Applied devices........305
References........305

3.11 (Al,Ga,In)(P,As) alloys emitting infrared luminescence

3.11.1 Compound semiconductors based on InP

Semiconductors for which bandgaps correspond to a long wavelength spectral region (1 to 1.6 µm) are important for optical fiber communication using silica fibers exhibiting extremely low loss and low dispersion, *infrared* imaging, lightwave sensing, etc. Figure 83 depicts a diagram of lattice constant vs. bandgap of several compound semiconductors based on InP, InAs, GaAs, GaN and AlAs, which can emit light in this infrared region.

Semiconductor crystals for 1 to 1.6-µm wavelength emission. Ternary or quaternary semiconductor crystals are used since binary semiconductor crystals with 1 to 1.6-µm bandgaps are not available. Matching of lattice constants to substrates in crystal growth processes is important for fabricating semiconductor devices such as semiconductor lasers and light-emitting diodes (LEDs) with high current injection levels (>5 kA cm^{-2} µm^{-1}) or a high-output power density (>1 mW µm^{-2}) or for photodiodes used for low-noise detection of very weak optical signals.

The bandgap of a specific quaternary crystal can be varied widely while completely maintaining the lattice match to a binary crystal used as a substrate, as shown in Figure 83. An example is $Ga_xIn_{1-x}As_yP_{1-y}$, which utilizes InP (a = 5.8696 Å) as a substrate; the bandgap can be changed in the region of $0.7 \leq E_g \leq 1.35$ eV when the composition is adjusted along the vertical line. The corresponding emission wavelength ranges from 0.92 to 1.67 µm. The ternary materials lattice-matched to the InP substrate are $Al_{0.47}In_{0.53}As$ and $Ga_{0.47}In_{0.53}As$.

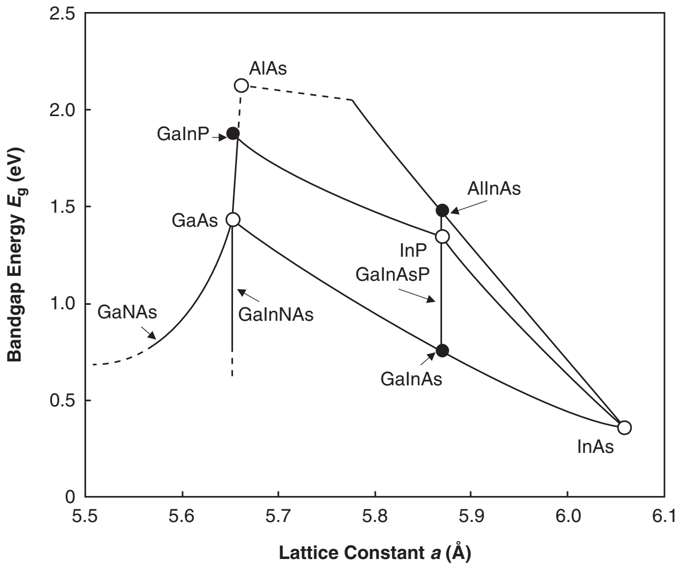

Figure 83 Diagram of lattice constant vs. bandgap for several compound semiconductors.

Possible compound crystals corresponding to light emission of 0.8 to 2 μm are as follows:

1. $Ga_xIn_{1-x}As_yP_{1-y}$ (InP): $0.92 < \lambda_g < 01.67$ (μm)
2. $(Ga_{1-x}Al_x)_yIn_{1-y}As$(InP): $0.83 < \lambda_g < 1.55$ (μm)
3. $Ga_{1-x}Al_xAs_ySb_{1-y}$(GaSb): $0.8 < \lambda_g < 1.7$ (μm)
4. $Ga_xIn_{1-x}As_ySb_{1-y}$(InAs): $1.68 < \lambda_g < 2$ (μm)
5. $Ga_xIn_{1-x}As_ySb_{1-y}$(GaSb): $1.8 < \lambda_g < 2$ (μm)
6. $Ga_xIn_{1-x}N_xAs_{1-x}$(GaAs): $1.1 < \lambda_g < 1.6$ (μm)

The binaries in the parentheses indicate the substrates to be used. Crystal growth of these materials is possible with a lattice mismatch ±0.1% or less. Among these, the heterostructure composed of $Ga_xIn_{1-x}As_yP_{1-x}$ and InP has been widely employed as a material for semiconductor lasers or photodiodes for lightwave systems.

The relationship between x, y, and the bandgap energy associated with $Ga_xIn_{1-x}As_yP_{1-y}$, which are lattice-matched to InP, can be expressed as follows.

$$x = \frac{0.466y}{1.03 - 0.03y}(0 \le x \le 1) \tag{41}$$

$$E_g(y) = 1.35 - 0.72y + 0.12y^2, \text{ (eV)} \tag{42}$$

which was phenomenologically obtained by Nahory et al.[1]

The values of x and y are no longer independent of one another, since the lattice constant must be adjusted so as to be matched to that of the InP substrate, 5.86875 Å. Consequently, the bandgap energy can be expressed by specifying the Ga or As contents. The band-structure parameters of GaInAsP/InP are summarized in Table 27.[2]

Longer-wavelength materials. Fluoride glass fibers have found use in long-distance optical communication in the 2- to 4-μm wavelength range. Signal loss in fluoride glass fibers is predicted to be one or two orders of magnitude lower than that for silica fibers. Also, this spectral band is important for LIDAR (Light Detection and Ranging) and optical

Table 27 The Band Structure Parameters of $Ga_xIn_{1-x}As_yP_{1-y}/InP$

Parameter	Dependence on the mole fractions x and y
Energy gap at zero doping	E_g [eV] = $1.35 - 0.72y + 0.12y^2$
Heavy-hole mass	$m^*_{hh}/m_0 = (1-y)[0.79x + 0.45(1-x)] + y[0.45x + 0.4(1-x)]$
Light-hole mass	$m^*_{lh}/m_0 = (1-y)[0.14x + 0.12(1-x)] + y[0.082x + 0.0261(1-x)]$
Dielectric constant	$\varepsilon = (1-y)[8.4x + 9.6(1-x)] + y[13.1x + 12.2(1-x)]$
Spin-orbit splitting	Δ [eV] = $0.11 - 0.31y + 0.09x^2$
Conduction-band mass	$m^*_e/m_0 = 0.080 - 0.039y$

From Agrawal, G.P. and Dutta, N.K., *Long-wavelength Semiconductor Lasers*, Van Nostrand Reinhold, New York, 1986, 85. With permission.

sensing. A potential material system to cover the wavelength range from 1.7 to 5 µm is GaInAsSb/AlGaAsSb.

3.11.2 Determination of GaInAsP/InP solid compositions

First, a review of the general concepts of crystal preparation for GaInAsP lattice-matched to InP, which has been commonly used in light-emitting devices. $Ga_xIn_{1-x}As_yP_{1-y}$ contains two controllable parameters, enabling independent adjustment of the lattice constant and the bandgap energy. The lattice constant $a(x,y)$ of $Ga_xIn_{1-x}As_yP_{1-y}$ is given as follows:

$$a(x,y) = a(\mathrm{GaAs})xy + a(\mathrm{GaP})x(1-y) + a(\mathrm{InAs})(1-x)y + a(\mathrm{InP})(1-x)(1-y) \tag{43}$$

According to measurements by Nahory et al.,[1] the binary lattice constants are: a(GaAs) = 5.653 Å, a(GaP) = 5.4512 Å, a(InAs) = 6.0590 Å, and a(InP) = 5.8696 Å. The following equation is obtained by inserting this data into Eq. 43:

$$a(x,y) = 0.1894y - 0.4184x + 0.013xy + 5.8696\ (\text{Å}) \tag{44}$$

The relation between x and y, therefore, is given by the following equation, when the $a(x,y)$ coincides with the lattice constant of InP:

$$0.1894y - 0.4184x + 0.0130xy = 0 \tag{45}$$

Usually, Eq. 45 is approximated as:

$$x = 0.467y \tag{46}$$

According to the theory by Moon et al.[3] and experimental results, the relation between the bandgap energy and compositions x and y is given by:

$$\begin{aligned} E_g(x,y) = 1.35 + 0.672x - 1.091y + 0.758x^2 + 0.101y^2 \\ -0.157xy - 0.312x^2y + 0.109xy^2 \end{aligned} \tag{47}$$

The bandgap energy calculated in terms of x and y using Eq. 47 agrees with the phenomenological results of Nahory et al.[1]

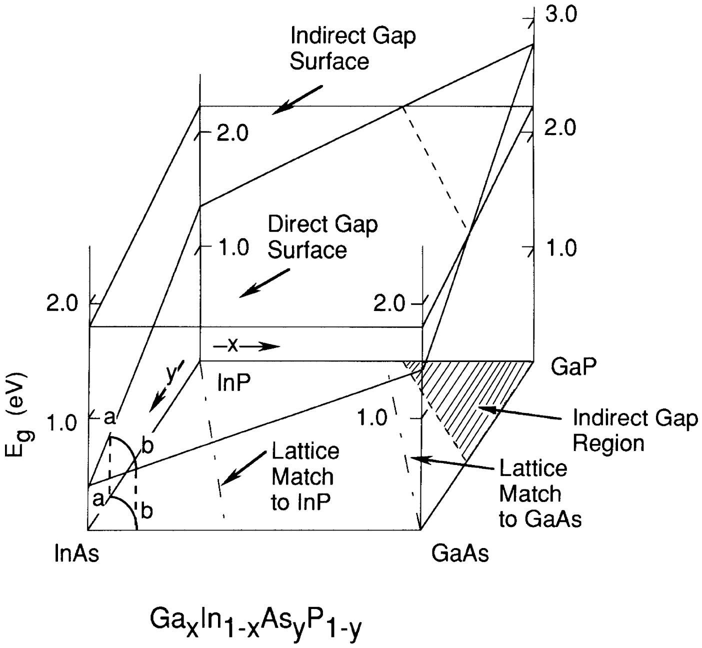

Figure 84 Bandgap energy vs. compositions x and y in $Ga_xIn_{1-x}As_yP_{1-y}$. (From Casey, H.C. and Panish, M.B., *Heterostructure Lasers*, Part B, Academic Press, New York, 1978. With permission.)

The bandgap energy vs. compositions x and y is illustrated in Figure 84.[4] With the aid of this figure, one can obtain the band structure of GaInAsP lattice-matched to InP for the entire set of allowed compositions of y. The bandgap of GaInAsP in the vicinity of GaP is seen to be indirect in the figure.

3.11.3 *Crystal growth*

Liquid phase epitaxy (LPE). In the case of liquid phase epitaxy, one has to determine the liquid composition of an In-rich melt in thermal equilibrium with the solid phase of the desired x and y compositions for $Ga_xIn_{1-x}As_yP_{1-y}$. The As composition y in the $Ga_xIn_{1-x}As_yP_{1-y}$ solid of the desired bandgap energy is given by Eq. 42 when its lattice constant is equal to that of InP. The Ga composition x is obtained by Eq. 46. In this way, the atomic fractions of Ga, As, and P in the In-rich melt that exists in equilibrium with the desired $Ga_xIn_{1-x}As_yP_{1-y}$ solid can be obtained. The actual weights of InP, InAs, and GaAs per gram of In can be estimated. The degree of lattice mismatching $|\Delta a/a|$ can be examined by X-ray diffraction and should be less than 0.05%.

Metal-organic chemical vapor deposition (MOCVD). In the metal-organic chemical vapor deposition (MOCVD) method, gas sources are used for growth of the structures.[5] To satisfy the lattice-match condition, the flow rates of trimethylindium and arsine (AsH_3) are fixed and the triethylgallium flow rate is adjusted. The phosphine (PH_3) flow rate is varied to obtain different compositions. Growth rates of InP and quaternary materials are about 2 µm/h, differing slightly for different alloy compositions. The compositions are calculated from the wavelength of the photoluminescence spectral peak intensities.

Chemical beam epitaxy (CBE). Trimethylindium and triethylgallium with H_2 carrier gas are used as Group III sources in chemical beam epitaxy (CBE) deposition.[6] Group V sources are pure AsH_3 and PH_3, which are precracked at 1000°C by a high-temperature cracking cell. Solid Si and Be are used as *n*-type and *p*-type dopants, respectively. The typical growth temperature is 500°C, which must be calibrated, for example, using the melting point of InSb (525°C). Typical growth rates for InP, GaInAsP (λ_g = 1.3 µm), and GaInAsP (λ_g = 1.55 µm) are 1.5, 3.8, and 4.2 µm/h, respectively.

Impurity doping control over wide ranges is one of the most important issues in the fabrication of optoelectronic devices. The advantages of using Be are that it is a well-behaved acceptor producing a shallow level above the valence band, and it can be incorporated into GaInAsP at a relatively high level (on the order of 10^{19} cm^{-3}).

The impurity levels of GaInAs grown by various epitaxial techniques are 3×10^{15} cm^{-3} by MBE, 8×10^{15} cm^{-3} by MOCVD, and 5×10^{14} cm^{-3} by CBE.

3.11.4 Applied devices

Semiconductor lasers emitting 1 to 1.6-µm wavelength. The optical fiber made of silica glass exhibits a very low transmission loss, i.e., 0.154 dB/km at 1.55 µm. The material dispersion of retractive index is minimum at the wavelength of 1.3 µm. These are advantageous for long-distance optical communications. Semiconductor lasers emitting 1.3-µm wavelength using lattice-matched GaInAsP/InP have been developed having low thresholds of about 10 mA and very long device lifetimes. The 1.3-µm wavelength system has been used since 1980 in public telephone networks and undersea cable systems.

In the 1990s, the 1.55-µm system was realized by taking the advantage of the minimum transmission loss. In this case, the linewidth of the light source must be very small, since the dispersion of the silica fiber is relatively large compared to that at 1.3 µm. Figure 85 exhibit an example of a single-mode laser structure that provides narrow linewidth even when modulated at high speed-signals.[7]

High-power semiconductor lasers emitting at 1.48 µm are employed as a pumping source for Er-doped optical fiber amplifier (EDFA). A surface-emitting laser operating at this wavelength is shown in Figure 86 and is expected to be used in long-wavelength networks and optical interconnects.[8]

For the purpose of substantially improving laser performance, quantum wells have been considered for use as the active region of semiconductor lasers. Figure 87 gives an example of quantum wire lasers employing a GaInAs/GaInAsP system that emits at 1.55 µm.[9]

Other optoelectronic devices. The counterpart of semiconductor lasers is a photodetector that receives the transmitted optical signal. Photodiodes having high quantum efficiencies in wavelength 1.3 to 1.6 µm band employ the GaInAs ternary semiconductors lattice-matched to InP as well. This system provides low-noise and high-speed photodiodes, i.e., PIN diodes and avalanche photodiodes (APDs). Infrared (IR) detectors and CCDs are important for infrared imaging. Illumination by IR LEDs are useful for imaging as well. Eye-safe radiation in the 1.3- to 1.55-µm range is another important issue in IR imaging.

References

1. Nahory, R.E., Pollack, M.A., Johnstone, W.D., and Barnes, R.L., *Appl. Phys. Lett.*, 33, 659, 1978.
2. Agrawal, G.P. and Dutta, N.K., *Long-Wavelength Semiconductor Lasers*, Van Nostrand Reinhold, New York, 1986, 85.
3. Moon, R.L., Antypas, G.A., and James, L.W., *J. Electron. Mater.*, 3, 635, 1974.
4. Casey, H.C. and Panish, M.B., *Heterostructure Lasers*, Part B, Academic Press, New York, 1978.
5. Manasevit, H.M., *Appl. Phys. Lett.*, 12, 156, 1968.
6. Tsang, W.T., *IEEE J. Quant. Electron.*, QE-23, 936, 1987.

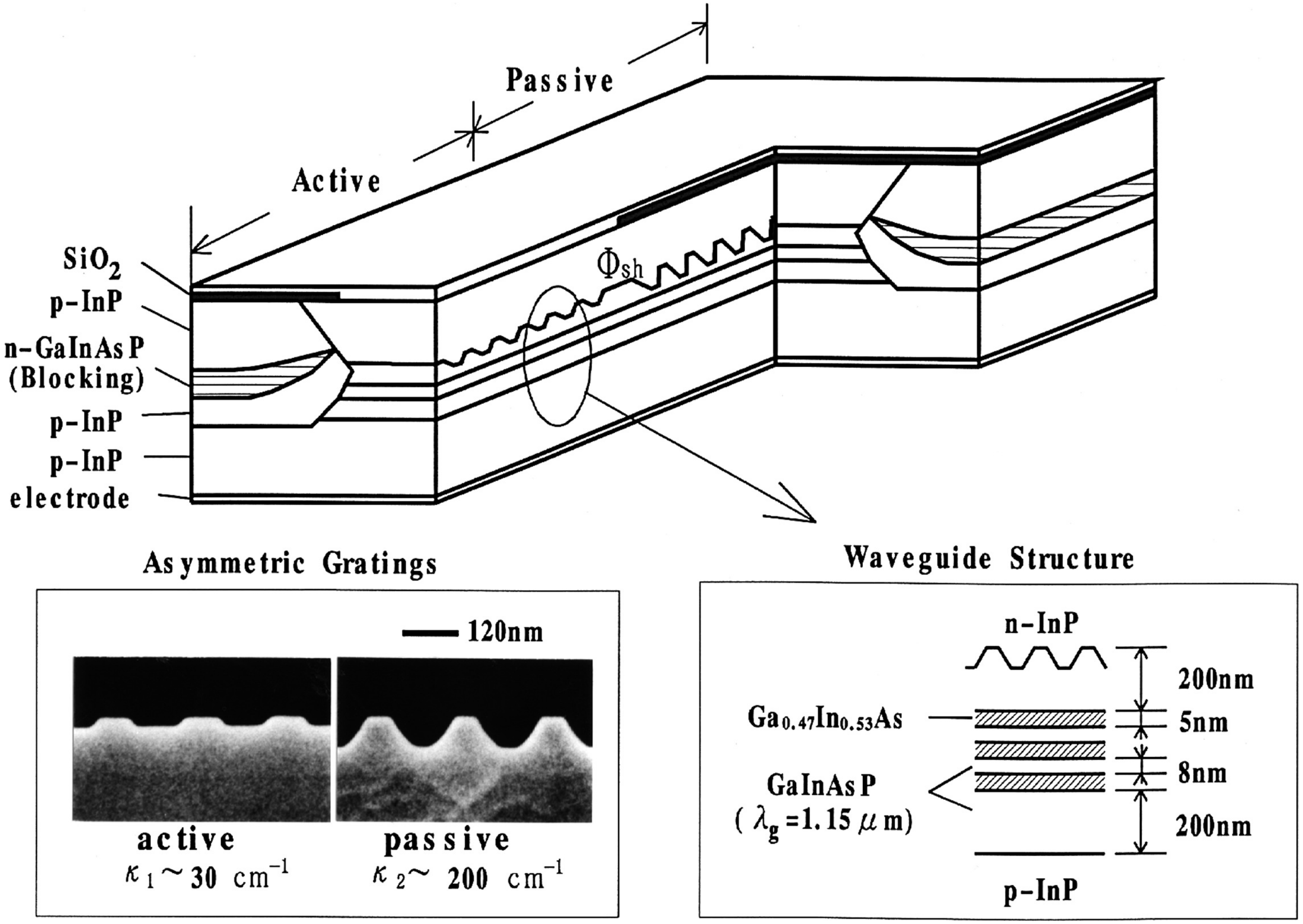
Passive
Active
SiO2
p-InP
n-GaInAsP (Blocking)
p-InP
p-InP
electrode
Φsh
Asymmetric Gratings
120nm
active
κ1 ~ 30 cm⁻¹
passive
κ2 ~ 200 cm⁻¹
Waveguide Structure
n-InP
200nm
Ga0.47In0.53As
5nm
8nm
GaInAsP
(λg = 1.15 μm)
200nm
p-InP

Figure 85 An example of single-mode laser. (From Shim, J.I., Komori, K., Arai, S., Suematsu, Y., and Somchai, R., *IEEE J. Quant. Electron.*, QE-27, 1736, 1991. With permission.)

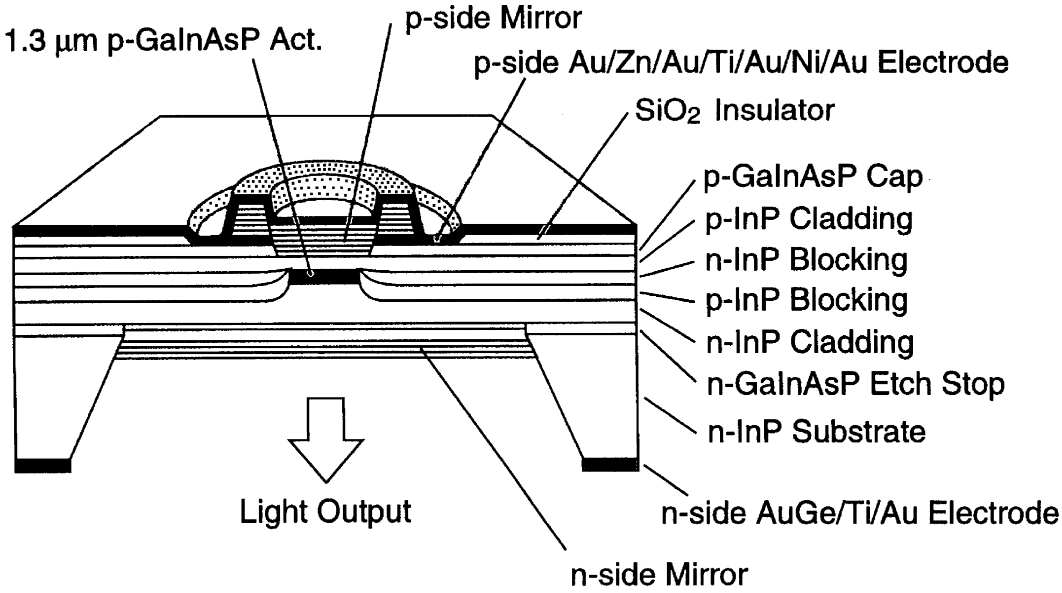
1.3 μm p-GaInAsP Act.
p-side Mirror
p-side Au/Zn/Au/Ti/Au/Ni/Au Electrode
SiO2 Insulator
p-GaInAsP Cap
p-InP Cladding
n-InP Blocking
p-InP Blocking
n-InP Cladding
n-GaInAsP Etch Stop
n-InP Substrate
Light Output
n-side AuGe/Ti/Au Electrode
n-side Mirror

Figure 86 An example of 1.48 μm surface emitting laser. (From Baba, T., Yogo, Y., Suzuki, T., Koyama, F., and Iga, K., *IEICE Trans. Electronics.*, E76-C, 1423, 1993. With permission.)

7. Shim, J.I., Komori, K., Arai, S., Suematsu, Y., and Somchai, R., *IEEE J. Quant. Electron.*, QE-27, 1736, 1991.
8. Baba, T., Yogo, Y., Suzuki, T., Koyama, F., and Iga, K., *IEICE Trans. Electronics.*, E76-C, 1423, 1993.
9. Kudo, K., Nagashima, Y. Tamura, S., Arai, S., Huang, Y., and Suematsu, Y., *IEEE Photon. Technol. Lett.*, 5, 864, 1993.

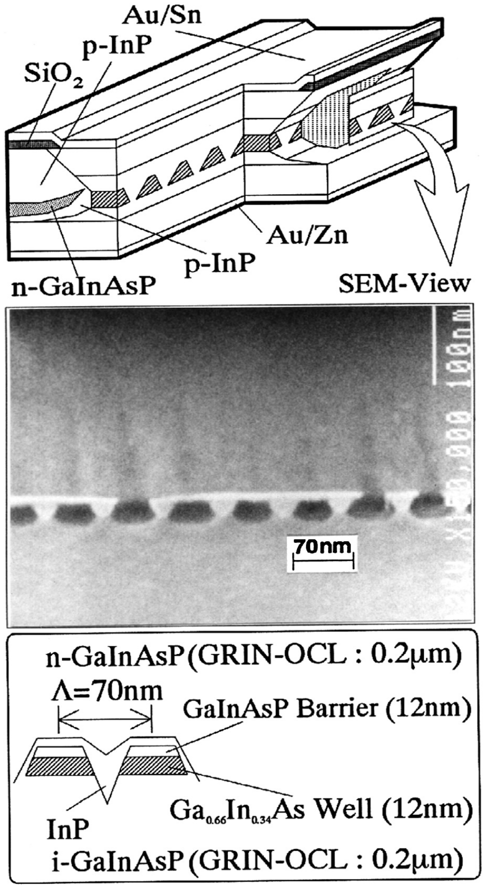
Au/Sn
p-InP
SiO$_2$
Au/Zn
p-InP
n-GaInAsP
SEM-View
100nm
70nm
n-GaInAsP (GRIN-OCL : 0.2μm)
Λ=70nm
GaInAsP Barrier (12nm)
InP
Ga$_{0.66}$In$_{0.34}$As Well (12nm)
i-GaInAsP (GRIN-OCL : 0.2μm)

Figure 87 An example of quantum wire lasers employing GaInAs/GaInAsP system to emit 1.55 μm wavelength. (From Kudo, K., Nagashima, Y. Tamura, S., Arai, S., Huang, Y., and Suematsu, Y., *IEEE Photon. Technol. Lett.*, 5, 864, 1993. With permission.)

chapter three — section twelve

Principal phosphor materials and their optical properties

Shuji Nakamura

Contents

3.12 GaN and related luminescence materials 309
  3.12.1 Introduction 309
  3.12.2 *n*-Type GaN 310
  3.12.3 *p*-Type GaN 310
  3.12.4 GaInN 311
  3.12.5 GaInN/AlGaN LED 312
  3.12.6 GaInN single-quantum well (SQW) LEDs 313
  3.12.7 GaInN multiquantum well (MQW) LDs 317
  3.12.8 Summary 321
References 321

3.12 GaN and related luminescence materials

3.12.1 Introduction

GaN and related materials such as AlGaInN are III-V nitride compound semiconductors with the wurtzite crystal structure and an energy band structure that allow direct interband transitions which are suitable for light-emitting devices (LEDs). The bandgap energy of AlGaInN varies between 6.2 and 1.95 eV at room temperature, depending on its composition. Therefore, these III-V semiconductors are useful for light-emitting devices, especially in the short-wavelength regions. Among the AlGaInN systems, GaN has been most intensively studied. GaN has a bandgap energy of 3.4 eV at room temperature.

Recent research on III-V nitrides has paved the way for the realization of high-quality crystals of GaN, AlGaN, and GaInN, and of *p*-type conduction in GaN and AlGaN.[1,2] The mechanism of acceptor-compensation, which prevents obtaining low-resistivity *p*-type GaN and AlGaN, has been elucidated.[3] In Mg-doped *p*-type GaN, Mg acceptors are deactivated by atomic hydrogen that is produced from NH_3 gas used to provide nitrogen during GaN growth. After growth, thermal annealing in N_2 ambience can reactivate the Mg acceptors by removing the atomic hydrogen from the Mg-hydrogen complexes.[3] High-brightness blue GaInN/AlGaN LEDs have been fabricated on the basis of these results, and luminous intensities over 2 cd have been achieved.[4–6] Also, blue/green GaInN single-quantum-well (SQW) LEDs with a narrow spectrum width have been developed.[7,8] These LEDs are now commercially available. Furthermore, recently, bluish-purple laser light emission at room-temperature (RT) in GaInN/GaN/AlGaN-based heterostructure laser diodes (LDs) under pulsed currents[9–14] or continuous-wave (CW) operation was demonstrated.[15–17] Recent studies of (Al,Ga,In)N compound semiconductors are described in this section.

3.12.2 n-*Type GaN*

GaN films are usually grown on a sapphire substrate with (0001) orientation (c face) at temperatures around 1000°C by the metal-organic chemical vapor deposition (MOCVD) method. Trimethylgallium (TMG) and ammonia are used as Ga and N sources, respectively. The lattice constants along the *a*-axis of the sapphire and GaN are 4.758 and 3.189 Å, respectively. Therefore, the lattice-mismatch between the sapphire and the GaN is very large. The lattice constant along the *a*-axis of 6H-SiC is 3.08 Å, which is relatively close to that of GaN. However, the price of a SiC substrate is extraordinarily expensive to use for the practical growth of GaN. Therefore, at present, there are no alternative substrates to sapphire from considerations of price and high-temperature properties, even as the lattice mismatch is large. Grown GaN layers usually show *n*-type conduction without any intentional doping. The donors are probably native defects or residual impurities such as nitrogen vacancies or residual oxygen.

Recently, remarkable progress has been achieved in the crystal quality of GaN films by employing a new growth method using buffer layers. Carrier concentration and Hall mobility, with values of 1×10^{16} cm^{-3} and 600 cm^2 Vs^{-1} at room temperature, respectively, have been obtained by deposition of a thin GaN or AlN layer as a buffer before the growth of a GaN film.[18] In order to obtain *n*-type GaN with high carrier concentrations, Si or Ge is doped into GaN.[19] The carrier concentration can be varied between 1×10^{17} and 1×10^{20} cm^{-3} by Si doping. Figure 88 shows a typical photoluminescence (PL) spectra of Si-doped GaN films. In the spectra, relatively strong deep-level (DL) emission around 560 nm and the band-edge (BE) emission around 380 nm are observed. The intensity of DL emissions is always stronger than that of BE emissions in this range of Si concentrations.

3.12.3 p-*Type GaN*

Formerly, it was impossible to obtain a *p*-type GaN film due to the poor crystal quality of GaN films. Recently, Amano et al.[1] succeeded in obtaining *p*-type GaN films by means of Mg doping and low-energy electron-beam irradiation (LEEBI) treatment after growth. In 1992, Nakamura et al.[20] found that low-resistivity *p*-type GaN films are also obtained by post-thermal annealing in N_2 ambience of Mg-doped GaN films. The resistivity of as-grown films is 1×10^6 Ω·cm. When the temperature is raised to 400°C in a N_2 ambience for annealing, resistivity begins to decrease suddenly. After annealing at 700°C, the resistivity, hole carrier concentration and hole mobility become 2 Ω·cm, 3×10^{17} cm^{-3} and 10 cm^2 V·s^{-1}, respectively.

These changes of the resistivity of Mg-doped GaN films are explained by the hydogenation process model in which atomic hydrogen produced from NH_3 during the growth is assumed to be the origin of the acceptor compensation. If low-resistivity *p*-type GaN films, which are obtained by N_2-ambient thermal annealing or LEEBI treatment, are thermally annealed in NH_3 ambience at temperatures above 400°C, they show a resistivity as high as 1×10^6 Ω·cm. This resistivity is almost the same as that of as-grown Mg-doped GaN films. Therefore, these results indicate that the abrupt resistivity increase in NH_3-ambient thermal annealing at temperatures above 400°C is caused by the NH_3 gas itself.

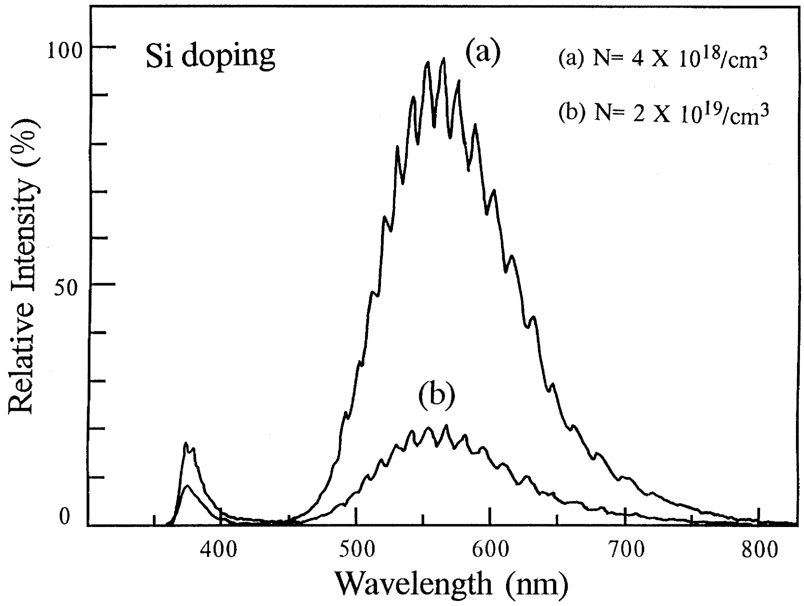

Figure 88 Room-temperature PL spectra of Si-doped GaN films. Both samples were grown under the same growth conditions but changing the flow rate of SiH_4. The carrier concentrations are (a) 4×10^{18} cm^{-3} and (b) 2×10^{19} cm^{-3}. (From Nakamura, S., Mukai, T., and Senoh, M., *Jpn. J. Appl. Phys.*, 31, 2883, 1992. With permission.)

Atomic hydrogen produced by the NH_3 dissociation at temperatures above 400°C is considered to be related to the acceptor compensation mechanism. A hydrogenation process whereby acceptor-H neutral complexes are formed during the growth of *p*-type GaN films has been proposed.[3] The formation of these complexes during film growth causes acceptor compensation. The N_2-ambient thermal annealing or LEEBI treatment after growth can reactivate the acceptors by removing atomic hydrogen from the neutral complexes. As a result, noncompensated acceptors are formed and low-resistivity *p*-type GaN films are obtained.

3.12.4 GaInN

The ternary III-V semiconductor compound, GaInN, is one of the candidates for blue to blue-green emitting LEDs, because its bandgap varies from 1.95 to 3.4 eV depending on the indium mole fraction. It was very difficult to grow high-quality single crystal GaInN films due to the high dissociation pressure of GaInN at the growth temperature. Recently, this difficulty has been overcome by means of the two-flow (TF)-MOCVD method,[21] and high-quality GaInN films have been obtained. Figure 89 shows the results of room-temperature PL measurements of high-quality GaInN films grown by this method. A strong sharp peak is observed at 400 nm in (a) and at 438 nm in (b). These spectra are due to BE emission of GaInN films because they have a very narrow halfwidth (about 70 meV).

Figure 90 shows the bandgap energy ($E_g(X)$) of $Ga_{(1-X)}In_XN$ films estimated from PL spectra at room temperature as a function of the indium mole fraction X.[22] The indium mole fraction of the GaInN films was determined by the measurements of the difference of the X-ray diffraction peak positions between GaInN and GaN films. Osamura et al.[23] showed that $E_g(X)$ in ternary alloys of $Ga_{(1-X)}In_XN$ has the following parabolic dependence on the molar fraction X:

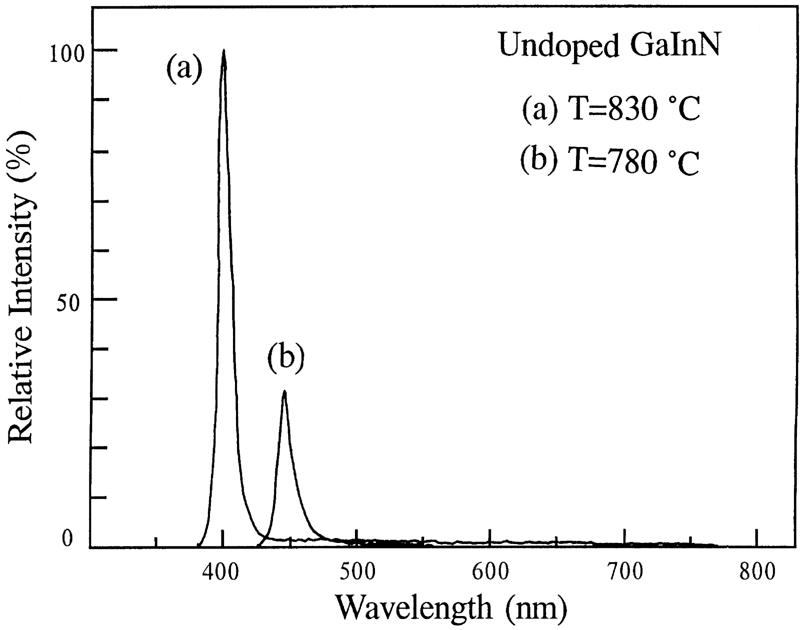

Figure 89 Room-temperature PL spectra of the GaInN films. Both samples were grown on GaN films under the same growth conditions but changing the growth temperature: (a) 830°C and (b) 780°C. (From Nakamura, S. and Mukai, T., *Jpn. J. Appl. Phys.*, 31, L1457, 1992. With permission.)

$$E_g(X) = (1-X)E_{g,\mathrm{GaN}} + XE_{g,\mathrm{InN}} - bX(1-X) \tag{48}$$

where $E_{g,\mathrm{GaN}}$ is 3.40 eV, $E_{g,\mathrm{InN}}$ is 1.95 eV, and the bowing parameter b is 1.00 eV. The calculated curve is shown by the solid line in the figure. Here, the bowing parameter, which is also called nonlinear parameter, shows downward deviation of the bandgap energy of ternary compounds compared to the linear relation between the bandgap energy of binary compounds, that is, from $(1–X)E_{g,\mathrm{GaN}} + XE_{g,\mathrm{InN}}$.

Figure 91 shows a typical room-temperature PL spectrum of a Zn-doped GaInN film.[22] It has two peaks. The shorter wavelength peak is due to BE emission of GaInN, and the longer wavelength peak is due to a Zn-related emission and has a large halfwidth (about 70 nm, i.e., about 430 meV).

3.12.5 GaInN/AlGaN LED

Figure 92 shows the structure of a GaInN/AlGaN double-heterostructure (DH) LED fabricated by Nakamura et al.[4–6,22] In this LED, Si and Zn are co-doped into the GaInN active layer in order to obtain a high output power. Zn-doped GaInN is used as the active layer to obtain strong blue emission, as shown in Figure 91. Mg-doped GaInN does not show strong blue emission, in contrast to the Zn-doped films.

Figure 93 shows the electroluminescence (EL) spectra of this system with forward currents of 0.1, 1, and 20 mA.[4–6,22] The typical peak wavelength and halfwidth are 450 and 70 nm, respectively, at 20 mA. The peak wavelength shifts to shorter wavelengths with increasing forward current. This blue shift suggests that the luminescence is dominated by the donor-acceptor (DA) pair recombination mechanism in the GaInN active layer co-doped with Si and Zn. At 20 mA, a narrower, higher-energy peak emerges around 385 nm. This peak is due to band-to-band recombination in the GaInN active layer. This peak is

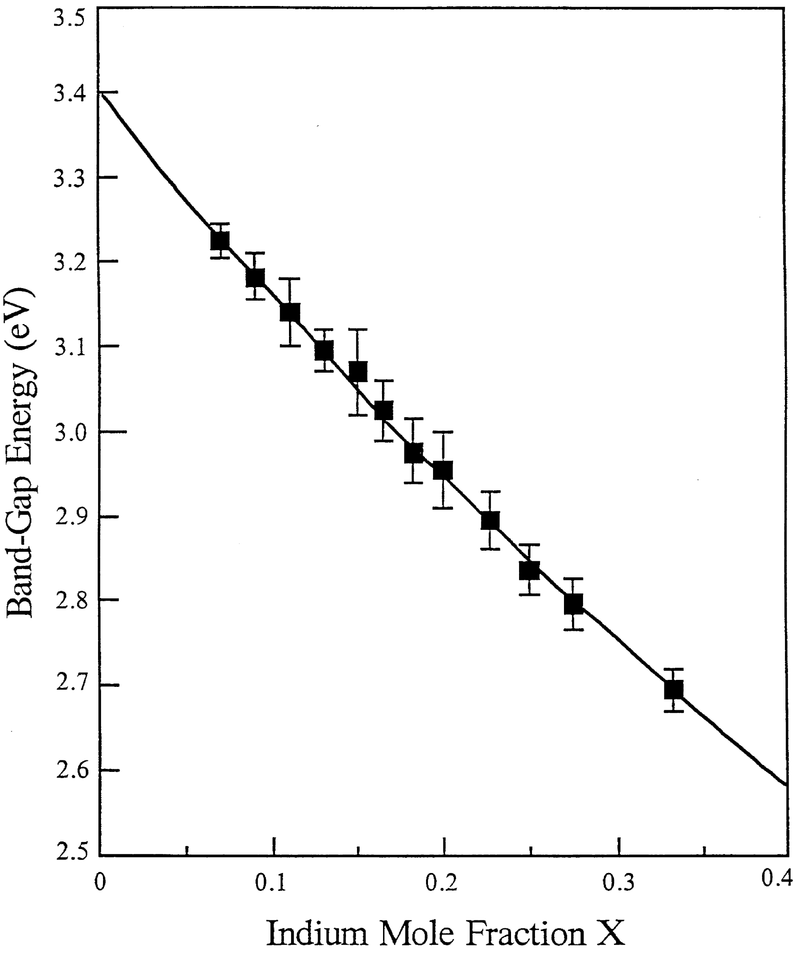

Figure 90 Bandgap energy of $Ga_{(1-X)}In_XN$ films as a function of the indium mole fraction X. (From Nakamura, S., *Jpn. J. Opt.*, 23, 701, 1994. With permission.)

resolved at injection levels where the intensity of impurity-related recombination luminescence is saturated. The output power of the GaInN/AlGaN DH blue LEDs is 1.5 mW at 10 mA, 3 mW at 20 mA, and 4.8 mW at 40 mA. The external quantum efficiency is 5.4% at 20 mA.[22] The typical on-axis luminous intensity with 15° conical viewing angle is 2.5 cd at 20 mA when the forward voltage is 3.6 V at 20 mA.

3.12.6 GaInN single-quantum-well (SQW) LEDs

High-brightness blue and blue-green GaInN/AlGaN DH LEDs with a luminous intensity of 2 cd have been fabricated and are now commercially available, as mentioned above.[4–6,22] In order to obtain blue and blue-green emission centers in these GaInN/AlGaN DH LEDs, the GaInN active layer was doped with Zn. Although these GaInN/AlGaN DH LEDs produced high-power light output in the blue and blue-green regions with a broad emission spectrum (FWHM = 70 nm), green or yellow LEDs with peak wavelengths longer than 500 nm have not been fabricated.[6] The longest peak wavelength of the EL of GaInN/AlGaN DH LEDs achieved thus far has been observed at 500 nm (blue-green) because the crystal quality of the GaInN active layer of DH LEDs deteriorates when the indium mole fraction is increased to obtain green band-edge

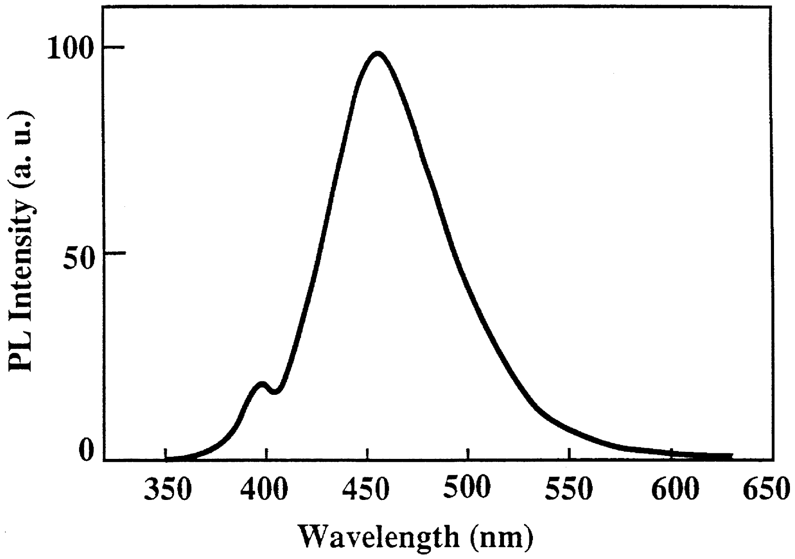

Figure 91 Room-temperature PL spectrum of a Zn-doped $Ga_{0.95}In_{0.05}N$ film. (From Nakamura, S., *Jpn. J. Opt.*, 23, 701, 1994. With permission.)

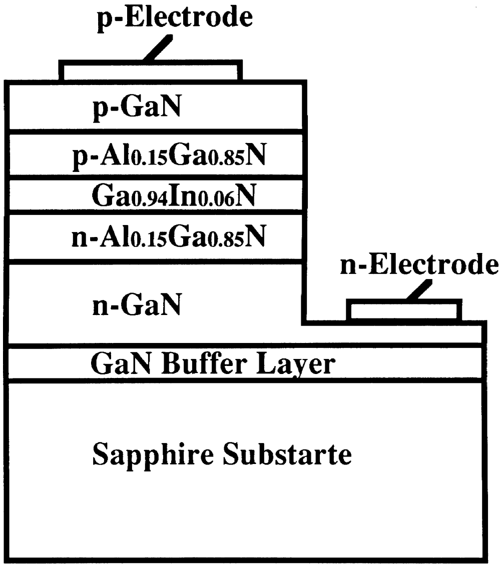

p-Electrode
p-GaN
p-Al0.15Ga0.85N
Ga0.94In0.06N
n-Al0.15Ga0.85N
n-Electrode
n-GaN
GaN Buffer Layer
Sapphire Substarte

Figure 92 Structure of the GaInN/AlGaN double-heterostructure blue LED. (From Nakamura, S., *Jpn. J. Opt.*, 23, 701, 1994. With permission.)

emission.[6] Quantum-well (QW) LEDs with thin GaInN active layers (about 30 Å) fabricated to obtain high-power emission from blue to yellow with a narrow emission spectrum[7,8] are described below.

The green GaInN SQW LED device structures (Figure 94) consist of a 300-Å GaN buffer layer grown at low temperature (550°C), a 4-µm-thick layer of *n*-type GaN:Si, a 30-Å-thick active layer of undoped $Ga_{0.55}In_{0.45}N$, a 1000-Å-thick layer of *p*-type $Al_{0.2}Ga_{0.8}N$:Mg, and a 0.5-µm-thick layer of *p*-type GaN:Mg. This is the SQW structure.

Figure 95 shows the typical EL of the blue, green, and yellow SQW LEDs containing different indium mole fractions of the GaInN layer, all at a forward current of 20 mA. The

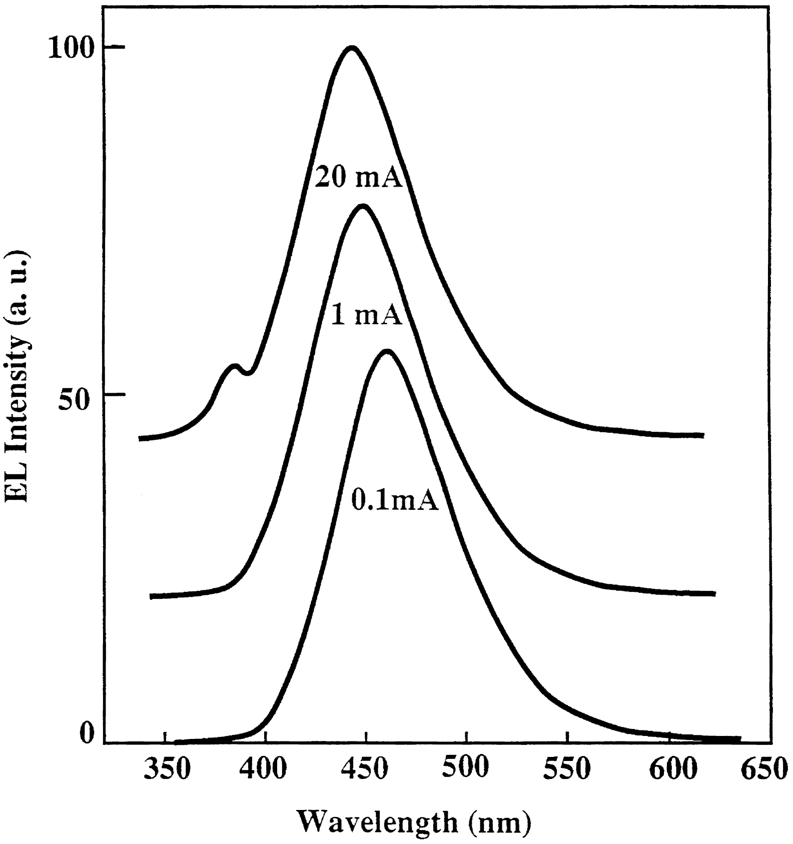

Figure 93 Electroluminescence spectra of a GaInN/AlGaN double-heterostructure blue LED. (From Nakamura, S., *Jpn. J. Opt.*, 23, 701, 1994. With permission.)

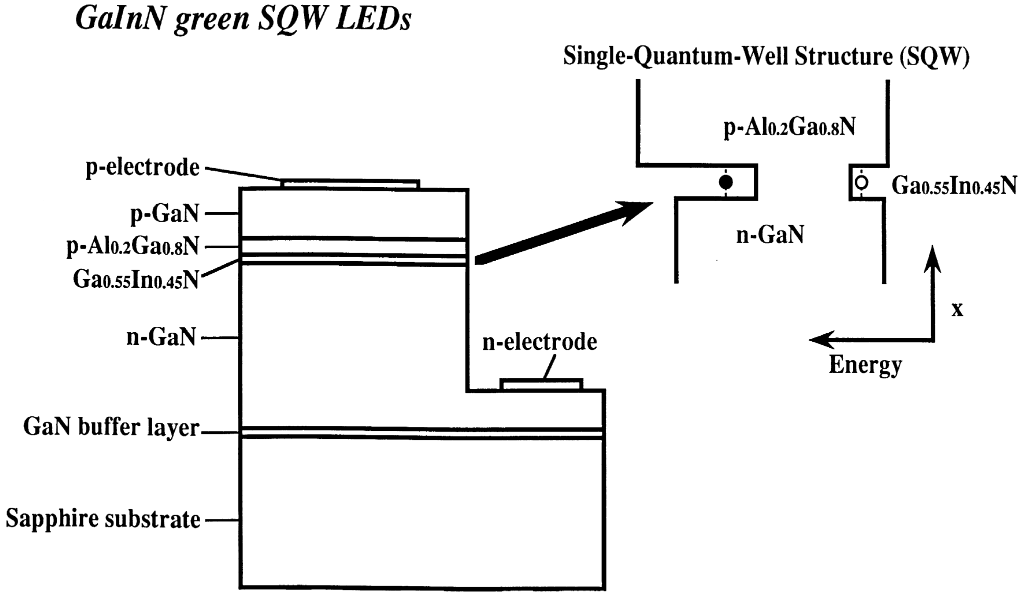
GaInN green SQW LEDs
Single-Quantum-Well Structure (SQW)
p-Al$_{0.2}$Ga$_{0.8}$N
Ga$_{0.55}$In$_{0.45}$N
n-GaN
x
Energy
p-electrode
p-GaN
p-Al$_{0.2}$Ga$_{0.8}$N
Ga$_{0.55}$In$_{0.45}$N
n-GaN
n-electrode
GaN buffer layer
Sapphire substrate

Figure 94 The structure of green SQW LED. (From Nakamura, S., Senoh, M., Iwasa, N., Nagahama, S., Yamada, T., and Mukai, T., *Jpn. J. Appl. Phys. Lett.*, 34, L1332, 1995. With permission.)

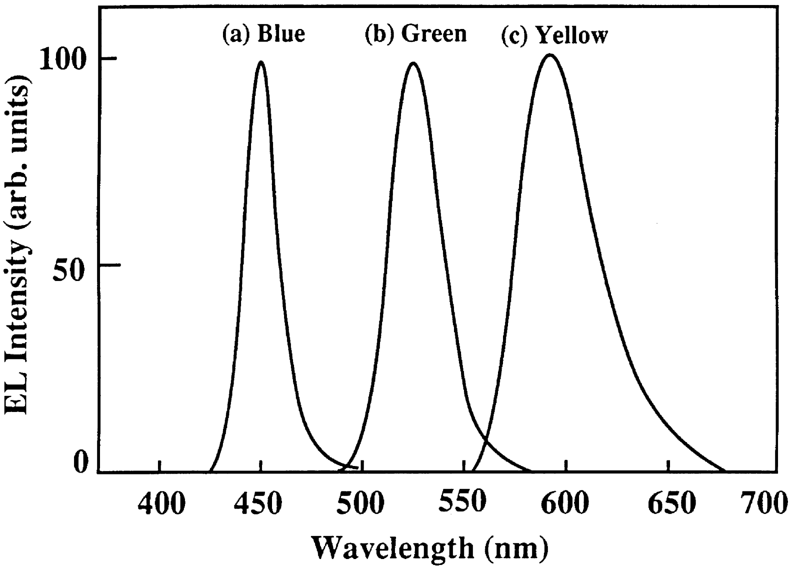

Figure 95 Electroluminescence of (a) blue, (b) green, and (c) yellow SQW LEDs at a forward current of 20 mA. (From Nakamura, S., Senoh, M., Iwasa, N., and Nagahama, S., *Jpn. J. Appl. Phys.*, 34, L797, 1995. With permission.)

peak wavelength and the FWHM of the typical blue SQW LEDs are 450 and 20 nm, respectively; of the green 525 and 30 nm; and of the yellow 600 and 50 nm, respectively. When the peak wavelength becomes longer, the FWHM of the EL spectra increases, probably due to the inhomogeneities in the GaInN layer or due to strain between well and barrier layers of the SQW caused by lattice mismatch and differences in the thermal expansion coefficients.

At 20 mA, the output power and the external quantum efficiency of the blue SQW LEDs are 5 mW and 9.1%, respectively. Those of the green SQW LEDs are 3 mW and 6.3%, respectively. A typical on-axis luminous intensity of the green SQW LEDs with a 10° cone viewing angle is 10 cd at 20 mA. These values of output power, external quantum efficiency, and luminous intensity of blue and green SQW LEDs are more than 100 times higher than those of conventional blue SiC and green GaP LEDs. By combining these high-power and high-brightness blue GaInN SQW, green GaInN SQW, and red AlGaAs LEDs, many kinds of applications such as LED full-color displays and LED white lamps for use in place of light bulbs or fluorescent lamps are now possible. These devices have the characteristics of high reliability, high durability, and low energy consumption.

Figure 96 is a chromaticity diagram in which the positions of the blue and green GaInN SQW LEDs are shown. The chromaticity coordinates of commercially available green GaP LEDs, green AlGaInP LEDs, and red AlGaAs LEDs are also shown. The color range of light emitted by a full-color LED lamp in the chromaticity diagram is shown as the region inside each triangle, which is drawn by connecting the positions of three primary color LED lamps. Three color ranges (triangles) are shown for differences only in the green LED (green GaInN SQW, green GaP, and green AlGaInP LEDs). In this figure, the color range of lamps composed of a blue GaInN SQW LED, a green GaInN SQW LED, and a red AlGaAs LED is the widest. This means that the GaInN blue and green SQW LEDs show much better color and color purity in comparison with other blue and green LEDs. Using these blue and green SQW LEDs together with LEDs made of AlGaAs, more realistic LED full color displays have been demonstrated.

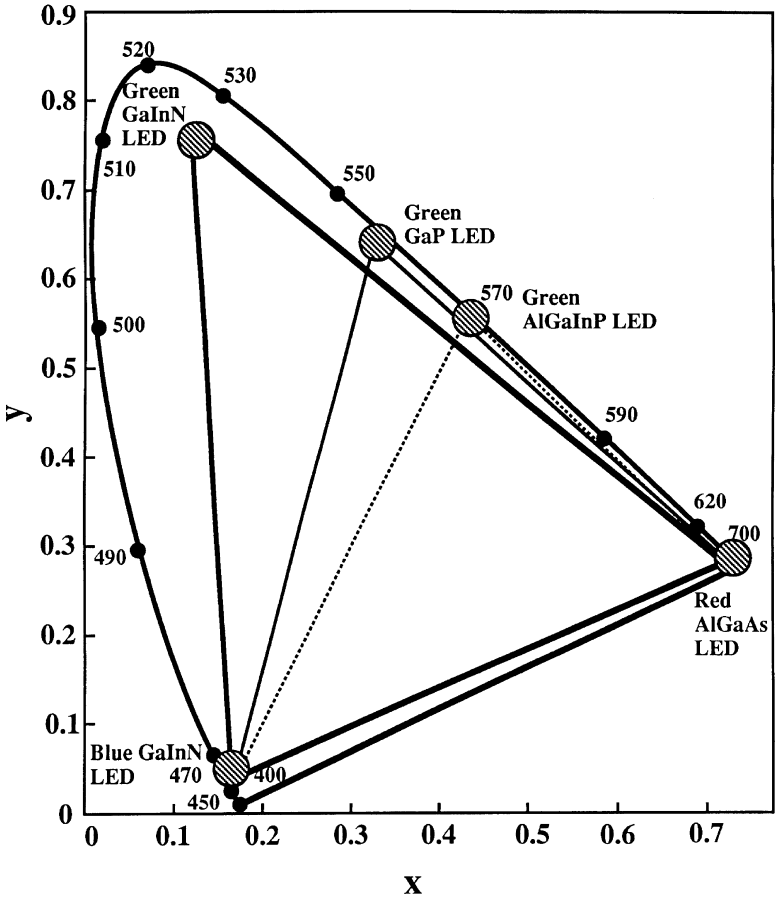

Figure 96 Chromaticity diagram in which blue GaInN SQW LED, green GaInN SQW LED, green GaP LED, green AlGaInP LED, and red AlGaAs LED are shown. (From Nakamura, S., Senoh, M., Iwasa, N., Nagahama, S., Yamada, T., and Mukai, T., *Jpn. J. Appl. Phys. Lett.*, 34, L1332, 1995. With permission.)

3.12.7 GaInN multiquantum-well (MQW) LDs

The structure of the GaInN MQW LDs is shown in Figure 97. The GaInN MQW LD device consists of a 300-Å-thick GaN buffer layer grown at a low temperature of 550°C, a 3-μm-thick layer of *n*-type GaN:Si, a 0.1-μm-thick layer of *n*-type $Ga_{0.95}In_{0.05}N$:Si, a 0.5-μm-thick layer of *n*-type $Al_{0.08}Ga_{0.92}N$:Si, and a 0.1-μm-thick layer of *n*-type GaN:Si. At this point, the MQW structure consists of four 35-Å-thick undoped $Ga_{0.85}In_{0.15}N$ well layers by 70-Å-thick undoped $Ga_{0.98}In_{0.02}N$ barrier layers. The four well layers form the gain medium. The heterostructure is then capped with a 200-Å-thick layer of *p*-type $Al_{0.2}Ga_{0.8}N$:Mg, a 0.1-μm-thick layer of *p*-type GaN:Mg, a 0.5-μm-thick layer of *p*-type $Al_{0.08}Ga_{0.92}N$:Mg, and a 0.5-μm-thick layer of *p*-type GaN:Mg. The *n*-type and *p*-type GaN layers are used for light-guiding, while the *n*-type and *p*-type $Al_{0.08}Ga_{0.92}N$ layers act as cladding for confinement of the carriers and the light from the active region.

Figure 98 shows typical voltage-current (V-I) characteristics and the light output power (L) per coated facet of the LD as a function of the forward DC current at RT. No stimulated emission was observed up to a threshold current of 80 mA, corresponding to a current density of 3.6 kA cm^{-2}, as shown in Figure 98. The operating voltage at the threshold was 5.5 V.

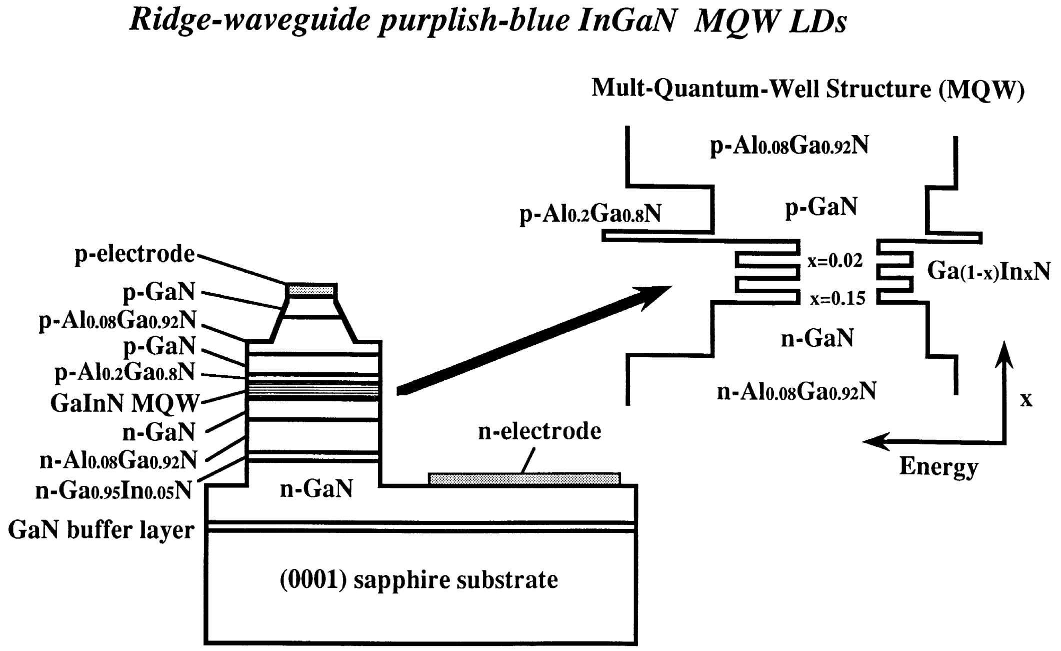
Ridge-waveguide purplish-blue InGaN MQW LDs
Mult-Quantum-Well Structure (MQW)
p-Al0.08Ga0.92N
p-Al0.2Ga0.8N
p-GaN
x=0.02
x=0.15
Ga(1-x)InxN
n-GaN
n-Al0.08Ga0.92N
x
Energy
p-electrode
p-GaN
p-Al0.08Ga0.92N
p-GaN
p-Al0.2Ga0.8N
GaInN MQW
n-GaN
n-Al0.08Ga0.92N
n-Ga0.95In0.05N
GaN buffer layer
n-GaN
n-electrode
(0001) sapphire substrate

Figure 97 The structure of the GaInN MQW LDs. (From Nakamura, S., Senoh, M., Nagahama, S., Iwasa, N., Yamada, T., Matsushita, T., Sugimoto, Y., and Kiyoku, H., Presented at the *9th Annual Meeting of IEEE Lasers and Electro-Optics Society,* Boston, PD1.1, Nov. 18-21, 1996. With permission.)

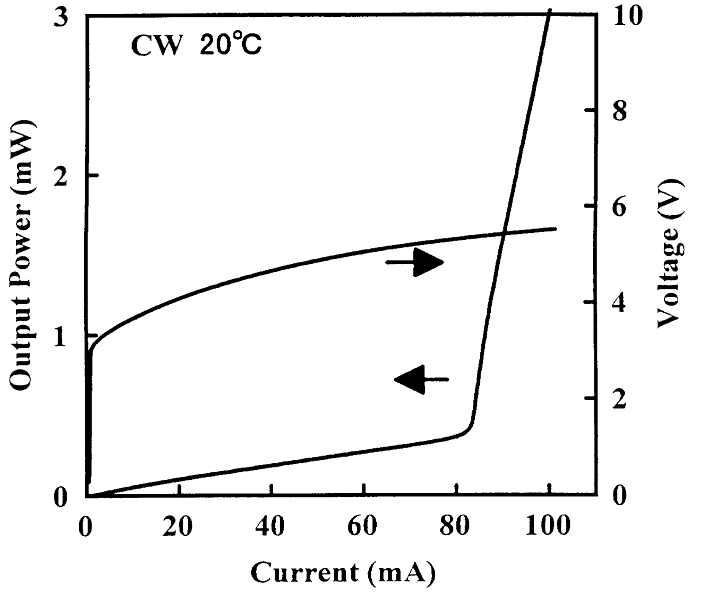

Figure 98 Typical light output power (L)-current (I) and voltage (V)-current (I) characteristics of GaInN MQW LDs measured under CW operation at RT. (From Nakamura, S., Senoh, M., Nagahama, S., Iwasa, N., Yamada, T., Matsushita, T., Sugimoto, Y., and Kiyoku, H., Presented at the *9th Annual Meeting of IEEE Lasers and Electro-Optics Society,* Boston, PD1.1, Nov. 18-21, 1996. With permission.)

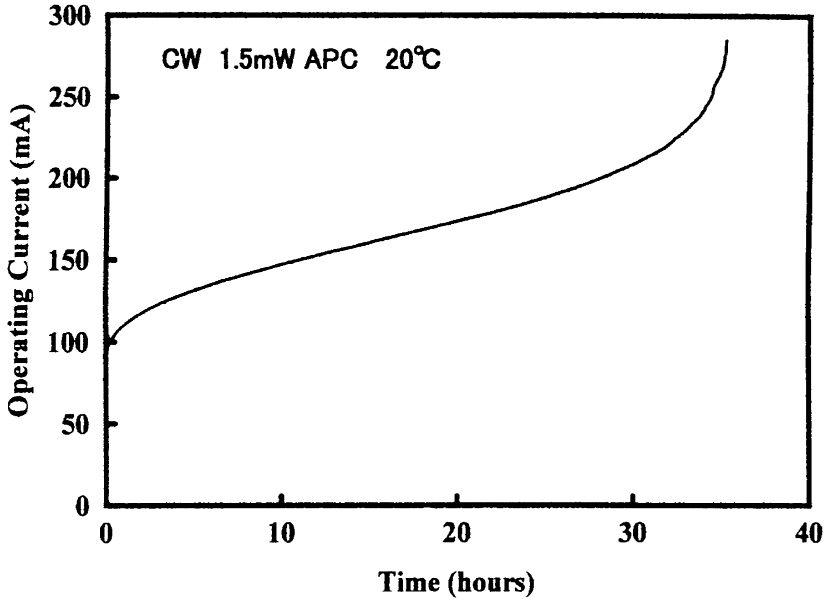

Figure 99 Operating current as a function of time for GaInN MQW LDs under a constant output power of 1.5 mW per facet controlled using an autopower controller. The LD was operated under DC at RT. (From Nakamura, S., presented at *Materials Research Society Fall Meeting*, Boston, N1.1, Dec. 2-6, 1996. With permission.)

Figure 99 shows the results of a lifetime test of CW-operated LDs carried out at RT, in which the operating current is shown as a function of time, keeping output power constant at 1.5 mW per facet using an autopower controller (APC). The operating current gradually increases due to the increase in the threshold current from its initial value; the current then increases sharply after 35 hours. This short lifetime is probably due to heating resulting from the high operating currents and voltages. Short-circuiting of the LDs occurred after the 35 hours, as mentioned above.

Figure 100 shows emission spectra of GaInN MQW LDs with various operating current under RT CW operation. The threshold current and voltage of this LD were 160 mA and 6.7 V, respectively. The threshold current density was 7.3 kA cm^{-2}. At a current of 156 mA, many longitudinal modes are observed with a mode separation of 0.042 nm; this separation is smaller than the calculated value of 0.05 nm, probably due to refractive index changes from the value used (2.54) in the calculation. Periodic subband emissions are observed with a peak separation of about 0.025 nm (ΔE = 2 meV). The origin of these subbands has not yet been identified. On increasing the forward current from 156 to 186 mA, the laser emission becomes single mode and shows mode hopping of the peak wavelength toward higher energy; the peak emission is at the center of each subband emission. Figure 101 shows the peak wavelength of the laser emission as a function of the operating current under RT CW operation. A gradual increase of the peak wavelength is observed, probably due to bandgap narrowing of the active layer caused by the temperature increase. At certain currents, large mode hopping of the peak wavelength toward higher energy is observed with increasing operating current.

The delay time of the laser emission of the LDs as a function of the operating current was measured under pulsed current modulation using the method described in Reference 14 in order to estimate the carrier lifetime (τ_s). From this measurement, τ_s was estimated to be 10 ns, which is larger than previous estimates of 3.2 ns.[14] The threshold

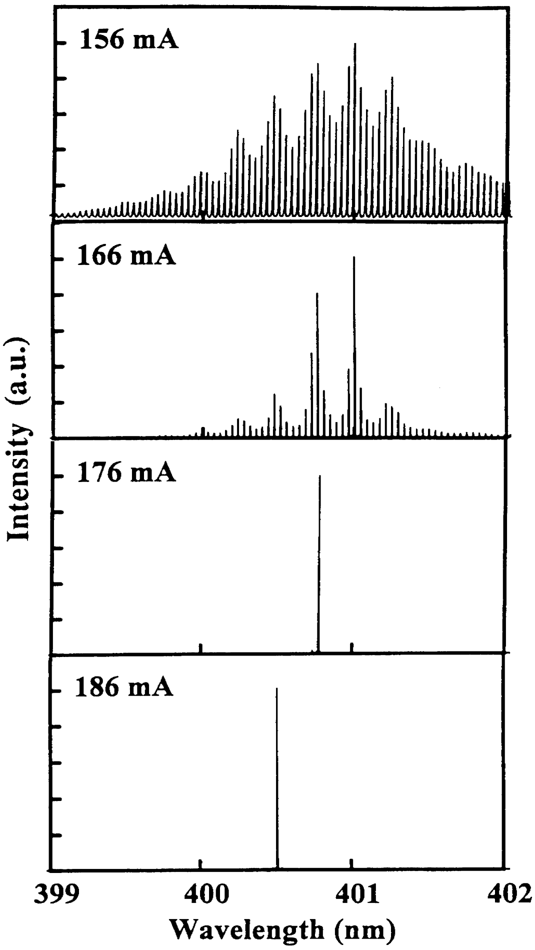

Figure 100 Emission spectra of GaInN MQW LDs with various operating currents under RT CW operation. (From Nakamura, S., presented at *Materials Research Society Fall Meeting*, Boston, N1.1, Dec. 2-6, 1996. With permission.)

carrier density (n_{th}) was estimated to be 2×10^{20} cm^{-3} for a threshold current density of 3.6 kA cm^{-2}, and an active layer thickness of 140 Å.[14] The thickness of the active layer was determined as 140 Å, assuming that the injected carriers were confined in the GaInN well layers. Other typical values are $\tau_s = 3$ ns, $J_{th} = 1$ kA cm^{-2}, and $n_{th} = 2 \times 10^{18}$ cm^{-3} for AlGaAs lasers and $n_{th} = 1 \times 10^{18}$ cm^{-3} for AlGaInP lasers. In comparison with other more conventional lasers, n_{th} in our structure is relatively large (two orders of magnitude higher), probably due to the large density of states of carriers resulting from their large effective masses.[14]

The Stokes' shift or energy differences between excitation and emission in GaInN MQW LDs can be as large as 100 to 250 meV at RT.[24–26] This means that the energy depth of the localized state of the carriers is 100 to 250 meV in these devices. Both the spontaneous emission and the stimulated emission of the LDs originates from these deep localized energy states.[24–26] Using high-resolution, cross-sectional transmission electron microscopy (TEM), a periodic indium composition fluctuation was observed in the LDs, probably caused by GaInN phase separation during growth.[25,26] Based on these results, the laser emission is thought to originate from GaInN quantum dot-like states formed in these structures. The many periodic subband emissions observed probably result from transitions between the subband energy levels of the GaInN quantum dots formed from

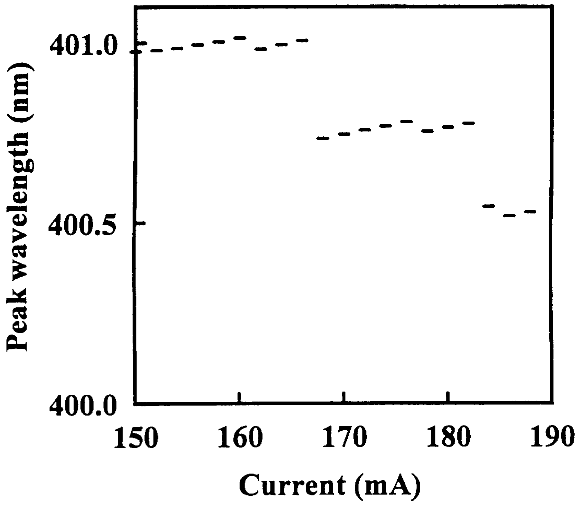

Figure 101 Peak wavelength of the emission spectra of the GaInN MQW LDs as a function of the operating current under RT CW operation. (From Nakamura, S., Characteristics of GaInN multi-quantum-well-structure laser diodes, presented at *Materials Research Society Fall Meeting*, Boston, N1.1, Dec. 2-6, 1996. With permission.)

In-rich regions in the GaInN well layers. The size of the GaInN dots is estimated to be approximately 35 Å from the high-resolution, cross-sectional TEM pictures.[25,26] It is difficult to control the size of GaInN dots that form in adjacent In-rich and -poor regions. The energy separation of each subband emission in Figure 100 is only about 2 meV, which is considered to be relatively small in comparison with the energy difference between the n = 1 and n = 2 subband energy transitions of other more controlled quantum dots. These periodic subband energy levels are probably caused between n = 1 subband levels of quantum dots with different dot sizes.

3.12.8 Summary

Superbright blue and green GaInN SQW LEDs have been developed and commercialized. By combining high-power, high-brightness blue GaInN SQW LEDs, green GaInN SQW LEDs, and red AlGaAs LEDs, many kinds of applications, such as LED full-color displays and LED white lamps for use in place of light bulbs or fluorescent lamps, are now possible. These devices have the characteristics of high reliability, high durability, and low energy consumption. RT CW operation of bluish-purple GaInN MQW LDs has been demonstrated recently with a lifetime of 35 hours. The carrier lifetime and the threshold carrier density were estimated to be 10 ns and 2×10^{20} cm^{-3}, respectively. The emission spectra of GaInN MQW LDs under CW operation at RT showed periodic subband emissions with an energy separation of 2 meV. These periodic subband emissions are probably due to the transitions between the subband energy levels of quantum dots formed from In-rich regions in the GaInN well layers. Further improvement in the lifetime of the LDs can be obtained by reducing the threshold current and voltage. The advances in this technology have been rapid in the past decade. Progress attained has been reviewed in a number of places.[27]

References

1. Amano, H., Kito, M., Hiramatsu, K., and Akasaki, I., *Jpn. J. Appl. Phys.*, 28, L2112, 1989.
2. Strite, S., Lin, M.E., and Morkoç, H., *Thin Solid Films*, 231, 197, 1993.

3. Nakamura, S., Iwasa, N., Senoh, M., and Mukai, T., *Jpn. J. Appl. Phys.*, 31, 1258, 1992.
4. Nakamura, S., *Nikkei Electronics Asia*, 3, 65, 1994.
5. Nakamura, S., Mukai, T., and Senoh, M., *Appl. Phys. Lett.*, 64, 1687, 1994.
6. Nakamura, S., Mukai, T., and Senoh, M., *J. Appl. Phys.*, 76, 8189, 1994.
7. Nakamura, S., Senoh, M., Iwasa, N., and Nagahama, S., *Jpn. J. Appl. Phys.*, 34, L797, 1995.
8. Nakamura, S., Senoh, M., Iwasa, N., Nagahama, S., Yamada, T., and Mukai, T., *Jpn. J. Appl. Phys. Lett.*, 34, L1332, 1995.
9. Nakamura, S., Senoh, M., Nagahama, S., Iwasa, N., Yamada, T., Matsushita, T., Kiyoku, H., and Sugimoto, Y., *Jpn. J. Appl. Phys.*, 35, L74, 1996.
10. Nakamura, S., Senoh, M., Nagahama, S., Iwasa, N., Yamada, T., Matsushita, T., Kiyoku, H., and Sugimoto, Y., *Jpn. J. Appl. Phys.*, 35, L217, 1996.
11. Nakamura, S., Senoh, M., Nagahama, S., Iwasa, N., Yamada, T., Matsushita, T., Kiyoku, H., and Sugimoto, Y., *Appl. Phys. Lett.*, 68, 2105, 1996.
12. Nakamura, S., Senoh, M., Nagahama, S., Iwasa, N., Yamada, T., Matsushita, T., Kiyoku, H., and Sugimoto, Y., *Appl. Phys. Lett.*, 68, 3269, 1996.
13. Nakamura, S., Senoh, M., Nagahama, S., Iwasa, N., Yamada, T., Matsushita, T., Sugimoto, Y., and Kiyoku, H., *Appl. Phys. Lett.*, 69, 1477, 1996.
14. Nakamura, S., Senoh, M., Nagahama, S., Iwasa, N., Yamada, T., Matsushita, T., Sugimoto, Y., and Kiyoku, H., *Appl. Phys. Lett.*, 69, 1568, 1996.
15. Nakamura, S., Senoh, M., Nagahama, S., Iwasa, N., Yamada, T., Matsushita, T., Sugimoto, Y., and Kiyoku, H., *Appl. Phys. Lett.*, 69, 3034, 1996.
16. Nakamura, S., Senoh, M., Nagahama, S., Iwasa, N., Yamada, T., Matsushita, T., Sugimoto, Y., and Kiyoku, H., First room-temperature continuous-wave operation of GaInN multi-quantum-well-structure laser diodes, presented at *9th Annual Meeting of IEEE Lasers and Electro-Optics Society*, Boston, PD1.1, Nov. 18-21, 1996.
17. Nakamura, S., Characteristics of GaInN multi-quantum-well-structure laser diodes, presented at *Materials Research Society Fall Meeting*, Boston, N1.1, Dec. 2-6, 1996.
18. Nakamura, S., *Jpn. J. Appl. Phys.*, 30, L1705, 1991.
19. Nakamura, S., Mukai, T., and Senoh, M., *Jpn. J. Appl. Phys.*, 31, 2883, 1992.
20. Nakamura, S., Mukai, T., Senoh, M., and Iwasa, N., *Jpn. J. Appl. Phys.*, 31, L139, 1992.
21. Nakamura, S. and Mukai, T., *Jpn. J. Appl. Phys.*, 31, L1457, 1992.
22. Nakamura, S., *Jpn. J. Opt.*, 23, 701, 1994.
23. Osamura, K., Naka, S., and Murakami, Y., *J. Appl. Phys.*, 46, 3432, 1975.
24. Chichibu, S., Azuhata, T., Sota, T., and Nakamura, S., *Appl. Phys. Lett.*, 69, 4188, 1996.
25. Narukawa, Y., Kawakami, Y., Fuzita, Sz., Fujita, Sg., and Nakamura, S., *Phys. Rev.*, B55, 1938R, 1997.
26. Narukawa, Y., Kawakami, Y., Funato, M., Fujita, Sz., Fujita, Sg., and Nakamura, S., Role of self-formed GaInN quantum dots for the exciton localization in the purple laser diodes emitting at 420 nm, *Appl. Phys. Lett.*, 70, 981, 1996.
27. Nakamura, S., and Fasol, G., *The Blue Laser Diode*, Springer - Verlag, Berlin, 2000.

chapter three — section thirteen

Fundamentals of luminescence

Hiroyuki Matsunami

Contents

3.13 Silicon carbide (SiC) as a luminescence material........323
    3.13.1 Polytypes........323
    3.13.2 Band structure and optical absorption........324
    3.13.3 Luminescence........324
        3.13.3.1 Luminescence from excitons........324
        3.13.3.2 Luminescence from donor-acceptor pairs........326
        3.13.3.3 Other luminescence centers........328
    3.13.4 Crystal growth and doping........329
    3.13.5 Light-emitting diodes........329
References........329

3.13 Silicon carbide (SiC) as a luminescence material

3.13.1 Polytypes

Silicon carbide (SiC) is the oldest semiconductor known as a luminescence material. This material shows polytypism arising from different stacking possibilities. In hexagonal close packing of the Si-C pair, the positions of the pair in the first and second layers are uniquely determined (A and B) as shown in Figure 102(a). However, in the third layer, there are two possibilities, either A or C as shown. In the former case, the stacking order becomes ABAB…, giving a wurtzite (hexagonal) structure, and the latter becomes ABCABC…, giving a zinc-blende (cubic) structure.

In SiC crystals, there can exist various combinations of these two structures, which give different stacking orders called polytypes. Among the many polytypes, 3C-, 6H-, and 4H-SiC appear frequently: these structures are shown in Figures 102(b)-(d) together with 2H-SiC (Figure 102(e)). Here, the number indicates the period of stacking order and the letter gives its crystal structure: C = cubic, H = hexagonal, R = rhombohedral. Since the position of each atom has a different configuration of nearest-neighbor atoms, the sites are crystallographically different; that is, they have cubic or hexagonal site symmetry. Hence, when an impurity atom substitutes into the position of Si or C, it gives rise to different energy levels depending upon the number of inequivalent sites present in the material. In 3C-SiC and 2H-SiC, only one cubic or one hexagonal site exists, respectively,

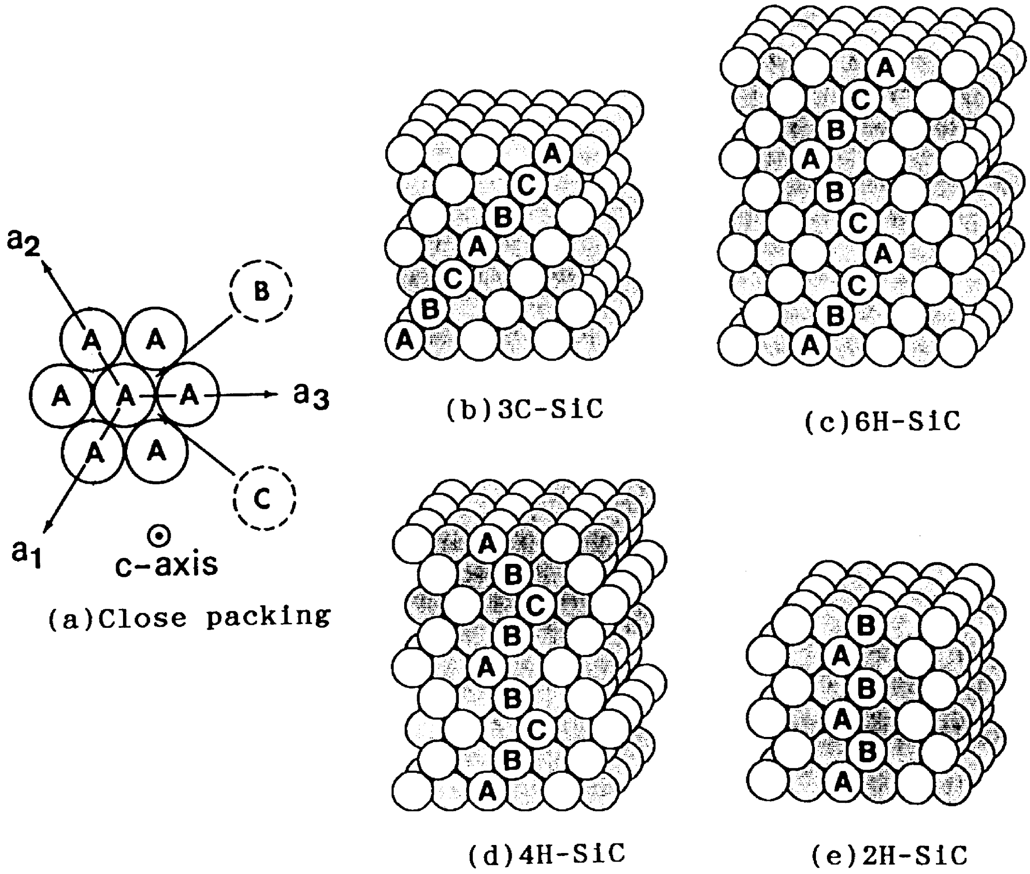

(a) Close packing

(b) 3C-SiC

(c) 6H-SiC

(d) 4H-SiC

(e) 2H-SiC

Figure 102 Position of Si-C pair in typical SiC polytypes. (a) Close packing of equal spheres (Si-C pair), (b) 3C-SiC, (c) 6H-SiC, (d) 4H-SiC, and (e) 2H-SiC.

whereas in 6H-SiC there exist one hexagonal and two cubic sites and in 4H-SiC one hexagonal and one cubic sites.

3.13.2 *Band structure and optical absorption*

Figure 103 shows the absorption spectra of different polytypes of SiC at 4.2K.[1] The spectra contain shoulder features related to phonon-assisted transitions, which are characteristics of indirect band structures. In the figure, the positions of the exciton bandgaps are shown. In Table 28, the values of exciton bandgaps and exciton binding energies are tabulated.[1] The characteristics near the fundamental absorption edge have quite similar structure for all the polytypes except 2H-SiC. This is due to the similarity of the phonons involved in optical absorption in the different polytypes.

3.13.3 *Luminescence*[1,2]

Since SiC has an indirect band structure, strong luminescence can be expected from the recombination of either bound excitons or donor-acceptor pairs.

3.13.3.1 *Luminescence from excitons*

Figure 104 depicts the photoluminescence spectrum from excitons bound at N donors in 3C-SiC.[1] From the energy difference between the exciton bandgap and the peak energy

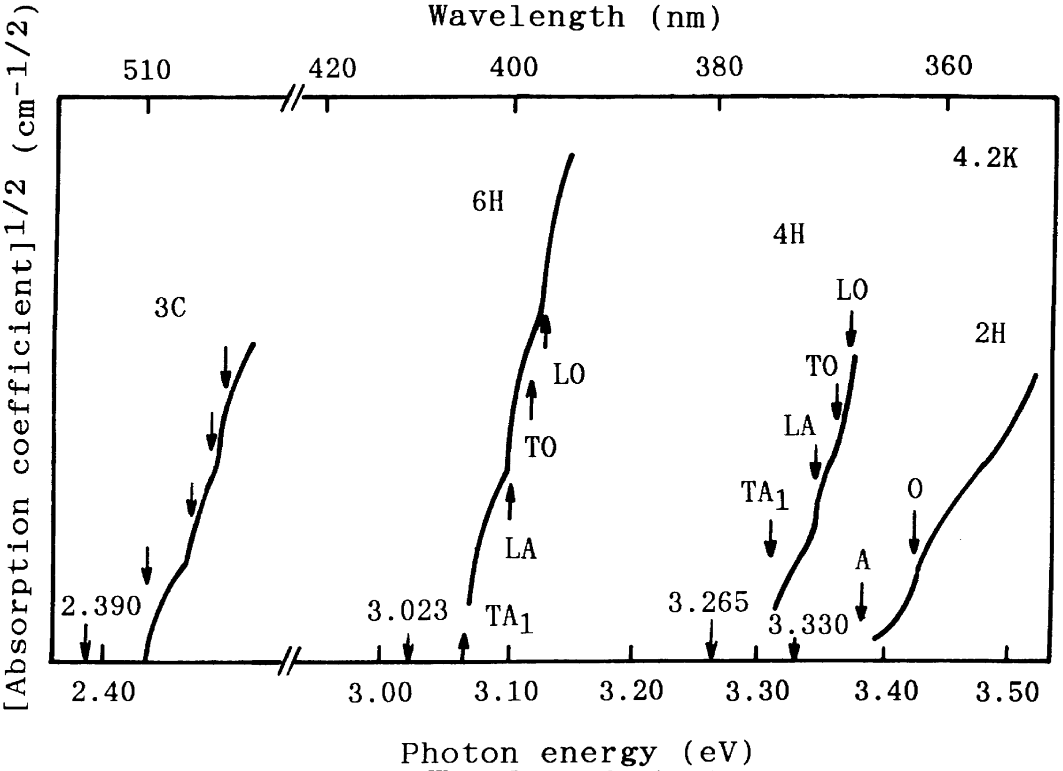

Figure 103 Absorption spectra for typical SiC polytypes. Exciton bandgap is shown for each polytype. (From Choyke, W.J., *Mater. Res. Bull.*, 4, S141-S152, 1969. With permission.)

Table 28 Bandgap Energies in Typical Polytypes of S:C

	E_{GX} (eV) 4.2K	E_{exc} (meV)	Conduction band minimum
3C (Zinc-blende)	2.390 (ID)[a]	13.5[b]	X[e]
6H	3.023 (ID)[a]	78[c]	U[f]
4H	3.265 (ID)[a]	20[d]	M[g]
2H (Wurtzite)	3.330 (ID)[a]	?	K[e]

Note: E_{GX}: Exciton bandgap, E_{exc}: Exciton binding energy.
ID: indirect band structure.
X, U, M, K: position in Brillouin zone.

[a] Choyke, W.J., *Mater. Res. Bull.*, 4, S141, 1969.

[b] Nedzvetskii, D.S. et al., *Sov. Phys. - Semicon.*, 2, 914, 1969.

[c] Sankin, V.I., *Sov. Phys. Solid State.*, 17, 1191, 1975.

[d] Dubrovskii, G.B. et al., *Sov. Phys. Solid State.*, 17, 1847, 1976.

[e] Herman, F. et al., *Mater. Res. Bull.*, 4, S167, 1969.

[f] Choyke, W.J., unpublished result, 1995.

[g] Patrick, L. et al., *Phys. Rev.*, 137, A1515, 1965.

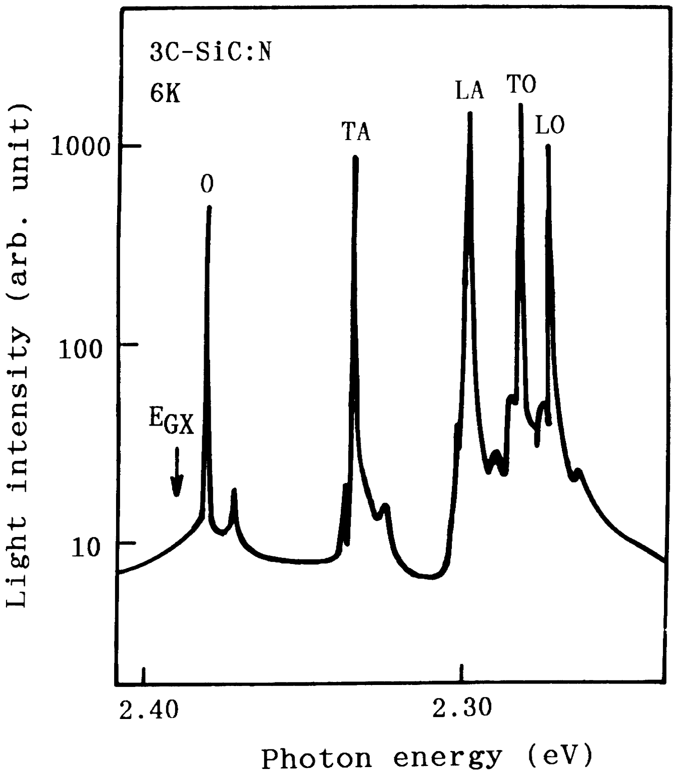

Figure 104 Photoluminescence spectrum of excitons bound at N donors in 3C-SiC. E_{GX} indicates the exciton bandgap. (0: zero phonon; TA: transverse acoustic; LA: longitudinal acoustic; TO: transverse optic; and LO: longitudinal optic). (From Choyke, W.J., *Mater. Res. Bull.*, 4, S141-S152, 1969. With permission.)

corresponding to the zero-phonon line, the exciton binding energy for N donors is estimated to be 10 meV. Since the resolution of peak energies is much better than that in the absorption spectra, the exact value of phonon energies can be obtained from the photoluminescence spectra.

In the photoluminescence spectrum of 6H-SiC, there exists a zero-phonon peak due to the recombination of excitons bound at N donors substituted into hexagonal C sites and two zero-phonon peaks due to those located in cubic C sites.[3] Since the energy levels of N donors in inequivalent (hexagonal, cubic) sites are different, the photoluminescence peaks have different energies.

3.13.3.2 Luminescence from donor-acceptor pairs

In SiC, N atoms belonging to the fifth column of the periodic table work as donors, and B, Al, and Ga in the third column work as acceptors. When donors and acceptors are simultaneously incorporated in a crystal, electrons bound at donors and holes at acceptors can create a pair due to the Coulombic force between electrons and holes. This interaction leads to strong photoluminescence through recombination and is known as donor-acceptor pair luminescence.

Figure 105 shows the photoluminescence spectrum from N-Al donor-acceptor pair recombination in 3C-SiC at 1.8K.[4] This gives a peculiar structure showing the recombination of electrons and holes in donor-acceptor pairs of type 2 with N donors replacing C and Al replacing Si. From a detailed analysis of this peculiar structure, the value of 310 meV is obtained for the sum of $E_D(N)$ and $E_A(Al)$, where $E_D(N)$ is the N-donor level

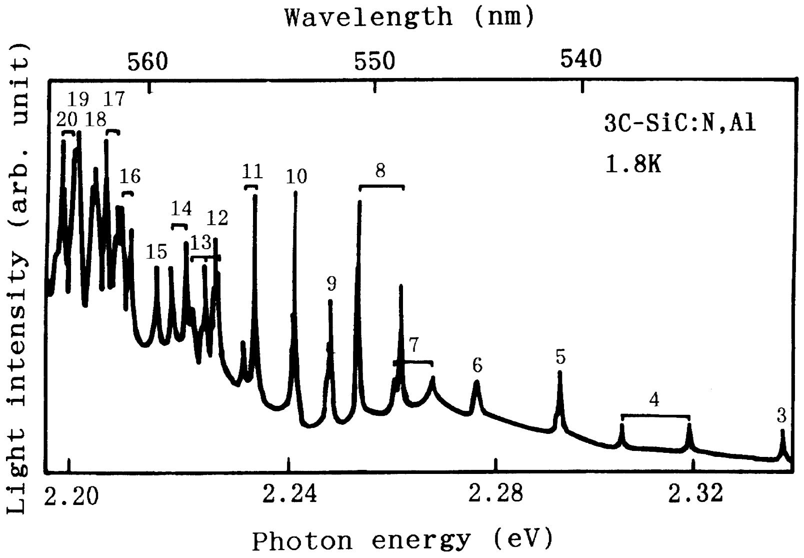

Figure 105 Photoluminescence spectrum of N donor-Al acceptor pair recombination in 3C-SiC. The number for each peak indicates the order of distance between donor and acceptor. (From Choyke, W.J. and Patrick, L., *Phys Rev.*, B2, 4959-4965, 1970. With permission.)

and E_A(Al) the Al-acceptor level. At 77K or higher, the spectrum changes to that due to the recombination of free electrons and holes bound at Al-acceptors (free-to-acceptor recombination) because of thermal excitation of electrons bound at N-donors to the conduction band. From the spectrum, the value of E_A(Al) can be determined precisely. Based on these studies, the values of E_A(Al) = 257 meV and E_D(N) = 53 meV were obtained.[2] From a similar analysis, the B- and Ga-acceptor levels can also be determined.

In most SiC polytypes, except for 3C-SiC and 2H-SiC, there are inequivalent sites, and impurities substituting into those sites give rise to different energy levels. Thus, spectra of donor-acceptor pair recombination and free-to-acceptor recombination can become complicated. As examples, donor-acceptor pair recombination spectra in 6H-SiC at 4.2K are shown in Figure 106(a) and free-to-acceptor recombination spectra at 77K in Figure 106(b).[5] Although the energy levels are different for different acceptors (B, Al, and Ga), the shapes of spectra are quite similar when the abscissa is shifted by an energy of the order of 0.05 eV, as shown in the figure.

The B series (peaks denoted as B) in the spectra show donor-acceptor pair luminescence for N donors in hexagonal C sites and Al acceptors, and the C series (peaks denoted as C) arising from N donors in cubic C sites and Al acceptors. Here, the energy levels of Al acceptors are thought to be very similar, whether they are in hexagonal or cubic Si sites. The subscripts in the figure are defined as follows: 0 implies a zero-phonon peak and LO implies peaks involving longitudinal optical phonons. Peaks A indicate free-to-acceptor recombination: A^a and A^b are due to acceptors substituting into hexagonal and cubic Si sites, respectively.

Since there are three different sites for donors and acceptors, respectively, in 6H-SiC, analysis for the peculiar structure observed in the spectra becomes very difficult. The photon energy, $h\nu(R)$, from donor-acceptor pair luminescence is given by $h\nu(R) \sim R^6 \exp(-4\pi c R^3/3)$, where R is the distance between a donor and an acceptor and c is larger of the donor or acceptor concentrations. By curve fitting of the above relation to the spectra, the value of $E_D + E_A$ can be obtained.[5] Since the value of E_A is calculated from free-to-acceptor recombination as in Figure 106(b), E_D can also be determined. Although

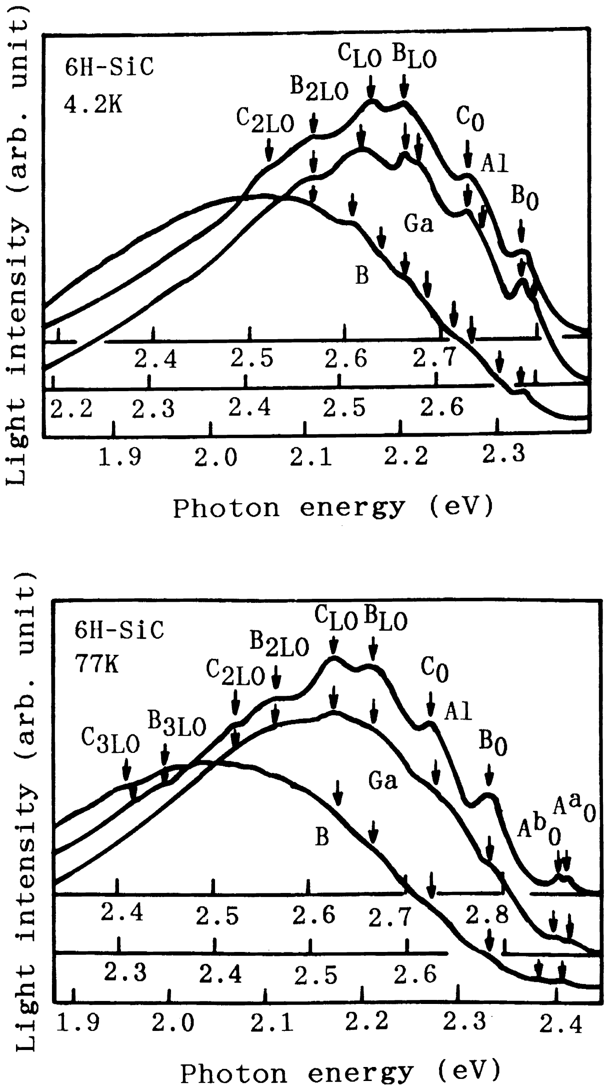

Figure 106 Photoluminescence spectra of (a) donor-acceptor pair recombination at 4.2K and (b) free-to-acceptor recombination at 77K in 6H-SiC doped with B, Al, and Ga. A_0: free-to-Al acceptor peak, (b) B_0: N-donor(hexagonal site)-Al acceptor, (c) C_0: N-donor(cubic site)-Al acceptor. LO indicates longitudinal phonon. (From Ikeda, M., Matsunami, H., and Tanaka, T., *Phys. Rev.*, B22, 2842-2854, 1980. With permission.)

one hexagonal site and two cubic sites exist in 6H-SiC, the difference between the energies for the two cubic sites seems to be very small. Curve fitting was carried out by assuming that the luminescence intensity related to cubic sites is two times larger than that related to hexagonal sites. The calculated energy levels of impurities are given in Table 29. In the table, the results of different polytypes are also shown.[5] In each polytype, the ratio between the acceptor energy levels for cubic and hexagonal sites is very small, whereas that of donor energy levels is large.

3.13.3.3 Other luminescence centers

In addition to the above luminescence centers, luminescence due to defects produced by ion implantation[2] and due to the localized centers such as Ti[2] have been reported.

Table 29 Energy Levels of Donor and Acceptors

		Energy level (meV)			
		Donor	Acceptor		
Polytype	Site	N	Al	Ga	B
3C-SiC	C	56.5	254	343	735
6H-SiC	C	155	249	333	723
	H	100	239	317	698
4H-SiC	C	124	191	267	647
	H	66			

From Ikeda, M., et al., *Phys. Rev.*, B22, 2842, 1980. With permission.

3.13.4 *Crystal growth and doping*

Crystals of SiC have been grown by the so-called Acheson method, in which a mixture of SiO_2 and C is heated to about 2000°C. To grow pure single crystals, the powdered SiC crystal mixture is sublimed in a specially designed crucible by the Lely method. Recent large-diameter (approximately 2-inch diameter) single crystal boules have been produced by a modified Lely method utilizing a SiC seed in the sublimation growth.

On those single crystals, epitaxial growth has been carried out by either liquid phase epitaxy (LPE) or vapor phase epitaxy (VPE). In LPE, molten Si in a graphite crucible is used as a melt in which a SiC substrate is dipped into.[6] In VPE, chemical vapor deposition (CVD) with SiH^4 and C_3H_8 has been widely used. To get a high-quality epitaxial layer at low temperatures, step-controlled epitaxy is used, which utilizes step-flow growth on off-oriented SiC substrates.[7]

Doping with third column elements as donors or fifth column elements as acceptors can be done easily through both in LPE and VPE.

3.13.5 *Light-emitting diodes*

Earlier, yellow light-emitting diodes (LEDs) of 6H-SiC utilizing N-B donor-acceptor pair luminescence were demonstrated; they were later replaced by $GaAs_{1-x}P_x$:N yellow LEDs. Blue LEDs of 6H-SiC *p-n* junction utilizing N-Al donor-acceptor pair luminescence are usually made by LPE[6] or VPE[7] methods. The mechanism for electroluminescence through injection of carriers was clarified by Ikeda et al.[8] A typical spectrum of blue LEDs is shown in Figure 107.[9] The spectral peak is located at 470 nm with a width of 70 nm for a forward current I_F of 20 mA (0.3×0.3 mm^2). The diode consists of LPE-grown Al-doped *p*-SiC/N-doped *n*-SiC/*n*-6H-SiC substrate. LEDs are fabricated with a *p*-side down structure, and the light comes through the *n*-SiC. The maximum external quantum efficiency is 0.023% ($I_F = 5$ mA). Since the blue LEDs utilize N-Al donor-acceptor pair luminescence in *n*-type epilayers, the brightness increases with incorporation of Al, and it exceeds 20 mCd ($I_F = 20$ mA).

References

1. Choyke, W.J., *Mater. Res. Bull.*, 4, S141-S152, 1969.
2. Choyke, W.J. and Patrick, L., *Silicon Carbide—1973*, Marshall, R.C., Faust, J.W., and Ryan, C.E., Eds., University of South Carolina Press, 1974, 261-283.
3. Choyke, W.J. and Patrick, L., *Phys. Rev.*, 127, 1868-1877, 1962.
4. Choyke, W.J. and Patrick, L., *Phys. Rev.*, B2, 4959-4965, 1970.
5. Ikeda, M., Matsunami, H., and Tanaka, T., *Phys. Rev.*, B22, 2842-2854, 1980.
6. Matsunami, H., Ikeda, M., Suzuki, A., and Tanaka, T., *IEEE Trans. Elec. Devices*, ED-24, 958-961, 1977.

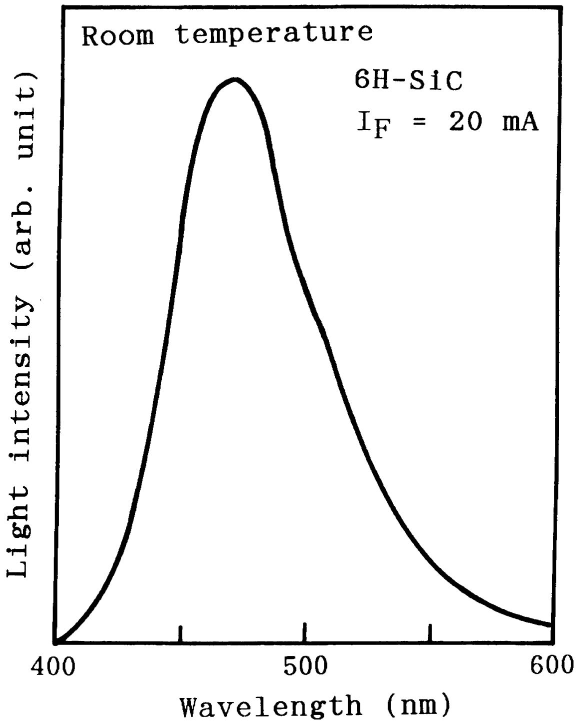

Figure 107 A typical spectrum of bright blue LEDs of 6H-SiC. (From Matsushita, Y., Koga, K., Ueda, Y., and Yamaguchi, T., *Oyobuturi*, 60, 159-162, 1991 (in Japanese).)

7. Shibahara, K., Kuroda, N., Nishino, S., and Matsunami, H., *Jpn. J. Appl. Phys.*, 26, L1815-L1817, 1987.
8. Ikeda, M., Hayakawa, T., Yamagiwa, S., Matsunami, H., and Tanaka, T., *J. Appl. Phys.*, 50, 8215-8225, 1979.
9. Matsushita, Y., Koga, K., Ueda, Y., and Yamaguchi, T., *Oyobuturi*, 60, 159-162, 1991, (in Japanese).

chapter three — section fourteen

Fundamentals of luminescence

Rong-Jun Xie, Naoto Hirosaki, and Mamoru Mitomo

Contents

3.14 Oxynitride phosphors 331
3.14.1 Introduction 331
3.14.2 Overview of oxynitride phosphors 332
3.14.3 Characteristics of typical oxynitride phosphors 333
3.14.3.1 $LaAl(Si_{6-z}Al_z)N_{10-z}O_z:Ce^{3+}$ (z = 1) 333
3.14.3.2 β-SiAlON:Eu^{2+} 333
3.14.3.3 $MSi_2O_2N_2:Eu^{2+}$ (M = Ca, Sr, Ba) 334
3.14.3.4 α-SiAlON:Eu^{2+} 335
3.14.3.5 $M_2Si_5N_8:Eu^{2+}$ (M = Ca, Sr, Ba) 335
3.14.3.6 $CaAlSiN_3:Eu^{2+}$ 337
3.13.4 Applications of oxynitride phosphors 337
References 338

3.14 Oxynitride phosphors

3.14.1 Introduction

Inorganic phosphors are composed of a host lattice doped with a small amount of impurity ions that activate luminescence. Most of these materials are oxides, sulfides, fluorides, halides, and oxysulfides doped with transition metal ions or rare-earth ions. Recently, with the advent of solid-state lighting technologies as well as the development of plasma and field emission display panels, a great number of traditional phosphors cannot meet the requirements for new applications, for example: (1) excitation by near-ultraviolet (UV) or visible light; (2) efficient emission of appropriate colors; and (3) survival at adverse environments. Therefore, novel phosphors with superior luminescent properties are being sought using new host materials.

The integration of nitrogen (N) in silicates or aluminosilicates produces a wide range of complex structures with increased flexibility compared to the oxosilicates, and thus a new class of materials, nitridosilicates, nitridoaluminosilicates, and sialons, are obtained.[1] These novel luminescent materials—the oxynitride phosphors—have been synthesized by doping with appropriate amounts of rare-earth activators.[2–20] The rare earths doped in the oxynitride phosphors usually enter into interstitial sites and are coordinated by (O, N) ions located at various distances. For those rare earths (i.e., Eu^{2+} and Ce^{3+}) emitting from their 5d excited state, which is strongly affected by the crystal-field environment (e.g., covalency, coordination, bond length, crystal-field strength), appropriate emission colors can be obtained by carefully selecting the host lattice. Due to a higher charge of N^{3-} compared with that of O^{2-} and because of the nephelauxetic effect (high covalency), the crystal-field splitting of the 5d levels of rare earths is larger and the center of gravity of the 5d states is shifted to low energy (i.e., longer wavelength) in these oxynitride compounds. Furthermore, the Stokes shift becomes smaller in a more rigid lattice, which results when more N^{3-} is incorporated. This will result in more versatile luminescent properties of oxynitride phosphors, increasing their range of applications. In this section, the characteristic features and potential applications of rare-earth-doped nitride phosphors are described.

3.14.2 Overview of oxynitride phosphors

Table 30 lists oxynitride phosphors reported in the literature in recent years. The host lattice of these phosphors is based on nitridosilicates, oxonitridosilicates, or oxonitridoaluminosilicates, which are derived from silicates by formal exchanges of O and Si by N and Al, respectively. The structure of these host lattices is built on highly condensed networks constructed from the corner-sharing (Si, Al)–(O, N) tetrahedra. The degree of condensation of the network structures (i.e., the molar ratio $Si:X > 1:2$, with $X = O, N$) is higher than the maximum value for oxosilicates ($1:4 \leq Si:O \leq 1:2$).[21] Consequently, these highly condensed materials exhibit high chemical and thermal stabilities. Moreover, the structural variabilities of this class of materials provide a significant extension of conventional silicate chemistry, forming a large family of Si–Al–O–N multiternary compounds.

Table 30 Emission Color and Crystal Structure of Oxynitride Phosphors

Phosphor	Emission color	Crystal structure	References
Y-Si-O-N:Ce^{3+}	Blue	—	[3]
$BaAl_{11}O_{16}N:Eu^{2+}$	Blue	β-Alumina	[2,4]
JEM:Ce^{3+}	Blue	Orthorhombic	[19]
$SrSiAl_2O_3N_2:Eu^{2+}$	Blue-green	Orthorhombic	[14]
$SrSi_5AlO_2N_7:Eu^{2+}$	Blue-green	Orthorhombic	[14]
$BaSi_2O_2N_2:Eu^{2+}$	Blue-green	Monoclinic	[18]
α-SiAlON:Yb^{2+}	Green	Hexagonal	[15]
β-SiAlON:Eu^{2+}	Green	Hexagonal	[17]
$MYSi_4N_7:Eu^{2+}$ (M = Sr, Ba)	Green	Hexagonal	[12]
$MSi_2O_2N_2:Eu^{2+}$ (M = Ca, Sr)	Green-yellow	Monoclinic	[18]
α-SiAlON:Eu^{2+}	Yellow-orange	Hexagonal	[7,8,10,11]
$LaSi_3N_5:Eu^{2+}$	Red	Orthorhombic	[6]
$LaEuSi_2N_3O_2$	Red	Orthorhombic	[6]
$Ca_2Si_5N_8:Eu^{2+}$	Red	Monoclinic	[5]
$M_2Si_5N_8:Eu^{2+}$ (M = Sr, Ba)	Red	Orthorhombic	[5]
$CaAlSiN_3:Eu^{2+}$	Red	Orthorhombic	[20]

The most usual approaches for synthesizing oxynitride phosphors are solid-state reactions and gas-reduction–nitridation. The solid-state reaction involves the reaction among chemical components including metals, nitride, and oxide starting powders at high temperatures (1400–2000°C) under an N_2 atmosphere. The nitridation reaction is generally performed in an alumina boat containing the oxide precursor powder loaded inside an alumina/quartz tube through which NH_3 or NH_3–CH_4 gas flows at appropriate rates at high temperatures (600–1500°C). The NH_3 or NH_3–CH_4 gas acts as both a reducing and nitridation agent.

3.14.3 *Characteristics of typical oxynitride phosphors*

3.14.3.1 *$LaAl(Si_{6-z}Al_z)N_{10-z}O_z{:}Ce^{3+}$ (z = 1)*

Crystal structure. The $LaAl(Si_{6-z}Al_z)N_{10-z}O_z$ (JEM) phase was identified in the preparation of La-stabilized α-SiAlON materials.[22] It has an orthorhombic structure (space group *Pbcn*) with a = 9.4303, b = 9.7689, and c = 8.9386 Å. The Al atoms and the (Si, Al) atoms are tetrahedrally coordinated by the (N, O) atoms, yielding an $Al(Si, Al)_6(N, O)_{10}^{3-}$ network. The La atoms are located in the tunnels extending along the [001] direction and are irregularly coordinated by seven (N, O) atoms at an average distance of 2.70 Å.

Luminescence characteristics. As shown in Figure 108, the emission spectrum of JEM:Ce^{3+} displays a broad band with the peak located at 475 nm under 368-nm excitation.[19] The emission efficiency (external quantum efficiency) is about 55% when excited at 368 nm. This blue phosphor has a broad excitation spectrum, extending from the UV to the visible range. When the concentration of Ce^{3+} or the z value increases, both the excitation and emission spectra are red shifted.

Preparation. The starting materials for JEM are Si_3N_4, AlN, Al_2O_3, La_2O_3, and CeO_2. The powder phosphor is synthesized by heating the powder mixture at 1800–1900°C for 2 h under 1.0 MPa N_2.

3.14.3.2 *β-SiAlON:Eu^{2+}*

Crystal structure. The structure of β-SiAlON is derived from β-Si_3N_4 by substitution of Al–O by Si–N, and its chemical composition can be written as $Si_{6-z}Al_zO_zN_{8-z}$ (z represents

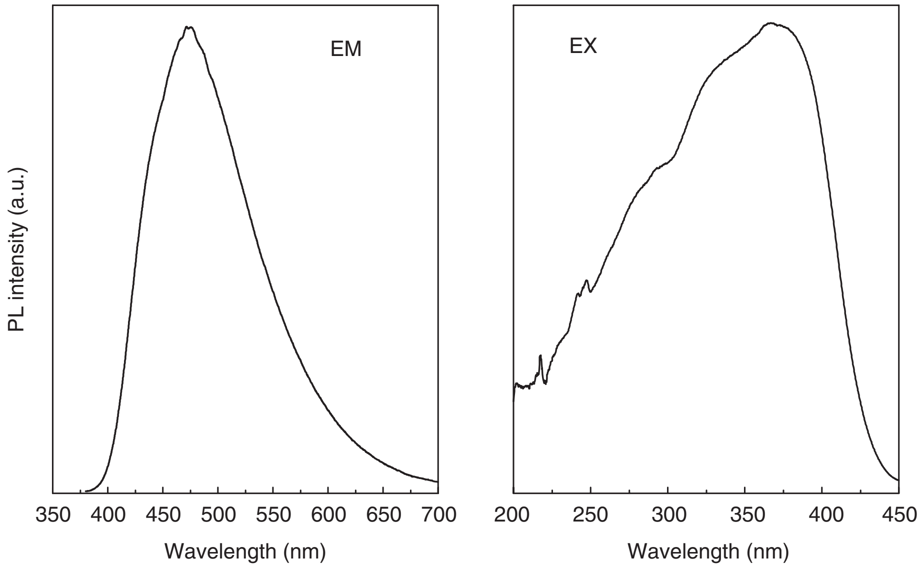

Figure 108 Emission and excitation of LaAl $(Si_{6-z}Al_z)N_{10-z}O_z{:}Ce^{3+}$ (z = 1).

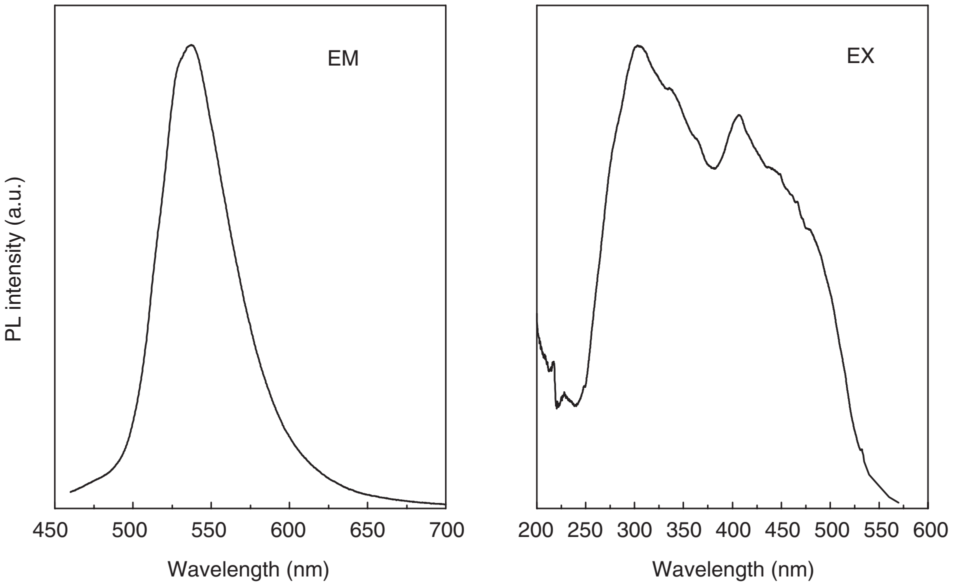

Figure 109 Emission and excitation of β-SiAlON:Eu^{2+}.

the number of Al–O pairs substituting for Si–N pairs and $0 < z \leq 4.2$).[23] β-SiAlON has a hexagonal crystal structure and the $P6_3$ space group. In this structure, there are continuous channels parallel to the c direction.

Luminescence characteristics. The β-SiAlON:Eu^{2+} phosphor gives intense green emission with the peak located at 538 nm,[17] as seen in Figure 109. The broad emission spectrum has a full width of half maximum of 55 nm. Two well-resolved broad bands centered at 303 and 400 nm are observed in the excitation spectrum. The broad excitation range enables the β-SiAlON:Eu^{2+} phosphor to emit strongly under near UV (390–410 nm) or blue-light excitation (450–470 nm). This green phosphor has a chromaticity coordinates of $x = 0.31$ and $y = 0.60$. The external quantum efficiency is about 41% when excited at 405 nm.

Preparation. Starting from Si_3N_4, AlN, Al_2O_3, and Eu_2O_3, the β-SiAlON:Eu^{2+} phosphor is synthesized at 1800–2000°C for 2 h under 1.0 MPa N_2. An Eu concentration of <1.0% is used.

3.14.3.3 $MSi_2O_2N_2$:Eu^{2+} (M = Ca, Sr, Ba)

Crystal structure. All $MSi_2O_2N_2$ compounds crystallize in a monoclinic lattice with different space groups and lattice parameters for M = Ca, Sr, Ba:$CaSi_2O_2N_2$, $P2_1/C$, $a = 15.036$, $b = 15.450$, $c = 6.851$ Å; $SrSi_2O_2N_2$, $P2_1/M$, $a = 11.320$, $b = 14.107$, $c = 7.736$ Å; $BaSi_2O_2N_2$, P_2/M, $a = 14.070$, $b = 7.276$, $c = 13.181$ Å.[18,24] A nitrogen-rich phase $MSi_2O_{2-\delta}N_{2+2/3\delta}$ (M = Ca, Sr, $\delta > 0$) has been identified, suggesting that some modifications of $MSi_2O_2N_2$ (M = Ca, Sr) exist depending on the synthesis temperature.

Luminescence characteristics. All $MSi_2O_2N_2$:Eu^{2+} phosphors have a broad-band emission spectrum with different full widths at half maximum: $CaSi_2O_2N$:Eu^{2+}, 97 nm; $SrSi_2O_2N$:Eu^{2+}, 82 nm; and $BaSi_2O_2N$:Eu^{2+}, 35 nm (see Figure 110). $CaSi_2O_2N$:6%Eu^{2+} shows a yellowish emission with a maximum at 562 nm. $SrSi_2O_2N$:6%Eu^{2+} emits green color with a maximum at 543 nm, and $BaSi_2O_2N$:6%Eu^{2+} yields a blue-green emission with a peak at 491 nm. The excitation spectrum of $CaSi_2O_2N$:6%Eu^{2+} shows a flat broad band covering the 300–450 nm range, whereas two well-resolved broad bands centered at 300 and 450 nm are seen in $SrSi_2O_2N$:6%Eu^{2+} and $BaSi_2O_2N$:6%Eu^{2+}, respectively.

Preparation. The $MSi_2O_2N_2$:Eu^{2+} phosphors are synthesized by heating the powder mixture of Si_3N_4, SiO_2 and alkaline-earth carbonates at 1600°C under 0.5 MPa N_2.

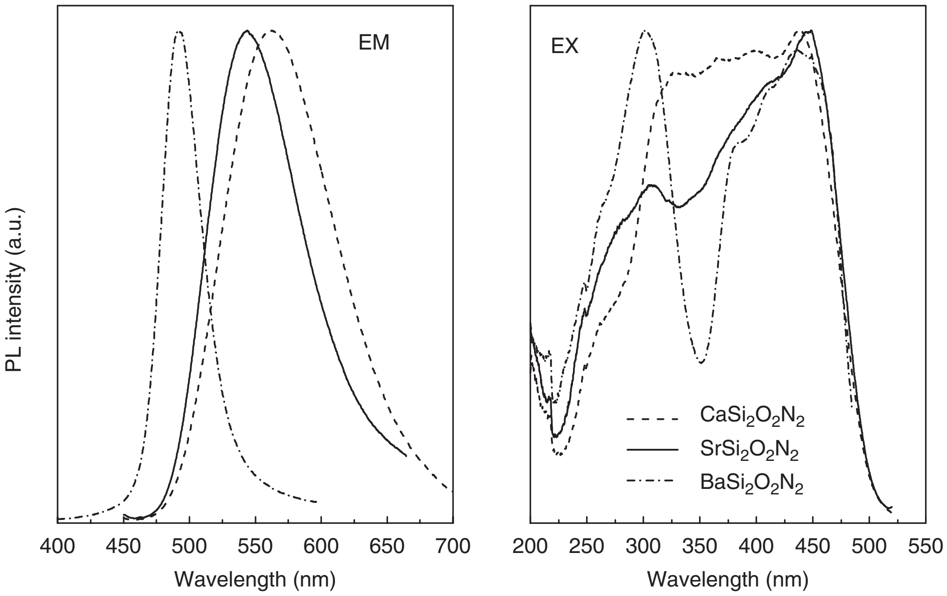

Figure 110 Emission and excitation of $MSi_2O_2N_2{:}Eu^{2+}$ (M = Ca, Sr, Ba).

3.14.3.4 α-SiAlON:Eu^{2+}

Crystal structure. α-SiAlON is isostructural to α-Si_3N_4. It has a hexagonal crystal structure and the *P*31*c* space group. The α-SiAlON unit cell content, consisting of four "Si_3N_4" units, can be given in a general formula $M_xSi_{12-m-n}Al_{m+n}O_nN_{16-n}$ (*x* is the solubility of the metal M).[25,26] In the α-SiAlON structure, *m*+*n* (Si–N) bonds are replaced by *m* (Al–N) bonds and *n* (Al–O) bonds; the charge discrepancy caused by the substitution is compensated by the introduction of M cations including Li^+, Mg^{2+}, Ca^{2+}, Y^{3+}, and lanthanides. The M cations occupy the interstitial sites in the α-SiAlON lattice and are coordinated by seven (N, O) anions at three different M-(N, O) distances.

Luminescence characteristics. α-SiAlON:Eu^{2+} phosphors give green-yellow, yellow, or yellow-orange emissions with peaks located in the range of 565–603 nm,[7,8,10,11] as shown in Figure 111. The broad-band emission spectrum covers from 500 to 750 nm with the full width of half maximum of 94 nm. The excitation spectrum of Eu^{2+} in α-SiAlON has two broad bands with peaks at 300 and 420 nm, respectively. The external quantum efficiency of the α-SiAlON:Eu^{2+} phosphor with optimal composition is about 58% when excited at 450 nm. By tailoring the composition of the host lattice and controlling the concentration of Eu^{2+}, the emission color of α-SiAlON can be tuned through a wide range.

Preparation. The Ca-α-SiAlON:Eu^{2+} phosphor is synthesized by solid-state reactions. The powder mixture of Si_3N_4, AlN, $CaCO_3$, and Eu_2O_3 is fired at 1600–1800°C for 2 h under 0.5 MPa N_2. The gas-reduction–nitridation method is also used to prepare α-SiAlON:Eu^{2+} phosphor.[16] It is synthesized from the CaO–Al_2O_3–SiO_2 system, by using an NH_3–CH_4 gas mixture as a reduction–nitridation agent. The Eu concentration in α-SiAlON phosphors varies from 0.5 to 10%.

3.14.3.5 $M_2Si_5N_8{:}Eu^{2+}$ (M = Ca, Sr, Ba)

Crystal structure. $Ca_2Si_5N_8$ has a monoclinic crystal system with the space group of *Cc*, whereas both $Sr_2Si_5N_8$ and $Ba_2Si_5N_8$ have an orthorhombic lattice with the space group of $Pmn2_1$.[27,28] The local coordination in the structures is quite similar for these ternary alkaline-earth silicon nitrides, half of the nitrogen atoms connecting two Si neighbors and the other half have three Si neighbors. Each Ca atom in $Ca_2Si_5N_8$ is coordinated by seven nitrogen

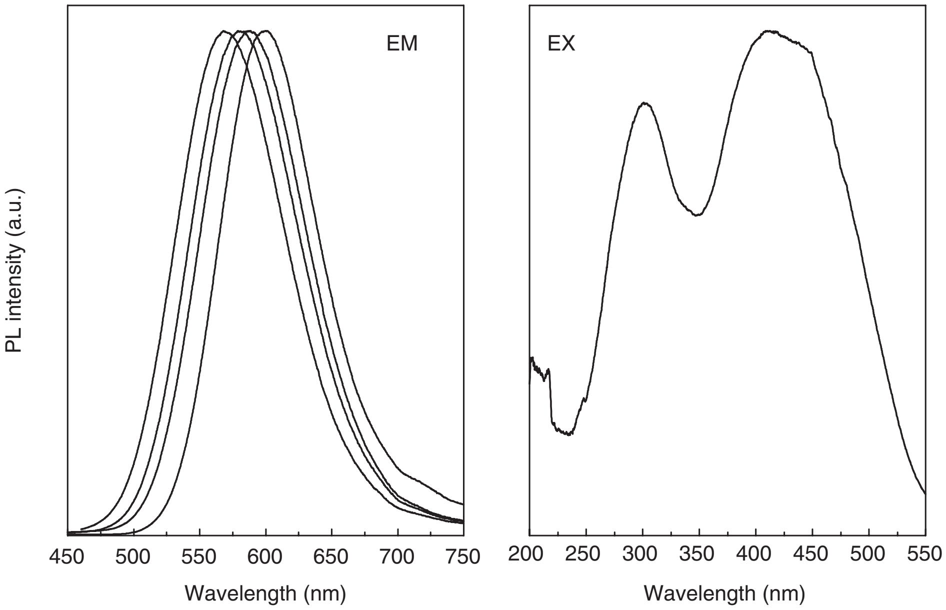

Figure 111 Emission and excitation of α-SiAlON:Eu^{2+}.

atoms, whereas Sr in $Sr_2Si_5N_8$ and Ba in $Ba_2Si_5N_8$ are coordinated by eight or nine nitrogen atoms.

Luminescence characteristics. $M_2Si_5N_8$:Eu^{2+} (M = Ca, Sr, Ba) phosphors give orange-red or red emission, as shown in Figure 112. A single, broad emission band is centered at 623, 640, and 650 nm for $Ca_2Si_5N_8$, $Sr_2Si_5N_8$, and $Ba_2Si_5N_8$, respectively. A red shift in the emission wavelength is observed with increasing the ionic size of alkaline-earth metals. The excitation spectrum resembles each other, indicating the chemical environment of Eu^{2+} in these materials is very similar. The excitation spectrum extensively shifts to longer wavelengths, with the peak located at 450 nm for all samples.

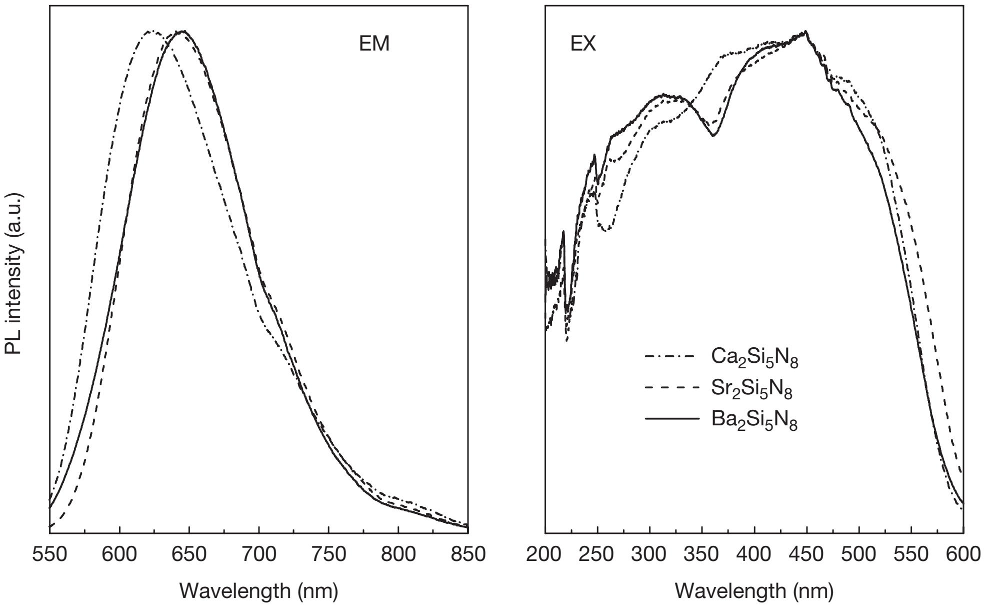

Figure 112 Emission and excitation of $M_2Si_5N_8$:Eu^{2+} (M = Ca, Sr, Ba).

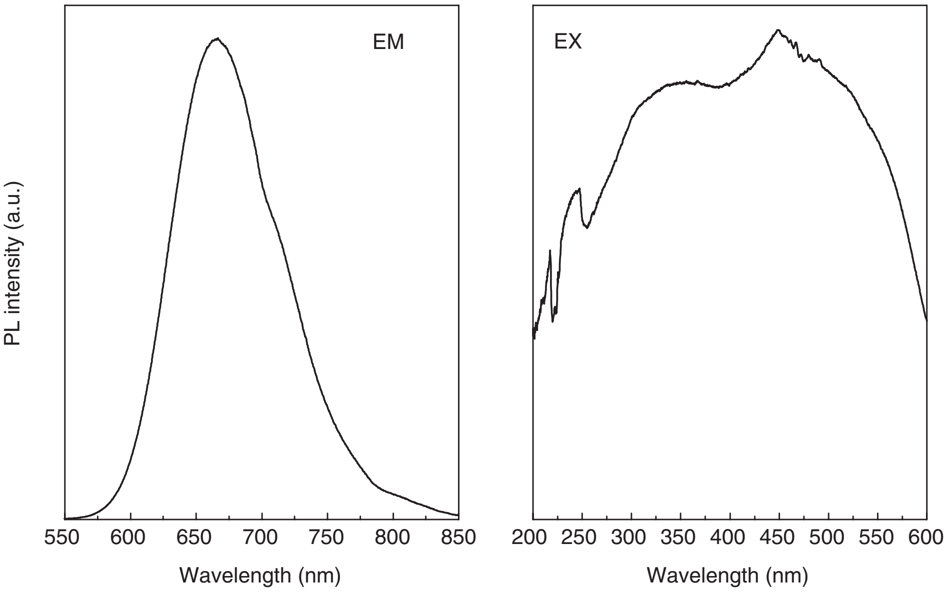

Figure 113 Emission and excitation of $CaAlSiN_3:Eu^{2+}$.

Preparation. The ternary alkaline-earth silicon nitrides are either synthesized by firing the powder mixture of Si_3N_4, M_3N_2, and EuN at 1600–1800°C under 0.5 MPa N_2 or prepared by the reactions of metallic alkaline-earths with silicon diimide at 1550–1650°C under nitrogen atmosphere.[5,27,28]

3.14.3.6 *$CaAlSiN_3:Eu^{2+}$*

Crystal structure. $CaAlSiN_3$ has an orthorhombic crystal structure and the space group of $Cmc2_1$, the unit cell parameter being $a = 9.8007$, $b = 5.6497$, and $c = 5.0627$ Å.[20] The Ca atoms are found in the tunnels surrounded by six corner-sharing tetrahedra of $(Al, Si)N_4$.

Luminescence characteristics. $CaAlSiN_3:Eu^{2+}$ is a red phosphor. The luminescence spectra are given in Figure 113. The excitation spectrum is extremely broad, ranging from 250 to 550 nm. Again a broad emission band centered at 650 nm is observed when excited at 450 nm. The chromaticity coordinates of red phosphor are $x = 0.66$ and $y = 0.33$. This phosphor has an external quantum efficiency as high as 86% under 450 nm excitation. The emission spectrum is red shifted with increasing Eu^{2+} concentrations.

Preparation. The $CaAlSiN_3:Eu^{2+}$ phosphor was synthesized by firing a powder mixture of Si_3N_4, AlN, Ca_3N_2, and EuN at 1600–1800°C for 2 h under 0.5 MPa N_2.

3.14.4 *Applications of oxynitride phosphors*

As shown in the previous section, oxynitride phosphors emit efficiently under UV and visible-light irradiation. This correlates well with the emission wavelengths of the UV chips or blue light-emitting diode (LED) chips, making their use as down-conversion phosphors in white LEDs feasible.

We have proposed that yellow α-SiAlON phosphors could be used to generate warm white light when combined with a blue LED. The first white LED lamp was reported by Sakuma et al. using an orange-yellow α-SiAlON:Eu^{2+} and a blue LED chip.[29] It emits warm white light with the color temperature of 2800 K. To obtain white LED lamps with high color rendering index, additional phosphors such as green and red phosphors are used. Sakuma et al. have reported white LEDs with various color temperatures and a color rendering index of >80 using β-SiAlON:Eu^{2+} (green), α-SiAlON:Eu^{2+} (yellow), and

$CaAlSiN_3:Eu^{2+}$ (red) phosphors.[30] Mueller-Mach et al. have used $(Ca,Sr,Ba)Si_2O_2N_2:Eu^{2+}$ (yellow-green) and $(Ca,Sr,Ba)_2Si_5N_8:Eu^{2+}$ (orange-red) phosphors to fabricate highly efficient white LEDs.[31]

References

1. Schnick, W., *Inter. J. Inorg. Mater.*, 3, 1267, 2001.
2. Jansen, S.R., de Hann, J.W., van de Ven, L.J.M., Hanssen, R., Hintzen, H.T., and Metselaar, R., *Chem. Mater.*, 9, 1516, 1997.
3. van Krevel, J.W.H., Hintzen, H.T., Metselaar, R., and Meijerink, A., *J. Alloy Compd*, 268, 272, 1998.
4. Jansen, S.R., Migchel, J.M., Hintzen, H.T., and Metselaar, R., *J. Electrochem. Soc.*, 146, 800, 1999.
5. Höppe, H.A., Lutz, H., Morys, P., Schnick, W., and Seilmeier, A., *J. Phys. Chem. Solids*, 61, 2001, 2000.
6. Uheda, K., Takizawa, H., Endo, T., Yamane, H., Shimada, M., Wanf, C.M., and Mitomo, M., *J. Lum.*, 87–89, 867, 2000.
7. van Krevel, J.W.H., van Rutten, J.W.T., Mandal, H., Hintzen, H.T., and Metselaar, R., *J. Solid State Chem.*, 165, 19, 2002.
8. Xie, R.-J., Mitomo, M., Uheda, K., Xu, F.F., and Akimune, Y., *J. Am. Ceram. Soc.*, 85, 1229, 2002.
9. Xie, R.-J., Hirosaki, N., Mitomo, M., Yamamoto, Y., Suehiro, T., and Ohashi, N., *J. Am. Ceram. Soc.*, 87, 1368, 2004.
10. Xie, R.-J., Hirosaki, N., Mitomo, M., Yamamoto, Y., Suehiro, T., and Sakuma, K., *J. Phys. Chem. B*, 108, 12027, 2004.
11. Xie, R.-J., Hirosaki, N., Sakuma, K., Yamamoto, Y., and Mitomo, M., *App. Phys. Lett.*, 84, 5404, 2004.
12. Li, Y.Q., Fang, C.M., de With, G., and Hintzen, H.T., *J. Solid State Chem.*, 177, 4687, 2004.
13. Xie, R.-J., Hirosaki, N., Mitomo, M., Suehiro, T., Xin, X., and Tanaka, H., *J. Am. Ceram. Soc.*, 88, 2883, 2005.
14. Xie, R.-J., Hirosaki, N., Yamamoto, Y., Suehiro, T., Mitomo, M., and Sakuma, K., *Jpn. J. Ceram. Soc.*, 113, 462, 2005.
15. Xie, R.-J., Hirosaki, N., Mitomo, M., Uheda, K., Suehiro, T., Xin, X., Yamamoto, Y., and Sekiguchi, T., *J. Phys. Chem. B*, 109, 9490, 2005.
16. Suehiro, T., Hirosaki, N., Xie, R.-J., and Mitomo, M., *Chem. Mater.*, 17, 308, 2005.
17. Hirosaki, N., Xie, R.-J., Kimoto, K., Sekiguchi, T., Yamamoto, Y., Suehiro, T., and Mitomo, M., *App. Phys. Lett.*, 86, 211905, 2005.
18. Li, Y.Q., Delsing, C.A., de With, G., and Hintzen, H.T., *Chem. Mater.*, 17, 3242, 2005.
19. Hirosaki, N., Xie, R.-J., Yamamoto, Y., and Suehiro, T., Presented at *the 66th Autumn Annual Meeting of the Japan Society of Applied Physics* (Abstract No. 7ak6), Tokusima, Sept. 7–11, 2005.
20. Uheda, K., Hirosaki, N., Yamamoto, H., Yamane, H., Yamamoto, Y., Inami, W., and Tsuda, K., Presented at *the 206th Annual Meeting of the Electrochemical Society (*Abstract No. 2073*)*, Honolulu, Oct. 3–8, 2004.
21. Schnick, W. and Huppertz, H., *Chem. Eur. J.*, 3, 679, 1997.
22. Grins, J., Shen, Z., Nygren, M., and Eskrtom, T., *J. Mater. Chem.*, 5, 2001, 1995.
23. Oyama, Y., and Kamigaito, O., *Jpn. J. Appl. Phys.*, 10, 1637, 1971.
24. Höppe, H.A., Stadler, F., Oeckler, O., and Schnick, W., *Angew. Chem. Int. Ed.*, 43, 5540, 2004.
25. Hampshire, S., Park, H.K., Thompson, D.P., and Jack, K.H., *Nature* (London), 274, 31, 1978.
26. Cao, G.Z. and Metselaar, R., *Chem. Mater.*, 3, 242, 1991.
27. Schlieper, T. and Schnick, W., *Z. Anorg. Allg. Chem.*, 621, 1037, 1995.
28. Schlieper, T. and Schnick, W., *Z. Anorg. Allg. Chem.*, 621, 1380, 1995.
29. Sakuma, K., Omichi, K., Kimura, N., Ohashi, M., Tanaka, D., Hirosaki, N., Yamamoto, Y., Xie, R.-J., and Suehiro, T., *Opt. Lett.*, 29, 2001, 2004.
30. Sakuma, K., Hirosaki, N., Kimura, N., Ohashi, M., Xie, R.-J., Yamamoto, Y., Suehiro, T., Asano, K., and Tanaka, D., *IEICE Trans. Electron.*, Vol.E88-C, 2005 (in press).
31. Mueller-Mach, R., Mueller, G., Krames, M.R., Höppe, H.A., Stadler, F., Schnick, W., Juestel, T., and Schmidt, P., *Phys. Stat. Sol.* (*a*) 202, 1727, 2005.

part three

Practical phosphors

chapter four — section one

Methods of phosphor synthesis and related technology

Kazuo Narita

Contents

4.1 General technology of synthesis 341
  4.1.1 Outline of synthesis processes 341
  4.1.2 Purification of raw materials 342
  4.1.3 Synthesis 342
    4.1.3.1 Matrix synthesis and activator introduction 342
    4.1.3.2 Raw material blend ratio 345
    4.1.3.3 Mechanism of solid-state reaction during firing 346
    4.1.3.4 Crucibles and atmospheres 347
  4.1.4 Fluxes 347
  4.1.5 Impurities and additives 349
  4.1.6 Particle size control 352
    4.1.6.1 Particle sizes of raw materials 353
    4.1.6.2 Fluxes 353
    4.1.6.3 Firing conditions 353
    4.1.6.4 Milling 353
    4.1.6.5 Particle classification 353
  4.1.7 Surface treatment 353
References 354

4.1 *General technology of synthesis*

4.1.1 *Outline of synthesis processes*

Almost all phosphors are synthesized by solid-state reactions between raw materials at high temperatures.* Figure 1 shows the general concept of the synthesis process. First, the high-purity materials of the host crystal, activators, and fluxes are blended, mixed, and then fired in a container. As the product obtained by firing is more or less sintered, it is crushed, milled, and then sorted to remove coarse and excessively crushed particles. In some cases, the product undergoes surface treatments.

---

* Single crystals and vacuum-deposited thin films are sometimes used as radioluminescent phosphors. (Chapter 7). Some electroluminescent devices have thin film- or epitaxially grown luminescent layers (Chapter 9).

4.1.2 Purification of raw materials

As small amounts of impurities sometimes change phosphor characteristics drastically, raw materials must be purified very carefully. Some typical cases are described below.

In case of the raw materials of zinc sulfide phosphors, iron-group ions have to be thoroughly removed. Two methods are employed for material purification,[1] namely the alkali process and the acid process. In the first stage of the latter, which is more frequently used, high-purity zinc oxide is dissolved in H_2SO_4. The solution is then brought into contact with metallic zinc to reduce iron and copper ions to the metallic state for removal. Then, H_2O_2 is added to oxidize the remaining ferrous ions to ferric ions. The ferric ions are precipitated with NH_4OH as $Fe(OH)_3$ and removed. The zinc ions in the solution are then precipitated as ZnS by supplying H_2S to the solution (See 6.2).

Calcium halophosphate phosphor, $Ca_5(PO_4)_3(F,Cl):Sb^{3+},Mn^{2+}$, one of the most important lamp phosphors, is usually synthesized from $CaHPO_4$, $CaCO_3$, CaF_2, $CaCl_2$, Sb_2O_3, and $MnCO_3$. Among these, $CaHPO_4$ and $CaCO_3$ provide 90% of the weight of the raw material mixture. The purification process of these two components is shown in Figure 2. The luminescence efficiency of the halophosphate phosphor is seriously affected not only by the presence of heavy metals, but also by Na. In commercial materials, heavy metals are controlled to within a few ppm, and Na to within 5 to 10 ppm.

In the rare-earth raw materials, separation of a single rare-earth ion from the others is most important. Figure 3 shows a typical refining process of a rare-earth ore.[2] In the case of Y_2O_3, the most frequently used rare-earth compound, rare earths other than Y are kept below 10 ppm, and the total amount of heavy metals below 10 ppm.

4.1.3 Synthesis

4.1.3.1 Matrix synthesis and activator introduction

A phosphor is composed of a host crystal, or matrix, and a small amount of activator(s). The common representation of a phosphor formula is exemplified by Zn_2SiO_4:Mn(0.02), where the first part tells us that the matrix is Zn_2SiO_4, and the last that 0.02 mol manganese activator was blended per 1 mole of matrix in the raw material mixture.

There are two different kinds of reactions in phosphor synthesis. In the first one, activator ions are introduced into an existing host material. A typical example of this kind is zinc sulfide phosphors, where following particle growth of the host crystal, diffusion of the activators into the ZnS lattice takes place. In the second scheme, host material synthesis and activator incorporation proceed simultaneously during firing, as shown in the following examples:

$$2\mathrm{ZnO} + \mathrm{SiO_2} + 0.02\mathrm{MnCO_3} \rightarrow \mathrm{Zn_2SiO_4}\!:\ \mathrm{Mn}^{2+}(0.2)\left(+\mathrm{CO_2}\uparrow\right) \tag{1}$$

$$\begin{gathered}6\mathrm{CaHPO_4} + 3\mathrm{CaCO_3} + 0.9\mathrm{CaF_2} + 0.1\mathrm{CaCl_2} + 0.1\mathrm{Sb_2O_3} + 0.4\mathrm{MnCO_3} \\ \rightarrow 2\mathrm{Ca_5}\left(\mathrm{PO_4}\right)_3\left(\mathrm{F_{0.9}Cl_{0.1}}\right):\mathrm{Sb}^{3+}(0.1),\mathrm{Mn}^{2+}(0.2)\left(+\mathrm{CO_2}\uparrow\right)\end{gathered} \tag{2}$$

Activators are added to raw material blends in the form of compounds (Sb_2O_3 and $MnCO_3$ in the above example), or as a component of a co-precipitate. A typical example for the latter is $Y_2O_3:Eu^{3+}$. In this case, synthesis by firing a physical mixture of Y_2O_3 and Eu_2O_3

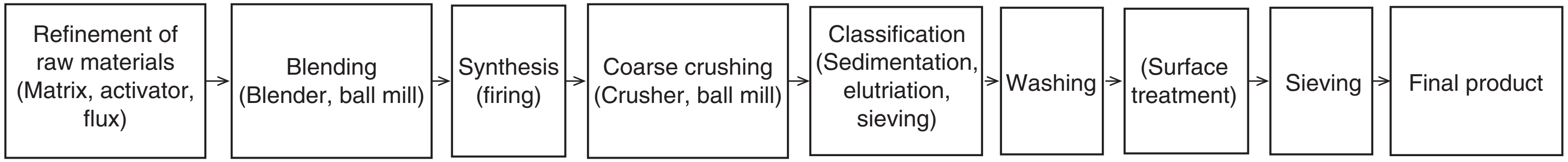
Refinement of raw materials (Matrix, activator, flux)
Blending (Blender, ball mill)
Synthesis (firing)
Coarse crushing (Crusher, ball mill)
Classification (Sedimentation, elutriation, sieving)
Washing
(Surface treatment)
Sieving
Final product

Figure 1 Phosphor synthesis processes.

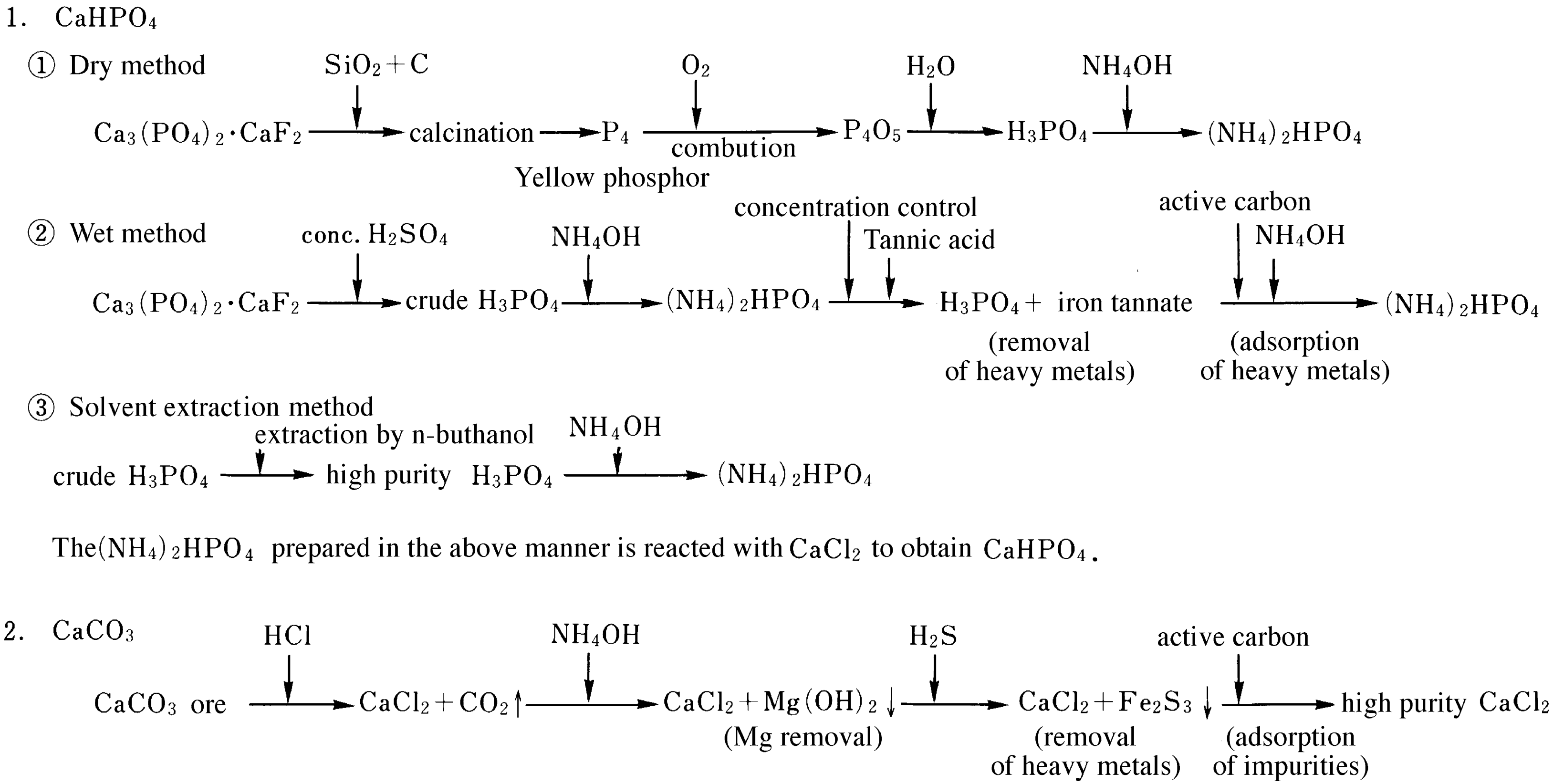
1. CaHPO4
① Dry method
SiO2+C
O2
H2O
NH4OH
Ca3(PO4)2·CaF2
calcination
P4
combution
P4O5
H3PO4
(NH4)2HPO4
Yellow phosphor
② Wet method
conc. H2SO4
NH4OH
concentration control
Tannic acid
active carbon
NH4OH
Ca3(PO4)2·CaF2
crude H3PO4
(NH4)2HPO4
H3PO4+ iron tannate
(NH4)2HPO4
(removal of heavy metals)
(adsorption of heavy metals)
③ Solvent extraction method
extraction by n-buthanol
NH4OH
crude H3PO4
high purity H3PO4
(NH4)2HPO4
2. CaCO3
HCl
NH4OH
H2S
active carbon
CaCO3 ore
CaCl2+CO2↑
CaCl2+Mg(OH)2↓
(Mg removal)
CaCl2+Fe2S3↓
(removal of heavy metals)
(adsorption of impurities)
high purity CaCl2

The $(NH_4)_2HPO_4$ prepared in the above manner is reacted with $CaCl_2$ to obtain $CaHPO_4$.

Figure 2 Refinement processes of $CaHPO_4$ and $CaCO_3$ for calcium halophosphate phosphor.

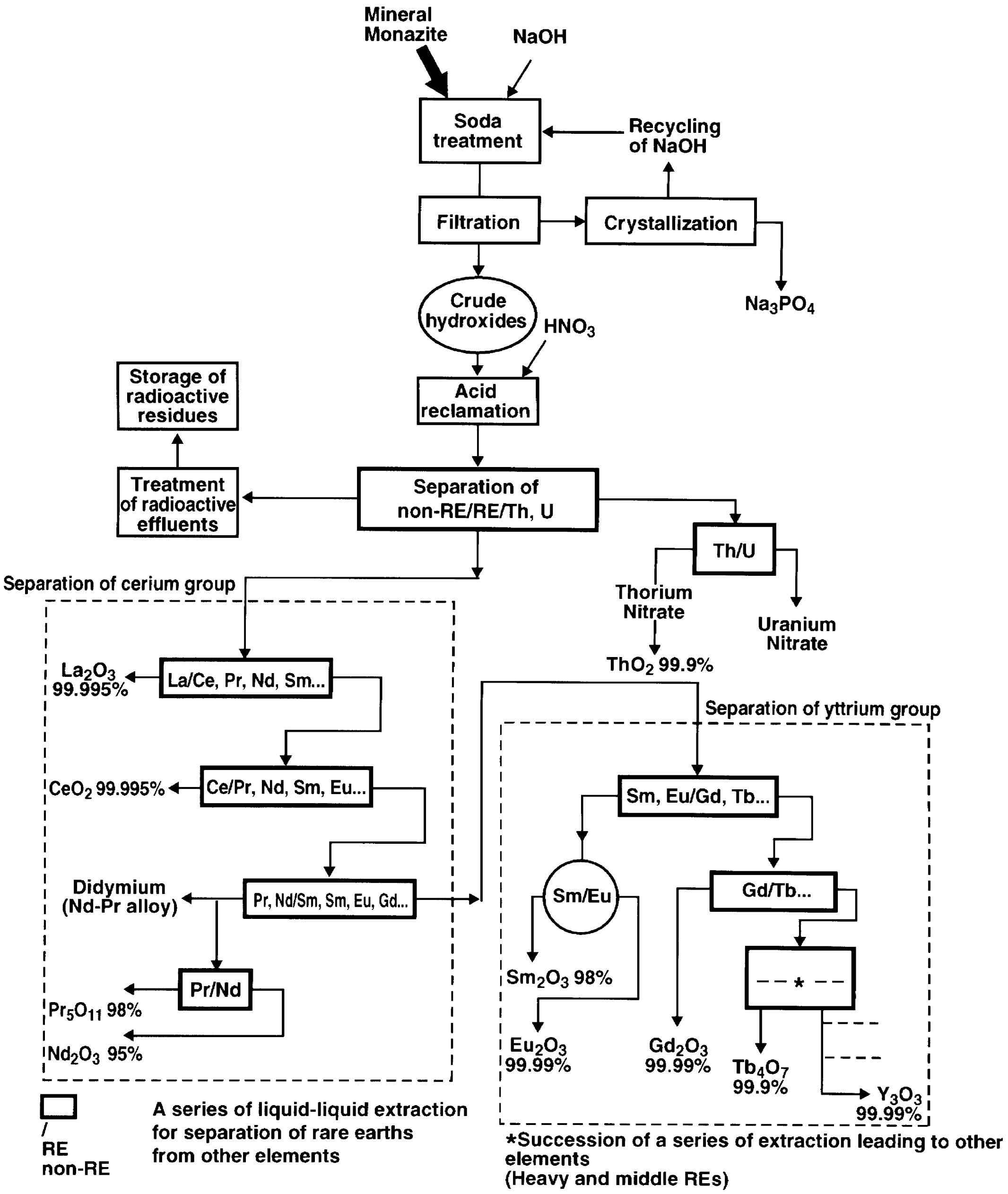
Mineral Monazite
NaOH
Soda treatment
Recycling of NaOH
Filtration
Crystallization
Na_3PO_4
Crude hydroxides
HNO_3
Acid reclamation
Storage of radioactive residues
Treatment of radioactive effluents
Separation of non-RE/RE/Th, U
Th/U
Thorium Nitrate
ThO_2 99.9%
Uranium Nitrate
Separation of cerium group
La_2O_3 99.995%
La/Ce, Pr, Nd, Sm...
CeO_2 99.995%
Ce/Pr, Nd, Sm, Eu...
Didymium (Nd-Pr alloy)
Pr, Nd/Sm, Sm, Eu, Gd...
Pr/Nd
Pr_5O_{11} 98%
Nd_2O_3 95%
Separation of yttrium group
Sm, Eu/Gd, Tb...
Sm/Eu
Gd/Tb...
Sm_2O_3 98%
Eu_2O_3 99.99%
Gd_2O_3 99.99%
Tb_4O_7 99.9%
Y_2O_3 99.99%
– – * – –
/ RE non-RE
A series of liquid-liquid extraction for separation of rare earths from other elements
*Succession of a series of extraction leading to other elements (Heavy and middle REs)

Figure 3 Refinement processes of rare-earth ore, monazite. (From Leveque, A. and Maestro, P., *Traité Genie des Procédés*, Les Techniques de l'Ingénieur, 1993, 1. With permission.)

does not yield an efficient phosphor. In the common factory process, Y_2O_3 and Eu_2O_3 are first dissolved in concentrated nitric acid, co-precipitated as oxalate, and then fired to obtain $(Y,Eu)_2O_3$.

4.1.3.2 *Raw material blend ratio*

In the case of the oxoacid-salt phosphor, raw materials are blended in a ratio deviating considerably from the stoichiometric composition of the final product (see 5.3.1). Calcium halophosphate phosphor, $Ca_5(PO_4)_3(F,Cl):Sb^{3+},Mn^{2+}$, presents a typical example. Figure 4

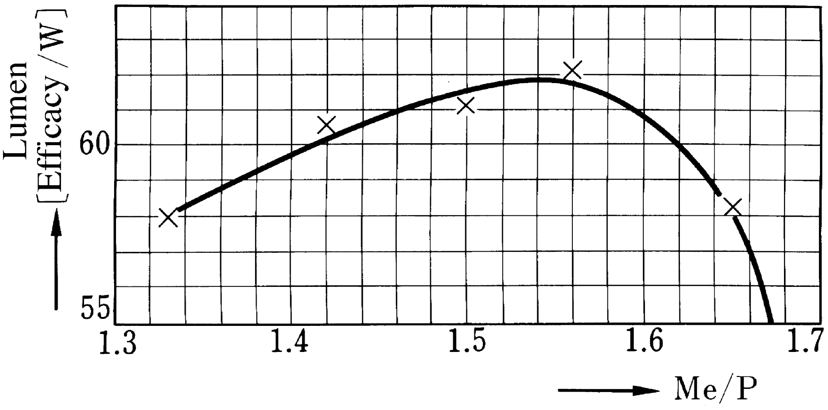

Figure 4 Relation between lamp efficacy and Me/phosphorus ratio of calcium halophosphate phosphor. Me stands for the sum of Ca, Sr, and Mn. (From Ouweltjes, J.L. and Wanmaker, W.L., *J. Electrochem. Soc.*, 103, 160, 1956. With permission.)

shows the relation between the molecular ratio of the total cations to phosphorus ions in this phosphor, Me/P, and the lamp efficacy.[3] As the Me/P ratio is increased and approaches the stoichiometric ratio 5/3 = 1.67, a sudden decrease of efficacy is observed. For this reason, 2 to 3% more phosphate than the stoichiometric composition is blended to the raw material mixture. The reason for the efficacy decrease at higher Me/P is that Sb added as an activator combines with excess Ca to form $Ca_2Sb_2O_7$, which precipitates out from the halophosphate matrix.[3] Also in Zn_2SiO_4, more SiO_2 is blended to ZnO than theoretically required.

The excess components either vaporize during firing or are consumed to create by-products. They can sometimes be washed away after the reaction. Because of these adjusting mechanisms, the resulting phosphors are usually very close to the stoichiometric composition.[4]

4.1.3.3 Mechanism of solid-state reaction during firing

The elementary processes taking place during firing can be investigated by such means as differential thermal analysis (DTA), thermogravimetric analysis (TGA), crystal structure identification by X-ray diffraction, microscopic observation, and chemical analysis. Some examples are given below.

Manganese-activated zinc silicate phosphor is synthesized from ZnO, SiO_2, and $MnCO_3$. The DTA studies of the raw material mixture show that ZnO and SiO_2 start reacting at about 770°C, where the reaction proceeds by diffusion of ZnO into the SiO_2 lattice.[5] The manganese ion is incorporated into the lattice in proportion to the amount of synthesized Zn_2SiO_4.

The $Y_2O_2S{:}Eu^{3+}$ phosphor, one of the most important components of the color TV screen, is unique in using an exceptionally large amount of flux (see 4.1.4). Details of the synthesizing reaction were studied using Y_2O_3 and Eu_2O_3 as the materials for the host crystal, S and Na_2CO_3 as sulfurizing agents, and K_3PO_4 as a flux.[6]

The substance Y_2O_3 can be converted to Y_2O_2S already at 700°C, but the reaction proceeds only slowly. At 1180°C, sulfurization is completed in a very short time, i.e., within 10 min. The Y_2O_2S particles formed in the initial stage of the reaction maintain the original shape of Y_2O_3 particles. This indicates that Y_2O_2S is first formed by a reaction between a vapor phase and a solid phase, i.e., between gaseous Na_2S_x or S_x and solid Y_2O_3. Following this process, the particles develop to larger, well-crystallized ones in the molten flux. The Eu^{3+} emission in Y_2O_2S is observed shortly after the matrix formation, suggesting quick diffusion of the Eu^{3+} ions into the lattice.

For fabrication of calcium halophosphate, $CaHPO_4$, $CaCO_3$, CaF_2, $CaCl_2$, Sb_2O_3, and $MnCO_3$ are usually used as raw materials. The process is more complicated than the examples described previously, as some of the above components decompose thermally.[7] By heating the starting mixture, $CaHPO_4$ decomposes first at 380 to 500°C to form $Ca_2P_2O_7$. Conversion of $CaCO_3$ to CaO follows at 770 to 920°C. At the same time, the apatite phase, $Ca_5(PO_4)_3(F,Cl)$, starts to appear. Above this temperature, a gas-phase reaction including POF_3 as an intermediate probably contributes to apatite formation.[8]

Diantimony trioxide, Sb_2O_3, in the initial mixture is oxidized at 450 to 520°C to Sb_2O_4.[7,9] This reacts with CaF_2 and CaO (formed by $CaCO_3$ decomposition) at 700 to 875°C to yield calcium antimonate ($Ca_4Sb_4O_{11}F_{12}$). At higher temperatures, the antimonate decomposes and gives Sb^{3+}, which is subsequently introduced into the apatite lattice. Part of Sb_2O_3 in the starting mixture is lost during firing by simple evaporation or as $SbCl_3$.

The behavior of the paramagnetic manganese ion can be traced by ESR.[10] In an inert or weakly reducing atmosphere, diffusion of manganese ion into the apatite lattice starts simultaneously with the formation of the apatite, is greatly accelerated at higher temperatures, and is completed at around 1100°C. In air, Mn^{2+} diffuses into the apatite lattice more slowly, the reaction becoming complete at around 1200°C. An intermediate phase, CaO:Mn, is observed during the reaction.

The synthesizing reaction of zinc sulfide phosphors is simpler, as only activator diffusion into the ZnS lattice and particle growth of ZnS take place. Studies on the luminescence mechanism of ZnS (see 3.4) show that, in green-emitting ZnS:Cu,Al or ZnS:Cu,Cl, copper and aluminum ions occupy Zn sites, and chlorine ions occupy sulfur sites. These ions are distributed randomly in the lattice. The diffusion coefficient of Cu into the ZnS lattice has been determined.[11]

4.1.3.4 *Crucibles and atmospheres*

In the phosphor industry, quartz and silicon carbide are the most frequently used container materials for firing phosphors. For phosphors requiring higher firing temperatures, (e.g., aluminate phosphors), alumina crucibles are employed.

Box-type furnaces are common for small-scale production. For large quantity production, tunnel-type, continuous furnaces are indispensable.

Firing is carried out either in air or in a controlled atmosphere. Phosphors activated with Tl^+, Pb^{2+}, Sb^{3+}, Mn^{2+}, Mn^{4+}, or Eu^{3+} ions can be fired in air, whereas phosphors activated with Sn^{2+}, Eu^{2+}, Ce^{3+}, or Tb^{3+} ions are fired in a reducing atmosphere.

As the reducing gas, nitrogen containing several percent hydrogen is most frequently used. The zinc sulfide phosphor is fired in a crucible that contains a small amount of sulfur, as ZnS is oxidized if directly exposed to air. When Al is employed as a co-activator (e.g., ZnS: Cu, Al), it is necessary to prevent its oxidation to Al_2O_3. For this purpose, a small amount of carbon powder is added to make the ambiance weakly reducing.[12]

Firing temperatures range from 900 to 1200°C for phosphate phosphors, 1000 to 1300°C for silicates, and 1200 to 1500°C for aluminates. For polymorphous materials such as zinc sulfides and alkaline earth orthophosphates, a firing temperature above or below the transition temperature of the two phases is selected so that the required crystal type is obtained.

4.1.4 *Fluxes*

The purpose of firing is not only to cause solid-state reactions but also to form well-crystallized particles with an appropriate average diameter. The substance added to the raw material mixture to help crystal growth is called a *flux*. Fluxes are usually compounds

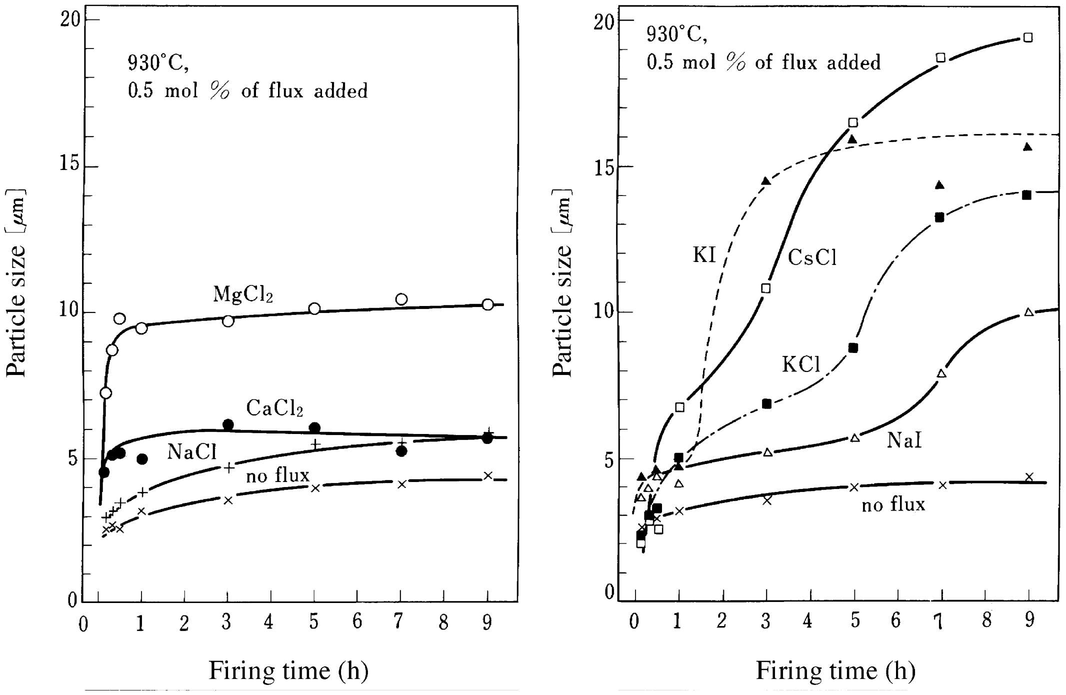

Figure 5 Relation between firing time and particle size in presence of various additives. (a) melting points of flux sulfides > firing temperature; (b) melting points of flux sulfides < firing temperature. (From Kawai, H., Abe, T., and Hoshina, T., *Jap. J. Appl. Phys.*, 20, 313, 1981. With permission.)

of alkali- or alkaline earth metals having low melting points. The halides are most frequently used.

Concerning the crystal growth of zinc sulfide phosphors during firing, it is known that the growth rate of the particle volume is constant for a constant firing temperature.[13] The crystal growth in this case is interpreted as being a result of particle-particle sintering. By adding a flux such as NaCl, particle growth is accelerated. The more flux added, the faster the growth rate. The activation energy of the crystal growth is around 89 kcal mol^{-1} when no flux is added. Presence of a flux reduces the energy to around 30 kcal mol^{-1}.

Among a number of halides studied as fluxes for zinc sulfide phosphors, only those that melt at the firing temperature (i.e., NaCl, $CaCl_2$, and alkali- and alkaline earth chlorides) are effective in promoting particle growth.[14] None of the halides whose melting points are higher than the firing temperature (NaF, $BaCl_2$) acts as a flux. These facts show that a liquid phase provided by the fluxes plays an important role.

When the fluxes melt, the surface tension of the liquid helps particles coagulate. The melt also makes it easier for particles to slide and rotate, provides chances of particle-particle contacts, and promotes particle growth.

Part of the added flux is sulfurized by contacts with ZnS. If the sulfides created in this manner do not melt during firing, no further particle growth takes place. If they melt, on the other hand, they cover the surface of the zinc sulfide particles. Part of the zinc sulfide dissolves into this liquid phase, diffuses to the particle-particle contact points, and precipitates there. By this process, particles make a second-stage growth. These two cases are compared in Figure 5.

Another important function of the flux is that it acts as a source of the co-activator. In case of ZnS:Ag,Cl and ZnS:Cu,Cl, the chlorine co-activator is supplied by a flux, NaCl. The Al co-activator of ZnS:Cu,Au,Al,[15] and ZnS:Cu,Al[12] is added as fluxes such as aluminum fluorides, nitrates, sulfates, etc. In these cases, it is common to add NH_4I as an auxiliary flux.

In the oxoacid phosphor, the flux is not always necessary, as usually some of the raw materials have low melting points or sublimation temperatures, and help crystal particles grow. In some cases, however, fluxes are added deliberately.

The $Y_2O_3:Eu^{3+}$ phosphor is usually fabricated by firing a co-precipitate of yttrium and europium oxalates. If no flux is added, firing has to be performed at very high temperatures (ca. 1400°C). By adding halides, the temperature can be reduced to 1200°C.

The $Y_2SiO_5:Ce^{3+},Tb^{3+}$ phosphor and a series of aluminate phosphors also need fluxes, as the raw materials of these phosphors have high melting points, and hardly react with each other. In the former, KF,[16] and in the latter, AlF_3 and MgF_2 have been found useful.[17]

The $Y_2O_2S:Eu^{3+}$ phosphor is fabricated by sulfurization of Y_2O_3 (see 4.1.3.3). To promote the reaction, K_3PO_4 is added as a flux.[18]

Generally, phosphates and borates do not need fluxes. In this group, the $Sr_5(PO_4)_3Cl:Eu^{2+}$ (= $3Sr_3(PO_4)_2 \cdot SrCl_2:Eu^{2+}$) phosphor presents an extraordinary example. The stoichiometric ratio of strontium phosphate and strontium chloride for this phosphor is 3:1. However, high luminescence efficiency is obtained only when this ratio in the raw material mixture is adjusted between 3:1.5 and 3:2; that is, the presence of a large excess of the chloride is required.[19] The more chloride added, the larger/becomes the particle size. Hence, it is obvious that the chloride is acting as a flux. After firing, the unreacted chloride can be removed easily by washing.

4.1.5 Impurities and additives

The presence of some impurity ions reduces luminescence efficiency, sometimes to a very great extent. On the contrary, there are some additives that influence phosphor characteristics in a positive way; they improve efficiency or decrease deterioration. The kind and quantity of the ions that change phosphor characteristics differ from phosphor to phosphor. Some examples are presented in the following.

It is well known that the iron group ions drastically reduce the luminescence efficiency of ZnS phosphors, and hence are called *killers*. In case of the ZnS:Cu,Al phosphor, Ni^{2+} has a stronger effect than Fe^{2+} and Co^{2+}. The presence of 10^{-6} mol Ni^{2+} in 1 mole of ZnS (ca. 0.6 ppm) results in an efficiency decrease of 30%; with 10^{-3} mol (ca. 600 ppm), no cathodoluminescence is observed[20] (See 3.7). A proposed mechanism for this phenomenon is either:

1. The iron group ions give rise to deep levels in the forbidden band, which act as nonradiative recombination centers for free electrons in the conduction band and holes in the valence band,

or

2. The excitation energy absorbed by the luminescence center is transferred to iron group ions without emitting radiation.[20]

The iron group ions also have adverse effects on oxoacid phosphors, but to a much smaller extent. The plaque brightness of a 3000K calcium halophosphate phosphor with various added impurities is shown in Table 1.[21] With the presence of 10 ppm Fe, Ni, or Co, the plaque brightness decreases by only 10%. In the case of Fe, this decrease can be explained by assuming that part of the 254-nm excitation radiation is absorbed by Fe.[22] In the cases of Ni and Co, however, plaque brightness is much lower than expected

Table 1 Influence of Impurities on the Plaque Brightness of a 3000K Calcium Halophosphate Phosphor

100 ppm addition		1,000 ppm addition		10,000 ppm addition	
Impurities	Plaque brightness	Impurities	Plaque brightness	Impurities	Plaque brightness
Ce	101.1	Al	100.5	Al	99.5
Al	100.9	Ce	98.8	Zr	95.2
Zr	100.9	Ag	88.8	Ce	93.2
Pb	100.8	S	97.8	La	92.5
Ga	100.8	Pb	97.7	Pb	91.7
La	100.6	Zr	97.6	Y	89.6
S	100.2	Si	97.5	In	89.2
Na	100.2	La	97.0	Sm	86.2
Si	100.1	In	96.9	Cs	83.5
Sm	99.8	Cs	96.7	S	79.7
Ag	99.7	Y	95.3	Pr	78.8
Cs	99.5	Sm	95.1	Nd	61.0
Mo	99.5	Mo	95.0	Na	48.5
Pr	99.5	Ga	94.8	Ag	46.7
Sn	98.9	Pr	92.5	Sn	45.8
Y	98.8	Nd	88.5	W	42.7
In	98.5	Na	88.5	Si	41.8
U	98.5	W	85.7	Mo	32.3
W	98.3	Sn	81.8	U	31.3
Nd	98.2	U	81.7	Ga	18.1
Ti	98.1	Cr	77.9	Cr	7.57
Cr	93.5	Fe	62.3	Ni	3.96
Cu	92.5	Ni	53.6	Fe	0.72
Ni	92.3	V	51.3	Cu	—
V	91.8	Cu	50.7	Co	—
Fe	91.7	Ti	44.9	V	—
Co	87.3	Co	39.6	Ti	—

Note: Normalized to the brightness for 1 ppm addition of each impurity.

From Wachtel, A., *J. Electrochem. Soc.*, 105, 256, 1958. With permission.

using the same assumption. This suggests the existence of energy transfer from activators to impurities.

In some cases, a small amount of added ions enhances luminescence efficiency. A typical example is Tb^{3+} in $Y_2O_2S{:}Eu^{3+}$. The presence of 10^{-4} to 10^{-2} atom% Tb^{3+} results in the improvement of cathodoluminescence efficiency, sometimes of up to several tens of percent, as shown Figure 6.[23] Praseodymium has the same effect.

As Figure 7 shows, the extent of efficiency improvement by Tb^{3+} depends on the current density of excitation. The true nature of the Tb^{3+} effect consists of the fact that efficiency saturation at high current density is diminished by Tb^{3+}. It is assumed that the Tb^{3+} additive eliminates quenching by nonlinear loss centers.[23]

Another example of a beneficial additive is cadmium in calcium halophosphate phosphor.[24] The presence of 1 to 2% Cd in halophosphates improves initial lumen output by about 2%. The commonly accepted interpretation of this effect is that Cd introduces an absorption band in the wavelength region between 180 and 190 nm and absorbs harmful 185-nm radiation, which otherwise creates color centers leading to the loss of exciting radiation.[25]

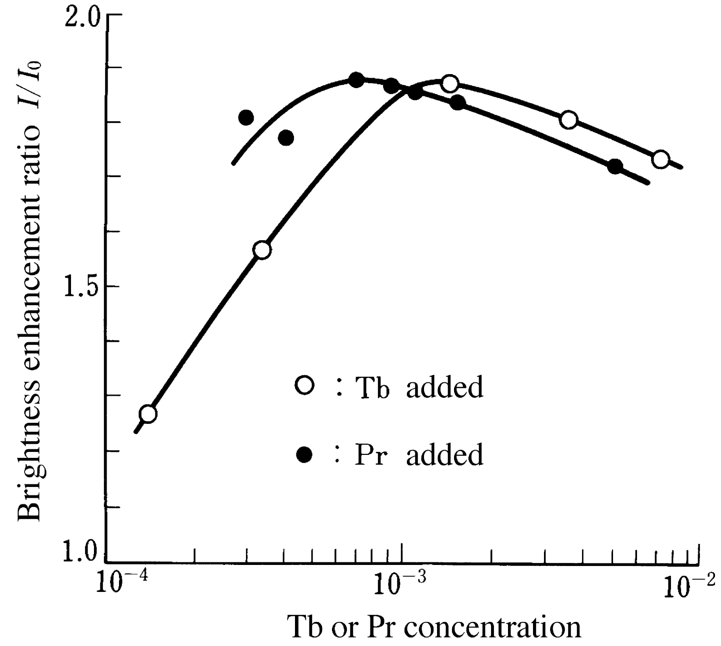

Figure 6 Emission intensity enhancement by Tb^{3+} or Pr^{3+} addition $Y_2O_2S:Eu^{3+}$ (normalized to intensity without addition.) Measured under cathode-ray excitation. (From Yamamoto, H. and Kano, T., *J. Electrochem. Soc.*, 126, 305, 1979. With permission.)

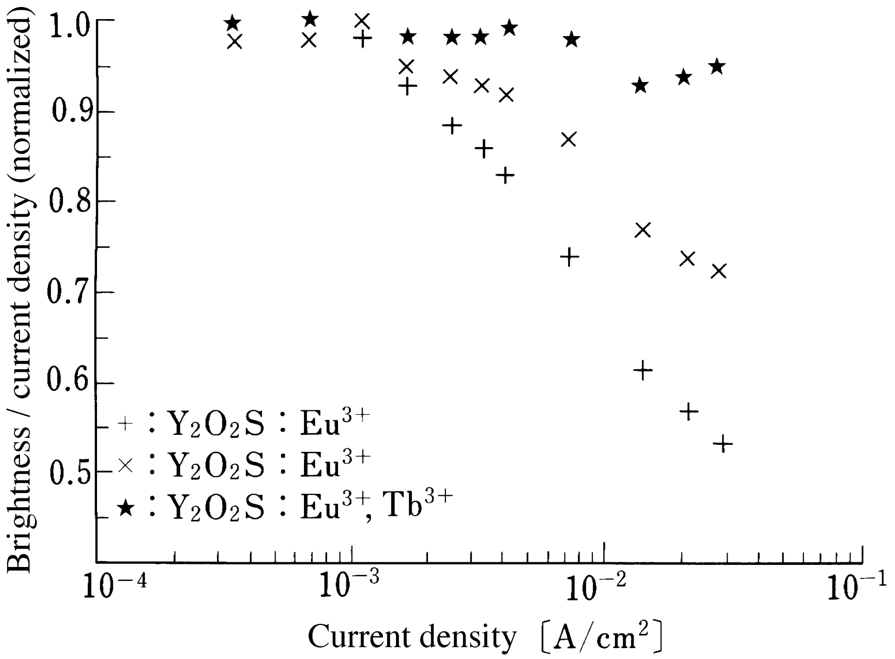

Figure 7 Relation between excitation current density and relative emission efficiency of $Y_2O_2S:Eu^{3+}$. +: $Y_2O_2S:Eu^{3+}$ prepared by firing in air. ×: $Y_2O_2S:Eu^{3+}$ phosphor annealed in sulphur atmosphere. ★: $Y_2O_2S:Eu^{3+},Tb^{3+}$ prepared by firing in air. (From Yamamoto, H. and Kano, T., *J. Electrochem. Soc.*, 126, 305, 1979. With permission.)

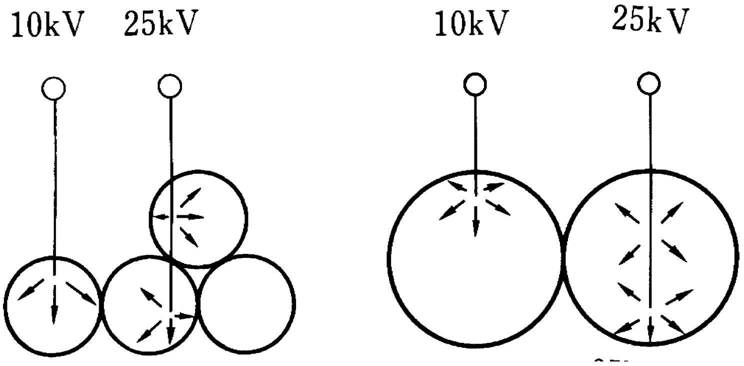

Figure 8 Penetration of cathode-ray into phosphor particles: (left) small particles; (right) large particles. (From Ozawa, L. and Hersh, H.N., *J. Electrochem. Soc.*, 121, 894, 1974. With permission.)

4.1.6 Particle size control

Practical phosphors must be prepared so that they can form a dense, pinhole-free coating on a substrate. This property is determined mainly by particle size distribution and surface treatment.

In case of a fluorescent lamp phosphor, the optimum coating thickness is roughly proportional to its mean particle size; that is, the smaller the particle size, the thinner the coating can be. When a mixture of phosphors is used, as is the case with three-band fluorescent lamps, the proportion of a component can be made smaller for the same emission color when its particle size can be made smaller. Therefore, a small particle size is advantageous for expensive phosphors. Fine-particle phosphors also yield denser coatings. When a phosphor is prepared in a condition that yields fine particles, on the other hand, luminescence efficiency tends to become lower. Phosphors having a small particle size and high efficiency would be most useful. The Y_2O_3:Eu^{3+} phosphor and some aluminate phosphors like $BaMg_2Al_{16}O_{27}$:Eu^{2+} and $(Ce^{3+},Tb^{3+})MgAl_{11}O_{19}$ can be made highly efficient at a mean particle diameter of about 3 μm. For halophosphate phosphors, on the other hand, a large diameter of about 8 μm or more is necessary to attain high efficiency, and a thick coating is required for obtaining optimum lamp efficiency. However, this causes little problem, as halophosphates are one of the most inexpensive phosphors.

Approximately the same rule applies for the cathodoluminescent phosphor. It is known that the optimum coating thickness of a phosphor on the cathode-ray tube is roughly 1.4 times the phosphor's mean particle diameter.[26]

Also in case of cathodoluminescence, phosphors having a large particle size have higher efficiency. The efficiency difference between large and small particles becomes more pronounced at larger accelerating voltages. It is postulated that the surface of phosphor particles is covered with a low-efficiency thin layer, and in case of smaller particles, impinging electrons have more chances to pass through this low-efficiency part than in case of larger particles (Figure 8); it follows that a larger portion of the electronic energy is dissipated with little emission. Again, higher efficiency and better coating properties must be balanced by adjusting the particle size. Usually, particle diameters between 5 and 7 μm are chosen for cathode-ray tubes.

For X-ray intensifying screens, the particle size is determined by considering efficiency, picture resolution, and picture quality. Particle diameters of 1 to 10 μm are selected in accordance with the applications of the screens.

The parameters that control the particle diameter in the phosphor preparation process are described in the following.

4.1.6.1 *Particle sizes of raw materials*

In the case of calcium halophosphates and strontium chlorophosphates, the particle shapes of $CaHPO_4$ or $SrHPO_4$, which occupy approximately 70% of the weight of the raw material mixtures, are inherited by the phosphors but with slightly increased particle diameters.[27] Therefore, the morphology of the hydrogen phosphates have to be carefully controlled in their preparation. Such close similarities of particle shapes between the starting materials and the final products, however, are not frequently observed.

4.1.6.2 *Fluxes*

As mentioned before (see Section 4.1.4), the flux used plays a determining role in the particle growth process. Each flux influences the particle size and the shape in a different way. Therefore, a combination of fluxes is sometimes used to obtain products with desired morphology.

4.1.6.3 *Firing conditions*

Higher firing temperatures and longer firing times result in larger particles. Particle growth is rapid in the initial stage of firing, and slows down after a certain period of time (see Figure 5).

4.1.6.4 *Milling*

Normally, the fired phosphor is obtained as a sintered cake. This is broken into smaller pieces and then milled into particles. Weak milling (i.e., separation of coagulated particles into primary ones) changes the efficiency little. However, primary particle destruction lowers efficiency. The possible reasons are that lattice defects created by phosphor crystal destruction act as nonradiative recombination centers, or that a nonluminescent, amorphous layer is formed on the surface of the particles. It is most important to select raw materials, fluxes, and firing conditions so as to avoid strong milling after firing.

4.1.6.5 *Particle classification*

Even by careful adjustment of materials, fluxes, and firing conditions, the phosphors obtained usually have a broad particle-size distribution. A process is necessary, therefore, to remove both very fine and coarse particles from the phosphor lots; this is done by means of sedimentation, elutriation, or sieving.

Sedimentation is usually used to separate very fine particles. In this process, phosphor batches are agitated in water and then left still until larger particles sediment. The remaining suspended, finer particles are removed by decantation. The sedimentation speed can be changed to some extent by adjusting acidity.

Elutriation is employed during a wet process, in which both washing and removal of coarse particles are carried out at the same time. Sieving is used to remove very large phosphor particles after firing.

4.1.7 *Surface treatment*

Zinc sulfide phosphors, as fired, are poorly dispersive in slurry. To improve dispersion, surface treatment is indispensable. The details are described in Section 4.1.2.

Cathodoluminescent phosphors other than zinc sulfides do not undergo surface treatments. However, coating with pigments is applied to the red-emitting $Y_2O_2S{:}Eu^{3+}$ for contrast improvement. Surface treatment sometimes also is applied to lamp phosphors in order to lower the lamp starting voltage or to minimize phosphor deterioration.

References

1. Leverenz, H., *An Introduction to Luminescence of Solids*, John Wiley & Sons, 1950, 473 (also Dover, 1968, 473).
2. Leveque, A. and Maestro, P., *Traité Genie des Procédés*, Les Techniques de l'Ingénieur, 1993, 1.
3. Ouweltjes, J.L. and Wanmaker, W.L., *J. Electrochem. Soc.*, 103, 160, 1956.
4. Rabatin, J.G., Gillooly, G.R., and Hunter, J.W., *J. Electrochem. Soc.*, 114, 956, 1967.
5. Takagi, K., *J. Chem. Soc. Jpn., Ind. Chem. Sec.*, 65, 847, 1962.
6. Kanehisa, O., Kano, T., and Yamamoto, H., *J. Electrochem. Soc.*, 132, 2033, 1985.
7. Wanmaker, W.L., Hoekstra, A.H., and Tak, M.G.A., *Philips Res. Rep.*, 10, 11, 1955; Kamiya, S., *Denki Kagaku*, 31, 246, 1963.
8. Rabatin, J.G. and Gillooly, G.R., *J. Electrochem. Soc.*, 111, 542, 1964.
9. Butler, K.H., Bergin, M.J., and Hannaford, V.M.B., *J. Electrochem. Soc.*, 97, 117, 1950.
10. Parodi, J.A., *J. Electrochem. Soc.*, 114, 370, 1967.
11. Shionoya, S. and Kikuchi, K., *J. Chem. Soc. Jpn., Pure Chem. Sec.*, 77, 291, 1956.
12. Martin, J.S., U.S. Patent 3,595,804, 1971.
13. Shionoya, S. and Amano, K., *J. Chem. Soc. Jpn., Pure Chem. Sec.*, 77, 303, 1956.
14. Kawai, H., Abe, T., and Hoshina, T., *Jap. J. Appl. Phys.*, 20, 313, 1981.
15. Oikawa, M. and Matsuura, S., Japanese Patent Disclosure (Kokai) 53-94281 (1978).
16. Watanabe, M., Nishimura, T., Omi, T., Kohmoto, K., Kobuya, A., and Shimizu, K., Japanese Patent Disclosure (Kokai) 53-127384.
17. Verstegen, J.M.P.J., Verlijsdonk, J.G., De Meester, E.P.J., and Van de Spijker, W.M.M., Japanese Patent Disclosure (Kokai) 49-77893 (1974), U.S. Patent 4,216,408, 1978.
18. Royce, M.R., Smith, A.L., Thomsen, S.M., and Yocom, P.N., *Electrochem. Soc. Spring Meeting Abstr.*, 1969, 86.
19. Pallila, F.C. and O'Reilly, B.E., *J. Electrochem. Soc.*, 115, 1076, 1968.
20. Tabei, M., Shionoya, S., and Ohmatsu, H., *Jap. J. Appl. Phys.*, 14, 240, 1975.
21. Wachtel, A., *J. Electrochem. Soc.*, 105, 256, 1958.
22. Narita, K. and Tsuda, N., *Bull. Chem. Soc. Japan*, 48, 2047, 1975.
23. Yamamoto, H. and Kano, T., *J. Electrochem. Soc.*, 126, 305, 1979.
24. Aoki, Y., Japanese Patent Publication (Kokoku) 29-967 (1954); Aia, M.A. and Poss, S.M., U.S. Patent 2,965,786; Japanese Patent Publication (Kokoku) 38-4325 (1963).
25. Apple, E.F., *J. Electrochem. Soc.*, 110, 374, 1963.
26. Ozawa, L. and Hersh, H.N., *J. Electrochem. Soc.*, 121, 894, 1974.
27. Wanmaker, W.L. and Radielovic, D., *Bull. Soc. Chim. France*, 1785, 1968; Kotera, Y., *J. Chem. Soc. Japan, Ind. Chem. Sec.*, 72, 55, 1969.

chapter four — section two

Methods of phosphor synthesis and related technology

Brian M. Tissue

Contents

4.2 Inorganic nanoparticles and nanostructures for phosphor applications.................355
  4.2.1 Synthesis and characterization 355
    4.2.1.1 Introduction..355
    4.2.1.2 Synthetic approaches 357
      4.2.1.2.1 Gas-phase methods 357
      4.2.1.2.2 Condensed-phase methods 359
      4.2.1.2.3 Nanocomposites 361
    4.2.1.3 Material characterization and analysis..363
    4.2.1.4 Optical spectroscopy for material characterization..........................364
  4.2.2 Size-dependent optical effects..366
    4.2.2.1 Introduction..366
    4.2.2.2 Structural and dopant distribution effects..367
      4.2.2.2.1 Structural effects on spectra 367
      4.2.2.2.2 Dopant distribution and segregation..368
    4.2.2.3 Dynamic effects 369
  4.2.3 Applications 370
    4.2.3.1 Introduction..370
    4.2.3.2 Analytical assays and imaging 371
  4.2.4 Summary and prospects 372
References..373

4.2 Inorganic nanoparticles and nanostructures for phosphor applications

4.2.1 Synthesis and characterization

4.2.1.1 Introduction

Nanoscale materials can exhibit new or enhanced structural, electronic, magnetic, and optical properties.[1–5] These size-dependent properties, coupled with the significant improvement in the spatial resolution of characterization and imaging methods during the last 20 years or so, have stimulated the development and study of nanomaterials. Researchers are active worldwide developing new preparation methods for nanoparticles and nanostructures to study their unique size-dependent properties and to apply them in functionally and technologically useful materials. A number of recent conference proceedings,[6,7] texts,[8] and general interest books[9,10] provide a survey of the wide range of current research in nanotechnology. Several recent reviews also provide more focused overviews of the size-dependent optical properties of metals, semiconductors, and insulators.[11–14] This discussion specifically introduces and reviews the preparation, characterization, advantages, and disadvantages of using nanostructured materials in phosphor applications. Forming a luminescent phosphor particle at the nanometer scale can change the structure, crystallinity, and intrinsic optical properties of the host, thereby affecting the characteristics and efficiency of a phosphor material.[15] Similarly, extrinsic effects such as quenching due to defects or contaminants on high-surface-area particles, or changes in radiative rates due to the surroundings will affect phosphor performance. Some of the key issues in using nanoscale materials in phosphor applications include the location, distribution, or segregation of any dopants present; quantum confinement effects in semiconductors; changes in the radiative and nonradiative relaxation rates due to size-dependent phonon dynamics, electron–phonon interactions, or surroundings; and the potential for optical enhancement or energy transfer to a luminescent center in a nanostructure.

As a working definition, I will restrict most of the discussion to nanostructured phosphor-type materials consisting of discrete nanoparticles with diameters of 100 nm or less and nanostructured films and composites with at least one component having a dimension of 100 nm or less. This section strives to provide an illustrative overview of the unique opportunities, technical issues, and potential uses of nanoscale materials for phosphors in lighting, optical displays, and analytical applications. It does not attempt to provide an exhaustive review of the current literature. To maintain a concise focus, most of the examples that I discuss are taken from studies of doped and undoped insulating phosphor materials. Nanoscale semiconductors (quantum dots) are being studied extensively for their unique size-dependent quantum-confinement effects,[16–18] and a number of books are available on the preparation and properties of these materials.[19–21] Some work on quantum dots and metal nanoparticles is included here, i.e., in the more general discussions on synthesis and characterization, but I have tried to avoid duplicating reviews of the large body of work on plasmonic and quantum-confined materials. Similarly, this section only touches briefly on the active research in porous silicon and related materials.[22,23]

There are a large number of well-known and newly developed methods for forming nanoparticles and nanoscale structures (grouped collectively as nanomaterials). The following section provides representative examples of procedures to create discrete nanoparticles, nanocomposites, and nanostructured films. For convenience I categorize the discussion of synthetic procedures for discrete nanoparticles into gas-phase and condensed-phase methods. Many of the preparation methods for discrete nanoparticles can be modified or extended to create nanostructured films and nanocomposites, although some types of nanostructures require completely novel approaches. The various synthetic methods are amenable to prepare metals, oxides, sulfides, fluorides, and mixed alloys, but no method is truly universal. The details of the different methods determine the distinct advantages and disadvantages for forming different types of materials, the ability to introduce dopants, and their compatibility with low-melting point substrates. Most of the preparation methods rely on homogeneous precipitation or on kinetic control to maintain the resulting particles or structures at the nanoscale. However, there are exceptions, with lithographic methods a notable one. Although not discussed in detail here, the scalability, cost, and environmental hazards of different preparation methods are receiving more attention as progress is made toward commercializing nanomaterials.[24]

The second part of this section discusses common material characterization methods that are indispensable to study size-dependent properties. Common analyses include the determination of size distribution, morphology, crystallinity, and phase purity. The last part of this section discusses examples of optical characterization that are oriented toward material characterization. Determining optical properties such as color purity and luminescence efficiency are certainly critical to the actual use of nanomaterials as phosphors, but these topics are treated in more depth in other chapters of this handbook.

4.2.1.2 Synthetic approaches

4.2.1.2.1 Gas-phase methods. A sampling of the wide variety of gas-phase synthetic methods in both inert and reactive atmospheres include:

- Laser or electron-beam heated vaporization and condensation[25,26]
- Flame and spray pyrolysis,[27,28] plasma processing,[29] and electrospray[30,31]
- Laser-driven reactions[32] and laser ablation[33,34]

A significant body of work published in the 1960s and 1970s provides the groundwork for understanding the gas-phase synthesis of nanoparticles.[35–37] Most of the early work concentrated on metals due to the simplicity of evaporating metals and the absence of problems with phase separation and oxygen deficiency. The models of nanoparticle formation determined for metals are applicable to most types of materials, and as-deposited nanoparticle films of metals, semiconductors, oxide insulators, and carbon soot show similar morphologies. Compared with gas-phase crystal or film growth methods, the key difference in the gas-phase formation of nanoparticles is that evaporation of starting material occurs in a buffer atmosphere to cool the evaporated material rapidly. Nanoparticles form in a distinct region of nucleation and particle growth, which depletes the supersaturation condition quickly so that any further particle growth occurs only by coalescence. Particle size is dependent on material properties and evaporation conditions, and the resulting particle sizes tend to follow a log–normal distribution.[38]

Figure 9 shows a simple arrangement for a gas-phase condensation method. In this example, a cw-CO_2 laser heats a spot on a ceramic target to vaporize material that forms as nanoparticles in the buffer gas atmosphere.[39] The nanoparticles deposit on some type of collector, which can be cooled, or have an applied electric bias.[34] Laser and electron-beam heating have the advantage of crucible-free methods as they can achieve very high vaporization temperatures. Laser heating, including laser ablation, has the additional advantage of not requiring the low chamber pressures necessary when using electron beams. The buffer gas pressure is a major factor that controls particle size and morphology. Figure 10 and Figure 11 show typical scanning electron micrographs of the morphology of films of gas-phase condensed nanoparticles. Chains of nanoparticles form a network (Figure 10) due to more rapid cooling and gas-phase aggregation at higher buffer gas pressures. At lower gas pressures, individual nanoparticles reach the collector surface, producing a denser columnar morphology (Figure 11). The individual nanoparticles are not resolved in these figures, but the morphology provides clues to the growth mechanisms. Different materials will have different transition pressures between these two morphologies. These results show that proper conditions must be used in different applications, such as using gas-phase methods to deposit nanoparticles on surfaces or synthesizing nanostructures using lithographic methods.

Dopants may be introduced in the target, but subsequent annealing is often necessary to obtain a single-phase material, a preferred phase, or to improve the crystallinity for the highest luminescence efficiency. Figure 12 shows transmission electron micrographs of Eu^{3+}:Y_2O_3 nanoparticles as prepared and after annealing.[40] The figure shows the typical

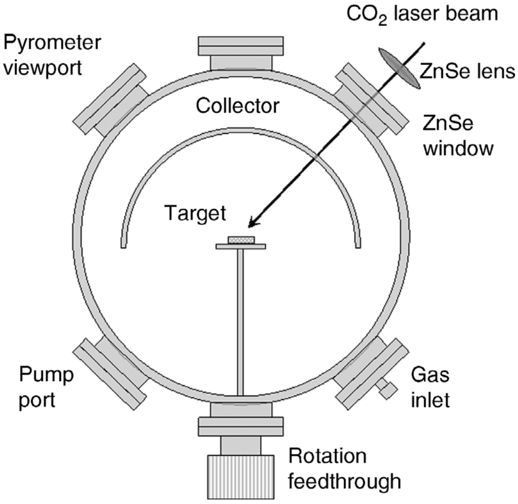
CO_2 laser beam
Pyrometer viewport
ZnSe lens
Collector
ZnSe window
Target
Pump port
Gas inlet
Rotation feedthrough

Figure 9 Schematic of a gas-phase condensation chamber to prepare nanoparticles. A cw-CO_2 laser vaporizes material from a ceramic target in an inert or reactive atmosphere. For scale, the typical target to collector distance is 5–20 cm. (Reprinted from Eilers, H. and Tissue, B.M., *Mater. Lett.*, 24, 261, Copyright (1995), with permission from Elsevier.)

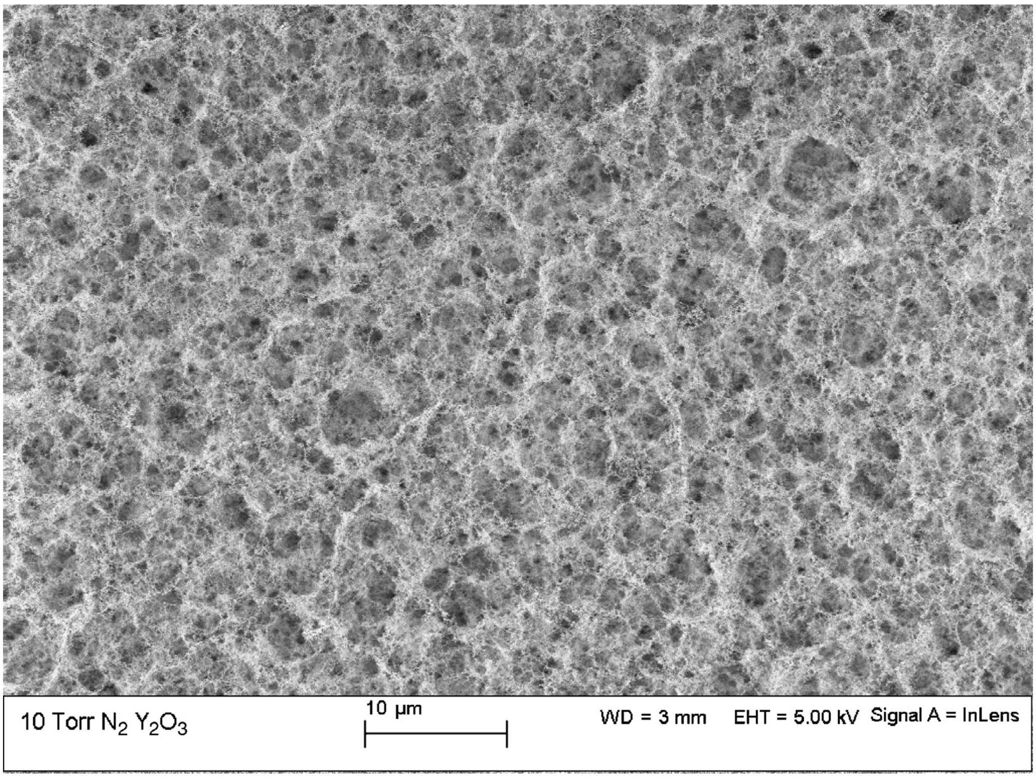
10 Torr N_2 Y_2O_3
10 μm
WD = 3 mm
EHT = 5.00 kV
Signal A = InLens

Figure 10 Scanning electron micrographs of gas-phase condensed Y_2O_3 nanoparticles prepared in a buffer gas of 10 Torr N_2 (W.O. Gordon, and B.M. Tissue, unpublished results).

increase in particle size that results on annealing. Figure 12 also shows the residual aggregation, which can be a problem for gas-phase prepared material in applications where dispersion of single particles is necessary. Many phosphor applications can be met

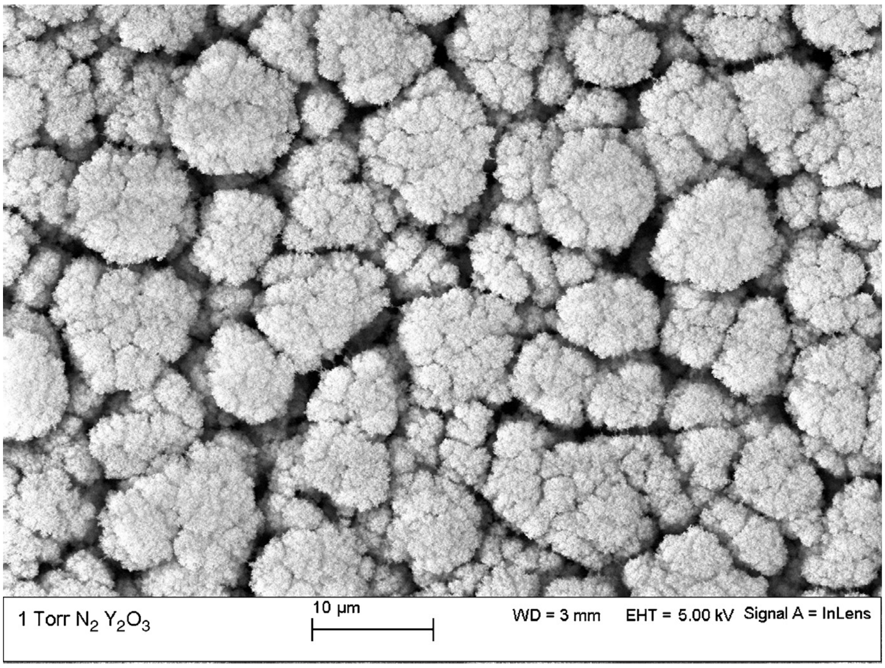

Figure 11 Scanning electron micrographs of gas-phase condensed Y_2O_3 nanoparticles prepared in a buffer gas of 1 Torr N_2 (W.O. Gordon, and B.M. Tissue, unpublished results).

by constructing particles on the scale of tens or hundreds of nanometers; however, new applications such as bioimaging can require smaller particles.[41] Grain growth can be suppressed using appropriate dopants,[42] and recently a two-step sintering process produced a full-density nanostructured yttria ceramic without late-stage grain growth.[43]

Flame and spray pyrolysis and electrospray methods result in more complex particle growth environments, but they provide very flexible methods to prepare a wide variety of nanoparticles.[44] Dopants are easily incorporated into precursors, but as in gas-phase methods, a subsequent anneal might be necessary to improve crystallinity and to optimize optical properties. These methods have the distinct advantage of operating continuously with a suitable collection system, and they have the potential to be incorporated into assembly-line types of production methods and monitoring systems.[26] Electrospray methods provide an additional control parameter as they use electric fields to affect the fine carrier droplets, thereby altering and controlling the morphology, dispersion, and deposition of material. This level of control is useful in placing nanoparticles in nanostructures and it also provides the ability to sort droplets by size.

4.2.1.2.2 Condensed-phase methods. As is the case with gas-phase methods, a large body of work precedes the recent surge of interest in developing new solution-phase methods for preparing nanoparticles. Much of the early work concentrated on preparation of "fine particles" with the goal of controlling the size, crystallinity, and dispersity of the resulting particles very precisely.[45] This early work provides the theoretical foundation to extend these solution-based methods to more complicated materials and to the preparation of self-assembled nanostructures.[46] The following list provides some examples of condensed-phase preparation methods:

- Homogeneous precipitation including sol–gel and hydrothermal methods[47–51]
- Templated synthesis,[52–54] self-assembly,[55,56] and "nanoreactor" synthesis[57–59]

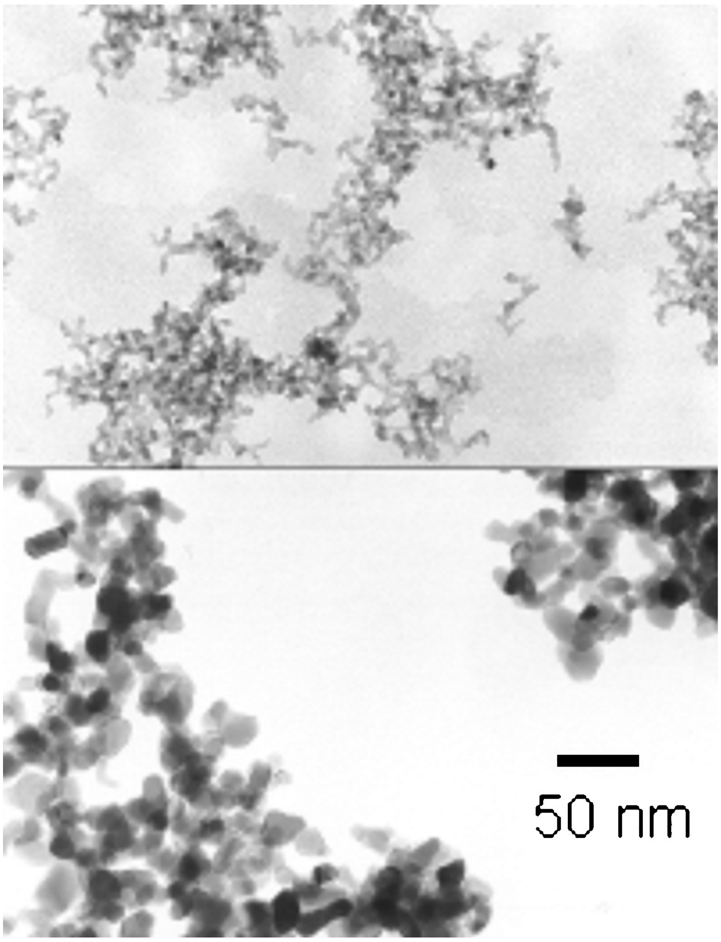

Figure 12 Transmission electron micrographs of Eu^{3+}:Y_2O_3 nanoparticles before and after annealing at 800°C for 24 h. The predominant particle sizes were 5±1 nm and 12±2 nm for the as-prepared and annealed samples, respectively. (Reprinted from Tissue, B.M. and Yuan, H.B., *J. Solid State Chem.*, 171, 12, Copyright (2003), with permission from Elsevier.)

- Combustion synthesis[60,61]
- High-energy mechanical milling[62,63]

The first group of methods are extensions of the well-known solution-phase methods, and the other three approaches are more recent methods.

The simplest solution-phase preparation method is the well-studied homogeneous precipitation. Related to homogeneous precipitation are the sol–gel and hydrothermal methods. Although these two methods are often used as low-temperature routes to incorporate ions and complexes into silica, they can also produce discrete nanoparticles.[64] Nanoscale particles are obtained by careful control of the synthesis conditions, and the reaction is stopped immediately after nucleation and before substantial growth of the particles. Using surfactants or other types of capping agents can aid in the precise control of a reaction, and, for many quantum dot materials, are necessary to protect the material from oxidation. A recent advance in postpreparation size control, demonstrated for some semiconducting materials, is the use of size-selective photoetching to reduce both the size and particle-size distribution of quantum dots.[65]

Extending the capping approach further, a number of synthetic methods use "nanoreactors" or "nanocontainers" to control particle nucleation and growth. An example is the use of solutions of reverse (or inverse) micelles, which are aqueous solutions contained within micelles in a nonpolar solvent. These micelles serve as nanocontainers for precipitation reagents. Mixing the micellar solutions initiates exchange of the micelle contents, with precipitation occurring within a protecting layer of surfactant. Further extending this approach are methods that involve extraction procedures of the resulting particles, such as the emulsion liquid-membrane or water-in-oil-in-water (W/O/W) approach.[66] This approach, like many solution-phase methods, has the advantage of being more easily incorporated into large-scale production methods similar to countercurrent extraction methods. The need for any subsequent annealing of precursor particles does introduce grain growth and can introduce impurities into the particles, which might be desirable or undesirable depending on the applications of the material.

Combustion or propellant synthesis is a popular method to produce gram quantities of phosphor materials. This method is simple and flexible, making it possible to optimize material composition and preparation conditions rapidly. An aqueous precursor solution containing metal salts, typically nitrates that serve as the oxidizer, and a fuel such as glycine is heated slowly in a furnace to evaporate water until rapid combustion occurs. The explosive nature of the reaction results in formation of nanoparticles with no subsequent particle growth. The particle size depends on the reaction temperature, which is controlled by adjusting the fuel-to-oxidizer ratio. Due to the heterogeneous nature of this approach, the synthesis requires careful reagent selection and control of the reaction conditions to minimize quenching entities, most notably hydroxide groups.[67,68] Annealing the as-prepared powders can also improve brightness by eliminating any residual nitrate or carbon. This method is not restricted to oxides and a number of different types of materials have been produced.

4.2.1.2.3 Nanocomposites. In this section, I describe preparation methods for several types of nanoscale structures ranging from nanoparticles embedded in matrices to core-shell particles and nanostructured films. One of the main advantages of producing nanoscale materials for phosphor applications is the possibility of optimizing the local environment for stability and enhanced efficiency and integrating luminescent materials with other device components. Preparing nanoscale composites also creates the potential to develop and investigate the properties of nontraditional optical materials. The reduced optical scattering of nanometer-size particles might permit the use of noncrystalline materials in applications that usually require high-quality crystals or glasses.[69]

A key aspect of applying nanomaterials in technological applications is protecting materials from degradation. The high surface area of nanocrystals compared with micrometer-size particles results in high reactivity and accelerated rates of reaction with water, oxygen, and CO_2. The luminescence intensity of the 10-nm Eu^{3+}:Y_2O_3 nanocrystals prepared by gas-phase condensation decreases by approximately half over a period of several months when stored in a laboratory desiccator. Similarly, the luminescence of many sulfide and selenide quantum dots can decrease rapidly if they are not capped or protected to prevent oxidation. Passivating the surfaces of nanoparticles can be accomplished using chemical reactions to coat or disperse the particles in a polymer or glass matrix.[70] There are a variety of both gas-phase and solution-phase synthesis and processing methods to prepare nanoparticles in polymeric matrices.[71,72] The simplest embedding method disperses nanoparticles in solution and puddles or spin-casts them in a polymer matrix. Very often the surfaces of solution-dispersed nanoparticles are modified chemically to obtain a more intimate dispersion during polymerization reactions.[73] Although capping and passivation coatings can provide protection from environmental degradation, they can also affect optical properties and introduce new reaction pathways at the nanoparticle surface.[74] The effects of surface modification can be detrimental to the optical properties,[75] but it also presents the possibility of embedding nanoparticles in matrices to optimize the physical properties of the composites[76] and introducing sensitizers for luminescent materials.[77]

Nanoparticles can be created in glass matrices by sol–gel methods,[78] or by forming nanocrystals in glass ceramics.[79,80] These materials can achieve optical properties similar to optically active dopants in crystals, but with the processibility and compatibility of a glass host. Sol–gel methods also provide approaches to co-dope molecular and other types of sensitizers in a host with luminescent ions.[81,82] As an example, the luminescence efficiency of europium and terbium benzoates doped into sol–gel silica increased by a factor of ten or more due to the benzoate sensitizer when excited at 290 nm. A similar enhancement, or antenna effect, is observed in self-assembled lanthanide-cored dendrimer complexes.[56] The dendrimer approach has received widespread attention due to the very precise control afforded by the "generational" synthetic approach and the ability to construct supramolecular assemblies.[83,84] Sol–gel techniques have also been used to dope lanthanides in SnO_2 xerogels[85] and in highly porous alumina nanostructured with dimensions of approximately 5 nm.[86] Trivalent lanthanides are difficult to substitute onto Al_2O_3 due to size mismatch between the large lanthanide and the small Al^{3+} cation. The highly porous alumina sample is interesting due to the unique nature of the host and size-resonant vibrations of the nanocrystals, which affect the dynamics of the dopant.[87] Glass–ceramic materials can have similar advantages; for example, preparing doped PbF_2 nanocrystals in silica has the optical characteristics of a crystalline fluoride in a glass matrix.[80]

A variety of methods have been developed for creating core-shell structures.[88] Such structures are useful for passivating or altering the surroundings of an optically active core, for placing an optically active material over a monodisperse support, or for forming a sensitizer–acceptor composite. Kong et al. used a sol–gel process to coat silica spheres with a Zn_2SiO_4:Mn phosphor layer (denoted as Zn_2SiO_4:Mn@SiO_2), which were efficient emitters at 521 nm under UV and electron excitation.[89] After annealing at 1000°C, the Zn_2SiO_4:Mn formed a crystalline shell on an amorphous SiO_2 core. In this case, the core-shell approach allowed preparation of an efficient phosphor material on a "scaffold" to obtain spherical morphology and narrow size distribution. In another example, chemical deposition was developed to produce core-shell particles of Eu^{3+}:Y_2O_3 on an Al_2O_3 core.[90] In this work, the core-shell composite could serve as a precursor for nanoparticles, and annealing between 600 and 900°C formed Eu^{3+}-doped $YAlO_3$ and $Y_3Al_5O_{12}$ nanoparticles. These annealing temperatures were lower than typical sintering temperatures for solid-state reactions of these materials.

A number of synthesis methods used to prepare discrete nanoparticles can be modified to grow nanostructured films. Some common approaches are spray pyrolysis, laser ablation, and chemical-vapor deposition methods.[91] The advantages of direct deposition of a luminescent thin film, compared to using particulate material, for display phosphors include better adhesion, lower outgassing, and higher resolution.[92] Field emission devices (FEDs) produce a high current density, and therefore create a higher heat load compared to conventional cathode ray tubes. Solid films can dissipate this heat load better than particulate films and reduce degradation problems and thermal quenching of the luminescence.[93] Films of Eu^{3+}:Y_2O_3 can achieve luminescence efficiencies which approach that of commercial phosphors, although many of the as-deposited films require high-temperature annealing.[92] Many factors, in addition to the quantum efficiency of the material or dopant, determine the overall luminescence efficiency of phosphor films. For example, the luminescence efficiency of Eu^{3+}:Y_2O_3 films prepared by pulsed-laser deposition on diamond-coated Si substrates was approximately a factor of two higher than that of films deposited directly on Si. The increase was attributed to reduced internal reflections due to a rough surface morphology produced by the diamond layer, and the best film (annealed at 700ºC) had 80% of the brightness of Eu^{3+}:Y_2O_3 powder.[94] As a final note, metalorganic chemical vapor deposition (MOCVD) methods have also proven useful for preparing luminescent films that are difficult to prepare or dope by other methods.[95] For preparing AlN:Eu films, an oxygen-activation method replaces high-temperature annealing, making the material synthesis compatible with other types of preparation methods for forming nanocomposites.

4.2.1.3 Material characterization and analysis

This section discusses various analytical methods to determine particle size, morphology, and phase purity. Key material parameters required to understand, control, and correlate material properties with optical performance include the average particle diameter and particle-size distribution (or feature dimension for nanostructures), crystallinity, and material shape or morphology. As sizes decrease below 10 nm, the percent variation in a distribution of only ±1 nm becomes quite significant. As an example, the peak emission wavelength of CdSe quantum dots changes from 550 to 650 nm when the particle size increases from 3 to 7 nm in diameter.[153] Obviously, the emission width will be very sensitive to the monodispersity of the nanoparticles.

Characterizing particle or feature size for nanocrystals and nanostructures is done routinely using scanning transmission electron microscopy (STEM), high-resolution transmission electron microscopy (HRTEM), scanning electron microscopy (SEM), scanning tunneling microscopy (STM), and atomic force microscopy (AFM).[96] TEM methods usually require dispersion of the particles, but, of all the microscopy methods listed here, HRTEM can provide the best spatial resolution of better than 0.2 nm.[97] Furthermore, the high-resolution imaging can identify defects and surface structures. An important aspect of the direct imaging methods is that they will reveal the shapes of nanomaterials, which can affect the optical characteristics of many types of materials.[11,98] AFM is being used more frequently, although preparing atomically thin AFM tips to image particles or features less than 10 nm can be very difficult. AFM has the potential to provide spatially resolved chemical information. The main advantage of SEM, STM, and AFM methods is that they can be used to study the morphology of as-prepared nanoparticles and nanocomposites. Direct size measurements obtained from images are often used in conjunction with other measurements such as powder X-ray diffraction (XRD) line widths and BET (Brunauer–Emmett–Teller) surface area measurements. These methods provide additional information on domain size (using XRD) and the fraction of contacted surface area, for example, in interparticle necks (using BET).

Combining diffraction and imaging characterization tools can provide a complete picture of the crystal phase, average particle diameter, particle-size distribution, and the morphology of the samples. Crystal phase confirmation and purity can be obtained by using powder XRD[99] and selected-area electron diffraction (SAED). SAED can analyze single nanoparticles that are 10 nm and larger.[100] Figure 13 compares the powder XRD patterns of two gas-phase condensed samples of Eu_2O_3 nanoparticles to a reference diffraction pattern of cubic Eu_2O_3. The two nanoscale samples were prepared at different buffer gas pressures to obtain different particle sizes. The XRD patterns show a clear difference in the structure compared with bulk cubic-phase Eu_2O_3 and also a difference in the amount of disorder between the two nanoparticle samples. Similarly, using electron diffraction patterns in TEM or the interference fringes in HRTEM images can also confirm the crystal phase of individual nanoparticles. In some cases, it is possible to correlate the phase and structural information obtained from microscopy and diffraction measurements with the optical properties.[101]

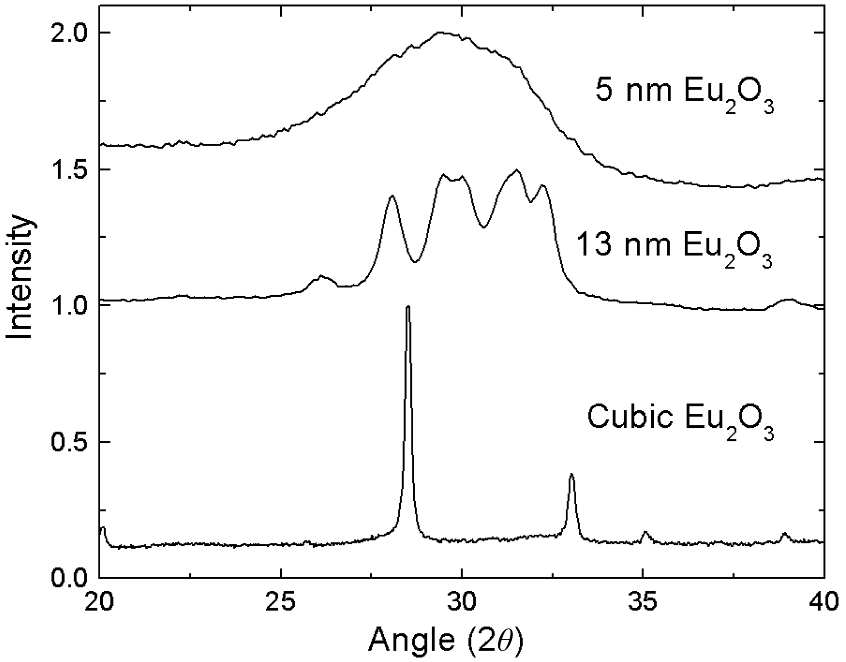

Figure 13 Powder X-ray diffraction patterns of two samples of nanoparticles of Eu_2O_3 prepared by gas-phase condensation and bulk cubic phase Eu_2O_3. (Reprinted from Eilers, H. and Tissue, B.M., *Mater. Lett.*, 24, 261, Copyright (1995), with permission from Elsevier.)

4.2.1.4 Optical spectroscopy for material characterization

Complete characterization of materials requires elemental analysis, which is often performed in an electron microscope using energy-dispersive X-ray spectrometry (EDXS) or by surface analytical techniques such as X-ray fluorescence, Auger electron spectroscopy, and X-ray photoelectron spectroscopy (XPS). XPS, extended X-ray absorption fine structure (EXAFS), and electron energy loss spectroscopy (EELS) can provide further details about the surface chemistry, structure, and local environment.[102] Elemental and qualitative analytical techniques are also necessary to identify intentional adsorbates or unintentional contaminants on a particle surface. Molecular spectroscopy such as Raman spectroscopy and Fourier transform infrared (FTIR) spectroscopy can characterize materials and help identify any surface contaminants or intentional capping agents. For example, shifts in the Raman lines in Y_2O_3:Eu^{3+} have been correlated with particle size and attributed to local surface strain.[103] Similarly, FTIR, nuclear magnetic resonance (NMR), Raman, UV-vis absorption, fluorescence, and other solution-phase characterization spectroscopies are useful for characterizing material precursors.[104]

As phosphors have strong optical emission, luminescence is a natural tool for characterizing materials, structures, and performances of phosphors. As noted above, optical spectroscopy can provide a sensitive measure of particle size, size distribution, and particle shapes for quantum dots and metals. Lifetime measurements can provide complementary information for characterizing multiple phases, defects, quenching, and environment effects. Although luminescence spectra, lifetimes, and quantum-efficiency measurements can be made with laboratory-scale spectrometers utilizing optical photons, electrons, or X-rays as excitation sources, detailed studies using vacuum-UV excitation may require sophisticated excitation sources.[105] Optical spectroscopic measurements are quite important to determine color purity and quantum efficiency of phosphor materials; however, the rest of this section concentrates on spectroscopic measurements that are applied to material characterization.

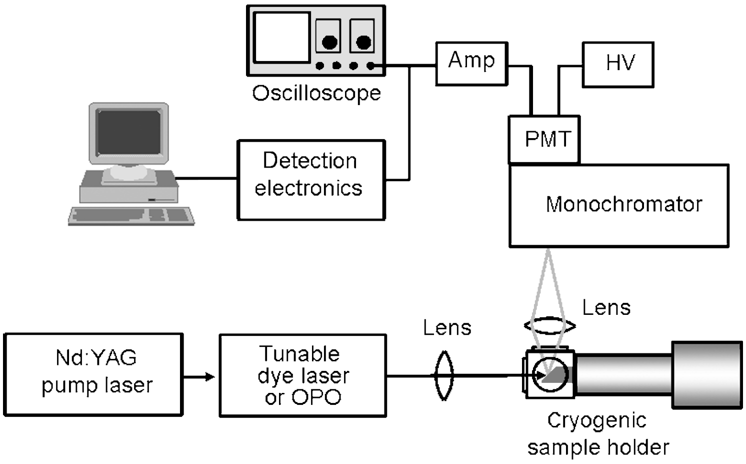

Figure 14 Schematic of an experimental setup to record laser-excited luminescence spectra and transient decay curves. The low-temperature capability provides greater detail for material characterization.

For the purpose of material characterization, samples are often cooled to low temperature (<77 K) to enhance the sensitivity and resolution in the optical spectra. Figure 14 shows a schematic of a typical laboratory-scale experimental setup for optical spectroscopy. A narrow line width laser can selectively excite an individual feature in an absorption spectrum to obtain high-resolution fluorescence spectra and time-resolved fluorescence transients. Similarly, disordered systems can be characterized by recording line-narrowed fluorescence spectra as the laser is tuned across the distribution of different sites. Absorption lines that produce the same fluorescence spectrum and fluorescence lifetimes are assigned to the same dopant phase or environment. The number of spectral lines, splitting pattern, the lifetime, and observations of energy transfer give clues to the local nature of each site. As an example, Figure 15 shows multiple phases in unannealed Eu^{3+}:Y_2O_3 nanoparticles prepared by gas-phase condensation. Recording the spectrum at low temperature was crucial to avoid broadening that would have obscured some of the line.

Spectroscopic studies range from basic luminescence spectroscopy and quantum efficiency measurements to high-resolution spectroscopic studies that investigate phonon dynamics and electron–phonon interaction as a function of particle size. For quantum dots and insulating materials doped with lanthanide and some transition metal ions, luminescence can serve as a sensitive probe of their local environment for material characterization. For lanthanide dopants, the position of the energy-level multiplets do not vary significantly from host to host, but the splitting patterns of the multiplets depend on the local site symmetry and crystal field. The optical spectra therefore consist of sharp lines that are characteristic of the local environment and serve as sensitive microprobes of the crystallographic sites the dopant occupies in the host. The luminescence dynamics depend on ion–lattice (electron–phonon) and ion–ion interactions and on the phonon spectrum of the host. Clustering of the lanthanide dopant changes the degree of ion–ion interactions, and therefore serves as a diagnostic to study dopant segregation or defect chemistry in a material.[106] Optical spectroscopy can therefore contribute to the understanding of the structure, phase distribution, crystallinity, phonon spectrum, electron–phonon interactions, and dopant distribution in nanostructured materials. Luminescence measurements are sensitive enough to detect a small number of emitting ions, as demonstrated by photoluminescence studies of thin films,[91] and they are sensitive to defect equilibrium,[106] phase transformations,[107,108] and the degree of disorder or crystallinity.[109] These spectroscopic studies can also be used to monitor the effects of material processing such as thermal

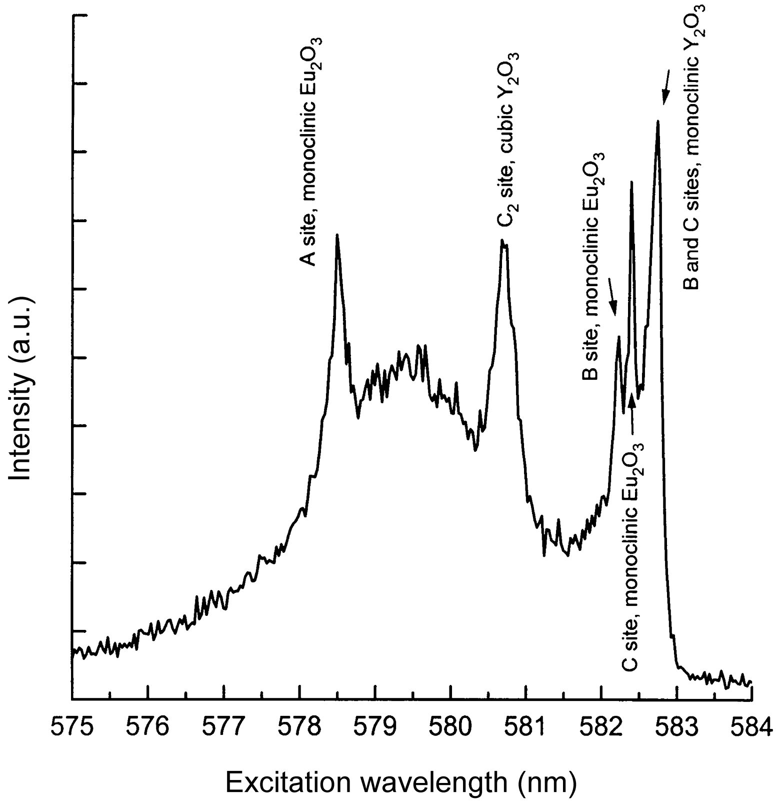

Figure 15 Low-temperature $^7F_0 \rightarrow {}^5D_0$ excitation spectrum of 5-nm $Eu^{3+}:Y_2O_3$ particles prepared by gas-phase condensation. The monoclinic phase has three sites labeled A, B, and C. Only the C_2 site of the cubic phase is observed for this transition, and the broad band at 579.4 nm is attributed to a disordered phase. (Reprinted from Tissue, B.M. and Yuan, H.B., *J. Solid State Chem.*, 171, 12, Copyright (2003), with permission from Elsevier.)

annealing, laser treatment, and plasma etching. As an example, Figure 16 shows the spectrum of $Eu^{3+}:Y_2O_3$ nanoparticles as a function of annealing temperature. These results, coupled with particle-size measurements, can show the optical characteristics for the acceptable degree of grain growth on annealing.

A very recent development in spectroscopic instrumentation is the ability to perform single-molecule or single-particle spectroscopy.[110] Such measurements can be performed using conventional and confocal fluorescence microscopes,[111] and with apertured or apertureless near-field scanning optical microscopy (NSOM).[112,113] Often the spatial resolution is dependent on the dispersion of single particles, since the nanoparticles are often smaller than the intrinsic resolution of the microscopes. Concurrent measurements of particle size with an AFM can be correlated with the results obtained using single-particle spectroscopy. Single-particle studies can remove the broadening and averaging that is inherent when exciting an ensemble of particles, and they can reveal interesting photophysics such as the blinking observed in quantum systems.[111,114]

4.2.2 Size-dependent optical effects

4.2.2.1 Introduction

One of the major driving forces for studying luminescent nanoparticles and nanostructures is the potential to use their size- and surroundings-dependent properties to optimize the

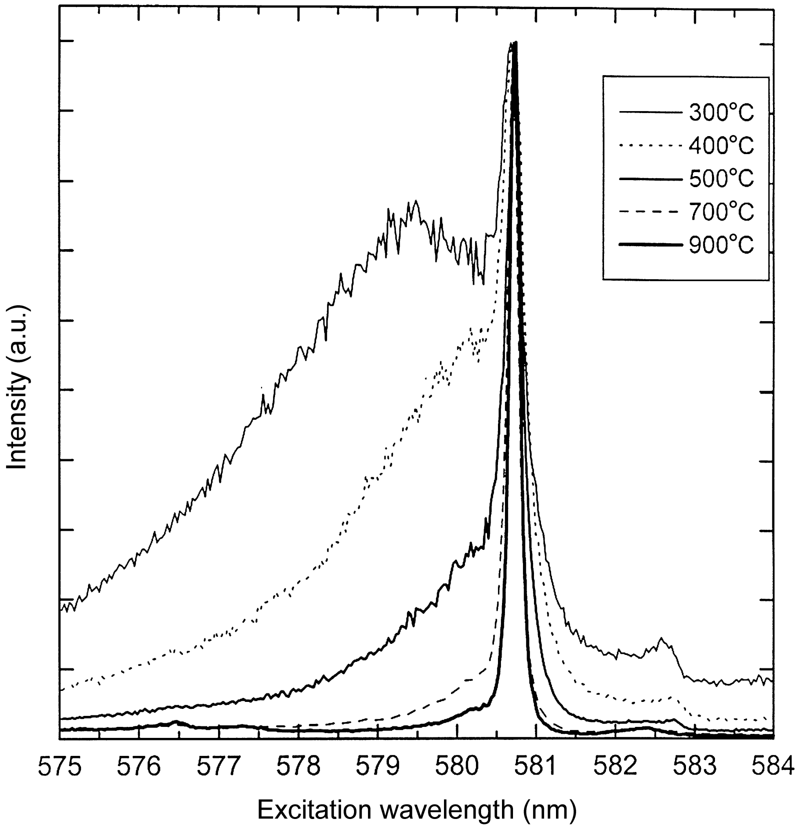

Figure 16 Low-temperature $^7F_0 \rightarrow {}^5D_0$ excitation spectra of 5-nm $Eu^{3+}:Y_2O_3$ particles as a function of annealing temperature. Anneal time for all samples was 24 h. The sharp peak at 580.7 nm is due to cubic phase $Eu^{3+}:Y_2O_3$. (Reprinted from Tissue, B.M. and Yuan, H.B., *J. Solid State Chem.*, 171, 12, Copyright (2003), with permission from Elsevier.)

spectral and dynamic properties of materials for technological applications. Work done during and since the 1990s has produced a fundamental understanding of the size dependence of luminescence for nanoscale metals, semiconductors, and doped materials. A number of phenomena remain to be explored more fully, especially those involving coupling, enhancement, and energy transfer of luminescent materials and centers within complex nanostructures. Luminescence efficiency of a material is often limited by multiple dynamic pathways that are sensitive to interactions with the host or surroundings.[115] Placing a luminescent center in a complex matrix introduces multiple avenues for the chemical and physical properties of the surroundings to affect luminescence. The dependence on the surroundings can be beneficial or detrimental depending on the application of the luminescent material. For example, sensitivity of luminescence to the surroundings, including enhancement or quenching strategies, which might be quite detrimental for a display phosphor could develop into an entirely new platform for creating chemical or biological assays or sensors. This section discusses some of the factors that affect how the particle dimensions, composition, processing, and morphology of a host affect the optical properties of a lanthanide dopant.

4.2.2.2 Structural and dopant distribution effects

4.2.2.2.1 Structural effects on spectra. Nanocrystals can form in new or metastable phases,[116] be distorted from the usual crystal phase, or have anisotropic shapes.[98] These physical differences can affect both the spectral and dynamics of luminescence.[117] As a relevant phosphor host example, micrometer-sized Y_2O_3 is stable in the cubic phase at ambient conditions, and the metastable monoclinic phase is obtained only by quenching Y_2O_3 powders from high temperature and under high pressure. Formation of the monoclinic structure in Y_2O_3 nanoparticles has been attributed to the Gibbs–Thomson effect, in which the increased surface tension converts the particle to the denser metastable phase. Subsequent work using a variety of preparation and annealing procedures have produced Y_2O_3 nanoparticles in both the cubic and monoclinic phases,[118–122] indicating that the resulting phase can probably depend on a number of factors during sample preparation and annealing. Some factors that can affect the resulting structure include the preferred faceting of nanocrystals, the presence of necks between particles,[123] and the significance of surface and adsorbate energies due to the very high surface-to-volume ratio.[99,124] During annealing of nanoparticles, resulting phases can be affected depending on the starting material—loose or compacted powders—and whether the initial particle-size distribution spans a critical particle size.[125] Work on Eu_2O_3 produced an optical spectra containing lines for the three crystallographic lattice sites of the monoclinic phase for 18 nm particles, and a broadened spectra, similar to the broad band in Figure 15 and Figure 16, for 4 nm particles.[126] On annealing, the 18-nm particles retained the monoclinic phase, but the smallest particles converted to the cubic phase. The possibility of a critical size in determining crystal structure, disorder, etc., will be a factor in the resulting optical properties.

4.2.2.2.2 Dopant distribution and segregation. From a fundamental standpoint, nanocrystals can provide model systems for studying luminescence from surfaces. The high surface-to-volume ratio of nanoparticles results in a significant fraction of all atoms in the particle being at or near a surface approximately 30–50%, as particle diameters approach a few nanometers. The high surface-to-volume ratio of nanoscale particles makes it possible to detect luminescence from ions at a surface, which is not possible in micrometer-size particles due to the overwhelming signal from ions in the interior of the particles. From a more practical standpoint, the details of the surface structure and chemistry can have a significant effect on the nonradiative decay pathways.[15] A number of optical spectroscopic studies have now correlated spectral changes with dopant ions at a particle surface. An early investigation studied high-surface-area Eu_2O_3 (≤100-nm diameter) prepared by thermal dehydration of $Eu(OH)_3$.[127] The intensity of the Eu^{3+} in the S_6 crystallographic site decreased compared with the C_2 site on exposure to water. The authors credit the change to the preferential chemical attack of water on the S_6 cation site. Observing this change would be unexpected for large particle sizes due to the large luminescence signal from ions in the interior of the particles, which obscure changes at the surfaces.

Depth profiling types of analysis, such as time-of-flight secondary ion mass spectrometry (TOF-SIMS), provide independent tools to measure dopant distribution in phosphor nanoparticles. Chakraborty et al. found a homogeneous distribution of dopants in $ZnS{:}Mn^{2+}$ and $Gd_2O_2S{:}Pr^{3+}$, but a much less homogeneous distribution in $SrAl_2O_4{:}Eu^{2+},Dy^{3+}$.[128] Doping of transition metals onto quantum dots, such as the $ZnS{:}Mn^{2+}$ example, is generally assumed to be distributed uniformly. Doping larger lanthanide ions into small lattice sites is more problematic. A large amount of work has been published on lanthanide luminescence from semiconductors such as ZnO. Recent work suggests that the lanthanides are not in the semiconductor lattice but are primarily on the surfaces or in the secondary phases.[129] For some lanthanides, the energy transfer from ZnO to the lanthanide can be efficient. Similar results have been found for a variety of synthesis methods for doping Eu^{3+} and Tb^{3+} in ZnS and CdS.[130]

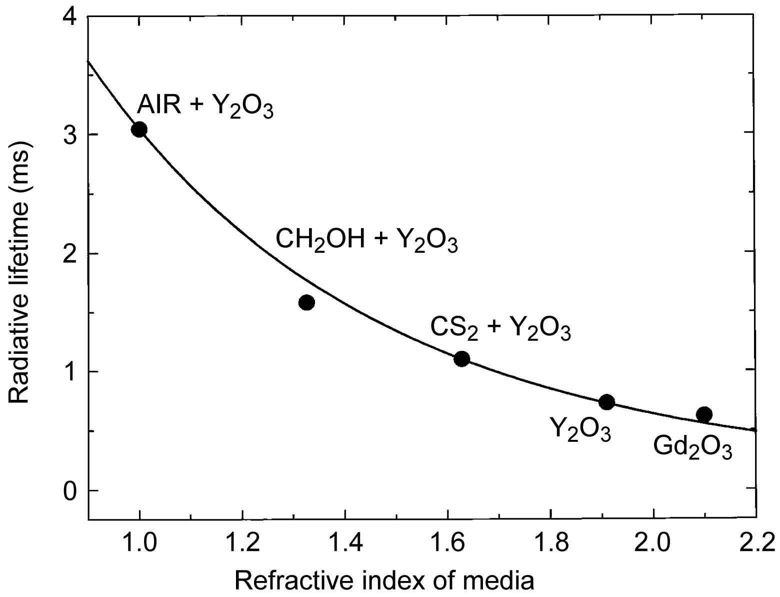

Figure 17 Room-temperature $^5D_0$ lifetime of cubic-phase Eu^{3+}:Y_2O_3 as a function of refractive index of the surroundings. The three left-most data points are for the 7-nm Eu^{3+}:Y_2O_3 particles dispersed in air, methanol (CH_3OH), and carbon disulfide (CS_2). The two right-most data points are for Eu^{3+} in bulk Y_2O_3 and Gd_2O_3. (Reprinted with permission from Meltzer, R.S., et al., *Phys. Rev. B*, 60, R14012, Copyright (1999) by the American Physical Society. http://prola.aps.org/abstract/PRB/v60/i20/pR14012-1)

4.2.2.3 Dynamic effects

Preparing phosphor materials in nanoscale forms creates problems due to sensitivity in the luminescence dynamics, which is not present for bulk materials. The luminescence dynamics, including quantum efficiency, can be affected by size-dependent effects on both radiative and nonradiative decay rates. The changes in radiative rates occur due to a dependence on the surroundings of the luminescent material or dopant.[75,131] Figure 17 shows the measured decay times of Eu^{3+}:Y_2O_3 nanoparticles dispersed in different media. The data could be explained by finding a filling factor between the nanoparticles and surroundings to find an effective refractive index of the Eu^{3+} surroundings.[131] This effect due to the surroundings is anticipated to be significant when the luminescence lifetime is dominated by radiative decay.

Changes in nonradiative rates can occur due to greater surface quenching or clustering and due to changes in the host phonon spectrum and in the electron–phonon interaction. These size-dependent changes in the optical properties can be very important for the technological applications of emissive materials. For example, reducing the particle size could be deleterious if close proximity of dopant ions to a relatively higher concentration of surface defects increases the quenching of optical emission.[149] A high surface-to-volume ratio is expected to affect the dopant and defect distributions between the interior, surface, and exterior (secondary phases) of the particles. Nanoscale materials provide the ability to control these defects to prepare energy-efficient phosphor materials. Ye et al. report changes in the charge-transfer excitation spectrum as a function of particle size, which is attributed to surface effects.[132] For 70-nm diameter particles, they also report that the Eu^{3+} concentration can reach 14% before the onset of concentration quenching, which is double the onset concentration of 6–8% for conventional phosphor material. This difference is attributed to a reduced energy-transfer rate due to the interfaces, so that less energy can migrate to quenching sites. The change in concentration quenching also suggests that the close proximity of the surface does not introduce a large number of quenching surface defects. Models of energy transfer average a distribution of distances between donor and acceptor sites, which might not be true in nanoscale systems. The observation of decay curves changing from multi- to single-exponential decays as particle size decreases to >6 nm for Eu_2O_3 nanoparticles supports this hypothesis.[133] Presumably, the distribution of cross-relaxation rates disappear for the smallest particle diameters by essentially eliminating the distribution of distances between the Eu ions. Donor–acceptor transfer in MBE films has also been observed to be modified due to restricted geometry and to become less effective in 2D geometry.[134] Energy transfer through space has been used to measure distances as great as approximately 8 nm in molecular systems.[135,136] Studying energy transfer between lanthanides in different host particles with dimensions of less than 10 nm will no doubt require a different theory than that for bulk materials.

Low-temperature work has shown a bottlenecking effect in the nonradiative decay of lanthanides in nanoparticles, seen experimentally as an increased intensity of hot-band absorptions.[137–139] Theoretical predictions show that the phonon density-of-states and the electron–phonon interactions are strongly modified in nanometer-size particles.[140] Whether such bottlenecking effects can be utilized to increase efficiency in phosphor materials operating at room temperature or higher is unknown. These same types of effects can also affect phonon-assisted energy transfer between dopants in nanoparticles.[141] Related to donor–acceptor energy transfer is interparticle luminescence enhancement or quenching due to surface plasma resonance (SPR) effects with metal nanoparticles.[142] The interparticle distance is obviously of importance in such nanocomposites, since some results show energy transfer from the metal to the luminescent emitter,[143] but other results show energy transfer from Eu^{3+} to Au nanoparticles.[144] Other work on nanocomposites containing metals and luminescent centers attribute differences in luminescence efficiency to local-field enhancements from surface plasmon resonance.[145,146] Research on energy transfer and enhancement in nanomaterials is at an early stage, and adapting appropriate theories to the details of nanocomposites is necessary to produce a clear understanding of such phenomena.

4.2.3 Applications

4.2.3.1 Introduction

Luminescent materials find a wide variety of applications as phosphors for fluorescent lighting,[147] display devices,[148] X-ray monitoring and imaging,[149] scintillators,[150] analytical assays,[151] and biomedical imaging.[152,153] Although outside the scope of this section, many of the materials discussed here also have promise as new or enhanced materials in related optical applications such as lasers,[154,155] solar-energy converters,[156] and optical amplifiers.[157] As display and lamp phosphors are discussed in detail elsewhere in this handbook, most of the following discussion concerns new applications of inorganic phosphors in analytical assays and bioimaging. Here I merely comment on some distinct advantages and issues of using nanoscale phosphors for lighting, displays, and related applications. Nanoparticles and nanostructured films of phosphor materials have obvious advantages for greater spatial resolution in high-definition displays.[158] Obtaining comparable efficiencies similar to micrometer-size phosphor materials will require optimizing the crystallinity, morphology, and stoichiometry of the material,[159] as well as the dependence on size and surroundings of the radiative and nonradiative decay rates as discussed above. The size of nanoscale phosphors can also change their excitation efficiency for different portions of the electromagnetic spectrum,[160] and plasma excitation sources have created more interest in vacuum-UV properties. Another promising application for nanostructured materials is, similar to phosphors, in FEDs.[161] These flat-panel displays use a cold-cathode (<1 keV) electron emitter tip to excite the phosphor screen. Luminescent nanostructured materials are attractive for FED applications because their small size allows complete penetration by the low-voltage electrons for efficient material utilization. The close proximity of the phosphor particles to the emitter tips requires that the phosphor does not outgas or sputter material that will poison the tips, and the high current excitation requires phosphors with low thermal quenching.[162] In addition to lamps and optical displays, a number of phosphor materials are used for long-persistence phosphors, thermometry,[163,164] and radiation dosimetry.[165] Thermoluminescence kinetics have been found to be different in nanoparticles,[166] and in one report the nanoscale material did not saturate as readily as microcrystals, giving the nanomaterials a larger dynamic range.[167]

4.2.3.2 Analytical assays and imaging

The small size and solubility of nanoscale materials makes it possible to replace molecular fluorophores with more robust phosphor particles, and a large amount of research effort is focused on preparing and characterizing luminescent nanoparticles for analytical and biomedical applications.[168] Affinity assays and immunoassays typically use molecular fluorophores or luminescent complexes as fluorescent tags, called reporters, for testing in environmental, food quality, drug, and biomedical applications. There are a variety approaches for using the luminescent probe, but a typical sandwich-type of assay is to immobilize the analyte or antigen on a supported nonspecific antibody and then to add an analyte-specific antibody that has the luminescent reporter attached. Measurement of luminescence after rinsing away unbound reporter provides a quantitative measure of the analyte concentration. Detection and quantitation of the analyte can be made based on a number of variations, including luminescence intensity (or quenching), energy transfer, and polarization anisotropy. Similar strategies to obtain selective binding and luminescence are used in bioimaging, with images being recorded in a fluorescence or confocal microscope.[169–171] The small size of luminescent inorganic nanoparticles allows them to replace fluorescent molecules or complexes in analytical applications and they might provide some unique advantages due to their size in relation to other materials and biological tissues.[172]

The longer lifetime and greater photostability of inorganic phosphors provides a significant advantage compared to molecular fluorophores in discriminating against background autofluorescence,[173,174] and using lanthanide-doped nanoparticles permits near-infrared (NIR) excitation of upconverted luminescence to avoid autofluorescence completely.[175–177] In general, the size tunability of quantum dot luminescence provides greater advantages when a number of discrete reporters are desired. For applications where background noise is problematic, lanthanide-doped materials with their longer lifetime and upconversion possibilities can perform better. In any given application, the details of the analysis will determine the best approach.

Using parallel detection and array-based diagnostics can provide a large gain in analytical efficiency, and a number of methods, e.g., Dip-Pen nanolithography, are being developed to create nanoarrays.[178] In addition to the long lifetime, other considerations for optimum application of luminescent nanoparticles in multispectral immunoassays include finding multiple reporters with distinct emission wavelengths to attach to different antibodies and having a common excitation wavelength for the different reporters. One example is shown in Figure 18. The Gd_2O_3 host absorbs UV excitation and the several different lanthanide dopants provide three-color capability. In this example, Dy^{3+} is the limiting reporter in applications with high background noise due to the shorter lifetime (on the order of 100 μs) compared with Tb^{3+} and Eu^{3+}.[179] Similar multicolor sets of materials have been developed with the advantage of upconverted luminescence.[180] These materials were ligand capped for dispersion in organic solutions and contained an Yb^{3+} co-dopant to provide a common excitation wavelength in NIR.

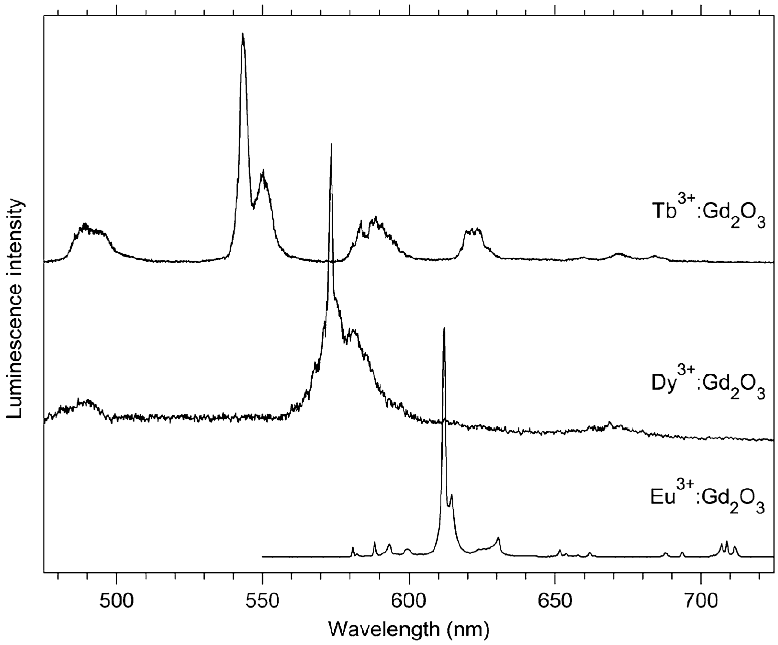

Figure 18 Luminescence spectra of lanthanide-doped Gd_2O_3 nanoparticles excited with a pulsed laser at 266 nm. Nanoparticles were annealed at 700°C for 1 h, resulting in grain growth to 10–15 nm. (Reprinted from Gordon, W.O., Carter, J.A., and Tissue, B.M., *J. Lumin.*, 108, 339, Copyright (2004), with permission from Elsevier.)

Despite the advantages of luminescent nanoparticles, there are several challenges to their use in analytical applications. Size-dependent effects can cause inhomogeneous spectral broadening due to disorder or heterogeneous dopant distribution, the luminescence dynamics can be sensitive to surface quenching and surroundings, and the nanomaterials must be sufficiently small and soluble to not alter the activity or solubility of the antibodies. The nanoparticles must also be attached to antibodies or other entities. A number of approaches have demonstrated effective surface chemistries for protecting the luminescent core, increasing solubility, and providing linkages to conjugate antibodies. Using core-shell approaches can form a solubilizing protective layer on the luminescent material, and also provide linking sites on the surface without loss of luminescence intensity (e.g., polysiloxane).[181] Nichkova et al. developed their materials to the point of using microcontact printing to create microarray immunoassays for use in confocal fluorescence microscopy.[151] The use of energy transfer or metal enhancement effects has been applied in assays and in sensing with molecular fluorophores for some time.[182] These effects are also observed for inorganic nanoparticles (see Section 3.3) and such approaches might lead to even more robust and flexible analytical methods for nanoscale inorganic phosphors.

4.2.4 *Summary and prospects*

Active research in nanostructured materials has resulted in a wide variety of new synthetic methods to prepare pure and doped luminescent materials. Continued development of new methods and refinement of existing methods are necessary to eliminate the need for high-temperature annealing and to develop scale-up procedures for preparing large quantities of nanoparticles. The defect and dopant chemistry in nanostructures is still an active area of research. I believe that strategies to control the location, distribution, or segregation of dopant ions in nanoparticles and multiple phases in nanocomposites have the potential for preparing high efficiency and robust phosphors for diverse applications. As many of the examples throughout these sections demonstrate, the potential for greater control of the optical properties of luminescent nanoparticles goes hand-in-hand with a greater sensitivity to detrimental effects of the surface and surroundings.[15] As the development of nanoscale inorganic phosphors for analytical applications has shown, many of these issues can be overcome with passivation methods.

The theoretical understanding of the size-dependent optical properties of isolated nanoparticles has made significant progress recently, and many issues concerning size-dependent spectral and dynamic phenomena have been identified.[11–13,183] That is not to say that the optical properties of any given material are predictable, especially for nanocomposites where there can be a distribution in morphologies or in the interactions between materials, which make optical properties very sensitive to interparticle distances. However, the advances in imaging and analytical methods provide the tools to correlate material characteristics and size-dependent optical properties for controlling the detrimental effects and optimizing performance in technological devices.

As a final comment, a number of recent news reports have questioned the safety of nanomaterials and nanotechnology. Although many scientists consider nanotechnology as the latest chapter in the evolution of scientific progress, history has shown that any new technology can have unintended and unpredictable effects on human health and the environment. Even more unpredictable is the public response to advances, with genetically modified foods being a recent example. The interest in studying and communicating the health and safety issues of nanotechnology at an early stage is a prudent response to past problems, because it is more easily addressed during the research and development stages than after the introduction of new materials in the marketplace.[184,185] As far as phosphor applications are concerned, most applications do not entail exposure of material to consumers, but nanoparticle preparations can pose hazards similar to those known for other ultrafine particles used or produced in other technologies.[186]

References

1. Suryanarayana, C., Nanocrystalline materials, *Inter. Mater. Rev.*, 40, 41, 1995.
2. Hadjipanayis, G.C. and Siegel, R.W., Eds., *Nanophase Materials: Synthesis–Properties—Applications; NATO ASI Series E*, Vol. 260, Kluwer, Dordrecht, 1993.
3. Komarneni, S., Nanocomposites, *J. Mater. Chem.*, 2, 1219, 1992.
4. National Materials Advisory Board, *Research Opportunities for Materials with Ultrafine Microstructures*, National Academy Press, Washington, DC, 1989; Andres, R.P., et al., Research opportunities on clusters and cluster-assembled materials, *J. Mater. Res.*, 4, 704, 1989.
5. Gleiter, H., Nanocrystalline materials, *Prog. Mater. Sci.*, 33, 223, 1989.
6. Komarneri, S., Parker, J.C., and Hahn, H., Eds., *Nanophase and Nanocomposite Materials III, MRS Symp. Proc.*, Vol. 581, Materials Research Society, Warrendale, PA, 2000.
7. Gonsalves, K., et al., *Surface Controlled Nanoscale and Microscale Materials for High Value Added Applications*, *MRS Symp. Proc.*, Vol. 501, Materials Research Society, Pittsburgh, 1998.
8. Di Ventra, M., Evoy, S., and Heflin Jr., J.R., Eds., *Introduction to Nanoscale Science and Technology*, Springer, New York, 2004.
9. Ratner, M.A. and Ratner, D., *Nanotechnology: A Gentle Introduction to the Next Big Idea*, Prentice Hall, Upper Saddle River, NJ, 2003.
10. Editors of Scientific America, *Understanding Nanotechnology*, Warner Books, New York, 2002.
11. Hao, E., Schatz, G.C., and Hupp, J.T., Synthesis and optical properties of anisotropic metal nanoparticles, *J. Fluoresc.*, 14, 331, 2004.
12. Murphy, C.J., et al., Anisotropic metal nanoparticles: Synthesis, assembly, and optical applications, *J. Phys. Chem. B*, 109, 13857, 2005.
13. Murphy, C.J. and Coffer, J.L., Quantum dots: A primer, *Appl. Spec.*, 56, 16A, 2002.

14. Bunzli, J.C.G. and Piguet, C., Taking advantage of luminescent lanthanide ions, *Chem. Soc. Rev.*, 34, 1048, 2005.
15. Abrams, B.L. and Holloway, P.H., Role of the surface in luminescent processes, *Chem. Rev.*, 104 5783, 2004.
16. Efros, A.L. and Rosen, M., The electronic structure of semiconductor nanocrystals, *Ann. Rev. Mater. Sci.*, 30, 475, 2000.
17. Nirmal, F. and Brus, L., Luminescence photophysics in semiconductor nanocrystals, *Acc. Chem. Res.*, 32, 407, 1999.
18. Brus, L.E., Efros, A.L., and Itoh, T., Eds., *Spectroscopy of isolated and assembled semiconductor nanocrystals*, special issue of *J. Lumin.*, 70, 1996.
19. Gaponenko, S.V., *Optical Properties of Semiconductor Nanocrystals, Cambridge Studies in Modern Optics*, Cambridge University Press, Cambridge, 2005.
20. Klimov, V.L., Ed., *Semiconductor and Metal Nanocrystals: Synthesis and Electronic and Optical Properties*, Marcel Dekker, New York, 2003.
21. Efros, A.L., Lockwood, D.J., and Tsybeskov, L., Eds., *Semiconductor Nanocrystals: From Basic Principles to Applications*, Kluwer, New York, 2003.
22. Heitmann, J., et al., Silicon nanocrystals: Size matters, *Adv. Mater.*, 17, 795, 2005.
23. Vial, J.C., Canham, L.T., and Lang, W., Eds., Proceedings of the Symposium on Light Emission from Porous Silicon, *J. Lumin.*, 57, 1993.
24. Masala, O. and Seshadri, R., Synthesis routes for large volumes of nanoparticles, *Ann. Rev. Mater. Res.*, 34, 41, 2004.
25. Hahn, H., Gas phase synthesis of nanocrystalline materials, *Nanostruct. Mater.*, 9, 3, 1997.
26. Swihart, M.T., Vapor-phase synthesis of nanoparticles, *Curr. Opin. Colloid Interface Sci.*, 8, 127, 2003.
27. Lindackers, D. and Roth, P., Formation of ceramic oxide nanoparticles in low pressure flames: Experiment and computer simulation, *Ber. Bunsen-Ges. Phys. Chem. Chem. Phys.*, 101, 1718, 1997.
28. Jain, S., Skamser, D.J., and Kodas, T.T., Morphology of single-component particles produced by spray pyrolysis, *Aerosol Sci. Tech.*, 27, 575, 1997.
29. Mangolini, L., Thimsen, E., and Kortshagen, U., High-yield plasma synthesis of luminescent silicon nanocrystals, *Nano Lett.*, 5, 655, 2005.
30. Salata, O.V., Tools of nanotechnology: Electrospray, *Curr. Nanosci.*, 1, 25, 2005.
31. Rulison, A.J. and Flagan, R.C., Synthesis of yttria powders by electrospray pyrolysis, *J. Amer. Ceram. Soc.*, 77, 3244, 1994.
32. Borsella, E., Botti, S., and Martelli, S., Nano-powders from gas-phase laser driven reactions: Characteristics and applications, *Mater. Sci. Forum*, 235–236, 261, 1997.
33. Lee, H.Y., Riehemann, W., and Mordike, B.L., Characterization of laser-sputtered nano-sized oxide powders, *Z. Metallk.*, 84, 79, 1993.
34. El-Shall, M.S., et al., Vapor phase growth and assembly of metallic, intermetallic, carbon, and silicon nanoparticle filaments, *J. Phys. Chem. B*, 107, 2882, 2003.
35. Kimoto, K., et al., An electron microscope study on fine metal particles prepared by evaporation in argon gas at low pressure, *Jpn. J. Appl. Phys.*, 2, 702, 1963.
36. Granqvist, C.G. and Buhrman, R.A., Ultrafine metal particles, *J. Appl. Phys.*, 47, 2200, 1976.
37. Tholen, A.R., Formation and interaction of small metal particles, *Acta Metal.*, 27, 1765, 1979.
38. Granqvist, C.G. and Buhrman, R.A., Log–normal size distributions of ultrafine metal particles, *Solid State Comm.*, 18, 123, 1976.
39. Eilers, H. and Tissue, B.M., Synthesis of nanophase ZnO, Eu_2O_3, and ZrO_2 by gas-phase condensation with cw-CO_2 laser heating, *Mater. Lett.*, 24, 261, 1995.
40. Tissue, B.M. and Yuan, H.B., Structure, particle size, and annealing of gas phase-condensed Eu^{3+}:Y_2O_3 nanophosphors, *J. Solid State Chem.*, 171, 12, 2003.
41. Niemeyer, C.M., Nanoparticles, proteins, and nucleic acids: Biotechnology meets materials science, *Angew. Chem., Int. Ed.*, 40, 4128, 2001.
42. Kleinlogel, C. and Gauckler, L.J., Sintering of nanocrystalline CeO_2 ceramics, *Adv. Mater.*, 13, 1081, 2001.

43. Chen, I.-W. and Wang, X.-H., Sintering dense nanocrystalline ceramics without final-stage grain growth, *Nature*, 404, 168, 2000.
44. Lebbou, K., Perriat, P., and Tillement O., Recent progress on elaboration of undoped and doped Y_2O_3, Gd_2O_3 rare-earth nano-oxide, *J. Nanosci. Nanotech.*, 5, 1448, 2005.
45. Matijevic, E., Preparation and properties of uniform size colloids, *Chem. Mater.*, 5, 412, 1993.
46. Sugimoto, T., Ed., *Fine Particles: Synthesis, Characterization, and Mechanisms of Growth*, Marcel Dekker, New York, 2000.
47. Chander, H., Development of nanophosphors—A review, *Mater. Sci. Eng., R*, 49, 113, 2005.
48. Levy, D. and Esquivias, L., Sol–gel processing of optical and electrooptical materials, *Adv. Mater.*, 7, 120, 1995.
49. Kwon, M.S., et al., Sol–gel synthesis and green luminescence of nanocrystalline Zn_2SiO_4:Mn phosphor, *J. Mater. Sci.*, 40, 4089, 2005.
50. Jiang, X.C., et al., Hydrothermal homogeneous urea precipitation of hexagonal YBO_3:Eu^{3+} nanocrystals with improved luminescent properties, *J. Solid State Chem.*, 175, 245, 2003.
51. Fang Y.P., et al., Systematic synthesis and characterization of single-crystal lanthanide orthophosphate nanowires, *J. Am. Chem. Soc.*, 125, 16025, 2003.
52. Fu, L., et al., Coating carbon nanotubes with rare-earth oxide multiwalled nanotubes, *Adv. Mater.*, 16, 350, 2004.
53. Xu, C.G., et al., 1D lanthanide halide crystals inserted into single-walled carbon nanotubes, *Chem. Comm.*, 24, 2427, 2000.
54. Hulteen, J.C. and Martin, C.R., A general template-based method for the preparation of nanomaterials, *J. Mater. Chem.*, 7, 1075, 1997.
55. Love, J.C., et al., Self-assembled monolayers of thiolates on metals as a form of nanotechnology, *Chem. Rev.*, 105, 1103, 2005.
56. Kawa, M. and Frechet, J.M., Self-assembled lanthanide-cored dendrimer complexes: Enhancement of the luminescence properties of lanthanide ions through site-isolation and antenna effects, *Chem. Mater.*, 10, 286, 1998.
57. Herrig, H. and Hempelmann, R., Microemulsion mediated synthesis of ternary and quaternary nanoscale mixed oxide ceramic powders, *Nanostruct. Mater.*, 9, 241, 1997.
58. Stein, A., Melde, B.J., and Schroden, R.C., Hybrid inorganic–organic mesoporous silicates—Nanoscopic reactors coming of age, *Adv. Mater.*, 12, 1403, 2000.
59. Pileni, M.P., Reverse micelles as microreactors, *J. Phys. Chem.*, 97, 6961, 1993.
60. Shea, L.E., et al., Synthesis of red-emitting, small particle size luminescent oxides using an optimized combustion process, *J. Am. Ceram. Soc.*, 79, 3257, 1996.
61. Polizzi, S., et al., Fractal aggregates of lanthanide-doped Y_2O_3 nanoparticles obtained by propellant synthesis, *J. Mater. Res.*, 16, 146, 2001.
62. Matteazzi, P. and Alcala, M., Mechanomaking of Fe/Al_2O_3 and FeCr/Al_2O_3 nanocomposites powders fabrication, *Mater. Sci. Eng. A*, 230, 161, 1997.
63. Yang, H.M., et al., Formation of zinc oxide nanoparticles by mechanochemical reaction, *Mater. Sci. Tech.*, 20, 1493, 2004.
64. Meyssamy, H., et al., Wet-chemical synthesis of doped colloidal nanomaterials: Particles and fibers of $LaPO_4$:Eu, $LaPO_4$:Ce, and $LaPO_4$:Ce,Tb, *Adv. Mater.*, 11, 840, 1999.
65. van Dijken, A., et al., Size-selective photoetching of nanocrystalline semiconductor particles, *Chem. Mater.*, 10, 3513, 1998.
66. Hirai, T. and Orikoshi, T., Preparation of Gd_2O_3:Yb,Er and Gd_2O_2S:Yb,Er infrared-to-visible conversion phosphor ultrafine particles using an emulsion liquid membrane system, *J. Colloid Interface Sci.*, 269, 103, 2004.
67. Zych, E., On the reasons for low luminescence efficiency in combustion-made Lu_2O_3:Tb, *Opt. Mater.*, 16, 445, 2001.
68. Zych, E., Meijerink, A., and Donega, C.D., Quantum efficiency of europium emission from nanocrystalline powders of Lu_2O_3:Eu, *J. Phys.: Condens. Matter*, 15, 5145, 2003.
69. Barber, D.B., et al., Amplification by optical composites, *Opt. Lett.*, 22, 1247, 1997.
70. Ethiraj, A.S., et al., Enhancement of photoluminescence in manganese-doped ZnS nanoparticles due to a silica shell, *J. Chem. Phys.*, 118, 8945, 2003.

71. Rajeshwar, K., de Tacconi, N.R., and Chenthamarakshan, C.R., Semiconductor-based composite materials: Preparation, properties, and performance, *Chem. Mater.*, 13, 2765, 2001.
72. Danev, G., Spassova, E., and Assa, J., Vacuum deposited polyimide—A perfect matrix for nanocomposite materials, *J. Optoelectron. Adv. Mater.*, 7, 1179, 2005.
73. Jarjayes, O. and Auric, P., Mossbauer investigations of γ-Fe_2O_3 nanocrystals embedded in polypyrrole, *J. Magn. Magn. Mater.*, 138, 115, 1994.
74. Kovalevskij, V., Gulbinas, V., and Scholes, G.D., Photomodification of CdSe nanocrystals incorporated in a poly(butylmethacrylate) polymer film, *J. Appl. Phys.*, 99, Art. No. 014305, 2006.
75. Wuister, S.F., Donega, C.D., and Meijerink, A., Local-field effects on the spontaneous emission rate of CdTe and CdSe quantum dots in dielectric media, *J. Chem. Phys.*, 121, 4310, 2004.
76. Zhou, H.S., et al., Synthesis and optical properties of coated nanoparticle composites, *J. Lumin.*, 70, 21, 1996.
77. Stipkala, J.M., et al., Light-induced charge separation at sensitized sol–gel processed semiconductors, *Chem. Mater.*, 9, 2341, 1997.
78. Bredol, M. and Schem, M., Luminescent materials: Glasses as substrate, matrix, and active medium, *Glass Sci. Technol.*, 78, 48, 2005.
79. Mortier M., et al., New progresses in transparent rare-earth doped glass ceramics, *Opt. Mater.*, 16, 255, 2001.
80. Mattarelli, M., et al., Tm^{3+}-activated transparent oxyfluoride glass ceramics: A study by Raman scattering of the nanocrystal size distribution, *Glass Phys. Chem.*, 31, 519, 2005.
81. Qian, G.D. and Wang, M.Q., Preparation and fluorescence properties of nanocomposites of amorphous silica glasses doped with lanthanide(III) benzoates, *J. Phys. Chem. Solids*, 58, 375, 1997.
82. Bredol, M., Gutzov, S., and Justel, T., Highly efficient energy transfer from Ge-related defects to Tb^{3+} ions in sol–gel-derived glasses, *J. Non-Cryst. Solids*, 321, 225, 2003.
83. Frechet, J.M.J., Dendrimers and other dendritic macromolecules: From building blocks to functional assemblies in nanoscience and nanotechnology, *J. Polym. Sci., Part A: Polym. Chem.*, 41, 3713, 2003.
84. Smith, D.K., Self-assembly using dendritic building blocks—Toward controllable nanomaterials, *Prog. Polym. Sci.*, 30, 220, 2005.
85. Ribeiro, S.J.L., Pulcinelli, S.H., and Santilli, C.V., SnO_2:Eu nanocrystallites in SnO_2 monolithic xerogels, *Chem. Phys. Lett.*, 190, 64, 1992.
86. Feofilov, S.P., et al., Sol–gel technology grown monolithic highly porous aluminum oxide with chromium and rare earth ions and size-resonant terahertz acoustic vibrations of nanocrystalline particles, *Mater. Sci. Forum*, 239–241, 687, 1997.
87. Feofilov, S.P., et al., Spectral hole burning in Eu^{3+}-doped highly porous γ-aluminum oxide, *Phys. Rev. B*, 54, R3690, 1996.
88. Pol, V.G., Reisfeld, R., and Gedanken, A., Sonochemical synthesis and optical properties of europium oxide nanolayer coated on titania, *Chem. Mater.*, 14, 3920, 2002.
89. Kong, D.Y., et al., Sol–gel synthesis and characterization of Zn_2SiO_4:Mn@SiO_2 spherical core-shell particles, *J. Electrochem. Soc.*, 152, H146, 2005.
90. Chen, X.Y., et al., Crystallization, phase transition, and optical properties of the rare-earth-doped nanophosphors synthesized by chemical deposition, *Nanotech.*, 14, 670, 2003.
91. Li, Q., Gao, L., and Yang, D.S., Recent advances in nanoscale luminescent materials of rare-earth compounds, *J. Inorg. Mater.*, 16, 17, 2001.
92. Hirata, G.A., et al., Pulsed laser deposition of $Y_3Al_5O_{12}$:Tb photoluminescent thin films, *J. Vac. Sci. Technol. A*, 14, 1694, 1996.
93. Itoh, S., et al., Problems and present status of phosphors in low-voltage full-color FEDs, *IEICE Trans. Electron.*, E82C, 1808, 1999.
94. Cho, K.G., et al., Improved luminescence properties of pulsed laser deposited Eu:Y_2O_3 thin films on diamond-coated silicon substrates, *Appl. Phys. Lett.*, 71, 3335, 1997.
95. Caldwell, M.L., et al., Visible luminescent activation of amorphous AlN:Eu thin-film phosphors with oxygen, *MRS Internet J. Nitride Semicond. Res.*, 6, 13, 2001.

96. Fernandez-Garcia, M., et al., Nanostructured oxides in chemistry: Characterization and properties, *Chem. Rev.*, 104, 4063, 2004.
97. Smith, D.J., The realization of atomic resolution with the electron microscope, *Rep. Prog. Phys.*, 60, 1513, 1997.
98. Wan, J.X., et al., Shape-induced enhanced luminescent properties of red phosphors: $Sr_2MgSi_2O_7$:Eu^{3+} nanotubes, *Eur. J. Inorg. Chem.*, 2005(20), 4031, 2005.
99. Zhang, H.Z. and Banfield, J.F., Understanding polymorphic phase transformation behavior during growth of nanocrystalline aggregates: Insights from TiO_2, *J. Phys. Chem. B*, 104, 3481, 2000.
100. Liu, J.Y., Scanning transmission electron microscopy and its application to the study of nanoparticles and nanoparticle systems, *J. Electron Micros.*, 54, 251, 2005.
101. Dinsmore, A.D., et al., Structure and luminescence of annealed nanoparticles of ZnS:Mn, *J. Appl. Phys.*, 88, 4985, 2000.
102. Tao, Y., et al., EXAFS studies of luminescence centres in Eu^{3+}-doped nanoscale phosphors, *Mater. Lett.*, 28, 137, 1996.
103. Zhang, K., et al., Enhanced luminescence and size effects of Y_2O_3:Eu^{3+} nanoparticles and ceramics revealed by X rays and Raman scattering, *J. Opt. Soc. Am. B*, 21, 1804, 2004.
104. Rosendo, A., et al., Synthesis, characterization and luminescence properties of Tb^{3+} and Eu^{3+}-doped poly(acrylic acid), *Mater. Lett.*, 57, 2885, 2003.
105. Wegh, R.T., et al., Extending Dieke's diagram, *J. Lumin.*, 87–89, 1002, 2000.
106. Wright, J.C., Laser spectroscopy of point-defect equilibria in insulators and transitions of insulators to superionic state, *Cryst. Latt. Def. Amorph. Mat.*, 12, 505, 1985.
107. Gutzov, S., et al., Chromium as a probe in amorphous and single-crystal zirconia, *Z. Phys. Chem.*, 205, 41, 1998.
108. Chen, W., et al., Structure, luminescence, and dynamics of Eu_2O_3 nanoparticles in MCM-41, *J. Phys. Chem. B*, 106, 7034, 2002.
109. Yen, W.M., Advances in the laser spectroscopy of solids—Introduction, *Top. Appl. Phys.*, 65, 1, 1989.
110. Bartko, A.P., et al., Observation of dipolar emission patterns from isolated Eu^{3+}:Y_2O_3-doped nanocrystals: New evidence for single-ion luminescence, *Chem. Phys. Lett.*, 358, 459, 2002.
111. Barnes, M.D., et al., On–off blinking and multiple bright states of single europium ions in Eu^{3+}:Y_2O_3 nanocrystals, *J. Phys. Chem. B*, 104, 6099, 2000.
112. Yatsui, T., et al., Observation of size-dependent features in the photoluminescence of zinc oxide nanocrystallites by near-field ultraviolet spectroscopy, *Appl. Phys. Lett.*, 80, 1444, 2002.
113. Kim, Z.H., Liu, B., and Leone, S.R., Nanometer-scale optical imaging of epitaxially grown GaN and InN islands using apertureless near-field microscopy, *J. Phys. Chem. B*, 109, 8503, 2005.
114. Mehta, A., et al., Size-correlated spectroscopy and imaging of rare-earth-doped nanocrystals, *Appl. Optics*, 42, 2132, 2003.
115. Stouwdam, J.W., et al., Lanthanide-doped nanoparticles with excellent luminescent properties in organic media, *Chem. Mater.*, 15, 4604, 2003.
116. Li, Z., Hahn, H., and Siegel, R.W., New phases of erbium oxides, *Mater. Lett.*, 6, 342, 1988.
117. Zhang, W.W., Optical properties of nanocrystalline Y_2O_3:Eu depending on its odd structure, *J. Colloid Interface Sci.*, 262, 588, 2003.
118. McKittrick, J., et al., Characterization of photoluminescent $(Y_{1-x}Eu_x)_2O_3$ thin films prepared by metallorganic chemical vapor deposition, *J. Am. Ceram. Soc.*, 83, 1241, 2000.
119. Nelson, J.A. and Wagner, M.J., Yttrium oxide nanoparticles prepared by alkalide reduction, *Chem. Mater.*, 14, 915, 2002.
120. Igarashi, T., et al., Relationship between optical properties and crystallinity of nanometer Y_2O_3:Eu phosphor, *Appl. Phys. Lett.*, 76, 1549, 2000.
121. Polizzi, S., et al., Investigation on lanthanide-doped Y_2O_3 nanopowders obtained by wet-chemical synthesis, *J. Mater. Chem.*, 12, 742, 2002.
122. Konrad, A., et al., Luminescence of bulk and nanocrystalline cubic yttria, *J. Appl. Phys.*, 90, 3516, 2001.

123. Skandan, G., et al., Phase characterization and stabilization due to grain size effects of nanostructured Y_2O_3, *Nanostruct. Mater.*, 1, 313, 1992.
124. Marks, L.D., Experimental studies of small-particle structures, *Rep. Prog. Phys.*, 57, 603, 1994.
125. Bagwell, R.B., Messing, G.L., and Howell, P.R., The formation of α-Al_2O_3 from theta-Al_2O_3: The relevance of a “critical size and diffusional nucleation” or “synchro-shear?”, *J. Mater. Sci.*, 36, 1833, 2001.
126. Eilers, H. and Tissue, B.M., Laser spectroscopy of nanocrystalline Eu_2O_3 and Eu^{3+}:Y_2O_3, *Chem. Phys. Lett.*, 251, 74, 1996.
127. Sheng, K.C. and Korenowski, G.M., Laser-induced optical-emission studies of Eu^{3+} sites in polycrystalline powders of monoclinic and body-centered cubic Eu_2O_3, *J. Phys. Chem.*, 92, 50, 1988.
128. Chakraborty, B.R., et al., TOF-SIMS and laser-SNMS investigations of dopant distribution in nanophosphors, *Nanotech.*, 16, 1006, 2005.
129. Bachir, S., et al., Photoluminescence of polycrystalline zinc oxide coactivated with trivalent rare-earth ions and lithium. Insertion of rare-earth ions into zinc oxide, *J. Lumin.*, 75, 25, 1997.
130. Bol, A.A., van Beek, R., and Meijerink, A., On the incorporation of trivalent rare earth ions in II-VI semiconductor nanocrystals, *Chem. Mater.*, 14, 1121, 2002.
131. Meltzer, R.S., et al., Dependence of fluorescence lifetimes of Y_2O_3:Eu^{3+} nanoparticles on the surrounding medium, *Phys. Rev. B*, 60, R14012, 1999.
132. Ye, T., et al., Combustion synthesis and photoluminescence of nanocrystalline Y_2O_3:Eu phosphors, *Mater. Res. Bull.*, 32, 501, 1997.
133. Tissue, B.M. and Bihari, B., Lanthanide luminescence as a probe of nanocrystalline materials, *J. Fluor.*, 8, 289, 1998.
134. Warren, G.T., et al., Excitation transfer in CaF_2:Eu^{2+},Sm^{2+} multilayered structures grown by MBE on Si(111), *J. Lumin.*, 76–77, 411, 1998.
135. Selvin, P.R., Lanthanide-based resonance energy transfer, *IEEE J. Sel. Top. Quant. Elec.*, 2, 1077, 1996.
136. Minoofar, P.N., Dunn, B.S., and Zink, J.I., Multiply doped nanostructured silicate sol–gel thin films: Spatial segregation of dopants, energy transfer, and distance measurements, *J. Am. Chem. Soc.*, 127, 2656, 2005.
137. Tissue, B.M., Synthesis and luminescence of lanthanide ions in nanoscale insulating hosts, *Chem. Mater.*, 10, 2837, 1998.
138. Liu, G.K., Zhuang, H.Z., and Chen, X.Y., Restricted phonon relaxation and anomalous thermalization of rare-earth ions in nanocrystals, *Nano Lett.*, 2, 535, 2002.
139. Liu, G.K., et al., Confinement of electron–phonon interaction on luminescence dynamics in nanophosphors of Er^{3+}:Y_2O_2S, *J. Solid State Chem.*, 171, 123, 2003.
140. Wolf, D., et al., Phonon-induced anomalous specific heat of a nanocrystalline model material by computer simulation, *Phys. Rev. Lett.*, 74, 4686, 1995.
141. Chen, X.Y., et al., Confinement on energy transfer between luminescent centers in nanocrystals, *J. Appl. Phys.*, 94, 5559, 2003.
142. Malta, O.L., Theoretical-analysis of the fluorescence yield of rare-earth ions in glasses containing small metallic particles, *Chem. Phys. Lett.*, 174, 13, 1990.
143. Louis, C., et al., Gold nano-antennas for increasing luminescence, *Adv. Mater.*, 16, 2163, 2004.
144. Guo, H., et al., Preparation and characterization of sol–gel derived Au nanoparticle dispersed Y_2O_3:Eu films, *J. Rare Earths*, 23, 600, 2005.
145. Hayakawa, T, Selvan, S.T., and Nogami, M., Field enhancement effect of small Ag particles on the fluorescence from Eu^{3+}-doped SiO_2 glass, *Appl. Phys. Lett.*, 74, 1513, 1999.
146. Selvan, S.T., Hayakawa, T., and Nogami, M., Remarkable influence of silver islands on the enhancement of fluorescence from Eu^{3+} ion-doped silica gels, *J. Phys. Chem. B*, 103, 7064, 1999.
147. Justel, T., Nikol, H., and Ronda, C., New developments in the field of luminescent materials for lighting and displays, *Angew. Chem., Int. Ed.*, 37, 3085, 1998.
148. Yamamoto, H. and Matsukiyo, H., Problems and progress in cathode-ray phosphors for high-definition displays, *J. Lumin.*, 48&49, 43, 1991.
149. Zych, E., Trojan-Piegza, J., and Kepinski, L., Homogeneously precipitated Lu_2O_3:Eu nanocrystalline phosphor for X-ray detection, *Sens. Actuators, B*, 109, 112, 2005.

150. Blasse, G., Scintillator materials, *Chem. Mater.*, 6, 1465, 1994.
151. Nichkova, M., et al., Microarray immunoassay for phenoxybenzoic acid using polymer encapsulated Eu:Gd_2O_3 nanoparticles as fluorescent labels, *Anal. Chem.*, 77, 6864, 2005.
152. Wang, F., et al., Luminescent nanomaterials for biological labeling, *Nanotech.*, 17, R1, 2006.
153. Michalet, X., et al., Quantum dots for live cells, *in vivo* imaging, and diagnostics, *Science*, 307, 538, 2005.
154. Kaminskii, A.A., Modern developments in the physics of crystalline laser materials, *Phys. Status Solidi A*, 200, 215, 2003.
155. Kaminskii, A.A. and Weber, M.J., *Crystalline Lasers: Physical Processes and Operating Schemes*, CRC Press, Boca Raton, FL, 1996.
156. Kawano, K., et al., Application of rare-earth complexes for photovoltaic precursors, *Sol. Energy Mater. Sol. Cells*, 48, 35, 1997.
157. Barber, D.B., et al., Amplification by optical composites, *Optics Lett.*, 22, 1247, 1997.
158. Yamamoto, H. and Matsukiyo, H., Problems and progress in cathode-ray phosphors for high definition displays, *J. Lumin.*, 48&49, 43, 1991.
159. Vecht, A., et al., Engineering phosphors for field emission displays, *J. Vac. Sci. Tech. B*, 17, 750, 1999.
160. Ledoux, G., et al., Synthesis and optical characterization of Gd_2O_3:Eu^{3+} nanocrystals: Surface states and VUV excitation, *Radiat. Meas.*, 38, 763, 2004.
161. Schwoebel, P.R. and Brodie, I., Surface-science aspects of vacuum microelectronics, *J. Vac. Sci. Tech. B*, 13, 1391, 1995.
162. Itoh, S., et al., Phosphors for full color low voltage FEDs, *Ext. Abs. 3rd Inter. Conf. Sci. Tech. Displ. Phosphors*, Nov. 1997, Huntington Beach, CA.
163. Allison, S.W., et al., Nanoscale thermometry via the fluorescence of YAG:Ce phosphor particles: Measurements from 7 to 77°C, Nanotech., 14, 859, 2003.
164. Alencar, M.A.R.C., et al., Er^{3+}-doped $BaTiO_3$ nanocrystals for thermometry: Influence of nanoenvironment on the sensitivity of a fluorescence-based temperature sensor, *Appl. Phys. Lett.*, 84, 4753, 2004.
165. Salah, N., et al., Luminescence characteristics of $K_2Ca_2(SO_4)_3$:Eu,Tb micro- and nanocrystalline phosphor, *Radiat. Eff. Def. Solids*, 159, 321, 2004.
166. Pandey, A., et al., Thermoluminescence and photoluminescence characteristics of nanocrystalline $LiNaSO_4$:Eu phosphor, *J. Phys. D: Appl. Phys.*, 36, 2400, 2003.
167. Salah, N., et al., TL and PL studies on $CaSO_4$:Dy nanoparticles, *Radiat. Meas.*, 41, 40, 2006.
168. Rosi, N.L. and Mirkin, C.A., Nanostructures in biodiagnostics, *Chem. Rev.*, 105, 1547, 2005.
169. Haraguchi, T., et al., Spectral imaging fluorescence microscopy, *Genes Cells*, 7, 881, 2002.
170. Paddock, S.W., Principles and practices of laser scanning confocal microscopy, *Mol. Biotech.*, 16, 127, 2000.
171. Buehler, C., et al., Single-photon counting multicolor multiphoton fluorescence microscope, *J. Fluor.*, 15, 41, 2005.
172. Gillies, G.T., Allison, S.W., and Tissue, B.M., Positive pressure infusion of fluorescent nanoparticles as a probe of the structure of brain phantom gelatins, *Nanotech.*, 13, 484, 2002.
173. Soukka, T., et al., Utilization of kinetically enhanced monovalent binding affinity by immunoassays based on multivalent nanoparticle-antibody bioconjugates, *Anal. Chem.*, 73, 2254, 2001.
174. Hemmila, I. and Mukkala, V.M., Time-resolution in fluorometry technologies, labels, and applications in bioanalytical assays, *Crit. Rev. Clin. Lab. Sci.*, 38, 441, 2001.
175. Niedbala, R.S., et al., Detection of analytes by immunoassay using upconverting phosphor technology, *Anal. Biochem.*, 293, 22, 2001.
176. Soukka T., et al., Photochemical characterization of upconverting inorganic lanthanide phosphors as potential labels, *J. Fluor.*, 15, 513, 2005.
177. Corstjens, P.L.A.M., et al., Lateral-flow and upconverting phosphor reporters to detect single-stranded nucleic acids in a sandwich-hybridization assay, *Anal. Biochem.*, 312, 191, 2003.
178. Clapp, A.R., et al., Quantum dot-based multiplexed fluorescence resonance energy transfer, *J. Am. Chem. Soc.*, 127, 18212, 2005.

179. Gordon, W.O., Carter, J.A., and Tissue, B.M., Long-lifetime luminescence of lanthanide-doped gadolinium oxide nanoparticles for immunoassays, *J. Lumin.*, 108, 339, 2004.
180. Yi, G.S. and Chow, G.M., Colloidal LaF_3:Yb,Er, LaF_3:Yb,Ho and LaF_3:Yb,Tm nanocrystals with multicolor upconversion fluorescence, *J. Mater. Chem.*, 15, 4460, 2005.
181. Louis, U., et al., Nanosized hybrid particles with double luminescence for biological labeling, *Chem. Mater.*, 17, 1673, 2005.
182. Aslan, K., Lakowicz, J.R. and Geddes, C.D., Metal-enhanced fluorescence using anisotropic silver nanostructures: Critical progress to date, *Anal. Bioanal. Chem.*, 382, 926, 2005.
183. Tanner, P.A., Synthesis and luminescence of nano-insulators doped with lanthanide ions, *J. Nanosci. Nanotech.*, 5, 1455, 2005.
184. NIOSH, *Approaches to Safe Nanotechnology: An Information Exchange with NIOSH*, National Institute for Occupational Safety and Health, Centers for Disease Control and Prevention, October 1, 2005; report available: http://www.cdc.gov/niosh/topics/nanotech/nano_exchange.html.
185. Roco, M.C. and Bainbridge, W.S., Eds., Societal implications of nanoscience and nanotechnology: Maximizing human benefit, *J. Nanopart. Res.*, 7, 1, 2005; and references therein.
186. Oberdörster, G., Oberdörster, E., and Oberdörster, J., Nanotoxicology: An emerging discipline evolving from studies of ultrafine particles, *Environ. Health Perspect.*, 113, 823, 2005.

chapter four — section three

Methods of phosphor synthesis and related technology

Weiyi Jia and Dongdong Jia

Contents

4.3 Preparation of phosphors by the sol–gel technology 381
  - 4.3.1 Sol–gel techniques 382
    - 4.3.1.1 Methodology 382
      - 4.3.1.1.1 Preparation of precursor solutions 382
      - 4.3.1.1.2 Hydrolysis 384
      - 4.3.1.1.3 Gelation 384
      - 4.3.1.1.4 Aging and drying 385
      - 4.3.1.1.5 Annealing and porosity control 385
      - 4.3.1.1.6 Technology for other materials 385
    - 4.3.1.2 Advantages and disadvantages of the sol–gel method 386
  - 4.3.2 Salted sol–gel method and combustion method 386
    - 4.3.2.1 Salted sol–gel method 386
    - 4.3.2.2 Combustion method 387
  - 4.3.3 Preparation of phosphors by the sol–gel method 388
    - 4.3.3.1 Nanoclusters embedded in SiO_2 glasses 388
    - 4.3.3.2 Nanoclusters of semiconductors embedded in SiO_2 glasses 389
    - 4.3.3.3 Organic–inorganic hybrid materials 389
    - 4.3.3.4 Thin films and coatings 389
    - 4.3.3.5 Aluminates 390
    - 4.3.3.6 Silicates 390
    - 4.3.3.7 Phosphate phosphors 390
    - 4.3.3.8 Borate phosphors 391
  - 4.3.4 Conclusion 391

References 391

4.3 Preparation of phosphors by the sol–gel technology

Phosphors used for most emissive display devices are in the form of powders. The quality of the display depends on the nature of the powders used; fine and uniform powders with good crystallinity are generally preferred. This is especially true in low-voltage applications such as in the field emission displays, currently of interest. In these devices, lower-energy electrons do not penetrate into phosphor grains very deeply, and in order to maintain efficiency the size of the phosphor grains has to be reduced to reflect this fact. The grain size of phosphors prepared via solid-state chemical reactions depends on the temperature and the length of the sintering process. Lower temperature and shorter sintering periods give rise to smaller-sized grain particles, but both the crystallinity and grain uniformity are poor if the treatment parameters do not allow the chemical reaction to be completed. To resolve this problem, wet methods of preparation are often used where aqueous solutions of specific constituent metallic salts are employed. The addition of $NH_4(OH)$ or oxalic acid causes the metallic hydroxides or oxalates to precipitate from the mixture. In these cases, the ingredients of the precipitate are in contact with each other at a molecular level, and an efficient chemical reaction normally occurs.

The sol–gel method of phosphor preparation is regarded as a wet method. A kind of metalorganic compounds, known as alkoxides of metals, are used as precursors. These metalorganic alkoxides are either in liquid form or are soluble in certain organic solvents. Through the use of appropriate reagents, the processes of hydrolysis and gelation can be induced to produce homogeneous gels from the mixture of alkoxides. To obtain powder or ceramic samples, the gels can be baked, sintered, and powdered as in other traditional methods. The sol–gel method is advantageous inasmuch as thin films or coatings of the phosphor can be formed on substrates directly and the sol–gel can be molded into designated forms.

In this chapter, the sol–gel technique is described in Section 4.3.1. A modified sol–gel technique called the salted sol–gel (SSG) method and an additional gel method called the combustion method are described in Section 4.3.2. Examples of a number of special materials and their applications are discussed in Section 4.3.3.

4.3.1 Sol–gel techniques

The sol–gel method is a chemical technique that uses metal alkoxides for the synthesis and production of glasses or ceramics through a series of chemical processes, including hydrolysis, gelation, drying, and thermal treatment. The sol–gel technique was developed as early as 1864; Graham[1] prepared gels of silica from aqueous salts, while Ebelmen[2] obtained silica gels from metal alkoxides. The potential of the sol–gel process was not appreciated until 1980, when it was rediscovered and found to be very useful in synthesizing various materials of practical importance. Since then the method has received considerable attention and has been investigated extensively.[3]

In general, a sol is defined as a colloid of solid particles suspended in a liquid; the particles consist of dense oxide or polymetric clusters formed by the precursors and reagents. A gel, on the other hand, is a composite substance consisting of a continuous solid skeletal structure, which results from the gelation of the sol; the gel forms cells that encapsulate colloidal liquids. This solute can be driven from the gel through thermal treatment, and solid glass or ceramic is produced in this way. As an example, the procedure for the preparation of doped SiO_2 sol–gel glasses is described in the following section. Similar procedures are applicable to other oxide compounds.

4.3.1.1 Methodology[3]

4.3.1.1.1 Preparation of precursor solutions. The initial raw materials for sol–gel preparations consist of metal alkoxides either in the solid or in the liquid form (Table 2). An alkoxide is a metalorganic compound in which a hydrogen atom belonging to the

Table 2 List of Some Commonly Used Metal Alkoxides and Recommended Solvents for Solids

Name	Chemical formula	Solvents
Aluminum isopropoxide	$Al(OC_3H_7^i)_3$	Isopropanol
Aluminum *n*-butoxide	$Al(OC_4H_9^n)_3$	*n*-Butanol
Aluminum *sec*-butoxide	$Al(OC_4H_9^s)_3$	Liquid
Barium ethoxide	$Ba(OC_2H_5)_2$	Ethanol
Barium isopropoxide	$Ba(OC_3H_7^i)_3$	Isopropanol
Bismuth isopropoxide	$Bi(OC_3H_7^i)_3$	Isopropanol
Triethyl borate	$B(OC_2H_5)_3$	Liquid
Trimethyl borate	$B(OCH_3)_3$	Liquid
Tributyl borate	$B(OC_4H_9)_3$	Liquid
Calcium ethoxide	$Ca(OC_2H_5)_2$	Ethanol
Calcium methoxide	$Ca(OCH_3)_2$	Methanol
Cerium isopropoxide	$Ce(OC_3H_7^i)_3$	Isopropanol
Chromium isopropoxide	$Cr(OC_3H_7^i)_3$	Isopropanol
Copper ethoxide	$Cu(OC_2H_5)_2$	Ethanol
Dysprosium isopropoxide	$Dy(OC_3H_7^i)_3$	Toluene–isopropanol
Erbium isopropoxide	$Er(OC_3H_7^i)_3$	Toluene–isopropanol
Gadolinium isopropoxide	$Gd(OC_3H_7^i)_3$	Toluene–isopropanol
Gallium isopropoxide	$Ga(OC_3H_7^i)_3$	Liquid
Germanium methoxide	$Ge(OCH_3)_4$	Liquid
Germanium ethoxide	$Ge(OC_2H_5)_4$	Liquid
Germanium isopropoxide	$Ge(OC_3H_7^i)_4$	Liquid
Hafnium *n*-butoxide	$Hf(OC_4H_9^t)_4$	Liquid
Indium isopropoxide	$In(OC_3H_7^i)_3$	Isopropanol
Lanthanum isopropoxide	$La(OC_3H_7^i)_3$	Isopropanol
Lithium isopropoxide	$Li(OC_3H_7^i)$	Isopropanol
Lithium methoxide	$Li(OCH_3)$	Methanol
Triethyl phosphite	$P(OC_2H_5)_3$	Liquid
Triisopropyl phosphite	$P[OCH(CH_3)_2]_3$	Liquid
Tributyl phosphite	$P(OC_4H_9)_3$	Liquid
Trimethyl phosphite	$P(OCH_3)_3$	Liquid
Lead isopropoxide	$Pb(OC_3H_7^i)_2$	Isopropanol
Magnesium methoxide	$Mg(OCH_3)_2$	Methanol
Magnesium ethoxide	$Mg(OC_2H_5)_2$	Ethanol
Manganese isopropoxide	$Mn(OC_3H_7^i)_2$	Isopropanol
Molybdenum isopropoxide	$Mo(OC_3H_7^i)_5$	Isopropanol
Proseodymium isopropoxide	$Pr(OC_3H_7^i)_3$	Toluene–isopropanol
Rare-earth isopropoxide	$R(OC_3H_7^i)_3$	Isopropanol
Tetraethoxysilane (TEOS)	$Si(OC_2H_5)_4$	Liquid
Tetramethoxysilane (TMOS)	$Si(OCH_3)_4$	Liquid
Strontium isopropoxide	$Sr(OC_3H_7^i)_2$	Isopropanol
Thallium ethoxide	$Tl(OC_2H_5)$	Liquid
Tin *tert*-butoxide	$Sn(OC_4H_9^t)_4$	Liquid
Titanium (IV) ethoxide	$Ti(OC_2H_5)_4$	Liquid
Titanium (IV) methoxide	$Ti(OCH_3)_4$	Methanol
Titanium (IV) isopropoxide	$Ti(OC_3H_7^i)_4$	Liquid
Titanium (IV) isobutoxide	$Ti[(CH_3)_2CHCH_2O]_4$	Liquid
Tunsten (VI) ethoxide	$W(OC_2H_5)_6$	Ethanol
Tunsten (VI) isopropoxide	$W(OC_3H_7^i)_6$	Isopropanol
Yttrium isopropoxide	$Y(OC_3H_7^i)_3$	Isopropanol
Zinc isopropoxide	$Zn(OC_3H_7^i)_2$	Isopropanol
Zirconium *n*-propoxide	$Zr(OC_3H_7^n)_4$	*n*-Propanol
Zirconium *n*-butoxide	$Zr(OC_4H_9^n)_4$	*n*-Butanol

hydroxyl (OH) group of an alcohol is replaced by a metal atom. As the sol–gel method is a wet chemical method, a proper solvent is needed to convert solid alkoxides, if used, into liquid form. Some alkoxide solutions are commercially available (see Table 2). Doping or activator ions are introduced either through another alkoxide solution or by using an aqueous solution of the doping ions. This liquid mixture of the metal alkoxides is stirred for an extended period. To stimulate hydrolysis, a mixture of water, alcohol, hydrochloric acid (pH approximately 2–5) is added.

Since the chemical and physical processes involved are similar for all metal alkoxides, we use silicon alkoxides as an illustrative example for the preparation of sol–gel materials. For these matrices, TMOS (tetramethoxysilane, $Si(OCH_3)_4$, liquid) or TEOS (tetraethoxysilane, $Si(OC_2H_5)_4$, liquid) is commonly used. They react readily but are not soluble in water. A solvent such as methanol (MeOH) or ethanol (EtOH) is normally used to produce the precursor solution.

4.3.1.1.2 Hydrolysis[3,4]. A mixture of water, alcohol, and HCl is prepared so that it has a pH of 2–5, with HCl acting as a catalyst in this process. This acidic solution is added slowly (dropwise) into the precursor alkoxide mixture. The reaction of alkoxides with water is called hydrolysis. In hydrolysis, a hydroxyl (OH) group attaches itself to the metal atom by replacing the alkoxide (OR) group in TMOS or TEOS. A typical reaction goes as

$$(OR)_3 - Si - OR + H_2O \rightarrow (OR)_3 - Si - OH + ROH$$

where R stands for the alkyl (alkylic) radical, C_nH_{2n+1}. R = CH_3 for TMOS and R = C_2H_5 for TEOS. Hydrolysis can occur with any one of the OR groups of the molecule. If the sol–gels are to be doped, an aqueous solution containing the doping ion/ions is also blended in during the hydrolysis step.

4.3.1.1.3 Gelation[3,4]. With proper thermodynamic conditions, gelation occurs. Gelation is a continuous process in which two partially hydrolyzed molecules begin to connect and intertwine with each other with the release (condensation) of water when in an aqueous solution

$$(OR)_3 - Si - OH + HO - Si - (OR)_3 \rightarrow (OR)_3 - Si - O - Si - (OR)_3 + H_2O$$

Alcohol, ROH, is released when an alcohol solution is employed:

$$(OR)_3 - Si - OR + HO - Si - (OR)_3 \rightarrow (OR)_3 - Si - O - Si - (OR)_3 + ROH$$

ROH is an alcohol, where ROH = C_2H_5OH for TEOS and CH_3OH for TMOS.

With continuing gelation, larger structures are produced by polymerization, wherein chains of polymers can cross-link to form three-dimensional clusters. Small clusters suspended in the liquid constitute the sol, and through the gelation process these clusters begin to grow by combining with monomers or other clusters while releasing or condensing water or alcohol. Different metal alkoxides can also coalesce to form “compound” clusters.

Several factors affect the rate of sol and gel formation including the temperature, the relative concentration of the alkoxide precursors, water, and solvent, and the pH of the total admixture. In most cases, sol–gel synthesis is carried out at room temperature, though both the sol and gel formation rates are known to increase with increasing temperature. Because water and alkoxysilanes are immiscible, a common solvent such as alcohol is also normally used as a homogenizing agent.

In our example, silica gels prepared at low pH (<3) and low water content (less than 4 mol% water per mole of alkoxide) produce primarily linear polymers with low cross-link density. Additional cross-links form during gelation and the polymer chains become increasingly entangled. Silica gels prepared under more normal conditions (pH approximately 5–7) or with higher water content produce highly branched clusters, which behave as discrete species; these clusters link together during gelation. At still higher pH and excess water content, colloidal silica is formed. Links between clusters keep on multiplying until a giant cluster forms that spans the vessel. During gelation, the viscosity and the elastic modulus of the solution increase rapidly. The final spanning cluster forms a skeletal framework that encloses cells containing the liquid phase (water or alcohol) and defines the gel phase. The solid network retards the escape of the liquid and prevents structural collapse.

4.3.1.1.4 Aging and drying. Aging leads to changes in the structure and other properties of the gel through further condensation, dissolution, and reprecipitation of monomers or oligomers. Syneresis or spontaneous shrinkage of the network of the gel takes place as bond formation or attraction between clusters induces a contraction of the network and expulsion of liquid from the pores.

Drying by evaporation under normal conditions gives rise to pressure within the pores, which causes shrinkage of the gel network. Pressure gradients develop through the volume of the gels, so that the networks are compressed more at the surfaces than in the bulk. This may cause, if the gradients are too large, cracking of the sample.

After shrinkage stops, further evaporation drives the meniscus of the liquids into the bulk and the rate of evaporation decreases. The resulting dried gel is called a xerogel. Xerogels are useful in the preparation of dense ceramics and are also interesting because of their high porosity and large surface area; these materials are useful as catalytic substrates, filters, and vapor sensors.[5,6]

4.3.1.1.5 Annealing and porosity control. Additional heat treatment of the sol–gel is required to produce pore-free ceramic materials; sintering at high temperatures results in densification driven by interfacial energy considerations. By heating, the gel constituents move by viscous flow or diffusion so as to reduce the solid–vapor interfacial areas, and hence reduce porosity. Removal of organics takes place by endothermic carbonization near 200°C, followed by exothermic oxidation at temperatures between 300 and 400°C. For the silicate system of our example, the exothermic process is suppressed if the gels are heated under inert conditions, where oxidation is prevented. The temperature interval between 400 and 525°C represents a region where considerable skeletal densification occurs with little associated weight loss. Structural relaxation, a process by which free excess volume is removed by diffusive motion of the network, is the predominant shrinkage mechanism in this temperature interval. The condensation (water or alcohol) and pyrolysis reactions that occur during heating liberate a large volume of gas that can generate high pressures, and because of low permeability of the small pores in the network, this may cause cracking when the samples are heated between room temperature and 400°C. At 800°C, there is partial densification of the sol–gel; by 900°C, the gel is completely densified leaving only a trace of silanols (Si-OH).

4.3.1.1.6 Technology for other materials. The technology to prepare other oxide compounds is similar to that described for SiO_2. For example, for preparing Al_2O_3, $Al(OC_4H_9)_3$ (liquid) can be used (see Table 2). Hydrolysis can be carried out at 80°C with 1 mole of aluminum *sec*-butoxide (ASB), 100 moles H_2O, and 0.07 mole of HCl. Alumina sol, wet gels, and dried gels can be obtained by hydrolysis, gelation, and drying, respectively, as discussed above.[7] By annealing at 500°C, monolithic transparent γ-alumina can be obtained. When annealed at 1200°C, the alumina becomes α-phase.[7] For complex compounds, a network between different metals is randomly formed through oxygen bonds.

For ceramic powders, cracking is not a major concern, and the heating process can be done rapidly.[8] The annealing temperature should be higher than 1000°C in order to get rid of any organic groups, especially OH, which is known to quench luminescence efficiently through nonradiative vibrational relaxation.[9]

4.3.1.2 Advantages and disadvantages of the sol–gel method

The sol–gel technique presents us with the following advantages:

1. High homogeneity of the chemical composition of the materials produced. Molecule-level homogeneous multicomponent materials can be obtained. Because of the better homogeneity, contributions to the spectra of these materials from inhomogeneous sources are generally expected to be smaller than those encountered in unordered systems.
2. High uniformity of doping ion distribution. No "local" concentration quenching will occur because of impurity clustering, and higher doping concentration becomes possible.
3. Processing temperature can be very low. This allows the doping of fragile organic and biological molecules into porous inorganic materials and the fabrication of organic–inorganic hybrid materials.
4. The microstructure (porosity and size of pores) of the materials can be controlled. Nanoscale uniform pores can be obtained at intermediate processing temperatures while high-density materials can be produced with higher annealing temperature.
5. Thin films and multilayer coatings of sol–gel materials can be readily prepared by spinning or dipping methods during the gelation period.
6. The sol–gel procedures produce little unintentional contamination. No milling and grinding are needed, as these processes are known to contaminate samples. Fluxes, such as B_2O_3, H_3BO_3, and NH_4Cl, which are commonly used in ceramic technology and contaminate the end products, are no longer needed. When phosphor powders are prepared by the sol–gel method, powdering may be used and trace of foreign particles can be blended in. This "contamination" does not enter into the lattice of powders and will not affect the optical properties of the phosphor.

The technique has the following disadvantages:

1. When transparent samples are used, such as laser media, the drying and annealing processes have to be slow and deliberate; otherwise, cracks and striations will appear in the samples.
2. It is difficult to completely remove the residual hydroxyls from the sol–gel materials. In order to get rid of these organic groups, samples have to be annealed above 1000°C and this may produce undesirable side effects.

4.3.2 Salted sol–gel method and combustion method

4.3.2.1 Salted sol–gel method

Conventional sol–gel methods are well suited for the production of small amounts of phosphors, in quantities used for thin-film coating, but are not practical for producing large amounts of phosphors in general. Many metal alkoxides are solids and their solubility in organic solvents is low. For example, 100 ml of commercial yttrium isopropoxide, $Y(OC_3H_7)_3$, in toluene–isopropanol only contains an equivalent of 2 g of Y_2O_3. Therefore, production of phosphor-containing yttrium by the sol–gel method is both inefficient and expensive. In addition, the large amounts of vapor produced by the organic solvent may also be a source of environmental problems.

Recently, a novel modified sol–gel method, the salted sol–gel process, has been developed.[10] In this method, metal alkoxides and solutions of various inorganic salts are used in combination. As noted in Table 2, many of the alkoxides are in liquid form and they contain one or more constituents of the standard phosphors (aluminates, silicates, borates, or phosphates).

Most of commercial phosphors are aluminates, silicates, borates, or phosphates. One of the sources of phosphors is liquid alkoxides (listed in Table 2). Water–alcohol solutions of salts containing the other constituents can be prepared and blended into liquid alkoxides. The water in the solution plays a role in hydrolysis, and the salts are repelled and entrapped in the gel network. A relatively uniform mixture of salted gels can be obtained this way. The salts to be used should have high resolubility. This process requires an accurate amount of solvent for the salts introduced; the amount should be sufficient for hydrolysis but insufficient to redissolve some salts.

The SSG technology provides the possibility of producing large amounts of phosphors in the form of ultrafine or nanoscaled powders economically. In this method, the multichemical compositions can be uniformly mixed at almost the molecular level. Complete chemical reaction and much better crystallinity can be obtained at lower sintering temperature and shorter sintering period. Fine phosphor powders of nanometer size and good crystallinity have been obtained in this way.[11]

$Y_3Al_5O_{12}$:Ce is taken as an example. This material is widely used as a downconverter in commercial LED-phosphor white light sources. The melting points of Y_2O_3 and Al_2O_3 are 2410°C and 2072°C, respectively. Therefore, sintering temperatures for the production of YAG powders are normally very high. For YAG, at temperatures below 1300°C, no garnet phase is formed, but with the aid of a flux, BaF_2 (20 mol%), a complete garnet phase can be formed above 1500°C.[12] In the SSG method, ASB and an aqueous solution of yttrium/cerium nitrates (or acetates) are used. The rare-earth solution is added into ASB while stirring vigorously for a few minutes. Hydrolysis is exothermic and proceeds very fast; alcohol will evaporate during this process and fumes are produced. The formed gels become a kind of slurry and are baked to dry at about 80°C. The garnet phase is formed at 800°C, as the characteristic yellow emission begins to be produced by the powders. X-ray diffraction reveals that fair crystallinity is obtained in samples sintered at 1200°C. The complete garnet phase is formed at 1350°C or above. Figure 19 shows the dependence of the luminescence intensity of YAG-1%Ce^{3+} prepared by the SSG method on sintering temperatures.[11] Maximum luminescence intensity is obtained in the sample when the sintering temperature is at or above 1350°C. For comparison, Figure 19 also shows similar results for YAG-Tb prepared by solid-state reaction (SSR) with or without the flux, BaF_2 (data taken from Ohno and Abe[12]).

Several key points need to be addressed: (1) The amount of water used to dissolve the nitrates should be kept at a minimum. Using less water to dissolve the nitrates (acetates) at higher temperature (60°C) is recommended. (2) ASB can be diluted using isopropanol. Diluted ASB gives more uniform gels. (3) Certain amount of polyalcohol (such as ethylene glycol) can be added into the aqueous salt solutions to prevent the clusterization of nitrates or acetates in the gel network. (4) A small amount of flux can also be added to further reduce the sintering temperature and improve crystallinity.

4.3.2.2 *Combustion method*[13–15]

In the combustion method, all the precursors used are salts such as nitrates or acetates. A proper amount of organic "fuel" such as glycine ($C_2H_5NO_2$, powder, melting point 234°C, soluble in water),[13] urea (NH_2CONH_2, powder, melting point 134°C, soluble in

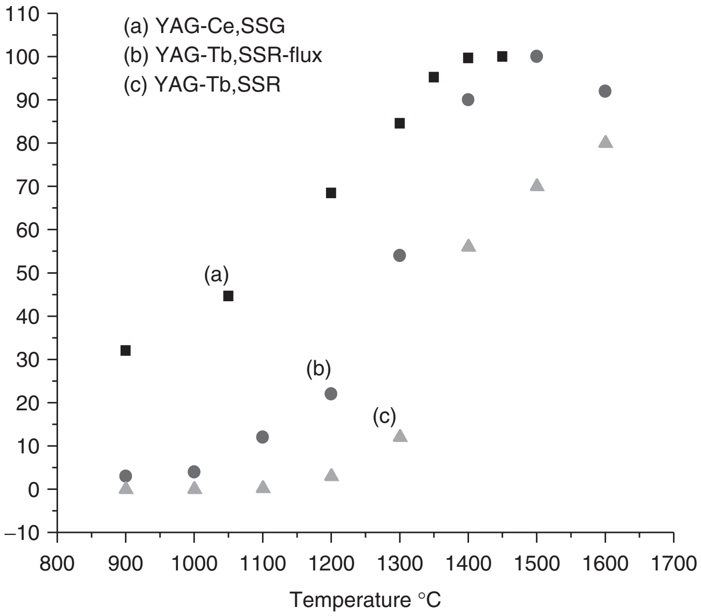

Figure 19 Relative intensity of luminescence of YAG-1% Ce^{3+} by the SSG method, sintered at different temperatures. For comparison, results of YAG-Tb obtained by solid state reaction (SSR) are also shown. (From K. Ohno and T. Abe).[12]

water), ethylene glycol ($HOCH_2CH_2OH$, liquid, miscible in water),[14] triethanolamine (TEA, $(HOCH_2CH_2)_3N$, liquid, melting point 21.2°C, miscible in water)[15] etc. is added to the aqueous solution of the salts. The mixture is heated on a hot plate to vaporize the water until gels result. The gels are then put in an oven preheated to 300–500°C. Vigorous combustion occurs and puffy powders are obtained. Before the final sintering, the powders are fired at 600–800°C in air (or oxygen) to completely burn off all the organic residues. In the case of $Y_3Al_5O_{12}$:Ce^{3+}, the garnet phase starts to form above 750°C. SEM imaging reveals the powders are skeletal with bone size in tens of nanometers.[11]

4.3.3 *Preparation of phosphors by the sol–gel method*

The sol–gel method has been widely used to prepare a number of phosphors for displays and other materials of technical importance. We cite a number of representative examples below.

4.3.3.1 *Nanoclusters embedded in SiO_2 glasses*

Willi Lehmann reported in 1975 that very efficient luminescence was observed in, what he called, heterogeneous materials, such as SiO_2:CaX_2-Eu^{2+}/Mn^{2+} (where X = Cl, Br, or I), prepared by solid-state reactions.[16] These materials are similar to those found in the nanoclusters in SiO_2 which have been developed recently via the sol–gel method described in Section 4.3.1.[17–20] There are two ways to prepare such nanophosphor composites: (1) Colloids (sols) of phosphors prepared from the appropriate precursors are blended into TEOS or TMOS; the gelation process then proceeds as described before to form composites of SiO_2 gels and clusters of phosphors. Heat treatment is needed to finalize the form of the nanocomposites. (2) Nanophases can be obtained by phase aggregation from doped SiO_2 during thermal treatments. These nanophosphor-embedded silica glasses are transparent, and can be used for displays and in laser devices.[21,22]

SiO_2 doped with Eu^{3+} or with Eu^{3+} and Y^{3+} is used as an illustrative example to demonstrate the growth of these materials. Eu^{3+}-doped SiO_2 sol–gel glasses have been extensively studied in recent years,[18–21] as the $^5D_0 \rightarrow ^5F_2$ transition of Eu^{3+} at 612 nm has implications in various display technologies. The precursors used were tetraethoxysilane (TEOS = $Si(OC_2H_5)_4$ or $Si(OEt)_4$), yttrium isopropoxide $Y(OC_3H_7^i)_3$ in toluene–isopropanol, mixed with ethanol and water in a molar ratio of 1:0.1:1:1. HCl is added slowly as catalysis occurs until the pH of the solution reaches ~2.5. The mixture is stirred for several hours using ultrasound. While stirring, an aqueous solution of $EuCl_3$ is also added till the required doping level is attained. Hydrolysis of the alkoxide produces a wet gel which is dried slowly at 45°C in air in a plastic cuvette sealed with paraffin and perforated with pin holes to allow the evaporate to escape. After about 2 weeks, a clear transparent SiO_2 dry gel is obtained. The dry gels are annealed in air above 900°C in order to increase the density of the samples, and thereby their luminescence intensity. In the annealing process, the temperatures are raised at a rate of less than 30°C/h in order to get crack-free samples. The solubility of rare earth in SiO_2 glass is very limited. During the annealing process, the rare-earth ions may immigrate, aggregate, and form clusters. Because of concentration quenching due to clusterization of Eu, weak luminescence and short lifetime (0.8 ms) are observed in 1% Eu-doped SiO_2. However, much stronger luminescence and longer lifetime (1.8 ms) are detected in 1% Eu,10%Y-doped SiO_2 due to dilution of Eu in clusters of Y_2O_3.[23] The result indicates that the rare-earth oxides aggregate in the form of nanoclusters in the SiO_2 matrix.

4.3.3.2 *Nanoclusters of semiconductors embedded in SiO_2 glasses*

Nanoclusters of semiconductors embedded in glasses show interesting nonlinear optical and quantum confinement properties and have been extensively studied.[24,25] For preparing these composite materials, a solution of metal alkoxides (TEOS or TMOS in case SiO_2 is used as a host) and colloids of semiconductors are prepared in advance. Techniques used to prepare colloids of semiconductors may vary; in the case of PbS, $Pb(ClO_4)_2$ methanolic solution is used, which reacts with injected H_2S gas flow at about 70°C. Dodecane thiol, $CH_3(CH_2)_{11}SH$, needs to be added in the solution to stabilize the clusters of PbS and prevent aggregation.[26] For preparing CdS-nanocrystals-embedded SiO_2, $Cd(NO_3)_2.4H_2O$ can be used.[27]

The colloids of the semiconductors are then mixed with TEOS to form a uniform mixture by stirring. During the gelation process, the sols are entrapped in the SiO_2 gel network.

4.3.3.3 *Organic–inorganic hybrid materials*[28]

To prepare organic–inorganic hybrid materials, a solution of dyes, polymers, or biological substances are mixed with the metal alkoxides as in the first step described above. This can also be accomplished by soaking xerogels in an appropriate doping organic solution. The xerogels of silica prepared at step 4.3.1.1.4 are porous and water–alcohol is normally entrapped in the pores. These gels can be directly used as a host that can be "doped" with a solution of dyes, polymers, or biological substances as the organic solution easily diffuses into the pores of the gels. The gels can be annealed at 100–400°C to reduce porosity and the size of pores, and then be used as the host of the organic species. Depending on the type of organic species, the transparent hybrid materials can be used to make tunable lasers.[29]

4.3.3.4 *Thin films and coatings*

The most important applications of the sol–gel method are in the preparation of thin films of phosphors. At the step 4.3.1.1.2 when the solution becomes uniform and when hydrolysis begins, thin film coatings can be started by dipping substrates into the sol–gel solution or by spinning substrates. In the latter, a proper amount of solution is dripped on the spinning substrate to produce the film. The film is then annealed to increase in density and to increase its adhesive strength to the substrate. To produce thicker films, the processes can be repeated to produce multiple layers.

Various thin films have been fabricated for different applications. Erbium (Er) or other rare-earth-doped germania–silica thin films are fabricated for optical waveguide and amplifiers.[30] Indium and tin oxide thin films are fabricated for transparent conducting electrodes.[31] Antireflective and scratch-resistant surface coating of tantalum oxide for CRTs have also been produced.[32]

In the preparation of thin films of ZnO,[33] zinc 2-ethylhexanoate ($Zn[OOCCH(C_2H_5)C_4H_9]_2$) was dissolved in 2-ethylhexanoic acid ($C_4H_9(C_2H_5)CHCOOH$) and ethylacetate ($CH_3COOC_2H_5$). A mixture of distilled water and HCl was blended dropwise into the solution. The mixture was stirred for 30 min. A quartz substrate was dipped into the solution and dried in an oven at 200°C for 20 min. The dipping and drying process was repeated five times in order to get thicker films. The thin films were finally annealed at 800°C in air for one and half hours. The films showed a strong emission band at 530 nm.

4.3.3.5 *Aluminates*

Aluminates are a major kind of phosphors used in lighting and in displays. In Section 4.3.2, the SSG method was described for the preparation of $Y_3Al_5O_{12}:Ce^{3+}$. Other aluminates can also be synthesized by a similar procedure. Aluminates can also be prepared by the conventional sol–gel method, in which all the precursors are alkoxides or their solutions.

4.3.3.6 *Silicates*

Silicate phosphors, such as Zn_2SiO_4: Mn^{2+}, can be synthesized by the conventional sol–gel method, as described in Section 4.3.1. They can be also fabricated by the SSG method. As an example, the preparation of the blue phosphor $Sr_2MgSi_2O_7:Eu^{2+}$ is described here. TEOS and an aqueous solution of Sr and Mg nitrates were used. The specific weight of high-concentration water solution of the nitrates is much higher than that of TEOS. As a result, TEOS floats above the nitrate solution. The hydrolysis process is very slow. In order to speed up the process and to get uniform gels, the mixture is rapidly stirred in an ultrasonic bath set at a constant temperature of 65°C. The resulting white gels were baked at 80°C and the powders were slightly ground and fired at 700°C in air in a furnace. The powders are then sintered at 1150°C for 2 h in N_2+5% H_2 gas flow. The phosphor was also prepared by the standard solid-state reaction route under sintering temperature of 1200°C in N_2+5% H_2 gas flow. The peak emission intensity at 470 nm of the SSG-derived sample was found more than 40% stronger than that of the solid reaction sample.[11]

4.3.3.7 *Phosphate phosphors*

Phosphate phosphors, such as $Zn_3(PO_4)_2:Mn^{2+}$, $Sr_3(PO_4)_2:Eu^{2+}$, and $LnPO_4$, can be synthesized by the sol–gel procedure. The corresponding metal alkoxide solutions are uniformly blended with phosphorus alkoxides such as triethyl or trimethyl phosphates (both are liquids). Water and ethanol can be used to trigger hydrolysis and gelation processes. The gels can be baked dry and then sintered at 900–1100°C to obtain phosphor powders.

A modified procedure has been used for $LnPO_4$ activated with Eu^{3+} when some commercial alkoxides are not available.[34] First potassium isopropanolate is produced by the reaction of metallic potassium with isopropanol. Phosphorus and rare-earth alkoxides are formed in situ by the chemical reaction of P_2O_5 and $LnCl_3$ with the potassium isopropanolate solution. The white gels are collected by centrifugation and washed with distilled water several times to eliminate the KCl produced by the chemical reaction.

4.3.3.8 Borate phosphors

Borate phosphors, for example $YBO_3:R^{3+}$, can be fabricated in a similar way as the phosphates.[35] In this case, in addition to other metal alkoxides, liquid boric alkoxides, such as trimethyl borate $B(OCH_3)_3$ or triethyl borate $B(OC_2H_5)_3$, are used.

4.3.4 Conclusion

In the last two decades, sol–gel technology has developed rapidly and has been applied to the synthesis of a number of photoelectronic materials. This method is especially useful for preparing nanophosphor-embedded composites, luminescent thin films, and nanopowders of phosphors. A modification of the technique (i.e., SSG) allows the synthesis of large quantities of phosphor materials in a fairly economical way.

References

1. Graham, T., *J. Chem. Soc.*, 17, 318, 1864.
2. Ebelmen, M., *Ann. Chim. Phys.*, 16, 129, 1864.
3. Brinker, C.J., and Scherer, G.W., *Sol–Gel Science*: *The Physics and Chemistry of Sol–Gel Processing*, Academic Press, San Diego, 1990.
4. Livage, L., Henry, M., and Sanchez, C., *Prog. Solid State Ch.*, 18, 183, 1988.
5. MacCraith, B.D., McDonagh, C.M., O'Keeffe, G., McEvoy, A.K., Butler, T., Sheridan, F.R., *Sol–Gel Coating for Optical Chemical Sensors and Biosensors*, SPIE Sol–Gel Optics III, 2288, 518, 1994.
6. Levy, D., Serna, C.J., Serrano, A., Vidal, J., Oton, J.M., *Gel Glass-Dispersed Liquid-Crystal Optical Shutters*, SPIE Sol–Gel Optics II, 1758, 476, 1992.
7. Yoldas, B.E., *Amer. Ceram. Soc. Bull.*, 54, 286, 1975.
8. Jayachandran, M., Chockalingam, M.L., Lakshmanan, A.S., *Sol–gel Synthesis of Cadmium Tin Oxide Powder*, SPIE Sol–Gel Optics III, 2288, 745, 1994.
9. Jia, W., Brundage, R.T., and Yen, W.M., Isotope effects in the multiphonon relaxation of hydrated and deuterated cesium chloromanganate ($CsMnCl_3.2H_2O,2D_2O$), *Phys. Rev. B*, 27, 41, 1983.
10. Dongdong, J., Shaffer, V.C., Weyant, J.E., Goonewardene, A., Guo, X., Zou, Y.K., Li, K., and Jia, W., *Symposium of Solid-State Lighting Materials and Devices*, 2006 MRS Spring Meeting, April 17–21, 2006, San Francisco.
11. Dongdong, J., Li, K., Zou, K., and Jiang, H., Boston Applied Technology, Inc. Technique Report, 2005.
12. Ohno, K., and Abe, T., *J. Electrochem. Soc.*, 133, 638, 1986.
13. Shea, L.E., McKittrick, J., Lopez, O.A., *J. Am. Ceram. Soc.*, 79, 3257, 1996.
14. Narayanan, R., and Laine, R.M., *Appl. Organomet. Chem.*, 12, 919, 1997.
15. Waldner, K.F., Laine, R.M., Dhumrongvaraporn, S., Tayaniphan, S., and Narayanan, R., *Chem. Mater.*, 8, 2850, 1996.
16. Lehmann, W., *J. Electrochem. Soc.*, 122, 748, 1975.
17. Costa, Vilma C., Lochhead, Michael, J., and Bray, Kevin, L., Fluorescence line-narrowing study of Eu^{3+}-doped Sol–gel silica: Effect of modifying cations on the clustering of Eu^{3+}, *Chem. Mater.*, 8, 783, 1996.
18. Lochhead, Michael, J. and Bray, K.L., Rare-earth clustering and aluminum codoping in sol–gel silica: Investigation using europium (III) fluorescence spectroscopy, *Chem. Mater.*, 7, 572, 1995.
19. Jia, W., Liu, H., Feofilov, S.P., Meltzer, R., and Jiao, J., Spectroscopic study of Eu^{3+}-doped and Eu^{3+},Y^{3+}-codoped SiO_2 sol–gel glasses, *J. Alloy Compd.*, 311 (1), 11, 2000.
20. Jia, W., Wang, Y., Santiago, M., Castro, L., and Liu, H., Photoluminescence of $Eu^{3+}:Y_2O_3$ nanoclusters embedded in SiO_2 glass, *Mat. Res. Soc. Symp. Proc.*, Vol. 519, 271, 1998.
21. Boulton, J.M., Teowee, G.T., Bommersbach, W.M., Uhlmann, D.R. *Second-Harmonic Generation from Sol–Gel Derived Ferroelectric and Piezoelectric Thin Films*, SPIE Sol–Gel Optics II, 1758, 292, 1992.

22. Reisfeld, R., Prospects of sol–gel technology towards luminescent materials, *Opt. Mater.*, 16, 1, 2001.
23. Weiyi, J., Wang, Y., Fernandez, F., Wang, X., Huang, H., and Yen, W.M., Photoluminescence of Ce^{3+},Tb^{3+}:Y_2O_3 nanoclusters embedded in SiO_2 sol–gel glasses, *Mat. Sci. Eng. C*, 572, 55, 2001.
24. Yamane, M., Takada, T., Mackenzie, J.D., Li, C.-Y., *Preparation of Quantum Dotes by the Sol–Gel Process*, SPIE Sol–Gel Optics II, 1758, 577, 1992.
25. Tseng, J.Y., Li, C.-Y., Takada, T., Lechner, C., Mackenzie, J.D., *Optical Properties of Metal Cluster-Doped ORMOSIL Nanocomposites*, SPIE Sol–Gel Optics II, 1758, 612, 1992.
26. Guglielmi, M., Martucci, A., Righini, G.C., Pelli, S., *CdS- and PbS-Doped Silica–Titania Optical Waveguide*, SPIE Sol–Gel Optics III, 174, 1994.
27. Minti, H., Eyal, M., Reisfeld, R., Berkovic, G., *Chem. Phys. Lett.*, 183, 277, 1991.
28. Dunn, B., and Zink, J.I., 1991. Optical properties of sol–gel glasses doped with organic molecules, *J. Mater. Chem.*, 1, 903, 1991.
29. Rahn, M.D., King, T.A., *Characreristics of Dye-Doped Ormosil Lasers*, SPIE Sol–Gel Optics, 2288, 364, 1994.
30. Martucci, A., Guglielmi, M., Fick, J., Pelli, S., Forastiere, M.A., Righini, C.C., Battaglin, C., *Germania Sol–Gel Waveguide for Optical Amplifiers*, SPIE Sol–Gel Optics V, 3943, 2, 2000.
31. Perry, C.C., McGiveron, J.K., Harrison, P.G., *Aqueous Sol–Gel Routes to Conducting Films of Indium Oxide and Indium-Tin-Oxide*, SPIE Sol–Gel Optics V, 3943, 270, 2000.
32. Belleville, P.F., Prené, P., Lambert, B., *UV-Cured Sol–Gel Broadband Antireflective and Scratch-Resistant Coating for CRT*, SPIE Sol–Gel Optics V, Vol. 3943, 67, 2000.
33. Jia, W., Monge, K., Xu, W., and Katiyar, R., spectroscopy of pure and Eu^{3+}-doped ZnO, *Integr. Ferroelectr.*, 42, 357, 2002.
34. Nedelec, J.M., Mansuy, C., Mahiou, R., *J. Mol. Struct.*, 651–653, 165, 2003.
35. Boyer, D., Bertrand-Chadeyron, G., Mahiou, R., Caperaa, C., and Cousseins, J-C., *J. Mater. Chem.*, 9, 211, 1999.

chapter four — section four

Methods of phosphor synthesis and related technology

Shuji Inaho and Takashi Hase

Contents

4.4 Surface treatment 393
  4.4.1 Protection of particles 393
  4.4.2 Improvement of coating properties 394
    4.4.2.1 Phosphors used in monochrome CRTs 394
    4.4.2.2 Color CRT phosphors 395
  4.4.3 Improvement of contrast (pigment coating) 395
  4.4.4 Methods of surface treatment 396
References 397

4.4 Surface treatment

Surface treatment is usually used to improve the characteristics of as-fired phosphors for practical application. Particularly for zinc sulfide phosphors, surface coating is indispensable. In spite of the importance of this treatment, few research reports on surface treatment have been published and only a part of the knowledge has been disclosed in patents.

The purposes of surface treatment are broadly classified into three categories: protection of particles, improving the coating characteristics of the phosphor screen during fabrication of cathode-ray tubes (CRTs), and improving the contrast of the phosphor screen (pigment coating). Here, the surface treatments for the phosphors used in CRTs for each of the three instances above are described.

4.4.1 Protection of particles

The phosphors used in CRTs usually have particle sizes between 4 and 12 µm, which provide high emission efficiency and are optimized for the CRT manufacturing process. The phosphor particles suffer damage in several ways. For example, the crystals are broken by physical forces such as pressure, abrasion, and shock[1,2]; they are oxidized at the surface by heat produced in CRT manufacturing; and their emission intensity is reduced or the emission color is changed by diffusion of impurities.

The phosphors can be protected from chemical change by surface treatment. Currently known examples are the SiO_2 coating of zinc sulfide surfaces with sodium silicate solution[4] to reduce darkening of the sulfide surface by moisture and ultraviolet light, a phenomenon referred to as blacking,[3] and the coating of easily hydrolyzed calcium sulfide surfaces with organic waterproofing compounds.[4]

The manufacture of CRTs involves baking at temperatures from 400 to 450°C to remove organic materials such as the polyvinyl alcohol (PVA) used in phosphor coating or the acrylic emulsion film used to form the aluminum reflection film. One example of surface treatment to protect the phosphor from this heat is the use of a phosphate coating to control surface oxidation and yellowish-brown coloration of ZnS and (Zn,Cd)S during baking.[5,6] Another example is the phosphate coating of blue-emitting ZnS:Ag to prevent the change of the emission color to green as a result of contamination of the phosphor with copper ions.[7]

4.4.2 *Improvement of coating properties*

CRTs in current use are broadly classified into three categories according to their use: motion picture displays (used in entertainment TVs), graphic and character displays (used in computer monitors, etc.), and instrumentation displays (oscilloscopes, radar screens, etc.).

The phosphor particles are coated onto the inner surface of the panel glass to form a thin uniform layer (the fluorescent screen). The fluorescent screen must have the optimized thickness* (usually from 10 to 30 μm) that provides the maximum brightness over the entire screen.

The phosphor screen must be free of defects such as irregularities or pinholes, and it must adhere to the glass tube surface well enough so that it does not separate from the surface during the manufacturing process.

In color CRTs, phosphors that emit in the three primary colors (red, blue, and green) are applied in a fine mosaic pattern (see 4.3). Naturally, the patterning must be done accurately and mixing of the different colors (color contamination) must be avoided. To obtain a fluorescent screen of high quality, surface treatment that is suitable for the phosphor application method is required. In the following, surface treatments for various phosphor application methods are described.

4.4.2.1 *Phosphors used in monochrome CRTs*

In the process of forming fluorescent screens by the sedimentation method (see 4.3), the supernatant liquid is decanted after the phosphor has settled on the glass surface. If the adhesion of the phosphor screen to the glass surface (wet adhesion strength) is insufficient, the layer will separate from the glass surface; if the adhesion of the layer after drying (dry adhesion strength) is insufficient, the fluorescent layer will separate during the process of forming the emulsion film for the aluminum reflective layer.

This wet adhesion strength and dry adhesion strength basically vary with the concentrations of potassium silicate and electrolyte present during settling. The effect of surface treatment is thought to be the strengthening of both the wet and dry adhesion strengths by controlling the gelling speed of the SiO_2 and the amount of adsorption on the phosphor surface. Accordingly, the surface treatment effect is not so great as for the color CRT phosphors.

The surface treatment for practical phosphors employs phosphates or silicates. There is, however, not much information in the literature about monochrome CRT phosphors.

---

* As a measure of the screen thickness, phosphor weight per unit screen area or the screen weight is often used.

4.4.2.2 *Color CRT phosphors*

Color CRTs mainly use the color selection grid (shadow mask or aperture grill) scheme. In this case, the electron beam that passes through the color selection grid causes the phosphors in a fixed red-blue-green pattern to fluoresce. To attain sufficient resolution, the red-blue-green phosphor pattern must be very fine, with stripes or dots about 0.2 mm wide. Displays for characters or graphics must have an even higher resolution, and the pattern must thus be even finer.

Spin coating using a slurry is the most widely used coating method (see 4.3). Here, surface treatment serves the purposes of forming a dense, uniform fluorescent layer by increasing the phosphor dispersion in the slurry, and also preventing missing stripes or missing dots by increasing the adhesion of the fluorescent layer to the glass surface and preventing color contamination between the phosphors of different colors.

The quality of the phosphor screen (packing density, uniformity, and adhesion) is greatly affected by the phosphor dispersion in the slurry. While formerly the phosphor dispersion in the slurry was improved through such means as grinding in a ball mill, the resulting damage to phosphor particles decreased the luminescence efficiency. For that reason, phosphor treatments to obtain high dispersion in slurry without the use of mechanical means have been considered in recent years. Drying is the indispensable final stage in the production of phosphors; in the drying process, however, the phenomenon known as blocking occurs. In blocking, clumps of several phosphor particles can form by cohesion due to the surface tension of water. While alternative ways such as using alcohol or surfactants can be considered,[8,9] surface treatment with silicate compounds or silicon dioxide are practically used.

These surface treatments are also effective against the color contamination described above. For sulfide phosphors, the firing conditions and the method of treatment after firing strongly affect the surface characteristics, greatly changing the zeta potential, i.e., the dynamical surface potential, of the phosphor in water.[10] Fogging of the glass surface and color contamination are considered to be caused by the zeta potential between the phosphors. The effect of the surface treatment can thus be thought of as an appropriate adjustment of the zeta potential resulting from a change in the nature of the phosphor surface. There is also an example of examining the adhesion strength of the phosphor in CRT panels in relation to the contact charge.[11]

Another means of reducing color contamination is surface treatment with a phosphate.[7] The effect of this treatment is thought to be making the relatively hydrophobic sulfide phosphor hydrophilic by the introduction of ions to the phosphor surface.

4.4.3 *Improvement of contrast (pigment coating)*

When the part of the screen excited by the electron beam is made as bright as possible while other parts are as dark as possible, the screen contrast is high and the resulting image is clearly visible. Although each phosphor particle is normally transparent to visible light, the surface of the phosphor screen is highly reflective because of light diffusion due to the many minute particles that make up the screen. The result is that the screen appears white. Lowering the optical transmittance of the face glass so as to absorb outside light incident on the CRT is one countermeasure, but this method is inadequate because it also reduces the screen luminosity by absorption of the phosphor emissions. The black matrix method, in which a black coating is applied to the areas not covered by the phosphor stripes (or dots), is very effective, but it only covers from 30 to 50% of the surface area, the rest remaining white.

Thus, the method of coating the phosphor screen itself so as to reduce its reflectivity was conceived. This method, referred to as pigment coating, was made practical around

1975. Pigment coating is now used for some monochrome CRTs and almost all color CRTs. A black coating is effective from the viewpoint of reducing the reflectivity of the phosphor screen, but it absorbs the phosphor emission as well as ambient light. Thus, a coating that has the same color as the emission is used; that is to say, blue-emitting phosphors are coated with blue, and red-emitting phosphors are coated with red pigments. Green-emitting phosphors are not usually treated in this way; this is because, in the case of the commonly used sulfide phosphors, the phosphor itself is green, and no suitable highly reflective green pigment is available.

The pigment coating materials must be capable of withstanding high temperatures and must be chemically stable so as to endure the CRT manufacturing processes. The pigment particle size is less than 1 μm, one tenth the size of the phosphor particles. Thus, if the pigment is simply mixed into the slurry, the pigment particles will separate from the phosphor, making it difficult to obtain a homogeneous layer. For this reason, the pigment must be bound to the phosphor surface with a binding agent. The binding agent may be either an organic compound or an inorganic compound, but organic compounds have the advantages of providing strong binding and can be removed along with the PVA by the baking process. Specific examples are given in 4.4.4.

4.4.4 *Method of surface treatment*

Surface treatment involves two processes: cleaning the phosphor particles and coating the phosphor particle surfaces.

The purpose of the cleaning process is to remove the residue, which mainly consists of the flux added to aid particle growth and diffusion of the activator into the crystal during firing. This residue is harmful to the CRT manufacturing process and decreases CRT performance because it is converted into a gas by the electron beam used in CRTs. The gas thus produced reduces the vacuum in the CRT and creates the possibility of reactions with the electrode material. The cleaning to remove the residue is produced by washing phosphor particles with acid or alkaline chemicals; only in the case of highly water-soluble material is it sufficient to wash with deionized water.

The coating is generally done in water, as explained below. First, after sufficient cleaning, the phosphor is suspended in deionized water and the coating agent is added while stirring. The result is that the surfaces of the phosphor particles are covered with a film or very fine particles of the coating agent. In a case where the coating agent is generated by a chemical reaction, the reagent is sometimes initially added to the solution in the form of very fine particles. In addition to inorganic materials, organic surfactants for improving dispersion are also used. These organic materials and the organic binder used for binding pigments to the phosphor surface are completely removed by baking during the CRT manufacturing process. The inorganic coating materials, however, remain as they are. If the coating is excessive, the inorganic coating material will absorb electron beam energy, thus lowering the efficiency of the CRT. For this reason, the coating amount is kept to less than 1wt% relative to the phosphor, except for special cases such as pigment binding.

As a specific example, the coating of a phosphor with silicates for the purpose of improving dispersion in the slurry and preventing color contamination is described. First, the phosphor is suspended in deionized water and the prescribed amount of a soluble silicate such as potassium silicate is added. Then, an aqueous solution of a soluble salt of Zn, Al, Y, Mg, Ba, or Ca is slowly added with stirring. This generates an amorphous oxide that adsorbs to the phosphate.[12–16] The phosphor is then cleaned, dehydrated, and dried. Another method is to add a colloidal silicate (e.g., Ludox by Dupont or Snowtex by Nissan Chemical) to the phosphor suspension for adsorption to the phosphate surface.[17] The process for coating with phosphates to prevent color contamination is about the same as for silicates. That is, a prescribed amount of a soluble salt, such as an alkaline salt of orthophosphoric acid or pyrophosphoric acid, is added to the phosphor suspension and, while stirring, an aqueous solution of a sulfate, nitrate, or acetate of Al, Zn, Ca, Ba, etc. is added. These metal ions and the phosphate ions bind to form nonsoluble salts that coat the phosphor surfaces.[18,19] Other methods include the formation of organic silane on the phosphor surfaces[20] and the mixing of fine particles of oxides of B, Al, Ti, Ga, Ge, As, Nb, Mo, Sn, Sb, Ta, W, or other metals for adsorption to the phosphor surfaces.[21–23] The various methods described here are sometimes used in combination to increase the effectiveness of the coating.

While pigmenting methods, on the other hand, are protected by various patents, the important points are sufficient contact between the pigment and the phosphor particles, and good dispersion of the phosphor particles. In a method first proposed by RCA,[24] the pigment particles are thoroughly dispersed in a polyvinyl pyrrolidon solution, while the phosphor particles are dispersed in a gelatin solution. The two solutions are then mixed so that the pigment adheres to the phosphor.

Many other methods have been proposed to increase the adhesion of the pigments and to improve the dispersion of the phosphor. One example is a method in which the phosphor particles and pigment particles are charged with opposite polarities and brought into contact by means of a binder, thus achieving adhesion through electrostatic attraction.[25] Another example is to achieve adhesion by adding a monomer resin such as acrylic resin or styrene to the phosphor suspension.[26,27] Other examples are the adsorption to the phosphor surface of latex colloid particles that have ionic functional groups, such as ethylene vinyl chloride or butadiene, followed by adsorption of the pigment,[28] the mixing of gelatin and gum arabic as a binder,[29] the combination of acrylic emulsion cations and anions,[30] and the use of polystyrene and acrylic resins.[31] Many patents have been issued for such methods that employ organic compounds. There are also many other examples using silicates and aluminates,[32,33] and silane films[34] as binding intermediaries.

References

1. Sekine, T. and Kotera, Y., *J. Luminesc.*, 12/13, 1976.
2. Takagi, K., and Ishii, T., Proc. 26th Annual Conf. Chem. Soc. Jpn., 2J40, 1972.
3. Shionoya, S., *J. Chem. Soc. Japan, Ind. Chem. Sec.*, 52, 79, 1949.
4. Isojima, T., Japanese Patent Disclosure (Kokai) 50-26782 (1975).
5. de Boer, F. and Broos, J., *Electrochem. Tech.*, Jan. Feb., 1966.
6. Takizawa, T., Torii, T., and Tanabe, N., Japanese Patent Publication (Kokoku) 49-43076 (1974).
7. Schaller, E., Japanese Patent Publication (Kokoku) 40-28648 (1965).
8. Isojima, J. and Oikawa, M., Japanese Patent Publication (Kokoku) 52-5034 (1977).
9. Isojima, T., Takayama, Y., and Inoue, M., Japanese Patent Publication (Kokoku) 51-12032 (1976).
10. Levy, B., *J. Electrochem. Soc.*, 106, 218, 1959.
11. Tamatani, M. and Oguchi, T., *Tech. Digest, Phosphor Res. Soc. 181st Meeting*, July, 1980 (in Japanese).
12. Isojima, T. and Oikawa, M., Japanese Patent Publication (Kokoku) 50-15747 (1975).
13. Isojima, T. and Kubo, R., Japanese Patent Publication (Kokoku) 55-4793 (1980).
14. Yokota, K., Japanese Patent Publication (Kokoku) 47-13242 (1972).
15. Matsuura, S., Japanese Patent Publication (Kokoku) 47-13481 (1972).
16. Fermoiren, G.A.W. and Grafeslein, Y.Y.K., Japanese Patent Publication (Kokoku) 50-3615 (1975).
17. Kato, A., Japanese Patent Publication (Kokoku) 46-35425 (1971).
18. Takizawa, T., Torii, T., Tanaka, Y., and Omatoi, S., Japanese Patent Publication (Kokoku) 49-43075 (1974).
19. Takizawa, T., Torii, T., and Tanabe, N., Japanese Patent Publication (Kokoku) 49-43076 (1974).

20. Otake, Y. and Ito, T., Japanese Patent Publication (Kokoku) 53-17555 (1978).
21. Yokota, Y., Miyagawa, T., Tanaka, Y., and Torii, T., Japanese Patent Publication (Kokoku) 47-7521 (1972).
22. Yokota, T., Miyagawa, T., Tanaka, Y., and Torii, T., Japanese Patent Publication (Kokoku) 44-11769 (1969).
23. Hosokoshi, K., Japanese Patent Publication (Kokoku) 47-21352 (1972).
24. Lipp, S.A., Japanese Patent Disclosure (Kokai) 50-56146 (1975).
25. Kato, A. and Yaguchi, M., Japanese Patent Disclosure (Kokai) 52-133088 (1977).
26. Tsugukuni, H. and Takahashi, T., Japanese Patent Disclosure (Kokai) 52-133089 (1977).
27. Shimizu, Y., Japanese Patent Disclosure (Kokai) 55-164282 (1980).
28. Rotia, J.S. and Brenin, F.B., Japanese Patent Disclosure (Kokai) 52-109488 (1977).
29. Kanda, K., Kotera, N., Murakami, S., Yoshida, C., Eguchi, S., Iwasaki, K., and Iwamoto, I., Japanese Patent Disclosure (Kokai) 53-5088 (1978).
30. Oba, Y., Kano, T., Hayashi, M., Takada, H., Kanda, K., and Eguchi, S., Japanese Patent Disclosure (Kokai) 53-76181~4 (1978).
31. Azuma, H., Kida, N., Ogura, R., and Tokida, K., Japanese Patent Disclosure (Kokai) 53-76740 (1978).
32. Oba, Y. and Manabe, T., Japanese Patent Disclosure (Kokai) 54-37081 (1979).
33. Sumida, T., Wakatsuki, T., and Koga., Y., Japanese Patent Disclosure (Kokai) 52-107287~8 (1977).
34. Ubugaki, N., Ito, T., Otake, Y., and Tsukagoshi, H., Japanese Patent Disclosure (Kokai) 52-107769 (1977).

chapter four — section five

Methods of phosphor synthesis and related technology

Yoshifumi Tomita

Contents

4.5 Coating methods 399
  4.5.1 Cathode-ray tubes 399
    4.5.1.1 Screen structure 400
    4.5.1.2 Phosphor coating process 400
References 403

4.5 *Coating methods*

4.5.1 *Cathode-ray tubes*

Phosphors widely used for screens of cathode-ray tubes are powdered materials, the size of which ranges from a few micrometers up to about 10 µm. The accumulated knowledge from various powder coating technologies for the paint and printing industries has played an important role in the development of the phosphor coating process. The resulting process, however, had to meet stricter requirements to develop reliable phosphor screens, as follows.

Generally, the manufacturing of cathode-ray tubes starts with the phosphor coating process and is followed by several other processes, such as baking and evacuating, to make the completed tubes. The screen efficiency and color of the emission must be maintained, while avoiding spotting and other irregularities that may arise from contaminants present throughout the tube-making processes. The finished products must also maintain a high performance level throughout their lifetime following exposure to extended electron beam bombardment.

With these requirements, the coating process is designed to avoid adhesive materials that adversely affect the phosphors. Deleterious effects to the manufacturing process include mechanical damage to the phosphor grains, and the introduction of killer centers that reduce the phosphor efficiency and change the color of emission. Also, adhesives with poor bake-out properties cannot be employed in the phosphor coating process. Various organic polymers are widely used as the best adhesive to make uniform powder layers in the paint industry. In phosphor coating, however, one must give careful consideration to the bake-out properties of polymers. The process is then designed to give a uniform screen

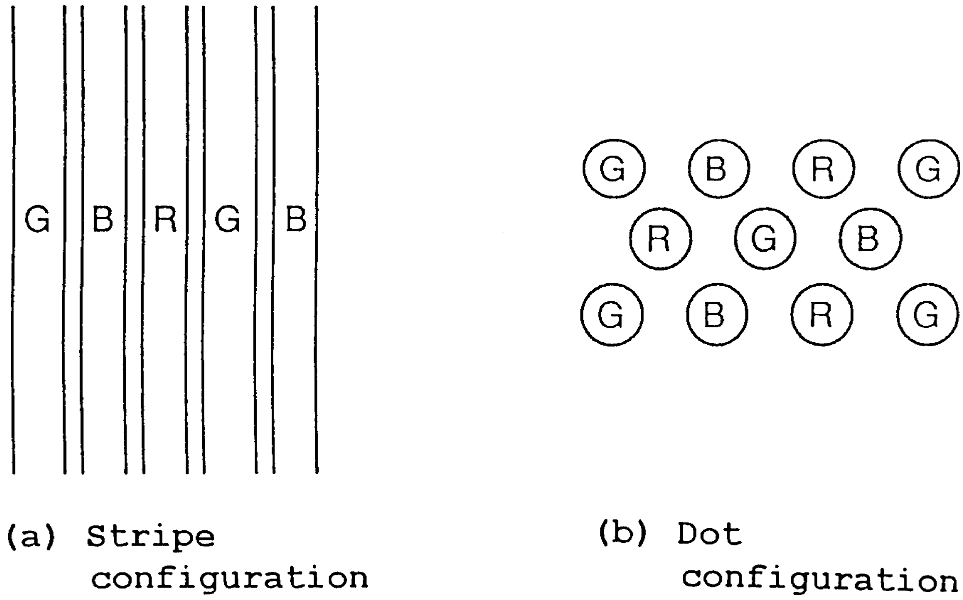

Figure 20 Mosaic screen of three primary colors: (a) stripe configuration; (b) dot configuration.

across the entire face plate glass; the latter can have any shape and this depends on the tube type. The current processes being used are summarized, along with screen structures, in the following sections.

4.5.1.1 Screen structure

Monochrome screen. Monochrome screens are used in black-and-white television tubes, oscilloscope tubes, monochrome monitor tubes, and individual projection tubes (green, blue, red) used for color television. Here, monochrome implies a single color over the entire tube screen. Blending of different phosphors is often employed to realized the desired color.

Multilayer screen. This group includes the screens of radar tubes and penetration tubes (voltage modulation tubes for color). Phosphors on different emission colors are coated layer by layer, with or without insulating film between neighboring layers, depending upon the tube requirements.

Mosaic screen. Mosaic screens are used for color television tubes and color monitor tubes, and are technically very promising. Phosphors of different emission colors (green, blue, red) are deposited in fine two-dimensional patterns of the face plate glass. Figure 20 shows examples of mosaic screens composed of the three primary colors (green, blue, red) (a) in a stripe and (b) a dot configuration.

4.5.1.2 Phosphor coating process

Settling process.[1] The setting process is very unique and highly adaptable to coating monochrome screens in bottle-shaped tubes. The process has a long history and is attractive because it is the only process feasible for monochrome tubes. Figure 21 shows the settling steps. A bulb is set horizontally neck-side up. An aqueous (aq.) solution of electrolytes is poured into the bulb. An aqueous silicate suspension of phosphor powders is then added quickly through a funnel with a perforated tip. The bulb remains still until

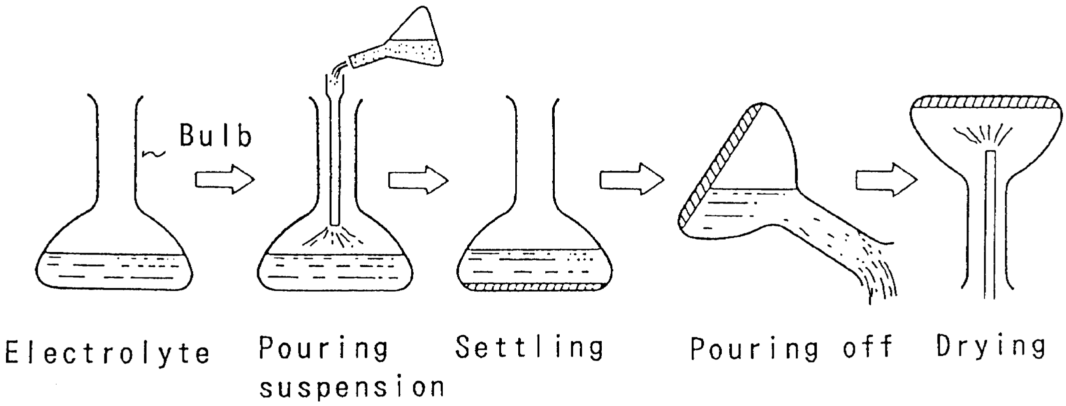

Figure 21 Steps in the settling process.

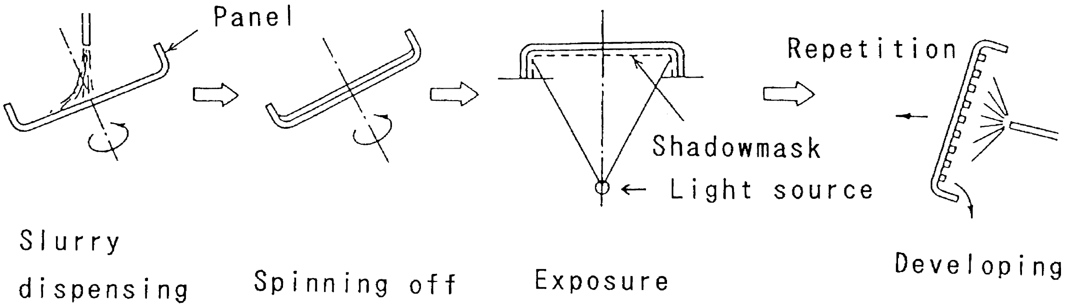

Figure 22 Steps in the slurry process.

the phosphor powders settle down onto the bottom (face plate) and binding by the silicate is completed. The surplus solution in the bulb is smoothly decanted so as to avoid any damage to the deposited screen. Finally, the screen is dried by blowing hot air into the bulb. Repetition of the above process allows for the formation of multilayered screens.

Gelation of silicates on the surface of phosphor grains and of the glass takes place by electrolyte ions (Ba, K, etc.), resulting in siloxane bridges (O-Si-O) between grains and between the phosphor and the glass.

Slurry process.[2] The slurry process is the typical process used for manufacturing mosaic screens. Figure 22 shows the steps in the process: A suspension is prepared by dispersing phosphor powders in an aqueous polyvinyl alcohol (PVA) solution. An aqueous dichromate solution is added to the suspension to make the mixture photosensitive. The mixture is called a slurry; hence, the name of the process. A glass panel is set face-down in a spin-coating machine. The slurry is dispensed onto the panel while the glass is rotated slowly with a small tilt angle. The slurry is allowed to spread evenly on the inside surface of the panel without bubbles and using a minimal slurry volume. The panel rotation is then increased to obtain the desired screen thickness on the panel. Any excess slurry is recycled. The coating on the panel is dried with an infrared heater.

The panel is then exposed to light after an appropriate shadow-mask (or an aperture grill) has been placed within the panel. The exposure system is equipped with an ultraviolet (UV) light source (mercury-arc lamp) at the site corresponding to the deflection center of the electron gun of the cathode-ray tube to be finished; the system is equipped with a lens that equalizes the light beam path to that of the electron beam trajectory, and with a shader plate that controls the light intensity distribution along the panel surface. Generally, a pattern size (dot diameter or stripe width) increases with light intensity for a given exposure time. Therefore, the distribution of the light intensity along the panel surface has to be controlled by employing the shader plate, which corrects the intensity of light from the arc lamp. After exposure, the coating is developed by spraying hot water to wash out phosphors in unexposed areas.

The PVA-dichromate system works here as a negative photoresist. The slurry process, in a word, is photolithographic, employing a shadow-mask as a photomask. The only difference between the slurry process and other photolithographic processes is that a given shadow-mask cannot be used to expose other individual panels, whereas a general photomask is repeatedly used to reproduce the same patterns on many substrates.

Dusting process.[3] In the dusting process, an aqueous dichromate-PVA solution is dispensed onto a panel glass in the same way as for the slurry process. Dry phosphor powders are then blown directly onto the PVA-filmed panel before the film gets a chance to dry out. By this process, phosphor powders adhere to the panel. Dusting is named after the manner in which dry phosphor powders are placed on the screen. The subsequent procedures are exactly the same as those used in the slurry process. A positive feature of the dusting process comes from the result that phosphors are applied separately as dry powders, not as suspended powders in photosensitive solutions. In this way, the complexity of mixing and controlling the suspension may be avoided, and phosphors of fairly large grain size, which would normally settle in the suspension, can be used for coating. The screen thickness is controlled by the thickness and drying temperature of the photosensitive film and by the dusted volume of phosphors.

Phototacky process.[4] This process has also been developed for mosaic screens, and features the use of phototackifiable materials instead of the conventional photosensitive materials. The former material becomes tacky or sticky only when exposed to UV light. An aqueous solution of phototacky material is prepared by dissolving a diazonium double salt (e.g., *p*-diazo-N,N-dimethylaniline chloride-zinc chloride) in aqueous polymer solution (e.g., polypropylene glycol alginate). The solution is spin-coated on a face plate glass, and the film is exposed to UV light through a shadow-mask. Phosphor powders are dusted right on the exposed film. The dusted panel is developed by blowing air to remove phosphors lying on the unexposed areas. Repetition of the process two more times from exposure steps for the other two colors provides a mosaic screen.

In this process, high-definition patterns can be obtained because the exposure is initially only on photosensitive film, which contains no phosphor powder; the latter tends to scatter the light beam, blurring the edges of the pattern. The mechanism of phosphor adhesion comes from the result that upon exposure to light, a diazonium double salt with zinc chloride decomposes into nitrogen and a resinous mixture of zinc chloride, *p*-chloro-N,N-dimethylaniline, plus other compounds. The zinc chloride in the mixture is hygroscopic, and absorbs the ambient moisture, resulting in a tacky solution.

Others. Improvements in phosphor coating technology have been continuously sought since the advent of cathode-ray tubes in order not only to improve screen performance, but to streamline the manufacturing processes. In the following, some of these concepts are discussed. Not all processes that have evolved can be justified in terms of their immediate practical value; some are very promising for specific objectives, not necessarily CRTs, and require sophistication not presently available on an industrial scale.

Printing.[5] For printing, a phosphor ink is prepared by mixing phosphor powders with some organic liquid vehicle. The ink is applied to a substrate through a mesh screen. The mesh screen is patterned with an ink-blocking layer that makes it possible to print the mosaic design. The process is used in some electroluminescent panel (phosphor dispersion type) and vacuum fluorescent displays. Printing was used for phosphor screen processes during the early periods of color television tubes; later, printed flat glass plates were incorporated directly into the tube assembly.

Electrophoresis.[6] A phosphor grain suspended in an appropriate medium can be surrounded with a double layer of electric charge created by the selective adsorption of ions onto the grain surface; this can result in an electrokinetic potential that produces grain migration under an applied DC voltage. By selecting the appropriate ion species and their concentration, phosphor grains can be uniformly deposited either on a cathode or on an anode plate. A glass plate with a transparent electroconductive layer is used as the substrate. This process is very useful in the preparation of uniform screens of high packing density. This is because the electrostatic force is much stronger than gravity in driving phosphor grains to settle more rapidly onto the substrate; in addition, because electroosmosis takes place at the electrode (substrate) surface, the liquid medium in the spaces between grains is squeezed out from the immobilized phosphor grain layer.

Electrophotography.[7] The process is, in principle, almost the same as that of an electrostatic charge-driven copy machine or xerography for office use. Issues are how to impart and electrostatic charge on phosphor grains, how to identify a highly transparent photoelectroconductive material (PEC), and how to fix the charged grains firmly on a substrate. In this process, exposed areas of a charged PEC on the substrate, previously coated with a transparent electroconductive film, lose the charge, and charged phosphor grains of the same polarity adhere to those areas by induction. This process is thought to be quite promising for mosaic color screen fabrication.

References

1. Sadowski, M., *J. Electrochem. Soc.*, 95, 112, 1949.
2. Saulnier, T., *J. Electrochem. Technol.*, 4, 1-2, 27, 1966.
3. Levy, S., *J. Electrochem Soc.*, 101, 99, 1954.
4. Nonogaki, S., *Abstr. Electrochem. Soc.*, 1982 Meeting, 812.
5. Kikuchi, M., Presented at *IEEE Chicago Conference*, June 4, 1981.
6. McGee, J.D., *Advances in Electronics and Electron Physics*, 22A, 571, 1966, Academic Press.
7. Tomita, Y., Japanese Patent Publication (Kokoku), 48-12547, 1973.

chapter four — sections six–eight

Methods of phosphor synthesis and related technology

Shigeharu Nakajima* and Yuji Itsuki

- 4.6 Fluorescent lamps 405
  - 4.6.1 Phosphor suspensions 405
  - 4.6.2 Types of phosphor suspensions 405
  - 4.6.3 Preparation of phosphor suspensions 406
  - 4.6.4 Characteristics and manufacturing methods of adhesive additives 407
  - 4.6.5 Method of adding adhesives 408
  - 4.6.6 Coating method 408
- 4.7 Mercury lamps 409
- 4.8 Intensifying screens (Doctor Blade Method) 410
- References 411

4.6 *Fluorescent lamps*

The lighting industry constitutes the largest consumer of phosphor materials and produces the largest quantity of phosphor-related products in the form of fluorescent lamps. The phosphor coating process for the manufacturing of these lamps has evolved into a comparatively simple procedure, a desirable feature for the industry.

4.6.1 *Phosphor suspensions*

First, a high-viscosity solution is prepared by dissolving a binding agent in an organic solvent or deionized water in a concentration range of 0.5 to 3.0 wt%. This solution is called a vehicle.[1] A phosphor suspension prepared by dispersing phosphors in the vehicle is used as a coating solution. Further, an adhesive additive from 1 to 5 wt% of the phosphors is added to the suspension to obtain better adhesion of the phosphor layer to the inner surface of glass tubes.

4.6.2 *Types of phosphor suspensions*

As shown in Table 3, the vehicles are classified into two types: organic vehicles and water-based vehicles.

---

* Shigeharu Nakajima is deceased.

Table 3 The Mixing Amount of the Vehicles with 100 g of Phosphors and the Viscosity of the Suspensions

	Composition and viscosity	Organic suspension		Water-based suspension
Vehicle	Solvent	Butyl acetate	Xylene	Deionized water
	Binding agent and Concentration in solvent	NC 1 wt% (2000 s)	EC 1.8 wt%	PEO 0.6 wt% pH 8.7
	Viscosity (cP)	23	40	69
	Mixing amount (g)	126	104	150
Suspension	Viscosity (cP)	56	51	76
Drying condition Temperature, air velocity		30–35°C 2 m s^{-1}		65–80°C 1–10 m s^{-1}

Note: NC : nitrocellulose; EC : ethyl cellulose; PEO : polyethylene oxide; cp : rotational viscosimeter (TOKYO KEIKI E type) 50 rpm, 22°C.

Nitrocellulose or ethyl cellulose is usually used as a binding agent for organic vehicles. For water-based vehicles, on the other hand, ammonium polymethacrylate, polyethylene oxide, hydroxypropyl cellulose, hydroxyethyl cellulose, carboxymethyl cellulose, a co-polymer of maleic acid anhydride and isobuthylene, or a co-polymer of maleic acid anhydride and polymethyl vinyl ether are used.

In the past, ammonium polymethacrylate was widely used as a binding agent in water-based vehicles. However, it is very difficult to use ammonium polymethacrylate for the coating of tri-color phosphors, because it reacts with tri-color phosphors and causes the agglomeration of phosphors. In view of these facts, the main binding agent of the water-based vehicle has been changed to polyethylene oxide in recent years.

Comparing the characteristics of these two types of phosphor suspensions, the processes of coating and drying are easier when an organic suspension is used. However, solvents such as butyl acetate and xylene cost more than deionized water, have strong odors, and require equipment for the prevention of fire or explosion. Although water-based suspensions tend to generate bubbles during the coating process and require higher temperatures in the drying process than organic suspensions, the consideration of industrial and environmental safety has made it the trend to use water-based suspensions. However, for some kinds of phosphors whose water resistance is low, organic vehicles are still used.

4.6.3 Preparation of phosphor suspensions

Table 3 shows examples of the mixing ratio of phosphors to vehicles in typical phosphor suspensions. These suspensions are used for manual coating of the glass tubes for fluorescent lamps (diameter, 32 mm; nominal power, 40 W) with halophosphate phosphors. For halophosphate phosphors made by Nichia, a treatment to improve dispersion is made beforehand, so that uniform coating films are obtained only by simply mixing the phosphors with the vehicle.

In the case of using phosphors that are not treated, the phosphor suspension should be ball-milled or colloid-milled to disperse the phosphor particles into the vehicle sufficiently. The thickness of the phosphor coating is controlled by adjusting the viscosity and specific gravity of the phosphor suspension. In general, a Ford viscosimeter[2] (a cup-shaped instrument) is used for measuring the viscosity, and a floating hydrometer is used to measure the specific gravity. In the case of water-based suspensions, the concentration of binding agent is generally 0.5 to 3.5 wt% in vehicle, and the pH value is maintained between 7 and 9 by the addition of ammonium hydroxide (NH_4OH). The weight ratio of phosphors to water-based vehicles in the suspension is about 1:1.5. To decrease the surface tension of the phosphor suspension, one or two kinds of nonionic or anionic surface-active agents are used. To prevent foaming in the coating process, a nonionic antifoaming agent can be added to the suspension.

4.6.4 *Characteristics and manufacturing methods of adhesive additives*

An adhesive additive is a material added to the phosphor suspension to prevent chipping-off of the phosphor layer from the inner surface of a glass tube. Prior to 1953, chipping-off did not occur very frequently because milling was utilized. At that time phosphor suspensions were milled to obtain optimum sized particles, and the fine particles resulting from milling gave sufficient adherence. However, at the time the manufacture of circular fluorescent lamps was started (in 1953), chipping-off of the phosphor layers became a problem because the adherence of fine particles was insufficient for extension to glass tubes during the bending process. To solve this problem, adhesive additives were introduced for the first time.

The required physical and optical characteristics of adhesive additives are:

1. They absorb little radiation in the ultraviolet and visible regions.
2. Their sintering temperature should be similar to the forming temperature of the glass tube.
3. They should be stable under long-term exposure to ultraviolet rays.
4. They should be stable in the suspension.

Borates of alkaline earths are typical examples of thermomelting adhesives.[3,4] These borates can be obtained by the precipitation method.

An example of borate preparation is as follows:

$$3.2H_3BO_3 + 0.7BaCl_2 + 0.3CaCl_2 \xrightarrow[\mathrm{pH = 8,\ 50°C}]{NH_4OH} \left(Ba_{0.7}Ca_{0.3}\right)O \cdot 1.6B_2O_3 \tag{3}$$

Borates prepared in this way begin to fuse at about 650°C, and change into a fused state at 850°C.

Because of the improvement in particle size control, the particle size distribution of the phosphor had been made sharper and both rough and fine particles are eliminated; as a result, the milling process is no longer needed. However, this new process has reduced the amount of fine particles that acted as adhesives, with the result that serious chipping-off problems arose even for straight tubes.

In this case, super-fine particles such as colloidal alumina made by DEGUSSA AG, or pyrophosphates of alkaline earth prepared by precipitation, are employed as adhesives. These fine particles are thought to fill the spaces among phosphor particles and strengthen their adherence to glass.

An example of the pyrophosphate preparation is as follows:

$$CaCl_2 + H_3PO_4 \xrightarrow[\mathrm{70°C}]{NH_4OH,\ \mathrm{pH = 5}} CaHPO_4 \xrightarrow{\mathrm{800°C}} Ca_2P_2O_7 \tag{4}$$

Table 4 Examples of Adhesive Slurries

	Vehicle	Percentage by weight (%)	Adhesive additive	Percentage by weight (%)
For straight tubes	Deionized water	70	Calcium pyrophosphate	30
For circular tubes	Butyl acetate (NC 1%)	85	Calcium pyrophosphate (5) Barium calcium borate (10)	15
	Xylene (EC 1.5%)	85	Same as above	15

Note: NC : nitrocellulose, EC: ethyl cellulose.

These adhesive additives are added to phosphor suspensions alone or as a mixture. For the coating of straight tubes, alumina or pyrophosphate are used in both organic and water-based suspensions. Due to the speed-up of lamp manufacturing, the previously mentioned borates are added to fine adhesives, such as pyrophosphate or alumina in organic suspensions, to obtain higher adherence. In the coating process of circular fluorescent lamps, borates or the above-mentioned mixture is used in organic suspensions. However, these compounds are difficult to use in the water-based coating process of circular fluorescent lamps because borates are unstable in water and phosphor suspensions containing borates must be used within a few days of preparation. If the suspensions are left for a longer time, the borate ion causes the agglomeration of phosphors, lowering the adherence of the layer. To solve these problems, borates made water-resistant by adding phosphorus,[5] water-resistant low melting-point glass,[6] and eutectic melt frits[7] of calcium pyrophosphate and calcium tetraborate [$Ca_2P_2O_7{\cdot}CaB_4O_7$] (melted into a glass and then shattered into fine particles) have been developed. Further, borates of rare earths also are in present use.

4.6.5 Method of adding adhesives

Though borate adhesive additives and fine-grain adhesive additives are on the market, their adhesive efficiency is low when they are simply mixed with the phosphor suspension. To obtain better adhesive efficiency, the adhesive additives must be added in the ratio shown on Table 4 to a vehicle or a solvent of the same kind as the suspension, and then they must be wet-ground to form a slurry. The coating suspension should contain adhesive additive from 1 to 5 wt% of phosphors. The addition of more than 5 wt% may deteriorate the characteristics of lamps, such as their initial lumen output and lumen maintenance.

4.6.6 Coating method

The coating suspension is made to flow down along the inner surface of a glass tube. The excess suspension drops into a trough at the bottom of the tube. This excess suspension is collected from the trough and mixed with new suspension for reuse. After the tube is coated, warm or hot air is made to flow into the tube to dry the suspension and form a phosphor film on the inner surface of the glass tubes. Organic compounds (binding agent, etc.) in the phosphor layer are removed by baking the tubes at 500 to 600°C. Examples of the drying condition are shown in Table 3.

There is an optimum thickness of the coated phosphor film. When the thickness of a phosphor film is thinner than this optimum value, the phosphor does not absorb ultraviolet radiation sufficiently; thus, the luminous output of the lamp is low. On the other hand, if the phosphor film is too thick, some fluorescent light will be absorbed by the phosphor layer, and some will be reflected back into the lamp, thus also lowering the lumen output.

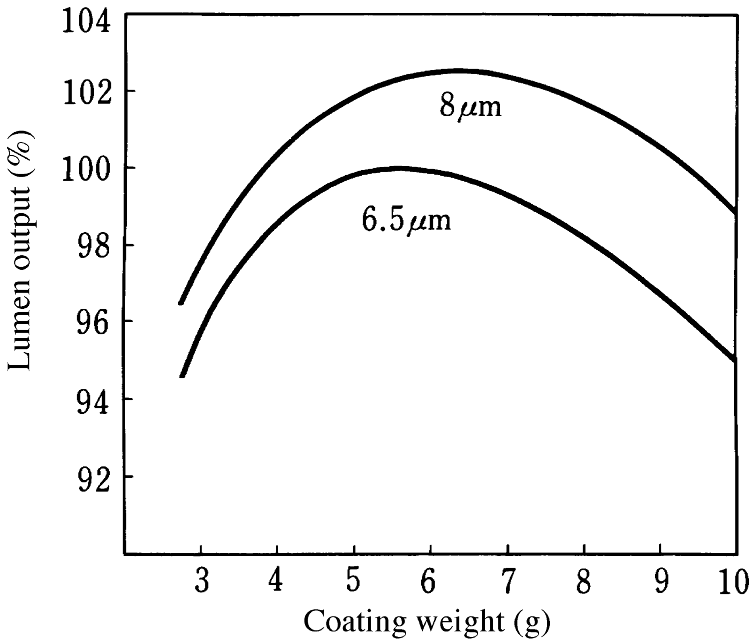

Figure 23 The relationship between the coating weight of phosphors and lumen output (calcium halophosphate phosphors, 4 feet, 32 mmϕ bulbs; the particle diameter is measured by the air-permeability method). (From Nichia Chemical Industries, Ltd., *Technical Information: Halophosphate Phosphor*, 1982 (in Japanese). With permission.)

Figure 23 shows the relationship between the amount of applied phosphors and the luminous output[8] (the thickness of a coated film is indicated by the weight of the applied phosphors per tube). In general, if the particle size of the phosphor increases, the optimum thickness also increases. As illustrated in Figure 24,[8] it is helpful to have a graph showing the relationship between the coating weight of the phosphor and the diffuse transmittance of the phosphor layer. Diffuse transmittance is measured by a light detector placed outside the phosphor-coated glass tube with a light source placed inside the glass tube.

If the thickness of the phosphor layer is not uniform throughout the length and circumference of the tube, the luminous output will be lower than expected. To obtain a uniform phosphor film, the viscosity and specific gravity of the phosphor suspension in the coating process, as well as the temperature and air velocity in the drying process, should be carefully controlled.

4.7 Mercury lamps

Unlike the fluorescent lamps, the mercury lamp is spheroid in shape. Phosphors are coated onto the inner surface of the outer glass envelope of a mercury lamp. The suspension or the electrostatic coating method can be used in the production of mercury lamps. The suspension coating process is similar to the coating process of fluorescent lamps; the coating suspension is sprayed into the glass envelope using a nozzle.

In the electrostatic coating method,[9] the glass envelope is heated to 150 to 300°C to increase the electrical conductivity to 10^9 to 10^{11} $S{\cdot}m^{-1}$. The inner surface of the glass envelope is positively charged by voltages of 40 to 80 kV. The nozzle with the negative electrode is inserted into the glass envelope to spray phosphor powder onto the inner

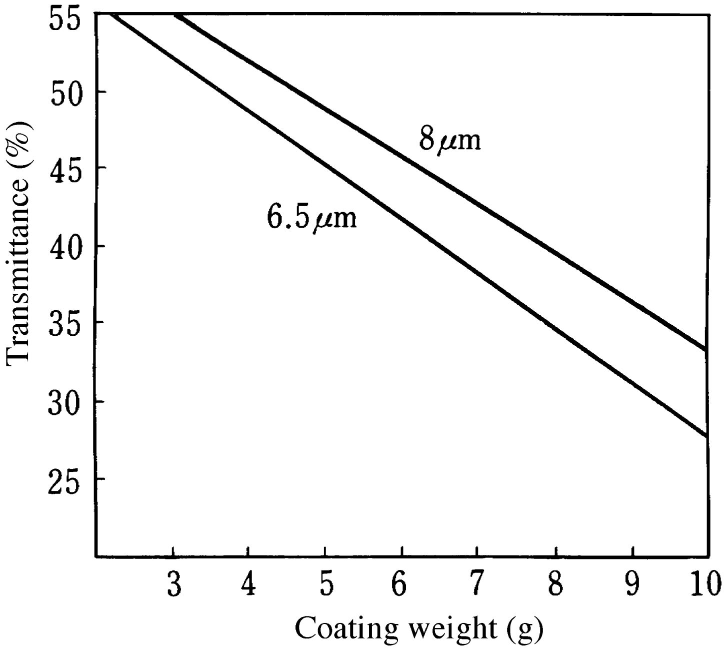

Figure 24 The relationship between the coating weight of phosphors and diffuse transmittance (the same sample as in Figure 23 is used). (From Nichia Chemical Industries, Ltd., *Technical Information: Halophosphate Phosphor,* 1982 (in Japanese). With permission.)

surface of the envelope. After that, if necessary, the glass envelope is filled with steam, and then baked at a relatively low temperature (200 to 400°C) in order to enhance the adhesion of the phosphor layer to the glass. To improve the fluidity of the phosphor suspension during the spraying process, a small amount of colloidal silica (AELOSIL, etc.) is mixed with the phosphor. The silica acts as an adhesive when phosphors are coated.

4.8 Intensifying screens (Doctor Blade Method)

Intensifying screens require a phosphor layer thickness of more than 70 μm and are manufactured without a baking process. The Doctor Blade Method, well known in the field of paper, paint, and ceramics manufacturing, is usually used.

A vacuum-defoamed organic slurry containing a higher concentration of phosphors, which has high viscosity with a small amount of an organic polymer, is supplied to the container shown in Figure 25. The slurry flows out from the small opening at the bottom of the doctor blade edge onto a moving thin organic polymer film and forms a phosphor layer on the film. The thickness of the coating layer is controlled by the distance between the blade edge and the film and by the sliding speed of the film. After the coated film is cut to proper size, a plastic sheet is stuck on the phosphor side of the coated film to protect the phosphor layer.

A precipitation method employing a low-viscosity slurry is also used. In this method, larger phosphor particles are precipitated comparatively quickly because of their larger weight, and are distributed preferentially in the bottom of the phosphor layer. As a result, the filling-up density of the bottom layer is increased. However, coatings prepared by this method are susceptible to damage through mechanical forces such as bending.

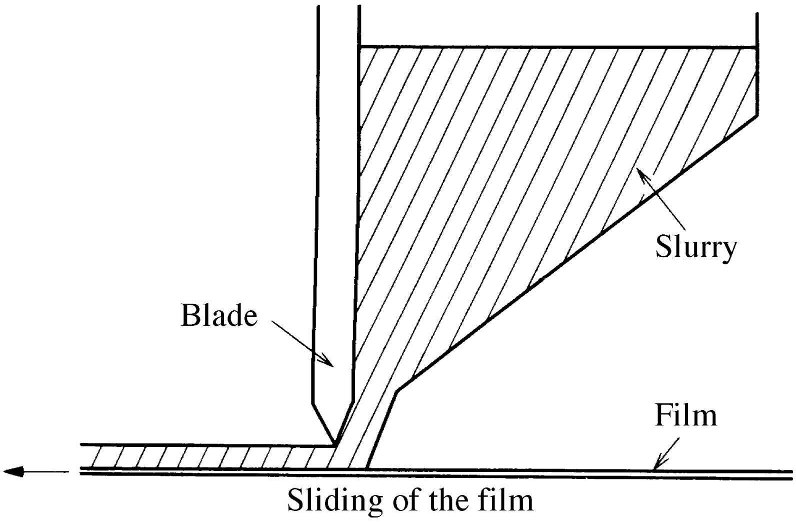

Figure 25 Doctor Blade Method.

References

1. JIS (Japan Ind. Std.) K 5400 (1979) Testing Methods for Paints; JIS (Japan Ind. Std.) K 5500 (1977) Glossary of Paint Terms.
2. JIS (Japan Ind. Std.) K 5402 (1971) Ford Cup for Determining Consistency of Coatings; JIS (Japan Ind. Std.) Z 8809 (1978) Standard Liquids for Calibrating Viscometers.
3. Sabato, C., Ito, Z., and Suzuki, T., Japanese Patent Publication (Kokoku) 34-3786 (1959).
4. Kamiya, S., Japanese Patent Publication (Kokoku) 37-515 (1962).
5. Narita, J., Yamasaki, H., and Tanaka, N., Japanese Patent Disclosure (Kokai) 57-108188 (1982).
6. Shingai, M., Hagiwara, M., Nakano, M., and Ohno, Y., Japanese Patent Disclosure (Kokai) 57-187367 (1982).
7. Fan, A. K. and Chiola, V., Japanese Patent Disclosure (Kokai) 57 -96080 (1982); Taubner, F. R., Chiola, V., and Fan, A. K., Japanese Patent Disclosure (Kokai) 57-98970 (1982).
8. Nichia Chemical Industries, Ltd., *Technical Information: Halophosphate Phosphor,* 1982 (in Japanese).
9. Ito, T., *J. Illum. Eng. Japan*, 70, 221, 1986; Shindo, N., Japanese Patent Disclosure (Kokai) 53-122269 (1978); Shindo, N. and Iwafuji, Y., Japanese Patent Disclosure (Kokai) 54 -62673 (1979).

chapter four — section nine

Methods of phosphor synthesis and related technology

Masaaki Tamatani

4.9 Dispersive properties and adhesion strength 413
  4.9.1 Properties required for phosphor screens 413
  4.9.2 Environment for screening process 413
  4.9.3 Dispersion 414
  4.9.4 Adhesion strength 415
References 419

4.9 Dispersive properties and adhesion strength

4.9.1 Properties required for phosphor screens

It is desirable for a phosphor screen to have a smooth surface free of irregularities and stained spots, complete uniformity over the entire screen, high packing density, and an appropriate adhesive strength to the substrate. Methods for manufacturing such good quality screens have been developed based mainly on the experience acquired in phosphor coating processes developed by fluorescent lamp and cathode-ray tube (CRT) manufacturers. Some of the accumulated know-how has appeared in patent specifications. However, only a few scientific papers systematically describing the factors that govern screen properties have been published thus far.

4.9.2 Environment for screening process

Irregularities and stained spots in phosphor screens are caused by foreign matter in the phosphor powder or in the suspending liquid, by abnormally large or aggregated phosphor particles, and by contaminated substrate glass. In the case of ZnS-type phosphors, heavy metals (mainly copper) from the air sometimes contaminate part of the phosphor screen and change the luminescence color.[1] To prevent such defects, phosphor screening for CRTs is usually performed in a clean room.

High stability in the properties of phosphor suspension slurries is required for producing good screens, since a slurry is used repeatedly in the production lines; the same slurry may be used for several days. After prolonged use in the manufacturing process, aqueous slurries for color CRTs and for fluorescent lamps sometimes begin to produce pinhole or crack defects in phosphor screens due to changes in the viscosity and pH values. This may be brought about by the change in particle size distribution within the slurry and in its composition during repeated use. In some cases, such deterioration is also caused by bacterial propagation from water and/or air into phosphor slurries.[2]

4.9.3 Dispersion

A well-dispersed slurry, in which individual particles exist without aggregation, is required for preparing a phosphor screen with high packing density* and without irregularities and stained spots. To obtain good dispersion, mechanical dispersing methods such as hard grinding or cracking of a phosphor should be avoided as much as possible, since luminescence properties are usually degraded when phosphor particles are cracked. Therefore, during the firing (solid-state reaction) process of phosphor production, sintering between particles should be minimized. For this reason, it is important to select well-dispersed powders of raw materials and to optimize firing conditions (time, temperature, atmosphere, quantity of raw materials, kind and quantity of flux agents for crystal growth, deviation from the stoichiometric composition, etc.). For the same reason, such processes as washing phosphors with water or acid, classifying particle size in a liquid, light ball milling, colloidal particle deposition on phosphor particle surfaces, and repeated sieving, are necessary after the firing.

The degree of slurry dispersion depends on particle wettability in the liquid and on the forces acting between particles.[5] As the particle size decreases, the particles tend to aggregate because the wettability decreases; further, the effect of external forces such as the gravitational or stirring force also decreases and becomes weaker than the attraction between particles. In order to increase the wettability, particle surfaces are often treated with deposits of solventphilic organic or inorganic surfactant agents or colloids.

Van der Waals attractive and electrostatic repulsive forces acting between particles influence the dispersion. For example, ZnS particles** without surface treatment aggregate in water due to the strong Van der Waals forces. When pyrophosphate ions are added to the slurry, the aggregation disappears abruptly at concentrations when the adsorbed pyrophosphate ions form a monolayer on the particle surfaces.[6] This occurs because the electrostatic repulsive force resulting from the ionic charges on the particle surfaces overcomes the Van der Waals attractive force between particles. In other words, particles are either aggregated or dispersed, depending on whether the absolute value of the zeta potential*** corresponding to the charges on the particles is below or above a certain threshold value, as shown in Figure 26. In the case of Y_2O_2S, it is also known that the dispersion improves as the zeta potential increases.[7] Electric charges on a particle in water are generated when the pH value deviates from the isoelectric point**** of the particle. During the sedimentation process for forming a phosphor screen in a monochrome CRT, particle dispersion is usually good; this is because the pH value of the potassium silicate solution used as the suspending medium in this case is higher than the isoelectric points of almost all phosphors. In the case of the slurry method, organic surfactant agents adsorbed on a particle also contribute

---

* High packing density is desirable specially for a screen to obtain high resolution and to protect the glass substrate from direct bombardment of electrons (CRTs) or mercury ions (fluorescent lamps). Recently, effects of phosphor particle shape and depositing method have been studied. Good dispersion of a pearl-like spherical particle phosphor[3] as well as physical force brought about by the centrifugal sedimentation[4] produces high packing density.

** In this experiment, weight-averaged particle size was 6.7 μm by the microscope observation method.[6]

*** More precisely, the potential difference at a solid-liquid interface that contributes effectively to interfacial electrokinetic phenomena.

**** A pH value of the solution in which particles lose surface charges.

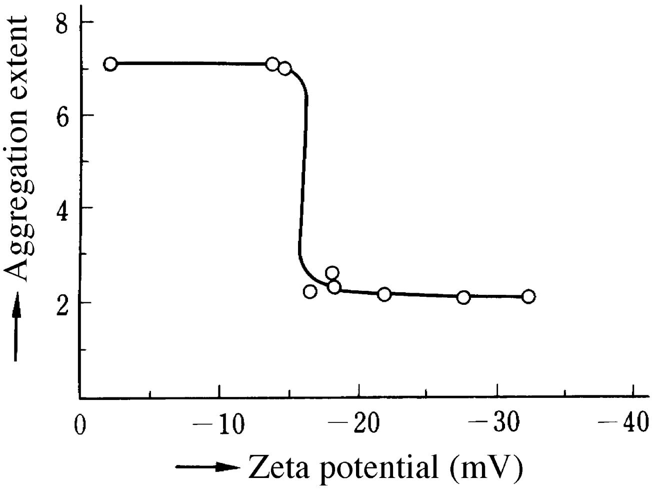

Figure 26 Aggregation extent as a function of zeta potential for a ZnS phosphor. (From Shionoya, S. and Ishikawa, T., *J. Chem. Soc. Japan Ind. Chem. Soc.*, 58, 900, 1955 (in Japanese). With permission.)

to the dispersion because they produce electric charges on the phosphor particles, in addition to increasing the wettability as described above.

Dispersion is often evaluated based on particle size-related properties, such as particle size distribution in a liquid and the ratio of average particle sizes measured using different methods (microscope, sedimentation, Coulter counter, etc.). Sedimentation volume and speed are other measures, because more aggregation results in larger sedimentation volumes and higher sedimentation speeds when the phosphors being tested have the same primary particle size.* Another important slurry property is how easily phosphors can be dispersed again after sedimentation. Therefore, it is difficult to judge whether a slurry is good or bad for practical use based only on the sedimentation volume and speed. The most widely accepted method for evaluating the slurry screening properties is an indirect one, where the dispersion is evaluated by visual inspection of the screen surface produced for qualities such as screen thickness, flatness, and uniformity. This is a practical approach inasmuch as the screen, not the slurry, is the commercial product that is finally viewed by the user.

4.9.4 Adhesion strength

Phosphor particles coated in fluorescent lamps and monochrome CRTs should have sufficient adhesion strength to the glass substrate and to other particles. The forces acting at the interfaces between the particles and the substrate and between the particles themselves are the Van der Waals and electrostatic forces, and the liquid interfacial tension;[8] their overall adhesion strength increases with the number of contact points. External gravitational or mechanical forces that act against the adhesion work more weakly on particles with smaller mass. Therefore, phosphor adhesion is strong when the phosphor particles are small and/or planar in shape. It is also strong in a screen structure having high packing density where small particles fill vacant spaces within a particle layer on a substrate. In addition, small particles tend to sinter to other particles and to a substrate during the device baking process, resulting in strong adhesion strength. The high adhesion strength of small particles has been confirmed in experiments using halophosphate phosphors on a glass substrate.[9]

---

* Particle size when all particles are separated from each other. Aggregated particles are called secondary particles.

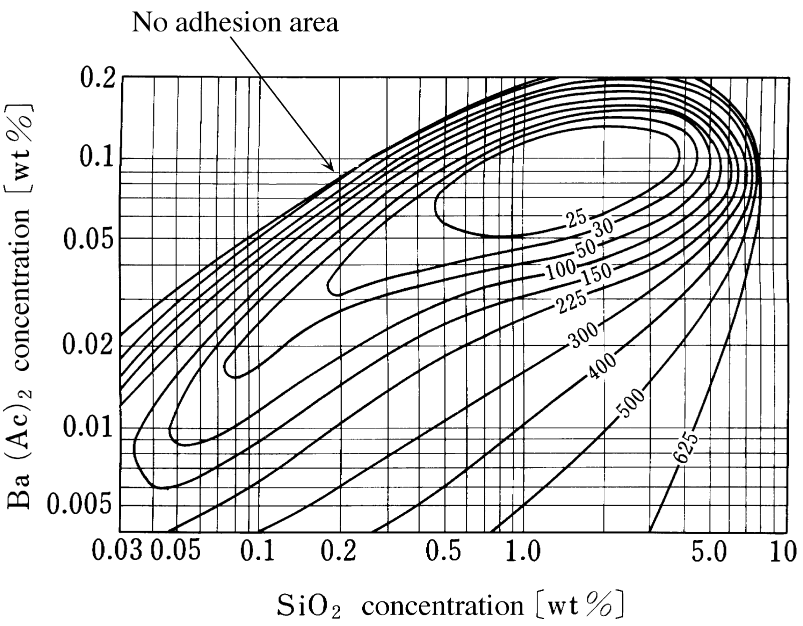

Figure 27 Contour lines showing equal wet adhesion strengths for P4 phosphor. (Numbers in the figure show size (mm^2) of the area where phosphor particles are blown off by a water stream with a constant pressure.) (From Miyakawa, S., Yoshikawa, S., and Naitou, M., *Dai-Nippon-Toryou Shahou*, 14, 22, 1961 (in Japanese). With permission.)

For a monochrome CRT, the adhesion strength of a phosphor screen to a substrate in an aqueous solution (wet adherence) is evaluated by measuring the size of a small circular area produced by removing the phosphor particles by means of a water jet stream; the impinging jet is produced under constant pressure through a small nozzle. The larger the area cleared by the jet, the lower the adhesion strength. Adhesion strength is governed by the concentration of potassium silicate and barium salts (or electrolytes such as potassium sulfate) in the settling solution, as shown in Figure 27.[10] Strong adhesion is found in certain regions of the concentration, though it varies somewhat depending on the kind of phosphors being deposited. It is known that low adhesion is due to the repulsive force produced when both the substrate glass and the phosphors have large negative zeta potentials in the settling solution.[11] The zeta potentials vary depending on such factors as phosphor firing conditions, kind of dopant, surface treatments, and the composition of the settling solutions.[12] After the drying process, the adhesion strength of a screen (dry adherence) increases with the potassium silicate concentration in the settling solution. In practice, the composition of the settling solution is selected so as to provide sufficient strength in both wet and dry adhesion.

In a color CRT, phosphor patterns of stripes (or dots) are photolithographically formed, generally in the order green, blue, and red (or blue, green, and red), through the repetition of the following processes: deposition of a photosensitive phosphor slurry, drying, ultraviolet photoexposure to harden the desired stripe pattern through a shadow mask, and development. The last process washes away with water the nonhardened phosphor layers at the nonphotoexposed areas. Picture qualities such as color reproducibility and white uniformity are degraded when phosphor particles laid down during one process invade the stripe positions that should be filled with other phosphors, or when phosphor particles deposited during a subsequent process adhere to the phosphor stripes that have already been formed, as shown in Figure 28. Some manufacturers call the former defect "residue," to distinguish

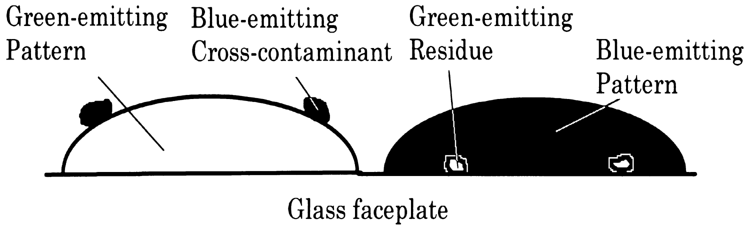

Figure 28 Residue and contamination in the case of the blue-emitting phosphor coating after the green.

it from the latter, called "cross-contamination." Adhesion should be weak at areas other than the photoexposed areas, while it should be strong at the photoexposed areas.

The adhesion strength of the phosphor screen is evaluated by the water jet impinging method similar to that used in the monochrome CRT. More practically, however, it is evaluated by the photoexposure method; reduction in exposure time to ultraviolet light for the photosensitive phosphor screen through a photomask leads to insufficient hardening at the stripe (or dot) edges. Then, narrower stripes (smaller dots), which are easily peeled off during the development process, are produced. If smaller phosphor stripe (or dot) sizes are obtained without peeling when the exposing time is successively reduced, stronger adhesion strength at the photoexposed areas has been achieved.

The photosensitive slurry is a suspension liquid containing a dispersed phosphor in an aqueous solution of polyvinyl alcohol (PVA), a dichromate compound (usually ammonium dichromate (ADC)), several kinds of surfactants, and other additives. Ultraviolet irradiation from a high-pressure mercury lamp reduces the dichromate (Cr^{6+}) to chromate (Cr^{3+}) ion; the Cr^{3+} ions form PVA networks insoluble in water by bridging reactions.[13] The photosensitivity depends on several factors such as temperature, concentration of the dichromate, nature and quantity of the surfactants, pH and viscosity of the slurry, and the particle size distribution and surface treatment of the phosphor. Figure 29 shows the pH dependence of light transmission spectra of the dichromate.[14] Usually, the pH is controlled to keep it at a neutral or slightly basic value.

The depth to which the exposing ultraviolet light penetrates the phosphor layer is an important factor affecting the adhesion strength to the substrate, since, within the layer, the portion close to the glass substrate as well as the portion close to the layer surface should be sufficiently hardened. A higher proportion of small particles in the particle size distribution causes larger light scattering and reduces the penetration depth. Better dispersion of the phosphor leads to higher adhesion strength. To improve the adherence, the screen is at times photoexposed from the face plate side (back exposure), though UV is usually applied from the shadow mask side.

Precoating the etched glass faceplate with a PVA film is known to increase the adhesion strength by forming ester bonds between the silanol group of the glass and PVA.[15,16] Polystyrene latex precoating and addition of polymer emulsion to the slurry are considered useful for improving the photosensitivity at the photoexposed pattern areas or for relaxing the strains produced during the drying and developing processes.[17]

Factors that influence the adhesion strength at the unexposed area (degree of the residue and cross-contamination) occur first during the phosphor coating process, according to a number of patent specifications. For example, (1) phosphor particles are trapped in the precoat layer, such as PVA, when the layer is swelled by successive applications of phosphor slurry;[18] (2) phosphor particles are trapped in the residual photosensitive PVA layers used to form black stripes that are not completely removed in processing;[19] (3) phosphor particles are deposited at substrate portions that have geometrically uneven

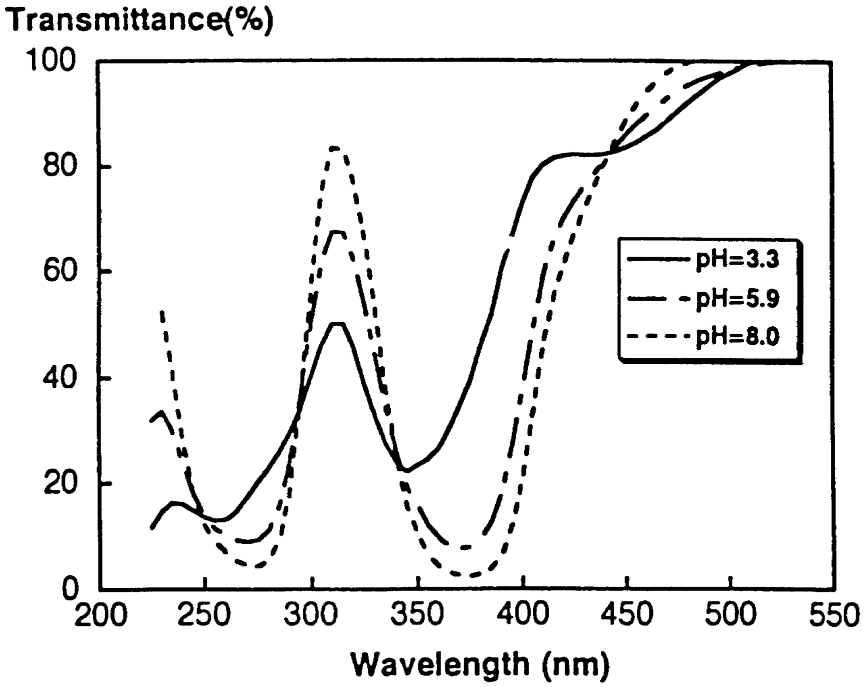

Figure 29 pH dependence of the transmission spectra of Cr^{6+} oxyanions. (From Takahashi, F., Mikami, T., and Hase, T., *Display and Imaging*, 3, 71, 1994 (in Japanese). With permission.)

structures;[20] (4) phosphor stripes, when hardened insufficiently, capture additional phosphor particles deposited in a later step;[21] and (5) insufficient development leaves phosphor particles in the wrong or at undesired stripe positions.[22] In addition, the extent of residue and contamination depends also on slurry conditions such as the quantity ratio of the phosphors to photosensitive liquid, the pH of the slurry, and the nature and quantity of surfactant agents in the slurry.[23] Furthermore, the adhesion depends on the kind of phosphors being used, the particle size and shape, surface treatments,[24] and pigment coatings on the particle surfaces.[25]

The main reason for the existence of such a large number of factors controlling the adhesion of the phosphor particles to the unexposed areas is that adhesion strength is determined by the properties of the interface between the phosphors and the substrate, rather than by the phosphors or substrates themselves. This was demonstrated by experimentally as follows. When coatings of phosphors *1* and *2*, with differently treated surfaces, were applied to glass panel *a*, the residue level for *1* was better than that for *2*. These results were, however, often reversed when the phosphors were applied to glass panel *b* whose precoat had a composition different from that used for *a*.

In some cases, the electrostatic force acting at the interface between a phosphor particle and the substrate plays a leading role in the residue and in cross-contamination. Under certain conditions, there is a correlation between the residue level and the zeta potentials for pigmented red-emitting phosphors.[26] For ZnS phosphors, more residue is observed with the increase in the contact electric charge generated between the panel precoat material and phosphors coated with metal oxide colloid particles.[27] This fact is explained as follows. When two dissimilar materials are in contact, equal electric charges with opposite polarity are induced on each surface, causing electrostatic attraction between them. For a simple metal oxide, the contact charging tendency is correlated to the electronegativity of the metal ion as shown in Figure 30.[28a] It is also correlated to the zeta

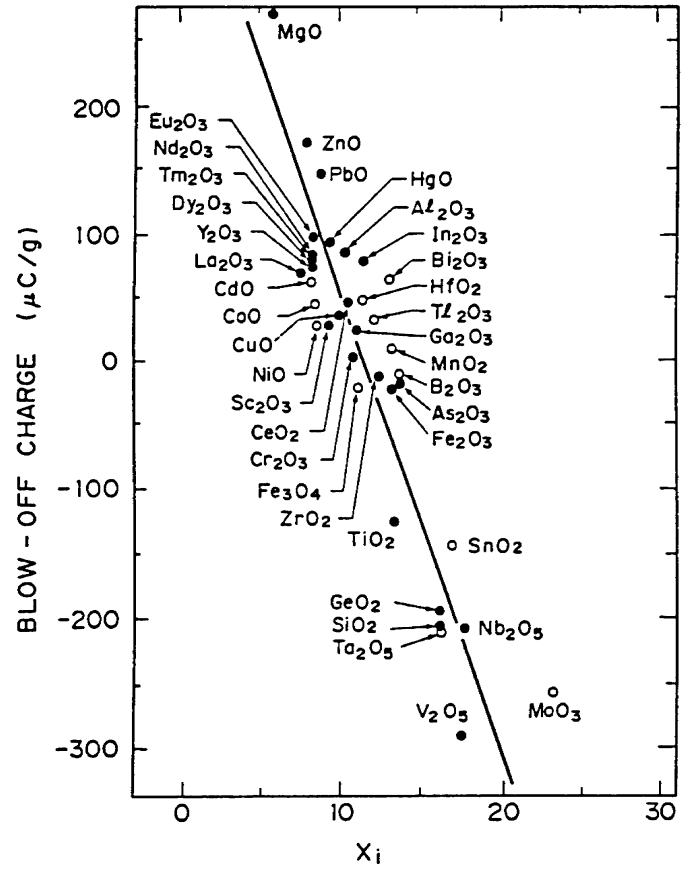

Figure 30 Charging tendency for oxides as a function of generalized electronegativity X_i for metal ions. Blow-off charge means the electric charge amount generated when an oxide powder makes contact with a reference iron powder using the blow-off method. (From Oguchi, T. and Tamatani, M., *J. Electrochem. Soc.*, 133, 841, 1986. With permission.)

potential in water.[28b] Therefore, the residue level may be minimized by adjusting the amount and kinds of surface deposit oxides so as to give the phosphor particles a characteristic contact charging tendency close to that of a given substrate.

References

1. Japanese Patent Publication (Kokoku) 40-28648 (1965); 48-20107 (1973).
2. Japanese Patent Publication (Kokoku) 53-24210 (1978); Japanese Patent Disclosure (Kokai) 54-26975 (1979); 54-52689 (1979); 54-109087 (1979); 55-163747 (1980), etc.
3. Albessard, A.K., Tamatani, M., Okumura, M., Matsuda, N., Hattori, H., and Motoki, S., *Proc. Asia Display '95*, 643, 1995.
4. Uehara, Y., Nakayama, K., Asano, T., and Matsukiyo, H., *Electrochem. Soc. Fall Meeting*, Abstr. 556, 1994.
5. Koishi, M. and Tsunoda, T., *Funtai no hyoumen kagaku (Surface Chemistry of Powders)*, Nikkan Kogyo Shinbun Press, Tokyo, 1975, 181 (in Japanese).
6. Shionoya, S. and Ishikawa, T., *J. Chem. Soc. Japan Ind. Chem. Soc.*, 58, 900, 1955 (in Japanese).
7. Kitahara, H., Kumata, T., and Manabe, T., *Shikizai (Colored Materials)*, 52, 475, 1979 (in Japanese).
8. Kubo, K., Jinbo, G., Suito, E., Takahashi, H., and Hayakawa, S., Eds., *Funtai (Powders)*, Maruzen, Tokyo, 1979, 324 (in Japanese).

9. Kikuchi, G. and Tsunoda, T., *Shikizai (Colored Materials)*, 52, 119 and 174, 1979; *ibid.*, 53, 691, 1980 (in Japanese).
10. Miyakawa, S., Yoshikawa, S., and Naitou, M., *Dai-Nippon-Toryou Shahou (Dai-Nippon-Toryou Reports)*, 14, 22, 1961 (in Japanese).
11. Hazel, J.F. and Schnable, G.L., *J. Electrochem. Soc.*, 100, 65, 1953.
12. Levy, B., *J. Electrochem. Soc.*, 106, 218, 1959.
13. Grimm, L., Hilke, K.-J., and Scharrer, E., *J. Electrochem. Soc.*, 130, 1767, 1983.
14. Takahashi, F., Mikami, T., and Hase, T., *Display and Imaging*, 3, 71, 1994 (in Japanese).
15. Larach, S. and McGowan, J.E., *RCA Review*, 45, 335, 1984.
16. Scharrer, E., Grimm, L., Mayatepek, H., and Ritsert, W., *J. Electrochem. Soc.*, 130, 1762, 1983.
17. Yamamoto, H. and Ohba, Y., *Hyoumen (Surface)*, 18, 233, 1980 (in Japanese).
18. Japanese Patent Disclosure (Kokai) 51-82563 (1976); 52-139359 (1977); 53-86568 (1978).
19. Japanese Patent Disclosure (Kokai) 50-147279 (1975); 52-64868 (1977); 51-142965 (1976).
20. Japanese Patent Disclosure (Kokai) 50-57377 (1975); 51-142967 (1976).
21. Japanese Patent Disclosure (Kokai) 52-67254 (1977); 53-59359 (1978); 51-16862 (1976).
22. Japanese Patent Disclosure (Kokai) 50-75362 (1975); 50-134362 (1975).
23. Japanese Patent Disclosure (Kokai) 50-11373 (1975); 51-85606 (1976); 53-45965 (1978).
24. Japanese Patent Disclosure (Kokai) 55-41649 (1980).
25. Trond, S.S., *SID Digest*, 171, 1980.
26. Bolte, G., *Farbe und Lack*, 88, 528, 1982.
27. Tamatani, M. and Oguchi, T., *Electrochem. Soc. Spring Meeting*, Abstr. No. 487, 1982
28. Oguchi, T. and Tamatani, M., (a) *J. Electrochem. Soc.*, 133, 841, 1986; (b) *Wear*, 168, 91, 1993.

chapter five — section one

Phosphors for lamps

Kohtaro Kohmoto

Contents

5.1 Construction and energy conversion principle of various lamps 421
  5.1.1 Optical radiation sources using phosphors 421
  5.1.2 Fluorescent lamps (low-pressure mercury discharge lamps) 421
    5.1.2.1 Lamp construction 421
    5.1.2.2 Principle of energy conversion 423
    5.1.2.3 Conversion of energy 425
    5.1.2.4 General characteristics 426
References 426

5.1 Construction and energy conversion principle of various lamps

5.1.1 Optical radiation sources using phosphors

Various systems in which phosphors in combination with suitable excitation sources have been developed and are widely used. Among these systems, the optical radiation source for lighting (lamps) is one of the most representative applications of phosphors. Table 1 shows features of typical light sources (lamps) that use the optical radiation from phosphors or their intrinsic radiation. Lamp construction, principles of energy conversion, energy conversion efficiencies, and other important aspects of several principal light sources shown in Table 1 are described in this section.

It is not the aim of this chapter to discuss the physical phenomena involved in the energy conversion process of phosphor; these are discussed elsewhere in this handbook.

5.1.2 Fluorescent lamps (low-pressure mercury discharge lamps)[1–10]

5.1.2.1 Lamp construction

It is well known that among light sources using phosphors, fluorescent lamps are most widely used and are produced in the largest quantity. Nowadays, many types of fluorescent lamps are being manufactured. However, the fundamental construction of the fluorescent lamp shown in Figure 1 is common to all: lamps are essentially constructed with a glass tube, the inside wall being coated with a phosphor layer, and electrodes sealed at both ends.

Table 1 Light Sources Utilizing Optical Radiation form Phosphors

Lamp designation	Exciting source for phosphor	Wavelength of exciting source (nm)	Irradiance of exciting source at phosphor (Wm^{-2})	Ratio of phosphor radiation to total (%)	Principal application field	Remarks
Fluorescent lamps	UV radiation from low-pressure Hg-rare gas arc discharge plasma	185 and 254 (line spectra)	250–450	≃85	General lighting	
Fluorescent high-pressure mercury lamps	UV radiation from high-pressure Hg gas arc discharge plasma	297, 313 and 365 (line spectra)	600–900	≃20	General lighting	
Metal halide lamps	Optical radiation from high-pressure Hg-metal halide gas arc discharge plasma	Depends on kind of metal	—	<2*	General lighting	*Obtain diffuse light
Fluorescent glow lamps	UV radiation from negative glow discharge of low-pressure Xe and/or Kr gas	Line spectra shorter than 400*	10–20	>90	Indicator lamp	*Mainly at 140–280 nm
Fluorescent sign tubes	UV radiation from low-pressure Hg-Ar gas glow discharge plasma	254 (line spectrum)	50–100	≃80	Luminous sign	
Cold-cathode fluorescent lamps	UV radiation from low-pressure Hg-rare gas or rare gas(es) discharge plasma	254 or UV line spectra	50–150	≃80	Back light for LCD display	
Electrode-less fluorescent lamp	UV radiation from high-frequency-induced gas discharge plasma	254 or UV radiation*	100–200	≃85	Maintenance lamp	*Sometimes broad band
LED (Dichromatic white)	Optical radiation from blue-emitting LED chip (InGaN)	400–500 (continuous)	5–20	≃50	Local lighting, backlight	
LED (UV LED + phosphor white)	UV radiation from UV emitting LED chip (InGaN)	330–420 (continuous)	5–20	≃90	Local lighting, backlight	

Since the previous editon more than 10 years have passed. During these 10 years, different LED (light-emitting diode) sources have been developed and at present white LEDs are expected to be used for general lighting purposes. White LEDs are applying phosphors to emit white light. As phosphors in LEDs are playing a very important part of the energy conversion process from electric energy to optical radiation energy, LEDs are also added to Table 1.

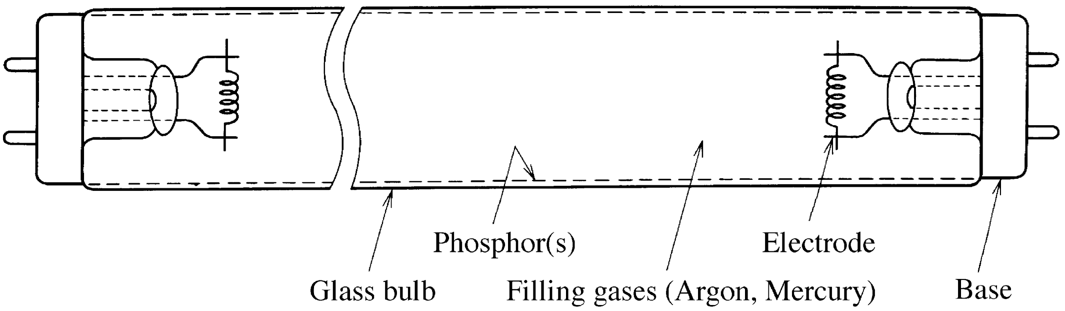

Figure 1 Fundamental construction of the fluorescent lamp.

The general term "electrode" refers to both positive and negative terminals for the electric discharge of the fluorescent lamp. The negative electrode is called a cathode and the positive electrode is called an anode. However, for alternating current (AC) operation, the electrode at each end serves alternately as the cathode and anode.

As fluorescent lamps are generally operated with AC power sources, the two electrodes at both ends of lamps have the same construction. Each of the electrodes consists of a doubly-coiled (or triply-coiled) tungsten filament coated with an electron-emissive material, such as barium-calcium-strontium oxide. In one AC cycle, the discharge current flows from the electron-emitting tungsten wire of one electrode to the other and, in the next cycle, the discharge current flows in the reverse direction. Inside the tube, a tiny amount of mercury and a small amount of a rare gas, such as argon, are also placed. Both the mercury and rare gas are added after the electrodes have been sealed to the tube and the air inside the tube has been evacuated. The pressure of the rare gas is usually 0.2 to 0.7 kPa (1.5 to 5.2 Torr). The pressure of the mercury vapor during lamp operation is of prime importance. It is well known that the saturation vapor pressure is dependent on the temperature. Since the tube contains excess mercury, the temperature of the coldest spot on the tube wall determines the mercury vapor pressure throughout the tube. The optimum mercury vapor pressure for common fluorescent lamps is 0.5 to 1.4 Pa (3.7 to 10.5 mTorr), which corresponds to the vapor pressure of Hg at about 40°C. Hence, fluorescent lamps are designed so that the temperature of the coldest point of the tube wall during normal operation is about 40°C.

5.1.2.2 Principle of energy conversion[11]

After the arc discharge has taken place in the tube, partly ionized plasma is formed in the positive column of the discharge. First, the electric input energy to the lamp is mostly converted to ultraviolet (UV) radiation energy (wavelength, 185 and 254 nm) through a specific energy conversion process in the plasma. This UV radiation is converted further to optical radiation by the phosphor(s) coated on the inside wall of the glass tube.

During normal operation of the fluorescent lamp with the rated conditions, a uniform electric field of about 1 V cm^{-1} is formed in the positive column of the discharge between the two electrodes, and electrons in this plasma are accelerated in the direction of the anode. During this acceleration, the kinetic energy of the electrons increases gradually. Since the ions in this plasma have a much larger mass than the electrons, the ions do not move very much and the electric input energy to the fluorescent lamp is mostly converted to the kinetic energy of the electrons. During this acceleration, the electrons collide with other particles to create the plasma and other forms of energy.

Various energy conversion processes occur, depending on the plasma density and the kinetic energy of the electrons just before the collisions. In the case where the electron kinetic energy is smaller than 4.66 eV, collisions between an electron and a neutral mercury or a neutral rare gas atom are elastic and result in slight changes in the electron's motion, with little energy conversion to heat. (The conversion rate to heat energy due to one elastic collision is very small. Since the number of elastic collisions is very large, however, the total amount of energy converted to heat reaches 30% of the input energy.)

When the electron kinetic energy becomes larger than 4.88 eV, an electron can excite the neutral mercury atoms to the 6^3P_1 energy level. Mercury atoms excited to this state will make a transition to the ground state (6^1S_0) in a very short time with energy difference being emitted as optical radiation or photons. The emitted radiation is, of course, in the form of a line spectrum; in the case of the Hg 6^3P_1 to 6^1S_0 transition, the wavelength is 254 nm in the UV region. The phosphor coated on the inside wall of the fluorescent lamp tube is mainly excited by this UV radiation and emits down-converted visible radiation.

When the electron kinetic energy becomes larger yet, the neutral mercury atoms can be excited to much higher energy levels through inelastic collisions with the electrons. For kinetic energy higher than 6.67 eV, the mercury atoms may be excited to the 6^1P_1 level. This excited atom decays to the ground state in a short time, via the same process as the 6^3P_1 transition emitting 185-nm UV radiation, which also excites the phosphor(s).

As the kinetic energy of electrons becomes much higher, or when electrons collide with mercury atoms excited to the level of 6^3P_1, 6^1P_1, or other metastable states, the atoms may be excited to even higher energy levels. Mercury atoms excited in this way never make direct transitions to the ground state but decay to lower excited levels. The optical radiation emitted corresponds to the energy difference between the two interacting levels. As the wavelengths of these optical radiations are rather long compared with the two UV lines discussed above, they have less probability of exciting phosphors and are directly emitted to the outside of the tube.

When the kinetic energy of electrons becomes larger than 10.38 eV, which is larger than the ionization potential of the mercury atom, neutral mercury atoms may be ionized by colliding with such electrons. (Excited mercury atoms can also be ionized by colliding with electrons with high kinetic energy (build-up ionization).) Electrons released from the neutral mercury atoms to the positive column will soon start to be accelerated by the electric field and, as before, some electrons can contribute to the emission of UV radiation while others contribute to build-up ionization.

Since ionized mercury atoms in the positive column are far heavier than electrons, they are not significantly affected by the electric field and may gradually diffuse to the tube walls. In the course of this diffusion, they may recombine with electrons and return to neutral state.

Auxiliary rare gases, such as argon and krypton, have a density in the plasma that is much higher than that of the vaporized mercury, these gaseous atoms also collide with the electrons in the positive column. However, the excitation and ionization potentials of both of these rare gases are higher than those of mercury: in argon, for example, the lowest excitation potential is 11.6 eV and the ionization potential is 15.75 eV. Hence, the probabilities of their excitation and/or ionization in the discharge plasma are very small.

Therefore, almost all collisions between electrons and rare gas atoms are elastic and have no direct effects on the characteristics of the optical radiation emitted from the fluorescent lamp. During each of these elastic collisions, the direction of the electrons is changed; practically, this is equivalent to increasing the electrode distance. By filling the tube with a suitable amount of rare gas, the actual physical length of the fluorescent lamp can be shortened. Such a rare gas is called a buffer gas.

Other than serving as a buffer gas, argon can serve another function. The potential of the metastable state of argon is 11.5 eV and this is slightly larger than the ionization

Table 2 Energy Conversion Ratio in Positive Column of Fluorescent Lamp

Discrimination		Rate (%)
Radiation	185 nm	5
	254 nm	60
	others	6
Elastic collision loss		28
Recombination loss		1
Total		100

potential of mercury. Argon is not ionized in collisions within the discharge plasma; however, many argon atoms are excited to their metastable states. These excited argon atoms can contribute effectively to the ionization of neutral mercury by collisions. As a result of this contribution, the breakdown voltage of the fluorescent lamp is lowered, and the lamp can be made to operate at a lower input voltage. This phenomenon is called the Penning effect. This effect is also well known in argon-neon discharges.

In the case of mercury-krypton discharge, the potential of the krypton metastable state is much lower than the ionization potential of mercury. Consequently, the Penning effect does not occur. If krypton is added to argon as a buffer gas in a fluorescent lamp (mercury-argon-krypton type fluorescent lamp), the breakdown voltage is actually increased slightly and this type of fluorescent lamp is more difficult to start than the mercury-argon type discussed previously.

5.1.2.3 Conversion of energy

As described above, the electric energy supplied to the fluorescent lamp is converted to other forms of energy, such as optical (ultraviolet) radiation and heat energy. Table 2 shows the conversion ratio of the input electric energy to other forms of energy for a standard type fluorescent lamp. About 65% of the input energy is converted to UV radiation, which is used to excite phosphors; in addition, approximately 6% is converted to visible radiation, which is directly emitted to the outside of the tube. The balance of the electric energy is not converted to optical radiation, and can be designated as an energy loss. About 3% of the energy is lost at the electrodes, and about 26% is converted to heat energy through elastic collisions in the positive column.

The UV radiation is further converted to visible radiation by the phosphors. Since the UV-visible energy conversion ratio is about 40%, 23% of the input electric energy is finally converted to visible radiation. If the visible radiation emitted directly by the positive column is added to this, the total sum will reach 25%.

These values are applicable to conventional standard fluorescent lamps. Recently, many additional types of fluorescent lamps have been developed and commercialized, such as the compact fluorescent lamp, the slimmer tube type fluorescent lamps for special use, and the electrodeless fluorescent lamps. In these lamps, some lamp dimension is specifically different from the standard type; the plasma density in the positive column and the kind of buffer gases used can also differ. Consequently, the energy conversion ratio can be different from the values cited in Table 2.

For the slimmer tube type fluorescent lamps designed for special uses, such as backlight lamps for the liquid crystal displays (LCDs), there is not only a mercury-argon discharge but also a discharge in the rare gas. In these fluorescent lamps, the energy conversion mechanism and the conversion ratio are slightly different from those of conventional fluorescent lamps. These types of lamps will be discussed later.

5.1.2.4 General characteristics[12–17]

Since the fluorescent lamp converts electrical energy to optical radiation, the conversion efficiency should be as high as possible. Many factors affect fluorescent lamp efficiency. The efficiency is also related to the phosphors that are used. In this section, however, only the relationship between tube diameter and lamp efficiency will be described.

Recently, the dimensions of fluorescent lamps have been reduced. The dimension is closely related to the density of electrons, ions, neutral gas (mercury atom), and buffer gas in the plasma. As processes of energy conversion vary depending on these densities, the lamp dimension—especially the tube diameter—becomes the important factor in designing fluorescent lamps.

Conversion efficiency of electrical input energy to UV radiation varies with the tube diameter. If the 254-nm UV radiation produced in the fluorescent lamp plasma encounters neutral mercury atoms before reaching the inside wall of the tube, it may be reabsorbed by the atoms into the 6^3P_1 state. This excited mercury atom will normally reemit the 254-nm UV radiation. However, if the excited atoms collide with other particles in the plasma before reemission, the atoms can produce radiation with wavelengths different from 254 nm. This means that the 254-nm radiation can be down-converted before reaching the phosphor layer, thereby decreasing the conversion efficiency. In a normal lamp, this reexcitation-reemission process is estimated to occur several hundred times before the UV radiation from one excited atom reaches the wall. If the tube diameters are large, the chance of energy down-conversion increases and the opportunity for 254-nm radiation quenching is enhanced. This means that the total UV radiation reaching the phosphor in larger-diameter tubes is smaller than in lamps having the desirable normal tube size.

On the other hand, in a case where the tube diameter becomes smaller, the ratio of the tube circumference to the cross-section becomes larger. Consequently, the ions and the electrons that have migrated to the vicinity of the tube wall by ambipolar diffusion recombine more frequently, and the rate of electron and ion extinction becomes greater. This effect makes the electron temperature (corresponding to the average kinetic energy of electrons) in the plasma rise. However, in much slimmer fluorescent lamps, the electron temperature can become too high and the probability of exciting a mercury atom to the 6^3P_1 state decreases. These discussions are applicable also to 185-nm UV radiation.

According to the above, the energy conversion efficiency (the luminous efficacy of fluorescent lamps) decreases when the tube diameter is increased or decreased. In other words, there is an optimum tube diameter range for fluorescent lamp design.

Strictly speaking, the optimum diameter for the 254-nm conversion is slightly larger than that of the 185-nm conversion. For phosphors that are more efficiently excited by 185-nm UV radiation, such as those used for the three-band fluorescent lamps, the optimum tube diameter can be made smaller than for those using conventional calcium halophosphate phosphors. Recently developed compact fluorescent lamps having slimmer tubes (diameter, 15–20 mm) use three-band phosphors, as do far slimmer tubular fluorescent lamps operated with high-frequency electric power supplies (diameter, 26 mm).

References

1. Harada, T., *Kogen (Light Sources)*, Kyoritsu Shuppan, Tokyo, 1944 (in Japanese).
2. Amick, C.L., *Fluorescent Lighting Manual*, McGraw-Hill Book Co., New York, 1947.
3. Forsythe, W.E. and Adams, E.Q., *Fluorescent and Other Gaseous Discharge Lamps*, Murry Hill, London, 1948.
4. Harada, T., *Hodento (Discharge Lamps)*, Ohm-sha, Tokyo, 1950 (in Japanese).
5. Zwikker, C., *Fluorescent Lighting*, Philips Technical Library, Eindhoven, 1952.
6. Honjo, I., *Keikoutou (Fluorescent Lamps)*, Kyoritsu Shuppan, Tokyo, 1954 (in Japanese).

7. Itoh, T., *Keikoutou-Shoumei Nyumon (Introduction to Fluorescent Lighting)*, Denki Shoin, Tokyo, 1954 (in Japanese).
8. Summer, W., *Ultraviolet and Infrared Engineering*, Sir Issac Piman & Sons, New York, 1962.
9. Elembaas, W., *Fluorescent Lamps*, Philips Technical Library, Eindhoven, 1971.
10. Waymouth, J.F., *Electric Discharge Lamps*, MIT Press, Boston, 1971.
11. Kenty, C., *J. Appl. Phys.*, 21, 1309, 1950.
12. Hashimoto, T., Someya, A., and Hanada, T., *Toshiba Rev.*, 18, 1116, 1963 (in Japanese).
13. Someya, T., Kohmoto, K., and Ebara, H., *CIE Compte Rendu*, 19th Session, Kyoto, 1979.
14. Kamiya, S. and Shibata, H., *Tech. Digest, Phosphor Res. Soc. 119th Meeting*, 1967 (in Japanese).
15. Kamiya, S. and Shibata, H., *Natl. Tech. Rep.*, 27, 339, 1981 (in Japanese).
16. Kohmoto, K., Hayashi, M., Funabashi, T., and Hirai, A., *Toshiba Rev.*, 38, 115, 1983 (in Japanese).
17. Hirota, T. and Suzuki, A., *J. Illum. Eng. Jpn.*, 67, 552, 1983 (in Japanese).

chapter five — section two

Phosphors for lamps

Shigeru Kamiya

Contents

5.2 Classification of fluorescent lamps by chromaticity and color rendering properties 429
References 435

5.2 *Classification of fluorescent lamps by chromaticity and color rendering properties*

There are many kinds of fluorescent lamps of different chromaticities and different color rendering properties. According to the appropriate or particular application, lamps with suitable color chromaticity and color rendering can be chosen. In Japan, the classification of fluorescent lamps for general lighting is described in the *JIS Standard Z9112*[1] in accordance with the chromaticity and color rendering properties.

Classification by light source color. The described chromaticity ranges of five different colors in *JIS* are shown in Figure 2, together with the IEC specification. Designations and symbols of these five colors are shown in Table 3 as compared with those commonly used outside Japan. The 5000-K lamp is exceptionally popular in Japan.

Classification by color rendering properties. Various kinds of descriptive wording are used by manufacturers to describe the degree of improvement in the color rendering of their lamps; words such as Deluxe type, Super Deluxe type, Natural Color, etc. are commonly encountered. *JIS* first introduced a standard designation system according to the color rendering indices and characteristics of the spectral power distribution.

Fluorescent lamps with wide band spectra are classified into four types: ordinary type, color rendering A type, color rendering AA type, and color rendering AAA type, depending on the degree of improvement of the color rendering indices. The minimum required values of the general color rendering index and special color rendering indices of the lamp belonging to each category are given in Table 4. For narrow band fluorescent lamps, in addition to the requirement for color rendering indices, the ratio of the radiant flux within the three specified band wavelength regions to that in the entire visible wavelength region are specified. The symbol for narrow band lamps satisfying the values described in Table 5 is designated as EX.

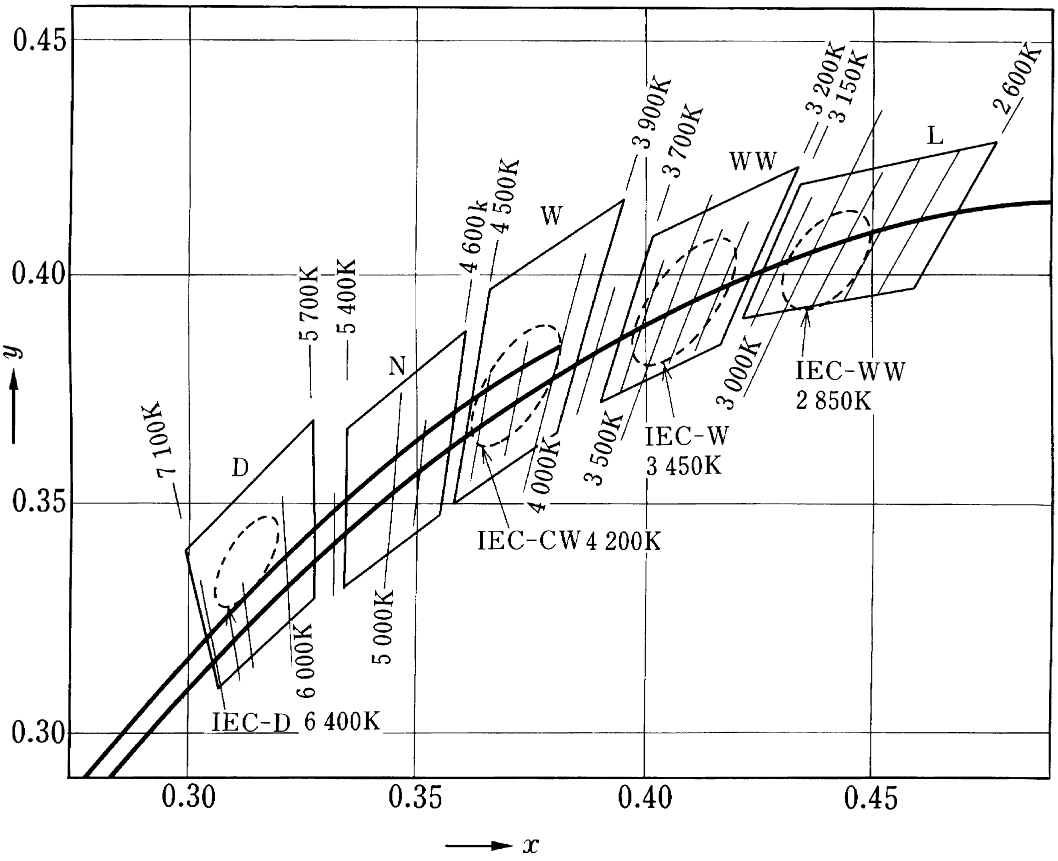

Figure 2 Chromaticity range of light source colors of fluorescent lamps. (From *JIS Standard Z 9112*, 1990. With permission.)

Table 3 Chromaticity Range of Light Source Colors of Fluorescent Lamps

JIS 9112				
Classification	Symbol	T_{cp} (K)	IEC Publ. 81	
Daylight	D	5700–7100	Daylight	(D)
Day white	N	4600–5400	—	
White	W	3900–4500	Cool white	(CW)
Warm white	WW	3200–3700	White	(W)
Incandescent color	L	2600–3150	Warm white	(WW)

Note: Correlated color temperature T_{cp} values are informative reference.
From *JIS Standard Z 9112*, 1990. With permission.

Fluorescent lamps with wide emission bands. Ordinary fluorescent lamps employ calcium halophosphate phosphors, which have a broad continuous spectra. Emission intensity in the region longer than 600 nm, however, is insufficient to reproduce reddish colors correctly. To improve this shortcoming, various combinations of phosphors have been investigated to realize a continuous emission spectrum close to that of reference light sources such as synthetic daylight and full radiator (blackbody radiator). Lamps constructed with this concept are called wide-band spectrum lamps. For ordinary lamps, only the general color rendering index Ra is specified because these lamps are produced with

Table 4 Minimum Values of Color Rendering Indices of Fluorescent Lamps with Wide Emission Bands

Classification of color rendering property	Light source color	Symbol	Minimum value of color rendering index							
			Ra	R9	R10	R11	R12	R13	R14	R15
Ordinary type	Daylight	D	69							
	Day white	N	67							
	White	W	57							
	Warm white	WW	54							
	Incandescent color	L	50							
Color rendering A	Day white	N-DL	75							65
	Incandescent color	L-DL	65							50
Color rendering AA	Daylight	D-SDL	88	76						88
	Day white	N-SDL	86	72						86
	White	W-SDL	84	68						84
	Warm white	WW-SDL	82	64						82
Color rendering AAA	Daylight	D-EDL	95	88	88	93	88	93	93	93
	Day white	N-EDL	95	88	88	93	90	93	93	93
	Incandescent color	L-EDL	90	80	78	85	78	85	90	88

From *JIS Standard Z 9112*, 1990. With permission.

Table 5 Minimum Value of Color Rendering Indices of Three-Band Fluorescent Lamps

Light source color	Symbol	Minimum value of color rendering index		Minimum value of three-band radiant flux ratio (r_t)
		Ra	R15	
Day white	EX-N	80	80	50
Incandescent color	EX-L	78	78	50

Note: $r_t = \frac{P_B + P_G + P_R}{R_T} \times 100$

where PB, PG, PR are radiant flux within the wavelength ranges of 445–470, 525–550, and 595–620 nm, respectively. PT is total radiant flux within the visible wavelength region.

From *JIS Standard Z 9112*, 1990. With permission.

calcium halophosphate phosphors alone. For lamps belonging to the category of color rendering A, the special color rendering index R15, which corresponds to the reproduction of the typical Japanese female face skin color, is specified in addition to Ra. This specification is understandable because color reproduction of facial appearances is very important in daily human interactions. Type AA lamps are required to have the necessary color rendering properties for use in general lighting. Another special color rendering index, R9, is specified for this purpose. For color rendering AAA type lamps, all the special color rendering indices are specified in order to meet such applications as color evaluation and inspection. Typical spectral power distribution curves of the wide-band emission lamps are shown in Figure 3.

Fluorescent lamps with narrow emission bands. The distinctive features of this type of fluorescent lamp is that it possesses a discontinuous spectral power distribution. Most of the emission is intentionally concentrated in specific wavelength regions. In the rest of the wavelength region, no or very weak emission is produced. As is well known, most natural light sources produce a continuous spectrum. Efforts to improve the color render-

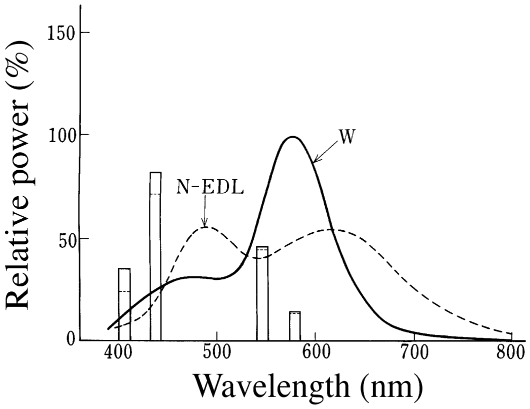

Figure 3 Spectral power distribution curves of fluorescent lamps with wide emission bands.

ing of artificial light sources concentrated on how to realize spectral power distributions approximating those of the natural light throughout the entire visible wavelength range. High color rendering lamps with the wide-band emission are based on this concept. In implementing this concept, part of the emission energy was generally distributed to the both ends of the visible wavelength region, i.e., deep blue and red, resulting in the decrease of the total luminous efficacy of the lamps. This means that high luminous efficacy and high color rendering properties cannot stand together.

This limitation, however, has been eased by developing a better understanding of the chromatic response of the human eye. Since 1970, extensive research on the color vision of the human eye has been carried out. As a result, it became clear that the color discrimination sensitivity of the human eye depends strongly on the wavelength, as does the sensitivity for brightness. It was confirmed that the sensitivity of the human eye is concentrated within a relatively narrow spectral region centered at 450, 540, and 610 nm. It was also confirmed that most colors can be reproduced using a light source with an emission spectrum consisting a combination of very narrow emission bands at these wavelengths. Calculated results suggest the possibility of attaining Ra 85 lamps by a simple combination of these three emission lines.[2,3] These research results offered alternate means to improve the color rendering property of fluorescent lamps. According to this new concept, high efficacy and high color rendering are compatible with each other because it is no longer necessary to distribute emission energy into regions of low luminous sensitivity. The first report of a fluorescent lamp based on this new concept was made by Haft and Thornton in 1972.[4] They obtained an Ra 83 lamp having a color temperature of 4200K using the phosphor combination of $3Sr_3(PO_4)_2{\cdot}SrCl_2{:}Eu^{2+}$, $Zn_2SiO_4{:}Mn^{2+}$, and $Y_2O_3{:}Eu^{3+}$ as the blue-, green-, and red-emitting components, respectively. The luminous output was comparable to that of ordinary lamps with calcium halophosphate phosphors. The spectral power distribution curve of this lamp is shown in Figure 4. This lamp illustrated the new concept, but was not commercialized due to the relatively poor maintenance characteristics of the phosphors.

The commercialization of a practical lamp had to wait for the development of better phosphors for this purpose. In 1974, a series of rare-earth activated aluminate phosphors was invented by Verstegen.[5] Fluorescent lamps employing $BaMg_2Al_{16}O_{27}{:}Eu^{2+}$ as the blue-emitting component, $CeMgAl_{11}O_{19}{:}Tb^{3+}$ as the green-emitting component, and $Y_2O_3{:}Eu^{3+}$ as the red-emitting component offered equivalent luminous output to that of the lamps employing the common calcium halophosphate phosphor; the lamps attained an Ra value as high as 85 throughout the color temperature range of 2500 to 6500K.[6] An example of the

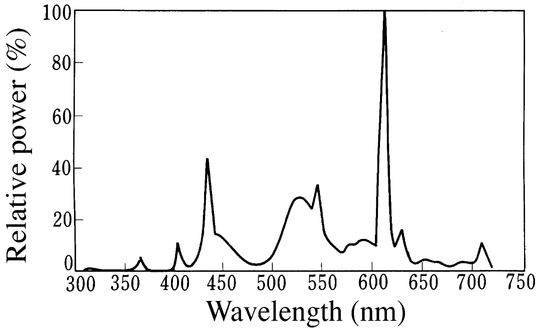

Figure 4 Spectral power distribution of a fluorescent lamp with narrow emission bands. (From Haft, H.H. and Thornton, W.A., *J. Illum. Eng. Soc.*, 2-1, 29, 1971. With permission.)

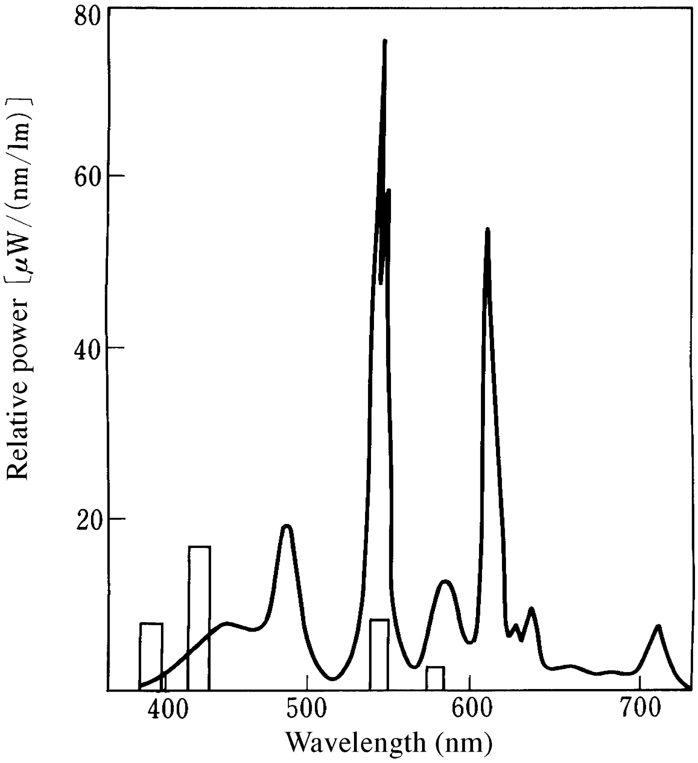

Figure 5 Spectral power distribution of a fluorescent lamp with narrow emission bands. (From Verstegen, J.M.P.J., Radielovic, D., and Vrenken, L.E., *J. Electrochem. Soc.*, 121, 1627, 1974. With permission.)

spectral power distribution is shown in Figure 5. From a comparison of Figures 4 and 5, it is obvious that the latter has a much sharper and more intense emission band in the green region than does the former. This contributes to the higher luminous output.

Since that time, various blue- and green-emitting phosphors have been developed and commercially deployed; the red-emitting component, Y_2O_3:Eu^{3+} has remained the same throughout. The lamp efficacy has also been improved from 80 lm W^{-1} at the time of first announcement to nearly 100 lm W^{-1} when combined with energy-saving lamp designs. Overall, however, the spectral power distribution curve has remained almost the same. Figure 6 depicts a typical example of the spectral power distribution of a 5000-K lamp of

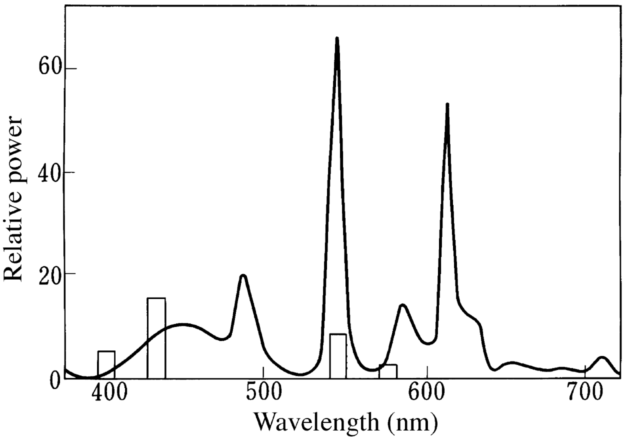

Figure 6 Spectral power distribution of a 5000K three-band fluorescent lamp.

the *three narrow emission band type* (usually called *three-band lamp*), which is most commonly used in Japan today.

The addition of an extra emission in the 490-nm region increases the Ra value to 88 with only a small sacrifice of lamp efficacy.[7] For this purpose, several kinds of blue/green-emitting phosphors are being used in commercial lamp products in Japan. The highest Ra values can be obtained by adding a deep red emission. However, this decreases the lamp efficacy.

Illumination by the narrow-band lamps produces several specific lighting effects that are not observed when conventional lamps are used. First, under illumination by a narrow-band lamp, the required illuminance level can be lowered from that produced by ordinary lamps to give a sensation of an equivalent brightness in places where chromatic color objects exist. That is, the human eye senses a higher brightness under illumination by the narrow-band lamps than by ordinary lamps when the illuminance level is equivalent. Although this effect has commonly been observed experimentally under illumination—even using conventional, high color rendering lamps of wide emission band—the effect was not recognized in the practical situation due to the extremely low luminous output of these lamps. In the case of narrow-band lamps, this effect is observed because these lamps have equivalent luminous output to that of the ordinary lamp. Second, the light from the narrow-band lamps reproduces the object color preferably and vividly. Finally, illumination by the narrow-band lamps gives a clear and limpid appearance to color objects. All these effects are considered to originate from the distinctive emission spectrum of the narrow-band lamps. As for the detail of color rendering indices, refer to 17.6.

Phosphors utilized for three-band lamps. Phosphors presently utilized for three-band lamps are shown in Table 6. $(Sr,Ca,Ba)_5(PO_4)_3Cl:Eu^{2+}$ and $BaMg_2Al_{16}O_{27}:Eu^{2+}$ are two main classes of blue-emitting phosphors. The ratio of Ca:Ba:Sr of the former phosphor differs from manufacturer to manufacturer in order to optimize the emission spectrum according to a specific lamp design. For the latter phosphor, partial replacement of Ba by other alkaline earth metals and small deviation from the formulated composition are also introduced by various manufacturers to optimize the emission spectrum. As for the green-emitting phosphors, three kinds of phosphors—namely $CeMgAl_{11}O_{19}:(Ce^{3+}):Tb^{3+}$, $LaPO_4:Ce^{3+}:Tb^{3+}$ and $GdMgB_5O_{10}:Ce^{3+}:Tb^{3+}$—are being used. $Y_2O_3:Eu^{3+}$ remains the only available phosphor for the red-emitting component. For the purpose of improving Ra values, blue/green-emitting $(Ba,Ca,Mg)_5(PO_4)_3Cl:Eu^{2+}$, $Sr_4Al_{14}O_{25}:Eu^{2+}$ and $2SrO{\cdot}0.84P_2O_5{\cdot}0.16B_2O_3:Eu^{2+}$ phosphors are

Table 6 Phosphors Utilized in Three-Band Lamps

	Emission color	Chemical composition
Main	Blue	$(Sr,Ca,Ba)_5(PO_4)_3Cl:Eu^{2+}$ $BaMg_2Al_{16}O_{27}:Eu^{2+}$
	Green	$CeMgAl_{11}O_{19}:(Ce^{3+}):Tb^{3+}$ $LaPO_4:Ce^{3+}:Tb^{3+}$ $GdMgB_5O_{10}:Ce^{3+}:Tb^{3+}$
	Red	$Y_2O_3:Eu^{3+}$
Auxiliary	Blue-green	$(Ba,Ca,Mg)_5(PO_4)_3Cl:Eu^{2+}$ $2SrO{\cdot}0.84P_2O_5{\cdot}0.16B_2O_3:Eu^{2+}$ $Sr_4Al_{14}O_{25}:Eu^{2+}$

being used. The actual combination of these phosphors used in lamps varies either by manufacturer or lamp type. Detailed characteristics of the phosphors are described in Section 5.3.2.

References

1. *JIS Standard Z 9112*, 1990.
2. Thornton, W.A., *J. Opt. Soc. Am.*, 61, 1155, 1971.
3. Koedam, M. and Opstelten, J.J., *Lighting Res. Tech.*, 3, 205, 1971.
4. Haft, H.H. and Thornton, W.A., *J. Illum. Eng. Soc.*, 2-1, 29, 1972.
5. Verstegen, J.M.P.J., *J. Electrochem. Soc.*, 121, 1623, 1974.
6. Verstegen, J.M.P.J., Radielovic, D., and Vrenken, L.E., *J. Electrochem. Soc.*, 121, 1627, 1974.
7. Takahashi, M., Shibata, H., and Iwama, K., *Natl. Tech. Rept.*, 38, 582, 1992.

chapter five — sections three and four

Phosphors for lamps

Kohtaro Kohmoto

Contents

5.3 High-pressure mercury lamps 437
    5.3.1 Lamp construction 437
    5.3.2 Principle of energy conversion 438
    5.3.3 Conversion of energy 439
    5.3.4 Phosphors for lamp applications....439
5.4 Other lamps using phosphors 441
    5.4.1 Other HID lamps....441
    5.4.2 Fluorescent glow lamps 441
    5.4.3 Fluorescent sign tube (luminous tube)....442
    5.4.4 Cold cathode fluorescent lamp 442
    5.4.5 Electrodeless fluorescent lamp....443
References....443

5.3 *High-pressure mercury lamps*[1–5]

5.3.1 *Lamp construction*

Although the radiation from the phosphors does not play a large role in light output, phosphors are used for some high-pressure mercury and metal-halide lamps. Among these lamps, phosphors for the high-pressure mercury lamps play an important role in improving the color radiated from the lamp, and the lamps with phosphor coatings are known as fluorescent mercury lamps.

The fundamental construction of the high-pressure mercury lamp is shown in Figure 7. The lamp consists of an inner tube (burning tube), which converts the input electrical energy to optical radiation energy, and an outer bulb, the functions of which are to protect the inner tube, keep the temperature of the inner tube high, and make the actual installation of the lamps easier. The phosphors are coated on the inside wall of the outer bulb.

The inner tube is usually made of quartz and filled with 2.5 to 4.0 kPa (18.7 to 30 Torr) of argon gas and a small amount of mercury. The amount of mercury is precisely controlled so that it all vaporizes under the rated operating condition; at this time, the pressure reaches 300 kPa (2.96 atm). After the discharge is started, a stable discharge state is reached in the inner tube, and the balance of the electrical energy is converted to optical radiation in this plasma.

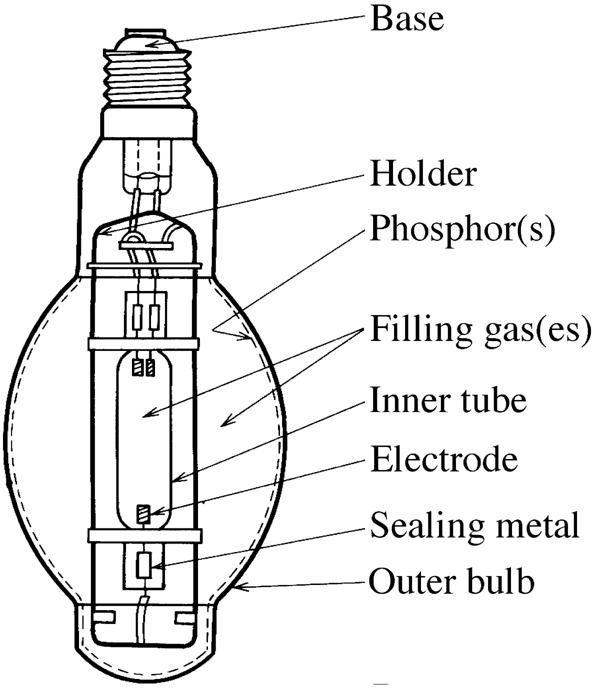

Figure 7 Fundamental construction of a fluorescent high-pressure mercury discharge lamp.

5.3.2 *Principle of energy conversion*

Since the mercury vapor pressure after reaching the stable operating state is higher than that found in fluorescent lamps (low-pressure mercury discharge lamps) and the plasma density in the inner tube is also higher, the energy conversion process is slightly different. In this higher density plasma, electrons collide with other plasma particles before their kinetic energy becomes large enough to excite and/or ionize the particles. Almost all collisions in the high-pressure mercury discharge plasma can be considered as elastic, and only a very small part of the energy is lost through collisions. However, as the plasma density is very large and number of elastic collisions is enormous, the total amount of the energy lost is large, and is mostly converted to heat energy. The temperature of the inner tube becomes higher, and the plasma density and temperature also increase to the point where mercury atoms in the plasma are excited sufficiently by thermal energy to emit radiation. The plasma then is said to have reached a thermal equilibrium state.

Since the conversion process in high-pressure mercury discharge lamps is different, the spectrum emitted contains a larger portion of the visible region than in low-pressure mercury discharge lamps. In the fluorescent mercury lamp also, the UV radiation emitted from the inner tube is partly converted to visible radiation by phosphors coated on the inside wall of outer bulb.

As for general type high-pressure mercury discharge lamps, the power input per unit length of the inner tube is 40 to 50 W cm^{-1} after reaching the stable operating state. Then, as mentioned, all of the mercury inside the inner tube is vaporized and its pressure will reach 300 kPa (2.96 atm), which is much higher than that of fluorescent lamps. As mentioned above, the temperature and the plasma will reach thermal equilibrium in which the electrical energy (electron energy) is converted mainly to thermal energy by elastic collisions with a part also lost through the inner tube wall by heat conduction and convection.

Table 7 Energy Conversion Ratio in Inner Tube of High-Pressure Mercury Discharge Lamp

Discrimination		Rate (%)
Radiation	<300 nm	7.3
	302 nm	1.8
	313 nm	3.0
	365 nm	4.9
	Other UV	1.8
	405 nm	2.2
	436 nm	3.7
	545 nm	4.2
	577 nm	4.4
	Other visible	0.5
	Infrared	15
Convection and conduction loss		46.9
Electrode loss		4.3
Total		100.0

At the thermal equilibrium state, the mercury atoms in the plasma are excited and/or ionized through thermal energy, and some of the excited mercury atoms emit optical radiation. As the density of mercury atoms is very large, UV radiation through transitions to the ground state (185 and 254 nm) is mostly reabsorbed by mercury atoms and is not emitted from the inner tube. The optical radiation from high-pressure mercury lamps consists mainly of radiation produced by transitions from the excited levels 6^3D and 7^3S to the next lower energy levels. They are predominantly line spectral radiations, with wavelengths of 297, 313, 365, 405, 436, 545, and 577 nm.

5.3.3 *Conversion of energy*

Table 7 shows the typical conversion ratio of input electric energy in a standard high-pressure mercury discharge lamp.

5.3.4 *Phosphors for lamp applications*

As is shown in Table 7, about 10% of the input electrical energy in high-pressure mercury discharge lamps is converted into the four-line spectra in the visible region. The optical radiation of these four-line spectra can be used directly for general lighting. However, good color rendering properties cannot be obtained by lighting with only these four lines. In particular, as there is no visible radiation in the wavelength region longer than 600 nm, the light output appears bluish-white, and the rendering of red colors is not satisfactory.

In order to improve the color and the color rendering properties of the output, a phosphor that converts the ultraviolet radiation from the inner tube to red is coated on the inside surface of the outer bulb. As the exciting radiation consists of the 297, 313, and 365-nm lines shown in Table 7, phosphors different from those for fluorescent lamps are used. Further, it is required that the conversion efficiency of the phosphors does not decrease, even at higher temperatures above 300°C.

As mentioned, phosphors suited for these purposes are fundamentally red-emitting phosphors. However, for other purposes, such as adjusting the color temperature of the light output and improving the luminous efficacy of the lamp, blue/green-emitting phos-

Table 8 Phosphors for Fluorescent High-Pressure Mercury Discharge Lamps

Material designation	Chemical composition	Optical properties Peak (nm)	Color	Applicable lamp type
Phosphate	$(Sr,M)(PO_4)_2:Sn^{2+}$, M = Mg,Zn	630	Orange-red	Standard
Germanate	$4MgO{\cdot}GeO_2:Mn^{4+}$ $4(MgO,MgF_2)GeO_2:Mn^{4+}$	660	Deep red	Standard
Yttrate	$Y_2O_3:Eu^{3+}$	613	Red	Standard
Vanadate	$YVO_4:Eu^{3+}$, $Y(P,V)O_4:Eu^{3+}$	619	Red	Standard
	$Y(P,V)O_4:In^{+}$	460	Blue-white	Standard
Halo-silicate	$Sr_2Si_3O_82SrCl_2:Eu^{2+}$	485	Blue-green	Color improved
Aluminate	$(Ba,Mg)_2Al_{16}O_{24}:Eu^{2+}$	450	Blue	Color improved
	$(Ba,Mg)_2Al_{16}O_{24}:Eu^{2+},Mn^{2+}$	515	Green	Color improved
	$Y_2O_3Al_2O_3:Tb^{3+}$	545	Green	Color improved

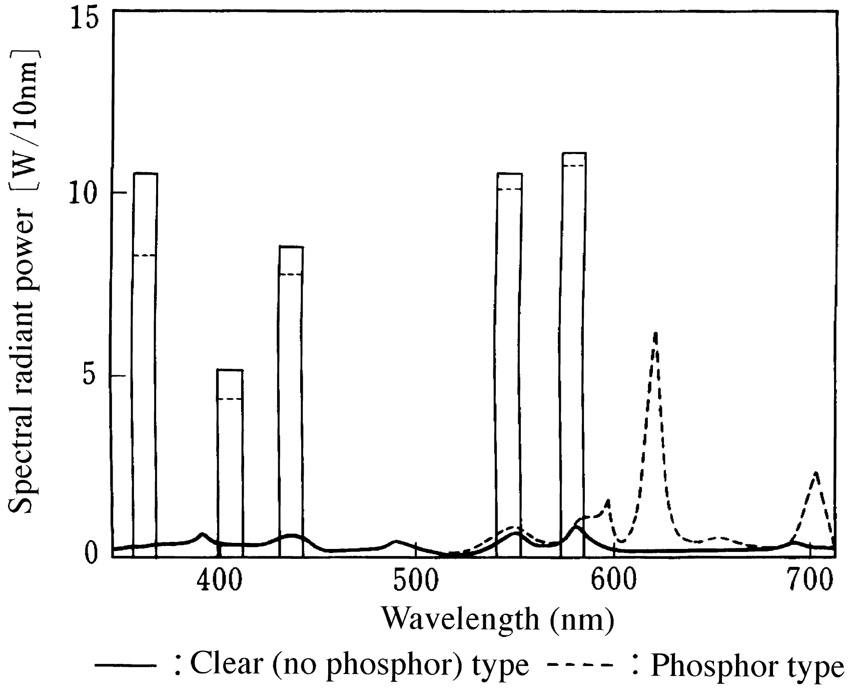

Figure 8 Spectral radiant power distribution of high-pressure mercury discharge lamps (400-W, no phosphor, and red phosphor type).

phors or deep red-emitting phosphors are often applied. Table 8 gives the chemical formula and peak wavelengths of the phosphors used in high-pressure mercury lamps. Figure 7 depicts the spectral power distribution of a typical fluorescent mercury lamp, comparing it with that of a general clear-type high-pressure mercury lamp (without phosphor coatings). Table 9 reveals examples of the improvements in color temperatures, color rendering properties, and luminous efficacy through the use of suitable phosphors.

Since the visible radiation from the inner tube of mercury lamps is directly used for lighting, transmittance of the phosphor layer needs to be properly adjusted. For this reason, the phosphor layer thickness in mercury lamps is usually thinner than that used in fluorescent lamps.

Table 9 Improvement of Optical Properties of High-Pressure Mercury Discharge Lamps by Phosphors (400-W type)

Color of phosphors	Lamp luminous efficacy ($\mathrm{lm\ W^{-1}}$)	Luminous color & correlated color temperature (K)	General color rendering index (R_a)
No phosphor (clear type)	51	Bluish-white (5800)	23
Red	55	Pinkish-white (4100)	44
Red+blue+green	59	White (4200)	50
Red+deep red	53	Incandescent lamp color (3300)	55

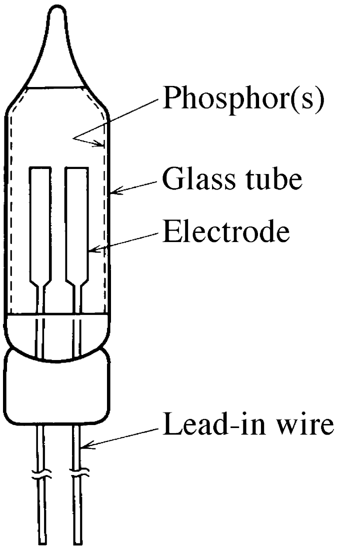

Figure 9 Fundamental construction of a fluorescent glow lamp.

5.4 *Other lamps using phosphors*

5.4.1 *Other HID lamps*[4–5]

For other HID (high-intensity discharge) lamps, some metal-halide lamps and high-pressure sodium discharge lamps also have a phosphor layer coated on the inside wall of the outer bulb. Since these lamps do not emit much UV radiation from the inner tube, the optical radiation emitted from the phosphor does not contribute to the final output. For these lamps, the phosphor is not used to improve the output color of the optical radiation, but to alter the spatial distribution of light by diffusing the output in order to reduce lamp glare.

5.4.2 *Fluorescent glow lamps*[6–7]

Fluorescent glow lamps are used as indicators in various appliances, in the same way as neon glow lamps, LEDs, etc. are used. Figure 9 shows the fundamental structure of a typical fluorescent glow lamp, which is identical to the conventional neon glow lamp. When a suitable current is supplied to the two electrodes, a glow discharge is started.

In the case of neon glow lamps, the bulbs are filled with 5 to 15 kPa (38 to 113 Torr) neon gas, and the optical radiation from the negative glow region of the discharge is used directly. For fluorescent glow lamps, other rare gases (e.g., krypton and/or xenon) are employed. UV radiation is emitted from the negative glow region of this discharge, and this UV radiation is converted to visible radiation by the phosphor coated on the inside wall of the bulb.

Since the emission color of neon glow lamps is reddish-orange, phosphors emitting other colors, such as green and blue, are usually selected to provide distinguishable characteristics in combination with the neon glow lamps. In order to obtain UV radiation from the negative glow discharge efficiently, 3 to 10 kPa krypton or xenon gas are used in the bulbs, producing UV radiation in the 140- to 280-nm region. Phosphors used in fluorescent lamps are also used in these bulbs.

5.4.3 Fluorescent sign tube (luminous tube)[8–10]

For advertisement displays, information signs etc., discharge lamps with longer and slimmer tubes are widely used. One of the typical lamps used for these purposes is the neon sign tube. These tubes have an outside diameter of 10 to 15 mm (the standard size is 14 mm) and overall lengths of 3 m or longer. The original neon signs were filled with 0.1 to 0.3 kPa (0.8 to 2.3 Torr) neon; the output color is the fundamental reddish-orange color, generated by the neon gas discharge plasma.

In order to make displays or advertisements more effective, other colors are desirable. For this reason, fluorescent sign tubes were developed. The fundamental structure of the fluorescent sign tube is identical with that of the neon sign tube except phosphors are coated on the inside wall of the tube and different filling gases are used. As in fluorescent lamps, mercury and rare gases are employed, and the UV radiation from the glow discharge plasma of these gases is used to excite the phosphors. The same phosphors used for fluorescent lamps are used here; monochromatic color phosphors (such as pure blue, green, yellow, and violet) are preferred in displays or advertisements.

This type of tube is specified in terms of the Japanese Industrial Standard (JIS). Leakage transformers with a high secondary open-circuit voltage of 6 to 15 kV are used for these discharges.

5.4.4 Cold cathode fluorescent lamp

Recently, devices using LCD (liquid crystal device) display terminals, such as LCD TVs, personal computers, word processors, and display accessories for the car, have been widely commercialized. For these displays, a back light is used in order to improve visibility. This back light is usually a small-sized cold cathode fluorescent lamp.

As the size of the lamps is determined by the size and dimension of the display devices, the electrical ratings and dimensions vary widely and no starndardization has been achieved. As an example, a slimmer fluorescent lamp having an overall length of 150 mm and a diameter of 6 mm has been developed and is being used.

The fundamental composition and construction of cold cathode fluorescent lamps are similar to those of conventional fluorescent lamp except for the electrodes. Metal electrodes are used as the cold cathodes. And white-emitting phosphors are generally applied. Recently, three-band type, white-emitting phosphors have obtained wide usage, especially for the back light of color LCD display terminals.

As for the gas used in the discharge plasma, a mercury-argon mixture is customarily used. However, rare gases such as argon, krypton, and xenon are also used on occasions; for example, to compensate for a decrease in the light output at low temperatures. In these applications, the phosphor on the inside surface of the tube wall is excited by UV radiation from the rare gas discharge plasma. Recently, panel-type cold cathode fluorescent lamps were developed and their applications are currently being examined.

5.4.5 *Electrodeless fluorescent lamp*[30,31]

Radiation sources using phosphors exploit UV radiation from discharge plasmas for excitation phosphors. Recently, an electrodeless fluorescent lamp consisting of only a sealed glass envelope coated with phosphors on the inner wall, and with plasma-forming filling gases has been developed and put to practical usage. A suitable intense electric field is applied from the outside of this glass envelope, producing a discharge and forming a plasma. The electric field energy is converted into UV radiation in this plasma and phosphors are excited to produce optical radiation in this way.

Since a mercury/rare gas, a rare gas, or a suitable mixture of rare gases is used to fill the glass envelope, the same phosphors as those used in conventional fluorescent lamps are used here.

Electrodeless lamps have a longer life than radiation sources containing electrodes. These lamps are finding popular acceptance for this reason. A recent electrodeless fluorescent lamp being marketed consists of an electrodeless envelope and a high-frequency generator integrated into a single device.

References

1. Harada, T., *Kogen (Light Sources)*, Kyoritsu Shuppan, Tokyo, 1944 (in Japanese).
2. Forsythe, W.E. and Adams, E.Q., *Fluorescent and Other Gaseous Discharge Lamps*, Murry Hill, London, 1948.
3. Harada, T., *Hodento (Discharge Lamps)*, Ohm-sha, Tokyo, 1950 (in Japanese).
4. Waymouth, J.F., *Electric Discharge Lamps*, MIT Press, Boston, 1971.
5. Elembaas, W., *The High Pressure Mercury Vapour Lamps and Their Applications*, Philips Technical Library, Eindhoven, 1966.
6. Kohmoto, K., Dobashi, Y., and Kishimoto, T., *Toshiba Rev.*, 29, 763, 1974 (in Japanese).
7. Kohmoto, K., Ohtani, T., and Dobashi, Y., *Proc. 1976, Annual Conf. IEI Jpn.*, No. 8, 1976 (in Japanese).
8. Oohira, K., *Neon Sign*, Ohm-sha, Tokyo, 1964 (in Japanese).
9. *JIS Z 7615*, 1973, Neon Tubings, 1973 (in Japanese).
10. *JIS Z 8109*, 1991, Luminous Tube Transformers, 1991 (in Japanese).
11. Iseki, Y., Yamashita, H., Yamazaki, H., and Furuya, T., *Proc. 1995, Annual Conf. IEI Jpn.*, No. S-4, 1995 (in Japanese).
12. Hollister, D., *LD & A*, 11, 48, 1976.

chapter five — section five

Phosphors for lamps

Kazuo Narita

Contents

5.5 Characteristics required for lamp phosphors 445
  5.5.1 Characteristics of ultraviolet excitation 445
  5.5.2 Luminescence efficiency 445
  5.5.3 Luminescence spectra 446
  5.5.4 Temperature characteristics 446
  5.5.5 Stability 447
    5.5.5.1 Causes of phosphor deterioration 447
    5.5.5.2 Long-term lumen maintenance 448
References 449

5.5 Characteristics required for lamp phosphors

In selecting practical lamp phosphors, the following characteristics are taken into consideration.

5.5.1 Characteristics of ultraviolet excitation

The phosphor for fluorescent lamps is excited primarily by the 254-nm Hg resonance line. Therefore, the phosphor must absorb this radiation strongly, and convert it into fluorescence efficiently. Since the advent of the three-band fluorescent lamp, however, high-load fluorescent lamps (lamps with a smaller diameter or compact lamps) are becoming popular, and excitation by 185-nm radiation is also becoming important.[29]

In high-pressure mercury lamps, approximately equal amounts of ultraviolet energy are radiated into three wavelength regions, 220–290 nm, 290–330 nm, and 330–380 nm. In order to fully utilize this energy, phosphors that have excitation bands extending into a longer wavelength region up to 380 nm are desired.

5.5.2 Luminescence efficiency

In this chapter, luminescence efficiency is defined as the product of the absorbance of excitation radiation and the quantum efficiency, where the quantum efficiency is the ratio between the number of emitted photons and the number of photons absorbed by a

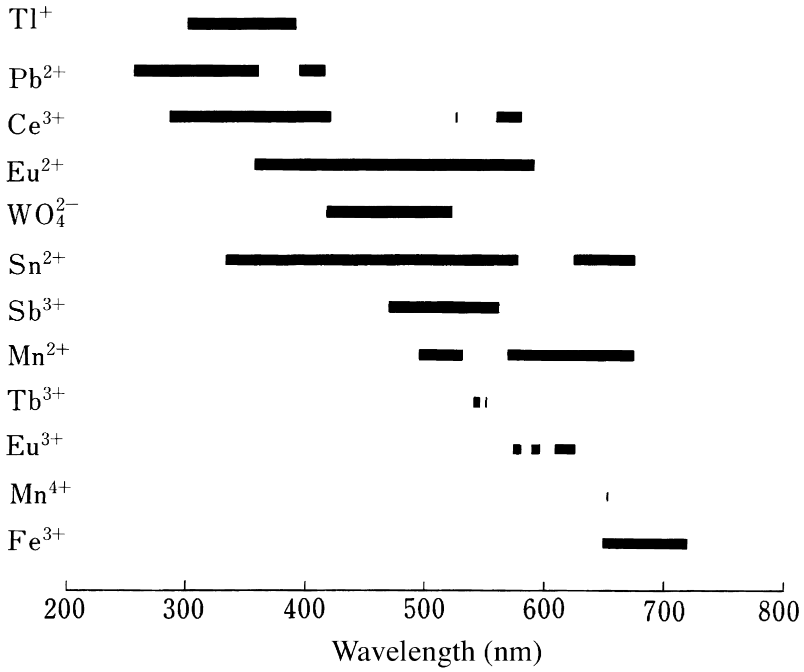

Figure 10 Position of emission peaks of various activators.

phosphor. Quantum efficiency values of phosphors currently in use for fluorescent lamps can be calculated from lamp efficacy. The values range between 0.55 and 0.95, the most frequent values being around 0.70 (see 5.6.1). This reveals that there are still possibilities for improving these phosphors with respect to efficiency.

5.5.3 *Luminescence spectra*

The emission spectra of lamps requested by users range from near-ultraviolet to far-red. By selecting phosphors, it is possible to obtain emissions anywhere between 285 and 720 nm. The peak wavelength is determined primarily by activators (Figure 10).

In lamps for general lighting, the halfwidth of luminescence emission bands exerts great influence on lamp efficacy and color rendition. By combining phosphors having broad emission bands, a lamp with high color rendition can be obtained, but its efficacy is rather low. On the other hand, combinations of blue, green, and red narrow-band emissions of rare-earth activators give lamps with high efficacy and satisfactory color rendering.

5.5.4 *Temperature characteristics*

In general, luminescence efficiency decreases at higher temperatures. In the case of a fluorescent lamp, which is operated at around 40°C, the decrease is very small. However, for high-pressure mercury lamps, in which the temperature of the phosphor coating rises to 300°C, phosphors that maintain high efficiency at such temperatures are necessary.

A model has been proposed that predicts the temperature dependence of luminescence efficiency.[30,31] According to this theory, the necessary condition for phosphors to keep high efficiency at high temperatures is that, in the configurational coordinate model of the luminescence center, the difference of the equilibrium positions in the ground- and excited states is small. For this to be true, the following criteria must be fulfilled:

1. If charge transfer is involved in the excitation process (e.g., Eu^{3+}-activated and tungstate phosphors), then:

   the activator ion radius > the host crystal cation radius

2. When the activator is directly excited (e.g., Tl^{+}-, Eu^{2+}-, and Ce^{3+}-activated phosphors),

   the host crystal cation radius > the activator ion radius

This has been confirmed to be true for a series of phosphors having identical crystal structures.[31]

5.5.5 *Stability*

5.5.5.1 *Causes of phosphor deterioration*

Phosphors are damaged by various causes in the course of the lamp manufacturing process and during lamp operation. The chemical compositions, firing conditions, additives, and surface treatment of phosphors have been studied to keep the phosphors' initial efficiency as unchanged as possible. In the following, some processes that cause phosphor deterioration are described.

Lamp baking. After forming a phosphor film on a lamp wall, the film is dried and the remaining organic binder is decomposed by heating the tube to around 500°C. Usually, the plaque brightness of the phosphor removed from the lamp wall after this process is 7 to 9% lower than the initial brightness. Two explanations are possible for this observed decrease. The first is that, in case of the phosphors fired in a reducing atmosphere (e.g., Eu^{2+}-activated phosphors), the activators are made partially inactive by oxidation. This kind of deterioration can be made considerably smaller by optimizing activator concentration or matrix composition. The second source of decrease in efficiency is that fine carbon particles created by incomplete combustion of the organic binder sometimes absorb exciting radiation and the emission.

The decrease in plaque brightness can be controlled by changing baking conditions. If the lamp baking temperature is lowered, more free carbon is created and plaque brightness becomes much lower. At higher baking temperatures, on the contrary, little carbon is freed and the decrease in brightness is negligible. As a matter of fact, the initial lamp efficacy depends little on the extent of variations in the plaque brightness through baking conditions as long as the phosphor used is oxidation resistant.[32]

Color centers. When irradiated with 185-nm Hg radiation, phosphors generally become slightly colored and their luminescence efficiency decreases.[33] By heating or exposure to 254-nm Hg radiation, the coloration is easily bleached. As this process can be repeated without leaving any permanent change, the coloration is attributed to the formation of color centers, which is a reversible process. The observed decrease of luminescence efficiency is caused by the fact that part of 254-nm exciting radiation is absorbed by the color center and dissipated nonradiatively. If the absorption of the excitation by the phosphor itself is made stronger by increasing the activator concentration, the proportion of the exciting energy absorbed by the color center becomes smaller, and the efficiency decrease is reduced. Some additives, or deliberately added impurities, suppress color center formation.[33] An attempt was made to diminish phosphor damages by 185-nm radiation by providing an absorbing layer, YAG:Ce, on the phosphor coating.[34] The lumen decrease in the first several minutes of lamp burning is attributed to color centers.[35,36]

Mercury adsorption. After long-term lamp operation, the whole phosphor coating becomes grayish; by heating the lamp slightly from the outside, this coloration fades away. As this process is reversible, it is assumed that absorption and desorption of mercury are taking place. According to one theory,[37] mercury adsorption is facilitated when the electronegativity of the phosphor cation exceeds 1.4. From this viewpoint, the poor performance commonly observed in $Zn_2SiO_4:Mn^{2+}$ and other Zn-containing phosphors can be attributed to the fact that the electronegativity of Zn is 1.6. Concerning the deterioration of $Zn_2SiO_4:Mn^{2+}$, however, there is another interpretation (i.e., ion bombardment; see below).

In the case of calcium halophosphate phosphors, the lumen output decrease D[%] is related to Hg concentration in the phosphor H[ppm], which is expressed as $D = 1.16H$. However, mercury deposition is not the direct cause of lumen deterioration.[38]

A recent experiment[39] suggests that mercury is adsorbed either as metallic Hg or HgO, where HgO causes lamp deterioration while Hg does not. The amount of adsorbed HgO becomes larger with an increase in the difference of electrostatic charging potential of HgO and the phosphor. The above-mentioned YAG:Ce coating of phosphors is also effective in diminishing HgO adsorption.[34]

After long-term operation, gray-appearing rings are observed at both ends of a fluorescent lamp, i.e., in the area close to cathodes. These rings are also caused by Hg adsorption. Some phosphors cause a more rapid formation of these rings than others. However, it is not yet clear which elements or compounds accelerate this kind of adsorption.

Ion bombardment. The $Zn_2SiO_4:Mn^{2+}$ phosphor is known as one of the most vulnerable phosphors. As mentioned above, this is sometimes attributed to mercury adsorption.

In another experiment in which deterioration of this phosphor caused by discharge in an argon atmosphere was investigated,[40] it was found that the extent of the deterioration of the phosphor was approximately the same, irrespective of the presence of mercury. Hence, it was concluded that the deterioration could not be attributed to mercury adsorption, but to the formation of an amorphous, nonluminescent layer on the phosphor particle surface by Ar^+- and/or Hg^+-ion bombardment.

Reaction with glass. Poorer lumen maintenance is observed when soda-lime, rather than lead-glass, is used as the material for the lamp bulb.[41] However, the plaque brightness of the phosphors—once removed from the two kinds of lamp envelopes—show little difference. Therefore, it is postulated that a reaction between the glasses and mercury is the cause of the difference. Extensive studies have been performed to clarify the mechanism of the glass-mercury reaction.[42–46] Coatings between the glass wall and phosphor layer have been found effective in preventing mercury penetration into the glass.[43,46]

5.5.5.2 *Long-term lumen maintenance*

The following empirical formula has been proposed to describe the gradual decrease of lumen output during lamp operation over a period of several thousand hours.[47]

$$L_0 - L_t = A\left(1 - e^{-at}\right) + B\left(1 - e^{-bt}\right) + C\left(1 - e^{-ct}\right) \tag{1}$$

Here, L_0 and L_t are lumen outputs at operation times 0 and t, respectively, A, B, and C are parameters, and a, b, and c are rate constants. Eq. 1 suggests that three reactions with different rate constants are involved. Another formula is proposed for the case in which the formation of a nonluminescent layer is assumed (see *Ion bombardment* above.):

$$L_t = L_0 e^{-\sqrt{t/r}} \tag{2}$$

However, correlation between physical or chemical changes of phosphors, including those described in 5.5.5.1 and long-term lumen maintenance is rather complicated, and there is no generally accepted interpretation as to the cause(s) of the long-term change of lumen output. Consequently, the improvement of lamp performance has been made in an empirical manner. In the case of lamps using halophosphates, the lumen output decrease after 5000-hour operation was about 18% in 1950, but had been reduced to 10% by 1970.[48]

References

29. Tanimizu, S. and Nakano, M., *Proceedings of 1983 Annual Conference of IEI Japan*, 11, 1983.
30. Blasse, G., *J. Chem. Phys.*, 51, 3529, 1969.
31. Blasse, G. and Bril, A., *Philips Tech. Rev.*, 31, 304, 1970.
32. Narita, K., *Tech. Digest, Phosphor Res. Soc. 183th Meeting*, Nov., 1980, 13 (in Japanese).
33. Flaherty, J.M., *J. Electrochem. Soc.*, 128, 131, 1981.
34. Saito, M., Honda, H., and Tamatani, M., *Proceedings of the 25th Anniversary Session of Tokyo Branch, the Illuminating Engineering Institute, Japan*, 1995, 20.
35. Vrenken, L.E., de Vette, T.M., and Van der Wolf, R.W., *Illum. Eng.*, 59, 59, 1964.
36. Apple, E.F. and Aicher, J.O., *Proc. Int. Conf. Luminescence*, Budapest, 1966, 2013.
37. Peters, R.C., Vrenken, L.E., Couvbenberg, W.D., and Ligthart, A.S., U.S. Patent 4,335,330, 1982. Japanese Patent Disclosure (Kokai) 54-42874 (1979).
38. Kreidler, E.R., *Electrochem. Soc. Meeting Abstr.*, Spring 1980, 217.
39. Ito, H., Yuge, Y., Taya, A., Tamatani, M., and Terashima, K., *J. Illum Eng. Jpn.*, 76, 16, 1992.
40. Lehman, W., *J. Electrochem. Soc.*, 130, 426, 1983.
41. Lowry, E.T., *J. Electrochem. Soc.*, 95, 242, 1949.
42. Mulder, B.J. and van Heusden, S., *J. Electrochem. Soc.*, 130, 440, 1983.
43. Verhees, P.W.C., *Proceedings of the 5th International Symposium on the Science and Technology of Light Sources*, York, 1989, 105:L.
44. Thaler, E.G., Wilson, R.H., Doughty, D.A., and Beers, W.W., *J. Electrochem. Soc.*, 142, 1968, 1995.
45. Doughty, D.A., Wilson, R.H., and Thaler, E.G., *J. Electrochem. Soc.*, 142, 3542, 1995.
46. Tomioka, H., Higashi, T., and Iwama, K., *Proceedings of the 7th International Symposium on the Science and Technology of Light Sources*, Kyoto, 1995, 103:P.
47. Lowry, E.F. and Mager, E.L., *Illum. Eng.*, 44, 98, 1949.
48. Butler, K.H., *Fluorescent Lamp Phosphors*, Pennsylvania State University Press, 1980, 75.

chapter five — section six

Phosphors for lamps

Shigeru Kamiya and Hideo Mizuno

Contents

5.6 Practical lamp phosphors 451
- 5.6.1 Introduction....451
- 5.6.2 Phosphors for fluorescent lamps....452
  - 5.6.2.1 Halophosphate phosphors....452
  - 5.6.2.2 Phosphate phosphors....462
  - 5.6.2.3 Silicate phosphors....470
  - 5.6.2.4 Aluminate phosphors....478
  - 5.6.2.5 Tungstate phosphors....484
  - 5.6.2.6 Other phosphors....486

References....493

5.6 Practical lamp phosphors

5.6.1 Introduction

Lamp phosphors are divided into two main categories: those for fluorescent lamps and the others for high-pressure mercury lamps. All lamp phosphors in practical use are either oxides or oxyacid salts. As mentioned in 5.1, those phosphors are excited by ultraviolet (UV) rays generated in the rare gas/mercury discharge spaces. The strongest UV radiation generated in fluorescent lamps is located at 254 nm, whereas the dominant UV radiation in the high-pressure mercury lamps is located at 365 nm. The working temperatures of the phosphors during lamp operation are also quite different. Therefore, different kinds of phosphors are utilized for these two lamps.

Requirements for the practical use of phosphors in fluorescent lamps are high emission efficacy under excitation with 254-nm radiation and physical and chemical stability in the rare gas/mercury discharge space. A typical phosphor that satisfies these requirements is calcium halophosphate. The calcium halophosphate phosphors activated with antimony and manganese, invented by Mckeag et al. in 1942, have served as a strong driving force for the popularization of fluorescent lamps. Thanks to various improvements, calcium halophosphate is still being used as a mainstream fluorescent lamp phosphor. Recently, the halophosphates have also been adapted to accommodate a new series of Eu^{2+}-activated phosphors. The blue-emitting phosphor utilized for three-band lamps is an example of a halophosphate.

Various kinds of phosphate phosphors have also been employed for fluorescent lamps. For example, the $(Sr,Mg)_3(PO_4)_2:Sn^{2+}$ phosphor is utilized as the orange-emitting component in high color rendering fluorescent lamps; this phosphor has also been applied for the purpose of color correction and efficacy improvements in high-pressure mercury lamps. Typical phosphate phosphors activated with rare-earth ions are $Sr_2P_2O_7:Eu^{2+}$ (used for diazo photocopy lamps), $2SrO{\cdot}0.84P_2O_5{\cdot}0.16B_2O_3:Eu^{2+}$ (employed as the blue/green-emitting component in extremely high color rendering fluorescent lamps), and $LaPO_4:Ce^{3+},Tb^{3+}$ (which is most commonly used in three-band lamps as the green-emitting component in Japan).

Among the silicate phosphors, $Zn_2SiO_4:Mn^{2+}$ has been well known for a long time. The efficacy of this phosphor is reasonably high. However, due to the poor maintenance during lamp operation, this phosphor is being replaced by other phosphors co-activated with Ce^{3+} and Tb^{3+}. The $BaSi_2O_5:Pb^{2+}$ phosphor utilized for black-light lamps is another example of a silicate phosphor. Tungstate phosphors belong to the group of the self-activated phosphors. $CaWO_4$ and $MgWO_4$ phosphors have also been around for a long time. Aluminate phosphors are relatively new and have also been introduced into fluorescent lamps. The blue-emitting $BaMg_2Al_{16}O_{27}:Eu^{2+}$ and green-emitting $CeMgAl_{11}O_{19}:Tb^{3+}$ phosphors have played an important role in commercializing the three-band fluorescent lamp.

In addition to the above-mentioned phosphors, $Y_2O_3:Eu^{3+}$ is very important because it is the only available red-emitting phosphor for three-band fluorescent lamps. The $3.5MgO{\cdot}0.5MgF_2{\cdot}GeO_2:Mn^{4+}$ phosphor is also the only practical phosphor suitable for fluorescent lamps as the deep red component. This phosphor is also used for color correction purposes in high-pressure mercury lamps.

Only a few kinds of phosphors are utilized in high-pressure mercury lamps because phosphors are required to maintain a high efficacy at ambient temperatures as high as 250 to 300°C in addition to good conformity with the 365-nm UV radiation. Typical phosphors being used in high-pressure mercury lamps include $YVO_4:Eu^{3+}$ and $Y(V,P)O_4:Eu^{3+}$. The blue/green-emitting $BaMg_2Al_{16}O_{27}:Eu^{2+},Mn^{2+}$ and $Sr_2Si_3O_8{\cdot}2SrCl_2:Eu^{2+}$ phosphors are utilized in combination with trivalent europium-activated phosphors to improve the color rendering index of high-pressure mercury lamps.

The emission characteristics and primary usage of the principal phosphors used in the past and in current use are summarized in Tables 10, 10A, and 11. Phosphors utilized for fluorescent lamps are classified according to the host materials in Table 10, while Table 10A shows a rearrangement of these phosphors in terms of the particular luminescence centers.

5.6.2 *Phosphors for fluorescent lamps*

5.6.2.1 *Halophosphate phosphors*

Calcium halophosphate activated with trivalent antimony and divalent manganese phosphors were invented by Mckeag et al. in 1942. Thanks to their various positive features, these phosphors became the main fluorescent lamp phosphors shortly thereafter. The extensive research that followed resulted in remarkable improvements in lamp quality. The lamp efficacy of the standard 40-W fluorescent lamp was increased to 80 lm W^{-1} in 1970 from 60 lm W^{-1} in 1954. It may be said fairly that the invention of calcium halophosphate phosphors was the principal technical driving force behind fluorescent lamps being transformed into the most important light source of today.

A new series of phosphors activated with divalent europium has been successively developed by adopting this stable matrix composition of alkaline earth halophosphates.

Table 10 Phosphors for Fluorescent Lamps (Host Compound Grouping)

Chemical composition	Luminescence color	Peak wavelength (nm)	Halfwidth (nm)	Application	Emission spectrum (Fig. No)	Quantum eff.	Lumin. eff. (lm W^{-1})
Halophosphate phosphors							
1-1 $3Ca_3(PO_4)_2{\cdot}Ca(F,Cl)_2{:}Sb^{3+}$ (BW)	Blue-white	480	140	Color lamp	11	0.96	57
1-2 $3Ca_3(PO_4)_2{\cdot}Ca(F,Cl)_2{:}Sb^{3+},Mn^{2+}$ (D)	Daylight	480, 575	—	Standard lamp	11	0.97	72
1-2 $3Ca_3(PO_4)_2{\cdot}Ca(F,Cl)_2{:}Sb^{3+},Mn^{2+}$ (W)	White	480, 575	—	Standard lamp	11	0.97	80
1-2 $3Ca_3(PO_4)_2{\cdot}Ca(F,Cl)_2{:}Sb^{3+},Mn^{2+}$ (WW)	Warm white	480, 580	—	Standard lamp	11		
1-3 $Sr_{10}(PO_4)_6Cl_2{:}Eu^{2+}$	Blue	447	32	Three-band lamp	16	0.97	12
1-4 $(Sr,Ca)_{10}(PO_4)_6Cl_2{:}Eu^{2+}$	Blue	452	42	Three-band lamp	16		
1-5 $(Sr,Ca)_{10}(PO_4)_6{\cdot}nB_2O_3{:}Eu^{2+}$	Blue	452	42	Three-band lamp			
1-6 $(Sr,Ca,Mg)_{10}(PO_4)_6Cl_2{:}Eu^{2+}$	Blue-green	483	88	High color rend.	13		
Phosphate phosphors							
2-1 $Sr_2P_2O_7{:}Sn^{2+}$	Blue-green	464	105	High color rend.	18	0.94	35
2-2 $(Sr,Mg)_3(PO_4)_2{\cdot}Sn^{2+}$	Orange	620	140	High color rend.	20	0.96	56
2-3 $Ca_3(PO_4)_2{:}Tl^{+}$	Ultraviolet	328	56	Photochemical	22		
2-4 $(Ca,Zn)_3(PO_4)_2{:}Tl^{+}$	Ultraviolet	310	41	Sun lamp	22		
2-5 $Sr_2P_2O_7{:}Eu^{2+}$	Blue	420	28	Photocopy lamp	24		
2-6 $SrMgP_2O_7{:}Eu^{2+}$	Blue	394	25	Photocopy lamp	24		
2-7 $Sr_3(PO_4)_2{:}Eu^{2+}$	Blue	408	35	Photocopy lamp	24		
2-8 $2SrO{\cdot}0.84P_2O_5{\cdot}0.16B_2O_3{:}Eu^{2+}$	Blue-green	480	85	High color rend.	26	0.93	62
2-9 $LaPO_4{:}Ce^{3+},Tb^{3+}$	Green	543	6	Three-band lamp	28		
2-10 $La_2O_3{\cdot}0.2SiO_2{\cdot}0.9P_2O_5{:}Ce^{3+},Tb^{3+}$	Green	543	9	Three-band lamp		0.93	130
2-11 $BaO{\cdot}TiO_2P_2O_5$	Blue-white	483	167	Color correction	30		
Silicate phosphors							
3-1 $Zn_2SiO_4{:}Mn^{2+}$	Green	525	40	Color lamp	32	0.87	109
3-2 $CaSiO_3{:}Pb^{2+},Mn^{2+}$	Orange	610	87	High color rend.	32		
3-3 $(Ba,Sr,Mg)_3Si_2O_7{:}Pb^{2+}$	Ultraviolet	370	68	Insect catching	34		
3-4 $(Ba,Mg,Zn)_3Si_2O_7{:}Pb^{2+}$	Ultraviolet	295	27	Photochemical	34		
3-5 $BaSi_2O_5{:}Pb^{2+}$	Ultraviolet	350	39	Black light	34		
3-6 $Sr_2Si_3O_8{\cdot}2SrCl_2{:}Eu^{2+}$	Blue-green	490	70		36	0.93	57
3-7 $Ba_3MgSi_2O_8{:}Eu^{2+}$		435	90		36		
3-8 $(Sr,Ba)Al_2Si_2O_8{:}Eu^{2+}$	Blue	400	25		36		

Table 10 Phosphors for Fluorescent Lamps (Host Compound Grouping) (continued)

Chemical composition	Luminescence color	Peak wavelength (nm)	Halfwidth (nm)	Application	Emission spectrum (Fig. No)	Quantum eff.	Lumin. eff. (lm W^{-1})
3-9 $Y_2SiO_5:Ce^{3+},Tb^{3+}$	Blue-green	543	12	High color rend.	38	0.92	124
Aluminate phosphors							
4-1 $LiAlO_2:Fe^{3+}$	Infrared	735	62	Plant growth	46		
4-2 $BaAl_8O_{13}:Eu^{2+}$	Blue-green	480	76	High color rend.			
4-3 $BaMg_2Al_{16}O_{27}:Eu^{2+}$	Blue	452	51	Three-band lamp	39	1.03	20
4-4 $BaMg_2Al_{16}O_{27}:Eu^{2+},Mn^{2+}$	Blue-green	450, 515	—	Photocopy	41	0.79	82
4-5 $Sr_4Al_{14}O_{25}:Eu^{2+}$	Blue-green	493	65	High color rend.	45		
4-6 $SrMgAl_{10}O_{17}:Eu^{2+}$	Blue	465	65				
4-7 $CeMgAl_{11}O_{19}:Ce^{3+},Tb^{3+}$	Green	543	6	Three-color lamp	43	0.97	118
Borate phosphors							
5-1 $Cd_2B_2O_5:Mn^{2+}$	Pink	620	79	(Color correct.)	51	0.88	41
5-2 $SrB_4O_7F:Eu^{2+}$	Ultraviolet	360	16	Black light	52		
5-3 $GdMgB_5O_{10}:Ce^{3+},Tb^{3+}$	Green	543	11	Three-band lamp	53		
5-4 $GdMgB_5O_{10}:Ce^{3+},Mn^{3+}$	Orange	630	80	High color rend.	54		
5-5 $GdMgB_5O_{10}:Ce^{3+},Tb^{3+},Mn^{2+}$	Yellow	543, 630	—		54		
Tungstate phosphors							
6-1 $CaWO_4$	Blue	415	112	Color correction	47		
6-2 $(Ca,Pb)WO_4$	Blue	435	120	Color lamp	47	0.81	19
6-3 $MgWO_4$	Blue-white	480	138	Color correction	47	1.00	57
Other phosphors							
7-1 $Y_2O_3:Eu^{2+}$	Red	611	5	Three-band lamp	49		73
7-2 $Y(V,P)O_4:Eu^{2+}$	Red	619	5	Color correction		0.99	43
7-3 $YVO_4:Dy^{3+}$	White	480, 570	—	Light white lamp	50	0.90	
7-4 $MgGa_2O_4:Mn^{2+}$	Green	510	30	Photocopy lamp	55	0.75	55
7-5 $6MgO \cdot As_2O_5:Mn^{2+}$	Deep red	655	15	(High color rend)	56	0.88	22
7-6 $3.5MgO \cdot 0.5MgF_2 \cdot GeO_2:Mn^{4+}$	Deep red	655	15	High color rend.	57	0.75	19

Note: Quantum efficiency is the relative value when that of $MgWO_4$ is referred as 1.00. Luminous efficacy is the value obtained in standard 40-W fluorescent lamps.[1] The parenthesized application is being restricted from environmental respects.

Table 10A Phosphors for Fluorescent Lamps (Luminescence Center Grouping)

Luminescence center	Chemical composition	Peak wavelength (nm)	Luminescence color	Emission spectrum (Fig. No)	No. in Table 10
Tl^+	$(Ca,Zn)_3(PO_4)_2{:}Tl^+$	310	Ultraviolet	22	2-5
	$Ca_3(PO_4)_2{:}Tl^+$	328	Ultraviolet	22	2-4
Mn^{2+}	$MgGa_2O_4{:}Mn^{2+}$	510	Green	55	7-4
	$BaMg_2Al_{16}O_{27}{:}Eu^{2+},Mn^{2+}$	(450), 515	Green	41	4-4
	$Zn_2SiO_4{:}Mn^{2+}$	525	Green	32	3-1
	$3Ca_3(PO_4)_2\cdot Ca(F,Cl)_2{:}Sb^{3+},Mn^{2+}$	(480), 575	Warm white	11	1-2
	$CaSiO_3{:}Pb^{2+},Mn^{2+}$	610	Orange	32	3-2
	$Cd_2B_2O_5{:}Mn^{2+}$	620	Pink	51	5-1
	$GdMgB_5O_{10}{:}Ce^{3+},Mn^{2+}$	630	Orange	54	5-4
	$GdMgB_5O_{10}{:}Ce^{3+},Tb^{3+},Mn^{2+}$	(543), 630	Orange	54	5-5
Sn^{2+}	$Sr_2P_2O_7{:}Sn^{2+}$	464	Blue	18	2-1
	$(Sr,Mg)_3(PO_4)_2{:}Sn^{2+}$	620	Orange	20	2-2
Eu^{2+}	$SrB_4O_7F{:}Eu^{2+}$	360	Ultraviolet	52	5-2
	$SrMgP_2O_7{:}Eu^{2+}$	394	Blue	24	2-6
	$(Sr,Ba)Al_2Si_2O_8{:}Eu^{2+}$	400	Blue	36	3-8
	$Sr_3(PO_4)_2{:}Eu^{2+}$	408	Blue	24	2-7
	$Sr_2P_2O_7{:}Eu^{2+}$	420	Blue	24	2-5
	$Ba_3MgSi_2O_8{:}Eu^{2+}$	435	Blue	36	3-7
	$Sr_{10}(PO_4)_6Cl_2{:}Eu^{2+}$	447	Blue	16	1-3
	$BaMg_2Al_{16}O_{27}{:}Eu^{2+},Mn^{2+}$	450, (515)	Blue	41	4-4
	$(Sr,Ca)_{10}(PO_4)_6Cl_2{:}Eu^{2+}$	452	Blue	16	1-4
	$(Sr,Ca)_{10}(PO_4)_6\cdot nB_2O_3{:}Eu^{2+}$	452	Blue		1-5
	$BaMg_2Al_{16}O_{27}{:}Eu^{2+}$	452	Blue	39	4-3
	$SrMgAl_{10}O_{17}{:}Eu^{2+}$	465	Blue		4-6
	$BaAl_8O_{13}{:}Eu^{2+}$	480	Blue-green		4-2
	$2SrO\cdot 0.84P_2O_5\cdot 0.16B_2O_3{:}Eu^{2+}$	480	Blue-green	26	2-8
	$(Sr,Ca,Mg)_{10}(PO_4)_6Cl_2{:}Eu^{2+}$	483	Blue-green	13	1-6
	$Sr_2Si_3O_8\cdot 2SrCl_2{:}Eu^{2+}$	490	Blue-green	36	3-6
	$Sr_4Al_{14}O_{25}{:}Eu^{2+}$	493	Blue-green	45	4-5
Pb^{2+}	$(Ba,Mg,Zn)_3Si_2O_7{:}Pb^{2+}$	295	Ultraviolet	34	3-4
	$BaSi_2O_5{:}Pb^{2+}$	350	Ultraviolet	34	3-5
	$(Ba,Sr,Mg)_3Si_2O_7{:}Pb^{2+}$	370	Ultraviolet	34	3-3
Sb^{3+}	$3Ca_3(PO_4)_2\cdot Ca(F,Cl)_2{:}Sb^{3+}$	480	Blue-white	11	1-1
	$3Ca_3(PO_4)_2\cdot Ca(F,Cl)_2{:}Sb^{3+},Mn^{2+}$	480, (575)	Blue-white	11	1-2
Tb^{3+}	$CeMgAl_{11}O_{19}{:}Ce^{3+},Tb^{3+}$	543	Green	43	4-7
	$LaPO_4{:}Ce^{3+},Tb^{3+}$	543	Green	28	2-9
	$La_2O_3\cdot 0.2SiO_2\cdot 0.9P_2O_5{:}Ce^{3+},Tb^{3+}$	543	Green		2-10
	$Y_2SiO_5{:}Ce^{3+},Tb^{3+}$	543	Green	38	3-9
	$GdMgB_5O_{10}{:}Ce^{3+},Tb^{3+}$	543	Green	53	5-3
	$GdMgB_5O_{10}{:}Ce^{3+},Tb^{3+},Mn^{2+}$	543, (630)	Green	54	5-5
Eu^{3+}	$Y_2O_3{:}Eu^{3+}$	611	Red	49	7-1
	$Y(V,P)O_4{:}Eu^{3+}$	619	Red		7-2
Dy^{3+}	$YVO_4{:}Dy^{3+}$	(480), 570	White	50	7-3
Fe^{3+}	$LiAlO_2{:}Fe^{3+}$	735	Infrared	46	4-1
Mn^{4+}	$6MgO\cdot As_2O_5{:}Mn^{4+}$	655	Deep red	56	7-4
	$3.5MgO\cdot 0.5MgF_2\cdot GeO_2{:}$	655	Deep red	57	7-5
WO_4^{2-}	$CaWO_4$	415	Blue	47	6-1
	$(Ca,Pb)WO_4$	435	Blue	47	6-2
	$MgWO_4$	480	Blue-white	47	6-3
TiO_4^{4-}	$BaO\cdot TiO_2\cdot P_2O_5$	483	Blue-white	30	2-11

Table 11 Phosphors for High-Pressure Mercury Lamps

Chemical composition	Luminescence color	Peak wavelength (nm)	Half-width (nm)	Application	Emission spectrum (Fig. No)[a]
$YVO_4:Eu^{3+}$	Red	619	5	Ordinary lamp	58
$V(V,P)O_4:Eu^{3+}$	Red	619	5	Ordinary lamp	58
$(Sr,Mg)_3(PO_4)_2:Sn^{2+}$	Orange	620	40	Color improv. lamp	61
$3.5MgO\cdot 0.5MgF_2\cdot GeO_2:Mn^{2+}$	Deep red	655	15	Color improv. lamp	57
$Y_2SiO_5:Ce^{3+},Tb^{3+}$	Green	543	—	Color improv. lamp	58
$Y_2O_3\cdot Al_2O_3:Tb^{3+}$	Green	545	—	Color improv. lamp	66
$Y_3Al_{15}O_{12}:Ce^{3+}$	Greenish-yellow	540	12	Low color temp. lamp	68
$BaMg_2Al_{16}O_{27}:Eu^{2+},Mn^{2+}$	Blue-green	450, 515	—	Color improv. lamp	70
$Sr_2Si_3O_8\cdot 2SrCl_2:Eu^{2+}$	Blue-green	490	7	Color improv. lamp	72
$Sr_{10}(PO_4)_6Cl_2:Eu^{2+}$	Blue	447	32	Color improv. lamp	16
$(Sr,Mg)_3(PO_4)_2:Cu^{2+}$	Blue-green	490	75	Color improv. lamp	74

[a] See 5.6.3.

These phosphors are being used for fluorescent lamps that have high color rendering properties.

$3Ca_3(PO_4)_2\cdot Ca(F,Cl)_2:Sb^{3+},Mn^{2+}$

Crystal structure. These phosphors have a hexagonal structure and a crystal shape identical with natural apatite. The Ca atoms occupy two different sites: Ca atoms in Ca(I) sites are surrounded by six oxygen atoms and those in Ca(II) sites are contiguous with halogen atoms. In cases where the halogen is F, Ca(II) and F atoms are situated in the same crystal plane. When the halogen is Cl, however, Ca(II) cannot remain in the same crystal plane, due to the larger ionic radius of Cl.[2] The difference between these two configurations—namely, F-apatite and Cl-apatite—results in different luminescence properties. The configuration of (F,Cl)-apatite is the same as that of Cl-apatite. Although there are many reports concerning the sites of Sb and Mn, the consensus seems to be that these ions are capable of replacing Ca ions at both types of sites. While manganese ions are generally distributed rather uniformly in the crystal bulk, antimony ions are found mostly on the surface region of the crystal.[3] Partial substitution of Ca by Sr is easy, and partial substitution by Ba or Cd is also possible. The Cd Cl-apatite belongs to another phosphor group.[4]

Emission characteristics. This phosphor series is typical of doubly activated phosphors. Energy transfer from Sb^{3+} to Mn^{2+} can be understood in terms of Dexter's resonance transfer theory. The Sb^{3+} emission peak in calcium halophosphate is located at ~480 nm at room temperature and is not influenced by the kind of halogen in the host. The emission peak of Mn^{2+} in calcium fluorophosphate is located at ~575 nm, whereas that of calcium chlorophosphate is located at ~585 nm. The manganese emission peak in calcium fluorochlorophosphate is located between these wavelengths, depending on the F:Cl ratio. Emission colors from blue-white to warm-white are easily obtained by choosing an appropriate Mn:Sb ratio. A typical example is shown in Figure 11; with increases in the Mn^{2+} concentration, the Mn^{2+} emission intensifies, while the Sb^{3+} emission is suppressed. When the $Mn^{2+}:Sb^{3+}$ ratio is 1, the peak intensity of the Mn^{2+} emission is 1.2 times that of the Sb^{3+} emission. The Sb^{3+} emission vanishes when the ratio rises above 3.3. The Mn^{2+} emission peak shifts to shorter wavelength when Ca is substituted by Sr.

At 83K, the Sb^{3+} emission is composed of a main emission band peaking at ~500 nm and a subband peaking at ~390 nm. With rising temperatures, the main emission band

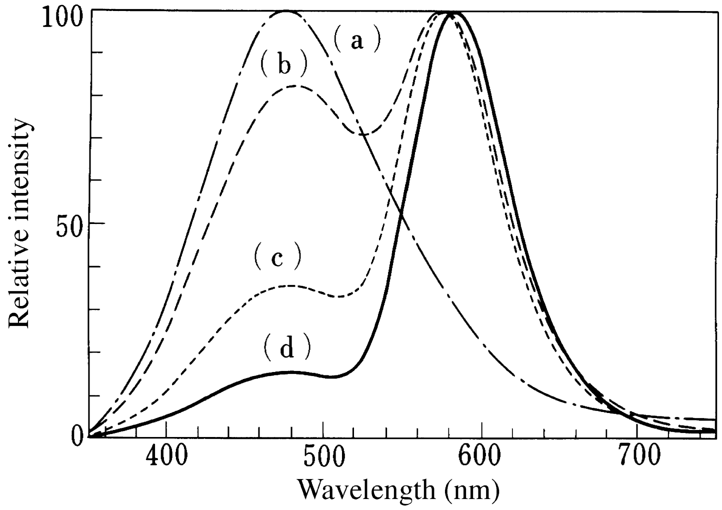

Figure 11 Emission spectra of various calcium halophosphate phosphors activated by Sb^{3+} and Mn^{2}: (a) blue-white Mn^{2+}:Sb^{3+} = 0:0.15 mol per $6PO_4$; (b) daylight Mn^{2+}:Sb^{3+} = 0.08:0.08 mol per $6PO_4$; (c) cool white Mn^{2+}:Sb^{3+} = 0.17:0.08 mol per $6PO_4$; (d) warm white Mn^{2+}:Sb^{3+} = 0.24:0.08 mol per $6PO_4$. (From Kamiya, S. and Mizuno, H., unpublished results. With permission.)

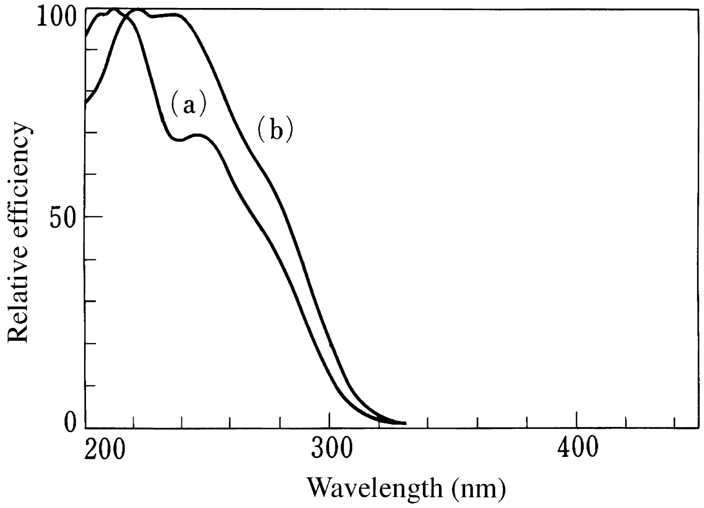

Figure 12 Excitation spectra of calcium halophosphate phosphor activated by Sb^{3+} and Mn^{2+}: (a) Sb^{3+} emission; (b) Mn^{2+} emission. (From Kamiya, S. and Mizuno, H., unpublished results. With permission.)

shifts to shorter wavelength and becomes broader.[5] The subband is not observed in the Sr halophosphate phosphor and its emission peak is located at ~500 nm at room temperature.[6] Addition of Cd results in the shift of the Mn^{2+} emission to longer wavelength. As is clear from the excitation spectra shown in Figure 12, this phosphor series has good conformity with the 254-nm resonance radiation line generated in the low-pressure mercury discharge.

Temperature dependence. The manganese emission maintains relatively good characteristics at high temperatures. Almost 90% of the emission intensity is retained, even at 200°C, without a shift in the emission peak. The antimony emission band, however, shifts to shorter wavelengths with increasing ambient temperature. This results in a decrease of the luminous efficacy.[5] Therefore, the application of these phosphors for high-loading fluorescent lamps is limited.

Degradation characteristics. Halophosphate phosphors are relatively stable among all lamp phosphors in current use. However, an initial short-term degradation still exists. The degradation is caused by color center formation under irradiation with 185-nm UV radiation, which is a component in low-pressure mercury discharges.[7–9] During the initial period of lamp operation, this phenomenon is pronounced. A brightness depression of 5 to 6% is observed within the first 10 minutes of lamp operation. After 1 hour of operation, the depression rate reaches 8 to 10%. The F-apatite phosphor has a lower depression rate than Cl- or (F,Cl)-apatite phosphors. With increases in the Sb concentration, the depression rate decreases. Partial replacement of Ca by Cd also results in remarkable diminution of the depression rate.[8] Due to the fear of environmental contamination, however, this means of improvement has been abandoned. Besides the degradation caused by color center formation, the maintenance of light output during the lamp operation is strongly affected by lamp manufacturing conditions and by the kind of glass used in the envelope. The surface smoothness of the phosphors is another important factor that exerts influence on the maintenance of light output, as well as the efficacy of the lamps.

Preparation. $CaHPO_4$, $CaCO_3$, CaF_2, $CaCl_2$, Sb_2O_3, and $MnCO_3$ are most commonly used as starting materials. The compounds NH_4F and NH_4Cl are also used to provide the halogen components. The preferred mixing ratio of these materials lies in a range that deviates from the stoichiometric value. A slight excess of PO_4 gives favorable results. The preferred range of the Me:PO_4:F,Cl ratio lies between 9.8:6.0:1.6 and 9.95:6.0:1.9.[10] These components are usually mixed by means of a dry system, such as ball mill and/or double corn mixer. Mixed materials are filled in crucibles or dishes and fired in an electric furnace at ~1200°C for several hours. The firing time depends on the quantity of material mixture in the vessel. The most important factor during the firing process is atmospheric control. Although atmospheric control can be attained using a reducing or inert gas flow, fine adjustment of the ventilation system is normally used for control. After crushing and milling the sintered cakes, the powdered phosphors are washed by acid or alkaline solution in order to make the crystal surface smooth. Removal of particles that are too fine is also essential for improved lamp efficacy as well as for better maintenance characteristics.[11,12] For this reason, various means—either a dry or wet system utilizing sedimentation and centrifugation—are being employed. The control of crystal shape and particle size distribution of phosphors is quite important for practical lamp application. These phosphor characteristics strongly depend on those of the $CaHPO_4$ raw material.

Use. Phosphors containing both Sb^{3+} and Mn^{2+} are widely used for the standard warm-white, white, and daylight fluorescent lamps used for general lighting purposes. These phosphors are also utilized as the main component of the phosphor blend for Class A improved color rendering type lamps. Calcium halophosphate makes up the first layer in the double-layer construction of three-band fluorescent lamps.[13] The phosphor activated by Sb^{3+} alone is used for blue-white color lamps and for color correction purposes of general lighting lamps.

$(Ba,Ca,Mg)_{10}(PO_4)_6Cl_2:Eu^{2+}$ [14]

Crystal structure. This phosphor belongs to the hexagonal Cl-apatite structure. Its lattice constant varies continuously, depending on the Ca:Ba ratio; the site occupied by Eu has not been determined.

Emission characteristics. The peak wavelength of emission changes with the Ca:Ba ratio. With increasing Ca content, the emission peak shifts to longer wavelengths and the emission

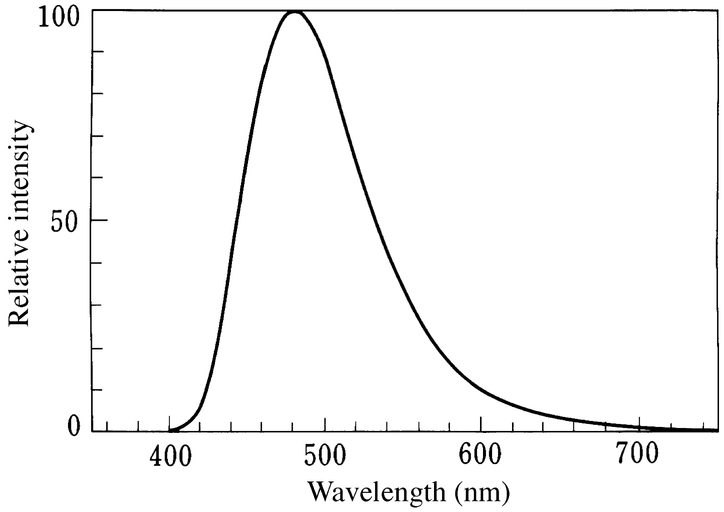

Figure 13 Emission spectrum of (Ba,Ca,Mg)$_{10}$(PO$_4$)$_6$Cl$_2$:Eu^{2+}. (From Kamiya, S. and Mizuno, H., unpublished results. With permission.)

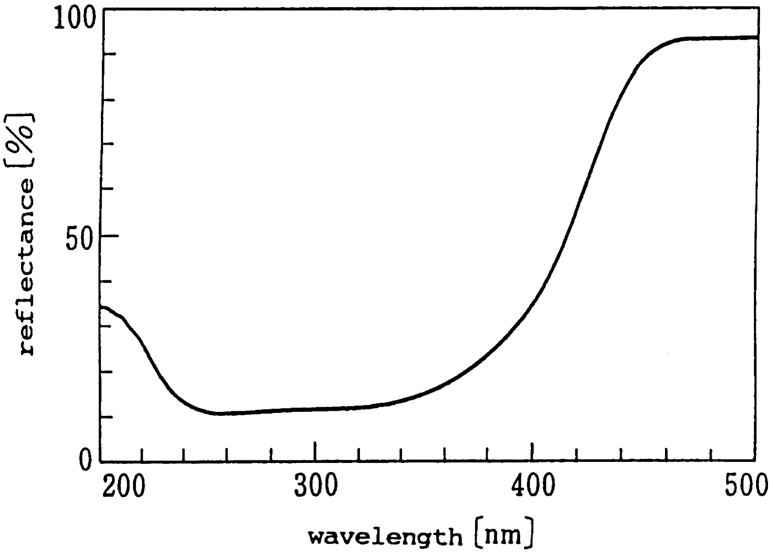

Figure 14 Spectral reflection of (Ba,Ca,Mg)$_{10}$(PO$_4$)$_6$Cl$_2$:Eu^{2+}. (From Kamiya, S. and Mizuno, H., unpublished results. With permission.)

becomes broader. Partial replacement of Ca by Mg is effective in improving the efficacy as well as the maintenance. In Figure 13, the spectral power distribution of a typical example of this phosphor is shown. As is clear from the figure, the emission peak is located at ~483 nm and the spectrum is asymetrical. Whereas a steep emission energy decrease is observed in the shorter wavelength side, the emission in the longer wavelength side is gently sloping and extends beyond 600 nm. The absorption band of these phosphors is well into the blue region of the spectrum, as is clear from the spectral reflection curves shown in Figure 14. This property is useful in suppressing the intensity of mercury lines in the blue region, resulting in improvement of the color rendering property of fluorescent lamps. The excitation spectrum also extends into the blue region, as is shown in Figure 15.

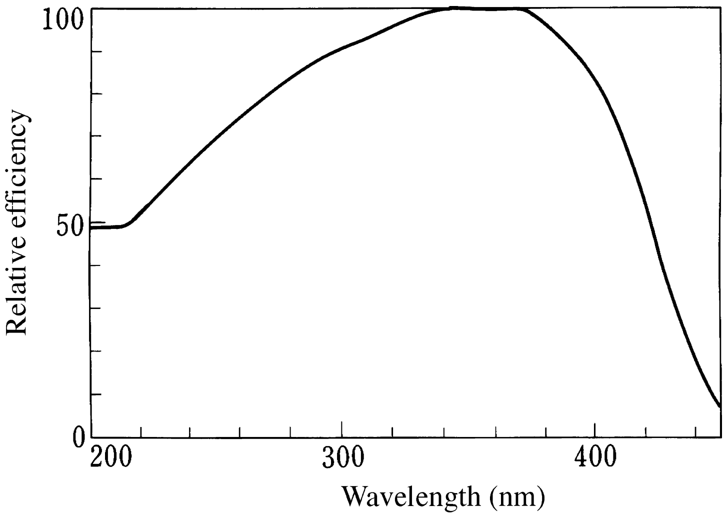

Figure 15 Excitation spectrum of $(Ba,Ca,Mg)_{10}(PO_4)_6Cl_2{:}Eu^{2+}$. (From Kamiya, S. and Mizuno, H., unpublished results. With permission.)

Preparation. A mixture of $BaHPO_4$, $BaCO_3$, $CaCO_3$, MgO, NH_4Cl, and Eu_2O_3 is fired at 800 to 1000°C in air for several hours. After milling and sieving the sintered cake, a second firing is carried out at the same temperature as the first in a slightly reducing atmosphere for several hours. The stoichiometric composition ratio of the total metal components to phosphoric acid gives optimal results. When the Ca content is 1 mole:$6PO_4$ and that of Mg is 0.1 mole:$6PO_4$, the emission peak is located at 467 nm. With increasing Ca content, the emission peak shifts to longer wavelengths and reaches 497 nm when the Ca content is 3 mole:$6PO_4$. The Eu concentration to obtain the highest efficacy is around 0.2 mole:$6PO_4$. The preferable Mg content lies in the 0.1–0.2 mole:$6PO_4$ range.

Use. The blend of this phosphor with a $(Sr,Mg)_3(PO_4)_2{:}Sn^{2+}$ phosphor makes it possible to construct the fluorescent lamps with high color rendering Class AAA, even when a simple single-layer coating is employed.

$Sr_{10}(PO_4)_6Cl_2{:}Eu^{2+}$ *and* $(Sr,Ca,Ba)_{10}(PO_4)_6Cl_2{:}Eu^{2+}$

Crystal structure. Among the alkaline earth halophosphate crystals, only Cl-apatite gives efficient emission by activation with divalent europium. The lattice constant and spectral power distributions are dependent on the ratio of the metal species.[15]

Emission characteristics. The Eu^{2+}-activated Sr Cl-apatite gives a sharp emission spectrum peaking at 447 nm, as shown in Figure 16(a).[16] Partial replacement of Sr by Ca results in the shift of the emission peak to longer wavelength, and the emission spectrum becomes asymmetric in the long-wavelength region. The emission peak shifts to 452 nm when 1 mole Sr is replaced by Ca, as shown in Figure 16(b). Although the replacement of Sr by Ba is supposed to result in the shift of the emission peak to shorter wavelengths, a systematic study of the Sr-Ba system has not been made. When 1 mole each Ca and Ba replace Sr, the emission peak wavelength is found at 445 nm. Incorporation of a small amount of Ba serves to improve the degradation characteristics of the phosphor.[15] It is also reported that an increase in the emission intensity is observed when a small amount of phosphate is replaced by borate.[15] The excitation spectrum is also affected by the composition of the matrix, especially in the wavelength region shorter than 300 nm. In Figure 17, the excitation spectra of a typical Sr-Ca Cl-apatite

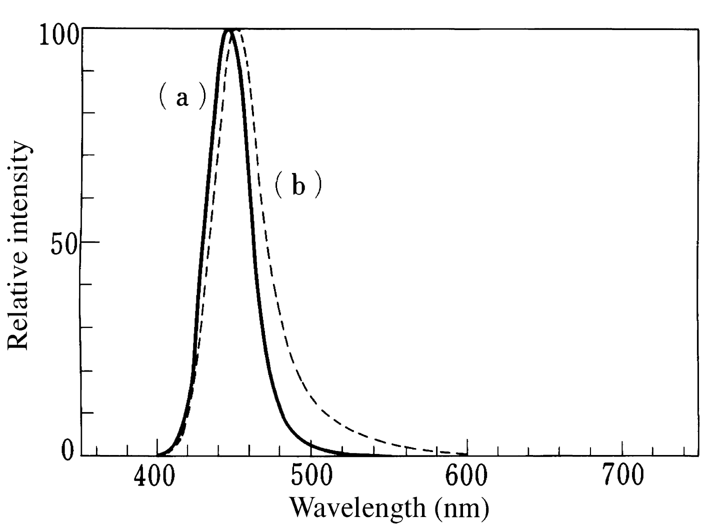

Figure 16 Emission spectra of $(Sr,M)_{10}(PO_4)_6Cl_2:Eu^{2+}$: (a) M = 0; (b) M = 0.1 Ca. (From Kamiya, S. and Mizuno, H., unpublished results. With permission.)

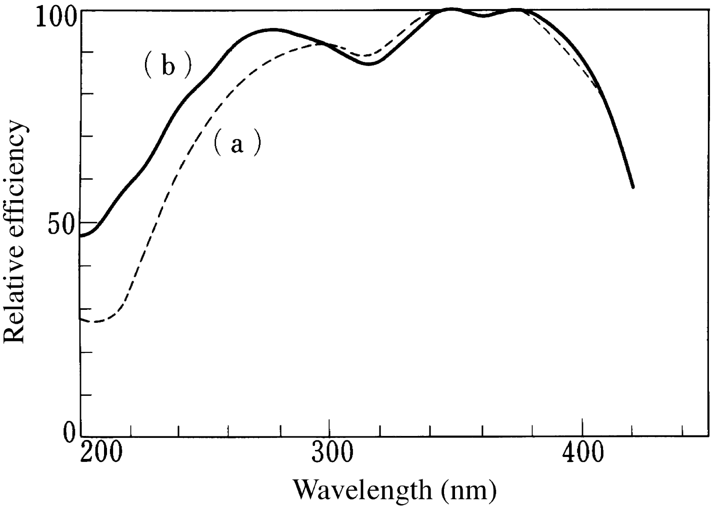

Figure 17 Excitation spectra of $(Sr,Ca)_{10}(PO_4)_6Cl_2:Eu^{2+}$: (a) without B_2O_3; (b) with B_2O_3. (From Kamiya, S. and Mizuno, H., unpublished results. With permission.)

with and without borate incorporation are shown. This series of phosphors has a broad excitation band resulting in good response to both short- and long-wavelength UV excitation.

Preparation. A mixture of raw materials, such as $SrHPO_4$, $SrCO_3$, $SrCl_2$, $CaCl_2$, $BaCl_2$, and Eu_2O_3 in the desired ratio, is fired at 1000 to 1200°C in a slightly reducing atmosphere. The sintered cake is converted to the powder in the usual way. The ratio of the total metal components to the sum of the phosphate and borate combined is adjusted, preferably to the stoichiometic value. The appropriate Eu concentration used is around 0.03 mole:$6PO_4$.

Use. These phosphors are mainly used for the blue color component of three-band fluorescent lamps.

5.6.2.2 Phosphate phosphors

Phosphate compounds have been utilized as host materials of lamp phosphors for many years, thanks to their relatively low material cost, easy synthesis, and reasonable stability in lamp application. The development of the first synthesized alkaline earth phosphate phosphor can be traced back to 1938. In the 1960s, rare-earth-activated alkaline earth phosphate phosphors were practically used in photocopying fluorescent lamps. This was the first application of rare-earth-activated phosphors in fluorescent lamps and represented a landmark in the history of fluorescent lamp development.

Recently, rare-earth-activated, green-emitting phosphate phosphors have successively been developed for three-band lamps as competitive materials to aluminate phosphors.

Phosphates are still being explored as one of the promising matrix crystals for new lamp phosphor development.

$Sr_2P_2O_7$:Sn^{2+}

Crystal structure. The $Sr_2P_2O_7$ crystal is dimorphic. A high-temperature treatment results in the α phase crystal, whereas the β phase is formed at low temperature. The practical phosphor belongs to the α type.

Emission characteristics. The emission color of alkaline earth pyrophosphates activated by divalent tin varies from blue to green depending on the species of the alkaline earth metal.[17–19] The Sr pyrophosphate phosphor has a relatively broad emission band peaking at 464 nm, as shown in Figure 18. The color coordinate of the emission is calculated to be $x = 0.160$, $y = 0.179$. The excitation spectrum of this phosphor is shown in Figure 19. In addition to efficient excitation by UV radiation of wavelength shorter than 300 nm, this phosphor can also be excited by electron beam or by X-ray.

Preparation. Raw materials are ordinarily chosen from $SrHPO_4$, $SrCO_3$, $(NH_4)_2HPO_4$, and SnO. To preserve the divalent state of tin, a slightly reducing atmosphere is required during the firing process. Preferable firing temperatures are ~900 to 1000°C. The amount of Sn is in the vicinity of 1 to 2 mol%.

Use. This phosphor was occasionally utilized to improve the color rendering property of fluorescent lamps.

$(Sr,Mg)_3(PO_4)_2$:Sn^{2+}

Crystal structure[21,22]*.* When pure $Sr_3(PO_4)_2$ is heated to between 1000 and 1600°C and then rapidly cooled down to room temperature, a rhombohedral structure is obtained. Above 1305°C, transition into a structure similar to β-$Ca_3(PO_4)_2$ has been identified by differential thermal analysis. This means that the crystal structure of pure $Sr_3(PO_4)_2$ is always rhombohedral at room temperature, independent of the synthesis temperature. However, partial replacement of Sr, either by Mg, Ca, Zn, or Cd, makes it possible to keep the β-$Ca_3(PO_4)_2$ structure even at room temperature. Only the β type phosphate gives efficient fluorescence.

Emission characteristics. Mg in too large an amount gives a strongly sintered phosphor cake, resulting in low emission intensity. The highest brightness is obtained in the β-type structure but only at a critical composition close to the border where α and β-type structures co-exist.[22] As shown in Figure 20, this phosphor has a broad emission band with a peak at 620 nm. The highest quantum efficiency is obtained when 11 mol% $Sr_3(PO_4)_2$ is replaced by $Mg_3(PO_4)_2$. In this case, the efficiency reaches 0.96. Such high efficiency is not observed in the Ca or Cd compounds. When the Sr-Mg phosphate is used, the luminous efficacy of a 40-W fluorescent lamp is as high as 56 lm W^{-1}. The excitation spectrum shown in Figure 21 illustrates clearly that this phosphor is also efficiently excited by the 365-nm

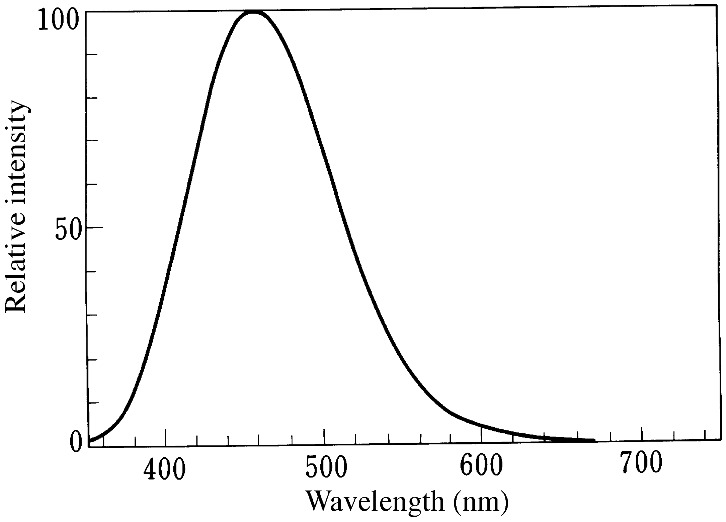

Figure 18 Emission spectrum of $Sr_2P_2O_7$:Sn^{2+}. (From Kamiya, S. and Mizuno, H., unpublished results. With permission.)

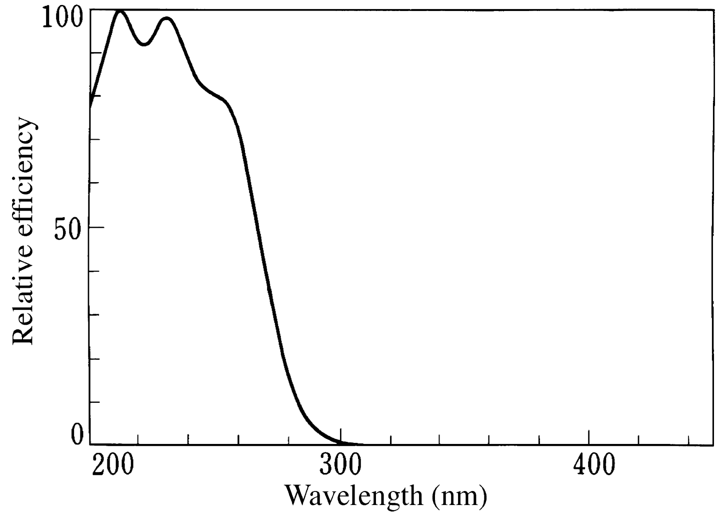

Figure 19 Excitation spectrum of $Sr_2P_2O_7$:Sn^{2+}. (From Kamiya, S. and Mizuno, H., unpublished results. With permission.)

radiation generated in the high-pressure mercury discharge. Thanks to this excitation characteristic and the excellent high-temperature characteristics, this phosphor has been widely used for the purposes of color correction and efficacy improvement in high-pressure mercury lamps.

Preparation. $SrHPO_4$, $SrCO_3$, $3MgCO_3 \cdot Mg(OH)_2 \cdot 3H_2O$, and SnO are commonly used as raw materials. The preferred Sn concentration is 2 to 4 mol%. Firing is carried out at 1000 to 1200°C in a slightly reducing atmosphere for several hours. Special caution must be taken for atmospheric control to preserve Sn in the divalent state during the firing process. The sintered cake is milled to a powder by ordinary means.

Use. This phosphor is very important as the red-emitting component of extremely high color rendering fluorescent lamps of Class AAA.

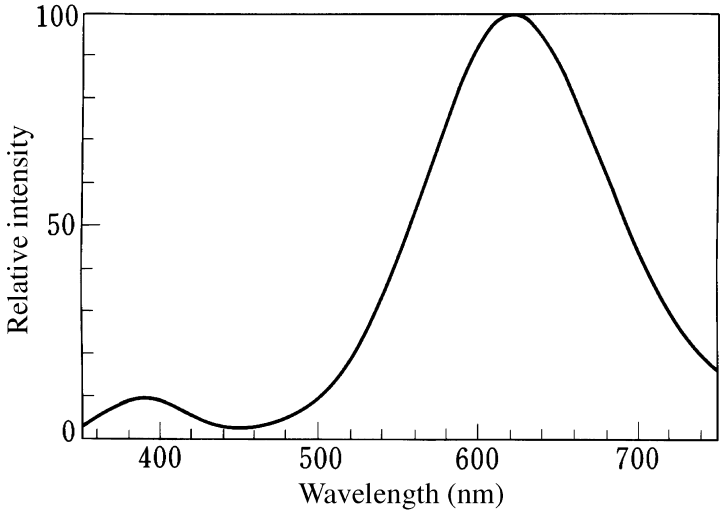

Figure 20 Emission spectrum of $(Sr,Mg)_3(PO_4)_2$:Sn^{2+}. (From Kamiya, S. and Mizuno, H., unpublished results. With permission.)

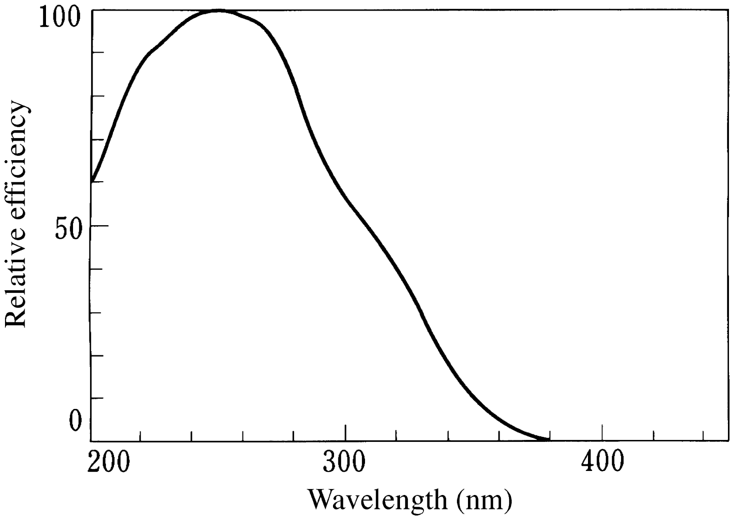

Figure 21 Excitation spectrum of $(Sr,Mg)_3(PO_4)_2$:Sn^{2+}. (From Kamiya, S. and Mizuno, H., unpublished results. With permission.)

$(Ca,Zn)_3(PO_4)_2$:Tl^+

Crystal structure. The $Ca_3(PO_4)_2$ crystal is dimorphous. The α phase forms at temperatures higher than 1180°C and the β phase crystal forms below that temperature. For practical lamp phosphors, Ca-Zn orthophosphate has been used as the matrix composition in order to shift emission peaks for a particular application.

Emission characteristics. The emission peak of $Ca_3(PO_4)_2$:Tl^+ is located at 328 nm, as shown in Figure 22(a).[23] This peak wavelength deviates from the erythematic sensitivity peak of 298 nm. Shifting of the emission peak is possible by partial replacement of Ca by Zn. With an increase in the Zn amount, the emission peak shifts to shorter wavelengths. The composition in practical use is $(Ca_{0.9},Zn_{0.1})_3(PO_4)_2$:$Tl^+$, with emission peak located at 310 nm, i.e., nearer to the erythematic sensitivity peak, as shown in Figure 22(b).[24] Partial replacement of Ca by Zn does not alter the excitation spectrum significantly, as shown in

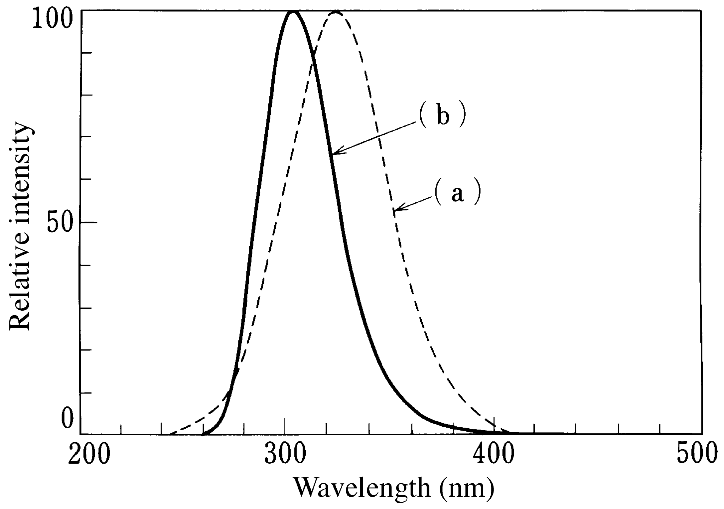

Figure 22 Emission spectra of (a) $Ca_3(PO_4)_2{:}Tl^+$ and (b) $(Ca,Zn)_3(PO_4)_2{:}Tl^+$. (From Kamiya, S. and Mizuno, H., unpublished results. With permission.)

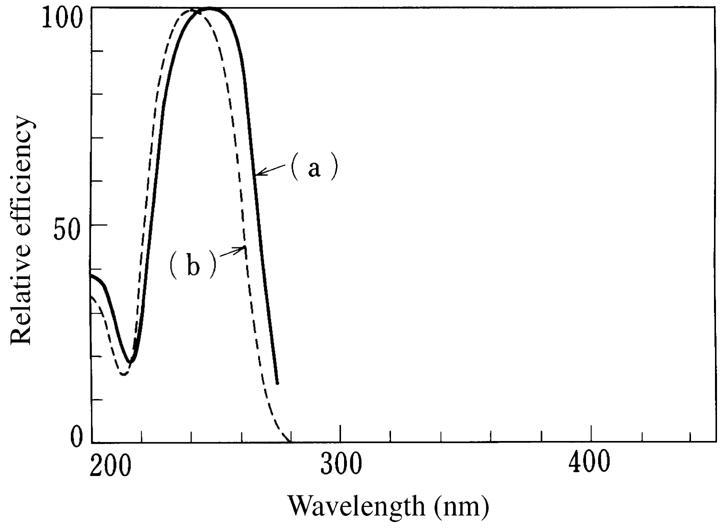

Figure 23 Excitation spectra of (a) $Ca_3(PO_4)_2{:}Tl^+$ and (b) $(Ca,Zn)_3(PO_4)_2{:}Tl^+$. (From Kamiya, S. and Mizuno, H., unpublished results. With permission.)

Figure 23. 40-W fluorescent lamps employing this phosphor generate 7.5 to 8.0 W of UV radiation with an output of 1.3 to 1.75 W at the erythematic wavelength.

Preparation. Usually, $CaHPO_4$, $CaCO_3$, ZnO, and $TlNO_3$ are used as starting materials. The blended materials are then fired at 900 to 1000°C in air. A favorable result is obtained by firing at relatively low temperatures because this minimizes the evaporation loss of Tl. The optimal Tl concentration is ~3 to 4 mol%.

Use. This phosphor is exclusively utilized for fluorescent sun lamps.

$Sr_2P_2O_7{:}Eu^{2+}$ and $(Sr,Mg)_2P_2O_7{:}Eu^{2+}$

Crystal structure. The crystal structure of these phosphors have been identified as orthorhombic α type. The lattice constants of $Sr_2P_2O_7$ are a = 8.98 Å, b = 13.13 Å, and c = 5.40 Å.

Emission characteristics. Because the divalent Eu ion emission originates from an electric dipole transition between the $4f^65d$ and $4f^7$ configurations, its emission spectrum is relatively broad and the spectrum is influenced strongly by the matrix structure.[26–28] According to X-ray analysis, Sr-Mg pyrophosphate has a different structure from either Sr or Mg pyrophosphates. The emission peak of $(Sr,Mg)_2P_2O_7:Eu^{2+}$ is located at 394 nm, whereas that of $Sr_2P_2O_7:Eu^{2+}$ is located at 420 nm, as shown in Figure 24(a) and(b), respectively. As shown in Figure 25, the excitation spectra of both phosphors extend to the long-wavelength UV region. High excitation probability of these phosphors at 254 nm explains their suitability for fluorescent lamp application. The quantum efficiency of the optimized phosphors under 250- to 270-nm excitation reaches 0.95. The temperature dependence of the efficiency of these phosphors is somewhat inferior to that of $Sr_3(PO_4)_2:Eu^{2+}$ discussed below. The quenching temperature of the emission is ~200°C.

Preparation. $SrHPO_4$, $MgNH_4PO_4$, and Eu_2O_3 are commonly used as raw materials. Firing is made at 1000 to 1200°C in a slightly reducing atmosphere for several hours. Preferred Eu concentrations are ~2 mol%.

Use. These phosphors are used for fluorescent lamps in photochemical application; particular use is in photocopying lamps for diazo-sensitive paper systems.

$Sr_3(PO_4)_2:Eu^{2+}$

Crystal structure[27,28]*.* The crystal phase of $Sr_3(PO_4)_2$ changes from α to β or β to α type at 1305°C. This transition temperature decreases by 125 to 150°C when Eu^{2+} ions are incorporated. Crystals heated to temperatures higher than 1000°C and then cooled rapidly show the α phase. This procedure assumes that the crystal phase of this phosphor is always of the α type, independent of firing temperature. The emission intensity, however, depends strongly on the firing temperature. A high brightness phosphor is obtained only by high-temperature firing where β type formation takes place prior to temperature quenching.

Emission characteristics. The emission peak of this phosphor is located at 408 nm, as shown in Figure 24(c). When the Sr is partially replaced by either Mg, Ca, Zn, or Cd, β type structures are obtainable even at room temperature. The emission intensity of Eu^{2+}-activated phosphors employing these materials as hosts is insufficient for practical application.[28] The peak height of $Sr_3(PO_4)_2:Eu^{2+}$ is only about 70% that of $Sr_2P_2O_7:Eu^{2+}$ at room temperature; however, this situation is reversed at high temperatures.[29] In addition, the excitation spectrum of this phosphor is different from those of the pyrophosphate phosphors. As shown in Figure 25(c), two separate bands are clearly observable in the excitation spectrum.

Preparation. A mixture of $SrHPO_4$, $SrCO_3$, and Eu_2O_3 is commonly employed as the starting material. Firing is made at 1200 to 1250°C in a slightly reducing atmosphere for several hours. Addition of a small excess of Sr yields improved results. The appropriate Eu concentration is ~2 mole.

Use. These phosphors are used for fluorescent lamps in photochemical applications, particularly photocopying using diazo-sensitive paper systems.

$2SrO\cdot 0.84P_2O_5\cdot 0.16B_2O_3:Eu^{2+}$ [30]

Crystal structure. This phosphor matrix is obtained by partial replacement of P_2O_5 by B_2O_3 in $Sr_2P_2O_7$. X-ray analysis, however, shows that the crystal structures of these two materials are different from each other.

Emission characteristics. This phosphor gives a blue-green emission whose peak is located at 480 nm, as shown in Figure 26. This phosphor is efficiently excited not only by 254-nm radiation, but also by the 405- and 436-nm mercury lines owing to its broad excitation

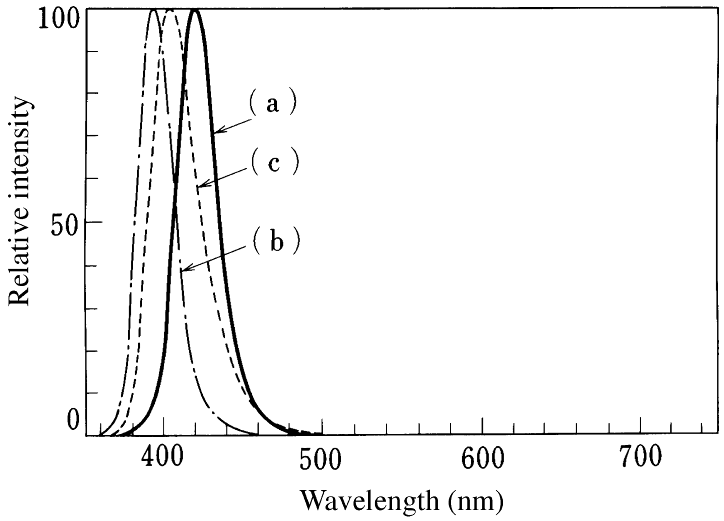

Figure 24 Emission spectra of (a) $Sr_2P_2O_7:Eu^{2+}$; (b) $(Sr,Mg)_2P_2O_7:Eu^{2+}$; and (c) $Sr_3(PO_4)_2:Eu^{2+}$. (From Kamiya, S. and Mizuno, H., unpublished results. With permission.)

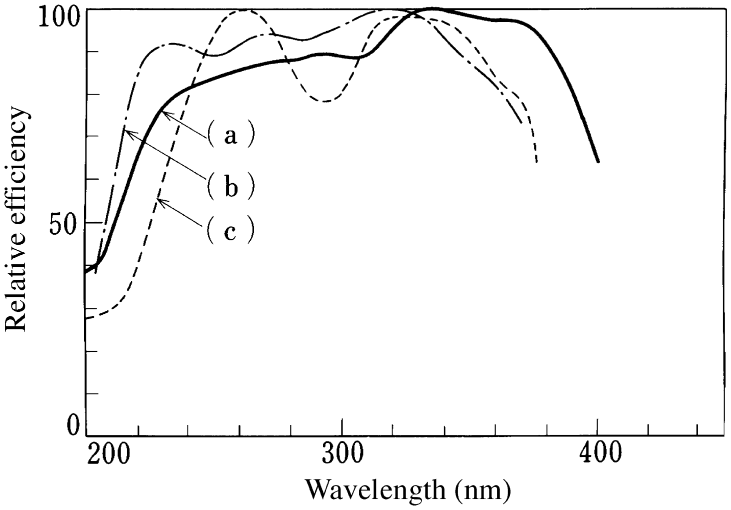

Figure 25 Excitation spectra of (a) $Sr_2P_2O_7:Eu^{2+}$; (b) $(Sr,Mg)_2P_2O_7:Eu^{2+}$; and (c) $Sr_3(PO_4)_2:Eu^{2+}$. (From Kamiya, S. and Mizuno, H., unpublished results. With permission.)

spectrum; the latter extends from the UV all the way into the visible, as shown in Figure 27. The luminous efficacy of 62 lm W^{-1} when used in a 40-W fluorescent lamp is higher than that of the calcium halophosphate phosphor activated with trivalent antimony.

Preparation. The starting materials are $SrHPO_4$, $SrCO_3$, H_3BO_3 (99.5%), and Eu_2O_3. Firing is made at 1100 to 1250°C in a slightly reducing atmosphere for several hours. Eu concentrations of 2 to 3 mol% are normally used.

Use. This phosphor is utilized for Class AAA high color rendering fluorescent lamps as its blue/green-emitting component. The absorption spectrum extending to the blue color region has the advantage of suppressing the mercury emission lines in the blue region, which normally influence the color rendering property of fluorescent lamps unfavorably. Proper combination of this phosphor with an orange-emitting phosphor makes it possible

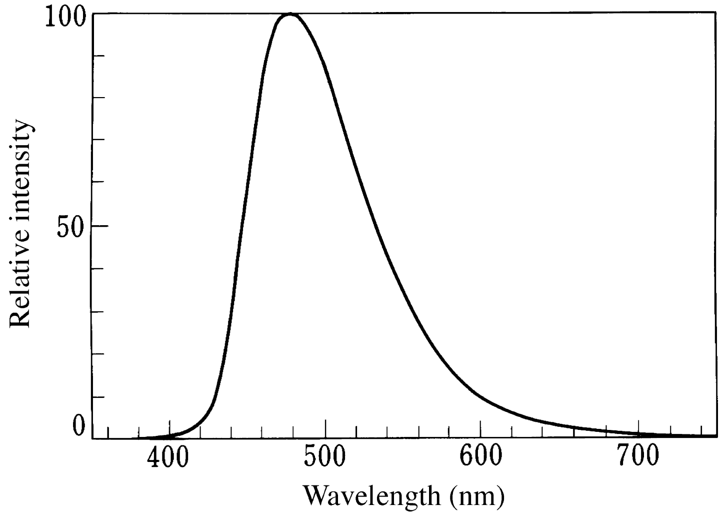

Figure 26 Emission spectrum of $2SrO{\cdot}0.84P_2O_5{\cdot}0.16B_2O_3{:}Eu^{2+}$. (From Kamiya, S. and Mizuno, H., unpublished results. With permission.)

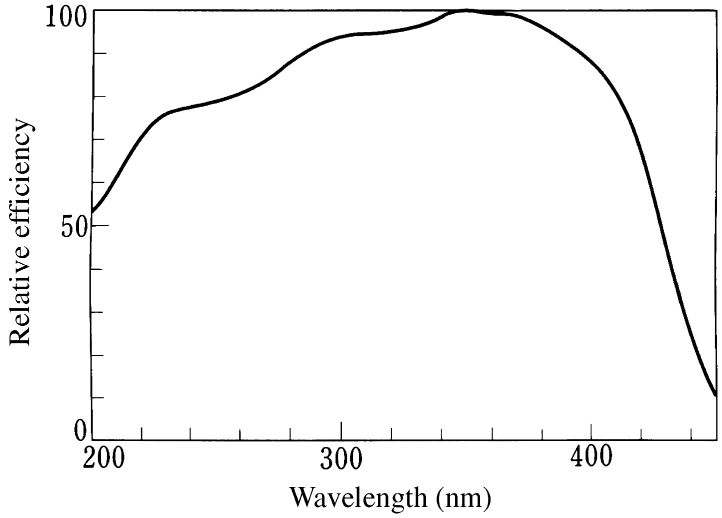

Figure 27 Excitation spectrum of $2SrO{\cdot}0.84P_2O_5{\cdot}0.16B_2O_3{:}Eu^{2+}$. (From Kamiya, S. and Mizuno, H., unpublished results. With permission.)

to obtain Class AAA lamps even with a single-layer coating (i.e., without coating with a filter layer).

$LaPO_4{:}Ce^{3+},Tb^{3+}$

Crystal structure. The rare-earth orthophosphates, specifically Ce and Y family compounds, form monazite and xenotite crystals, respectively. This phosphor belongs to the monazite crystal group, as determined by X-ray analysis.[31] The $La_2O_3{\cdot}0.9P_2O_5{\cdot}0.1SiO_2{:}Ce^{3+},Tb^{3+}$ phosphor obtained by partial replacement of P_2O_5 by SiO_2 belongs to the same family.[32]

Emission characteristics. The Tb^{3+} emission of $LaPO_4$ involves the 5*d*-4*f* transition process. The $LaPO_4{:}Tb^{3+}$ phosphor does not give an efficient emission under 254-nm excitation due to the low absorption coefficient at that wavelength. Co-activation by Ce^{3+}, however,

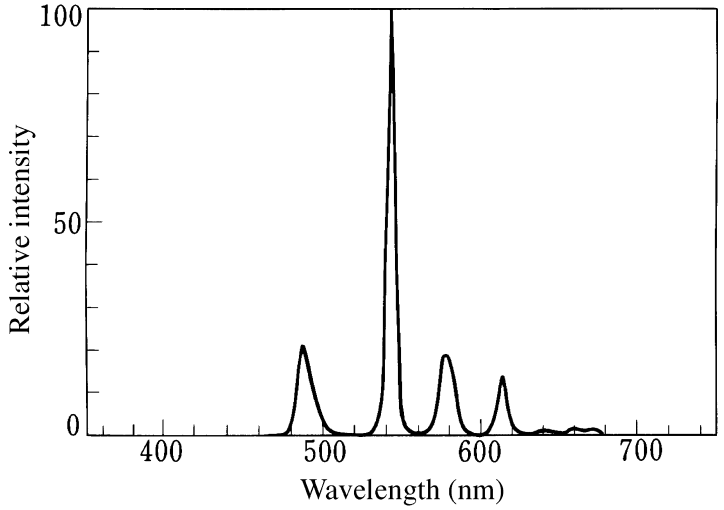

Figure 28 Emission spectrum of $LaPO_4:Ce^{3+},Tb^{3+}$. (From Kamiya, S. and Mizuno, H., unpublished results. With permission.)

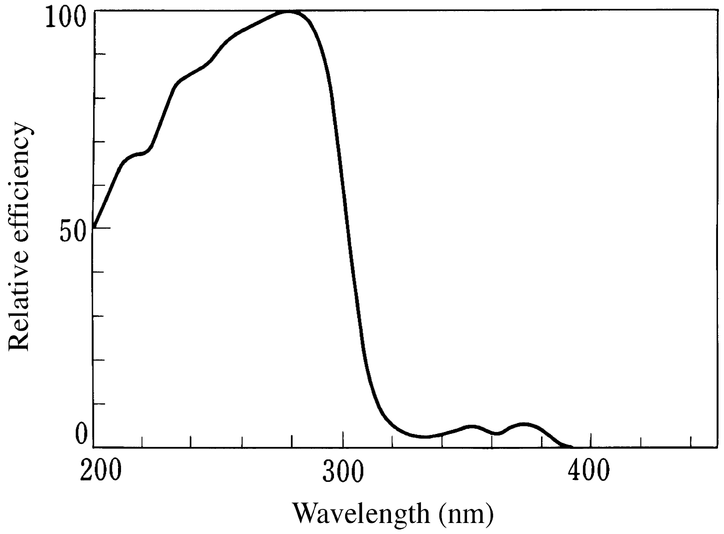

Figure 29 Excitation spectrum of $LaPO_4:Ce^{3+},Tb^{3+}$. (From Kamiya, S. and Mizuno, H., unpublished results. With permission.)

results in a remarkable increase in emission intensity since Ce^{3+} acts as an efficient sensitizer to Tb^{3+}.[33–35] Energy transfer from Ce^{3+} to Tb^{3+} can be explained in terms of a resonant transfer process similar to those occurring in ordinary doubly activated phosphors. As is clear from Figure 28, the emission spectrum of this phosphor peaks at 543 nm, showing the distinctive character of Tb^{3+} emission. The excitation spectrum given in Figure 29 shows good conformity with 254-nm absorption.

Temperature dependence. One of the drawbacks of this phosphor is its relatively high sensitivity to ambient temperature effects. The temperature dependence of the emission intensity of this phosphor is strongly related to the Ce concentration.[36] The quenching temperature for the luminescence decreases with increasing Ce concentration. For example, for a Ce concentration that gives the highest intensity at room temperature, the emission intensity falls by nearly 90% at 150°C. On the other hand, the emission of a phosphor containing less Ce, with an intensity of 95% of the maximum at room temperature, increases nearly 100% in intensity at 150°C. Therefore, the Ce concentration of this phosphor has to be properly adjusted to the wall temperatures of the lamp in which the phosphor is to be used. Phosphors with lower Ce concentrations, of up to half of the optimal amount used in standard tubular fluorescent lamp applications, yield better results in the compact fluorescent lamps with an outer envelope (so-called incandescent lamp type) where wall temperatures are extremely high.

Preparation. The commonly used raw materials for this phosphor are La_2O_3, CeO_2, Tb_4O_7, and $(NH_4)_2HPO_4$. The optimal Tb concentration is ~0.2 to 0.3 mol:PO_4. As mentioned above, the Ce concentration must be chosen according to the application, and ranges from 0.15 to 0.4 mol:PO_4. Firing is made at 1150 to 1200°C in a slightly reducing atmosphere for several hours. The sintered cake is milled to the powder by ordinary means.

Use. This phosphor is currently being extensively used in three-band lamps as the green-emitting component.

$BaO{\cdot}TiO_2{\cdot}P_2O_5$

Crystal structure. The crystal structure of this phosphor is unknown. Below 790°C, the crystal structure of pure $Ba_2P_2O_7$ is known as the α phase. By heat treatment above 790 °C, transition to the γ phase takes place. Only the γ phase gives bright fluorescence.

Emission characteristics. This phosphor belongs to class of materials activated by complex ions. The emission center of this phosphor is the TiO_4^{4-} ion complex. Its emission spectrum is similar to that of the $MgWO_4$ phosphor, as is shown in Figure 30. The emission peak is located at 483 nm. The emission intensity is not significantly influenced by the TiO_2 concentration. The Ti:Ba mole ratio of the practical phosphor is ~0.3. The excitation spectrum of the phosphor is shown in Figure 31. A remarkable feature of this phosphor is its very long decay time: the after-glow time of 100 μs is twice as long as that of the $MgWO_4$ phosphor.[20] The luminous efficacy in a 40-W fluorescent lamps can be as high as 50 lm W^{-1}.

Preparation. $BaHPO_4$, $(NH_4)_2HPO_4$, and TiO_2 are usually used as raw materials. Both the rutile and anatase type TiO_2 can be used for this purpose. Around 2 mol% BaF_2 is often added as a flux. Firing is made in air at temperatures between 900 and 1000°C. The sintered cake is milled to powder form by ordinary means.

Use. This phosphor had been utilized as a replacement for the $MgWO_4$ phosphor for color correction purposes in Class AA high color rendering fluorescent lamps.

5.6.2.3 *Silicate phosphors*

The Mn^{2+}-activated zinc silicate and zinc-beryllium silicate were the most important fluorescent lamp phosphors until 1949. These phosphors, however, lost their prominence as soon as the calcium halophosphate phosphors activated with antimony and manganese were introduced. From 1947 to 1957, Pb^{2+}-activated alkaline earth silicate phosphors were successively developed; these materials have efficient UV emissions. Three applications have been of special interest. The barium-zinc silicate phosphor, having an emission peak at 295 nm, was used in fluorescent sun lamps that emit erythematic light. Barium disilicate phosphors, having an emission peak at 350 nm, find application in black-light lamps; and barium-strontium-magnesium silicate phosphors with an emission peak at 370 nm, were used for insect catching and for photocopy lamps for diazo-sensitive paper systems. These phosphors, however, have mostly been replaced by rare-earth-activated phosphate phosphors.

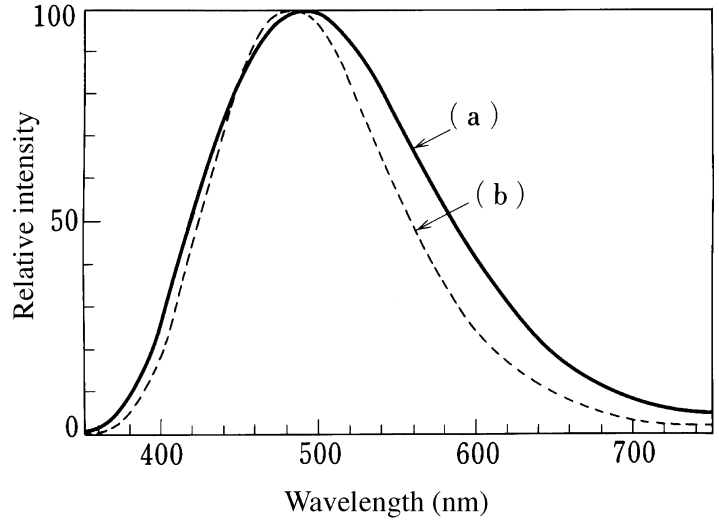

Figure 30 Emission spectra of (a) BaO·TiO_2·P_2O_5 and (b) $MgWO_4$. (From Kamiya, S. and Mizuno, H., unpublished results. With permission.)

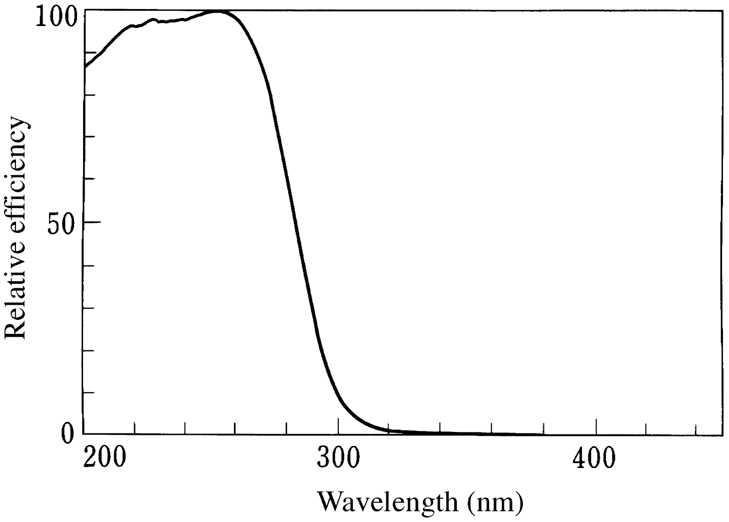

Figure 31 Excitation spectrum of BaO·TiO_2·P_2O_5. (From Kamiya, S. and Mizuno, H., unpublished results. With permission.)

Recently, the Eu^{2+}-activated silicate phosphors have attracted much attention. Complex silicate, halosilicate, and aluminosilicate phosphors containing Ba, Sr, and/or Mg have been developed. Depending on the host material, blue- to blue/green-emitting phosphors can be obtained.

Zn_2SiO_4:Mn^{2+}

Crystal structure. The crystal structure of the Zn silicate phosphor is isomorphous with the mineral willemite and has hexagonal symmetry. A part of Zn^{2+} can be replaced by Be^{2+} to form a solid solution.

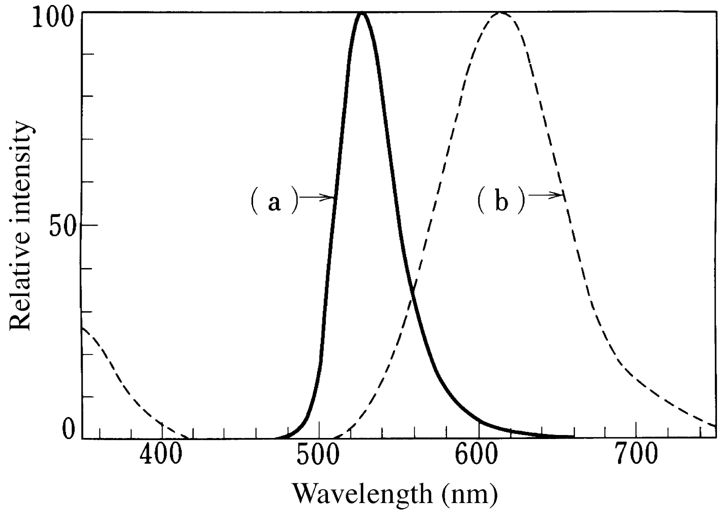

Figure 32 Emission spectra of (a) $Zn_2SiO_4:Mn^{2+}$ and (b) $CaSiO_3:Pb^{2+},Mn^{2+}$. (From Kamiya, S. and Mizuno, H., unpublished results. With permission.)

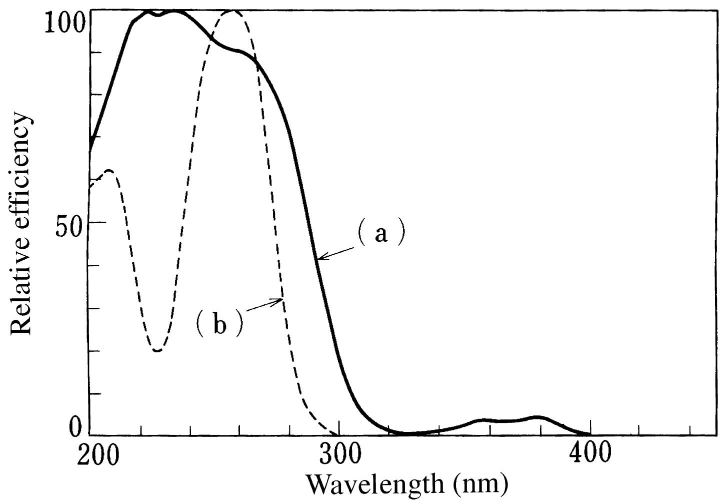

Figure 33 Excitation spectra of (a) $Zn_2SiO_4:Mn^{2+}$ and (b) $CaSiO_3:Pb^{2+},Mn^{2+}$. (From Kamiya, S. and Mizuno, H., unpublished results. With permission.)

Emission characteristics. Under 253.7-nm UV excitation, the $Zn_2SiO_4:Mn^{2+}$ phosphor shows a bright green emission peak located at 525 nm, as shown in Figure 32(a). This phosphor has a strong excitation band in the wavelength range of 200 to 280 nm, as shown in Figure 33(a). Hence, this phosphor is well suited for 253.7-nm excitation. Its quantum efficiency can reach 0.87 with this excitation. Partial replacement of Zn by Be brings about a new emission band with a peak located at 610 nm. By changing the Be:Zn ratio, a wide range of colors from green to orange can be obtained.

Preparation. ZnO, SiO_2, and $MnCO_3$ are commonly used as starting materials. Optimal results are obtained with the mixing ratio $1.5ZnO:SiO_2:0.08MnCO_3$. The mixture is fired at 1200°C in air for several hours. The sintered cake is milled and fired again in air at 1200 to 1300°C for several hours. Although the stoichiometric $ZnO:SiO_2$ ratio is

2:1, the highest brightness can be obtained when excess SiO_2 is introduced in the starting blend.

Use. The Zn silicate phosphor is one of the oldest lamp phosphors. Its efficiency and color purity are reasonably high. Nevertheless, its practical application in fluorescent lamps is limited due to its rather poor maintenance characteristics. Beside its application in green color lamps, this phosphor was once employed in lamps for electrostatic photocopying equipment, because of a good spectral match. This application, however, had been taken over either by the $MgGa_2O_4$:Mn^{2+} or Tb^{3+}-activated aluminate phosphors. Until 1950, the Zn-Be silicate phosphor was the most important phosphor, as it was used as the main component of white/daylight fluorescent lamps. This application has been taken over by the calcium halophosphate phosphors. Also, due to the toxicity of beryllium compounds, this phosphor is no longer in use.

$CaSiO_3$:Pb^{2+},Mn^{2+}

Crystal structure. Calcium metasilicate, $CaSiO_3$, has a low-temperature (β type) and a high-temperature form (α type). The β type is isomorphous with the mineral wollastonite and has triclinic symmetry. Whereas undoped $CaSiO_3$ fired at 1150°C belongs to the α type, Ca silicate phosphors activated with Pb^{2+} and Mn^{2+} form the β type, even when fired at temperatures higher than 1200°C, because the transition temperatures, α to β, rise when a solid solution of $CaSiO_3$ and $MnSiO_3$ is formed.[37]

Emission characteristics. This phosphor is a typical doubly activated phosphor. The emission peak of Pb^{2+} in this phosphor is located at 330 nm and that of the Mn^{2+} is located at 610 nm, as shown in Figure 32(b). The $CaSiO_3$:Pb^{2+} phosphor emits ultraviolet rays peaked at 330 nm. Once the Mn^{2+} is incorporated, this band almost disappears and red emission becomes dominant.[38,39] When the concentration of Mn^{2+} is lower than 0.1 mol%, the crystal form of the phosphor is α type and it emits a yellowish-green fluorescence peaked at 560 nm. When the Mn^{2+} concentration is increased up to 1 mol%, the crystal form changes to the β type and red emission peaked at 610 nm appears. This phosphor has a relatively high quantum efficiency (0.8) under 253.7-nm excitation.[38]

Preparation. The starting materials, SiO_2, $CaCO_3$, PbO, and $MnCO_3$, are mixed in the ratio 0.75CaO:SiO_2:0.06PbO:0.05MnO. The mixture is fired at 1200°C in air for several hours. The sintered cake is milled and then fired again at the same temperature in a water vapor atmosphere for several hours.

Use. In the past, this phosphor was widely used for high color rendering fluorescent lamps as the orange-red emitting component. This application, however, has been taken over by either $(Sr,Mg)_3(PO_4)_2$:Sn^{2+} or Y_2O_3:Eu^{3+} phosphors.

$(Sr,Ba,Mg)_3Si_2O_7$:Pb^{2+} [40]

Crystal structure. Both $Sr_2MgSi_2O_7$ and $Ba_2MgSi_2O_7$ have been identified by X-ray analysis as having a single phase. $Sr_2MgSi_2O_7$ is isomorphous with $Ca_2MgSi_2O_7$ (akaermanite), having tetragonal symmetry. Eighty percent of Sr^{2+} in crystalline $Sr_2MgSi_2O_7$ can be replaced by Ba^{2+} to form a solid solution. When more than 80% Sr^{2+} is replaced by Ba^{2+}, the X-ray difraction shows mainly lines belonging to $Ba_2MgSi_2O_7$ crystal.

Emission characteristics. The emission peak of the $Sr_2MgSi_2O_7$:Pb^{2+} phosphor is located at 325 nm. With increasing Ba^{2+}, the emission peak shifts to longer wavelength until it reaches 370 nm with 80% of the Sr^{2+} replaced. When more than 80% of the Sr^{2+} is replaced by Ba^{2+}, an emission band peaked at 330 nm, belonging to $Ba_2MgSi_2O_7$:Pb^{2+}, becomes dominant. This observation agrees well with the results from X-ray diffraction. The emission and

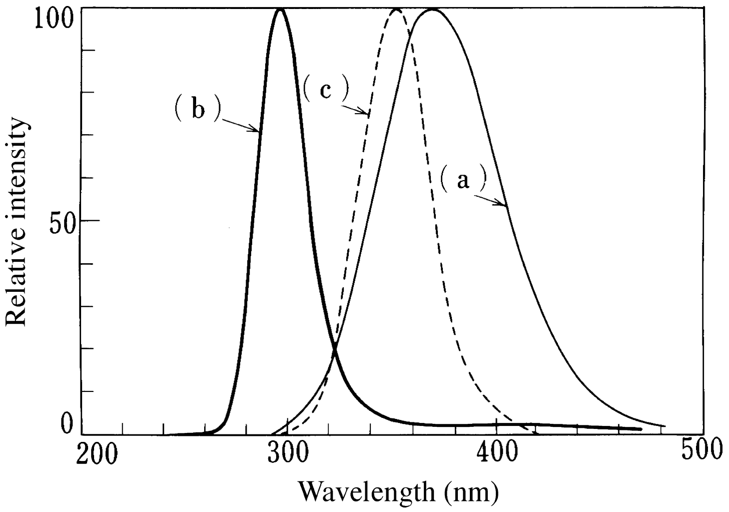

Figure 34 Emission spectra of (a) $(Sr,Ba,Mg)_3Si_2O_7:Pb^{2+}$; (b) $(Ba,Zn,Mg)_3Si_2O_7:Pb^{2+}$; and (c) $BaSi_2O_5:Pb^{2+}$. (From Kamiya, S. and Mizuno, H., unpublished results. With permission.)

excitation spectra of the $Sr_{0.6}Ba_{1.4}MgSi_2O_7:Pb^{2+}$ phosphor are shown in Figure 34(a) and 35(b), respectively.

Preparation. A slurry is made of $SrCO_3$, $BaCO_3$, $MgCO_3$, and SiO_2 in the mole ratio 0.6:1.4:1.0:2.0 with water. Some 3% of a Pb compound, usually $Pb(NO_3)_2$ in an aqueous solution, is added to the mixture. The paste is dried and milled. The resulting powder is fired at ~1050°C in air for several hours.

Use. The phosphor had been used in diazo copying lamps until the $SrP_2O_7:Eu^{2+}$ phosphor was introduced. Currently, it is used in lamps for photochemical and insect-catching purposes.

$(Ba,Zn,Mg)_3Si_2O_7:Pb^{2+}$ [40]

Crystal structure. The fluorescence and the phase diagrams of the Pb^{2+}-activated BaO-MgO-SiO_2 and BaO-ZnO-SiO_2 systems have been reported. Both $BaMg_2SiO_2O_7$ and $BaZn_2SiO_2O_7$ have been identified by X-ray analysis as having single phases. The similarity between these two phosphors indicates that they are isomorphous; it has been also confirmed that these compounds can make a solid solution. Thermal analysis indicates that $(Ba,Zn)_3Si_2O_7$ has a reversible crystallographic transition at about 270°C. Due to this transition, this phosphor detaches easily from the tube wall during fluorescent lamp production. However, the transition disappears when more than 0.05 mole Zn^{2+} is replaced by Mg^{2+}. Thus, practical usable phosphors employ the composition $BaZn_{1.9}Mg_{0.1}Si_2O_7:Pb^{2+}$.

Emission characteristics. The emission peak of $BaZn_2Si_2O_7:Pb^{2+}$ phosphor is located at 303 nm, whereas that of the $BaMg_2Si_2O_7:Pb^{2+}$ phosphor is at 290 nm. The emission intensity of the latter is lower than that of the former. These two phosphors form solid solutions with emission peak position depending on the Mg:Zn ratio. The emission peak shifts to shorter wavelengths with increases in the Mg^{2+} content. The emission intensity decreases when more than 20% of the Zn^{2+} is replaced by Mg^{2+}; however, at low replacement levels, an increase in the emission intensity is observed. As the intensity decreases, another emission band (370-nm peak) appears. The emission peak of the practical phosphor $BaZn_{1.9}Mg_{0.1}Si_2O_7:Pb^{2+}$ is located at 295 nm, as shown in Figure 34(b). Its excitation spectrum is shown in Figure 35(b).

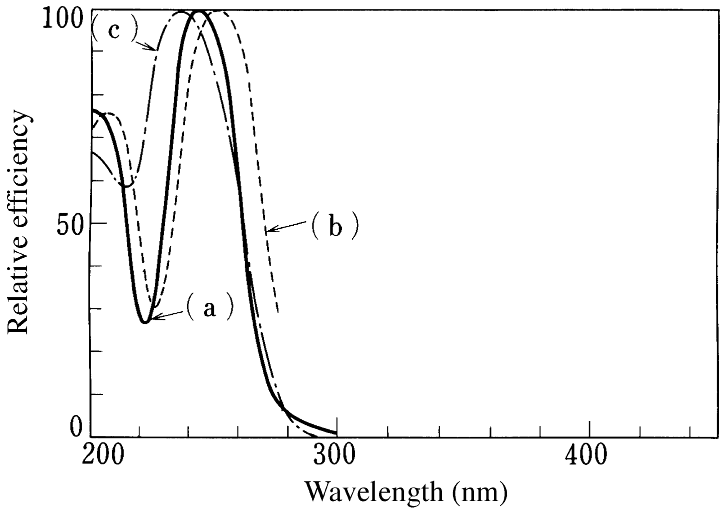

Figure 35 Excitation spectra of (a) $(Sr,Ba,Mg)_3Si_2O_7:Pb^{2+}$; (b) $(Ba,Zn,Mg)_3Si_2O_7:Pb^{2+}$; and (c) $BaSi_2O_5:Pb^{2+}$. (From Kamiya, S. and Mizuno, H., unpublished results. With permission.)

Preparation. A slurry is made of $BaCO_3$, ZnO, MgO, and SiO_2 with water. The mixing ratio of $BaCO_3$ is made lower than the stoichiometric ratio, $BaO{\cdot}1.9ZnO{\cdot}0.1MgO{\cdot}SiO_2$; 1 mol% of Pb^{2+}, usually as $Pb(NO_3)_2$ in an aqueous solution, is added to the blend. The paste is dried and milled. The resulting powder is fired at 1100 to 1200°C in air for several hours.

Use. This phosphor was used for fluorescent sun lamps. This application, however, has been taken over by the $(Ca,Zn)_3(PO_4)_2:Tl^+$ phosphor due to relatively poor maintenance characteristics.

$BaSi_2O_5:Pb^{2+}$ [41,42]

Crystal structure. The $BaSi_2O_5:Pb^{2+}$ phosphor is isomorphous with the mineral sanbornite and has rhombic symmetry.

Emission characteristics. The $BaSi_2O_5:Pb^{2+}$ phosphor shows a strong UV emission peaked at 350 nm under 253.7-nm excitation. The emission and excitation spectra are shown in Figures 34(c) and 35(c), respectively.

Preparation. The starting materials are SiO_2 and $BaCO_3$.The highest brightness is obtained when 5 mol% SiO_2 in excess of the stoichiometric ratio is blended; 3 mol% Pb^{2+}, usually $Pb(NO_3)_2$ in an aqueous solution, is also added. The mixed paste is dried and milled. The resulting powder is fired in air at 1100 to 1250°C for a few hours.

Use. This phosphor is used for black-light lamps.

$Sr_2Si_3O_8{\cdot}2SrCl_2:Eu^{2+}$

Crystal structure. The Eu^{2+}-activated alkaline earth halosilicate phosphors were invented by Leete and Mckeag.[43] X-ray analysis shows that this phosphor has a novel crystal structure that is different from that of other Sr silicates. Detailed luminescence characteristics have been reported.[44] However, a definitive crystal structure for these materials has not been established.

Emission characteristics. This phosphor emits blue-green luminescence and its emission peak is located at 490 nm, as shown in Figure 36(a). Besides this main emission band, an additional band peaking at 425 nm due to $SrCl_2:Eu^{2+}$ occasionally appears in the sintered product. This emission band can be removed by washing with water.[45] The excitation spectrum of this phosphor is shown in Figure 37(a). The luminescence mechanism of this phosphor can be explained by the $4f^7$-$4f^65d$ excitation and emission model for Eu^{2+}. Owing to the splitting of *d* states, the excitation spectrum shows a broad band extending from 200 to 450 nm. This phosphor has good temperature characteristics under 365-nm excitation; the brightness at 330°C retains 50% of its room-temperature value.

Preparation. The starting materials—$SrCO_3$, SiO_2, and $SrCl_2$ in the ratio of 2:3:2 with $0.01Eu_2O_3$—are mixed with pure water. The paste is dried at 120°C and prefired at 850°C for 3 hours. The prefired cake is milled and then refired for a few hours at 950°C in a slightly reducing atmosphere of nitrogen containing 2% hydrogen by volume. The sintered product is cooled in this atmosphere and milled to a powder. Finally, the powder is washed with water to remove the remaining $SrCl_2$.

Use. This phosphor was considered as the blue-green component for high color rendering fluorescent lamps, but was not widely used due to shortfalls in its maintenance characteristics. The phosphor is currently employed for color correction of high-pressure mercury lamps because of its high temperature properties.

$Ba_3MgSi_2O_8:Eu^{2+}$

Crystal structure. The crystal structure of the Me_3(Me=Ca,Sr, Ba)$MgSi_2O_8:Eu^{2+}$ phosphor is isomorphous with the mineral merwinite ($Ca_3MgSi_2O_8$), which has rhombic symmetry.[40]

Emission characteristics. The emission spectra of the Me_3(Me=Ca,Sr,Ba)$MgSi_2O_8:Eu^{2+}$ phosphor depend on the species of alkaline earth metal used in the compound. The emission peak of the phosphor containing Ca is located at 475 nm, and those of the phosphors containing Sr or Ba are located at 460 and 440 nm, respectively.[46] The emission spectrum of the $BaMgSi_2O_8:Eu^{2+}$ phosphor is shown in Figure 36(b). The phosphor has a quantum efficiency of 0.50 under the 250–270-nm excitation. As is clear from Figure 37(b), the excitation spectrum of this phosphor extends from 200 to 460 nm. Therefore, this phosphor can be excited even by blue light.

Temperature dependence. The temperature dependence of the emission intensity of $Me_3MgSi_2O_8:Eu^{2+}$ (Me=Ca,Sr,Ba) phosphors depends on the alkaline earth species involved. Corresponding to the change of Me, going from Ca to Sr or to Ba, temperature characteristics become better. The emission intensity of $Ba_3MgSi_2O_8:Eu^{2+}$ at 270°C is about 50% of that observed at room temperature.

Preparation. The raw materials—$BaCO_3$, $MgCO_3$, and very fine SiO_2—are mixed in the mole ratio 3:1:2 with 0.01 mole Eu_2O_3. The mixture is fired at 1100 to 1300°C for a few hours in a slightly reducing atmosphere, preferably a mixture of 5 volume percent hydrogen in nitrogen. The sintered product is cooled in this atmosphere.

Use. Since the $Ba_3MgSi_2O_8:Eu^{2+}$ phosphor has a narrow blue emission band, it is used for color correction purposes. The phosphor co-activated with Mn^{2+} has the characteristic manganese orange emission band peaking at 620 nm in addition to the Eu^{2+} 443-nm band. This phosphor finds its application in plant growth lamps.[47]

$(Sr,Ba)Al_2Si_2O_8:Eu^{2+}$

Crystal structure. Feldspar is the general classification for the mineral structure containing the three-dimensional silicon-aluminum-oxygen framework. The frameworks of all the alkaline earth feldspars are the same. The crystal symmetries, however, are different, depending on the size of the species involved. The Sr-feldspar ($SrAl_2Si_2O_8$) has triclinic

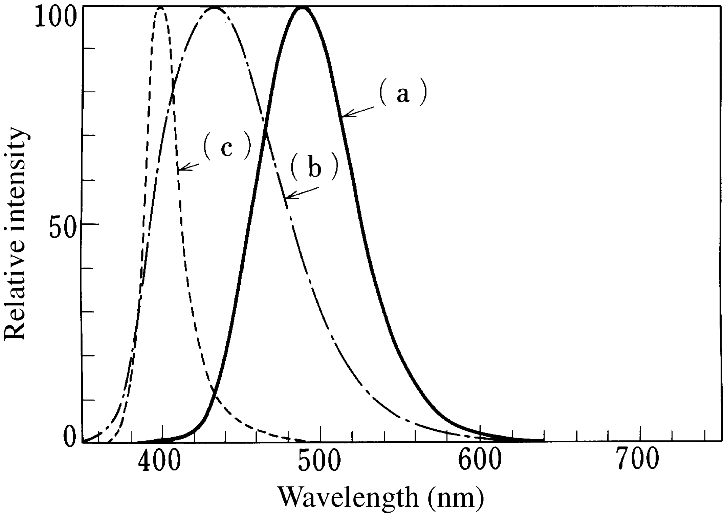

Figure 36 Emission spectra of (a) $Sr_2Si_3O_8{\cdot}2SrCl_2{:}Eu^{2+}$; (b) $Ba_3MgSi_2O_8{:}Eu^{2+}$; and (c) $(Sr,Ba)Al_2Si_2O_8{:}Eu^{2+}$. (From Kamiya, S. and Mizuno, H., unpublished results. With permission.)

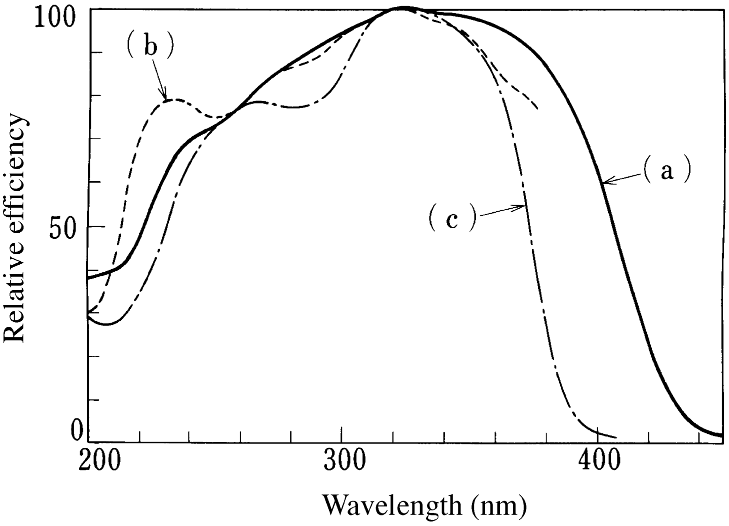

Figure 37 Excitation spectra of (a) $Sr_2Si_3O_8{\cdot}2SrCl_2{:}Eu^{2+}$; (b) $Ba_3MgSi_2O_8{:}Eu^{2+}$; and (c) $(Sr,Ba)Al_2Si_2O_8{:}Eu^{2+}$. (From Kamiya, S. and Mizuno, H., unpublished results. With permission.)

symmetry, while the Ba-feldspar ($BaAl_2Si_2O_8$) has monoclinic symmetry. The Sr-Ba feldspar forms a solid solution up to Sr contents of 40 mol%.[48,49]

Emission characteristics. The Sr-feldspar phosphor activated by Eu^{2+} shows the strongest emission when 40 mol% Sr^{2+} is replaced by Ba^{2+}. The emission and excitation spectra of $Sr_{0.6}Ba_{0.4}Al_2Si_2O_8{:}Eu^{2+}$ are shown in Figure 36(c) and 37(c), respectively.

Preparation. Starting materials—$SrCO_3$, $BaCO_3$, α-Al_2O_3, and Eu_2O_3—are mixed in the mole ratio $0.6SrO{:}0.4BaO{:}Al_2O_3{:}2SiO_2{:}0.01Eu_2O_3$ with 10 weight% NH_4Cl. The mixture is fired at temperatures of 1150 to 1400°C in a slightly reducing atmosphere, preferably a mixture of 5% hydrogen in nitrogen by volume.

Use. The $Sr_{0.6}Ba_{0.4}Al_2Si_2O_8{:}Eu^{2+}$ phosphor can be used in diazo photocopying lamps.

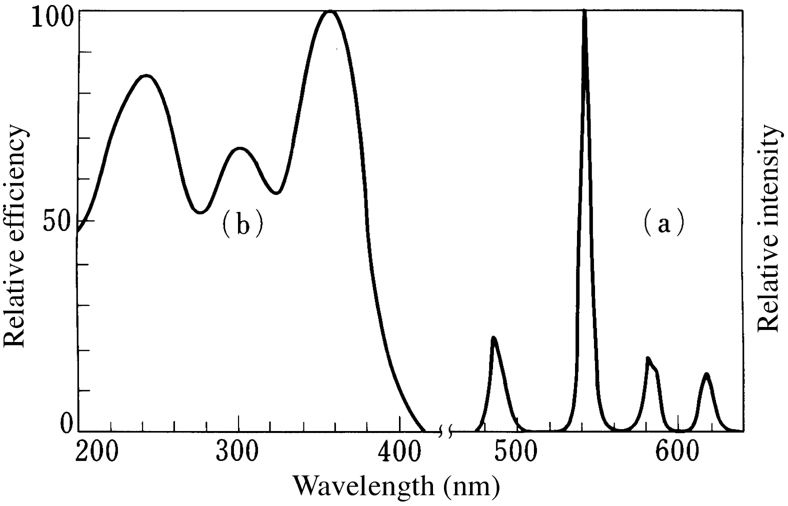

Figure 38 Emission and excitation spectra of Y_2SiO_5:Ce^{3+},Tb^{3+}. a = emission; b = excitation (From Kamiya, S. and Mizuno, H., unpublished results. With permission.)

Y_2SiO_5:Ce^{3+},Tb^{3+}

Crystal structure. The Y_2SiO_5 phosphor has monoclinic symmetry.[50]

Emission characteristics. The Y_2SiO_5:Ce^{3+},Tb^{3+} phosphor has a narrow green emission band, as shown in Figure 38(a). The fluorescence of this phosphor is attributed to the Tb^{3+} $^5D_4 \rightarrow {}^7F_3$ transition. The excitation spectrum of the phosphor shown in Figure 38(b) is a composite of the Y_2SiO_5:Tb^{3+} and Y_2SiO_5:Ce^{3+} spectra and indicates that Ce^{3+} sensitizes Tb^{3+}.[51,52]

Temperature dependence. The temperature dependence of this phosphor depends strongly on the Ce^{3+} concentration. The quenching temperature becomes lower with increasing Ce^{3+} content.

Preparation. Y_2O_3 and very fine SiO_2 are mixed in the mole ratio 1:1 with 0.01 mole Tb_4O_7 and CeO_2. The mixture is fired at 1100 to 1400°C in a slightly reducing atmosphere for several hours.

Use. This phosphor can be used as the green component in three-band fluorescent lamps. However, the higher material cost of this phosphor compared to other Tb^{3+}-activated phosphors has precluded its widespread practical application. The phosphor is being employed in high-pressure mercury lamps for color correction purposes, since it can be efficiently excited by 365-nm UV radiation.

5.6.2.4 *Aluminate phosphors*

Aluminate phosphors were first introduced to three-band fluorescent lamps by Verstegen et al.[53] in 1974. Popularization of these lamps for general lighting has made the aluminates the important lamp phosphors. Most of the aluminate phosphors are activated by rare-earth ions and require high-temperature firing for synthesis. Accordingly, their emission efficiency and stability are excellent and various aluminate phosphors are being extensively used, notwithstanding their high price. The excellent stability of these phosphors makes it possible to develop very high-loading fluorescent lamps such as compact fluorescent and high-loading photocopying lamps.

$BaMg_2Al_{16}O_{27}$:Eu^{2+}

Crystal structure. This phosphor has a crystal structure similar to hexagonal β-alumina, which is well known in the $Na_2O \cdot 11Al_2O_3$ compound.[54–56] The compound $BaMg_2Al_{16}O_{27}$[57]

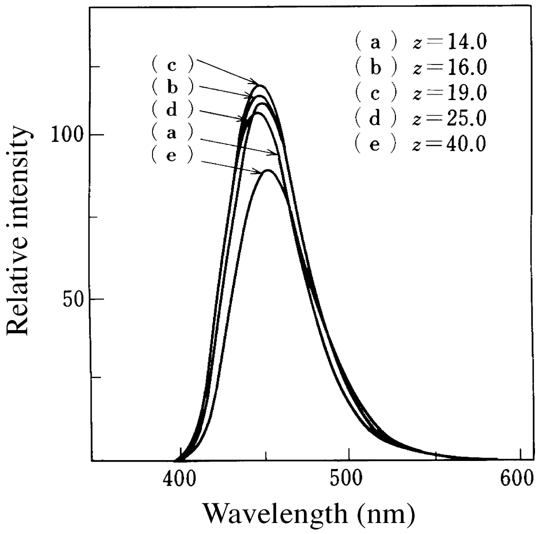

Figure 39 Emission spectra of $Ba_{0.07}Mg_{2.0}Al_zO_{3/2z+3}$:$Eu^{2+}_{0.13}$. (From Kamiya, S. and Mizuno, H., unpublished results. With permission.)

is a member of the β-alumina family. The matrix crystal is composed of the replacement of Na^+ by Ba^{2+} and of the partial replacement of Al^{3+} by Mg^{2+} in the $Na_2O{\cdot}11Al_2O_3$ crystal, thus attaining the electric charge compensation.[58] The Eu^{2+} activator is situated at the Ba^{2+} site.

Emission characteristics. This phosphor has a blue emission peak at ~450 nm, originating from a $4f^65d$ to $4f^7$ transition of the Eu^{2+} ion. Because the 5*d* electron is involved in the excitation process, the emission spectrum is strongly influenced by the crystal field strength. The crystal structure can be classified into five types according to the lattice site where the Ba^{2+} ion is located and the difference of the stacking of the spinel lattice and the Ba^{2+}-containing layers. The Ba^{2+} ion enters into different lattice sites depending on small differences in the matrix composition. As the Eu^{2+} activator substitutes into Ba^{2+} sites, its emission spectrum is affected by the matrix composition as well. When the phosphor composition is $Ba_{0.87}Mg_{2.0}Al_zO_{3/2z+3}$:$Eu_{0.13}{}^{2+}$, the variations of the emission and excitation spectra as the function of the z value are those shown in Figures 39 and 40, respectively. As seen in the figures, the emission peak shifts to longer wavelengths with increasing z value. These figures also illustrate that the *d* orbital splitting varies with the change of the crystal field. The replacement of Ba^{2+} (ionic radius = 1.33 Å) by either Sr^{2+} (ionic radius = 1.12 Å) or by Eu^{2+} (ionic radius = 1.13 Å) induces a change of the crystal field as well. With increases in either Sr^{2+} concentration or in the Eu^{2+}:Ba^{2+} mole ratio, the emission peak shifts continuously to longer wavelengths. The emission peak moves to 465 nm when all Ba^{2+} ions are replaced by Sr^{2+} [53,58] and to 475 nm when replaced by Eu^{2+}.[58] In the latter case, however, the emission intensity decreases due to concentration quenching. When the mole ratio of Eu^{2+}:Ba^{2+} becomes higher than 0.4, the luminescence is quenched rapidly. The thermal behavior of this phosphor is also influenced by the composition. The T_{50} value (the temperature at which the emission intensity falls to 50% of that at room temperature) is 610°C. The T_{50} value decreases when either the Eu^{2+} concentration or the Al_2O_3 ratio is increased. This fact indicates that the probability of a nonradiative transition process depends on the state of the matrix crystal field as well as the Eu^{2+} concentration. The quantum efficiency of this phosphor is very high. The measured value according to conventional methods appears to exceed 1.00.

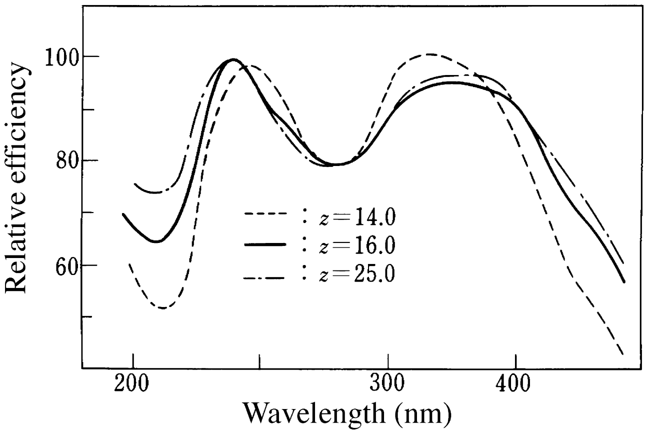

Figure 40 Excitation spectra of $Ba_{0.87}Mg_{2.0}Al_zO_{3/2z+3}:Eu^{2+}_{0.13}$. (From Kamiya, S. and Mizuno, H., unpublished results. With permission.)

Preparation. The compounds $BaCO_3$, $Mg_4(CO_3)_3OH{\cdot}3H_2O$, and Eu_2O_3 are commonly used as the starting materials. An appropriate amount of flux material is usually added. The mixture is fired at ~1200°C in a slightly reducing atmosphere (for example, 2% H_2/N_2) for several hours. After cooling in that atmosphere, the sintered cake is reduced to a powder by ordinary means. The sieved powder is fired again under the same conditions as the first firing. In the second firing, a wet gas flow is maintained to yield the most favorable results. AlF_2 and $BaCl_2$ are often used as fluxes. The amount of flux to be added influences the hardness of sintered cake and the particle size of the finished phosphor. The appropriate Eu^{2+} concentration is around 0.1 to 0.2 mole per 2 moles MgO.

Use. This phosphor is being used extensively for three-band lamps as the blue-emitting component. The high durability of this phosphor under intense UV irradiation allows this phosphor to be used in very high loading fluorescent lamps.

$BaMg_2Al_{16}O_{27}$:Eu^{2+},Mn^{2+}[53]

Crystal structure. This phosphor is obtained by partial replacement of Mg^{2+} in $BaMg_2Al_{11}O_{27}:Eu^{2+}$ by Mn^{2+}. The Mn^{2+} ion enters the Mg^{2+} site and is surrounded by oxygen atoms in a tetrahedral coordination.[60]

Emission characteristics. As is well known, the Mn^{2+} *d-d* transition is forbidden. In the β-alumina structure, its oscillator strength is as small as $\sim 10^{-7}$.[61] Therefore, the Mn^{2+} emission by direct excitation is not observable in this phosphor. However, nonradiative energy transfer from Eu^{2+} to Mn^{2+} results in an efficient green emission peaked at ~515 nm. In Figure 41, the emission spectra for different Mn^{2+} concentrations are shown. With increasing Mn^{2+} concentration, the Mn^{2+} emission intensifies, whereas the Eu^{2+} emission becomes weaker. The excitation spectra for the Mn^{2+} and for Eu^{2+} emissions are quite similar, as shown in Figure 42. These spectra prove that the Mn^{2+} emission originates from energy transfer from Eu^{2+} ions. The energy transfer mechanism is the dipole-quadrupole interaction according to the theory of Dexter.[61]

Preparation. Except that $MnCO_3$ is used as an additional component, the preparation method is identical with that of $BaMg_2Al_{16}O_{27}:Eu^{2+}$. The Mn^{2+} concentration can be chosen to yield the desirable emission spectrum as indicated in Figure 42.

Use. This phosphor can also be used for high-loading fluorescent lamps such as photocopying lamps.[62] The phosphor is occasionally employed for the purposes of color cor-

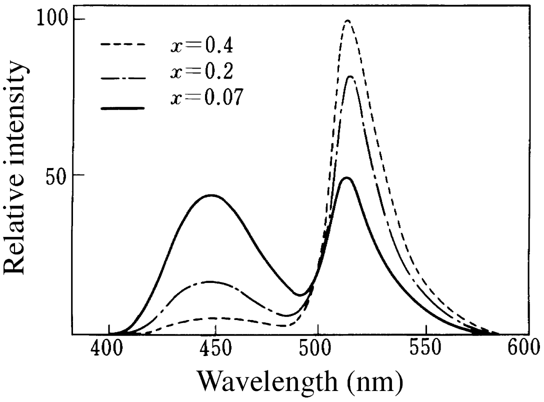

Figure 41 Emission spectra of $Ba_{0.8}Mg_{1.93}Al_{16}O_{27}$:$Eu^{2+}_{0.2}$,$Mn_x^{2+}$. (From Kamiya, S. and Mizuno, H., unpublished results. With permission.)

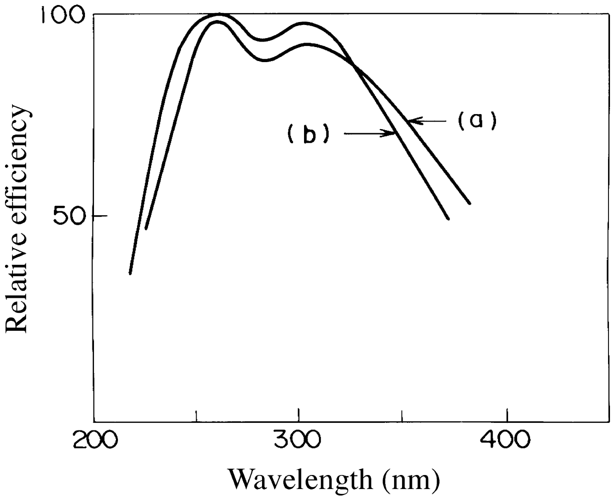

Figure 42 Excitation spectra of $Ba_{0.8}Mg_{1.93}Al_{16}O_{27}$:$Eu^{2+}_{0.2}$,$Mn^{2+}$: (a) excitation corresponding to Mn^{2+} emission; (b) excitation corresponding to Eu^{2+} emission. (From Kamiya, S. and Mizuno, H., unpublished results. With permission.)

rection. Thanks to its excellent temperature characteristics, this phosphor is also applicable to high-pressure mercury lamps.[63]

$CeMgAl_{11}O_{19}$:Ce^{3+},Tb^{3+}

Crystal structure. This phosphor has the same magnetoplumbite structure as the $PbFe_{12}O_{19}$ crystal. The matrix structure of this phosphor can be derived from full substitution of Pb^{2+} by Ce^{3+} and Fe^{3+} by Al^{3+} and Mg^{2+} in the $PbFe_{12}O_{19}$ structure.[60] The incorporation of Mg^{2+} is for charge compensation purposes. This phosphor has the hexagonal symmetry of β-alumina compounds. The crystal has a structure in which a crystal plane containing Ce^{3+}, Tb^{3+}, O^{2-}, and Al^{3+} ions is placed between every cubic spinel configuration.[58]

Emission characteristics. The emission spectrum is shown in Figure 43. The Tb^{3+} emission originates from $^5D_4$ to ^7F_j (where j = 3, 4, 5, 6) transition. The dominant emission is observed at 545 nm, corresponding to the $^5D_4$-$^7F_5$ transition. The fine structure observed in each emission band is attributed to perturbation by the crystal field. The excitation spectra

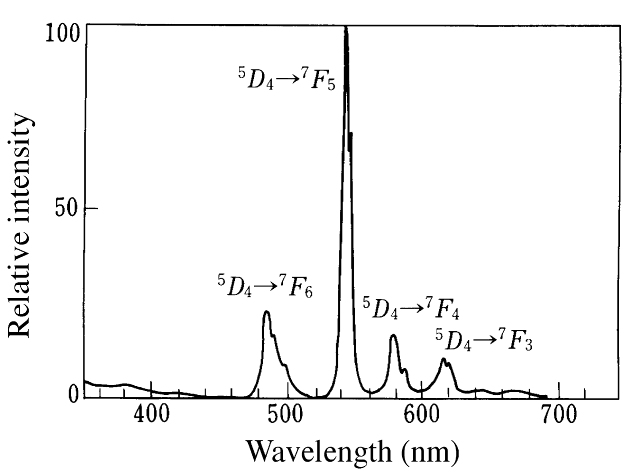

Figure 43 Emission spectrum of $CeMgAl_{11}O_{19}$:Ce^{3+},Tb^{3+}; excitation corresponding to Tb^{3+} emission. (From Kamiya, S. and Mizuno, H., unpublished results. With permission.)

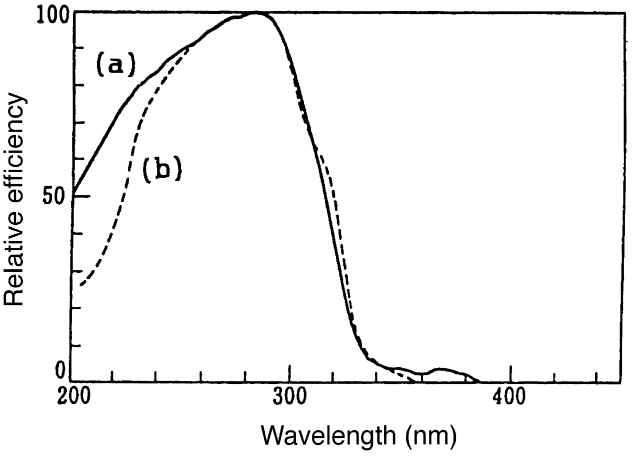

Figure 44 Excitation spectra of $CeMgAl_{11}O_{19}$:Ce^{3+},Tb^{3+}. (a) for Tb^{3+} emission ($^5D_4 \rightarrow ^7F_5$), (b) for Cl^{3+} emission. (From Kamiya, S. and Mizuno, H., unpublished results. With permission.)

corresponding to the Ce^{3+} emission observed at ~350 nm and the Tb^{3+} emission caused by the $^5D_4$-$^7F_5$ transition are shown in Figure 44. These spectra resemble each other, and this implies that the energy absorbed by the Ce^{3+} ion through the *f-d* transition is transferred efficiently to Tb^{3+}. The energy transfer mechanism is the dipole-quadrupole interaction between the ions.[64] The Ce^{3+} emission band disappears when the mole ratio Ce^{3+}:Tb^{3+} approaches 2.[65] The quantum efficiency of this phosphor has been improved from 0.80 reported at the time of development[58] to 0.97.[1] The luminous efficacy in 40-W fluorescent lamps reaches 120 lm·W^{-1}.

Preparation. A mixture of CeO_2, Tb_2O_3, α-Al_2O_3, $Mg_4(CO_3)_3OH \cdot 3H_2O$ and an appropriate amount of flux material is fired at 1200 to 1400°C in a slightly reducing atmosphere for several hours. A wet H_2/N_2 gas mixture is preferable for this purpose. After cool-down in this atmosphere, the sintered cake is reduced to a powder by ordinary means. The sieved powder is fired again under the same conditions as the first firing. Halide and borate compounds are often used as fluxes. The optimal molar ratio of Ce^{3+}:Tb^{3+} is approximately 0.67:0.33.

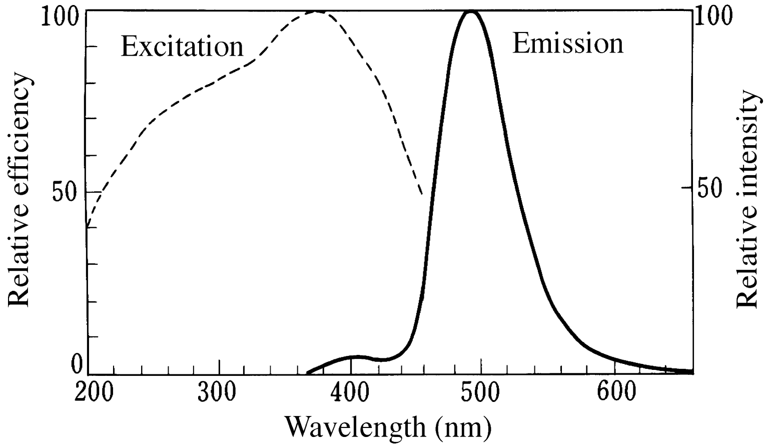

Figure 45 Emission and excitation spectra of $Sr_4Al_4O_{25}$:Eu^{2+}. (From Kamiya, S. and Mizuno, H., unpublished results. With permission.)

Use. This phosphor is used widely as the green-emitting component of three-band lamps. The high durability of this compound against intense UV radiation makes it possible to utilize this phosphor for very high-loading fluorescent lamps.[62]

$Sr_4Al_{14}O_{25}$:Eu^{2+} [66]

Crystal structure. This phosphor has a rhombic structure. The lattice constants are a = 4.9 Å, b = 24.8 Å, and c = 8.5 Å.

Emission characteristics. The emission and excitation spectra are shown in Figure 45. A blue-green main emission band peaked at 490 nm and a weak subband at 400 nm are observed. The excitation and emission are caused by the $4f^7$-$4f^65d$ direct transition of Eu^{2+}. The excitation spectrum extends to ~450 nm. The body color of the phosphor appears greenish-yellow. Other phosphors belonging to the SrO-Al_2O_3 system are $SrAl_2O_4$:Eu^{2+} and $SrAl_{12}O_{19}$:Eu^{2+}.[57] The emission peaks of these phosphors are located at 520 and 400 nm, respectively. Accordingly, strict control of manufacturing conditions is required to obtain a homogeneous $Sr_4Al_{14}O_{25}$:Eu^{2+} phosphor crystal.

Preparation. In addition to $SrCO_3$, α-Al_2O_3, and Eu_2O_3, an appropriate amount of flux material is required in the starting materials. The mixture of these compounds is fired at ~1200°C in a slightly reducing atmosphere (for example, 2% H_2/N_2) for several hours. After cool-down in such an atmosphere, the sintered cake is reduced to a powder by ordinary means. The sieved powder is fired again at 1300°C in a slightly reducing atmosphere, preferably a wet H_2/N_2 gas mixture, for several hours. Borate compounds give favorable results when used as fluxes. The optimal result is obtained when around 0.1 mol of Sr^{2+} is replaced by Eu^{2+} ions.

Use. This phosphor is utilized as the blue/green-emitting component of Class AA and AAA high color rendering fluorescent lamps. The addition of this phosphor to ordinary three-band lamps is useful for further improvement to their color rendering index.[68]

$LiAlO_2$:Fe^{3+} [69]

Crystal structure. According to ASTM data, $LiAlO_2$ has several different crystal structures. However, no definite report on the relationship between the Fe^{3+} emission and the crystal phase has been found.

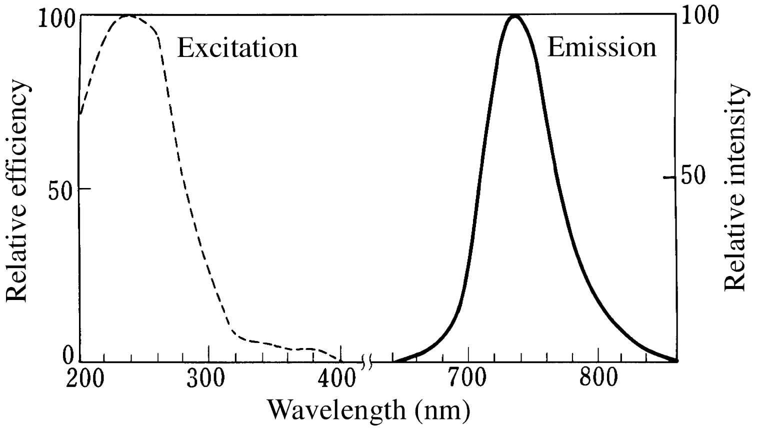

Figure 46 Emission and excitation spectra of $LiAlO_2:Fe^{3+}$. (From Kamiya, S. and Mizuno, H., unpublished results. With permission.)

Emission characteristics. The emission and excitation spectra are shown in Figure 46. This phosphor emits near-infrared radiation peaked at ~735 nm. The excitation and emission are ascribed to the *d-d* transitions of Fe^{3+}.

Preparation. Mixing of the raw materials such as $Al(OH)_3$, Li_2CO_3, and $Fe(NO_3)_3$ is usually carried out by a wet process. After drying, the mixture is placed in a crucible with lid and gradually heated to 900°C. The prefired material is pulverized and then fired at 1250°C in air for several hours. The sintered cake is milled to a powder and fired again under the same conditions as the preceding firing. The appropriate amount of Fe^{3+} is ~1 mol%.

Use. Besides $LiAlO_4:Fe^{3+}$, several other kinds of Fe^{3+}-activated aluminate phosphors have been reported.[70,71] These phosphors are exclusively utilized in special fluorescent lamps for plant growth and the selection of agricultural products by light irradiation.

5.6.2.5 Tungstate phosphors

Tungstate phosphors belong to a group of so-called self-activated phosphors. Pure crystals of tungstates and molybdates generate bright intrinsic luminescence under UV excitation. The luminescence originates from the ion complexes WO_4^{2-} and MoO_4^{2-}, respectively. (See Section II.3.4.) Typical examples of this phosphor type are $CaWO_4$ and $MgWO_4$. These phosphors have been in practical use for quite a long time.

$CaWO_4$ and $(Ca,Pb)WO_4$

Crystal structure. The $CaWO_4$ phosphor is isomorphous with the mineral schelite and has tetragonal symmetry. In this structure, the W^{6+} ion is situated at the center of a tetrahedron composed of four O^{2-} to form the WO_4^{2-} ion complex.

Emission characteristics. The emission peak of the $CaWO_4$ phosphor is located at 415 nm under 253.7-nm UV excitation, as shown in Figure 47(a). When a small amount of Pb^{2+} ion is incorporated to replace Ca^{2+} in this phosphor, the emission intensity increases and the emission peak shifts to longer wavelength. When 0.05 mole Ca^{2+} is replaced by Pb^{2+}, the emission intensity increases by 1.5 times and the peak shifts to 435 nm, as shown in Figure 47(b). The shift is attributed to the distortion of WO_4^{2-} tetrahedron brought about by the partial replacement of Ca^{2+} by Pb^{2+}. The incorporation of Pb^{2+} results in the broadening of excitation spectrum on the longer wavelength side, as shown in Figure 48. The emission lifetime of the phosphors can be as short as 10^{-5} to 10^{-7} s.

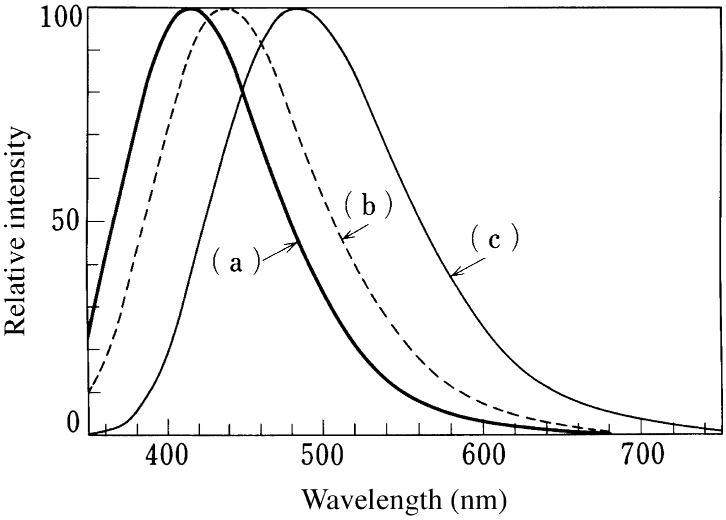

Figure 47 Emission spectra of (a) $CaWO_4$, (b) $(Ca,Pb)WO_4$, and (c) $MgWO_4$. (From Kamiya, S. and Mizuno, H., unpublished results. With permission.)

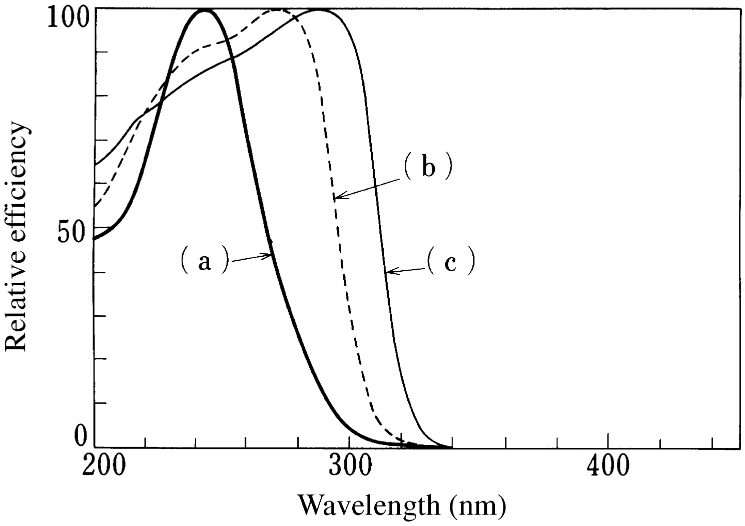

Figure 48 Excitation spectra of (a) $CaWO_4$, (b) $(Ca,Pb)WO_4$, and (c) $MgWO_4$. (From Kamiya, S. and Mizuno, H., unpublished results. With permission.)

Preparation. A mixture of WO_3 and $CaCO_3$ is fired in air at ~1100°C for several hours. Excess Ca in the material blend gives favorable results. For the preparation of the $(Ca,Pb)WO_4$ phosphor, 0.05 mole PbO/WO_4 is added to the mixture. The fired and further milled product is finally washed with 3% hydrochloric acid to remove the excess CaO remaining in the phosphor.

Use. Formerly, this phosphor was utilized in insect-catching lamps. At present, its application is limited to blue color lamps, especially in fluorescent signs.

$MgWO_4$

Crystal structure. The crystal structure of the $MgWO_4$ phosphor is isomorphous with the mineral wolframite (slightly distorted scheelite), which has monoclinic symmetry.

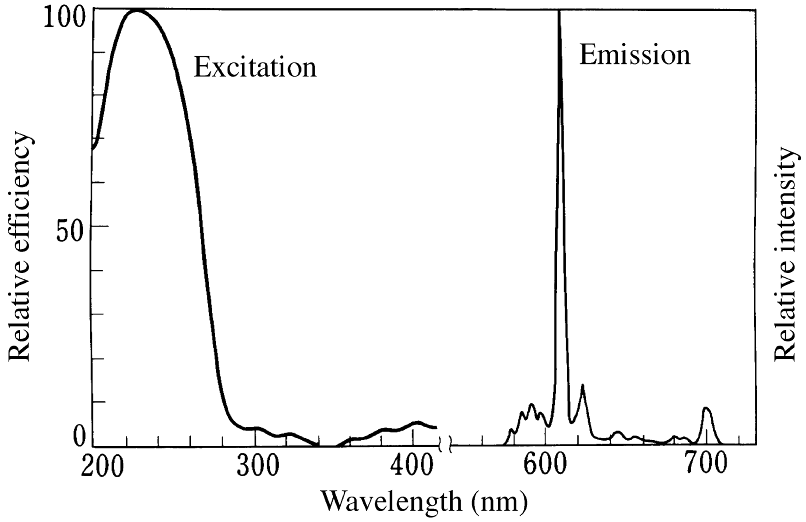

Figure 49 Emission and excitation spectra of Y_2O_3:Eu^{3+}. (From Kamiya, S. and Mizuno, H., unpublished results. With permission.)

Emission characteristics. The $MgWO_4$ phosphor has a broad, blue-white emission and its peak is located at 480 nm, as shown in Figure 47(c). The emission intensity of the phosphor decreases with the addition of almost any kind of impurity element. As shown in Figure 48(c), the excitation spectrum is even broader than that of the (Ca,Pb)WO_4 phosphor. The quantum efficacy of this phosphor is highest among traditional phosphors. Therefore, this phosphor has been adopted as the standard sample for quantum efficiency measurement. Though the quantum efficiency is nearly one, actual efficiency is reported to be around 0.85.[72]

Preparation. A mixture of WO_3 and MgO is fired in air at ~1150°C for several hours. Excess Mg in the material blend gives favorable results. The sintered cake is crushed and milled to a powder. Then the powder is fired again under the same conditions as the preceding firing. The excess MgO remaining in the phosphor is removed by washing with 3% hydrochloric acid.

Use. This phosphor was a very important phosphor as the blue-white color-emitting component for general lighting purposes in the earliest fluorescent lamps. At present, its main application is for blue-white color lamps, especially in fluorescent signs.

5.6.2.6 Other phosphors

Y_2O_3:Eu^{3+}

Crystal structure. The crystal structure of this phosphor is cubic and Eu^{3+} ions occupy the two Y^{3+} sites of C_2 and S_6 symmetry.

Emission characteristics. The excitation and emission spectra of this phosphor are shown in Figure 49. The very narrow emission band originates from the ${}^5D_0 \rightarrow {}^7F_2$ transition of Eu^{3+}.

Preparation. Although this phosphor can be prepared by simple dry mixing of Y_2O_3 and Eu_2O_3 with an appropriate flux followed by firing in air, an efficient phosphor is obtained by utilizing only $(Y,Eu)_2O_3$ that has been prepared by co-precipitation. This material is usually prepared by heat decomposition of the co-precipitated compound of Y and Eu oxalates. High-temperature firing with a small amount of flux results in a phosphor with high emission intensity as well as good durability. Firing is carried out at 1300 to 1400°C in air for several hours. The sintered cake is reduced to a powder and finally washed with

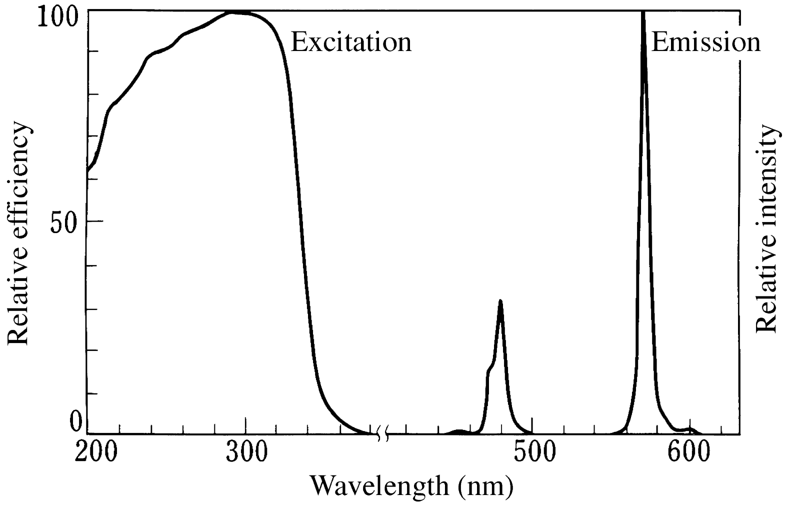

Figure 50 Emission and excitation spectra of YVO_4:Dy^{3+}. (From Kamiya, S. and Mizuno, H., unpublished results. With permission.)

water to remove the residual flux. Borates and halides are commonly employed as flux materials. The optimal Eu^{3+} concentration lies between 0.03 and 0.05 mole per mole Y_2O_3.

Use. This phosphor is the only existing red-emitting phosphor used in three-band fluorescent lamps.

YVO_4:Dy^{3+}

Crystal structure. The crystal structure of this phosphor has been identified as belonging to the tetragonal zircon type.[73]

Emission characteristics. The emission and excitation spectra are shown in Figure 50. Under excitation with UV radiation, an emission consisting of two narrow bands, at 570 and 480 nm, appears. As the Dy^{3+} ion does not absorb UV radiation of wavelength longer than 250 nm, the emission originates from the transfer of energy from the matrix. Pronounced concentration quenching due to Dy^{3+}-Dy^{3+} interaction is observed. The optimal Dy^{3+} concentration is as low as 0.5 mol%. This is nearly one tenth of the optimal Eu^{3+} concentration in the same matrix. The quantum efficiency is reported to be 0.65.[74]

Preparation. A mixture of Y_2O_3, V_2O_5, and Dy_2O_3 is fired at 1000 to 1300°C in air. For efficient performance, the complete removal of excess V_2O_5 by washing is required.

Use. This phosphor was once employed in fluorescent lamps of high luminous efficacy (but lower color rendering property).

$Cd_2B_2O_5$:Mn^{2+}

Crystal structure. This phosphor is reported to be isostructural with $Mg_2B_2O_5$.[75] More detailed studies of structure have not been reported.

Emission characteristics. The emission and excitation spectra are shown in Figure 51. Under short-wavelength UV excitation, a bright pink emission is generated. This phosphor is one of the typical host activation phosphors, but the energy absorption and transfer processes leading emission have not been fully investigated.

Preparation. $Cd(NO_3)_2 \cdot 4H_2O$, $(NH_4)_2B_4O_7$, and $MnCO_3$ are usually employed as the starting materials. The mixture is placed in an evaporating dish and gradually heated and mixed

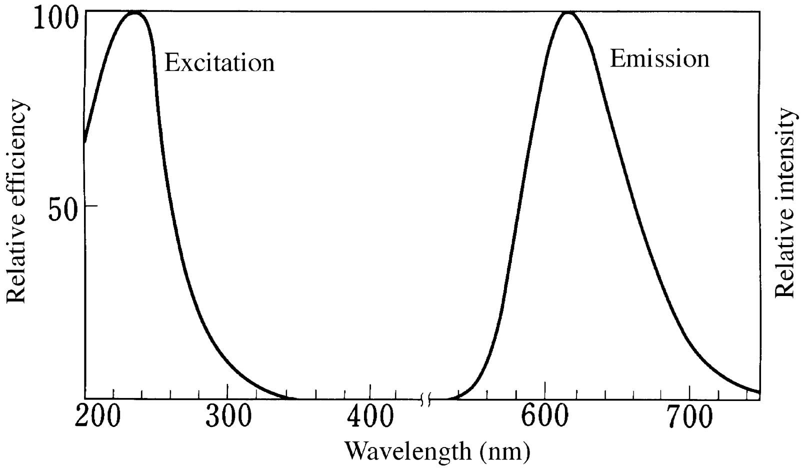

Figure 51 Emission and excitation spectra of $Cd_2B_2O_5$:Mn^{2+}. (From Kamiya, S. and Mizuno, H., unpublished results. With permission.)

by stirring. The heating is continued until all water and other gases generated by the heat decomposition are removed. The dry mixture prepared by this process is crushed and then milled. The powdered mixture is prefired at 650°C in air for several hours. The sintered material is pulverized to a fine powder and is then fired again at 800°C for several hours in a crucible with lid. The optimal results are obtained with a ratio of 1.5CdO:B_2O_3:0.04Mn.

Use. This phosphor was widely utilized for early fluorescent lamps as the red-emitting component. Due to the poor maintenance characteristics and environmental problems, this phosphor is no longer used.

$SrB_4O_7F:Eu^{2+}$ [76]

Crystal structure. The structure of this material is not known.

Emission characteristics. The emission and excitation spectra are shown in Figure 52. A narrow band emission is obtained under a wide range of UV-wavelength excitation.

Preparation. $SrCO_3$, H_3BO_3, and Eu_2O_3 are dissolved in nitric acid. After adjusting the solution temperature to 90°C, NH_4OH is gradually added; $SrB_6O_{10}\cdot 5H_2O$ is produced in this way. A mixture of this material and SrF_2 is prefired at 400°C in air for several hours. The prefired material is crushed and milled thoroughly. Final firing is made at 900 to 1000°C in a slightly reducing atmosphere for several hours. The appropriate Eu^{2+} concentration is ~2 mol%.

Use. This phosphor is used exclusively for black-light fluorescent lamps in place of Pb^{2+}-activated phosphors.

$GdMgB_5O_{10}:Ce^{3+},Tb^{3+}$ [77]

Crystal structure. This phosphor has monoclinic symmetry and is isostructural with $LaCoB_5O_{10}$, $NdCoB_5O_{10}$, and $SmCoB_5O_{10}$.

Emission characteristics. The emission and excitation spectra of this phosphor are shown in Figure 53. The excitation energy absorbed by Ce^{3+} is transferred to Tb^{3+}, resulting in a distinctive Tb^{3+} emission. It has been reported that a part of the energy is transferred through Gd^{3+}, i.e., through a path indicated as $Ce^{3+} \rightarrow (Gd^{3+})_n \rightarrow Tb^{3+}$. The luminous output of this material in a 40-W fluorescent lamp is higher than that of $CeMgAl_{11}O_{19}$:Tb^{3+}, and slightly lower than that of $LaPO_4$:Ce^{3+},Tb^{3+}.[78]

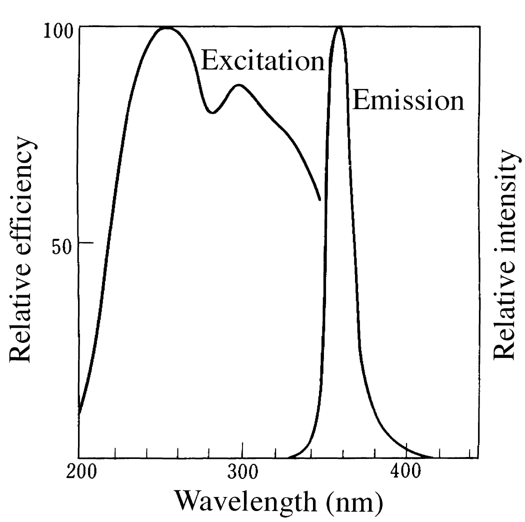

Figure 52 Emission and excitation spectra of $SrB_4O_7F:Eu^{2+}$. (From Kamiya, S. and Mizuno, H., unpublished results. With permission.)

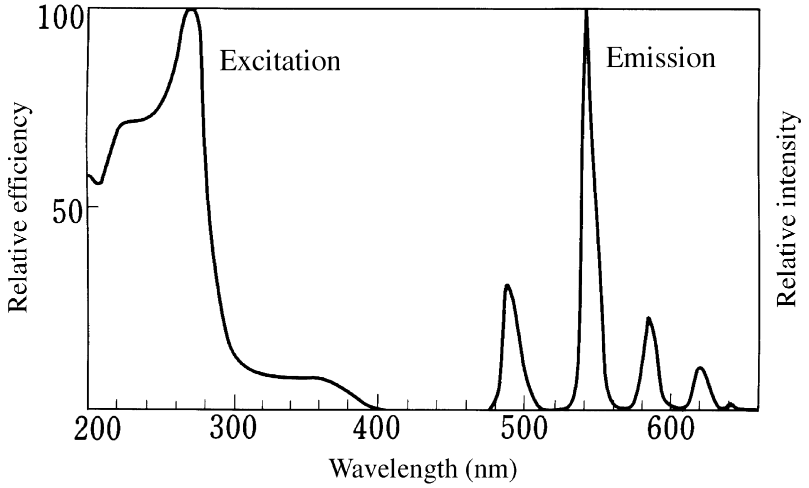

Figure 53 Emission and excitation spectra of $GdMgB_5O_{10}:Ce^{3+},Tb^{3+}$. (From Kamiya, S. and Mizuno, H., unpublished results. With permission.)

Preparation. A stoichiometric ratio of Gd_2O_3, MgO, CeO_2, Tb_2O_3 and an excess amount of H_3BO_3 are mixed. The optimal CeO_2 and Tb_2O_3 amounts are 0.05 and 0.1 mole, respectively. The fixture is fired at 1000 to 1050°C in a slightly reducing atmosphere for several hours. Repeated firing is effective in producing a homogeneous phosphor. Excess boric acid remaining in the phosphor must be removed by washing.

Use. This phosphor is exclusively utilized for three-band fluorescent lamps as the green-emitting component. The color rendering index of lamps employing this phosphor is slightly higher than that with $LaPO_4:Ce^{3+},Tb^{3+}$ and $CeMgAl_{11}O_{19}:Tb^{3+}$ phosphors.[78]

$GdMgB_5O_{10}:Ce^{3+},Mn^{2+}$ and $GdMgB_5O_{10}:Ce^{3+},Tb^{3+},Mn^{2+}$[77]

Crystal structure. The $GdMgB_5O_{10}$ matrix produces other practical phosphors by co-activation with Ce^{3+} and Mn^{2+} or with Ce^{3+}, Tb^{3+}, and Mn^{2+}. The crystal structures of these phosphors are identical to that of $GdMgB_5O_{10}:Ce^{3+},Tb^{3+}$.

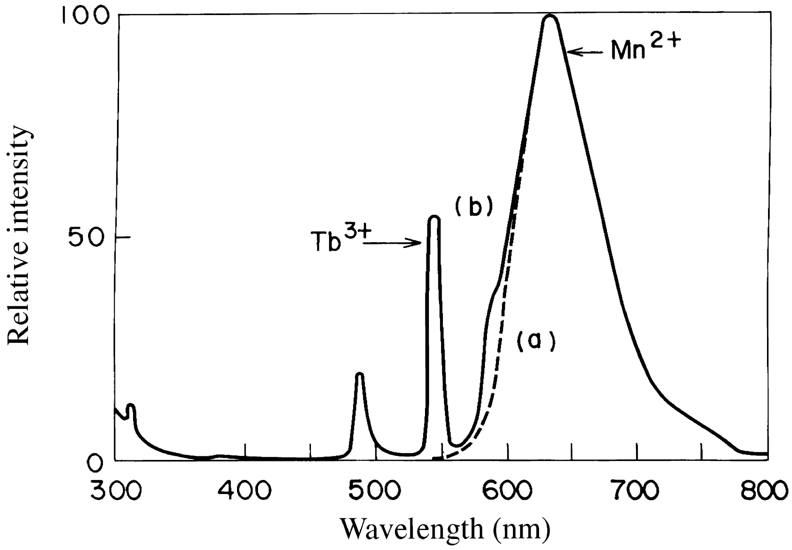

Figure 54 Emission spectra of (a) $GdMgB_5O_{10}:Ce^{3+},Mn^{2+}$ and (b) $GdMgB_5O_{10}:Ce^{3+},Tb^{3+},Mn^{2+}$. (From Kamiya, S. and Mizuno, H., *Proc. 6th Int. Symp. Science Technology of Light Sources*, Budapest, 1992, No. 2-I. With permission.)

Emission characteristics. The Ce^{3+} and Mn^{2+} co-activated $GdMgB_5O_{10}$ phosphor has an Mn^{2+} emission band in the orange-red region, the peak of which is located at 630 nm as shown in Figure 54. The Mn^{2+} emission in this material appears at the longest wavelength among all practical phosphors. By adding of Tb^{3+} to the Ce^{3+} and Mn^{2+} co-activated phosphor, a Tb^{3+} emission appears together with the Mn^{2+} emission. Curve (b) in Figure 54 is an example of this spectra. The intensity ratio of the emissions depends on the mole ratio of $Mn^{2+}:Tb^{3+}$. Although the co-existence of Tb^{3+} and Mn^{2+} emissions has been observed in other phosphors,[79] the emission spectrum of this phosphor is very attractive for practical application in fluorescent lamps.

Preparation. Except for the addition of $MnCO_3$, the preparation method for this compound is identical with that of $GdMgB_5O_{10}:Ce^{3+},Tb^{3+}$ mentioned above. The highest Mn^{2+} emission intensity is obtained when around 0.1 mole Mn^{2+} replaces Mg^{2+} ions.

Use. Combinations of the $GdMgB_5O_{10}:Ce^{3+},Tb^{3+},Mn^{2+}$ and the $Sr_4Al_{14}O_{25}:Eu^{2+}$ phosphors can result in high color rendering fluorescent lamps of Ra = 95 throughout the color temperature range of 3000 to 5000K.[80] The Ce^{3+} and Mn^{2+} co-activated phosphor is expected to play an important future role replacing Sn^{2+}-activated phosphors.

$MgGa_2O_4:Mn^{2+}$

Crystal structure. This phosphor has the spinel structure. It has been established that a part of the Mg occupies sites of octohedral instead of tetrahedral symmetry.[81]

Emission characteristics. As shown in Figure 55, this phosphor has a relatively narrow green emission band peaked at ~510 nm. The emission peak shifts to longer wavelengths with increasing Mn^{2+} levels. The highest emission intensity is obtained when the $Mn^{2+}:Mg^{2+}$ ratio is 0.01, and when the peak wavelength is at 510 nm. As is clear from the excitation spectrum in Figure 55, this phosphor is excited efficiently by short-wavelength UV radiation. The quantum efficiency under 254-nm excitation is 0.81, which is close to that of $Zn_2SiO_4:Mn^{2+}$. The durability and temperature characteristics of the phosphor are fairly good.

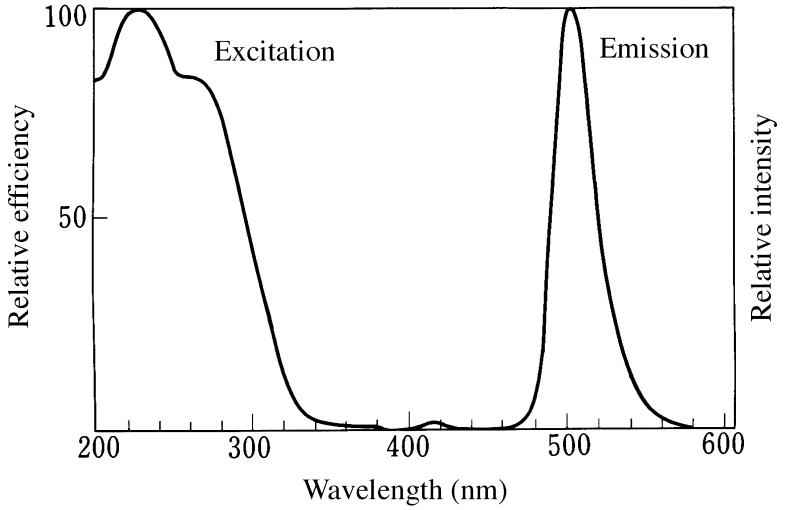

Figure 55 Emission and excitation spectra of $MgGa_2O_4:Mn^{2+}$. (From Kamiya, S. and Mizuno, H., unpublished results. With permission.)

Preparation. A mixture of raw materials in the ratio $MgO:Ga_2O_3:0.01MnCO_3$ is fired at 1400°C in air for at least 10 hours. The sintered cake is crushed and then milled thoroughly. The final firing is made at 1200°C in a slightly reducing atmosphere for several hours.[82,83]

Use. This phosphor was utilized exclusively in lamps for electrostatic photocopying equipment in place of $ZnSi_2O_4:Mn^{2+}$ phosphor. However, this application has mostly been taken over by Ce^{3+} and Tb^{3+} co-activated phosphors.

$6MgO{\cdot}As_2O_5:Mn^{4+}$

Crystal structure. Although the detailed crystal structure has not been identified, this phosphor has a different structure from $Mg_3(AsO_4)_2$, as determined by X-ray analysis.[84]

Emission characteristics. The tetravalent manganese ion has a $3d^3$ electron configuration, and the energy difference between excited and ground states does not depend on the crystal field strength. (See Section II.3.2.4.) Consequently, a narrow band luminescence appears, accompanied by fine structure due to phonons, as shown in Figure 56.[85] This phosphor has a broad excitation spectrum extending to visible wavelengths as shown in Figure 56.

Preparation. A mixture of MgO, H_3AsO_4, and $MnCO_3$ is prepared in the ratio $6MgO:As_2O_5:0.01MnO_2$. Firing is carried out at ~1100°C in air for several hours.

Use. This phosphor was particularly used in Class A and Class AA high color rendering fluorescent lamps as the deep red-emitting component. However, due to possible environmental contamination by poisonous arsenic compounds, the practical use of this phosphor has ceased.

$3.5MgO{\cdot}0.5MgF_2{\cdot}GeO_2:Mn^{4+}$

Crystal structure. This phosphor has orthorhombic symmetry and is isostructural with $Mg_{28}Ge_{10}O_{48}$.[86]

Emission characteristics. Among the $MgO\text{-}GeO_2$ compounds activated by Mn^{4+}, the most efficient emission is obtained when the Mg:Ge mole ratio is 4:1. Partial replacement of MgO by MgF_2 is effective in improving the high-temperature characteristics.[87] The emission

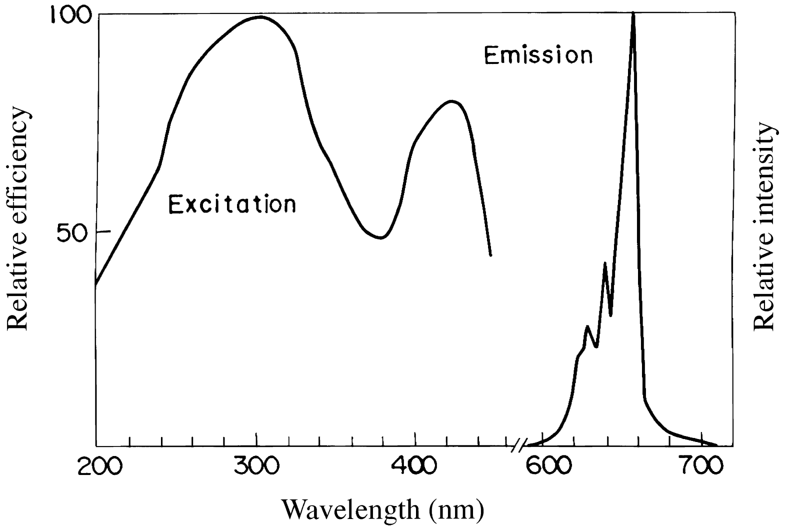

Figure 56 Emission and excitation spectra of 6MgO·As_2O_5:Mn^{4+}. (From Kamiya, S. and Mizuno, H., unpublished results. With permission.)

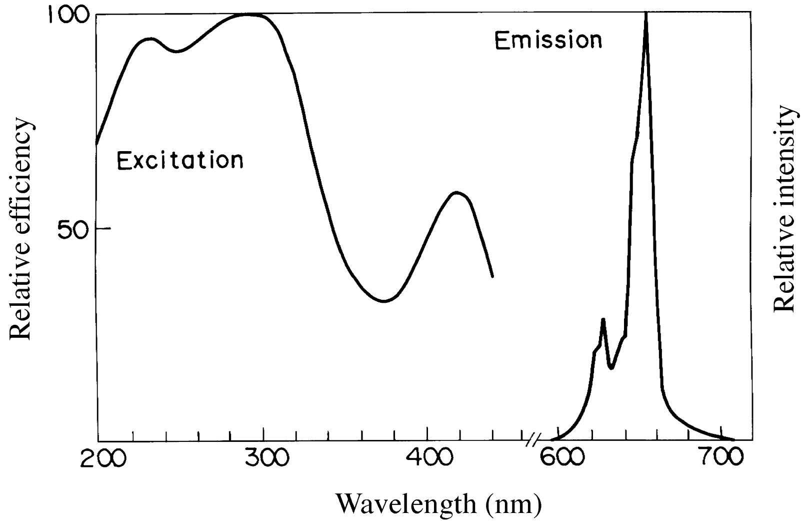

Figure 57 Emission and excitation spectra of 3.5MgO·0.5MgF_2·GeO_2:Mn^{4+}. (From Kamiya, S. and Mizuno, H., unpublished results. With permission.)

and excitation spectra are shown in Figure 57. and are quite similar to those of the 6MgO·As_2O_5:Mn^{4+} phosphor.

Preparation. A mixture of MgO, MgF_2, GeO_2, and $MnCO_3$ in the ratio 3.5MgO:0.5MgF_2:GeO_2:0.01MnO_2 is prefired at ~1000°C in air for several hours. The prefired product is crushed and then milled thoroughly before the final firing, which is made at 1200°C in air for more than 10 hours.

Use. This phosphor is the only available deep red-emitting phosphor and was indispensable in making Class AAA high color rendering fluorescent lamps. This phosphor was also exclusively utilized for color correction purposes of the high-pressure mercury lamps. However, both applications have been taken over by rare-earth activated phosphors. The phosphor is currently being used only for lamps with special application.

References

1. Narita, K., *J. Illum. Eng. Japan.*, 69, 65, 1985 (in Japanese).
2. Apple, E.F. and Ishler, W.E., Effect of cooling rate on calcium halophosphate phosphors, in *Proc. Int. Conf. Luminescence of Organic and Inorganic Materials*, New York, 1962, 576.
3. Robbins, D., in *The Electrochemical Society Spring Meeting Abstracts*, Los Angeles, 1962, 31.
4. Ropp, R.C., *J. Electrochem. Soc.*, 110, 113, 1963.
5. Kamiya, S. and Masuda, M., *Denki Kagaku*, 32, 679, 1964 (in Japanese).
6. Butler, K.H., Halophosphate phosphors, in *Fluorescent Lamp Phosphors*, The Pensylvania State University Press, Penn. State, 1980, 219.
7. Singleton, J.H. and Suchow, L., *J. Electrochem. Soc.*, 110, 36, 1963.
8. Apple, E.F., *J. Electrochem. Soc.*, 110, 374, 1963.
9. Kamiya, S. and Shibata, H., *Denki Kagaku*, 35, 718, (in Japanese).
10. Ouweltijes, J.L. and Wanmaker, W.L., *J. Electrochem. Soc.*, 103, 160, 1956.
11. Ouweltijes, J.L., *Electrizitats Verwertung*, 11-12, 1958.
12. Martyny, W.C., U.S. Patent 3,047,512, 1962.
13. ter Vrugt, J.W., Manders, L.W.J., and Wanmaker, W.L., *Light. Res. Tech.*, 7, 23, 1975.
14. Taya, A., Narita, K., Akiyama, Y., Asada, M., and Shinra, K., *Tech. Digest, Phosphor Res. Soc. 192nd Meeting*, 1982 (in Japanese).
15. Nakamoto, M., Nishimura, T., Kohmoto, K., and Ebara, H., in *Proc. IES Annual Conference*, Atlanta, 1982, No. 15.
16. Palilla, F.C. and O'Reilly, B.E., *J. Electrochem. Soc.*, 115, 160, 1968.
17. Ropp, R.C. and Mooney, R.W., *J. Electrochem. Soc.*, 115, 160, 1960.
18. Ranby, P.W., Mash, D.H., and Henderson, S.T., *Br. J. Appl. Phys.*, Suppl. 4, S18, 1955.
19. Mckeag, A.H. and Steward, E.G., *Br. J. Appl. Phys.*, Suppl. 4, S16, 1955.
20. Henderson, S.T. and Ranby, P.W., *J. Electrochem. Soc.*, 98, 479, 1951.
21. Koelmans, H. and Cox, A.P.M., *J. Electrochem. Soc.*, 104,442, 1957.
22. Sarver, J.F., Hoffman, M.V., and Hummel, F.A., *J. Electrochem. Soc.*, 108, 1103, 1961.
23. Froelich, H.C., *J. Electrochem. Soc.*, 92, 241, 1947.
24. Nagy, R., Wollentin, K.W., and Lui, C.K., *J. Electrochem. Soc.*, 97, 29, 1950.
25. Wanmaker, W.L. and ter Vrugt, J.W., *Philips Res. Rept.*, 22, 355, 1967.
26. Hoffman, M.V., *J. Electrochem. Soc.*, 115, 560, 1968.
27. Lagos, C.C., *J. Electrochem. Soc.*, 117, 1189, 1970.
28. Looney, J.R. and Brown, J.J., Jr., *J. Electrochem. Soc.*, 118, 470, 1971.
29. Ohta, J., Yamazaki, K., and Ohtani, M., *Mitsubishi Denki Giho*, 44, 1442, 1970 (in Japanese).
30. Murakami, S., Anzai, Y., Itoh, H., Doi, S., and Awazu, K., *Mitsubishi Denki Giho*, 52, 701, 1978 (in Japanese).
31. Nakajima, S., Ichinomiya, K., Okada, K., Tsuchikura, K., and Kashiwagi, M., *Tech. Digest, Phosphor Res. Soc. 186th Meeting*, 1981 (in Japanese).
32. Terajima, K., Kimura, Y., Sakakibara, Y., and Nira, H., *Tech. Digest, Phosphor Res. Soc. 186th Meeting*, 1981 (in Japanese).
33. Boucet, J.C. and Fong, F.K., *J. Chem. Phys.*, 60, 34, 1974.
34. Ropp, R.C., *J. Electrochem. Soc.*, 115, 531, 1968.
35. Hoffman, M.V., *J. Electrochem. Soc.*, 118, 1508, 1971.
36. Ichinomiya, K., Nakajima, S., Sumoto, H., and Arai, K., *Tech. Digest, Phosphor Res. Soc. 233th Meeting*, 1990 (in Japanese).
37. Harrison, D.E., and Hoffman, M.V., *J. Electrochem. Soc.*, 106, 800, 1959.
38. Froelich, H.C., *J. (and Trans.) Electrochem. Soc.*, 93, 101, 1948.
39. Merril, J.B. and Shulman, J.H., *J. Opt. Soc. Am.*, 38, 471, 1948.
40. Klasens, H.A., Hoekstra, A.H., and Cox, A.P.M., *J. Electrochem. Soc.*, 104, 93, 1949.
41. Clapp, R.H. and Ginther, R.J., *J. Opt. Soc. Am.*, 37, 355, 1947.
42. Butler, K.H., *Trans. Electrochem. Soc.*, 91, 265, 1947.
43. Leete, C.R.J. and Mckeag, A.H., British Patent, 1,087,655, 1967.
44. Burrus, H.L. and Nicholson, K.P., *J. Luminesc.*, 3, 467, 1971.
45. Butement, F.D.S., *Trans. Faraday Soc.*, 44, 617, 1948.

46. Blasse, G., Wanmaker, W.L., ter Vrugt, J.W., and Bril, A., *Philips Res. Rept.*, 23, 189, 1968.
47. Barry, T.L., *J. Electrochem. Soc.*, 115, 733, 1968.
48. Laud, K.R., Gibbons, E.F., Tien, T.Y., and Stadler, H.L., *J. Electrochem. Soc.*, 118, 918, 1971.
49. Isaacs, T.J., *J. Electrochem. Soc.*, 118, 1009, 1971.
50. Peters, T.E., *J. Electrochem. Soc.*, 116, 986, 1969.
51. Watanabe, M., Terajima, K., Kimura, Y., and Nishimura, T., *The Electrochemical Society, Spring Meeting Abstracts*, Boston, 1979, Abstract No. 225.
52. Watanabe, M., Nishimura, T., Kohmoto, K., Shimizu, K., and Narita, K., *Tech. Digest, Phosphor Res. Soc. 167th Meeting*, 1977 (in Japanese).
53. Verstegen, J.M.P.J., Radielovic, D., and Vrenken, L.E., *J. Electrochem. Soc.*, 121, 1627, 1974.
54. Braun, P.B., *Philips Res. Rept.*, 12, 491, 1957.
55. Blasse, G. and Bril, A., *Philips Res. Rept.*, 22, 481, 1967.
56. Matsui, Y., *J. Crystal Soc. Japan*, 24, 165, 1982 (in Japanese).
57. Verstegen, J.M.P.J., *J. Electrochem. Soc.*, 121, 1623, 1974.
58. Stevels, A.L.N. and Schrama de Pauw, A.D.M., *J. Electrochem. Soc.*, 123, 691, 1976.
59. Kamiya, S. and Shibata, H., *Natl. Tech. Rept.*, 27, 339, 1981 (in Japanese).
60. Sommerdijk, J.L. and Stevels, A.L.N., *Philips Tech. Rev.*, 37, 221, 1977.
61. Stevels, A.L.N. and Verstegen, J.M.P.J., *J. Luminesc.*, 14, 207, 1976.
62. Nohmi, K., Honmoh, M., Iwama, K., and Kamiya, S., *Natl. Tech. Rept.*, 27, 339, 1981 (in Japanese).
63. Iwama, K., Yamaguchi, M., and Watarai, Y., *J. Illum. Eng. Japan*, 60, 41, 1976 (in Japanese).
64. Verstegen, J.M.P.J., Sommerdijk, J.L., and Verriet, J.G., *J. Luminesc.*, 6, 425, 1973.
65. Sommerdijk, J.L. and Verstegen, J.M.P.J., *J. Luminesc.*, 9, 415, 1974.
66. van Kemendo, J.T.C. and Hoeka, G.P.F., *Electrochemical Society, Spring Meeting Abstracts*, San Francisco, 1983, Abstract No. 607.
67. Froelich, H.C., U.S. Patent 2,392,814, 1946.
68. Shibata. H. and Ikai, Y., *Natl. Tech. Rept.*, 33, 301, 1987 (in Japanese).
69. Lehmann, W. and Wachtel, A., U.S. Patent 3,857,054, 1974.
70. Kohmoto, K., *Proc. 1980 Annual Conf. IEI Jpn.*, No. 13 (in Japanese).
71. Mochel, V.D., *J. Electrochem. Soc.*, 113, 398, 1966.
72. Bril, A. and Hoekstra, W., *Philips Res. Rept.*, 16 356, 1961.
73. Brixner, L.H. and Abramson, E., *J. Electrochem. Soc.*, 112, 70, 1965.
74. Sommerdijk, J.L. and Bril, A., *J. Electrochem. Soc.*, 122,952, 1975.
75. Bloch, S., Burley, G., Perlof, A., and Mason, R.D., *J. Res. NBS*, 62, 95, 1959.
76. Chenot, C.F., U.S. Patent 3,431,215, 1969.
77. de Hair, J.Th.W. and van Kemenade, J.T.C., *Proc. Int. Symp. Science and Technology of Light Sources*, Toulouse, 1983, Abstract No. 54.
78. Kamiya, S., *Proc. Int. Symp. Science and Technology of Light Sources*, Budapest, 1992, Paper No. 2I.
79. Higashi, T., Tanaka, K., and Iwama, K., *Tech. Digest, Phosphor Res. Soc. 232th Meeting*, 1990 (in Japanese).
80. van Kemenade, J.T.C., Berns, E.G., and Peters, R.C., *CIE 20th Session*, Amsterdam, 1983, Paper No. D702.
81. Huber, M., *J. Chem. Phys.*, 57, 202, 1960.
82. Brown, J.J., *J. Electrochem. Soc.*, 114, 245, 1967.
83. Wanmaker, W.L., ter Vrugt, J.W., and de Bres, J.G.C.M., *Philips Res. Rept.*, 22, 304, 1967.
84. Kostiner, E. and Bless, P.W., *J. Electrochem. Soc.*, 119, 548, 1972.
85. Tranvnicek, M., Kröger, F.A., Botden, T.P.J., and Zalm, P., *Physica*, 18, 33, 1952.
86. Bless, P.W., von Dreele, R.B., Kostiner, E., and Hughes, R.E., *J. Solid State Chem.*, 4, 262, 1972.
87. Thornton, L., *J. Opt. Soc. Am.*, 40, 579, 1950.

chapter five — section seven

Phosphors for lamps

Katsuo Murakami

Contents

5.7 Phosphors for high-pressure mercury lamps 495
  5.7.1 YVO_4:Eu^{3+}, Y(P,V)O_4:Eu^{3+} 495
  5.7.2 $(Sr,Mg)_3(PO_4)_2$:Sn^{2+}..498
  5.7.3 3.5MgO·0.5MgF_2·GeO_2:Mn^{4+} 499
  5.7.4 Y_2SiO_5:Ce^{3+},Tb^{3+} 499
  5.7.5 Y_2O_3·nAl_2O_3:Tb^{3+} [26] 501
  5.7.6 $Y_3Al_5O_{12}$:Ce^{3+} (YAG:Ce^{3+}) 502
  5.7.7 $BaMg_2Al_{16}O_{27}$:Eu^{2+},Mn^{2+} 502
  5.7.8 $Sr_2Si_3O_8$·2$SrCl_2$:Eu^{2+}..503
  5.7.9 $Sr_{10}(PO_4)_6Cl_2$:Eu^{2+} [33] 503
  5.7.10 $(Sr,Mg)_3(PO_4)_2$:Cu^{+} [35] 505
References 505

5.7 Phosphors for high-pressure mercury lamps

5.7.1 YVO_4:Eu^{3+}, Y(P,V)O_4:Eu^{3+}

Crystal structure. Europium-activated YVO_4 and Y(P,V)O_4 phosphors have the tetragonal zircon ($ZrSiO_4$) structure, crystallizing in the D_{4h}^{19}-I4/amd space group.[1,2] The Eu^{3+} ion enters the Y^{3+} site. The lattice constant of unactivated YVO_4 are a_0 = 7.12 Å and c_0 = 6.29 Å.[3–5] If a part of the vanadate group is replaced by the phosphate group, then a phosphate-vanadate solid solution is formed and the lattice constants a_0 and c_0 decrease almost linearly as the content of the phosphate group increases.[3] There are many reports stating that the mixed crystal forms a xenotime (YPO_4) structure, similar to that of zircon.

Emission characteristics. Unactivated YVO_4 produces a broad blue emission with ultraviolet (UV) excitation.[6] By adding the activator Eu^{3+}, this blue emission is quenched and, as shown in Figure 58, a line spectrum emission in the red with a peak at 619 nm appears. The main emission lines near 610 to 620 nm are assigned to the Eu^{3+} electric dipole transitions from the $^5D_0$ to $^7F_2$ states, while the weaker emission near 593 nm is ascribed to magnetic dipole transitions from $^5D_0$ to $^7F_1$. The reason for the $^5D_0$ to $^7F_2$

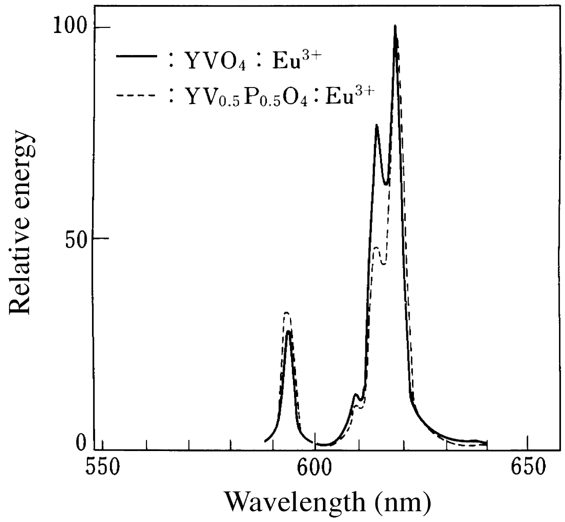

Figure 58 Emission spectra of YVO_4:Eu^{3+} and Y(P,V)O_4:Eu^{3+}. (Observed by the author.)

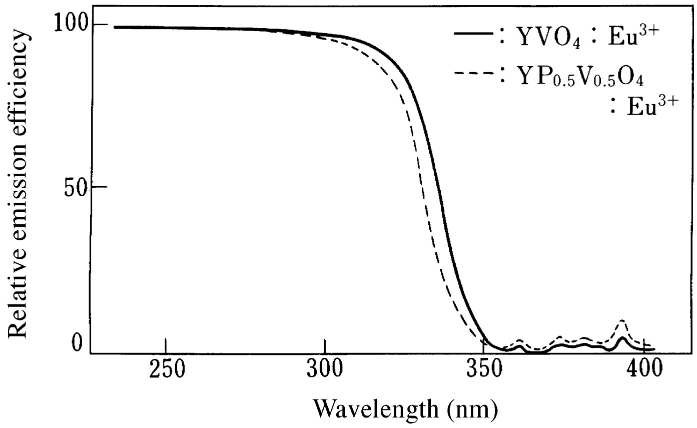

Figure 59 Excitation spectra of YVO_4:Eu^{3+} and Y(P,V)O_4:Eu^{3+}. (Observed by the author.)

transitions being dominant is that the host material has no inversion center. By introducing the phosphate group, the sub-emission near 593 nm increases.

Figure 59 shows the excitation spectra of the YVO_4:Eu^{3+} and Y(P,V)O_4:Eu^{3+}. The broad excitation band extending to 330 nm is attributed to the host crystal. The energy absorbed by the host is transferred to Eu^{3+} and produces the red emission. The mechanism of energy absorption by the host lattice is not the same in the long and short wavelength regions; these absorptions are related to charge-transfer processes involving V-O and Y-O bonds, respectively.[6]

When the vanadate group is replaced by the phosphate group, the excitation cut-off wavelength moves to shorter wavelength. Consequently, the brightness under 365 nm excitation drops as the phosphate content increases, while that under 254-nm excitation changes little, even when the amount of phosphate group reaches about 80%. If a very small amount of Bi^{3+} is added to YVO_4:Eu^{3+}, a new absorption band due to Bi^{3+} appears near 350 nm; the energy absorbed by Bi^{3+} is transferred to Eu^{3+} thereby enhancing the 365-nm excitation brightness.[9,10]

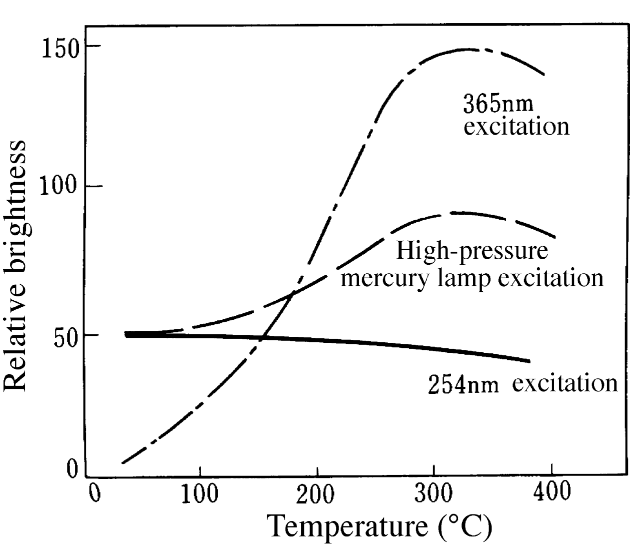

Figure 60 Temperature characteristics of YVO_4:Eu^{3+}. (Observed by the author.)

Temperature characteristics. The YVO_4:Eu and $Y(P,V)_4$:Eu phosphors have temperature characteristics suitable for high-pressure mercury lamps, and exhibit higher emission efficiencies at lamp operation temperatures over 300°C than at room temperature. Figure 60 shows the temperature characteristics of YVO_4:Eu^{3+}. The temperature dependence of its efficiency changes with excitation wavelength; that is, the emission intensity due to 365-nm excitation increases greatly as temperatures become higher, while the intensity due to 254-nm excitation depends little on temperature. The temperature characteristics improve as the amount of phosphate incorporation is increased.[7]

Depreciation characteristics. The luminous flux maintenance of the YVO_4:Eu^{3+} and $Y(P,V)O_4$:Eu^{3+} phosphors for a 400-W high-pressure mercury lamp is reported to be 80 and 85% after 8000 hr of operation, respectively.[11]

Preparation. Y_2O_3, Eu_2O_3, V_2O_5, and $(NH_4)_2HPO_4$ are generally used as raw materials; NH_4VO_3 has also been used as the vanadium source. Proper amounts of these materials are mixed, put into crucibles, and fired at about 1000 to 1150°C for several hours. H_3BO_3 is sometimes added as a flux. It is important to keep the mixing ratio of the raw materials close to stoichiometric. If the amount of Y_2O_3 + Eu_2O_3 is too large, the phosphor body color will be slightly yellow; and if it is too small, the phosphor turns brown and at the same time the brightness drops drastically.[12,13] Preferable Eu^{3+} concentrations are about 0.05 mol per 1 mol host material. These phosphors can also be prepared by a wet process; that is, YVO_4:Eu^{3+} and YPO_4:Eu^{3+} are precipitated separately, the precipitates are mixed with a flux, and then fired.[14] The vanadium to phosphorus ratio V:P of $Y(P,V)O_4$:Eu^{3+} is usually adjusted to about 1.

Use. Since it was demonstrated in 1966 that YVO_4:Eu^{3+} was a suitable phosphor for high-pressure mercury lamps, it quickly replaced $(Sr,Mg)_3(PO_4)_2$:Sn^{2+} and $3.5MgO\cdot 0.5MgF_2\cdot GeO_2$:$Mn^{2+}$, which had widely been used.[17–21] Later, $Y(P,V)O_4$:Eu^{3+}, having better temperature characteristics, was introduced and has become the most important red phosphor for high-pressure mercury lamps. This phosphor is widely used not only for fluorescent mercury lamps of the general, the improved color rendering, and the low color temperature types, etc., but also for metal halide lamps. The efficiency of the 400-W

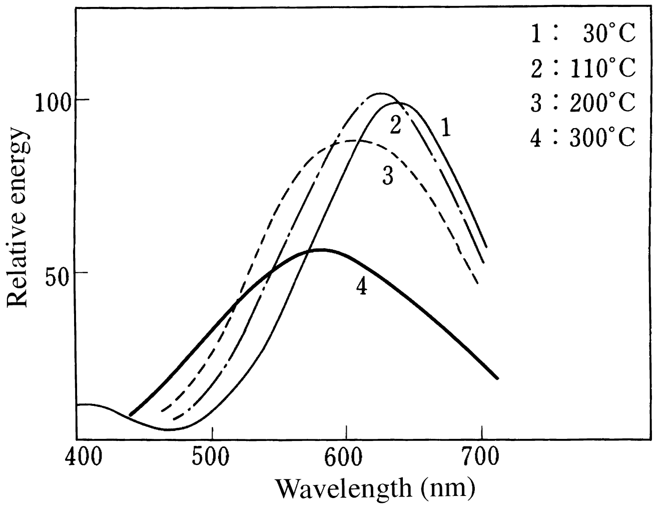

Figure 61 Emission spectra of $(Sr,Mg)_3(PO_4)_2$:$Sn^{2+}_{0.04}$. (Observed by the author.)

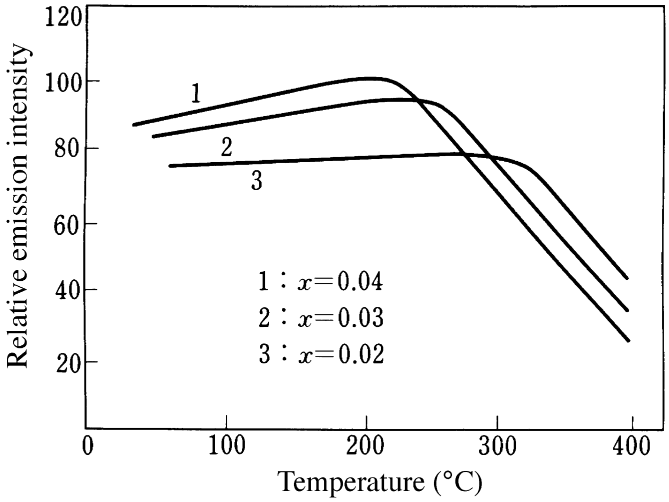

Figure 62 Temperature characteristics of $(Sr,Mg)_3(PO_4)_2$:Sn_x^{2+}. (Observed by the author.)

high-pressure mercury lamp using YVO_4:Eu is ca. 54 lm·W^{-1} and that using $Y(P,V)O_4$:Eu^{3+} ca. 55 lm W^{-1}.[11]

5.7.2 *$(Sr,Mg)_3(PO_4)_2$:Sn^{2+} (see 5.6.2)*

Emission characteristics. Figure 20 in 5.6.2 shows the emission spectrum of the tin-activated Sr, Mg orthophosphate phosphor at room temperature. Figure 61 shows changes of its emission spectrum vs. temperature. The peak moves to shorter wavelengths as the temperature increases.

Temperature characteristics. Figure 62 shows the temperature characteristics of the emission of the phosphor. Temperature quenching in this phosphor changes considerably with increasing concentration of the activator (Sn^{2+}).[22] The Sn^{2+} concentration in terms of the Sn:2P ratio is normally ca. 0.02.

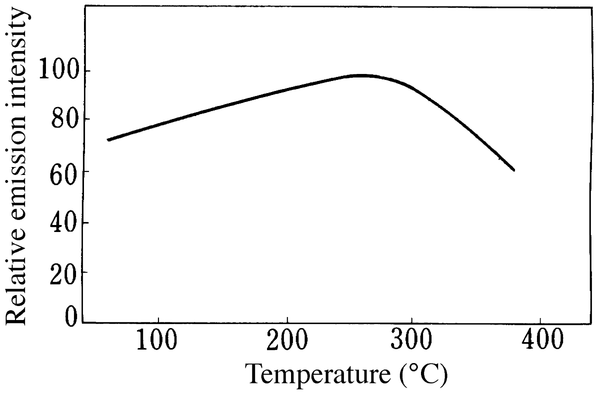

Figure 63 Temperature characteristics of $3.5MgO{\cdot}0.5MgF_2{\cdot}GeO_2{:}Mn^{4+}$ (365-nm excitation). (Observed by the author.)

Use. When only this phosphor is used in high-pressure mercury lamps, it gives off a silver-white light with high efficiency. Hence, it has been employed as a common phosphor for this purpose. Currently, however, it is used as a supplementary component to $YVO_4{:}Eu^{3+}$ or $Y(P,V)O_4{:}Eu^{3+}$, etc., in general or in improved color rendering type fluorescent mercury lamps.

5.7.3 $3.5MgO{\cdot}0.5MgF_2{\cdot}GeO_2{:}Mn^{4+}$ *(see 5.6.6)*

Temperature characteristics. Figure 63 shows the temperature characteristics of Mn^{4+}-activated fluorogermanate. Emission intensity reaches a maximum at about 260°C, with the emission due to Mn^{4+} in the deep red portion of the spectrum.

Use. The phosphor is used as a deep red emission phosphor for high-pressure mercury lamps. Since its body color is yellow, it absorbs blue mercury lines at 405 and 436 nm, and is used for low color temperature type fluorescent mercury lamps in combination with $YVO_4{:}Eu^{3+}$ or $Y(P,V)O_4{:}Eu^{3+}$. When this phosphor mixture is coated on a SiO_2 film, a low color temperature of 3000K (incandescent lamp color) is obtained.[23]

5.7.4 $Y_2SiO_5{:}Ce^{3+},Tb^{3+}$ *(see 5.6.3)*

Emission characteristics[24]*.* The main peak in the excitation spectrum of $Y_2SiO_5{:}Tb^{3+}$ containing no Ce^{3+} is located at 248 nm, and the phosphor produces a green emission due to the Tb^{3+} $^5D_4$-^7F_j transitions. However, this emission is barely excited by the 365-nm mercury line of the high-pressure mercury lamp. If Ce^{3+} is introduced as a sensitizer for Tb^{3+}, the excitation spectrum shows not only a peak near 304 nm, but also a stronger peak at 360 nm due to Ce^{3+}-Tb^{3+} transfer, thus producing a green emission.

The relation between Ce^{3+} concentration and the Tb^{3+} green emission intensity is shown in Figure 64. The curves show different dependencies for 254- and 365-nm excitation. The maximum emission intensity for 254-nm excitation is obtained when the ratio Ce:Me = 0.01, while for 365-nm excitation Ce:Me = 0.03. Here, Me stands for Y+Ce+Tb. The relation between Tb^{3+} concentration and emission intensity shows a similar pattern for both 254- and 365-nm excitation, having the maximum at about Tb:Me = 0.10 to 0.20. The lamp efficacy is 68 $lm{\cdot}W^{-1}$ for a 400-W lamp.

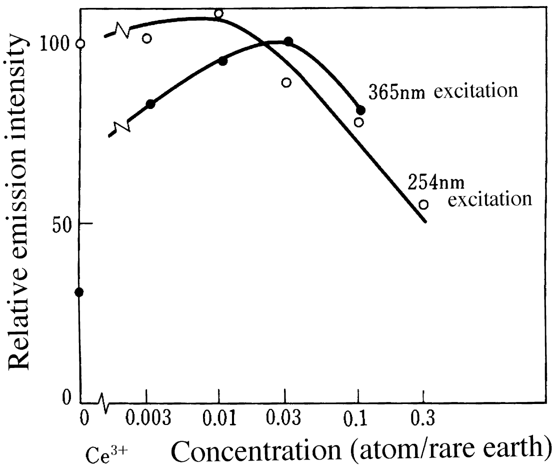

Figure 64 Emission intensity vs. Ce concentration of Y_2SiO_5:Ce^{3+},Tb^{3+}. (From Watanabe, M., Nishimura, T., Komoto, K., Shimizu, K., and Narita, K., *Tech. Digest, Phosphor Res. Soc. 167th Meeting*, 1977 (in Japanese). (With permission.)

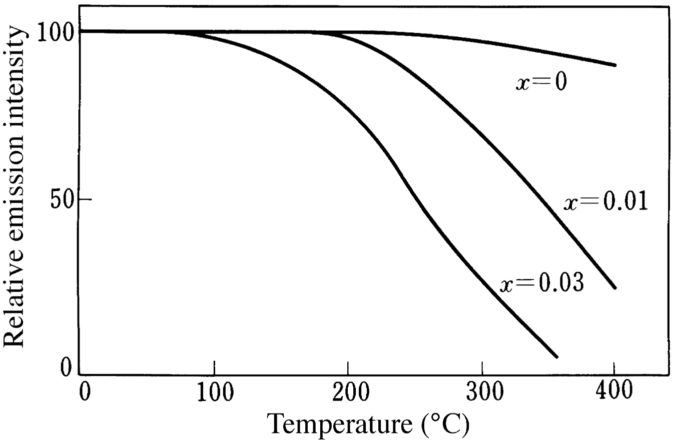

Figure 65 Temperature characteristics of Y_2SiO_5:Ce_x^{3+},Tb^{3+}. (From Watanabe, M., Nishimura, T., Komoto, K., Shimizu, K., and Narita, K., *Tech. Digest, Phosphor Res. Soc. 167th Meeting*, 1977 (in Japanese). (With permission.)

Temperature characteristics[24]. Although Y_2SiO_5:Tb^{3+} shows little drop of emission intensity at temperatures as high as 200 to 300°C, temperature quenching is apt to take place by the introduction of Ce^{3+}, as shown in Figure 65. For this reason, the Ce^{3+} concentration is adjusted to a value most suitable for the high-pressure mercury lamp operating temperature and 365-nm excitation intensity.

Preparation[24,25]. Y_2O_3, CeO_2, Tb_4O_7, and SiO_2 are mixed with fluxes such as KF, LiF, and LiBr, etc. The mixture is fired at 1000 to 1300°C in a slightly reducing atmosphere.

Use[24,25]. This phosphor is used for improved color rendering type mercury lamps mixed with YVO_4:Eu^{3+} and $Sr_{10}(PO_4)_6Cl_2$:Eu^{2+}.[24,25]

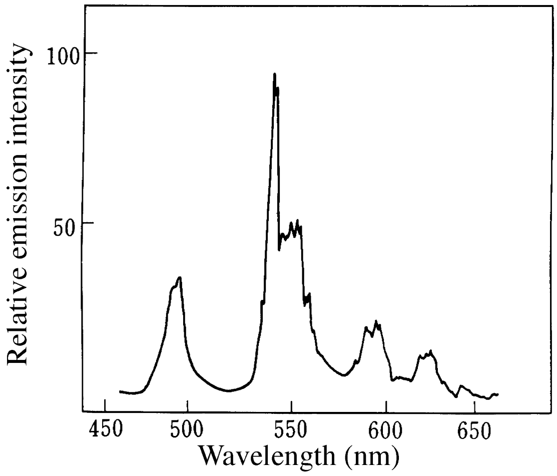

Figure 66 Emission spectrum of terbium-activated yttrium aluminates (365-nm excitation). (From Inoshima, H., Matsuoka, M., and Ide, S., *Tech. Digest, Phosphor Res. Soc. 162nd Meeting*, 1976 (in Japanese). (With permission.)

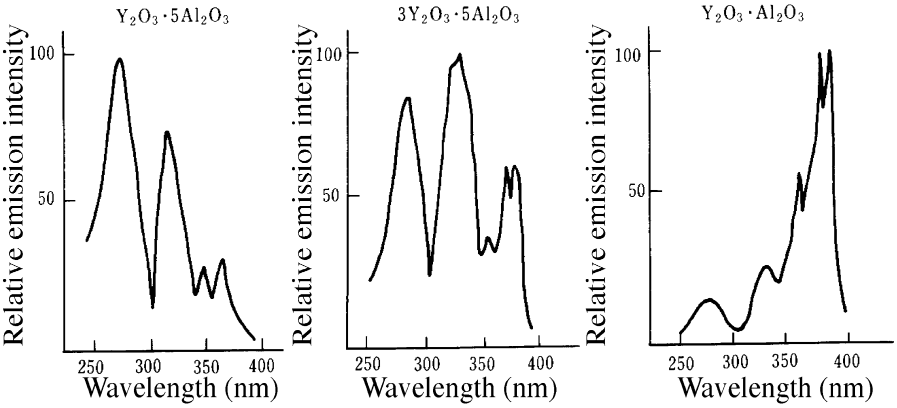

Figure 67 Excitation spectra of terbium-activated yttrium aluminates (room temperature). (From Inoshima, H., Matsuoka, M., and Ide, S., *Tech. Digest, Phosphor Res. Soc. 162nd Meeting*, 1976 (in Japanese). (With permission.)

5.7.5 $Y_2O_3{\cdot}nAl_2O_3{:}Tb^{3+}$ [26]

Emission characteristics. Figure 66 shows the emission spectrum of $Y_2O_3{\cdot}nAl_2O_3{:}Tb^{3+}$. Tb^{3+} emission lines with peaks at near 490, 545, 595, and 620 nm are observed. The emission color is yellow-white. The excitation spectrum is shown in Figure 67. It changes depending on the Y:Al ratio, and its maximum peak moves to longer wavelengths as the Al concentration decreases. The lamp efficacy is 68 lm W^{-1} for a 400-W lamp.

Temperature characteristics. There is a small decrease in the emission intensity up to near 300°C. Excitation and emission characteristics at high temperatures are identical with those observed at room temperature.

Preparation. Y_2O_3, Al_2O_3, and Tb_4O_7 are mixed with a fluoride flux. The mixture is then fired in a slightly reducing atmosphere.

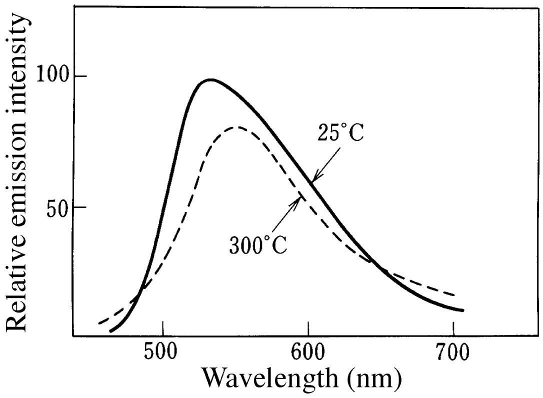

Figure 68 Emission spectra of $Y_3Al_5O_{12}$:Ce^{3+}. (From Hoffman, M.V., *Journal I.E.S.*, 6, 89, 1977. (With permission.)

Use. Mixing this phosphor with YVO_4:Eu^{3+} has no effect in improving the efficiency of high-pressure mercury lamps, but is has been reported that if this phosphor is coated on the YVO_4:Eu^{3+} layer to form a double coating, then the efficiency is improved by 8%.[26]

5.7.6 $Y_3Al_5O_{12}$:Ce^{3+} (YAG:Ce^{3+})

Emission characteristics. Figure 68 shows the emission spectrum of $Y_3Al_5O_{12}$:Ce^{3+}. There is an emission peak near 540 nm at room temperature, but it moves to longer wavelengths at higher temperatures. This phosphor is not excited by the 254 or 365-nm UV rays efficiently, but is by the 436-nm mercury line.

Preparation. Proper amounts of Y_2O_3, Al_2O_3, and CeO_2 are mixed and fired at about 1400 to 1500°C. The optimum Ce^{3+} concentration varies, depending on operational temperature conditions, i.e., at room temperature, it is 1 to 2 mol% and at 300°C it is about 0.5 mol%.[27]

Use. The phosphor has its absorption in the blue region, i.e., it absorbs and suppresses the 436-nm mercury line; thus, it can effectively lower the color temperature of high-pressure mercury lamps. It is consequently used in low color temperature lamps combined with Y(P,V)O_4:Eu^{3+}.

5.7.7 $BaMg_2Al_{16}O_{27}$:Eu^{2+},Mn^{2+} (see 5.6.4)

Temperature characteristics. Temperature quenching of the doubly activated $BaMg_2Al_{16}O_{27}$ is controlled by the Eu^{2+} ion, becoming more pronounced as the Eu^{3+} concentration increases. Figure 69 shows the temperature characteristics of the Eu^{2+} and Mn^{2+} emissions. Figure 70 shows the variation of the emission spectrum with temperature. There is a difference in the temperature quenching rates of the Eu^{2+} and Mn^{2+} emissions; thus, the emission color of the phosphor changes as the temperature rises.

Use. A mixture of this phosphor with Y(P,V)O_4:Eu^{3+} is used to improve color rendering type mercury lamps. When the Mn^{2+} concentration is adjusted to Mn:(Mg+Mn) = 0.07:2, the lamp emission color and skin color rendition become more preferable.[29,30]

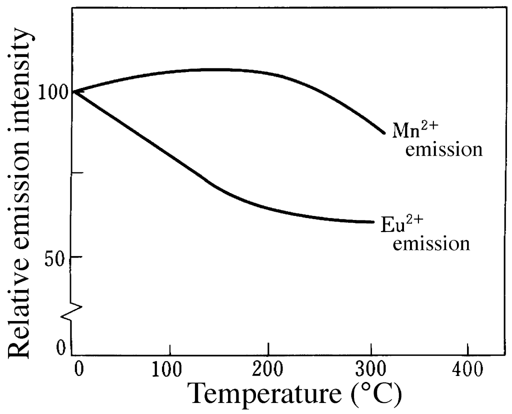

Figure 69 Temperature characteristics of $BaMg_2Al_{16}O_{27}$:Eu^{2+},Mn^{2+}. (From Iwama, K., Takakawa, M., Kobayashi, Y., *Tech. Digest, Phosphor Res. Soc. 159th Meeting*, 1974 (in Japanese). (With permission.)

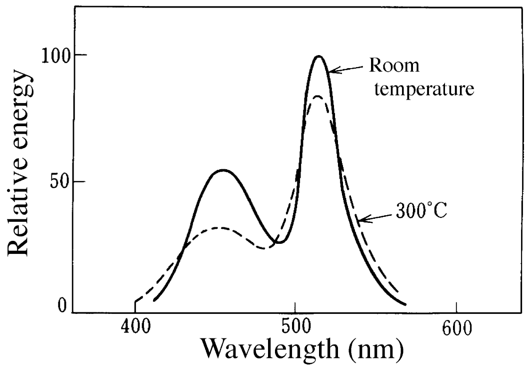

Figure 70 Emission spectra of $BaMg_2Al_{16}O_{27}$:Eu^{2+},Mn^{2+}. (From Iwama, K., Takakawa, M., Kobayashi, Y., *Tech. Digest, Phosphor Res. Soc. 159th Meeting*, 1974 (in Japanese). (With permission.)

5.7.8 $Sr_2Si_3O_8 \cdot 2SrCl_2$:$Eu^{2+}$ (see 5.6.3)

Temperature characteristics[31,32]. Figures 71 and 72 show the temperature dependence of the luminescence efficiency and the emission spectrum of $Sr_2Si_3O_8 \cdot 2SrCl_2$:$Eu^{2+}$, respectively. The emission peak at 250°C is observed at 480 nm, which is about 10 nm shorter in wavelength than that at room temperature. Lamp efficacy is 65 $lm \cdot W^{-1}$ for 400 W.

Use. This substance has good temperature characteristics. Because it emits in the wavelength region between the 436- and 546-nm mercury lines where there is no mercury emission, it is used together with such red-emitting phosphors as YVO_4:Eu^{3+} and $3.5MgO \cdot 0.5MgF_2 \cdot GeO_2$:$Mn^{4+}$, etc. for improved color rendering type fluorescent mercury lamps.[32]

5.7.9 $Sr_{10}(PO_4)_6Cl_2$:Eu^{2+} [33] (see 5.6.1)

Temperature characteristics. Figure 73 shows the temperature characteristics of Eu^{2+}-activated Sr-chlorapatite. At 200°C, this phosphor maintains about 50% of its emission intensity at room temperature. It has a broad excitation spectrum in the ultraviolet region, and both 254- and 365-nm mercury lines can be used to excite the phosphor.

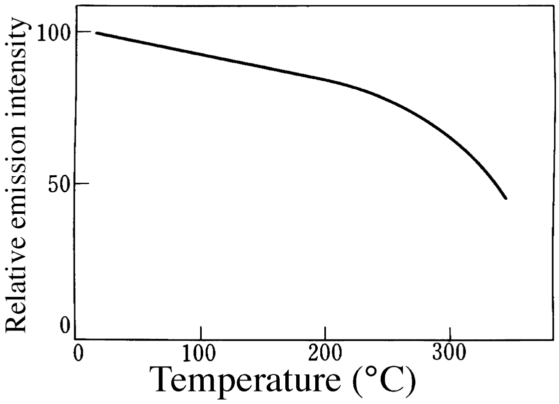

Figure 71 Temperature characteristics of $Sr_2Si_3O_8{\cdot}2SrCl_2:Eu^{2+}$. (Observed by the author.)

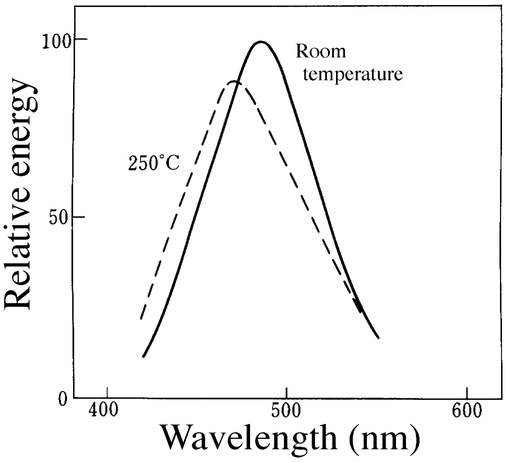

Figure 72 Emission spectra of $Sr_2Si_3O_8{\cdot}2SrCl_2:Eu^{2+}$. (Observed by the author.)

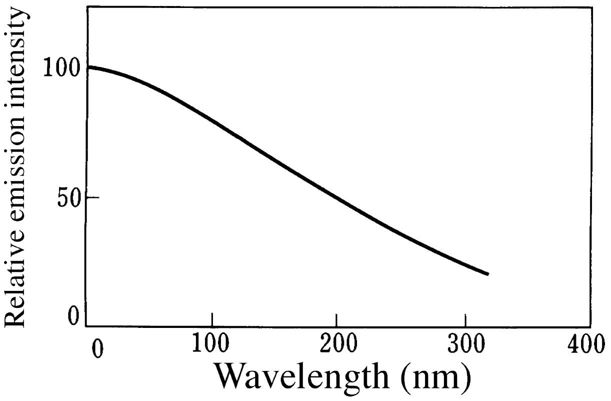

Figure 73 Temperature characteristics of $Sr_{10}(PO_4)_6Cl_2:Eu^{2+}$. (Observed by the author.)

Use. The phosphor is used for improved color rendering type fluorescent mercury lamps, but the color rendering indexes are not improved by a two-component mixture with $Y(P,V)O_4:Eu^{3+}$.[32,34] A three-component mixture that includes a green-emitting phosphor is effective for this purpose.

5.7.10 $(Sr,Mg)_3(PO_4)_2$:Cu^{+} [35]

Crystal structure. The copper-activated Sr,Mg-orthophosphate phosphor has the β-$Ca_3(PO_4)_2$ crystal structure. The $Sr_3(PO_4)_2$ phosphor containing no Mg is rhombohedral at room temperature, and produces only a faint deep blue emission when activated by Cu^{+}. If part of Sr is replaced by Al, Zn, Ca, Mg, Cd, etc., then it takes the β-$Ca_3(PO_4)_2$ form and produces a strong blue-green emission.

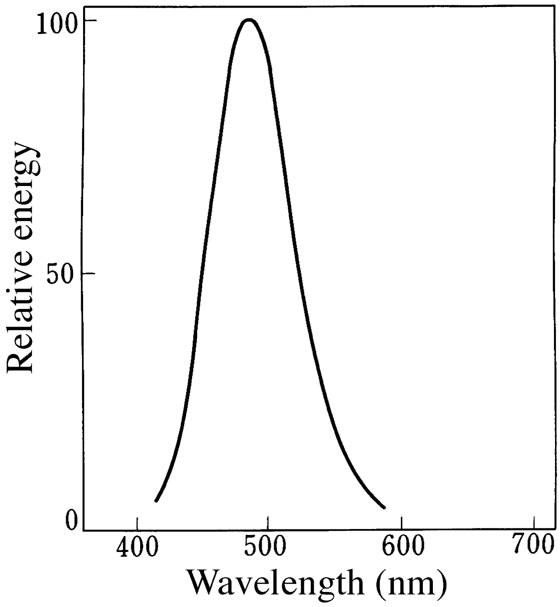

Figure 74 Emission spectra of $(Sr,Mg)_3$:$(PO_4)_2$:Cu^{+}. (Observed by the author.)

Emission characteristics. Figure 74 shows the emission spectrum of $(Sr,Mg)_3(PO_4)_2$:Cu^{+}. Its plaque brightness when excited with 254-nm radiation is higher than that of $CaWO_4$ or $Ca(PO_4)_6$·$Ca(F,Cl)_2$:Sb^{3+}.

Preparation. A mixture of $SrHPO_4$, $CuSO_4$, MgO, $SrCO_3$, Al_2O_3, etc. is fired at 1160 to 1240°C in a reducing atmosphere. A slight excess of phosphate gives better results, i.e., Me:P_2O_5 = 2.90 to 2.95.

Use. This phosphor has good temperature characteristics, and has been used for improved color rendering type fluorescent mercury lamps in conjunction with a red-emitting phosphor, but the Cu^{+} activator is easily oxidized by heating. Since better blue-green phosphors such as $Sr_2Si_3O_8$·$2SrCl_2$:Eu^{2+} and $BaMg_2Al_{16}O_{27}$:Eu^{2+},Mn^{2+} have become available, this phosphor is no longer in use.

References

1. Broch, E., *Phys. Chem.*, 20, 345, 1993.
2. Levine, A.K., Palilla, F.C., *Applied Physics*, 5, 118, 1964.
3. Aia Michael, A., *J. Electrochem. Soc.*, 114, 367, 1967.
4. Levine, E.M., *J. Am. Ceram. Soc.*, 50, 7, 1967.
5. Swanson, H.E., McMurdic, H.F., Marris, M.C., and Evans, E.H., *Standard X-ray diffraction powder patterns*, Natl. Bur. Std. (U.S.) Monograph No. 25, Section 5, 1967.

6. Datta, R.K., *Trans. Metallurg. Soc. AIME*, 239, 355, 1967.
7. Wanmaker, W.L., Brill, A., Ter Vrugt, J.W., and Broos, J., *Philips Res. Repts.*, 21, 270, 1966.
8. Hoshina, T., *Oyo Butsuri*, 49, 202, 1980 (in Japanese).
9. Toma, S.Z., Micus, F.F., and Mathers, J.E., *J. Electrochem. Soc.*, 114, 953, 1967.
10. Datta, R.K., *J. Electrochem. Soc.*, 114, 1057, 1967.
11. Luscher, T.W., Datta, R.K., *Illum. Eng.*, 65, 49, 1970.
12. Ropp, R.C., *J. Electrochem. Soc.*, 115, 940, 1968.
13. Wanmaker, W.L. and Berlijadon, J.G., Japanese Patent Publication (Kokoku) 44-24411 (1974).
14. Graf, J.A., Heitmajor, H.R., Japanese Patent Disclosure (Kokai) 49-52191 (1969).
15. *Illum. Eng.*, 62, 1, 1967.
16. Palilla, F.C. and Levine, A.K., *The Electrochem. Soc. Spring Meeting*, 1966, Abstr. 34.
17. Miyake, S., Otagaki, Y., *J. Illum. Eng. Japan*, 52, 368, 1968 (in Japanese).
18. Shimazu, H., Obara, A., and Miyazaki, K., *Toshiba Rev.*, 23, 1585, 1968 (in Japanese).
19. Hirota, T., Ogura, K., *J. Illum. Eng. Japan*, 52, 638, 1968 (in Japanese).
20. Ota, J., Tomonaga, A., Tamazaki, S., and Otani, M., *Mitsubishi Denki Giho*, 42, 1081, 1968 (in Japanese).
21. Toison, M.L., *Lux*, 44, 363, 1967.
22. Limbach, H.W., Japanese Patent Publication (Kokoku) 35-17821 (1960).
23. Rokosz, F., Sausville, J.W., van Broekhoven, J., *J. I.E.S.*, 3, 95, 1973.
24. Watanabe, M., Nishimura, T., Komoto, K., Shimizu, K., and Narita, K., *Tech. Digest, Phosphor Res. Soc. 167th Meeting*, 1977 (in Japanese).
25. Watanabe, M., Nishimura, T., Komoto, K., Kobuya, T., and Shimizu, K., Japanese Patent Disclosure (Kokai) 53-127384 (1978).
26. Inoshima, H., Matsuoka, M., and Ide, S., *Tech. Digest, Phosphor Res. Soc. 162nd Meeting*, 1976 (in Japanese).
27. Hoffman, M.V., *Journal of I.E.S.*, 6, 89, 1977.
28. Verstegen, J.M.P.J., Radielovic, D., Vrenken, L.E., *J. Electrochem. Soc.*, 121, 1627, 1974.
29. Iwama, K., Takakawa, M., Kobayashi, Y., *Tech. Digest, Phosphor Res. Soc. 159th Meeting*, 1974 (in Japanese).
30. Iwama, K., Yamaguchi, M., Watarai, Y., *J. Illum. Eng. Japan*, 60, 41, 1976 (in Japanese).
31. Burrus, H.L., Nicholson, K.P., *J. Luminesc.*, 3, 467, 1971.
32. Murakami, K., Otani, M., and Awazu, K., *Tech. Digest, Phosphor Res. Soc. 159th Meeting*, 1974 (in Japanese).
33. Palilla, F.C. and O'Reilly, B.E., *J. Electrochem. Soc.*, 115, 1076, 1968.
34. Opstelten, J.J., Radielovic, D., and Wanmaker, W.L., *J. Electrochem. Soc.*, 120, 1400, 1973.
35. Wanmaker, W.L. and Bakker, C., *J. Electrochem. Soc.*, 106, 1027, 1959.

chapter five — section eight

Phosphors for lamps

Richard S. Meltzer

Contents

5.8 Quantum-cutting phosphors 507
  5.8.1 Introduction 507
  5.8.2 Cascade emission 508
  5.8.3 Cross-relaxation energy transfer 515
    5.8.3.1 Quantum cutting with the Gd-Eu couple 517
    5.8.3.2 Sensitization of Gd^{3+} 520
      5.8.3.2.1 Sensitization of Gd^{3+} with 4f→5d transitions of rare-earth ions 520
      5.8.3.2.2 Sensitization of Gd^{3+} with ns^2 ions 524
      5.8.3.2.3 Sensitization of Gd^{3+} with host lattice absorption 525
    5.8.3.3 Cross-relaxation energy transfer with parity-allowed f–d transitions. 525
  5.8.4 Quantum cutting using host lattice states—Auger and other processes 527
  5.8.5 Conclusions 528
Acknowledgments 529
References 529

5.8 *Quantum-cutting phosphors*

5.8.1 *Introduction*

Quantum cutting provides a means to obtain two or more photons for each photon absorbed. It therefore serves as a downconverting mechanism with quantum efficiency greater than unity and it offers the prospect of providing improved energy efficiency in lighting devices.

Currently, the primary excitation of phosphors in fluorescent lamps is achieved by UV excitation from a Hg discharge. While it generates electromagnetic radiation at about 70% efficiency, over 90% of the radiation occurs in the UV region at 254 nm. Conversion of UV light to visible light is accomplished by phosphors that introduce additional losses, predominantly due to the large energy difference between the exciting photon and the emitted photon; the resulting lamp energy efficiencies are at best 33%. Improvements in fluorescent lamps have been incremental with small improvements in efficiency through tailoring of the Hg discharge or optimization of the efficiency of phosphors that convert the UV into visible light. Major improvements will therefore require a conceptually new approach.

Plasma displays take advantage of a Xe discharge that emits vacuum ultraviolet (VUV) photons in the 147–170 nm range to produce visible light. These have secured a sizable share of the commercial display market. To make this possible, new phosphors were required to optimize the efficiency of the display using VUV excitation. It would be highly desirable to utilize rare-gas discharge in general lighting applications as well. While the Xe discharge is now approaching the efficiency of mercury discharges, the larger energy of the VUV photons inherently limits the energy efficiency of a phosphor if only one visible photon is generated per VUV photon produced in the discharge. Therefore, new phosphors with quantum efficiencies greater than 1 are required for this purpose. To actually make the Xe discharge-based fluorescent lamps more energy efficient than the currently used Hg-based tubes, quantum efficiencies above 150% must be achieved. A quantum-splitting phosphor would therefore serve this need. The discovery of such phosphors for VUV excitation would be advantageous, as it would lead toward the realization of a highly efficient and environmentally benign lighting technology. Lamps having improved efficiency would decrease the energy consumption for lighting, a major part of the world energy budget, thereby reducing the costs of lighting and the consumption of fossil fuels that contribute to environmental problems. In addition, the replacement of Hg in a standard fluorescent lamp by a rare-gas (VUV) excitation source would eliminate environmental concerns regarding the disposal of Hg-based lamps.

In order to obtain quantum-cutting phosphors with quantum efficiencies exceeding unity, the lanthanide ions are obvious candidates for this purpose due to their energy level structures that provide metastable levels from which quantum-cutting processes are possible. The VUV levels of many of the lanthanides have been recently measured, thereby providing the starting point from which new phosphors may be designed.[1,2]

As far back as the 1950s, it was realized that it is possible, from energy conservation principles, to obtain two visible photons for each absorbed UV photon.[3] Examples of materials that emit two visible photons per absorbed UV photon were discovered in the early 1970s when it was shown that cascade emission from the high-energy $^1S_0$ level of Pr^{3+} can yield two visible photons in a sequential two-step radiative process.[4,5] Unfortunately, it is usual for the high-lying energy levels of a single lanthanide ion that the branching ratio (which determines the division of the emission over the UV, visible, and IR spectral regions) is unfavorable for obtaining visible emission of two photons; rather the radiation is emitted preferentially to the lower levels producing a single VUV or UV photon. However, by using a combination of two lanthanide ions, resonant energy transfer can be used to yield high visible quantum yields; internal quantum efficiencies as high as 190% have been demonstrated.[6] In the next section, we review cascade or two-step photon emission as a method of obtaining quantum cutting. In the following section, we consider the use of cross-relaxation energy transfer (CRET) using a pair of rare-earth ions. Finally, we discuss the case of quantum splitting by Auger processes.

5.8.2 *Cascade emission*

The simplest quantum-cutting scheme utilizes a two-step photon emission on a single ion, referred to as photon cascade emission (PCE). Despite the tendency of an ion to have the greatest transition probability to the lowest-lying states, or maximum photon energy, thereby preventing efficient PCE, for the Pr^{3+} ion excited to its high-lying $^1S_0$ state, spin selection rules favor transitions to its singlet states, especially the $^1I_6$ state. This results in emission at 406 nm, thereby making quantum cutting possible. Emission from the $^1S_0$ state of Pr^{3+} was first observed by Elias et al. in 1973.[7] Shortly thereafter, highly efficient PCE

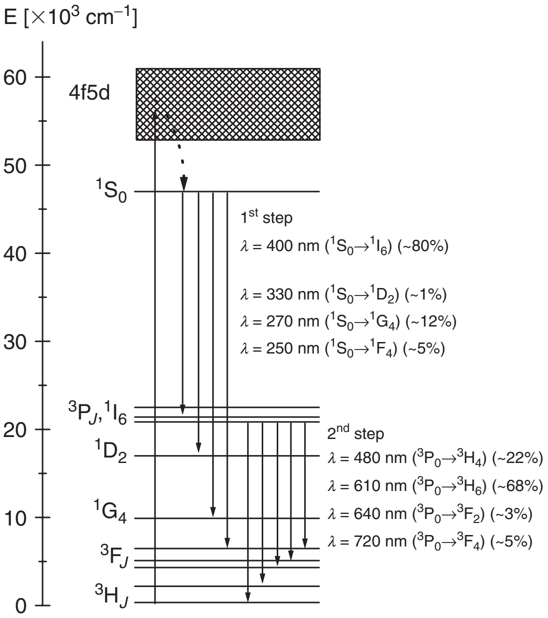

E [×10³ cm⁻¹]
60
50
40
30
20
10
0
4f5d
¹S₀
³P_J, ¹I₆
¹D₂
¹G₄
³F_J
³H_J
1st step
λ = 400 nm (¹S₀→¹I₆) (~80%)
λ = 330 nm (¹S₀→¹D₂) (~1%)
λ = 270 nm (¹S₀→¹G₄) (~12%)
λ = 250 nm (¹S₀→¹F₄) (~5%)
2nd step
λ = 480 nm (³P₀→³H₄) (~22%)
λ = 610 nm (³P₀→³H₆) (~68%)
λ = 640 nm (³P₀→³F₂) (~3%)
λ = 720 nm (³P₀→³F₄) (~5%)

Figure 75 Energy level scheme of Pr^{3+} showing two-step emission. The percent values in parenthesis are the branching ratios for YF_3:Pr^{3+}. (From Kuck, S., Sokolska, I., Henke, M., Scheffler, T., and Osiac, E., *Phys. Rev. B,* 71, 165112, 2005. With permission.)

for Pr^{3+} in the visible region was reported in YF_3 by Piper et al.[4] and by Sommerdijk et al.[5] in 1974.

This process, which has been demonstrated for the Pr^{3+} ion in a number of hosts, is illustrated in Figure 75. The energy of the 4f5d state is sensitive to the environment of the ion since the wave function of the 5d electron extends much further out from the nucleus than the 4f electrons, which are more shielded from the crystalline fields of the surrounding ions. It requires a host where the Pr^{3+} ion experiences a weak crystal field, which occurs when the Pr^{3+} ion sits at a site of high coordination number or high electronegativity, so that the 4f5d state lies above the $^1S_0$ state as shown in Figure 75. Methods for identifying hosts in which the $4f^2$ $^1S_0$ state lies below that of the lowest 4f5d state have been described based on the spectroscopy of Ce^{3+} or Eu^{2+} in the same host.[8] A VUV photon is absorbed by the strong parity-allowed transition from the $^3H_4$ ground state to the 4f5d excited state of the Pr^{3+} ion. Fast relaxation populates the metastable $^1S_0$ state. This state radiates to its lower-lying states but preferentially to the spin singlet states because these transitions are favored by the $\Delta S = 0$ spin selection rule. This produces the first photon. While transitions at the shortest wavelengths usually have the largest radiative rates, which for Pr^{3+} would tend to promote UV emission, in YF_3 and many other hosts emission to $^1I_6$ at 406 nm has the largest branching ratio. The $^1I_6$ state undergoes rapid nonradiative multiphonon relaxation to the $^3P_0$ state, which emits the second photon in the visible region. It was shown that the theoretical quantum yield in YF_3 could be as large as 1.4 ± 0.15 in a sample containing 0.1% Pr^{3+} provided there were no losses. Detailed experimental studies of the quantum yield and branching ratios for emission into the different final states showed that the actual quantum yield in the visible (380–750 nm) was 1.27, which is fairly constant when the Pr^{3+} concentration is in the range of 0.1 to 1%.[9]

This study illustrates some of the many difficulties in obtaining a useful phosphor. In order to provide high absorption of the VUV photon, the Pr^{3+} concentration must be sufficiently high. However, cross relaxation which nonradiatively depopulates the $^3P_0$

state, involved in generation of the second photon, already becomes active above a Pr^{3+} concentration of 0.1%; the quantum yield of this state is only 0.61 at such a low doping level. In addition, the first photon is only of limited use in lighting applications since 80% of the photons in the first step occur in the violet region at 406 nm, a wavelength that does not produce good luminous efficiency. Most of the remaining 20% occurs at even shorter wavelengths in the UV, making such emissions useless in a visible lamp unless this is converted to visible radiation by a secondary phosphor.

Cascade emission of Pr^{3+} has now been demonstrated in a large number of fluoride materials where the $^1S_0$ state of Pr^{3+} lies below the 4f5d states. The emission spectra for many fluorides are compared in Figure 76. Note the dominance of the $^1S_0 \rightarrow {}^1I_6$ transition at 406 nm in all of these hosts. Its relative intensity is maximum for YF_3 and LuF_3, making these the materials of highest expected visible quantum yield. Like YF_3, both LuF_3 and $BaMgF_4$ also exhibit strong PCE with theoretical visible quantum yields of 1.6 and 1.3, respectively, based on a Judd–Ofelt analysis,[10] but their actual quantum yields have not been measured. In $KMgF_4$:Pr^{3+}, the theoretical branching ratio is reduced to 0.6 resulting in a maximum visible quantum yield of 1.24.[11]

For some fluorides, host absorption may compete with the 4f5d absorption. For example, while quantum splitting by PCE has been observed[12] for Pr^{3+} in $LaZrF_7$ and α-$LaZr_3F_{15}$, self-trapped exciton (STE) emission also occurs at 10 K. If the STE were to transfer its energy to the $^1S_0$ state of Pr^{3+}, this could be an effective means of sensitizing the quantum cutting. Indeed, at room temperature the STE emission is absent and the excitation spectrum of the Pr^{3+} emission indicates that the exciton state does transfer energy to Pr^{3+}. Unfortunately, this energy transfer occurs to the ^3P states and not to the $^1S_0$ state of Pr^{3+}, circumventing the quantum-splitting channel. Also, in these systems, the quantum yield is reduced by the quenching of the $^1D_2$ emission. $SrAlF_5$:Pr^{3+} has also been shown to exhibit cascade emission[13] under VUV excitation into the 4f5d states of Pr^{3+} where the branching ratio to $^1I_6$ is rather high. Here again, under band gap excitation below 110 nm, STE emission is observed at low temperatures but thermal release of the trapped charges leads to excitation of Pr^{3+}. It has been reported that the visible light yield from $SrAlF_5$:Pr^{3+} even exceeds that of YF_3:Pr^{3+}, but such comparisons are complicated by the fact that this is a strong function of Pr^{3+} concentration, and thus a full study of both materials as a function of Pr^{3+} concentration would be required.[14] Under X-ray excitation, $SrAlF_5$:Pr^{3+} also exhibits $^1S_0$ emission at 350 K, whereas only STE emission is observed at 100 K.[15] This suggests that thermally induced energy transfer occurs from the STE to the $^1S_0$ state of Pr^{3+}. In $NaMgF_3$:Pr^{3+}, PCE with a good branching ratio to $^1I_6$ has also been reported. Although PCE occurs both for the excitation of the 4f5d state of Pr^{3+} and the host excitation below 120 nm, the host excitation leads to some direct excitation of the ^3P states of Pr^{3+}, partially defeating the quantum splitting in $NaMgF_3$:Pr^{3+} as was previously described for $LaZrF_7$ and α-$LaZr_3F_{15}$.[16]

As noted above, concentration quenching of the $^3P_0$ emission due to CRET often limits the visible quantum yield as it reduces the efficiency of the second step in the PCE. It is possible to control this loss by selecting materials where the rare-earth ions are inherently well separated due to the crystal structure. One such example is $K_5Li_2PrF_{10}$ where the rare-earth ions do not share a common ligand, inhibiting CRET. At 8 K, $^3P_0$ emission is observed[17] even for a sample fully concentrated in Pr^{3+}, but at 300 K $^3P_0$ emission is quenched. However, for a sample with a 1% Pr^{3+} concentration in $K_5Li_2LaF_{10}$:Pr^{3+}, $^3P_0$ emission and PCE still occur at room temperature.

On the basis of Judd–Ofelt calculations, the total quantum yield for two-step emission for Pr^{3+} can be as high as 1.99.[18] The Judd–Ofelt theory parameterizes the intensities of all the transitions with the $4f^n$ configuration of any rare-earth ion in a host in terms of three parameters. On the basis of such an analysis, the theoretical visible quantum yields for a

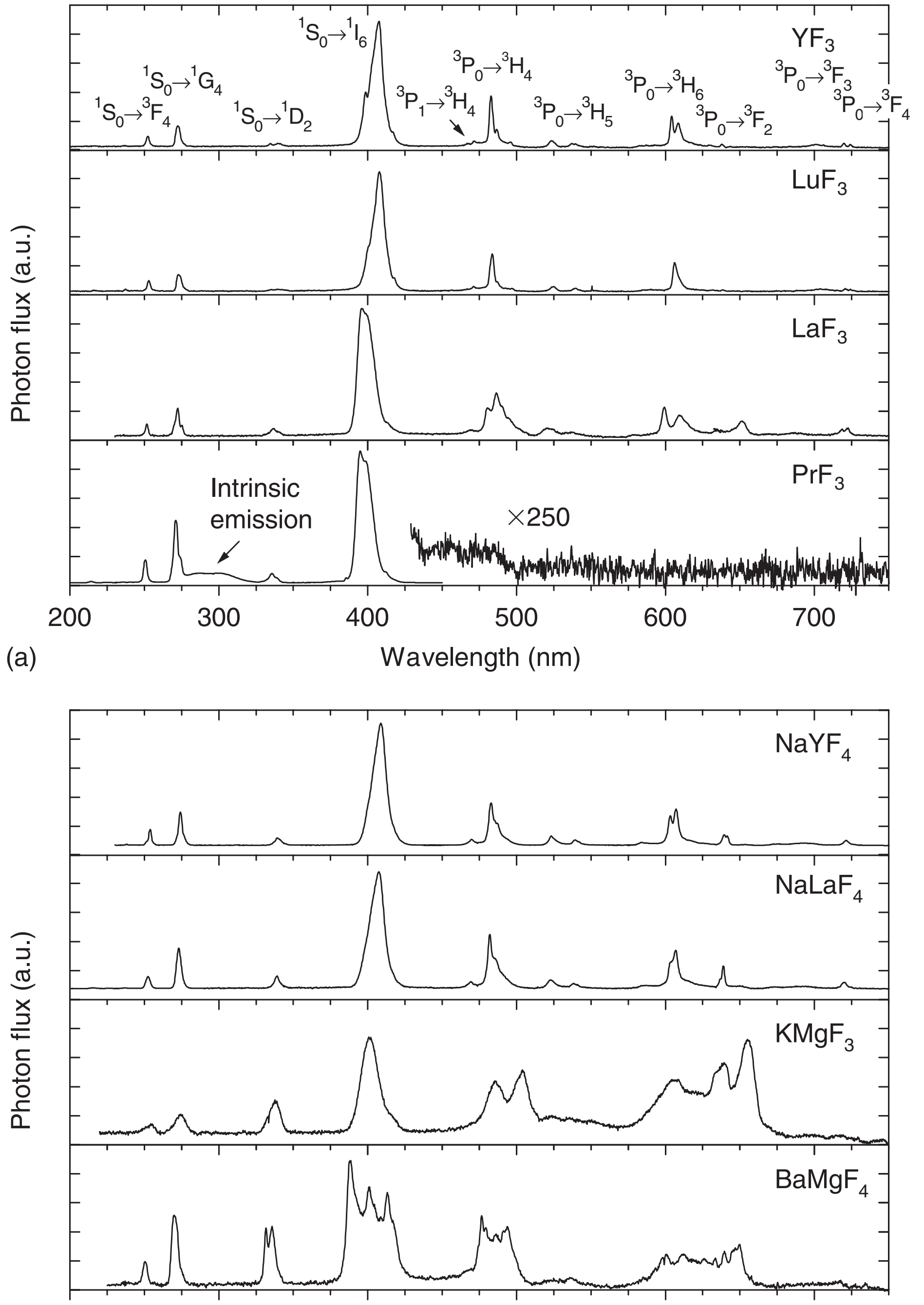

Figure 76 Room temperature emission spectra (uncorrected) under excitation at approximately 190 nm ($KMgF_3$: 172 nm) of the pure cascade emitters YF_3, $NaYF_4$, LaF_3, $NaLaF_4$, LuF_3, $KMgF_3$, $BaMgF_4$, and PrF_3. (From Kuck, S., Sokolska, I., Henke, M., Scheffler, T., and Osiac, E., *Phys. Rev. B*, 71, 165112, 2005. With permission.)

number of hosts have been summarized by Rodnyi et al.[19] and by Kuck et al.[20,21] For most materials, the branching ratio for the $^1S_0\rightarrow{}^1I_6$ transition is lower than in YF_3, where it is

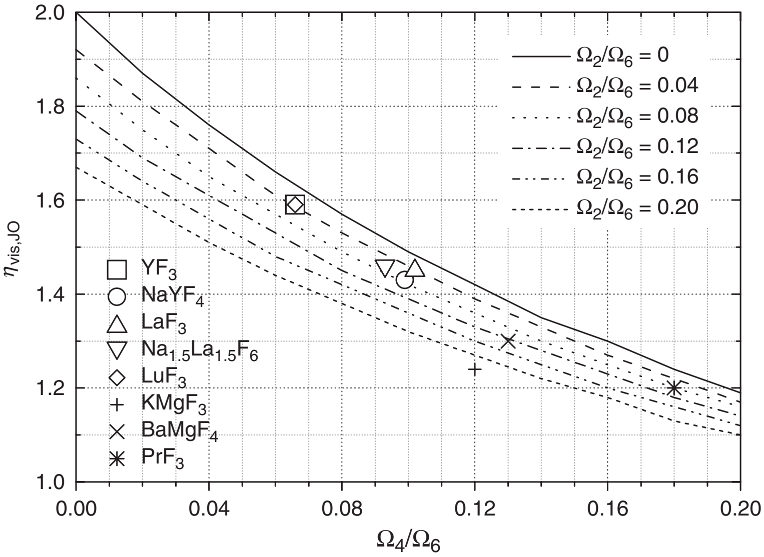

Figure 77 Calculated visible quantum efficiency $\eta_{vis,JO}$ for different ratios of the Judd–Ofelt parameters Ω_2/Ω_6 and Ω_4/Ω_6. The values for the pure cascade emitters are also indicated. (From Kuck, S., Sokolska, I., Henke, M., Scheffler, T., and Osiac, E., *Phys. Rev. B*, 71, 165112, 2005. With permission.)

0.86. The branching ratio is most favorable where the ratios of the Judd–Ofelt parameters, Ω_2/Ω_6 and Ω_4/Ω_6, are small. The theoretical visible quantum yield as a function of the ratio of Judd–Ofelt parameters is summarized in Figure 77. The most favorable situation occurs when these ratios are both zero, for which a quantum yield close to 2 is possible. These theoretical quantum yields for a number of fluorides containing Pr^{3+} are also shown in Figure 77. So far, $YF_3:Pr^{3+}$ remains the material of highest measured visible quantum yield, but such absolute quantum yield measurements are rare.

Pr^{3+}-doped PCE phosphors suffer from the fact that the first photon occurs in the violet spectral region, which is too short a wavelength for useful luminous efficiency. One solution would involve converting this emission to longer wavelengths through CRET. In this type of energy transfer both the donor and acceptor are left in an excited state so that they can each emit a photon, fulfilling the quantum-cutting objective. This will be discussed more fully in the next section, but we briefly discuss it here in the context of Pr^{3+}, as it offers an alternative to PCE. This idea was tried in $YF_3:Pr^{3+}$ co-doped with Sm^{3+}, Eu^{3+}, Dy^{3+}, Er^{3+}, or Tm^{3+}.[22] Although there was spectral overlap between the 406 nm emission from $^1S_0$ of Pr^{3+} and absorption of each of these ions, no energy transfer to the co-dopant ions was observed. For the case of YF_3 co-doped with Pr^{3+} and Eu^{3+}, it was shown that one reason for the absence of energy transfer was the quenching of the $^1S_0$ state by a low-energy metal-to-metal charge transfer state (Pr^{4+}–Eu^{2+}) for Pr–Eu pairs.[23] The use of energy transfer was also tested in Pr^{3+}, Mn^{2+} co-doped $SrAlF_5$, $CaAlF_5$, and $NaMgF_3$ where there is good spectral overlap between the $^1S_0 \rightarrow {}^1I_6$ emission at 406 nm and the $^6A_1 \rightarrow {}^4E_g,{}^4A_{1g}$ absorption of Mn^{2+}. Unfortunately, such energy transfer was not observed.[24] The failure of this idea is probably related to the fact that the transitions involved in the energy transfer are parity forbidden in both cases. In addition, for Mn^{2+} they are also spin forbidden. Therefore, the dipole–dipole energy transfer rates at these low concentrations of dopants (<1%) are incapable of competing with the $^1S_0$ radiative rate, which exceeds 10^6 s^{-1}.

Although oxides tend to have larger crystal fields than fluorides, such that the lowest 4f5d state for Pr^{3+} lies below the $^1S_0$ state, it was shown recently that certain oxides containing sites with high coordination number exist such that PCE can also occur. Srivastava and coworkers demonstrated the effect in Pr^{3+}-doped $SrAl_{12}O_{19}$,[25] $LaMgB_5O_{10}$,[26] and LaB_3O_6.[27] In these oxides, the branching ratios were less favorable for the transition to $^1I_6$ and their quantum yields were not expected to exceed unity. They also illustrate an additional problem; in oxides, the phonon energies are much larger than in fluorides, promoting multiphonon and other nonradiative processes that either eliminate or reduce the efficiency of $^3P_0$ emission, which comprises the second step in the quantum cutting. SrB_4O_7 and $Sr_{0.7}La_{0.3}Al_{11.7}Mg_{0.3}O_{19}$ are two other oxides, in which the $^1S_0$ state lies below the 4f5d state, exhibiting cascade emission.[28] They also suffer from the problem, discussed earlier for the fluorides—their band gaps are sufficiently small that Xe discharge excitation excites preferentially the host absorption rather than the 4f5d state of Pr^{3+}. Energy transfer from the host to the Pr^{3+} $^1S_0$ state is then required for quantum cutting. For example, in SrB_4O_7 the branching ratio to $^1I_6$ is relatively high. However, the excitation spectrum below 175 nm is dominated by the host lattice features rather than the 4f5d Pr^{3+} states and these clearly do not produce as high an efficiency of Pr^{3+} emission when compared with excitation of the 4f5d state. In SrB_6O_{10}, this effect is so severe that excitation into the band state is totally ineffectual in exciting Pr^{3+}.[29]

In the Pr^{3+}-doped sulfates, e.g., MSO_4 (M = Ba, Sr, Ca), the $^1S_0$ state, and the lowest 4f5d states are nearly degenerate.[30] In $CaSO_4$, the 4f5d state lies below the $^1S_0$ state so that only broad $4f5d \rightarrow 4f^2$ emission is observed. For $BaSO_4$ at low temperatures, sharp intraconfigurational transitions within $4f^2$ are seen indicating that $^1S_0$ lies below the 4f5d states, and hence PCE can occur. However, as the temperature is increased, emission from 4f5d increases relative to that of $^1S_0$ as lowest 4f5d states are thermally populated. At room temperature, PCE is therefore ineffective.[31] In $SrSO_4$, only $^1S_0$ emission is observed for excitation into the 4f5d state of Pr^{3+} at 187 nm, with a favorable branching ratio for the 406 nm transition to $^1I_6$.[32] Unfortunately, the $^3P_0$ emission in the second step in quantum splitting is strongly quenched.

The proximity of these two states results in mixing of the $4f^2$ $^1S_0$ level with the 4f5d states and this can strongly affect both the radiative rate of $^1S_0$ and the relative intensities of 4f5d and $^1S_0$ emissions. The effect of this mixing has been calculated for Pr^{3+} in $SrAl_{12}O_{19}$ and the relative intensities of the different transitions from $^1S_0$ have been estimated.[33] The results lead to the conclusion that in this host the $^1S_0$ state couples most strongly to states in the middle of the 4f5d configuration. The calculated intensity for $^1I_6$ is somewhat underestimated compared with the measured values, but this may be related to its strongly vibronic character.[34] The actual quantum yield is also hindered by the $^3P_0$ internal quantum efficiency, which is only about 70% even for very low Pr^{3+} concentrations.[35] The mixing has also been examined experimentally in $BaSO_4$ by applying pressure to alter the energy gap between the lowest 4f5d and the $^1S_0$ states.[36] Both the relative intensities of 4f5d to that of $^1S_0$ and the $^1S_0$ lifetime were measured as a function of pressure. The results were explained by a simple model in which the $^1S_0$ state is coupled to the lowest 4f5d state that is 325 cm^{-1} higher in energy by an off-diagonal matrix element of about 80 cm^{-1}.

Although most attempts to achieve quantum cutting by PCE have utilized Pr^{3+}, the scheme can be applied quite generally to any metastable high-lying level. In order to achieve efficient quantum cutting, the first photon must arise from emission that occurs with high probability to some intermediate state. Then the intermediate excited state must radiate efficiently to a lower state. Thus, even ions that emit from the $4f^{n-1}5d$ state could generate efficient PCE. However, in all known cases, the parity-allowed transitions to states in the $4f^n$ configuration occur with a strong preference to very low-lying levels so that the first step occurs in the VUV or UV defeating quantum cutting. Thus, one must look for high-lying metastable levels of the $4f^n$ configuration; the $^1S_0$ state of Pr^{3+}, already described in detail, has been demonstrated to be an excellent example.

Quantum cutting by PCE has been examined for Gd^{3+} in $LiYF_4$ whose ^6G states at about 50,000 cm^{-1} are metastable.[37] There are no excited states below 31,000 cm^{-1}. The ^6G state can radiate to the ground state at 204 nm, which would not produce quantum cutting, or to its ^6P, ^6I, or ^6D states. Transitions to ^6P occur in the red but the second step in the PCE involving emission from the ^6P levels would occur at 312 nm in the UV. An additional ion could be incorporated into the lattice to which the ^6P Gd^{3+} ions could transfer their energy, yielding a second visible photon. However, transitions to ^6I and ^6D occur in the IR. In some materials, like $LiYF_4$ where the $U^{(6)}$-reduced matrix elements of the electric dipole operator dominate, the matrix elements for transitions to ^6I are in fact much larger that those to ^6P so that it may dominate the first step in the PCE.[38] As a result, the visible quantum yield for Gd^{3+} in $LiYF_4$ is expected to be quite low. However, this may not be the case in other hosts. PCE has also been reported for Gd^{3+} in $GdBaB_9O_{16}$.[39]

The case of Tm^{3+} was considered theoretically by Pappalardo.[18] Its energy level structure is similar to that of Pr^{3+} but expanded by a factor of 2 by the larger spin–orbit coupling. The $^1S_0$ state is at too high an energy to be useful. Thus, it is the ^3P and $^1I_6$ metastable states from which quantum splitting must occur. Judd–Ofelt calculations of branching ratios indicate that the strongest transitions will occur to the low-lying manifolds, preventing visible PCE.

Both Er^{3+} and Ho^{3+} have high-lying states that are likely to be metastable in the VUV and which can be populated by absorption to the $4f^{n-1}5d$ states; these have the potential for PCE. A major issue in their application is the presence of many excited states that yield transitions not only throughout the visible region, but also in the UV and IR regions, which will not be useful in phosphors. Nonetheless, if certain transitions in the visible region dominate, a useful phosphor could be possible.

The cases of Ho^{3+} in $LiYF_4$ and YF_3 were investigated by Peizel et al.[40] Sufficiently large gaps within the $4f^{10}$ configuration exist below the $^3P(1)_2$ level at 62,970 cm^{-1} and the $^1D(3)_3$ level at 45,166 cm^{-1} (gaps of about 2200 cm^{-1} in both cases) for these states to emit radiation. Indeed, emission from $^1D(3)_2$ was observed from both fluorides to most of the lower-lying states. While much of the radiation was in the UV to the ^5I manifold, emission to ^5F in the visible region also occurred from which a second visible photon can be produced. For $YLiF_4$, the $^3P(1)_2$ state will not emit since the lowest 4f5d state lies slightly lower in energy, but in YF_3 the lowest 4f5d state lies higher in energy so that emission from this state was observed. However, not surprisingly, much of the emission is in the UV with no dominant transitions in the visible region for the first step in the PCE; thus, Ho^{3+} is probably not a good candidate for quantum splitting by PCE.

Calculations for the PCE of Er^{3+} have shown, based on the Judd–Ofelt theory, that visible quantum efficiencies of up to 112% are possible for a host with appropriate Judd–Ofelt parameters.[41] The energy level structure for Er^{3+} is shown in Figure 78. On the basis of the energy gaps between manifolds, emission from the high-lying states can be expected from $^2P_{3/2}$, $^4D_{1/2}$, $^2F_{7/2}$, and, if the 4f5d state of Er^{3+} lies very high (above 65,000 cm^{-1}), emission can also be expected from $^2F(2)_{5/2}$. The results depend on the level initially selected for PCE and on the Judd–Ofelt parameters. For example, if emission originates from the $^2F_{7/2}$ level and if Ω_6 is the dominant Judd–Ofelt parameter, then 112% quantum efficiency is possible. If emission commences from $^2P_{3/2}$ and if Ω_4 is the dominant term, then a quantum efficiency of 107% is theoretically possible. In reality, there will be some losses; more than one of these levels will emit due to multiphonon relaxation and the Judd–Ofelt parameters will not be the ideal values in the calculation. As a result, the visible quantum efficiency is not likely to exceed 100% for Er^{3+}. As an example, in Figure 78, the emission spectrum of Er^{3+} in YPO_4 is shown. In this host, the lowest 4f5d level lies just

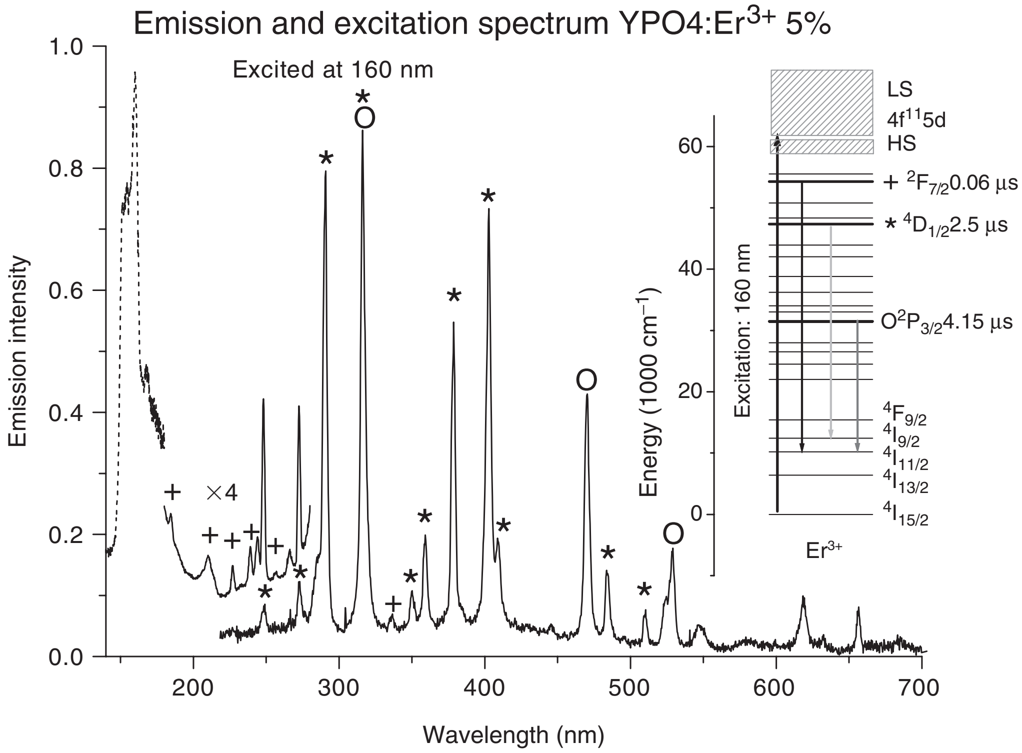

Figure 78 Excitation and emission spectra of YPO_4:Er^{3+} 5% excited at 160 nm. The insert shows the energy level diagram of Er^{3+} with measured lifetimes. Transitions are identified according to their initial state using + ($^2F_{7/2}$), * ($^4D_{1/2}$), or O ($^2P_{1/2}$). (Measured by the author.)

below $^2F(2)_{5/2}$ so that only three high-lying levels are expected to show emission. Indeed emission from all three states is observed as can be seen from the identification of the levels based on studies of their lifetimes. While there is significant emission in the visible region, it appears that in this host the Judd–Ofelt parameters are such that most of the emission occurs in the UV so that the visible quantum yield will fall well below 1. If another ion can be found, which when co-doped in the host will cross-relax with the excited ion, it may be possible to convert this UV radiation into the visible spectrum. This is discussed in the next section.

It must be concluded from the above discussion that commercially viable phosphors for lamps or plasma displays based on rare-gas discharge excitation of PCE remains a challenging task. Success is limited by (1) excessive emission outside the visible region, (2) nonradiative losses which appear as rare-earth concentrations are increased to promote efficient absorption of VUV radiation, and (3) competition from host absorption which often does not efficiently couple to the high-lying levels.

5.8.3 *Cross-relaxation energy transfer*

An alternative scheme to develop an efficient quantum-cutting phosphor is to utilize a pair of ions that can share the initial excitation energy. The CRET process is illustrated in Figure 79 in which the initially excited ion (state A3) undergoes a nonradiative transition (A3→A2) to an intermediate excited state (A2) accompanied by an energy-conserving transition of a neighboring ion from its ground state (B1) to some excited state (B2). This would leave both ions in excited states, each of which could emit a visible photon. While

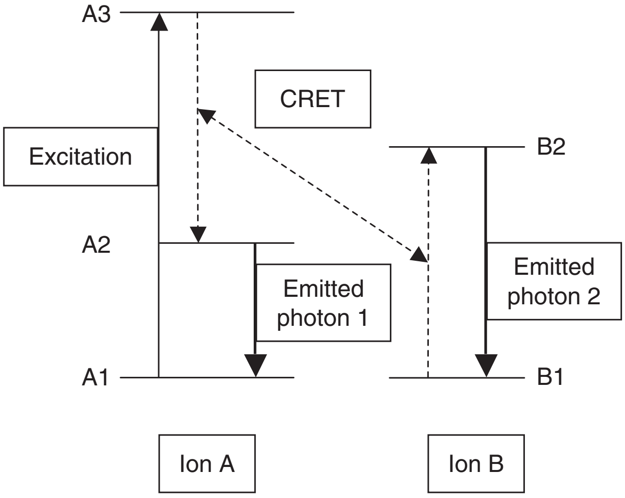

Figure 79 Description of cross-relaxation energy transfer (CRET). After ion A is initially excited, it undergoes a CRET with ion B such that ion A makes a transition A3→A2 while ion B makes a resonant transition B1→B2 (shown by the dashed lines). Both ions emit photons from their respective excited states A2 and B2.

this idea has been known for a long time, and serves as one of the main mechanisms for concentration quenching, it has been demonstrated by Meijerink's group as an efficient means of quantum splitting. They showed that for the Gd^{3+}–Eu^{3+} pair of ions, an internal quantum efficiency of 190% was possible, opening the way to serious consideration of this approach.[6]

Critical to the success of these concepts is the need for rapid CRET among a pair of ions since it must compete effectively with the radiative emission of the initially excited ion (sensitizer). This radiative rate is typically 10^3–10^6 s^{-1} for forbidden $4f^n \rightarrow 4f^n$ transitions and 10^6–10^8 s^{-1} for parity-allowed $4f^{n-1}5d \rightarrow 4f^n$ transitions.

CRET can occur by multipole–multipole interactions or by exchange interactions.[42] At typical nearest neighbor distances, exchange will usually dominate. At more dilute concentrations, typical of phosphors, the short-range exchange-mediated transfer rate will have decreased to the point that the dipole–dipole (or other multipole–multipole) interactions, which fall off more slowly as R^{-6}, will dominate. The dipole–dipole transfer rate can be written in terms of the oscillator strengths of the optical transition connecting the initial and final states of the pair of ions participating in the cross relaxation.[43] This is expressed as

$$P_{AB}^{dd} = (2/3)(2\pi/\hbar)(e^2/R^3)^2(3\hbar/2m_e)^2(1/\omega)^2 f_A f_B S \tag{3}$$

where ω is the transition frequency of each ion involved in the cross relaxation, f_A and f_B are the oscillator strengths of the transitions occurring on the two ions, and S is the spectral overlap of the emission and absorption of these two transitions. Substituting values for the constants and expressing the transition energy, $\Delta E = \omega$, in eV, the spectral overlap integral in cm^{-1}, and the ion–ion separation in angstroms, the transition rate (in s^{-1}) can be calculated as

$$P_{AB}^{dd} = \left(1.4{*}10^{24} \cdot f_A f_B S\right) \Big/ \left(\Delta E^2 R^6\right) \tag{4}$$

For typical 4f–4f oscillator strengths of 10^{-6}, a transition energy of 3 eV, and a perfect spectral overlap of transitions on the two ions (total resonance) whose widths at room temperature are 10 cm^{-1} ($S = 0.1$ cm^{-1}), yields a rate of 8×10^6 s^{-1} for ions separated by a typical nearest-neighbor distance of 3.5 Å. This corresponds to the situation of resonant energy transfer between two nearest neighbor ions that would occur in a stoichiometric rare-earth system. For a 5% concentration of ions, for which the nearest neighbor is much more distant, this rate will drop by more than two orders of magnitude to ~10^5 s^{-1}. However, while this CRET rate is competitive with the radiative rate, it will require an ideal energy match for the transitions on the two ions of the couple and a high level of dopant concentration such that other unwanted nonradiative processes may severely interfere with the operation of the phosphor. For exchange interactions, the weak oscillator strengths of the f–f transitions involved in the energy transfer are not relevant in determining the energy transfer rates since they involve an overlap of the wave functions of the two ions, usually through an intervening anion (superexchange).

In designing a phosphor, one need not be limited to f–f transitions on both ions of the couple. Estimates for energy transfer rates in the case of a $4f^{n-1}5d \rightarrow 4f^n$ transition (abbreviated as f–d) on one of the ions can also be made for dipole–dipole interactions using Eq. 4. Let us first obtain an estimate for the case of nearest neighbors separated by about 3.5 Å. Typical oscillator strengths can be estimated as 10^{-2} for the 4f–5d transition and 10^{-6} for the 4f–4f transition. Since the $4f^{n-1}5d \rightarrow 4f^n$ is broad, typically about 1000 cm^{-1}, one can reasonably anticipate a spectral overlap of 10^{-3} cm^{-1} leading to an estimated transfer rate of about 10^9 s^{-1} as has been observed by Wegh et al.[44] For a sample with a reduced concentration of 5% in one of the species, this rate would reduce to about 10^7–10^8 s^{-1} and might still compete effectively with the radiative rate for the $4f^{n-1}5d$ levels of the lanthanides. The conditions for exact spectral overlap are much less stringent for the case of $4f^{n-1}5d \rightarrow 4f^n$ transitions because of their much larger spectral widths.

For the case of $4f^{n-1}5d \rightarrow 4f^n$ transitions on both ions of the couple, one can anticipate extremely fast energy transfer rates. Assuming oscillator strengths of 10^{-2} for both ions, one can expect rates of 10^{12} s^{-1} for nearest neighbor transfer, reducing to 10^8 s^{-1} for samples with 1% concentration of dopants.

The energy transfer rates as a function of ion–ion separation for the various possible types of transitions assuming dipole–dipole interactions are summarized in Figure 80. In this example, oscillator strengths are assumed to be 10^{-1} (for all allowed f–d transitions) and 10^{-6} (for all parity-forbidden f–f transitions). The use of parity-allowed f–d transitions on one or both ions would appear to offer great potential for implementing CRET in rare-earth-doped systems. It is much more forgiving with respect to transition energy matches on the two ions of the couple, and it may be competitive with radiative rates for lower dopant concentrations. Even at distances of 7 Å, the rates for f–d transitions on one ion coupled to an f–f transition of the other are estimated at 10^8 s^{-1}.

5.8.3.1 *Quantum cutting with the Gd–Eu couple*

The specific case of CRET process for the Gd^{3+}–Eu^{3+} pair[45] is shown in Figure 81. In this case, the host is Eu^{3+}-doped $GdLiF_4$ and it is a 4f–4f transition on both ions of the pair that is active. After initial excitation of the ^6G state of Gd^{3+}, a CRET occurs, identified by the dashed arrows labeled 1 in Figure 81, whereby the Gd^{3+} ion undergoes a nonradiative transition to its ^6P state while the Eu^{3+} ion undergoes a transition from its thermally populated $^7F_1$ state to its $^5D_0$ state. The excited Eu^{3+} is responsible for the first visible photon. Resonant energy migration among excited Gd^{3+} ions occurs from within the ^6P state until the energy resides nearby another Eu^{3+} ion to which it can transfer its energy. The curved arrow, labeled 2, indicates this. The second excited Eu^{3+} ion produces the second visible photon, achieving quantum splitting. While the internal quantum efficiency

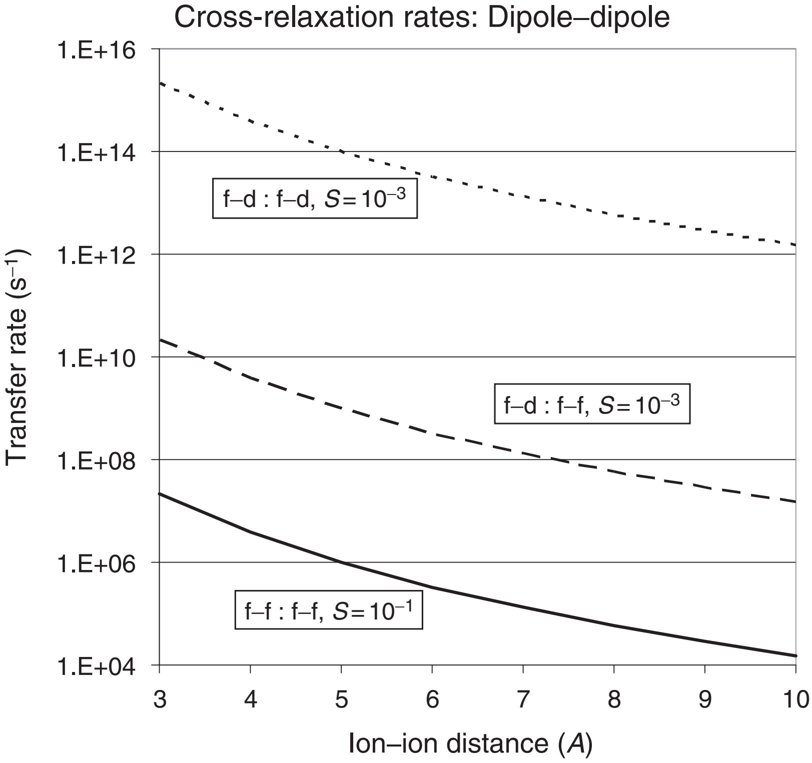

Figure 80 Calculated dipole–dipole energy transfer rates as a function of ion–ion distance. Assumed oscillators strengths are 10^{-1} (parity-allowed f–d transitions) and 10^{-6} (parity-forbidden f–f transitions). The cases depicted are for f–d transitions on both ions (dotted curve), a f–d transition on one ion and f–f transition on the other (dashed), and f–f transitions on both ions (solid). The assumed spectral overlap intergrals are shown in the boxes (in cm^{-1}).

is very high, in practice this will not produce a useful phosphor because the absorption of the VUV photon by Gd^{3+} is very weak as this involves a parity-forbidden and a spin-forbidden transition. Therefore, a sensitizer is required for applications. Proof of the quantum cutting was provided by comparing the Eu^{3+} emission intensity ratio, $^5D_0/^5D_1$, for excitation at 202 nm of the ^6G quantum-cutting state with that of 273 nm excitation of ^6I. As shown in Figure 82, it was determined that excitation at 202 nm produced a ratio almost twice of that produced for the 273 nm excitation; the detailed evaluation provided an internal quantum efficiency of 190%. However, because of the weak absorption by Gd^{3+}, the actual measured quantum efficiency is only about 32% with respect to input photons.[46]

The fact that this quantum efficiency was relatively insensitive to the Eu^{3+} concentration suggested that rapid energy migration among the Gd^{3+} ions was essential for the high quantum yield.[45] The rate of the energy transfer processes is strongly dependent on distance for both dipole–dipole and exchange interactions, and thus the Gd^{3+} and Eu^{3+} ions must be in close proximity. The energy migration provides a means to ensure that Gd^{3+} excitation resides near Eu^{3+} for part of its lifetime as it hops through the lattice.

The mechanism for the CRET within the Gd–Eu pair has not been ascertained but it is very likely that exchange interactions dominate since Gd^{3+} is stoichiometric in the host; as a result, every Eu^{3+} ion is a nearest neighbor to Gd^{3+} with which it can undergo CRET. Rapid resonant energy migration among the Gd^{3+} ions ensures that the excitation will find a site adjacent to a Eu^{3+} ion. Studies of the Gd–Nd pair, discussed below with regard to

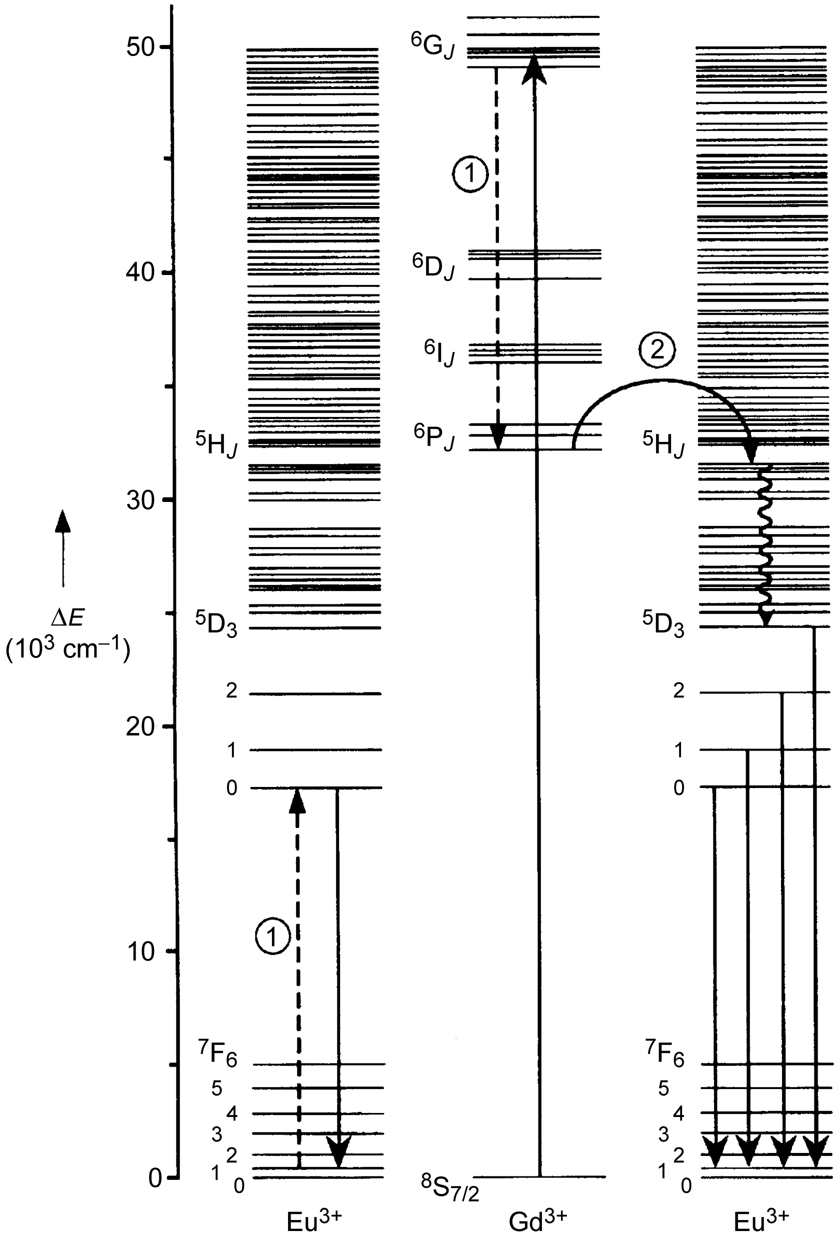

Figure 81 Energy level diagrams of Eu^{3+} and Gd^{3+} showing the cross-relaxation energy transfer process that leads to quantum splitting. The dotted arrows labeled 1 identify the resonant CRET which leave the first Eu^{3+} ion in its $^5D_0$ state from which the first photon is produced. The curved arrow labeled 2 describes the subsequent energy transfer from Gd^{3+} to a second Eu^{3+}, which produces the second photon. (From Wegh, R.T., Donker, H., Oskam, K., and Meijerink, A., *J. Lumin.*, 82, 93, 1999. With permission.)

sensitization of Gd^{3+}, demonstrate that for this system exchange dominates the CRET. It is likely that the same is true for the Gd–Eu pair.

Quantum splitting of the Gd^{3+}–Eu^{3+} couple has now been demonstrated in a large number of fluorides. The list, along with their estimated internal quantum efficiencies, includes GdF_3:Eu^{3+} (180%),[45] BaF_2:1% Gd, 1% Eu (194%),[47] $NaGdF_4$:Eu^{3+} (160%),[48] KGd_2F_7

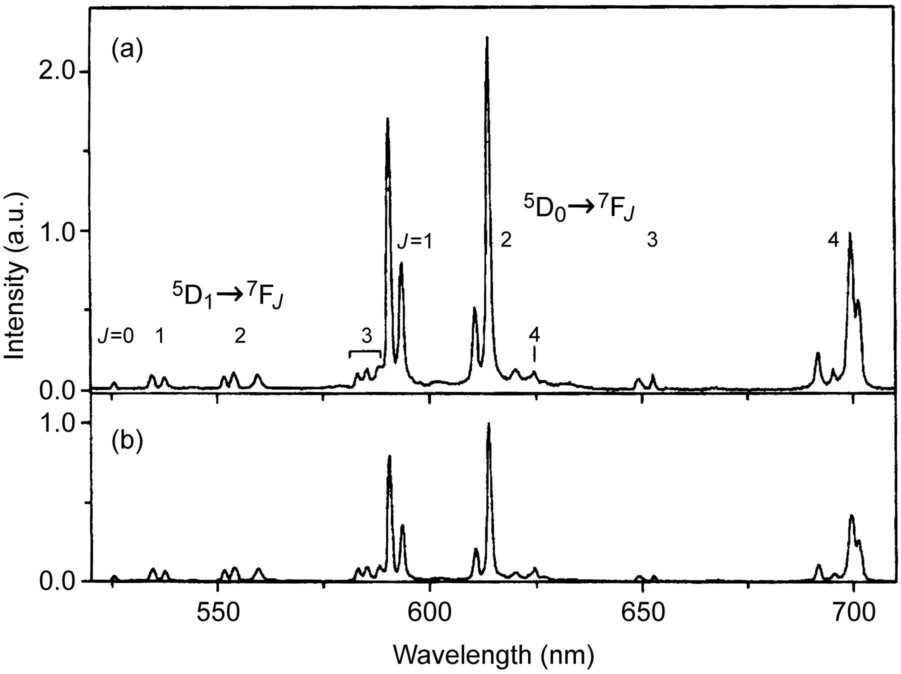

Figure 82 Emission spectra of LiGdF$_4$: Eu^{3+} 0.5% upon (a) $^8S_{7/2} \rightarrow {}^6G_J$ excitation on Gd^{3+} (202 nm) and (b) $^8S_{7/2} \rightarrow {}^6P_J$ excitation on Gd^{3+} (273 nm), both at 300 K. The spectra are scaled on the $^5D_1 \rightarrow {}^7F_J$ emission intensity. (From Wegh, R.T., Donker, H., Oskam, K., and Meijerink, A., *J. Lumin.*, 82, 93, 1999. With permission.)

and KGd$_3$F$_{10}$:Eu^{3+} (165%),[49] RbGd$_3$F$_{10}$:Eu^{3+} (150%),[50] KGdF$_4$:Eu^{3+} (175%),[51] and CsGd$_2$F$_7$:Eu^{3+} (150%).[52] The high efficiency of BaF$_2$:1% Gd, 1% Eu is surprising, but it is well known that in BaF$_2$ the Ln^{3+} ions form clusters which may provide the required proximity for Gd^{3+} and Eu^{3+}.

5.8.3.2 Sensitization of Gd^{3+}

As noted, sensitization is required if the Gd–Eu couple is to be applied successfully. The requirements of a good sensitizer are that it should:

- absorb the VUV photons of the rare-gas discharge efficiently;
- transfer its energy to the ^{6}G state of Gd^{3+}, made possible by good spectral overlap of the emission of the sensitizer and absorption of the activator;
- not produce quenching of visible emission from the activator.

There are a number of possible ways in which Gd^{3+} could be sensitized, which are now considered. These include (1) sensitization with the f–d transition on another lanthanide, (2) sensitization using the allowed s–p transition on a heavy ns^2 ion, or (3) sensitization with the host valence-conduction band transition.

5.8.3.2.1 Sensitization of Gd^{3+} with 4f→5d transitions of rare-earth ions. Allowed f–d transitions of many of the rare-earth ions occur in the VUV.[53] Tm^{3+} and Nd^{3+} have both been shown to sensitize Gd^{3+} in GdLiF$_4$ but they each also provide an alternate cross-relaxation pathway for energy transfer, which is more efficient than the Gd–Eu CRET. As a result, after the CRET, the Tm^{3+} and Nd^{3+} ions are left in low-lying excited states, which yield, for the first photon, IR emission. This of course defeats the goal of a visible quantum cutter. For Tm^{3+}, the dominant CRET pathway involves a nonradiative transition $^6G \rightarrow {}^6I$

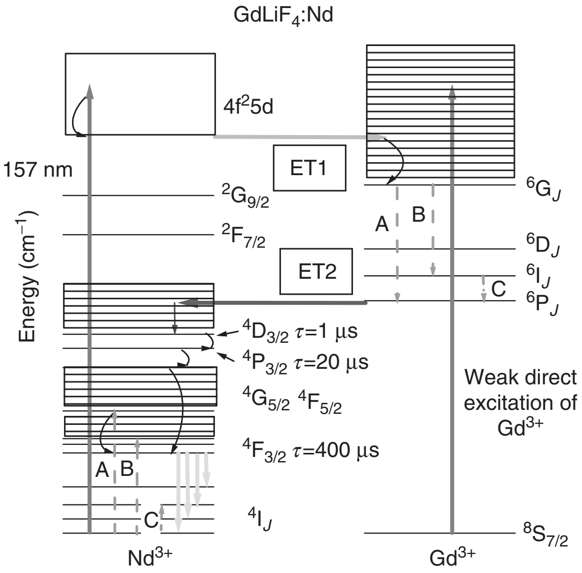

Figure 83 Energy level diagrams of Nd^{3+} and Gd^{3+} in $GdLiF_4$:Nd with the relevant energy levels labeled. The open box represents the $4f^25d$ band of Nd^{3+}. The boxed areas with horizontal lines represent energy regions with a high density of $4f^n$ levels. ET1 and ET2 indicate resonant energy transfer processes. Labels A, B, and C denote three cross-relaxation energy transfer processes. Some of the intrinsic lifetimes are indicated. (From Jia, W., Zhou, Y., Feofilov, S.P., Meltzer, R.S., Jeong, J.Y., and Keszler, D., *Phys. Rev. B*, 72, 075114, 2005. With permission.)

on Gd^{3+} and $^3H_4 \rightarrow {}^3H_4$ on Tm^{3+}.[38] A possible explanation for the dominance of the Gd–Tm couple over the Gd–Eu couple, under conditions in which dipole–dipole interactions dominate over exchange, is that the largest electric dipole-reduced matrix elements occur for the $^6G_{7/2} \rightarrow {}^6I_J$ transitions of Gd^{3+} in $GdLiF_4$.[38] According to Eq. 3, the CRET rate is proportional to the oscillator strength of the Gd^{3+} transition ($f_{Gd} \propto (U^{(6)})^2$), which is two orders of magnitude greater for the $^6G_{7/2} \rightarrow {}^6I_J$ transitions of Gd^{3+} relative to that of the $^6G_{7/2} \rightarrow {}^6P_J$ transitions. The required resonance for CRET in Tm^{3+} occurs for the $^6G_{7/2} \rightarrow {}^6I_J$ transition of Gd^{3+}, whereas for Eu^{3+} the energy resonance occurs for the $^6G_{7/2} \rightarrow P_J$ transition.

The Gd–Nd couple has been studied in great detail, especially its dynamics.[54] This provides a great deal of insight into the CRET process responsible for quantum cutting. As for the Gd–Tm couple, it is the $^6G_{7/2} \rightarrow {}^6I_J$ transitions of Gd^{3+} that dominate in the CRET. The energy level diagrams are shown in Figure 83. It shows the relevant $4f^3$ and $4f^7$ energy levels of Nd^{3+} and Gd^{3+}. Boxed regions with horizontal lines indicate a high density of states of the two $4f^n$ configurations for which rapid multiphonon relaxation will populate the lowest metastable levels. The open box represents the $4f^25d$ band of Nd^{3+}. The $4f^65d$ band of Gd^{3+} is off the energy scale and is not relevant here. The long vertical arrow represents the VUV excitation of Nd^{3+} into the $4f^25d$ band. Rapid energy transfer to a nearly resonant $4f^7$ state of Gd^{3+}, labeled by ET1, followed by rapid nonradiative relaxation, populates the ^6G_J states of Gd^{3+}. Although CRET from the $^6G_{7/2}$ state of Gd^{3+} can occur via two paths, labeled by the dashed arrows A and B, pathway B dominates. This involves a transition $^6G_{7/2} \rightarrow {}^6I_J$ on Gd^{3+} coupled with a $^4I_{9/2} \rightarrow {}^4F_{5/2}$, $^2H_{9/2}$, or $^4F_{7/2}$ transition on Nd^{3+}. A comparison of the energy level diagrams for Gd^{3+} and Nd^{3+} indicate that the transitions labeled B are likely to have good resonances. The larger reduced matrix elements for the $^6G_{7/2} \rightarrow {}^6I_J$ transitions would help to explain the dominance of this CRET pathway as for the Gd–Tm couple if dipole–dipole interactions dominate. ^6I_J then further relaxes to ^6P_J via a second CRET process, shown by the dashed arrows labeled C in Figure 83, and this excites the $^4I_{13/2}$ state of Nd^{3+}. The occurrence of these energy transfer processes is supported by the dynamical studies discussed below. The ^6P_J states of Gd^{3+} then transfer their energy to the nearly resonant $4f^3$ states of Nd^{3+}, as shown by the solid arrow labeled ET2. Above the $^4D_{3/2}$ state of Nd^{3+} there is a very dense, almost continuous group, of energy levels from the $4f^3$ configuration among which the $^2L_{17/2}$ at ~32,000 cm^{-1} is in closest resonance with the $^6P_{7/2}$ states of Gd^{3+}. Once excited, these will relax almost immediately to the $^4D_{3/2}$ level, which exists long enough to produce observable emission. Its decay, whose lifetime is about 1 μs, is dominated by nonradiative relaxation to the $^2P_{3/2}$ level which exists much longer with a lifetime of ~20 μs. These and subsequent multiphonon relaxations ultimately feed the $^4F_{3/2}$ level, leading to the emission of a second IR photon. The absolute experimentally determined quantum yield, which is dominated by IR emission, has been estimated as 1.05 ± 0.3.[54]

When a sample of $GdLiF_4$ containing 2% Nd^{3+} is excited at 157 nm with a molecular F_2 laser, one sees a buildup of the $^6P_{7/2}$ transition of Gd^{3+} at 313 nm, as shown in Figure 84 by the bold solid curve.[54] This buildup has two components. One is very fast, at a rate that exceeds the time resolution of these experiments (<50 ns, limited by some background scattered light from the laser discharge and defect luminescence), which represents about 20% of the population feeding. The second is a slower buildup over several microseconds, representing about 80% of the feeding. The cause of these two components becomes clear from the dynamics of the ^6I emission of Gd^{3+} at 281 nm, shown by the dotted curve in Figure 84. Its decay rate coincides with the $^6P_{7/2}$ population buildup rate. Also shown by the dot–dashed curve is the emission at 866 nm from the $^4F_{3/2}$ state of Nd^{3+}, which also builds up within the temporal resolution of the experiment. Thus we conclude, as suggested by an earlier discussion of the reduced matrix elements, that cross relaxation process B from Figure 76 is the dominant one in quantum splitting. However, the fact that the $^6P_{7/2}$ population does have a very fast component indicates that there may also be a contribution from the CRET process labeled as A in Figure 83. The relaxation of Gd^{3+} from ^6I to ^6P in a few microseconds occurs through the CRET process labeled C in Figure 83. In this process an Nd^{3+} ion is excited from the $^4I_{9/2}$ ground manifold to $^4I_{13/2}$, for which there is a good resonance match with the $^6I \rightarrow {}^6P$ transitions on Gd^{3+}.

The behavior of the dynamics of process C and its concentration dependence provides important information on the role of donor–donor energy transfer among the Gd^{3+} ions. The relaxation rate scales nearly linearly with concentration as expected for a Gd–Nd CRET. The nearly exponential relaxation processes for all concentrations suggest that energy migration among the Gd^{3+} ions is fast compared with the CRET relaxation rates. In such cases, the Gd^{3+} excitation samples all sites, thereby spending a fraction of its time nearby an Nd^{3+} ion with which it can undergo CRET. If, after energy transfer from the $4f^25d$ state of Nd^{3+} to Gd^{3+}, the energy remained localized on the Gd^{3+} ion, the CRET rates would be highly nonexponential.

The excited Gd^{3+} ions in the $^6P_{7/2}$ state then undergo energy transfer to the nearly resonant $4f^3$ states of Nd^{3+} at a rate described by the decay of the Gd^{3+} $^6P_{7/2}$ emission. Proof of this second step is obtained by monitoring the $^4D_{3/2}$ emission under 157 nm excitation. It is observed that this emission closely follows the $Gd^{3+} \rightarrow {}^6P_{7/2}$ population with a small delay and that it has zero population immediately after the laser excitation (see Figure 84). The fact that the $^4D_{3/2}$ population closely follows the excited Gd^{3+} population demonstrates that energy transfer from Gd^{3+} to Nd^{3+} does occur, a process that is necessary for the second step of the quantum-splitting process.

Estimates of the maximum CRET rate for process B, based on Eq. 4 which assumes dipole–dipole interactions, indicate that under the most favorable conditions it can have a maximum value of $\sim 5 \times 10^6$ s^{-1} if all transitions of the two ions were resonant. Even this extreme assumption falls well short of explaining the observed rate of $>2 \times 10^7$ s^{-1} and

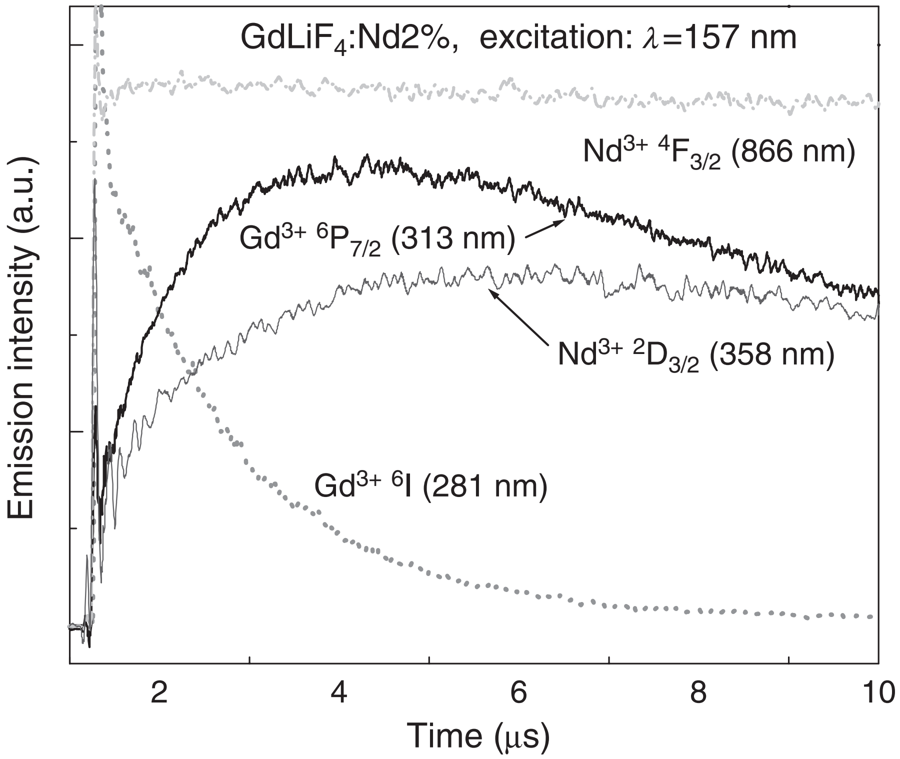

Figure 84 Time evolution of the ^6I (281 nm) and $^6P_{7/2}$ (313 nm) emission intensities of Gd^{3+} and the $^4D_{3/2}$ and $^4F_{3/2}$ emission intensities of Nd^{3+} in a GdLiF$_4$:Nd2% sample under 157 nm pulsed laser excitation. (From Jia, W., Zhou, Y., Feofilov, S.P., Meltzer, R.S., Jeong, J.Y., and Keszler, D., *Phys. Rev. B*, 72, 075114, 2005. With permission.)

would require the absence of fast donor–donor transfer, which seems unlikely. Thus, the above analysis of the experiments points strongly to the dominant role of exchange interactions in facilitating the CRET responsible for quantum splitting in GdLiF$_4$:Nd. This conclusion is probably valid for the Gd–Eu pair as well, since the CRET step appears very fast there as well despite the fact that the relevant Eu^{3+} oscillator strengths are even smaller than those for Nd^{3+}. Thus, the quantum splitting appears to require nearest-neighbor interactions facilitated by rapid energy migration within the donor system and hence, the requirement for stoichiometric or very highly concentrated Gd systems. Studies of quantum splitting as a function of Gd^{3+} concentration support this conclusion.[55]

Er^{3+} has also been shown capable of sensitizing Gd^{3+} in GdLiF$_4$:Er^{3+},Tb^{3+}.[44] In this system, Er^{3+} serves a double role both as sensitizer and replacement for Eu^{3+} to provide the CRET channel. For Ln^{3+} with more than half-filled 4f shells, there is a high-spin (HS, sextet for Er^{3+}) and a low-spin (LS, quartet) state in the 4f^{10}5d configuration, as shown on the right portion of Figure 85. Er^{3+} is excited to its 4f^{10}5d low-spin state by a VUV photon. This is followed by a CRET involving an allowed 5d–4f transition on Er^{3+} and a 4f–4f transition on Gd^{3+}. The spectral overlap between the 5d→4f transitions of Er^{3+}, shown by the dark bars on the left in Figure 85, and the absorption transitions from the ground state of Gd^{3+} shown by the vertical lines below the Er^{3+} transitions, are good for a number of pathways especially those indicated by the dashed lines labeled 1 and 2. These leave Er^{3+} in either the ^4G_J or ^4F_J states, which relax rapidly to $^4S_{3/2}$, producing the first photon. Pathways leaving Er^{3+} in the ^4I_J levels also exist and will limit the quantum efficiency for visible emission. After CRET, the excited Gd^{3+} ion transfers its energy to Tb^{3+}, which emits

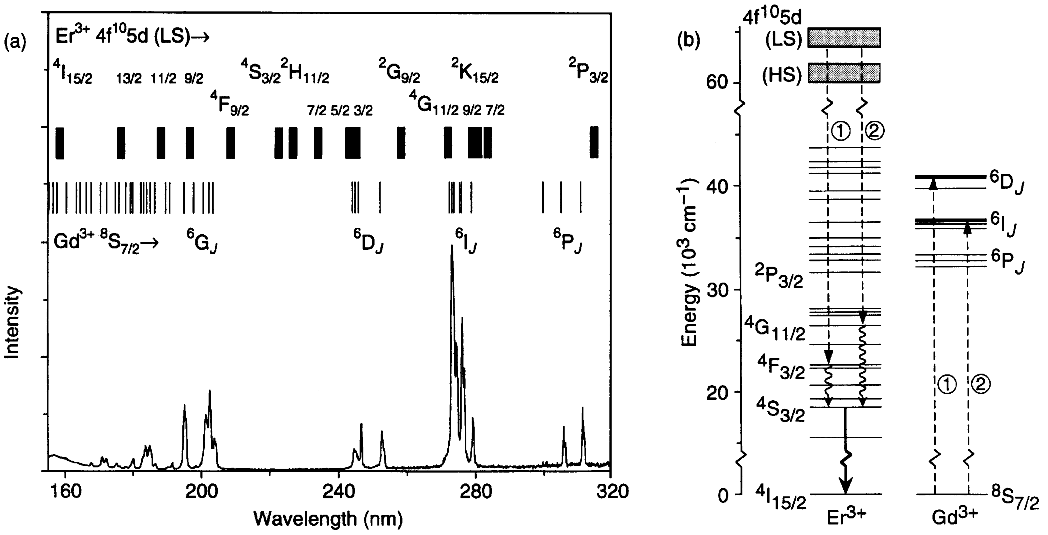

Figure 85 Excitation spectrum of LiGdF4:Eu^{3+} 0.1% monitoring $^5D_0 \rightarrow {}^7F_2$ emission of Eu^{3+} (614 nm) at 300 K. The vertical lines above the spectrum denote the spectral positions of all Gd^{3+} excitations in this region. The broad vertical bars denote the spectral positions of all Er^{3+} emissions from the low-spin $4f^{10}5d$ state in this region. (b) Energy level diagram for LiGdF4:Er^{3+}, showing the cross-relaxation possibilities between Er^{3+} and Gd^{3+} required for visible quantum cutting. (From Wegh, R.T., van Loef, E.V.D., and Meijerink, A., *J. Lumin.*, 90, 111, 2000. With permission.)

a second visible photon from its $^5D_3$ or $^5D_4$ states. A comparison of the lifetimes of the high-spin and low-spin $4f^{10}5d$ states of Er^{3+} in LiYF$_4$ and LiGdF$_4$, which are both very fast (nanoseconds), provides strong evidence that even when one of the transitions in the CRET is parity allowed, exchange interactions still dominate over dipole–dipole energy transfer. Estimates of the efficiency of the energy transfer process show that about 30% of the excited Er^{3+} ions cross-relax with Gd^{3+} such that Er^{3+} is left in an excited state above $^4S_{3/2}$, which can lead to visible emission. This implies a maximum quantum efficiency of 130% for visible emission. Since some UV emission occurs, the calculated maximum visible quantum efficiency of this system is 110%, but nonradiative processes will further reduce this value probably undermining the application of this phosphor.

5.8.3.2.2 Sensitization of Gd^{3+} with ns^2 *ions.* Sensitization of Gd^{3+} by Pb^{2+} has recently been considered.[56] Pb^{2+} falls in a class of ions whose ground states lie in the ns^2 configuration and whose first excited states are contained in the ns^{1}np^1 configuration containing the ^3P and ^1P levels. These states occur in the deep UV or vacuum UV. These ns^2 ions include Ga$^+$, In$^+$, Tl$^+$, Ge^{2+}, Sn^{2+}, Pb^{2+}, Sb^{3+}, and Bi^{3+}. Their lowest excited state is the $^3P_0$ level whose transition from the ground state is strongly forbidden. The next levels are the $^3P_1$ and $^3P_2$ states whose transitions from the ground state are spin-forbidden but which are nonetheless quite strong due to spin–orbit coupling. These could be used to absorb the VUV photons. Above these is the $^1P_1$ level, which is spin-allowed from the ground state. The actual location of the levels of the ns^{1}np^1 excited states depends strongly on the host lattice since these ns and np electrons are not shielded by outer-electron shells. After excitation to the $^1P_0$ and $^3P_{1,2}$ states, resonant energy transfer to the ^6G levels of Gd^{3+} could be utilized to sensitize the Gd–Eu CRET.

A recent study of Pb^{2+} in BaF$_2$/GdF$_3$ containing Pb^{2+} on the Ba site and Eu^{3+} on the Gd site has shown that Pb^{2+} can be used to sensitize the Gd^{3+}–Eu^{3+} couple in these mixed crystals.[56] In this system, it is the higher energy $^3P_2$ emission that sensitizes ^6G. Unfortunately, the efficiency of quantum splitting is only 20% and is limited by back-transfer from the ^6G state of Gd^{3+} to the lower ($^3P_0$ and $^3P_1$) levels of Pb^{2+}. Spectroscopic studies of Pb^{2+} in a number of other fluorides have shown that in $KMgF_3$ the $^3P_1$ emission lies sufficiently high so that it might be possible for it to directly sensitize ^6G of Gd^{3+}.[56]

While the optical properties of many of the ns^2 ions have been characterized in alkali halides[57] and some oxides,[58] spectroscopic studies of ns^2 ions in other hosts are few. However, for Bi^{3+} it is known that the $^3P_1$ emission peak occurs at 280 nm in metaphosphates (LnP_3O_9)[59] and 250 nm in YPO_4 at room temperature and is not significantly quenched up to 330°C.[60] Sb^{3+} is known as an efficient sensitizer in mercury discharge-excited phosphors. The 6s6p levels of Tl^+ in alkali halides can be even higher than those of Pb^{2+}.[61] $^3P_1$ emission of Tl^+ in $KMgF_3$ peaks at about 210 nm[62] and could provide effective sensitization of the ^6G state of Gd^{3+}. In considering the application of ns^2 ions, it is desirable to have hosts containing large sites of high coordination to provide the highest possible energies for the ns^1np^1 excited states.

5.8.3.2.3 Sensitization of Gd^{3+} with host lattice absorption. Sensitization of Gd^{3+} using the intrinsic excited states of the host would be most desirable because it does not require additional doping of ions into the system and the host provides very strong absorption of the VUV excitation light. This requires that the host excited state transfers its energy effectively to ^6G of Gd^{3+}. This could occur if the host emission were to overlap the Gd^{3+} absorption to ^6G at about 204 nm (or higher-lying states of Gd^{3+} which relax predominantly to ^6G) or if some efficient intersystem crosses between the STE and the Gd^{3+} ^6G potential surface.

Intrinsic emission of solids at or below 200 nm is rare. Typically, after host absorption, emission will occur from the STE state that involves a large Stokes shift. Such host emission has been studied in alkaline-earth fluorides[63] and oxides.[64] The shortest wavelength emission reported occurs for $ScPO_4$, which peaks at 211 nm but extends beyond the lowest ^6G level at 204 nm, making sensitization of quantum splitting a possibility.

5.8.3.3 Cross-relaxation energy transfer with parity-allowed f–d transitions

Having considered CRET based on 4f–4f transitions on both ions of the pair, we now examine the case of 4f–5d transitions on (1) one or (2) both of the ions. While we have considered a few examples in describing sensitization of Gd^{3+}, we now consider the situation more generally. These processes can be understood by returning to Figure 79. For case (1), after excitation of the $4f^{n-1}5d$ state of the sensitizer (state A3), an energy transfer occurs in which the first ion undergoes a parity-allowed transition to a lower-lying excited state of its $4f^n$ configuration (state A2) while the second ion is excited from its ground state (B1) to an excited state within its $4f^{n'}$ electronic configuration (B2). Both ions are thus left in excited states from which they can each emit a visible photon, accomplishing quantum cutting. As noted in Section 5.8.3.1, CRET rates involving parity allowed f–d transitions on one or both ions of a pair can be very fast even in diluted systems. The scheme requires that the decay rate of the $4f^{n-1}5d$ state of the sensitizer in the singly doped material be less than the CRET rate with the second ion (activator) of the pair. As the 4f–5d transitions are allowed electric dipole processes, they provide strong direct VUV absorption of the exciting photons.

The Pr–Tm pair, where both ions are present as dopants, has been examined in several hosts where the lowest Pr^{3+} 4f5d level lies below $^1S_0$, the usual case for oxides.[65] Here Pr^{3+} serves as the sensitizer transferring part of its energy to the Tm^{3+} ion, which participates as the activator. The situation is illustrated in Figure 86. For this pair, the Pr^{3+} undergoes a transition from its 4f5d state to a lower-lying state of the $4f^2$ configuration while a nearly resonant transition occurs on Tm^{3+} from its $^3H_6$ ground state to its ^3P_J states. Two energy-conserving CRET pathways, labeled A and B, are shown in Figure 86 (insert). However, as seen in Figure 86, in double-doped samples containing 1% Pr^{3+} and 5% Tm^{3+} there is no evidence of the Pr^{3+} excitation features when detecting only Tm^{3+} emission, (for comparison, see the excitation spectra of the singly doped Pr^{3+} samples in Figure 86). This indicates that there is no significant CRET in either YBO_3 or YPO_4, despite the fact that the required resonances are present. This is a disappointing result, which suggests that it may not be so easy to implement a scheme involving 5d→4f transition on the first ion and 4f→4f transition on the second ion unless one of the ions is either stoichiometric as part of the host or very high concentrations of at least one of the ions is utilized. Nonetheless, there are many other possible ion pairs and hosts that should be examined. Some general guidelines for identifying these materials are outlined below.

It has been found in many fluorides and in some oxides that several of the rare lanthanides fluoresce strongly in VUV. It therefore follows that these levels are metastable. The radiative decay rates of the $4f^{n-1}5d$ levels of the rare-earth ions are typically 10^7–10^8 s^{-1} for the lighter rare earths and about 10^6 s^{-1} for the heavier rare earths where the high-spin state lies lowest.[66] Since the spin of this lowest level exceeds that of any of the states of the $4f^n$ configuration, the transitions are all spin-forbidden and therefore weaker. In some of the fluorides containing the heavier lanthanides, emission is seen from both the low-spin and high-spin states if their splitting is sufficiently large relative to the maximum phonon energies of the material.[66] Thus, it may be possible to consider schemes that utilize either or both of these states. Cross-relaxation rates would then have to compete with the

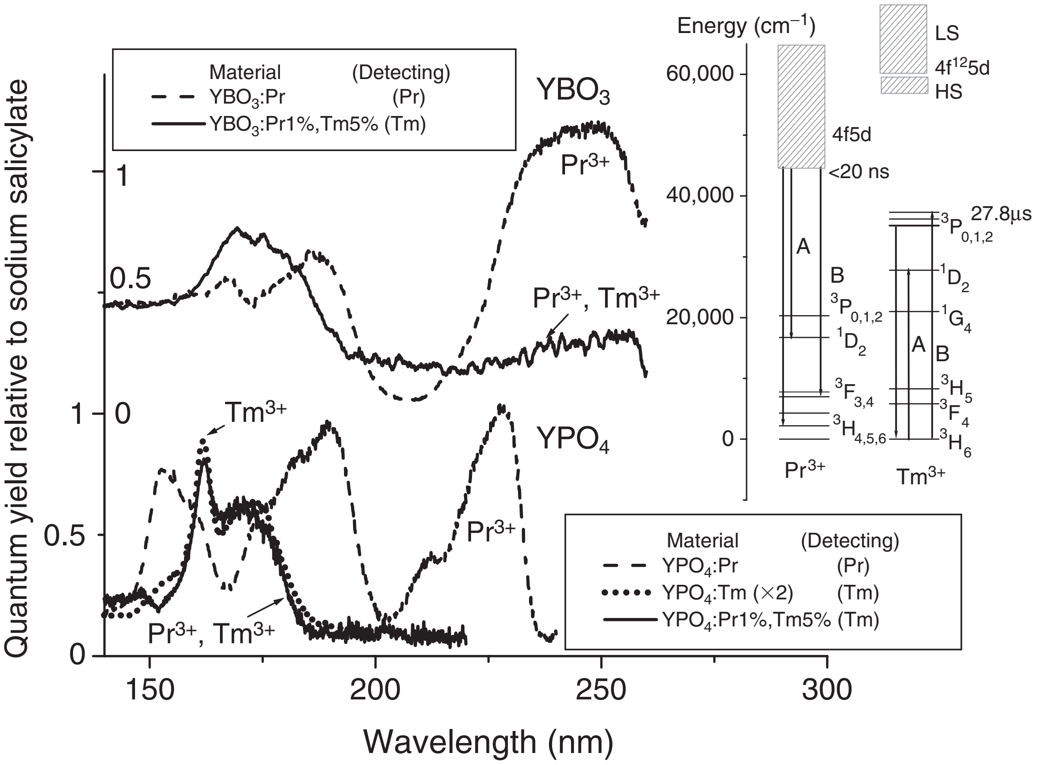

Figure 86 Excitation spectra at room temperature demonstrating the absence of Pr^{3+} to Tm^{3+} CRET in YPO_4 and YBO_3. None of the features of the Pr^{3+} excitation spectra appear in double-doped samples when only the Tm^{3+} emission is detected. The excitation spectra of the double-doped samples are not to scale. The insert shows the energy levels of Pr^{3+} and Tm^{3+} with two resonant CRET pathways labeled A and B. (Measured by the author.)

radiative rates. The fact that they are metastable makes them attractive candidates for CRET and multiphoton emission.

A number of considerations apply to the design of such phosphors. A sufficiently large gap must exist between the lowest $4f^{n-1}5d$ level and lower-lying states of the $4f^n$ configuration: about 5000 cm^{-1} for oxides with maximum phonon energies of about 1000 cm^{-1} and about 3000 cm^{-1} for fluorides with lower phonon energies. Here, hosts with lower phonon energies are better than those with higher energies. Although it will be necessary to satisfy the resonance condition on the cross relaxation, the large bandwidth of the 4f–5d transition implies that a resonance mismatch of 1000 cm^{-1} or more is still acceptable. It also follows that all of the crystal field transitions between one $^{2S+1}L_J$ manifold and another of the f^n configuration will satisfy the resonance condition, since the crystal field splittings within these manifolds are smaller than the bandwidth of the f–d transitions. As absorption of the activator at the excitation wavelength should be avoided or minimized, it may be necessary to use as low a concentration of the activator as possible.

The ions other than Pr^{3+} that are proven VUV emitters from their $4f^{n-1}5d$ configuration in fluoride hosts include[66,67] Nd^{3+}, Ho^{3+}, Er^{3+}, and Tm^{3+}. Nd^{3+} is of lower priority because of its poor visible emission properties. In oxides, VUV emission has been observed[68] for Nd^{3+} and Er^{3+} in YPO_4 but studies of such emission for other ions in oxides are very limited.

The energy locations of the lowest level of the $4f^{n-1}5d$ configuration of rare-earth ions with respect to their $4f^n$ ground states can be estimated quite well based on the work of Dorenbos.[53] The energy or the lowest $4f^{n-1}5d$ state can be expressed in terms of a host-dependent crystal depression energy, referred to as $D(A)$ where (A) identifies the host, and an energy, ΔE^{Ln}, that depends on the specific rare-earth ion. The emission of the sensitizer will involve the energy difference between the energy of the $4f^{n-1}5d$ state and the energy of the final state within the $4f^n$ configuration involved in the CRET less than the Stokes shift of the emission, which also depends only on the host and is typically between 1500 and 4000 cm^{-1}. As noted previously, for the heavier rare earths, there is a high-spin state about 2500–3000 cm^{-1} below the low-spin state for the relevant ions Ho^{3+}, Er^{3+}, and Tm^{3+}.[66]

One then needs to select the activator for the couple. The energy resonance condition requires that the lowest $4f^{n-1}5d$ emission energy must equal the appropriate $4f^n$ transition energy of the activator. Since the energy levels of the $4f^n$ states are well known and are nearly independent of the host, it is then possible to identify suitable ion pairs and hosts that satisfy the condition for resonant CRET pathways. As the cross-relaxation rates will depend on the particular oscillator strengths involved on the two ions, they will be quite variable from one host to another. At this time it is not possible to predict which transitions will have the largest oscillator strengths, although spin-allowed transitions should be the strongest in general.

The conditions required for case (2) utilizing parity-allowed f–d transitions on both ions of the couple are restrictive for trivalent rare-earth ions. Only Ce^{3+} as an activator ion has its $4f^{n-1}5d$ level at sufficiently low energy to emit visible emission, thereby providing the first photon in the quantum cutting. Evaluating whether the resonant condition of the CRET will be satisfied can be ascertained from the energy difference of the $4f^{n-1}5d$ state of Ce^{3+} and that of the sensitizing Ln^{3+} ions, given by ΔE^{Ln}, and from the $D(A)$ of the chosen host. In addition, the sensitizer must be chosen such that the transition resonant with the Ce^{3+} absorption must create a final $4f^n$ state for the sensitizer that provides for visible emission for the second photon. Satisfying all these conditions places severe limits on acceptable ions and hosts.

5.8.4 Quantum cutting using host lattice states—Auger and other processes

It has been demonstrated that quantum yields in excess of 1 occur in a number of materials excited into the host band states.[69,70] These include some well-known phosphors such as

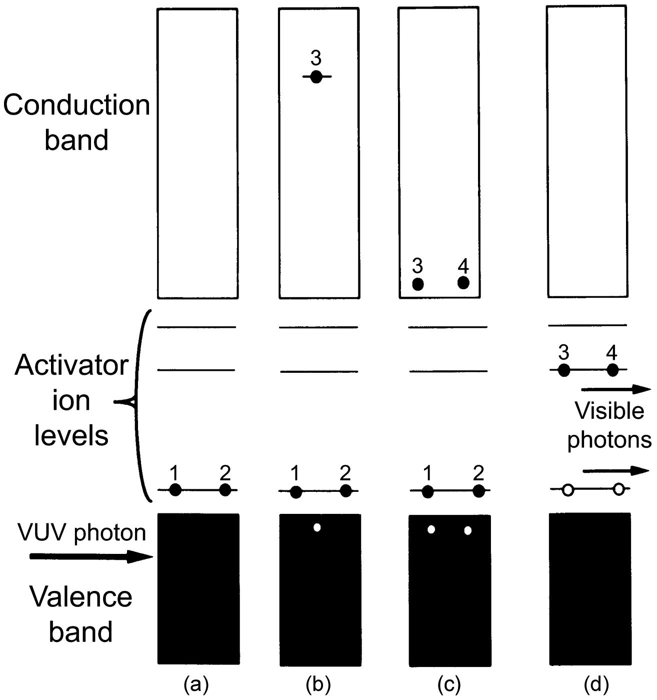

Figure 87 Interband Auger process. (a) Initial configuration before absorption of the VUV photon. Electrons 1 and 2 are the valence electrons of the activator ions. (b) Configuration after VUV absorption and creation of the first electron–hole pair. (c) Configuration after relaxation of the first electron to the bottom of the conduction band and creation of the second electron–hole pair. (d) Migration of electron–hole pairs to activator sites, leading to recombination and photon emission. (From Berkowitz, J.K. and Olsen, J.A., *J. Lumin.*, 50, 111, 1991. With permission.)

Zn_2SiO_4:Mn and Y_2O_3:Eu. This can occur when the photon energy exceeds twice the band gap energy but in practice, the quantum yield does not exceed unity until the photon energy is significantly greater than twice the band gap. In this Auger process, shown schematically in Figure 87, the initially excited electron transfers a portion of its energy to another electron promoting it to the conduction band and leaving the first electron also in the conduction band. Recombination of these electron-hole pairs at the activator sites gives rise to the emission of two photons. As discussed in several reviews by Ronda,[71,72] a minimum in the quantum yield usually occurs at about 2.5 times the band gap, often near the peak in the Xe discharge which has been the focus for excitation of phosphors in quantum-cutting lamps. While other rare gases can produce larger photon energies, as the exciting photon energy increases, the effective energy efficiency goes down, ultimately compromising the use of these rare gases unless quantum yields even greater than 2 can be found. Thus, barring the discovery of a material with much improved properties, useful quantum-splitting phosphors based on host lattice excitation and Auger processes do not seem likely.

5.8.5 Conclusions

The task of developing commercially viable quantum-splitting phosphors is very difficult. Successful materials must satisfy simultaneously a number of requirements including good absorption of VUV photons, emission of both photons in the visible region, quantum efficiencies in excess of 150%, resistance to damage by VUV photons, etc. Two schemes have shown considerable promise; cascade emission and CRET. In both cases, existing materials are still inadequate with respect to one or more of the necessary conditions. While excellent cascade emission from Pr^{3+} has been demonstrated, the emission does not occur in the desired part of the spectrum. Thus, either other ions must be identified, which yield suitable photon cascade emission or energy transfer schemes need to be found that convert the 406 nm emission from the first step to longer wavelengths. Phosphor schemes based on CRET using concentrated Gd^{3+} hosts have demonstrated excellent internal quantum efficiencies and suitable visible emission but effective sensitization of Gd^{3+} has still not been successfully implemented. Despite these difficulties and the current absence of a demonstrated phosphor, the potential rewards of improved lamp efficiencies and elimination of Hg dictate that research on quantum-splitting phosphors should continue.

Acknowledgments

The author is appreciative of support from the U.S. National Science Foundation (Grant 0305400) for his own work on quantum-splitting phosphors, some of which appears in this chapter. Thanks are also due to Sergey Feofilov, Douglas Keszler, Kailash Mishra, and Madis Raukas for many useful discussions. Stefan Kuck kindly supplied his original drawings that are reproduced as Figure 75, Figure 76, and Figure 77.

References

1. Wegh, R.T., Meijerink, A., Lamminmaki, R.-J., and Holsa, J., *J. Lumin.*, 87–89, 1002, 2000.
2. Peijzel, P.S., Meijerink, A., Wegh, R.T., Reid, M.F., and Burdick, G.W., *J. Solid. State Chem.*, 178, 448, 2005.
3. Dexter, D.L., *Phys. Rev.*, 108, 630, 1957.
4. Piper, W.W., DeLuca, J.A., and Ham, F.S., *J. Lumin.*, 8, 344, 1974.
5. Sommerdijk, J.L., Bril, A., and de Jager, A.W., *J. Lumin.*, 8, 341, 1974.
6. Wegh, R.T., Donker, H., Oskam, K., and Meijerink, A., *Science*, 283, 663, 1999.
7. Elias, L.R., Heaps, W.S., and Yen, W.M., *Phys. Rev.*, 88, 4989, 1973.
8. van der Kolk, E., Dorenbos, P., van Eijk, C.W.E., Vink, A.P., Fouassier, C., and Guillen, F., *J. Lumin.*, 97, 212 2002.
9. Kuck, S., Sokolska, I., Henke, M., and Osiac, E., *Chem. Phys.*, 310, 139, 2005.
10. Kuck, S. and Sokolska, I., *Chem. Phys. Lett.* 364, 273, 2002.
11. Sokolska, I. and Kuck, S., *Chem. Phys.* 270, 355, 2001.
12. van der Kolk, E., Dorenbos, P., and van Eijk, C.W.E., *Opt. Commun.*, 197, 317, 2001.
13. Vink, A.P., Dorenbos, P., de Haas, J.T.B., Donker, H., Rodnyi, P.A., Avanesov, A.G., and van Eijk, C.W.E., *J. Phys.: Condens. Matter*, 14, 8889, 2002.
14. Rodnyi, P.A., Mishin, A.N., and Potapov, A.S., *Opt. Spectrosc.*, 93, 714, 2002.
15. Vink, A.P., Dorenbos, P., and van Eijk, C.W.E., *J. Solid. State Chem.*, 171, 308, 2003.
16. Le Masson, N.J.M., Vink, A.P., Dorenbos, P., Bos, A.J., van Eijk, C.W.E., and Chaminade J.P., *J. Lumin.*, 101, 175, 2003.
17. Solarz, P., Dominiak-Dzik, G., Lisiecki, R., and Ryba-Romanowski, W., *Radiat. Meas.*, 38, 603, 2004.
18. Pappalardo, R., *J. Lumin.*, 14, 159, 1976.
19. Rodnyi, P.A., Potapov, A.S., and Voloshinovskii, A.A., *Opt. Spectrosc.*, 96, 862, 2004.
20. Kuck, S., Sokolska, I., Henke, M., Doring, M., and Scheffler, T., *J. Lumin.*, 102–103, 176, 2003.
21. Kuck, S., Sokolska, I., Henke, M., Scheffler, T., and Osiac, E., *Phys. Rev. B*, 71, 165112, 2005.
22. Zachau, M., Zwaschka, F., and Kummer, F., *Proc. Electrochem. Soc.*, 97–29, 314, 1998.
23. Vergeer, P., Babin, V., and Meijerink, A. *J. Lumin.*, 114, 267, 2005.

24. van der Kolk, E., Dorenbos, P., van Eijk, C.W.E., Vink, A.P., Weil, M., and Chaminade, J.P., *J. Appl. Phys.*, 95, 7867, 2004.
25. Srivastava, A.M. and Beers, W.W., *J. Lumin.*, 71, 285, 1997.
26. Srivastava, A.M., Doughty, D.A., and Beers, W.W., *J. Electrochem. Soc.*, 143, 4113, 1996.
27. Srivastava, A.M., Doughty, D.A., and Beers, W.W., *J. Electrochem. Soc.*, 144, L190, 1997.
28. van der Kolk, E., Dorenbos, P., and van Eijk, C.W.E., *J. Phys.: Condens. Matter*, 13, 5471, 2001.
29. Rodnyi, P.A., Berezovskaya, I.V., Voloshinovskii, A.S., Stryganyuk, G.B., and Potapov, A.S., *Opt. Spectrosc.*, 94, 550, 2003.
30. van der Kolk, E., Dorenbos, P., Vink, A.P., Perego, R.C., and van Eijk, C.W.E., *Phys. Rev. B*, 64, 195129, 2001.
31. Vink, A.P., Dorenbos, P., and van Eijk, C.W.E., *Phys. Rev. B*, 66, 075118, 2002.
32. Vink, A.P., van der Kolk, E., Dorenbos, P., and van Eijk, C.W.E., *J. Alloy Compd.*, 341, 338, 2002.
33. Huang, S.H., Wang, S.J., Meltzer, R.S., Srivastava, A.M., Setlur, A.A., and Yen, W.M., *J. Lumin.*, 94–95, 119, 2001.
34. Huang, S.H., Lu, L., Jia, W., Wang, S.J., Yen, W.M., Srivastava, A.M., and Setlur, A.A., *Chem. Phys. Lett.*, 348, 11, 2001.
35. Huang, S.H., Wang, S.J., Chen, B.J., Jia, D., and Yen, W.M., *J. Lumin.*, 102–103, 344, 2003.
36. Wang, J.W., Turos-Matysiak, R., Grinberg, M., Yen, W.M., and Meltzer, R.S., *J. Lumin.*, in press, 2006.
37. Wegh, R.T., Donker, H., and Meijerink, A., *Phys. Rev. B,* 56, 13841, 1997.
38. Peijzel, P.S., Schrama, W.J.M., and Meijerink, A., *Mol. Phys.*, 102, 1285, 2004.
39. Yang, Z., Lin, J.H., Su, M.Z., Tao, Y., and Wang, W., *J. Alloy Compd.*, 308, 94, 2000.
40. Peizel, P.S., Wegh, R.T., Meijerink, A., Holsa, J., and Lamminmaki, R.-J., *Opt. Commun.*, 204, 195, 2002.
41. Peijzel, P.S. and Meijerink, A., *Chem. Phys. Lett.*, 401, 241, 2005.
42. Dexter, D.L., *J. Chem. Phys.*, 21, 836, 1953.
43. Kushida, T., *J. Phys. Soc.* (*Japan*), 34, 1334, 1973.
44. Wegh, R.T., van Loef, E.V.D., and Meijerink, A., *J. Lumin.*, 90, 111, 2000.
45. Wegh, R.T., Donker, H., Oskam, K., and Meijerink, A., *J. Lumin.*, 82, 93, 1999.
46. Feldmann, C., Justel, T., Ronda, C.R., and Wiechert, D.U., *J. Lumin.*, 92, 245, 2001.
47. Liu, B., Chen, Y., Shi, C., Tang, H., and Tao, Y., *J. Lumin.*, 101, 155, 2003.
48. You, F.T., Wang, Y.X., Lin, J.H., and Tao, Y., *J. Alloy Compd.*, 343, 151, 2002.
49. Kodama, N. and Watanabe, Y., *Appl. Phys. Lett.*, 84, 4141, 2004.
50. You, F.T., Huang, S.H., Liu, S.M., and Tao, Y., *J. Solid. State Chem.*, 177, 2777, 2004.
51. You, F.T., Huang, S.H., Liu, S.M., and Tao, Y., *J. Lumin.*, 110, 95, 2004.
52. Karbowiak, M., Mech, A., and Ryba-Romanowski, W., *J. Lumin.*, 114, 65, 2005.
53. Dorenbos, P., *J. Lumin.*, 91, 155, 2000.
54. Jia, W., Zhou, Y., Feofilov, S.P., Meltzer, R.S., Jeong, J.Y., and Keszler, D., *Phys. Rev. B*, 72, 075114, 2005.
55. Zhou, Y., Feofilov, S.P., Jeong, J.Y., Keszler, D.A., and Meltzer, R.S., *J. Lumin.*, 264, 119, 2006.
56. Babin, V., Oskam, K.D., Vergeer, P., and Meijerink, A., *Radiat. Meas.*, 38, 767, 2004.
57. Fukuda, A., *J. Phys. Soc.* (*Japan*), 27, 96, 1969.
58. van der Steen, A.C. and Dijcks, L.T.F., *Phys. Status Solidi B*, 104, 283, 1981.
59. Oomen, E.W.J.L. and Blasse, G., *J. Solid State Chem.*, 75, 201, 1988.
60. Justel, T., Huppertz, P., Mayr, W., and Wiechert, D.U., *J. Lumin.*, 106, 225, 2004.
61. Ranfagni, A., Mugnai, D., and Bacci, M., *Adv. Phys.*, 32, 823, 1983.
62. Aminov, I.K., Nikitin, S.I., Silkin, N.I., Shakhov, A.A., and Yusupov, R.V., *J. Phys.: Condens. Matter*, 14, 13835, 2002.
63. Beaumont, J.H., Hayes, W., Kirk, D., and Summers, G.P., *Proc. Roy. Soc., Ser. A*, 315, 1970.
64. van Pieterson, L., Heeroma, M., de Heer, E., and Meijerink, A., *J. Lumin.*, 91, 177, 2000.
65. Jia, W., Zhou, Y., Keszler, D.A., Jeong, J.Y., Jang, K.W., and Meltzer, R.S., *Phys. Status Solidi C* 2, 48, 2005.

66. Wegh, R.T. and Meijerink, A., *Phys. Rev. B,* 60, 10820, 1999.
67. Becker, J., Gesland, J.Y., Yu, N., Kirikova, Krupa, J.C., Makhov, V.N., Runne, M., Queffelec, M., Uvarova, T.V., and Zimmerer, G., *J. Alloy Compd*., 275–277, 205, 1998.
68. Peijzel, P.S., Vergeer, P., Meijerink, A., Reid, M.F., Boatner, L.A., and Burdick, G.W., *Phys. Rev. B*, 71, 045116, 2005.
69. Ilmas, E.R. and Savikhina, T.I., *J. Lumin.*, 1/2, 702, 1970.
70. Berkowitz, J.K. and Olsen, J.A., *J. Lumin.*, 50, 111, 1991.
71. Ronda, C.R., *J. Alloy Compd*., 225, 534, 1995.
72. Ronda, C.R., *J. Lumin.*, 100, 301, 2002.

chapter five — section nine

Phosphors for lamps

Hiroto Tamaki and Yoshinori Murazaki

Contents

5.9 Phosphors for white light-emitting diodes 533
  5.9.1 Brief history of the white-LED phosphor development 533
  5.9.2 Structure and features of white LEDs 534
  5.9.3 White LEDs excited by blue light 534
    5.9.3.1 The blue-YAG white system 534
    5.9.3.2 Phosphors other than YAG:Ce 538
      5.9.3.2.1 Nitride phosphors 538
      5.9.3.2.2 Oxynitride phosphors 540
  5.9.4 White LEDs based on UV- or near-UV-emitting LEDs 540
  5.9.5 White emission obtained by three primary color LEDs 542
  5.9.6 Challenge of white LEDs in the future 542
References 542

5.9 Phosphors for white light-emitting diodes

Recently light-emitting diodes (LEDs), particularly white LEDs, have attracted much attention as new and economically advantageous all solid-state light sources. The development of LEDs has also stimulated research on phosphors used for white LEDs; this area is presently the most active in the field of phosphors. This section describes the state-of-the-art phosphors for white LEDs, which currently constitutes an area of high interest.

5.9.1 Brief history of the white-LED phosphor development

In 1991, Nichia Corporation pioneered the development of blue LEDs based on (In,Ga)N. This invention already raised the concept of an LED combined with a phosphor as was seen in a patent issued at this period.[1] It was 1996 when a white LED composed of a blue LED and a yellow-emitting $Y_3Al_5O_{12}:Ce^{3+}$ (denoted as YAG:Ce in this section) was first commercialized. The combination of blue and yellow light gives the sensation of white color by the principle of complimentary colors.[2,3] Since their introduction, this type of white LEDs, known as the “blue-YAG white”, has captured a substantial market because of their attractive properties such as compactness, light weight, and quick response.[4] These advantages fit quite well to the rapidly growing demand for backlighting small-sized liquid crystal displays, typically used in devices such as cellular phones and digital cameras. Since 1998, these LEDs have played a role in the automobile industry, because their high efficiency, high reliability, and low driving voltage satisfy the requirements in car illumination and gauge displays. At present, white LEDs have replaced the majority of other light sources for both the interior and exterior illumination of cars.

Since the beginning of the twenty-first century, high-power LEDs, which can be operated with input power of 1–3 W, have been placed in the market. This type of LED has an emitting area about ten times larger than that of conventional blue LEDs which is 350 μm^2. With their small size suitable for portable use and their high efficiency, these LEDs are now used as flashlights or spotlights. These lighting sources are expected to continue to increase their market share by invading areas such as general purpose illumination, headlights, and backlights for large-screen liquid crystal displays.

In the past few years, high-power UV LEDs have been developed by a number of companies and institutions. This has stimulated the research and development of phosphors, which can be excited by UV LEDs, emitting the three primary colors, blue, green, and red; white LEDs as well as devices emitting intermediate colors can then be obtained with the proper admixture of these tricolor phosphors. The white LEDs based on UV LEDs are superior to "blue-YAG white" in some respects; their high color-rendering performance in general illumination applications, their uniformity in the emitted white color, and wider chromaticity of backlight for liquid crystal displays are some of the apparent advantages. However, such devices have not been marketed on a large scale, because of lifetime and efficiency considerations.

Recently many reports and patents have been published on yellow phosphors other than YAG:Ce, for example thiogallates, silicates, SiAlON compounds, and oxynitrides activated mostly with Eu^{2+}.[5–12] As for emission color other than yellow, a red-emitting nitride phosphor, $(Sr,Ca)_2Si_5N_8:Eu^{2+}$, was developed and warm-white LEDs using this compound and YAG:Ce deposited on a blue LED was commercialized in 2003.[13] This technology has led to the production of white LEDs with high color-rendering index, the average index R_a being above 90, at any color temperature. This is generally accomplished by adding a red component (phosphor) to the emission spectrum of conventional "blue-LED YAG." The development of these warm-white LEDs has led to their applications in general purpose illumination like meeting household lighting demands. Since the development of $(Sr,Ca)_2Si_5N_8:Eu^{2+}$, a variety of phosphors including other nitrides have been developed, as shown in Table 12 and Table 13.

5.9.2 Structure and features of white LEDs

Presently three kinds of white LEDs have been proposed and constructed, as follows:

1. A yellow phosphor or two phosphors (red and green) are mounted on a blue LED.
2. A combination of two or more phosphors, spanning the blue to red spectrum, is applied to a UV or violet LED (365–420 nm).
3. Three LEDs of the primary colors are combined with each other.

The following section reviews (1) and (2), which use phosphors, in more detail.

5.9.3 White LEDs excited by blue light

5.9.3.1 The blue-YAG white system

As described above, the blue-YAG white is the white LED system invented first and is still the principal device found in the market. The device structure of this system is

Table 12 Luminescence Color and Chemical Composition of LED Phosphors

Type	Chemical composition	Luminescence color
Sulfide	(Ca,Sr)S:Eu [5]	Red
	ZnS:Cu,Al [6]	Green
Thiogallate	$CaGa_2S_4$:Eu [5]	Yellow
	$SrGa_2S_4$:Eu [5]	Green
Nitride	$(Ca,Sr)_2Si_5N_8$:Eu [17]	Red
	$CaSiAlN_3$:Eu [18]	Red
	$CaSiN_2$:Eu [19]	Red
Oxynitride	$BaSi_2O_2N_2$:Eu [11]	Blue-green
	$(Sr,Ca)Si_2O_2N_2$:Eu [11]	Yellow-green
	$Cax(Si,Al)_{12}(O,N)_{16}$:Eu [9, 10]	Orange
Silicate	$(Ba,Sr)_2SiO_4$:Eu [7]	Green
	Sr_2SiO_4:Eu [8]	Yellow
	$Ca_3Sc_2Si_3O_{12}$:Ce [20]	Green
Aluminate	$SrAl_2O_4$:Eu	Green
	$Sr_4Al_{14}O_{25}$:Eu	Blue-green

Table 13 Luminescence Color and Chemical Composition of UV and NUV LED Phosphors

Type	Chemical composition	Luminescence color
Apatite	$(Ca,Sr)_5(PO_4)_3Cl$:Eu	Blue
	$(Ca,Sr)_5(PO_4)_3Cl$:Eu,Mn	Blue-orange
Aluminate	$BaMgAl_{10}O_{17}$:Eu	Blue
	$BaMgAl_{10}O_{17}$:Eu,Mn	Blue-green
Oxysulfide	Y_2O_2S:Eu	Red
	Gd_2O_2S:Eu	Red
	La_2O_2S:Eu	Red
Silicate	$(Sr,Ba)_3MgSi_2O_8$:Eu	Blue
Others	$Ba_3MgSi_2O_8$:Eu,Mn [26]	Red
	Zn_2GeO_4:Mn	Yellow-green
	$LiEuW_2O_8$ [25]	Red

schematically shown in Figure 88 and with its emission spectrum shown in Figure 89. As shown in an emission and excitation spectra in Figure 90, the phosphor YAG:Ce absorbs the emission from a blue LED at 460 nm efficiently and converts it to a broad-band yellow emission. Internal quantum efficiency of this phosphor has been reported to be higher than 90%.[14] The blue emission, which is not used in excitation of the yellow light, is used as the blue component of the white emission, resulting in a small energy loss. This is a big advantage compared with the white LEDs based on UV-LEDs and is a feature of the structure seen in blue-YAG white LEDs.

The phosphor YAG:Ce has certain advantages as discussed below.

Emission color can be tuned in a wide range. Partial substitution of Y with Gd and Al with Ga can shift the emission wavelength of Ce between 510 and 590 nm without decreasing efficiency noticeably. By using just a single compound of YAG:Ce, one can obtain white emission of almost any color temperature, except for the warm white equivalent to an incandescent lamp. Luminescence and excitation spectra of YAG:Ce compounds with modified compositions are shown in Figure 91 and Figure 92, respectively. The color range obtained by YAG:Ce compositions is shown in Figure 93.

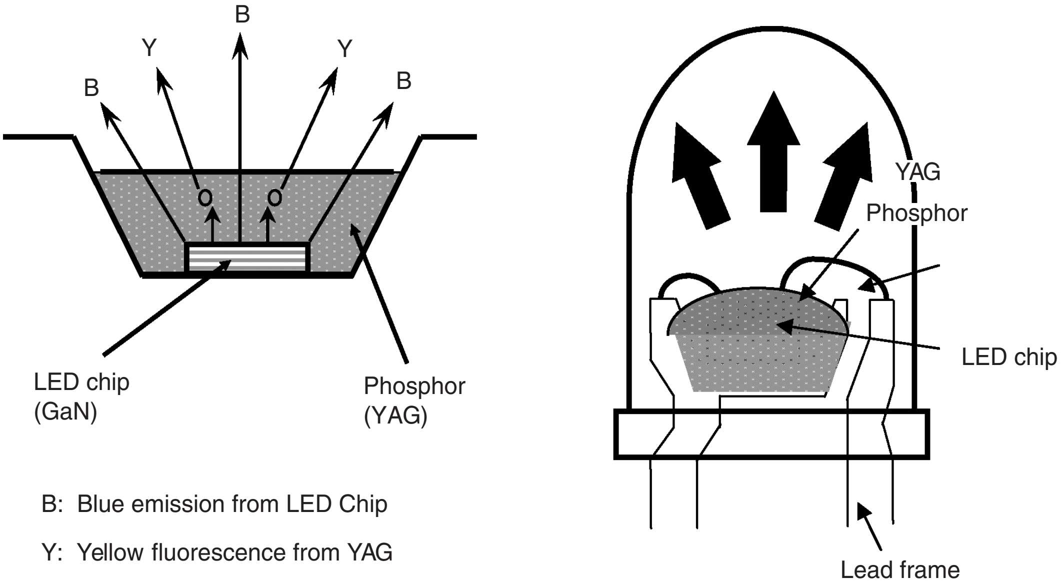
B
Y
Y
B
B
LED chip
(GaN)
Phosphor
(YAG)
B: Blue emission from LED Chip
Y: Yellow fluorescence from YAG
YAG
Phosphor
LED chip
Lead frame

Figure 88 The structure of a blue-YAG white LED (right) and a schematic illustration of light output from the diode.

The rugged crystal structure leads to chemical stability. The YAG:Ce phosphor deteriorates only slightly even under severe conditions by virtue of the rigid garnet-type crystal structure. As shown in Figure 94, Al ions occupy both a six-coordinated site in the center of an octahedron and a four-coordinated site in the center of a tetrahedron and Y ions substitute for an eight-coordinated site in the center of a dodecahedron.[15] The activator, Ce^{3+} ion, substitutes for the Y site.

The broad luminescence band contributes to high color-rendering index. The luminescence spectrum is composed of a band with a half width as wide as 130 nm. This broad emission band results in a high color-rendering index, which is well suited to light sources for general purpose illumination.

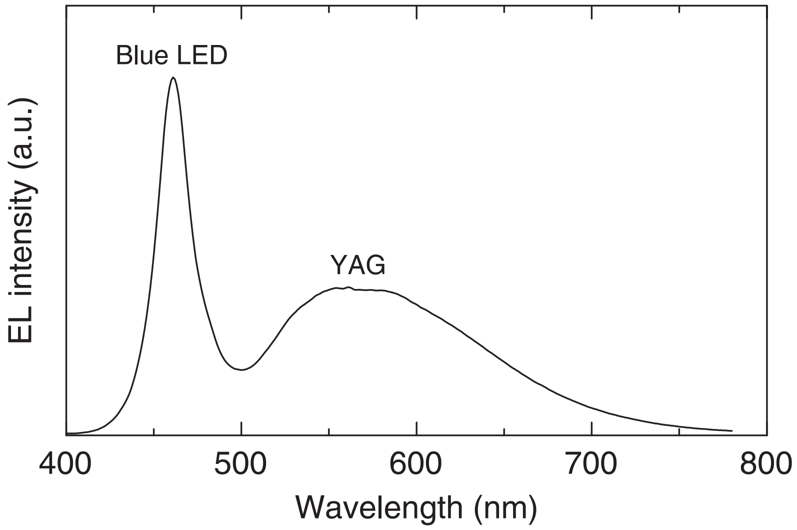

Figure 89 Emission spectrum of a blue-YAG white LED.

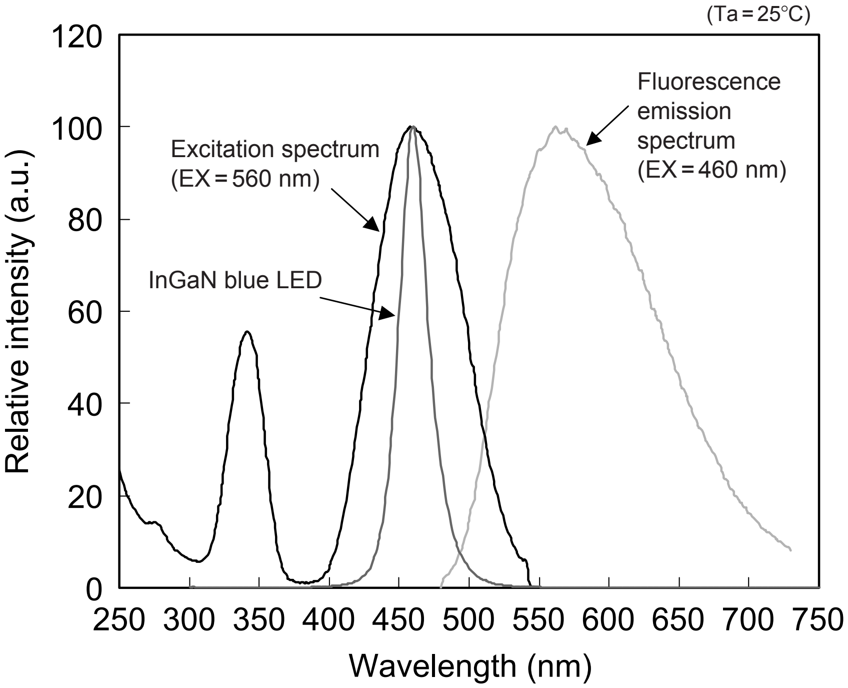

Figure 90 Emission and excitation spectra of YAG phosphor.

The Ce^{3+} luminescence has short persistence. The Ce^{3+} luminescence in YAG has a lifetime as short as 10^{-7}–10^{-8} s, which is advantageous for display applications. Such short persistence is due to 4f–5d transitions, which are parity- and spin-allowed.[16]

The manufacturing process is easy and inexpensive. The manufacturing process is well established; the mass production process is safe and easy. This is because YAG has been used for many years as a laser host and as phosphors for fluorescent lamps and CRTs.[17] The

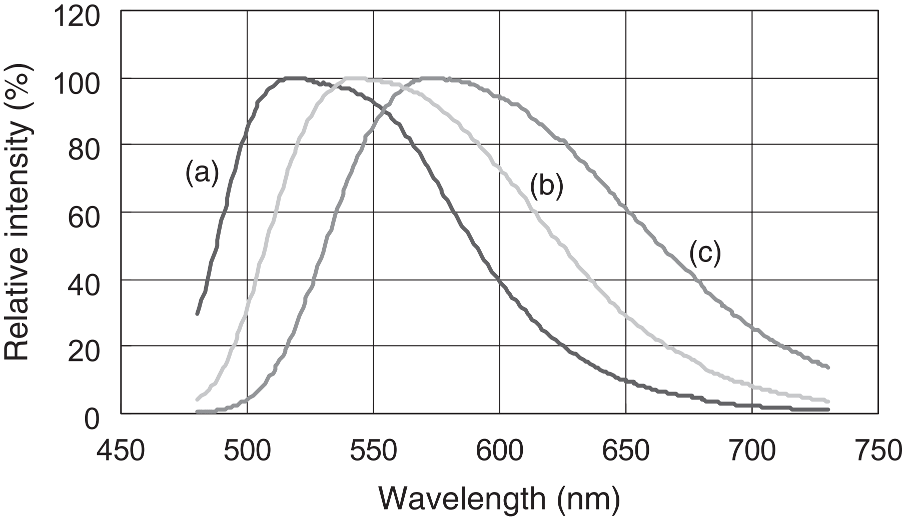

Figure 91 Emission spectra of YAG phosphors
(a) $Y_3(Al,Ga)_5O_{12}$:Ce; (b) $Y_3Al_5O_{12}$:Ce; (c) $(Y,Gd)_3Al_5O_{12}$:Ce.

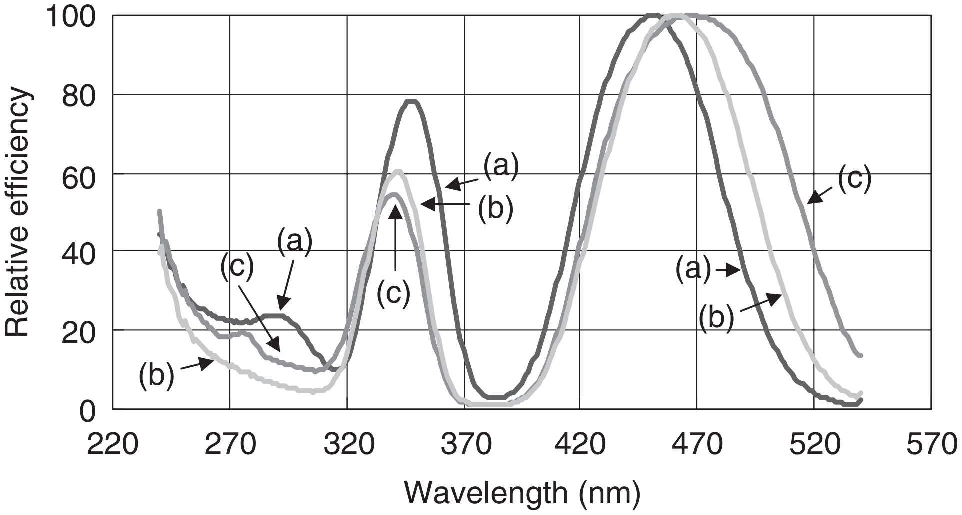

Figure 92 Excitation spectra of YAG phosphors.
(a) $Y_3(Al,Ga)_5O_{12}$:Ce; (b) $Y_3Al_5O_{12}$:Ce; (c) $(Y,Gd)_3Al_5O_{12}$:Ce.

material also has the advantage of low production costs, since it is made from inexpensive starting materials like alumina and yttria.

5.9.3.2 Phosphors other than YAG:Ce

Blue-emitting phosphors other than YAG:Ce include sulfides, thiogallates, nitrides, oxynitrides, silicates, and aluminates. Typical compositions and their emission colors are summarized in Table 12.

In the subsequent section, nitrides and oxynitrides are discussed in greater detail, since they have attracted most attention among the materials listed above.

5.9.3.2.1 Nitride phosphors. Nitride phosphors activated with a rare-earth ion are characterized by chemical stability caused by strong chemical bonding, by excitation and

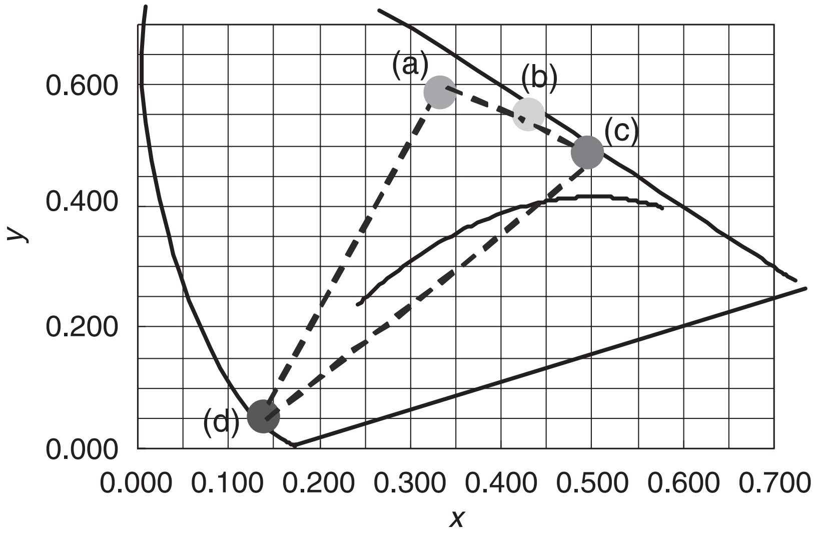

Figure 93 Chromaticity diagram of a blue-LED and YAG phosphors.
(a) $Y_3(Al,Ga)_5O_{12}$:Ce; (b) $Y_3Al_5O_{12}$:Ce; (c) $(Y,Gd)_3Al_5O_{12}$:Ce; (d) blue LED.

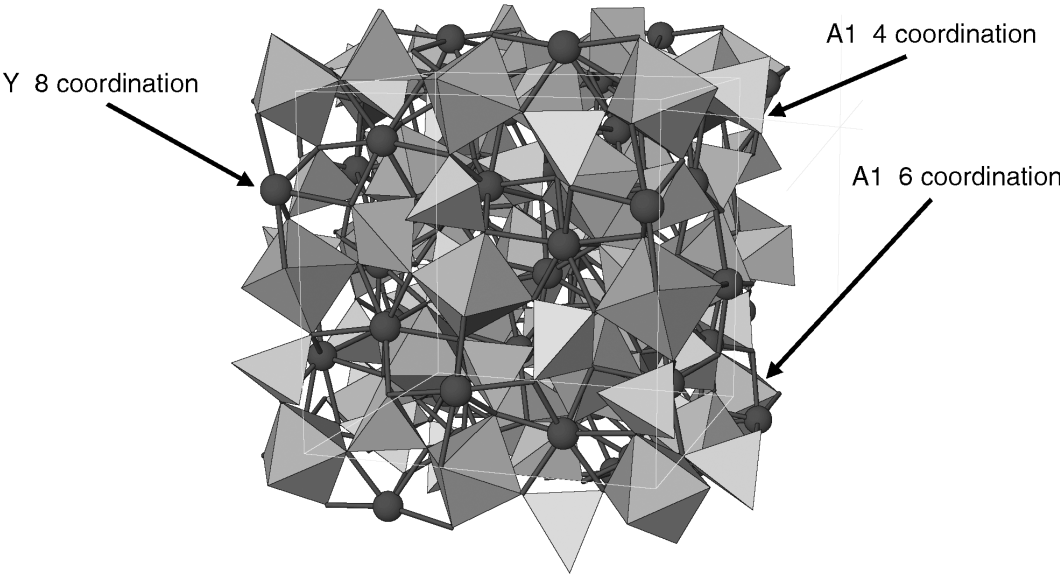

Figure 94 Crystalline structure of YAG phosphor.

emission bands at long wavelength due to large covalency, and by wide selectivity in their chemical composition.[21] The material first commercialized was the $(Ca,Sr)_2Si_5N_8{:}Eu^{2+}$ system. As shown in Figure 95, the luminescence peak of this material is at 610 nm for 100% Ca composition and 620 nm for 100% Sr composition, while it is shifted to 650 nm for the solid solution composed with 50% Ca and 50% Sr. This is an exceptional property of a solid solution. Development of this type of phosphors has enabled the production of LEDs with warm-white color and with high color-rendering index. The luminescence spectra of these types of LEDs are shown in Figure 96. With these products, LEDs have found increasing acceptance as new sources of lighting.

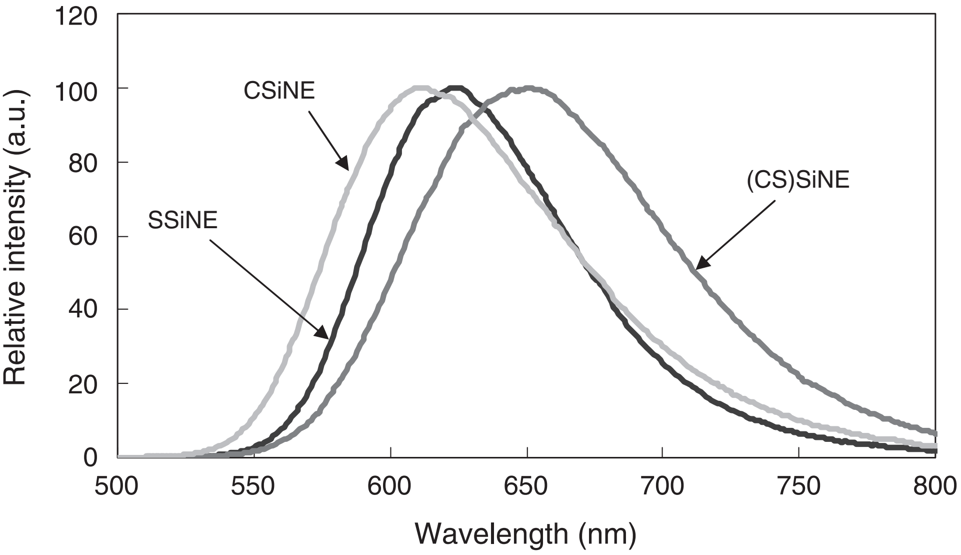

Figure 95 Emission spectra of $(Ca,Sr)_2Si_5N_8{:}Eu$ phosphor.

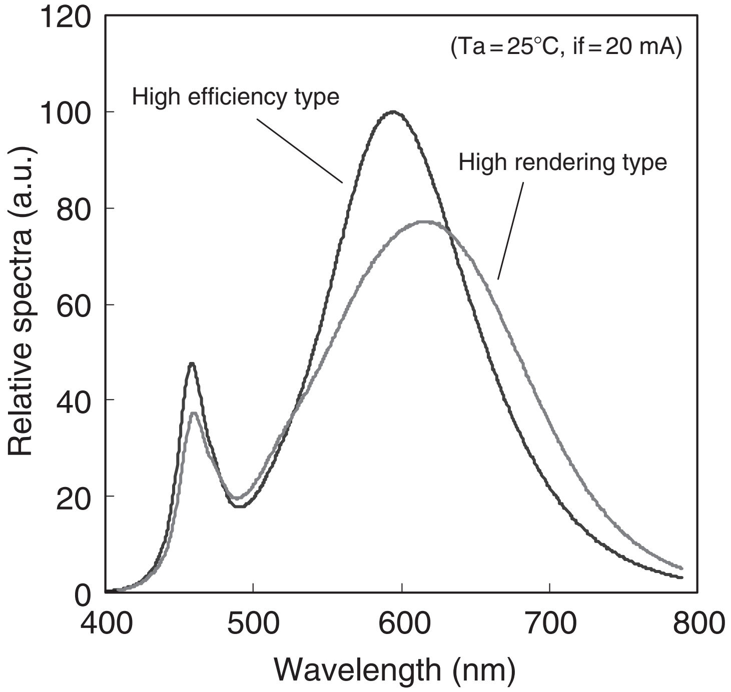

Figure 96 Emission spectra of high efficiency-type LED and high rendering-type LED.

Among other nitrides, attention has also been paid to $CaAlSiN_3:Eu^{2+}$, which shows a deep red luminescence peaking at 650 nm. Figure 97 shows the luminescence and excitation spectra.

To synthesize nitride phosphors, nitrides such as Ca_3N_2, Sr_3N_2, Si_3N_4, AlN, and EuN are used as starting materials. After weighing, the constituents are mixed in a glove box filled with N_2 gas and are heated at 1400–1900°C under 1–10 atm of N_2 or a reducing gas atmosphere. Phosphors obtained by this process are stable in air and can be treated just like any conventional oxide phosphors.

5.9.3.2.2 Oxynitride phosphors. $BaSi_2O_2N_2:Eu^{2+}$ with blue-green luminescence, $(Sr,Ca)Si_2O_2N_2:Eu^{2+}$ with yellow-green luminescence,[11] an α-SiAlON compound, $Ca_x(Si,Al)_{12}(O,N)_{16}:Eu^{2+}$ with orange-yellow emission,[9,10] and a β-SiAlON compound, $Si_{6-z}Al_zO_zN_{8-z}:Eu^{2+}$,[22] with green emission have been reported. Among them, $Ca_x(Si,Al)_{12}(O,N)_{16}:Eu^{2+}$ phosphors can provide a warm-white luminescence efficiently by itself. For more details refer to 3.14.

5.9.4 *White LEDs based on UV- or near-UV-emitting LEDs.*

LEDs of this type convert all the emission from UV- or near-UV LEDs to visible light by using phosphors (Figure 98). For this purpose, we can use the phosphors listed in Table 13 as well as those introduced above. Accordingly, we can design emission color with large flexibility using a wide selection and combination of phosphors, particularly white with high color-rendering index and an expanded range of color in the chromaticity diagram for backlighting of liquid crystal displays. The system has the additional advantage that its emission chromaticity depends little on the amount of phosphors mounted on the LED chip, because in principle the phosphors used absorb most of the UV- or near-UV emissions. Accordingly, variation of LED emission color can be reduced. However,

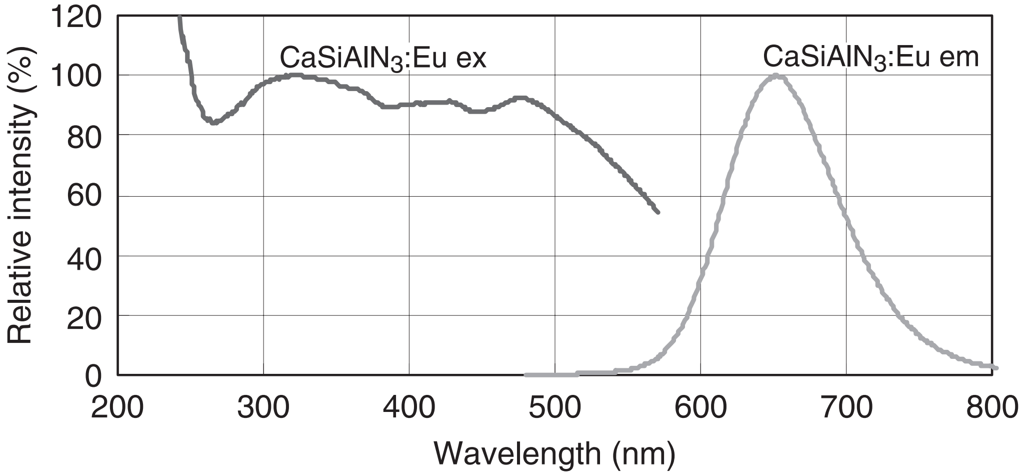

Figure 97 Emission and excitation spectra of $CaSiAlN_3$:Eu phosphor.

this system also has some disadvantages, which compensate for the above advantages as shown below. At present, these drawbacks make it difficult for this system to have a high enough quality to be commercialized.

1. Resin for packaging or molding is solarized by the UV light, resulting in considerable degradation of light output over time.
2. Luminescence efficiency tends to be lowered in comparison with the blue-YAG white system, because most of the visible light has to be obtained from the emission from phosphors. In order for phosphors to absorb as much of the excitation light as possible, a phosphor layer should be thick enough. Consequently, luminescence from the phosphor is scattered inside the thick powder layer and the light output may be adversely affected.
3. To provide white color, two or more kinds of phosphors are necessary. In many cases phosphors differ from each other in their temperature dependence of luminescence properties, lifetimes, and durability. Such unbalance in the properties may give rise to changes in emission color when under operation.
4. UV light used for excitation may be hazardous to users if it leaks outside the LEDs.

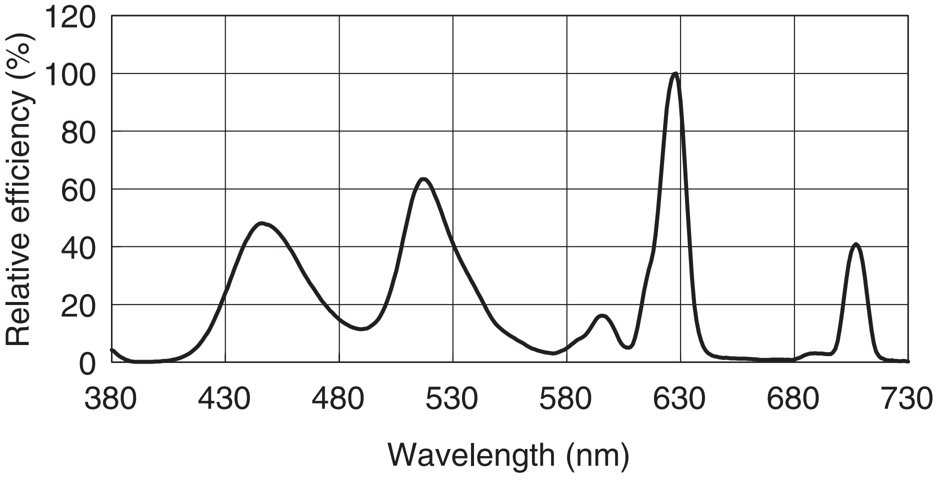

Figure 98 Emission spectrum of UV-LED phosphors.

5.9.5 *White emission obtained by three primary color LEDs*

This system is composed of three LEDs, each of which emits red, green, or blue light, respectively. No phosphors are used in these devices. The emission of LEDs can be designed in a wide range of tailored wavelengths and is endowed with a high color-rendering index. When this light source is used as a backlight of a liquid crystal display, it provides a wide range of color reproducibility, more than 100% NTSC color region.

This is a promising light source, as demonstrated by their successful application to large-screen liquid crystal displays. There remain, however, some drawbacks in this system. First, LEDs with different emission colors differ in temperature dependence and lifetimes of their light outputs, resulting in an unbalanced white hue as a function of time. To compensate for such a difference, complicated driving circuits are required. Moreover, LEDs are more expensive than cold-cathode fluorescent lamps (CCFLs); the latter are thus more popular for backlighting liquid crystal displays. At present, these drawbacks make it difficult for this specific market to be expanded.

5.9.6 *Challenge of white LEDs in the future*

For the major blue-YAG white system, LED types with an average color-rendering index R_a higher than 80 and a luminous efficiency of 100 lm/W will be achieved and marketed in the near future. Their performance is equivalent to or even higher than that of highly efficient three-color fluorescent lamps. Development of red-emitting nitride phosphors has solved the problem of high color-rendering light sources. However, current manufacturing processes of the nitride phosphors are not suited to mass production. To meet the predicted large demand for such LEDs, a new process to synthesize the required phosphors simply and economically in a large scale will need to be developed.

For the backlighting of liquid crystal displays, which forms a growing market, a combination of UV LEDs and phosphors emitting in three primary colors presents us with a challenging problem. If this technology is not practical, the target will be the development of green and red phosphors, which are excited by blue light and have a luminescence spectrum confined in a narrow wavelength range.

References

1. Nakamura, S., Mukai, T., and Senoh, M., *Appl. Phys. Lett.*, 64, 1687–1689, 1994.
2. Bando, K., Sakano, K., Noguti, Y., and Shimizu, Y., *Tech. Digest, Phosphor Res. Soc., 264th Meeting*, 5, 1996 (in Japanese).
3. Bando, K., Sakano, K., Noguti, Y., and Shimizu, Y., *J. Light Vis. Environ.*, 22, No.1, 2–5, 1998.
4. Narukawa, Y., Nagahama, S., Tamaki, H., and Mukai, T., *Jpn. J. Appl. Phys.*, 74 , No.11, 1423–1432, 2005.
5. Muller-Mach, R., Muller, G.O., Krames, M.R., and Trottier, T., *IEEE J. Sel. Top. Quantum Electron.*, 8, No.2, 339–345, 2002.
6. Taguti, T., *J. Light Vis. Environ.*, 27, No.3, 131–139, 2003.
7. Starrick, D., et al., *Proceedings of Phosphor Global Summit*, 2003.
8. Park, J.K., Lim, M.A., Kim, C.H., Park, H.D., Park, J.T., *Appl. Phys. Lett.*, 82, 683, 2003.
9. Xie, R.J., Mitomo, M., Uheda, K., Xu, F.F., and Akimune., *J. Am. Ceram. Soc.*, 85, 1229, 2002.
10. van Krevel, J.W.H., van Rutten, J.W.T., Mandal, H., Hintzen, H.T., and Metselaar, R., *J. Solid State Chem.* 165, 19, 2002.
11. Li, Y.Q., Delsing, A.C.A., de With, G., and Hintzen, H.T., *Chem. Mater.* 17, 3242–3248, 2005.
12. Yamada, M., Naitou, T., Izuno, K., Tamaki, H., Murasaki, Y., Kameshima, M., and Mukai, T., *Jpn. J. Appl. Phys.*, 42, No.2, L20, 2003.
13. Oshio, S., *Tech. Digest, Phosphor Res. Soc. 310th Meeting*, 2005 (in Japanese).
14. Galasso, F.S., *Structure and Properties of Inorganic Solids*, Pergamon Press, New York, 1970.

15. *Phosphor Handbook*, edited by S. Shionoya and W. M. Yen, CRC Press, Florida, pp. 187, 1998.
16. *Phosphor Handbook*, edited by S. Shionoya and W. M. Yen, CRC Press, Florida, pp. 440, 1998.
17. Hoppe, H.A., Lutz, H., Morys, P., Schnick, W., and Seilmeier, A., *J. Phy. Chem. Solids*, 61, 2001, 2000.
18. Uheda, K., Hirosaki, N., Yamamoto, H., Yamane, H., Yamamoto, Y., Inami, W., and Tsuda, K., *Abst. 206th Electochem. Soc. Meeting*, Honolulu, p. 2073, 2004; Uheda, K., Hirosaki, N., Yamamoto, Y., Naito, A., Nakajima, T., and Yamamoto, H., *Electrochem. Solid State Lett*. 9, H22, 2006.
19. Lee, S.S., Lim, S., Sun, S-S., and Wager, J.F., *SPIE*, Vol. 3241, 75–83, 1997.
20. Shimomura, Y. and Kijima, N., *Abst. Jpn. Appl. Phys. Soc. 65th Fall Meeting*, No.3, p. 1285, 2004 (in Japanese).
21. Brunner, H., et al., *Proceedings of Phosphor Global Summit*, 2003.
22. Hirosaki, N., Xie, R.J., Kimoto, K., Sekiguti, T., Yamamoto, Y., Suehiro, T., and Mitomo., M., *Appl. Phys. Lett*. 86, 211905, 2005.
23. Sakuma, K., Omichi, K., Kimura, N., Ohashi, M., Tanaka, D., Hirosaki, N., Yamamoto, Y., Xie, R.J., and Suehiro, T., *Opt. Lett*. 29, 2001, 2004.
24. Doxsee, D., *Extended Abst. of the International Symp. on the Light for the 21st Century*, Tokyo, 2002.
25. Odagi, T., Takagi, K., Hashimoto, K., and Toda, Y., Shikizai 74, 495, 2001 (in Japanese).
26. Umetsu, Y., Okamoto, S., Yamamoto, H. and Mita, Y., *Tech. Digest, Phosphor Res. Soc., 306th Meeting*, 23, 2005 (in Japanese).

chapter six — section one

Phosphors for cathode-ray tubes

Taisuke Yoshioka and Masataka Ogawa

Contents

6.1 Cathode-ray tubes 545
- 6.1.1 Principle and structure of cathode-ray tubes 545
- 6.1.2 Color CRTs 548
- 6.1.3 Oscilloscope CRTs 551
- 6.1.4 Other types of CRTs 551
  - 6.1.4.1 Storage tube 551
  - 6.1.4.2 CRT for radar 553
  - 6.1.4.3 Printing CRT 553
  - 6.1.4.4 Flying-spot scanner CRT 553
  - 6.1.4.5 Display tubes 554
  - 6.1.4.6 Projection CRT 554
  - 6.1.4.7 Flat CRT 554
  - 6.1.4.8 CRT for giant screens 555

References 555

6.1 Cathode-ray tubes

6.1.1 Principle and structure of cathode-ray tubes

The cathode-ray tube (CRT), more popularly called the Braun tube in Japan and some other countries after its inventor, Professor Karl Ferdinand Braun, is the most widely used display device. It has applications ranging from color television sets and giant screens to computers. An excellent book describing the past developments of CRTs has been published.[1] The structure of a typical CRT is shown in Figure 1. The glass vacuum envelope has a neck tube, a funnel, and a face plate. On the back of the face plate, there is a phosphor screen. The electron gun that generates the electron beam is inside the neck tube. The electron-beam deflection device is placed in the area between the neck tube and funnel. The deflection plates are positioned inside the neck tube and the deflection yoke is positioned outside the neck tube.

Hot electron emission is generated by heating the filament, which in turn heats the cathode. The emitted hot electrons are formed into a beam by controlling the voltage applied to the grids in the gun and the anode. The first grid is a control grid that modulates

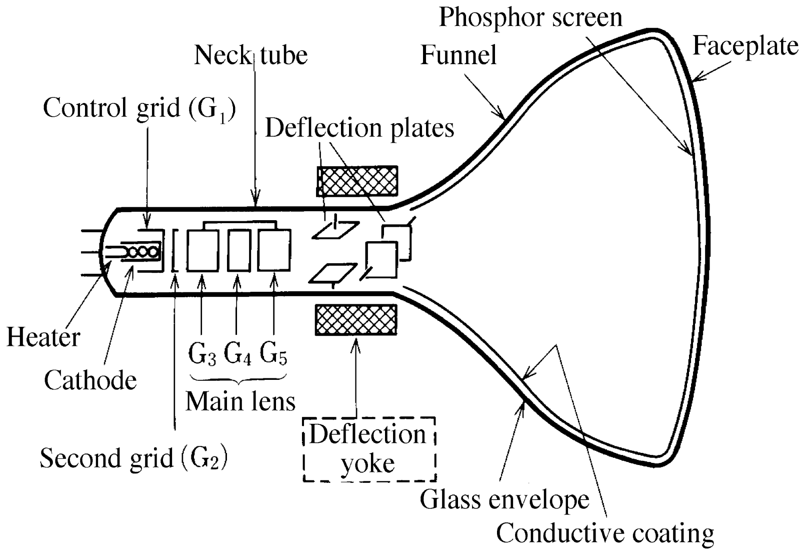

Figure 1 Structure of cathode-ray tube (either a deflection yoke or deflection plates are used).

the magnitude of the electron beam current. By adjusting the voltage between the first grid and the second grid, a crossover is formed where the beam diameter is minimized. The crossover is analogous to the object point in geometrical optics and its image is formed on the phosphor screen after passage through the main lens. The quality of the crossover, therefore, determines the quality of the image on the phosphor screen. Between the second and the third grid, the electron beam is accelerated by a high electric field, thus forming a prefocusing lens, which reduces the divergence angle of the beam.

There are two types of main lenses: electrostatic focusing and electromagnetic focusing. An electrostatic focusing main lens is commonly employed in commercial CRTs. Depending on the configuration of the electron gun and the voltages applied to the grids, there are bipotential focusing (BPF) and unipotential focusing (UPF) electron guns, as shown in Figure 2. In the BPF type, several to several tens of kilovolts is applied to the fourth grid, while approximately 20% of this voltage is applied to the third grid, thus forming the main lens between these grids. With the UPF type, a common high voltage is applied to the third and fifth grids, while the fourth grid remains at zero potential. The design principle of an electron gun is to obtain the sharpest possible beam spot on the phosphor screen by choosing the geometry of the gun and the voltages applied to the grids. A multistage convergence type gun has been developed with a combination of these lenses.[2–5] As an extension of the multistage device, a gun having a large-diameter lens at the last stage has also been proposed.[6]

In electromagnetic focusing, a high voltage is applied to the third grid and instead of employing a convergence grid, a coil or a permanent magnet is placed on the neck tube for beam convergence. When a magnetic field is formed parallel to the electron beam, its force on the electrons results in a spiral motion of electrons in the direction of propagation. The period of this spiral motion of electrons depends on the magnetic field strength and is independent of the angle of divergence of the electron beam. An electron emitted from the center of the beam axis will, therefore, be back in the same position after one full period. Since the magnetic coil is placed outside of the neck tube, the effective lens diameter can be larger than in electrostatic focusing, where the lens diameter is limited by the diameter of the neck tube. The larger the lens diameter, the smaller the spherical aberration, which will result in a finer beam spot on the screen. One disadvantage of magnetic focusing is

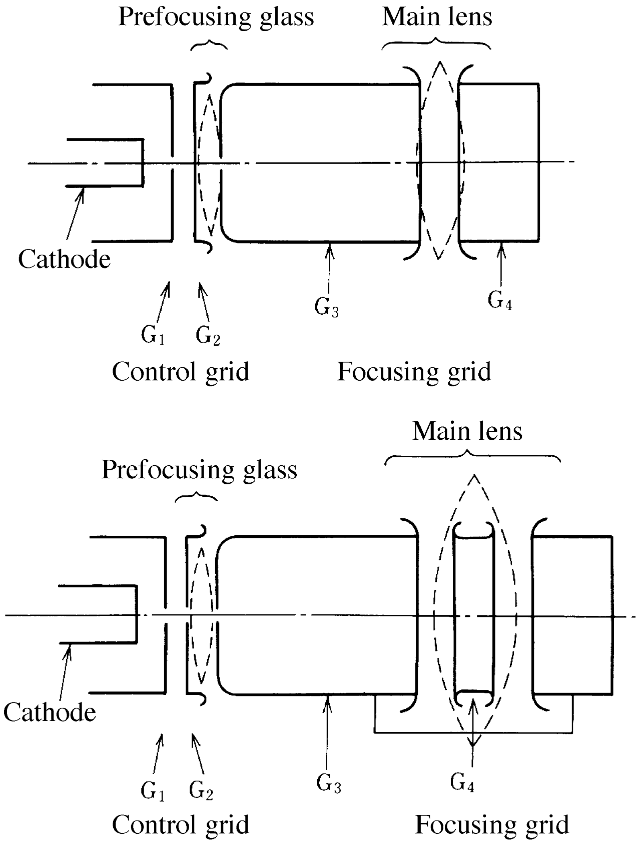

Figure 2 Schematic of a bipotential gun (top) and a unipotential gun (bottom).

that it is difficult to apply in color CRTs because the magnetic field gives a rotational motion to all three electron beams, confounding their geometrical relation.

Electron beams can be deflected by an electrostatic field as well as by a magnetic field. In electrostatic deflection, two pairs of plates are employed to deflect the beam horizontally and vertically, as is shown in Figure 1. A major disadvantage of electrostatic deflection is that the deflection sensitivity is low; hence, a large deflection angle is difficult to achieve. The advantage of this method of deflection, however, is that the deflection plates themselves require virtually no electrical power and can be operated at high frequency since the plates have very small inductance. In electromagnetic deflection, a deflection yoke is employed. Using this technique, a wide deflection angle can be readily achieved and the depth of the CRT can be shortened. Almost all image display CRTs employ this method of beam deflection. Since the yoke is subject to inductance, the high frequency response of magnetic deflection is smaller than that of electrostatic deflection.

The phosphors employed in CRTs are generally considered to be insulators. When the phosphors are irradiated by an electron beam, they tend to charge electrically. When a phosphor screen is negatively charged, the potential of the screen is lowered with respect to that of the cathode and consequently the beam trajectory is disturbed, resulting in distortion of the image on the screen. Also, ions generated by the cathode can collide with the screen and the phosphor may be "burned," thus reducing the light intensity emitted from the phosphor. In order to avoid these phenomena and to enhance and reflect light output from the phosphor in the viewing direction, the phosphor is coated with a thin aluminum film by vacuum evaporation (metal-backed phosphor screen).

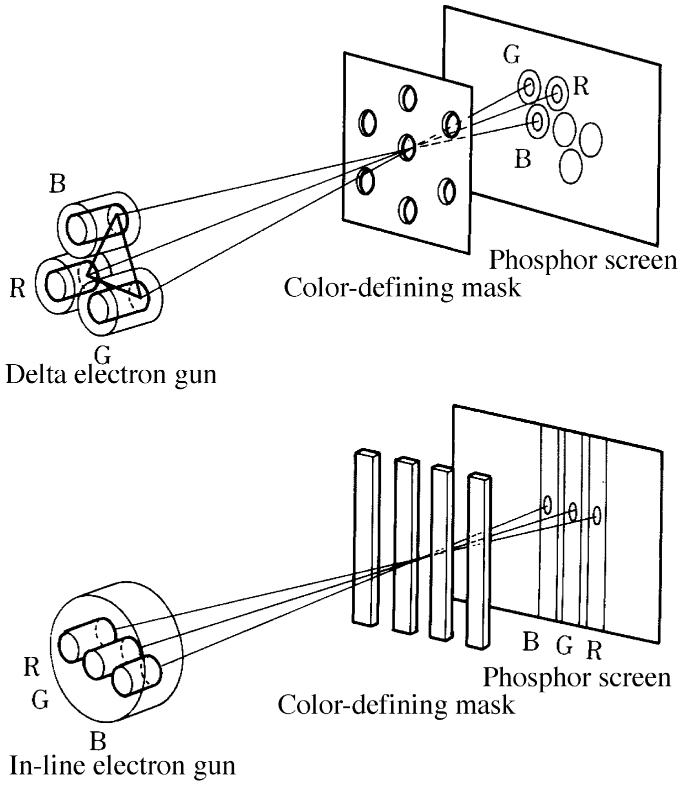

Figure 3 Geometry of delta configuration (top) and in-line configuration (bottom) of electron gun, color-defining masks, and phosphor screen.

6.1.2 Color CRTs

In a color CRT, intensities of the three primary colors (red, green, and blue) emitted from the corresponding phosphors are independently controlled. A conventional color CRT delivers three electron beams and has the corresponding three primary-color phosphors.[7]

There are two types of electron gun configurations for the three-beam color CRT: delta and in-line.[8] Figure 3 shows the geometrical relations of the gun configurations, their color-defining masks (shadow masks), and phosphor screens. As shown in Figure 4, the geometry of the phosphor screen for a color picture tube is circular, elliptical, or stripe-patterned and the structure of the color-defining mask corresponds to these phosphor patterns. The single mask hole corresponds to a single set of phosphor triplets (red, green, and blue), and each electron beam lands only on a particular color phosphor. The color-defining mask, consisting of slots with connecting webs, is utilized in conjunction with an in-line gun.

As an extension of the in-line configuration, a unique electron gun, called the trinitron electron gun, was developed, as shown in Figure 5.[9–10] This figure was produced in the course of computer simulation of electron beam trajectories in the gun. The trinitron gun generates three electron beams with a single gun, whereas a conventional type employs three independent guns. It utilizes a single, large-diameter lens for the three electron beams in common, thus minimizing spherical aberration and producing bright and sharp images on the screen. The trinitron gun has a common first grid for all the electron beams, and beam modulation is achieved by changing the cathode potential with respect to the first

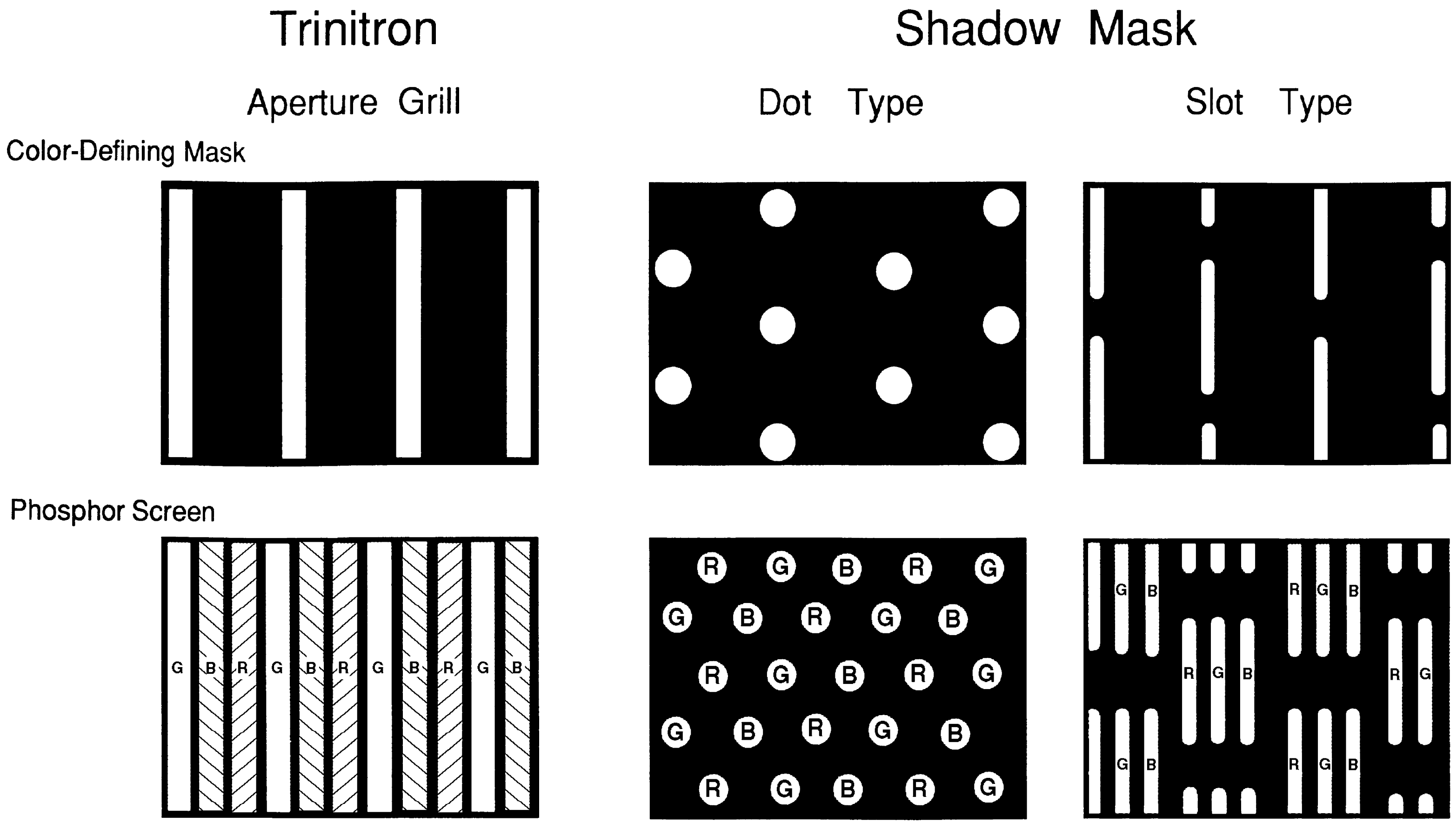
Trinitron
Shadow Mask
Aperture Grill
Dot Type
Slot Type
Color-Defining Mask
Phosphor Screen
G B R G B R G B R G B
R G B R G
G B R G B
R G B R G
G B R G B
R G B R G
G B
R G B
R G B
R G
G B
R G B

Figure 4 Geometry of color-defining mask and corresponding phosphor patterns.

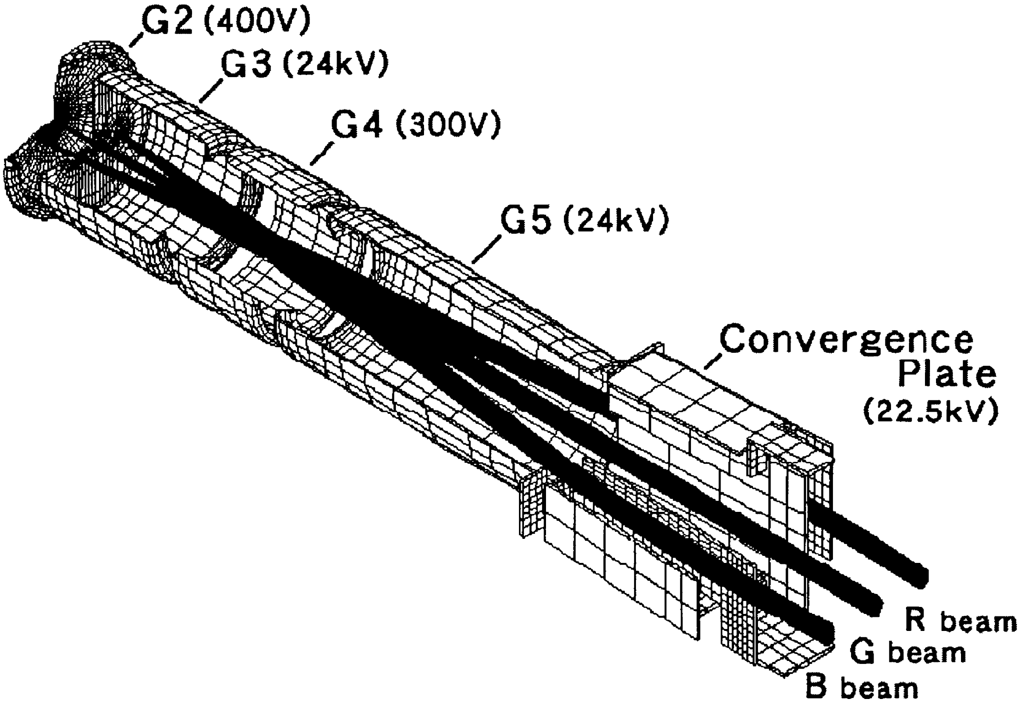

Figure 5 Computer simulation of electron beam trajectories in a trinitron gun, showing all three beams passing through a common focusing lens. (From Abe, G., Kawakubo, T., Hane, K., Ohno, H., Hirata, T., Watanabe, K., and Saitoh, T., *Proc. 6th Sony Research Forum*, 373, 1996. With permission.)

grid. The color CRT with a trinitron gun employs triplet phosphor stripes with an aperture grill and a cylindrical face plate (see Figure 4).

The electron beams in a color CRT are deflected electromagnetically and, at the same time, the deflection yoke corrects the trajectory of the three electron beams so they land on the corresponding phosphors over the entire phosphor screen. This is called self-convergence.

The Chromatron and beam-index tubes have been proposed as special types of color CRT in which only one electron beam is employed. In the Chromatron tube, there are 400 sets of three-color phosphor stripes aligned vertically on the screen. A control voltage applied to a wire grid placed immediately behind and aligned with the phosphor stripes is used to deflect the beam (which normally is aimed at the green stripes) slightly to the left to strike the red stripes or slightly to the right to strike the blue stripes.[11] In the beam-index tube, the position of the electron beam is detected by either light or secondary electrons emitted from the index phosphor stripes provided within the screen. The beam-position information is fed back into the color-switching signal to generate the correct color on the screen.[12–14]

A conventional color CRT has an aspect ratio (ratio of the horizontal to vertical dimensions of the screen) of 4:3. A wider screen, with an aspect ratio of 16:9, has recently become available to display high-definition images.[15]

In order to enhance the contrast of the picture image on the screen, an ambient-light-absorbing graphite layer is placed between the phosphors.[16] Blue and red pigments are coated on the blue and red phosphor particles to obtain a similar enhancement of the contrast ratio and to improve the color fidelity.[17] Another way to achieve the same effect is to place red, green, and blue inorganic filters between the front panel and the corresponding color phosphors.[18–19]

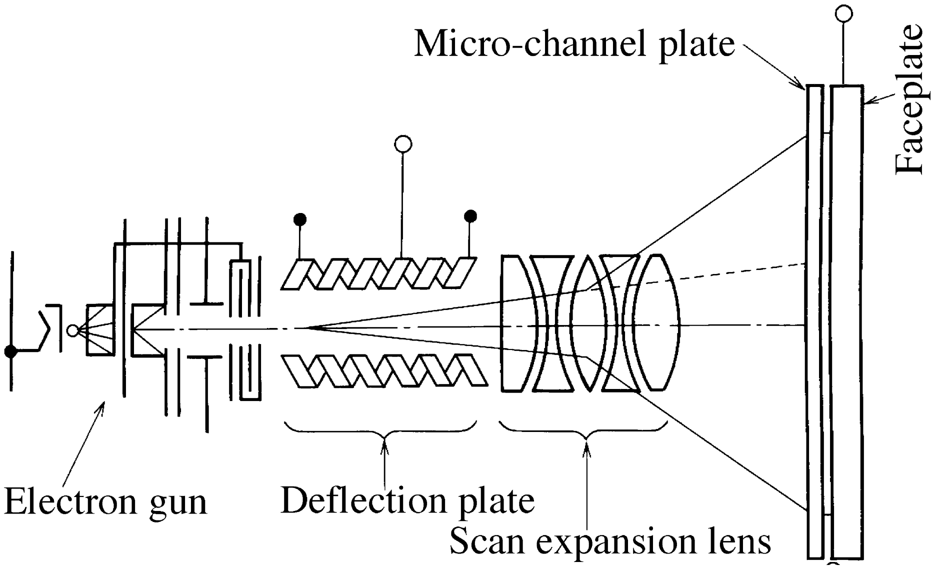

Figure 6 A sophisticated electron gun for oscilloscope CRT with micro-channel plate.

6.1.3 Oscilloscope CRTs

Cathode ray tubes for instrumental use are often called oscilloscope tubes and are widely used for the observation of electrical signals. Their basic structure is the same as that of a monochrome cathode ray tube but with highly sophisticated electron optics. Compared with a conventional picture tube, the oscilloscope CRT is required to have better beam-deflection sensitivity, linearity, and high-frequency response.

An electrostatic deflection technique and a flat face plate are commonly used for the oscilloscope. For use at frequencies higher than several hundred MHz, a single deflection plate is not able to produce sufficient deflection sensitivity. As shown in Figure 6, an extremely refined electron gun with three quadrupole lenses and a scan-expansion lens system is employed for this purpose.[20–23] To further improve oscilloscope CRT performance, the micro-channel plate was invented.[23] The micro-channel plate is a large array of microscopic electron multipliers. The micro-channels are placed in front of the phosphor screen. When the electron beam impinges on a micro-channel, secondary electrons are emitted and accelerated from the inside wall of the micro-channel by a voltage difference between the channel and the anode, thus increasing the electron beam current. This also increases the light output, enabling the observation of extremely high frequency waveforms. These techniques are useful for the observation of single-shot, high-speed phenomena.

Beyond the 1-GHz frequency region, the scan-converter tube, shown in Figure 7, is employed.[24,25] This tube consists of two facing electron guns with a silicon-diode target array positioned between them.[26–28] A writing gun generates a fast signal waveform directly on the target, discharging the target diodes. Then, as the reading gun scans at a much slower rate over these "written" diodes, the reading gun beam current flows to reverse the bias of the diode. The amount of beam current returning to the target is digitized and the acquired digital data is used to reconstruct the original fast waveform.

6.1.4 Other types of CRTs

6.1.4.1 Storage tube

The storage tube has a memory function for electric signals built in within the CRT.[29,30] Figure 8 shows the structure of a direct-view storage tube. The operating principle of

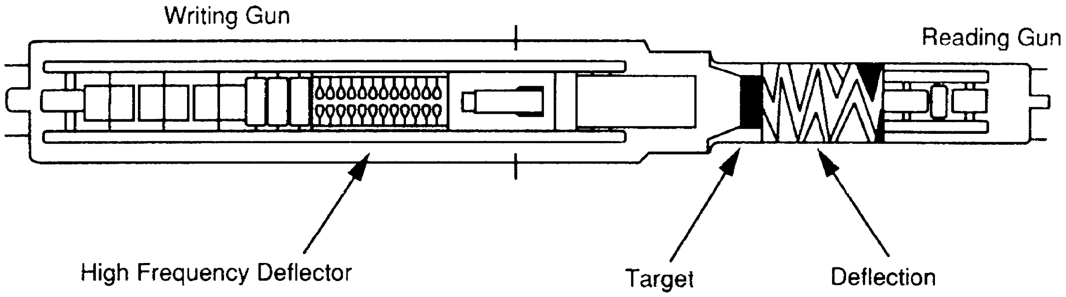
Writing Gun
Reading Gun
High Frequency Deflector
Target
Deflection

Figure 7 A scan converter tube. (From SCD1000/5000 Operator Manual, Tektronix, Inc. With permission.)

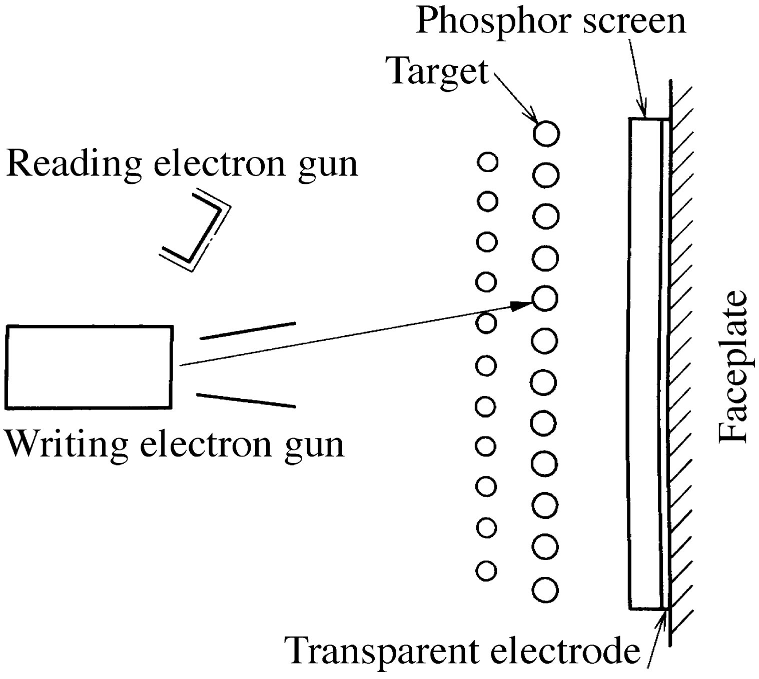
Phosphor screen
Target
Reading electron gun
Writing electron gun
Faceplate
Transparent electrode

Figure 8 Direct observation tube.

the direct-view tube is to utilize secondary electron emission of a dielectric target. The scanning electron beam modulated by the electric signal from the writing electron gun impinges on the dielectric target. If the electric potential of the dielectric target with respect to the writing gun is adjusted so that its secondary electron emissivity ratio is larger than unity, the target is charged positive and its potential will increase. This increase in potential is proportional to the modulation of the writing electron beam, and hence proportional to the electric signal to be observed. The reading gun uniformly irradiates the entire target; the latter acts as a control grid, so that the beam from the reading gun reaches the phosphor screen, producing light only in areas where the writing beam has been.

Because of the abundant availability of digital memory, recent oscilloscopes have a digital-storage capability, as described in the 6.1.3. Together with software development, data processing such as averaging, peak detection, and fast-Fourier transform, is readily performed through a graphics-user interface.[31]

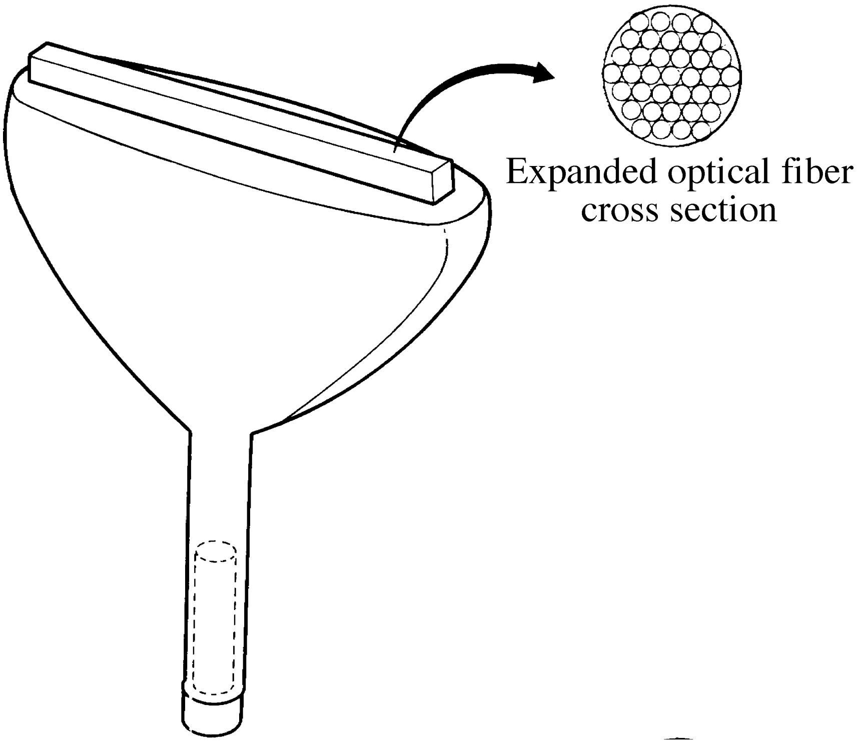

Figure 9 Optical-fiber printing tube.

6.1.4.2 CRT for radar

In order to display both an azimuth angle and distance to target in a single indicator, a plan position indicator (PPI) mode has been employed. The time delay between the pulse transmitted from the radar transmitter and the return pulse is proportional to the distance from the antenna to the target. The return pulse is amplified and is applied to the CRT grid to modulate the intensity. Since the period of electron beam rotation over the screen (synchronized with the rotation of the radar antenna) is relatively long, in order to retain an image on the screen until the next beam scan, a long-decay phosphor is required. Recently, digital technology has replaced this type of CRT employing long-decay phosphors. A computer-controlled 20 × 20-inch square, full-color CRT with 2048 × 2048 pixels has been developed for the aviation application.[32]

6.1.4.3 Printing CRT

Images and characters can be hard-copied onto photographic film by a printing CRT.[33] The film motion provides scanning along one axis while the orthogonal axis is scanned electrically. A bundle of optical fibers with a phosphor layer is used as a face plate and allows direct contact with the film. Using three primary-color phosphor stripes, color recording is possible. An electrostatic printing CRT with a thin-film conductive face plate that allows the electron beam to pass through has been proposed.[34] A typical structure of a printing CRT is illustrated in Figure 9.

6.1.4.4 Flying-spot scanner CRT

This type of CRT is used to convert film images to electrical signals that can then be reproduced on a display.[35] The CRT must have a fine beam-spot with an extremely fast-decay phosphor (less than 10^{-7} s). The CRT produces a source of a narrow beam of scanning light that passes through the color film to be scanned and is then detected by a photodetector. From the scanning signal and the detected light intensity, an electrical image signal can be obtained.

6.1.4.5 *Display tubes*

This class of CRT is used to display characters, figures, and picture images in applications such as computer terminals. Compared with a conventional color TV, this CRT is required to have higher resolution and greater contrast. To achieve these requirements, a smaller pitch of the color-defining mask is employed to produce a smaller electron-beam spot, resulting in a smaller light spot. A high-resolution 14-inch CRT has a 0.2 to 0.3-mm phosphor pattern pitch, versus 0.6-mm for a conventional CRT, and the phosphor particle-size distribution must be optimized accordingly.[36]

A CRT with a multilayer phosphor screen separated by dielectric layers has been developed as a display tube.[37,38] The penetration depth of the electron can be changed by changing the acceleration voltage. When the acceleration voltage is low, the electron is absorbed by the first phosphor layer and fluorescent light is emitted. When the voltage is raised so that the electron beam passes through the first layer but is absorbed by the second, a mixture of two colors is emitted. This type of CRT is called a beam penetration tube.

Another way to display a multicolor image is to utilize a mixture of phosphors having different current-density vs. brightness characteristics.[39] Some phosphors exhibit a brightness that increases linearly with current density; whereas in others, the brightness saturates in the higher current-density region. Thus, a mixture of two such phosphors can be designed to emit different color light depending on the current density. Both the current-sensitive and penetration CRTs have inherently a high-resolution capability because they do not require color-defining masks, but their capability to display a wide range of colors is somewhat limited.

One of the ways of reproducing a color picture image is to have the eye average the colors over time at each position on the screen. A combination of liquid-crystal optical retarders, color polarizers, and a monochrome CRT using a P45 phosphor makes this effect possible.[40,41] The operating principle is illustrated in Figure 10. For polarizing the CRT light and performing the initial separation into color components, this system has two sets of color polarizers. The first set is cyan and red (P1). The second set is yellow and blue (P2), and serves to separate the blue component from the green. The final element, a neutral-density polarizer (P3), limits the orientation of the final color to the vertical axis. By selecting the appropriate combination of direction of polarization produced by the two liquid crystals (C1 and C2) with respect to the color polarizers, a red, green, or blue image can be generated.

6.1.4.6 *Projection CRT*[42]

This type of CRT is basically the same as a monochrome CRT except that it has a lens in front of the face plate to enlarge the image of the CRT to project it onto a large screen. As is shown in Figure 11, a projection CRT having a combination of Schmidt lens and concave reflecting mirror has been proposed.[43] High brightness and small distortion of image are the prime requirements of a projection CRT. The CRT is operated under extremely high current density, and to avoid temperature quenching of the phosphor, the face plate is kept cool by means of circulating air or a liquid coolant. For this purpose, a coolant sealed in front of the face plate has also been proposed.[44]

6.1.4.7 *Flat CRT*

There is an obvious limitation to reducing the depth of a conventional CRT. For applications where there is a severe space limitation, a flat CRT has been proposed, as is shown in Figure 12. The deflection of the electron beam is in the horizontal and vertical direction, as well as in depth.[45]

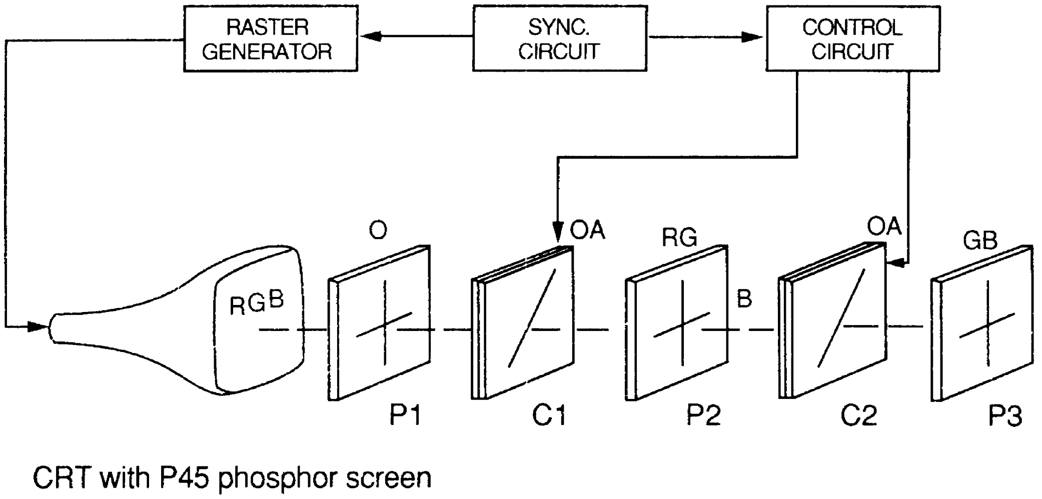
RASTER GENERATOR
SYNC. CIRCUIT
CONTROL CIRCUIT
O
OA
RG
OA
GB
RGB
B
R
P1
C1
P2
C2
P3
CRT with P45 phosphor screen

Figure 10 A multicolor display tube employing liquid crystals as optical retarders and color polarizers. (From Bos, P.J., Thomas, B., and Vante, R., *Eurodisp '84 Proc.*, 7, 1984. With permission.)

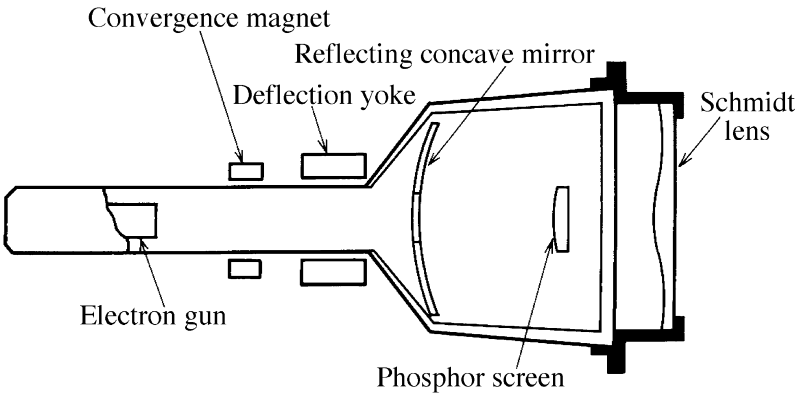
Convergence magnet
Reflecting concave mirror
Deflection yoke
Schmidt lens
Electron gun
Phosphor screen

Figure 11 Projection tube with Schmidt lens and reflecting concave mirror.

6.1.4.8 CRT for giant screens

For a very large display area, a single CRT cannot achieve the desired brightness. Instead, an assembly of special small tubes is proposed. Three primary-color tubes make up one pixel, and the pixels are arranged to form a screen with dimensions of several meters to several tens of meters. One example of such a tube is shown in Figure 13.[46] A box-type unit in which a multiple of pixels is contained and a large screen constructed from such units have also been commercialized, as is shown in Figure 14.[47–49]

References

1. Keller, P.A., *The Cathode-Ray Tube, Technology, History, and Application*, Palisades Press, New York, 1991.
2. Kanai, H., Yamazaki, E., and Watanabe, Y., *IEEE Trans. Electron. Devices*, ED-23, 45, 1976.
3. Palac, K., *IEEE Trans. Consumer Electronics*, CE-22, 289, 1976.
4. Hamano, Y., Koshigoe, S., and Ogawa, Y., *Sci. Rpt. of Res. Committee on Elctr. Equip. for TV.*, ED-460, 21, 1979 (in Japanese).
5. Morrell, A.M., *IEEE Trans. Consumer Electronics*, CE-28, 290, 1982.

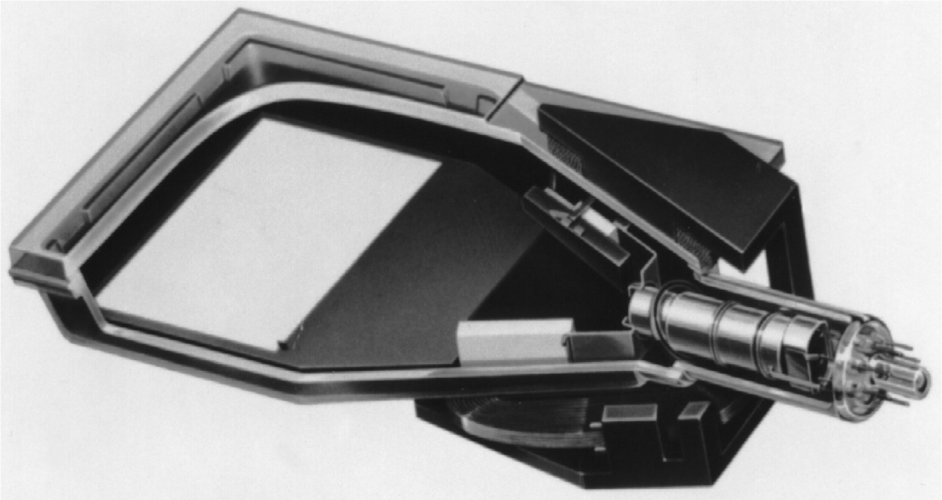

Figure 12 Cut-away view of a flat CRT. (From Ohkoshi, A., Sato, H., Nakano, T.N., and Hatanaka, M., *IEEE Trans. Consumer Electronics*, CE-28, 431, 1982. With permission.)

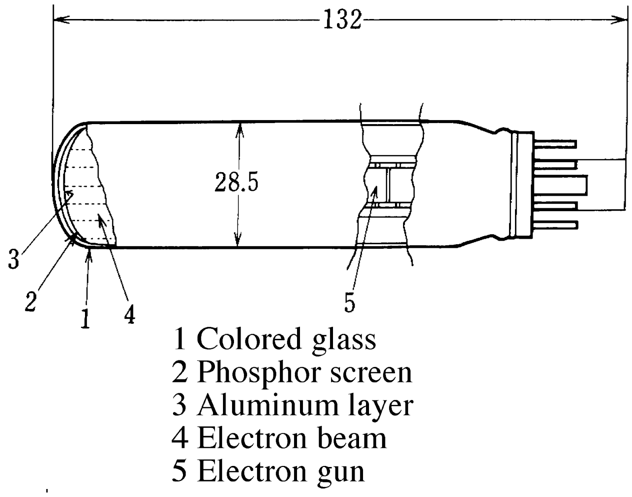

Figure 13 One CRT in a red, green, and blue triplet for a giant screen. (From Kobayashi, H. and Awazu, K., *Illum. Eng. Inst. Japan*, 5, 22, 1981. With permission.)

6. Saito, T., Kikuchi, M., and Sovers, O.J., *J. Appl. Phys.*, 50, 6123, 1979.
7. Law, H.B., *RCA Rev.*, 12, 466, 1951.
8. Morrell, A., *IEEE Trans. Consumer Electronics*, CE-22, 1, 1976.
9. Yoshida, S., Ohkoshi, A., and Miyaoka, S., *IEEE Trans. Broadcast & Television Receiver*, BTR-14, 19, 1968.
10. Abe, G., Kawakubo, T., Hane, K., Ohno, H., Hirata, T., Watanabe, K., and Saitoh, T., *Proc. 6th Sony Research Forum*, 373, 1996.
11. Dressler, R., *Proc. IRE*, 41, 851, 1953.
12. Barnett, G.F., Bingley, F.J., Parsons, S.L., Pratt, G.W., and Sadoesky, M., *Proc. IRE*, 44, 1115, 1956.
13. Turner, J.A., *Bien. Display Conf. Rec.*, 83, 1976.
14. Ohkoshi, A., Tohyama, T., Yukawa, T., and Tohyama, A., *IEEE Trans. Consumer Electronics*, CE-27, 433, 1981.
15. Uba, T., Omae, K., Ashiya, R., and Saita, K., *IEEE Trans. Consumer Electronics*, 34, 85, 1988
16. Fiore, J.P. and Kaplan, S.H., *IEEE Trans.*, BTR-15, 267, 1969.

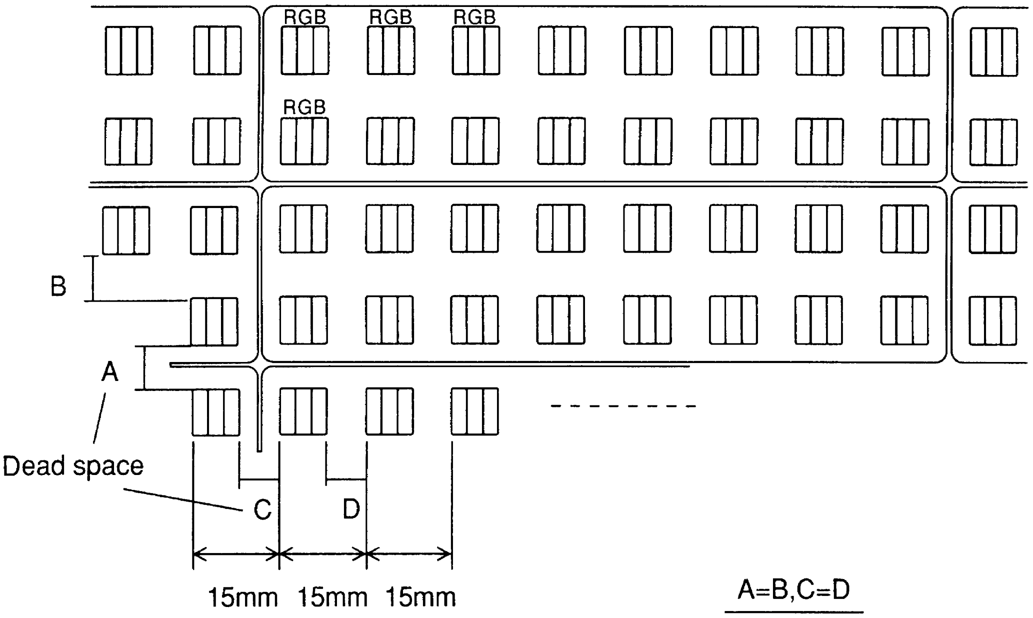

Figure 14 Alternative design of a CRT for a giant screen. (From Hayashi, H., Muchi, T., Ozeki, M., Masatoki, T., and Arae, T., *SID89 Digest*, 98, 1989. With permission.)

17. Ikegaki, M., Ito, T., Otake, Y., and Tsukagoshi, H., *Toshiba Rev.*, 31, 724, 1976 (in Japanese)
18. Ohno, K., *SID 94 Digest*, 584, 1994.
19. Itou, T., Matsuda, H., and Onodera, M., *SID 95 Digest*, 25, 1995.
20. Endo, S., *Natl. Tech. Rep.*, 25, 271, 1979.
21. Odenthal, C., *SID 77 Digest*, 134, 1977.
22. Janko, B., *SID 79 Digest*, 68, 1979.
23. Odenthal, C.J., *Electro-Optical System Design*, 27, 1979.
24. *Cathode-Ray Tubes: Getting Down to Basics*, Tektronix, Inc., 1985.
25. SCD1000/5000 Operator Manual, Tektronix, Inc.
26. Edens, G., *SID 70 Digest*, 60, 1970.
27. Sang, E., *SID73 Digest*, 104, 1973.
28. Arai, H., *Nikkei Electronics*, 67, 4.22, 1974 (in Japanese).
29. Anderson, R.H., *IEEE Trans. Electron. Devices*, ED-14, 838, 1967.
30. Curtin, C., *SID77 Digest*, 132, 1977.
31. Keller, P.A., *SID77 Digest*, 132, 1977.
32. Sodo, M., Ashiya, R., Uba, T., Murata, A., and Amano, Y., *SID86 Digest*, 338, 1998.
33. Wurtz, J.E., *J. Appl. Photographic Engineering*, 6, 73, 1980.
34. Uno, Y., *J. Inst. Television Eng.*, 29, 563, 1975 (in Japanese).
35. Wurtz, J., *Comput. Graphics World*, Feb., 25, 1985.
36. Fushiki, K., *Nikkei Electronics*, 104, 10.15, 1979 (in Japanese).
37. Koller, L.R. and Williams, F.E., U.S. Patent No. 2,590,018, 1952.
38. Rawdin, E., Shwartz, J., and Smilowitz, S., *SID81 Digest*, 94, 1981.
39. Ohkoshi, A., Takeuchi, O., Kambayashi, K., and Yukawa, T., *IEEE Trans. Electron. Devices*, ED-14, 838, 1967.
40. Bos, P.J., Thomas, B., and Vante, R., *Eurodisp '84 Proc.*, 7, 1984.
41. Bos, P.J. and Johnson, Jr., P.A., U.S. Patent No. 5,387,920, 1995.
42. Good, W.E., *IEEE Trans. Consumer Electronics*, CE-21, 206, 1975.
43. Suzuki, Y., Masuda, M., Inoue, T., and Tominaga, T., *Natl. Tech. Rep.*, 25, 226, 1979 (in Japanese).
44. Kikuchi, M., Kobayashi, K., Chiba, T., and Fujii, Y., *IEEE Trans. Consumer Electronics*, CE-27, 478, 1981.

45. Ohkoshi, A., Sato, H., Nakano, T.N., and Hatanaka, M., *IEEE Trans. Consumer Electronics*, CE-28, 431, 1982.
46. Kobayashi, H. and Awazu, K., *Illum. Eng. Inst. Japan*, 5, 22, 1981.
47. Ohkoshi, A., *SID85 Digest*, 87, 1985.
48. Nakagawa, H. and Ohkoshi, A., *SID86 Digest*, 246, 1986.
49. Hayashi, H., Muchi, T., Ozeki, M., Masatoki, T., and Arae, T., *SID89 Digest*, 98, 1989.

chapter six — section two

Phosphors for cathode-ray tubes

Shuji Inaho and Takashi Hase

Contents

6.2 Phosphors for picture and display tubes 559
  6.2.1 Phosphors for black-and-white television tubes 559
  6.2.2 Phosphors for monochrome display tubes 568
  6.2.3 Phosphors for color television tubes 571
  6.2.4 Phosphors for color display tubes 580
References 584

6.2 *Phosphors for picture and display tubes*

6.2.1 *Phosphors for black-and-white television tubes*

Required characteristics. Among the characteristics particularly required of phosphors for black-and-white television picture tubes are (1) white emission when excited by the electron beam, (2) relatively short after-glow persistence for display of moving pictures, (3) powder form that is suitable for sedimentation coating, and (4) high efficiency with long-term stability.

Practical phosphors. The following four types of phosphors are used in current black-and-white television picture tubes:

1. ZnS:Ag + (Zn,Cd)S:Cu,Al
2. ZnS:Ag + (Zn,Cd)S:Ag
3. (Zn,Cd)S:Ag,Au,Al
4. ZnS:Ag + ZnS:Cu,Al + $Y_2O_2S:Eu^{3+}$

The first of the above is the combination of a blue-emitting silver-activated zinc sulfide phosphor and a yellow-emitting copper- and aluminum-activated zinc-cadmium sulfide phosphor. The second composition uses the same blue-emitting phosphor as the first, together with yellow-emitting silver-activated zinc-cadmium sulfide. The third composition is zinc-cadmium sulfide activated by silver, gold, and aluminum. This is a single-component phosphor that emits white light. The fourth composition does not contain cadmium and has somewhat lower luminescence efficiency than the first three phosphors.

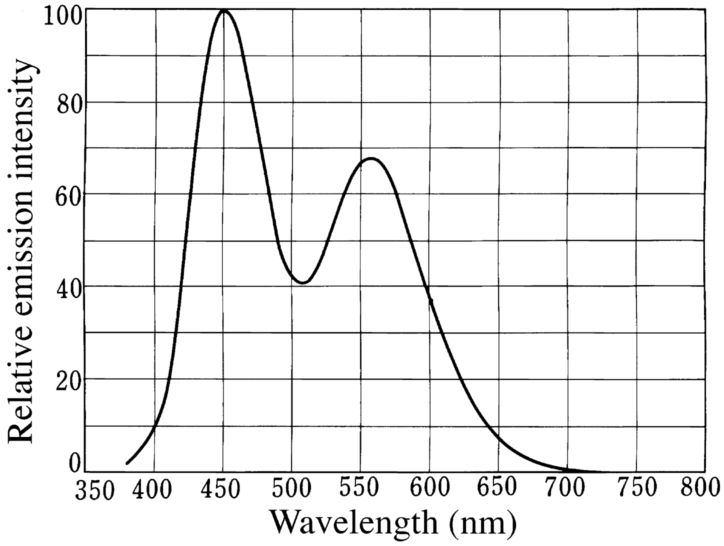

Figure 15 Emission spectrum of P4 phosphor [ZnS:Ag + (Zn,Cd)S:Cu,Al]. (From Kasei Optonix, Inc., unpublished results. With permission.)

Currently, the first of the above phosphors is the one most often used in black-and-white television screens. The third has demerits in having a lower luminescence efficiency than the first two, and a narrower range of color adjustment, because it is a single-component phosphor. Nevertheless, because the single-component composition makes it possible to achieve a highly uniform phosphor screen, this phosphor is applied in the very small CRTs used in viewfinders of television cameras.

Here we describe the most frequently used ZnS:Ag (0.01–0.03 wt%) + (Zn,Cd)S:Cu(0.002–0.03 wt%),Al phosphor in detail. An example of the emission spectrum of this phosphor is shown in Figure 15.[1] In this case, the chromaticity coordinates are x = 0.275 and y = 0.290. The after-glow persistence characteristics are shown in Figure 16.[1] The chromaticity coordinates can be adjusted by changing the weight ratio of zinc to cadmium in the yellow phosphor component or by changing the mixing ratio of the blue and yellow phosphor components. The emission spectra for phosphors of cadmium sulfide weight percentages of 12%, 17% and 20% are shown, respectively, as No. 1, No. 2, and No. 3 in Figure 17.[1] The emission spectrum of the blue phosphor component is shown in Figure 18.[1] The chromaticity coordinates for the above blue component phosphor and No. 1 and No. 2 yellow component phosphors are shown in Figure 19.[1] The chromaticity coordinates of mixed materials can be controlled by changing the mixing ratios of the three phosphors. The chromaticity coordinates within the triangle in Figure 19.[1] are theoretically attainable using the three phosphor components.[1]

The second of the four phosphors listed above is exactly the same as the first other than having a different activator for (Zn,Cd)S (Ag rather than Cu). The chromaticity coordinate of this phosphor can be controlled by varying the proportion of cadmium sulfide, in the same way as for the Cu-activated phosphor, but a different amount of cadmium sulfide is required to obtain a given chromaticity (Figure 20[2]).

The chromaticity coordinate of the third phosphor consisting of a single-component (i.e., white-emitting (Zn,Cd)S:Ag,Au,Al) can be controlled by changing the ratio of zinc sulfide to cadmium sulfide in the base material or by varying the amount of Ag and Au activators. A typical emission spectrum is shown in Figure 21[1]; the controllable region of the chromaticity coordinates is shown in Figure 22.[3]

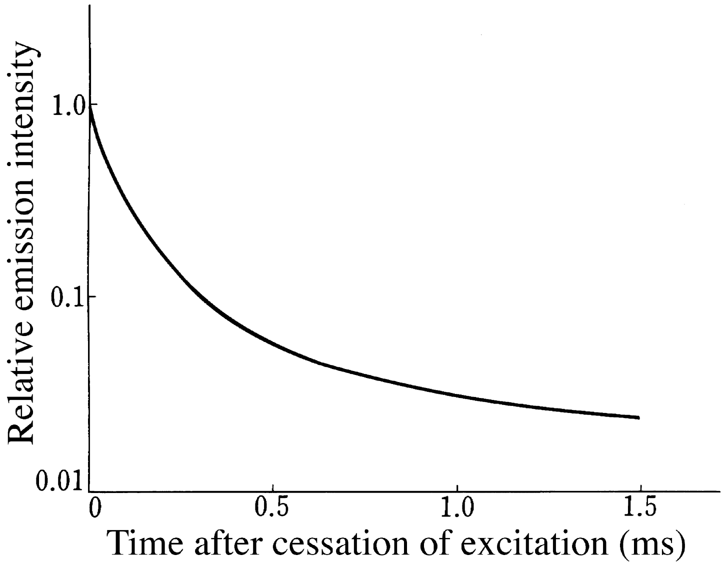

Figure 16 After-glow persistence characteristics of P4 phosphor. (From Kasei Optonix, Inc., unpublished results. With permission.)

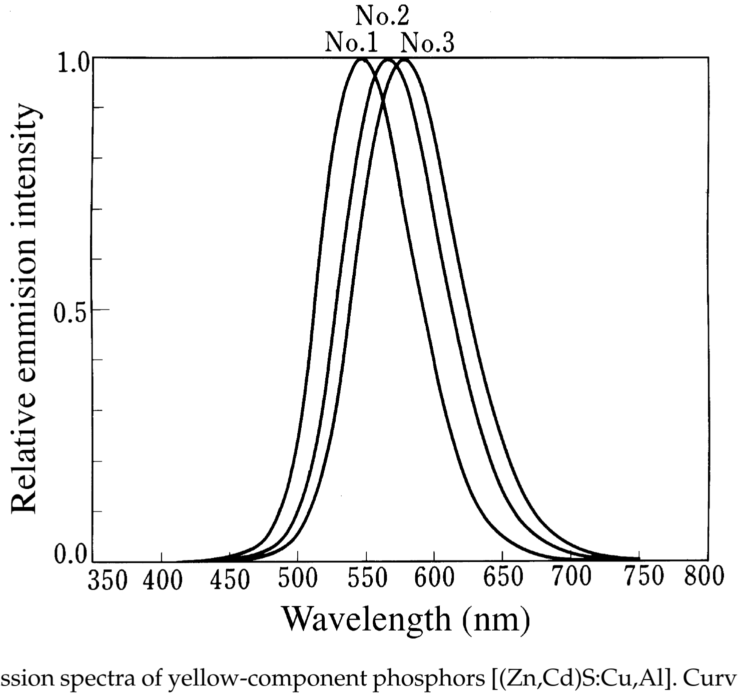

Figure 17 Emission spectra of yellow-component phosphors [(Zn,Cd)S:Cu,Al]. Curves No. 1, No. 2, and No. 3 are for phosphors of cadmium sulfide weight percentages of 12, 17, and 20, respectively. (From Kasei Optonix, Inc., unpublished results. With permission.)

The fourth phosphor in the above list is basically the same as the phosphor used in current color television tubes. A ZnS:Cu,Al phosphor containing no cadmium is used as the green component; a red phosphor is mixed in to attain white emission.

Cautions in application. As described above, the most frequently used phosphors currently are two-color mixtures. While the desired white color can be obtained by chang-

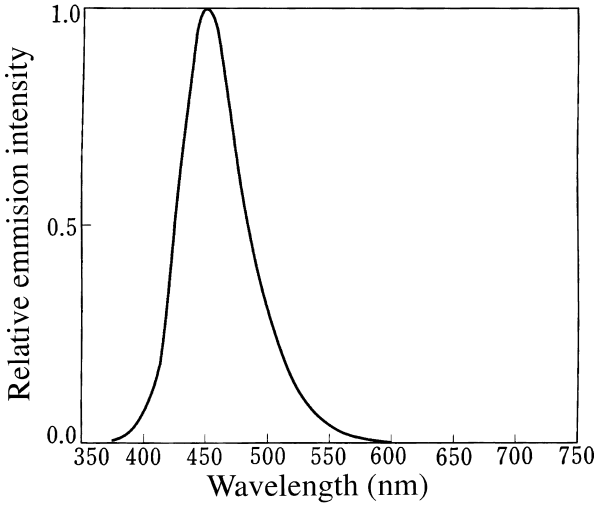

Figure 18 Emission spectrum of the blue-component phosphor (ZnS:Ag). (From Kasei Optonix, Inc., unpublished results. With permission.)

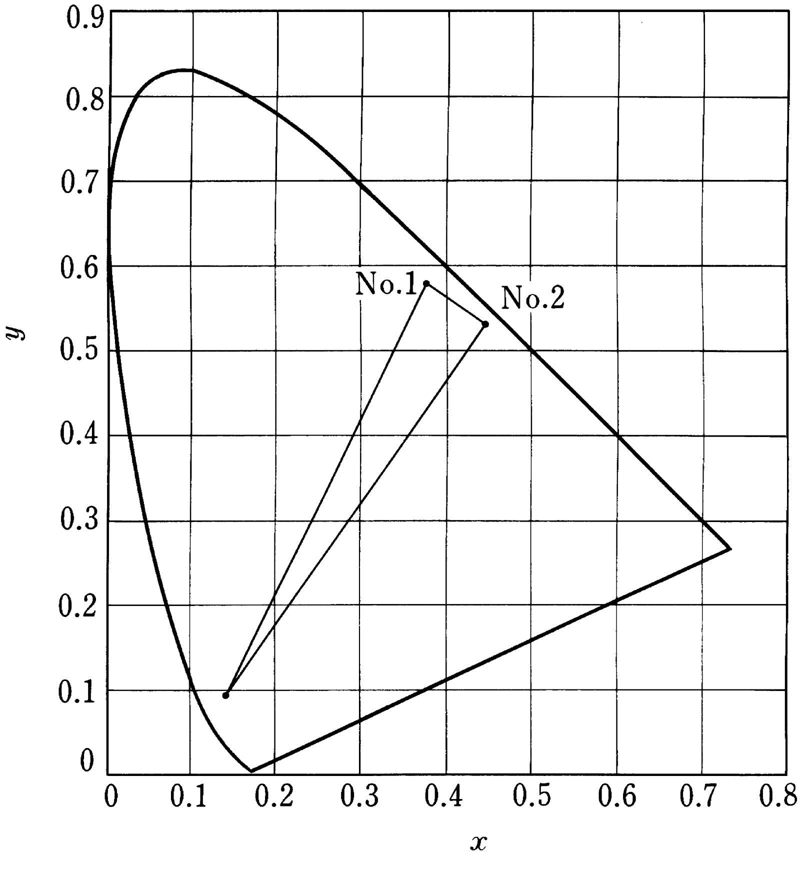

Figure 19 Chromaticity coordinates of the blue (ZnS:Ag) and No. 1 and No. 2 yellow [(Zn,Cd)S:Cu,Al] component phosphors. No. 1 and No. 2 correspond to those in Figure 17. (From Kasei Optonix, Inc., unpublished results. With permission.)

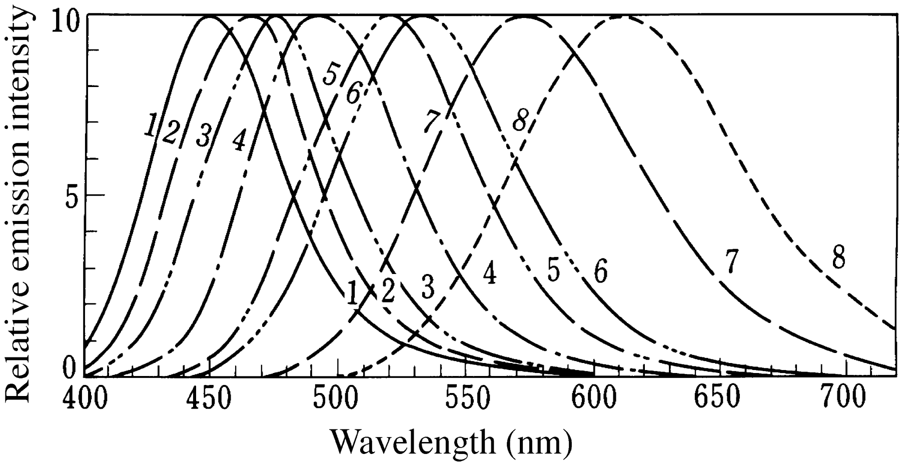

Figure 20 Emission spectra of cubic (Zn,Cd)S:Ag(0.005 wt%). All phosphors were produced by firing with 2% NaCl and 0.004% Ag at 780°C. The compositions corresponding to the various curves are as shown below. (From Leverenz, H.W., *An Introduction to Luminescence of Solids,* John Wiley & Sons, New York, 1950, 197. With permission.)

Curve		1	2	3	4	5	6	7	8
Mole ratio	ZnS	10	9.5	9	8	7	6	5	4
	CdS		0.5	1	2	3	4	5	6
Peak intensity	6-kV CR excitation	104	90	104	109	120	107	88	78
	365-nm UV excitation	45	27	36	51	55	53	66	56

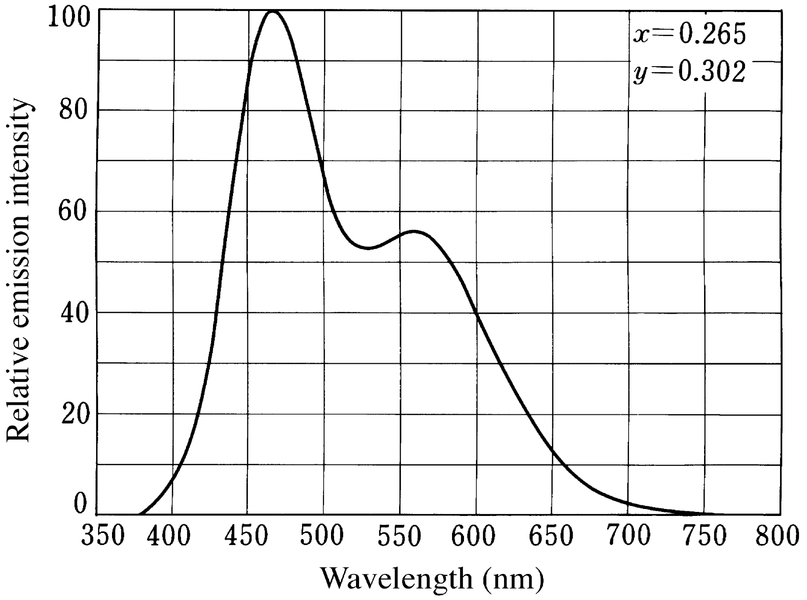

Figure 21 Emission spectrum of the (Zn,Cd)S:Ag,Au,Al phosphor. (From Kasei Optonix, Inc., unpublished results. With permission.)

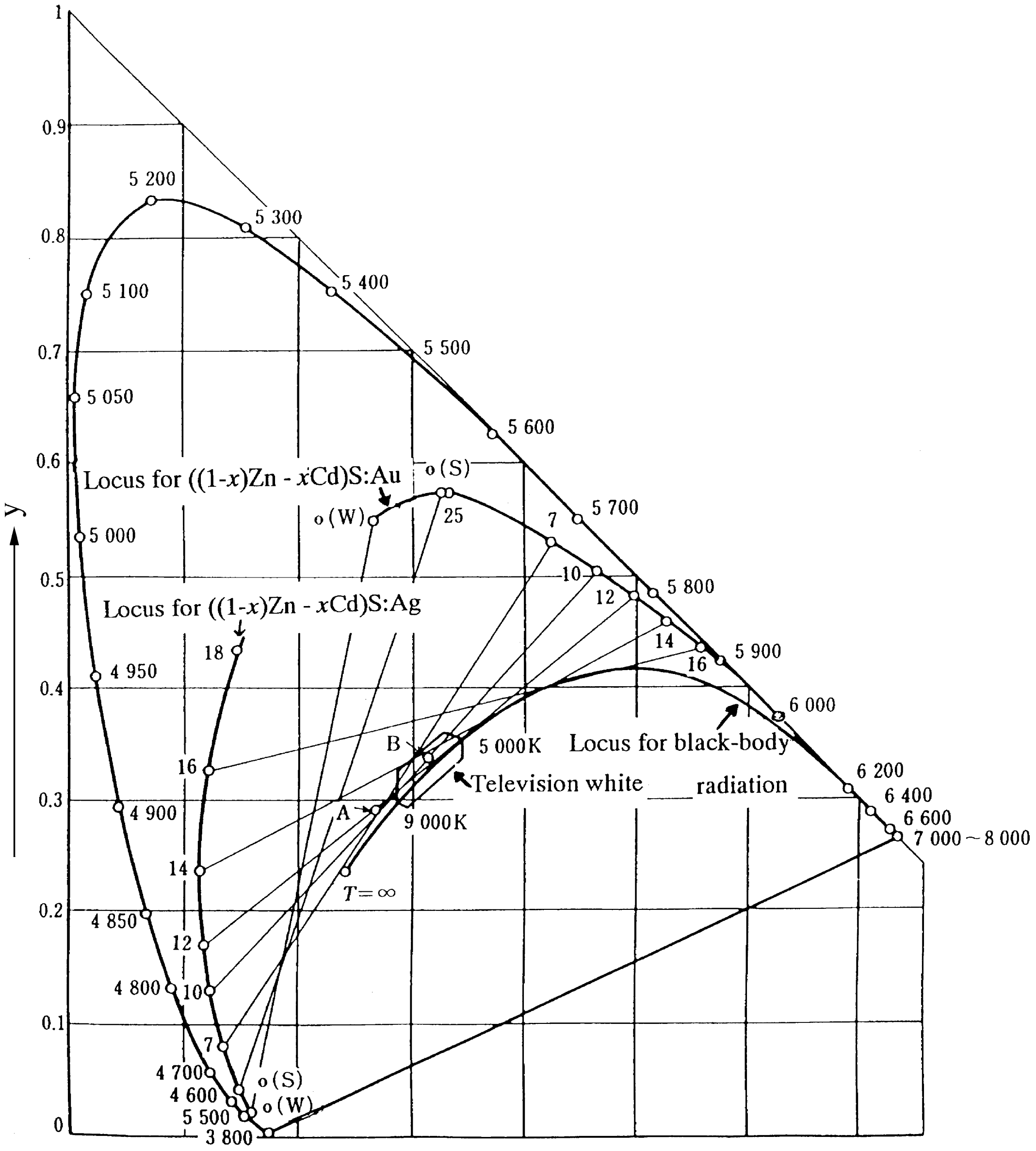

Figure 22 Controllable region of the chromaticity coordinates for the (Zn,Cd)S:Ag and (Zn,Cd)S:Au phosphor systems. (From Kröger, F.A., Bril, A., and Dikhoff, J.A.M., *Philips Res. Rep.*, 7, 241, 1952. With permission.)

ing the mixing ratio of the two-color phosphors, there are certain problems that require attention in actual practice. The phosphors are usually coated on monochrome cathode-ray tubes (CRTs) by the sedimentation method. (See 4.2.) Thus, if the two-component phosphors have different sedimentation rates, the two components separate, making the screen nonuniform. Accordingly, considering the specific gravities of the phosphors, the

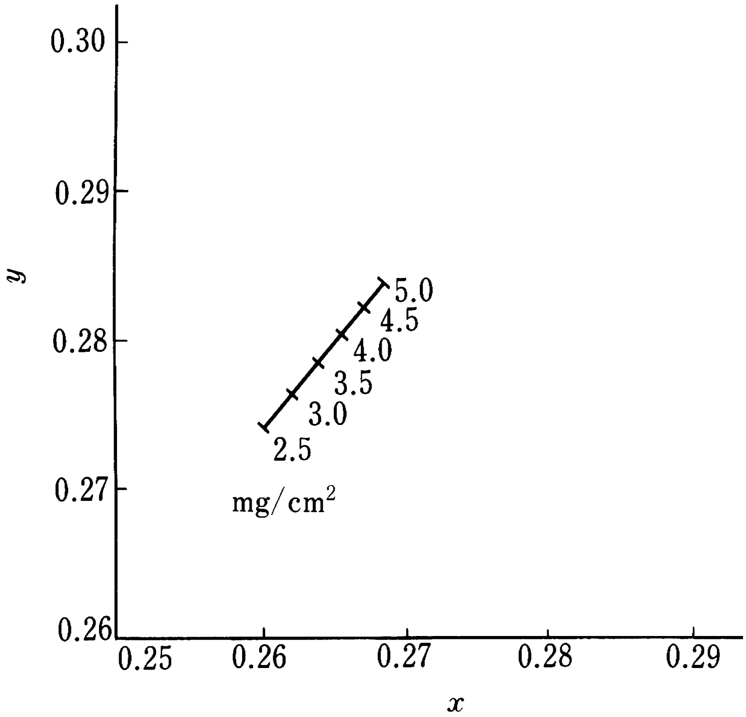

Figure 23 Color change in P4 phosphor with coating density (mg·cm^{-2}). (From Kasei Optonix, Inc., unpublished results. With permission.)

particle size and particle size distribution must be adjusted. Even when the same coating rate condition is attained, the emission color can vary somewhat according to the coating weight per unit area. This is because the light emitted by the blue component phosphor is absorbed by the yellow component. An example of this change in color with the coating weight is shown in Figure 23.[1] In the case of coating on an actual CRT, changes in such conditions as the water temperature and cushion height can also produce color variations, so a high level of control is needed to attain strict color accuracy.

On the other hand, in order to obtain a defect-free phosphor screen, the wet adhesion strength, which is required during the decanting of the supernatant liquid after phosphor sedimentation, and the dry adhesion strength, which is required during the water spraying that is done after the phosphor screen drying process, are important characteristics that need to be considered. (See 4.2.)

The wet adhesion strength and the dry adhesion strength are both affected by the surface condition of the phosphor. They vary greatly with the concentration of potassium water glass and the concentration of electrolytes such as barium salts during sedimentation. The dry adhesion strength increases with higher concentrations of potassium water glass and with lower concentrations of barium salts, while the wet adhesion strength has an optimum concentration for each of those two factors. A typical iso-adhesion line diagram is shown in Figure 24.[1] The wet adhesion strength shown in this figure by numerical values is the area, measured as the product of the minor axis and the major axis (mm^2), of the ellipse-like part in which phosphor is peeled off by the water flow of a certain pressure from a nozzle onto the phosphor surface. Thus, a smaller value indicates greater strength.

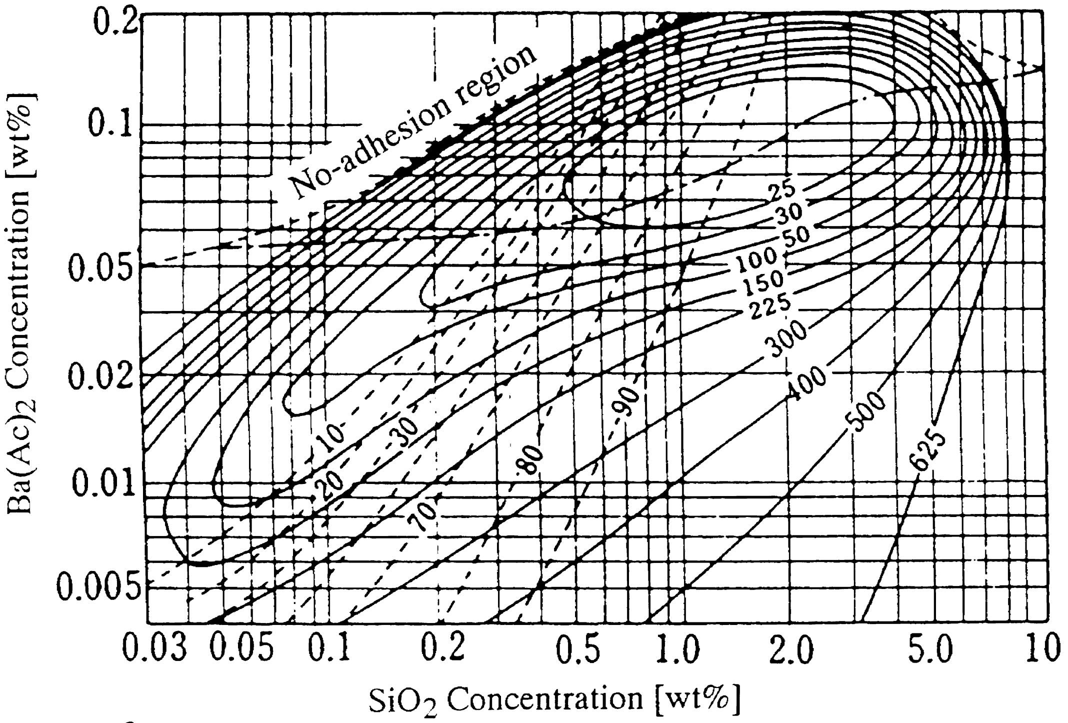

Figure 24 Iso-adhesion line diagram for P4 phosphor. Potassium water glass (silicate) solution: setting: 35°30' drying: 60°30' ——: Wet adhesion strength [mm^2] —·—: White muddiness boundary ----: Dry adhesion strength [lb/in^2] ----: Wet adhesion boundary. (From Kasei Optonix, Inc., unpublished results. With permission.)

Synthesis methods. The synthesis of sulfide phosphors involves the following three main steps.

Preparation of highly pure zinc sulfide (or cadmium sulfide)
Blending and firing
Treatment after firing

Synthesis of the blue phosphor

1. **Preparation of highly pure zinc sulfide:** To synthesize the blue phosphor ZnS:Ag, the first requirement is highly pure zinc sulfide. The most common production method is to have hydrogen sulfide react with a zinc salt solution to obtain a zinc sulfide precipitate ($Zn^{2+} + H_2S \rightarrow ZnS + 2H^+$). Zinc salts that are used are zinc sulfate, zinc chloride, or other such salts. Although these salts are obtained by reacting metallic zinc with mineral acids, this reaction becomes more difficult as the purity of the zinc increases (Figure 25[1]). If zinc oxide is used, dissolution becomes easier.

   Next, to the zinc solution an oxidizing agent such as hydrogen peroxide or bleaching powder is added to precipitate iron, manganese, and other heavy metals; then, after filtering, additional zinc is added to replace the heavy metals and thus purify the zinc solution. This zinc solution is reacted with hydrogen sulfide to obtain a zinc sulfide precipitate. The precipitate is rinsed with water to remove the acid by-products. This process produces the precipitate from an acidic solution;

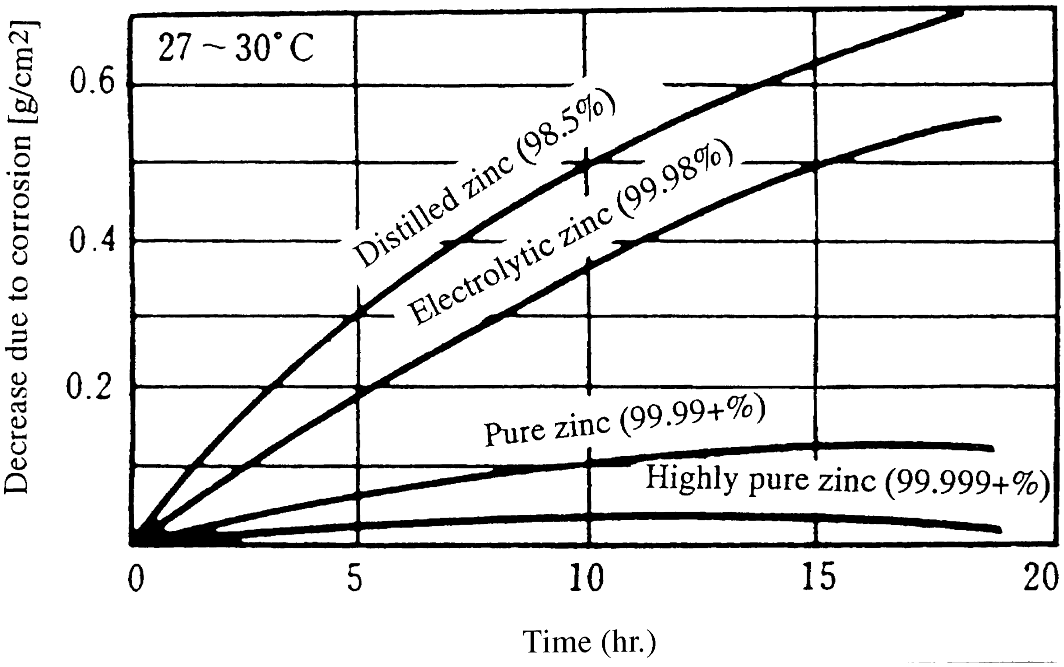

Figure 25 Corrosion of various types of zinc by 1N H_2SO_4 solution. (From Kasei Optonix, Inc., unpublished results. With permission.)

there are also methods for obtaining the precipitate from an alkaline solution without the use of hydrogen sulfide.[3–8] The reactions for two such examples are shown below.

$$Zn(OH)_2 + (H_2N)_2CS \rightarrow ZnS + (H_2N)_2CO + H_2O$$

$$(CH_3CO_2)_2Zn + (NH_4)_2S \rightarrow ZnS + 2(CH_3CO_2NH_4)$$

Precipitates from chlorides contain residual chloride ions that diffuse into the host material during firing and degrade the emission characteristics of the phosphor. Thus, care is required in using this process. It is also possible to add silver, copper, or other such activators at the time of the above-described sulfide precipitation; the metals also co-precipitate out as sulfides.[9]

2. **Blending and firing:** 0.01 wt% silver in the form of silver sulfate or silver nitrate is added to the zinc sulfide obtained as described above. Chlorides such as NaCl and $MgCl_2$[10] are also added to provide the chlorine co-activator and also to act as the flux. After thorough blending, the mixture is fired for several hours in a quartz crucible or quartz boat at temperatures from 850 to 1000°C[11] in a sulfurizing atmosphere.
3. **Treatment after firing:** The fired cake is washed well with water to remove flux and other residues. Surface treatment is done to improve the coating characteristics. (See 4.2.) The phosphor is then dried and sieved, completing the production process.

The flowchart of the process beginning with the zinc sulfide raw material is shown in Figure 26.[1]

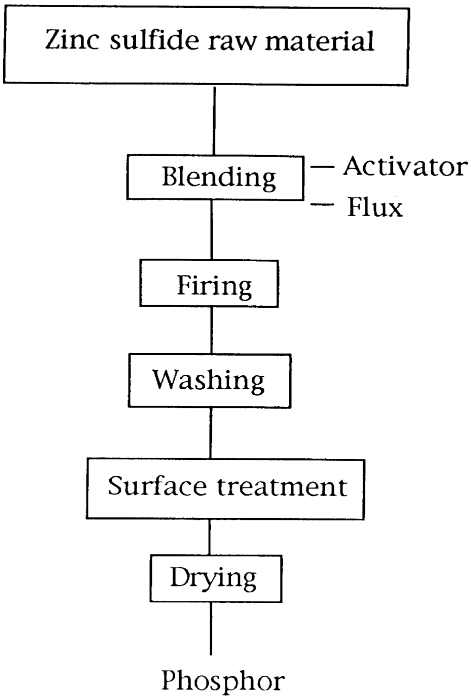

Figure 26 ZnS:Ag blue phosphor synthesis processes. (From Kasei Optonix, Inc., unpublished results. With permission.)

Synthesis of the yellow phosphor

1. **Preparation of the highly pure raw material:** The raw materials for the (Zn,Cd)S:Cu,Al phosphor are zinc sulfide and cadmium sulfide. While these two raw materials can be separately prepared by the method described above for the blue phosphor and then combined in the required proportions at the time of phosphor synthesis to form the (Zn,Cd)S, it is also possible to make a solution of zinc and cadmium salts prepared in the required proportions, and to react the mixture with hydrogen sulfide to obtain the zinc-cadmium coprecipitate.
2. **Blending and firing:** In place of the silver activator in ZnS:Ag, copper and aluminum are added as the activator and co-activator, respectively. To ensure sufficient diffusion of the aluminum co-activator into the host material during firing, the sulfurizing atmosphere must be stronger than that used in the synthesis of ZnS:Ag.

6.2.2 *Phosphors for monochrome display tubes*

CRTs for displays require higher resolution than entertainment television CRTs because they display characters and graphics rather than moving images. To attain higher vertical resolution, the number of scanning lines must be increased. The number of scanning lines is determined by the ratio of the horizontal to the vertical scanning frequencies (f_H:f_V). Thus, to increase the number of scanning lines, it is necessary to either increase the horizontal scanning frequency or decrease the vertical scanning frequency.

Increasing the horizontal scanning frequency makes it necessary to increase the bandwidth of the video signal, which would add costs to production and be difficult to implement for monochrome displays, which have the merit of being inexpensive. Decreasing the vertical scanning frequency, on the other hand, reduces the number of frames that

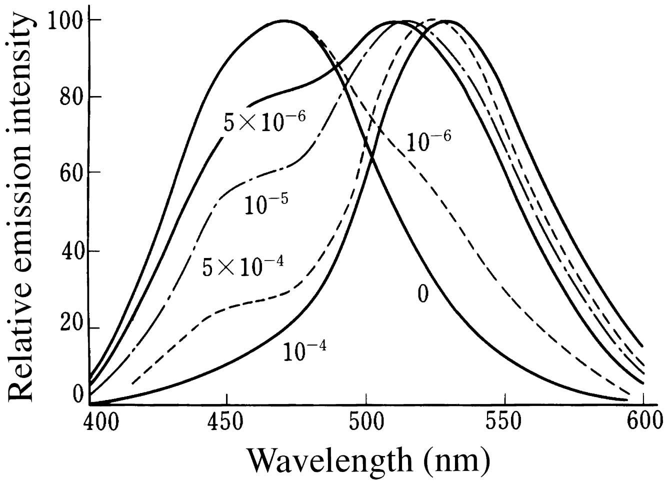

Figure 27 Relationship between the amount of copper in ZnS:Cu and the emission spectrum (figures in the curves indicate Cu wt%). (From Takagi, K. and Yamada, Y., *Optical Properties of Semiconductors Simplified*, Sanpo, Tokyo, 1965, 143 (in Japanese). With permission.)

can be displayed per second (= f_V). This creates flicker, so that in this case, phosphors with long persistent after-glow are required.

Required characteristics. Display tubes must have a higher resolution than entertainment television tubes, and the entire screen must be completely free of defects. Accordingly, the phosphors used in these tubes must have better dispersion and more stable adhesion characteristics. Moreover, as described earlier, ordinary monochrome display tubes generally operate with a low vertical scanning frequency, so the phosphor must also have long persistent after-glow.

Practical phosphors. The cubic-ZnS:Cu (≅ 0.01 wt%) phosphors (P31) are short-persistent and well known for their use in the early oscilloscopes. The color purity of these phosphors varies with the concentration of the copper activator (Figure 27[12]).

When the vertical scanning frequency is lowered for the purpose of increasing the resolution, Zn_2SiO_4:Mn^{2+} (2×10^{-3} to 1×10^{-2} g-atom/mol), As (≅1×10^{-4} g-atom/mol) (P39) is used. This phosphor differs from the Zn_2SiO_4:Mn^{2+} (2×10^{-3} to 1×10^{-2} g-atom/mol) (P1) phosphor in decay characteristics. As shown in Figure 28,[12] this phosphor has a longer decay time than Zn_2SiO_4:Mn^{2+}, which has a decay time of 25 ms (10% decay time). One drawback of these phosphors, synthesized using Zn_2SiO_4 as the host, is their susceptibility to burning by the electron beam. However, this weak point is being improved as a result of research on synthesis methods.[13]

In addition to the green-emitting phosphors described above, white-emitting phosphors are also used. Many of the short-persistent type are yellowish in color, having the same composition as the P4 (ZnS;Ag + (Zn,Cd)S;Ag) phosphors. P40 (ZnS;Ag + (Zn,Cd)S;Cu) is a white phosphor of moderate persistence. This phosphor, like P4, is a mixture of blue and yellow phosphors. It has the same composition as the P7 (ZnS;Ag + (Zn,Cd)S;Cu) phosphors used in radar screens. In the case of P7, the blue and yellow phosphors are coated on the tube separately, forming a two-layer structure (Figure 29[1]). On the other hand, in the case of P40, the two components are mixed as powders and coated together in a single layer. A point of difference between P40 and P4 is that the yellow component of the former has a long persistence.

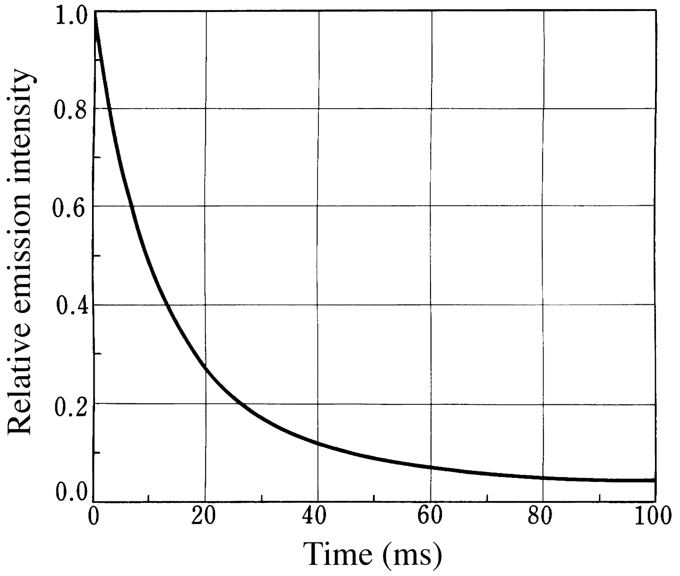

Figure 28 Decay curve of Zn_2SiO_4:Mn^{2+},As (P39) phosphor. (From Kasei Optonix, Inc., unpublished results. With permission.)

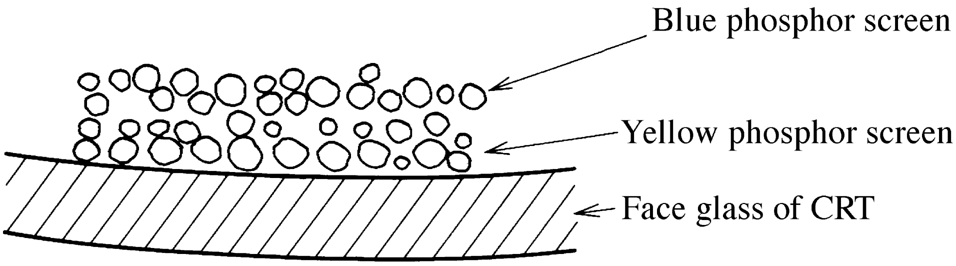

Figure 29 Structure of the P7 phosphor screen. (From Kasei Optonix, Inc., unpublished results. With permission.)

The fact that the persistence for excitation by ultraviolet light is longer than that for excitation by the electron beam is utilized to obtain a long-persistent yellow phosphor. That is to say, the yellow phosphor is excited simultaneously by both the electron beam and the emission of the blue phosphor, thus exhibiting long persistence. Thus, strictly speaking, the P40 phosphor emission by the electron beam is white, but the persistent color is yellow. The emission spectrum of the blue phosphor is located in a shorter wavelength region than in the case of the ordinary P4 phosphor, so as to serve as a better excitation source through the yellow phosphor. The persistence of the yellow phosphor through excitation by ultraviolet light is lengthened by techniques such as high-temperature firing and by reduction of the copper concentration in the synthesis process. The decay characteristics of the yellow phosphor for excitation by ultraviolet light and by electron beam are shown in Figure 30.[14]

For displays that users observe for long time, research on the emission color and persistence from the viewpoints of the labor environment and ergonomics has been performed recently. As a result of such research, phosphors for which emission colors are slightly more yellowish (known as paper white or egg-shell white) than the white color of the phosphors used in ordinary black-and-white television tubes are now being used.

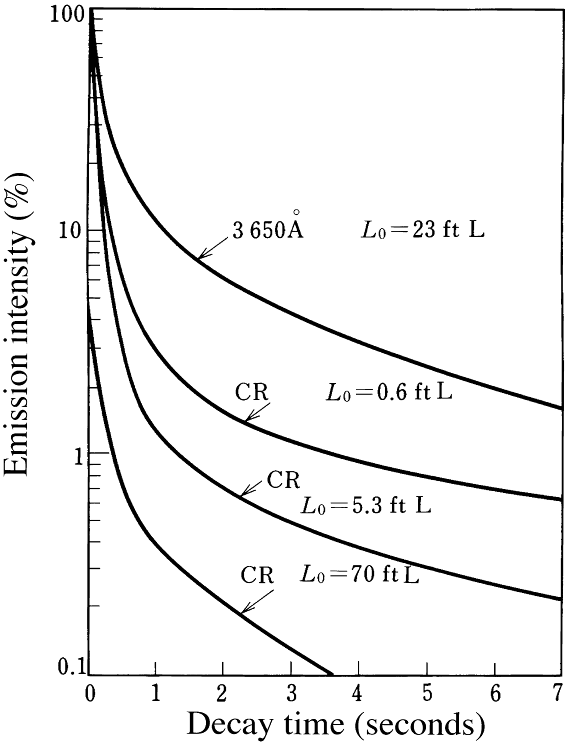

Figure 30 Decay curves of hex. $Zn_{0.9}Cd_{0.1}S$:Cu(0.0073 wt%) phosphor after ultraviolet (3650 Å) and cathode-ray excitation. (From Leverenz, H.W., *An Introduction to Luminescence of Solids*, John Wiley & Sons, New York, 1950, 264. With permission.)

Cautions in application. The color shift described in 6.2.1.1 is not a problem for single-component phosphors. However, the same cautions as described in 6.2.1.1 for synthesis and handling are necessary.

Synthesis methods. The synthesis of sulfide phosphors was discussed in Section 6.2.1.1. The synthesis of $Zn_2SiO_4:Mn^{2+}$,As (P39) can be accomplished in the same way as for the P1 phosphors except that As must be added at the blending stage. The synthesis of P1 has been discussed often in the literatures since the early days.[15] In a typical synthesis, ZnO, SiO_2, and manganese salt in powder form are mixed well and fired for several hours at 1000°C or above. The theoretical molar ratio of ZnO to SiO_2 in zinc orthosilicate is 2, but in actual practice it is better to add the SiO_2 in slight surplus (i.e., use a molar ratio of less than 2). The amount of manganese used in practice is about 1.5%.[16]

6.2.3 Phosphors for color television tubes

Since the time when the phosphors for three colors to be used in color television tubes were first developed, there has been continuous improvement in their basic characteristics. In particular, luminescence efficiencies have increased. The combinations of the phosphors for the three colors employed up until the present time are listed in Table 1.[1] The original blue phosphor was ZnS:Ag (0.01–0.03 wt%) and it is still being used. The original green phosphor $Zn_2SiO_4:Mn^{2+}$ (P1) is, among the currently known green phosphors, the one that has the highest color purity. However, P1 has insufficient luminescence efficiency for use in television tubes, and its decay is rather long (about 25 ms to 10% decay time). For these

Table 1 Historical Changes of Phosphors for Practical Use in Color Television Picture Tubes

	Blue	Green	Red
1	ZnS:Ag	Zn_2SiO_4:Mn^{2+}	$Zn_3(PO_4)_2$:Mn^{2+}
2	ZnS:Ag	(Zn,Cd)S:Ag	(Zn,Cd) S:Ag
3	ZnS:Ag	(Zn,Cd)S:Ag	YVO_4:Eu^{3+}
4	ZnS:Ag	(Zn,Cd)S:Cu,Al	Y_2O_2S:Eu^{3+} or Y_2O_3:Eu^{3+}
Current	ZnS:Ag	ZnS:Au,Cu,Al or ZnS:Cu,Al	Y_2O_2S:Eu^{3+}

From Kasei Optonix, Ltd., unpublished data. With permission.

reasons, it is no longer used for television tubes. For the red phosphor, $Zn_3(PO_4)_2$:Mn^{2+} (1×10^{-2} to 1×10^{-1} g-atom/mol) (P27) was originally used. This phosphor has excellent color purity, but has insufficient luminescence efficiency and too long a decay time (~40 ms). Further, it is susceptible to hydrolysis and thus unstable. This phosphor posed serious difficulties in application.

To avoid the problems noted above in using these green and red phosphors, sulfide phosphors were adopted in 1962. By controlling the quantity of cadmium in the composition formula (Zn,Cd)S:Ag of the green and red phosphors, so as to attain the respective chromaticity coordinates of $x = 0.24$ and $y = 0.56$, and $x = 0.65$ and $y = 0.34$, the luminescence efficiency was increased by a factor of 1.7 relative to the former CRTs that employed oxysalt phosphors.[17]

Since 1965, rare-earth red phosphors such as YVO_4:Eu^{3+} (3–5 mol%), Y_2O_3:Eu^{3+} (3–5 mol%), and Y_2O_2S:Eu^{3+} (3–5 mol%) have come into use. The green phosphor has been changed from the silver-activated system to one that is copper activated, (Zn,Cd)S:Cu,Al. In response to the ecological concerns beginning in the 1970s, green phosphors have been replaced by phosphors that do not contain cadmium, that is, ZnS:Cu(0.004–0.04 wt%),Al(0.003–0.03 wt%) or ZnS:Au(0–0.04 wt%),Cu,Al. At about the same time, phosphor dispersion techniques were improved so that phosphors could be applied to the tubes without ball milling.

This history of the change in the phosphors is also the history of increasing luminescence brightness of CRTs. Great improvements in the brightness were achieved, accompanied by improvements in the structure of CRTs. From about 1976, brightness was sacrificed to some extent for improvement in contrast. To obtain better image quality in bright surroundings, the technique of coating phosphor particles with color pigments was introduced. At present, pigment coating of blue and red phosphors is common practice.

In the following, an explanation of the basic characteristics required of phosphors for use in color television tubes is given. The phosphors in use until now and the synthesis methods for some typical phosphors is also described.

Basic characteristics required of phosphors for use in color TVs. Superior characteristics for color CRTs include a wide color reproduction range, the ability to display images with high contrast, relatively high resolution, no flickers or after-images, and a long operating lifetime. To attain such performance, the following characteristics are required of the phosphors used in these CRTs.

1. High color purity of the emission color
2. High emission efficiency and an appropriate after-glow persistence
3. Long life
4. Suitability for the CRT manufacturing processes and stability of quality (application characteristics)

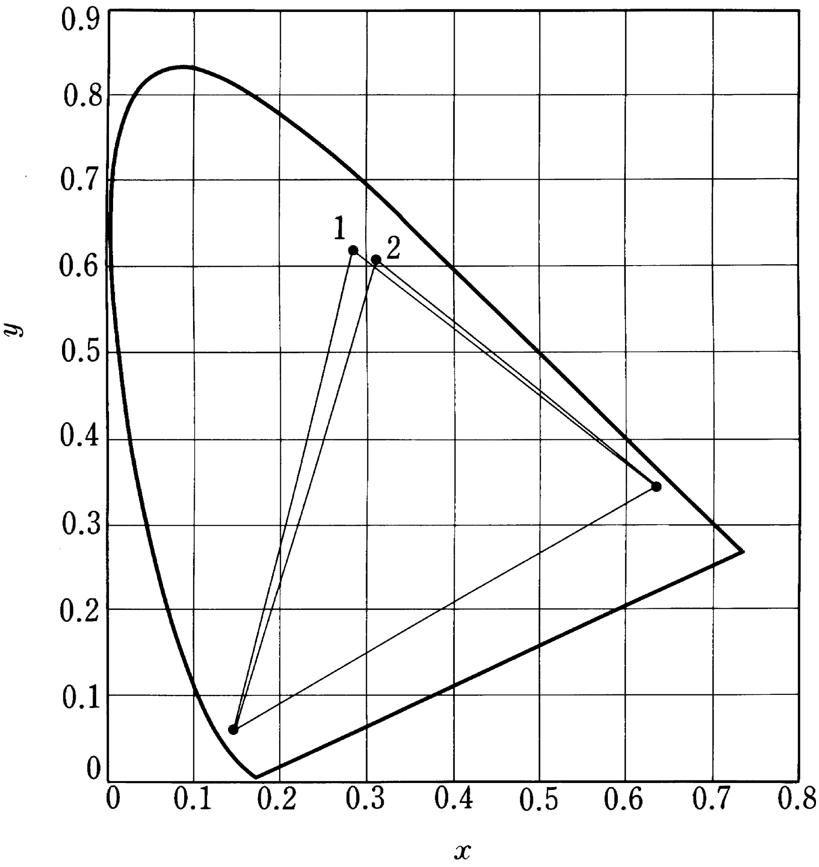

Figure 31 Chromaticity coordinates of the three colors of current color CRTs. The green phosphor (1) is ZnS:Cu,Al and (2) is ZnS:Au,Cu,Al. (From Kasei Optonix, Inc., unpublished results. With permission.)

These four items are explained below.

To achieve a broad color reproduction range for CRTs, the red, green, and blue phosphors should have *high color purity*. In practice, the chromaticity coordinates of the three color phosphors are chosen according to the relationship with visibility, the relationship with electric current balance among the three color phosphors, and other such factors. The chromaticity coordinates of the three colors and the color reproduction ranges for typical current phosphors are shown in Figure 31.[1]

Along with color, another very important CRT characteristic is *brightness*. When watching a television screen in a bright place, the screen must be brighter than the external light. Thus, phosphors with high emission efficiency are needed. At the same time, the balance among the three colors must be maintained; that is, it is important that there be no large imbalance between the currents that excite the three color lights which are being emitted to produce white light.

The television image is formed by the electron beam scanning across the phosphor screen. In the NTSC format used in Japan, the U.S., and various other countries, the scanning frequency is 60 Hz. Thus, if the phosphors have a certain degree of persistent after-glow after excitation, it brings about a desirable effect of preventing the sensation of screen flicker. If the after-glow is too long, on the other hand, it has an undesirable effect that moving bright areas in the image leave perceptible trails. The after-glow of phosphors in current use is from 100 to 200 μs for the sulfide phosphors and from 1 to 2 ms for the rare-earth phosphors, so the problem just described is not encountered.

Concerning the problem of phosphor life, in the case of large electric currents such as in the projection TVs that will be described later, there are problems of the coloration and the reduction in the emission efficiency of the phosphors. Under the conditions of ordinary entertainment television CRTs, however, phosphor life is rarely a problem as long as there is sufficient quality control in the manufacturing processes.

The properties of the phosphors themselves determine principally the performance characteristics described above. Thus, to improve these characteristics further, it is desirable to discover phosphors with new properties. In recent years, however, there have been no new phosphors discovered that could be used for these applications.

On the other hand, the ease of the use of phosphors (i.e., suitability for the CRT manufacturing processes) has become extremely important for improving productivity in today's mass production of CRTs; improvement is being made year by year in this area. The most striking progress has been in dispersing the phosphors; in the past, ball milling was used in the slurry production process to achieve better dispersion and thus obtain a more uniform phosphor screen, but now the dispersion of the phosphor particles has been improved to such an extent that ball milling is no longer required. As a result, the degradation of the phosphor luminescence efficiency caused by physical damage to the phosphor particles during the ball milling has been avoided, and CRTs with greater brightness have become possible to manufacture. Surface treatment for preventing the missing of phosphor dots or stripes in the photographic development process has also been improved, which has helped to increase the yield in CRT manufacturing.

Practical phosphors. The phosphors of the three colors in current use are described here in detail, focusing on the synthesis methods.

Blue phosphors. From the time when color television was invented up to the present, ZnS:Ag(0.01–0.03 wt%) has remained unchanged as the blue phosphor. This phosphor is described in 6.2.1.1, the section on phosphors for black-and-white TVs, but the surface treatment applied to them is different when they are used in color television picture tubes. While pigment-coated phosphors are currently in the mainstream, partially unpigmented phosphors are also coming into use. The unpigmented phosphors are given ordinary silicate surface treatment while the pigmented phosphors are coated with cobalt blue or ultramarine blue. (See 4.2.) The reflection spectra for cobalt blue and ultramarine blue are shown in Figure 32[1]; the respective reflection spectra for the ZnS:Ag phosphor with a 2% coating of these pigments are shown in Figure 33.[1]

Green phosphors. $Zn_2SiO_4:Mn^{2+}$ and (Zn,Cd)S:Ag have been replaced by ZnS:Cu,Al or ZnS:Au,Cu,Al as the green phosphor because of the problems associated with the use of cadmium. As described in the section on phosphors for black-and-white television picture tubes, the luminescent color of (Zn,Cd)S:Cu,Al can be freely selected by changing the molar ratio of Zn to Cd. In the case of ZnS:Au,Cu,Al, the luminescent color can be easily varied from green to yellow by controlling the concentrations of gold and copper (Table 2 and Figure 34).[18] In the case of the ZnS:Cu,Al phosphor, the luminescent color is more or less constant. A typical emission spectrum is shown in Figure 35.[1]

In the synthesis of the green phosphors described above, copper, gold, or other activator or co-activators are added to the high-purity zinc sulfide (or a prescribed amount of high-purity cadmium sulfide when cadmium is included) described earlier. Then flux is added. After thorough blending, the mixture is fired in a quartz crucible or boat from 900 to 1100°C under a sulfurizing atmosphere. The cake is then thoroughly rinsed and silicate surface treatment completes the process.[18–20]

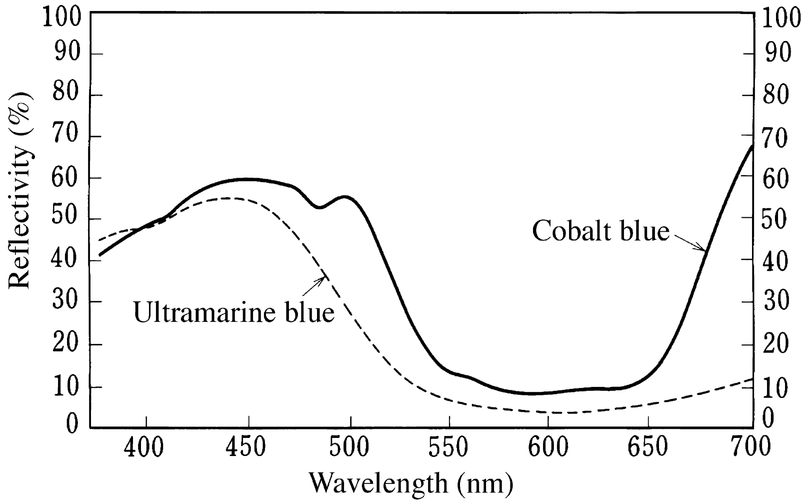

Figure 32 Reflection spectra of blue pigments. (From Kasei Optonix, Inc., unpublished results. With permission.)

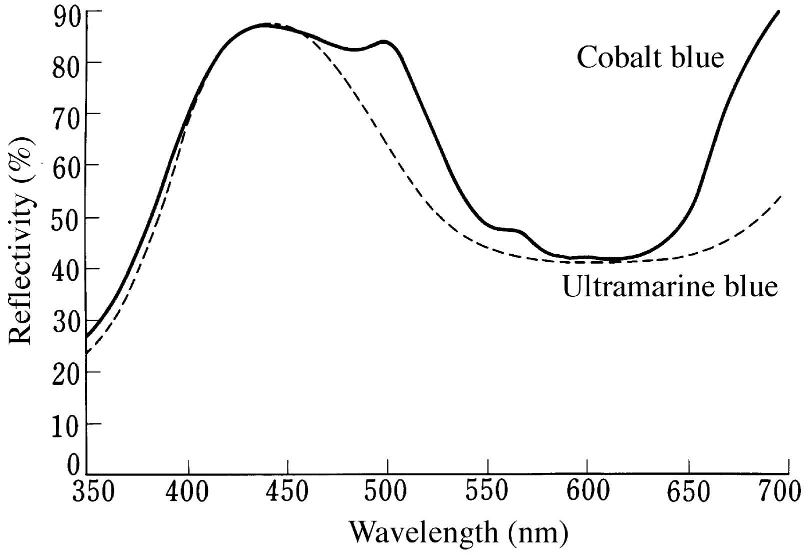

Figure 33 Reflection spectra of ZnS:Ag phosphor coated with cobalt blue and with ultramarine blue. (From Kasei Optonix, Inc., unpublished results. With permission.)

Red phosphors. Up to about 1965, the sulfide phosphors (Zn,Cd)S:Ag were used for red phosphors; after that, they were replaced by rare-earth phosphors, raising the brightness of color television to a higher level. The first rare-earth phosphor to be adopted was $YVO_4:Eu^{3+}$.[21,22] Subsequently, $Y_2O_3:Eu^{3+}$ was actively studied and made practical.[23,24] These phosphors, however, suffered from hydrolysis in the phosphor screen production process; this degraded slurry characteristics and reduced the luminescence efficiency of the phosphors. After a solution to this problem was found, these stabilized phosphors came into use.[25–27] Later, $Y_2O_2S:Eu^{3+}$ was developed and this phosphor is currently most widely used as the red phosphor for color televisions.[26–31] Typical emission spectra for these three types of phosphors are shown in Figures 36, 37, and 38.[1]

Table 2 Relationship Between Emission Color (chromaticity coordinates) and Activator Concentration in ZnS:Au,Cu,Al (wt%)

Cu	Au	Al	x	y	lm W^{-1}
0.01	0.01	0.01	0.301	0.598	492
0.01	0.02	0.01	0.317	0.598	498
0.01	0.03	0.01	0.331	0.596	504
0.01	0.04	0.01	0.346	0.589	506
0.01	0.05	0.01	0.344	0.592	506
0.01	0.05	0	0.267	0.582	470
0.01	0.05	0.005	0.291	0.616	499
0.01	0.05	0.01	0.310	0.608	504
0.01	0.05	0.02	0.332	0.590	501
0.01	0.05	0.03	0.341	0.591	502
0.01	0.05	0.04	0.343	0.588	501
0.01	0.05	0.05	0.340	0.589	499
0.002	0.05	0.01	0.319	0.577	487
0.004	0.05	0.01	0.305	0.598	494
0.006	0.05	0.01	0.297	0.607	495
0.008	0.05	0.01	0.302	0.610	499
0.01	0.05	0.01	0.299	0.612	499

From Matsuura, S., Koga, Y., Ito, T., and Tamatani, M., *Tech. Digest, Phosphor Res. Soc. 166th Meeting*, 1977, 5 (in Japanese). With permission.

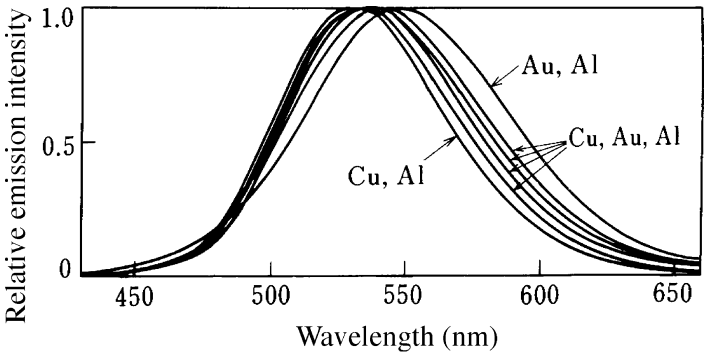

Figure 34 Emission spectra of ZnS:Au,Cu,Al phosphors. (From Matsuura, S., Koga, Y., Ito, T., and Tamatani, M., *Tech. Digest, Phosphor Res. Soc. 166th Meeting*, 1977, 5 (in Japanese). With permission.)

Synthesis methods. The synthesis of $Y_2O_2S:Eu^{3+}$ is given here. The rare-earth raw materials are highly pure oxides of yttrium and europium. Although the name of the rare-earth elements would indicate that they are found in extremely small quantities on the earth, the Clarke numbers for Ce, Y, Nd, La, and Gd range within the fiftieth. These numbers are three to four orders of magnitude larger than the Clarke numbers for platinum and gold. There are over 200 kinds of ores that contain rare-earth elements. The main ores are listed in Table 3,[1] and the compositions are listed in Table 4.[1] High-quality ores are found in China, India, Brazil, Finland, Canada, and countries formerly in the Soviet Union. The ore processing methods include the sulfate method and the alkali method. These two methods have their respective merits and demerits, but the tendency is to use the alkali method for large-scale production and the sulfate method for small-scale production.[32–36]

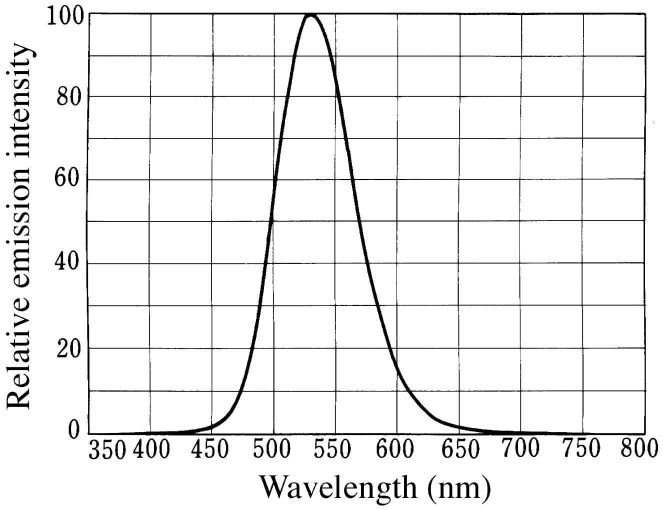

Figure 35 Emission spectrum of the ZnS:Cu,Al phosphor. (From Kasei Optonix, Inc., unpublished results. With permission.)

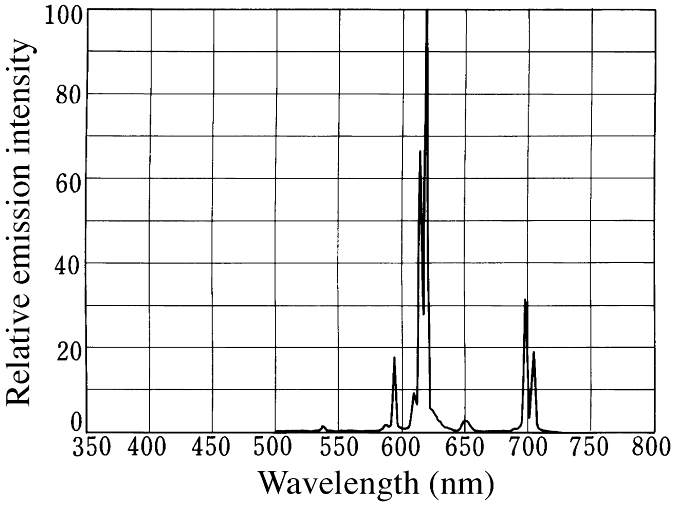

Figure 36 Emission spectrum of the YVO_4:Eu^{3+} phosphor. (From Kasei Optonix, Inc., unpublished results. With permission.)

The synthesis method of the Y_2O_2S:Eu^{3+} phosphor according to U.S. Patent USP–3418246 is described as an example. Y_2O_3 and Eu_2O_3 are dissolved in hydrochloric acid and co-precipitated as oxalates. Since the chromaticity coordinates of the emission varies with the Eu concentration (Figure 39),[1] it is necessary to perform this co-precipitation with the prescribed concentration of Eu. The precipitate is oxidized by heating in air and then fired for 1 hour at 1100°C in a hydrogen sulfide atmosphere.

An improvement in this method is to use the mixture of sulfur and sodium carbonate in place of hydrogen sulfide. Arsenates, germanates, phosphates, and sulfates of alkaline metals are used as fluxes.[28,29] With progress in purification techniques and an increase in the accuracy of material analysis, the enhancement effect of the Eu emission by Tb and Pr was discovered.[37] The phosphors obtained by the above methods are, as for the blue ZnS:Ag phosphor, rinsed well, given surface treatment, and pigmented when nec-

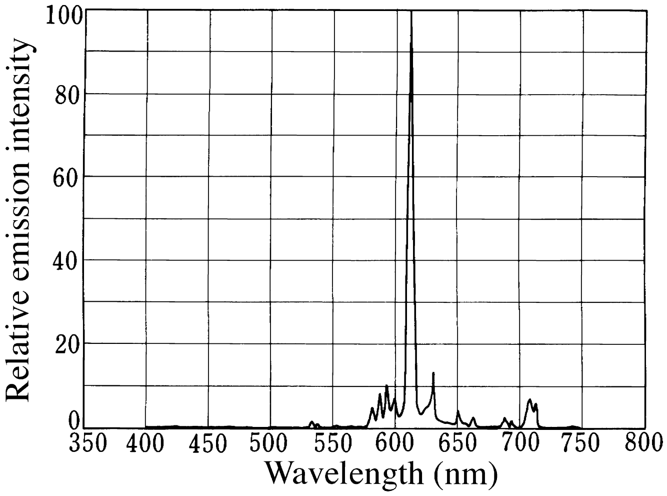

Figure 37 Emission spectrum of the $Y_2O_3:Eu^{3+}$ phosphor. (From Kasei Optonix, Inc., unpublished results. With permission.)

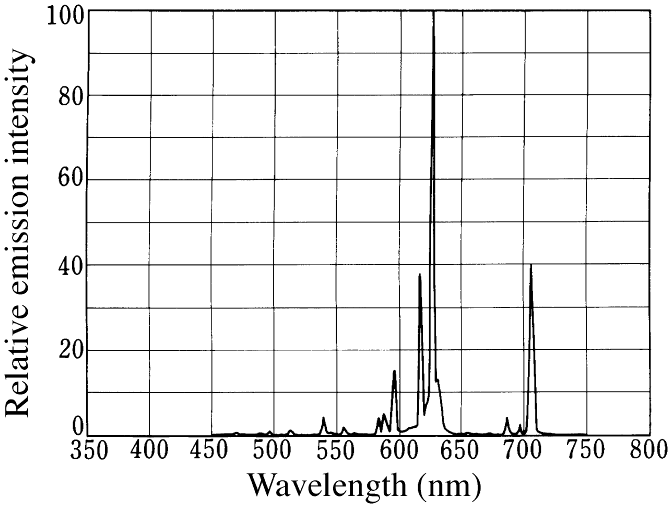

Figure 38 Emission spectrum of the $Y_2O_2S:Eu^{3+}$ phosphor. (From Kasei Optonix, Inc., unpublished results. With permission.)

essary. The available pigments include cadmium red (Cd(S,Se)) and iron oxide red (Fe_2O_3), but the latter is most widely used for its thermal stability and to avoid environmental pollution. Examples of reflection spectra of cadmium red and iron oxide red are shown in Figure 40[1]; reflection spectra of the $Y_2O_2S:Eu^{3+}$ phosphor coated with these pigments are shown in Figure 41.[1] Diagrams of the various stages of the $Y_2O_2S:Eu^{3+}$ phosphor synthesis described above are provided in the following figures. The rare-earth oxalate co-precipitation and decomposition processes are shown in Figure 42, the phosphor synthesis processes are shown in Figure 43,[1] and the pigment coating process is shown in Figure 43.[1]

Table 3 Main Rare Earth Ores

Ore	Chemical formula	Specific gravity	Crystal system
Monasite	(LR[a],Th)$\mathrm{PO_4}$	4.9–5.3	Monoclinic
Bastnaesite	$\mathrm{(LR)FCO_3}$	4.9–5.2	Hexagonal
Xenotime	(HR[a],Th)$\mathrm{PO_4}$	4.5–4.6	Tetragonal
Gadolinite	$\mathrm{Be_2Fe(LR,HRO)_2(SiO_4)_2}$	4.0–4.5	Monoclinic
Allanite	$\mathrm{(HR,LR,Fe,Ca,Al)Si_3O_{12}}$	5.5–6.0	Monoclinic
Cerite	$\mathrm{H_2(Ca,Fe)Ce_3Si_3O_{13}}$	4.8–4.9	Orthorhombic
Fergusonite	$\mathrm{HR(Nb,Ta)O_4}$	5.8	Tetragonal
Samarskite	$\mathrm{(Ca,Ca,UO_2)_3(LR,HR)_2(Nb,Ta)_6O_{21}}$	5.6–5.8	Orthorhombic

[a] LR: light rare-earth element; HR: heavy rare-earth element.

From Kasei Optonix, Inc., unpublished data. With permission.

Table 4 Example of the Compositions of the Main Rare-Earth Ores

	Bastnaesite (California)	Monasite (Australia)	Xenotime (Malaysia)
$\mathrm{R_2O_3}$	68–72	62.8	54.1
$\mathrm{ThO_2}$	<0.1	6.6	0.8
$\mathrm{U_2O_3}$	—	0.3	0.3
BaO	1.2		
SrO	0.7		
F	4.7		
$\mathrm{CO_2}$	20.0		
CaO	0.2	0.2	
$\mathrm{SiO_2}$	2.4	1.1	
$\mathrm{Fe_2O_3}$	<0.5	1.6	
$\mathrm{P_2O_5}$	<0.5	26.3	26.2
$\mathrm{InR_2O_3}$			
$\mathrm{La_2O_3}$	32.0	20.2	0.5
$\mathrm{CeO_2}$	49.0	45.3	5.0
$\mathrm{Pr_6O_{11}}$	4.4	5.4	0.7
$\mathrm{Nd_2O_3}$	13.5	18.3	2.2
$\mathrm{Sm_2O_3}$	0.5	4.6	1.9
$\mathrm{Eu_2O_3}$	0,1	0.05	0.2
$\mathrm{Gd_2O_3}$	0.3	2.0	4.0
$\mathrm{Tb_4O_7}$			1.0
$\mathrm{Dy_2O_3}$			8.7
$\mathrm{Ho_2O_3}$	0.1		2.1
$\mathrm{Er_2O_3}$		2.0	5.4
$\mathrm{Tm_2O_3}$			0.9
$\mathrm{Yb_2O_3}$			6.2
$\mathrm{Lu_2O_3}$			0.4
$\mathrm{Y_2O_3}$	0.1	2.1	60.8

Note: Concentrated ore, %.

From Kasei Optonix, Inc., unpublished results. With permission.

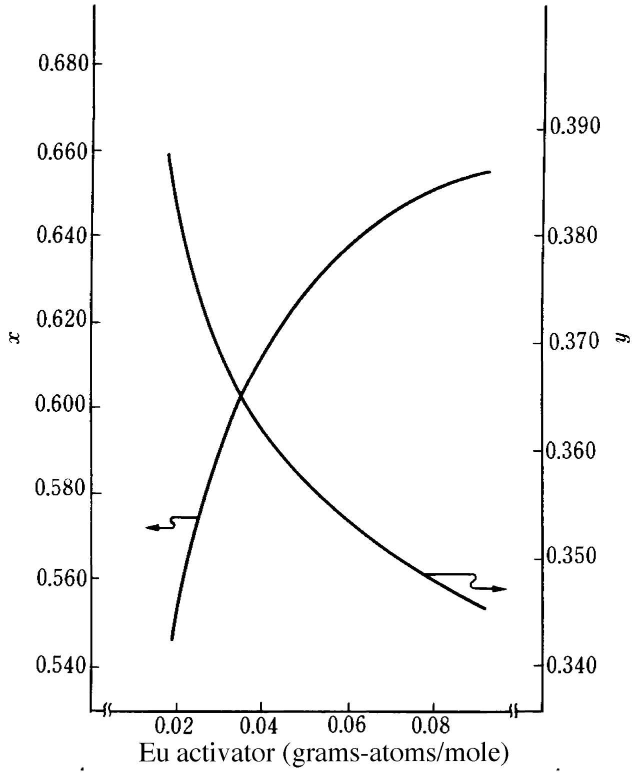

Figure 39 Eu^{3+} activator concentration and chromaticity coordinates, x and y, for $Y_2O_2S:Eu^{3+}$ phosphor. (From Kasei Optonix, Inc., unpublished results. With permission.)

6.2.4 Phosphors for color display tubes

Characteristics required of phosphors for use in color display tubes. The production of CRTs for color displays has expanded greatly in recent years. The main features of these CRTs are their higher resolution and image quality compared to entertainment color television CRTs. These features are required for the display of static characters and various types of graphics. In current shadow-mask (aperture grill) CRTs, the resolution is determined by the hole pitch of the mask (Figure 44).[1] The shadow masks used in entertainment color CRTs have a hole pitch of about 0.8 mm, but current high-resolution display CRTs have pitches as small as 0.2 mm. A shadow mask with such a small pitch must be very thin, in which case the miss-landing of the electron beam due to the doming of the screen becomes a major problem. The phosphor dot size for a pitch of 0.2 mm is 100 µm or less. Furthermore, so as to make the display of fine characters and graphics, faults in the phosphor screen are more serious than in an entertainment television screen. For a 14-inch screen, the phosphor dot number is 700,000 for each color, or 2.1 million in all. In addition to the obvious need to eliminate the missing of dots, color mixing and discoloration must be prevented, and uniformity over the entire phosphor screen is required. Because of these requirements, the good edge shape of dots, the absence of color mixing, and other conditions are regarded as more important in phosphor screens for color displays than those for entertainment television CRTs.

Practical phosphors. As described in 6.2.1.2 on phosphors for use in monochrome displays, phosphors with long after-glow persistence have usually been employed in order

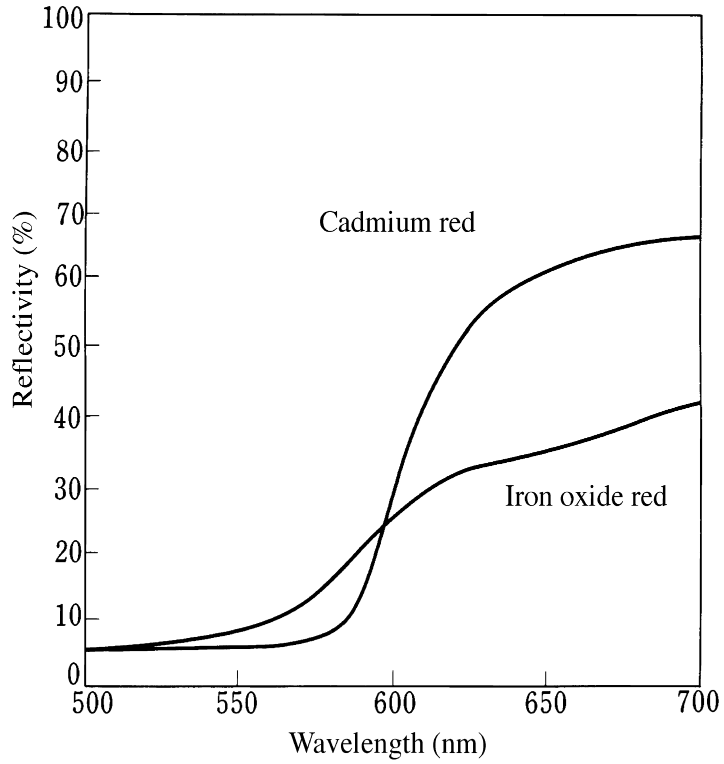

Figure 40 Reflection spectra of red pigments. (From Kasei Optonix, Inc., unpublished results. With permission.)

to prevent flicker. Recently, another way in which the horizontal scanning frequency is doubled or quadrupled to develop the NTSC format frequency has evolved. In this way, the refresh rate is raised so that the brighter short-persistent phosphors can be used. Phosphors with the same compositions as those used in color TVs are used, but with smaller particle sizes, making them suitable for use in the fine-pitch screens. Moreover, while in color television, the reproduction of natural color images is required and thus the color reproduction range should be as wide as possible, natural color reproduction is not required in the case of color displays. In particular, because the blue color causes fatigue in human eyes, phosphors of white-blue color are commonly used.

Green phosphors. As short-persistent green phosphors, ZnS:Cu,Al or ZnS:Au,Cu,Al are widely used. These are the same compositions employed in color TVs. For the long-persistent type, Zn_2SiO_4:Mn^{2+},As (P39) was used. The short-persistent and long-persistent phosphors are selected according to the relationship between the luminescence brightness and flicker; it is also possible to obtain intermediate characteristics by using mixtures of the two.

The persistence and luminescence brightness characteristics of the Zn_2SiO_4:Mn^{2+},As phosphor are governed by the amount of As in the composition; as the amount of As increases, the persistence increases, but the brightness decreases.[13] The persistence characteristics of this phosphor also vary with the electron beam excitation conditions. Specifically, higher excitation current densities result in shorter persistence times.

Red phosphors. Similar to the green phosphors, the red phosphors include short-persistent, long-persistent, and intermediate-persistent types. Main short-persistent phosphors currently used are those used in color television, i.e., Y_2O_2S:Eu^{3+} and related Eu^{3+} com-

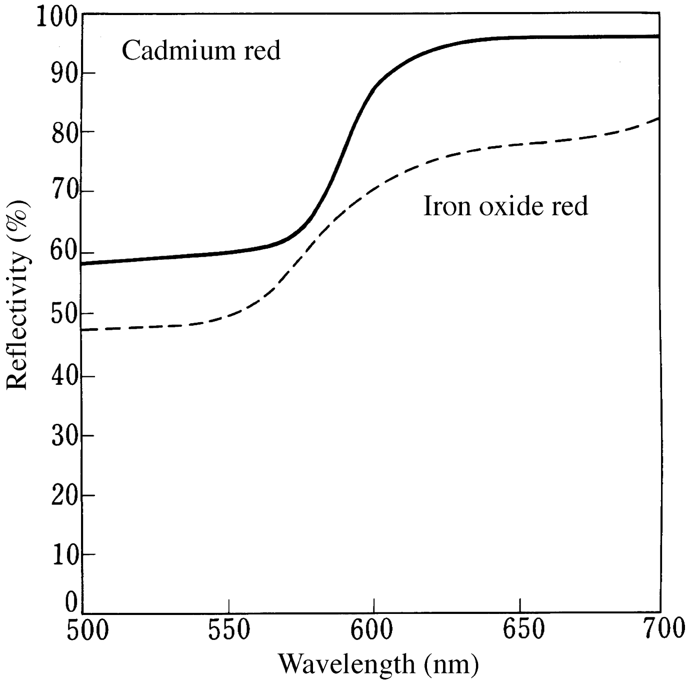

Figure 41 Reflection spectra of Y_2O_2S:Eu^{3+} phosphor coated with red pigments. (From Kasei Optonix, Inc., unpublished results. With permission.)

pounds. As long-persistent phosphors, $Zn_3(PO_4)_2$:Mn^{2+} (P27) was used. As the intermediate-persistent phosphors, mixtures of the long-persistent and short-persistent phosphors are used. The $Zn_3(PO_4)_2$:Mn^{2+} phosphor was originally used as the red phosphor in color television picture tubes, as mentioned above. The crystal structure of this phosphor host is β-$Zn_3(PO_4)_2$, and the persistent time was approximately 30 ms. For use as a long-persistent phosphor, very small amounts of Ca or Mg are substituted for Zn to change the crystal structure to γ-$Zn_3(PO_4)_2$. By doing so, the persistent time is changed to approximately 120 ms. Moreover, the emission spectrum of the γ-type phosphor is shifted toward shorter wavelengths relative to that of the β-type, so that the brightness becomes higher.

The decay curves of the two types of $Zn_3(PO_4)_2$:Mn^{2+} phosphors are shown in Figure 45[1]; their emission spectra are shown in Figure 46.[1] Unlike the green Zn_2SiO_4:Mn^{2+}, the decay times of these phosphors do not vary with the electron beam excitation conditions and are quite constant, which makes the phosphors easy to use. However, these phosphors are susceptible to hydrolysis, so that care is required in handling them.

Blue phosphors. As short-persistent blue phosphors, ZnS:Ag or ZnS:Ag mixed with other short-persistent phosphors to produce a somewhat whitish tint is used. When a long-persistent phosphor is needed, a mixture of ZnS:Ag with P39 or P27 was used as a measure against flicker, as no suitable phosphor of the simple composition is currently available.

It has been reported that the persistent time is lengthened somewhat by using gallium or indium as the co-activator for silver-activated sulfide phosphors.[38] The composition formula is ZnS:Ag (0.01–0.03 wt%),Ga(0.001–0.02 wt%) or ZnS:Ag,In.

Synthesis methods. The synthesis of the green phosphors (short-persistent sulfide phosphors and long-persistent P39) is described in 6.2.1.1 and 6.2.1.2; for the synthesis of the blue phosphors, see 6.2.1.1.

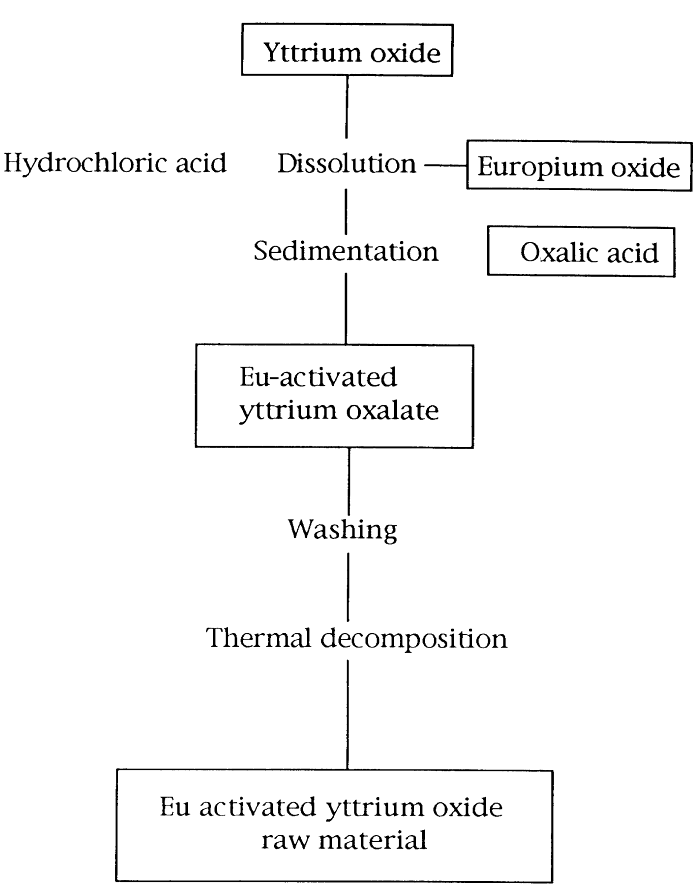
Yttrium oxide
Hydrochloric acid
Dissolution
Europium oxide
Sedimentation
Oxalic acid
Eu-activated yttrium oxalate
Washing
Thermal decomposition
Eu activated yttrium oxide raw material

Figure 42 Rare-earth oxalate co-precipitation and decomposition processes. (From Kasei Optonix, Inc., unpublished results. With permission.)

The synthesis of the red phosphor γ-$Zn_3(PO_4)_2$:Mn^{2+} (P27) is described here. This synthesis needs stricter optimum conditions than that of the β-type. Several methods for synthesizing stable phosphors have been proposed. An example of these methods is the replacement of some of zinc in the compound with magnesium.[39,40] Zinc oxide, magnesium oxide, orthophosphoric acid or diammonium phosphate, and manganese carbonate are mixed, either in wet or dry conditions. The mixture is fired in a quartz crucible from 900 to 1150°C. The molar ratio of zinc to magnesium, the molar ratio of (zinc + magnesium) to phosphorus, and the concentration of magnesium all affect the luminescence brightness and persistence of the phosphor.[39–41] The β-type phosphor is produced at higher firing temperatures. As the firing temperature is increased, there is a tendency for the emission color shifts toward longer wavelengths and the persistence to become shorter. As a result, there is a complex relationship between the composition ratios described above and the firing conditions; the synthesis conditions must be controlled according to the objectives for the phosphors being produced.

Recently, the demand for color display CRTs has increased year to year as the popularity of personal computers has increased rapidly. The screen resolution has steadily evolved from medium-resolution screens with dot pitches of 0.4 mm to high-

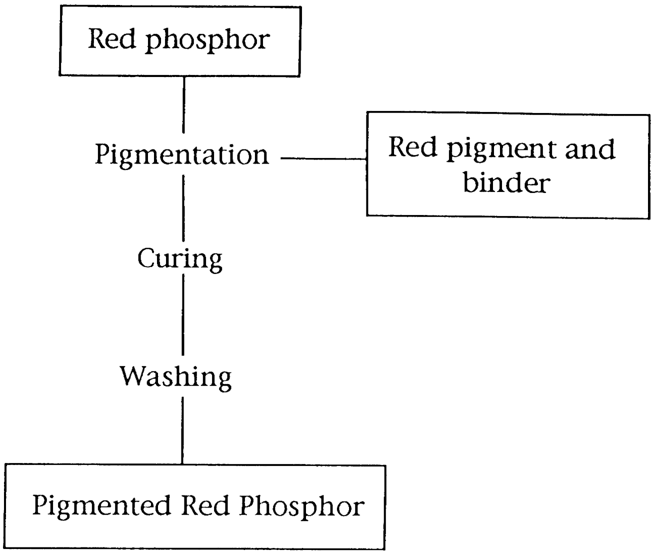
Red phosphor
Pigmentation
Red pigment and binder
Curing
Washing
Pigmented Red Phosphor

Figure 43 Pigment coating processes. (From Kasei Optonix, Inc., unpublished results. With permission.)

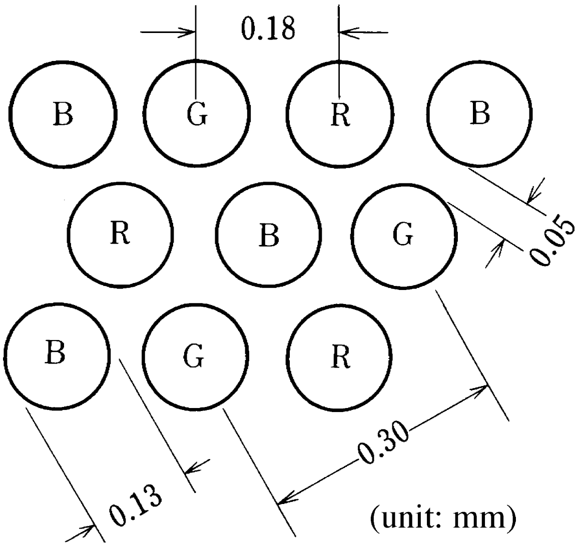
0.18
B
G
R
B
R
B
G
0.05
B
G
R
0.30
0.13
(unit: mm)

Figure 44 Phosphor screen with 0.3-mm hole pitch. (From Kasei Optonix, Inc., unpublished results. With permission.)

resolution dot pitches of 0.3 mm and further on to super-high-resolution dot pitches as small as 0.2 mm. There is also a trend toward increasing screen size from the usual 12-inch screens to sizes between 14 and 17 inches.

The demands placed on the characteristics of phosphor screens of color display CRTs by the increasing resolution are not only higher brightness and better color characteristics, but also better coating characteristics such as phosphor screen precision, dot shape, color shifting, and adhesion, all of which have become extremely important issues.

References

1. Kasei Optonix, Ltd., unpublished data.
2. Leverenz, H.W., *An Introduction to Luminescence of Solids*, John Wiley & Sons, New York, 1950, 197.

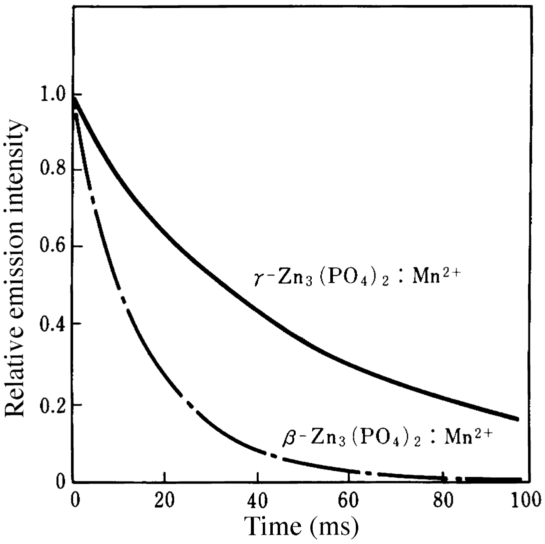

Figure 45 Decay characteristics of β- and γ-$Zn_3(PO_4)_2$:Mn^{2+} phosphors. (From Kasei Optonix, Inc., unpublished results. With permission.)

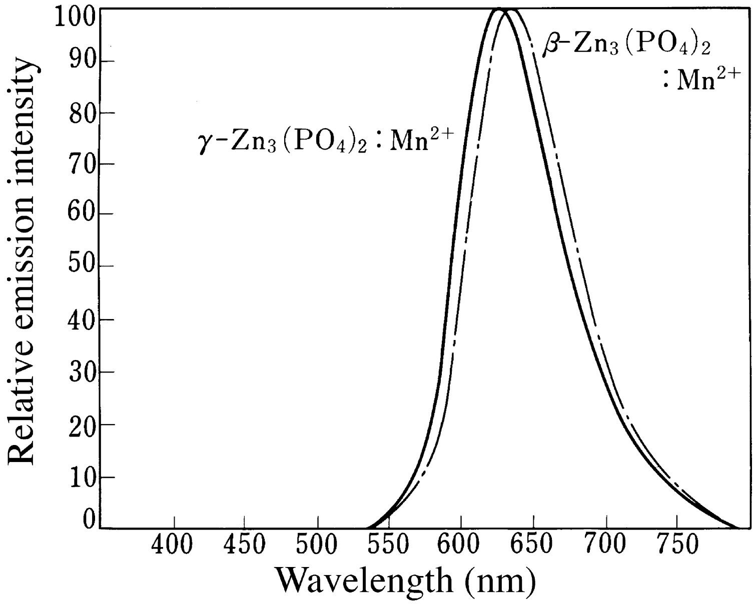

Figure 46 Emission spectra of β- and γ-$Zn_3(PO_4)_2$:Mn^{2+} phosphors. (From Kasei Optonix, Inc., unpublished results. With permission.)

3. Kröger, F.A., Bril, A., and Dikhoff, J.A.M., *Philips Res. Rep.*, 7, 241, 1952.
4. Leverenz, H.W., *An Introduction to Luminescence of Solids*, John Wiley & Sons, New York, 1950, 473.
5. Mellor, J.W., *A Comprehensive Treatise on Inorganic and Theoretical Chemistry*, Longmans, London, 1969, Vol. IV, 473.
6. Nakano, E., *J. Chem. Soc. Jpn., Ind. Chem. Sec.*, 63, 565, 1960.
7. Nakano, E., *J. Chem, Soc. Jpn., Ind. Chem. Sec.*, 71, 304, 1968.
8. Washizuka, S., *Bunseki Kagaku (J. Anal. Chem. Jpn.)*, 10, 585, 1961.
9. Nakano, E., *J. Chem, Soc. Jpn., Pure Chem. Sec.*, 84, 363, 1963.
10. Kotera, Y., *Phosphors and Their Application*, Ohm-sha, Tokyo, 1963 (in Japanese).

11. Radio Technology Society, Color Television Tube Testing Committee, *Research on 17-inch Color Television Tubes*, 1961, (in Japanese).
12. Takagi, K. and Yamada, Y., *Optical Properties of Semiconductors Simplified*, Sanpo, Tokyo, 1965, 143 (in Japanese).
13. Masuda, M., Hayashi, A., and Aoyama, T., *Natl. Tech. Rep.*, 12, 1088, 1982.
14. Leverenz, H.W., *An Introduction to Luminescence of Solids*, John Wiley & Sons, New York, 1950, 264.
15. Leverenz, H.W., *RCA Review*, 5, 131, 1940.
16. Takagi, K., *Research Concerning the Manufacture of Inorganic Phosphors*, 1961, 72 (in Japanese).
17. Toriu, T., Miyagawa, T., and Ozawa, R., *Tech. Digest, Phosphor Res. Soc. 88th Meeting*, 1961, 5 (in Japanese).
18. Matsuura, S., Koga, Y., Ito, T., and Tamatani, M., *Tech. Digest, Phosphor Res. Soc. 166th Meeting*, 1977, 5 (in Japanese).
19. Miyagawa, T., Nagashima, Y., and Murakami, S., *Tech. Digest, Phosphor Res. Soc. 131st Meeting*, 1970, 3 (in Japanese).
20. Tamatani, M. and Inoue, N., Japanese Patent Disclosure (Kokai) 47-38586 (1972).
21. Van Uitert, L.G., Linares, R.C., Soden, R.R., and Ballman, A.A., *J. Chem. Phys.*, 36, 702, 1962; U.S. Patent 3,152,085 (1964).
22. Levine, A.K. and Palilla, F.C., *Appl. Phys. Lett.*, 5, 118, 1964.
23. Chary, N.C., *J. Appl. Phys.*, 34, 3500, 1963.
24. Ropp, R.C., *J. Opt. Soc. Am.*, 57, 213, 1967.
25. Yokota, Y., Miyagawa, T., Tanaka, Y., and Torii, T., Japanese Patent Publication (Kokoku) 44-11769 (1969).
26. Yokota, Y., Miyagawa, T., Tanaka, Y., and Torii, T., Japanese Patent Publication (Kokoku) 50-21213 (1975).
27. Ninagawa, C., Yoshida, O., and Ashizaki, S., Japanese Patent Publication (Kokoku) 46-17394 (1971).
28. Royce, M.R., Smith, A.L., Thomsen, S.M., and Yocom, P.N., *Extended Abstr. Electrochem. Soc. (135th Meeting)*, 1969, No. 86.
29. Shrader, R.E., Royce, M.R., and Yocom, P.N., *Extended Abstr. Electrochem. Soc., (139th Meeting)*, 1971, No. 41.
30. Robbins, D.J., *J. Electrochem. Soc.*, 123, 1219, 1976.
31. Hoshina, T., Imanaga, S., and Yokono, S., *J. Luminesc.*, 15, 455, 1977.
32. Iizumi, S., *Kagaku Binran (Chemical Handbook)*, Maruzen, Tokyo, 1973 (in Japanese).
33. Arakawa, T. and Shimizu, H., *Tech. Digest, Phosphor Res. Soc. 173rd Meeting*, 1978, 12 (in Japanese).
34. Sato, M., *J. Chem. Soc. Jpn. Ind. Chem. Sec.*, 65, 1500, 1962.
35. Shiokawa, J., *J. Chem. Soc. Jpn. Ind. Chem. Sec.*, 65, 524, 1962.
36. Toyama, I. and Nakamura, T., *J. Chem. Soc. Jpn. Ind. Chem. Sec.*, 68, 1201, 1965.
37. Yamamoto, H. and Kano, T., *J. Electrochem. Soc.*, 126, 305, 1979.
38. Hase, T. and Yoshida, H., Japanese Patent Disclosure (Kokai) 58-120521 (1983).
39. Awazu, K. and Matsunaga, K., Japanese Patent Disclosure (Kokai) 58-18471 (1983).
40. Lehmann, W., *J. Electrochem. Soc.*, 127, 503, 1980.
41. Yamamoto, H., Megumi, K., Kasano, H., Suzuki, T., Uehara. Y., Morita, Y., and Ishigaki, T., *Tech. Digest, Phosphor Res. Soc. 198th Meeting*, 1983, 12 (in Japanese).

chapter six — section three

Phosphors for cathode-ray tubes

Katsutoshi Ohno

Contents

6.3. Phosphors for projection and beam index tubes....587
  6.3.1 Phosphors for projection tubes....587
  6.3.2 Phosphors for beam index tubes....594
References....596

6.3 *Phosphors for projection and beam index tubes*

6.3.1 *Phosphors for projection tubes*

One of the methods for achieving large television screens is the projection television system; in this system, a bright color picture produced by a cathode-ray tube (CRT) is magnified by a lens and projected onto a large screen to produce an image. The brightness of such a large screen depends on a variety of characteristics, including the brightness of the cathode-ray tube. The size of the projection tube is relatively small so as to make the television set without the screen as compact as possible. To make the projection tube as bright as possible, the current voltage for exciting the phosphor must be increased over normal CRT conditions. This means that the type of phosphors that can be used in projection tubes needs to meet more stringent requirements than those of direct-viewing tubes in terms of brightness saturation, temperature, lifetime, and other performance characteristics. In other words, phosphors used in direct-viewing tubes cannot be directly applied as-is to projection tubes.

At present, $Y_2O_3:Eu^{3+}$ is being used to produce red, and ZnS:Ag,Cl to produce blue in projection tubes, although their performance is not necessarily satisfactory. For the green, the behavior of various phosphors described below needs to be examined carefully since the intensity of green emission effects overall brightness the most. This section discusses the three most important characteristics of projection-tube phosphors: that is, *brightness saturation*, *temperature characteristics*, and *lifetime*. The characteristics of the phosphors obtained using an 8-inch projection tube* are compared with those obtained for direct-viewtube phosphors. This section then describes methods for synthesizing representative and practical projection-tube phosphors.

---

* Although the phosphor screen of the projection tube was manufactured using a printing method, the precipitation method was used for the $CaS:Ce^{3+}$ phosphor only. The coating thickness was optimized to achieve maximum brightness.

Brightness saturation and characteristics. Two methods are employed to express the brightness saturation characteristics of phosphors: (1) the current/brightness characteristics, in which brightness changes are measured as excitation current is varied, and (2) the focus voltage/brightness characteristics, in which brightness changes are determined as the focus voltage of the electron gun is varied while keeping the excitation current fixed. Strictly speaking, however, brightness saturation characteristics are usually expressed as the dependence of the brightness on the excitation current density, which means that neither of the above methods expresses the saturation characteristics correctly. More specifically, in the first method, the focus of the electron beam changes as the excitation current is increased; these changes appear in the form of cross-sectional area changes of the electron beam. Thus, if the electron beam is initially in focus on the screen at a given excitation current, I_k, the beam will defocus when the current is changed. In the second method, the focus voltage and the cross-sectional area of the electron beam do not have a linear relationship and thus the brightness is not simply related to the voltage changes. In addition, the focus voltage in projection tubes is fixed to that at the time of setting so that the second method again does not truly replicate the phosphor characteristics under actual operating conditions. Nevertheless, in terms of a practical means for carrying out phosphor evaluation, both the *current/brightness characteristics* and *focus-voltage/brightness characteristics* methods are considered effective, and experimental results for these two methods are shown below.

In Ohno's measurements under the current/brightness characteristics method, the voltage was set to 27 kV and the projection tube was placed into a "just-infocus" state with the cathode currents I_k = 290 μA for red, 230 μA for blue, and 430 μA for green. The same I_k currents were used for measurements in the focus-voltage/brightness characteristics method.

Current/brightness characteristics are shown in Figures 47 and 48. As can be seen in the figures, the slope of the plots changes in the neighborhood of the I_k corresponding to the "just-infocus" state. The change in the slope is large, particularly when the brightness saturation is remarkable. This can be attributed to the effect of defocusing, as described above. From these figures, the value of γ is defined by the expression $B = I_k\gamma$, where B is brightness. Table 5 lists γ values for I_k between 50 and 2000 μA.

Focus voltage/brightness characteristics are shown in Figures 49 and 50. The change in brightness (ΔB_r) obtained from these figures is shown in Table 6, where 100% is taken to be maximum brightness.

Both methods clearly indicate serious problems in brightness saturation characteristics of the blue ZnS:Ag,Al presently in use.

Temperature characteristics. The applied power in a projection tube is large compared with that in a direct-view tube, while the size of the projection tube's screen is relatively small, so that the power is concentrated in a small area, which leads to an increase in the phosphor surface temperature. The temperature characteristics of the phosphors employed therefore pose an important issue. Details of the rise in temperature in tubes have been documented by Kikuchi et al.,[1] and these data are reproduced in Table 7.

The temperature rise in phosphors is considered to cause the following problems: brightness drop, due to the occurrence of temperature quenching in phosphors and the shift from white balance. Here, white balance means the ratio of I_k (R.G.B.) to get white on the screen. Figure 51 shows the change in brightness due to the temperature rise of various phosphors; that is, their temperature characteristics or thermal dependence. In the figure, the temperature on the horizontal axis is for the outside of the glass face of an 8-inch projection tube. The temperature at the surface of the phosphors may actually be higher.

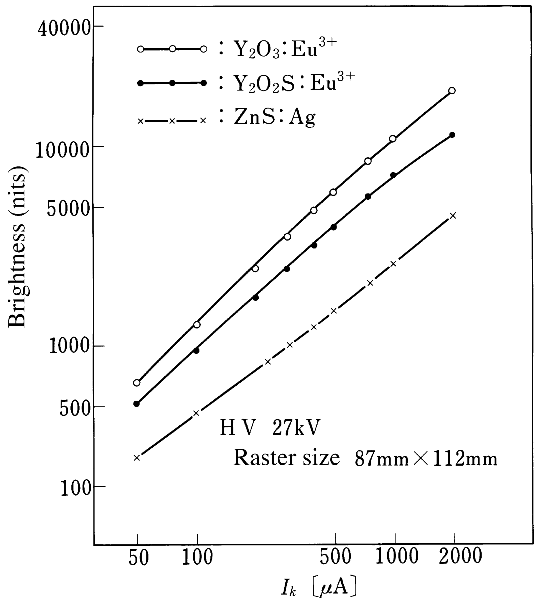

Figure 47 Cathode current dependence of the brightness of Y_2O_3:Eu^{3+}, Y_2O_2S:Eu^{3+}, and ZnS:Ag,Cl.

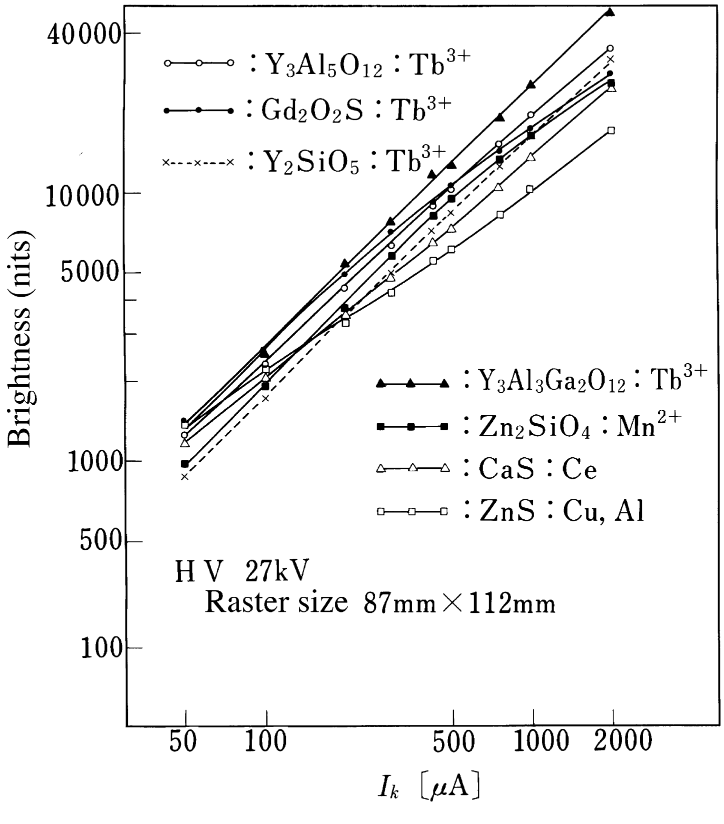

Figure 48 Cathode current dependence of the brightness of YAG:Tb^{3+} and various other green phosphors.

Table 5 γ Values of Several Phosphors for I_k Between 50 and 2000 μA

Phosphor	γ	Phosphor	γ
$Y_2O_3:Eu^{3+}$	0.92	$Y_2SiO_5:Tb^{3+}$	0.98
$Y_2O_2S:Eu^{3+}$	0.85	$Zn_2SiO_4:Mn^{2+}$	0.85
$Gd_2O_2S:Tb^{3+}$	0.84	$Y_3Al_5O_{12}:Tb^{3+}$	0.91
ZnS:Cu,Al	0.67	$Y_3Al_3Ga_2O_{12}:Tb^{3+}$	0.97
ZnS:Ag,Al	0.75	$CaS:Ce^{3+}$	0.82

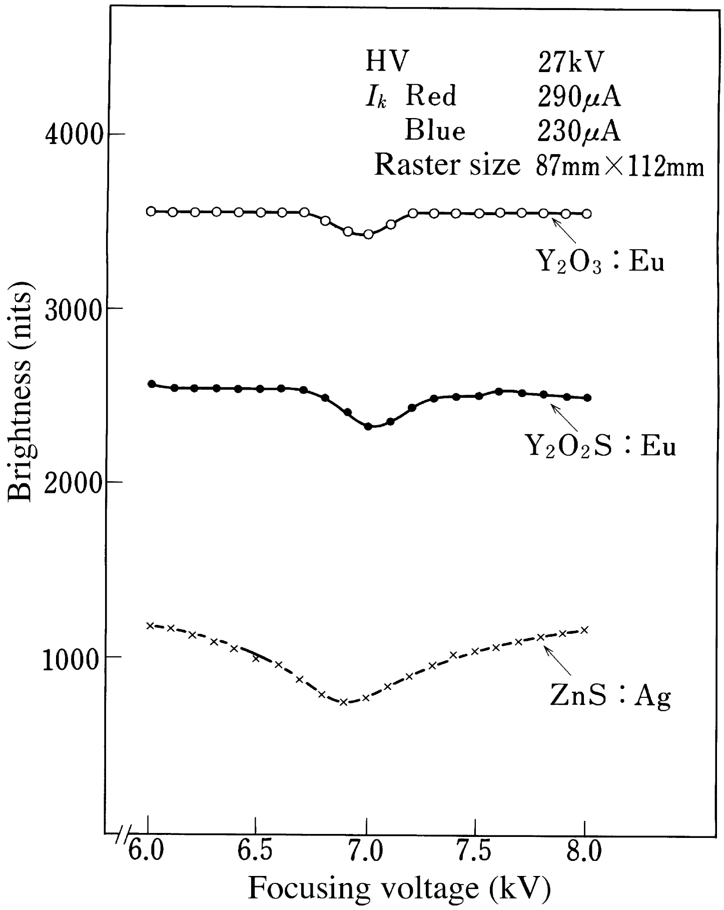

Figure 49 Focusing voltage dependence of the relative brightness of $Y_2O_3:Eu^{3+}$, $Y_2O_2S:Eu^{3+}$, and ZnS:Ag,Cl.

According to Table 7, the glass panel temperature can reach 70 to 100°C at room temperature (25°C). A number of cooling methods has therefore been proposed.[1] One of them is liquid cooling, and the temperature rise when applying it is shown by the values in parentheses in Table 7.

Figure 51 shows that $Gd_2O_2S:Tb^{3+}$, which is widely used as a green phosphor, exhibits a brightness drop of 10% at 60°C and 35% at 100°C from room temperature. If this phosphor is used, various effects will be apparent since the green spectral area is

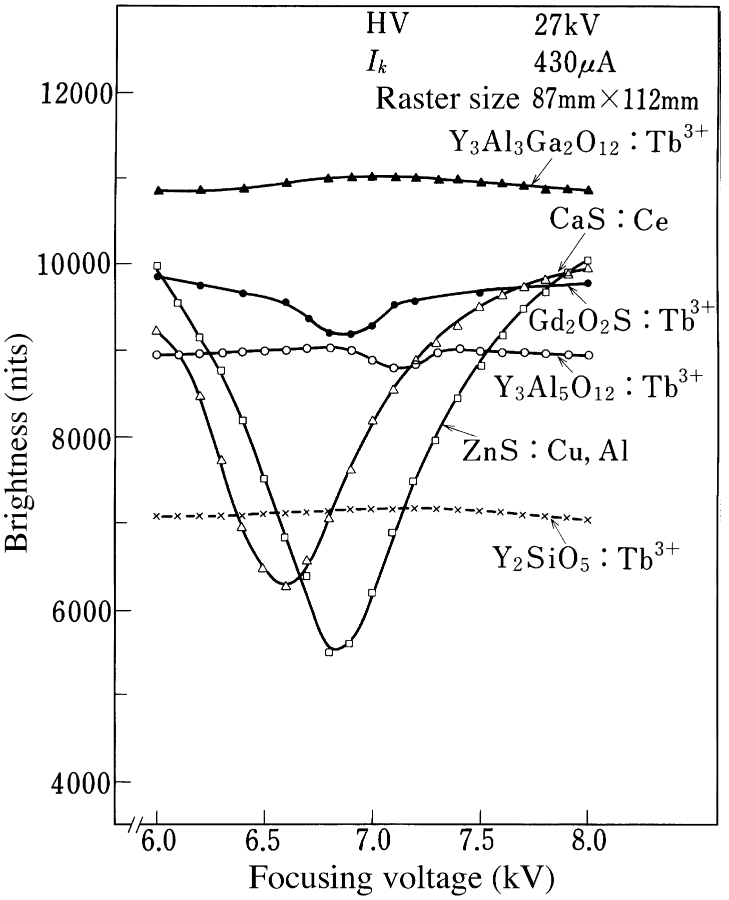

Figure 50 Focusing voltage dependence of the relative brightness of $Y_3Al_5O_{12}$:Tb^{3+} and various other green phosphors.

Table 6 Change in Brightness (ΔB_R)

Phosphor	ΔB_R	Phosphor	ΔB_R
Y_2O_3:Eu^{3+}	3%	Y_2SiO_5:Tb^{3+}	1.5%
Y_2O_2S:Eu^{3+}	12%	$Y_3Al_5O_{12}$:Tb^{3+}	2%
Gd_2O_2S:Tb^{3+}	5%	$Y_3Al_3Ga_2O_{12}$:Tb^{3+}	1.5%
ZnS:Cu,Al	37%	CaS:Ce^{3+}	30%
ZnS:Ag,Al	31%		

Table 7 Temperature Rise of Glass Panel Surface of Projection CRT

Raster size	Applied power (W cm^{-2})	Temperature rise after excitation
96 × 71 mm	0.17	68°C (46°C)^a
48 × 35.5 mm	0.67	120°C (78°C)

Note: HV: 26 kV, I_k: 430 μA.

( )^a Temperature rise in the case of using liquid cooling.

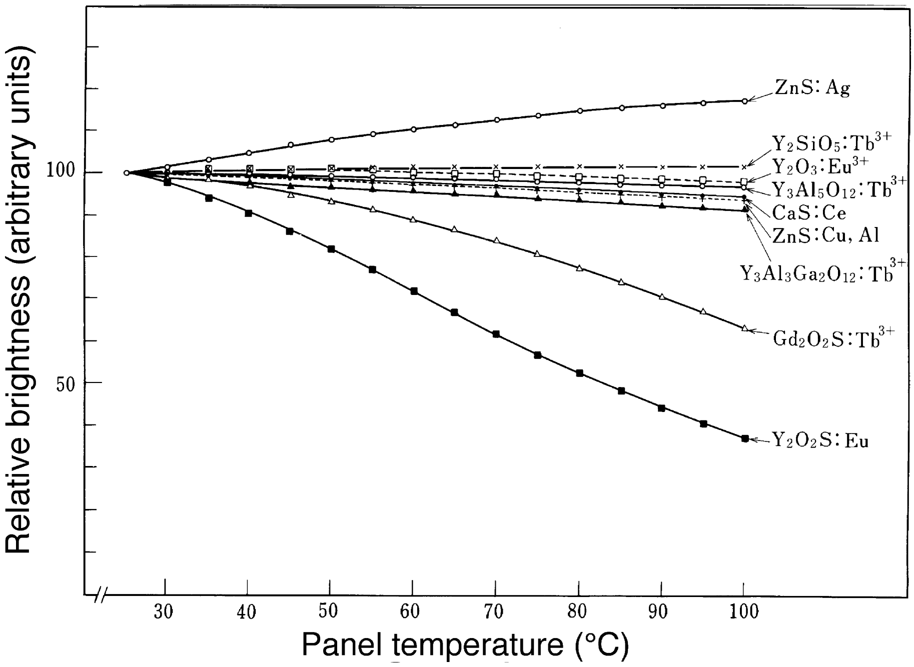

Figure 51 Temperature dependence of the luminescence intensity of various phosphors.

responsible for up to 60 to 70% of the total brightness. Brightness drop will produce additional related problems; what appeared white on the screen will become pinkish and deviations will occur in the white balance of the projection. In practical application, the latter poses a bigger problem, since the human eye is more sensitive to changes in color than to changes in brightness. Moreover, aberrations from white balance are a function of time following the placement of a projection tube into operation (eventually becoming constant). Therefore, setting the initial operational parameters for red, blue, and green is a serious and difficult problem for projection tube manufacturers. To make projection tubes brighter in the future and to assure reliable operation, the development of phosphors that do not exhibit temperature quenching is essential because of the general trend to increase input powers.

Lifetime. The lifetime (deterioration of luminescence efficiency) of phosphors can be said to be a more serious problem than those associated with brightness saturation and temperature characteristics, once the television set has been handed over to the user. Long-term brightness drop in phosphors has been attributed to various factors, such as phosphor compositional changes and color-center formation in hosts due to generated heat. In any case, phosphors undergo change according to the amount of applied power (in conjunction with beam-spot diameter), heat radiation in the projection tube, etc. The discussion here must be limited solely to qualitative aspects because only the evaluation of the relative strengths of phosphors made by using a demountable equipment could be used in judgment.

In this evaluation, DC excitation was applied at an accelerating voltage of 16 kV, and the excitation current and excitation time were varied to determine the relative strengths of phosphors based on brightness drop and changes in body color. The results are shown in Table 8, where strength is rated as VS (very strong), S (strong), W (weak), or VW (very weak). Because establishing what is "good" for a lifetime depends on excitation power

Table 8 Relative Strengths of Several Phosphors Based on Brightness Drop and Changes in Body Color

Phosphor	R.S.	Phosphor	R.S.
Y_2O_3:Eu^{3+}	S	Y_2SiO_5:Tb^{3+}	VW
Y_2O_2S:Eu^{3+}	S	Zn_2SiO_4:Mn^{2+}	W
Gd_2O_2S:Tb^{3+}	S	$Y_3Al_5O_{12}$:Tb^{3+}	VS
ZnS:Cu,Al	VW	$Y_3Al_3Ga_2O_{12}$:Tb^{3+}	VS
ZnS:Ag,Cl	VW	CaS:Ce^{3+}	VW

Note: Relative strength (R.S.) is related as VS > S > W > VW.

and is arbitrary, it is not possible to make generalizations here on the lifespan of the phosphors; it can be said, however, that the blue phosphor ZnS:Ag,Al has a problem with longevity. In addition to the above kind of qualitative study, there has recently been a fairly detailed quantitative evaluation of phosphor lifetime and an investigation as to the cause of phosphor degradation by electron beams.[2]

The preceding discussion has described the three most important characteristics of phosphors used in projection tubes: i.e., brightness saturation, temperature characteristics, and lifetime, giving the performance of various phosphors as examples. As mentioned, the characteristics of the green phosphor influence the overall system performance the most. Green phosphors such as LaOCl:Tb^{3+}[3] and $InBO_3$:Tb^{3+}[4] are now being put to use, in addition to those described above.

Synthesis of $Y_3Al_5O_{12}$:Tb^{3+} (YAG). $Y_3Al_5O_{12}$:Tb^{3+} can be taken as the representative example of green phosphors; the method for synthesizing this material is described below. The first point of concern when synthesizing this phosphor is how to obtain YAG in a single phase. There are three well-known compounds in the Y_3O_3-Al_2O_3 family: $Y_4Al_2O_9$ (yttrium aluminum monoclinic, YAM); $YAlO_3$ (yttrium aluminum perovskite, YAP); and $Y_3Al_5O_{12}$ (yttrium aluminum garnet, YAG). Among these, the easiest to form is YAM; accordingly, it is somewhat difficult to form the other phases, because deviations from the proper stoichiometric ratios can easily take place. A method has been reported by which single-phase YAG can be formed by repeated firing processes.[5,6] A simple synthesis method has not yet been found to put this phosphor to practical use. The following describes the formation of YAG and a typical YAG synthesis method.

YAG formation.[7] As mentioned before, YAM and YAP often co-exist as by-products with YAG. Figure 52 shows intensity changes in characteristic X-ray diffraction peaks for these compounds with firing temperature. It is indicated that YAM appears first, YAP second, and YAG last, as the firing temperature is increased. Each curve in the figure is normalized to its highest intensity. The samples were fired at various temperature for 2 h and quenched rapidly to room temperature. Using BaF_2 as a flux, the firing temperatures that give the highest peak intensity for YAM and YAP are 200~300°C lower than those without BaF_2. In the latter case, YAG does not appear, even when fired to 1300°C. When BaF_2 is added, however, YAG begins to form even at 900°C. These results indicate that YAG crystallizes through the formation of YAM and YAP. Figure 53 shows the relative brightness of these samples as a function of firing temperature. From Figures 52 and 53, it can be seen that the relative brightness is proportional to the amount of single-phase YAG contained in the product. Thus, this allows one to conclude that single-phase crystallinity of cubic YAG:Tb^{3+} is a key factor in luminescence efficiency.

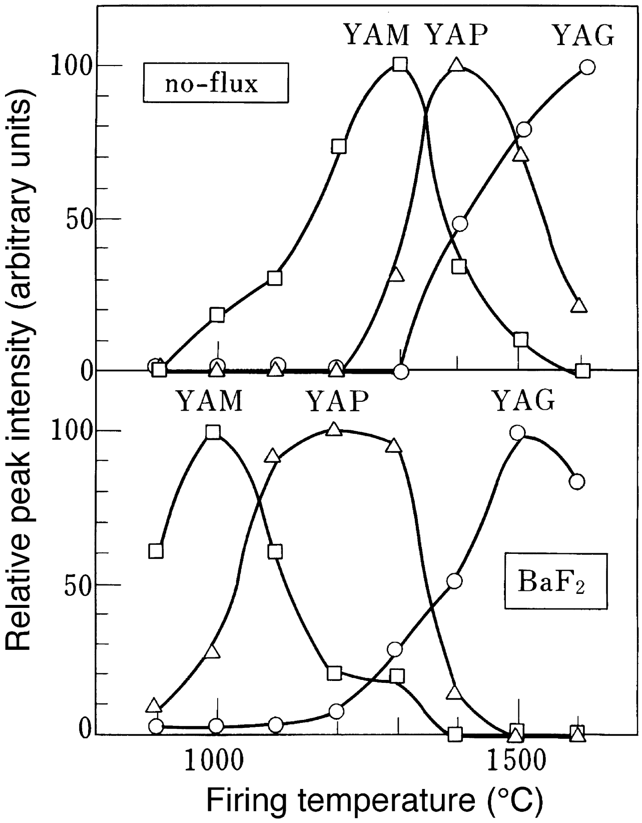

Figure 52 Changes of the X-ray diffraction peak intensity of $Y_4Al_2O_9$ (YAM), $YAlO_3$ (YAP), and $Y_3Al_5O_{12}:Tb^{3+}$ (YAG) with firing temperature. (From Ohno, K. and Abe, T., *J. Electrochem. Soc.*, 133, 638, 1986. With permission.)

YAG synthesis method. YAG samples are prepared by solid-state reaction. About 20 mol% BaF_2 is mixed with stoichiometric amounts of Y_2O_3,Tb_4O_7 and Al_2O_3 in ethanol. After being dried, the mixture is fired in a loosely sealed aluminum crucible at 1500°C for 2 hours. After firing, the sample is washed with 2*N* HNO_3 to remove residual flux reagent.

Figures 48, 49, and 50 show the brightness saturation characteristics and temperature characteristics of YAG:Tb and several other phosphors. The emission spectrum is shown in Figure 54 and a SEM photograph of the YAG microcrystals is shown in Figure 55.

6.3.2 *Phosphors for beam index tubes*

Another TV system is the so-called index system that uses indexing phosphors as a color selection mechanism instead of using shadow masks or aperture grills. Important characteristics needed for phosphors used in indexing are short decay time and high emission intensity. To achieve short decay times, the electronic transitions providing the emission must be electric dipole-allowed. These transitions include the *d-f* transition in Ce^{3+} and some divalent rare-earth ions such as Eu^{2+}, Sm^{2+}, and Yb^{2+}. Among these ions, Ce^{3+} exhibits the fastest decay and is the only activator used in index tube phosphors.[8]

To achieve the second important characteristic, i.e., high emission intensity, not only must the phosphor have a high energy efficiency, but the sensitivity of the device to detect the emission of indexing phosphors must also be considered. The ratio I_p/τ, where I_p is

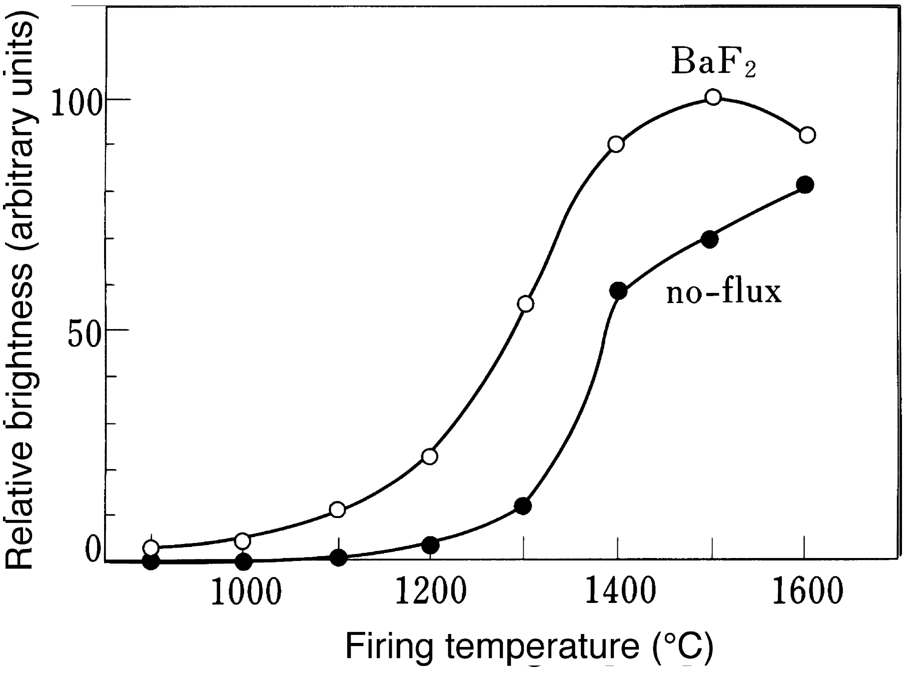

Figure 53 Relative brightness of YAG:Tb^{3+} as a function of firing temperature for the cases of no flux and BaF$_2$. (From Ohno, K. and Abe, T., *J. Electrochem. Soc.*, 133, 638, 1986. With permission.)

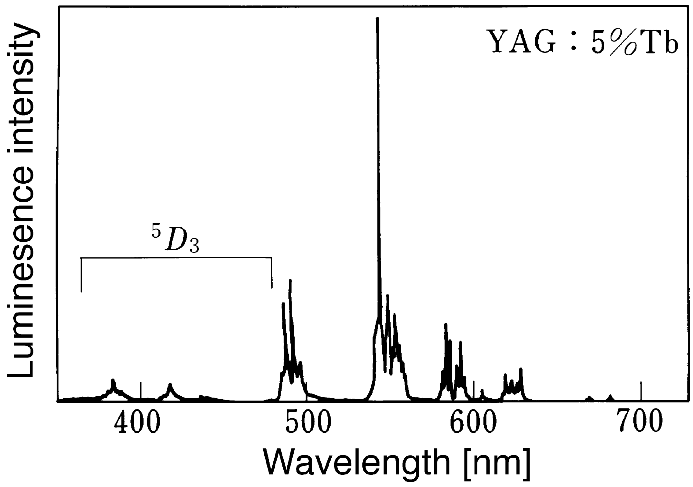

Figure 54 Cathodoluminescence spectrum of $Y_3Al_5O_{12}$:5% Tb^{3+}. (From Ohno, K. and Abe, T., *J. Electrochem. Soc.*, 133, 638, 1986. With permission.)

emission intensity and τ is decay time, and can be used as a figure of merit for the index signal. Other characteristics—such as filming, degradation, etc.—must of course be considered, as in other TV phosphors. Among all the short-persistence phosphors, those that can be put to practical use are Y_2SiO_5:Ce^{3+}, $YAlO_3$:Ce^{3+}, and $Y_3Al_3Ga_2O_{12}$:Ce^{3+}. Which of these three phosphors is put to use depends on the sensitivity of the pickup device (photocell, PIN diode, etc.). The characteristics of these three phosphors are shown in Table 9.[9–11]

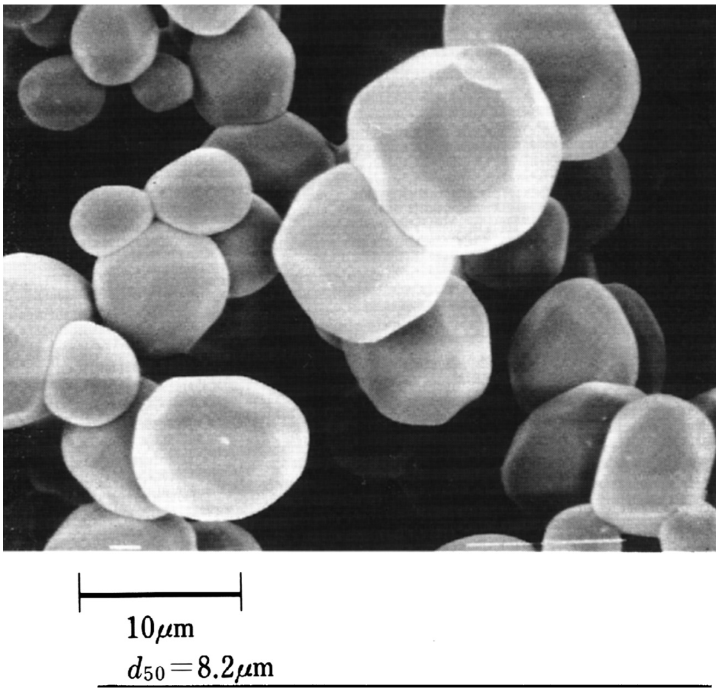

Figure 55 Scanning electron micrographs of $Y_3Al_5O_{12}$:Tb^{3+} microcrystals.

Table 9 Luminescence Characteristics of Several Indexing Phosphors

Phosphor	Energy efficiency (%)	Emission peak (nm)	1/10 Decay time (ns)
Y_2SiO_5:Ce^{3+}	7.7%	415	80
$Y_3Al_3Ga_2O_{12}$:Ce^{3+}	4.5%	520	120
$YAlO_3$:Ce^{3+}	5.0%	370	85

References

1. Kikuchi, M., Kobayashi, K., Chiba, Y., and Fujii, T., *IEEE Trans.*, CE-2, 3.280, 1982.
2. Matsukiyo, S., Yamamoto, H., Uehara, and Morita, Y., *Tech. Report Inst. TV Eng. Jpn.*, ED 943, 1, 1986.
3. Tsuda, N., Tamatani, M., and Sato, Y., *Tech. Digest, Phosphor Res. Soc. 199th Meeting*, 1984.
4. Morita, Y., Uehara, Y., Matsukiyo, H., Yamamoto, H., and Kano, T., *Abst. Inst. Electron. Inform. Commun. Eng. Jpn.*, 2-79, 1986.
5. Naka, J. and Tanaka, J., *Koggyo Kagaku Zasshi*, 69, 1112, 1966.
6. Abell, J.S., *J. Mater. Soc.*, 9, 527, 1974.
7. Ohno, K. and Abe, T., *J. Electrochem. Soc.*, 133, 638, 1986.
8. Bril, A. and Blasse, G., *J. Electrochem. Soc.*, 117, 346, 1970.
9. Ohno, K. and Hoshina, T., *Tech. Digest, Ins. Elect. Engnr. Jpn.*, EFM-81-9, 1981.
10. Takeuchi, I. and Miyamoto, N., *Abst. Jpn. Soc. Appl. Phys. Spring Meeting*, 30, 1977.
11. Tanaka, T. and Kishimoto, S., *Tech. Report Inst. TV Eng. Jpn.*, ED 595, IPD 62-5, 25, 1981.

chapter six — sections four and five

Phosphors for cathode-ray tubes

Kenzo Awazu*[*] and Noritsuna Hashimoto

Contents

6.4 Phosphors for observation tubes 597
  6.4.1 Phosphors for oscilloscope tubes 597
  6.4.2 Phosphors for storage tubes 598
  6.4.3 Phosphors for radar tubes 599
6.5 Phosphors for special tubes 600
  6.5.1 Phosphors for giant-screen display tubes 600
  6.5.2 Phosphors for color television tubes of beam penetration type 602
  6.5.3 Phosphors for flying-spot scanner tubes 603
References 606

6.4 Phosphors for observation tubes

6.4.1 Phosphors for oscilloscope tubes

Because of the response of the human eye, green-emitting phosphors have been used in oscilloscope applications to provide high visibility. The phosphor Zn_2SiO_4:Mn^{2+} (P1) has been most commonly used from the beginning. For the observation of fast or high-frequency phenomena, the electron beam (e-beam) sweep time is short and the emission build-up time of the phosphor needs to be considered. Short decay-time phosphors generally have fast response properties and meet this requirement. For this reason, a group of zinc sulfide phosphors such as hex.ZnS:Ag,Cu,Al (P2) and cub.ZnS:Cu,Cl (P31) has been employed. In selecting phosphors, the dependence of luminescence efficiency on the anode voltage should also be taken into consideration.

Oscilloscopes used for taking photographs require a phosphor that, first, has blue emission matching the spectral sensitivity of photographic films and, second, has a fast response. For this purpose, cub.ZnS:Ag,Cl (P11) has been used. For the observation of transient and high-speed phenomena having slow repetition frequency, a long decay-time phosphor P7 (see 6.2.2.3) had been employed. However, the storage tube (see 6.2.2.2) rather than an oscilloscope tube is more appropriate for this application.

Zn_2SiO_4:Mn^{2+} (P1). This common phosphor has steadily been improved with respect to its efficiency and resistance to electron bombardment, thanks to progress in

---

[*] Kenzo Awazu is deceased.

synthesis methods. In the early days, it was necessary to blend SiO_2 in surplus to ZnO in the raw material mixture in order to avoid coloration after firing and to keep the fluctuation of emission properties small. The brown coloration of the mixture arises if reactants are insufficient to prevent manganese ions from attaining higher valence states. Nowadays, however, high-performance P1 phosphors can be prepared by optimizing the conditions of raw material preparation and phosphor synthesis.

In a typical preparation, 2 moles ZnO, 1.1–1.2 moles SiO_2, and 0.6 moles MnO_2 are mixed by ball milling. The particle sizes of the raw materials have to be within the 2- to 3-μm range to facilitate the solid-state reaction. Firing is made at 1300–1350°C in air. The SiO_2 raw material should be selected with particular care; amorphous colloidal silica is generally used. The emission peak of this phosphor is 525 nm, and the halfwidth is ~44 nm. The 10% decay time is 25 ms. The particle size depends on preparation conditions and is usually between 4 and 6 μm.

hex.ZnS:Ag,Cu,Cl (P2). Aqueous solutions of $Ag(NO_3)$ and $CuSO_4$ are mixed with the ZnS powder, and then dessicated. The amount of Ag and Cu is 0.01–0.03 wt% ZnS. Firing is made at ~1200°C in an inert gas (N_2) atmosphere, with the addition of about 2 wt% NaCl as flux. The excess flux is washed away after firing. The peak wavelength of the main emission band is 543 nm. A smaller peak exists at ~460 nm. The 10% decay time is 30–100 μs, depending on the excitation density.

Phosphors with faster response are required for short sweep-time observations. To obtain ample brightness in this case, anode voltages have to be made higher. When the anode voltage is in the 4- to 5-kV range, the efficiency of P2 is higher than that of P1.[80] The average particle size is 8 to 10 μm.

cub.ZnS:Cu,Cl (P31). An aqueous solution of Cu ion is poured onto ZnS. The amount of Cu is 0.03 wt% of ZnS; 2 wt% NaCl is added as a flux. Firing is made at about 900°C in an N_2 atmosphere. The excess flux is removed by washing. The average particle size of the phosphor is 4–7 μm. The main emission peak is observed at 530 nm. A subpeak appears at 450 nm at higher excitation density so that the emission spectrum becomes broad. The 10% decay time is ~40 μs. This phosphor has been widely used for its high response speed and efficiency at high anode voltage.

cub.ZnS:Ag,Cl (P11). An aqueous solution of $AgNO_3$ is poured onto ZnS. The amount of Ag is 0.016 wt% of ZnS; 2 wt% NaCl is added as a flux. Firing is made at 950°C in air. The average particle size is 6–8 μm. The emission peak lies at 460 nm and the half width of the emission band is 70 nm. The 10% decay time varies form 30 to 70 μs, depending on the excitation density. This phosphor is used in oscilloscopes that are photographed because its emission spectrum fits well with the spectral sensitivity of photofilms.

6.4.2 *Phosphors for storage tubes*

The storage tube is equipped with a target that can store electric charges, and two electron guns for writing and reading images. The target consists of a gold-plated nickel mesh on which a 1–2 μm-thick MgF_2 film is deposited. A picture image is drawn on the target by the writing beam, and stored as a pattern of electric charges. The electrostatic field of the charges on the target controls the defocused reading beam, and the picture image is transferred onto the phosphor screen. In this way, a picture with a good half-tone quality is obtained. The stored image can be maintained for extended periods unless intentionally erased. As the reading beam is supplied continuously, the brightness of the phosphor screen can reach 2000 ft-L. For this reason, the storage tube is used in the cockpit of airplanes as the so-called *daylight display.*

(Zn,Cd)S:Ag,Cl (P20). A mixture of ZnS and CdS with the molar ratio of 6:4 is prepared. Further, 0.02 wt% Ag and fluxes in the form of 4 wt% NaCl and 2 wt% $BaCl_2$ are added. The mixture is fired at 1200°C in an N_2 atmosphere.

Since high resolution is required for storage tubes, the phosphor screen must be extremely uniform. For this reason, the average particle size of the phosphor is controlled to fall within the 6–8-μm range, and the particle size distribution is made relatively narrow. The wavelength of the emission peak is 560 nm and the halfwidth of the emission is 110 nm. The emission color is yellow-green. The 10% decay time is 18 ms under pulse excitation of current density 2 μA cm^{-2} and duration 16.7 ms.

6.4.3 *Phosphors for radar tubes*

Radar systems have been applied to meteorological observation, air traffic control, and marine traffic control. A long decay or persistent phosphor is required for displaying radar echoes on the screen.

hex.ZnS:Ag,Cl + (Zn,Cd)S:Cu,Cl (P7). Two-layer phosphor screens are used in radar tubes. The first layer (i.e., the layer on the electron-gun side) is made of blue-emitting hex.ZnS:Ag,Cl, and the second layer on the face panel side is made of yellow-green-emitting (Zn,Cd)S:Cu,Cl. The blue light from the first layer excited by an e-beam stimulates the second layer to emit long-persisting yellow-green light. The light from the second layer is observed through a yellow filter. While the second layer has an ideal decay time, it is only poorly cathodoluminescent. This is the reason why the second layer is excited by the light from the first layer.

To synthesize hex.ZnS:Ag,Cl, ZnS powder is mixed with 0.02 wt% Ag and fluxes (NaCl and $BaCl_2$). The mixture is then fired at 1250°C in an N_2 atmosphere. The particle size is adjusted to a few micrometers or less so that the phosphor can strongly absorb electron energy.

The starting materials of (Zn,Cd)S:Cu,Cl are ZnS and CdS mixed in the ratio of 9:1, 0.005 wt% Cu and NaCl. The mixture is fired at 800–900°C in an N_2 atmosphere. The phosphor having a diameter of several tens of micrometers is employed because the decay time becomes longer with larger particle size. The 10% decay time of the first layer is 50 μs. The emission peak of the second layer, excited by 445-nm radiation from the first layer, is 555 nm and the 10% decay time is 300 ms or longer. The two-layer screen is prepared by sedimentation. First, the second layer is deposited, and then the first layer is coated on the second layer. The total cathodoluminescence efficiency of this kind of the screen is properly low. Therefore, the transmission spectrum of the yellow filter and the level of the ambient light should be adjusted carefully.

Zn_2SiO_4:Mn^{2+},As (P39). In this phosphor, traps created in the host crystal make the decay time longer. The composition of this phosphor is basically the same as Zn_2SiO_4:Mn^{2+} (P1) except that 0.1 wt% As_2O_3 is added in the raw material. Firing at 1250°C in air makes the arsenic atoms dissolve in the host crystal as AsO_4^{3-}. The decay time becomes longer with increasing amounts of As_2O_3, but the brightness decreases. The wavelength of the emission peak is 525 nm (i.e., the same as P1), but the color purity is higher. The 10% decay time is 150 ms. These properties are suitable for radar tubes that are operated by random scanning. This phosphor has also been used for “flickerless” display tubes.

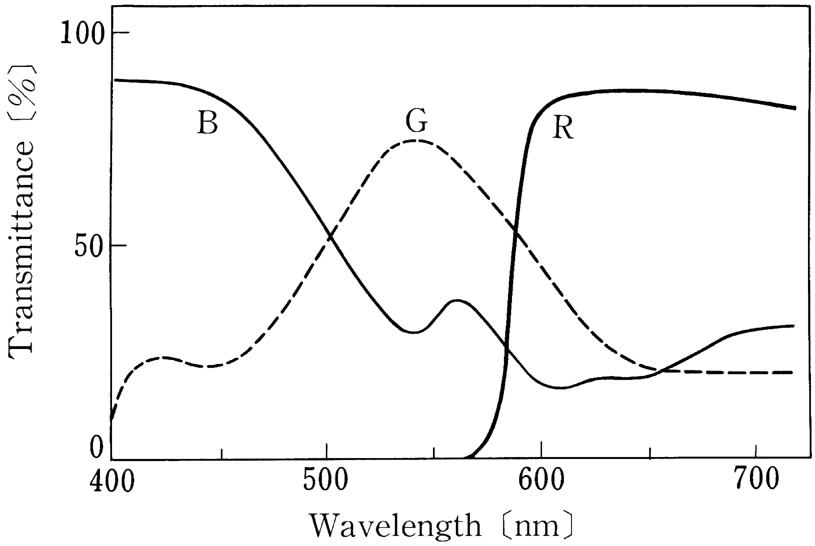

Figure 56 Transmittance spectra of colored glasses for three primary color tubes. (From Kobayashi, H. and Awazu, K., *J. Light & Vis.*, 5, 22, 1981. With permission.)

Other phosphors. Several long-decay fluoride phosphors activated by Mn^{2+} are well known. Representative phosphors of this group are $(Zn,Mg)F_2:Mn^{2+}$ (P12, P38); $(K,Mg)F_3:Mn^{2+}$ (P19); and $MgF_2:Mn^{2+}$ (P33). They emit orange light, but have a tendency to degrade under electron bombardment. In particular, the random-sweep type radar tubes have such a high excitation density in the center of the tube that their operating time is limited. For this reason, these phosphors are not used frequently in practical tubes.

6.5 *Phosphors for special tubes*

6.5.1 *Phosphors for giant-screen display tubes*

Several types of tubes have been developed as components of outdoor giant-screen displays. The displays can be classified into two categories. One consists of an array of monochrome tubes, each having one of three different colors, while the other is composed of tricolor matrix tubes. The display of the first type, which goes under the trade name Diamond Vision™, is described here. The standard screen size is 10.8 m × 7.2 m, and consists of 38,400 tubes.[81] The dimension of a single tube is 28.6 mm in diameter and 132 mm in length. The tube is made up of a color glass bulb, a phosphor screen, and an electron gun. The electron beam is defocused to excite the whole area of the phosphor screen without scanning.

Figures 56 and 57 show the transmission and emission spectra of the three kinds of the monochromatic tubes, respectively. The color glasses make the color purity of emitted light higher as compared with that of the phosphors themselves, the improvement color saturation being most pronounced for the green component (Figure 58). The color glasses also have such effects that they diminish the reflection of ambient light and increase the contrast of color tone. By modulating the excitation pulses, the brightness can be controlled to 32 different levels.[82] The power consumption of a tube is about 2 W, so the total power consumption of a large-size screen is only one tenth that of a system using incandescent lamps.

Table 10 shows the brightness and chromaticity coordinates of the three primary color tubes. To create a white color having the color temperature of 9300 K, the brightness ratio

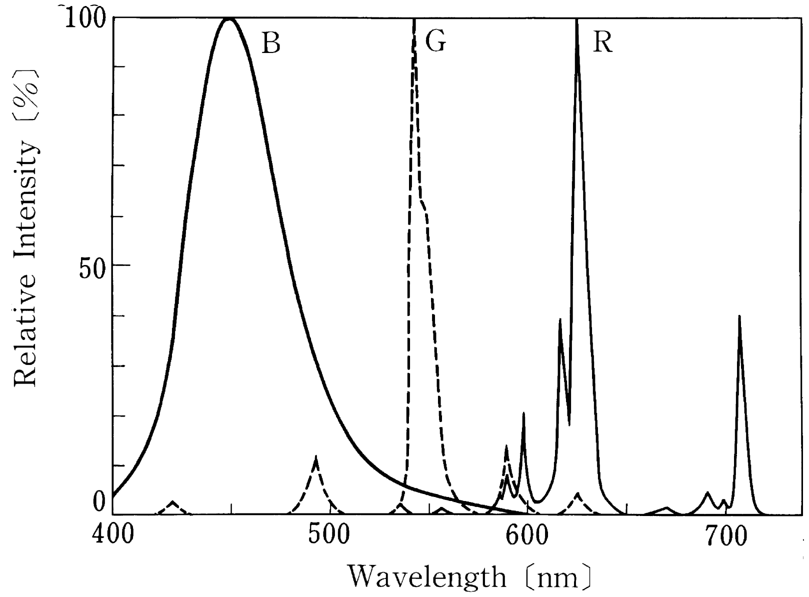

Figure 57 Emission spectra of three primary color tubes. (From Kobayashi, H. and Awazu, K., *J. Light & Vis.*, 5, 22, 1981. With permission.)

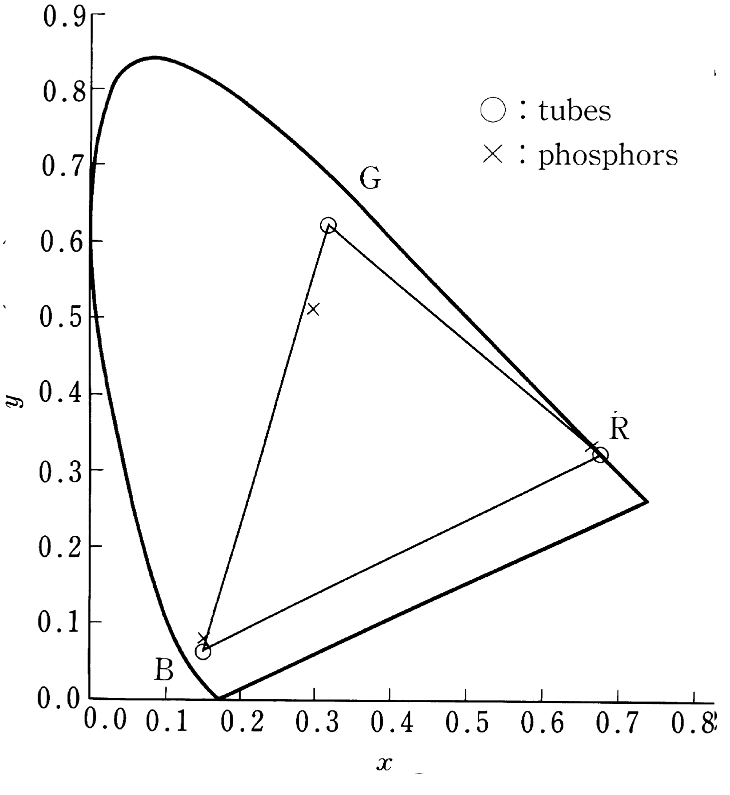

Figure 58 Chromaticity coordinates of three primary color tubes. (From Kobayashi, H. and Awazu, K., *J. Light & Vis.*, 5, 22, 1981. With permission.)

Table 10 Chromaticity Coordinate and Luminance of Three Color Primary Tubes

Phosphors	CIE chromaticity x	CIE chromaticity y	Luminance (cd m^{-2})
B; ZnS:Ag,Cl	0.1472	0.0642	1700
G; Gd_2O_2S:Tb	0.3134	0.6310	8000
R; Y_2O_2S:Eu	0.6661	0.3329	4200

of R, G, and B components must be 13:80:7, so each color unit is made up of one red (R), two green (G), and one blue (B) tubes.

Blue phosphor. The hex.ZnS:Ag,Cl (P22) phosphor, which is widely used for color picture tubes, is used for blue-emitting tubes in this application.

Green phosphors. $Gd_2O_2S:Tb^{3+}$ (P43) or $Y_3Al_5O_{12}:Tb^{3+}$ (P53) phosphors, both used in projection tubes, are applied in the green component.

Red phosphors. The $Y_2O_2S:Eu^{3+}$ (P22) and $Y_2O_3:Eu^{3+}$ phosphors, both used in color picture tubes, are applied in red-emitting tubes.

The current-brightness property of each phosphor is different, but brightness control can be made without problem by modulating the pulse width. The temperature characteristic poses no problem either because the surface temperature of the tubes does not rise above ~60°C when room temperature is around 20°C, or in the outdoors where natural cooling exists.

6.5.2 Phosphors for color television tubes of beam penetration type

This type of tube has a multilayer phosphor screen, in which the emission color changes with the penetration depth of the electron beam in the phosphor screen.[83] This tube is suitable for high-resolution graphic displays because it does not have a shadow mask that sets a limit to resolution. The problem in this system is in the need for fast switching of high-acceleration voltage; recently, however, a new electrical circuit for switching in 10 μs with low power consumption was proposed,[84] which would, in effect, make this type of tube practical.[85]

In a typical tube, there are green- and red-emitting phosphor layers with a nonluminescent dielectric layer between them, so that four colors (i.e., green, yellow, orange, and red) can be created. The materials usually employed are:

1. Green phosphor: $Zn_2SiO_4:Mn^{2+}$ (P1), with an average particle size of 2–3 μm.
2. Red phosphor: $YVO_4:Eu^{3+}$ (P22), with an average particle size of ~3 μm.
3. Dielectric layer: Titanium dioxide, TiO_2 (rutile structure) with an average particle size of 0.2–0.3 μm.

The particle size distribution of the phosphors is adjusted by elutriation to obtain a thin and high-density layer. The green, intermediate, and red layers are deposited in this order by sedimentation. In the case of large tubes such as the 23-inch type, particular care is necessary for the screening process. The temperature of water and air must be kept constant to inhibit the convection of water, and the vibration of the screening machine must be eliminated. The intermediate layer improves the uniformity of the red layer and minimizes the mixing of the red and green phosphors, making the distinction of emission color more clear.

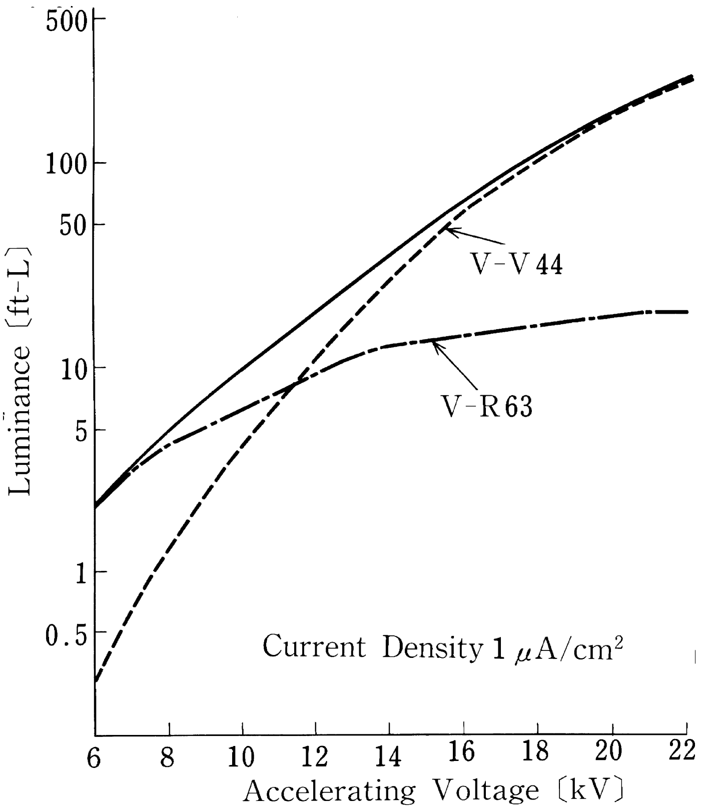

Figure 59 Brightness properties of beam penetration type tubes.

Figure 59 shows the brightness of the phosphor screen of a 23-inch tube as a function of the accelerating voltage. The blue and red components in emission picked up by V-44 and R-63 TOSHIBA sharp-cut color filters glasses, respectively, are also shown in Figure 59. Figure 60 shows the relation between the chromaticity coordinates of the emission and the accelerating voltage on the CIE chromaticity diagram. The change of color with accelerating voltage is suitable for random scan radars or for industrial graphics displays.

6.5.3 Phosphors for flying-spot scanner tubes

From the beginning of television system development, flying-spot scanner tubes have been used to pick up movie-film images. The bright point scanned on the phosphor screen is focused on the film through an optical lens system. The intensity of the light transmitted through the film changes with the density of the image on the film. In this way, the image is converted to light intensity, and detected by a photosensor. For this purpose, high brightness, high resolution, short decay time, and uniformity are required for the phosphor screen. The emission spectra of the phosphors must suit the spectral sensitivity of the detector. The phosphors $Ca_2MgSi_2O_7:Ce^{3+}$ (P16) and ZnO:Zn (P24) have been used for color and monochrome scanners, respectively. However, they have low efficiency and fast degradation. Currently, the following improved phosphors are used.

1. $Y_3Al_5O_{12}:Ce^{3+}$ (P46): The peak wavelength of the emission is 530 nm and the 10% decay time is 150 ns.

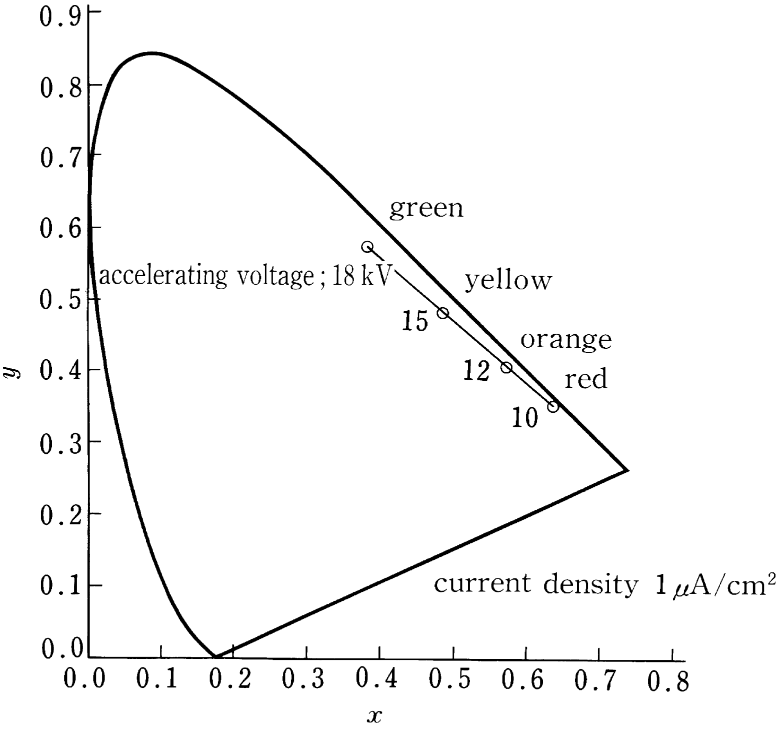

Figure 60 Chromaticity coordinate dependence on accelerating voltage of beam penetration type tubes.

2. Y_2SiO_5:Ce^{3+} (P47): The peak wavelength of the emission is 400 nm and the 10% decay time is 70 ns.
3. {P46(70%) + P47(30%)} (P48): The peak wavelengths of the emission are 400 and 525 nm, and the 10% decay time is 120 ns.
4. $Y_3(Al,Ga)_5O_{12}$:Ce^{3+} (PYG): The peak wavelength of the emission is 515 nm and the 10% decay time is 120 ns.[86]

The P48 screen is composed of two phosphors to create a broad-emission spectrum for reading color film images. The difference between the electrochemical properties of the two phosphors sometimes causes slight particle aggregation in the screening process. This aggregation results in noise on the optical image. For this reason, the $Y_3(Al,Ga)_5O_{12}$:Ce^{3+} phosphor is more suitable because its emission alone can cover a broad wavelength region, including the blue, as shown in Figure 61.

The synthesis method for $Y_3(Al,Ga)_5O_{12}$:Ce^{3+} is as follows. A mixture of Y_2O_3 (2.94 moles), Al_2O_3 (2.3 moles), Ga_2O_3 (2.7 moles), and $Ce_2(C_2O_4)_3$ (0.03 mole) is prepared by ball milling. The mixed materials are fired at 1550°C for 5 hours in air. The final particle size of the phosphor is adjusted to be under 5 μm.

Particles greater than 3 μm are removed by elutriation. A uniform phosphor screen is necessary because an irregular surface creates noise signals. For this purpose, the sedimentation method is used. The concentrations of sodium silicate and barium acetate should be optimized to keep the dispersion of the phosphor slurry as high as possible in the screening process.

The frequency response of color flying-spot scanner tubes is shown in Figure 62. Tubes with a $Y_3(Al,Ga)_5O_{12}$:Ce^{3+} screen have a good response in the high-frequency region.

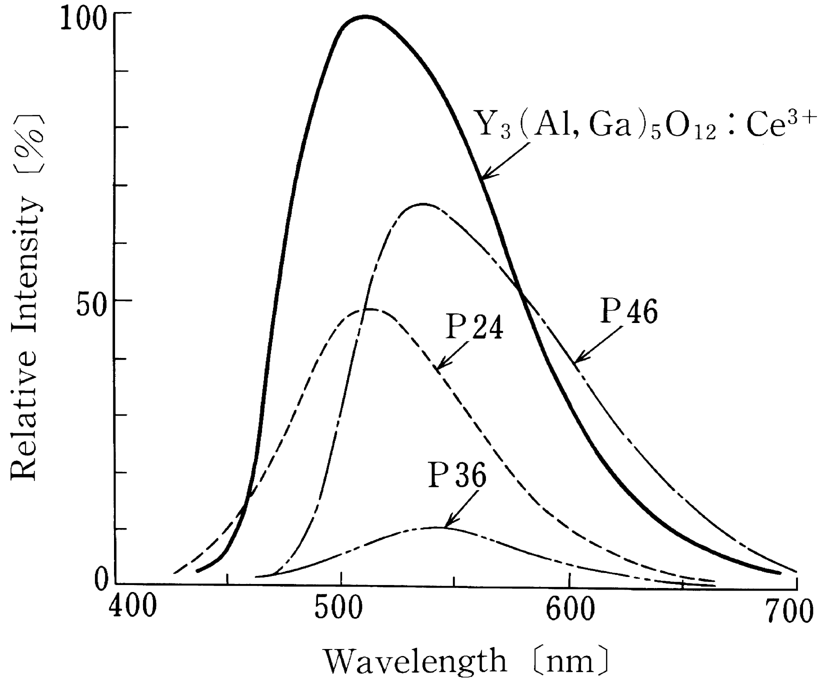

Figure 61 Emission spectra of flying-spot scanner tubes (compared under same conditions). (From Kobayashi, H., Ueba, Y., Takano, Y., and Awazu, K., *Mitsubishi Denki Giho (Mitsubishi Electric Technical Report)*, 48, 1121, 1974 (in Japanese). With permission.)

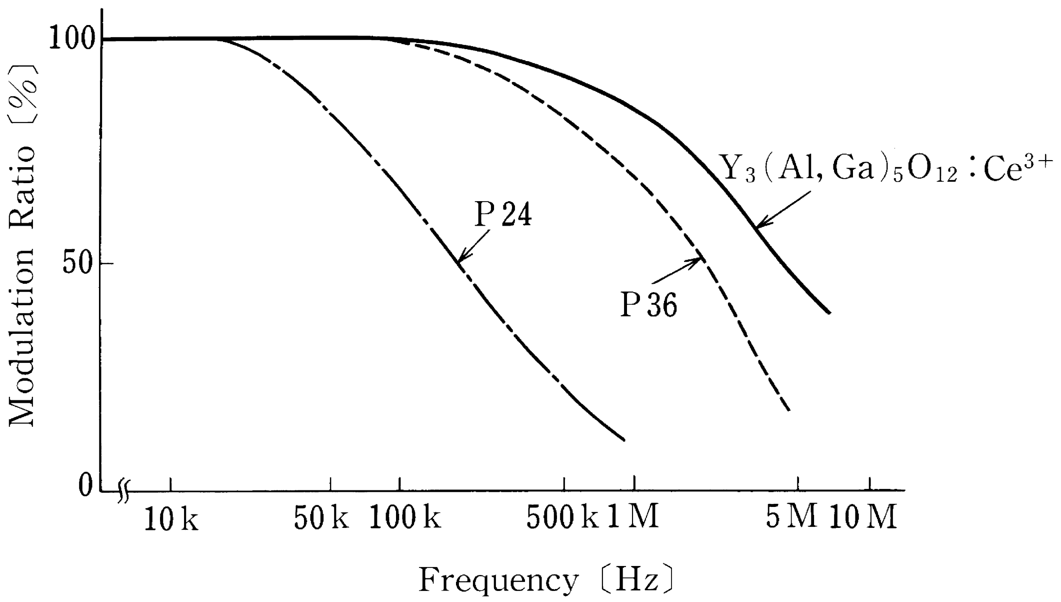

Figure 62 Response of color flying-spot scanner tubes (excited by sine wave). (From Kobayashi, H., Ueba, Y., Takano, Y., and Awazu, K., *Mitsubishi Denki Giho (Mitsubishi Electric Technical Report)*, 48, 1121, 1974 (in Japanese). With permission.)

Table 11 Relative Intensity of Color Flying-Spot Scanner Tubes

	Phosphors		
Color	P24 (std)	P36	$Y_3(Al,Ga)_5O_{12}$:Ce^{3+}
Blue	1.0	0.1	0.9
Green	1.0	0.2	2.1
Red	1.0	0.4	2.6

Moreover, the degradation of this screen is small: for example, emission intensity is more than 80% of the initial, even after a 3000-hour electron bombardment with an accelerating voltage of 20 kV and current density of 2 μA cm^{-2}. The three color components of this phosphor are measured using color filters (V-V45, V-G55, and V-R60) and a photosensor, and are shown in Table 11. The P24 phosphor is used as reference. The values of (Zn,Cd)S:Ag,Ni (P36) are shown for comparison.

The flying-spot scanner tube has been applied not only as a film image reader, but also to check photo-masks used in semiconductor processing.

References

1. Ooshima, I., *Densikeisoku (Electronic Measurement)*, 7, 63, 1967 (in Japanese).
2. Kobayashi, H. and Awazu, K., *J. Light & Vis.*, 5, 22, 1981.
3. Kurahashi, K. and Kobayashi, H., *SID International Symposium*, April 30, 1981.
4. Herold, E.W., *RCA Rev.*, 12, 445, 1951.
5. Kurahashi, K. and Ikehata, S., *Abstr. Inst. TV. Eng. Jpn.*, 13, 265, 1975 (in Japanese).
6. Kurahashi, K. and Ikehata, S., *Nikkei Electronics*, 10/20, 100, 1975 (in Japanese).
7. Kobayashi, H., Ueba, Y., Takano, Y., and Awazu, K., *Mitsubishi Denki Giho (Mitsubishi Electric Technical Report)*, 48, 1121, 1974 (in Japanese).

chapter six — section six

Phosphors for cathode-ray tubes

Shuji Inaho and Takashi Hase

Contents

6.6 Listing of practical phosphors for cathode-ray tubes 607
References 607

6.6 Listing of practical phosphors for cathode-ray tubes

The P numbers frequently used in this handbook are phosphor screen symbols specified by the Electronics Industries Association (EIA) of the U.S. These symbols have been used since 1945. The Japan Industrial Standard (JIS) B numbers are used in Japan, and the PRO symbols are used in Europe.

A new, unified international designation system, known as the Worldwide Phosphor Type Designation System (WTDS) was established in 1982. Table 14, which was compiled from other sources,[1] mainly uses the WTDS symbols; former symbols are also provided for comparison.

The WTDS symbols usually consist of two letters of the alphabet. The first letter indicates the criterion of phosphor screen emission color; the second letter indicates difference in the screen's emission color from the criterion. The meanings of the initial letters used in the symbol are listed in Table 12.

The meanings of the symbols for the 1/10 persistence time used in the next to last column of the phosphor table are listed in Table 13.[1]

The designation of symbols for new phosphor screens is being done by the JT-31 Committee of EIA.

Reference

1. *Optical Characteristics of Cathode Ray Tubes*, formulated by EIA Engineering Panel Advisory Council, EIA Publication No. 116-A December 1985.

Table 12 Meaning of the Initial Letters in the WTDS Symbols

Letter	Meaning
A	Violet tinged with red, purple, bluish-purple
B	Blue tinged with purple, blue tinged with green
D	Three-color phosphor screen for color TVs; the colors are clearly different from X or XX.
G,H	Green tinged with blue, green, green tinged with yellow
K	Greenish-yellow
L	Orange, pink tinged with yellow
R	Orange tinged with red, red, red tinged with purple, pink, pink tinged with purple
S	Phosphor screen for two-color display
V	Multicolor phosphor whose color varies with voltage
W	White
X (1 letter)	Phosphor screen for color TVs
X (2 letters)	Three-color phosphor screen for data displays; colors are close to X.
Y	Greenish-yellow, yellow, orangish-yellow
Z	Phosphor screens not belonging to any of the above categories

From EIA Engineering Panel Advisory Council, *Optical Characteristics of Cathode Ray Tubes*, EIA Publication No. 116-A, December 1985.

Table 13 Meaning of Symbols for 1/10 Decay Time

Symbol	10% Decay time
VL	1s or more
L	100 ms–1s
M	1–100 ms
MS	10 μs–1 ms
S	1–10 μs
VS	10 μs or less

From EIA Engineering Panel Advisory Council, *Optical Characteristics of Cathode Ray Tubes*, EIA Publication No. 116-A, December 1985.

Table 14 Registered CRT Phosphor Screens

	Former symbols				Emission color		Peak wavelength (nm)	Chromaticity coordinates		1/10 Persistence time	Main uses
WTDS symbol	EIA	JIS	PRO	Composition example	During excitation	After excitation		*x*	*y*		
AA	P16	B16	AA	$Ca_2MgSi_2O_7$:Ce^{3+}	Ultraviolet	Ultraviolet	385	0.199	0.016	VS	Flying-spot equipment, photographic applications
BA			BA		Violet-blue	—	400	0.164	0.015	VS	Flying-spot equipment
BB			BB	ZnS:Ag, Ni	Violet-blue	Violet-blue	435	0.170	0.050	MS	
BC			BC	ZnS:Ag,Al	Violet	—	435	0.170	0.024	S	
BD			BD	ZnS:Ag,Ni	Blue	—	400	0.198	0.220	VS	
BE	P11	B11	BE	ZnS:Ag	Blue	Blue	460	0.139	0.148	MS	Photographic applications
BF			BF	(Ca,Mg)SiO_3:Ti	Blue	—	420	0.164	0.108	MS	
BG	P35		BG	Zn(S,Se):Ag	Yellowish-green	Yellowish-blue	456	0.200	0.245	MS	Oscilloscopes
BH	P47	B47	BH	Y_2SiO_5:Ce^{3+}	Violet-blue	Violet-blue	400	0.166	0.101	VS	Flying-spot equipment, photographic applications
BJ	P5	B5	BJ	$CaWO_4$:W	Blue	Blue	420	0.169	0.132	MS	Photographic applications
BK	P37	B37		ZnS:Ag,Ni	Greenish-blue	Violet-blue, violet	465	0.143	0.208	VS	Flying-spot equipment, photographic applications
BL	P52	B52		Zn_2SiO_4:Ti	Violet-blue	Violet-blue	400	0.157	0.075	MS	Photographic applications
BM	P55	B55		ZnS:Ag	Blue	Blue	450	0.150	0.070	MS	Projection tubes
DA	A			Y_2O_2S:Eu^{3+}	Red	Red	—	0.615	0.360	M	
				(Zn,Cd)S:Cu,Al	Yellowish-green	Yellowish-green	—	0.300	0.600	M	

Table 14 Registered CRT Phosphor Screens (continued)

	Former symbols				Emission color		Peak wavelength (nm)	Chromaticity coordinates		1/10 Persistence time	
WTDS symbol	EIA	JIS	PRO	Composition example	During excitation	After excitation		*x*	*y*		Main uses
				ZnS:Ag+(Zn,Cd)S:Cu,Al	White	White	—	0.230	0.240	M	
DB	P54	B54		$Y_2O_2S:Eu^{3+}$	Red	Red	—	0.625	0.350	M	Character displays
	B			$ZnS:Cu,Al+Y_2O_2S:Eu^{3+}$	Green	Green	—	0.280	0.610	MS	Graphic displays
				ZnS:Ag+ZnS:Cu,Al	White	White	—	0.281	0.311	MS	
DC	C			$Y_2O_2S:Eu^{3+}+(Zn,Mg)_3(PO_4)_2:Mn^{2+}$	Reddish-orange	Reddish-orange	—	0.627	0.345	L	
				$Zn_2SiO_4:Mn^{2+}(As)+(Zn,Mg)_3(PO_4)_2:Mn^{2+}$ + ZnS:Ag	White	White	—	0.230	0.240	L	
						Red					
DD	E			$Zn_3(PO_4)_2:Mn^{2+}+Y_2O_2S:Eu^{3+}$	Red	Red	—	0.630	0.350	L	
				$Zn_2SiO_4:Mn^{2+},As+ZnS:Cu$	Green	Green	—	0.230	0.670	M	
				$Zn_2SiO_4:Mn^{2+},As+Zn_3(PO_4)_2:Mn^{2+}$	Light blue	Light blue	—	0.230	0.240	M	
DE	G			$Zn_3(PO_4)_2:Mn^{2+}+Y_2O_2S:Eu^{3+}$	Red	Red	—	0.630	0.350	L	
				$Zn_2SiO_4:Mn^{2+},As+ZnS:Cu$	Green	Green	—	0.220	0.670	M	
				$ZnS:Ag,Cu,Ga,Al+Zn_2SiO_4:Mn^{2+},As$	Blue	Blue	—	0.152	0.128	M	
DF				$Y_2O_2S:Eu^{3+}$	Red	Red	—	0.610	0.342	M	
				$Zn_2SiO_4:Mn^{2+},As+ZnS:Cu,Al,Au$	Green	Green	—	0.250	0.650	M	
				$ZnS:Ag+ZnS:Cu,Al+Y_2O_2S:Eu^{3+}$	Light blue	Light blue	—	0.230	0.240	MS	
DG				$Y_2O_2S:Eu^{3+}$	Red	Red	—	0.610	0.342	M	
				$Zn_2SiO_4:Mn^{2+},As+ZnS:Cu,Al$	Green	Green	—	0.250	0.650	M	
				$ZnS:Ag+ZnS:Cu,Al+Y_2O_2S:Eu^{3+}$	Light blue	Light blue	—	0.230	0.240	MS	
DH				$Y_2O_2S:Eu^{3+}$	Reddish-orange	Reddish-orange	—	0.625	0.350	M	
				$Zn_2SiO_4:Mn^{2+}(As)$	Yellowish-green	Yellowish-green	—	0.210	0.700	L	
DJ				$ZnS:Ag+Zn_2SiO_4:Mn^{2+}(As)+Y_2O_2S:Eu^{3+}$	White	White	—	0.230	0.240	M	
				$Y_2O_2S:Eu^{3+}$	Reddish-orange	Reddish-orange	—	0.615	0.360	M	

Table 14 Registered CRT Phosphor Screens (continued)

WTDS symbol	Former symbols			Composition example	Emission color		Peak wavelength (nm)	Chromaticity coordinates		1/10 Persistence time	Main uses
	EIA	JIS	PRO		During excitation	After excitation		x	y		
				$(Zn,Cd)S:Cu,Al+Zn_2SiO_4:Mn^{2+}(As)$	Yellowish-green	Yellowish-green	—	0.250	0.655	M	
DK				$ZnS:Ag+(Zn,Cd)S:Cu,Al$	White	White	—	0.230	0.240	M	
				$Y_2O_2S:Eu^{3+}+Zn_3(PO_4)_2:Mn^{2+}$	Red	Red	—	0.620	0.345	M	
				$Zn_2SiO_4:Mn^{2+}+ZnS:Cu,Al$	Green	Green	—	0.250	0.640	M	
				$ZnS:Ag,Al+ZnS:Ag,Ga$	Blue	Blue	—	0.152	0.062	M	
GA	P40	B40		$ZnS:Ag+(Zn,Cd)S:Cu$	White		—	0.276	0.312	Blue to S	Low-speed rate displays
						Yellowish-green	—			Yellow to L	
GB	P32	B32	GB	$(Zn,Cd)S:Cu+(Ca,Mg)SiO_3:Ti$	Violet-blue		—				Radar
						Yellowish-green	—	0.340	0.515	L	
GD			GD		Yellowish-green	—	525	0.335	0.460	M	
GE	P24	B24	GE	$ZnO:Zn$	Green	Green	510	0.245	0.441	S	Flying-spot equipment
GF			GF	$ZnS:Cu$	Green	Green		0.240	0.520	L	
GG	P15	B15	GG	$ZnO:Zn$	Green	Green	504	0.246	0.439	S	Flying-spot equipment, photographic applications
GH	P31	B31	GH	$ZnS:Cu$	Green	Green	520	High luminance		MS	Oscilloscopes
								0.193	0.420		
								Low luminance			
								0.226	0.528		
GJ	P1	B1	GJ	$Zn_2SiO_4:Mn^{2+}$	Yellowish-green	Yellowish-green	525	0.218	0.712	M	Oscilloscopes, radar
GK			GK	$Zn_2SiO_4:Mn^{2+}$	Yellowish-green	Yellowish-green	525	0.218	0.712	M	

Table 14 Registered CRT Phosphor Screens (continued)

WTDS symbol	Former symbols EIA	JIS	PRO	Composition example	Emission color During excitation	After excitation	Peak wavelength (nm)	Chromaticity coordinates x	y	1/10 Persistence time	Main uses
GL	P2	B2	GL	ZnS:Cu	Yellowish-green	Yellowish-green	543	0.279	0.534	MS	Oscilloscopes
GM	P7	B7	GM	ZnS:Ag	Violet-blue		—	0.151	0.032	Blue to MS	Oscilloscopes, radar
				(Zn,Cd)S:Cu	Yellowish-green	Yellowish-green	—	0.357	0.537	Yellowish-green to L	
GN			GN	Layer 1	Greenish-blue	Green	—	0.167	0.223	MS	
				Layer 1	Green	Green	—	0.239	0.434		
GP			GP	ZnS:Cu,Ag,Cl	Bluish-green	Green	520	High luminance			
								0.180	0.365	MS	
					Green	Green	—	Low luminance			
								0.190	0.430	MS	
GQ			GQ	(Zn,Cd)S:Cu,Al+black pigment	Yellowish-green	Yellowish-green	—	0.265	0.550	MS	
GR	P39	B39	GR	$Zn_2SiO_4:Mn^{2+},As$	Yellowish-green	Yellowish-green	525	0.223	0.698	L	Low-speed rate displays, radar
GS				(Zn,Cd)S:Ag,Ni	Yellowish-green	Yellowish-green	530	0.320	0.530	VS	
GT				(Zn,Cd)S:Ag,Ni	Bluish-green	Bluish-green	490	0.190	0.370	VS	
GW	P42	B42	GW	$ZnS:Cu+Zn_2SiO_4:Mn^{2+},As$	Yellowish-green	Yellowish-green	520	0.238	0.568	M	Low-speed rate displays, radar
GX	P44	B44	GX	$La_2O_2S:Tb^{3+}$	Yellowish-green	Yellowish-green	544	0.300	0.596	M	Displays
GY	P43	B43	GY	$Gd_2O_2S:Tb^{3+}$	Yellowish-green	Yellowish-green	544	0.333	0.556	M	Displays
GZ				$Zn_2SiO_4:Mn^{2+},As$+black pigment <GH> <GR>	Yellowish-green	Yellowish-green	525	0.223	0.698	M	

Table 14 Registered CRT Phosphor Screens (continued)

WTDS symbol	Former symbols			Composition example	Emission color		Peak wavelength (nm)	Chromaticity coordinates		1/10 Persistence time	Main uses
	EIA	JIS	PRO		During excitation	After excitation		*x*	*y*		
HA				$ZnS:Cu$ (15%) + $Zn_2SiO_4:Mn^{2+}$, As (85%) + black pigment <GH> <GR>	Yellowish-green	Yellowish-green	525	0.220	0.660	M	
HB				$ZnS:Cu+Zn_2SiO_4:Mn^{2+},As$	Yellowish-green	Yellowish-green	521	0.215	0.650	M	
KA	P20	B20	KA	$(Zn,Cd)S:Ag$	Yellowish-green	Yellowish-green	560	0.426	0.546	MS to M	
KB				$(Zn,Cd)S:Ag$	Yellowish-green	Yellowish-green	495	0.380	0.520	VL	
KC			KC	$(Zn,Cd)S:Cu,Al$	Yellowish-green	Yellowish-green	560	0.426	0.559	M	
KD				$(Zn,Cd)S:Cu,Al$+red pigment	Yellowish-green	Yellowish-green		0.425	0.550	MS	
KE	P28			$(Zn,Cd)S:Cu$	Yellowish-green	Yellowish-green	550	0.370	0.540	L	Radar
KF	P36	B36		$(Zn,Cd)S:Ag,Ni$	Yellowish-green	Yellowish-green	550	0.400	0.543	VS	Flying-spot equipment
KG	P46	B46		$Y_3Al_5O_{12}:Ce^{3+}$	Yellowish-green	Yellowish-green	530	0.365	0.595	VS	Flying-spot equipment
KH	P48	B48		$Y_3Al_5O_{12}:Ce^{3+}$ (70%) +$Y_2SiO_5:Ce^{3+}$ (30%)	Yellowish-green	Yellowish-green		0.365	0.474	VS	Flying-spot equipment
KJ	P53	B53		$Y_3Al_5O_{12}:Tb^{3+}$	Yellowish-green	Yellowish-green	544	0.368	0.539	M	Head-up displays
KK				$Y_2O_2S:Tb^{3+}$	Yellowish-green	Yellowish-green	544	0.341	0.586	M	Projection tubes
LA			LA	$Cd_5Cl(PO_4)_3:Mn^{2+}$	Orange	Orange	590	0.557	0.442	M	
LB	P12	B12	LB	$(Zn,Mg)F_2:Mn^{2+}$	Orange	Orange	590	0.557	0.442	L	Radar
LC	P26	B26	LC	$(KF,MgF_2):Mn^{2+}$	Orange	Orange	585	0.573	0.426	VL	Radar
LD	P33	B33	KD	$MgF_2:Mn^{2+}$	Orange	Orange	585	0.559	0.440	VL	Radar
LE				$(KF,MgF_2):Mn^{2+}$	Orange	Orange	590	0.530	0.420	VL	

Table 14 Registered CRT Phosphor Screens (continued)

WTDS symbol	Former symbols			Composition example	Emission color		Peak wavelength (nm)	Chromaticity coordinates		1/10 Persistence time	Main uses
	EIA	JIS	PRO		During excitation	After excitation		*x*	*y*		
LF	P19	B19		$(KF,MgF_2):Mn^{2+}$	Orange	Orange	590	0.572	0.422	L	Radar
LG			LG	$(Zn,Mg)F_2:Mn^{2+}$	Orange	Orange	600	0.559	0.440	VL	
LH			LH	$(Zn,Mg)F_2:Mn^{2+}+ZnS:Ag$	Violet	Orange	—	0.559	0.440	VL	
LJ	P25	B25		$CaSiO_3:Pb,Mn^{2+}$	Orange	Orange	610	0.569	0.429	M	Display equipment
LK	P38	B38		$(Zn,Mg)F_2:Mn^{2+}$	Orange	Orange	600	0.591	0.407	VL	Low-speed rate displays
LL	P57	B57		$Zn_2SiO_4:Mn^{2+}+MgF_2:Mn^{2+}$	Yellowish-green		—	0.218	0.712	M	Radar
						Orange	—	0.573	0.426	VL	Radar equipment
LM			LM	$(Zn,Cd)S:Cu,Al$	Orange	Orange	—	0.547	0.446	MS	
LN			LN	$Y_2O_3:Eu^{3+}$ (80%)+$ZnS:Cu,Al$ (20%)	Orange	Orange	611	0.535	0.433	MS	
LP			LP	$Zn_3(PO_4)_2:Mn^{2+}$ (85%) +$Zn_2SiO_4:Mn^{2+},As$ (15%)	Orange	Orange	640	0.545	0.435	L	
RA			RA		Reddish-orange	—	640	0.665	0.335	M	
RB			RB	$Y_2O_3:Eu^{3+}$	Reddish-orange	Reddish-orange	611	0.630	0.365	M	
RC	P13			$MgSiO_3:Mn^{2+}$	Reddish-orange	Reddish-orange	640	0.670	0.329	M	
RD	P21			$MgF_2:Mn^{2+}$	Reddish-orange	Reddish-orange	605	0.539	0.373	L	Radar
RE	P27			$Zn_3(PO_4)_2:Mn^{2+}$	Reddish-orange	Reddish-orange	635	0.674	0.326	M	Color monitor TVs
RF	P56	B56		$Y_2O_3:Eu^{3+}$	Red	Red	611	0.640	0.335	M	Projection tubes
SA	P29			$ZnS:Cu$	Yellowish-green	Yellowish-green		0.279	0.534	MS	
				$CaSiO_3:Pb,Mn^{2+}$	Orange	Orange		0.569	0.429	M	

Table 14 Registered CRT Phosphor Screens (continued)

WTDS symbol	Former symbols			Composition example	Emission color		Peak wavelength (nm)	Chromaticity coordinates		1/10 Persistence time	Main uses
	EIA	JIS	PRO		During excitation	After excitation		*x*	*y*		
VA	P49	B49		YVO_4:Eu^{3+}, 6kV	Reddish-orange	Reddish-orange	619	0.672	0.327	M	Graphics displays
				Zn_2SiO_4:Mn^{2+}, 17kV	Yellowish-green	Yellowish-green	522	0.315	0.615	M	Alphanumeric displays
VB	P50	B50		Y_2O_3:Eu^{3+}, 8kV	Reddish-orange	Reddish-orange	619	0.655	0.340	M	Multicolor displays
				(Zn,Cd)S:Ag,Ni, 15kV	Yellowish-green	Yellowish-green		0.398	0.546	MS	
VC	P51	P51		Y_2O_3:Eu^{3+}, 6kV (Zn,Cd)S:Ag,Ni, 12kV	Reddish-orange	Reddish-orange		0.675	0.325	M	Multicolor displays
VD				Y_2O_3:Eu^{3+}, 8kV	Reddish-orange	Reddish-orange		0.591	0.380	M	Graphic, alphanumeric, and pictorial displays
				Zn_2SiO_4:Mn^{2+}, 13kV	Yellowish-green	Yellowish-green		0.344	0.465	M	
				ZnS:Ag, 18kV	Bluish-green	Bluish-green		0.230	0.361	M	
VE				YVO_4:Eu^{3+}, 8kV	Reddish-orange	Reddish-orange		0.604	0.360	M	
				ZnS:Cu, 17kV	Yellowish-green	Yellowish-green		0.355	0.510	VL	
WA			WA	ZnS:Ag+(Zn,Cd)S:Ag	White	White		0.313	0.329	M	
WB	P45	B45	WB	Y_2O_2S:Tb^{3+}	White	White		0.253	0.312	M	Displays
WC			WC	ZnS:Ag+(Zn,Cd)S:Ag (black pigmentation)	White	White		0.265	0.285	MS	
WD			WD	P22 red and P4 blue/yellow mixture	White	White		0.355	0.395	M	
WE				Y_2O_2S:Tb^{3+},Sm^{3+}	White			0.265	0.285	MS	

Table 14 Registered CRT Phosphor Screens (continued)

WTDS symbol	Former symbols			Composition example	Emission color		Peak wavelength (nm)	Chromaticity coordinates		1/10 Persistence time	Main uses
	EIA	JIS	PRO		During excitation	After excitation		*x*	*y*		
WF	P17			ZnO:Zn +(Zn,Cd)S:Cu	White	Yellow		0.302	0.390	Blue to S Yellow to L	
WG	P23			ZnS:Ag+(Zn,Cd)S:Ag	White	White		0.364	0.377	MS	Direct viewing television
WH			WH	$Zn_3(PO_4)_2$:Mn^{2+} (40%) Zn_2SiO_4:Mn^{2+},As (40%) ZnS:Ag (20%)	White	White		0.253	0.305	L	
WJ				ZnS:Ag+(Zn,Cd)S:Cu,Al	White	White		0.310	0.355	MS	
WK				ZnS:Ag+(Zn,Cd)S:Cu,Al	White	White		0.310	0.355	M	
WL				ZnS:Ag+(Zn,Cd)S:Cu,Al	White	White		0.310	0.355	M	
WM				ZnS:Ag+Zn_2SiO_4:Mn^{2+},As+Zn_2SiO_4:Mn^{2+},As+$Zn_3(PO_4)_2$:Mn^{2+}	White	White		0.280	0.310	M	
WN				ZnS:Ag+Zn_2SiO_4:Mn^{2+},As+(Zn,Cd)S:Cu,Al,Ga	White	White		0.280	0.310	M	
WP				ZnS:Ag+Zn_2SiO_4:Mn^{2+},As+$Zn_3(PO_4)_2$:Mn^{2+}+(Zn,Cd)S:Cu,Al	White	White		0.280	0.310	M	
WW	P4	B4	WW	ZnS:Ag+(Zn,Cd)S:Ag	White	White		0.265	0.285	MS	Entertainment television
XX	P22	B22		ZnS:Ag	Blue	Blue		0.146	0.052		Color TV
				Zn_2SiO_4:Mn^{2+}	Green	Green		0.218	0.712		
				$Zn_3(PO_4)_2$:Mn^{2+}	Red	Red		0.674	0.326		
XX	P22	B22		ZnS:Ag	Blue	Blue		0.155	0.060		Color TV
				(Zn,Cd)S:Ag	Green	Green		0.285	0.600		
				(Zn,Cd)S:Ag	Red	Red		0.663	0.337		
XX	P22	B22		ZnS:Ag	Blue	Blue		0.157	0.047	MS	Color TV
				(Zn,Cd)S:Ag	Green	Green		0.260	0.600		
				YVO_4:Eu^{3+}	Red	Red		0.650	0.325		
XX	P22	B22		ZnS:Ag	Blue	Blue		0.150	0.068	MS	Color TV
				(Zn,Cd)S:Ag	Green	Green		0.300	0.600		
				Y_2O_2S:Eu^{3+}	Red	Red		0.628	0.337		
XX	P22	B22		ZnS:Ag	Blue	Blue		0.150	0.070	MS	Color TV

Table 14 Registered CRT Phosphor Screens (continued)

WTDS symbol	Former symbols EIA	JIS	PRO	Composition example	Emission color During excitation	After excitation	Peak wavelength (nm)	Chromaticity coordinates x	y	1/10 Persistence time	Main uses
				(Zn,Cd)S:Cu	Green	Green		0.330	0.590		
				$Y_2O_2S:Eu^{3+}$	Red	Red		0.640	0.335		
XX	P22	B22		ZnS:Ag	Blue	Blue		0.155	0.067	MS	Color TV
				(Zn,Cd)S:Cu	Green	Green		0.343	0.591		
				$Y_2O_2S:Eu^{3+}$	Red	Red		0.623	0.342		
XX	P22	B22		$Y_2O_2S:Eu^{3+}$	Reddish-orange	Reddish-orange		0.630	0.345	M	Color TV
				ZnS:Cu,Al	Yellowish-green	Yellowish-green		0.297	0.597	M	
				ZnS:Ag	Violet-blue	Violet-blue		0.149	0.070	M	
XB	D			$Zn_3(PO_4)_2:Mn^{2+}+Y_2O_2S:Eu^{3+}$	Red	Red		0.630	0.350	M	
				$Zn_2SiO_4:Mn^{2+}$,As+ZnS:Cu	Green	Green		0.220	0.670	M	
				ZnS:Ag	Blue	Blue		0.151	0.064	MS	
XC	F			$Y_2O_2S:Eu^{3+}$	Red	Red		0.610	0.342	M	
				$Zn_2SiO_4:Mn^{2+}$,As+ZnS:Cu,Au,Al	Green	Green		0.230	0.650	M	
				ZnS:Ag	Blue	Blue		0.151	0.064	MS	
XE				$Y_2O_2S:Eu^{3+}+Zn_3(PO_4)_2:Mn^{2+}$	Reddish-orange	Reddish-orange		0.620	0.345	M	
				$Zn_2SiO_4:Mn^{2+}$+ZnS:Cu,Al	Yellowish-green	Yellowish-green		0.250	0.640	M	
				ZnS:Ag,Al+ZnS:Ag,Ga	Violet-blue	Violet-blue		0.152	0.062	M	
XY	Y			$Y_2O_2S:Eu^{3+},(Zn,Mg)_3(PO_4)_2:Mn^{2+}$	Reddish-orange	Reddish-orange		0.627	0.345	L	
				$Zn_2SiO_4:Mn^{2+}(As)$	Yellowish-green	Yellowish-green		0.210	0.699	L	
				ZnS:Ag	Violet-blue	Violet-blue		0.149	0.070	M	
YA				$(Zn,Be)_2SiO_4:Mn^{2+}$	Orangish-yellow	Orangish-yellow		0.540	0.460	M	
				(Zn,Cd,Mg)Silicate:Mn^{2+}							

Table 14 Registered CRT Phosphor Screens (continued)

	Former symbols				Emission color			Chromaticity coordinates			
WTDS symbol	EIA	JIS	PRO	Composition example	During excitation	After excitation	Peak wavelength (nm)	*x*	*y*	1/10 Persistence time	Main uses
YB	P3			$(Zn,Be)_2SiO_4:Mn^{2+}$	Orangish-yellow	Orangish-yellow	600	0.523	0.469	M	Monochrome television
YC	P14			ZnS:Ag+(Zn,Cd)S:Cu	Blue	Orangish-yellow		0.150	0.093	MS	Displays for military use
								0.504	0.443	M	
YD	P41	B41		$(Zn,Mg)F_2:Mn^{2+}+Ca_2MgSi_2O_7:Ce^{3+}$	Orangish-yellow	Orangish-yellow		0.541	0.456	L	Light pens
										VS	
ZA	P10			Not a luminescent material (KCl)						VL +variable	
ZB	P34			ZnS:Pb,Cu	Bluish-green	Yellowish-green	540	0.235	0.364	VL	Oscilloscopes, radar

chapter seven — sections one and two

Phosphors for X-ray and ionizing radiation

Norio Miura

Contents

7.1 Phosphors for X-ray intensifying screens and fluorescent screens 619
  7.1.1 X-ray intensifying screens....619
    7.1.1.1 Functions and methods of use....620
    7.1.1.2 Performance of intensifying screens....620
    7.1.1.3 Required phosphor characteristics....621
    7.1.1.4 Characteristics of practical phosphors....622
    7.1.1.5 Phosphor synthesis....623
  7.1.2 Phosphors for X-ray fluorescent screens....625
    7.1.2.1 Applications of X-ray fluorescent screens....625
    7.1.2.2 Phosphors used in X-ray fluorescent screens....626
    7.1.2.3 Structure and characteristics of X-ray fluorescent screens....626
7.2 Phosphors for thermoluminescent dosimetry....629
  7.2.1 The principle of thermoluminescent dosimetry....629
  7.2.2 Characteristics required of phosphors....630
  7.2.3 Characteristics of phosphors in practical use....631
    7.2.3.1 Energy dependence....631
    7.2.3.2 Glow curve....631
    7.2.3.3 Thermoluminescence spectrum....631
    7.2.3.4 Supralinearity....631
    7.2.3.5 Fading....632
  7.2.4 Examples of main uses....633
References....633

7.1 Phosphors for X-ray intensifying screens and X-ray fluorescent screens

7.1.1 X-ray intensifying screens

X-ray intensifying screens are used in radiological diagnosis and in industrial nondestructive testing. In the former case, the objective is to reduce the amount of radiation exposure to patients; in the latter case, the objective is to shorten the testing time.

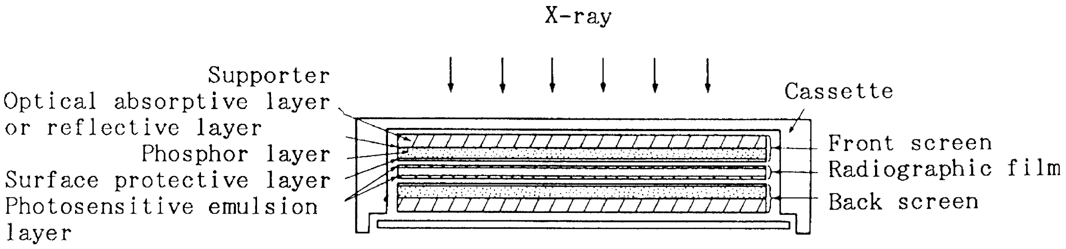

Figure 1 Method of using X-ray intensifying screens and radiographic film, and the structure of intensifying screens.

7.1.1.1 Functions and methods of use

X-ray intensifying screens are used to increase the speed of radiographic films by making use of the emission from phosphors excited by X-rays. A radiographic film consists of a 175-μm-thick transparent film base coated on both sides with silver halide photosensitive emulsion layers that are approximately 5-μm thick. Within the X-ray energy region used for radiological diagnosis, the X-ray absorption by the emulsion layer is inefficient, at best about 1%, so the direct sensitivity of the film to X-rays is very low.

For that reason, intensifying screens are employed, as shown in Figure 1. The radiographic film is sandwiched between two screens, each of which consists of an optically reflective layer or an optically absorptive layer coated on a supporter base. Over that layer, first a phosphor layer and then a protective surface layer are applied.

Intensifying screens have the following functions.

1. Reduce the patient's exposure to radiation.
2. Reduce blurring of the image due to subject movement by shortening the exposure time.
3. Reduce geometric blur by making it possible to use a small focus X-ray tube.
4. Make possible the use of portable X-ray equipment and extend the life of the X-ray tube.
5. Increase the contrast of the radiograph.

7.1.1.2 Performance of intensifying screens

While the primary function of an intensifying screen is to reduce the amount of exposure to radiation or to reduce the exposure time, there is at the same time a need to increase the accuracy of diagnosis or inspection by enhancing the quality of the image obtained and to extend the lifetime of the equipment.

The extent of sensitization by intensifying screens is, as shown conceptually in Figure 2, expressed in terms of the spectral sensitivity of the radiographic film, F_λ, and the emission spectrum of the intensifying screen, E_λ, as the radiographic speed, $S = ½E_\lambda \cdot F_\lambda d\lambda$.

The actual speed of a screen-film system is evaluated by mounting a standard intensifying screen and a test screen together on one cassette at the same time, exposing them to a fixed exposure dose in more than 10 different places, and varying the distance according to the inverse square law. The relative sensitivity of the specimen is then determined from the characteristic curve of the measured image density versus exposure dose.

The image quality of intensifying screens is evaluated by sharpness, graininess, and contrast. Sharpness is evaluated as a response function (modulation transfer function: MTF) by taking a radiograph of a test chart and optically measuring the blurred image

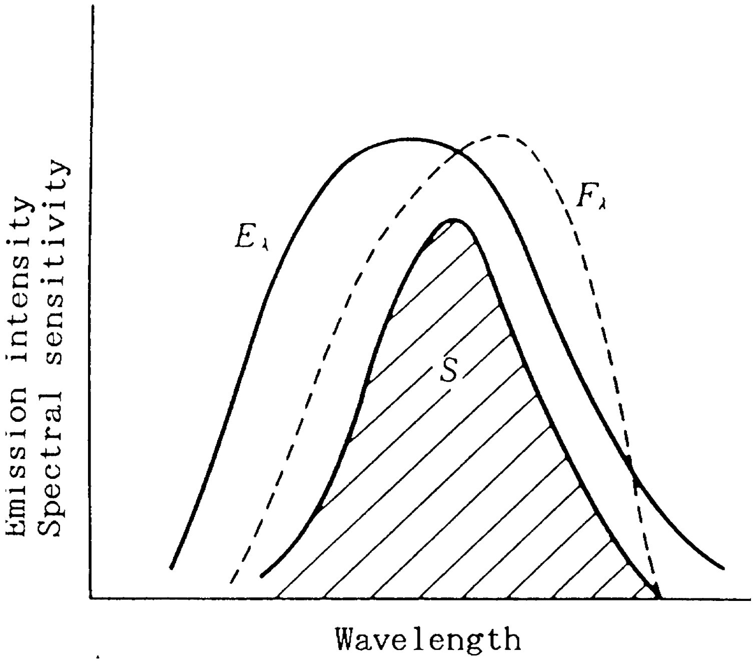

Figure 2 Concept of radiographic speed in X-ray intensifying screens.

at various spatial frequencies (image sizes). Graininess is evaluated by scanning an exposed radiograph image with a microdensitometer to measure changes in density, and then taking the Fourier transformation of these density changes to obtain a Wiener spectrum. Contrast can be changed by altering the X-ray absorption characteristics of the phosphor compound used in intensifying screens.

7.1.1.3 Required phosphor characteristics

The following characteristics are required of phosphors for use in X-ray intensifying screens.

1. *High emission efficiency:* In radiological diagnosis, as noted before, the most important objectives are to minimize the patient's radiation exposure dose and to obtain a radiograph of high image quality. To attain these objectives, the phosphors must have a high emission efficiency. In industrial nondestructive testing, testing efficiency requires the same characteristics.
2. *Strong X-ray absorption:* In contrast to the cases of ultraviolet or cathode-ray excitation, most substances are highly transparent to X-rays. To obtain efficient emission, therefore, the phosphors must have a large X-ray absorption coefficient. Accordingly, the phosphor must be composed of elements that have high atomic numbers. The characteristic graininess is also important with respect to X-ray quanta utilization efficiency.
3. *Emission spectrum matched to the spectral sensitivity of the radiographic film:* There are two types of radiographic films: a blue-sensitive type, which has a spectral sensitivity peak between 350 and 430 nm, and an orthochromatic type, which has spectral sensitivity up to the green light region.
4. *Short emission decay time:* Because the screen is used repeatedly, persistent emission after exposure to X-rays can cause double-exposure with the preceding image and lower the contrast by raising the base density. It is particularly unacceptable for

the phosphor to have even a small amount of persistent after-glow following exposure to X-rays or light.

5. *Durability:* Degradation by X-ray radiation or by the moisture in air must be minimized.
6. *Dispersion:* To obtain a homogeneous phosphor layer, the phosphor must disperse well in the coating slurry without forming coagulated particles.

7.1.1.4 Characteristics of practical phosphors

$CaWO_4$. Of all phosphors for use in X-ray intensifying screens, $CaWO_4$ has been used for the longest time in combination with blue-sensitive radiographic film.

The $CaWO_4$ phosphor is a typical self-activated phosphor. It exhibits blue emission with a peak at 420 nm. This phosphor includes tungsten in the host composition, and has a large specific gravity (6.1) and a large X-ray absorption coefficient. An excellent radiographic image quality can be obtained with an intensifying screen that employs this phosphor. For that reason, $CaWO_4$ intensifying screens still enjoy widespread use.

$Gd_2O_2S:Tb^{3+}$. This phosphor is most frequently used among the rare-earth phosphors. It has excellent X-ray absorption, emission efficiency, short after-glow after X-ray excitation, and chemical stability. It has a green emission with a peak at 545 nm in its line spectrum.

Because of its green emission, X-ray intensifying screens employing this phosphor are used with orthochromatic-type radiographic films dye-sensitized to emissions ranging from blue to green.

This combination has made it possible to take radiographs of high image quality at a high speed.

$BaFCl:Eu^{2+}$. Of the $Ba_{1-x}Sr_xFCl_{1-y}Br_y:Eu^{2+}$ system phosphors, $BaFCl:Eu^{2+}$ has a high X-ray emission efficiency and an emission spectrum with a peak at 380 nm, which is well matched with the spectral sensitivity of blue-sensitive radiographic film. The speed of $BaFCl:Eu^{2+}$ intensifying screens is from two to five times faster than that of CaWO4 screens. This screen yields excellent sharpness because the cross-over effect* is very small due to its short emission wavelength, but the graininess is very poor. While the emission decay time after X-ray excitation is long, it can be reduced to an acceptable level by additives such as KCl.

$BaFBr:Eu^{2+}$, of the same phosphor group, has better X-ray absorption and emission efficiency than $BaFCl:Eu^{2+}$, but is inferior in terms of moisture resistance and emission decay characteristics.

$LaOBr:Tb^{3+}$ and $LaOBr:Tm^{3+}$. These phosphors emit in the blue region and have high emission efficiencies. Intensifying screens employing them provide high speed in combination with a blue-sensitive radiographic film. The Tb-activated compound was put to practical use. Recently, the Tm-activated material has taken over, as it has emission at shorter wavelength, which is more effective in reducing the blurring caused by cross-over.

This phosphor has the disadvantage of being degraded by moisture, so various moisture-proof treatments are required. Moreover, these crystals are flat-shaped platelets, so the image quality of the screen is not very good.

---

* The cross-over effect is a phenomenon that occurs during radiographic exposure when the light emitted by the intensifying screen passes through the contacting emulsion layer of the radiographic film and exposes the emulsion layer on the opposite side. While this phenomenon increases speed, it reduces sharpness.

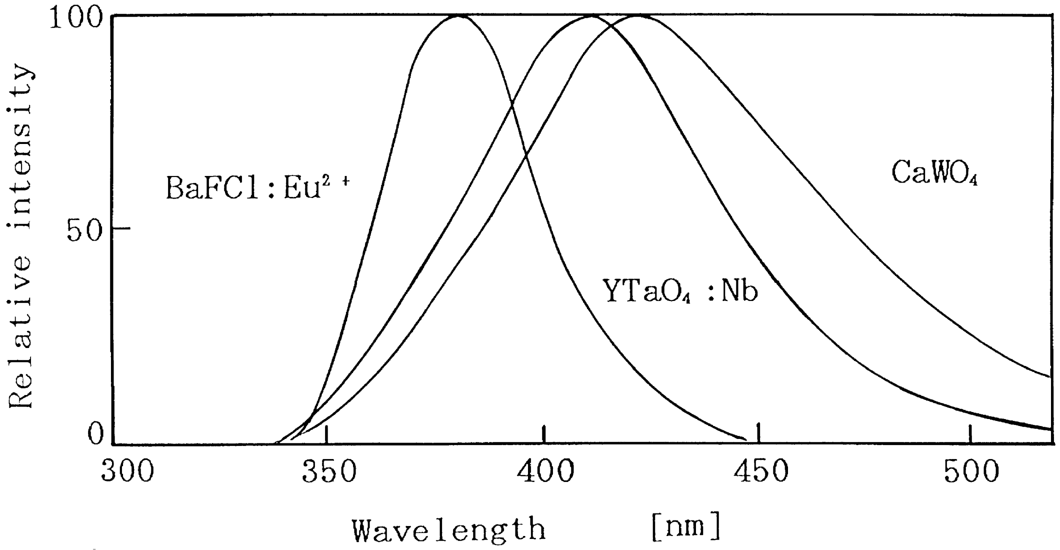

Figure 3 Emission spectra of phosphors for X-ray intensifying screens (I).

$YTaO_4$ and $YTaO_4$:Nb. The matrix compound $YTaO_4$ contains Ta, which has an atomic number of 73, and has a large specific gravity (7.5). It also has a higher X-ray absorption coefficient than $CaWO_4$.

The Nb-activated $YTaO_4$ phosphor has a blue emission with a peak at 410 nm and an emission efficiency twice that of $CaWO_4$. Used with blue-sensitive radiographic film, intensifying screens that employ this phosphor offer high speed (approximately two to three times that of $CaWO_4$ screens).

Self-activated $YTaO_4$ phosphors have an emission peak at 337 nm in the near-ultraviolet region. By using screens employing this phosphor together with a radiographic film that is sensitive to near ultraviolet light, a high degree of sharpness can be obtained. The reasons for this increase in sharpness are that the phosphor's short wavelength emission suffers only low optical dispersion, and in addition, the cross-over effect is greatly reduced.

$La_2O_2S:Tb^{3+}$. This phosphor is of the same group as $Gd_2O_2S:Tb^{3+}$. It has an even higher green emission intensity and must be used with orthochromatic film. Radiation from ^{138}La, an isotope of La, and from other radioactive species like ^{227}Ac and ^{227}Th contained in the material sometimes causes a photographic problem.

Some other phosphors are also used in practical X-ray intensifying screens; for example, $BaSO_4:Eu^{2+}$, $Y_2O_2S:Tb^{3+}$, and ZnS:Ag. The emission spectra of the most important phosphors described above are shown in Figure 3 and Figure 4. The X-ray absorption coefficients are shown in Figure 5.

The various characteristics of X-ray phosphors are summarized in Table 1.

7.1.1.5 Phosphor synthesis

While the phosphors used in intensifying screens are synthesized in the same way as phosphors for other uses, the syntheses of $CaWO_4$ and Gd_2O_2S:Tb as typical examples are described here.

$CaWO_4$. The purity of the materials used in synthesizing phosphors is important to the characteristics of brightness and persistence; in particular, the concentrations of metallic elements such as Fe, Mo, P, As, Sb, Mn, Ni, and Co must be 0.5 ppm or less. The

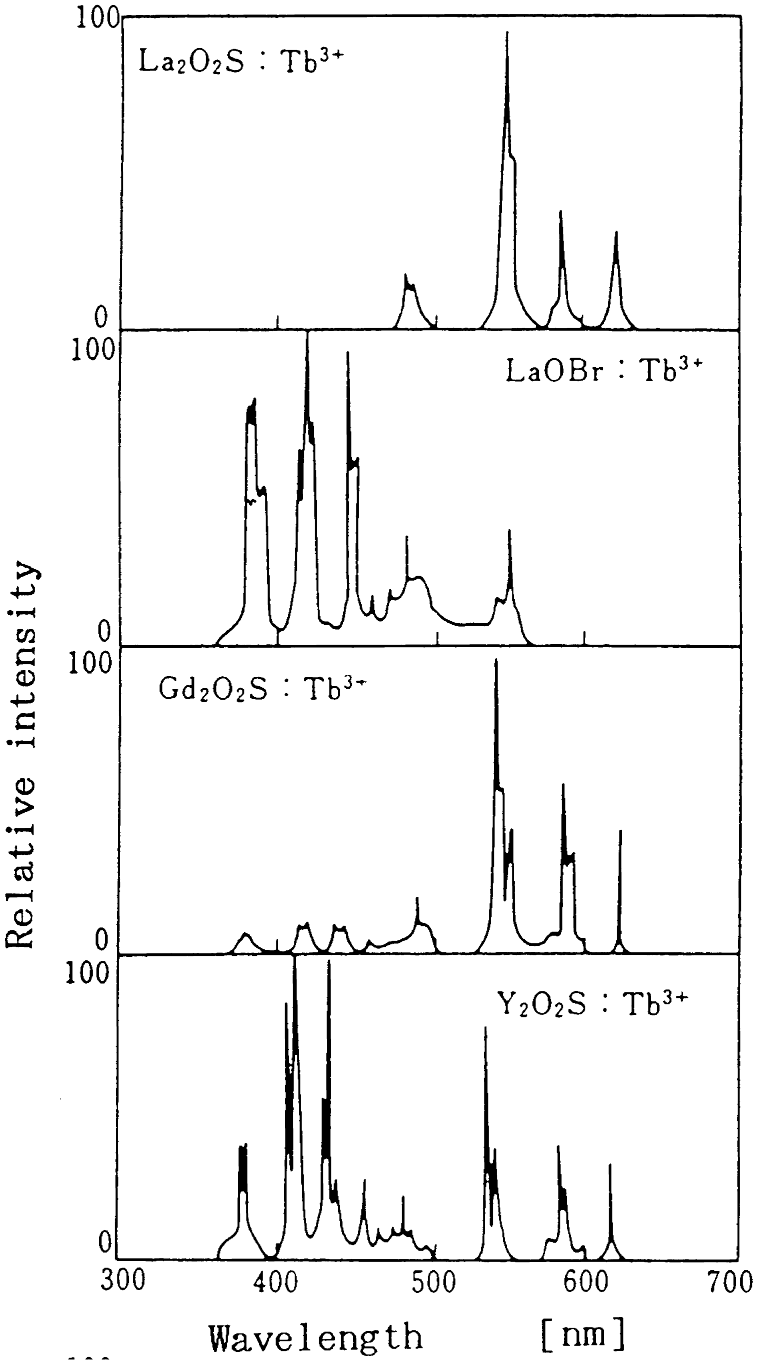

Figure 4 Emission spectra of phosphors for X-ray intensifying screens (II).

production stream for $CaWO_4$ synthesis by the wet precipitation method is shown in Figure 6. There is also a direct synthesis method in which high-purity tungstate is fired with calcium carbonate at high temperature.

Gd_2O_2S:Tb^{3+}. The synthesis process of this phosphor is shown in Figure 7. High-purity Gd_2O_3 and Tb_4O_7 are first dissolved in a mineral acid; then an oxalic acid solution

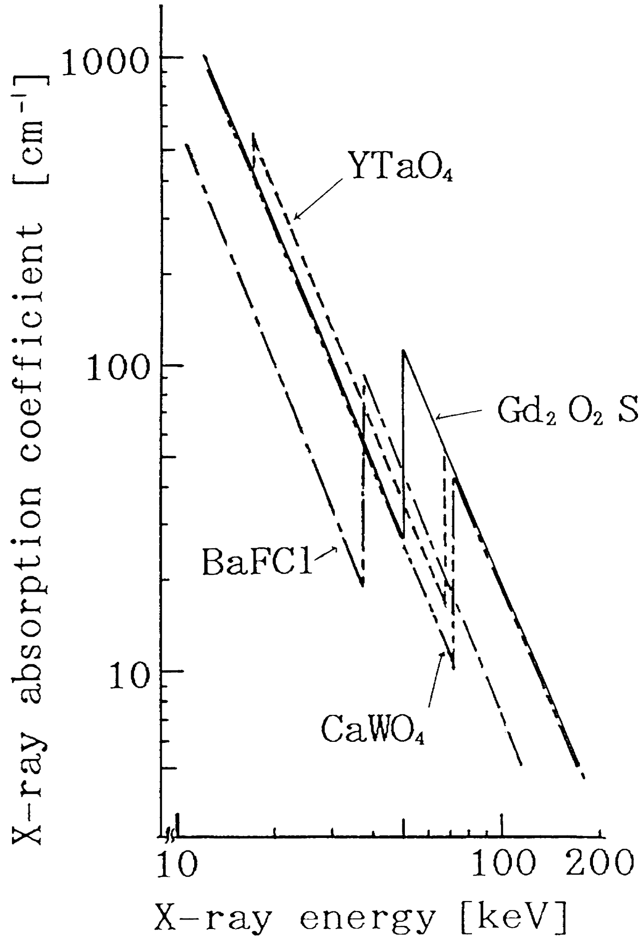

Figure 5 X-ray absorption coefficients of phosphors for X-ray intensifying screens.

is added to obtain a rare-earth oxalate co-precipitate. The oxalate is thermally decomposed in an oxidizing atmosphere to return a high-purity rare-earth oxide. To that oxide, Na_2CO_3 and sulfur are added and the mixture is fired at a high temperature in a sulfuric atmosphere to produce an oxysulfide phosphor. In this process, the sulfur is added in excess of the amount theoretically required by the synthesis reaction.

The phosphor can also be synthesized directly by thoroughly mixing Gd_2O_3, Tb_4O_7, sulfur, and Na_2CO_3, and then firing the mixture at high temperature.

7.1.2 Phosphors for X-ray fluorescent screens

X-ray fluorescent screens are used mainly in radiological group health examination and in radiological fluoroscopy for luggage check at airports. These screens require the same phosphor characteristics as intensifying screens. In particular, a phosphor that has a large X-ray absorption coefficient and high emission efficiency is needed.

7.1.2.1 Applications of X-ray fluorescent screens

X-ray fluorescent screens are used in the following ways.

Table 1 Various Characteristics of X-ray Phosphors

Phosphor	Emission spectrum		Emission efficiency (%)	X-ray absorption		Specific gravity	Crystal structure
	Emission color	Peak wavelength (nm)		Effective atomic number	K-edge (keV)		
$BaFCl:Eu^{2+}$	Violet	380	13[a,b]	49.3	37.38	4.7	Tetragonal
$BaSO_4:Eu^{2+}$	Violet	390	6[a,b]	45.5	37.38	4.5	Rhombic
$CaWO_4$	Blue	420	5[c]	61.8	69.48	6.1	Tetragonal
$Gd_2O_2S:Tb^{3+}$	Green	545	13[d]	59.5	50.22	7.3	Hexagonal
$LaOBr:Tb^{3+}$	Whitish-blue	420	20[e]	49.3	38.92	6.3	Tetragonal
$LaOBr:Tm^{3+}$	Blue	360, 460	14[e]	49.3	38.92	6.3	Tetragonal
$La_2O_2S:Tb^{3+}$	Green	545	12.5[d]	52.6	38.92	6.5	Hexagonal
$Y_2O_2S:Tb^{3+}$	Whitish-blue	420	18[a,b]	34.9	17.04	4.9	Hexagonal
$YTaO_4$	Ultraviolet	337	—	59.8	67.42	7.5	Monoclinic
$YTaO_4:Nb$	Blue	410	11[f]	59.8	67.42	7.5	Monoclinic
ZnS:Ag	Blue	450	17[d]	26.7	9.66	3.9	Hexagonal
(Zn,Cd)S:Ag	Green	530	19[d]	38.4	9.66/26.7	4.8	Hexagonal

[a] Measured value by cathode-ray excitation.

[b] From Stevels, A.L.N. and Pingault, F., *Philips Res. Rep.*, 30, 277, 1975.

[c] From Coltman, J.W., Ebbighausen, E.G., and Altar, W., *J. Appl. Phys.*, 18, 583, 1947.

[d] From de Pooter, J.A. and Bril, A., *J. Electrochem. Soc.*, 122, 1086, 1975.

[e] From Rabatin, J.A., *Abstr. Electrochem. Soc., Spring Meeting*, 825, 1978.

[f] From Brixner, L.H. and Chen, H.-Y., *J. Electrochem. Soc.*, 130, 2435, 1983.

1. The direct radiography exposure time is determined by watching the X-ray image on the fluorescent screen during fluoroscopic examination.
2. The fluorescent screen is mounted on a mirror camera and used in radiographic fluoroscopy for group health examination.
3. Medical diagnosis, luggage inspection at airports, and nondestructive industrial testing is accomplished by capturing the image on the fluorescent screen with an image pickup tube and observing the image on a TV monitor.

7.1.2.2 Phosphors used in X-ray fluorescent screens

In the early days of X-rays, $BaPt(CN)_4{\cdot}4H_2O$ phosphor was used. However, because of its high cost and chemical instability, this phosphor was later replaced by $ZnSiO_4:Mn^{2+}$ and $CdWO_4$.

Around 1930, (Zn, Cd)S:Ag was developed. This phosphor greatly increased the brightness of fluorescent screens, and is currently still in use. About 10 years ago, $Gd_2O_2S:Tb^{3+}$ came into use for applications in combination with a mirror camera or image pickup tube, as described above.

7.1.2.3 Structure and characteristics of X-ray fluorescent screens

As can be seen from the structure illustrated in Figure 8, an X-ray fluorescent screen is composed of a reflective layer deposited on one side of a high-quality paper or plastic base, with a 200- to 300-µm-thick phosphor layer coated on top.

In fluorescent screens for radiology use, (Zn, Cd)S:Ag phosphors are used; an emission peak wavelength at 525 nm, providing a spectral luminous efficacy that allows the X-ray image on the fluorescent screen to be seen by the human eye. Because brightness is a very important requirement, a large-grain (average 20 to 40 µm) phosphor is used.

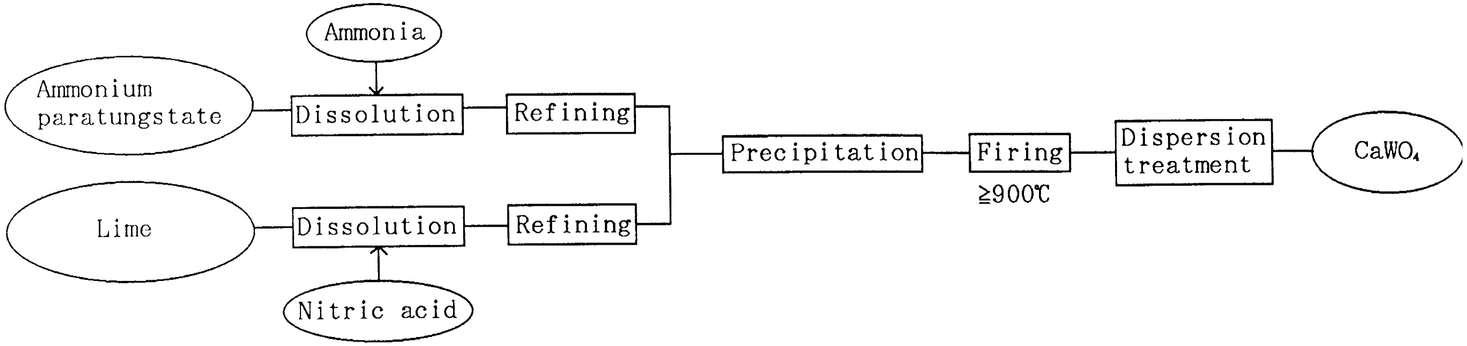
Ammonia
Ammonium paratungstate
Dissolution
Refining
Lime
Dissolution
Refining
Nitric acid
Precipitation
Firing
≧900℃
Dispersion treatment
CaWO₄

Figure 6 Production process of the $CaWO_4$ phosphor.

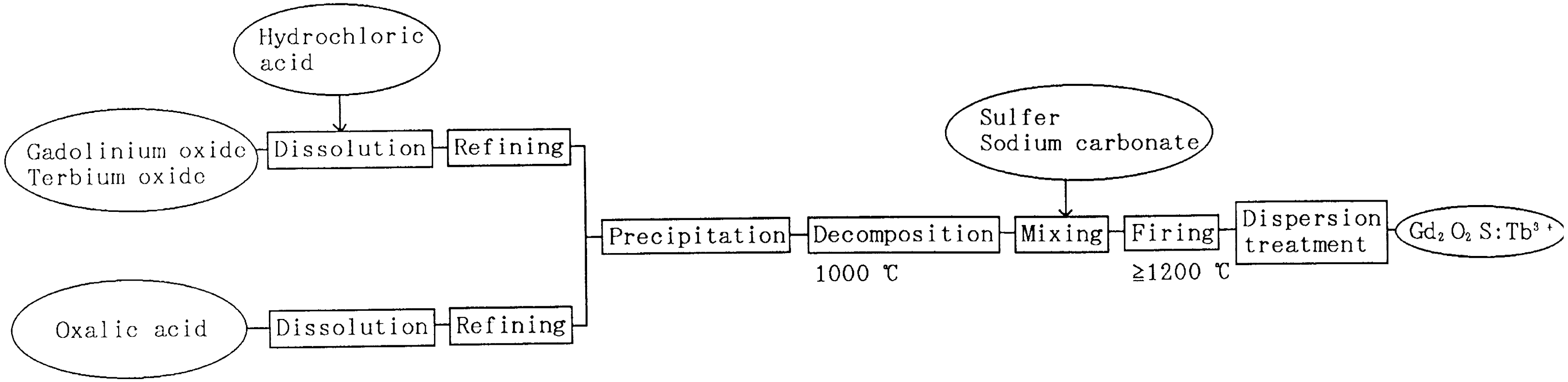
Hydrochloric acid
Gadolinium oxide
Terbium oxide
Dissolution
Refining
Oxalic acid
Dissolution
Refining
Precipitation
Decomposition
1000 ℃
Sulfer
Sodium carbonate
Mixing
Firing
≧1200 ℃
Dispersion treatment
Gd₂O₂S:Tb³⁺

Figure 7 Production process of the $Gd_2O_2S{:}Tb^{3+}$ phosphor.

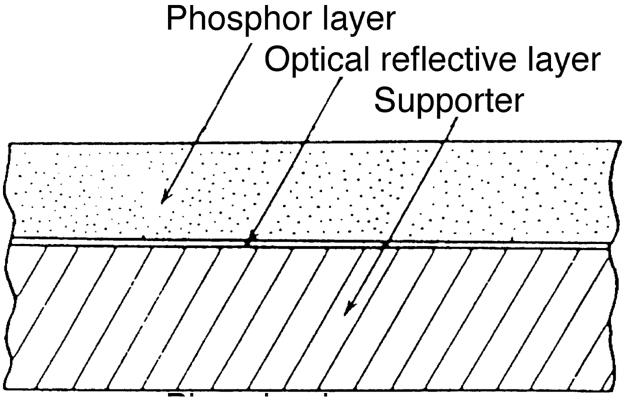

Figure 8 Structure of an X-ray fluorescent screen.

In a fluorescent screen for direct viewing, the minimum identifiable image size, *d*, is related to the brightness of the screen, *B*, and the contrast of the screen, *C*, by the following equation.

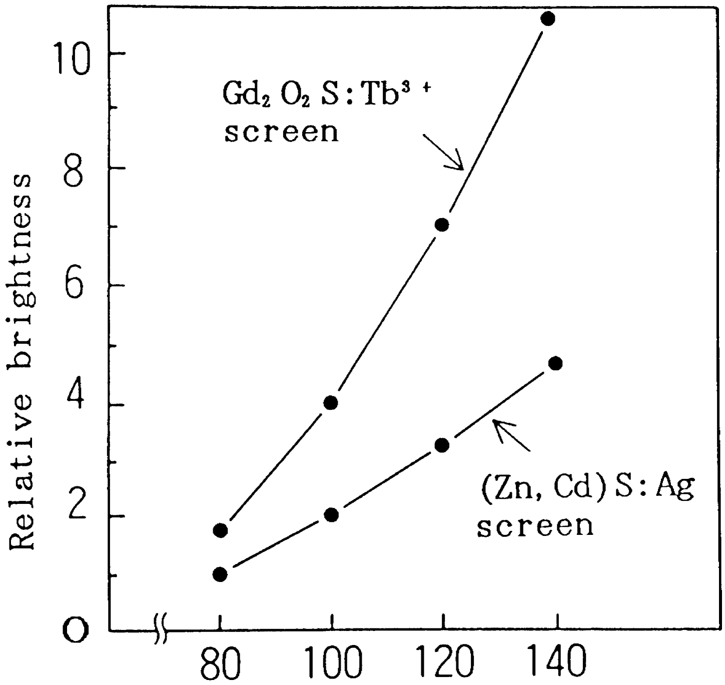

Figure 9 Comparison of the speed of $Gd_2O_2S:Tb^{3+}$ and (Zn, Cd)S:Ag fluorescent screens.

$$d = \frac{k}{C\sqrt{B}} \tag{1}$$

Fluorescent screens for fluoroscopy use the (Zn, Cd)S:Ag phosphor, which has an emission peak at 540 nm, matching the spectral sensitivity of a radiographic film. Recently, screens using the $Gd_2O_2S:Tb^{3+}$ phosphor have been replacing (Zn, Cd)S:Ag screens. The $Gd_2O_2S{:}Tb^{3+}$ fluorescent screens are superior to the (Zn, Cd)S:Ag phosphor screens in such basic characteristics as speed (the product of the X-ray absorption coefficient and the emission efficiency) and sharpness. The speed characteristics of fluorescent screens for fluoroscopy under the conditions of chest radiography are compared in Figure 9; sharpness characteristics are compared for the same conditions in Figure 10.

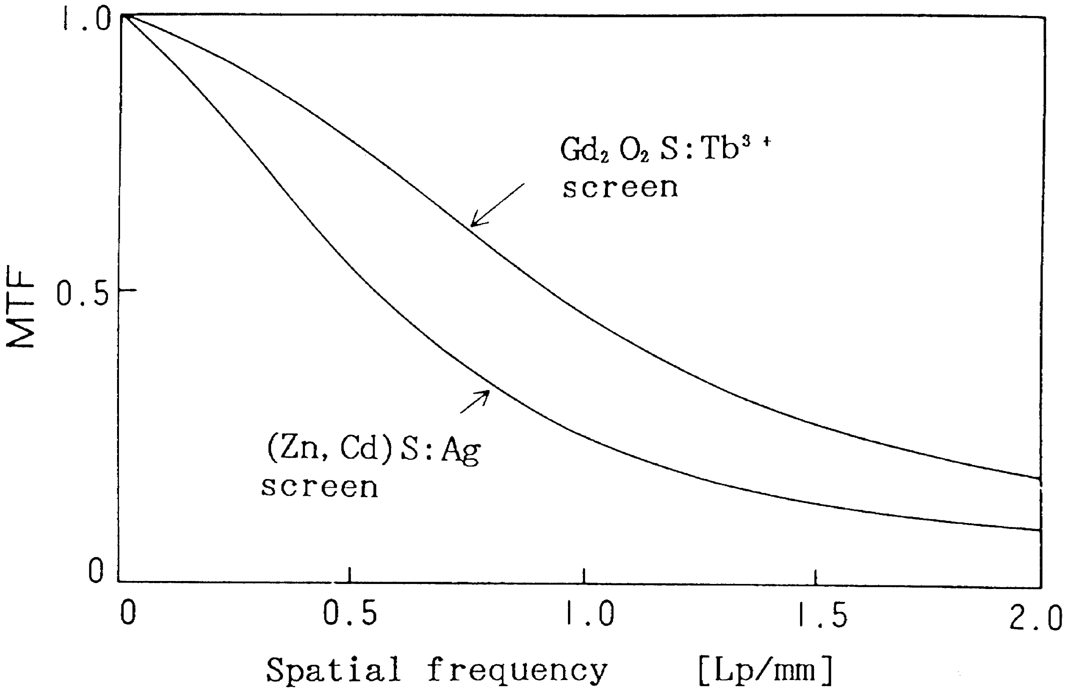

Figure 10 Comparison of the sharpness of $Gd_2O_2S{:}Tb^{3+}$ and (Zn, Cd)S:Ag fluorescent screens.

7.2 *Phosphors for thermoluminescent dosimetry*

7.2.1 *The principle of thermoluminescent dosimetry*

When substances that have been irradiated by X-rays or gamma rays are heated, a phenomenon called thermoluminescence can occur. An example of the application of this phenomenon in the measurement of radiation is the thermoluminescent dosimeter system. The function of phosphors in that system are explained below.

Irradiated phosphors absorb some of the radiant energy, producing free electrons and holes within the phosphor crystals. The electrons are captured by lattice defects (F-center, etc.), creating a metastable state. If a phosphor in that state is heated, the captured electron is released and recombines with a trapped hole, returning to the ground state. By that recombination, luminescence is produced. Thermoluminescent phosphors are so designed that they remain in the metastable state and do not easily radiate the trapped energy unless subjected to an intentional external disturbance such as heating.

The detailed mechanism of thermoluminescence varies with the substance. This is a complex issue, but consider here a simple system that has only one type of metastable state. Let n be the number of luminescence centers that are in the metastable state, $s\exp(-\varepsilon/kT)$ the probability of release from the metastable state, and $dT/dt = \beta$ the rate of temperature increase of the phosphor. Then,

$$-\frac{dn}{dt} = ns\exp\frac{-\varepsilon}{kT} \tag{2}$$

By replacing *dt* by *dT* and integrating the above equation, one obtains:

$$\log\frac{n}{n_0} = -\int_{T_0}^{T} \frac{s}{\beta}\exp\left(\frac{-\varepsilon}{kT}\right)dT \tag{3}$$

The symbol n_0 is the number of luminescence centers in the metastable state at the temperature at which the excitation was applied, T_0. Therefore, the thermoluminescence intensity is given as:

$$I(T) = n_0 s\exp\left(\frac{-\varepsilon}{kT}\right)\exp\int_{T_0}^{T}\left(-\frac{s}{\beta}\right)\exp\left(\frac{-\varepsilon}{kT}\right)dT \tag{4}$$

From this solution, the following conclusions are derived:

1. When s and β are constant, the glow-peak temperature is more or less proportional to ε.
2. As s/β becomes large, the maximum temperature of the glow curve shifts toward lower temperatures.
3. The area under the glow curve is proportional to the number of initially trapped electrons, n_0. Meanwhile, the following relationship holds for n_0:

$$n_0 \doteqdot ABRNt = ABRD\ldots \tag{5}$$

Here, N is the number of traps, B is the probability that a trap captures an electron, R is the radiation intensity, t is the irradiation time, and A is a constant of proportionality. From this one can see that the number of trapped electrons is proportional to the radiation dose, $D(R \times t)$. Therefore, the dose can be measured by determining either the peak height of, or the area under, the glow curve.

7.2.2 Characteristics required of phosphors

Phosphors for use in thermoluminescent dosimeters (TLD) must have the following characteristics.

1. High concentration of electron (or hole) traps
2. High emission efficiency by the electrons (or holes) thermally released from the traps
3. Large trap depth, ε, and small frequency factor, s
4. Trap depth distribution to have a small energy range (single level if possible)
5. A thermal emission spectrum that is in a relatively short wavelength region
6. Traps, luminescence centers, and crystalline lattice that are not damaged or otherwise changed by radiation
7. For use in biomedicine, an effective atomic number of the phosphor to be close to 7.4, the effective atomic number of a living organism

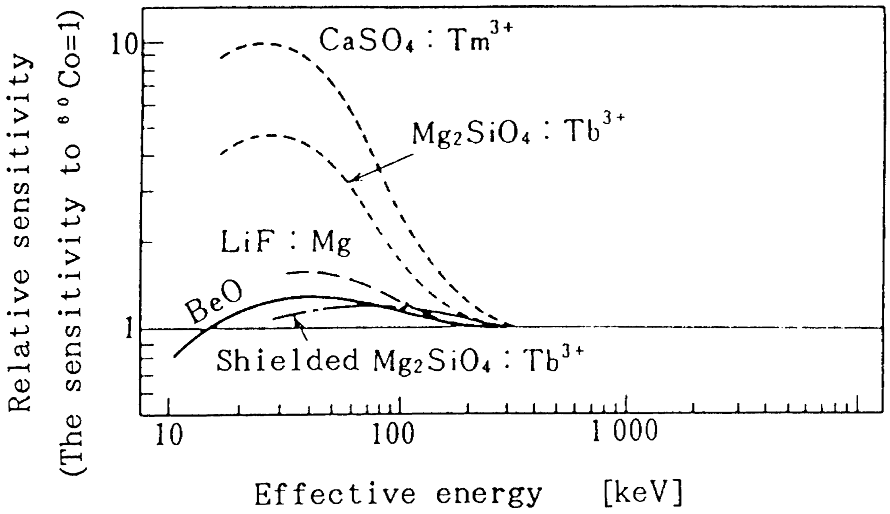

Figure 11 Energy characteristics for various TLDs.

7.2.3 Characteristics of phosphors in practical use

7.2.3.1 Energy dependence

If the sensitivity of the phosphor, or the intensity of its thermoluminescence, is dependent on the photon energy of the radiation, errors will be caused in the dose measurement. The extent of such a change in luminescence intensity is related to the radiation absorption characteristics of the phosphor host crystal material: the larger the effective atomic number of the phosphor, the greater becomes the dependence of its sensitivity on the energy of the radiation.

The energy characteristics of typical TLD phosphors are shown in Figure 11. Even when a phosphor has a large energy dependence, it is possible to make that dependence smaller by using a specially shaped metal shield for the TLD element. (See the Mg_2SiO_4:Tb^{3+} shielding effect shown in Figure 11.)

Phosphors that have a weak energy dependence generally have low sensitivity.

7.2.3.2 Glow curve

For the TLD application, it is desirable that the shape of the glow curve is as simple as possible, and that there is a glow peak located near 200°C. When the glow curve is complex on the low-temperature side, an undesirable fading effect occurs. When the glow curve is complex on the high-temperature side, on the other hand, time is required to dissipate the energy remaining after the radiation measurement has been performed. The glow curves of typical phosphors are shown in Figure 12.

7.2.3.3 Thermoluminescence spectrum

The thermoluminescence spectrum has to match the spectral sensitivity of the photodetector. A typical thermoluminescence spectrum is shown in Figure 13.

7.2.3.4 Supralinearity

When the irradiation dose is increased at a constant radiation energy, the relationship between the sensitivity and the absorbed dose is linear within the dynamic range from 10^5 to 10^6. For large doses, this relationship exhibits supralinearity, as shown in Figure 14. The reason for this supralinearity is that, above certain doses, a new glow peak appears on the high-temperature side of the main glow curve, making the nonlinearity large.

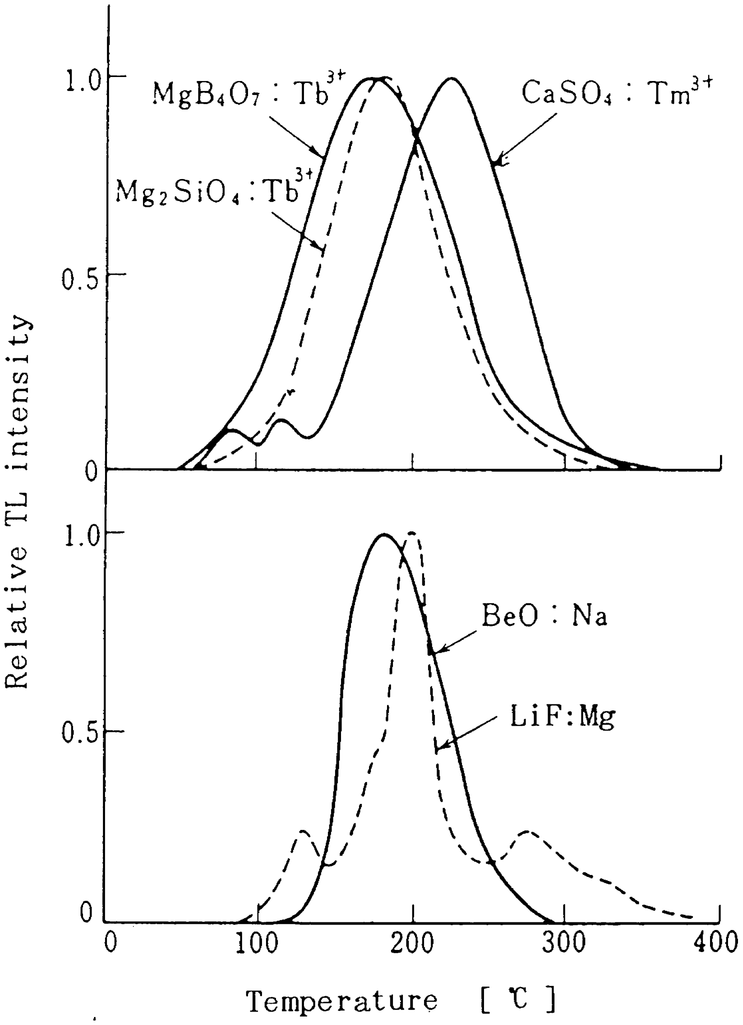

Figure 12 Glow curves for various TLDs.

The dose at which the supralinearity appears and its degree depend not only on the type of phosphors, but also on the quality of the radiation.

7.2.3.5 Fading

The phenomenon of thermoluminescence fading in the dark is related to the shape of the glow curve in the low-temperature region (shallow traps); the temperature dependence of fading varies with that curve shape. That is to say, for phosphors that have shallow traps, fading is caused by the gradual thermal activation of trapped electrons at room temperature. This phenomenon complicates the correction process in the measurement of radiation. Furthermore, fading occurs also through exposure to visible light. This is because the charge carriers excited by the radiation can be released not only by heat, but also by optical energy.

The characteristics of the main phosphors used for TLD are listed in Table 2.

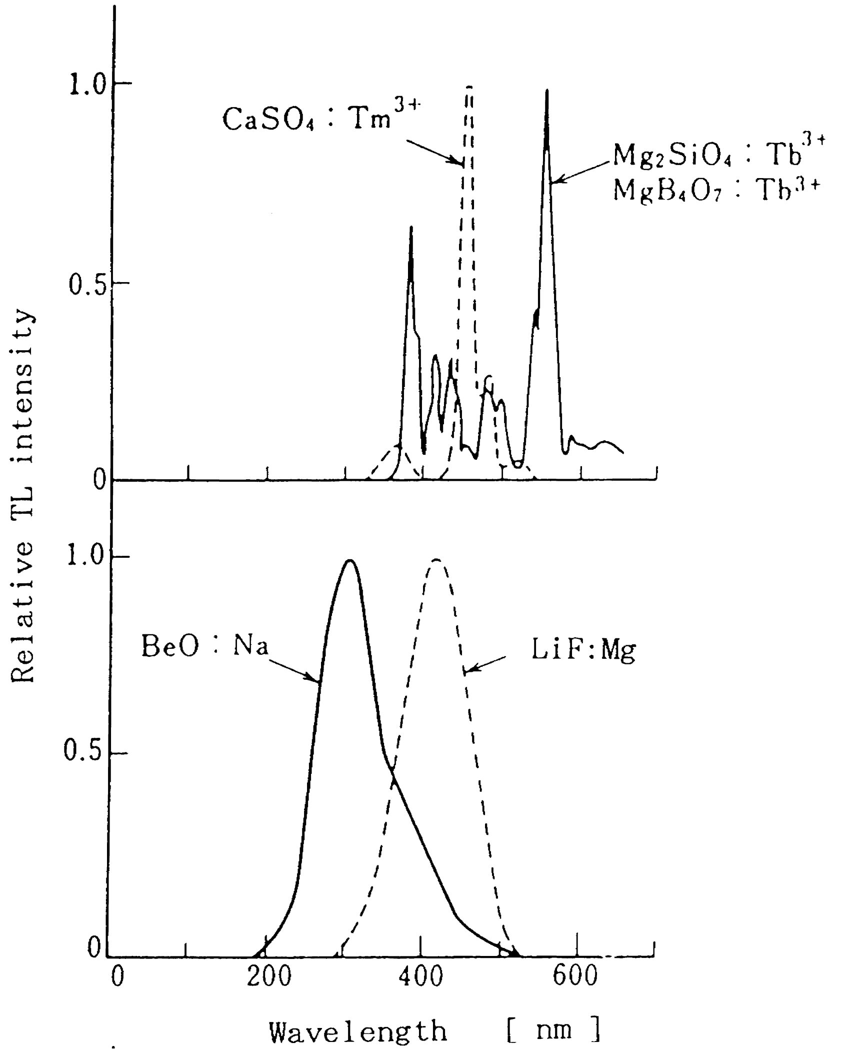

Figure 13 Thermoluminescence spectra for various TLDs.

7.2.4 Examples of main uses

While the phosphors are sometimes used in powder form, they are mostly packed into glass tubes (diameter 2 mm, length 12 mm) or formed into solids, such as thin disks, rods, or pellets, using heat-resistant resin or ceramics, and mounted in a holder for use.

The main uses of the dosimeters are to control the exposure levels of individuals who are engaged in radiation-related work, for environmental monitoring of facilities that employ radiation, for the measurement of dosage in radiation therapy and leakage in X-ray diagnostic equipment, and for dosimetry in medical diagnosis.

References

1. Stevels, A.L.N. and Pingault, F., *Philips Res. Rep.*, 30, 277, 1975.
2. de Pooter, J.A. and Brill, A., *J. Electrochem. Soc., Solid-state Science and Technology*, 122, 1086, 1975
3. Rabatin, J.A., *Abstracts of the Electrochem. Soc., Spring Meeting*, 825, 1978.

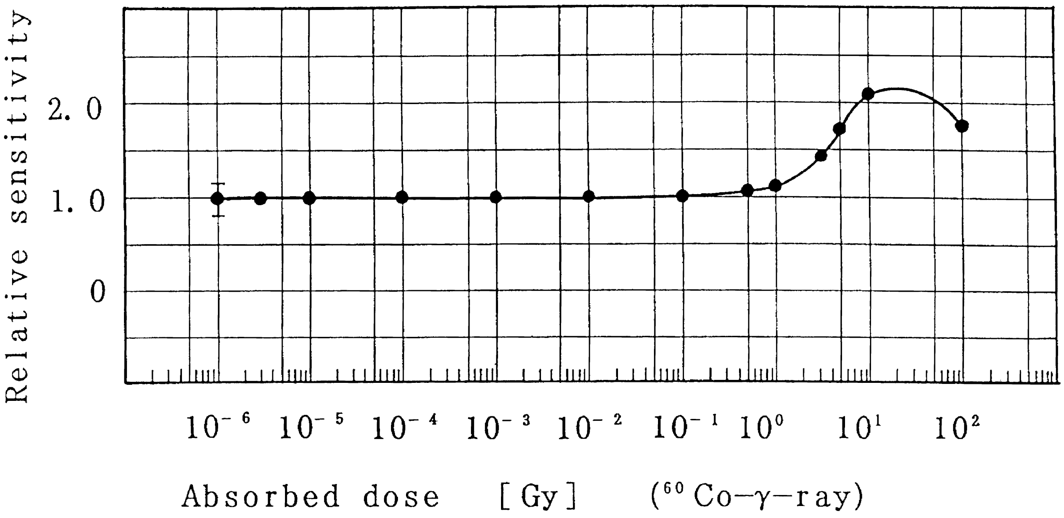

Figure 14 Supralinearity of Mg_2SiO_4:Tb^{3+} TLD elements.

4. Brixner, L.H. and Chen, H.-Y., *J. Electrochem. Soc., Solid-State Science and Technology,* 130, 2435, 1983.
5. Coltman, J.W., Ebbighausen, E.G., and Altar, W., *J. Appl. Phys.,* 18, 583, 1947.
6. Strum, R.E. and Morgan, R.H., *Am. J. Roentgenol.,* 62, 617, 1949.
7. Kasei Optonix, Ltd., *Kyokko Thermoluminescent Dosimetry System Technical Data.*

Table 2 Various Characteristics of Main TLD Phosphors

TLD	$Mg_2SiO_4:Tb^{3+}$	$MgB_4O_7:Tb^{3+}$	$Li_2B_4O_7:Cu,In,Si$	$LiF:Mg^{2+}$	$CaSO_4:Tm^{3+}$	$CaF_2:Mn^{2+}$
Effective atomic number	11.1	8.4	7.4	8.14	15.5	16.5
Dominant peak wavelength (nm) of TL spectrum	560	560	400	400	452	500
Glow peak temperature (°C)	190	180	180	195	200	260
Energy dependency (30 keV/^{60}Co)	4.5	3.0	1.0	1.5	13	13
Linearity	10 µSv–10 Sv	10 mSv–100 Sv	1 mSv–100 Sv	1 mSv–50 Sv	100 µSv–10 Sv	100 µSv–10 Sv
Fading	1%/month	10%/month	10%/month	5%/month	15%/month	30%/month

chapter seven — section three

Phosphors for X-ray and ionizing radiation

Masaaki Kobayashi and Mitsuru Ishii

Contents

7.3 Scintillators....637
- 7.3.1 Inorganic crystal scintillators....640
  - 7.3.1.1 Scintillators for γ-ray camera....641
  - 7.3.1.2 Scintillators for XCT....641
  - 7.3.1.3 Scintillators for PET....642
  - 7.3.1.4 Scintillators for nuclear and high energy physics detectors....643
  - 7.3.1.5 Scintillators for neutron detection....646
  - 7.3.1.6 Industrial applications....648
  - 7.3.1.7 New scintillators....648
- 7.3.2 Ceramics and glasses....650
- 7.3.3 Organic scintillators....651

References....651

7.3 Scintillators

The fluorescence caused by incident radiations such as α, β, and γ-rays is called scintillation. Scintillators are mainly used in detection and measurement of energy, position, and time of the incident radiation. Although scintillation can occur for all materials, efficient scintillators have to satisfy the following requirements: (1) fast deexcitation; (2) high efficiency of emitting UV or visible light; and (3) transparency of the material to its own emission. A sketch of a typical scintillation counter is given in Figure 15(a). The photosensor as a readout device is usually a photomultiplier tube (PMT) or a Si PIN photodiode (PD) or an avalanche photodiode (APD). It should be noted that the light output in practical detectors depends on the spectral match between the emission and the photosensors. Light outputs are compared between PMTs and PDs for typical scintillators by Sakai[1]. There is a wide variety of inorganic (crystals, ceramics, glasses, gases, liquids) and organic (crystals, liquids, plastics) scintillators, depending on the application. Characteristics of typical scintillators are given in Table 3. Inorganic crystals and plastic scintillators are most widely used. Emphasis is made on inorganic crystals, followed by a brief description of ceramic, glass, and organic scintillators.

Table 3 Characteristics of Typical Scintillators

Scintillators	μ[a] at 150/511 keV cm^{-1}	Effective Z Z_{eff}	Density g/cm^{-3}	Radiation length/ cm	Decay constant /ns	Emission peak/nm	LY[b] 10^3 ph/MeV	Index of refraction n[c]	Hygro-scopicity	M.P./ °C	Radiation hardness[d] /Gy	Cleavage	Applications (Nucl.= Nuclear and particle detectors)
Inorganic crystals													
NaI:Tl$^+$	2.24/ 0.34	50.8	3.67	2.59	230	415	40	1.85	Strong	651	10	(100)	XCT, PET, Nucl.
CsI:Tl$^+$	3.30/ 0.44	54.1	4.53	1.86	1050	550	48	1.8	Slight	621	10	None	XCT, Nucl.
CsI	3.30/ 0.44	54.1	4.53	1.86	10/1000	305/>400	~1.6/~0.4	1.8	Slight	621	10^{2-3}	None	Nucl.
LiI:Eu^{2+}	2.73/ 0.39	52.3	4.08	2.18	1400	470-485	12	1.96	Strong	446		(100)	Neutron
CsF	3.16/ 0.44	53.2	4.11	2.23	2.8	390	2	1.48	Strong	682	$<10^2$	(100)	PET
CaF_2:Eu^{2+}	0.47/ 0.269	17.1	3.19	6.72	940	420	19	1.47	No	1403		(111)	Nucl.
BaF_2	3.14/ 0.46	52.7	4.89	2.03	0.6/620	220/310	2/6	1.56	Little	1354	10^{4-5}	(111)	PET, Nucl.
CeF_3	4.04/ 0.59	53.3	6.16	1.66	30	375	2	1.68	No	1443	10^{3-4}	(0001)	Nucl.
$LaBr_3$:Ce^{3+}	2.57/ 0.47	46.9	5.3	1.88	30(90%)	370	61	~1.9	Strong	783			PET, Nucl.
ZnS:Ag	0.84/ 0.34	27.4	4.09	3.45	72(α)	450	60(α)	2.36	No	1850		poly.	α Detection
LiF-ZnS:Ag	~0.49/ ~0.20		2.36	~6.0	~1000	450	160/*n*th		No			poly.	Neutron
ZnO:Ga	1.21/ 0.47	28.4	5.61	2.53	1.5(α)	385(α)	16(α)	2.01(D)	No	1975			Nucl.
$CdWO_4$	7.94/ 0.89	64.2	7.90	1.10	5000	470	16	2.3	No	1272	10^6	(010)	XCT
$ZnWO_4$	7.91/ 0.90	64.9	7.87	1.16	5000	475	11	2.1	No	1220		(010)	XCT
$PbWO_4$	13.04/ 1.15	75.6	8.28	0.89	<3/<20	420	0.2–0.3	2.2	No	1123	10^{5-6}	(101)	Nucl.
$Bi_4Ge_3O_{12}$	10.42/ 0.98	75.2	7.13	1.12	300	480	6	2.15	No	1050	10^{2-3}	None	XCT, PET, Nucl.
$Bi_4Si_3O_{12}$	10.88/ 0.98	77.3	6.8	1.15	100	480	1.2	2.06	No	1030	10^{3-4}	None	Nucl.

$Gd_2SiO_5:Ce^{3+}$	5.73/ 0.71	59.5	6.71	1.38	30-60/600	430	9	1.85	No	1900	>10^6	(100)	PET, Nucl.
$Lu_2SiO_5:Ce^{3+}$	8.34/ 0.88	66.4	7.40	1.14	40	420	27	1.82	No	2050	10^6	None	PET, Nucl.
$YAlO_3:Ce^{3+}$	1.38/ 0.45	33.5	5.35	2.77	28	370	16	1.94	No	1875	10^{2-3}	None	PET, Nucl.
$LuAlO_3:Ce^{3+}$	8.71/ 0.96	64.9	8.34	1.08	18(75%)	350	10	1.97	No	1960		None	PET, Nucl
$Lu_3Al_5O_{12}:Ce^{3+}$	6.30/ 0.75	62.9	6.73	1.45	70	535	12	1.84	No	2043		None	XCT, PET
$LuBO_3:Ce^{3+}$	7.52/ 0.77	66.0	6.8	1.28	21	375,410	50	1.59(D)	No	1650			XCT
Ceramics, glasses, and organic scintillators													
$Y_{1.34}Gd_{0.6}0_3:Eu^{3+},Pr$	3.43/ 0.56	51.5	5.92	1.74	10^6	610		1.96	No	~2400		poly.	XCT
$Gd_2O_2S: Pr^{3+},Ce$	6.89/ 0.79	61.1	7.34	1.16	3000	510	28	2.2	No	>2000	10^{2-3}	poly.	XCT
$SCG1:Ce^{3+}$	1.37/ 0.32	44.4	3.49	4.14	100	430	0.5	1.61	No		10^4	glass	Nucl.
Li-glass:Ce^{3+} (GS20)	0.40/ 0.21	25.2	2.48	10.9	100	395	6/*n*th	1.55	No	1200		glass	Neutron
Gd_2O_3-glass:Ce^{3+}	4.48/ 0.59	59.0	5.63	1.84	<500	380	1		No			glass	Nucl.
Anthracene	0.18/ 0.11	5.91	1.25	34.5	31	440	16	1.62	No	217	10^4	(001)	Nucl.
Liquid scinti.	0.13/ 0.081	5.86	~0.88	~51	3.5	425	8	1.51	—	—	10^4	—	Nucl.
Plastic scinti.	0.15/ 0.096	5.87	~1.03	~42	1-4	375–445	8–10	1.58	No	350	10^5	None	Nucl.

a) Absorption coefficient for X-rays.

b) Light yield for high-energy electrons unless indicated otherwise.

c) At the wavelength of the peak emission except for D = sodium D-line (589.3 nm).

d) A rough measure of the accumulated absorbed dose (g-rays) that causes a reduction of 1 to 2% in the optical transmittance per thickness of X0.

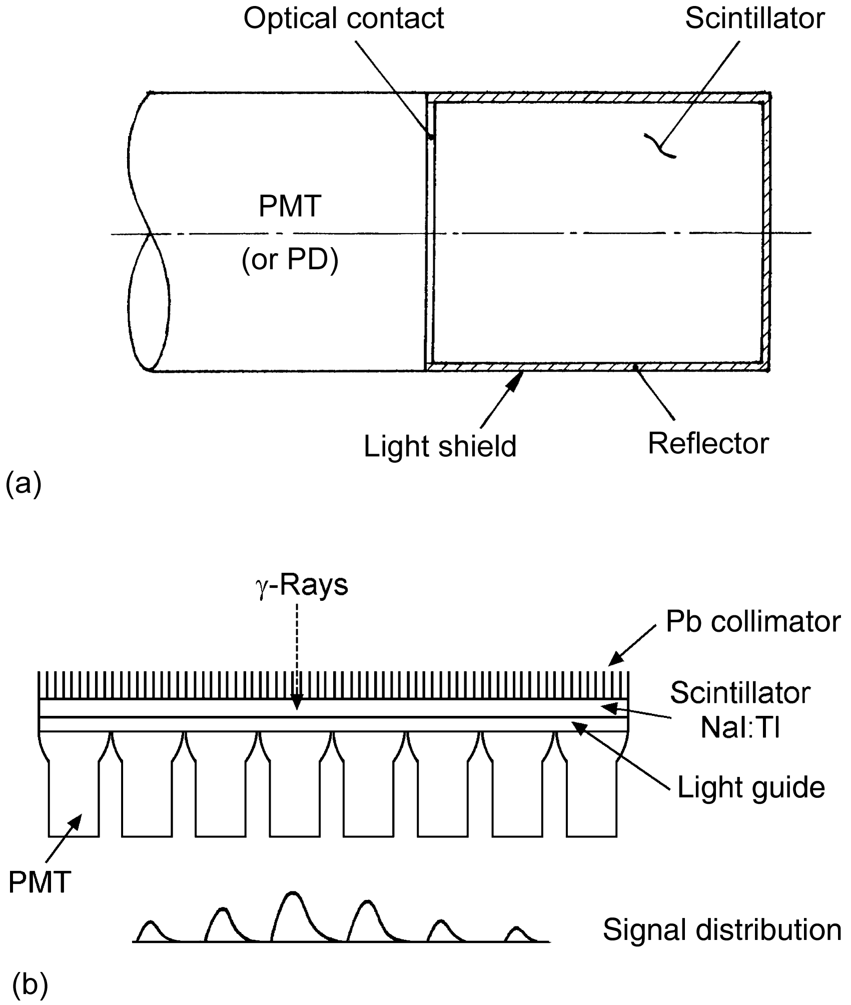

Figure 15 Sketch of a typical scintillation counter (not to scale). (a) Silicone grease, silicone oil, and air are frequently used for the optical contact, and Al foil, teflon, white papers, MgO powder, and BaSO$_4$ for the reflector. (b) Sketch of a γ camera.

7.3.1 Inorganic crystal scintillators

Inorganic crystal scintillators have been widely used in medical diagnoses; γ-ray (or X-ray) detectors such as the γ-ray camera[2] since 1958, X-ray computed tomography[3] (XCT) since 1973, and positron emission tomography[4] (PET) since 1975 have been used. They are also used in nuclear, high-energy, and astrophysics experiments as detectors of γ-rays and charged particles, and in industrial applications as γ-ray detectors. Reviews of scintillators and their applications are available.[5–11] NaI:Tl$^+$ has been used since Hofstadter[12] discovered its scintillation due to the s^2–sp transitions of Tl$^+$ in 1948. Scintillation of Bi$_4$Ge$_3$O$_{12}$[13] (BGO) was discovered by Weber and Monchamp[14] in 1973. BGO is one of the most outstanding scintillating crystals established after the discovery of NaI:Tl$^+$, and has taken over from NaI:Tl$^+$ in many applications. While the scintillation of BGO was at first assigned to the s^2–sp transitions of Bi^{3+}, it is now thought to be due to the radiative recombination of excitons; the bandgap is $\sim$5.0 eV and the binding energy of excitons $\sim$0.2 eV.[15,16] This explanation is more natural since the electron energies of the host Bi^{3+} ions should have a band structure. $Gd_2SiO_5:Ce^{3+}$ ($GSO:Ce^{3+}$) was discovered by Takagi and Fukazawa[17] in 1983 while studying the doping of heavy oxides with various additives. They found[18] fast (decay constant $\tau \sim 30$ ns) and efficient scintillation due to the 4f–5d transitions of Ce^{3+}. The discovery of $GSO:Ce^{3+}$ prompted the search for other Ce-doped scintillators. The very fast component in BaF_2 ($\tau \sim 0.8$ ns) arising from cross-luminescence[19] (or core valence luminescence[20]) due to the transition of electrons from the F^- valence band (2p) to the core Ba^+ valence band (5p) was unraveled in the latter half of the 1980s. Since then, other scintillators having cross-luminescence have been sought. In addition to the crystals mentioned above, many other scintillation crystals are now used including $CdWO_4$ (CWO), $PbWO_4$ (PWO), $Lu_2SiO_5:Ce^{3+}$ ($LSO:Ce^{3+}$), $CsI:Tl^+$, and CsI.

All of these scintillators have a common feature of containing heavy elements that give large absorption coefficients for radiation. Another important feature is that the decay should be fast except for some applications such as XCT. Fast decay can be obtained in the following luminescence mechanisms:

1. 4f–5d-allowed radiative transitions of rare-earth ions (Ce^{3+}, Pr^{3+}, etc.)
2. Cross-luminescence
3. Thermally quenched luminescence
4. Charge transfer luminescence (Yb^{3+}–Yb^{2+}, etc.)
5. Near-band-edge semiconductor luminescence (GaO:Ga, etc.)

7.3.1.1 Scintillators for γ-ray camera

The γ-ray camera, usually referred as the Anger camera[2,7], takes pictures of γ-rays emitted from isotopes [^{99m}Tc(141 keV), ^{123}I(159 keV), ^{201}Tl(~75 keV)] introduced into human bodies. As shown in Figure 15(b), the γ-rays pass through a collimator consisting of many parallel fine holes and are detected with a large-area (up to 80 cm diameter) single scintillator plate which is read out with several tens of PMTs. Due to the necessary conditions of (1) large light output, (2) fast decay, and (3) large crystal plate, $NaI:Tl^+$ is usually employed. In the so-called single-photon emission computer tomography (SPECT), a three-dimensional image of the radioactivity distribution is reconstructed by rotation or by using multiple γ-cameras.

7.3.1.2 Scintillators for XCT

X-rays are attenuated in passing through the patient. In XCT,[7] the intensity of the attenuated X-rays is measured with scintillators and a three-dimensional X-ray image is reconstructed by rotating the X-ray tube and the detector. To improve the contrast and resolution of the image and achieve high speed, many small-size detector elements are arranged azimuthally in the third and fourth generation units (Figure 16) and the X-ray source is rotated at high speed. As many as 1000 individual detector elements with a width of about 1 mm for each element[7] are used.

The main requirements[21] for scintillators are (1) large absorption coefficient, (2) large light output, (3) reasonably fast decay (<1 ms) with small afterglow (<0.01% at 3 ms after termination of irradiation), and (4) minimization of both radiation damage and gain hysteresis (<2% at ~5 Gy, 1Gy = 100 rad). $NaI:Tl^+$ has the advantage of large light output but suffers from strong hygroscopicity and large afterglow (0.5–5.0% after 3 ms), adversely affecting imaging quality. BGO is superior to $NaI:Tl^+$ with respect to smaller afterglow(0.005% after 3 ms), larger absorption coefficient (more than four times), and easy handling (absence of hygroscopicity). The XCT apparatus can be made compact if PDs or APDs can be used instead of PMTs. The small light output of BGO (7–10% of $NaI:Tl^+$),

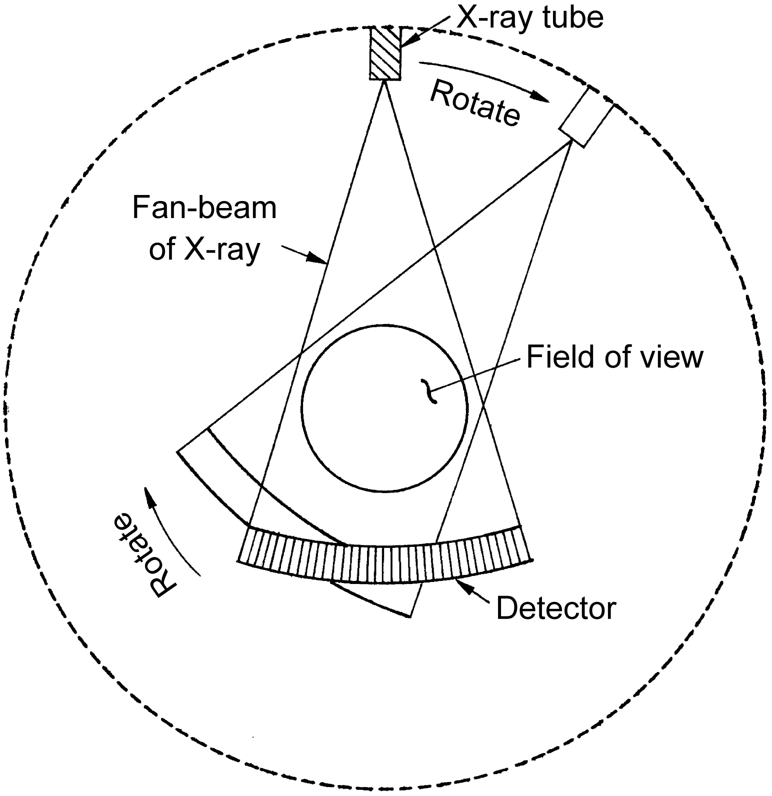

Figure 16 A typical scheme of X-ray CT detectors of the third generation.

however, makes the use of PDs difficult, since PDs have much larger noise levels than PMTs, thus degrading the contrast of the image. CsI:Tl$^+$ has as large a light output as NaI:Tl$^+$, and the emission wavelength of 550 nm (Figure 18) matches PDs well, but the afterglow (0.7–1.5% after 20 ms) is not small enough. CsI:Tl$^+$ has the additional drawbacks of positive hysteresis in its light output (increase of light output after the start of irradiation) as large as +13.5%[21] and hygroscopicity. CWO is nonhygroscopic and has a small afterglow (0.005% after 3 ms), a large absorption coefficient (3.5 times NaI:Tl$^+$), and large light output (38% of NaI:Tl$^+$). The decay spectrum[22] for γ-rays consists of two components: $\tau \sim 1.1$ μs at the beginning followed by a slow tail with 15 μs. ZnWO4 (ZWO) is similar to CWO, with a slightly lower density and a slightly smaller light output. CWO is toxic while ZWO is not. CWO with the PD readout is most frequently employed in current applications besides the ceramic scintillator[21] Gd_2O_2S:Pr^{3+},Ce^{3+} (described later) and Xe gas ionization chambers. Although GSO:Ce^{3+} can be one of the best candidates, a sizable positive hysteresis of light output, similar to that in CsI:Tl$^+$, is a difficulty against practical use.

7.3.1.3 Scintillators for PET

In PET, a medical reagent containing positron-emitting radioisotopes such as ^{11}C, ^{13}N, and ^{15}O is prescribed to a patient; the two γ-rays (511 keV) emitted in opposite directions resulting from positron–electron annihilation are registered with detectors arranged in a ring around the patient[7] (see Figure 17) using a coincidence technique. From the distribution of the coincident 2γ events, the radioactivity distribution in a slice of the human body is computed to reconstruct a three-dimensional image. To obtain good space and time resolutions, the scintillators must have (1) large absorption coefficient for 511 keV γ-rays,

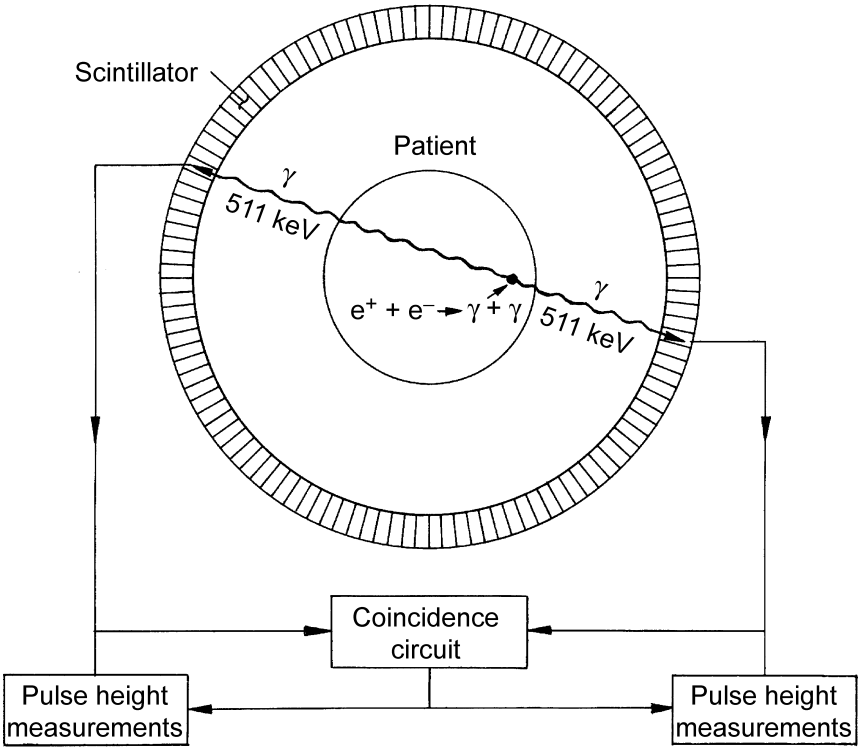

Figure 17 A typical scheme of a ring of PET detectors.

(2) fast decay, and (3) a large light output. NaI:Tl$^+$ was first used and then replaced by BGO. In a large PET system of BGO, the entire detector can be made of as many as 30 rings, each ring consisting of as many as several hundred crystals. Each crystal has a typical size of 5 × 5 mm^2 in cross-section and 30 mm in length. The space resolution reaches 2–3 mm. Although GSO:Ce^{3+} has the advantages of fast decay ($\tau \sim$ 50 ns, being one sixth that of BGO) and large light output (three times that of BGO), its absorption coefficient is smaller than BGO by 50% and this is a limitation in achieving high spatial resolution.[23] Improvements in the light output (by 20%) and the transmittance in the short wavelength region has been recently achieved by co-doping Zr.[24] LSO:Ce^{3+},[25] resembles GSO:Ce^{3+} in scintillation characteristics but considerably heavier. This material can be, therefore, more ideal for PET but is substantially more expensive than both BGO and GSO:Ce^{3+}. Actually, LSO:Ce^{3+} crystals suffer from a local nonuniformity in the light output, which may be due to the small nonuniformity in the dopant concentration. The effort to reduce nonuniformity is still continuing.

7.3.1.4 Scintillators for nuclear and high energy physics detectors

Typical old scintillators[26] for the detection of γ-rays, β-rays, and α particles were alkali halides[27,28] such as NaI:Tl$^+$ and CsI:Tl$^+$ (due to high stopping power), CaF$_2$:Eu^{2+}, and ZnS:Ag (large light output ratio for α/β~2), respectively. A wide variety of scintillating crystals are currently used in γ-ray detectors, sometimes called electromagnetic (EM) calorimeters;[29,30] these include NaI:Tl$^+$, CsI:Tl$^+$, CsI(nondoped), BGO, BaF$_2$, GSO:Ce^{3+}, and PWO. As the count rate and/or the energy of γ-rays increases with the beam intensity and/or energy of particle accelerators, the following conditions become important: (1) short radiation lengths X_0 (large absorption coefficients), (2) decay constants as short as or shorter than tens of nanoseconds, (3) radiation hardness against the radiation environment, and (4) availability of long (20 X_0 or longer) crystals. Large light output per unit energy deposited is not always important, especially at very high energies (much higher than GeV), since the total energy deposited is large. In large-scale, high-energy experiments, the total scintillator volume per detector sometimes reaches 1–10 m^3 or more, making low cost materials also important.

For applications in nuclear physics experiments,[31] NaI:Tl$^+$ has been used for a long time,[32] initially as single crystals with ever-increasing sizes, up to 50 cm in both diameter and depth, and then in arrays of many crystals. NaI:Tl$^+$ and BGO have been used as active shielding materials in Compton-suppressed spectrometers[33] that use Ge semiconductor detectors in in-beam γ-ray spectroscopy. Use of GSO:Ce^{3+} is increasing due to the advantage of larger light output (more than three times) and faster decay (more than six times) than BGO. CsI:Tl$^+$ has a capability of pulse-shape discrimination and is used for the identification of different Z particles. For studying heavy-ion reactions, BaF$_2$ provides the advantage of excellent time resolution because the fast component (at shorter wavelengths than ~240 nm, Figure 19) decays with $\tau \sim 0.6$ ns. The fast/slow component ratio is the largest for γ-rays and decreases with increasing Z for the nuclear particles, thereby enabling particle identification. CaF$_2$:Eu^{2+} gives a large light output (40% of NaI:Tl$^+$) at 420 nm (Figure 18) with a dominant decay component of $\tau \sim 1$ μs. As the band gap is large (12.1 eV), photoluminescence cannot be excited as in BaF$_2$. CsF is heavy ($X_0 = 2.0$ cm) and gives a light output of 6% that of NaI:Tl$^+$ and a fast decay component of $\tau \sim 2.8$ ns for γ-rays (but as slow as 200 ns for α-particles).[34] Even though CsF is strongly hygroscopic it can be used as an efficient detector of γ-rays with fast timing.

γ-rays with energies much higher than 1 MeV cause an electromagnetic cascade shower through pair production and bremsstrahlung in the detector. In order to measure precisely the energy of the incident γ-rays, the detector size should be as large as or larger than the shower size, so as to minimize the shower leakage. The shower depth increases slowly with the γ-ray energy roughly in proportion to its logarithm, and the required depth of

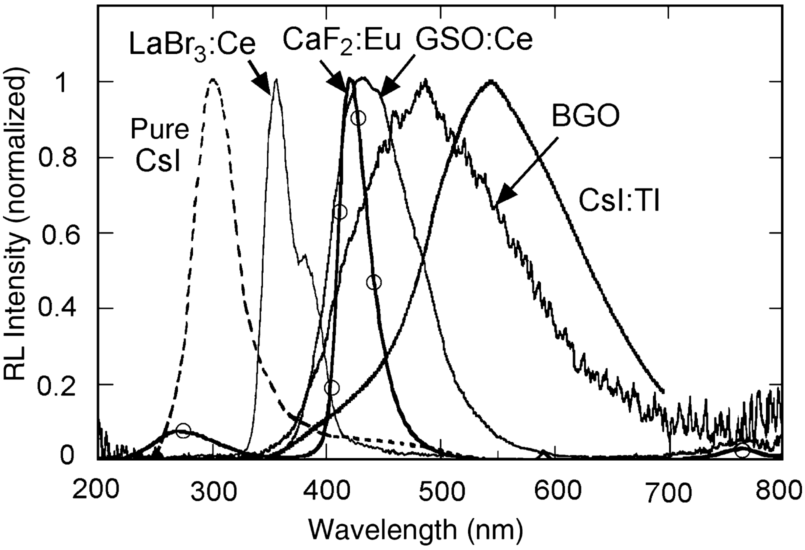

Figure 18 Normalized radioluminescence spectra of CsI:Tl$^+$, CsI[38], LaBr$_3$:Ce^{3+}, CaF$_2$:Eu^{2+}, BGO, and GSO:Ce^{3+} for X- or γ-rays. The CsI:Tl$^+$ and CsI data are taken from [38], while data for LaBr$_3$:Ce^{3+} are taken from [74]. In CaF$_2$:Eu^{2+}, the height of the 270 nm peak depends on the crystal purity.

the detector is typically as large as 20 X_0. NaI:Tl$^+$ and BGO are most commonly used; for example, the crystal ball[35] at Stanford Linear Accelerator Center (SLAC) consists of 672 NaI:Tl$^+$ (~41 cm long) crystals with PMT readout. The BGO detector[36] at European Organization for Nuclear Research (CERN) consists of 11,600 crystals (~24 cm long) assembled in a barrel shape with PD readout. Efforts to make BGO faster by doping with various additives such as Ce^{3+} have not yet been successful. Although GSO:Ce^{3+} is expensive compared with BGO, work continues on GSO:Ce^{3+} to increase the reliability in growing large size crystals (larger than 100 mm diameter × 300 mm length), signaling the possibility of deploying GSO:Ce^{3+} crystals on a large scale for high-energy purposes in the near future. By increasing the Ce amount, for example, from 0.5 to 2 mol%, the decay constant can be reduced from 50 ns to less than 30 ns with the reduction of the light yield of only 20%. GSO:Ce^{3+} has an excellent radiation hardness, in the vicinity of 10^{6-7} Gy.[23]

CsI:Tl$^+$ has a shorter radiation length ($X_0 = 1.86$ cm) and is easier to handle (much weaker hygroscopicity) than NaI:Tl$^+$. However, its longer decay time (~1 μs) is a problem for high count rate applications. The CLEO detector[37] at the Cornell electron-positron storage ring consists of about 8000 CsI:Tl$^+$ crystals with a total volume of ~7 m^3 with PD readouts. The emission spectrum of CsI:Na$^+$ peaks at 410 nm and fits the response of PMTs better. CsI:Na$^+$ is faster ($\tau = 650$ ns) but much more hygroscopic than CsI:Tl$^+$. Nondoped CsI has the advantage that its fast component[32] ($\tau \sim 10$ ns at ~305 nm, Figure 18) is four times larger than its slow component ($\tau \sim 1$ μs at >400 nm, Figure 18), although the light yield is only one twentieth that of CsI:Tl$^+$.

For the efficient use of BaF$_2$, selective readout of the fast component ($\tau \sim 0.6$ ns at λ = 220 nm, Figure 19) is necessary. Various methods[39] have been elaborated elsewhere including the use of quartz window PMTs, solar blind CsTe PMTs, band-pass filters, and wavelength filters or shifters. BaF$_2$ has been intensively studied[40] for possible use at the high

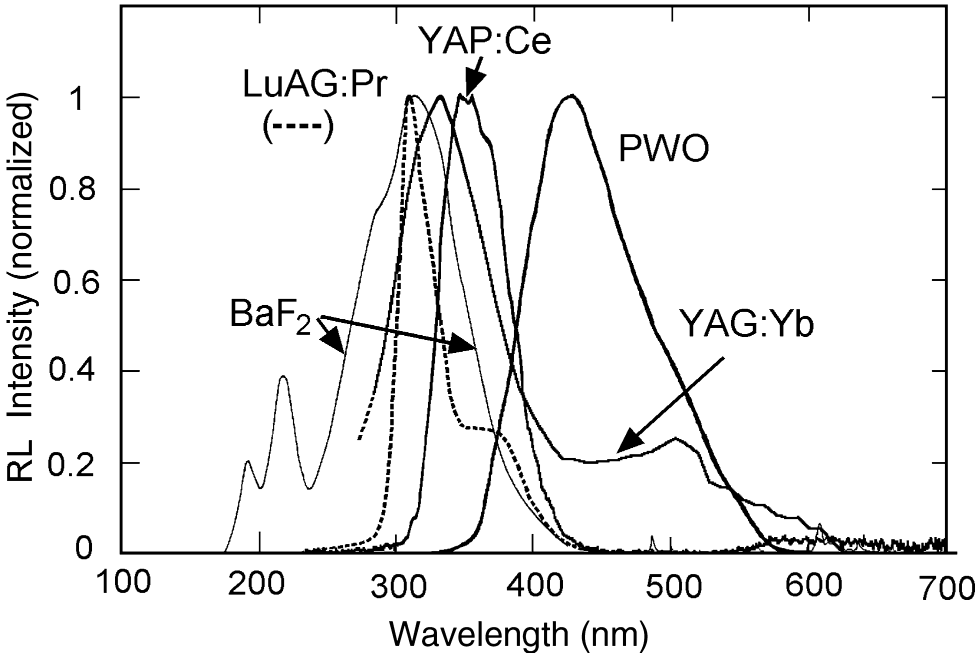

Figure 19 Normalized radioluminescence spectra of BaF$_2$, YAP:Ce^{3+}, PWO, YAG:Yb^{3+}, and LuAG:Pr^{3+} for X-rays. LuAP:Ce^{3+} is similar to YAP:Ce^{3+} in the shape of the emission spectra, while LuAG:Yb^{3+} is similar to YAG:Yb^{3+}.

energy pp collider superconducting super collider (SSC), especially since the possibility exists in optical bleaching of any radiation damages. Taking full advantage of BaF_2 (i.e., fast component) at high energies, however, has not yet been realized in any large-scale detectors due to the present limitation on the available size (10–15 X_0) of the crystals and insufficient radiation hardness in large-size crystals. BaF_2 detectors[41] incorporated in a periodic structure of thin crystals and low-pressure multiwire proportional chambers (MWPC) and treated with UV/VUV photosensitive materials (for example, tetrakisdimethylaminoethylene (TMAE)) have a capability of measuring the longitudinal development of showers and allow for particle identification between, for example, e/π.

PWO has the shortest radiation length of $X_0 = 0.92$ cm among all the established scintillators. Due to thermal quenching of the luminescence of WO_4^{2-} ions, the light output at room temperature is as small as 5% that of BGO. After rediscovery in 1992,[42,43] PWO was intensively studied as a dense and fast scintillator for calorimeters at high energies. In addition to the intrinsic very fast (less than a few nanoseconds) blue component (Figure 19), a slow green component can appear with much larger light intensity, depending on the defects and impurities present. In addition to the improvements made by removing harmful Mo^{6+} impurities, dramatic improvements[44,45] in the transmittance at short wavelengths, radiation hardness, and suppression of slow components were obtained around 1997–1999 by doping trivalent rare-earth ions such as La^{3+}, Gd^{3+}, and Y^{3+}. These dopants can compensate the crystal defects of Pb^{3+} and O^- that would cause the slow component. Crystals of good quality with more than 25 X_0 are available. The PWO detector[46] at LHC (CERN) consists of 83,000 crystals (~23 cm long) assembled in a barrel shape with APD readout.

Although $YAP:Ce^{3+}(YAlO_3:Ce^{3+})$[47] ($X_0 = 2.77$ cm) is lighter than $LSO:Ce^{3+}$ ($X_0 = 1.14$ cm), it has an absorption coefficient similar to $NaI:Tl^+$, a decay constant as short as 30 ns, and a light output as large as CWO. The emission wavelength of 350 nm (Figure 19) is shorter than in many other Ce^{3+}-doped oxide crystals. While single crystals of YAP are difficult to grow in large-size due to noncongruent composition, it has good mechanical characteristics. The overall good scintillation as well as mechanical characteristics give a unique position to the small-size precision YAP crystals in practical applications as well as in model studies.

7.3.1.5 Scintillators for neutron detection

In addition to the X-ray analysis of materials, neutron analysis is becoming important in biochemistry as seen in DNA analysis as well as in other fields of biology, materials science, chemistry, physics, and so on. Probes of thermal neutrons instead of X-rays and γ-rays can give information on light atoms like H, C, N, and O in materials. New intense neutron sources are being planned and built. Requirements for the scintillators to detect intense thermal neutrons with a good position resolution are (1) large light output, (2) fast decay, and (3) suppression of background γ-rays due to inefficiency or discriminating capability. Traditional scintillators[48] include LiF/ZnS:Ag, Li-glass, and $LiI:Eu^{3+}$. LiF/ZnS:Ag gives a large light output of 160,000 ph/neutron with the α/β ratio of ~0.44. While the decay is as slow as 1 μs for neutrons due to an existence of slow component, it is faster (order of 10 ns) for γ-rays, giving a capability of discriminating γ-rays. As LiF is added to ZnS:Ag powder crystals with an organic binder, LiF/ZnS:Ag is opaque, giving a limitation in the efficient readout from thin plates. Li-glass gives a much smaller light output (6000 ph/neutron) at ~385 nm[49] (Figure 20) with a smaller α/β ratio of ~0.3. Compared with LiF/ZnS:Ag, the decay is much faster (<100 ns for both neutrons and γ-rays) but the discrimination against γ-rays is poorer. Due to the advantage of efficient γ-ray discrimination, LiF/ZnS:Ag is used in large detector systems. While $LiI:Eu^+$ gives large light output (50,000 ph/neu-

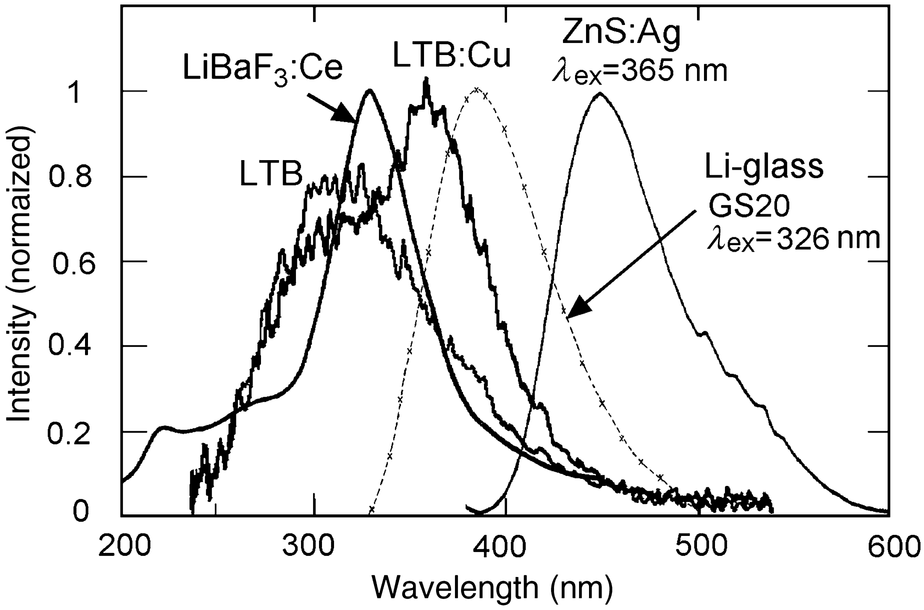

Figure 20 Emission spectra of Li-glass GS20,[49] ZnS:Ag, nondoped and Cu^+-doped LTB ($Li_2B_4O_7$), and $LiBaF_3$:Ce^{3+},[50] under UV (for the first two) or X-ray (for the rest) excitation. They are normalized at the peak except nondoped LTB, which is shown relative to LTB:Cu^+. A transparent crystal was used for ZnS:Ag. For $LiBaF_3$:Ce^{3+}, the emission was measured within 50 ns to suppress the slow STE luminescence.

tron), the slow decay (τ~ 1 μs) and the strong hygroscopicity are the disadvantages. As the traditional scintillators do not fit all the requirements to a satisfactory level, intense efforts are devoted to developing new scintillators. Nondoped $LiBaF_3$ and $LiBaF_3$:Ce^{3+} give a fast cross-luminescence for γ-rays and not for neutrons, enabling discrimination against γ-rays.[49] The luminescence in $LiBaF_3$:Ce^{3+} consists of three components; cross-luminescence at 220 nm (τ~ 1 ns), Ce^{3+} luminescence at 325 nm (~30 ns), and a slow component due to STE origin at 280 nm (~15 μs). While the total light output is moderate (3,500 ph/neutron), the slow component occupying one third of it is a disadvantage. LTB:Cu^{3+} ($Li_2B_4O_7$:Cu^+) has a density of 2.42 g cm^{-3} and an emission peak at 365 nm (Figure 20). The light output is roughly 200 ph/neutron and the decay is fast (τ~ 1 ns order), indicating strong thermal quenching at room temperature. Nondoped LTB gives ~140 ph/neuron at 320 nm (Figure 20) with a similarly short decay time. The small light outputs of doped or nondoped LTB create limitations in two-dimensional readouts when ^{6}Li is used as a converter of neutrons to α-rays. However, LTB may be useful for neutron detection at high rates, with high spatial resolution. A new method[51] was proposed for using ^{10}B as a converter of a neutron to an α-ray and an additional γ-ray (95% branching ratio) of 0.48 MeV. To reject background γ-rays, coincidence is taken between the fast α-ray signal from LTB and the γ-ray signal from a fast-response scintillator such as Y_2SiO_5:Ce^{3+} (τ~ 42 ns) coupled to the LTB plate or powder. Many other scintillators containing Li and Gd have been intensively developed at Delft.[48] While some of them either give large light output or fast decay or both, they have disadvantages like hygroscopicity or the background γ-ray signals produced in heavy elements (Gd). Research and development of better new scintillators remain to be done.

7.3.1.6 *Industrial applications*

Scintillators also play an important role in well logging.[52] Underground natural resources can be searched for by drilling bore holes 5000 m below and remotely operating a γ-ray detector, called a sonde, to measure the natural radioactivity of geologic formations. In some cases, the sonde also carries a γ-ray source or a neutron source to irradiate the formation. The γ-rays coming back to the sonde are detected with a scintillator. The scintillators used for these purposes have (1) large volumes, (2) high atomic number, (3) short decay times, (4) large light output, and (5) small dependence on temperature. The operational environment is extreme with temperatures as high as 150°C. While NaI:Tl^+ has been most widely used so far, faster and higher Z_{eff} scintillators are required in order to achieve higher count rate capability and detection efficiency. Although BGO has much larger Z_{eff} than NaI:Tl^+, BGO has a much larger dependence on temperature[53] than NaI:Tl^+; the light output of BGO (NaI:Tl^+) decreases by 70% (12%) when the temperature rises from room temperature to 100°C. GSO:Ce^{3+} appears promising[53] because of its relatively high volumetric detection efficiency and a temperature dependence of the light output similar to that of NaI:Tl^+. The CT scanning technologies, used in medical diagnoses, also are applicable to nondestructive industrial or safety inspections.[54,55] The importance of quick and reliable safety inspection is ever increasing at airports and elsewhere. While detection of metallic weapons is straightforward by the CT scanning technique, discovery of chemical bombs requires more sophisticated techniques. The indices of explosives are (1) abundance of N (12–38% of weight), (2) small abundance of H (2–7%) and C, and (3) density of about 1.6 g cm^{-3}. Among these indices, the N abundance is the most important. To detect N abundance, γ-rays of the characteristic energies, both their energies and positions are detected precisely for 10.8 MeV γ-rays emitted from activated N* and for 9.17 MeV γ-rays to be absorbed by the ground-state N. For this purpose, scintillators like NaI;Tl^+, BGO, GSO:Ce^{3+}, LSO:Ce^{3+}, etc. are used for precision γ-ray detectors.

7.3.1.7 *New scintillators*

Lately, many new Ce^{3+}-activated scintillators[56] have been studied, including LSO:Ce^{3+},[25] $LuAlO_3$:Ce^{3+}, (LuAP:Ce^{3+}),[57] BaF_2:Ce^{3+},[58] $LaBr_3$:Ce^{3+}, and $LuBO_3$:Ce^{3+}. LSO:Ce^{3+}, previously mentioned, has excellent radiation hardness (10^{4-5} Gy). If the remaining nonuniformity could be removed in the future, it can find much wider applications. $LuAlO_3$:Ce^{3+} is similar to but much heavier ($X_0 = 1.08$ cm) than $YAlO_3$:Ce^{3+} and has been considered for use in PET. The reported scintillation characteristics scatter to some large extent. LuAP is not congruent in composition, similar to YAP. To improve the instability, LuYAP,[59] a mixed solution of LuAP and YAP, and LuGAP,[60] that of LuAP and GAP ($GdAlO_3$), have been studied to take advantage of the stable and good mechanical properties of YAP and congruent composition of GAP, respectively. Among rare-earth garnet scintillators, YAG:Ce^{3+}($Y_3Al_5O_{12}$:Ce^{3+}) is widely used as imaging screens (P46); the emission occurs at 530 nm with the main decay constant of 88 ns.[61] Since the density of 4.55 g cm^{-3} is not very large, LuAG($Lu_3Al_5O_{12}$) with a density of 6.73 g cm^{-3} is more interesting as the host. LuAG:Ce^{3+} (emission at 510 nm, light output~6000 ph/MeV, $\tau \sim 70$ ns,)[57,62] is similar to YAG:Ce^{3+} in the scintillation characteristics. Compared with LuAG:Ce^{3+}, LuAG:Pr^{3+} gives the emission peak at a shorter wavelength of 310 nm (Figure 19) with a larger intensity of about ~10,000 photons/Mev (ph/Mev) and a shorter decay constant of ~26 ns. It is necessary to study the origin (impurities or defects) of an intense and slower ($\tau \sim \mu$s) component accompanying the fast component, and to improve the crystal growth.

One of the most significant intrinsic scintillators developed, after the discovery of BGO, are PWOs, mentioned earlier. To search for new efficient scintillators quickly, without going through the time-consuming process of growing single crystals, Derenzo et al.[63] irradiated many powdered compounds and measured their scintillations. This study triggered the rediscovery of PWO. BSO ($Bi_4Si_3O_{12}$)[64] is similar to BGO in many respects, but its decay time ($\tau \sim 100$ ns) is one third and the light output is one fifth that of BGO due to thermal quenching at room temperature. BSO is as radiation hard as or harder than BGO by an order of magnitude.

Yb-containing crystals have been studied intensively due to twofold interests: first, fast luminescence is possible in the charge-transfer allowed transition between Yb^{2+} and Yb^{3+} and second, Yb has potential uses in the detection of solar neutrinos and the search for dark matter. YAG:Yb^{3+}, YbAG ($Yb_3Al_5O_{12}$), and LuAG:Yb^{3+} are of congruent compositions. Among them, YAG:Yb^{3+} has been most deeply studied; the density is 4.55 g cm^{-3} for the host and increases with heavy Yb^{3+} doping. At room temperature, the light output is 13% of BGO for 15 mol% Yb doping, and the emission occurs at 330 nm (Figure 19) with a decay constant $\tau \sim 7$ ns. When the temperature is decreased, the light output increases, reaching the maximum (six times that of BGO) at ~100 K. The decay at 100 K is still fast ($\tau \sim 45$ ns) indicating that the temperature dependence is not typical thermal quenching. The obtained result shows that both a large light output and fast decay can be obtained at a reasonably low temperature of 100 K.[65]

As for fluorides, if the concentration of Ce^{3+} doped into BaF_2 is increased to 1.0 mol%,[58] the dominant decay component becomes fast ($\tau < 100$ ns); the total light output of the fast and slow (340 ns) components reaches 70% of that of pure BaF_2. CeF_3[66,67] was enthusiastically developed for possible use in high-energy physics experiments. CeF_3 has fast scintillation ($\tau \sim 30$ ns) and its light output is 4–5% that of NaI:Tl^+. Radiation damage is small for doses up to 10^4 Gy in small-size crystals, but significantly large in large-size crystals. There remain difficulties in growing crystals of good quality longer than 10 X_0. This tendency is common to large-size fluoride crystals. In the crystal growth, a fluoride scavenger, MF_m, (CdF_2, PbF_2, CF_4, etc.) is usually added to the melt to remove H_2O by converting it to HF gas and the oxide of M. The evaporation of H_2O, HF, and the oxide of M are close enough from the surface but not enough from the deep inside of the crystal, leaving them as impurities. CdF_2 is dense ($X_0 = 1.73$ cm) and fast ($\tau \sim 7$ ns),[68] while its light output is small (0.25% of NaI:Tl^+). It is, however, nonhygroscopic and optically clear above 220 nm, and has its emission peak at 520–580 nm. Its radiation hardness is improved significantly by doping with Ce^{3+}.[20] PbF_2, with $X_0 = 0.95$ cm, is very dense and is known to emit only Cherenkov radiation at room temperature as a result of thermal quenching of scintillation.[69] Doping PbF_2 with small amounts of additives has been attempted in order to obtain scintillation, but without much success. Its radiation hardness is of the order of 10^2 Gy.[70] LuF_3:Ce^{3+} is heavy (density = 8.29 g cm^{-3}, $X_0 = 1.04$ cm), and gives emission at 310 nm with a light output of ~8000 ph/MeV and $\tau \sim 23$ ns.[71] The growth of a single crystal, however, is difficult due to phase transformation as seen in the case of GdF_3. LuF_3:Ce^{3+} may find an application in small crystals or ceramics. While GdF_3 is also heavy (density = 7.06 g cm^{-3}, $X_0 = 1.33$ cm), the energy transfer from Gd^{3+} to Ce^{3+} or Pr^{3+} dopant ions is not efficient,[72] resulting in much smaller light output and slower decay than in the LuF_3 host. Since most binary fluorides have already been investigated, multicomponent fluorides[20] are now being studied systematically for efficient scintillation.

Extensive studies[73] carried out at Delft on rare-earth halide crystals have revealed that some of them have excellent scintillation characteristics of large light output and fast decay, although they have medium density and are strongly hygroscopic. $LaBr_3$:Ce^{3+} (density = 5.3 g cm^{-3}) gives 61,000 ph/MeV at 360 nm (Figure 18) with a dominant decay of $\tau \sim 30$ ns.[74] When the halogen ion becomes heavy, the halide becomes heavy and the band gap E_g decreases : 11.4 eV for F, 7.0 eV for Cl, 5.6 eV for Br, and 3.6 eV for I. Smaller E_g is preferable for increasing the number of emitted photons, as far as it is large enough to enable visible or UV emission. In addition to $LaBr_3:Ce^{3+}$, $LuI_3:Ce^{3+}$ (density = 5.6 g cm^{-3}) is also promising:[75] it gives large light output (40,000 ph/MeV) at 475 nm with a dominant decay of $\tau \sim 31$ ns.

The characteristic features of cross-luminescence[19] (or core-valence luminescence[20]) are fast decay ($\tau <$ ns), emission in the UV/VUV range, and very small temperature dependence of the emission. The fast decay is appropriate for detectors that require subnanosecond time resolution. Many candidates, in addition to the well-known BaF_2, have been examined, including CsF, RbF, $KMgF_3$, $KCaF_3$, KYF_4, $LiBaF_3$, and $CsCaCl_3$. No cross-luminescence systems have been found that yield more than 5% of the emission of $NaI:Tl^+$ in the fast component. BaF_2 seems to remain the best from its overall scintillation characteristics and availability in large crystal forms. Molding of small-size grains of heavy single crystals into a transparent “solvent” may be useful especially when large-size crystals are difficult to grow. Plastics can be considered as solvents. Both the density and the light output, however, are smaller than those of the single crystal. Matching of the index of refraction between the crystal and the solvent is important in obtaining efficient transmission of the light. The old neutron detectors comprising polycrystalline ZnS and nonscintillating plastics, known as “Hornyak button” belong to this class of scintillators. More recently, the above technique has been considered for BaF_2.[76] Although its index of refraction ($n = 1.56$) is relatively small among the heavy crystal scintillators, it is too large to be matched to a solvent.

7.3.2 *Ceramics and glasses*

Luminescent ceramics[7,21] such as $(Y,Gd)_2O_3:Eu^{3+},Pr^{3+}$ (density = 5.92 g cm^{-3}), $Gd_2O_2S:Pr^{3+},Ce^{3+}$ (7.34 g cm^{-3}), and $Gd_3Ga_5O_{12}:Cr^{3+},Ce^{3+}$ (7.09 g cm^{-3}) have been shown to be promising for use in XCT. They are polycrystalline materials with grain sizes typically in the range of tens of microns. For $(Y,Gd)_2O_3:Eu^{3+},Pr^{3+}$, the 4f–4f transition ($^5D_J \rightarrow {}^7F_J$) of Eu^{3+} gives the scintillation. Co-doping of Pr^{3+} lowers the afterglow but decreases light output. For $Gd_2O_2S:Pr^{3+},Ce^{3+}$, the 4f–4f transition ($^3P_0 \rightarrow {}^3H_J,{}^3F_J$) of Pr^{3+} gives the scintillation and Ce^{3+} lowers the afterglow. $Gd_2O_2S:Pr^{3+},Ce^{3+}$ is now used in XCT detectors due to the advantage of 1.8 times larger light output in spite of a smaller density compared with $CdWO_4$, the main XCT scintillator. $LuBO_3:Ce^{3+}$ has been studied for a new efficient scintillator.[77] While it has high-temperature (density = 7.4 g cm^{-3}, vaterite) and low-temperature (6.9 g cm^{-3}, calcite) phases, the latter seems to be more practical in the growth. The scintillation in $LuBO_3:Ce^{3+}$ ceramics occurs at around 410 nm (as shown in Figure 21) with an integrated light output nine times that of BGO with the dominant decay of $\tau \sim 21$ ns. Growth of single crystals is not easy due to the phase transition at 1310°C. If transparent or translucent ceramics could be successfully produced, this material may be promising for X-ray CT.

As for scintillating glasses, a typical one, SCG1,[78] based on SiO_2 and BaO and activated with Ce^{3+}, has a density of 3.4 g cm^{-3} and its light output is five times the Cherenkov radiation observed. Ce^{3+}-containing heavy fluoride glasses, such as fluorohafniates (HFG),[79,80] have a density as large as 6 g cm^{-3} while the light output is as small as 10–30 % of SCG1. Recently, new heavy scintillating glasses mainly based on Gd_2O_3 have been developed with Ce^{3+} or Tb^{3+} doping for luminescence centers. The Gd_2O_3- (20 mol%) and Lu_2O_3- (10 mol%) based glasses with Ce^{3+} doping[81] for nuclear detectors have a density of 5.63 g cm^{-3} and give 1000 ph/MeV around 380 nm (Figure 21) with a dominant decay of $\tau < 500$ ns. These are much heavier than SCG1, still giving a light output twice as large as that of SCG1. The Gd_2O_3- (up to 40 mol%) based glasses with Tb doping[82] for X-ray detectors have a typical density of 6.0 g cm^{-3}. These give a light output 26% of BGO with a decay constant of 1.8 ms. The emission arises from the 4f–4f transition of Tb^{3+} with the dominant peak at 540 nm.

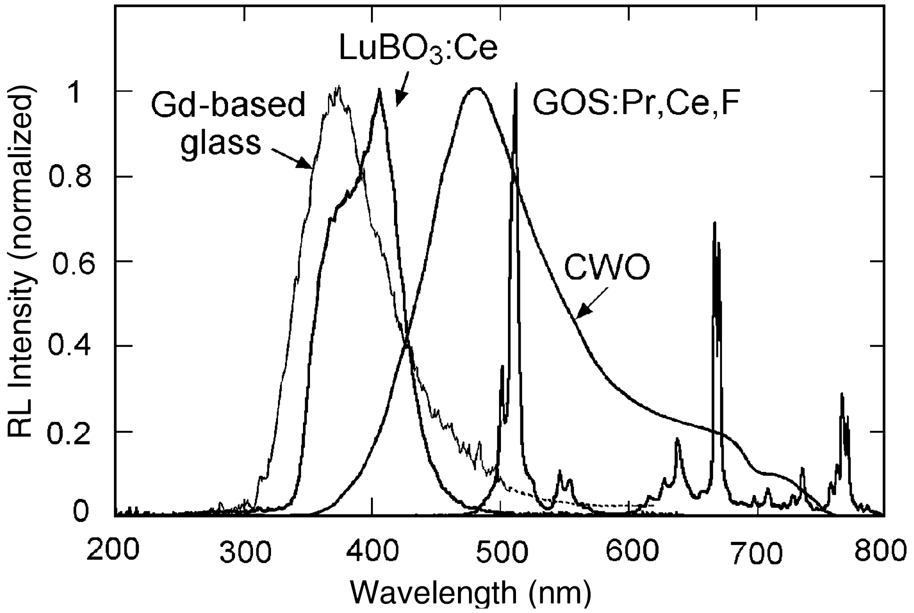

Figure 21 Normalized radioluminescence spectra of CWO,[22] GOS(Gd_2O_2S):Pr^{3+},Ce^{3+},F^+, $LuBO_3$:Ce^{3+}, and Gd_2O_3-based glass:Ce^{3+} for X-rays. A powder sample of Gd_2O_2S:Pr^{3+},Ce^{3+},F^+ and a ceramic disk of $LuBO_3$:Ce^{3+} were used in measurement.

7.3.3 Organic scintillators

Organic scintillators[26,30] (crystals, liquids, and plastics) used for the detection of charged particles have the following characteristic features: (1) small density not much larger than 1.0 g cm^{-3}, (2) fast decays in the order of nanoseconds, and (3) mostly composed of C and H. Scintillations[26,30] occur in the deexcitation ($S_1 \rightarrow S_0$) of the π-electron in the benzene ring. The most widely used organic crystals are anthracene ($C_{14}H_{10}$), *trans*-stilbene ($C_{14}H_{12}$), *p*-terphenyl (TP, $C_{18}H_{14}$), and quarterphenyl ($C_{24}H_{18}$); these compounds are all aromatic hydrocarbons based on benzene structures. Anthracene gives a light output as large as 40% of NaI:Tl^+ and has a fast decay ($\tau \sim 30$ ns). It is, however, not easy to produce large-sized crystals. Liquid scintillators have the advantage that large volumes can be obtained in any shape by dissolving organic crystal scintillators like TP as a primary solute in solvents like toluene. Sometimes wavelength shifters such as POPOP [1,4 di-(2-(5-phenyloxazolyl))-benzene, $C_{24}H_{16}N_2O_2$] are added as a secondary solute in order to obtain good spectral matching between the emission and the photosensors (PMTs). Liquid scintillators are, however, not versatile, requiring hermetic containers. Plastic scintillators have been developed to solve this problem by adding scintillators into plastics. A typical plastic scintillator consists of polystylene (C_8H_8) or polyvinyltoluene (C_9H_{10}) as a base scintillator, TP as a primary solute, and a wavelength shifter tetraphenylbutadiene, ($C_{28}H_{22}$) (TPB) as a secondary solute. They are widely used as general-purpose detectors for charged particles.

References

1. Sakai, E., *IEEE Trans. Nucl. Sci.*, NS-34, 418, 1987.
2. Anger, H.O., *Rev. Sci. Instrum.*, 29, 27, 1958.
3. Hounsfield, G.N., *Brit. J. Radiol.*, 46, 1016, 1973.
4. Ter-Pogossian, M.M., Phelps, M.E., Hoffman, E.J., and Mullani, N.A., *Radiology*, 114, 89, 1975.

5. Farukhi, M.R., Scintillation detectors for CT applications, *Workshop on Transmission and Emission Computed Tomography*, Seoul, July 1978.
6. Ishii, M. and Kobayashi, M., *Prog. Cryst. Growth Ch.*., 23, 245, 1991.
7. Blasse, G. and Grabmaier, B.C., *Luminescent Materials*, Springer, Berlin, 1994.
8. Rodnyi, P.A., *Physical Processes in Inorganic Scintillators*, CRC Press, New York, 1997.
9. Korzhik, M.V., *Physics of Scintillators Based on Oxide Single Crystals* (Russian), Belarussian State University, Minsk, 2003.
10. Nikl, M., *Phys. Status Solidi A*, 178, 2000, 595.
11. Nikl, M., *Meas. Sci. Technol*. 17, 2006, R37.
12. Hofstadter, R., *Phy. Rev.*, 74, 100, 1948; *Phys. Rev.,* 75, 796, 1949.
13. Gevay, G., *Prog. Cryst. Growth Ch.*, 15, 145, 1987.
14. Weber, M.J. and Monchamp, R.R., *J. Appl. Phys.*, 44, 5495, 1973.
15. Ivanov, V.Y., Kruzhalov, A.V., Pustovarov, V.A., and Petrov, V.L., *Nucl. Instrum. Methods A*, 261, 150, 1987.
16. Antonangeli, F., Zema, N., and Piacentini, M., *Phys. Rev. B*,37, 9036, 1988.
17. Takagi, K. and Fukazawa, T., *Appl. Phys. Lett*., 42, 43, 1983.
18. Hoshina, T., *J. Phys. Soc. Jpn.*, 48, 1261, 1980.
19. Van Eijk, C.W.E., Experimental and theoretical studies of cross-luminescence, *Proc. Crystal 2000*, Chamonix, September 1992, De Notaristefani, F., Lecoq, P., and Schneegans, M., Eds., Frontiers, France, p. 161.
20. Sobolev, B.P., Rodnyi, P.A., Kobayashi, M., Vasilchenko, V.G., Motin, Yu.D., and Krechko, Yu.A., *Multicomponent Crystals Based on Heavy Metal Fluorides for Radiation Detectors*, Institut d'Estuadis Catalans, Barcelona, 1994.
21. Grescovich, C., Cusano, D., Hoffman, D., and Riedner, R.J., *Am. Ceram. Soc. Bull.,* 71, 1120, 1992.
22. Kinloch, D.R., Novak, W., Raby, P., and Toepke, I., *IEEE Trans. Nucl. Sci.* NS-41, 752, 1994.
23. Ishii, M., Kobayashi, M., Ishibashi, H., Akiyama, S., and Melcher, C.L., R&D of Ce-doped GSO scintillation crystals, *Proc. γ-ray Detector Physics and Applications*, San Diego, July 1994, SPIE Vol. 2305, 68.
24. Shimizu, S., Sumiya, K., Ishibashi, H., Senguttuvan, N., Redkin, B.S., Ishii, M., Kobayashi, M., Susa, K., and Maruyama, H., *IEEE Trans. Nucl. Sci.*, NS-50, 778, 2003.
25. Melcher, C.L. and Schweitzer, J.S., *Nucl. Instrum. Methods A,* A314, 212, 1992.
26. Birks, J.B., *The Theory and Practice of Scintillation Counting*, Pergamon Press, Oxford, 1964.
27. Van Sciver, W., *IRE Trans. Nucl. Sci.*, NS-3, 39, 1956.
28. Vasil'eva, N.N., γ- and photoluminescence of alkali iodides, in *Lebedev Physics Institute Series* 39, Consultants Bureau, New York, 1969, 219.
29. Gratta, G., Newman, H. and Zhu, R.-Y., *Ann. Rev. Nucl. Part. Sci.*, 14, 453, 1994.
30. Majewski, S. and Zorn, C., *Instrumentation in High Energy Physics*, A*dvanced Series on Directions in High Energy Physics* 9, Sauli, F., Ed., World Scientific, Singapore, 1992, chap. 3, 157.
31. Matulewics, T., Heavy scintillators in nuclear physics, *Proc. Crystal 2000*, Chamonix, September 1992, De Notaristefani, F., Lecoq, P. and Schneegans, M., Eds., Frontiers, France, p. 33.
32. Paul, P., Large NaI detectors, in *Nuclear Spectroscopy and Reactions*, Academic, 1974, Part A, 345.
33. Sharpey-Schafer, J.F. and Simpson, J., *Prog. Part. Nucl. Phys.*, 21, 293, 1988.
34. Moszynski, M., Gresset, C., Vacher, J., and Odru, R., *Nucl. Instrum. Methods,* 179, 271, 1981.
35. Kirkbride, G.I., et al., *IEEE Trans. Nucl. Sci.*, NS-26, 1535, 1979.
36. Schneegans, M., *Nucl. Instrum. Methods A*, 257, 528, 1987.
37. Bebek, C., *Nucl. Instrum. Methods A*, 265, 258, 1988.
38. Kubota, S., Sakuragi, S., Hashimoto, S. and Ruan(Gen), J., *Nucl. Instrum. Methods A*, 268, 275, 1988.
39. Sugimoto, S., Fukai, K., Mori, K., Ide, S., Kaneko, H., Takagi, H., and Kobayashi, M., *Nucl. Instrum. Methods A*, 336, 179, 1993.
40. Zhu, R.-Y., *Nucl. Instrum. Methods A*, 340, 442, 1994.
41. Anderson, D.F., Charpak, G., Kusmierz, W., Pavlopoulos, P., and Suffert, M., *Nucl. Instrum. Methods*, 228, 33, 1984.

42. Kobayashi, M., Ishii, M., Usuki, Y., and Yahagi, H., $PbWO_4$ scintillator at room temperature, *Proc. Crystal 2000*, Chamonix, September 1992, De Notaristefani, F., Lecoq, P., and Schneegans, M., Eds., Frontiers, France, p. 375.
43. Nagornaya, L. and Ryzhikov, V., Fast scintillators based on large "heavy" tungstate single crystals, ibid., p. 367.
44. Kobayashi, M., Usuki, Y., Ishii, M., Yazawa, T., Hara, K., Tanaka, M., Nikl, M., and Nitsch, K., *Nucl. Instrum. Methods A*, 399, 261, 1997.
45. Kobayashi, M., Usuki, Y., Ishii, M., Senguttuvan, N., Tanji, K., Chiba, M., Hara, K., Takano, H., M., Nikl, M., Bohacek, P., Baccaro, S., Cecilia, A., and Diemoz, M., *Nucl. Instrum. Methods A*, 434, 412, 1999.
46. Lecoq, P. The lead tungstate calorimeter of the CMS experiment at LHC, *Proc. SCINT95*, Delft, August–September 1995, Dorenbos, P. and van Eijk, C.W.E., Eds., Delft University Press, p. 52.
47. Baryshevsky, V.G., Korzhik, M.V., Moroz, V.I., Pavlemko, V.B., Fyodorov, A.A., Smirnova, S.A., Egorycheva, O.A., and Kachanov, V.A., *Nucl. Instrum. Methods B*, 58, 291, 1991.
48. Van Eijk, C.W.E., *Radiat. Prot. Dosim.*, 110, 5, 2004.
49. Spowart, A.R., *Nucl. Instrum. Methods.*, 140, 19, 1977.
50. Gektin, A., Voronova, V., Voloshinovski, A., and Zimmer, G., Fast scintillations in pure and Ce-doped $LiBaF_3$, *Proc. SCINT97*, Shanghai, September 1997, Zhiwen, Y, Peijun, L., Xiqi, F., and Zhilin, X., Eds. CAS, Shanghai Branch Press, p. 121.
51. Katagiri, M., Sakasai, K., Matsubayashi, M., Takahashi, H., and Nakazawa, M., *Nucl. Instrum. Methods A*, 513, 374, 2003.
52. Melcher, C.L., *Nucl. Instrum. Methods B*, 40/41, 1214, 1989.
53. Melcher, C.L., Schweitzer, J.S., Manente, R.A., and Peterson, C.A., *IEEE Trans. Nucl. Sci.*, NS-38, 506, 1991.
54. Melcher, C.L., Industrial applications of scintillators, *Proc. Crystal 2000*, Chamonix, September 1992, De Notaristefani, F., Lecoq, P., and Schneegans, M., Eds., Frontiers, France, p. 75.
55. Goldberg, M.B., Application of scintillators in security inspection systems, ibid., p. 137.
56. Weber, M.J., Ce-activated crystal and glass scintillators, ibid., p. 99.
57. Lempicki, A., Randles, M.H., Wisniewski, D., Balcerzyk, M., Brecher, C., and Wojtowicz, A.J., *IEEE Trans. Nucl. Sci.*, 42, 280, 1995.
58. Visser, R., Dorenbos, P., Van Eijk, C.W.E., Hollander, R.W., and Schotanus, P., *IEEE Trans. Nucl. Sci.*, NS-38, 178, 1991.
59. Kunter, C., Aiginger, H., Auffray, E., Glodo, J., Kapusta, M., Lecoq, P., Moszynski, M., Schneegans, M., Szupryczynski, P., and Wojtowicz, A.J., Scintillation properties and mechanism in $Lu_{0.8}Y_{0.2}AlO_3$:Ce, *Proc. SCINT2001*, Chamonix, September 2001; Auffray, E., Chipaux, R., Lecoq, P., Pedrini, C., and Schneegans, M., Eds., *Nucl. Instrum. Methods A*, 486, 176, 2002.
60. Chval, J., Clement, D., Giba, J., Hybler, J., Loude, J.-F., Mares, J.A., Mihokova, E., Morel, C., Mejezchleb, K., Nikl, M., Vedda, A., and Zaidi, H., *Nucl. Instrum. Methods A*, 443, 331, 2000.
61. Moszynski, M., Ludziejewski, T., Wolski, D., Klamra, W., and Norlin, L.O., *Nucl. Instrum. Methods A*, 345, 461, 1994.
62. Catalogue of Crytur Ltd., Czech Republic, 2003.
63. Derenzo, S.E., Moses, W.W., Cahoon, J.L., Perera, R.C.C., and Litton, J.E., *IEEE Trans. Nucl. Sci.*, NS-37, 203, 1990.
64. Kobayashi, M., Ishii, M., Harada, K., and Yamaga, I., *Nucl. Instrum. Methods A*, 372, 45, 1996.
65. Guerassimova, N., Garnier, N., Dujardin, C, Petrosyan, A.G., and Pedrini, C., *Chem. Phys. Lett.*, 339, 197, 2001.
66. Anderson, D.F., *IEEE Trans. Nucl. Sci.*, NS-36, 137, 1989; Moses, W.W. and Derenzo, S.E., *IEEE Trans. Nucl. Sci.*, NS-36, 173, 1989.
67. Crystal Clear Collaboration, *Nucl. Instrum. Methods A*, 332, 373, 1993.
68. Jones, R.V. and Polland, J.H., *Proc. Phys. Soc.*, 79, 358, 1962.
69. Eijkelenkamp, A.J.H., *J. Lumin.*, 15, 217, 1977.
70. Anderson, D.F., Kobayashi, M., Woody, C.L., and Yoshimura, Y., *Nucl. Instrum. Methods A*, 290, 385, 1990.
71. Moine, B., Dujardin, C., Lautesse, H., Pedrini, C., Combes, C.M., Belsky, A., Martin, P., and Gesland, J.Y., *Material Science Forum*, 239–241, 245, 1997.

72. Kobayashi, M., Nakamura, R., Ishii, M., Solovieva, N., and Nikl, M., *Jpn. J. Appl. Phys.*, 42, 1648, 2003.
73. Dorenbos, P., Our research (past and future) on scintillators, *Proc. KEK-RCNP International School for Scintillating Crystals*, Tsukuba, November 2003, Kobayashi, M. and Sugimoto, S., Eds., KEK-Proceedings 2004-4, p. 15.
74. van Loef, E.V.D., Dorenbos, P., van Eijk, C.W.E., Kramer, K.W., and Gudel, H.U., Scintillation properties of $LaBr_3$:Ce^{3+} crystals, *Proc. SCINT2001*, Chamonix, September 2001, p. 254.
75. Glodo., J, Shah, K.S., Klugerman, M., Wong, P., Higgins, B., and Dorenbos, P., Scintillation properties of LuI_3:Ce, *Proc. SCINT2003*, Valencia, September 2003; Ballestor, F., Bemlloch, J.M., Diaz, J., Lerche, C.W., Sanchez, F., and Sebastia, A., Eds, *Nucl. Instrum. Methods A*, 537, 279, 2005.
76. Kubota, S., Motobayashi, T., Ruan(Gen), J., Murakami, T., and Kasagi, J., *IEEE Trans. Nucl. Sci.*, NS-34, 438,1987.
77. Zhang, L., Madej, C., Pedrini, C., Dujardin, C., Gacon, J.C., Moine, B., Kamenskikh, I., Belsky, A., Shaw, D.A., and Mac Donald, M.A., Fast UV luminescence of Ce^{3+} and Pr^{3+} ions in lutetium orthoborate with the calcite or vaterite structure, *Proc. SCINT97,* Shanghai, September 1997, Zhiwen, Y, Peijun, L., Xiqi, F., and Zhilin, X., Eds. CAS, Shanghai Branch Press, p. 303.
78. Kobayashi, M., Yoshimura, Y., Iwahori, J., Yoshida, H., Takeutchi, F., Chiba, M., and Ito, H., *Nucl. Instrum. Methods*, 196, 239, 1982.
79. Devitsin, E.G., Dmitruk, L.N., Kozlov, V.A., Komar, A.A., Kotov, M.I., Popov, L.S. and Potashov, S.Yu., Heavy scintillating fluoride glasses as promising materials for EM calorimetry in H.E. physics, *Proc. Crystal 2000*, Chamonix, September 1992, De Notaristefani, F., Lecoq, P., and Schneegans, M., Eds., Frontiers, France, p. 401.
80. Dafinei, L., Auffray, E., Lecoq, P., and Schneegans, M., Heavy fluoride glasses as an alternative to crystals in H.E. physics calorimetry, *Mat. Res. Soc. Symp. Proc.,* 348, 217, 1994.
81. Kobayashi, M., Fu, J., and Sugimoto, S., Ce-doped heavy scintillating glasses with high Ln_2O_3 concentrations (Ln = La,Y,Gd,Lu), to be published in *Proc. SCINT2005*, Crimia, September 2005.
82. Fu, J., Kobayashi, M., and Parker, J.M., Terbium-activated heavy scintillating glasses, submitted to *Optical Materials*, 2006.

chapter seven — section four

Phosphors for X-ray and ionizing radiation

Takeshi Takahara

Contents

7.4 Phosphors for X-ray image intensifiers 655
  7.4.1 Overview 655
  7.4.2 Required characteristics 655
  7.4.3 Phosphors for input screens 656
  7.4.4 Phosphors for output screens 657
References 657

7.4 Phosphors for X-ray image intensifiers

7.4.1 Overview

The X-ray image intensifier (hereafter referred to as I.I.) converts an X-ray image into a visible one and is mainly used for medical purposes. Figure 22 shows its simplified cross-section.

The X-ray that penetrates through a specimen excites the input phosphor screen and is converted into visible light. It is then converted into photoelectrons by the photocathode located on the back of the input phosphor screen. The photoelectrons are accelerated through the focus electrode and converge on the anode. These electrons subsequently excite the output phosphor screen to form a visible image. Thus, a typical I.I. uses two different kinds of phosphors one for the input and one for output screens.

7.4.2 Required characteristics

The I.I. to be used for medical service is required to possess the following characteristics in order to perform diagnoses with a minimal X-ray dose:

1. High image brightness and S/N ratio
2. Sufficient image resolution

In order to satisfy these requirements, the phosphor for the input screen must have:

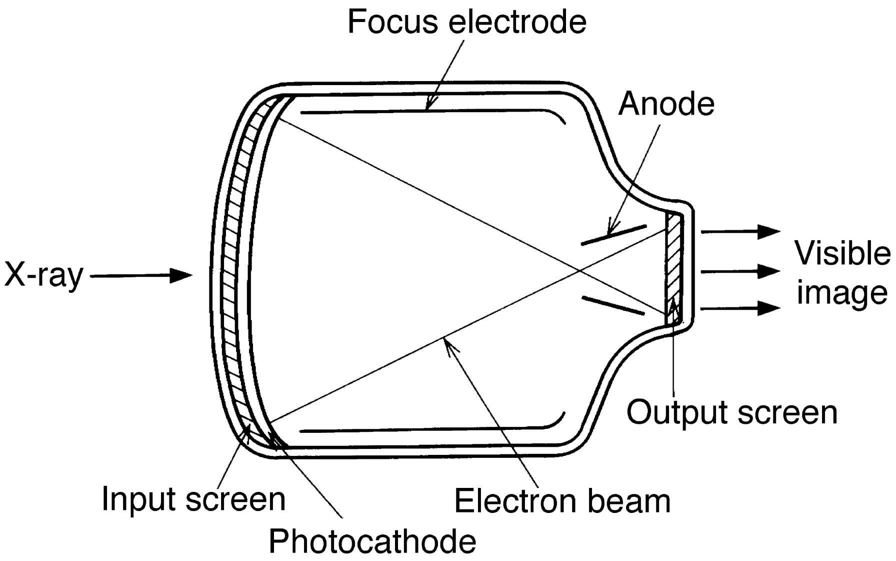

Figure 22 Simplified structure of an X-ray image intensifier.

1. Large X-ray absorptivity, that is, high specific gravity and a composition which includes elements of large average atomic number
2. High luminescence efficiency under X-ray excitation
3. An emission spectrum matched to the spectral response of the photocathode

The phosphor for the output screen is required to have a high luminescence efficiency under excitation by a low-density electron beam with smaller beam currents than in ordinary cathode-ray tubes.

The resolution of an I.I. is determined by the structure of the fluorescent screen (the size, packing density, etc. of the constituent phosphor particles). The forming methods of the phosphor screen are classified into the following two groups:

1. Film coating methods (electrodeposition, centrifugal sedimentation, etc.)
2. Vapor deposition methods (vacuum deposition, vapor phase growth, etc.)

In the film coating method, the fluorescent screen is made by piling up phosphor particles. In general, a screen prepared by this method is very efficient. However, its packing density is comparatively small, and its S/N ratio and resolution are rather poor due to diffusion of light inside the phosphor particle layer and on its rough surface. In the vapor deposition method, the fluorescent screen is made so compact that the packing density is about 100%; hence, its resolution is generally satisfactory. In many cases, the vapor-deposited fluorescent screen has considerably lower light emission efficiency than that prepared by the film coating method. However, since the demand for improved resolution of the input screen is strong, CsI:Na thin films prepared by the vapor deposition method are used at present, as will be described in 7.4.3.

7.4.3 Phosphors for input screens

As the phosphor for the input screen, the green-emitting (Zn,Cd)S:Ag was used formerly. In order to improve brightness and resolution, however, $Gd_2O_2S:Tb^{3+}$ was also used for some time.

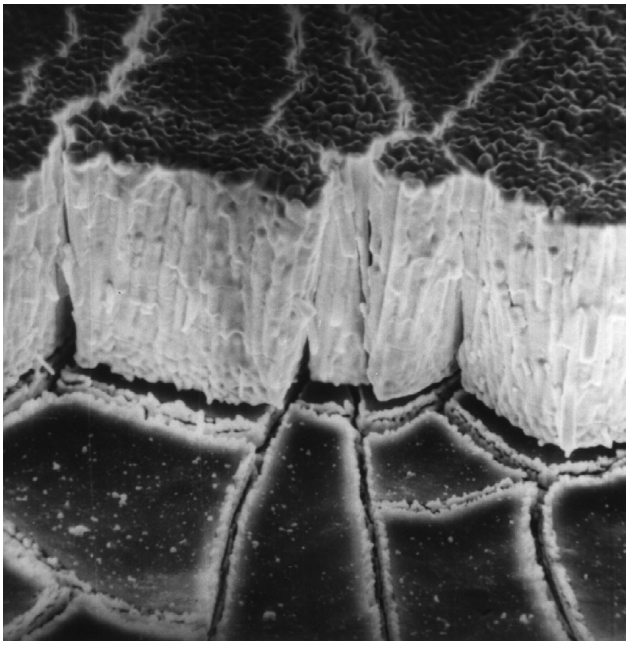

Figure 23 A TEM photograph of the cross-section of a CsI:Na input screen.

In the 1970s, the CsI:Na fluorescent screen, as shown in Figure 23, was successfully fabricated by the vapor deposition method, and mosaic cracks, called light-guide structure, were introduced. This method has been a great success in improving resolution.[1,2] As a result, this screen is presently being used.

Unlike ordinary phosphors, CsI is water soluble, degrades in the presence of moisture, and is inconvenient to handle, but it has a low melting point (~600°C). This property makes it a desirable substance to be used in the vapor deposition method. Figure 24 shows the emission spectra of CsI:Na and conventional (Zn,Cd)S:Ag, together with the spectral sensitivity of the photocathode.

7.4.4 *Phosphors for output screens*

For the output screen, zinc sulfide-type phosphors such as ZnS:Cu, (Zn,Cd)S:Cu, and (Zn,Cd)S:Ag are generally used. These phosphors have a high luminescence efficiency and are widely used in cathode-ray tubes. In the case of I.I., the signal current density is about 10 nA cm^{-2}, which is only 1/100 that used in cathode-ray tubes. Hence, one hardly needs to worry about the current saturation effect on brightness, which is problematic for cathode-ray tubes.

Synthesis methods of these phosphors are nearly identical with those of phosphors for cathode-ray tubes. However, it has become a general practice to make use of only phosphors with a particle diameter of 1 to 2 μm to form the output screen, as shown in Figure 25, by means of various film-coating methods (electrodeposition, sedimentation, etc.). Similar to the input screen, various kinds of vapor deposition methods of the ZnS-type phosphors have been considered, but none of them have reached the practical use level with respect to brightness.

References

1. Minami, H., Harao, N., and Tsuneoka, T., *Toshiba Rev.*, 30, 1005, 1975.
2. Washida, H., *Adv. Electron. Electron Phys.*, 52, 201, 1979.

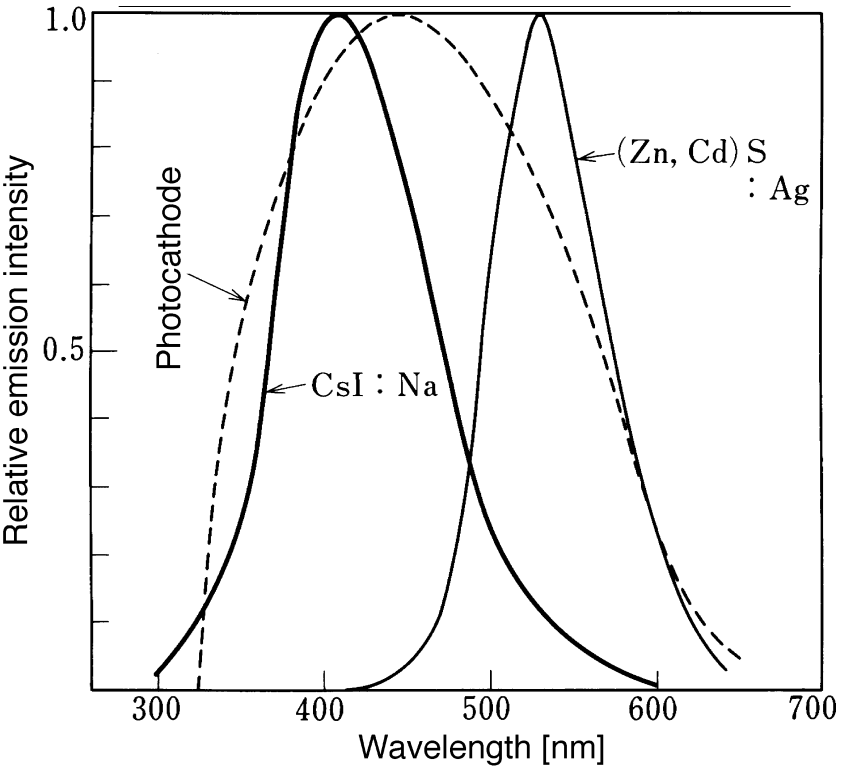

Figure 24 Emission spectra of input screen phosphors and spectral response of the photocathode.

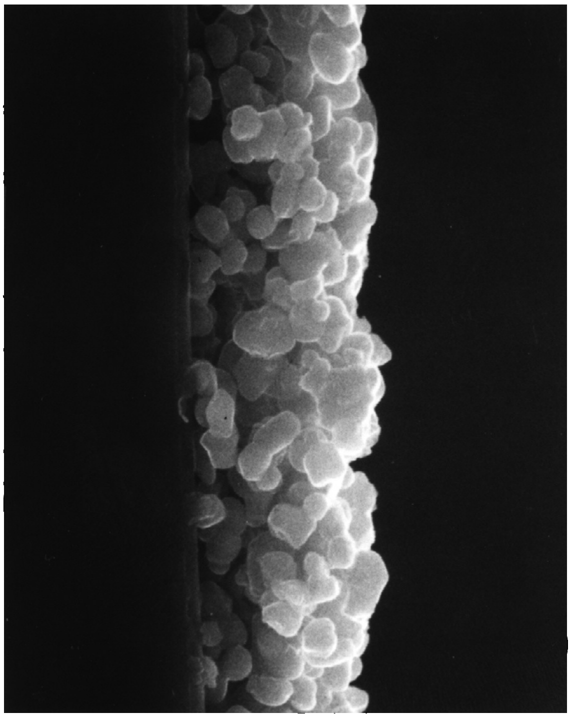

Figure 25 An SEM photograph of the cross-section of a ZnCdS:Ag output screen.

chapter seven — section five

Phosphors for X-ray and ionizing radiation

Kenji Takahashi

7.5 Photostimulable phosphors for radiographic imaging....659
  7.5.1 Introduction....659
  7.5.2 Properties and mechanism of PSL in BaFX:Eu^{2+} (X = Cl, Br, I)....660
  7.5.3 Characteristics of the imaging plate IP....662
  7.5.4 Radiographic image formation by means of the IP....663
References....664

7.5 Photostimulable phosphors for radiographic imaging

7.5.1 Introduction

The first attempt of radiographic imaging by means of photostimulated luminescence (PSL) was reported in 1947;[1] here, the PSL image corresponding to the X-ray image obtained on a chalcogenide photostimulable phosphor sheet was printed out on a photographic film using uniform infrared irradiation. In those days, PSL was investigated vigorously in terms of developing infrared-to-visible image converters; this interest waned soon thereafter. Although a few ideas of radiographic imaging by means of PSL were proposed after the first paper, no practical systems were developed until the following innovation in 1978.

In 1978, it was discovered that BaFX:Eu^{2+} (X = Cl,Br,I) is a photostimulable material, and the first patent for a radiographic imaging method utilizing this phosphor was filed by Fuji Photo Film and Dai Nippon Toryo (presently Kasei Optonix).[2]

The technical announcement of a system specifically using this patent was made in 1981 and the first-generation computed radiography (CR) system for medical diagnostics was developed in 1983 by Fuji Photo Film. The method employed is explained as follows[3]: After the radiographic image is transferred to an imaging plate (IP), i.e., a two-dimensional photostimulable detector for ionizing radiation such as X-rays, β-rays, γ-rays, ultraviolet light, etc., the plate is scanned point by point by a He-Ne laser beam of 633 nm light in an image reader. A series of the PSL emission corresponding to the scanned pixels is detected by a photomultiplier tube through a high-efficiency light guide to be converted into the electric signals as a function of time. These analog signals are logarithmically

Table 4 Typical Photostimulable Phosphors Investigated for Radiographic Imaging

Phosphors	Peak wavelength of stimulation spectrum (nm)	Peak wavelength of emission spectrum (nm)	Life time of PSL (μs)	References
$Ba_2B_5O_9Br:Eu^{2+}$	<500, 620	430	1.0	[7]
$BaBr_2:Eu^{2+}$	580, 760	400	0.5	[5]
$BaFBr:Eu^{2+}$	600	390	0.8	[3]
$BaFCl:Eu^{2+}$	550	385	7.4	[3]
$Ba_{12}F_{19}Cl_5:Eu$		440		[20]
$BaFI:Eu^{2+}$	610, 660	410	0.6	[3]
$Ba_5(PO_4)_3Cl:Eu^{2+}$	680	435		[9]
$Ba_5SiO_4Br_6:Eu^{2+}$	<500, 610	440	0.7	[8]
$Ca_2B_5O_9Br:Eu^{2+}$	500	445		[21]
$CaS:Eu^{2+},Sm^{3+}$	1180	630	0.05	[14]
$CsBr:Eu^{2+}$	680	440	0.7	[22, 26]
$CsI:Na^{+}$	720	338	0.7	[12]
$KCl:Eu^{2+}$	560	420	1.6	[10]
$LaOBr:Bi^{3+},Tb^{3+},Pr^{3+}$	(565–650)	360	10	[13]
$LiYSiO_4:Ce$	<450	410	0.038	[21]
$RbBr:Tl^{+}$	680	360	0.3	[11]
$RbI:T1^{+}$	730	420		[11]
$SrAl_2O_4:Eu^{2+},Dy^{3+}$	(532, 1064)	(520)	0.108	[23]
$Sr_2B_5O_9Br:Eu^{2+}$	<500	423		[21]
$SrBPO_5:Eu^{2+}$	640	390		[24]
$SrFBr:Eu^{2+}$	530	390	0.6	[6]
$SrS:Eu^{2+},Sm^{3+}$	1020	590	0.05	[14]
$Y_2SiO_5:Ce^{3+}$	<500, 620	410	0.035	[15]
$Y_2SiO_5:Ce^{3+},Sm^{3+}$	670	410	0.035	[15]

amplified and converted into digital signals. By processing these signals through a computer, the computed radiograph can be reconstructed.

This method has found application in the fields of bioscience and materials science in areas such as autoradiography, X-ray diffraction experiments, transmission electron microscopy, etc., and is called radioluminography (RLG). In addition, these IPs can be used as neutron detectors by introducing compounds with elements such as ^{6}Li or ^{Nat}Gd, which react with neutrons and produce secondary particles or γ-rays to excite the phosphor in the IP.[4]

Recently, the activities in the research and development of PSL have been revitalized and various kinds of new photostimulable phosphors for radiographic imaging have been reported. Typical phosphors are listed in Table 4; $BaFX:Eu^{2+}$ remains the most commonly used material.[26–27]

7.5.2 Properties and mechanism of PSL in $BaFX:Eu^{2+}$ (X = Cl,Br,I)

The emission spectra and stimulation spectra (excitation spectra of PSL) of $BaFCl:Eu^{2+}$ (BFC), $BaFBr:Eu^{2+}$ (BFB), and $BaFI:Eu^{2+}$ (BFI) are shown in Figure 26.[3] The emission spectra peak around 400 nm. The emission is due to the $5d \rightarrow 4f$ allowed transition of Eu^{2+} ions. The lifetimes of the emissions of BFB and BFI are shorter than 1 μs (see Table 4).

The mechanism of PSL in $BaFBr:Eu^{2+}$ was first proposed by Takahashi et al.[16] The proposed mechanism was initially controversial; however, continued experimental work

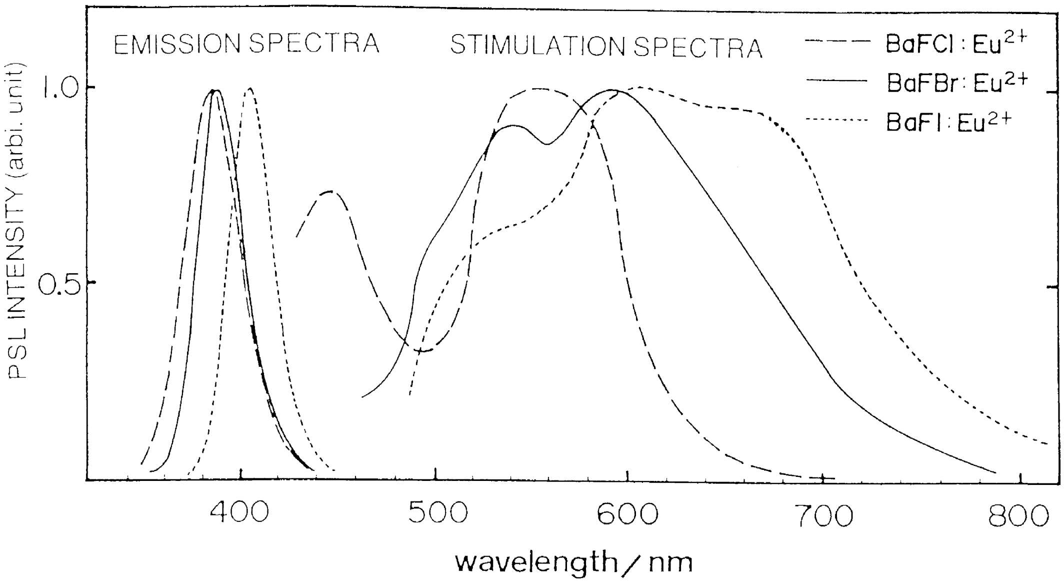

Figure 26 The emission and stimulation spectra of BaFCl:Eu^{2+}, BaFBr:Eu^{2+}, and BaFI:Eu^{2+}. (From Sonoda, M., Takano, M., Miyahara, J., and Kato, H., *Radiology*, 148, 833, 1983. With permission.)

by Takahashi and co-workers,[17] coupled with numerical simulations, confirmed all of the aspects of the model. The model is as follows:

BaFBr crystals have the tetragonal structure of PbFCl (P4/nmm; D^7_{4h}). Measurements of electron spin resonance (ESR) spectra revealed that F centers are formed by X-ray irradiation, and that there are two types of F centers, i.e., F(Br^-) and F(F^-) centers.[18] In a heavily X-rayed BaFBr:Eu^{2+} single crystal, the absorption spectrum due to F centers, the stimulation spectrum, the excitation spectrum of photostimulated photoconductivity (PSPC), and the fading spectrum of ESR signals all correspond well with each other. Here, the fading spectrum implies the spectrum which induces fading of the ESR signal intensity caused by F center absorption. The stimulation spectrum after the photoionization excitation by ultraviolet light is almost the same as that after X-ray excitation.

In the ultraviolet region, there is a broad absorption band at 270 nm due to the 4*f*-5*d* transition of Eu^{2+} ions. In the region shorter than 250 nm, the absorption spectrum, the excitation spectrum of photoconductivity, and the formation spectrum of PSL centers nearly the same manner in the shorter wavelengths (up to 200 nm) region. PSL centers are efficiently formed by the Eu^{2+} photoionization absorption at 190 nm.

BaFBr:Eu^{2+} phosphors prepared by firing in an oxidizing atmosphere show red line luminescence from Eu^{3+} ions, in addition to the violet Eu^{2+} luminescence. In these phosphors, the intensity of the Eu^{2+} luminescence decreases under strong irradiation by 337-nm nitrogen laser light, with a simultaneous increase in the intensity of the Eu^{3+}. After producing PSL by red light, both intensities return to the initial values.

PSL and PSPC intensities both decrease in the same manner with decreasing temperature below room temperature. This indicates that in the PSL process, electrons trapped at F centers return to Eu^{3+} ions via the conduction band, and using this, the energy levels of F(Br^-) and F(F^-) centers can be determined.

Figure 27 shows the energy level diagram and the PSL process in BaFBr:Eu^{2+}. By X-ray or ultraviolet light irradiation, Eu^{2+} ions are ionized and converted to Eu^{3+} ions either directly or by trapping holes, while electrons excited to the conduction band are trapped by F^+ centers (halogen ion vacancies) to form F centers. With green to red light irradiation

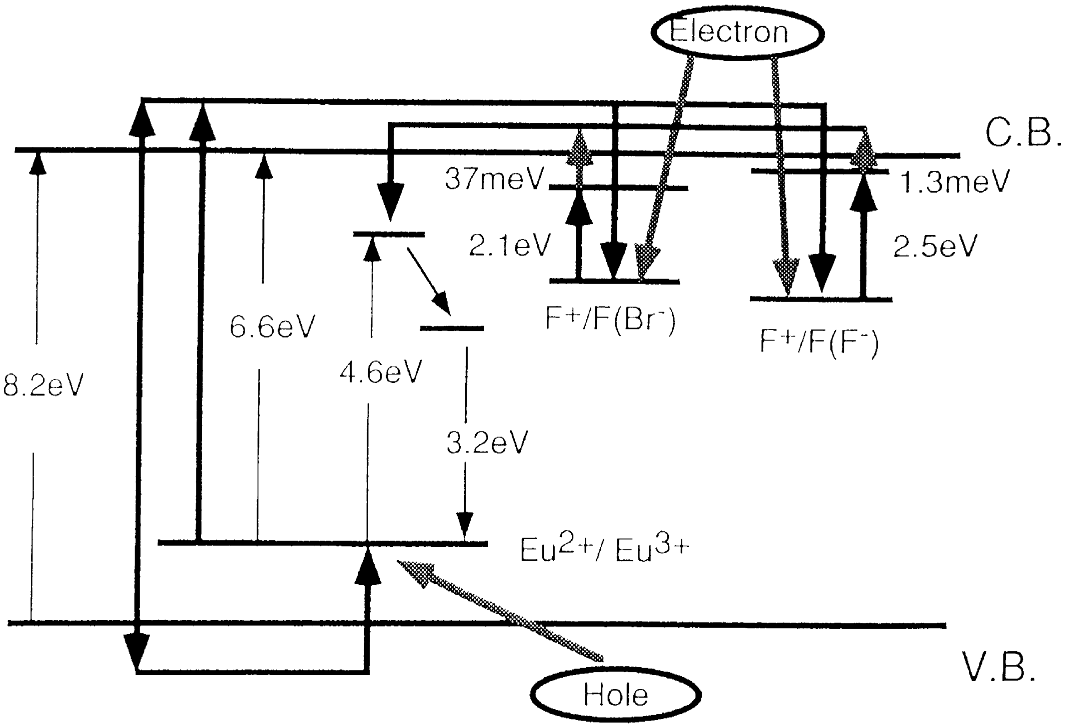

Figure 27 The energy level diagram and the PSL process in BaFBr:Eu^{2+}. (From Iwabuchi, Y., Mori, N., Takahashi, K., Matsuda, T., and Shionoya, S., *Jpn. J. Appl. Phys.*, 33, 178, 1994. With permission.)

to cause PSL, trapped electrons are released to the conduction band and return to Eu^{3+} ions, converting them to Eu^{2+} ions in an excited state; luminescence is produced by these ions.

This mechanism assumes essentially bimolecular kinetics for the PSL process. A numerical analysis of the dependence of PSL intensity on the intensity of the irradiating radiation on the basis of the bimolecular kinetics shows that linearity holds over an extended range under practical conditions.[17]

7.5.3 *Characteristics of the imaging plate IP*

The typical IP is composed of a support such as a polyethylenetelephtalate (PET) film, a phosphor layer where photostimulable phosphor particles are bound by organic polymers, and a surface protective layer consisting of a thin PET film or a fluoride polymer coating.

The lifetime of BFB is so short that it is possible to read an image of a large area with a high scanning density in a short period of time. By partially substituting iodine for bromine in BFB, more F^+ centers can be made by firing, which results in higher PSL intensity; in this case, both the emission spectrum and the stimulation spectrum shift to longer wavelength. For example, the stimulation spectrum of $BaFBr_{0.85}I_{0.15}:Eu^{2+}$, which is widely used in commercial IPs, matches the wavelengths of a He-Ne laser (633 nm) as well as that of visible semiconductor laser (about 680 nm) used in CR systems. In both cases, the phosphor emission can be separated efficiently from the laser light because their wavelengths are sufficiently different from each other.

When the IP is read out using a fixed amount of stimulation light energy, the dependence of the light emission on the irradiated dose of ionizing radiation is exactly linear over a range of more than $1{:}10^5$.

Fading is a phenomenon whereby PSL intensity decreases with the passage of time between its excitation by ionizing radiation and its stimulation by a laser light. This is caused by the thermal release or diffusion of trapped electrons and/or holes. In case of long exposure times to constant radiations, the linearity between the exposure time and the PSL intensity can be affected by fading. However, the linearity between the radiation dose and the PSL intensity within an IP is maintained, which makes it possible to measure the relative dose distribution quantitatively. Fading increases with passing time and rising temperature. It is also influenced by the wavelength and the energy of the reading light.

7.5.4 Radiographic image formation by means of the IP

The image quality of the IP is not determined solely by itself. It is influenced by the reader optical system, the reader electrical system, and the digital image processing system. Figure 28 shows the imaging steps and the factors governing the image quality in CR and RLG systems.[19]

The diffusion of the stimulating laser light in the IP extends the scanning aperture practically and decreases the sharpness of the system. On the other hand, the diffusion of the emitted light does not affect the sharpness. The noise is composed of the quantum noise of the absorbed ionizing radiations, the quantum noise of the emitted photons, and the structure noise of the IP. Fading causes the increase of the photon quantum noise only. Pixel sizes from 25 × 25 μm to 200 × 200 μm are available now, allowing the choice of the proper reader system. The IP can be used repeatedly since the residual energy of the absorbed ionizing radiation in it after being read can be erased by exposing it to a large dose of visible light. As the IP is highly sensitive to ionizing radiation, it is influenced by ambient natural radioactive elements and by cosmic rays. When reading the IP under high-sensitivity conditions, the plate should first be erased to remove the effects of radiation prior to imaging, especially if it is left in the dark for a long period. The use of a shield case made of lead is also effective for the improvement of the S/N ratio under long time exposure conditions, as is often the case with autoradiography.

CR and RLG systems have the following advantages:

1. With wider dynamic range and excellent linearity, more quantitative information is provided.
2. Radiation doses can be reduced. Especially in the field of autoradiography and transmission electron microscopy where intensifying screens are not used because of low resolution, higher speeds and lower detection limits compared with the conventional film method can be attained.
3. New methods of diagnosis or measurement can be developed.
4. The image data is obtained in digital form so that it can be easily processed, analyzed, stored, and transmitted.

CR and RLG systems have opened new fields of application for photostimulable phosphors and are being accepted widely; thus, a new era of PSL is just beginning.

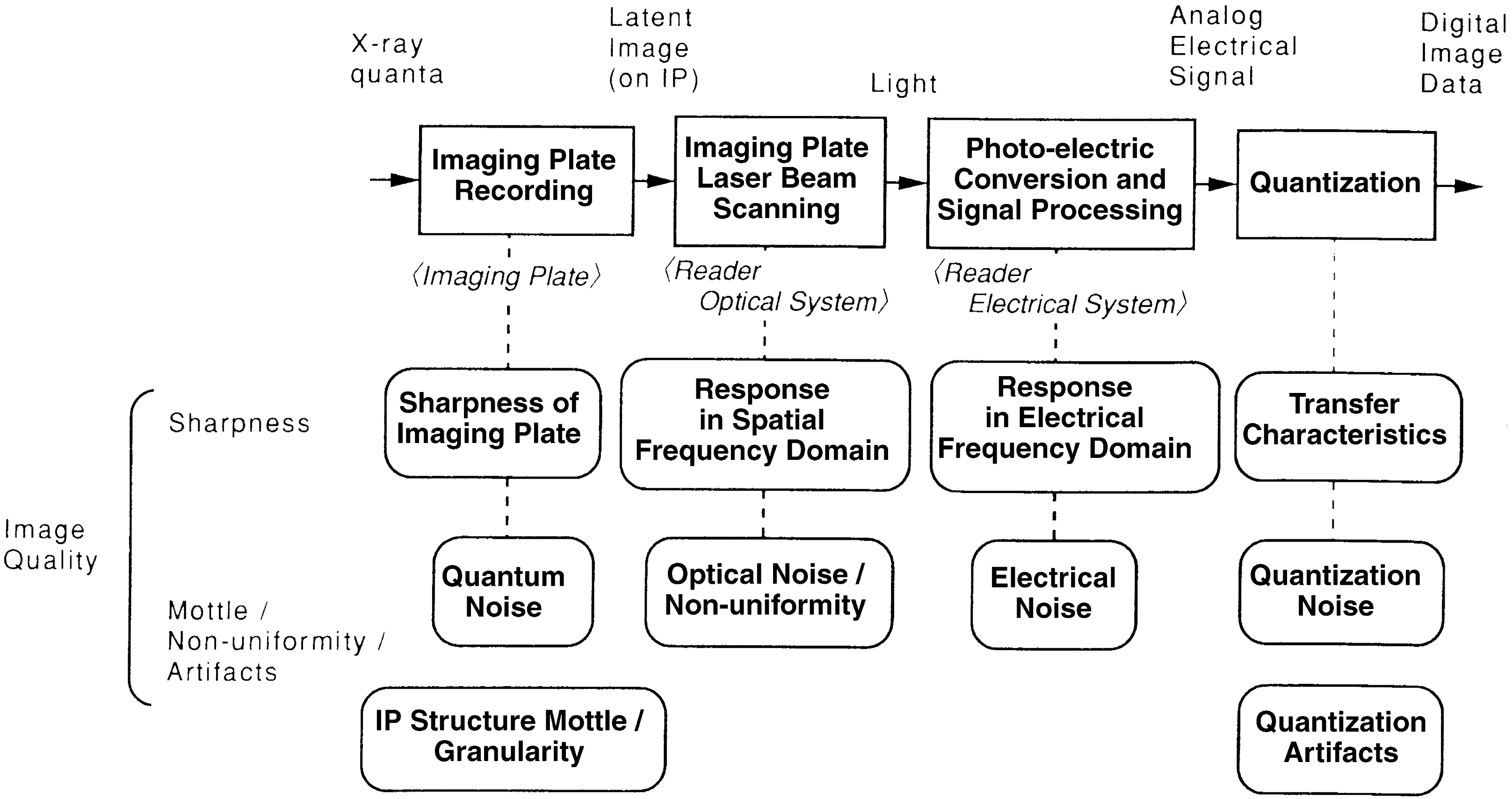
X-ray quanta
Latent Image (on IP)
Light
Analog Electrical Signal
Digital Image Data
Imaging Plate Recording
Imaging Plate Laser Beam Scanning
Photo-electric Conversion and Signal Processing
Quantization
⟨Imaging Plate⟩
⟨Reader Optical System⟩
⟨Reader Electrical System⟩
Image Quality
Sharpness
Sharpness of Imaging Plate
Response in Spatial Frequency Domain
Response in Electrical Frequency Domain
Transfer Characteristics
Mottle / Non-uniformity / Artifacts
Quantum Noise
Optical Noise / Non-uniformity
Electrical Noise
Quantization Noise
IP Structure Mottle / Granularity
Quantization Artifacts

Figure 28 The imaging steps and the factors governing the image quality of CR and RLG systems. (From Kato, H., *Computed Radiography*, Tateno, Y., Iimuma, T., and Takano, M., Eds., Springer-Verlag, Tokyo, 1987, chap. 3. With permission.)

References

1. Berg, O.E. and Kaiser, H.F., *J. Appl. Phys.*, 18, 343, 1947.
2. Kotera, N., Eguchi, S., Miyahara, J., Matsumoto, S., and Kato, H., Japanese Patent Disclosure (Kokai) 55-12145 (1980).
3. Sonoda, M., Takano, M., Miyahara, J., and Kato, H., *Radiology,* 148, 833, 1983.
4. Niimura, N., Karasawa, Y., Tanaka, I., Miyahara, J., Takahashi, K., Saito, H., Koizumu, S., and Hidaka, K., *Nucl. Instr. Meth. Phys. Res. A*, 349, 521, 1994.
5. Iwase, N., Tadaki, S., Hidaka, S., and Koshino, N., *J. Luminesc.*, 60&61, 618, 1994.
6. Hosoi, Y., Saito, H., Kojima, Y., Arakawa, S., and Takahashi, K., Mammographic imaging properties of an experimental SrFBr:Eu^{2+} imaging plate, in *Proc. SPIE 1651: Medical Imaging: Instrumentation,* The Soc. Photo-opt. Instr. Engineers, Washington, 1992, 236.
7. Meijerink, A. and Blasse, G., Properties of Eu^{2+}-activated bariumbromoborate, $Ba_2B_5O_9Br$-Eu^{2+}, a new storage phosphor for X-ray imaging, in *Proc. Lumin. Sci. and Techn. (ECS'88-24)*, Srtruck, C.W., DiBartolo, B. and Yen, W.M., Eds., Electrochem. Soc., Pennington, 1989, 279.
8. Meijerink, A. and Blasse, G., *Mater. Chem. Phys.*, 21, 261, 1989.
9. Sato, M., Tanaka, T., and Ohta, M., *J. Electrochem. Soc.*, 141, 1851, 1994.
10. Nanto, H., Murayama, K., Usuda, T., Taniguchi, S., and Takeuchi, N., Two-dimensional X-ray sensor utilizing photostimulated luminescence in europium-doped potassium chloride single crystals, in *Proc. SPIE 1736: X-ray Detector Physics and Applications*, Hoover, R.B., Ed., The Soc. Photo-opt. Instr. Engineers, Washington, 1993, 10.
11. Amitani, K. and Honda, S., Properties of RbX:Tl(X = Br,I) photostimulable phosphors, presented at the *174th Electrochem. Soc. Meeting*, Chicago, Oct. 9 to 14, 1988.
12. Kano, T., Takahashi, T., Okajima, K., Umetani, K., Ataka, S., Yokouchi, H., and Suuki, R., *Appl. Phys. Lett.*, 48, 1117, 1986.
13. Rabatin, J.G. and Brines, M., Thermal and photostimulated luminescence of LaOBr:Bi,Pr,Tb, presented at the *170th Electrochem. Soc. Meeting*, San Diego, Oct. 19 to 24, 1986.
14. Gasiot, J., Braunlich, P., and Fillard, J.P., *Appl. Phys. Lett.*, 40, 376, 1982.
15. Meijerrink, A., Schipper, W.J., and Blasse, G., *J. Phys. D: Appl. Phys.*, 24, 997, 1991.
16. Takahashi, K., Kohda, K., Miyahara, J., Kanemitsu, Y., Amitani, K., and Shionoya, S., *J. Luminesc.*, 31&32, 266, 1984.
17. Iwabuchi, Y., Mori, N., Takahashi, K., Matsuda, T., and Shionoya, S., *Jpn. J. Appl. Phys.*, 33, 178, 1994.
18. Takahashi, K., Miyahara, J., and Shibahara, Y., *J. Electrochem. Soc.*, 132, 1492, 1985.
19. Kato, H., Image reading: conversion to digital signals, in *Computed Radiography,* Tateno, Y., Iimuma, T., and Takano, M., Eds., Springer-Verlag, Tokyo, 1987, chap. 3.
20. Rey, J.M. and Bill, H., *J. Lumin.*, 97, 224, 2002.
21. Knitel, M.J., Hommels, B., Dorenbos, P., van Eijk, C.W.E., Berezovskaya, I., and Dotsenko V., Nucl. *Instr. Meth. Phys. Res. A*, 449, 595, 2000.
22. Leblans, P.J.R., Struye, L., and Williams, P., *New Needle Crystalline CR Detector*, in *Proc. SPIE 4320*, 2001, 59.
23. Jia, W., Yuan, H., Holmstrom, S., Liu, H., and Yen, W.M., *J. Lumin.*, 83–84, 465, 1999.
24. Karthikeyani, A. and Jagannathan, R., *J. Lumin.*, 86, 79, 2000.
25. Takahashi, K.,*J. Lumin.*, 100, 307, 2002.
26. Rowlands, J.A., *Phys. Med. Biol.* 47, R123, 2002.
27. Schweizer, S., *Phys. Stat. Sol.* (a), 187, 335, 2001.

chapter eight — sections one and two

Phosphors for vacuum fluorescent displays and field emission displays

Kiyoshi Morimoto and Shigeo Itoh

Contents

8.1 Vacuum Fluorescent Displays 667
  8.1.1 Structure of vacuum fluorescent display panels 668
    8.1.1.1 VFD structure 668
    8.1.1.2 Operation of VFDs 670
    8.1.1.3 Electrical and optical characteristics of VFDs 670
  8.1.2 Required phosphor characteristics 671
    8.1.2.1 Low-energy electron-excited phosphors 671
    8.1.2.2 Some characteristics required of phosphors 672
  8.1.3 Low-energy electron-excited phosphors 674
8.2 Field Emission Displays (FED) 681
  8.2.1 Structure of FED 681
  8.2.2 Phosphors for use in FED 682
    8.2.2.1 Requirements for phosphors for FEDs 682
    8.2.2.2 Phosphors for color FEDs 683
References 685

8.1 Vacuum Fluorescent Displays

The vacuum fluorescent display (VFD) was invented in Japan in 1965, and is now a practical display device.[1] In the beginning, there was the single-digit round tube, which was later developed into the multi-digit round tube and then into the flat multi-digit panel.[2] At first, these devices were used almost entirely in calculators, but now they have a wide range of applications, including audio and video equipment, household electronics, automobiles, office equipment, and instrumentation.[3]

VFD tubes operate in the same way as cathode-ray tubes (CRTs): electrons emitted from a cathode are accelerated and controlled so as to bombard an anode that is coated with a phosphor; excited by the electrons, the phosphor emits light (cathodoluminescence). The difference from cathode-ray tubes, however, is that the kinetic energy of the accelerated electrons is much smaller in VFD tubes. That is to say, the phosphors in CRTs are excited by electrons driven by an extremely high accelerating voltage, ranging from kilovolts to tens of kilovolts (i.e., a high-energy electron beam), whereas the phosphors in VFDs are excited by electrons driven by a low voltage of from about 10 to 100 V (i.e., a low-energy electron beam).

Because of charging and other reasons, the phosphors used in CRTs either do not luminesce at all under the low-energy electron beams characteristic of VFDs, or if they do luminesce, the obtained luminance is too low for practical application.

Accordingly, the phosphors used in VFDs must have characteristics that differ from phosphors excited by ordinary cathode rays. It would thus not be an exaggeration to say that the development of phosphors that can be excited by low-energy electron beams (low-energy electron beam phosphors) made VFDs practical and led to their present widespread application in many fields.[4]

8.1.1 Structure of vacuum fluorescent display panels

The VFDs currently manufactured and used in Japan and the rest of the world are based on VFD panels that employ glass substrates. Such panels became practical in 1972. Thus, in this section, the structure of these flat VFDs, unless specifically stated otherwise, are described.

8.1.1.1 VFD structure

The VFD, in principle, is one type of cathode-ray tube, similar to CRTs used in TVs. In these devices, accelerated electrons from a cathode bombard a phosphor, producing luminescence. However, unlike CRTs where the electron beam is constructed into a fine beam that is scanned over the phosphor layer from top to bottom so as to produce an image, in the VFD the electron beam is broadly diffused and the desired display is achieved by producing luminescence from phosphor layer segments irradiated selectively by the diffused beam.

The basic structure of a VFD, as shown in Figure 1, consists of filamentary cathodes, a grid (electrode for controlling and accelerating the electron beam), and an anode substrate (display electrodes, wiring, etc.) arranged in that order at specified distances. Leads and terminals are then attached, the assembly is covered with a front glass, exhausted and hermetically sealed to form a triode vacuum tube with multiple anodes and directly heated cathodes.

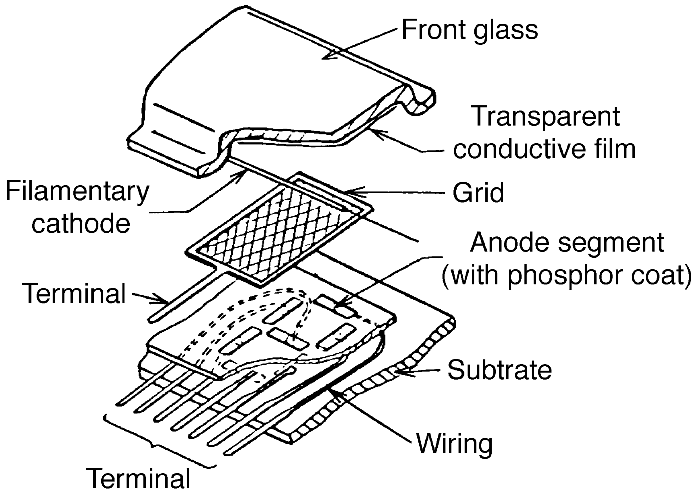

Figure 1 Basic structure of flat VFD.

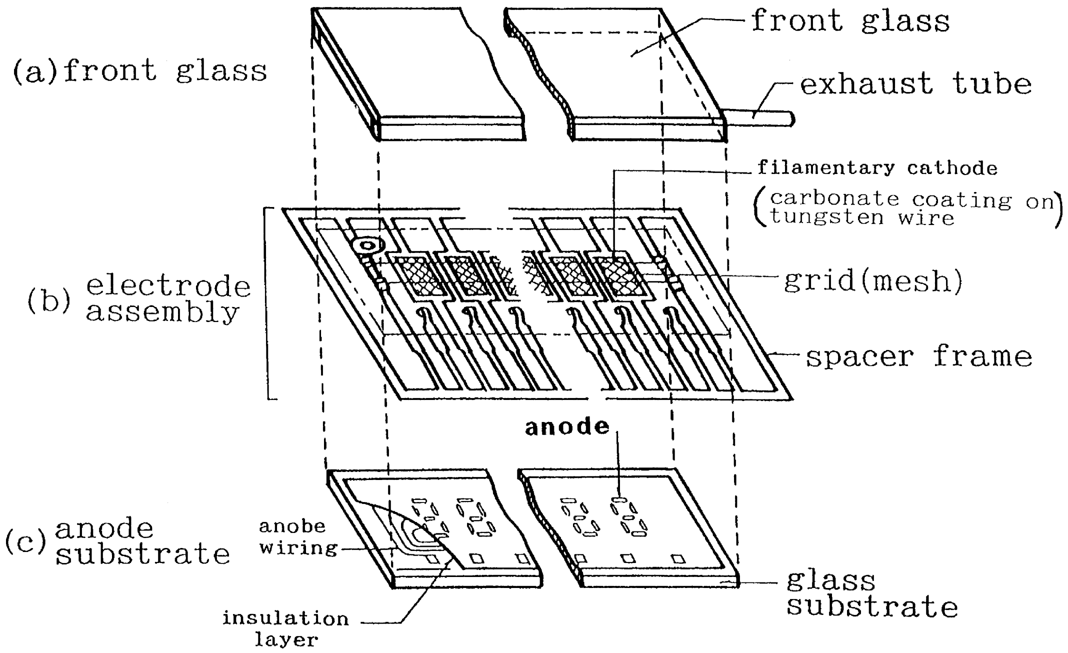
(a)front glass
front glass
exhaust tube
filamentary cathode
(carbonate coating on tungsten wire)
(b) electrode assembly
grid(mesh)
spacer frame
anode
(c) anode substrate
anobe wiring
insulation layer
glass substrate

Figure 2 Configuration of flat VFD.

The overall structure of the device is shown in more detail in Figure 2, where (a) is the front glass, (b) is the electrode assembly, and (c) is the wired and phosphor-coated anode substrate. Figure 3 shows the electrode unit.

The filamentary cathode is thin tungsten wire (with a diameter of 5 to 30 µm) covered with an electron-emitting material. The overall diameter of the filament is 15 to 50 µm so as not to obstruct the display. Usually, from one to ten of these filamentary cathodes are stretched across the display in parallel, depending on the height of the characters in the display and on the anode voltage across the electrode.

The grid is extremely fine mesh formed by photoetching thin metal plates (30 to 50 µm thick). They ensure that the display luminescence of the anode is emitted in the forward

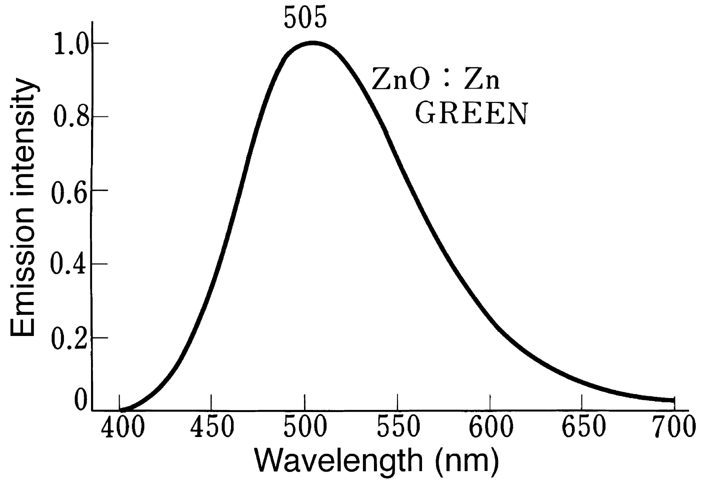

Figure 3 Emission spectrum of VFD using ZnO:Zn phosphor.

direction with good efficiency. There are two grid leadout arrangements. In one, there are separate leadouts for each digit position of the display; in the other, leadouts are shared by all digit positions. The grid leadout arrangement is dependent on the driving method.

The anode is divided into a number of segments that form the character, symbol, or diagram to be displayed. The desired display is obtained from the combination of these individual anode segments. The surface of each segment is covered with the ZnO:Zn phosphor, which luminesces at very low voltages.

The anode substrate is a glass plate on the surface of which anode wiring and terminals, an insulation layer with through-holes for connecting wiring and electrodes, the anodes, and the phosphor are successively formed by screen printing or some other method.

The electrode unit is mounted on the anode substrate. On the electrode unit is placed a front glass, whose inner surface is covered with a transparent conductive film (NESA film). These three elements are sealed with frit cement and the air within the assembly is exhausted. The surrounding frame is then cut off, the terminals are tinned with solder, edging is done, and the device is tested.

There are two major wiring methods. One is for dynamic driving, and so the anodes for each digit position of the display are connected in parallel to the common wiring; the other method is for static driving, so all of the anodes have separate leadouts.

8.1.1.2 *Operation of VFDs*

When a current flows in the filamentary cathode (see Figure 1), the temperature of the cathode rises to an average of about 600°C and thermoelectrons are released by the electron-emitting material on the cathode surface. In this state, if a positive voltage is applied to the anodes and the grid, the thermoelectrons emitted from the cathode are accelerated by the electric field generated between the anodes and grid on one side and the filamentary cathodes and transparent conductive film on the other. After passing through the grid, the electrons bombard the phosphor on the anodes. The phosphors excited by those electrons luminesce.

If the voltage applied to either the anodes or grid is zero or negative, the electrons do not reach the anode and luminescence does not occur. Using this fact, the figure to be displayed (numeral, character, etc.) can be displayed in the desired digit by applying a positive voltage simultaneously to the anode segments corresponding to the figure and to the grid corresponding to the digit position.

Even if the voltage is applied to anode segments of other digits, while the grid is applied with negative voltages (2 to 7 V), those anodes will not luminesce.

8.1.1.3 *Electrical and optical characteristics of VFDs*

The VFD characteristics include the cathode characteristics, the on characteristics, the cut-off characteristics, and the luminescence characteristics.

The cathodes of VFDs are designed to operate in the space-charge limited region, as are ordinary vacuum tubes. When the display is active (the on state), the voltages on the grid and on the anodes are about the same. Thus, the *luminance*, L (cd m^{-2}) in the on state is expressed as:

$$L \cong 3.2 E_p \cdot J_p \cdot D_u \cdot \eta \tag{1}$$

where E_p is the anode voltage (V), J_p is the anode current density (mA cm^{-2}), D_u is the duty cycle, and η is the luminous efficiency of the phosphor (lm W^{-1}).

The emission spectrum of green-emitting ZnO:Zn, the most representative of the low-energy electron-excited phosphors, is shown in Figure 3. The luminescence peak wavelength is 505 nm. The spectral distribution covers the entire visible region, from 400 to 700 nm.

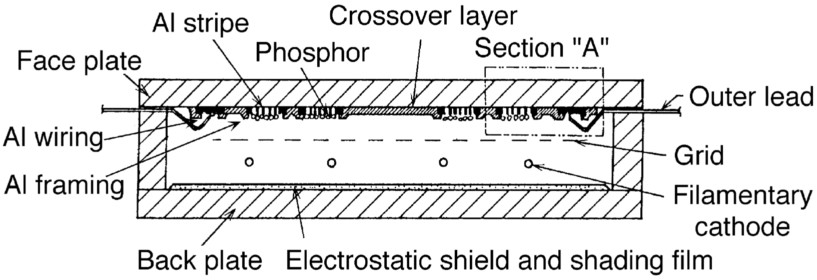

Figure 4 Cross-section of front luminous VFD.

The basic structure, operating principle, and characteristics of VFDs were described above. The other type of VFD is represented by the front luminous VFD (FLVFD),[5] in which the luminescence of the phosphor is observed through the phosphor, the anodes and the glass face plate (Figure 4), and which can display various types of diagrams, Japanese characters, and images as well as numerals, letters, and symbols.

8.1.2 Required phosphor characteristics

8.1.2.1 Low-energy electron-excited phosphors

The phosphors used in VFDs are usually called low-energy electron-excited phosphors. While there is not yet a clear definition for low-energy electron beams, such phosphors are generally used with electron beams of several hundred electron-volts or less.

The phosphors used in ordinary CRTs are excited by electron beams of thousands of electron-volts to tens of thousands of electron-volts, and the secondary electrons emitted from the phosphor surface cause a current flow. Present VFDs, however, must normally operate at accelerating voltages for which the ratio of secondary electrons emitted according to that principle (i.e., the secondary electron yield, δ) is less than 1.0.

If δ exceeds 1, anode segments may luminesce even without a signal voltage applied, thus causing display errors.

Furthermore, in the case of VFDs, the driver is most often an integrated circuit or LSI chip; thus, even when high-voltage resistant elements are used, for example, the voltage is about 100 V. These points lead to the conclusion that the voltage levels used in CRTs cannot be considered for use in VFDs.

When injected into a substance, low-energy electron beams of less than 100 eV or less excite mainly the valence electrons in the material (inter-band excitation or plasmon excitation), and immediately lose that energy. Accordingly, the penetration depth of the injected primary electrons is extremely shallow, about 10 Å as calculated by the well-known relationship for high-energy electron beams:

$$R = bV^n \tag{2}$$

where R is the penetration distance length (mm), V is the voltage (kV), and b and n are empirical values for the phosphor. This means that the excitation is limited to the phosphor surface only. In addition, few secondary electrons are emitted.[6]

The ratio of emitted secondary electrons to injected primary electrons is less than 1.0, so a negative charge is generated on the surface of ordinary phosphors (mostly near-insulators). That surface charge negates the accelerating electric field and thus prevents luminescence.

8.1.2.2 *Some characteristics required of phosphors*

Some of the characteristics required of the phosphors used in VFDs in actual practice are given.

1. *Conductivity to prevent charging of the phosphor surface.* For VFDs, the anode voltage is usually about 10 to 100 V, and the anode current is about 2 to 10 mA cm^{-2}. Thus, to suppress the voltage drop in the phosphor layer to 1.0 V (10%) or less, the resistance of the phosphor layer must be 500 Ω cm^{-2} or less. In this case, the layer thickness is usually about 30 μm (Figure 5).
2. *An essentially low emission threshold voltage.* Even if the phosphor has a low resistance, it will not be suitable if its emission threshold voltage is above 10 V, because it will have weak luminescence at low voltages. The emission threshold voltage should be less than 10 V, with 5 V being the normal. The threshold for ZnO:Zn phosphors is 2.2 V (Figure 6).
3. *Efficient luminescence by low-energy electron beam excitation without luminance saturation.* While highly efficient luminescence is naturally desirable, the electrons excite only the surface of phosphor particles in low-energy electron beam excitation; thus, the luminous efficiency is generally low (about 10 lm W^{-1} for ZnO:Zn). For this reason, the density of defects and luminescence centers on the surface is important. Also, phosphors for which the luminance saturates with voltage (current) are not suitable for use with dynamic driving or in devices mounted in automobiles and other environments in which the ambient illumination is bright (Figure 7).
4. *Stability against heat treatments during the VFD manufacturing process.* During VFD manufacture, processes such as baking and sealing unavoidably expose the phosphors to high-temperature atmospheres of 500°C or higher for several tens of minutes. Phosphors with properties that are degraded by such heat treatments are unsuitable (Figure 8).
5. *Long lifetime under low-energy electron beam excitation.* Even some phosphors that do not deteriorate under high-energy electron beam excitation exhibit remarkable deterioration in lifetime testing under low-energy electron beam excitation (Figure 9).
6. *Low-level release of harmful substances*, as in poisonous oxide cathodes.

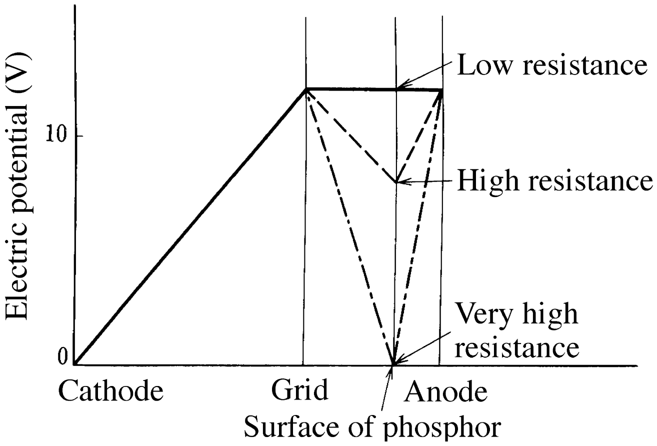

Figure 5 Dependence of phosphor surface electric potential on resistance of phosphor layer.

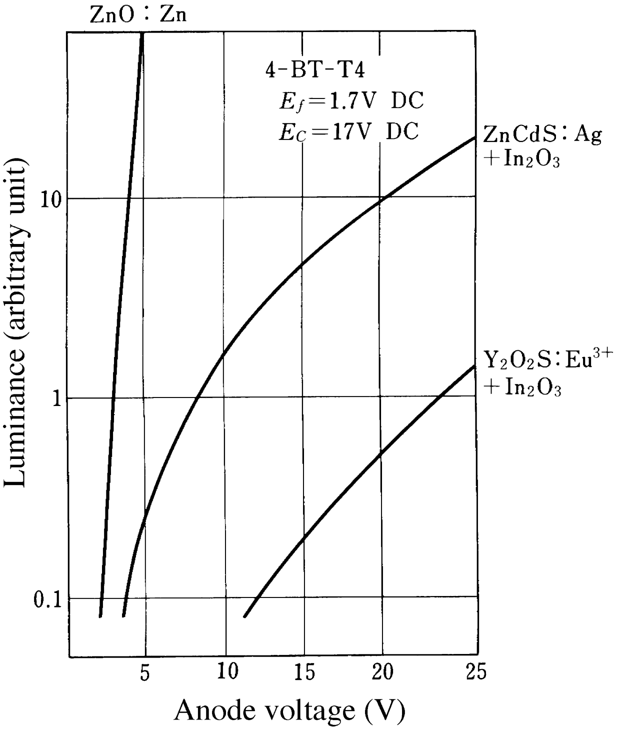

Figure 6 Characteristics of emission threshold voltage of phosphors.

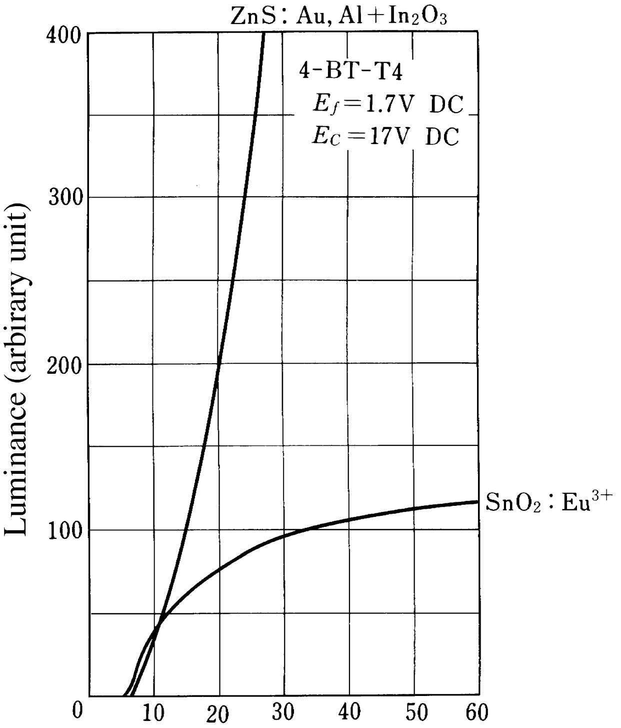

Figure 7 Characteristics of luminance saturation in phosphors.

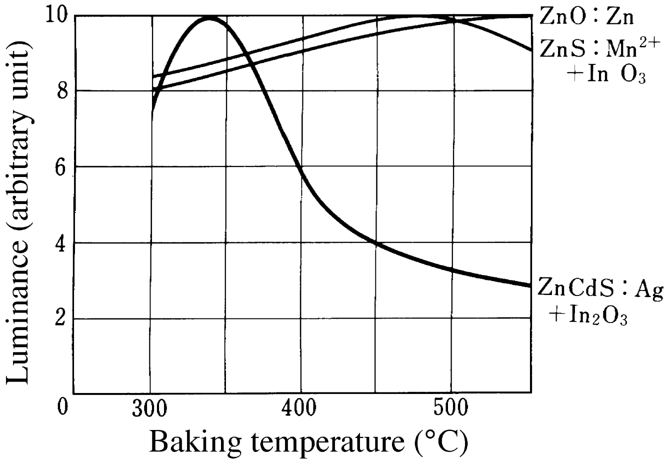

Figure 8 Luminance degradation by heat treatment.

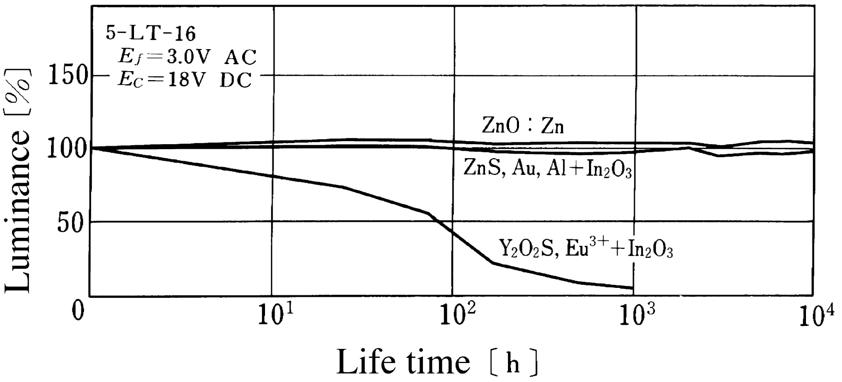

Figure 9 Luminance deterioration in lifetime testing.

8.1.3 Low-energy electron-excited phosphors

With the expansion of the application of users, many types of low voltage phosphors have developed. To obtain the high efficiency of low energy electron excitation, low voltage phosphor must have moderate conductivity. This conductivity can be achieved in the following three ways.

1. Use a conductive material for the phosphor base,
   Examples : ZnO:Zn, SnO_2:Eu^{3+} [7], $ZnGa_2O_4$, $SrTiO_3$:Pr,Al, GaN:Zn.
2. Mix a conductive material in with a phosphor (conductive mixture type phosphors)[8],
   Examples : ZnS:Ag + In_2O_3, ZnS:Cu + ZnO, Y_2O_2S:Eu^{3+} + SnO_2.
3. Dope conventional phosphors with impurities to make them conductive (doped type phosphors)[9].
   Examples : ZnS:Ag,Cu,Al.

Of these three type of phosphors, type1 and 2 are most used at present.

The characteristics of representative phosphors for low-energy electron-excited phosphors are described bellow.

1) ZnO:Zn

As described above, green –emitting ZnO:Zn phosphors have been mainly used in VFD devices, and their green luminescence was well known as a representative image of VFDs. As ZnO:Zn phosphor was obtained by baking ZnO in a reducing atmosphere without activators, it is written down ZnO:Zn customarily. Baking in a reducing atmosphere makes about 5-15 ppm of excess Zn and the amount of them is proportional to green luminescence, it is thought that the luminescent is related to the interstitial Zn or vacancy O.

2) Sulfide phosphors

With the expansion of usage and application field of VFDs, demand for multicolor displays has surged. As the first stage multicolor low voltage phosphors, sulfide phosphors, such as ZnS:Cu, Al and (Zn,Cd)S:Ag, Cl phosphors with fine powder of In_2O_3 to provide adequate conductivity were used due to the excellent luminous efficiency, wide luminescent spectra and quick response time. However, it is found that the sulfide phosphors could degrade the electron emissivity of the oxide cathode in certain operating condition, there is some restriction to use for color VFDs. Moreover, phosphors contain Cd shall never been used any longer because of the environmental problem.

It is reported that the surface of sulfide phosphors is decomposed by electron irradiation especially it depends on the existence of H_2O by the result of the mass analysis, SEM observation, AES and ESCA analysis[10]. Figure 10 shows the SEM images of ZnS:Zn and $(Zn_{0.22}Cd_{0.78})S$:Ag,Cl before and after the electron irradiation with accelerated condition.

Unlike to CRTs, the electrons from oxide coated filaments directly excites the phosphor surface without metal back coat film which is only a few *mm* away from filments in case of VFDs, the decomposed materials and gases of the phosphor surface causes the deterioration of cathode filaments.

3) $ZnGa_2O_4$ and $ZnGa_2O_4$:Mn phosphor

The $ZnGa_2O_4$ phosphor[11] for blue luminescence and $ZnGa_2O_4$:Mn phosphor[12] for green were investigated for the low voltage phosphors of VFDs.

Figure 11 shows the SEM images of $ZnGa_2O_4$ observed after the irradiation under accelerated condition. In Figure 11, no appreciable change was observed on the $ZnGa_2O_4$ phosphor surface. At the same time, AES analysis was made for the surface of phosphor and the indium tin oxide (ITO) films located close to phosphor to catch the evaporated materials from the $ZnGa_2O_4$ phosphor under the electron irradiation. We could not find any significant change on the surface of the $ZnGa_2O_4$ phosphor and the ITO films before and after the electron irradiation under accelerated condition. It was expected that toughness of the condition of electron irradiation in VFDs, compared to sulfide phosphors.

$ZnGa_2O_4$ phosphor is a compound oxide of ZnO and Ga_2O_3, crystallizing in the spinel structure, and its optical band gap is about 4.4 eV. This phosphor shows blue luminescence with a spectral peak at 470 nm and a chromaticity at $X = 0.170$ and $Y = 0.130$ and the color is somewhat whitish.

The dependence of luminous intensity on the anode voltage is shown in Figure 12 and the dependence on the anode current is shown in Figure 13 The luminous intensity is still lower than that of the ZnS:Cl, but a luminance of about 800 cd/m^2 was obtained at an anode voltage of 30 V. In Figure 13 saturating tendency is observed. It is probably due to insufficient concentration of the luminescence center of this phosphor specimen.

Figure 14 shows the temperature quenching of the luminous intensity of the $ZnGa_2O_4$ phosphor. The value of the intensity is normalized by the value at an ambient temperature of 25 degree Celsius. The self-activated ZnS:Cu,Al shows a luminance decrease down to 45% at 85 degree Celsius., and to nearly 0% at 150 degree Celsius. On the other hand, the $ZnGa_2O_4$ phosphor keeps better condition and excellent resistance to the ambient temper-

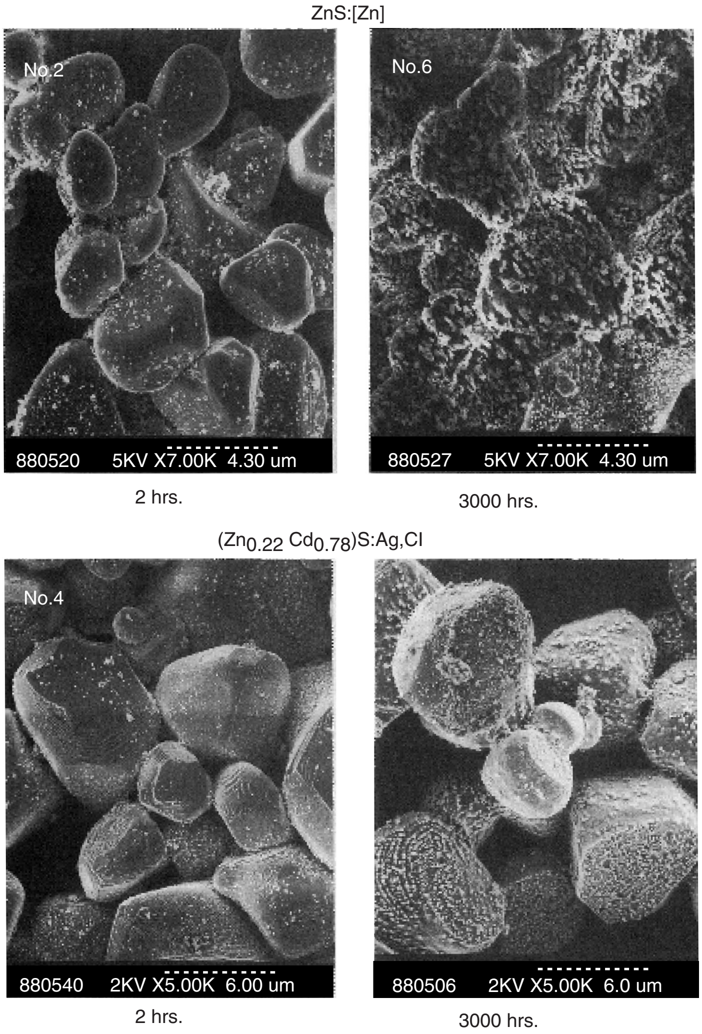
ZnS:[Zn]
No.2
880520 5KV X7.00K 4.30 um
No.6
880527 5KV X7.00K 4.30 um
2 hrs.
3000 hrs.
(Zn0.22 Cd0.78)S:Ag,Cl
No.4
880540 2KV X5.00K 6.00 um
880506 2KV X5.00K 6.0 um
2 hrs.
3000 hrs.

Figure 10 The SEM images of ZnS:Zn and $(Zn_{0.22}Cd_{0.78})$S:Ag, Cl before and after the electron irradiation under accelerated condition.

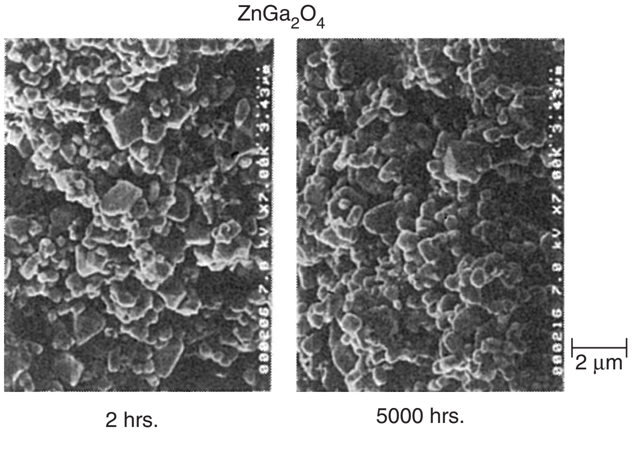
ZnGa2O4
2 μm
2 hrs.
5000 hrs.

Figure 11 SEM images of $ZnGa_2O_4$ observed after the irradiation under accelerated condition.

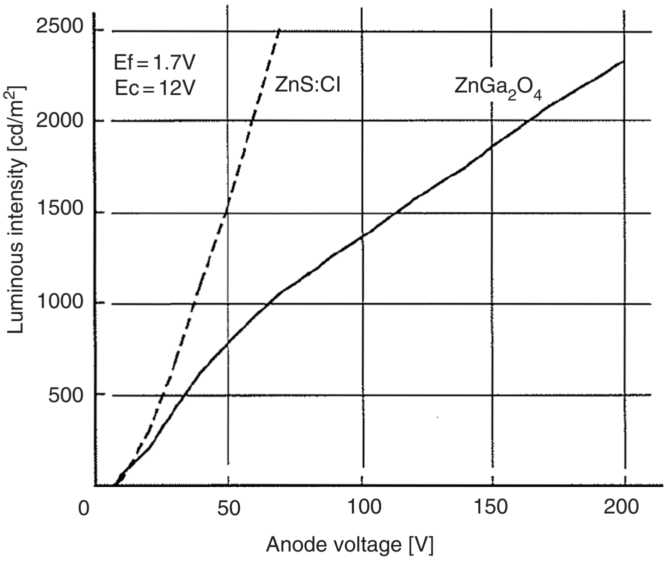

Figure 12 The dependence of luminous intensity on the anode voltage.

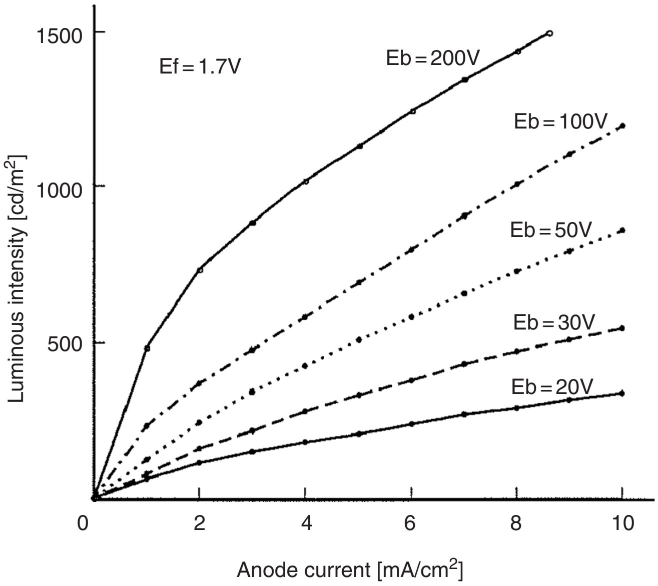

Figure 13 The dependence of luminous intensity on the anode current.

ature. This favorable resistance to temperature shows that the $ZnGa_2O_4$ phosphor is suitable for the automotive applications.

$ZnGa_2O_4$:Mn phosphor was investigated to green phosphor for VFDs. Figure 15 shows a typical emission spectrum of the $ZnGa_2O_4$:Mn phosphor together with a spectrum of the ZnS:Cu,Al green phosphor for comparison. The smaller spectral half width for $ZnGa_2O_4$:Mn phosphor indicates its better green colorimetric purity and the color coordinate of X = 0.105 and Y = 0.720 for VFDs than ZnS:Cu,Al.

Figure 16 shows the luminous intensity dependence on the anode voltage.

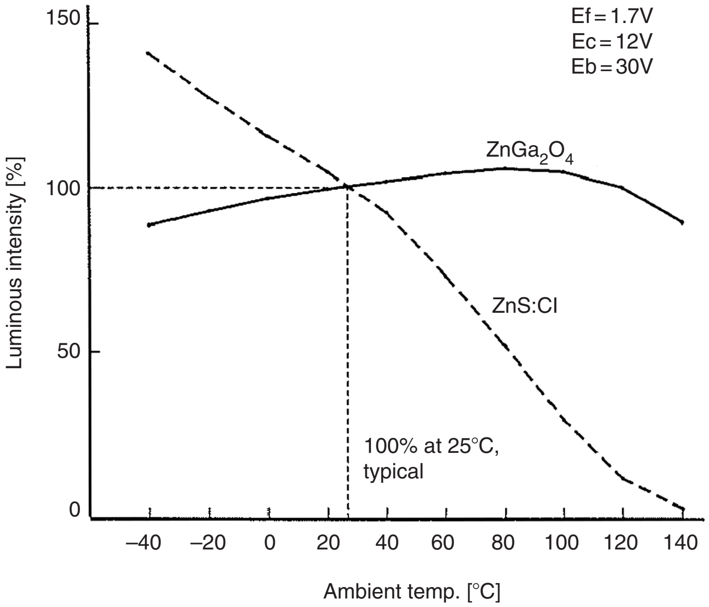

Figure 14 Luminous dependence on ambient temperature of the VFD.

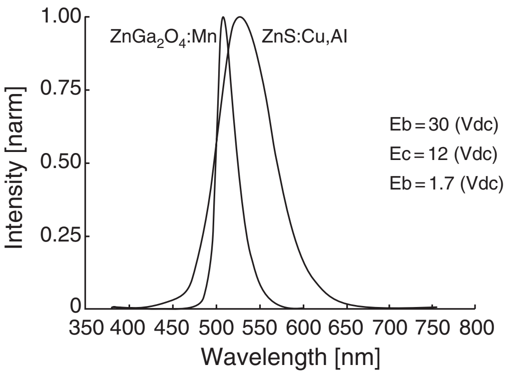

Figure 15 Typical cathodoluminescent spectrum of the $ZnGa_2O_4$:Mn phosphor.

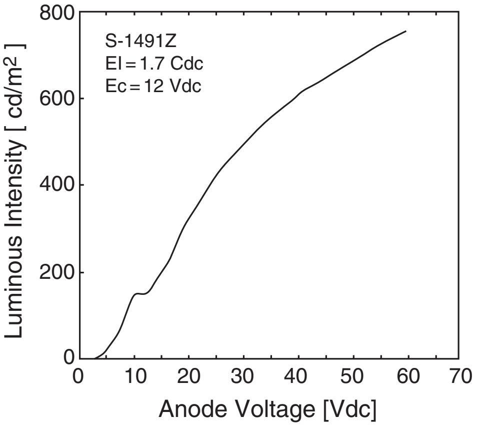

Figure 16 Dependence of luminous intensity on anode voltage.

4) SrTiO$_3$:Pr^{3+}

A new red phosphor, SrTiO$_3$:Pr^{3+}, was developed for low voltage phosphor[13]. This phosphor was made of SrTiO$_3$ which is well known as a dielectric material and has perovskite structure, with doping Pr as red luminescent center added with Al. The Al-addition effect for improving the luminescent efficiency is the main characteristic of this phosphor. Figure 17 shows images of SEM of an Al-added SrTiO$_3$:Pr^{3+} compared with those of an Al-free sample. Little difference is found in the mean particle size, which is 1-2 μm and with no apparent coalescence of particles. Crystal habit is developed more in the Al-added sample.

The effect of Al addition on the photoluminescence intensity, and VFD luminance vs DC anode Voltage are shown in Figure 18 and 19 respectively.

Apparently, SrTiO$_3$:Pr^{3+} scarcely emits luminescence when Al ions are not added, while the luminescence efficiency increase drastically with the addition of Al. A samples with 17 mol% Al(OH)$_3$ which is adding Al compound in the preparation process shows a luminance of 800 cd/m^2 at 50 V. CIE color coordinates are shown in Figure 20 together with the color coordinates of other red phosphors. From Figure 20, it is clear that the SrTiO$_3$:Pr^{3+} phosphor has an excellent color purity as low-voltage phosphor emitting red light.

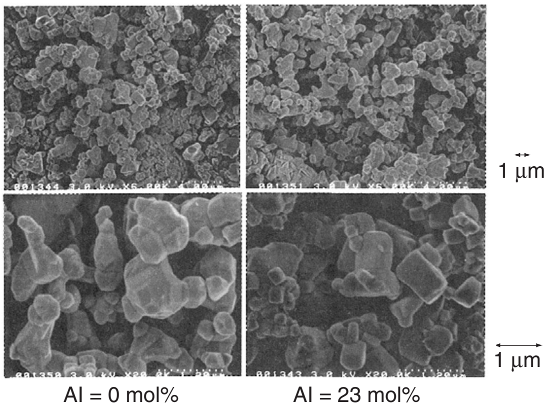

Figure 17 SEM images of an Al-added SrTiO$_3$:Pr^{3+} compared with those of an Al-free sample.

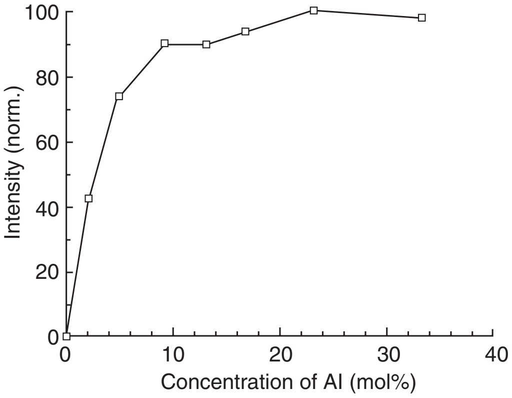

Figure 18 Photoluminescence intensity against a nominal Al concentration of SrTiO$_3$:Pr^{3+}.

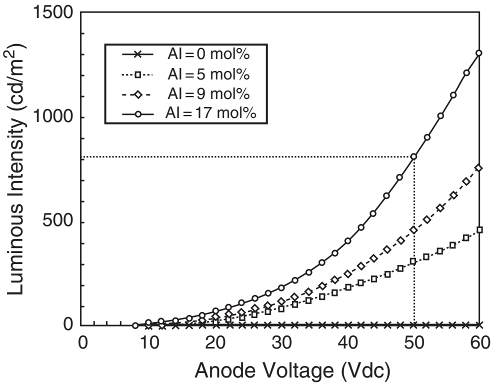

Figure 19 Luminance of VFDs mounted with $SrTiO_3$:Pr^{3+} as a function of the anode voltage. Samples with different Al concentration were used.

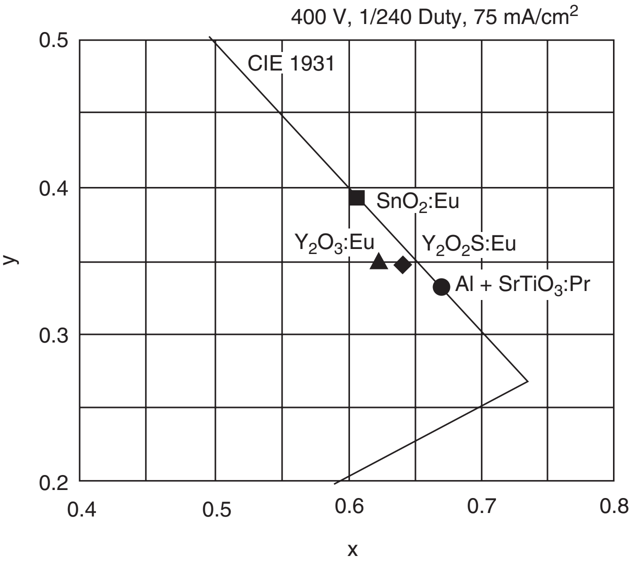

Figure 20 CIE color coordinates of $SrTiO_3$:Pr^{3+} and conventional red phosphors.

5) GaN:Zn

Blue-emitting phosphors, GaN:Zn for VFDs have developed[14]. Figure 21 shows particle shapes of a GaN:Zn phosphor observed by SEM. The luminous efficiency and luminance of GaN:Zn phosphor was improved by control of a luminescence spectrum by a change in Zn concentration.

Figure 22 shows the luminance of the VFDs, which use GaN:Zn phosphors, against the anode voltage. In this figure, a GaN:Zn phosphor and a conventional blue phosphor $ZnGa_2O_4$ are compared. The VFD luminance at 50Vdc anode voltage is 650 cd/m^2. As shown by this result, the luminance of GaN:Zn has a nearly linear voltage dependence, which is better than that of $ZnGa_2O_4$. Also for the current dependence, the luminance of GaN:Zn has a good linearity. The GaN:Zn phosphor has an advantage of relatively small luminance saturation against the anode voltage and current.

Figure 23 shows the results of luminance lifetime tests for VFDs employing GaN:Zn phosphors. It is found that the luminance of GaN:Zn is maintained quite well . As a result. GaN:Zn phosphor has come close to practical usage for VFDs.

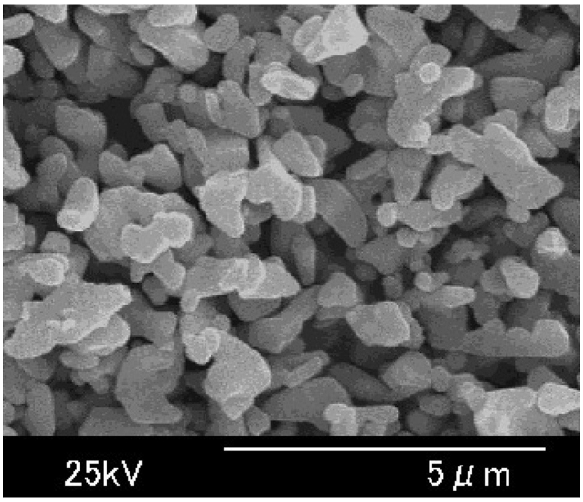

Figure 21 A SEM image of GaN:Zn phosphor.

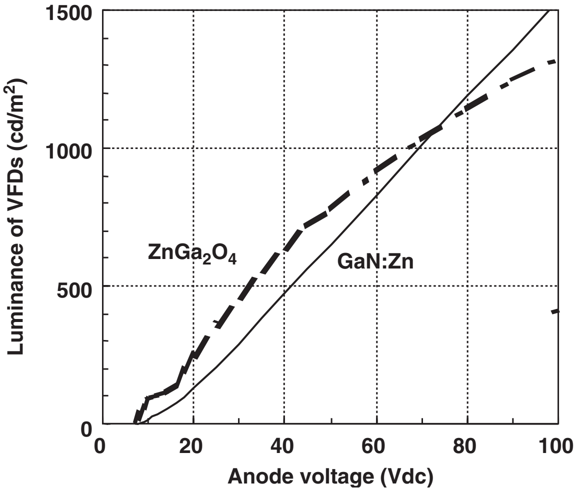

Figure 22 Luminance of VFDs against the anode voltage. Phosphor samples are GaN:Zn and $ZnGa_2O_4$.

8.2 Field Emission Displays (FED)

8.2.1 Structure of FED

Field emission displays (FED) are drawing attentions as one of the most promising flat panel displays. Currently, the development stage of Spindt-type FEDs with Mo emitter is close to an end. The mono-color Spindt-type FEDs are being supplied to the market, also the color FEDs are ready to mass production. The other electron sources of the FED including nano-carbon materials are now being actively developed. FED is also expected as a low power consumed display device, because the power, in principle, is consuming at the light emitting part only. FEDs will be developed and used for the applications from small, medium size panels to large-size TVs.

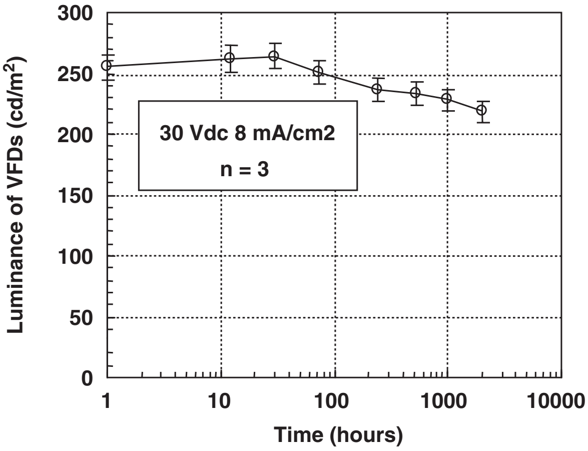

Figure 23 Luminance longevity characteristics of VFDs with GaN:Zn phosphors.

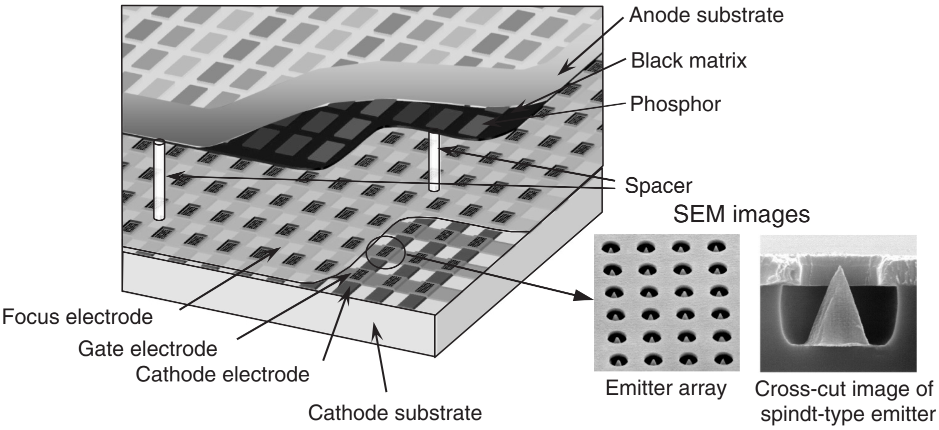
Anode substrate
Black matrix
Phosphor
Spacer
SEM images
Focus electrode
Gate electrode
Cathode electrode
Cathode substrate
Emitter array
Cross-cut image of
spindt-type emitter

Figure 24 The typical structure of Spindt Type Color FED.

Figure 24 shows the typical structure of Spindt Type Color FED [15,16].

Figure 25 shows the photographs of Spindt –type 14.4 inch-SVGA color FED panel and Table 1 shows the property of it. In this FED Y_2O_3:Eu was used for red, $ZnGa_2O_4$:Mn for green and Y_2SiO_5:Ce for blue.

8.2.2 Phosphrs for use in FED

8.2.2.1 Requirements for phosphors for FEDs

Phosphor for low voltage FEDs must satisfy the following requirements[17].

i. High luminance under anode voltage is less than 10 kV, anode current density is a few mA/cm².
ii. Less decomposition and evolution of gases, substances which increases the work function of emitters.
iii. Small temperature quenching under high current density.
iv. Quick response.
v. Fine and well-dispersed grains for high-resolution screens.
vi. Stable in the heat treatment of the panel manufacturing process.

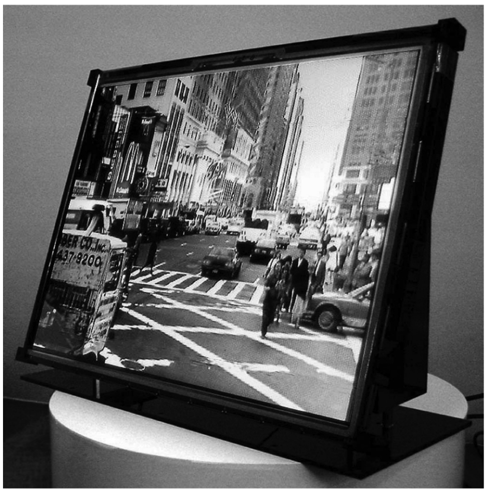

Figure 25 The photographs of Spindt –type 14.4 inch-SVGA color FED panel.

Table 1 property of the Spindt –type 14.4 inch-SVGA color FED panel

Panel size (mm)	311.3 (H) × 242 (V)
Screen size (mm)	292.80 (H) × 219.60 (V)
Pixel format	800 (RGB) × 600
Pixel pitch (mm)	0.122 (RGB) × 0.366
Panel gap (mm)	0.6
Panel thickness (mm)	2.8
Luminance (cd/m^2)	500

Table 2 Phosphors for Color FEDs

Color	Phosphor	Luminous efficiency η (lm/W)*	CIE chromaticity		Response (μs)	
			x	y	Rise-up	Remainig luminance
red	$SrTiO_3$:Pr	0.4	0.670	0.329	105	200
	Y_2O_3:Eu	0.7	0.60	0.371	273	2000
	Y_2O_2S:Eu	0.57	0.616	0.368		900
Green	$Zn(Ga,Al)_2O_4$:Mn	1.2	0.118	0.745	700	9000
	$Y_3(Al,Ga)_5O_{12}$:Tb	0.7	0.354	0.553	650	6500
	Y_2SiO_5:Tb	1.1	0.333	0.582	400	3900
	ZnS:Cu,Al	2.6	0.301	0.614	27	35
blue	Y_2SiO_5:Ce	0.4	0.159	0.118	2>	2>
	$ZnGa_2O_4$	0.15	0.175	0.186	800	1200
	ZnS:Ag,Cl	0.75	0.145	0.081	28	34
	GaN:Zn	0.20	0.166	0.126	5	5

8.2.2.2 Phosphors for color FEDs

Table 2 shows the luminous efficiency and chromaticity coordinate of phosphors having high possibility to be used for color FEDs. The response time of luminescence is expressed by the rise time (t_r) of the luminance when the pulsed voltage is applied to the anode, and the fall time (t_f) after the applied voltage is turned off. This table includes $ZnGa_2O_4$[11],

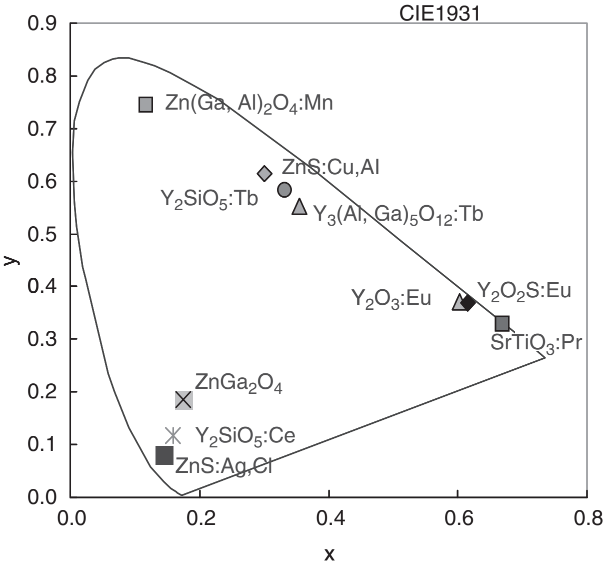

Figure 26 CIE color coordinates of phosphors.

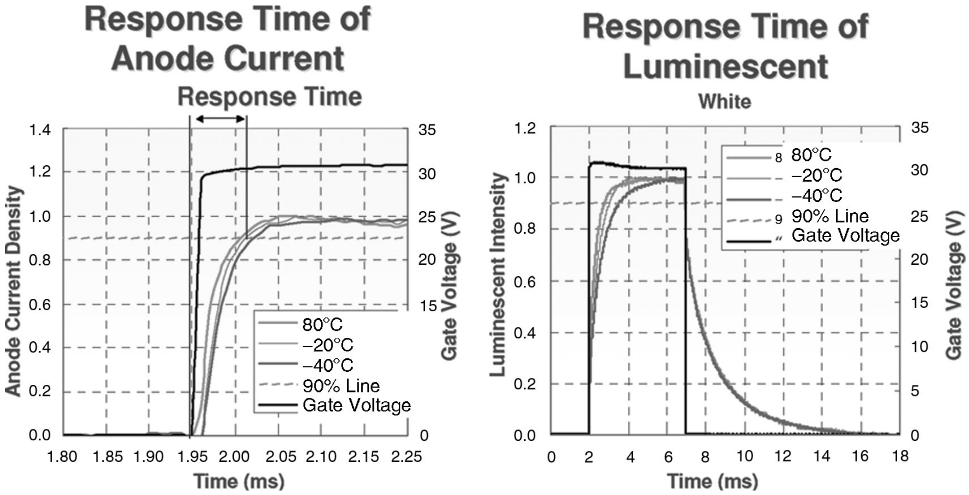

Figure 27 Response time vs. Temperature.

ZnGa$_2$O$_4$:Mn[12], SrTiO$_3$:Pr[13] and GaN[14] developed by authors. These phosphors are of low resistance and get cathodoluminescence in the low voltage excitement.

From the result of the excitation depth by low voltage electron beam, the synthesis method and condition of phosphors are being improved in consideration of the surface status and optimum luminescent center of low voltage phosphors. But the luminous efficiency of these phosphors decrease remarkably with an increase in the current density. In other words, high current density leads to unnecessary power consumption, inducing the decomposition of phosphor. Figure 26 shows the CIE color coordinates of phosphors in Table 2 and Figure 27 shows Response time of anode current and luminescence vs. Temperature of 14.4 inch-SVGA color FED panel. It shows that FED can image high speed moving picture.

References

1. Ohkubo, M., Japanese Patent Publication (Kokoku) 45-20223 (1970).
2. Morimoto, K., *Denshi Tenbou*, 11-9, 34-38, 1974 (in Japanese).
3. Morimoto, K. and Pykosz, T.L., Trend in vacuum fluorescent display, in *Electronic Display and Information Systems and On-board Electronics*, P103, 820264, 1982, 69.
4. Morimoto, K., Multi-Color Fluorescent Display, in *Tech. Digest, Jpn. Soc. Prom. Sci., 125th Committee, 90th Meeting, Proc.*, No. 341, 21-27, 1979 (in Japanese).
5. Morimoto, K. and Dorris, J.M., Front luminous vacuum fluorescent display, in *An Update on Automotive Electronic Displays and Information Systems*, P123, 830044, 1983, 67.
6. Kukimoto, H., in *Hikaribussei Handobukku*, Shionoya, S., Toyozawa, Y., Koda, T., and Kukimoto, H., Eds. Asaka syoten, March 1984, 511 (in Japanese).
7. Matsuoka, T., Nitta, T., Kasahara, Y., Tsuchiya, M., and Hayakawa, K., The preparation and low energy electron (LEE) excitation of SnO_2:Eu powder phosphor, in J. Electrochem. Soc.,125, 1,1978.
8. Kagami, A., Mimura, Y., Narita, K., and Kanda, K., Development of low energy cathode ray phosphors, in *Tech. Digest, Jpn. Soc. Prom. Sci., 125th Committee, 90th Meeting, Proc.*, No.340, 13-20, 1979 (in Japanese).
9. Nakayama, T. and Kukimoto, H., *Tech. Digest, JSAP, Div., Solid State Phys. Apr., Meeting, 375*, 17, 1978 (in Japanese).
10. Itoh, S., Kimizuka, T., and Tonegawa, T., "Degradation Mechanism for Low Voltage Cathodoluminescence of Sulfide Phosphors" J. Electrochem. Soc., Vol. 136, No. 6, June (1989) pp. 1819–1823.
11. Itoh, S., Toki, H., Sato, Y., Morimoto, K., and Kishino, T., "The $ZnGa_2O_4$ Phosphor for Low-Voltage Blue Cathodoluminescence" J. Electrochem. Soc., Vol. 138, No. 5, May 1991, pp. 1509–1512.
12. Toki, T., Kataoka, H., and Itoh, S., "$ZnGa_2O_4$:Mn Green Cathodoluminescent Phosphor for VFDs" *Technical Digest of Japan Display'92*, 1992, pp. 421–423.
13. Itoh, S., Toki, H., Tamura, K. and Kataoka, F., "A New Red-Emitting Phosphor, $SrTiO_3$:Pr^{3+} for Low-Voltage Electron Excitation", Jpn. J. Appl. Phys. Vol. 38 (1999) Part 1, No. 11, Nov. 1999, pp. 6387–6391.
14. Sato, Y., Takahashi, H., Tamaki, H., and Kameshima, M., "Luminescence Properties of a Blue Phosphor, GaN:Zn for VFDs" *Proceedings of The Ninth International Display Workshops (IDW'02)*, 2002, pp. 951–954.
15. Itoh, S., Tanaka, M., Tonegawa, T., Obara, Y., Naito, Y., Niiyama, T., Kobayashi, H., Sato, Y., Toriumi, M., Takeya, Y., Taniguchi, M., Namikawa, M., Yamaura, T. and Kawasaki, H., *Proceedings of the IDW'04*, Niigata, 2004, pp. 1189–1192.
16. Itoh, S., and Tanaka, M., "Current Status of Field-Emission Displays" PROCEEDINGS OF THE IEEE, Vol. 90, No. 4, April, 2002, pp. 514–520.
17. Itoh, S., Toki, H., Kataoka, F., Tamura, K., and Sato, Y.,: Phosphor for Full-Color Low-Voltage FEDs", Extended Abstracts of The Third International Conference on the Science and Technology of Display Phosphors, 1997, pp. 275–278.

chapter nine — section one

Electroluminescence materials

Masaru Yoshida, Akiyoshi Mikami, Toshio Inoguchi, and Noboru Miura

Contents

9.1 Inorganic electroluminescence materials 687
  9.1.1 Introduction....687
  9.1.2 Thin-film type....688
    9.1.2.1 Device structure....688
    9.1.2.2 Material requirements for the constituent layers 689
    9.1.2.3 Deposition methods for the constitutional layers 692
    9.1.2.4 Characteristics....694
    9.1.2.5 Recent developments in EL displays....699
  9.1.3 Thick-film-dielectric electroluminescent (TDEL) displays....705
References....706

9.1 Inorganic electroluminescence materials

9.1.1 Introduction

The high-field electroluminescence (EL) phenomenon was discovered by Destriau in 1936.[1] Light emission was observed from ZnS phosphor powder dispersed in castor oil and sandwiched between two electrodes when a high AC voltage was applied. Until 1950, when transparent electrically conductive films made of SnO_2 were developed, no effort was made to develop practical devices using this phenomenon. With the use of these SnO_2 transparent conductive films, AC powder EL devices (commercial name, Panelite) were developed by Sylvania. This triggered worldwide research and development on EL devices.

During the period from the latter half of the 1950s to the first half of the 1960s, basic studies on AC powder EL devices were actively carried out, aiming at flat light sources for wall illumination. However, these EL devices exhibited insufficient luminance and stability for practical use. The lifetime, which is defined as the operating time over which the luminance decreases to one half of the initial value, remained in the range of a few hundred to a thousand hours. In the mid-1960s, a carrier injection-recombination type light-emitting diode was realized using a GaAs single-crystal *p-n* junction. Research interest in solid-state EL devices was completely transferred to the LED. Thus, the first era of EL development drew to a close.

In 1968, the second era of EL development began with two EL devices. The first was a DC powder EL device that was made possible by coating powder EL phosphor surfaces with copper ions.[2] The second was an AC thin-film EL device using ZnS thin films doped with rare-earth fluorides.[3] The development of these devices became possible by advances in electronics and material science, especially in new process technologies. Thus, these devices began to be studied again, since the technical advantages of producing large-area multiplexed displays were expected at relatively lower production costs when compared to the LED as information display equipment in electric computers.

In 1974, Inoguchi et al. reported that a triple-layered, thin-film EL devices, consisting of $ZnS:Mn^{2+}$ EL layer sandwiched by a pair of insulating layers, showed high luminance and an unusually long life, both of which were unsolved problems during the first era of EL development.[4] Further, Mito et al. showed that these EL panels could be used as a TV imaging system.[5] In the autumn of the same year, a remarkable hysteresis behavior in the luminance-voltage characteristics was reported in the same triple-layered, thin-film EL device. Since then, the so-called "second generation" EL device was the subject of much attention and triggered worldwide investigations because of the high probability of these devices finding practical application in information displays.

In regard to the production of thin-film EL panels, Uede et al. and Tekeda et al. reported on practical EL display units and practical application technologies of $ZnS:Mn^{2+}$ EL display panels.[6,7] With the use of these technologies, mass production of 6-inch diagonal matrix EL panels began in April of 1983 in Japan.[8] Since then, the AC thin-film EL panels with the triple-layered structure have been continually improved with new phosphor materials for red, green and blue colors, along with fabrication techniques for the formation of the phosphor and the insulating layers. At this time, both multicolor and full-color EL units have been realized.

The first-generation powder-type EL devices have also been developed, showing steady improvement in luminance and reliability. These powder-type EL devices are used as back lights for liquid crystal displays.

9.1.2 Thin-film type[9,10]

Thin-film electroluminescence devices are classified into two types: AC and DC type EL devices. The DC type devices have remained on a laboratory level because the luminous efficiency and reliability problems have not been overcome. The AC type devices are also divided into a single-insulating layer type and a double-insulating layer type, as shown in Figure 1. A device of the former type with ZnS host materials doped with various rare-earth centers was reported for the first time by Kahng et al.[3,11] The interest in this type has faded away because of poor reliability. On the other hand, the latter type structure has been the center of research and development since Inoguchi et al.[4] reported a high luminance and a long lifetime.

The research and development on both colorization and enlarging the display information capacity have been done with the aim of enriching the applications of EL devices.

In this section, the AC thin-film EL devices with the double-insulating layered structure are described in detail.

9.1.2.1 Device structure

A schematic structure of the AC thin-film EL device is shown in Figure 1(b), where a thin-film phosphor layer is sandwiched between thin-film insulating layers.[4,8,10] These thin films are sequentially deposited on an ITO (indium tin oxide)-coated substrate, and an Al rear electrode is deposited on the second insulating layer. EL emission can be observed only when an AC voltage on the order of 200 V is applied between the ITO and Al electrodes. The EL emission mechanism is described in Section II.2.10.

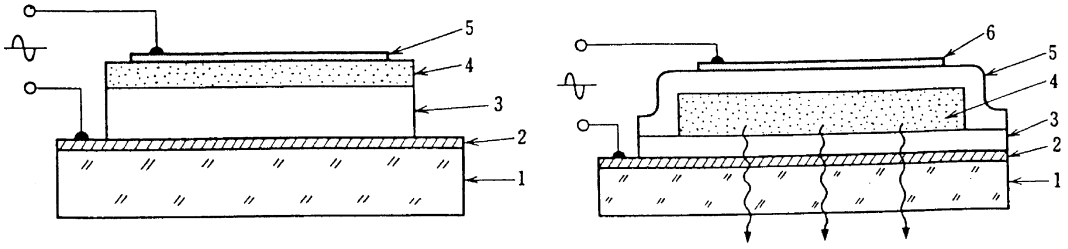

(a)

1 — glass substrate
2 — transparent electrode
3 — insulating layer
4 — phosphor layer (ZnS:Mn)
5 — back electrode

(b)

1 — glass substrate
2 — transparent electrode (ITO)
3 — insulating layer (~3000Å)
4 — phosphor layer (ZnS:Mn ~7000Å)
5 — back electrode (A1)

Figure 1 Schematic structure of two thin-film EL devices. (a) a single-insulating layer type EL device; (b) a double-insulating layer type EL device. (From Chase, E.W., Hoppelwhite, R.T., Krupka, D.C., and Kalong, D., *J. Appl. Phys.*, 40, 2512, 1969. With permission.)

This type of EL device has the following advantages:

1. Double-insulating layers can protect the phosphor layer against moisture penetration from outside to ensure higher stability.
2. A steady high electric field of up to 10^6 V cm^{-1} can be applied to the phosphor layer without a catastrophic electric breakdown, because the insulating layers block electron flow from the both electrodes into the phosphor layer.
3. An internal polarization field caused from trapped charges at the interfaces between the phosphor layer and the insulating layer increases or modulates the effective electric field applied to the phosphor layer under AC driving conditions. As a result, luminous efficiency and luminance are increased, and a steep luminance vs. voltage (L-V) characteristic is obtained, as shown in Figure 2.[12] The threshold voltage in this figure is defined by a voltage corresponding to a luminance of 1 cd/m^2.

9.1.2.2 Material requirements for the constituent layers

EL phosphor materials. In general, a phosphor consists of a host material doped with an activator, which acts as the light-emitting center. The requirements for the host materials are as follows:

1. The host materials have a bandgap large enough to emit visible light without absorption.
2. On excitation by a high electric field on the order of 10^6 V cm^{-1}, an electron avalanche is produced.
3. The lattice can accept a suitable activator that emits visible light.

Host materials satisfying the above requirements are limited to II-VI compounds such as ZnS, ZnSe, SrS, and CaS etc.[13–21] ZnS is the most widely used material among the above host materials.

The requirements for the luminescent centers are as follows:

1. Luminescent centers must have a large cross-section for the impact excitation mechanism.

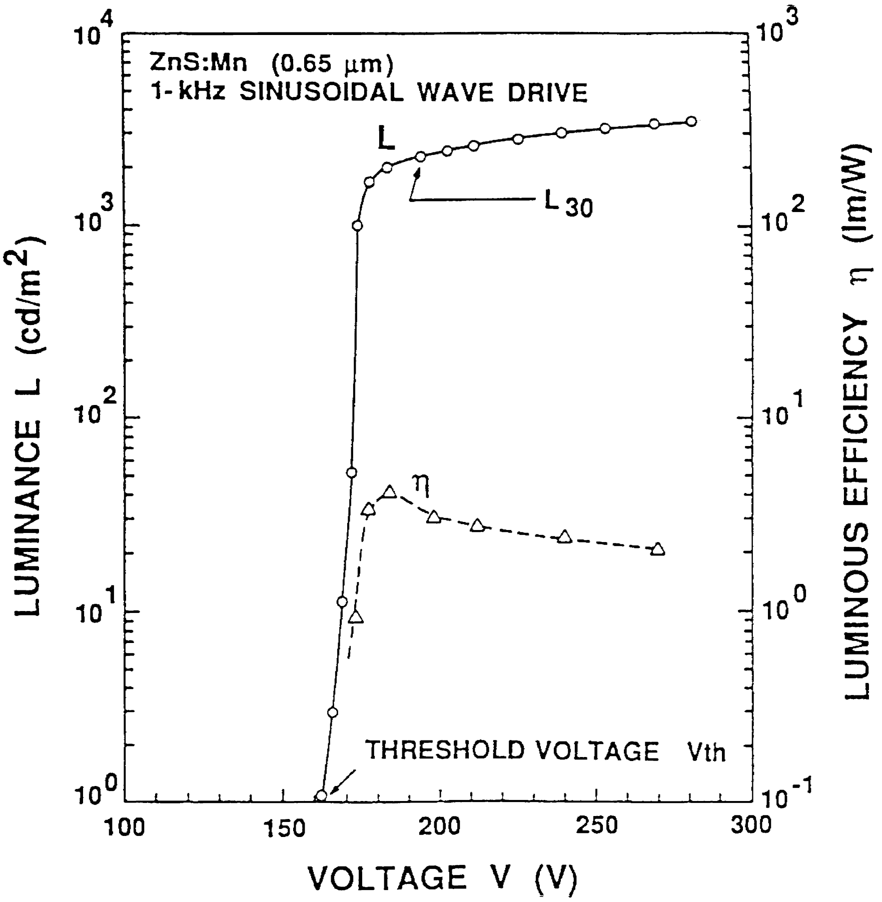

Figure 2 Typical luminance vs. voltage (L-V) and luminous efficiency vs. voltage (η-V) characteristics of a double-insulating layered AC thin film EL device. (From Mikami, A., Terada, K., Okibayashi, K., Tanaka, K., Yoshida, M., and Nakajima, S., *J. Cryst. Growth*, 110, 381, 1991. With permission.)

2. Luminescent centers must be chosen with an appropriate ionic radius and valency in order to be stable in a high electric field environment.
3. Isolated luminescent centers are suitable to exhibit high luminous efficiency because of efficient impact excitation by high-energy electrons.

From the above requirements, transition metal ions, such as Mn^{2+}, and rare-earth ions, such as Tb^{3+}, Sm^{3+}, Tm^{3+}, Pr^{3+}, Eu^{2+}, and Ce^{3+}, are found to be suitable luminescent centers.[11,13–21]

ZnS host materials doped with Mn^{2+} have proved to be one of the most useful phosphors. These materials emit a yellowish-orange light with a single peak around 585 nm; the highest brightness is obtained at the Mn concentration of about 0.5 wt%. In the case of rare-earth ions, their fluorides are generally used as the doping materials.[11]

Donor-acceptor type phosphors, such as ZnS doped with Cu and Al widely used for cathode-ray tubes, show poor EL performance under high electric fields.

Insulating materials. The insulating layers play an important role in the stability of the double-insulating layered EL devices and also in the control of EL characteristics. The following properties are required.

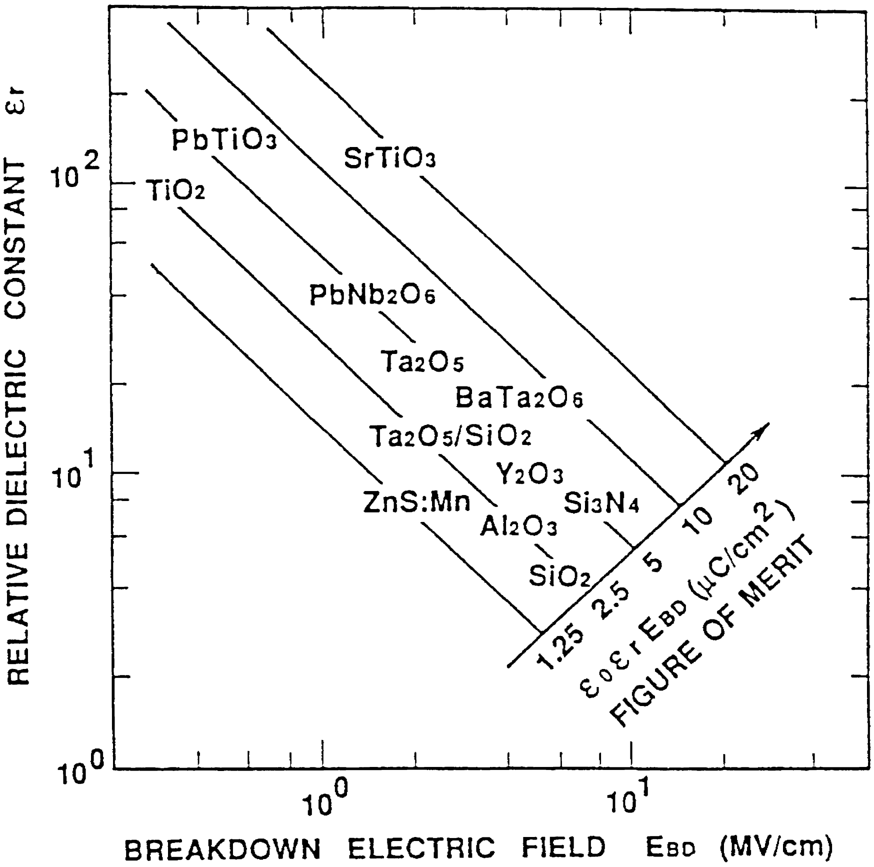

Figure 3 Relative dielectric constant vs. breakdown electric field (ε_r–E_{BD}) characteristics of typical dielectric materials used for a double-insulating, thin-film EL device. (From Fujita, Y., Kuwata, J., Nishikawa, M., Tohda, T., Matuoka, T., Abe, A., and Nitta, T., *Proc. Soc. Inf. Disp.*, 25, 177, 1984. With permission.)

1. High breakdown electric field strength (E_{BD}) to ensure the stability and to prevent electric breakdown
2. High dielectric constant (ε_0, ε_r) to reduce the driving voltage
3. Small number of pinholes to prevent moisture penetration and electric breakdown
4. Good adhesion to the upper and lower layers

Two types of dielectric insulating materials are mainly used, based on the above: (1) amorphous oxides and nitrides, such as Al_2O_3, SiO_2, TiO_2, Ta_2O_5, and Si_3N_4,[7] and (2) ferroelectric materials, such as $BaTiO_3$, $SrTiO_3$, and $PbTiO_3$.[22–24] Figure 3 shows the relative dielectric constant vs. breakdown electric field characteristics of typical dielectric materials used for the double-insulating layered devices.[24] The figure of merit in this figure is the product of the dielectric constant and the breakdown electric field strength. The figure of merit reflects the maximum trapped charge density at the interface between the phosphor layer and the insulating layer. In practical devices, a complex film such as Al_2O_3/TiO_2, and a composite film such as Si_3N_4/SiO_2 are used to ensure the above requirements.[7,25]

Another important characteristic for EL devices is the breakdown mode; there are two modes, a propagating and a self-healing breakdown mode. In the former mode, the electric breakdown occurring in the small area within a pixel, propagates to neighboring places, resulting in a large-area electric breakdown. In the latter mode, on the other hand, the electric breakdown remains at the initial spot. Insulating thin films for EL devices must exhibit the self-healing breakdown mode. Dielectric thin films with large dielectric constants tend to have the propagation breakdown mode. By coupling the latter with other dielectric thin films such as $Ba_2Ta_2O_6$, the breakdown mode can be converted into the self-healing mode.[24]

Transparent conducting materials. Material requirements for the transparent conducting films used for EL devices are large conductivity and high transmittance. The large conductivity is especially needed to obtain display uniformity and to decrease the power consumption due to heating in the transparent conducting films. At the initial stages of EL development, SnO_2 thin films (commercial name, NESA) were used, having a resistivity of about 10^{-3} Ω·cm. While these materials have excellent stability, they are not currently used because of the difficulty of electrode patterning by chemical etching. At this time, indium thin oxide (ITO:In_2O_3-10 wt% SnO_2) materials are widely used because of the ease of chemical etching and a lower resistivity (about 10^{-4} Ω·cm). This material has a tendency to undergo oxidation-reduction reactions, resulting in a change in both the resistivity and transmittance. Careful attention must be paid to its stability during the fabrication process of EL devices.

9.1.2.3 Deposition methods for the constitutional layers

Phosphor layers. A large number of deposition methods have been investigated to increase the luminance of the EL displays; electron-beam deposition (EBD),[6,7] atomic-layer epitaxy (ALE),[30] multisource deposition (MSD),[26] sputtering method (SP),[20] metal-organic chemical vapor deposition (MOCVD),[27] and low-pressure hydride-transport chemical vapor deposition (HT-CVD).[12] Among these methods, the EBD and ALE methods are used to fabricate commercially available EL displays. In this section, the EBD, ALE, and SP methods are explained. The SP method is introduced because this method was extensively studied in making ZnS:Tb^{3+},F^- phosphor layers.

EBD method. II-VI compound semiconductors (such as ZnS, etc.) used for the phosphor layer have different vapor pressures for the two constituents. In the case of the fabrication of ZnS:Mn^{2+}, the EBD method, which evaporates a ZnS pellet doped with Mn^{2+} by irradiation with an electron beam, is most generally used. This method is a variation on the flash evaporation method suitable for obtaining stoichiometry and reproducibility in ZnS:Mn^{2+} films, since both ZnS and Mn are sublimation materials. The substrate temperature is usually set between 200 and 250°C. Thermal annealing is performed in vacuum at approximately 550°C for about 1 hour after deposition of the ZnS:Mn^{2+} thin film.[28] Thermal annealing improves the crystallinity of the phosphor layer and accelerates the Mn diffusion. In the case of ZnS pellets doped with rare-earth fluorides such as TbF_3 and PrF_3 etc., much attention must be paid to the large particles observed during EB evaporation, since rare-earth fluorides are difficult to sublimate. For CaS- and SrS-based EL devices, the EBD method is mainly used.[29]

Sputtering method. The sputtering method has the possibility of being an inline process for mass production, since both phosphor layers and insulating layers can be grown by the same deposition method. However, a ZnS:Mn^{2+} phosphor layer deposited by this method shows a poorer EL performance than that obtained by the EBD method. This is due to the lower crystallite diameter and the lower stoichiometry produced by this method. On the other hand, EL devices with a ZnS:Tb^{3+},F^- phosphor layer deposited by the sputtering method shows the highest green emission because sputtering produces very uniform doping of Tb^{3+} into the ZnS host material.[19–21]

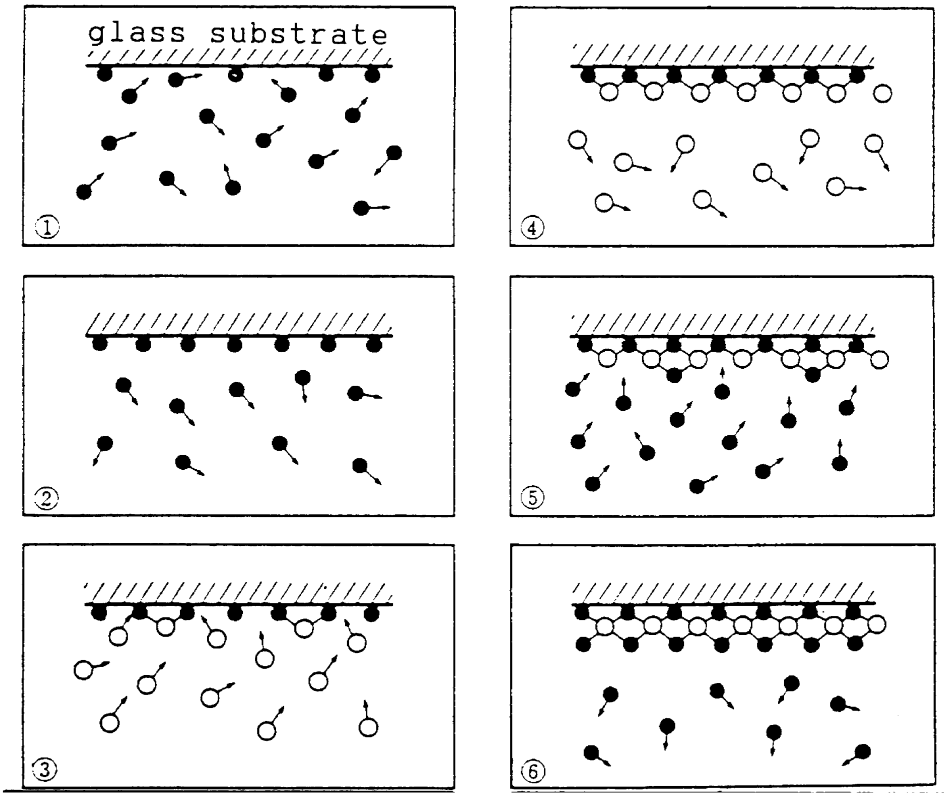

Figure 4 Conceptual explanation for a growth mechanism of an atomic-layer epitaxy (ALE) process for ZnS thin film using Zn vapor and S vapor as reactants. (●: Zn atom, ○: S atom) (From Suntola, T., Anston, J., Pakkala, A., and Linfors, S., in *Digest, 1980 SID Int. Symp. Soc. Information Display,* 1980, 108. With permission.)

ALE method. The ALE method is a type of chemical vapor deposition method. Single layers are sequentially formed by alternately supplying reactant vapors, of the constituent elements, to a substrate, as shown in Figure 4. Upon introduction of Zn vapor, a Zn monoatomic layer is formed by making Zn-O bonds on the surface of an oxygen-including glass substrate. Excess Zn vapor is flushed away and then S vapor is introduced. By making Zn-S bonds due to reaction of S with the Zn monoatomic layer, a S monoatomic layer is formed. Excess S vapor is also flushed away. By alternating of the reactant vapor, a ZnS thin film with good thickness uniformity and good crystallinity can be obtained. The most important growth parameter of the ALE method is the substrate temperature. Films grown at 350 and 500°C have cubic and hexagonal crystal structures, respectively. The low transition temperature between the cubic and hexagonal crystal structures is quite interesting, since the transition temperature is 1020°C in ZnS single crystals.

Insulating layers. At the initial development stage of EL devices, Y_2O_3 thin films, which can be easily deposited by the EBD method, were mostly used. However, the Y_2O_3 thin films tend to have oxygen deficiency, depending on the evaporation conditions, which result in a lower breakdown electric field.

SiO_2, Al_2O_3, and Si_3N_4 thin films, which are now extensively used, are deposited by a reactive sputtering method,[7] and $PbTiO_3$, $SrTiO_3$, and $Ba_2Ta_2O_6$ thin films with high dielectric constant are fabricated by the sputtering method.[22,24] The ALE method is also extensively used for the fabrication of Al_2O_3-TiO_2 composite insulating films.[25]

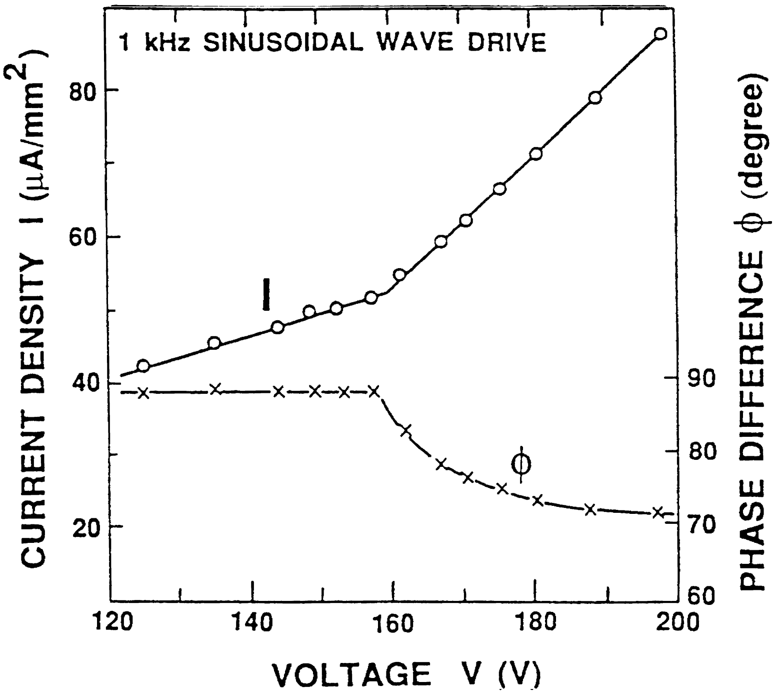

Figure 5 Current density vs. voltage (I-V) and phase difference vs. voltage (ϕ-V) characteristics of a double-insulating, thin-film EL device. (From Inoguchi, T. and Suzuki, C., *Nikkei Electronics*, 84, 1974 (in Japanese). With permission.)

Transparent conducting films. Considering that the transparent conducting film is located at the lowest position on the double-insulating layered EL devices, surface flatness is an important factor in addition to conductivity and transmittance. Poor flatness induces electric breakdown and nonuniform emission. ITO films deposited by the sputtering method have a very smooth surface and this method of deposition is in general use at the present time.

9.1.2.4 Characteristics

Electrical characteristics. EL devices exhibited current density vs. voltage (I-V) and phase difference vs. voltage (ϕ-V) characteristics under 1 kHz sinusoidal wave drive conditions, as shown in Figure 5. The I-V profile is given by two straight lines linked with a kink at the threshold voltage (V_{th}). The slope of the I-V characteristics below V_{th} corresponds to the total capacitances of the insulating layer, the phosphor layer, and the insulating layer in series. On the other hand, the slope above V_{th} corresponds to the total capacitances of only the insulating layers in series.[28] This indicates that the phosphor layer changes its capacitive characteristics into resistive characteristics. This behavior is confirmed by the ϕ-V characteristics.

Taking ZnS as an example, with increasing driving voltage, the average electric field in the phosphor layer at V_{th} reaches a value of $1–2 \times 10^6$ V cm^{-1} and remains at that value above V_{th}. From the above results, an equivalent-circuit model for EL devices can be proposed, as shown in Figure 6.[28]

Optical characteristics. When the phosphor layer becomes conductive above the V_{th}, an in-phase conduction current starts to flow through the phosphor layer, producing the EL emission. The luminance is proportional to the in-phase conduction current. Figure 7

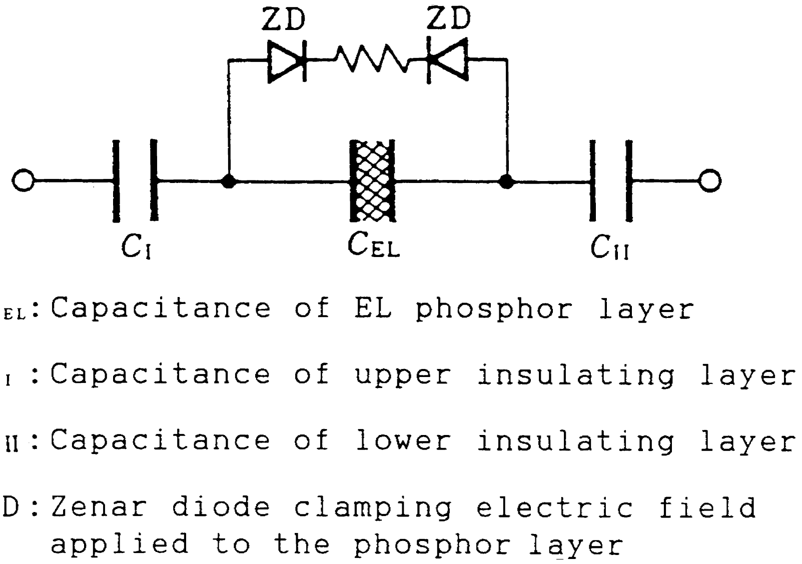
ZD
ZD
C_I
C_{EL}
C_{II}
C_{EL}: Capacitance of EL phosphor layer
C_I : Capacitance of upper insulating layer
C_{II} : Capacitance of lower insulating layer
ZD : Zenar diode clamping electric field applied to the phosphor layer

Figure 6 Equivalent circuit model of a double-insulating layer AC thin-film EL device. (From Inoguchi, T. and Suzuki, C., *Nikkei Electronics*, 84, 1974 (in Japanese). With permission.)

shows the schematic characteristics of the voltage waveform V, the current waveform I, and the EL emission waveform L under triangular-wave drive conditions.

The rise and decay times in the case of ZnS:Mn^{2+} EL devices are of the order of several microseconds and several milliseconds, respectively. The above times indicate that the luminance is directly proportional to the driving frequency, up to frequencies of several kHz. The same proportionality is expected to continue for frequencies up to the order of several 100 kHz. However, consideration must be paid to the influence on the time constant by: the resistivity of the transparent electrode, the output impedance of IC driver, and the capacitance of EL display panel.

Figure 8 shows typical luminance vs. voltage (L-V) characteristics. With an increase in the applied voltage, the luminance increases steeply above V_{th}, and then shows a tendency toward saturation, regardless of the luminescent centers.

In the case of ZnS:Mn^{2+} devices, a luminance of 5000–7000 cd m^{-2} and a luminous efficiency of 2–8 lm W^{-1} are obtained under a driving frequency of 5 kHz. In the case of the EL devices with rare-earth luminescent centers, the luminances are lower than those for ZnS:Mn^{2+}. The luminance of the ZnS:TbF_3 EL device (the most luminous device among the rare-earth-based devices) is about half that of ZnS:Mn^{2+}.

Figure 9 shows typical emission spectra of EL devices with the ZnS-based phosphor layers. The emission color in the case of ZnS:Mn^{2+}, ZnS:TbF_3, ZnS:PrF_3, ZnS:DyF_3, and ZnS:TmF_3 are yellowish-orange, green, white, yellowish-white, and blue, respectively. In the case of ZnS:PrF_3, there are two emission groups that center around 500 and 650 nm. These two groups roughly satisfy the complementary color relationship, resulting in a white sensation to the human eye.[13]

Reliability. In the development of EL devices, both short- and long-term reliability must be considered. Electrical breakdown is the main factor that determines the short-term reliability of these devices, since EL action is obtained under a high electric field of ~10^6 V cm^{-1}. The constituent layers must have an even surface with no pinholes. In addition, the insulating layers should exhibit high breakdown electric field strength. An aging process is needed to stabilize the luminance vs. voltage (L-V) characteristics, since

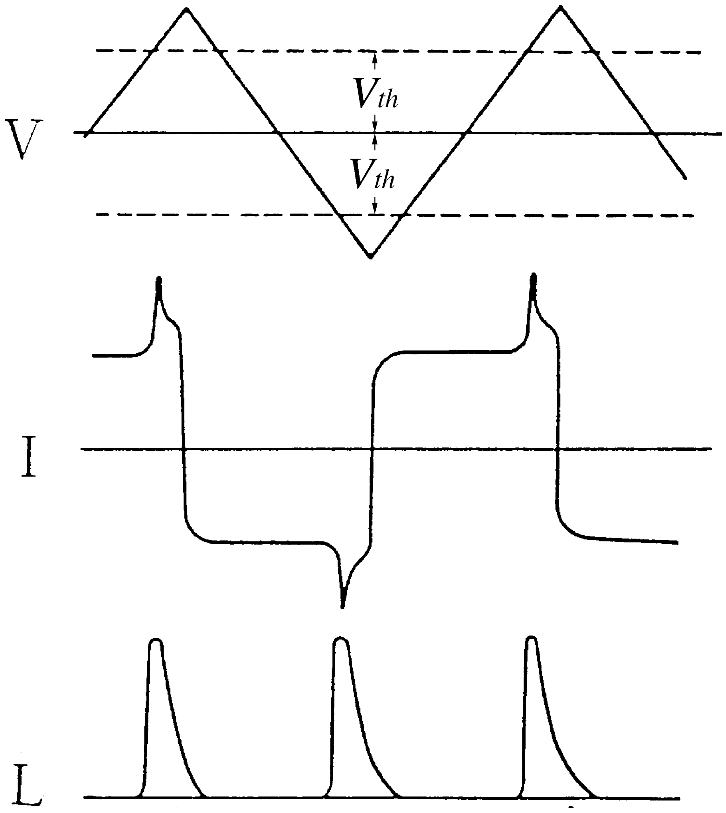

Figure 7 Schematic characteristics of the voltage waveform V, the current waveform I, and the EL-emission L, under triangular-wave drive conditions. (From Inoguchi, T. and Suzuki, C., *Nikkei Electronics*, 84, 1974 (in Japanese). With permission.)

the L-V characteristics of the as-fabricated EL devices shift toward higher voltages, as shown in Figure 10. Inoguchi et al. found that this shift is not a degradation phenomenon, but a stabilization phenomenon.[4,9] After this process, stable L-V characteristics are obtained, as shown in Figure 11.

With regard to long-term reliability, the peeling of thin films is the main lifetime-determining factor. Moisture (H_2O) penetrating the phosphor-insulating layer interface through the small dielectric breakdown holes causes peeling of thin films. During the EL operation, ionization of water that has penetrated occurs from hot-electron impact in the phosphor layer, generating H^+ and OH^- ions. H^+ ions combine at the interface to form hydrogen gas. The gas pressure lifts the second insulating layer from the phosphor layer, leading to peeling of the thin films.[31] Serious attention must be paid to sealing techniques in order to prevent moisture penetration from the atmosphere. In commercial EL devices, silicone oil and silica gel powders are placed in the glass-sealed EL device, as shown in Figure 12. A long lifetime of more than 30,000 hours has been achieved by employing this technique.

Hysteresis characteristics. When the Mn^{2+} concentration in the $ZnS:Mn^{2+}$ phosphor layer of the double-insulating layered EL devices exceeds an optimum concentration of 0.5 wt%, a hysteresis phenomenon is observed. This is shown in Figure 13.[32,33] This phenomenon is thought to result from the coupling between the polarization induced by

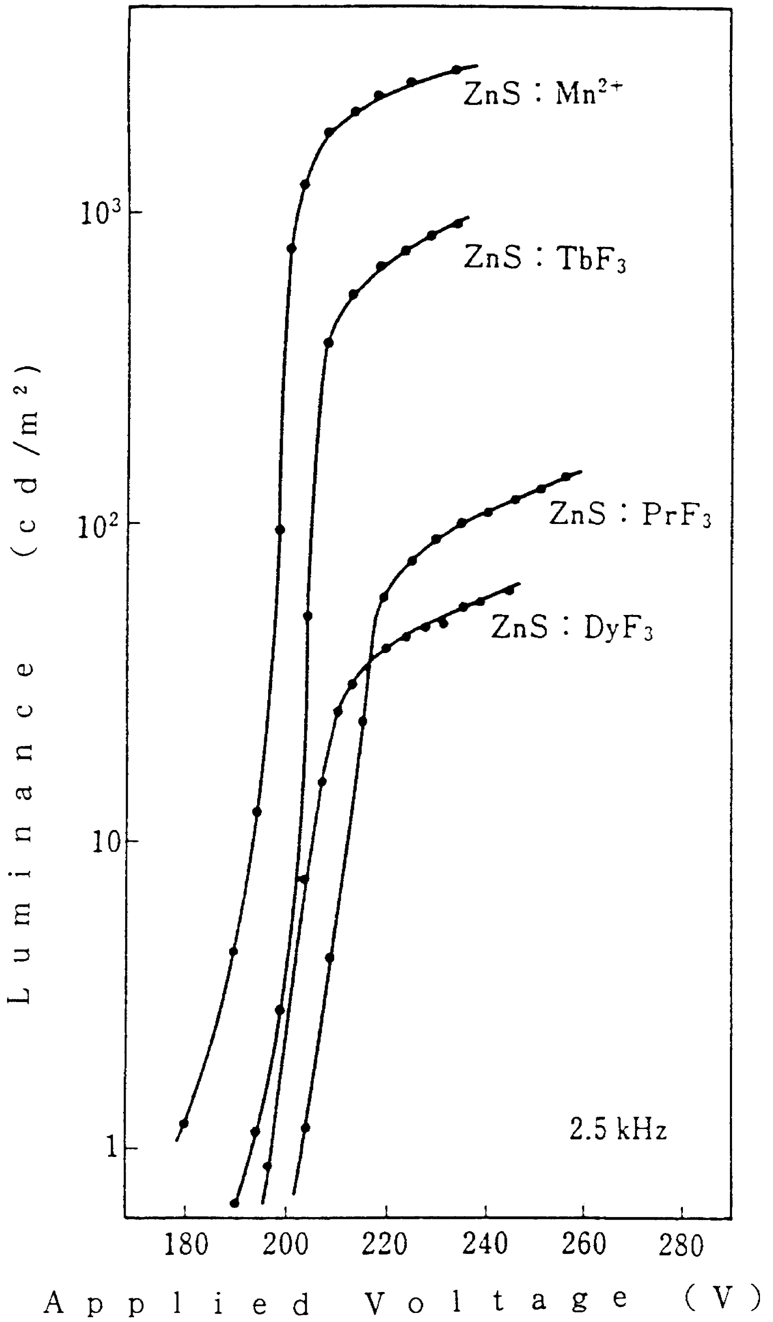

Figure 8 Typical luminance vs. voltage (L-V) characteristics of double-insulating layered AC thin-film EL devices using ZnS phosphor layers doped with various emission centers. (From Yoshida, M., Tanaka, K., Taniguchi, K., Yamashita, T., Kakihara, Y., and Inoguchi, T., in *Digest, 1980 SID Int. Symp. Soc. Information Display,* 1980, 106. With permission.)

the stored charge at the phosphor-insulating interface and the electron emission from the Mn^{2+}-related deep levels.

On increasing and decreasing the applied voltage, the polarization charge that modulates the applied electric field has a hysteresis due to the electrons supplied from the

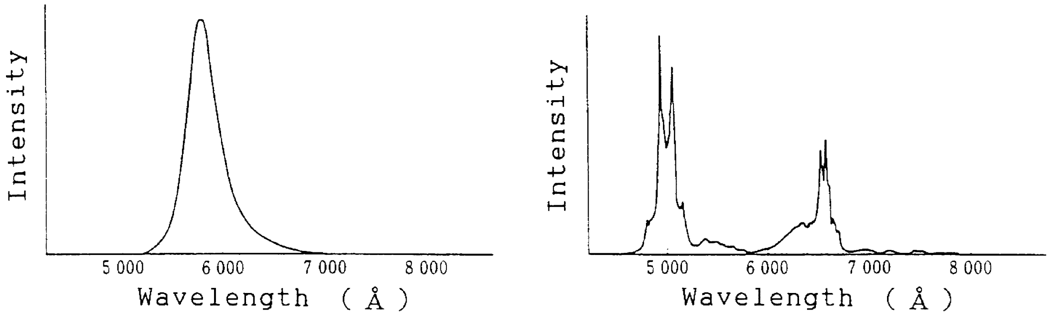

(a) $ZnS:Mn^{2+}$ (c) $ZnS:PrF_3$

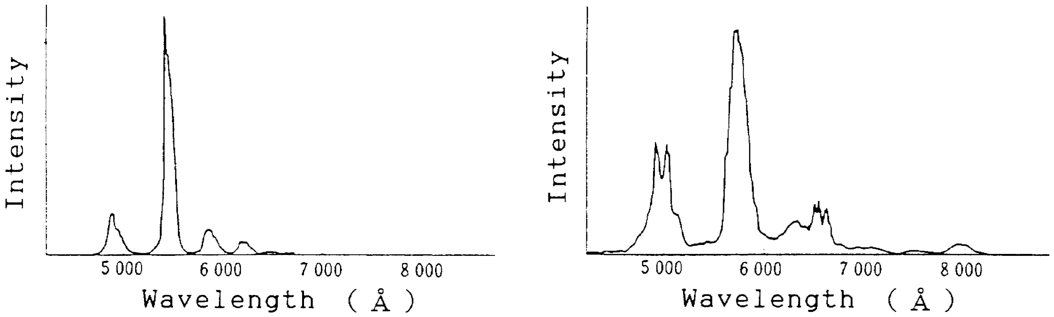

(b) $ZnS:TbF_3$ (d) $ZnS:DyF_3$

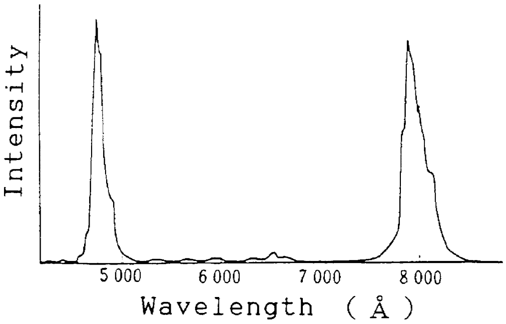

(e) $ZnS:TmF_3$

Figure 9 Typical emission spectra of double-insulating layer AC thin-film EL devices using ZnS phosphor layers doped with various emission centers.

deep level. This effect results in the observed hysteresis in the L-V characteristics. This hysteresis phenomenon is useful in providing a memory function to the EL devices. Figure 14 shows a schematic representation of the memory operation by electrical means. Luminous levels between L_{on} and L_{off} at a given sustained voltage (V_s) can be changed by adjusting the amplitude of the writing pulse ($V_s + V_w$) and the erasing pulse ($V_s - V_E$). This feature results in an analog memory because there are many luminous levels between L_{on} and L_{off}. This means that EL devices can display memory images with gray levels. Optically writing and erasing is also possible by irradiation with UV light.[5] The same kind of hysteresis phenomenon has also been observed in $CaS:Eu^{2+}$ and $SrS:Ce^{3+}$ EL devices.[16,17]

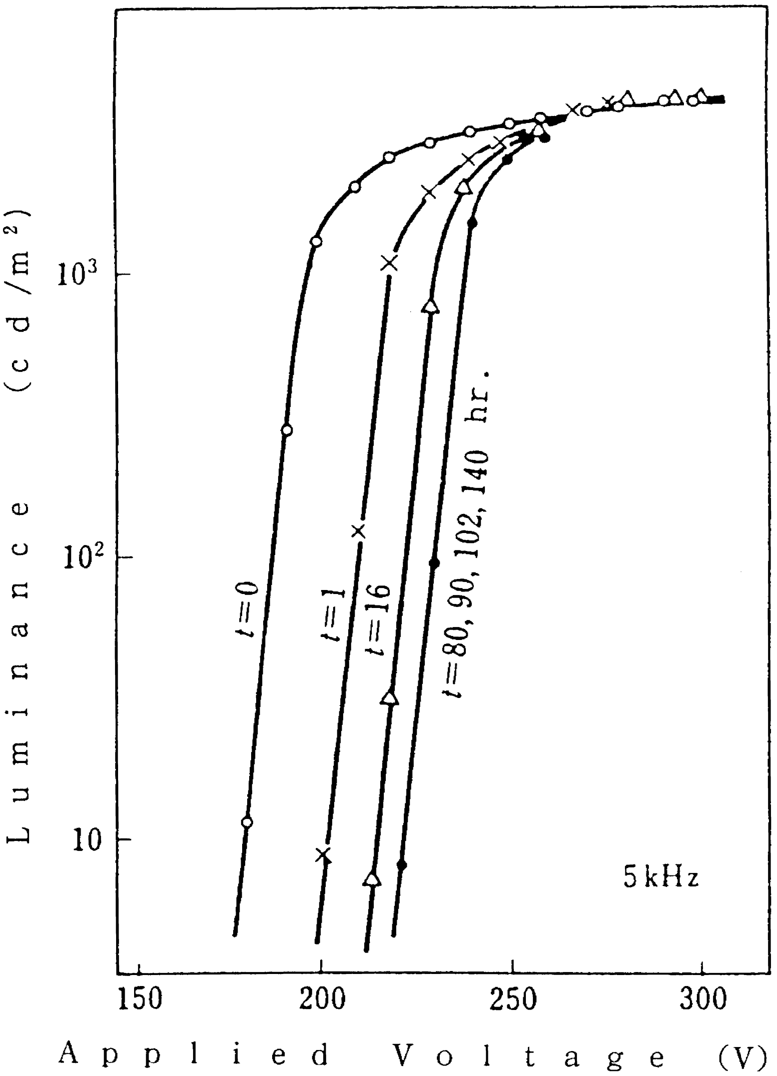

Figure 10 Aging characteristics of an as-fabricated EL device with double-insulating layered structure under a driving frequency of 5 kHz. (From Inoguchi, T., Takeda, M., Kakihara, Y., Nakata, Y., and Yoshida, M., in *Digest, 1974 SID Int. Symp. Soc. Information Display,* 1974, 84. With permission.)

9.1.2.5 Recent developments in EL displays

Since the first commercial monochrome EL displays were introduced in 1983, EL displays have made significant progress and a variety of products are now available; for example, in the case of $ZnS:Mn^{2+}$ monochrome EL panels, high-luminance devices with 200 cd m^{-2}, high-resolution devices with 1.3 million pixels, low-power consumption devices of less than 5 W in a 10.4-inch diagonal EL display, and high-contrast devices of more than 50:1 at 500 lux[34] are commercially available. In the case of color EL panels, red/green multicolor EL devices are now available.[35] These EL displays have found solid acceptance in industrial controller and medical controller applications, where the needs for ruggedness, wide temperature range, wide viewing angle, long life, and fast response time are critical.

Other recent developments—the high contrast monochrome EL display, red/green multicolor type EL display, and full-color EL display—are discussed below.

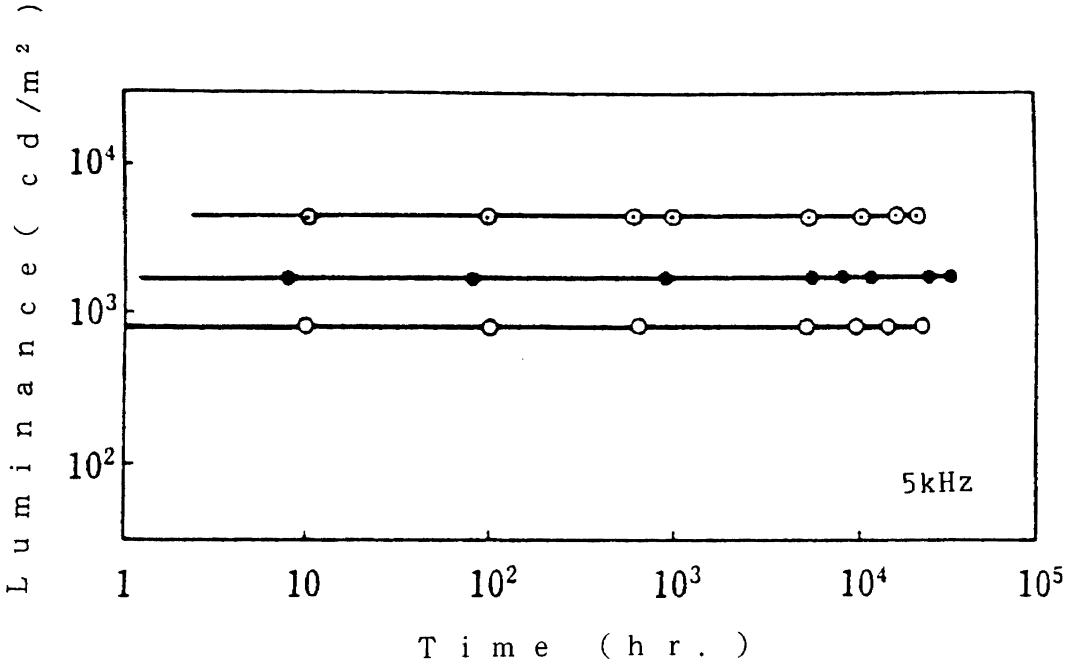

Figure 11 Aging characteristics of the double-insulating layered type AC thin-film EL device after a stabilization process. (From Inoguchi, T., Takeda, M., Kakihara, Y., Nakata, Y., and Yoshida, M., in *Digest, 1974 SID Int. Symp. Soc. Information Display,* 1974, 84. With permission.)

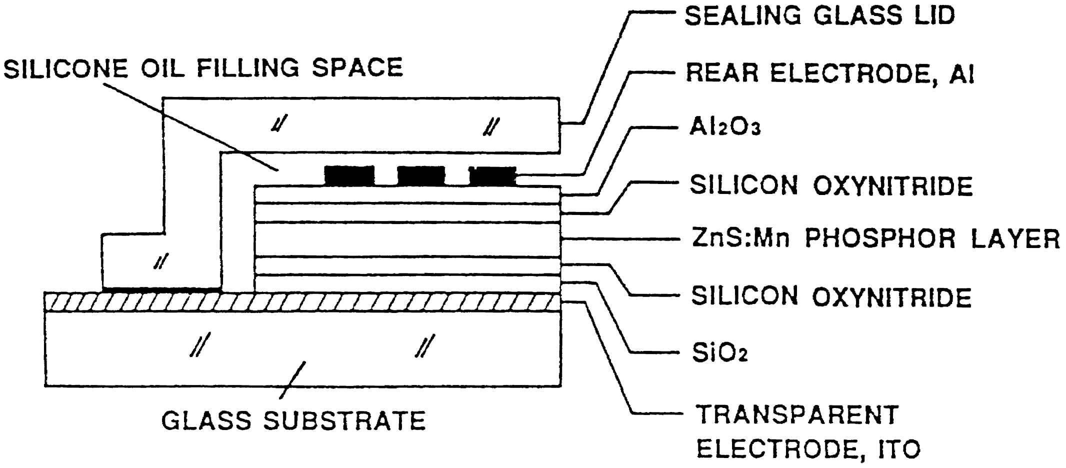
SEALING GLASS LID
SILICONE OIL FILLING SPACE
REAR ELECTRODE, Al
Al2O3
SILICON OXYNITRIDE
ZnS:Mn PHOSPHOR LAYER
SILICON OXYNITRIDE
SiO2
GLASS SUBSTRATE
TRANSPARENT ELECTRODE, ITO

Figure 12 Cross-sectional structure of commercially available thin-film EL devices with double-insulating layers. (From Takeda, M., Kanatani, T., Kishishita, H., Inoguchi, T., and Okano, K., in *Proc. Soc. Information Display,* 22, 57, 1981. With permission.)

High-contrast monochrome EL displays. The contrast ratio of the monochrome EL panel with the conventional structure as shown in Figure 15 is insufficient for outdoor applications due to the reflection of ambient light from the back aluminum electrode and light scattering off the rough upper surface of the phosphor layer.[34,35] One of the solutions to this problem is the use of a traditional circular polarizer (CP) attached to the panel. The CP filter enhances the contrast ratio by a factor of three. A super-high-contrast (SHC)

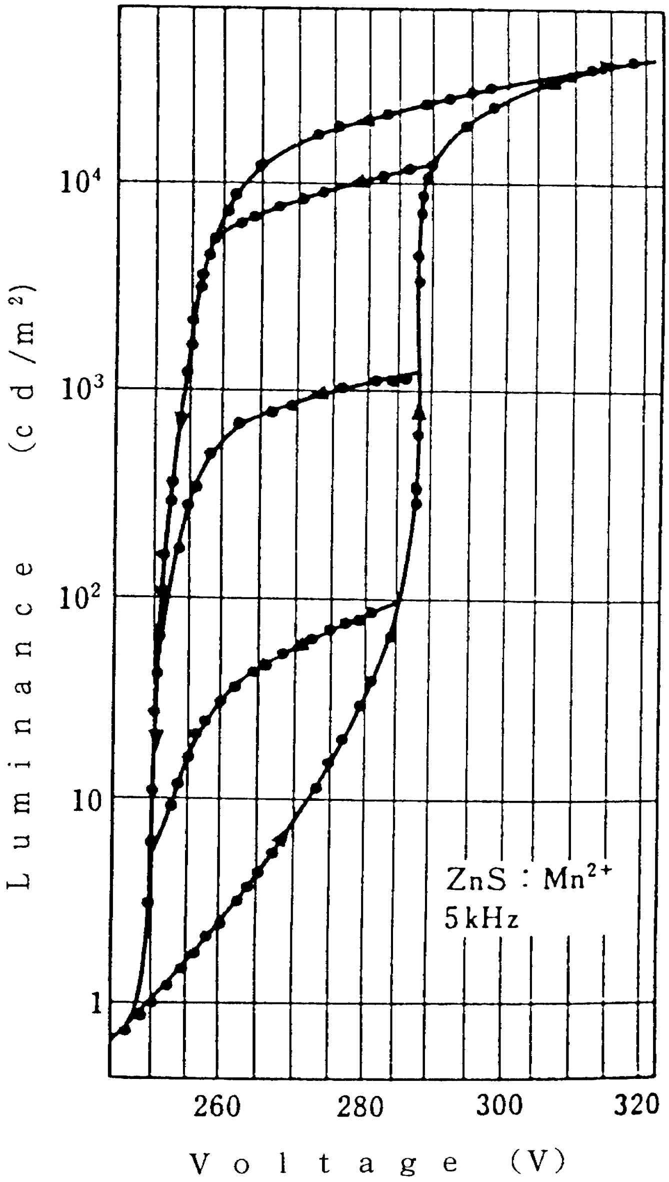

Figure 13 Hysteresis phenomenon observed in luminance vs. voltage (L-V) characteristics of an AC thin-film EL device. (From Yoshida, M., Kakihara, Y., Yamashita, T., Taniguchi, K., and Inoguchi, T., in *Proc. 9th Conf. Solid State Devices, Supplement to Jpn. J. Appl. Phys.*, 17, 127, 1978. With permission.)

monochrome EL display has been developed by a technique utilizing a new light-absorbing layer within the thin-film structure; this layer significantly reduces the reflections of ambient and internal light from the display's back metal electrode. The light-absorbing layer is constructed of a new insulating layer and a new black electrode. Figure 16 shows the comparison of the contrast ratio as a function of ambient illumination among the SHC panel and the conventional panel, both with and without a CP filter.[24,36] The SHC panel exhibits a contrast ratio of better than 50:1 in an ambient atmosphere of 500 lux, and 10:1 in a brighter outdoor ambient of 5000 lux.

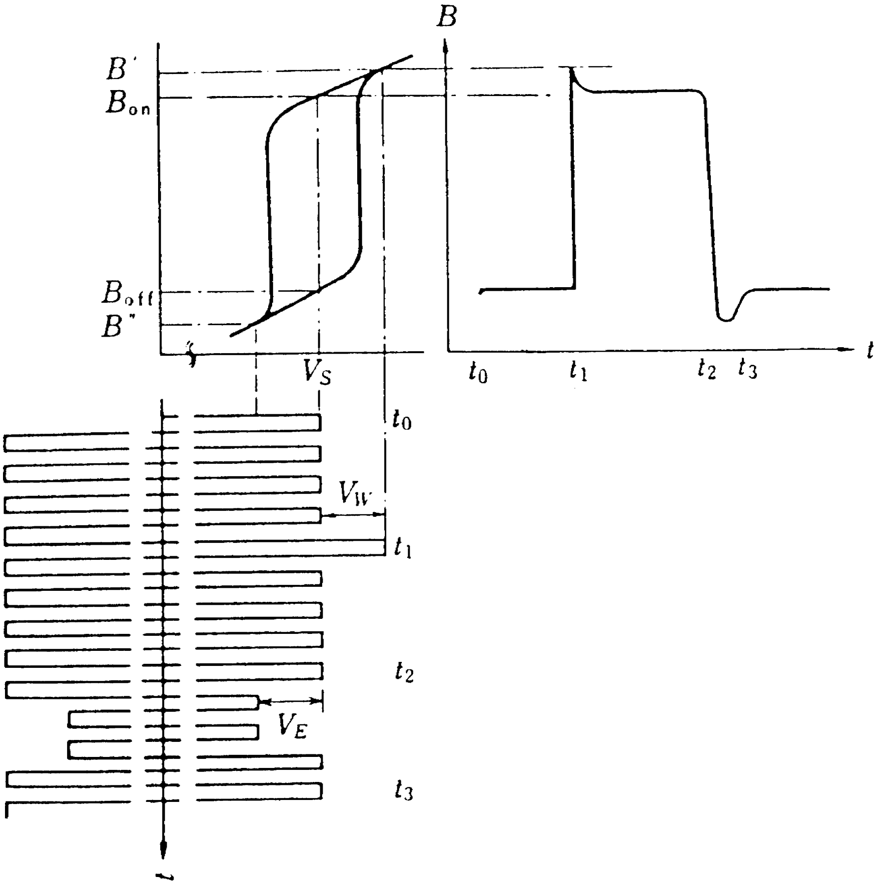
B
B'
B_on
B_off
B"
V_S
t
t_0
t_1
t_2
t_3
V_W
V_E

Figure 14 Schematic explanation for a memory operation in accordance with an L-V hysteresis loop. Luminous levels at the same sustaining voltage pulse from L_{off} to L_{on} and from L_{on} to L_{off} can be changed by applying a writing pulse ($V_s + V_w$) and an erasing pulse (V_s–V_E), respectively. (From Takeda, M., Kakihara, Y., Yoshida, M., Nakata, T., and Mito, S., *Proc. 6th Conf. Solid State Devices, Supplement to Jpn. J. Appl. Phys.*, 44, 103, 1975. With permission.)

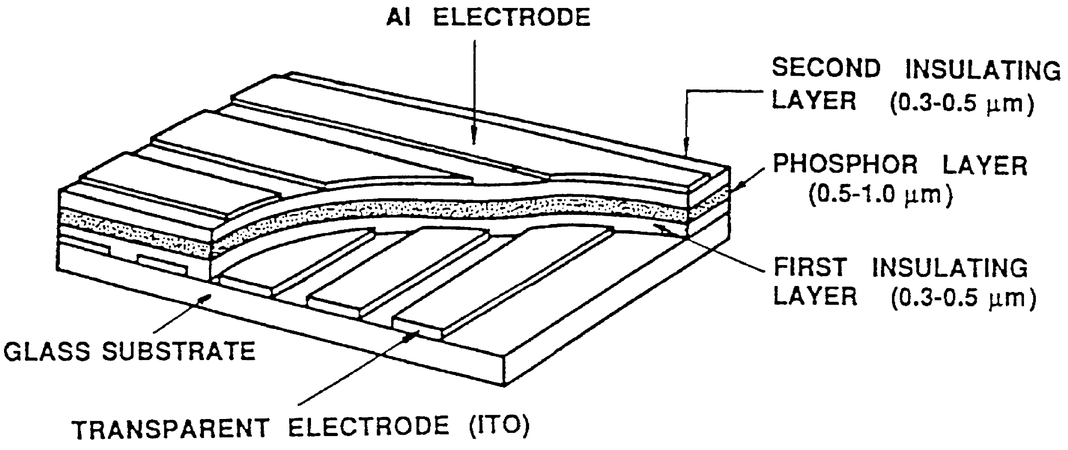
Al ELECTRODE
SECOND INSULATING LAYER (0.3-0.5 μm)
PHOSPHOR LAYER (0.5-1.0 μm)
FIRST INSULATING LAYER (0.3-0.5 μm)
GLASS SUBSTRATE
TRANSPARENT ELECTRODE (ITO)

Figure 15 Structure of double-insulating layer, thin-film EL device.

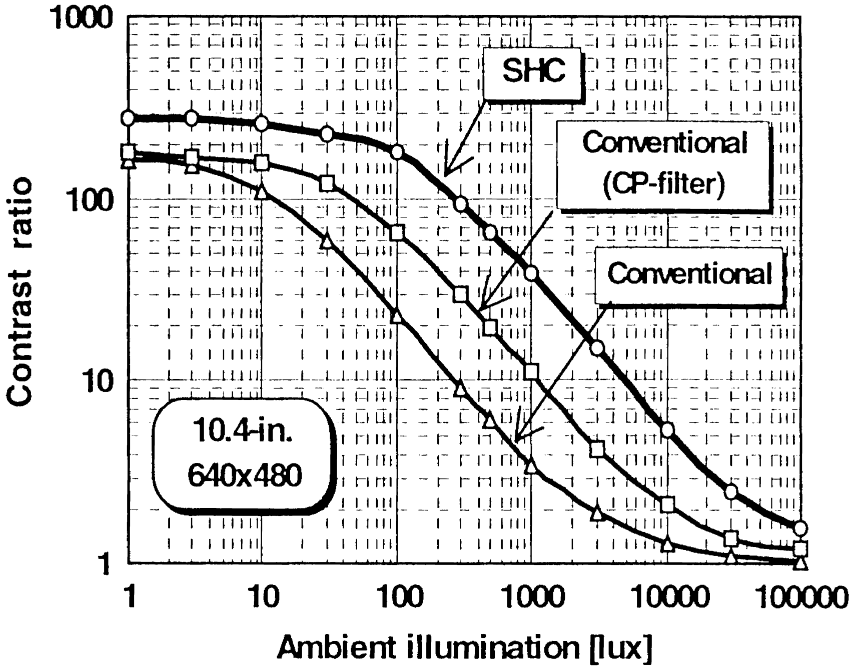

Figure 16 Contrast ratio of super high contrast (SHC) and conventional monochrome EL displays as a function of ambient illumination. (From Mikami, A., Tashima, I., and Kajikawa, F., in *Proc. 8th Int. Workshop Inorganic and Organic Electroluminescence in Berlin*, 1996. With permission.)

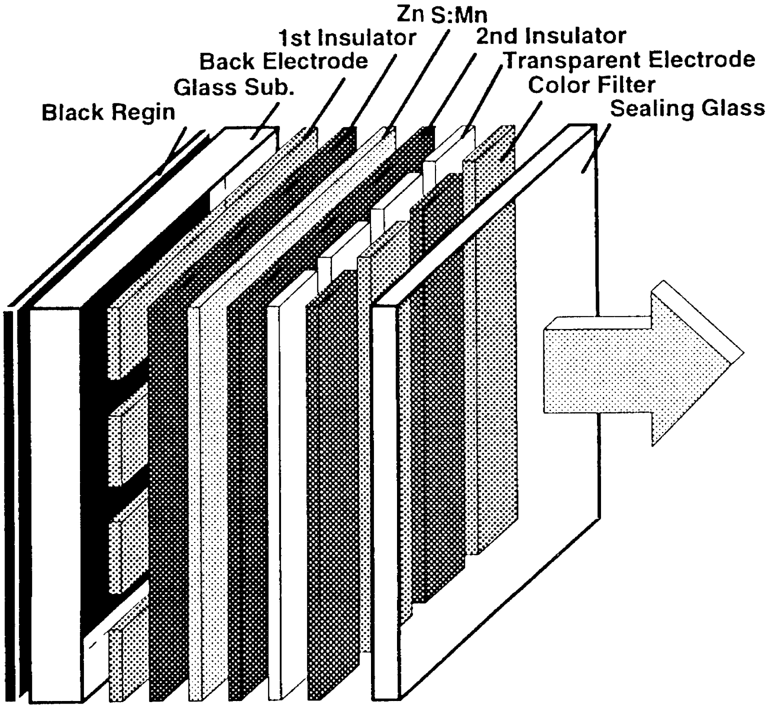
Zn S:Mn
1st Insulator
2nd Insulator
Back Electrode
Transparent Electrode
Glass Sub.
Color Filter
Black Regin
Sealing Glass

Figure 17 Schematic diagram of an inverted color thin-film EL structure with a patterned color filter. (From Mikami, A., Tashima, I., and Kajikawa, F., in *Proc. 8th Int. Workshop Inorganic and Organic Electroluminescence in Berlin*, 1996. With permission.)

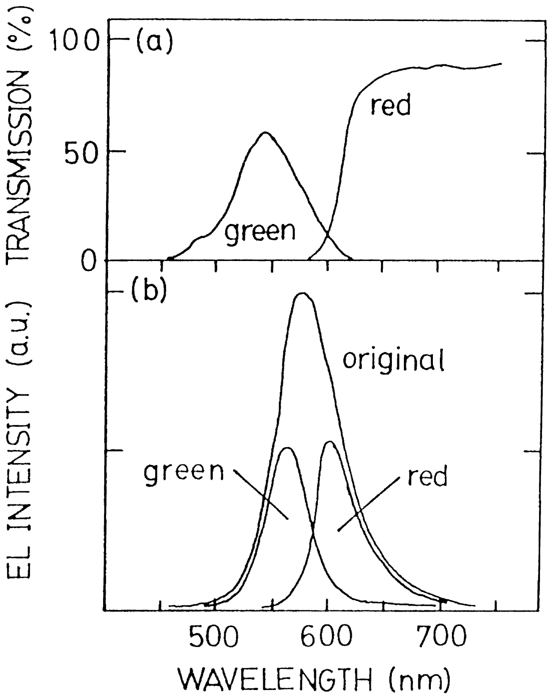

Figure 18 Emission spectrum change of ZnS:Mn^{2+} original light after passing through color filters. (a) transmission characteristics of color filters; (b) emission spectra after passing through green and red color filters. (From Okibayashi, K., Ogura, T., Terada, K., Taniguchi, K., Yamashita, T., Yoshida, M., and Nakajima, S., in *Digest, 1991 SID Int. Symp. Information Display,* 1991, 275. With permission.)

Red/green multicolor EL. Figure 17 shows the device structure of a red/green multicolor EL, which is the simplest structure for implementing a multicolor EL panel.[37] This structure takes advantage of the rather broad emission characteristics of the ZnS:Mn^{2+} phosphor in the green to red part of the spectrum and uses a filter to produce the primary red and green colors, as shown in Figure 18. In order to avoid parallax, it is necessary for the filter to be located in close to the EL film stack, and thus an inverted structure is used in which the lower electrode on the glass substrate is opaque and the upper electrode on the top of the thin-film stack is transparent. The display is therefore viewed through the color filter.

The combination of a broad-band phosphor with a patterned color filter appears to be a more promising approach for multicolor EL displays than the development of efficient EL phosphor materials that emit the primary colors.

Full-color EL. Table 1 shows phosphors for thin-film color inorganic EL displays. In 1990s, the red color obtained by filtering the ZnS:Mn^{2+} emission, and the ZnS:Tb^{3+} phosphor is used for the green emitter. As a blue emitter, SrS:Ce^{3+} has been revaluated as an efficient blue phosphor and extensively studied. Ce^{3+}-activated calcium thiogallate ($CaGa_2S_4$:Ce^{3+}),[38] SrS:Cu^{+},[39] and CaS:Pb^{2+}[40] phosphors were also investigated for the manufacture of blue emitters. In 1999, Miura et al.[41] developed $BaAl_2S_4$:Eu^{2+}, a bright and blue-emitting EL phosphor that satisfied the requirements (luminance, color purity, response time, and life) for full color displays. As a blue EL phosphor, $BaAl_2S_4$:Eu^{2+} far outperforms other blue EL phosphors. Many color phosphors followed the blue-emitting $BaAl_2S_4$:Eu^{2+} phosphor. $SrGa_2S_4$:Eu^{2+}[42] and $CaAl_2S_4$:Eu^{2+}[43] as green emitters, and red-emitting $MgGa_2O_4$:Eu^{3+}[44] and (Ca, Sr)Y_2S_4:Eu^{2+}[45] are promising materials.

Table 1 Color inorganic electroluminescent phosphors

Materials	Obtained Luminance (cd/m^2) (Drive frequency (Hz))	CIE color coordinates (CIE x, CIE y)
SrS:Ce^{3+}	L_{60}=317 (90)	(021, 0.36)
CaGa$_2$S$_4$:Ce^{3+}	L_{40}=10 (60)	(0.14, 0.20)
SrS:Cu^{+}	L_{45}=250 (240)	(0.19, 0.29)
CaS:Pb^{2+}	L_{25}=80 (60)	(0.15, 0.10)
BaAl$_2$S$_4$:Eu^{2+}	L_{60}=1681 (120)	(0.12, 0.08)
ZnS:Tb^{3+}	L_{60}=3574 (120)	(0.320, 0.600)
ZnMgS:Mn^{2+} with filter	L_{60}=625 (120)	(0.315, 0.680)
SrGa$_2$S$_4$:Eu^{2+}	L_{60}=686 (120)	(0.226, 0.701)
CaAl$_2$S$_4$:Eu^{2+}	L_{60}=1700 (120)	(0.13, 0.73)
BaAl$_2$S$_4$:Eu^{2+} with CCM (green)		(0.27, 0.65)
ZnS:Mn^{2+} with filter	L_{60}=830 (120)	(0.660, 0.340)
MgGa$_2$O$_4$:Eu^{3+}	L_{60}=203 (120)	(0.652, 0.348)
(Ca, Sr)Y$_2$S$_4$:Eu^{2+}		(0.67, 0.33)
BaAl$_2$S$_4$:Eu^{2+} with CCM (red)		(0.65, 0.35)

Color by blue method. Recently color by blue method was developed to replace the patterned phosphor system.[46] This method is similar to the white LED system. In order to obtain the red and green primary colors, color-changing medium frequency-convert the blue light to red and green. The frequency conversion materials are patterned over the subpixel sets for red and green with the similar process of CRT phosphor manufacturing, while blue light-emitting primary phosphor is used directly for the blue subpixel set. This method is as simple as the order color by white approach, but generates much higher luminance and energy efficiency due to the nature of the color conversion as compared to the filtering of white light. The color by blue method also improves the color uniformity, color saturation, contrast, and grayscale fidelity.

9.1.3 Thick-film dielectric electroluminescent (TDEL) displays

In the past 40 years, the effective lifetime of thin-film electroluminescence (EL) displays was extended and their brightness and contrast were boosted. However some limitation of thin-film EL has yet to be overcome, including relatively limited brightness and difficulty in scaling to large sizes. The thin dielectric layers used in thin-film EL displays are prone to pinhole defects and particulate contamination during manufacturing. Replacing the thin-film dielectric of thin-film EL displays with a thick-film, high-dielectric constant material overcomes the traditional limitations of thin-film EL without losing its advantages.[47] Figure 19 shows a structure of thick-film dielectric electroluminescent devices. The dielectric layers consists of a combination of materials 10–20 m thick, 20–100 times thicker than the traditional thin-film insulating layer. The thick dielectric film is formed by a simple screen-printing technique. Thick-film dielectric dramatically boosts dielectric strength and resistance to electric breakdown, eliminates the problem of pinhole defects, and substantially reduces susceptibility to contamination during processing. Thick-film dielectric gives high electric field; high-dielectric materials increase the transferred charge which acts as an excitation source for emission centers. The thick-film dielectric also improved the luminance–voltage characteristics than those realized with thin-film EL display, enabling easy grayscale control through amplitude modulation.

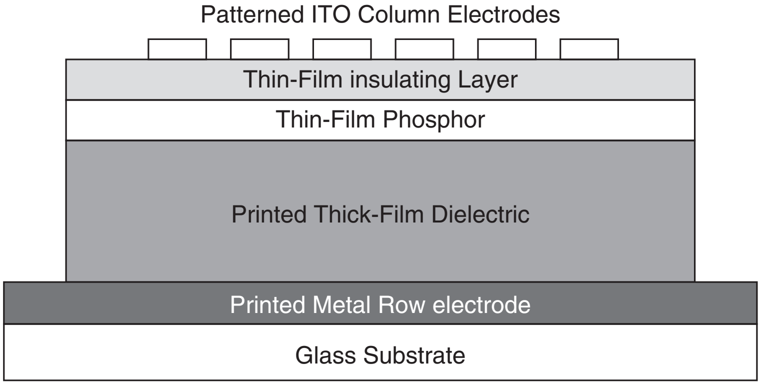
Patterned ITO Column Electrodes
Thin-Film insulating Layer
Thin-Film Phosphor
Printed Thick-Film Dielectric
Printed Metal Row electrode
Glass Substrate

Figure 19 Cross sectional structure of thick-film dielectric EL devices.

References

1. Destriau, G., *J. Chem. Phys.*, 33, 587, 1936.
2. Vecht, A., Werring, N.J., and Smith, P.J.F., *Br. J. Appl. Phys.*, 1, 134, 1968.
3. Kahng, D., *Appl. Phys. Lett.*, 13, 210, 1968.
4. Inoguchi, T., Takeda, M., Kakihara, Y., Nakata, Y., and Yoshida, M., in *Digest, 1974 SID Int. Symp. Society for Information Display,* 1974, 84.
5. Mito, S., Suzuki, C., Kanatani, Y., and Ise, M., in *Digest, 1974 SID Int. Symp. Society for Information Display,* 1974, 86.
6. Uede, H., Kanatani, Y., Kishishita, H., Fujimori, A., and Okano, K., in *Digest, 1981 SID Int. Symp. Society for Information Display,* 1981, 28.
7. Takeda, M., Kanatani, Y., Kishishita, H., Inoguchi, T., and Okano, K., in *Proc. Soc. Inf. Disp.*, 22, 57, 1981.
8. Takeda, M., Kanatani, Y., Kishishita, H., and Uede, H., *Advances in Display Technology III, SPIE Proceedings*, Vol. 386, 34, 1980.
9. Inoguchi, T. and Mito, S., *Electroluminescence in Topics in Appl. Phys.*, 17, Springer-Verlag, 1977, 196.
10. Mach, R. and Miller, G.D., *Phys. Stat. Sol. (a)*, 69, 11, 1982.
11. Chase, E.W., Hoppelwhite, R.T., Krupka, D.C., and Kalong, D., *J. Appl. Phys.*, 40, 2512, 1969.
12. Mikami, A., Terada, K., Okibayashi, K., Tanaka, K., Yoshida, M., and Nakajima, S., *J. Cryst. Growth*, 110, 381, 1991.
13. Yoshida, M., Tanaka, K., Taniguchi, K., Yamashita, T., Kakihara, Y., and Inoguchi, T., in *Digest, 1980 SID Int. Symp. Society for Information Display,* 1980, 106.
14. Vecht, A., in *Digest, 1980 SID Int. Symp. Society for Information Display,* 1980, 110.
15. Barrow, W.A., Coovert, R.E., King, C.N., and Ziuchkovski, M.J., in *Digest, 1986 SID Int. Symp. Society for Information Display,* 1986, 284.
16. Tanaka, S., Shanker, V., Shiiki, M., Deguchi, H., and Kobayashi, H., in *Proc. Soc. Inf. Disp.*, 26, 255, 1985.
17. Tanaka, K., Mikami, A., Ogura, T., Taniguchi, K., Yoshida, M., and Nakajima, S., *Appl. Phys. Lett.*, 48, 1730, 1986.
18. Ono, Y.A., Fuyama, M., Onisawa, K., Tamura, K., and Ando, M., *J. Appl. Phys.*, 66, 5564, 1989.
19. Ogura, T., Mikami, A., Tanaka, K., Taniguchi, K., Yoshida, M., and Nakajima, S., *Appl. Phys. Lett.*, 48, 1570, 1986.
20. Ohnishi, H., Yamasaki, Y., and Iwase, R., in *Proc. Soc. Inf. Disp.*, 28, 345, 1987.
21. Okamoto, K., Yoshimi, T., Nakamura, K., Kobayashi, T., Sato, S., and Miura, S., *Jpn. J. Appl. Phys.*, 28, 1378, 1989.
22. Okamoto, K., Nasu, Y., and Hamakawa, Y., in *Digest, '80 Biennial Disp. Res. Conf.*, 1980, 143.
23. Marello, V. and Onton, A., *IEEE Trans. Electron Device*, ED-27, 1767, 1980.

24. Fujita, Y., Kuwata, J., Nishikawa, M., Tohda, T., Matuoka, T., Abe, A., and Nitta, T., *Proc. Soc. Inf. Disp.*, 25, 177, 1984.
25. Törnqvist, R., Antson, J., Skarp, J., and Tanninen, V.P., *IEEE Trans. Electron Devices*, ED-30, 468, 1983.
26. Nire, T., Watanabe, T., Tsurumaki, N., Miyakoshi, A., and Tanda, S., *Electroluminescence, Springer Proceedings in Physics*, 38, Shionoya, H. and Kobayashi, H., Eds., Springer, Heidelberg, 1989.
27. Cattel, A.R., Cockayne, B., Dexter, K., Kirton, J., and Wright, P.J., *IEEE Trans. Electron Devices*, ED-30, 471, 1983.
28. Inoguchi, T. and Suzuki, C., *Nikkei Electronics*, 84, 1974 (in Japanese).
29. Tanaka, S., Deguchi, H., Mikami, Y., Shiiki, M., and Kobayashi, H., in *Proc. Soc. Inf. Disp.*, 28, 21, 1987.
30. Suntola, T., Anston, J., Pakkala, A., and Linfors, S., in *Digest, 1980 SID Int. Symp. Society for Information Display*, 1980, 108.
31. Okamoto, K., Wakitani, M., Sato, S., Miura, S., Andoh, S., and Umeda, S., in *Digest, 1983 SID Int. Symp. Society for Information Display*, 1983, 16.
32. Takeda, M., Kakihara, Y., Yoshida, M., Nakata, T., and Mito, S., in *Proc. 6th Conf. Solid State Devices, Supplement to Jpn. J. Appl. Phys.*, 44, 103, 1975.
33. Yoshida, M., Kakihara, Y., Tamashita, T., Taniguchi, K., and Inoguchi, T., in *Proc. 9th Conference on Solid State Devices, Supplement to Jpn. J. Appl. Phys.*, 17, 127, 1978.
34. Mikami, A., in *Tech. Digest, Int. Symp. Inorganic and Organic Electroluminescence*, 1994, 17.
35. Matuoka, T., Nakanishi, M., Tohda, T., and Abe, A., *IEEE Trans. Elect. Devices*, ED33, 1290, 1986.
36. Mikami, A., Yashima, I., and Kajikawa, F., in *Proc. 8th Int. Workshop on Inorganic and Organic Electroluminescence in Berlin*, 1996.
37. Okibayashi, K., Ogura, T., Terada, K., Taniguchi, K., Yamashita, T., Yoshida, M., and Nakajima, S., in *Digest, 1991 SID Int. Symp. Society of Information Display*, 1991, 275.
38. Barrow, W.A., Coovert, R.C., Dickey, E., King, C.N., Laakso, C., Sun, S.S., Tuenge, R.T., Wentross, R., and Kane, J., in *Digest 1993 SID Int. Symp. Society of Information Display*, 1993, 761.
39. Sun, S.S., Dickey, E., Kane, J., and Yocom, P.N., in *Conference Record of the 1997 Int. Display Research Conference*, 1997, 301.
40. Yun, S.J., Kim, Y.S., Kang, J-S., Park, S-H., Cho, K., and Ma, D-S., in *Digest 1999 SID Int. Symp. Society of Information Display*, 1999, 1142.
41. Miura, N., Kawanishi, M., Matsumoto, H., and Nakano, R., *Jpn. J. Appl, Phys.*, 38, L1291, 1999.
42. Benalloul, P., Barthou, C., Benoit, J., Eichenauer, L., and Zeinert, A., *Appl. Phys. Lett.* 63, 1954, 1993.
43. Kawanishi, M., Ono, Y., Nakagawa, R., Miura, N., Matsumoto, H., and Nakano, R., in *proc. 11th Int. Workshop on Inorganic and Organic Electroluminescence in Ghent*, 2002, 239.
44. Yano, Y., Oike, T., and Nagano, K., in *proc. 11th Int. Workshop on Inorganic and Organic Electroluminescence in Ghent*, 2002, 225.
45. Miura, N., in *Digest 2004 SID Int. Symp. Society of Information Display*, 2004, 1142.
46. Wu, X., Nakua, A., and Cheong, D., *Journal of the SID*, 12/3, 2004.
47. Wu. X., and Carkner D., in *Digest 2005 SID Int. Symp. Society of Information Display*, 2005, 108.

chapter nine — section two

Electroluminescence materials

Shosaku Tanaka, Hiroshi Kobayashi, Hiroshi Sasakura,
and Noboru Miura

Contents

9.2 Inorganic electroluminescence 709
  9.2.1 Powder phosphor type 709
    9.2.1.1 History 709
    9.2.1.2 AC powder EL 710
    9.2.1.3 DC powder EL 714
References 720

9.2 Inorganic electroluminescence

9.2.1 Powder phosphor type

9.2.1.1 History

In 1936, Destriau[1,2] discovered the phenomenon of light generation by the application of a high AC electric field in a ZnS powder phosphor dispersed in castor oil. This phenomenon is called high-field powder phosphor electroluminescence (EL),[1–9] and it differs from injection EL, which occurs in light-emitting diodes and is associated with processes within *p-n* junctions formed in semiconductor single crystals.

In the 1950s and early 1960s, enormous research efforts were devoted to AC powder phosphor EL with the aim to fabricate efficient illumination panels. Illumination applications and display applications using this type of EL, however, suffer from low luminance and significant luminance degradation in the course of operational times shorter than 500 hours.

During the period from the late 1970s to the 1980s and driven by computer applications, a need developed for flat panel instead of cathode-ray tube (CRT) displays. Thin-film EL, liquid crystal displays (LCDs), plasma display panels (PDPs), and light-emitting diode (LED) arrays were all investigated for the purpose of developing compact flat panel devices for alphanumeric and graphic information displays. In 1974, AC-driven, high-field, thin-film EL devices with high luminance and lifetimes as long as 10,000 hours were developed. It has been also demonstrated that these EL panels can be used for information display with high information contents. With additional industrial development, AC thin-film EL display panels are now commercially available.

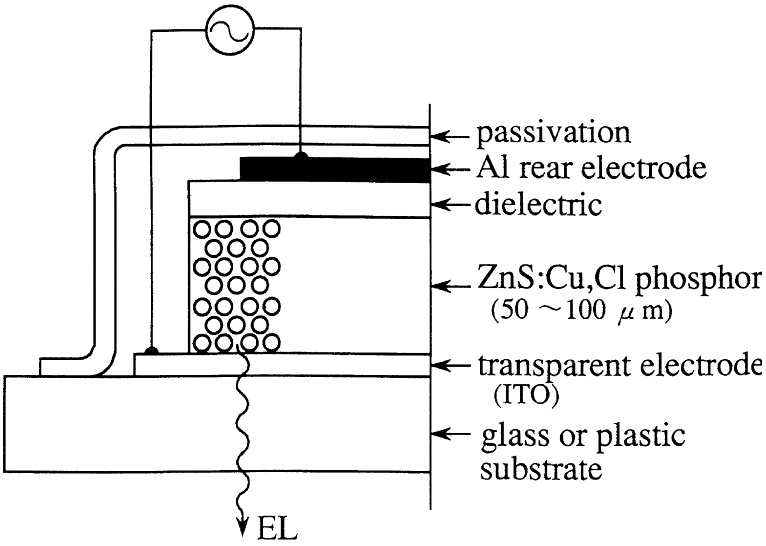

Figure 20 Typical structure of AC powder phosphor EL device.

This advance once again triggered research efforts on AC and DC powder phosphor EL. Generally, AC powder EL panels are expected to be used for back lighting of liquid crystal panels, whereas DC powder EL panels find usage in displays with multiplex capability for matrix addressing. In order to improve the characteristics of powder EL devices, preparation techniques of EL phosphors and a structure of the EL devices continue to be investigated actively.

9.2.1.2 AC powder EL

Structure of EL devices. The structure of a typical AC powder EL device is shown in Figure 20. The EL active layer, consisting of powder ZnS with particle size of 5 to 20 μm dispersed in a dielectric material, is sandwiched between two electrodes. The typical thickness of the EL active layer is 50 to 100 μm. The EL color of the film depends on activators of ZnS phosphors. The most common ZnS phosphor used is the green-emitting ZnS:Cu,Cl(or Al); in this material, the Cu activator behaves as an acceptor and is responsible for the color of the emission, while Cl(or Al) behaves as a donor. The amount of Cu added in the preparation process of these phosphors is 10^{-3} to 10^{-4} g per gram of ZnS, and is one order of magnitude larger than that added to ZnS phosphors used in CRTs. As discussed below, copper plays an important role in high-field powder EL in addition to acting as the activator. The dielectric can be an organic material, such as cyanoethylcellulose, which has a relatively high dielectric constant, or glass with a low melting point is sometimes used as a dispersor. The substrate for the device is glass or a flexible plastic coated with a transparent, conductive indium-tin oxide (ITO) thin-film electrode. In order to protect the EL device against catastrophic dielectric breakdown, an insulating layer, which consists of $BaTiO_3$ powder dispersed in another dielectric material, is often inserted between the EL active layer and the Al rear electrode.

EL characteristics. EL is observed when an AC voltage of about 100 to 200 V corresponding to an electric field of the order of 10^4 V cm^{-1} applied across the electrodes. Luminance-voltage characteristics of a typical EL device are shown in Figure 21. The observed dependence of the luminance (L) on the applied voltage (V) is expressed[3] by the equation:

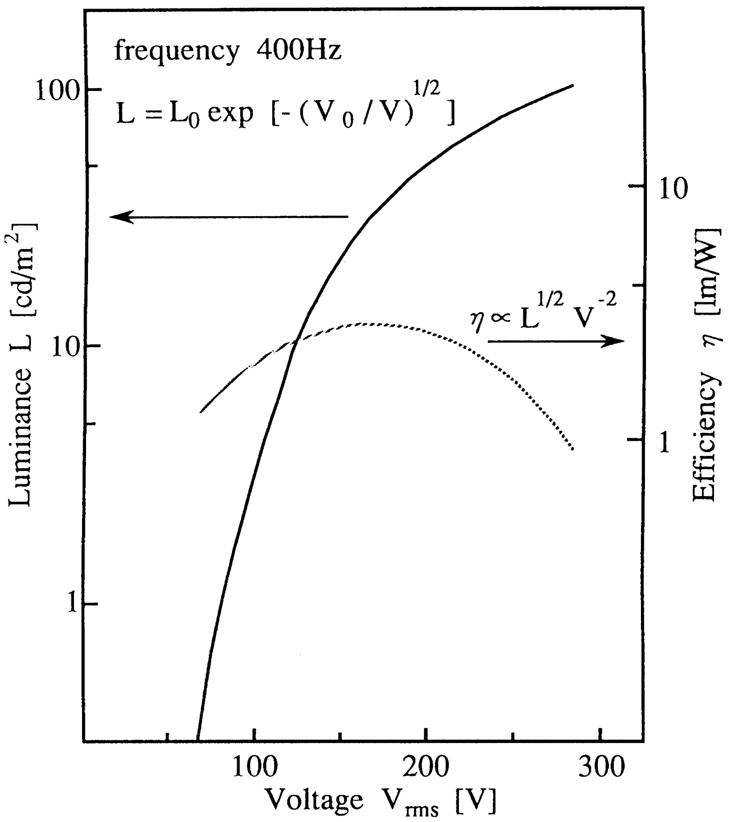

Figure 21 Typical luminance-voltage and efficiency-voltage characteristics of AC powder EL device. (From Zalm, P., *Philips Res. Rep.*, 11, 353, 417, 1956; Fischer, A.G., *J. Electrochem. Soc.*, 109, 1043, 1962. With permission.)

$$L = L_0 \exp\left(-\left(\frac{V_0}{V}\right)^{1/2}\right) \tag{1}$$

The parameters L_0 and V_0 depend on the particle size of the phosphor, the concentration of the powder in the dielectric, the dielectric constant of the embedding medium, and the device thickness. This equation is valid over 7 decades of the EL intensity.[3] It has been established empirically that one of the key parameters affecting EL characteristics is particle size, and a critical trade-off between the EL efficiency and operational life exists as follows. The efficiency increases in proportion to ~$d^{-1/2}$, where d is the particle size; this leads to the nonlinearity of the luminance-voltage dependence. The operational lifetime, however, decreases in proportion to ~d. In addition, the luminance increases with frequency in the frequency region of ~100 Hz to 10 kHz. Luminances up to 100 cd m^{-2} have been achieved for devices driven at a frequency of 400 Hz and a voltage of 200 V.

A typical voltage dependence of the EL efficiency, η, is also shown in Figure 21. Typical values of the efficiency are 1 to 5 lm W^{-1}. The efficiency increases initially with increased applied voltage up to a maximum, but then decreases gradually with further increases in voltage. The EL efficiency dependence on the voltage V is expressed by: $\eta = L^{1/2} V^{-2}$. The maximum efficiency is obtained at a voltage well below the highest luminance level.

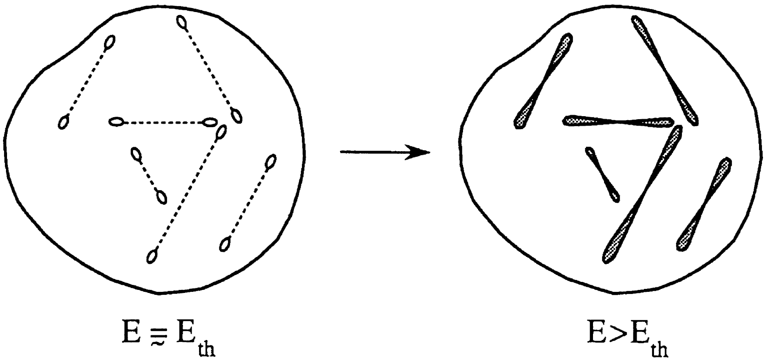

Figure 22 Typical microscopic view of EL from ZnS:Cu,Cl particles. Double EL comet lines at threshold voltage and above the threshold voltage are illustrated. (From Fischer, A.G., *J. Electrochem. Soc.*, 109, 1043, 1962. With permission.)

EL excitation mechanism. EL characteristics of Cu-activated ZnS phosphors can be understood if one considers the microscopic nature of the EL phenomenon. The best experimental observations and theoretical interpretation of EL were presented by Fischer in the early 1960s.[4–6] A careful study of the interior of ZnS:Cu,Cl particles using an optical microscope was performed.[4] It was observed that the shape of the light-emitting region within a single EL particle took the form of double lines with shapes similar to twinkling tails of a comet, as illustrated in Figure 22. Fisher found that each half of the double comet lines lit up alternately whenever the nearest electrode turned positive. As many as 20 or more comet line pairs are observed in one particle. The comet lines follow definite crystal orientations so that networks aligned with 60°-angles are often formed. Those lines making acute angles to the applied field are observed to be the brightest.

Based on these observed facts, Fischer[5,6] proposed the following model for the EL mechanism. ZnS EL powders are typically prepared by firing at high temperatures (1100–1200°C) where the hexagonal wurtzite phase predominates. When the powders are cooled, there is a phase transition to the cubic zinc-blende structure. Copper, previously mentioned as essential in the EL phenomenon, preferentially precipitates on defects formed in the hexagonal-to-cubic transformation with a concentration exceeding their solubility limit in ZnS. The Cu forms thin embedded Cu_xS needles in the crystal matrix. Cu_xS is known to be a *p*-type semiconductor. The applied electric field is concentrated at the tips of these needles. Thus, an applied field of 10^4 to 10^5 V cm^{-1} can induce a local field of 10^6 V cm^{-1} or more inside, sufficient to induce tunneling of holes from one end of the needle and electrons from the other to the ZnS:Cu,Cl lattice. A schematic band model of simultaneous emission of electrons and holes is illustrated in Figure 23. The electrons are captured in shallow traps, probably in Cl or Al donor sites, while the holes are trapped by the Cu recombination centers. When the field is reversed, the emitted electrons recombine with the trapped holes to produce EL.

The luminance-applied voltage relation can be explained by this bipolar field-emission model.[5] The instantaneous field-emission current I through the Cu_xS-ZnS contact follows the Fowler-Nordheim equation:

$$I = A\frac{E^2}{W^{3/2}}\exp\left(-B\frac{W^{3/2}}{E}\right) \tag{2}$$

where A and B are constants, E is the field strength, and W is the work function. In this case, the work function W corresponds to the energy difference between the electron

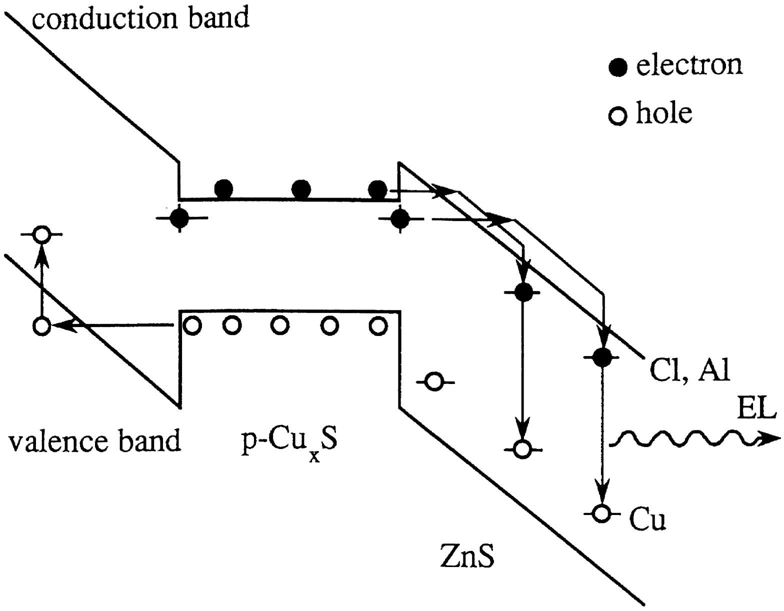

Figure 23 Schematic band model of simultaneous injections of electrons and holes from the opposite ends of a Cu$_x$S needle into the ZnS:Cu,Cl surrounding lattice. (From Fischer, A.G., *J. Electrochem. Soc.*, 110, 733, 1963; Fischer, A.G., Electroluminescence in II-VI compounds, in *Luminescence of Inorganic Solids*, Goldberg, P., Ed., Academic Press, New York, 1966, chap. 10. With permission.)

affinity of ZnS and that of Cu$_x$S. Assuming that the EL intensity is proportional to the current, the luminance may be expressed as:

$$L = L_0' \exp\left(-\frac{V_0'}{V}\right) \tag{3}$$

It has been established that L-V characteristics of single ZnS:Cu,Cl particles as well as those of EL devices made of powders with a uniform particle size obey this equation. The luminance-applied voltage relation of ordinary EL devices expressed by Eq. 1 is due to the fact that phosphor powders have a natural particle size distribution. Eq. 1 is derived through the summation of Eq. 3 over the distribution of L_0' and V_0' values.

Prior to Fischer's work mentioned above, another model[3] had been proposed to explain the L-V relation. In this model, the presence of a metallic Cu$_x$S to *n*-type ZnS junction similar to a Schottky barrier was postulated; EL excitation and emission were thought to take place in the depletion layer. Assuming that ionized donors with positive charge exist uniformly in the depletion layer, one can derive that the maximum electric field E_{max} is proportional to $V^{1/2}$, leading to the L-V relation of Eq. 1. In Fischer's model, however, it is unnecessary to postulate depletion layers with $E_{max} \sim V^{1/2}$ in front of the field-emitting junctions.

Recently, Ono et al.[10] have examined the profile of Cu-activated ZnS phosphor particles showing EL using a transmission electron microscope. They observed black speckles with diameters of 20 to 40 nm in the boundary of micro-twin crystals inside a ZnS particle. The speckles were considered to be some kind of precipitate. As a result of elementary analysis using electron probe microanalysis, it was shown that the composition of the black speckles is copper sulfide. Further, by measuring the wavelength of characteristic X-rays emitted from the copper, it was determined that the copper ion is monovalent, thus establishing

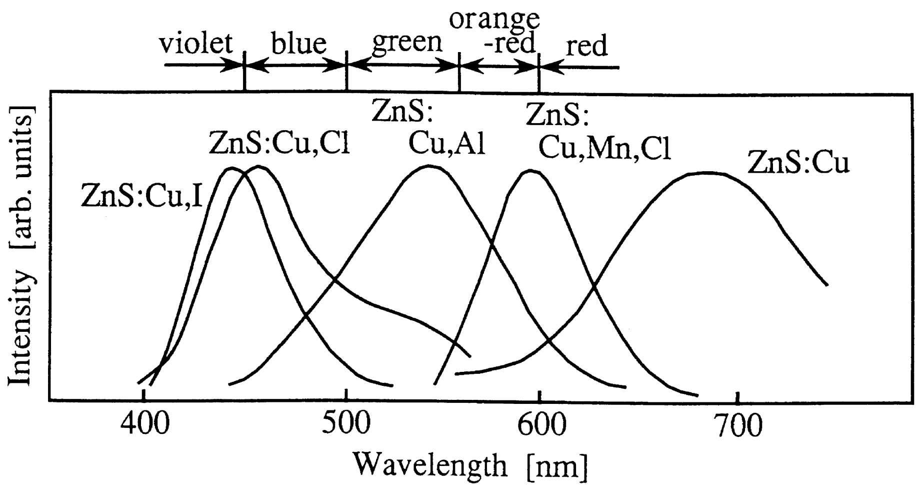

Figure 24 AC EL spectra of various kinds of ZnS powder phosphors.

that the precipitated phase is definitely Cu_2S. These workers proposed that Cu_2S precipitates in narrow needle shape along the micro-twin boundaries. Cu_2S is known to be a *p*-type semiconductor with high metallic conductivity. Therefore, the above observations provide clear experimental evidence for the validity of Fischer's model for the EL excitation mechanism. Thus, this mechanism has been established.

EL emission spectra. The emission spectra of AC powder EL devices are shown in Figure 24. Emission colors can be controlled by incorporating different luminescent centers in the phosphors. When the ZnS lattice is activated with Cu (activators) and Cl, I, or Al (co-activator), donor (co-activator)-acceptor (activator) pairs are formed. The EL is caused by the radiative recombination of electron-hole pairs at donor-accepting (D-A) pair sites. The combination of Cu and Al (ZnS:Cu,Al) produces a green (~550 nm) emission color. The combination of Cu and Cl (ZnS:Cu,Cl) gives blue (~460 nm) and green emission bands, their relative intensity depending on the relative amount of Cu to Cl. ZnS:Cu,I shows a blue emission. ZnS:Cu in which no co-activators are incorporated shows a red emission. By further incorporating Mn^{2+} ions into ZnS:Cu,Cl phosphors, the resultant ZnS:Cu,Mn,Cl shows a yellow emission (~580 nm) due to Mn^{2+}.

Degradation characteristics. Degradation is a key issue in applications of AC powder EL devices. Figure 25 shows a typical example of EL light output vs. time. The degradation rate depends on the driving conditions (such as frequency and luminance levels) and on environmental conditions, especially on temperature and humidity. A lifetime of 2000 hr, defined as the time required for the luminance to decrease to half its initial value, as shown in the figure, can be achieved only by careful protection of the device from the harmful effects of moisture. The luminance decay with time is usually expressed by: $L/L_0 = (1 + \alpha t)^{-1}$, where α is roughly proportional to the driving frequency.

Recently, EL degradation characteristics have been improved. Using power driving techniques that either maintain constant current or constant power, the lifetime of a device producing 200 cd m^{-2} has been extended to more than 3000 hr. These lifetimes meet the requirements for applications such as in back lighting of liquid crystal panels.

9.2.1.3 DC powder EL

Structure of EL devices. The pioneering work on DC powder EL was carried out by Vecht and collaborators.[11] The structure of a typical DC powder EL device is shown in

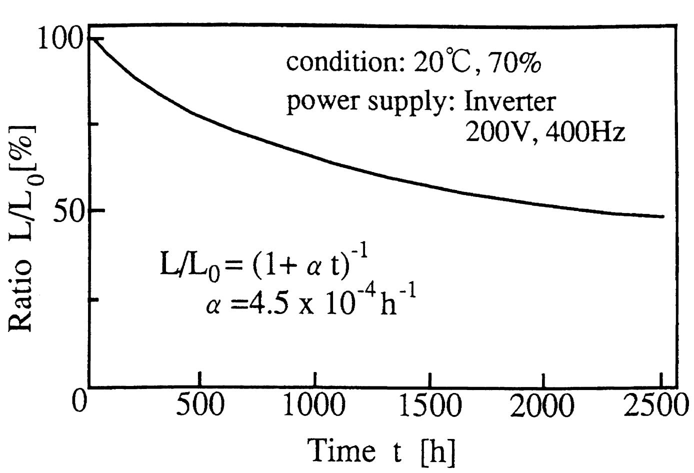

Figure 25 Typical luminance maintenance curve of AC powder EL device. (From Howard, W.E., *Proc. Soc. Inform. Display*, 22, 47, 1981. With permission.)

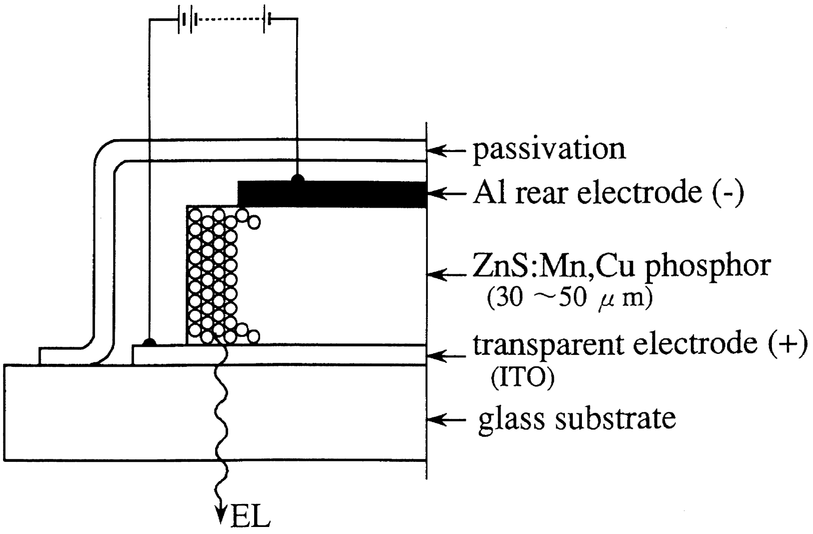

Figure 26 Typical structure of DC-powder phosphor EL device. (From Vecht, A., Werring, N.J., Ellis, R., and Smith, J.F., *Proc. IEEE*, 61, 902, 1973. With permission.)

Figure 26. A layer of ZnS:Mn,Cu phosphor powder with a small amount of binder is deposited on a glass substrate coated with a transparent ITO thin film. The typical thickness of the EL active layer is 30 to 50 μm. The rear Al electrode is evaporated onto the phosphor layer to complete the EL device. The transparent ITO and Al rear electrodes are positive and negative, respectively. This bias condition is used when the EL active layer is nearest the ITO transparent electrode, as mentioned below.

In the case of AC powder EL phosphors, the high-temperature firing and cooling in the phosphor preparation process produce conducting Cu_xS precipitates within the ZnS particles (particle size of 5 to 20 μm). On the other hand, for DC powder EL phosphors, an Mn^{2+}-doped ZnS powder composed of finer (0.5 to 1 μm) particles is used. A conductive Cu_xS surface layer is chemically formed on the ZnS particles by immersing the powder in a hot $CuSO_4$ solution. This treatment is called Cu-coating. Devices incorporating these powders are conductive and do not produce EL. To complete the fabrication process, a

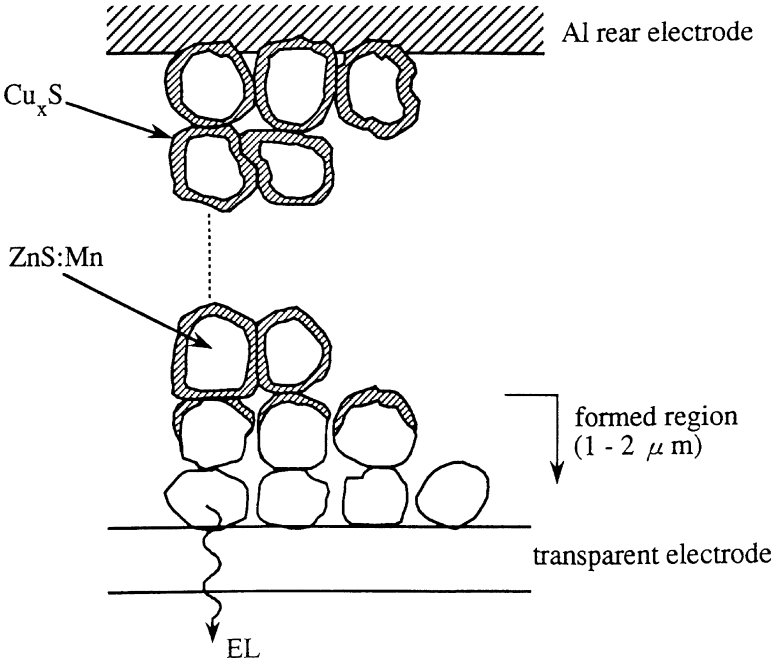

Figure 27 Microscopic structure of DC powder EL layer. (From Kirton, J., *Handbook on Semiconductors*, Vol. 4, Device Physics, North-Holland Publishing Company, Amsterdam, 1981, chap. 5C. With permission.)

process called *forming* is required. The forming process is discussed in the next section, together with the DC EL excitation mechanism. These EL devices emit yellow light (~590 nm) due to the Mn^{2+} centers. Since ZnS is sensitive to moisture and the device construction provides no protection for the phosphor powder, the entire structure must be sealed hermetically.

Forming process and EL excitation mechanism[7,11]. An EL device prepared as described above does not emit light and it must be "formed" to obtain EL emission. In the forming process, a DC voltage with the Al electrode negatively biased is applied to the device. A large current flows because the device is conductive before forming. The phosphor layer heats up, allowing Cu^+ ions to migrate toward the negative electrode. This produces a narrow Cu-free region adjacent to the ITO anode. The microscopic structure of the powder layer after "forming" is illustrated in Figure 27. Since the Cu-free region is less conductive, the greater part of the applied voltage is concentrated here and a high electric field appears across this region. When the formed region reaches thicknesses of 1 to 2 µm, the area begins to emit light. However, the formed region keeps growing slowly with time; as a result, the applied field decreases gradually and the process becomes self-limiting.

Quantitatively, since the thickness of the Cu-free formed region is of the order of 1 to 2 µm and the greater part of external applied voltage of the order of 100 V is applied across this region, an extremely high electric field of 10^6 V cm^{-1} (100 V per ~1 µm) is produced within this region. An energy band model corresponding to the microscopic structure of a DC powder EL device is shown in Figure 28. Electrons are injected from the Cu_xS layer, presumably by tunneling, into the Cu-free $ZnS{:}Mn^{2+}$ layer. These electrons are accelerated by the high field and excite the Mn^{2+} luminescent centers by impact. Thus, the excitation mechanism of Mn^{2+} centers in DC powder EL is essentially the same as that in AC thin-film EL (See 2.10).

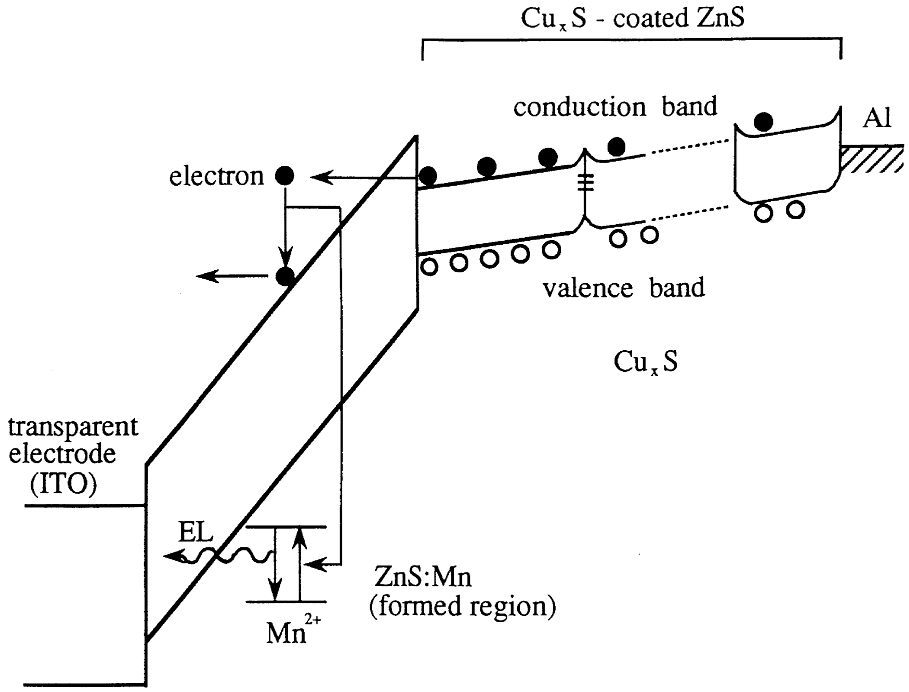

Figure 28 Energy band model of DC powder EL device. (From Kirton, J., *Handbook on Semiconductors*, Vol. 4, Device Physics, North-Holland Publishing Company, Amsterdam, 1981, chap. 5C. With permission.)

Current-applied voltage characteristics of DC EL devices after forming are shown in Figure 29 for several forming voltages V_f. A large current flows when voltages exceeding the forming voltage are applied to the device. To avoid further forming, DC EL devices are generally used under the condition that the driving voltage is kept lower than the forming voltage for the device.

EL characteristics. A typical luminance-voltage characteristic of a DC powder EL device is shown in Figure 30. The dependence of luminance (L) on applied DC voltage (V) is expressed by the following equation:

$$L = L_0 \exp\left\{\left(-V_0/V\right)^{1/2}\right\} \tag{4}$$

The discrimination ratio L(V):L(V/3), which is the evaluation factor for the nonlinear dependence of L-V curves, is defined as the ratio of the luminance obtained at applied voltage V to that obtained at V/3. Typical values of the discrimination ratio of a DC powder EL device are over 1000 due to a larger value of L_0, and are considerably higher than those for AC powder EL devices of less than 100. The dependence of the efficiency, η, on V is expressed by: $\eta = L_{1/2} V^{-2}$. A typical example is shown in Figure 30. The value of η is in a range 0.2 to 0.5 lm W^{-1}.

DC powder EL devices are suitable for use in display panels with x-y matrix electrodes because these devices have a higher discrimination ratio, thus allowing simple matrix addressing. In the case of EL display panels with N (200–400) row electrodes, the EL cell in each row electrode is addressed in a fraction of the field time, which is defined as the time required to address the entire row of electrodes. This corresponds to a pulsed voltage

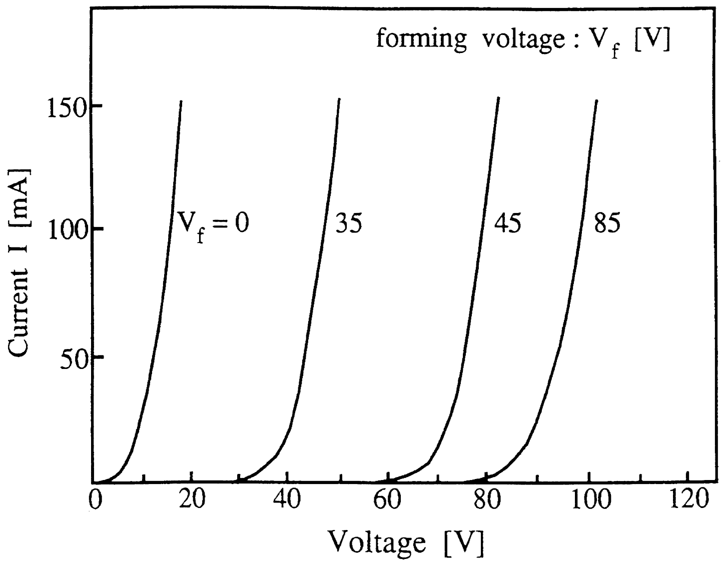

Figure 29 Current–applied voltage characteristics of DC powder EL device after forming at several forming voltages V_f. (From Kirton, J., *Handbook on Semiconductors*, Vol. 4, Device Physics, North-Holland Publishing Company, Amsterdam, 1981, chap. 5C. With permission.)

drive for EL cells with a low duty ratio of 1/N. In pulsed voltage excitation, DC EL devices can be operated beyond the forming voltage without producing further forming. This brings about a better discrimination ratio and higher luminance than those expected based on L-V curves for DC drive. This is schematically illustrated by the dashed extension of the curve in Figure 30.

Maintenance of luminance. Typical luminance maintenance curves of DC powder EL devices are shown in Figure 31. The cause of luminance degradation is not clear yet. In general, pulsed operation and low luminance operation lead to longer lifetimes. Devices operated at 85 cd m^{-2} can retain more than half of their initial luminance for more than 10,000 hours. This long lifetime is good enough for practical applications.

Color DC powder EL. Conventional DC powder EL devices based on the $ZnS:Mn^{2+}$ phosphor show yellow EL.[11] Using different powder materials and different luminescent centers, other EL colors can be obtained. Various EL devices based on ZnS and alkaline earth sulfides (CaS and SrS) doped with rare-earth ions have been developed, and DC EL has been demonstrated in these materials.[12,13] Rare-earth-doped ZnS shows DC EL in various colors; for example, blue (Tm^{3+}), green (Er^{3+} and Tb^{3+}), orange (Nd^{3+}), and red (Sm^{3+}). $CaS:Ce^{3+},Cl^-$-based devices produce green EL with luminances about one third of the standard value of the $ZnS:Mn^{2+}$ yellow EL device. $CaS:Eu^{2+},Cl^-$ and $SrS:Ce^{3+},Cl^-$ devices show red and blue-green EL, respectively. In order to improve the EL characteristics of phosphors for industrial display applications, further fundamental studies of luminescent materials are required.

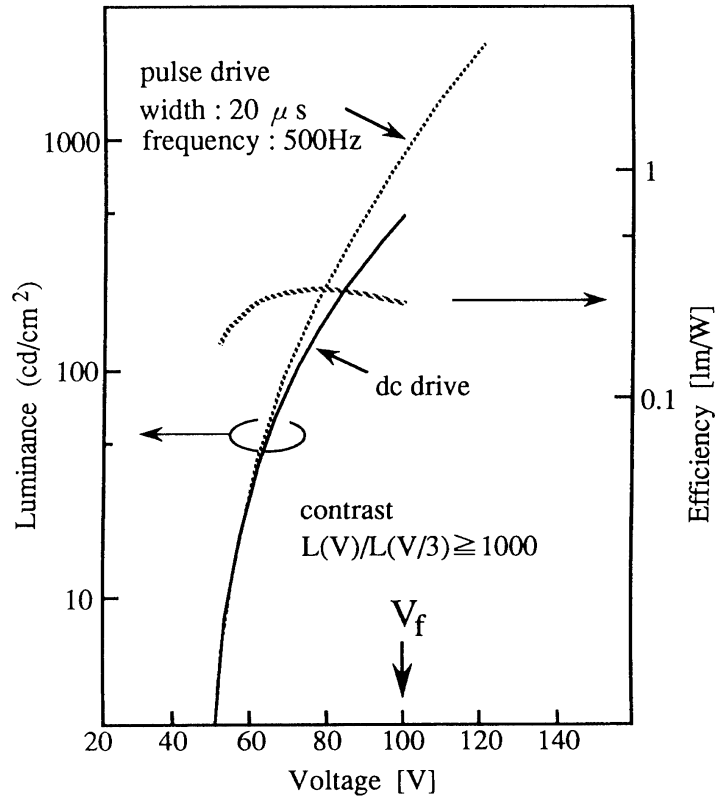

Figure 30 Typical luminance-voltage and efficiency-voltage characteristics of DC powder EL device. (From Kirton, J., *Handbook on Semiconductors*, Vol. 4, Device Physics, North-Holland Publishing Company, Amsterdam, 1981, chap. 5C; Howard, W.E., *Proc. Soc. Inform. Display*, 22, 47, 1981. With permission.)

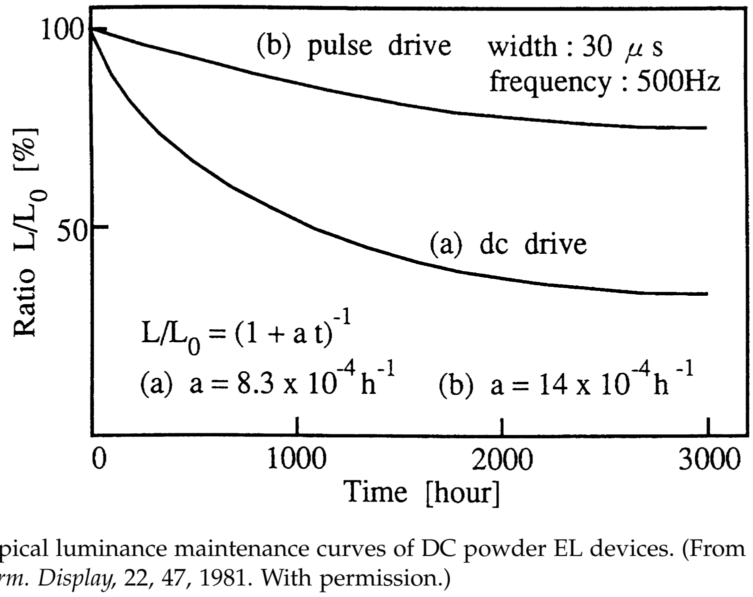

Figure 31 Typical luminance maintenance curves of DC powder EL devices. (From Howard, W.E., *Proc. Soc. Inform. Display*, 22, 47, 1981. With permission.)

References

1. Destriau, G., *J. Chim. Phys.*, 33, 620, 1936.
2. Destriau, G., *Phil. Mag.*, 38, 700, 774, 880, 1947.
3. Zalm, P., *Philips Res. Rep.*, 11, 353, 417, 1956.
4. Fischer, A.G., *J. Electrochem. Soc.*, 109, 1043, 1962.
5. Fischer, A.G., *J. Electrochem. Soc.*, 110, 733, 1963.
6. Fischer, A.G., Electroluminescence in II-VI compounds, in *Luminescence of Inorganic Solids*, Goldberg, P., Ed., Academic Press, New York, 1966, chap. 10.
7. Kirton, J., *Handbook on Semiconductors*, Vol. 4, Device Physics, North-Holland Publishing Company, Amsterdam, 1981, chap. 5C.
8. Theis, D., *J. Luminesc.*, 23, 191, 1981.
9. Howard, W.E., *Proc. Soc. Inform. Display*, 22, 47, 1981.
10. Ono, Y., Shiraga, N., Kadokura, H., and Yamada, K., *Inst. Electron. Inform. Commun. Eng., Tech. Rep.*, 89, No. 378, 1990.
11. Vecht, A., Werring, N.J., Ellis, R., and Smith, J.F., *Proc. IEEE*, 61, 902, 1973.
12. Waite, M.S. and Vecht, A., *Appl. Phys. Lett.*, 19, 471, 1971.
13. Higton, M., Vecht, A., and Mayo, J., *Digest 1978 SID Int. Symp., Soc. Inform. Display*, Los Angeles, 1978, 136.

chapter nine — section three

Electroluminescence materials

Chihaya Adachi and Tetsuo Tsutsui

Contents

9.3 Organic electroluminescence 721
  9.3.1 Electroluminescence in organic solids 721
  9.3.2 Useful materials for organic thin-film EL devices 723
  9.3.3 Polymeric materials for EL 727
  9.3.4 Electrophosphorescence for ultimate EL efficiency 728
References 730

9.3 *Organic electroluminescence*

9.3.1 *Electroluminescence in organic solids*

A review of the early work on electroluminescence (EL) in organic single crystals in the 1960s is very useful for understanding the more recent works on high-performance organic multilayered thin-film EL. In particular, Helfrich and Schneider studied the mechanism of EL in anthracene single crystals in the 1960s. They used anthracene cation- and anion-containing electrolyte solutions as an anode and cathode, respectively, and double charge injection of electrons and holes was only possible using solution contacts for both electrodes, leading to the production of bright EL.[1,2] Figure 32 shows the light intensity versus current density characteristics replotted from one of their original figures. It is seen that the emission intensity scales linearly with injected current density over more than three decades, providing clear evidence of charge injection, transport, and recombination processes which determine quantum efficiencies in terms of photons emitted per charge injected. Helfrich and Schneider also reported that the emission arose predominantly from a region near the positive electrode, indicating that electrons are injected and transported through the crystal to recombine with the holes injected from the positive electrode. This clearly shows that bulk-controlled charge transport and recombination control the process of charge-injection EL.

Following this early work, numerous reports on similar phenomena in a variety of aromatic hydrocarbon single crystals have appeared.[3–8] Over the years, the EL quantum efficiencies have steadily increased and unstable liquid contacts have been replaced with more stable solid electrodes. The development of stable, solid electrodes with good

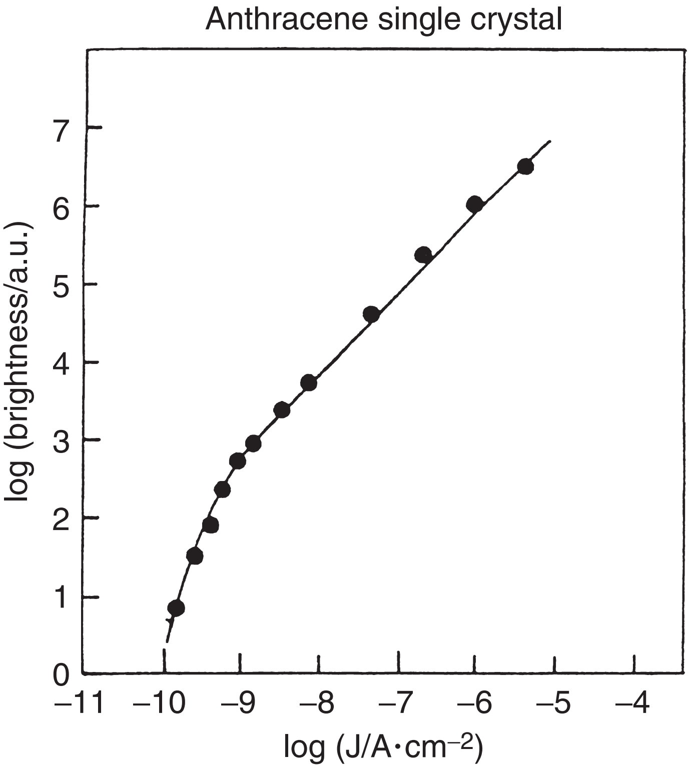

Figure 32 Emission intensity–current density relationship in the EL device made of an anthracene single crystal. (Adapted from data reported by Helfrich, W. and Schneider, W.G. *Phys. Rev. Lett.*, 14, 229, 1965.)

injection characteristics for both electrons and holes is an area deserving further attention and is one that should improve not only the EL efficiency, but also the overall device stability.

In molecular single crystals, the carrier densities are limited to low levels, since they require very high driving voltage, typically over 1000 V, to induce efficient carrier injection. Further, the injected positive and negative charges, which one refers to as electrons and holes for simplicity, are expected to exist as space charges due to the low carrier mobilities, i.e., there can be no local charge neutrality. This situation is clearly different from the inorganic-based semiconductor LEDs, in which minority charge carrier injection at a p–n junction determines the charge recombination process.

It is evident that EL devices made from organic single crystals are unsuitable for any application. The high voltages, the small emitting areas, and the difficulty in processing into display pixels due to typical molecular crystal dimensions are all factors that mitigate their utility. This unfavorable situation led to fabrications of thin-film structures and reports of charge-injection EL in Langmuir–Blodgett (LB) films, vacuum-sublimed polycrystalline films, and vacuum-sublimed amorphous glassy films.[9–14] Both the EL efficiencies and stabilities of such thin-film EL devices, however, remained low until the invention of double layer organic EL by Tang and VanSlyke in 1987.

Tang and VanSlyke fabricated high-performance EL devices made of vacuum-sublimed, double-layer organic thin films.[15] A maximum luminance in excess of 1000 cd/m^2, an external quantum efficiency of ~1% photon/electron, and an external energy conversion efficiency of 1.5 lm/W were achieved with a driving voltage below 10 V. Their report represented an important breakthrough in that it highlighted the possibilities for organic EL in flat-panel display applications and demonstrated a commercially viable level of performance.

The attainment of high performance organic EL by Tang and VanSlyke involved several key improvements. The first was the choice of organic materials, namely the use of aromatic diamine TAPC (1,1′-*bis*(di-4-tolylaminophenyl)cyclohexane) and the fluorescent metal chelate Alq_3 ((8-hydroxyquinolino)aluminum). TAPC has been extensively used in xerography as a hole transport material. Alq_3 is a robust material with intense green photoluminescence when in a film. Second, they demonstrated that ultrathin films with thicknesses of less than 60 nm provided improved stability. Third, the idea to combine two layers with complementary electronic and optical properties proved especially significant, allowing separate optimizations of the transport and emission properties. The final important improvement was in the choice of cathode materials. The Mg/Ag alloy cathode provides a favorable balance between low work function for efficient electron injection and relatively high stability under ambient conditions. Following this demonstration of the utility of double-layer devices, Adachi and coworkers at Kyushu University extended and generalized the concept to multilayer structures using electron transport materials.[16–21] The discovery of an oxadiazole derivative as an electron transport material expanded the range of novel EL device structures that could be fabricated, and a variety of new materials were confirmed to be useful for organic EL devices.

9.3.2 *Useful materials for organic thin-film EL devices*

Typical modern EL devices with two-layer structures are composed of a transparent indium–tin–oxide (ITO) anode, a hole transport layer (HTL), an electron transport layer (ETL), and a metal cathode (Mg/Ag alloy film, for example). The HTL fulfills the roles of assisting in the injection of holes from the ITO anode and transporting the injected holes into the two organic layers, while the ETL has the function of assisting in the injection of electrons from the metal cathode and the transport of the injected electrons. Recombination of holes and electrons occurs in the boundary regions between the two organic layers because of the stacking of HTL and ETL analogous to an inorganic p–n junction. When the recombination region is within an ETL, the ETL also serves as an emitting layer (EML). When the recombination occurs within the HTL, on the other hand, the HTL can serve as an EML. Thus, these devices are classified into two types: ITO/HTL/ETL(EML)/MgAg and ITO/HTL(EML)/ETL/MgAg. When bipolar materials that have the ability to transport both electrons and holes are available, one can use a three layer, double heterostructure in which an independent thin EML is sandwiched between HTL and ETL, ITO/HTL/EML/ETL/MgAg. Figure 33 summarizes three typical device structures.

An aromatic diamine, *N*,*N*′-diphenyl-*N*,*N*′-*bis*(3-methylphenyl)-1,1′-biphenyl-4,4′-diamine (TPD) has been used as a typical HTL material, and it exhibits excellent hole injection and transport properties, with a good electron-blocking capability at an HTL/ETL interface (Figure 34).[18] Although TPD has superior characteristics for HTL, the stability of vacuum-sublimed thin TPD films is insufficient for commercial applications due to the thin films' low glass transition temperature. HTL materials have been extensively developed and the oligomer structures of triphenylamine such as starburst polyamines (*m*-MTDATA) perform better than TPD. In some cases, double HTLs between an ITO electrode and EML have shown good performance.[22]

Several ETL materials that behave as EMLs have been reported. For example, Alq_3 is one of the best ETL (EML) materials. Other fluorescent pigments have also been developed. Fluorescent pigments (e.g., 1,8-naphthoylene-1′,2′-benzimidazole derivatives (NBIs)) that exhibit intense green to red fluorescence in a solid state have been shown to be useful as ETL (EML) materials. Figure 35 shows the typical EL performance of

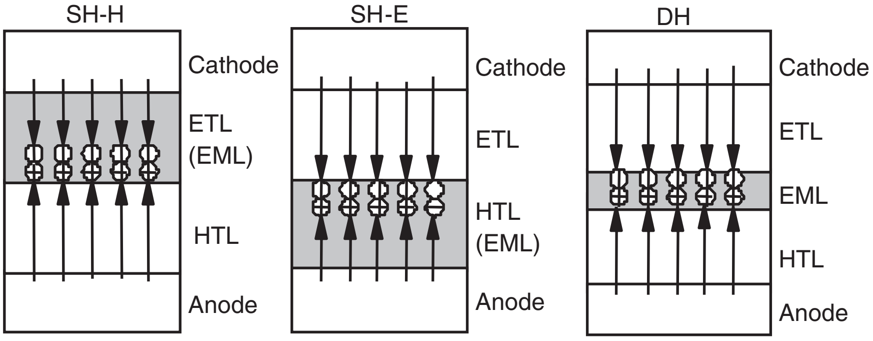

Figure 33 Three typical multilayer structures of thin film EL devices, single and double heterostructures. HTL, ETL, EML, ITO, and LiF/Al mean hole transport layer, electron transport layer, emission layer, indium–tin–oxide anode, and LiF/Al cathode, respectively. Carrier recombination and light emission occurs within the hatched regions. (From Tsutsui, T. and Saito, S. *Polymers for Electronics*, Kodansha Pub., Tokyo, 1990, 591. With Permission.)

double-layer devices with an ITO/TPD/NBI/MgAg structure. Devices with NBI-1 and NBI-2 exhibited a luminance of over 1000 cd/m^2. It was reported that the thin film-forming capability of NBIs with a thickness of ~50 nm most strongly affected the EL-device performance.[23]

When one plans to use the ITO/HTL(EML)/ETL/MgAg structure or the triple-layer structure with an independent EML, ETL materials with high exciton energies are required. The major requirements for this type of ETL material are summarized as follows:

1. ETL should form stable and uniform vacuum-sublimed thin films with a thickness of ~50 nm.
2. They should have rather strong electron affinity for electron injection and transport.
3. They should have high electron mobility for electron transport.
4. They should have large ionization potentials to prevent the injection of holes into a metal cathode without recombination with electrons.
5. They should have large exciton energies to prevent energy transfer from excitons produced by charge-carrier recombination within an EML to an ETL.

During the survey of ETL materials, an oxadiazole derivative, 2-(4′-biphenyl)-5-4″-*tert*-butylphenyl)-1,3,4-oxadiazole (*t*-Bu-PBD) was found to be useful as an ETL in the preparation of EL devices, especially blue EL devices using hole transporting materials as an EML.[18,19] However, the stability of vacuum-sublimed *t*-Bu-PBD thin film is not high enough for practical device applications (i.e., the film does not meet the first requirement). In some cases, Alq_3 can be used for the ETL, however, Alq_3 does not always satisfy the fourth and fifth requirements , due to the low energy gap characteristics and hole transport ability. Therefore, new ETL materials had to be designed and synthesized based on the knowledge that *t*-Bu-PBD has the right properties except the stability of vacuum-sublimed thin films. An oxadiazole derivative with the dimmer structure of *t*-Bu-PBD (named OXD-7) has been found to be one of the most suitable materials for ETL.[24,25] The electron transport properties of OXD-7 are almost the same as that of *t*-Bu-PBD, and the maximum emission wavelength, which can be used as a measure of exciton energy, is below 410 nm.

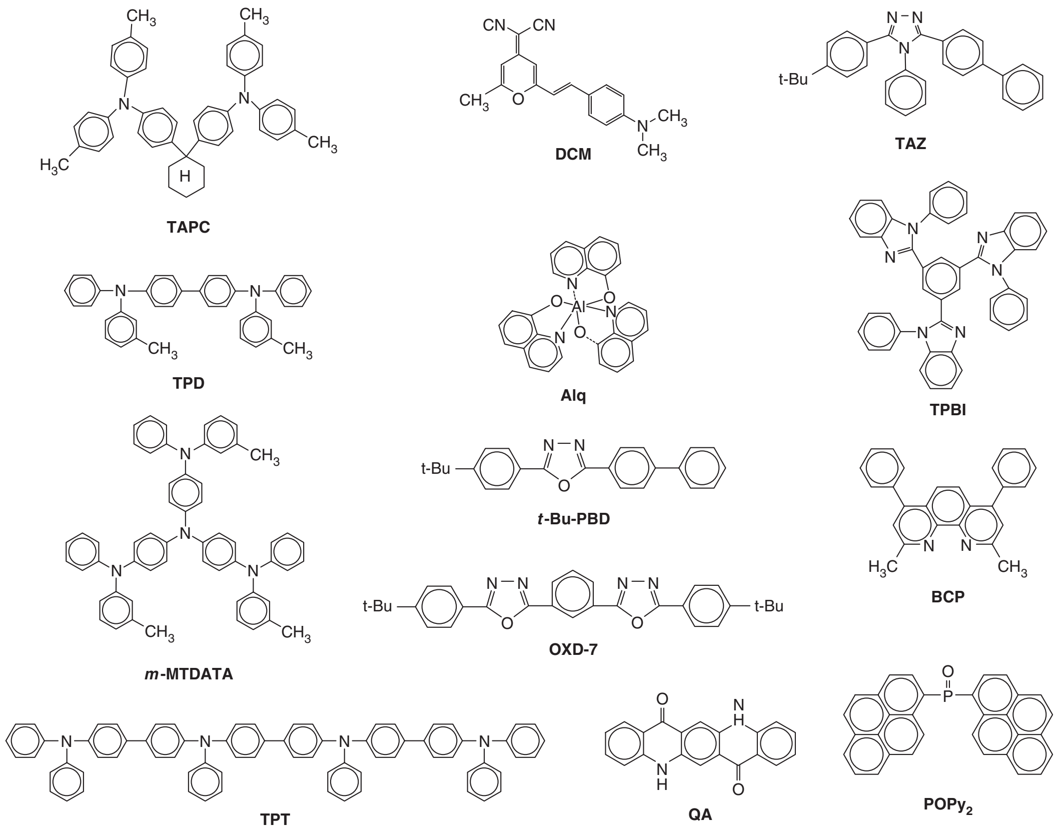

Figure 34 Molecular structures of HTL, ETL, and dopant used in the organic electroluminescence.

Vacuum-sublimed deposition of OXD-7 yields a uniform glassy film with higher softening temperatures than those of *t*-Bu-PBD. OXD-7 is quite stable; no degradation due to spontaneous crystallization was found after a 30-day storage period. More recently a new ETL material, 1,2,4-triazole derivative (TAZ), has been reported.[26] Other stable electron transport materials, such as BCP, TPBI, silole, and phosphine oxide derivatives, have enabled a great improvement in device stability lately.

Several molecules with high fluorescence quantum efficiency have also been utilized as emissive centers, namely by doping within ETL or HTL. The idea of doping is analogous to utilizing a triple-layer structure with a separate EML, which can avoid concentration quenching effects found in high-concentration solid films. The difficulty here is to ensure compatibility of the dopant with the host materials so that a stable, uniform dispersion can be obtained. For example, typical laser dyes, (4-dicyanomethylene-2-methyl-6–9-*p*-dimethylaminostyryl)-4H-pyran (DCM) and quinacridone (QA), have been used to increase EL efficiency and shift the emission colors.

The stability of sublimed, low molar mass materials in their as-deposited amorphous forms is dependent on ensuring that they have little tendency to crystallize. Glass-forming materials, of which TPD is a prime example, can now be molecularly designed. Extensive studies established that the addition of bulky substituents, generation of asymmetric skeletal structures, appendage of dimmer-like nonplanar structures, and the formation of dendric networks all promote the formation of stable glassy films upon vacuum sublimation.

Today, EML materials that emit blue, green, and red have been developed. Although green-emitting Alq_3 has the best EL characteristics among these molecular materials, excellent blue-emitting materials have also been reported. Their EL efficiencies have been greatly improved by using small amounts of emissive dopants in EML.

Experiments on a variety of HTL, ETL, and EML materials confirmed that the introduction of electron-accepting groups increases the electron injection and transport capabilities, whereas the introduction of electron-donating groups increases the hole injection and transport capabilities. Thus, an extended molecular design concept for charge transport and emissive materials has been established, which allows for the systematic design and synthesis of hole and electron injection and transport materials by simply replacing substituents on selected aromatic skeletons. Figure 36 shows examples of systematic molecular design. As an example the common aromatic skeleton is taken; an electron-donating diethylamino group or an electron-accepting cyano group modifies the electronic natures of the aromatic skeletons.

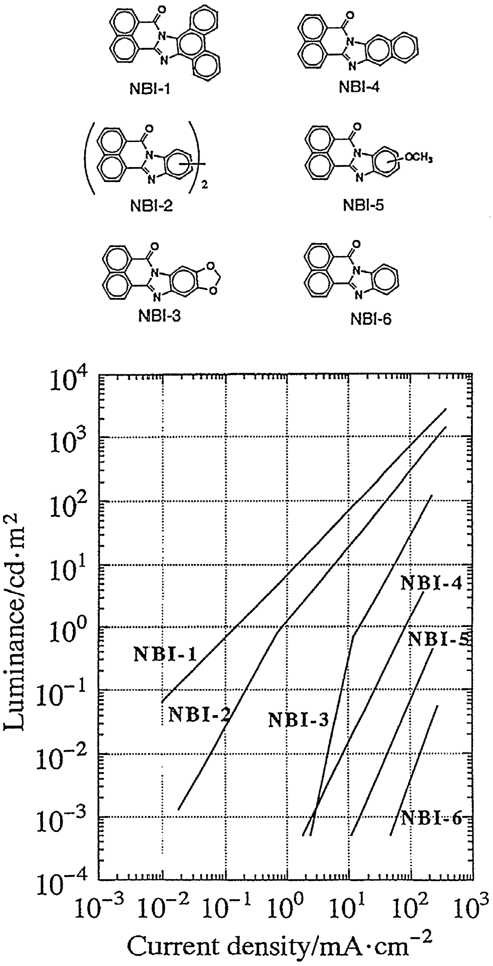

Figure 35 Luminance–current density relationship in ITO/TPD/NBI/MgAg devices. (From Tsutsui, T. and Saito, S. *Polymers for Electronics*, Kodansha Pub., Tokyo, 1990, 591.)

9.3.3 Polymeric materials for EL

In 1990, Burroughes and coworkers at Cambridge University reported that the conjugated polymer poly(*p*-phenylene vinylene) (PPV) could be utilized in single-layer EL devices.[27] The idea of incorporating conjugated polymers into EL devices was an innovation which attracted worldwide interest and elicited the participation of many other groups. The first PPV EL devices had low efficiencies compared with the then state-of-the-art sublimed small molecular devices, mainly due to a lack of balance in charge injection and transport. The efficiency was greatly increased by making use of many of the lessons learned from sublimed dye devices. For example, Heeger and coworkers[28] showed that a low work function calcium cathode gave a tenfold increase in efficiency. Similar improvements were observed using double-layer devices with an ETL consisting of polymethylmethacrylate-dispersed *t*-Bu-PBD.[29] In terms of ultimate efficiency, the combination of a PPV layer, as an HTL, with a cyano-substituted PPV derivative (CN-PPV) layer, as a combined ETL and EML, has given the best results.[30]

Many different π-conjugated polymers have been shown to be EL materials, including poly(*p*-phenylene) (PPP) and its derivatives, poly(3-alkylthiphene) (P3AT), polyphenylacetylene (PPA), and polyfluorenes.[31–33] Figure 37 summarizes the molecular structures of π-conjugated polymers useful for EL.

It should be stressed that the basic EL mechanism from charge injection to emission remains the same, even when fully conjugated polymers are introduced. This is because the emission in organic EL devices occurs via neutral excitations. It has been pointed out that the combination of different organic materials in EL devices is very promising.[34]

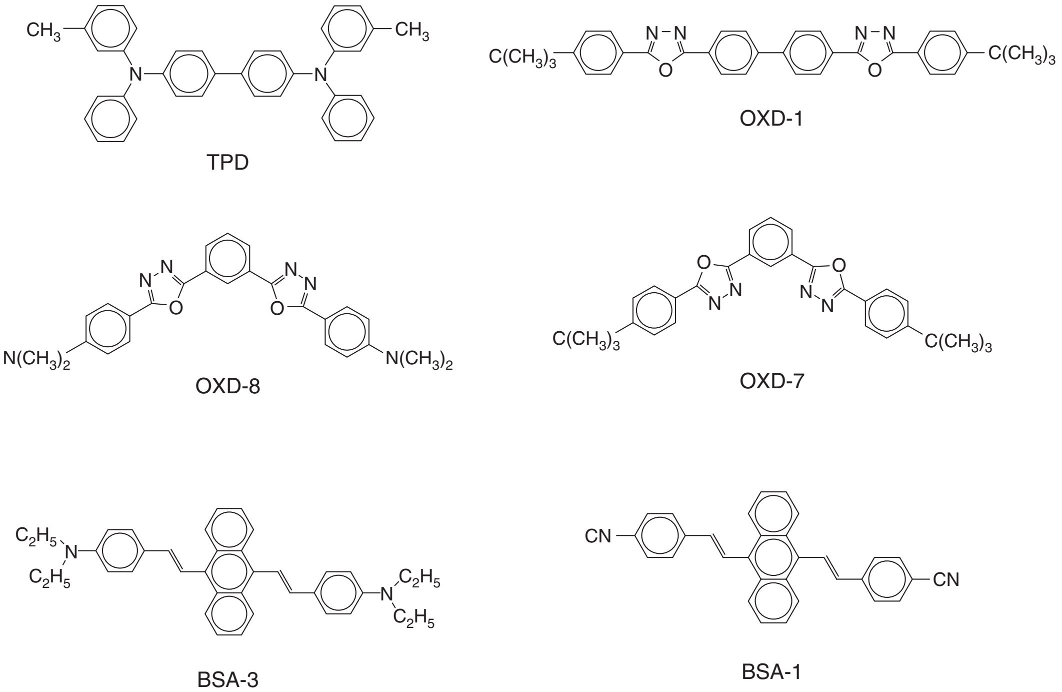

Figure 36 Model systems representing the possibility of systematic molecular design of hole and electron transport molecules.

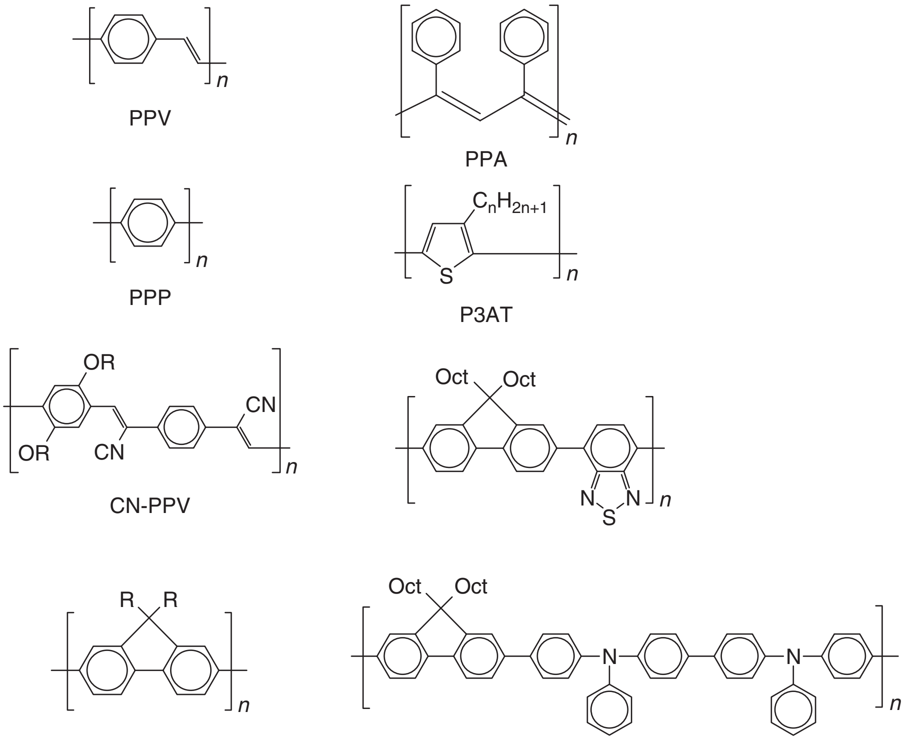

Figure 37 Molecular structures of π-conjugated polymers.

Multilayer device structures utilizing fully conjugated polymers have been fabricated; polymer-dispersed *t*-Bu-PBD was the first,[29] and a variety of charge transport layers have been tested.[30] EL devices using polymers having chromophores on a skeleton have been reported.[35,36] The possibility of using polymer-dispersed systems has also been experimentally verified.[37]

Today, a large variety of organic film-forming materials and systems—including vacuum-sublimed organic thin films, conjugated polymers, polymers containing chromophores, small molecule-polymer composite films, etc.—can be combined to fabricate EL devices with optimal performances. Single-, double-, triple-, and higher multilayer devices are readily accessible, and thousands of selections and combinations are conceivable.

9.3.4 *Electrophosphorescence for ultimate EL efficiency*

Electrophosphorescence (EP) in organic EL was first discovered in anthracene single crystals by Helfrich and Schneider in 1965, and EP from organic thin films was first reported using keto-coumarin and benzophenone derivatives.[38] Unfortunately, the relatively large nonradiative versus radiative decay rates of the triplet states at room temperature lead to very low light emission efficiency. For example, when benzophenone is doped into poly(methylmethacrylate) (PMMA), the external EL quantum efficiency was less than 1%[39] even at temperatures as low as 100 K. Phosphorescence is also possible in atomically forbidden transitions such as those observed in organolanthanide complexes. Examples of such EP are Eu(III)[TTA]phen, which is a red emitter, and similar Tb(III) complexes, which are green emitters. More recently, near infrared emission was observed using Nd(III) and Er(III) complexes. In Eu(III)[TTA]phen, excitation of the Eu(III) ion occurs via intersystem crossing (ISC) from the ligand singlet to the Eu(III) atomic state. Although energy transfer of both electrically generated singlets and triplets can lead to a high external

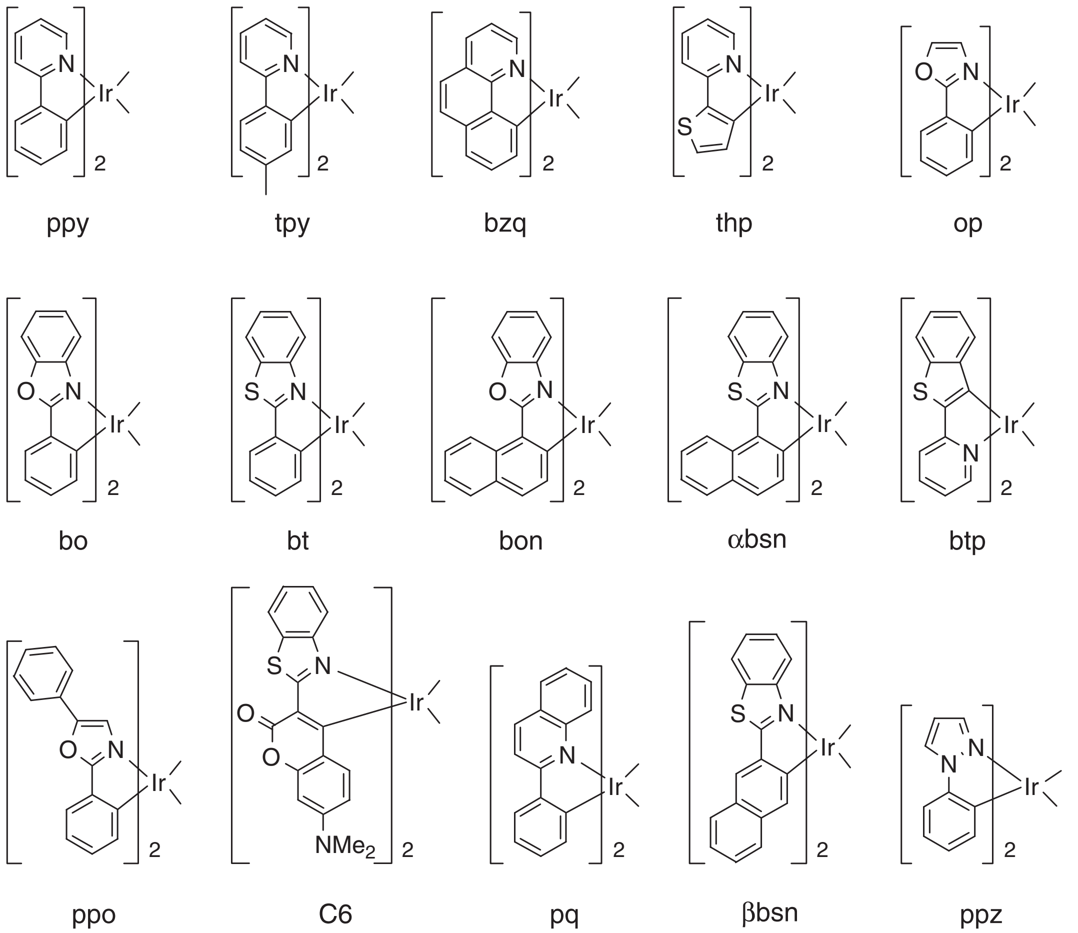

Figure 38 Molecular structures for electrophosphorescence.

efficiency in the lanthanides, the highest efficiency observed to date is ~2%.[40] The most significant problem with the lanthanide complexes is the long lifetime of the excited state. The forbidden d–f transition in Eu(III) has a radiative lifetime of 350 s, which allows for decay via competitive nonradiative processes, as well as via triplet–triplet (T–T) annihilation at high current density. Ultimately, these limitations may prevent the lanthanide complexes from having any practical application for high-efficiency EP.

In contrast, the short radiative triplet lifetimes in heavy metal organometallic compounds lead to a relatively high phosphorescence efficiency, approaching 100% even at room temperature.[41] For this class of compounds, a strong radiative transition moment of metal-to-ligand charge transfer (MLCT) states results from triplet mixing with the excited singlet state by spin–orbit coupling. Mixing reduces the phosphorescence lifetime, leading to high photoluminescent efficiencies. The mixing between singlet and triplet excited states also results in efficient ISC, allowing both singlet and triplet exciton recombination via phosphorescent emission. By this strategy, demonstrations of high-efficiency EP using the organometallic compound, *fac tris*(2-phenylpyridine)iridium (Ir(ppy)$_3$), and its derivatives resulted in a maximum 20%,[42] corresponding to 100% internal quantum efficiency. Also, a variety of emission colors, from blue to green, have been realized by optimizing organic ligands, and some EP devices based on these molecules have already been commercialized (Figure 38).

References

1. Helfrich, W. and Schneider, W. G., *Phys. Rev. Lett.*, 14, 229, 1965.
2. Helfrich, W. and Schneider, W. G., *J. Chem. Phys.*, 44, 2902, 1966.
3. Kawabe, M., Masuda, K., and Nambu, S., *Jpn. J. Appl. Phys.*, 10, 527, 1971.
4. Lohmann, F. and Mehl, W., *J. Chem. Phys.*, 50, 500, 1969.
5. Williams, D. A. and Schadt, M., *Proc. IEEE*, 58, 476, 1970.
6. Bradley, L.L.T., Schowob, H.P., Weitz, D., and Williams, D.F., *Mol. Cryst. Liq. Cryst.*, 23, 271, 1973.
7. Basurto, G. and Burshtein, J.Z., *Mol. Cryst. Liq. Cryst.*, 31, 211, 1975.
8. Glinski, J., Godlewski, J., and Kalinowski, J., *Mol. Cryst. Liq. Cryst.*, 48, 1, 1978.
9. Roberts, G.G., McGinnity, M.M., Barlow, W.A., and Vincett, P.S., *Solid State Commun.*, 32, 683, 1979.
10. Vincett, P.S., Barlow, W.A., Hann, R.A., and Roberts, G.G., *Thin Solid Films*, 94, 171, 1982.
11. Partridge, R.H., *Polymer*, 24, 748, 1983.
12. Era, M., Hayashi, S., Tsutsui, T., and Saito, S., *J. Chem. Soc., Chem. Commun.*, 557, 1985.
13. Hayashi, S., Wang, T.T., Matsuoka, S., and Saito, S., *Mol. Cryst. Liq. Cryst.*, 135, 355, 1986.
14. Hayashi, S., Etoh, H., and Saito, S., *Jpn. J. Appl. Phys.*, 25, L773, 1986.
15. Tang, C.W., and VanSlyke, S.A., *Appl. Phys. Lett.*, 51, 913, 1987.
16. Adachi, C., Tokito, S., Tsutsui, T., and Saito, S., *Jpn. J. Appl. Phys.*, 27, L269, 1988.
17. Adachi, C., Tokito, S., Tsutsui, T., and Saito, S., *Jpn. J. Appl. Phys.*, 27, L713, 1988.
18. Adachi, C., Tsutsui, T., and Saito, S., *Appl. Phys. Lett.*, 55, 1489, 1989.
19. Adachi, C., Tsutsui, T., and Saito, S., *Appl. Phys. Lett.*, 56, 799, 1990.
20. Adachi, C., Tsutsui, T., and Saito, S., *Appl. Phys. Lett.*, 57, 531, 1990.
21. Adachi, C., Tsutsui, T., and Saito, S., *Optoelectron-Devices*, 6, 25, 1991.
22. Shirota, Y., et al., *Appl. Phys. Lett.*, 65, 807, 1994.
23. Tsutsui, T. and Saito, S., Organic thin films for electroluminescence displays, in *Polymers for Electronics*, Tabata, Y., Mita, I., Nonogaki, S., Horie, K., and Tagawa, S., Eds., Kodansha Pub., Tokyo, 1990, 591.
24. Hamada, Y., Adachi, C., Tsutsui, T., and Saito, S., *Jpn. J. Appl. Phys.*, 31, 1812, 1992.
25. Tsutsui, T., Aminaka, E., Fujita, Y., Hamada, Y., and Saito, S., *Synth. Met.*, 55–57, 4157, 1993.
26. Kido, J., et al., *Jpn. J. Appl. Phys*., 32, L917, 1992.
27. Burroughes, J.H., et al., *Nature*, 347, 539, 1990.
28. Braun, D. and Heeger, A.J., *Appl. Phys. Lett.*, 58, 1982, 1991.
29. Brown, A.R., et al., *Appl. Phys. Lett.*, 61, 2793, 1992.
30. Greenham, N.C., Moratti, S.C., Bradley, D.D.C., Friend, R.H., and Holmes, A.B., *Nature*, 365, 628, 1993.
31. Grem, G., Leditzky, G., Ullrich, B., and Leising, G., *Adv. Mater.*, 4, 36, 1992.
32. Ohmori, Y., Uchida, M., Muro, K., and Yoshino, K., *Jpn. J. Appl. Phys*., 30, L1938, 1991.
33. Swanson, L.S., Lu, F., Shinar, J., Ding, Y.W., and Barton, T.J., *Proc. SPIE*, 1910, 101, 1993.
34. Tsutsui, T., and Saito, S., Organic multilayer electroluminescent diodes, in *Intrinsically Conducting Polymer: An Emerging Technology,* Aldissi, M., Ed., Kluwer Academic, The Netherlands, 1993, 23.
35. Hosokawa, C., Kawasaki, N., Sakamoto, S., and Kusumoto, T., *Appl. Phys. Lett.*, 61, 2503, 1992.
36. Sokolik, I., Yang, Z., Karasz, F.E., and Morton, D.C., *J. Appl. Phys*., 74, 3584, 1993.
37. Kido, J., Nagai, K., Okamoto, Y., and Skotheim, T., *Chem. Lett.*, 1267, 1991.
38. Helfrich, W. and Schneider, W.G., *Phys. Rev. Lett.*, 14, 229, 1965.
39. Morikawa, M., Adachi, C., Tsutsui, T., and Saito, S., "Multilayer-type organic solar-cells using phthalocyanines and perylene derivatives," presented at the *51st Autumn Mtg., Jpn. Soc. Appl. Phys.*, 1990. Paper 28a-PB-8.
40. Adachi, C., Baldo, M.A., and Forrest, S.R., *J. Appl. Phys.*, 87, 8049, 2000.
41. Kawamura, Y., Goushi, K. Brooks, J., Brown, J. J., Sasabe, H., and Adachi, C., *Appl. Phys. Lett.*, 86, 071104, 2005.
42. Adachi, C., Baldo, M.A., Thompson, M.E., and Forrest, S.R., *J. Appl. Phys.*, 90, 5048, 2001.

chapter ten — sections one–four

Phosphors for plasma display

Takehiro Kojima and Takayuki Hisamune

Contents

10.1 Plasma display panels 731
10.2 Discharge gases....734
10.3 Vacuum-ultraviolet phosphors and their characteristics....735
10.4 Characteristics of full-color plasma display panel 741
References....743

10.1 Plasma display panels

Plasma display panels (PDPs) can be defined as flat-panel information-display devices in which the pixels consist of small gas-discharge cells that radiate visible light directly or emit luminescence produced by phosphors. In the latter case, the phosphors are excited by ultraviolet light produced by the gas discharge controlled individually in each cell. Devices are usually classified into three classes based on the fundamental operation mechanisms and the structure: (1) the DC type having electrodes in direct contact with discharge gas as in a conventional fluorescent lamp; (2) the AC type in which the electrodes and discharge gas are isolated from each other by a dielectric layer deposited on the electrode; (3) a hybrid type that combines the structures of the AC and DC types.

In order to drive a large-area, high-resolution matrix-addressed PDP to high luminance using a line sequential scanning process, it is necessary to increase the fraction of the on-state period of the discharge in one field scanning period; this is done by introducing a memory function into the display cells. In this case, the discharge of display cells is forced to operate in a bistable (on/off) mode. High speed characteristics, with access times of 4 μs, are then required to display eight subfield (1-bit) pictures in one field period to reproduce a good (8-bit) picture in gray scale.

The memory function of DC-PDPs is obtained by lowering the firing voltage of selected (discharging) display cells compared to the firing voltage of other unselected cells; this is done while a sustaining pulse train, with voltages slightly lower than the firing voltage, is applied to all display cells. The firing voltage is lowered by the presence of priming agents, such as gas atoms excited to a metastable state. These priming agents are generated during cell discharge and the residue allows for the cell to refire upon arrival of the following sustaining pulse. The priming effect is very important in order to make

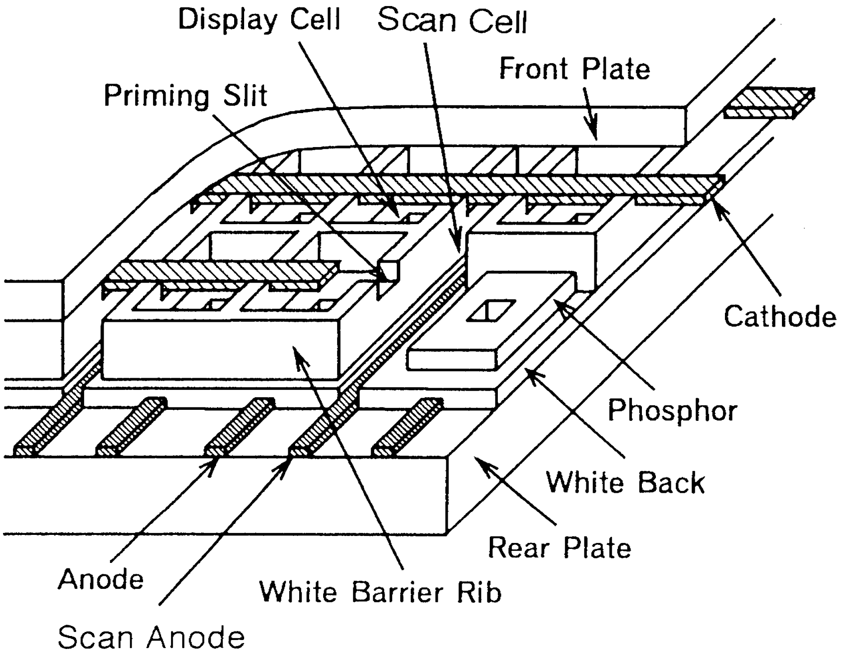

Figure 1 Structure of DC type PDPs. (From Murakami, Y., Koike, J., Oguri, Y., Hisamune, T., and Takahashi, A., *Tech. Rep. Inst. TV Eng. Japan*, 18, 68, 55, 1994 (in Japanese). With permission.)

panels operate with the desired characteristics of high speed, low noise, and stable cell selectivity. The time delay needed for firing, the fluctuation in delay, and the firing voltage are reduced in the discharge control of the cell itself and of the adjacent cells because of the supply of metastable gas particles.

Figure 1 shows a typical structure for DC panels.[1] The panels are operated by modulating the number of luminescence pulses in each display cell during one field period under feeding a sustaining pulse train to all display cells. Writing pulses are applied between pulses of the sustaining pulse train to turn on the display cell. A low-voltage pulse is enough to turn on display cells because the cells are primed by a discharge in the adjacent scan cell through a small priming slit between the cells. The scan cell has an opened-column structure and is used to obtain stable scanning and to prime the display cells. Luminescence of the display cell emitted following the low-voltage writing pulse is much weaker than that following the high-voltage sustaining pulse discharge; therefore, the display maintains a good contrast ratio. All selected display cells can discharge repetitively due to self-priming after a high-voltage discharge. This continues with each sustaining pulse until an erasing pulse is added to suppress the sustaining pulse voltage to an amplitude lower than the refiring voltage.

In this pulse memory scheme, stable 256 gray-scale (8-bit) pictures with a high contrast ratio (100:1 or more) have been displayed on a 500-line panel with a 4-μs repetition period of the sustaining pulses. 40-inch diagonal panels having 800 lines have also been operated using a 2-lines-at-a-time addressing technique and a panel structure in which all anode electrodes are divided into upper and lower subpanels; this scheme produces a high-definition TV picture without seams in the image.[2]

On the other hand, AC panels have an inherent memory function. Wall charges accumulate on the dielectric layer surface placed over the electrode during and just after a pulse discharge. The wall voltages produced by the charges are then added to the next

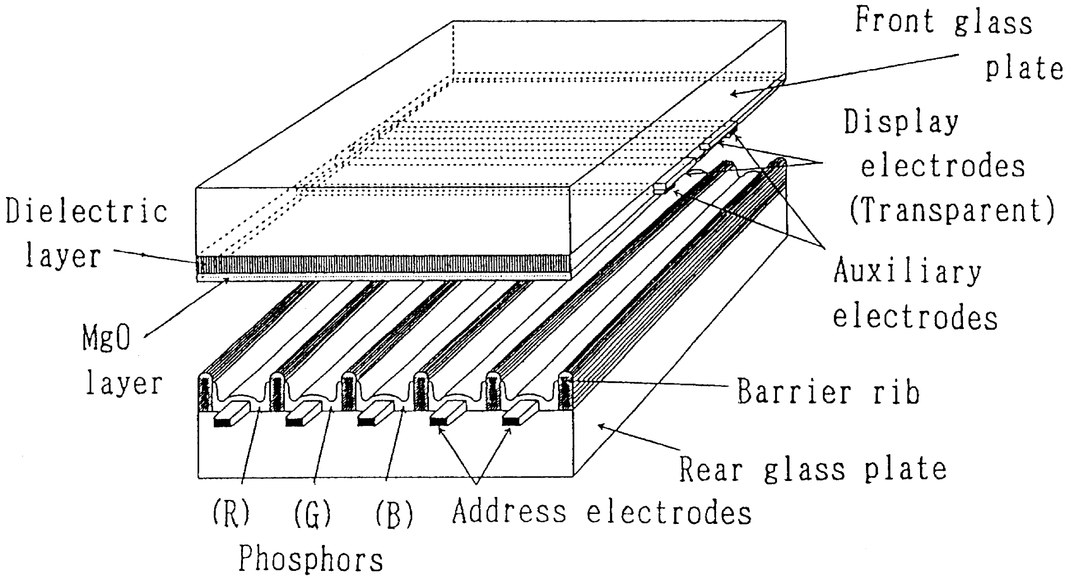

Figure 2 Structure of AC type PDPs. (From Yoshikawa, K., Kanazawa, Y., Wakitani, Y., Shinoda, T., and Otsuka, A., *Tech. Rep. Inst. TV Eng. Jpn.*, 16, 83, 17, 1992 (in Japanese). With permission.)

external sustaining pulse in the same polarity as the applied AC. All the on-state cells can then repeat the discharge without additional writing pulses; the unselected cells are kept in an undischarged condition since they are not exposed to sufficient discharge voltage. The generation and displacement of the wall charges in the specified cells are the basic technique used to drive the AC panel.

Figure 2 shows a typical structure for recent AC panels.[3] The writing operation is done by the removal of the wall charges from the unselected display cells in line sequence after all cells have been lit; only the selected cells have the wall charge, i.e., the selected (unerased) cells are written in the panel. The decay time of the wall charges is usually much longer than the decay of metastable state gas particles in DC cells. The time constant is determined by the insulating characteristics of the dielectric layer if there is no other disturbance. To display an image, all written cell lines can initiate their sustaining discharges simultaneously after the entire display cell lines have been written in line sequence. This can be done without regard for the difference of the write-in time between the lines. Therefore, the sustaining pulse frequency for display can be selected independently of that in the writing process.

Short access times of 3.3 μs, comparable to that of DC panels, have been obtained for AC panels. Thus, 256 gray-scale pictures have been displayed on a 21-inch diagonal, 480-line panel. The long time constant of the wall charge decay can broaden the sustaining pulse width in the AC PDPs. Another drive scheme in which multiple-line writing is accomplished in a single sustaining period is under development for another panel structure.[4]

Large-area, high-resolution memory panels are typically operated using a sustaining pulse train with a pulse width of 1 μs and repetition period of 3 to 4 μs in both DC and AC panels. Comparison of the vacuum ultraviolet (VUV) generation efficiency between AC and DC panels has not been analyzed quantitatively for a single cell or for a complete panel due to the complexity of the small cell structures and their transient discharge behavior. However, the basic analysis of the discharge process in a small cell space with discharge gas pressures of near 200 Torr has progressed recently.[5,6] 20- to 103-inch color PDPs have been developed recently by many manufacturers. A large-area (32- to 103-inch diagonal), full-color emissive flat panel display using the plasma scheme has been commercialized.

10.2 Discharge gases

PDPs displaying pictures with orange color radiation from the discharge of gas mixtures of Ne with Ar and/or Xe, etc. were used in many sizes and resolutions. Research and development of full-color displays have been actively pursued for a long time in Japan and recently have been commercialized.

The full-color representation of PDPs presently used is made possible through photoluminescence of the three primary colors from three kinds of phosphors coated in their respective discharge cells. Phosphors are excited by the VUV radiation produced by the gas-discharge in the display cells. Many kinds of visible radiation directly produced from the discharge of various gases do not possess the high-purity colors suitable for the full-color representation. Electrons generated in the gas discharge, which have low energies, can also be used to excite some kinds of phosphors, e.g., ZnO:Zn and others, that have been developed for vacuum fluorescent displays as described in Chapter 8.

The conversion efficiency from the electric input to the output of phosphor emission is presently low in full-color PDPs.[7] To overcome this problem, there is an approach that attempts to use high-energy electrons, instead of VUV radiation, to excite phosphors. Low-energy electrons are generated in the low-pressure discharge space in the rear of display cells. These electrons can be introduced into the display cell, which has a constricted structure with a smaller electrode gap than that in the electron-generation space. The firing voltage of this structure is very high, even at the low pressure of several Torrs. The electrons can then be accelerated to an energy that is close to the firing voltage without initiating discharge in the display cell. This high energy, up to several thousand volts, is enough to excite phosphors in a way similar to that of cathode-ray tubes (CRTs). High efficiency characteristics have been reported in some panels using this plasma cathode scheme.[8–10] However, a large-area and high-resolution panel has not yet been obtained because low pressure vessels that can endure atmospheric pressure are still difficult to manufacture since a flat-panel structure without spacers is required.

A picture element of the display panel consists of red (R), green (G), and blue (B) cells. The discharge gap of display cells is on the order of several hundred micrometers or less, and the minimum firing voltage is near 200 V at gas pressures of several hundred Torrs. The saturated gas pressure of mercury, which is generally used in fluorescent lamps, is 10^{-3} Torr at room temperature. Therefore, mercury cannot be used as a gas component applicable to PDP because its pressure is too low. To use it, the optimum operation temperature would need to be raised to 100°C or more.[11] Under these circumstances, the kinds of discharge gas that can be used in PDPs are limited to the mixture of rare gases emitting VUV radiation with a wavelength shorter than 200 nm. Thus, the phosphors used must be efficiently excited by the radiation of this wavelength region.

The discharge gas most widely adopted in present PDPs is Xe. In practice, a mixture of Xe and other rare gases is used. A resonance radiation line of Xe atoms at 147 nm, which is most intense, is used for excitation. The next most intense line is the radiation from an excited state of molecular Xe at 173 nm. Xe pressures recently tend to become higher and 173 nm radiation tends to become stronger to improve VUV radiation efficiency. As gas mixtures, combinations of Ne-Xe,[12] He-Xe,[13–16] Ar-Xe,[16,17] and He-(Ar, Kr,

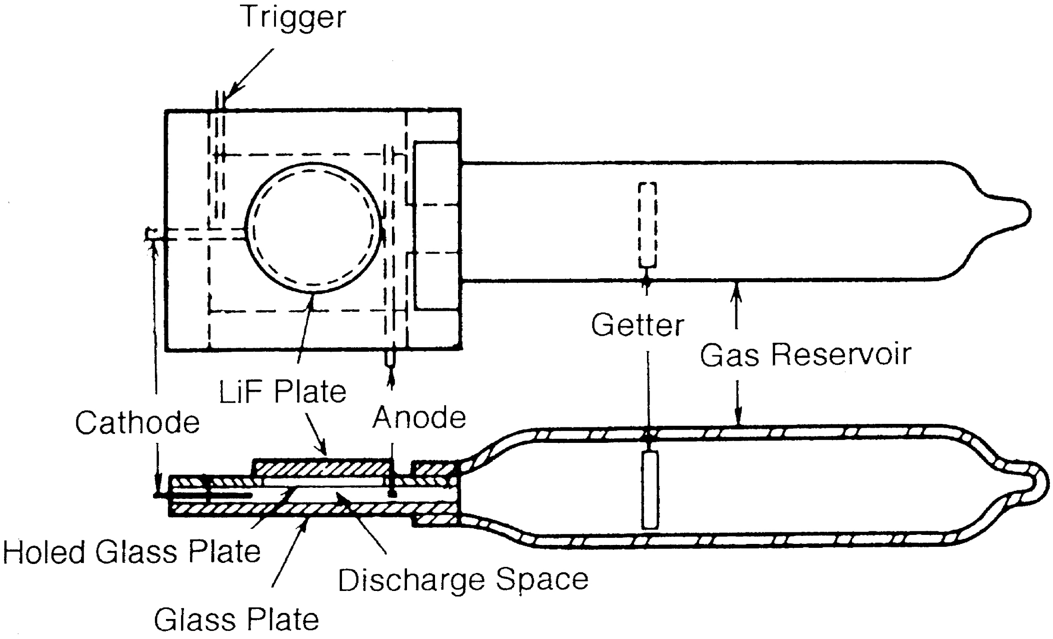

Figure 3 Structure of a simplified VUV light source. (From Koike, J., Kojima, T., Toyonaga, R., Takahashi, K., Kagami, A., and Hase, T., *Tech. G. Electron Device, Inst. TV Eng. Jpn.*, ED317, 1977 (in Japanese). With permission.)

Xe)[18] have been used. Rare gases other than Xe emit at shorter wavelengths and with less intensity.

10.3 *Vacuum-ultraviolet phosphors and their characteristics*

Excitation spectra of VUV phosphors were measured in the author's laboratory with a 0.5-m Seya-Namioka-type vacuum monochromator using sodium salicylate as the sample for reference (see 14.6).[19,20] The radiation source was a water-cooled capillary H_2 discharge lamp without a window.[21]

A VUV light source, shown in Figure 3, was used to excite the phosphors; this enabled measurements in an atmospheric environment without any special conditions, as mentioned below.[22] The VUV window was made of a cleaved LiF disk. The sample phosphor powder is simply placed on the LiF plate and held with tape; or else a phosphor slurry dispersed in alcohol without binder is thickly coated on the plate. Since the air layer between the plate and phosphor powder is very thin, the absorption of VUV light by the air is negligible in these measurements. Using a He-Xe mixture gas as the discharge gas, very intense and reproducible excitation similar to that in display cells can be easily realized.

Excitation uniformity, geometric stability between the light source and phosphor surface, and high excitation intensity are obtained reproducibly with this simple VUV light source by merely keeping the discharge current constant. Caution should be paid to the different thermal expansion coefficients of LiF and the glass vessel. The LiF plate should be attached to the vessel using a plastic sealant at room temperature; and a nonvolatile getter also should be used. Long lives (>10 years) have been obtained with getter reactivation made every 2 to 6 months. Thus, this lamp was used in the initial search for many kinds of phosphor materials and for the quantitative evaluation of luminescent

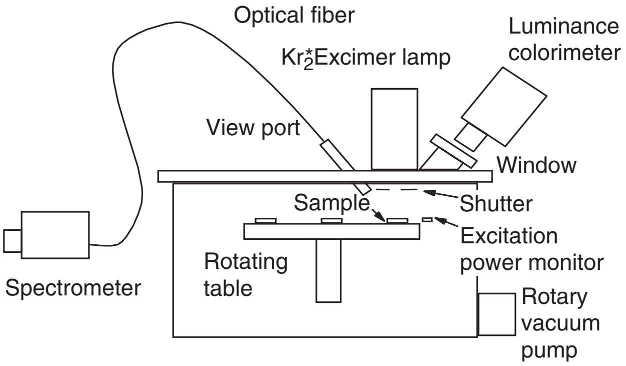

Figure 4 An example of a measuring system with a 146 nm excimer lamp for emission spectrum, luminance, and chromaticity under VUV excitation.

characteristics in the practical stages.[23] In addition to the above, a demountable vacuum vessel, in which a deuterium discharge lamp, bandpass filter of 25-nm bandwidth, and sample phosphors are assembled, was used for practical measurements of VUV phosphors.[24] A Kr_2 excimer lamp producing 146-nm emission has been developed. It is recently widely used in measurements of PDP phosphors. An example of the measurement system with the lamp is shown in Figure 4.

The search for VUV phosphors was performed with the focus on the requisite characteristics for practical PDPs toward the target of full-color display panels rather than multicolor panels. Luminescent characteristics were measured under the 147-nm excitation of the Xe resonance line in the He-Xe discharge, as described above. Excitation spectra were measured in the wavelength region of 100 to 300 nm at room temperature for selected materials.[25] The initial search was started with measurements on practical phosphors for CRTs and fluorescent lamps and has expanded to about 600 materials.

The following VUV phosphors have been reported as of the mid-1970s:

Blue-emitting phosphors	
$CaWO_4{:}Pb^{2+}$	Used in the initial stage of panel developments [26]
$CaWO_4{:}W$	Used in the initial stage of panel developments [14,27,28]
$Sr_3(PO_4)_2{:}Eu^{2+}$ [21]	
$Ba_3(PO_4)_2{:}Eu^{2+}$ [21]	
$Y_2SiO_5{:}Ce^{3+}$	Used in the initial stage of panel developments [21,29]
$YP_{0.85}V_{0.15}O_4$	short on color purity [30]
$SrMg(SiO_4)_2{:}Eu^{2+}$	Good color and efficiency [31]
$BaMg_2Al_{14}O_{24}{:}Eu^{2+}$	Long life [32]
$Sr_5Cl(PO_4)_3{:}Eu^{2+}$ [33]	
Green-emitting phosphors	
$Zn_2SiO_4{:}Mn^{2+}$	Good characteristics [26]
$Y_3(Al, Ga)_5O_{12}{:}Ce^{3+}$ [34]	
$BaMg_2Al_{14}O_{24}{:}Eu^{2+}, Mn^{2+}$	Long life [32]
$CeMgAl_{11}O_{19}{:}Tb^{3+}$	Long life [32]
$Mg(Ga, Al)_2O_4{:}Mn^{2+}$ [35]	
Red-emitting phosphors	
$YVO_4{:}Eu^{3+}$ [26]	
$Y_2O_3{:}Eu^{3+}$ [26]	Used in the initial stage of panel developments [23]
$YP_{0.65}V_{0.35}O_4{:}Eu^{3+}$ [29]	
$YBO_3{:}Eu^{3+}$	Long life [32]

Table 1 CIE Chromaticity Coordinates and Relative Luminous Efficiencies of VUV Phosphors

	Chromaticity coordinates		Relative luminous efficiency[a]
Phosphor	*x*	*y*	
NTSC[b] blue	0.14	0.08	
$CaWO_4:Pb^{2+}$	0.17	0.17	0.74
$Y_2SiO_5:Ce^{3+}$	0.16	0.09	1.1
$BaMgAl_{14}O_{23}:Eu^{2+}$	0.14	0.09	1.6
NTSC green	0.21	0.71	
$Zn_2SiO_4:Mn^{2+}$ (0.03 g atm/mole)	0.21	0.72	1.0
$BaAl_{12}O_{19}:Mn^{2+}$	0.16	0.74	1.1
$BaMgAl_{14}O_{23}:Mn^{2+}$	0.15	0.73	0.92
$SrAl_{12}O_{19}:Mn^{2+}$	0.16	0.75	0.62
$ZnAl_{12}O_{19}:Mn^{2+}$	0.17	0.74	0.54
$CaAl_{12}O_{19}:Mn^{2+}$	0.15	0.75	0.34
$YBO_3:Tb^{3+}$	0.33	0.61	1.1
$LuBO_3:Tb^{3+}$	0.33	0.61	1.1
$GdBO_3:Tb^{3+}$	0.33	0.61	0.53
$ScBO_3:Tb^{3+}$	0.35	0.60	0.36
$Sr_4Si_3O_8Cl_4:Eu^{3+}$	0.14	0.33	1.3
NTSC red	0.67	0.33	
$Y_2O_3:Eu^{3+}$	0.65	0.34	0.67
$Y_2SiO_5:Eu^{3+}$	0.66	0.34	0.62
$Y_3Al_5O_{12}:Eu^{3+}$	0.63	0.37	0.47
$Zn_2(PO_4)_2:Mn^{2+}$	0.67	0.33	0.34
$YBO_3:Eu^{3+}$	0.65	0.35	1.0
$Y_{0.65}Gd_{0.35}BO_3:Eu^{3+}$	0.65	0.35	1.2
$GdBO_3:Eu^{3+}$	0.64	0.36	0.94
$ScBO_3:Eu^{3+}$	0.61	0.39	0.94
$LuBO_3:Eu^{3+}$	0.63	0.37	0.74

Note: Measured under VUV excitation from He-Xe (2%) gas discharge (emits mainly resonance line of 147 nm from Xe).

[a] Normalized to the value of Zn_2SiO_4:Mn (0.03 g-atom/mol).

[b] NTSC: National Television Standard Committee.

From Koike, J., Kojima, T., Toyonaga, R., Kagami, A., Hase, T., and Inaho, S., *J. Electrochem. Soc.*, 126, 1008, 1979. With permission.

Besides the above, several phosphors with high quantum efficiencies under excitation with wavelength longer than 160 nm have been investigated.[36]

Table 1 shows chromaticity coordinates and relative radiant efficiencies (energy efficiencies) of various VUV phosphors investigated, which include those in practical use today.[25] Figures 5, 6, and 7 show excitation spectra of various phosphors in the wavelength region 100 to 300 nm.[25]

For the blue-emitting phosphors in Table 1, $BaMgAl_{14}O_{23}:Eu^{2+}$ has excellent high-efficiency excitation characteristics with two maxima at 180 and 250 nm and luminescent chromaticity near the NTSC (National Television Standard Committee) blue with the peak wavelength at 455 nm and a halfwidth of 55 nm.

As for the green phosphors, $Zn_2SiO_4:Mn^{2+}$ (0.03 g-atom/mol, optimized for CRTs) has found practical application. Although the optimum content of Mn is 0.06 g-atom/mol

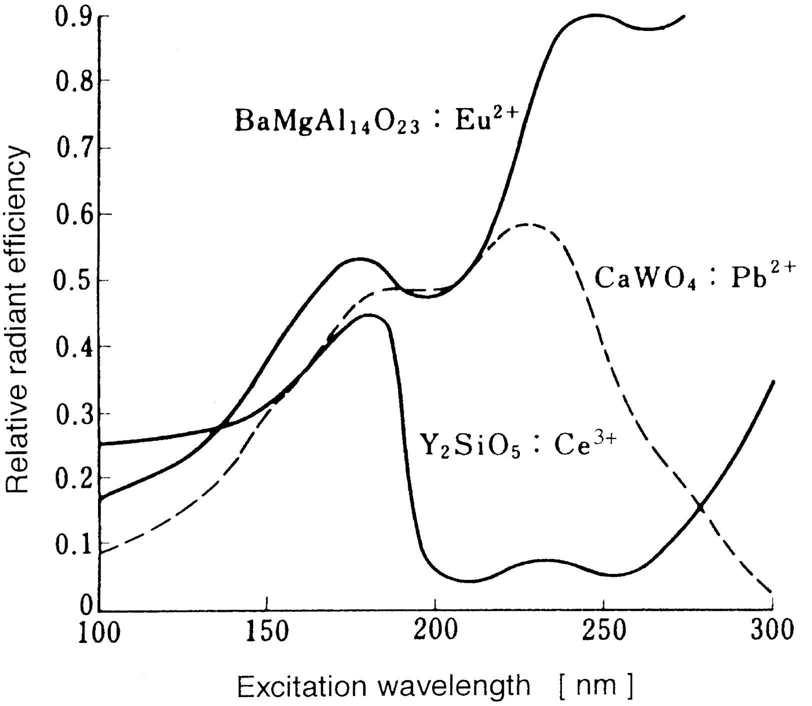

Figure 5 Excitation spectra of blue-emitting phosphors. (From Koike, J., Kojima, T., Toyonaga, R., Takahashi, K., Kagami, A., and Hase, T., *Tech. G. Electron Device, Inst. TV Eng. Jpn.*, ED317, 1977 (in Japanese). With permission.)

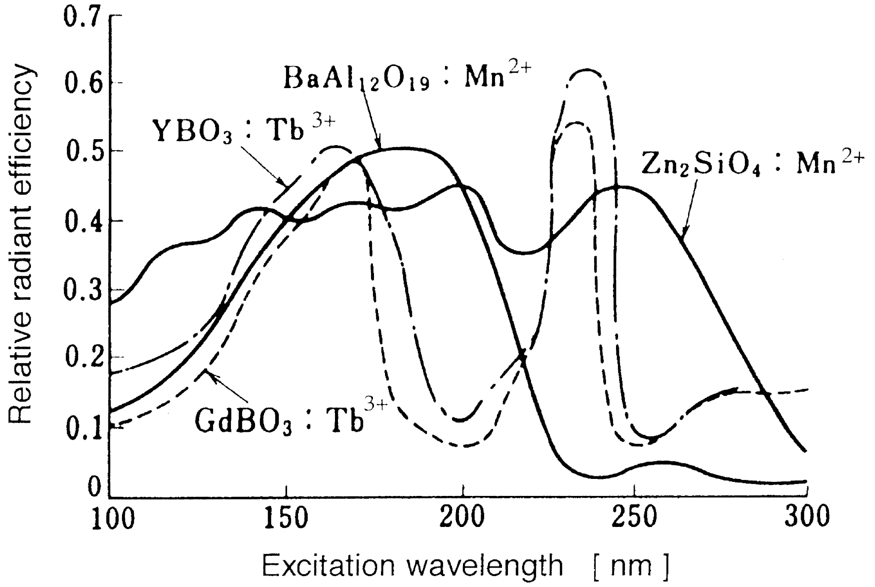

Figure 6 Excitation spectra of green-emitting phosphors. (From Koike, J., Kojima, T., Toyonaga, R., Takahashi, K., Kagami, A., and Hase, T., *Tech. G. Electron Device, Inst. TV Eng. Jpn.*, ED317, 1977 (in Japanese). With permission.)

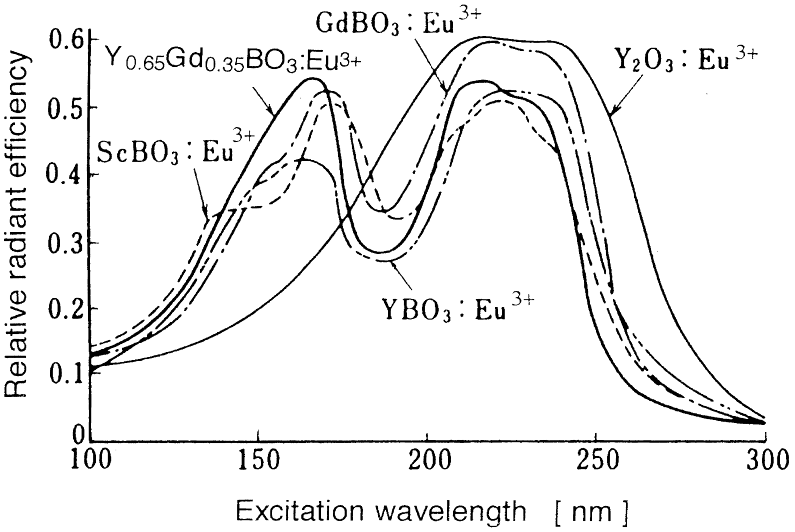

Figure 7 Excitation spectra of red-emitting phosphors. (From Koike, J., Kojima, T., Toyonaga, R., Takahashi, K., Kagami, A., and Hase, T., *Tech. G. Electron Device, Inst. TV Eng. Jpn.*, ED317, 1977 (in Japanese). With permission.)

for luminous efficiency by VUV excitation,[25] higher Mn concentrations of 0.1 g-atom/mol has recently been adopted because of a shorter decay time, one third of that of previously used $Zn_2SiO_4:Mn^{2+}$ (0.03 g-atom/mol), is obtained without a decrease in luminous efficiency.[1,37–39] Tb^{3+}-activated borate phosphors show high luminous efficiencies, but the chromaticity of their luminescence is not desirable because the emission spectrum contains many sharp lines around 545 nm, not a suitable for a green primary color. $BaAl_{12}O_{19}:Mn^{2+}$ shows not only good efficiency but also high luminescent color purity with a peak wavelength at 515 nm and halfwidth of 30 nm. These characteristics can broaden the color gamut compared to that of NTSC green. This phosphor is not luminous under 254- and 365-nm Hg line excitations, so that inconvenience is caused in the screen coating process; the latter is controlled by observing fluorescence under UV lamp excitation during PDP screen factories. Besides these phosphors, $Sr_4Si_3O_8Cl_{14}:Eu^{2+}$ also shows high efficiency characteristics. This phosphor, however, is only suitable for a color component of multicolor displays rather than that of full-color displays because of its greenish-blue luminescent color.

Table 2 Typical Properties of Practical Phosphors for PDPs.

Color	Composition	Chromaticity x	Chromaticity y	1/10 Decay time (ms)	Specific gravity
Blue	$BaMgAl_{10}O_{17}:Eu^{2+}$	0.146	0.047	<1	3.8
	$CaMgSi_2O_6:Eu^{2+}$	0.150	0.040	<1	3.4
Green	$Zn_2SiO_4:Mn^{2+}$	0.244	0.702	9	4.2
	(Ba,Sr,Mg)O $aAl_2O_3:Mn^{2+}$	0.145	0.747	14	3.8
	$(Y,Gd)BO_3:Tb^{3+}$	0.321	0.610	10	5.1
Red	$(Y,Gd)BO_3:Eu^{3+}$	0.641	0.356	11	5.1
	$Y(P,V)O_4:Eu^{3+}$	0.657	0.333	4	4.3

Of the red phosphors, borates of Sc, Y, Gd, or Lu activated with Eu^{3+} show an excitation peak at 160 to 170 nm, and their luminescence spectra, composed of 591-, 611 and 628-nm lines, give good hues and purities as the primary color. The $Y_{0.65}Gd_{0.35}BO_3:Eu^{3+}$ phosphor shows excellent characteristics for both efficiency and chromaticity of luminescence.[40] A 21 inch AC panel was put on the market in 1993 for the first time. It boosted research on PDPs and phosphors for constructing such panels. On the basis of descriptions above, phosphors have improved and some new phosphors have been introduced.[41–43] Table 2 shows the characteristics of phosphors practically used for PDP TVs. Figure 8 (a), (b), (c) shows emission spectra of blue, green, and red phosphors, respectively in Table 2. There are two or three kinds of phosphor in each color. The mixed phosphors are occasionally used to compensate the short properties of the others. As for the blue phosphor $BaMgAl_{10}O_{17}:Eu^{2+}$, it is widely used because of its high luminous efficiency and longer life than that of $BaMgAl_{14}O_{23}:Eu^{2+}$.[1] $CaMgSi_2O_6:Eu^{2+}$ is also used because of its longer lifespan,[44] although it is not excited efficiently under 173 nm radiation. As for the green phosphor $Zn_2SiO_4:Mn^{2+}$, it is mainly still used because of its high luminous efficiency. $YBO_3:Tb^{3+}$ or $(Y,Gd)BO_3:Tb^{3+}$ is used to reduce the firing voltage of the PDPs.[45] $(Ba,Sr,Mg)O.aAl_2O_3:Mn^{2+}$ takes the place of $BaAl_{12}O_{19}:Mn^{2+}$ because the former is superior to the later in color purity and luminous efficiency.[46] As for the red phosphor $(Y,Gd)BO_3:Eu^{3+}$, it is also mainly still used because of its high luminous efficiency. $Y(PV)O_4:Eu^{3+}$ is occasionally used to improve color purity although its luminance is lower than that of $(Y,Gd)BO_3:Eu^{3+}$.

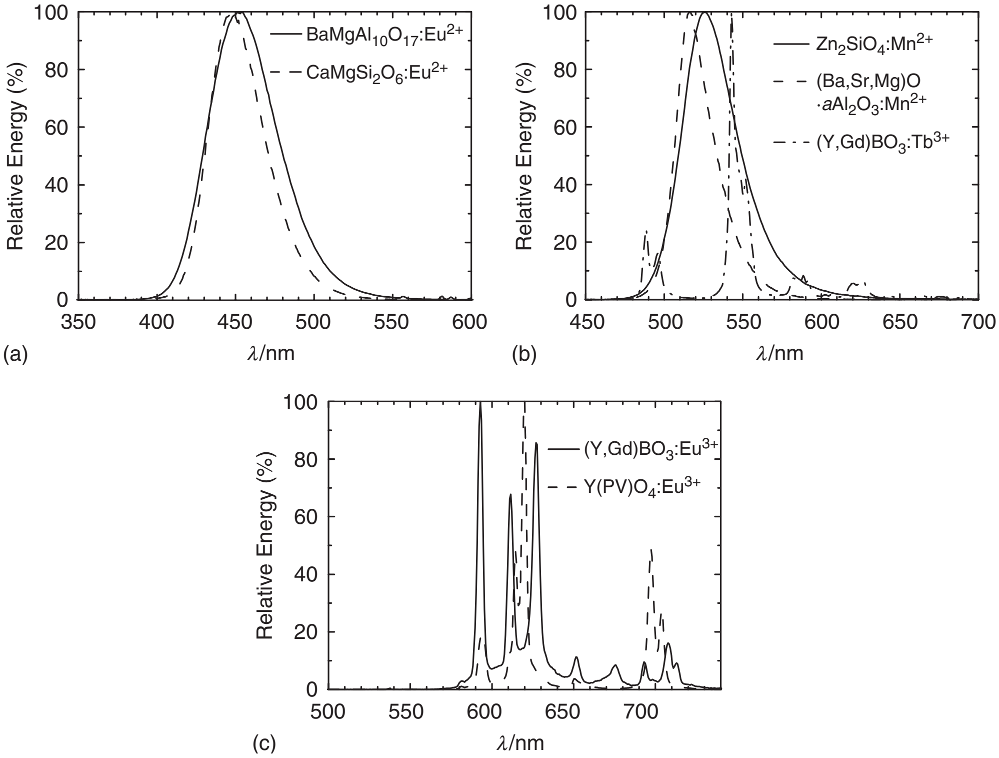

Figure 8 Emission spectra of (a) blue, (b) green, and (c) red practical phosphors for PDPs.

Table 3 Characteristics Comparison of Tricolor Phosphor Combinations Used in PDP

No.	Tricolor phosphor combination			Chromaticity coordinates at equal discharge current		Relative luminance for Illuminant C[a]
	B	G	R	x	y	
1	$CaWO_4:Pb^{2+}$	$Zn_2SiO_4:Mn^{2+}$	$Y_2O_3:Eu^{3+}$	0.34	0.44	58
2	$Y_2SiO_5:Ce^{3+}$	$Zn_2SiO_4:Mn^{2+}$	$Y_2O_3:Eu^{3+}$	0.31	0.38	100
3	$YP_{0.85}V_{0.15}O_4$	$Zn_2SiO_4:Mn^{2+}$	$YP_{0.65}V_{0.35}O_4:Eu^{3+}$	0.31	0.38	83
4	$BaMgAl_{14}O_{23}:Eu^{2+}$	$Zn_2SiO_4:Mn^{2+}$	$YBO_3:Eu^{3+}$	0.29	0.31	150
5	$BaMgAl_{14}O_{23}:Eu^{2+}$	$Zn_2SiO_4:Mn^{2+}$	$Y_{0.65}Gd_{0.35}BO_3:Eu^{3+}$	0.31	0.31	182
6	$BaMgAl_{14}O_{23}:Eu^{2+}$	$BaAl_{12}O_{19}:Mn^{2+}$	$Y_{0.65}Gd_{0.35}BO_3:Eu^{3+}$	0.30	0.31	172

[a] *Illuminant C*: Daylight at color temperature 6774K established by Commission Internationale de l'Eclairage.

From Koike, J., Kojima, T., Toyonaga, R., Takahashi, K., Kagami, A., and Hase, T., *Tech. G. Electron Device, Inst. TV Eng. Jpn.*, ED317, 1977 (in Japanese). With permission.

10.4 *Characteristics of full-color plasma displays*

Table 3 shows typical combinations of tricolor phosphors reported for PDPs in the time order of their development, along with their characteristic chromaticity coordinates of color at equal discharge current of the RGB cells and the relative luminance for the white color of Illuminant C ($x = 0.3101$, $y = 0.3161$) (see the footnote a in Table 3).[23] The relative luminous efficiency can be defined as a ratio of the luminance to total RGB cell currents, because the VUV intensity is proportional to the cell current. However, the discharge current of any display cell is limited to a constant value by many factors of the discharge characteristics of display cells, for example, color turbidity caused by irregular discharges

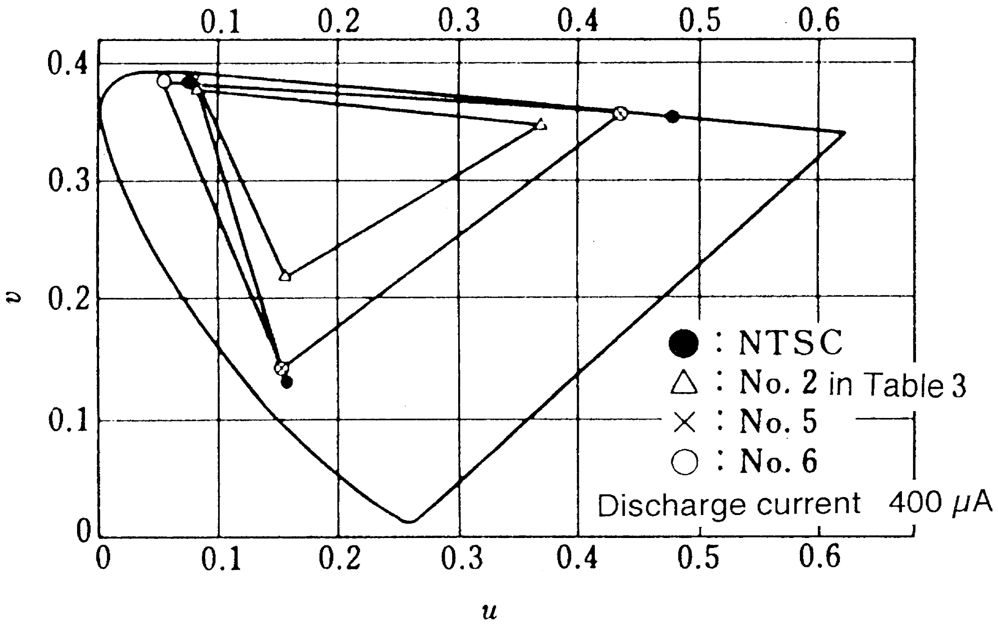

Figure 9 Color reproducing gamuts of PDPs for tricolor phosphor combinations. As to the Coordinates u and v, see Chapter 17. (From Kojima, T., Toyonaga, R., Sakai, T., Tajima, T., Sega, S., Kuriyama, T., Koike, J., and Murakami, H., *Proc. SID*, 20/3, 153, 1979. With permission.)

at over currents, etc. Therefore, the relative luminance, unlike the relative luminous efficiency, is calculated with the practical assumption that all RGB cells have a limit on their cell currents. When the white color is represented, the lumen contribution of RGB component colors is determined uniquely by their luminescence spectra. The luminance for white is limited by the current of the cell having the largest current contribution. Therefore, equal current contribution of RGB cell discharges is most desirable for high luminous efficiencies for Illuminant C. White luminances of combinations Nos. 4–6 shown in Table 3 have been improved by an increase in luminous efficiency and a decrease in current contributions of the red and blue phosphors relative to the green.

Figure 9 shows the reproduced color gamuts measured for PDPs.[47] The temperature dependence of the phosphor luminance in DC discharge are shown in Figure 10. The luminance deterioration after the baking process in fabrication is shown in Table 4.[48]

DC and AC PDPs up to 103 inch diagonal size have been manufactured recently with excellent display characteristics. Among the phosphors above, the No. 6 combination in Table 2 had been widely adopted for color PDPs in early stage. Main advantages of this combination are: (1) high conversion efficiency to visible luminescence from VUV excitation; (2) wide reproducible color gamut; (3) white color representation at equal discharge currents; and (4) no serious damage to other panel characteristics. A combination of $BaMgAl_{10}O_{17}:Eu^{2+}$ (blue), $Zn_2SiO_4:Mn^{2+}$ (green), and $(Y,Gd)BO_3:Eu^{3+}$ (red), is also mainly adopted recently.

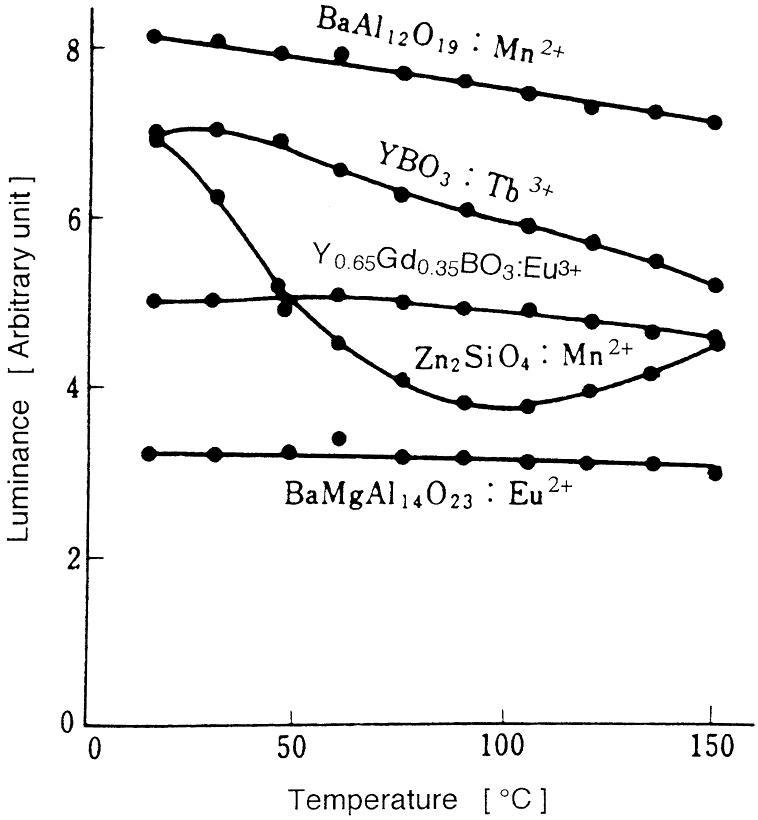

Figure 10 Temperature dependencies of the luminescence of typical phosphors under VUV excitation from He-Xe (2%) DC gas discharge. (From Koike, J., Okada, K., and Yokozawa, M., *NHK Giken Geppo*, 22, 176, 1979 (in Japanese). With permission.)

Table 4 Luminance Deteriorations of VUV Phosphors by the Baking Process for Panel Fabrication

Phosphors	Luminance ratio of after to before baking process
$Y_{0.65}Gd_{0.35}BO_3:Eu^{3+}$	0.91
$BaAl_{12}O_{19}:Mn^{2+}$	0.99
$Zn_2SiO_4:Mn^{2+}$	0.96
$BaMgAl_{14}O_{23}:Eu^{2+}$	0.88

From Koike, J., Okada, K., and Yokozawa, M., *MHK Giken Geppo*, 22, 176, 1979 (in Japanese). With permission.

In these phosphors, quantum efficiencies of 0.8 to 0.9 have been achieved.[40] Energy efficiencies, however, are limited to low values due to the large energy conversion ratio from 147 nm to the visible region. The long-term R&D issues for the future will focus on finding a discharge gas with a longer radiation wavelength than that of Xe having weak visible radiation and stability in low current discharges. Additionally, work is required in identifying phosphor materials having suitable excitation spectra and luminescent characteristics, together with improved VUV radiation efficiencies.

In the short-term, luminous efficiency and life issues of the PDPs are currently in development. Effective VUV excitation of the phosphor screen from gas discharges, efficient extraction of the phosphor luminescence through the screen, and screen forming techniques on the nonflat surface in small and complex cell structures, not the conventional coating on flat face plates, are very important for device improvements.

References

1. Murakami, Y., Koike, J., Oguri, Y., Hisamune, T., and Takahashi, A., *Tech. Rep. Inst. TV Eng. Jpn.*, 18, 68, 55, 1994 (in Japanese).
2. Seki, M., Kuriyama, T., Yamamoto, T., Katoh, T., Takei, T., Kawai, T., and Murakami, H., *NHK Giken R&D*, 26, 47, 1993 (in Japanese).
3. Yoshikawa, K., Kanazawa, Y., Wakitani, Y., Shinoda, T., and Otsuka, A., *Tech. Rep. Inst. TV Eng. Jpn.*, 16, 83, 17, 1992 (in Japanese).
4. Deschamps, J., *SID 94 Digest*, 21.1, 315, 1994.
5. Hashiguchi, S., *Display and Imaging*, 1, 301, 1993 (in Japanese).
6. Matsuzaki, H., Sakai, T., Murakami, H., Kitada, H., Takano, Y., and Murakami, Y., *NHK Giken R&D*, 30, 35, 1994 (in Japanese).
7. Imahori, Y., Matsuzaki, H., and Kamegaya, T., *NHK Tech. J.*, 28, 107, 1976 (in Japanese).
8. DeJule, M., Sobel, A., and Markin, J., *SID 83 Digest*, 13.3, 134, 1983.
9. Glaser, D., DeJule, M., Whelchel, C.J., Stone, C.S., Sobel, A., and Markin, J., *SID 83 Digest*, 13.4, 136, 1983.
10. Schauer, A., *Proc. Jpn. Display '83*, 234, 1983.
11. Matsuzaki, H., and Kamagaya, T., *Tech. Report Inst. Elect. Commun. Eng. Jpn.*, ED77-19, 43, 1977 (in Japanese).
12. Forman, J., *Proc. SID*, 13/3, 14, 1972.
13. Takashima, K., Nakayama, N., Shirouchi, Y., Iemori, T., Yamamoto, H., and Sato, S., *SID 73 Digest*, 7.4, 76, 1973.
14. Sakai, T., Koike, J., and Kojima, T., *Inst. TV Eng. Natl. Convention*, 12-7, 317, 1973 (in Japanese).
15. Fukushima, M., Murayama, S., Kaji, T., and Mikoshiba, S., *IEEE Trans. ED*, ED-22, 657, 1975.
16. Yokozawa, M., *Tech. Report, Inst. TV Eng. Jpn.*, 5, 4, 37, 1981 (in Japanese).
17. Hinson, D.C., and Bennett, R.A., *SID 74 Digest*, 11.1, 118, 1974.
18. Cola, R., *IEDM*, 10.5, 201, 1973.
19. Samson, J.A.R., *Techniques of Vacuum Ultraviolet Spectroscopy,* John Wiley & Sons, New York, 1967, 216.

20. Bril, A., and de Jager-Veenis, A.W., *J. Electrochem. Soc.*, 123, 396, 1976.
21. Koike, J., Sakai, T., Murakami, H., and Ohishi, I., *J. Inst. TV Eng. Jpn.*, 28, 1001, 1974 (in Japanese).
22. Kojima, T., Koike, J., and Toyonaga, R., *NHK Giken Geppo*, 19, 238, 1976 (in Japanese).
23. Koike, J., Kojima, T., Toyonaga, R., Takahashi, K., Kagami, A., and Hase, T., *Tech. G. Electron Device, Inst. TV Eng. Jpn.*, ED317, 1977 (in Japanese).
24. Takei, M., Tamura, A., Takahashi, K., and Wani, K., *Tech. Report Inst. TV Eng. Jpn.*, 16, 43, 1992 (in Japanese).
25. Koike, J., Kojima, T., Toyonaga, R., Kagami, A., Hase, T., and Inaho, S., *J. Electrochem. Soc.*, 126, 1008, 1979.
26. Brown, F.H., and Zayac, M.T., *Proc. SID*, 13/1, 52, 1972.
27. Fukushima, M., Murayama, Shinada, S., Sumioka, A., Oikawa, M., and Tanimizu, S., *Tech. G. Image Process. Display, Inst. TV Eng. Jpn.*, 7-15, 1, 1974 (in Japanese).
28. Kishimoto, S., Nishina, M., and Hinotani, K., *Hoden Kenkyu (Discharge Research)*, 50, 26, 1972 (in Japanese).
29. Tanimizu, S., and Suzuki, T., *36th Abstr. Jpn. Soc. Appl. Phys. Meeting*, 146, 1975 (in Japanese).
30. Okamoto, Y., and Mizushima, T., *6th Image Electrn. Conf.*, 97, 1975 (in Japanese).
31. Tanimizu, S., and Suzuki, T., *Abstr. 37th Jpn. Soc. Appl. Phys. Meeting*, 13, 1975 (in Japanese).
32. Akutsu, H., Nakagawa, Y., Okamoto, T., and Atsumi, T., *Tech. Report Inst. Electn. Commun. Eng. Jpn.*, 76, 65, 1976 (in Japanese).
33. Kaufman, R. G., *Biennial Display Conf.*, 45, 1976.
34. Koitabashi, M., and Awazu, K., *Tech. G. Light Source, Inst. Elect. Eng. Jpn.*, LS74-8, 1974 (in Japanese).
35. Yamashita, H., Andoh, S., and Shinoda, T., *SID 76 Digest*, 7.1, 80, 1976.
36. de Jager-Veenis, A.W. and Bril, A., *J. Electrochem. Soc.*, 123, 1253, 1976.
37. Kagami, A., Hase, T., Koike, J., Ohishi, I., Kojima, T., and Toyonaga, R., Japanese Patent 1093745, 1982.
38. Morell, A., and Goumard, N., *SID 92 Digest*, 10.1, 159, 1992.
39. Koike, J., *Tech. Digest, 250th Phosphor Res. Soc. Meeting*, 17, 1994 (in Japanese).
40. Koike, J., Kojima, T., Toyonaga, R., Takahashi, K., Kagami, A., and Hase, T., *Tech. Digest, 161st Phosphor Res. Soc. Meeting*, 1, 1979 (in Japanese).
41. Hisamune T., *Proc. IDW '02*, 685, 2002.
42. Hisamune T., Display 10-4, 55, 2004 (in Japanese).
43. Zhang, S., *SID 2005 Digest*, 26.4, 1142, 2005.
44. Yoshimatsu, R., Kunimoto, T., Ohmi, K., Tanaka, S., and Kobayashi, H., *Proc. Asia Display/IDW '01*, 1115, 2001.
45. Tachibana, H., Matsuda, A., Haruki, S., Kosugi, N., Wani, K., and Weber, L.F., *Proc. IDW '00*, 651, 2000.
46. Hisamune T., Nabu, M., Ohto, A., Oguri, Y., and Endoh, T., *J. Light & Vis. Env.*, 25, 19, 2001.
47. Kojima, T., Toyonaga, R., Sakai, T., Tajima, T., Sega, S., Kuriyama, T., Koike, J., and Murakami, H., *Proc. SID*, 20/3, 153, 1979.
48. Koike, J.A., Okada, K., and Yokozawa, M., *NHK* Giken Geppa, 22, 176, 1979 (in Japanese).

chapter ten — section five

Phosphors for plasma display panels

R. P. Rao

Contents

- 10.5 Plasma displays and phosphors 746
  - 10.5.1 Plasma display panels 746
    - 10.5.1.1 Introduction 746
    - 10.5.1.2 Structure and operation 747
  - 10.5.2 PDP phosphors 747
    - 10.5.2.1 Introduction 747
    - 10.5.2.2 Phosphor requirements 747
      - 10.5.2.2.1 Physical requirements 747
      - 10.5.2.2.2 Optical requirements 748
        - 10.5.2.2.2.1 Excitation 748
        - 10.5.2.2.2.2 Emission and brightness 750
        - 10.5.2.2.2.3 After-glow decay or persistence 751
        - 10.5.2.2.2.4 Color coordinates, gamut, and color temperature 751
        - 10.5.2.2.2.5 Saturation 751
        - 10.5.2.2.2.6 Degradation 751
      - 10.5.2.2.3 Electrical requirements 752
        - 10.5.2.2.3.1 Zeta potential and surface charge 752
    - 10.5.2.3 Phosphor preparation 753
      - 10.5.2.3.1 Solid-state reaction 753
      - 10.5.2.3.2 Sol–gel method 753
      - 10.5.2.3.3 Coprecipitation method 754
      - 10.5.2.3.4 Hydrothermal technique 754
      - 10.5.2.3.5 Spray pyrolysis 754
      - 10.5.2.3.6 Combustion synthesis 754
      - 10.5.2.3.7 Combinatorial chemistry method 754
    - 10.5.2.4 Phosphor Characterization 755
      - 10.5.2.4.1 Physical analysis 755
      - 10.5.2.4.2 Optical characteristics 755
  - 10.5.3 Potential phosphors 755
    - 10.5.3.1 Blue phosphors 756
      - 10.5.3.1.1 BAM phosphor 756

10.5.3.1.2 Tm^{3+}-activated lanthanum phosphate phosphor......756
10.5.3.1.3 Blend of LPTM and BAM......756
10.5.3.1.4 Eu^{2+}-activated alkaline earth alumina silicate phosphor......759
10.5.3.1.5 Gd^{3+}-activated yttrium–aluminum borate phosphor......759
10.5.3.1.6 Zr-, Mn-activated yttrium phosphate......759
10.5.3.2 Green phosphors......760
10.5.3.2.1 Mn^{2+}-activated zinc silicate phosphor......760
10.5.3.2.2 Mn^{2+}-activated alkaline earth aluminate phosphor..760
10.5.3.2.3 Mn^{2+}-doped lithium zinc germanate phosphor......761
10.5.3.2.4 Mn^{2+}-activated lanthanum aluminate phosphor......761
10.5.3.2.5 Tb^{3+}-activated green emitting phosphor......761
10.5.3.2.6 Tb^{3+}-activated phosphor blends......762
10.5.3.3 Red phosphors......763
10.5.3.3.1 Eu^{3+}-activated yttrium, gadolinium borate......763
10.5.3.3.2 Eu^{3+}-activated rare earth aluminum borate phosphor......764
10.5.3.3.3 Eu^{3+}-activated rare earth lithium borate and oxyborate phosphor......764
10.5.3.3.4 Eu^{3+}-activated rare earth aluminum phosphate phosphor......764
10.5.3.3.5 Eu^{3+}-activated rare earth phosphate phosphor......764
10.5.3.3.6 Eu^{3+}-activated rare earth barium zirconium borate phosphor......764
10.5.3.3.7 Eu^{3+}-activated rare earth oxide phosphor......764
10.5.4 Drawbacks and recent developments......765
References......765

10.5 Plasma displays and phosphors

10.5.1 Plasma display panel

10.5.1.1 Introduction

Because of its performance and scalability, the plasma display panel (PDP) is increasingly gaining attention over conventional cathode ray tube (CRT)-based TVs as a medium of large format (60+″) television (TV), particularly high definition TVs (HDTVs). Improvements have been made not only in size but also in other areas such as resolution, luminescence efficiency, brightness, contrast ratio, power consumption, and cost reduction. The performance of a PDP depends on a complicated set of factors, for instance, phosphors, gas mixture, dielectric layer, reflective layer, black matrix, electrodes, cell dimension and shape, nature, size and shape of electrodes, address waveforms, and operating voltages.[1,2] The performance and lifetime of a PDP is strongly related to the nature of phosphors and their resistance to energetic discharge ions and electrons, and solarization from vacuum UV (VUV) arising from the Xe/Ne gas discharge. Compared with standard emissive display such as CRTs (5–6 lm/W), the efficiency of a PDP is low (1–2 lm/W). To improve the overall efficiency of PDPs, considerable developments related to materials, design, process, and electronics have been under way for some time. Efforts are also being made to develop new and to improve existing phosphors. Because of the VUV wavelengths available from Xe discharges (147 and 173 nm), only a limited number of lamp phosphors are suitable for PDP applications. In addition to having high luminous efficiency, PDP phosphors should have longer life or stability, the required after-glow decay or persistence, suitable color coordinates, color temperature, and color saturation.

10.5.1.2 Structure and operation

The PDP was invented at the University of Illinois by Profs. Gene Slottow and Don Bitzer in the 1960s. The first panel, consisting of a 1″ × 1″ pixel attached to a glass vacuum system, was built for academic purpose.[3] The general structure of a single-substrate color AC plasma panel is shown in Figure 11. The front plate is made with the sustain and scanning electrodes, covered with a thick film of transparent dielectric layer that is coated with a thin protection layer of magnesium oxide (MgO) or related material. The back plate is made with the address electrodes, a thick dielectric reflective layer, glass barrier ribs, and red, green, and blue (R, G, B) emitting phosphors coated between the ribs by a screen-printing or ink-jet process. The two glass substrates are frit-sealed and filled with a neon–xenon gas mixture. When an alternating voltage waveform is applied across the front sustain electrodes, xenon atoms are excited by the discharge. The resulting Xenon VUV emission in turn excites the phosphors to reproduce visible radiation, which can be viewed through the transparent front plate.[4] Figure 12 shows a cross-sectional view of a typical PDP cell structure. The VUV radiation (130, 147, and 172 nm) output (7–12 eV) of the plasma source depends on the nature of the gas and the composition and pressure.[5] Every pixel is made up of three (R, G, B) separate subpixel cells, each with three different phosphors. By varying the pulses of current flowing through the different cells, the control system can increase or decrease the intensity of each subpixel color to create hundreds of different combinations of red, green, and blue. Compared with lamp or CRT phosphors, PDP phosphors need to satisfy more stringent requirements, as will be described in the following sections.

10.5.2 PDP phosphors

10.5.2.1 Introduction

As mentioned earlier, the phosphors employed in commercial plasma TVs should satisfy the following requirements: high quantum efficiency (QE), low reflectivity to VUV, high reflectivity to visible light, longevity, proper after-glow decay and persistence characteristics, and proper color coordinates or color gamut and temperature dependence required by the National Television System Committee (NTSC) standards. Various aspects of PDP phosphors have been reviewed in the past.[6–9] Phosphor requirements, preparation, and characteristics are briefly described in the following sections.

10.5.2.2 Phosphor requirements

10.5.2.2.1 Physical requirements. The morphology (phosphor particle size and shape), particle size distribution (PSD), body color, and rheology are the important physical requirements of PDP phosphors. The rheology of a paste depends on the size and shape of particles and the binders and vehicles used in paste formulations. Currently, PDPs are manufactured by depositing phosphor particles by screen-printing or by an ink-jet process on the complicated rib structure of the PDP cell back plate. The morphology, PSD, and phosphor thickness not only affect the PDP manufacturing process but also influence the performance of the cell. Various experimental methods have been used to improve the morphology of PDP phosphors. For example, preparing phosphor in the presence of various flux materials can modify its morphology and improve the luminescent characteristics.[10] The spherical shape of the phosphor particles helps to minimize the quantity of binder as well as the vehicles required to form the paste used to make the

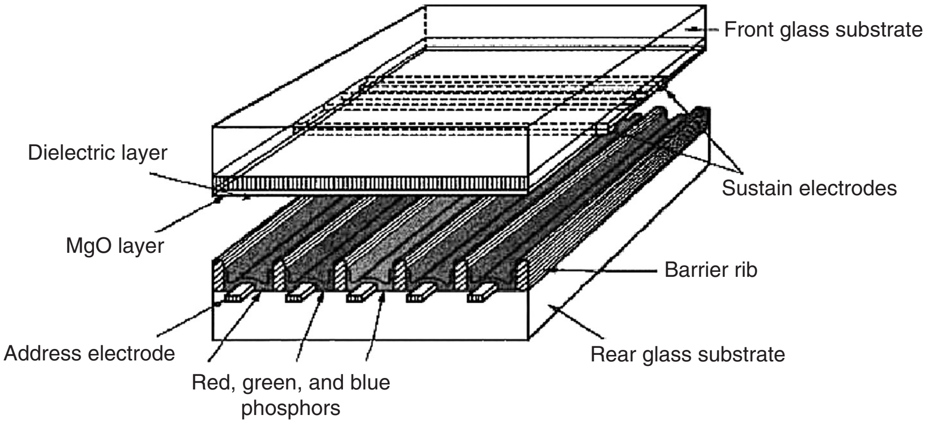
Front glass substrate
Dielectric layer
Sustain electrodes
MgO layer
Barrier rib
Address electrode
Rear glass substrate
Red, green, and blue phosphors

Figure 11 Cross-sectional view of AC plasma display panel.

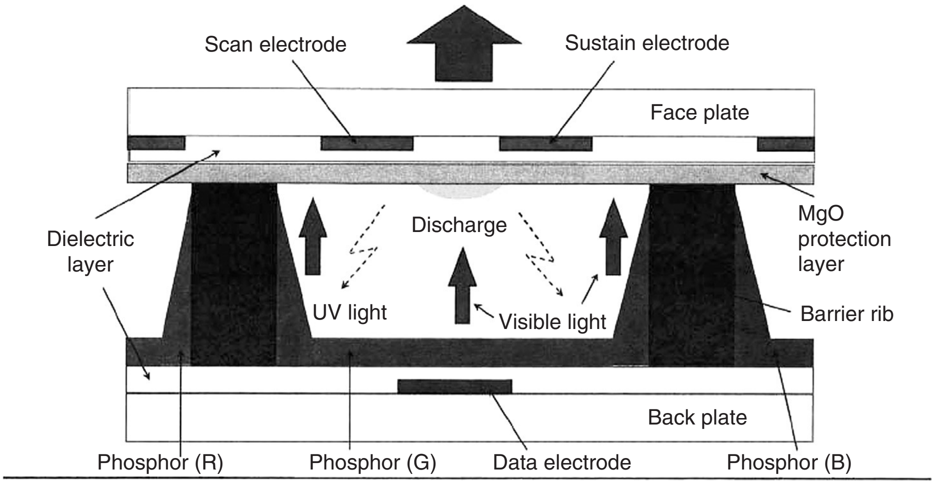
Scan electrode
Sustain electrode
Face plate
Dielectric layer
Discharge
MgO protection layer
UV light
Visible light
Barrier rib
Back plate
Phosphor (R)
Phosphor (G)
Data electrode
Phosphor (B)

Figure 12 Cross-sectional view of single cell (plasma display panel, PDP) with three different red, green, and blue emitting phosphors.

back plates. It is also known that thick films screen-printed with smaller size phosphor particles have higher packing density and better paste rheology.

10.5.2.2.2 Optical requirements. The following optical properties of phosphors need to be optimized in PDP applications.

10.5.2.2.2.1 Excitation. PDP phosphors should have a high conversion coefficient under VUV excitation. The photon energy from the plasma discharge is essentially absorbed by the phosphor matrices and then transferred to luminescent centers. The excitation properties and absorption coefficient of various PDP phosphors are well known.[11,12] Since the emission from plasma discharge (Xe/Xe*) is limited to two dominant spectral lines at 147 and 172 nm, most of the common luminescent materials do not absorb at these wavelengths. The band gaps of the majority of PDP phosphors currently in use lie below the energy of the plasma discharge; unlike common lamp phosphors, PDP luminescence entails band-to-band transitions. Depending on the ratio of gas mixture, the

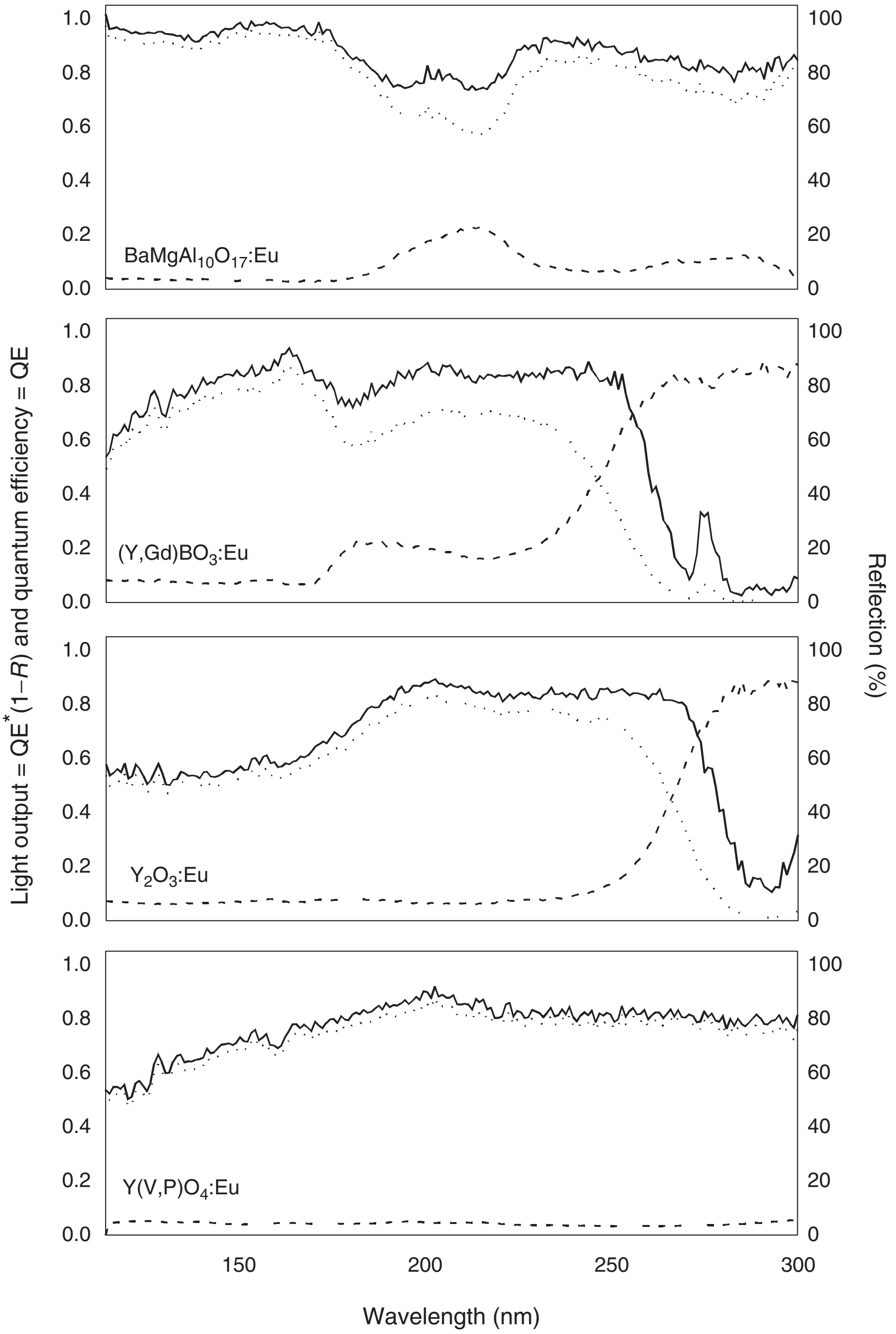

Figure 13 Reflection spectra (dashed line), spectral light output (LO, dotted line), and quantum efficiency (QE, solid line) of blue, red, and green emitting VUV phosphors. (From Justel, T., Krupa, J.C., and Wiechert, D.U., *J. Lumin.*, 93, 179, 2001. With permission.)

intensity of the two lines varies. Excitation and reflectance spectra and QEs of various PDP phosphors are well discussed and have been summarized.[13] Figure 13 presents the reflection spectra and the spectral light output and QE of some blue, red, and green emitting VUV phosphors.

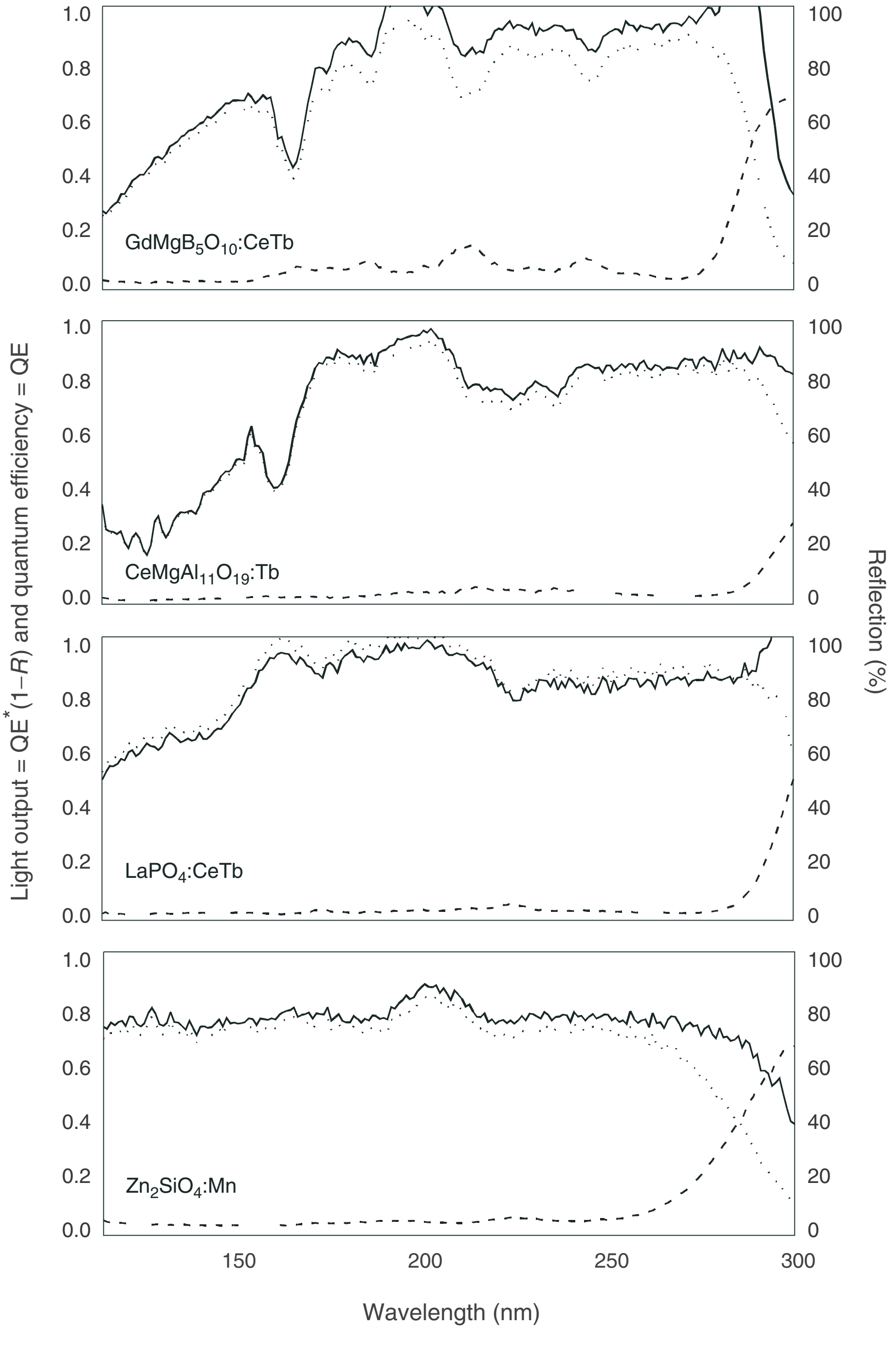

Figure 13 Continued

10.5.2.2.2.2 Emission and brightness. Brightness of a phosphor in a specified spectral energy distribution is a key in their performance in a display. Ideally, phosphor materials should have high QE, low reflectivity for VUV, and high reflectivity for visible light. Phosphors with higher QE not only minimize the power consumption but also reduce the cost of electronics required to operate the display. Phosphors currently in use have achieved QE in the range of 80–95%. The emission of three different (B, G, R) phosphors should satisfy the NTSC requirements. The emission characteristics of individual PDP phosphors are described in Section 10.5.3.

10.5.2.2.2.3 After-glow decay or persistence. For TV applications, short- as well as long-time persistence behavior of phosphors must be considered. Short-time persistence value, defined as the time for the decay to reach 10% of the initial brightness, should be between 6 and 9 ms. The long-time persistence component should contribute less than 0.25% to the initial brightness 2–10 s after the termination of excitation. The origin of long persistence is similar to that of fluorescence, but the metastable to ground state transition is forbidden. Emission occurs when thermal energy raises the electron to a state from which it can de-excite; therefore, this process or phosphorescence is temperature-dependent.

10.5.2.2.2.4 Color coordinates, gamut, and color temperature. The color purity of a phosphor depends on the spectral energy distribution of the emission. Generally, the color purity can be determined by measuring its x and y coordinates on a standard CIE color chart. The color gamut of a phosphor is represented as an area in the CIE 1931 chromaticity diagram, with the curved edge representing the monochromatic colors. Gamut areas typically have triangular shapes because most color reproduction is done with three primaries. Color temperature is a simplified way to characterize the spectral properties of emissions from phosphors. In reality the color of spectral energy distribution is determined by how much each point on the spectral curve contributes to the total output; the color temperature of most color TVs is in the 6500 to 9500 K range. Higher color temperatures are due to higher brightness and color saturation.

10.5.2.2.2.5 Saturation. Every PDP phosphor saturates when pumped with an increasing VUV flux; for example red (Y_2O_3:Eu and Y,GdBO_3:Eu) and blue (BaMg$Al_{10}O_{17}$:Eu) phosphors show luminescence saturation with strong VUV excitation. On the other hand, green (Zn_2SiO_4:Mn) phosphors exhibit luminescence saturation in all excitation regions, as shown in Figure 14.[14] Phosphor saturation leads to image sticking problems in the PDP displays and must be minimized or eliminated.

10.5.2.2.2.6 Degradation. When PDPs were initially introduced, phosphor degradation was a major concern and there are continuing efforts to improve the operational lifetimes of PDP phosphors. The degradation is related not only to optical exposure or solarization but also to thermal or heating processes. The degradation of PDP phosphors starts during the baking cycles, which is part of the manufacturing process, and continues during PDP operation. The degradation mechanisms involved in specific phosphors are not fully understood. Various factors responsible for the degradation reported in the literature include morphology of phosphor particles, crystal structure, surface effects, stability of activators, location of activators in the lattice, oxidation of activators, backing processes related to binder burn-off of back plate after printing the phosphors, frit seal and back fill of Xe–Ne gas, and ratio of gas mixture. Practically and unfortunately, BAM (B) exhibits a very low stability when compared with the stability of the other two phosphor components, red emitting (Y,Gd)BO_3:Eu^{3+} and green emitting $ZnSiO_4$:Mn^+ (P1), or the blend of P1 and (Y,Gd)BO_3:Tb^{3+}. The loss in luminance of RGB phosphors in a 42″ panel operated continuously for about 30,000 h in normal video image operations is shown in Figure 15. An improved version of BAM is now being used in comparison with the earlier version in this figure. Generally, degradation is moderate in the case of silicate and borate phosphors whereas it is high in the case of aluminate samples.

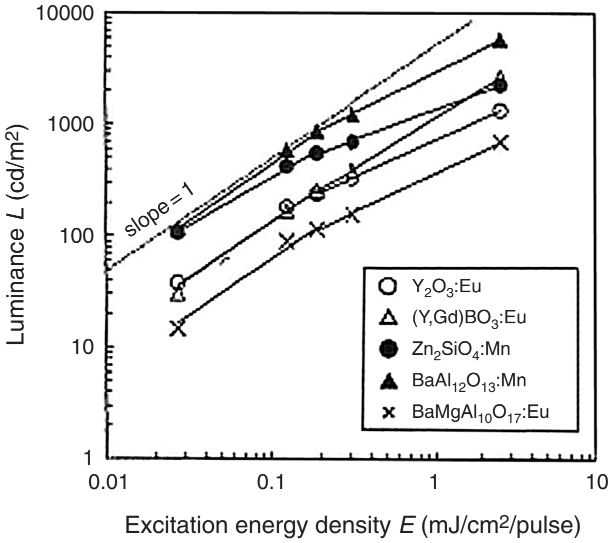

Figure 14 Dependence of luminescence of phosphor (L) on excitation energy density (E). (From Okazaki, C., Shiiki, M., Suzuki, T., and Suzuki, K., *J. Lumin.*, 87–89, 1280, 2000. With permission.)

10.5.2.2.3 Electrical requirements. In a PDP, if the three phosphors exhibit different electrical characteristics, its performance may be compromised. For example, the higher dielectric constant of zinc silicate phosphors is of particular concern as this component charges more than its blue and red counterparts and this results in a higher sustainer voltage.

10.5.2.2.3.1 Zeta potential and surface charge. The zeta potential and the surface charge of phosphor particles are important factors affecting the performance of a PDP phosphor. Zeta potential, exhibited by a phosphor particle in a suspension such as phosphor paste or slurry, has to be of optimum value so that phosphor particles can overcome the natural tendency to aggregate. The variation of charge on phosphor particles makes the addressing margin and background brightness from individual cells different.[15] To maintain uniform addressing, much higher ramp setup voltage needs to be applied to the green cell

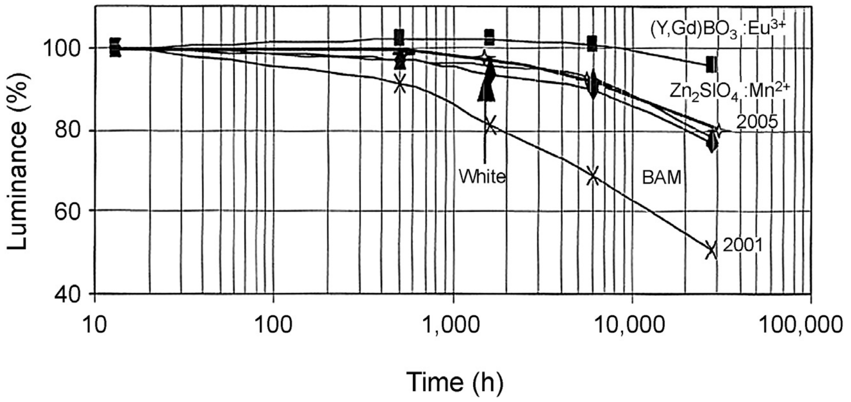

Figure 15 Degradation in luminance of red ((Y,Gd)BO_3:Eu^{3+}), green (Zn_2SiO_4:Mn^{2+}), and blue ($BaMgAl_{10}O_{17}$:Eu^{2+}) phosphor in a plasma display panel (PDP) operated for 30,000 h of normal (video image) operation.

(Zn_2SiO_4:Mn) than to the red and blue cells. Higher setup voltage brings higher background brightness and error discharges. The charging of phosphor not only affects the electrical characteristics of the cell but also modifies the surface properties of a particular phosphor. Luminescence efficiency also decreases with the accumulation of surface charge. The measured values of surface charge or zeta potentials (mV) of green emitting phosphors are +28.5 mV for YBO_3:Tb, –8.1 mV for $La_2Al_{22}O_{36}$:Mn,Li, and –52.3 mV for P1 phosphors.

10.5.2.3 Phosphor preparation

Almost all phosphor materials are synthesized or manufactured by a high-temperature solid-state reaction or by a sol–gel process.[16] During synthesis, a host matrix is formed from high-purity starting chemicals and the impurities, also known as activators and coactivators, are diffused into the crystal lattice in the required quantities. The activators are mostly responsible for the luminescence. In some cases, coactivators play an important role in diffusing the activators effectively into the crystal lattice and sometimes participate in keeping crystal neutrality through charge compensation. The synthesis sequence varies depending on the type of phosphor being prepared.[17,18] The following section describes the preparation of the PDP phosphors described in literature.

10.5.2.3.1 Solid-state reaction. The formation of a phosphor host and doping process by solid solution is critical and is highly dependent on the reaction temperature and conditions. Since the purity of starting chemicals is very important to the synthesis of phosphors, the starting chemicals are typically 99.9–99.999% in purity. It is important to minimize the concentration of specific contaminants such as Fe, Co, and Ni, which can seriously degrade phosphor performance. Required amounts of starting ingredients are mixed in the presence of an appropriate flux (if necessary) and fired at high temperatures (900–1500°C) in air or in a controlled atmosphere (N_2, C, CO, or N_2 with 2-5% of H_2). The calcination conditions such as firing temperature, duration of firing, firing atmosphere, and rate of heating and cooling for a particular phosphor are optimized empirically. The phosphor particle size and shape are also related to the morphology of starting chemicals and flux.[10] The presence of flux materials of low melting compounds such as alkali halides helps to complete the doping process at lower temperatures. In the past decade many publications on the subject of PDP phosphors have become available; most of the phosphors are prepared by a solid-state reaction. The general preparation procedure of solid-state reaction is well described in the literature.[16,19]

10.5.2.3.2 Sol–gel method. The sols are dispersions of colloidal particles in a liquid from which a gel can be formed. The gel is an interconnected, rigid network, having submicrometer pores and a polymeric chain whose average length is of the order of microns. Sol–gel processes are classified by the way the gels are dried: they are known as a sol–gel if they undergo normal drying above room temperature, as aerogels if dried at room temperature, and as xerogels if processed in vacuum. The particle size of the finished product is a function of the initial concentration of the starting sols, the gelation and drying process, calcination temperatures, and rates of cooling.

The sol–gel process has many advantages over conventional methods (high-temperature solid-state reaction) in the synthesis of fine powders, particularly phosphor materials. Since all the starting materials are mixed at the molecular level in the sol solution, a high degree of homogeneity is achievable. Doping of impurities (activators/coactivators) through solutions is straightforward, easy, and effective. The pores in properly dried gels are often extremely small and the components of a homogenous gel are intimately mixed. The surface area of powders produced from sol–gel is very high, allowing lower processing temperatures.[20]

It is known that phosphor materials are extremely sensitive to impurities, even at ppb levels. The above-described low-temperature process minimizes the potential for cross contamination. The selection of a precursor is crucial in the sol–gel process. The possible precursors for typical phosphor compositions are well compiled.[16] Many PDP phosphors, such as Zn_2SiO_4:Mn,[21] (Y,Gd)BO_3:Eu,[22] and BAM,[23] prepared by the sol–gel process show better particle morphology and brightness.

10.5.2.3.3 Coprecipitation method. The coprecipitation method is being employed to prepare submicron size and spherical-shaped phosphors for various display applications. In the coprecipitation method, solutions of salts containing the phosphor constituents are precipitated by adding suitable hydroxides, such as an ammonia solution or an oxalate. After filtering and drying, the precipitates are fired as required at designated temperatures. Since the starting precipitate is made of very small particles, coprecipitates generally need low firing temperatures to synthesize the required phosphors. For example, small and spherical-shaped (Y,Gd)BO_3:Eu^{3+} can be synthesized by the coprecipitation method.[24]

10.5.2.3.4 Hydrothermal technique. In the hydrothermal method, oxide- and silicate-based phosphors can be synthesized at low temperatures and under high pressures. In this method, the reaction is carried out in either an open or a closed system. In the open system, the solid is in direct contact with the reacting gases, which also serve as the pressure medium. In the seeded hydrothermal method, the presence of a polymeric stabilizer enhances the nucleation and crystallization processes of oxide particles under hydrothermal conditions.[25]

10.5.2.3.5 Spray pyrolysis. In recent years, spray pyrolysis has become another method to prepare submicron and spherical-shaped phosphors. Here, an ultrasonic spray generator is used to generate fine droplets of suitable precursors to the phosphor to be prepared. Every phosphor particle is of high phase purity as each particle arises from one droplet in which constituents are mixed homogeneously. The preparative conditions, concentration of precursors, nature of additives, and flow rate control the size and morphology of phosphor particles. The droplets are dried, decomposed, and crystallized in the dispersed phase when passing through a reactor at a high temperature for a short time (seconds). The disadvantage with this process is the hollowness of particles, which causes reduction in the brightness and the lifetime of the phosphor. Hollow phosphors are less stable thermally and mechanically. Attempts to synthesize various PDP phosphors by spray pyrolysis are relatively rare.[26–28]

10.5.2.3.6 Combustion synthesis. Combustion synthesis has been proposed to prepare oxide-based phosphors of smaller size particles. This method involves a highly exothermic reaction between an organic fuel and metal salts (oxidizers) in an aqueous solution. The reaction is initiated at low temperatures (around 500°C) and proceeds to completion in a few minutes. The peak reaction temperature depends on the fuel and oxidizer molar ratio (f/o). By utilizing various quantities of urea as a fuel, BAM phosphor obtained in this were found to about 20% as efficient as commercially available BAM. By milling phosphors obtained by this method, the brightness of BAM was found to improve considerably.[29]

10.5.2.3.7 Combinatorial chemistry method. Combinatorial chemistry method is mainly utilized in the pharmaceutical field to generate solution-based libraries. Recently, this method has been extended to the inventory of phosphor materials, particularly phosphor thin films for various display applications. This method is not very useful for identifying PDP-suitable materials.[30,31]

10.5.2.4 *Phosphor characterization*

Most phosphors are characterized by physical as well as optical means to determine their practical behavior. There are a number of methods used in the characterization, as described below.

10.5.2.4.1 Physical analysis. Thermal analysis (TA) such as thermogravimetric analysis and differential TA provides insight into the reaction kinetics. It also helps to optimize the nature of starting chemicals, firing temperatures, duration of firing, firing atmosphere, and cooling process. TA is being used effectively in the design of new phosphors. X-ray powder diffraction (XRD) is widely used for phase identification of crystal structure, composition, and quantitative analysis of mixed phases. Photon-induced X-ray emission (PXIE) technique is commonly employed to quantify various trace elements, from sodium to uranium, present in a particular phosphor down to the ppm level. Scanning or transmission electron microscopy is used to study the morphology of phosphor particles whereas PSD is determined with the help of the Coulter counter analyzer or by laser scattering.

10.5.2.4.2 Optical characteristics. Excitation, emission, persistence, and thermoluminescence studies are all used to characterize PDP phosphor materials. Optical spectral features allow us to determine the nature and concentration of the active centers. Persistence and thermoluminescence help us to quantify the nature of the defects present in the crystal lattice.

10.5.3 *Potential phosphors*

Since the picture quality of PDP TV depends mainly on the type of phosphors employed, the selection of the appropriate phosphors is of utmost importance. Currently, different combinations of phosphors are used by PDP manufacturers. The emission spectra from three different 42″ commercial display panels employing three different green phosphors, viz., $ZnSiO_4$:Mn, a $ZnSiO_4$:Mn + Y,$GdBO_3$:Tb blend, and a $BaAl_{12}O_{19}$:Mn+Y,$GdBO_3$:Tb blend, are shown in Figure 16.

All the three screens use the standard blue ($BaMgAl_{10}O_{17}:Eu^{2+}$) and the standard red (Y,$GdBO_3:Eu^{3+}$) phosphors. Luminescent characteristics of various PDP phosphors are compiled in Table 5.

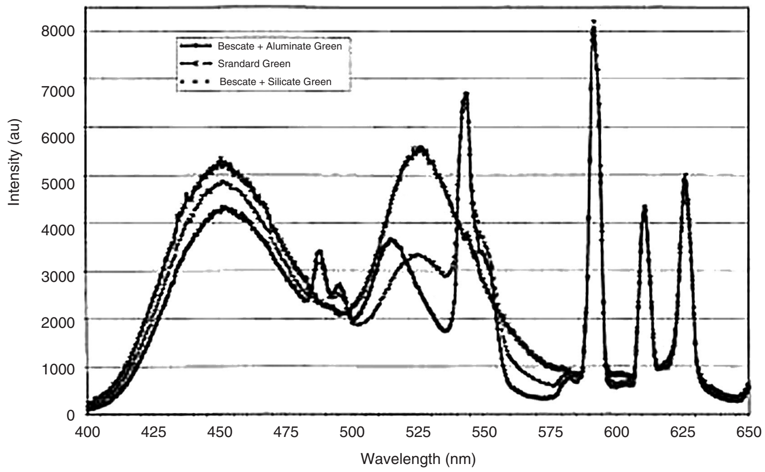

Figure 16 Emission spectra from a 42″ panel made with three different groups of phosphors. (a) BAM (blue), $ZnSiO_4$:Mn (green), and Y,$GdBO_3$:Eu (red), (b) BAM (blue), $ZnSiO_4$:Mn+Y,$GdBO_3$:Tb (green), and Y,$GdBO_3$:Eu (red) and © BAM (blue), $BaAl_{12}O_{19}$:Mn+Y,$GdBO_3$:Tb (green), and Y,$GdBO_3$:Eu (red). (From Rao, R.P., *J. Electrochem. Soc.*, 150, H165, 2003. With permission.)

Table 5 Luminescent Characteristics of Various PDP Phosphors

Serial number	Composition	Emission maximum (nm)	Color coordinates		Remarks	Ref.
			x	*y*		
		Blue phosphors				
1	NTSC		0.14	0.08	Standard from CRT TV	
2	$BaMgAl_{10}O_{17}$ Eu (BAM)	450	0.145	0.068	High brightness with poor stability	
3	$LaPO_4$:Tm (LPTM)	291, 348, 362, 452	0.141	0.037	Low brightness and good stability	[37]
4	BAM + LPTM	452	0.144	0.061	Normal brightness with better stability	[37]
5	$CaMgSi_2O_6$:Eu	450	0.192	0.074	Low brightness	[38]
6	$Sr_3Al_{10}SiO_{20}$:Eu	450	0.145	0.124	Low brightness	[39]
7	(Ca,Mg)$Al_2Si_2O_8$:Eu	450	—	—	Better thermal stability	[40]
8	YPO_4:Zr,Mn	292, 477	—	—	Off-the-color point	[42]
		Green phosphors				
1	NTSC		0.21	0.71	Standard from CRT TV	
2	$(Zn,Mn)_2SiO_4$ (P1)	528	0.233	0.702	Long decay and negative charging	
3	$Li_2ZnGe_3O_8$:Mn	524	0.254	0.02	Better thermal stability	[47]
4	Ba,O×Al_2O_3:Mn	517	0.145	0.747	Poor stability	[46]
5	$La_2Al_{22}O_{36}$:Mn,Li	515	0.125	0.772	Good stability and less negative charge	[49]
6	YPO_4:Tb^{3+}	542, 548	0.284	0.630	Bluish green	[57]
7	(Y,Gd)BO_3:Tb^{3+}	542	0.271	0.718	Bluish green	[51]
8	$LaPO_4$:Tb^{3+}	543	0.276	0.712	Bluish green	[51]
9	(Y,Gd)BO_3:Tb+P1	528, 542	0.275	0.645	Less negative charge	[51]
		Red phosphors				
1	NTSC		0.67	0.33	Standard from CRT TV	
2	(Y,Gd)BO_3:Eu^{3+}	593, 611, 626	0.641	0.352	Orange with high brightness	[60]

Table 5 Luminescent Characteristics of Various PDP Phosphors

Serial number	Composition	Emission maximum (nm)	Color coordinates		Remarks	Ref.
			x	y		
3	$(Y,Gd)_2O_3$: Eu^{3+}	611	0.652	0.337	Red with low brightness	
4	$Gd_{1.7}Li_{0.2}O_3$: $Eu_{0.1}$	611	—	—	Brightness improved	[61]
5	$Y,Gd(PO_4)$ Eu^{3+}	593, 611, 697	0.632	0.364	Stable low color purity	[57]
6	$(Y,Gd)BO_3$: $Eu+(Y,Gd)_2O_3$:Eu^3	593, 611, 626	0.646	0.342	Trade-off between color purity and brightness	[60]
7	$BaZr(BO_3)_2$: Eu	594, 615	0.668	0.331	Improved color point	[59]
8	$(Y,Gd)Al_3(BO_3)_2$:Eu	594, 615	0.668	0.331	Better color point	[53]
9	$Y(PV)O_4$:Eu	594, 611	0.627	0.346	High brightness	[58]
10	$YAl_3(BO_3)_4$: Eu	594, 617	0.668	0.331	Higher 617-nm emission	[53]
11	$GdAl_3(BO_3)_4$: Eu	595, 612	0.645	0.330	Less 594-nm contribution	[52]

10.5.3.1 Blue phosphors

There are a limited number of blue emitting phosphors satisfying all the requirements for TV and PDP applications compared with green and red emitting phosphors.

10.5.3.1.1 BAM phosphor. Presently, divalent europium-activated barium magnesium aluminate ($BaMgAl_{10}O_{17}$:Eu^{2+}, BAM) phosphor is used in PDPs as the blue emitting component due to its high QE, color purity, and availability. BAM phosphor has been used as a lamp phosphor and exhibits a hexaaluminate structure. The structure consists of $MgAl_{10}O_{16}$ spinel-type blocks with intervening Ba–O layers and crystallizes in the $P6_3/mmc$ space group. Because of its wide band gap (6.4 eV), host–lattice absorption occurs at wavelengths shorter than 190 nm.[32] The blue emission from Eu^{2+} has CIE chromaticity coordinates of $x = 0.145$ and $y = 0.124$ and is assigned to the $4f^6 5d^1$ to $4f^7$ transition. BAM exhibits a relatively short life when exposed to VUV flux. The degradation of BAM starts during the baking cycles, and through the manufacturing process, PDP operation results in further degradation through solarization. The emission peak of BAM: Eu^{2+} shifts toward the green during panel fabrication; in manufacturing this is known as the green shift. The mechanism involved in the degradation and green shift in BAM phosphor has been established.[33–36] Apparently, the morphology (hexagonal plate) of BAM phosphor particles is not favorable for screen-printing as well as ink-jet process. There are considerable ongoing efforts in improving the stability of this material.

10.5.3.1.2 Tm^{3+}-activated lanthanum phosphate phosphor. One of the alternatives to BAM is Tm^{3+}-activated lanthanum phosphate (LPTM). Lanthanum phosphate belongs to the monazite crystal group (monoclinic monazite crystal structure) and has a band gap

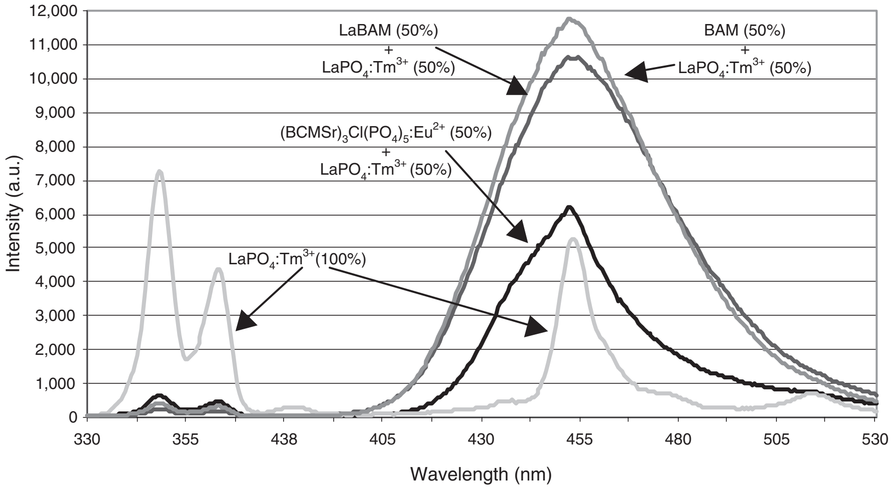

Figure 17 Emission spectra of BAM, LPTM phosphors, and blends of BAM and LPTM phosphors. (From Rao, R.P., *J. Lumin.*, 113, 271, 2005. With permission.)

around 8.0 eV. The emission from the LPTM samples after excitation with either 147 or 173 nm shows three narrow peaks in the UV region at 291, 348, and 362 nm corresponding to the $^1I_6 \rightarrow {}^3H_6$, $^1I_6 \rightarrow {}^3H_4$, $^1D_2 \rightarrow {}^3H_6$ transitions; the emission in the visible region at 452 nm corresponds to the $^1D_2 \rightarrow {}^3H_4$ transition.[37] In lamp phosphors, terbium- and cerium-activated lanthanum phosphates have high QEs, better stability at higher operating temperatures, and longer lifetimes, particularly under 254 and 185 nm UV excitation from high-pressure Hg vapor and compact fluorescent lamps. Tm^{3+}-activated phosphors have a few drawbacks, viz., low brightness, complicated energy levels, and concentration quenching and cross relaxation at relatively low concentrations.

10.5.3.1.3 Blend of LPTM and BAM. The brightness of LPTM phosphor is low when compared with the brightness of BAM phosphor, particularly for PDP applications. The UV energy generated during emission can be utilized to enhance the brightness by blending LPTM phosphors with a suitable UV-excitable blue emitting phosphor. Since the absorption spectrum of BAM extends from VUV to UV regions, the UV emission of LPTM can be used to pump BAM. LPTM is blended with BAM in various proportions, as well as with other blue emitting phosphors such as LaBaMgAl$_{10}$O$_{17}$:Eu^{2+} (LaBAM) and (Ba,Sr,Mg,Ca)$_3$Cl(PO)$_4$:Eu^{2+}. The emission characteristics, brightness, and degradation of these phosphor blends have been investigated. Emission spectra of LPTM–BAM phosphor blend and of LPTM and BAM are shown in Figure 17. As can be seen from the figure, the intensity of UV peaks in LPTM decreases and the intensity of the visible peak around 452 nm increases with the addition of BAM phosphor to LPTM. The peaks in the emission spectrum of LPTM completely disappear with the addition of 50% of BAM. The brightness level of a phosphor blend with 50% of BAM and 50% of LPTM is close to the brightness of BAM alone. Degradation of LPTM and LPTM–BAM blends have been studied in powder samples exposed to VUV and compared with the degradation of a standard BAM phosphor.[37] The degradation of LPTM phosphors and blends in a 42″ test panel has also been studied by operating the panel at accelerated operating conditions (10 × mode). It is observed that under these conditions the degradation of LPTM phosphor is minimal (<0.1%) whereas the degradation is severe in the case of BAM (>30%). By blending BAM

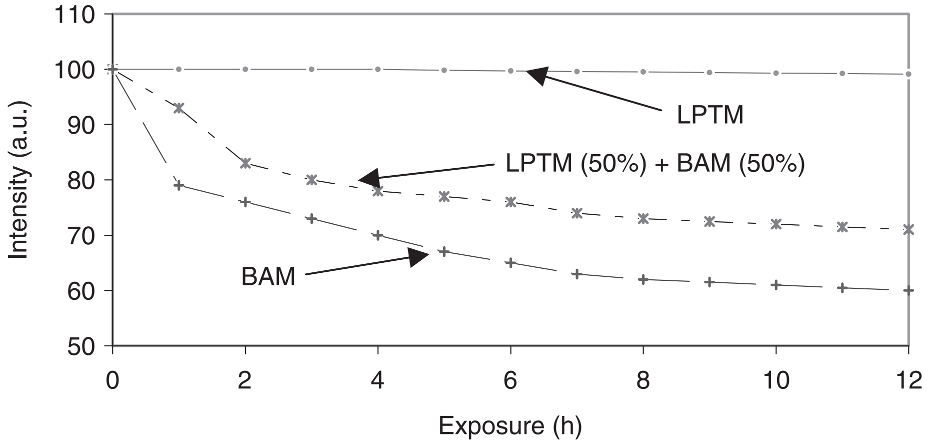

Figure 18 Degradation in intensity (normalized) of LPTM, LPTM (50%) + BAM (50%), and BAM phosphor powders after exposing to vacuum UV (VUV) lamp for different durations. (From Rao, R.P., *J. Lumin.*, 113, 271, 2005. With permission.)

with LPTM, the degradation observed is greatly reduced.[37] Figure 18 shows the level of degradation of LPTM, BAM phosphors, and LPTM–BAM phosphor blends. From the figure, it can be seen that the degradation of BAM is reduced by 50% by blending with 50% of LPTM phosphor. The nature of degradation observed in the panel is the same as observed in powder samples. It can thus be concluded that blending with LPTM can minimize the degradation of BAM without sacrificing the brightness. The overall morphology of the phosphor blends is improved. As the voids in BAM phosphor are filled with the smaller particles of LPTM, the packing density of the thick films (15–20 μm) of blends is also improved.

10.5.3.1.4 Eu^{2+}-activated alkaline earth alumina silicate phosphor. $CaMgSi_2O_6$:Eu,[38] $Sr_3Al_{10}SiO_{20}$:Eu,[39] and (Ba,Mg)$Al_2Si_2O_8$:Eu[40] are phosphors that have been suggested as alternatives to replace BAM. Although these phosphors show less degradation, their luminescence efficiency is much lower under VUV excitation than that of BAM phosphor. The emission is also shifted to longer wavelengths.

10.5.3.1.5 Gd^{3+}-activated yttrium–aluminum borate phosphor. Gd^{3+} activated yttrium –aluminum borate phosphor (YAB:Gd) has an intense line at 313 nm when under VUV excitation, which shows little degradation. The emission originates from the $^6P_{7/2}$ to $^8S_{7/2}$ transition of the Gd^{3+} ion. The emission peak of this phosphor overlaps the excitation of the BAM emission. When proper quantities of YAB:Gd are mixed with BAM, the UVU energy absorbed by YAB:Gd is efficiently transferred to the blue emission of BAM and the degradation characteristics of BAM improve. Although the proposed blend, as an alternate to BAM, shows less degradation as illustrated in Figure 19,[41] overall brightness is low when compared with BAM alone.

10.5.3.1.6 Zr-, Mn-activated yttrium phosphate. Yttrium phosphate activated with both Zr and Mn shows UV emission (291 nm) and a blue peak at 477 nm under VUV excitation. The blue emission originates from Mn^{2+} ions replacing Y^{3+} ions of YPO_4 and is assigned to the transition $^4T_1(^4G) \rightarrow {}^6A_1(^6S)$ of Mn^{2+}.[42] Considering the position of the emission peak and its lower brightness as compared with BAM, this material may not be a potential phosphor for PDP applications.

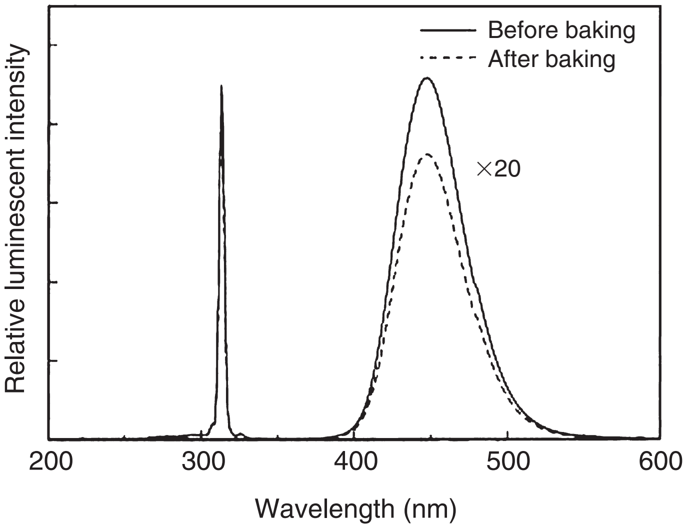

Figure 19 The emission spectra of $YAl_2(BO_3)_4$:Gd^{3+} and $BaMgAl_{10}O_{17}$:Eu^{2+} before and after vacuum UV (VUV) radiation. (From Yokosawa, N., Sato, G., and Nakazawa, E., *J. Electrochem. Soc.*, 150, H197, 2003. With permission.)

10.5.3.2 Green phosphors

The green component is very important as the human eye is most sensitive in this region. Green phosphors improve the color point of white light and boost the overall brightness of the display device. Manganese-activated zinc silicate phosphor (P1) is conventionally used in PDPs as the green emitting component due to its ready commercial availability and its high QE. However, compared with red and blue emitting phosphors, zinc silicate exhibits a wide spectrum of emission with low color purity, long persistence, and fast saturation with VUV flux. Apart from P1 phosphor, various other possible candidates as PDP green phosphors are described in the following sections.

10.5.3.2.1 Mn^{2+}-activated zinc silicate phosphor. Mn^{2+}-activated zinc silicate phosphor is known in mineral form as willemite and has a rhombohedral structure (space group R3). The substitution of Mn^{2+} ions for Zn^{2+} makes the material an excellent green emitting phosphor. The emission is attributed to the $^4T_{1s} \rightarrow {}^6A_{1g}$ forbidden transition of Mn^{2+}; it follows that the decay time of this emission is long (around 20 ms).[43] Because of its long decay time, this phosphor is less favorable for TV applications. The decay time can be reduced with higher doping concentrations of Mn. However, with higher Mn content, there is concentration quenching and the color coordinates shift. This material has been compared extensively with P1.[44] In addition to having long decay, P1 also has negative surface charge, which reduces the wall discharge and addressing margin of green cell in a PDP. This not only causes nonuniformity but also reduces the efficiency and requires higher discharge voltage. By surface-coating with metal oxides such as MgO, the negative discharge is slightly improved.[45]

10.5.3.2.2 Mn^{2+}-activated alkaline earth aluminate phosphor. Mn^{2+}-activated barium aluminate is being suggested in the place of P1 as the green emitting PDP phosphor due to its high efficiency and color purity.[46] The PL of this phosphor is due to transitions of $3d^5$ electrons of the Mn ion. There are several compositions of this compound containing between 1 mol of BaO and 6 mol of Al_2O_3, which are discussed in the literature. Compared

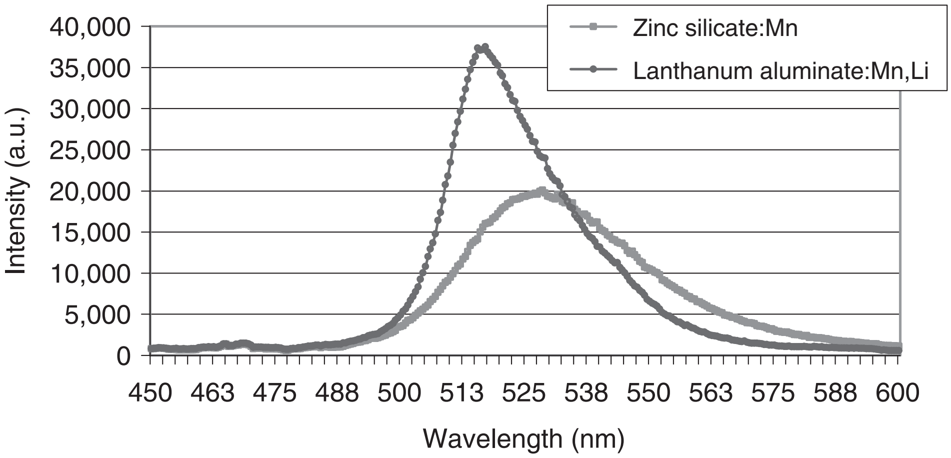

Figure 20 Emission spectra of P1 and Mn, Li-activated lanthanum aluminate phosphors.

with the operational lifetime of P1, its operational lifetime is short during PDP applications. Because of its poor stability, it is not a potential phosphor for PDP applications.

10.5.3.2.3 Mn^{2+}-doped lithium zinc germanate phosphor. Mn-activated lithium zinc germanate, $Li_2ZnGe_3O_8$:Mn (LZG:Mn), has a stronger absorption band in the 100- to 200-nm wavelength range. It shows an emission band peaking at about 524 nm. Because of its poor thermal stability, it is not suitable as a PDP phosphor. The addition of Ga^{3+} improves the thermal as well as the optical stability of this particular phosphor although not sufficiently.[47]

10.5.3.2.4 Mn^{2+}-activated lanthanum aluminate phosphor. Mn^{2+}-activated lanthanum aluminate phosphor with higher color purity is another potential candidate to replace P1 phosphors.[48] Its brightness increases twofold when Li^+ is added as a coactivator to provide charge compensation at the La^{3+} site. The emission spectra of $La_2Al_{22}O_{36}$:Mn,Li and P1 are shown in Figure 20. This phosphor shows higher color purity and lower surface charge when compared with P1 and has a good potential to replace it in this application.[49]

10.5.3.2.5 Tb^{3+}-activated green emitting phosphors. Because of their QE and thermal stability, Tb-activated green emitting lanthanum phosphate and borate phosphors have been well studied and are widely used in compact fluorescent lamps. Silicate and phosphate phosphors have a higher absorption at 147-nm wavelength, whereas borates have a higher absorption at 173-nm wavelength. The excitation spectra of Tb-activated phosphors show a number of strong absorption bands in this region corresponding to the crystal field components of Tb-excited $4f_75d$ state, making these phosphors suitable for PDP applications. The morphology of borate and phosphate phosphors is significantly superior to zinc silicate and aluminate phosphors. It has been shown that the borate-based Tb-activated green phosphors improved the uniformity of the discharge characteristics in AC PDPs.[15]

The emission spectra of Tb-doped yttrium gadolinium borate, lanthanum phosphate, and yttrium phosphate phosphors along with an emission spectrum of commercially available Mn-activated $ZnSiO_4$ are shown in Figure 21. In Tb-activated phosphors, the emission can be divided into three spectral regions, viz., 485–495 nm (bluish green), 535–555 nm (green), and 580–590 nm (yellow). YPO_4 exhibits a doublet in all the three emission regions whereas $LaPO_4$ shows solid peaks.[50] Because of its sizable contribution in the blue region, $LaPO_4$ is not considered to be a viable candidate to replace zinc silicate

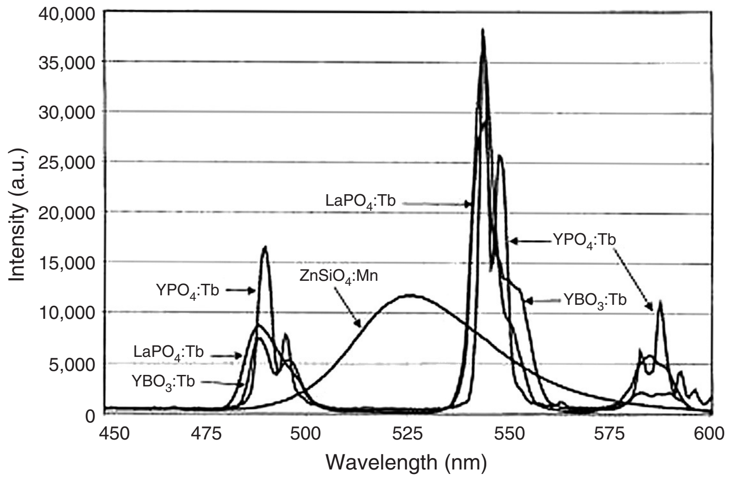

Figure 21 Emission spectra of (a) (Y,Gd) (BO_3):Tb, (b) $LaPO_4$:Tb, (c) YPO_4:Tb, and (d) $ZnSiO_4$:Mn phosphors recorded at room temperature under 147-nm excitation. (From Rao, R.P., *J. Electrochem. Soc.*, 150, H165, 2003. With permission.)

green phosphor. There are ongoing efforts to minimize the blue peak by using suitable optical filters. The fluorescence from Tb-activated phosphors mainly occurs in the transitions $^5D_3 \rightarrow {}^7F_j$ and $^5D_4 \rightarrow {}^7F_j$. Since the crystal field splits the levels into many sublevels a complicated spectrum is produced, particularly in the case of YPO_4:Tb phosphor.

At lower Tb concentrations, when the cross-relaxation probability is small, the transition from the $^5D_3$ state dominates as a blue emission. At higher concentrations of Tb, the cross-relaxation mechanism produces rapid population of the $^5D_4$ state at the expense of $^5D_3$, giving strong emission in the green region. With the increase in Tb concentration, the intensity of the blue peak decreases. At higher Tb concentrations, there is an additional peak in the yellow region arising from the $^5D_4 \rightarrow {}^7F_4$ transition. As color purity is very important for display applications, emissions in the blue and yellow regions are not desirable. For display applications, particularly TVs, it is preferable to have only one peak around 545 nm to obtain good color purity. By incorporating blue absorption dye in a neutral density filter, the contribution from the blue peak can be eliminated. Neutral density filters are being used in PDPs to eliminate unwanted colors.

10.5.3.2.6 Tb^{3+}-activated phosphor blends. As described above, Tb^{3+}-activated phosphors exhibit superior characteristics including excitation, morphology, negative charge, and optical and thermal stability. A little emission peak in the blue region makes these phosphors yellowish. To overcome the blue peak and to take advantage of the superior morphology and longer life of borate and phosphate phosphors, a blend of zinc silicate and yttrium borate phosphor is used in the manufacture of large-area PDPs.[51] The ratio of silicate, aluminate, borate, or phosphate can be varied depending on the required optical and electrical characteristics of a phosphor blend. The phosphor blends improve not only the optical properties but also the morphology.

The degradation of borates, phosphates, and blends with P1 is low when compared with that of P1. Figure 22 shows the loss of intensity of various screen-printed green phosphors: (a) $ZnSiO_4$:Mn, (b) $BaAl_{12}O_{19}$:Mn, (c) YBO_3:Tb (50%), (d) YBO_4:Tb, (e) $LaPO_4$:Tb, (f) blend of YBO_3:Tb (50%) + $ZnSiO_4$:Mn (50%), (g) blend of YBO_3:Tb (50%) + $BaAl_{12}O_{19}$:Mn, and (h) blend of YPO_4:Tb (50%) + $ZnSiO_4$:Mn (50%) after exposure to Xe flash lamp for

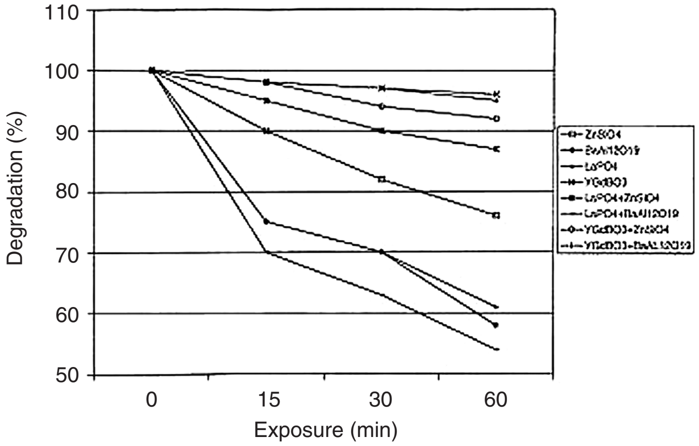

Figure 22 Degradation in intensity of various green emitting phosphors and phosphor blends exposed to Xe flash lamp (vacuum UV, VUV) for different durations. (a) $ZnSiO_4$:Mn, (b) $BaAl_{12}O_{19}$:Mn, (c) YBO_3:Tb (50%), (d) YBO_4:Tb, (e) $LaPO_4$:Tb, (f) blend of YBO_3:Tb (50%) + $ZnSiO_4$:Mn (50%), (g) blend of YBO_3:Tb (50%) + $BaAl_{12}O_{19}$:Mn, and (h) blend of YPO_4:Tb (50%) + $ZnSiO_4$:Mn (50%). (From Rao, R.P., *J. Electrochem. Soc.*, 150, H165, 2003. With permission.)

different durations. The degradation is moderate in the case of silicate phosphor whereas it is high in the case of aluminate samples. The level of degradation in the case of borate- and phosphate-based samples is negligible. The degradation of phosphor blends is relatively less when compared with that of aluminate- or silicate-based phosphors.

10.5.3.3 Red phosphors

The following are some of the red emitting PDP phosphors reported in the literature. Figure 23 shows the emission spectra of various red emitting phosphors identified as PDP phosphors.

10.5.3.3.1 Eu^{3+}-activated yttrium, gadolinium borate. Europium-activated yttrium, gadolinium borate [(Y,Gd)BO_3:Eu^{3+}] is an efficient red emitting phosphor that is currently used in PDPs due to its high QE, persistence characteristics, and reduced saturation.

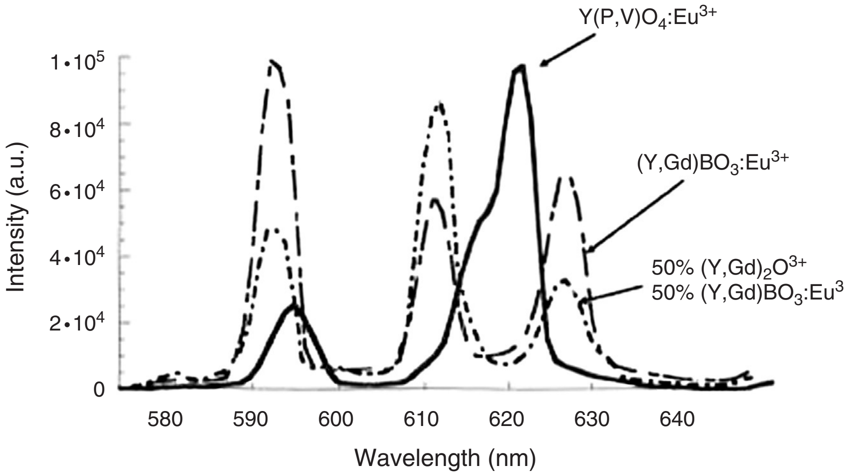

Figure 23 Emission spectra of Eu^{2+}-activated (Y,Gd)BO_3, (Y,Gd_2)O_3, YVO_4, YPO_4, and blend of 50% (Y,Gd)BO_3 and (Y,Gd)O_3 phosphors excited by 147-nm Xe lamp.

In general, the luminescence (emission) lines at 593, 611, and 627 nm correspond to $^5D_0 \rightarrow {}^7F_1$ (orange red) and $^5D_0 \rightarrow {}^7F_2$ (red) transitions of Eu. The peak and intensity of each red line (593, 611, and 627 nm) depend on the Eu and Gd concentrations. For lamp applications, all three lines at 593 nm (orange), 611 nm (red), and 627 nm (red) are acceptable. But in the case of displays, specifically for TV applications, it is preferable to have more of the red. Different Eu^{3+}-activated phosphors to replace rare earth (RE) borates are described briefly in the following sections.

10.5.3.3.2 Eu^{3+}-activated rare earth aluminum borate phosphor. Gadolinium aluminum borate crystallizes in hexagonal form where the Gd^{3+} ions are separated from each other by BO_3 groups without Gd^{3+} ions sharing the same oxygen ion. This results in a relatively large distance between the nearest Gd^{3+} neighbors.[52] The intense emission peak at 612 nm observed is due to the electric dipole transition, $^5D_0 \rightarrow F_2$, induced by the lack of inversion symmetry at the Eu^{3+} site. The color coordinates of this emission are close to that required by the NTSC color standard. In the case of $(Y,Gd)Al_3(BO_3)_4$:Eu, the emission spectrum is dominated by the 617-nm peak, which is more favorable as a TV phosphor.[53]

10.5.3.3.3 Eu^{3+}-activated rare earth lithium borate and oxyborate phosphors. Eu^{3+}-activated yttrium lithium borate, $Li_6(BO)_3$ and lithium lanthanum borate, $Li_3La_2(BO_3)_3$, and similar oxyborate phosphors are being considered for PDP applications due to their color point in the deep red. The probability for radiative dipole f–f transitions is generally higher in oxyborates. In these phosphors, the intensity of the orange line in the 582–600-nm wavelength range arising from the $^5D_0 \rightarrow {}^7F_1$ transition is less than that observed in RE borates while the emission due to $^5D_0 \rightarrow {}^7F_2$ in the wavelength range 600–640 nm is stronger.[54] Unfortunately, these phosphors are of low brightness.

10.5.3.3.4 Eu^{3+}-activated rare earth aluminum phosphate phosphor. PL studies of Eu^{3+}-activated yttrium aluminophosphate under VUV excitation show that their integrated intensities are higher than that of yttrium phosphate phosphors. The addition of Al improves the color purity due to the distortion of the crystal symmetry at the Eu site.[55]

10.5.3.3.5 Eu^{3+}-activated rare earth phosphate phosphor. It has been reported that lanthanum-based phosphors show high efficiency under VUV excitation when compared with other PDP phosphors due to their higher absorption in the VUV region.[56] In lanthanide phosphate–based phosphors, Gd^{3+} plays an important role in acting as a sensitizer. With the increase of Gd content, the brightness increases and reaches a maximum at 0.4 mol of Gd. Since the emission from Eu^{3+} corresponds to the $^5D_0 \rightarrow {}^7F_j$ transitions, the red and orange lines appearing are the same as in borate-based phosphors. There is no advantage over borate phosphor with regard to color purity in these phosphor systems.[57] The orange line is less intense in the case of $Y,Gd(PV)O_4$:Eu. It is also found that the addition of SiO_2 in the phospho-vanadate phosphor improves the morphology of the phosphor crystal.[58]

10.5.3.3.6 Eu^{3+}-activated rare earth barium zirconium borate phosphor. Eu^{3+}-activated $BaZr\ (BO_3)_2$ shows the strongest emission at 615 nm and it is due to the electric dipole $^5D_0 \rightarrow {}^7F_2$ transition arising from the noncentrosymmetric structure of the host lattice. The CTS excitation band of Eu^{3+} is enhanced by codoping Al^{3+} into the $BaZr(BO_3)_2$ lattice.[59]

10.5.3.3.7 Eu^{3+}-activated rare earth oxide phosphor. Eu^{3+}-activated yttrium oxide is used in lamp applications. It is also proposed as an alternate to the red emitting borate phosphor in PDP applications due to its color purity. Less intense emission peak at 593 nm assigned to the $^5D_0 \rightarrow {}^7F_1$ transition helps improve the color purity. The stability of this phosphor is not as good as that of borates. The stability can be improved by replacing a small portion of Y_2O_3 with Gd_2O_3. The complex of $(Y,Gd)_2O_3$ phosphor exhibits the same level of brightness and persistence with better stability. By blending $(Y,Gd)BO_3$ with $(Y,Gd)_2O_3$, color purity of the phosphor can be improved with a little loss in brightness.[60] It is reported that the brightness of these oxides can also be improved by codoping with L^+. Li^+ substitution in the lattice leads to a decrease in interstitial oxygen and an increase in the quantum yield.[61] Currently, PDP manufacturers are not willing to replace $(Y,Gd)BO_3:Eu^{3+}$ as a red emitting phosphor.

10.5.4 Drawbacks and recent developments

Currently, the PDP industry is able to manufacture TVs with an efficacy close to 2 lm/W, with a goal of 5 lm/W. If it reaches this goal the efficacy is still only 6% of the current lamp performance standard. The main concern of the industry is in reducing manufacturing costs and in lowering power consumption. To achieve these goals, the improvement of phosphors and phosphor-related technology is very important. Some of the issues such as image sticking, ghost imaging, moving picture distortion (MPD), gray scale, ambient light reflectivity, long-term after-glow decay (<0.25% of brightness), and dark room contrast are related to phosphors and need in-depth study.

The degradation of blue emitting BAM has been a real concern as it directly affects the life of a PDP TV. As shown in Figure 15, the life of BAM has improved tremendously recently; from 50% degradation to 20% degradation after 30,000 h of continuous normal operation. One of the leading PDP manufacturers claims that their 2006 product (TVs) has better blue phosphors with longer life. New phosphor preparation techniques as well as display manufacturing processes make this possible. Decay time of green phosphor has been reduced by blending with Tb-activated phosphors. Also, the new lanthanum aluminate phosphor has low negative charge as well as color point characteristics and it is poised to replace P1 or its blends. Poor chromaticity of borate-based red phosphor due to the presence of the orange line in the emission spectrum is not a real problem. Use of a front filter with orange absorption dye eliminates the orange peak from the red phosphor along with orange emission from Ne gas. Currently, the PDP industry is pretty much settled on BAM type phosphor as blue, Mn^{2+}- and Tb^{3+}-activated blends as green, and Eu^{3+}-activated RE borate as red emitting phosphors.

References

1. Weber, L., Color plasma displays, in SID Seminar Lectures, Society for Information Display, San Jose, Vol. 1, Seminar M-9, 2002.
2. Boeuf, J.P., Plasma display panels: Physics, recent developments and key issues, *J. Phys. D Appl. Phys.*, 36, R53, 2003.
3. Bitzer, D.L. and Slottow, H.G., The plasma display—A digitally addressable display with inherent memory, *Conf. Proc. AFIPS*, 29, 541, 1966.
4. Mikoshiba, S., Color plasma displays, in SID Seminar Lectures, Society for Information Display, San Jose, Vol. 1, Seminar M-4, 1997.
5. Seo, J.H., Jeong, H.S., Lee, J.Y., Yoon, C.K., Kim, J.K., and Whang, K.W., Vacuum ultraviolet emission characteristics from He–Ne–Xe gas discharge in an ac plasma display panel cell, *J. Appl. Phys.*, 88, 1257, 2000.
6. Koike, J., Kojima, T., and Toyonaga, R., New tricolor phosphors for gas discharge display, *J. Electrochem. Soc.*, 126, 1008, 1979.
7. Kim, C.H., Kwon, I.K., Park, C.H., Hwang, Y.J., Bae, H.S., Yu, B.Y, Pyun, C.H., and Hong, G.Y., Phosphors for plasma display panels, *J. Alloys Compd.*, 311, 33, 2000.

8. Bechtel, H., Justel, T., Glaser, H., and Wiechert, D.U., Phosphors for plasma-display panels: Demands and achieved performance, *J. SID*, 10, 63, 2002.
9. Hisamune, T., Technical trend of phosphors for plasma display panels, in Proceedings of International Display Workshop, Society for Information Display, San Jose, IDW02, 685, 2002.
10. Rao, P.R., Morphology and stability of flux grown blue emitting BAM phosphors for PDP applications, *J. Electrochem. Soc.*, 152, H115, 2005.
11. Hongpeng, Y., Hong, G., Zeng, X., Kim, C.H., Pyun, B.Y., and Bae, H.S., VUV excitation of $LnAl_3B_4O_{12}$:RE (Ln=Y,Gd; RE=Eu,Tb), *J. Phys. Chem.*, 61, 1985, 2005.
12. Moine, B., Mugnier, J., Boyer, D., Mahiou, R., Schamm, S., and Zanchi, G., VUV absorption coefficient measurements of borate matrices, *J. Alloys Compd.*, 323–324, 816, 2001.
13. Justel, T., Krupa, J.C., and Wiechert, D.U., VUV spectroscopy of luminescent materials for plasma display panel and Xe discharge lamps, *J. Lumin.*, 93, 179, 2001.
14. Okazaki, C., Shiiki, M., Suzuki, T., and Suzuki, K., Luminance saturation properties of PDP phosphors, *J. Lumin.*, 87–89, 1280, 2000.
15. Tachibana, H., Matsuda, A., Haruki, S., Kosugi, N., Wani, K., and Weber. L., in Proceedings of International Display Workshop (IDW), Society for Information Display (SID), San Jose, IDW00, 651, 2000.
16. Yen, W.M. and Weber, M.J., *Inorganic Phosphors (Compositions, Preparations and Optical Properties)*, CRC Press, Boca Raton, 2004.
17. Rao, R.P., *Preparation of Phosphor Materials in Luminescence, Phenomena, Materials and Devices*, Rao, R.P., Ed., Nova Science Publishers, New York, 345, 1992.
18. Kummer, F., The production of fluorescent lamp phosphors, in Proceedings of Physics and Chemistry of Luminescent Materials, Struck, C.W., Misra, K.C., and Bartolo, B.Di., Eds., *Electrochem. Soc. Pennington (NJ)*, 210, 1999.
19. Butler, K.H., *Fluorescent Lamp Phosphors*, The Pennsylvania State University Press, University Park (USA) 1980, Chap. 3.
20. Rao, R.P., Preparation and characterization of fine grain yttrium based phosphors by sol–gel process, *J. Electrochem. Soc.*, 143, 189, 1996.
21. Copeland, T.S., Lee, B.I, Qi, J., and Elrod, A.K., Synthesis and luminescent properties of Mn^{2+} -doped zinc silicate phosphors by sol–gel methods, *J. Lumin.*, 97, 168, 2002.
22. Rao, P.R., Method of making small particle red emitting phosphor, US Patent 6,284,155 B1, 2001.
23. Ravilisetty, P.R., Stable blue phosphor for plasma display panel applications, US Patent 6,830,706 B2, 2004.
24. Kim, K.N., Jung, H.K., and Park, H.D., Synthesis and characterization of red phosphor ((Y,Gd)BO_3:Eu by the co-precipitation method, *J. Mater. Res.*, 17, 907, 2002.
25. Lu, S.W., Copeland, T., Lee, B.I, Tong, W., Wagner, B.K., Park, W., and Zhang, F., Synthesis and luminescent properties of Mn^{2+} doped Zn_2SiO_4 phosphors by a hydrothermal method, *J. Phys. Chem. Solids*, 62, 777, 2001.
26. Kang, Y.C., Lim, M.A, Park, H.D., and Man, H., Ba^{2+} co-doped Zn_2SiO_4:Mn phosphor particles prepared by spray pyrolysis process, *J. Electrochem. Soc.*, 150, H7, 2003.
27. Jung, K.Y., Lee, D.Y, Kang, Y.C., and Park, H.D., Improved PL of $BaMgAl_{10}O_{17}$ blue phosphor prepared by spray pyrolysis, *J. Lumin.*, 105, 127, 2003.
28. Jung, K.Y., Kim, E.J., and Kang, Y.C., Morphology control and optimization of luminescent property of YBO_3:Tb phosphor particles prepared by spray pyrolysis, *J. Electrochem. Soc.*, 151, H69, 2004.
29. Bacalski, C.F., Cherry, M.A., Hirata, G.A., McKittrick, J.M., and Mourant, J., The effect of fuel-to-oxidizer ratio on luminescent properties and particle morphology of combustion-synthesized Eu activated Ba,Mg aluminate, *J. SID*, S1, 93, 2000.
30. Sohn, K.S., Park, E.S., Kim, C.H., and Park, H.D., Photoluminescence behavior of $BaAl_{12}O_{19}$:Mn phosphor prepared by pseudo-combinatorial chemistry method, *J. Electrochem. Soc.*, 147, 4368, 2000.
31. Sohn, K.S., Zeon, I.W., Chang, H., Lee, S.K., and Park, H.D., Combinatorial search for new red phosphors of high efficiency at VUV excitation based on the YRO_4 (R = As, Nb, P, V) system, *Chem. Mater.*, 14, 2140, 2002.

32. Howe, B. and Diaz, A.L., Characterization of host–lattice emission and energy transfer in $BaMgAl_{10}O_{17}:Eu^{2+}$, *J. Lumin.*, 109, 51, 2004.
33. Zhang, S., Kono, T., Ito, A., Yasaka, T., and Uchiike, H., Degradation mechanisms of the blue-emitting phosphor $BaMgAl_{10}O_{17}:Eu^{2+}$ under baking and VUV-irradiating treatments, *J. Lumin.*, 106, 39, 2004.
34. Dawson, B., Ferguson, M., Marking, G., and Diaz, A.L., Mechanisms of VUV damage in $BaMgAl_{10}O_{17}:Eu^{2+}$, *Chem. Mater.*, 16, 5311, 2004.
35. Bizarri, G. and Moine, B., On $BaMgAl_{10}O_{17}:Eu^{2+}$ phosphor degradation mechanism: Thermal treatment effects, *J. Lumin.*, 113, 199, 2005.
36. Misra, K.C., Raukas, M., Marking, G., Chen, P., and Boolchand, P., Investigation of fluorescence degradation mechanism of hydrated $BaMgAl_{10}O_{17}:Eu^{2+}$ phosphor, *J. Electrochem. Soc.*, 152, H183, 2005.
37. Rao, R.P., Tm^{3+} activated lanthanum phosphate: A blue PDP phosphor, *J. Lumin.*, 113, 271, 2005.
38. Kunimoto, T., Yamaguchi, S., Ohimi, K., and Kobayashi, H., Luminescent and aging characteristics of test-PDP panel using Gd-codoped $CaMgSi_2O_6$:Eu phosphors, IDW'04, 1081, 2004.
39. Kubota, S. and Shimada, M., $Sr_3Al_{10}SiO_{20}$:Eu as a blue luminescent material for plasma displays, *Appl. Phys. Lett.*, 81, 2749, 2002.
40. Im, W.B., Kim, Y, Kang, J.H., and Jeon, D.Y., Luminescent and aging characteristics of blue emitting $(Ca,Mg)Al_2Si_2O_8$:Eu (M=Ca,Ba) phosphor for PDP applications, *Solid State Commun.*, 134, 717, 2005.
41. Yokosawa, N., Sato, G., and Nakazawa, E., Improvement of luminescence degradation of PDP blue phosphor with new UV phosphor, *J. Electrochem. Soc.*, 150, H197, 2003.
42. Kaneyoshi, M. and Nakazawa, E., Luminescence of YPO_4:Zr and YPO_4:Zr,Mn under vacuum ultraviolet excitation, *J. Electrochem. Soc.*, 152, H80, 2005.
43. Morell, A. and El Khiati, N., Green phosphors for large plasma TV screens, *J. Electrochem. Soc.*, 140, 2019, 1993.
44. Barthou, C., Benoit, J., Benalloul, P., and Morell, A., Mn^{2+} concentration effect on the optical properties of Zn_2SiO_4:Mn phosphors, *J. Electrochem. Soc.*, 141, 524, 1994.
45. Hong, G.Y., Jeoung, B.W., Jeon, B.S., Yoo, J.S, Ha, C.H., and Whang, K.W., Improvement of discharge characteristics of $Zn_2SiO_4:Mn^{2+}$ phosphor layer in plasma display panels, *J. Electrochem. Soc.*, 151, H205, 2004.
46. Rao, R.P. and Devine, D.J., Method of making green emitting alkaline earth aluminate phosphor for VUV excited light emitting device, US Patent 6,423,248 B1, 2002.
47. Kim, J.H., Choi, I.K., You, Y.C., and Zang, D.S., A new synthesis of germanate phosphor and its PDP applications, IDW'04, 1089, 2004.
48. Tamatani, M., Fluorescence in β-Al_2O_3-like materials of K, Ba and La activated with Eu^{2+} and Mn^{2+}, *Jpn. J. Appl. Phys.*, 13, 950, 1974.
49. Ravilisetty, P.R., Green emitting phosphor material and plasma display panel using the same, US Patent 7,025,902 B2, 2006.
50. Di, W., Wang, X., Chen, B., Lai, H., and Zhao, X., Preparation, characterization and VUV luminescence property of YPO_4:Tb phosphor for a PDP, *Opt. Mater.*, 27, 1386, 2005.
51. Rao, R.P., Tb^{3+} activated green phosphors for plasma display panel applications, *J. Electrochem. Soc.*, 150, H165, 2003.
52. Wang, Y., Uheda, K., Takizawa, H., Mizumoto, U., and Endo, T., Synthesis of $Gd_{1-x}Eu_xAl_3(BO_3)_4$ $(0<x<1)$ and its PL properties under UV and VUV regions, *J. Electrochem. Soc.*, 148, G430, 2001.
53. Lee, K.G., Yu, B.Y., Pyun, C.H., and Mho, S., Vacuum ultraviolet excitation and PL characteristics of $(Y,Gd)Al_3(BO_3)_4$/Eu, *Solid State Commun.*, 122, 485, 2002.
54. Jubera, V., Chaminade, J.P., Garcia, A., Guillen, F., and Fouassier, C., Luminescent properties of Eu^{2+} activated lithium rare earth borates and oxyborates, *J. Lumin.*, 101, 1, 2003.
55. Kang, J.H, Im, W.B., and Jeon, D.Y., PL characteristics of new yttrium aluminophosphate phosphors under VUV excitation, IDW'04, 1159, 2004.

56. Wu, X, You, H., Cui, H., Zeng, X., Hong, G., Kim, C.H., Pyun, C.H., Yu, B.Y., and Park, C.H., Vacuum ultraviolet optical properties of (La,Gd)PO_4:RE^{3+} (RE=Eu,Tb), *Mater. Res. Bull.*, 37, 1531, 2002.
57. Rao, R.P. and Devine, D.J., RE-activated lanthanide phosphate phosphors for PDP applications, *J. Lumin.*, 87–88, 1260, 2000.
58. Okazaki, C., Suzuki, T., and Shiiki, M., Characterization of (Y,Gd)(P,V)O_4:Eu for PDP phosphor, IDW'03, 849, 2003.
59. Tian, L., Mho, S., Yu, B.Y., and Pyun, C.H., Enhanced PL and VUV absorption of BaZr$(BO_3)_2$:Eu^{3+} by Al^{3+} incorporation, *J. SID*, 12, 517, 2004.
60. Rao, P.R., Eu^{3+} activated red emitting phosphors for PDP applications, *SID 03 Digest*, 1219, 2003.
61. Park, J.K., Kim, J.M., Kim, K.N., and Kim, C.H., Effect of Li^+ on the luminescence properties of Gd_2O_3:Eu phosphor, *Electrochem. Solid State Lett.*, 7, H39, 2004.

chapter eleven — sections one–three

Organic fluorescent pigments

Sadayasu Miyahara

Contents

11.1 Daylight fluorescence and fluorescent pigments 769
11.2 Manufacturing methods of fluorescent pigments 771
  11.2.1 Lump resin pulverizing method 772
  11.2.2 Emulsification polymerization method 772
  11.2.3 Resin precipitation method 773
11.3 Use of fluorescent pigments 773
  11.3.1 Paints 773
  11.3.2 Printing 773
  11.3.3 Dyeing 774
  11.3.4 Tinted plastics 774
  11.3.5 Flaw detection 774
References 774

Organic fluorescent pigments are classified into coloring materials and whiteners. The former is used to add chromatic fluorescent color to various materials. The latter, which normally emits blue fluorescence, is added to white-colored materials to compensate for the blue-region absorption caused by small amounts of yellowish-brown impurities in the materials. Both types of organic fluorescent pigments have a wide range of applications; but in this chapter, fluorescent coloring materials and their diverse uses are described, focusing particularly on highly useful fluorescent pigments (properly called daylight fluorescent pigments).[1]

11.1 Daylight fluorescence and fluorescent pigments

Daylight fluorescence is the ability to fluoresce under excitation by radiation ranging from the blue-green to the near-ultraviolet. That is, the high-energy portion of the daylight spectrum, and thus to achieve a practical fluorescent effect in daylight. Daylight fluorescent pigments offer colors of extremely high luminosity for daylight or near-daylight illumination. They are usually simply called fluorescent pigments and this usage is employed herein.

Excitation and emission spectra of various fluorescent pigments are shown in Figures 1 and 2, respectively. Except for the blue fluorescent pigment, the excitation spectra of these

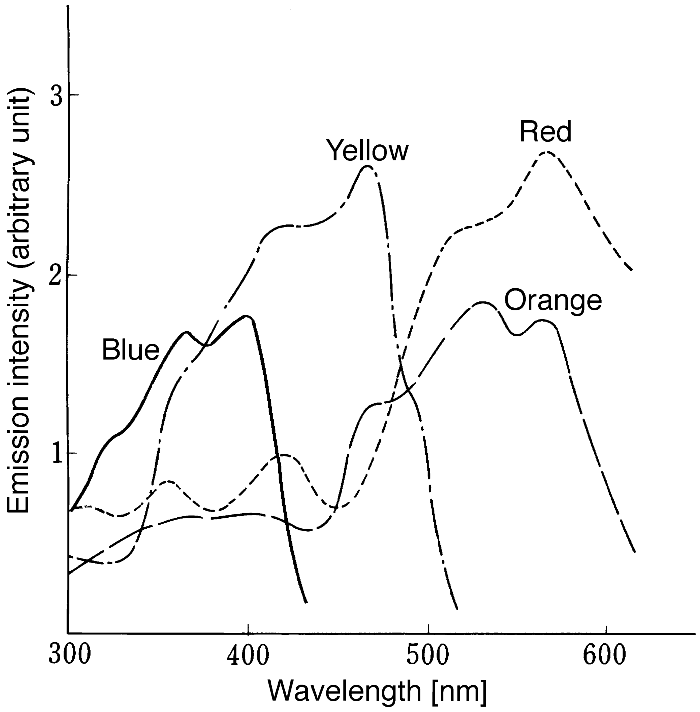

Figure 1 Excitation spectra of fluorescent pigments.

materials are mostly in the visible region. This explains why these fluorescent pigments fluoresce well under blue and green light excitation and why the color definition is nearly unchanged under daylight, even when an ultraviolet-absorbing agent is painted over the fluorescent pigment.

There are two types of fluorescent pigments: one consists of solid solutions of fluorescent dyes and synthetic resins, and the other is composed of color pigments. At present, the former type is in general use. With some exceptions, the color pigment type has low applicability because of its poor fluorescence characteristics and instability. The description given herein is limited to the solid solution type synthetic resin.

Fluorescent dyes have chemical structures and electronic states that are easily excited by light. They are also characterized by their chemical reactivity. In other words, these organic compounds can be highly unstable when exposed to light. Fluorescence is generally found mainly in unsaturated compounds that have π electrons. Ring compounds have higher fluorescence yields than chain compounds. Aromatic hydrocarbons in particular have high fluorescence yields, which increase in proportion to the number of benzene nuclei they contain. Molecules with contorted shapes generally do not exhibit fluorescence, but those that have flat structures do. Examples of some practical fluorescent dyes are listed in Table 1.

Fluorescent pigments of the solid solution type synthetic resins can be applied in areas where fluorescent dyes alone have been found to be impractical. However, technical problems still remain centered on the improvement of the stability of these solid solutions when exposed to sunlight. To protect fluorescent dyes against photodegradation while maintaining the desired fluorescent characteristics sometimes requires incompatible and contradictory requirements. Dissolving dyes in resins has made it possible to improve the stability of dyes against sunlight while not hindering the properties or applicability of the dyes.

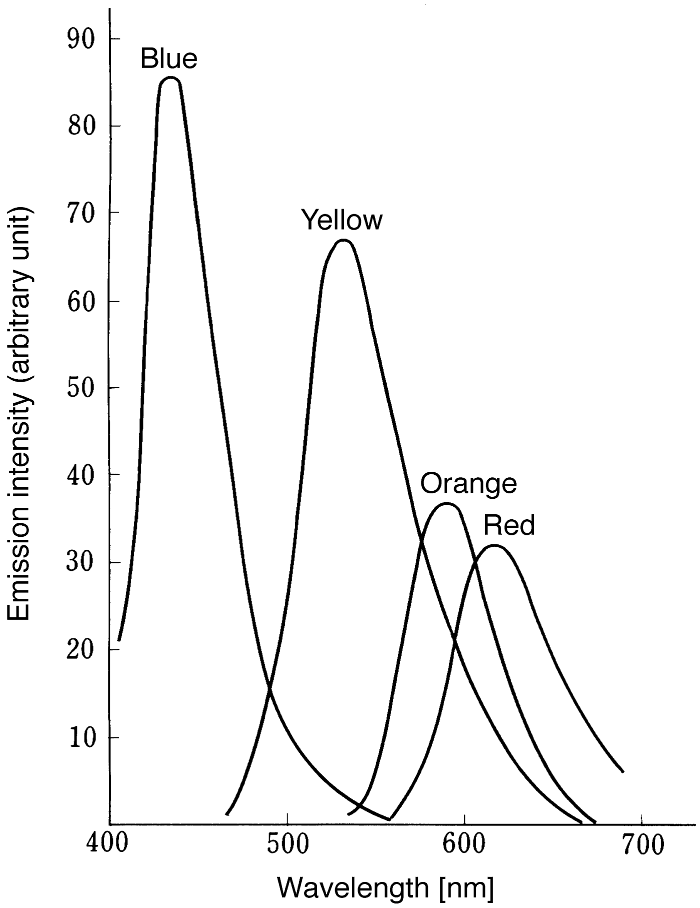

Figure 2 Emission spectra of fluorescent pigments excited by the 365-nm mercury line.

11.2 *Manufacturing methods of fluorescent pigments*

Fluorescent pigments in solid solution with synthetic resins can be manufactured by making fluorescent dyes dissolve in a transparent solid carrier materials. Attention must be given to the forces of interaction between the synthetic resin carrier and the fluorescent dye. This interaction strongly affects the intensity and color of the fluorescence and the stability of the pigment. Fluorescent dyes generally fluoresce when in dilute solution; the intensity of the fluorescence increases as the concentration of the dye increases. Above a certain concentration, however, the intensity decreases with increasing concentration. This phenomenon, known as concentration- or self-quenching, must also be considered when preparing fluorescent pigments in solid solution. Fluorescent dye concentrations are optimized so as to achieve a suitable balance between the fluorescence intensity and tinting power.

The synthetic resins used as carriers of the fluorescent dyes include polymethacrylate ester, polyvinyl chloride, polyvinyl chloride with acetate co-polymer, alkyd resin, benzoguanamine resin, and their co-condensation polymers. The dyes listed in Table 1 can be used as the fluorescent dyes in these pigments.

Next, typical manufacturing methods for fluorescent pigments of solid solution type synthetic resins are described.

Table 1 Fluorescent Dyes

Dye	Structure	Color under daylight[b]	Fluorescent color[b]
Brilliantsulfoflavine FF (C.I. 56205)[a]	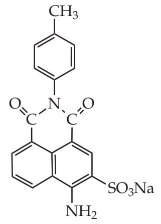	Yellow	Green to yellowish-green
Basic yellow HG (C.I. 46040)[a]	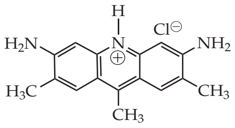	Yellow	Greenish-yellow to yellow
Eosine (C.I. 45380)[a]	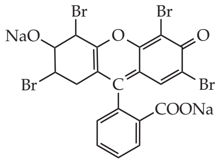	Red	Yellow to orange
Rhodamine 6G (C.I. 45160)[a]	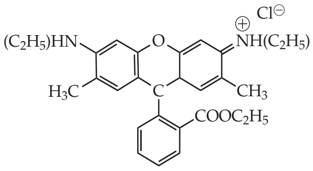	Red	Yellow to orange
Rhodamine B (C.I. 45170)[a]	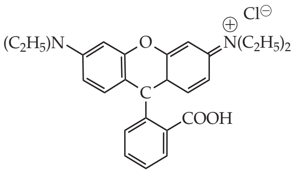	Pink	Orange to red

[a] Color index number.

[b] Color of dyed textiles.

11.2.1 *Lump resin pulverizing method*

Fluorescent dyes are added to melted synthetic resins, and then the resins are polymerized. An alternate way is to polymerized the resins first, and then add the fluorescent dyes. The lump resins obtained by cooling of the molten solutions are crushed and pulverized to obtain fluorescent pigments. By changing the resin composition, different kinds of pigments suitable for various uses can be obtained.

11.2.2 *Emulsification polymerization method*

In this method, the resin is polymerized in the presence of a fluorescent dye using an emulsifying agent and a stabilizer. An emulsified polymer also can be dyed directly. Depending on the application, the emulsified polymers can be used as is or after drying.

11.2.3 Resin precipitation method

After resins are dissolved in solvents with high solubility, different solvents with low solubility are added, and the resins are made to precipitate as fine particles. Fluorescent dyes are added either to the solutions in which pigments are dissolved, or to the resin particles that have precipitated. The precipitates are filtered out, dried, and used in the form of fine particles.

Of the production methods described above, the one currently used most often is the resin pulverization method (11.2.1). The reasons are that (1) the tinting power is high because pigments with distinct colors can be obtained even with high concentrations of fluorescent dye; (2) tints ranging from blue to red are easily made; and (3) the stability required for practical use is possible. On the negative side, much energy is required for the crushing and pulverizing process.

11.3 Use of fluorescent pigments

The properties of fluorescent pigments are determined by the type of fluorescent dye used and its concentration, the composition of the resin, the dyeing method, and the manufacturing method. The proper fluorescent pigment that has properties suitable for the intended application is selected through these combinations of factors.

11.3.1 Paints

Fluorescent paints are made by dispersing a fluorescent pigment in a varnish, including the normally dry type, the baked type, and the hardened type. The fluorescent paints have lightness that is at least three times as bright as the normal color under sunlight and further show distinct colors of high color purity. In the case of deep colors, the paints attract the human eye. In the case of light colors, their soft and clear tone create a refreshing sensation. Under fluorescent lamp or mercury lamp illumination, ordinary colors look dull, but fluorescent paints emit light under short wavelength radiation, which is a primary cause for reducing the color rendering properties of the lamps, thereby making objects brighter and clearer. Furthermore, when irradiated with a black-light lamp (main wavelength = 365 nm) in dark places, fluorescent paints can be seen with neon-lamp-like brightness. Sodium lamps are often used in expressway tunnels and other such places and have no color rendering properties; in this light, ordinary colors become indistinct. Coloration produced by fluorescent paints, however, is clearly distinguishable under sodium light illumination.

As noted, fluorescent paints have very high visibility under a variety of conditions. Therefore, they have a very broad range of applications. In the fields of advertisement and decoration, they are used in notices, signs, window stickers, posters, etc. In the fields of safety and disaster prevention, they are used as warning and instruction signs. Fluorescent paints effective for disaster prevention are specified in *JIS* (Japanese Industrial Standards) *Z 9106*, "Fluorescent Safety Colours—General Rules for Application."

Fluorescent paints are weak in covering power, so when they are used on objects that are not white, a white base coat must first be applied. These paints also have low resistance to weathering, so when used outdoors they must be coated with a transparent paint that contains an ultraviolet light-absorbing material to prevent discoloration.

11.3.2 Printing

Fluorescent inks are made by dispersing fluorescent pigments in a varnish that is suitable for the particular printing method to be used. They can be used in all types of printing, from offset and relief printing to gravure, newspaper rotary, and flexographic printing, independently of whether oil-based or water-based inks are used. Fluorescent inks are used in printed materials that require attractive and eye-catching color; these include packaging, magazine covers, posters, newspapers, and calendars. Recent improvements in fluorescent pigment characteristics for printing applications include distinct color types at high pigment concentrations, fine grain size (0.5 μm or less) pigments that are suitable for offset printing, and superior solvent resistance for use in gravure printing.

11.3.3 Dyeing

The main use of fluorescent pigments in dyeing is for textile printing. In this process, a binder is added to the fluorescent color base, consisting of a fluorescent pigment dispersed in a vehicle. The mixture is then printed onto the fabric.

The fluorescent color base is also often used together with a reactive dye. Reactive dyes produce distinct and stable colors when used in dyeing cotton. Yellows, greens, and blues are very attractive, but oranges, reds, and pinks produced in this way are not as attractive as those obtained through cation-dyed colors on acrylic textiles. Fluorescent color bases are used to compensate for this weakness. For example, the texture color, leaf color, etc. of a flower pattern can be printed with yellow, green, or blue reactive dyes, while the pink or red petals of the flowers need to be printed with the fluorescent color bases.

11.3.4 Tinted plastics

Fluorescent pigments are used to tint plastics such as polyethylene, polypropylene, and soft polyvinyl chloride. In selecting the fluorescent pigments, attention must be given to factors such as heat resistance and color transfer properties, depending on the molding method and tinting conditions to be used. Molded products of these plastics include markers, toys, and leisure goods.

11.3.5 Flaw detection

Because fluorescent dyes and fluorescent pigments fluoresce under ultraviolet radiation, a small amount of these dyes dissolved in solvent can be used as a flaw-detecting agent for welded and other machined parts. When applied to the parts to be inspected, they reveal flaws when examined under ultraviolet light. Another application involves the use of sand containing the pigment to investigate sand flow conditions.

Reference

1. Miyahara, S., *Shikizai Kyokaishi (Journal of the Japan Society of Colour Material)*, 58(2), 73-79, 1985 (in Japanese).

chapter twelve — section one

Other phosphors

Yoh Mita

Contents

12.1 Infrared up-conversion phosphors 775
  12.1.1 Introduction 775
  12.1.2 Brief review up to the present 775
  12.1.3 Mechanism and the materials for the up-conversion of luminescence 776
  12.1.4 Applications 780
    12.1.4.1 Detection of diode laser light 780
    12.1.4.2 Light sources 781
References 782

12.1 *Infrared up-conversion phosphors*

12.1.1 *Introduction*

In this section, characteristic features of infrared-to-visible up-conversion phosphors doped with trivalent rare-earth ions are described. Devices made with these materials and important applications of such materials and devices are also mentioned. It is widely known that certain kinds of trivalent rare-earth-activated phosphors emit intense visible luminescence under near-infrared light excitation. This up-conversion process takes place in the following way: higher lying excited states of a rare-earth ion are populated by two- or three-step successive excitations with infrared quanta or by energy transfers. A downward transition to the ground level or to an intermediate excited level produces the visible luminescence. The up-conversion efficiency is known to be strongly dependent upon choice of host materials, activator and sensitizer concentrations, etc. However, since elementary processes governing the up-conversion processes are physically simple in nature and well explored, it seems now possible to review the entire up-conversion phenomenon in a consistent manner.

Infrared stimulation of visible luminescence is an anti-Stokes emission process (see Chapter 7). This phenomenon is due to the liberation by infrared excitation of carriers stored in traps and is produced by a different mechanism. However, these two phenomena are used in the same application, i.e., the detection of infrared laser light.

12.1.2 *Brief review up to the present*

Generation of visible luminescence in rare-earth ion-doped materials as a result of successive photon absorption in excited levels was proposed in 1959 and has been termed "quantum counter action."[1] Today, the same effect is generally called excited-state absorption (ESA) in contrast with ground-state absorption (GSA). The effect is observed particularly at high excitation densities such as those produced by high-power laser light excitation or those encountered in single-mode optical fibers.

Substantial improvement in the up-conversion efficiencies was realized by incorporating the Yb^{3+} ion as a sensitizer and by exploiting energy transfers between rare-earth ions.[2] This scheme is often called energy transfer up-conversion (ETU) or addition of photons by transfer of energy (APTE). Since Yb^{3+} ions have a substantially larger optical cross-section and a lesser tendency for concentration quenching in comparison with other rare-earth ions, higher excitation densities can be realized. The absorbed energy can then be efficiently transferred to such ions as Er^{3+} or Tm^{3+}, giving rise to green and red or blue emission, respectively.[3,4]

The effect of Yb^{3+} sensitization was first reported in $NaWO_4$ microcrystals and approximately 50× improvement in up-conversion efficiency was observed.[2] Shortly thereafter, fluorides such as LaF_3 and YF_3 proved more suitable as host materials for rare-earth ion doping.[5] It was then found that the absorption band of Yb^{3+} ions provides a good match to the emission band of common GaAs:Si light-emitting diodes (LEDs) centering at 950 nm.[6] Extensive investigations have been carried out with the purpose of obtaining practical green-emitting LEDs by combining infrared-emitting LEDs with Er^{3+}- and Yb^{3+}-doped fluoride phosphors.[7–9] However, it soon became clear that these devices cannot compete with the more efficient green-emitting GaP LEDs, and interest for the systems has faded out.

Presently, the most important application of infrared up-conversion materials seems to be the detection of infrared light from laser diodes.[10,11] Since the visible emissions generated from these materials are quadratically or cubically dependent upon excitation intensity, detection is particularly favorable for intense or focused laser light.

In recent years, renewed interest has been directed toward up-conversion devices and materials. The interest is principally due to prospects for the realization of infrared up-conversion lasers pumped with laser diodes. The revival of interest for the up-conversion phenomenon is due to the advent of powerful and less costly 980-nm or 800-nm laser diodes that can be used as excitation sources and the appearance of new materials such as fluoride glass that can be manufactured in fiber form. The first report on an infrared up-conversion laser dates back to 1972, in which a BaY_2F_8 crystal doped with Ho^{3+} and Yb^{3+} was used and green laser oscillations were observed at liquid nitrogen temperature.[12] More recently, up-conversion lasers oscillating in the green or blue spectral regions have been reported in long fibers[13,14] or in materials under excitation with high-power lasers.[15,16]

12.1.3 *Mechanism and the materials for up-conversion of luminescence*

Several typical up-conversion schemes are illustrated in Figures 1(a) to (e). The energy levels of trivalent rare-earth ions are discussed elsewhere (see 3.3). The simplest way for realizing up-converted emission is to induce successive absorption in a single ion. This scheme, called ESA, is illustrated in Figure 1(a) for the Er^{3+} ion.

Efficient up-conversion emission is observed in fluoride phosphors doped with Er^{3+} and Yb^{3+} ions. In these phosphors, the green emission at 550 nm is generated as a result of two successive resonant energy transfers from Yb^{3+} to Er^{3+} ions, followed by nonradiative decay to the green-emitting level, ${}^4S_{3/2}$, as is depicted in Figure 1(b). A typical emission spectrum is shown in Figure 2(a) for YF_3:Yb^{3+},Er^{3+} phosphors pumped by a 980-nm emitting laser diode. In some Er^{3+}-doped phosphors, red emission from ${}^4F_{9/2}$ level predominates over the green emission. This is especially the case for phosphors such as

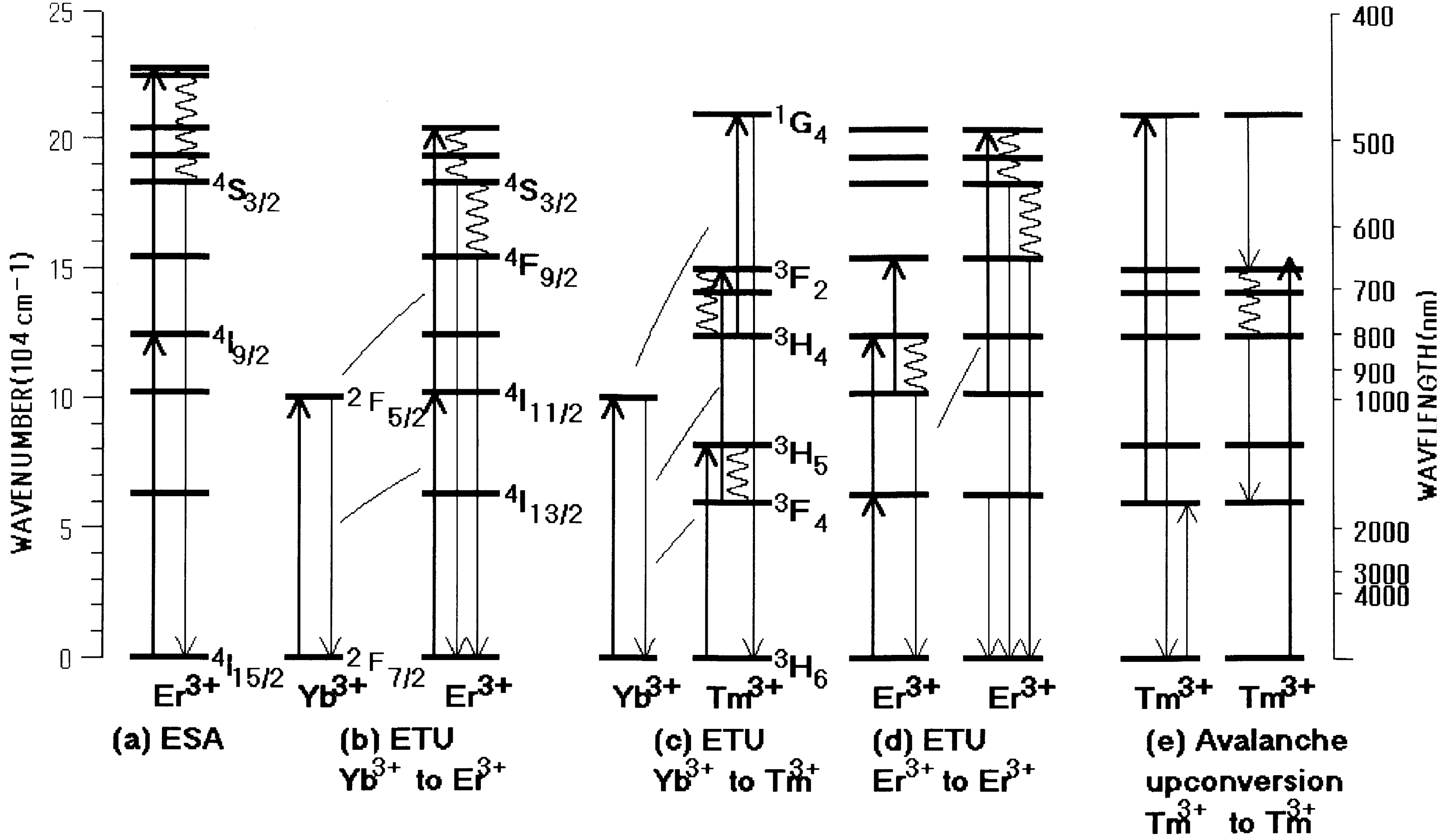
WAVENUMBER(104 cm−1)
25
20
15
10
5
0
WAVELENGTH(nm)
400
500
600
700
800
900
1000
2000
3000
4000
4S3/2
4I9/2
4I15/2
2F5/2
2F7/2
4S3/2
4F9/2
4I11/2
4I13/2
1G4
3F2
3H4
3H5
3F4
3H6
Er3+
Yb3+
Er3+
Yb3+
Tm3+
Er3+
Er3+
Tm3+
Tm3+
(a) ESA
(b) ETU
Yb3+ to Er3+
(c) ETU
Yb3+ to Tm3+
(d) ETU
Er3+ to Er3+
(e) Avalanche
upconversion
Tm3+ to Tm3+

Figure 1 Schematic illustrations of various up-conversion processes: (a) excited state absorption (ESA); (b) infrared up-conversion with two resonant energy transfers (Yb^{3+} to Er^{3+}); (c) same with three phonon-assisted energy transfers (Yb^{3+} to Tm^{3+}); (d) same with a more complicated energy transfer scheme in 1.5-μm light detection (Er^{3+} to Er^{3+}); (e) avalanche up-conversion (Tm^{3+} to Tm^{3+}).

the oxyhalides, which have larger phonon cut-off energies as compared to fluoride materials. Several possible excitation routes have been postulated for the red emission. All of these routes require multiphonon nonradiative decay to bridge large energy gaps or energy transfer steps assisted by the simultaneous emission of phonons to surmount the energy mismatch between two transitions.

Three successive phonon-assisted energy transfer steps from Yb^{3+} ions are required for generating the blue emission of Tm^{3+} ions, as shown in Figure 1(c). The blue emission from the $^1G_4$ level is accompanied by red emission, which arises from an intermediate transition terminating at the $^3F_4$ level. A typical emission spectrum for YF_3:Yb^{3+},Tm^{3+} phosphors is given in Figure 2(b).

There are several rare-earth ions, other than Yb^{3+}, that have relatively long excited-state lifetimes. The wavelengths can be extended from 1.0 µm to the 0.8-µm and 1.5-µm regions by using these ions. In Figure 1(d), a typical excitation route for generating visible emissions when using 1.5-µm excitation is depicted.

Recently, a new type of up-conversion luminescence, called avalanche up-conversion, has been reported in several Tm^{3+}-activated phosphors and has attracted considerable interest.[17,18] The mechanism of avalanche up-conversion is schematically shown in Figure 1(e). In this up-conversion scheme, the principal excitation takes place due to weak ground-state absorption combined with intense excited-state absorption. The up-conversion luminescence is weak under weak pump power. However, with increasing excitation power, the lower excited state becomes populated due to cross-relaxation between neighboring ions. This up-conversion luminescence is characterized by a threshold in the excitation power, above which a conspicuous increase of visible emission is observed. This up-conversion process is known to take place particularly at low temperatures and under high excitation intensity.

The following discussion on the up-conversion mechanism principally concerns ETU phenomena using Yb^{3+} as the sensitizer. Since the physical nature of the elementary processes involved in the up-conversion processes is well understood, the apparently complicated characteristics of ETU can be explained with relatively simple models in a straightforward manner. The elementary processes involved in the up-conversion phenomena include optical absorption both from ground (GSA) and excited states (ESA), radiative and nonradiative decay, and energy transfer. Energy transfer processes include those between different species of ions as well as those between the same kind of ions (known as energy migration or energy diffusion), and phonon-assisted transfers as well as resonant transfers. The nonradiative multiphonon decay rate is governed by the number of phonons needed to relax to the next lower level. It is known that the relaxation rate decreases approximately exponentially with the energy gap to the next lower level; in other words, with the number of emitted phonons.[19,20] The rate for the phonon-assisted energy transfer is also expected to be exponentially dependent upon the energy mismatch.[21]

Many important characteristics of up-conversion materials and devices can then be analyzed with a set of simple rate equations, taking various elementary processes into consideration. Results of such calculations and comparisons with experimental results are found in a number of publications.[2,9,22] However, it has also been shown that the simple rate equation model has limitations in some instances. Several important features are briefly reviewed in this article.

In many applications, fluoride materials such as YF_3 or BaY_2F_8 are considered to be advantageous. However, it has been shown recently that chlorides such as $BaCl_2$ are more suitable as hosts for Er^{3+} ions than the fluorides.[23] This is due to a lower phonon cut-off frequency in the chlorides than in the fluorides. The smaller phonon energy brings about

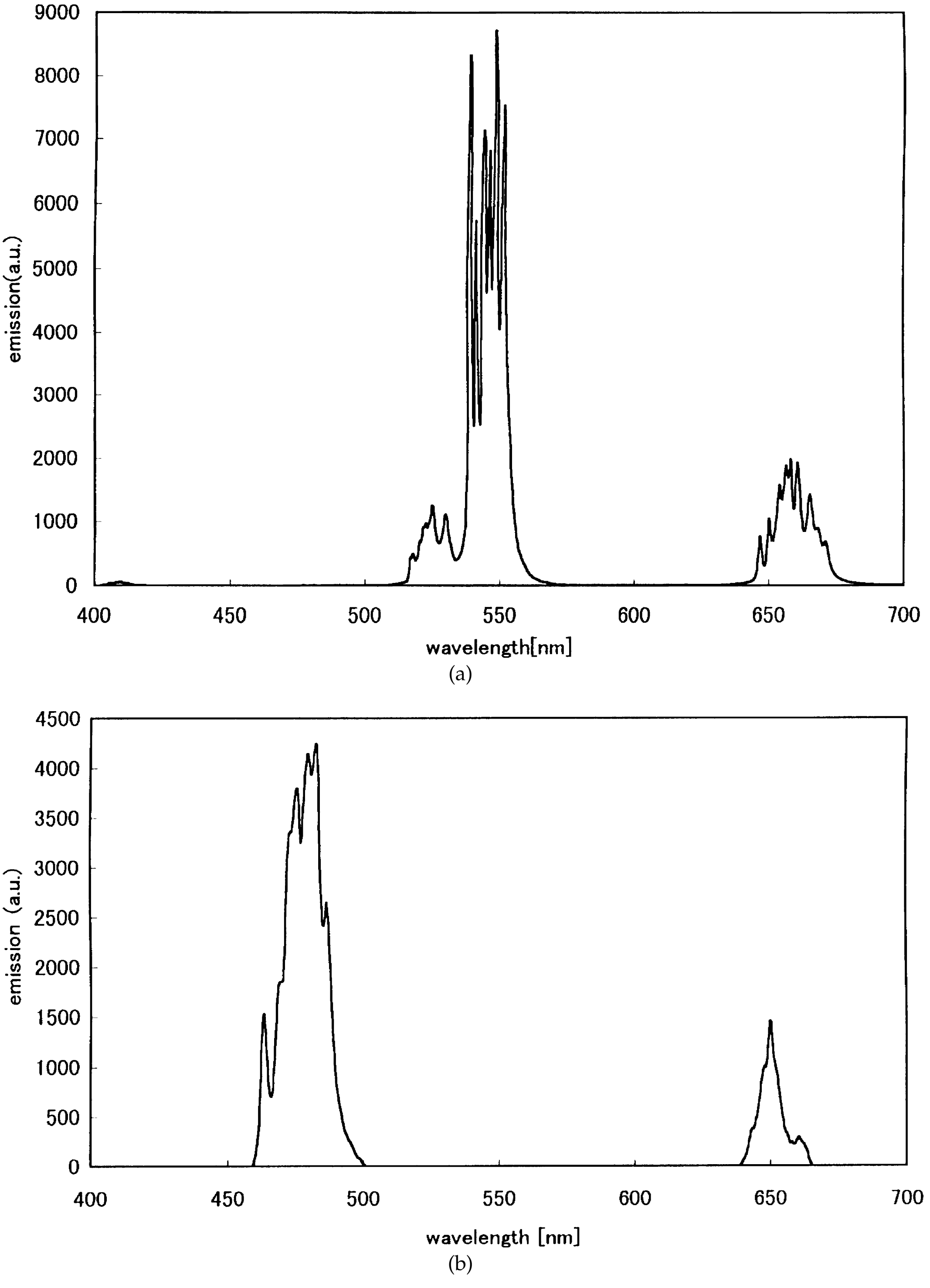

Figure 2 Typical up-conversion emission spectra under 980-nm light excitation in fluoride phosphors doped with Yb^{3+} as sensitizer: (a) $Y_{0.78}Yb_{0.20}Er_{0.02}F_3$; (b) $Y_{0.8}Yb_{0.2}Tm_{0.001}F_3$. (Observed by the author.)

Table 1 Chemical Compositions of the Representative Infrared Up-conversion Materials

Emission color	Typical composition	Ref.
Green	$Y_{0.78}Yb_{0.20}Er_{0.02}F_3$	7
	$NaY_{0.69}Yb_{0.30}Er_{0.01}F_4$	
	$BaY_{1.34}Yb_{0.60}Er_{0.06}F_8$	10
	$25ErCl_3$-$75BaCl_2$	23
Red	$Y_{0.74}Yb_{0.25}Er_{0.01}OCl$	7
Blue	$Y_{0.65}Yb_{0.35}Tm_{0.001}F_3$	7

slower multiphonon decay rates; in other words, longer lifetimes of the excited levels. Longer excited-state lifetimes are advantageous in generating up-conversion emission efficiently. The conversion efficiency for the green emission under both 0.98- and 1.5-μm excitation has improved dramatically in chloride host lattices as compared to that obtained in fluorides. An efficiency approximately 40 times higher than that of fluoride phosphors has been reported.[23] Since the chloride phosphors are susceptible to moisture, proper protection procedures are required for practical application.

Representative compositions of the up-conversion materials are shown in Table 1. In addition, there are several other interesting materials for infrared up-conversion phenomena. Fluoride glasses having ZrF_4 or AlF_3 as their main component have also proved to be good host materials for rare-earth ions.[24,25] Excited-state lifetimes of rare-earth ions in these glasses are slightly shorter than those found in fluoride crystals. However, since the materials are highly transparent and can be processed into various physical forms including fibers, glasses have notable merits in some applications; improvements both in the materials and their applications are currently still in progress. Vitroceramic materials, which are composites of microcrystalline fluoride crystals and oxide glass, also seem favorable for some applications. This is because these materials can be made with good luminescence properties and can be manufactured with arbitrary shapes and sizes.[26]

Up-conversion characteristics are also dependent upon geometrical factors. Since the up-conversion emission intensity is expected to have nearly a quadratic dependence upon the excitation density, the emission power is expected to be inversely proportional to the volume. The principal loss mechanism found in up-conversion devices is due to the infrared emission of Yb^{3+}.[22] In many infrared up-conversion fluoride crystals,[27] as well as in fluoride glass,[22] the Yb^{3+} emission spectrum overlaps its own absorption spectrum to a good extent. Since Yb^{3+} has a large absorption cross-section, an appreciable part of the emitted energy from Yb^{3+} is reabsorbed before it can escape from the material. The reabsorption effect is particularly significant when transparent up-conversion materials are contained in reflective cavities, as has been demonstrated both experimentally and analytically.[22]

12.1.4 *Applications*

12.1.4.1 *Detection of diode laser light*

A representative application of up-conversion phosphors is the detection of infrared diode laser light. Detectable wavelength regions with presently available phosphors can be determined from the excitation spectra shown in Figure 3. The spectra in the figure were taken for $Y_{0.8}Er_{0.2}F_3$ phosphors in the 0.8-μm region, for $Y_{0.78}Yb_{0.20}$,$Er_{0.02}F_3$ phosphors in the 1.0-μm region, and for $25ErCl_3$-$75BaCl_2$ phosphors in the 1.5-μm region.[23] Since the rare-earth ion absorption spectra are relatively insensitive to the host lattices, the applicable wavelength regions are not so different for different hosts. As noted before, detection is favorable under conditions of focused laser light, since the up-conversion emission intensity is nearly quadratic dependent upon the excitation intensity.

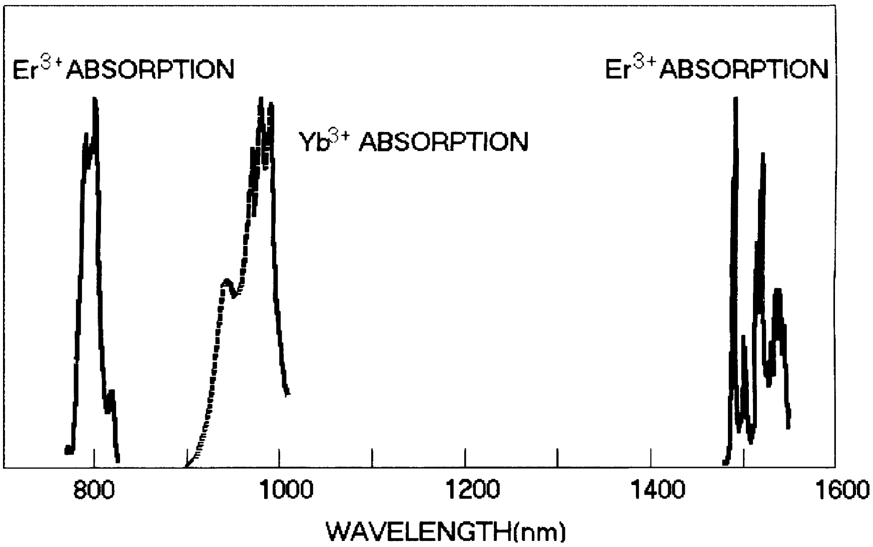

Figure 3 Excitation spectra of infrared up-conversion phosphors: $Y_{0.8}Er_{0.2}F_3$ phosphors for 0.8 μm regions; $Y_{0.78}Yb_{0.20},Er_{0.02}F_3$ phosphors for 1.0 μm region (observed by the author), and $25ErCl_3$-$75BaCl_2$ phosphors for 1.5-μm region. (From Ohwaki, J. and Wang, Y., *Jpn. J. Appl. Phys.*, 33, L334, 1994).

Laser light detection in the 1.5-μm wavelength region using Er^{3+}-doped phosphors is especially important[10] because this wavelength region corresponds to the loss minimum of silica optical fibers used in long-distance optical communications. As mentioned above, chlorides are more suitable as the host material[23] for this application and $BaCl_2:Er^{3+}$ phosphors are currently in use along with fluorides.

Another important wavelength region for optical communications is the 1.3-μm region corresponding to the dispersion minimum of silica optical fibers. It was shown very recently that Dy^{3+} ions added to Er^{3+}-doped phosphors act as sensitizers to Er^{3+}, absorbing 1.3-μm light. Multistep energy transfers take place from excited Dy^{3+} ions to Er^{3+} ions and green and red emission of Er^{3+} is generated.[28] As host materials for Dy^{3+} and Er^{3+}, bromides have been found to be more suitable than chlorides. In bromide hosts such as YBr_3, the conversion efficiency is two orders of magnitude higher than in chloride hosts.[28] This is reasonable since the phonon cut-off energy is considerably smaller in bromides than in chlorides.

It is interesting to compare the important features of up-conversion phosphors with those of infrared-stimulable phosphors. Commercially available infrared-stimulable phosphors are found as IR Phosphor Plate.[29] The sensitivity range of these phosphor plates covers the near infrared region to 1.3 μm. The phosphor plate can detect unfocused infrared light as well as focused laser emission. However, the phosphor plate requires ultraviolet charging prior to use and is limited both in brightness and duration. The principal constituents of the infrared stimulable phosphor plates are CaS activated with rare-earth ions. (See 3.6.)

12.1.4.2 Light sources

Recently, the conversion efficiency of up-conversion devices has been improved by utilizing a 980-nm laser diode as an excitation source and adopting a confined optical structure. It has been shown that a conversion efficiency from a 980-nm light to green light of nearly 4% can be obtained in fluoride glass containing both Er^{3+} and Yb^{3+} ions.[30]

Considerable interest has been directed toward laser diode-pumped visible up-conversion lasers. Since laser oscillations depend on the product of optical gain times the cavity length, most of the upconversion lasers reported have utilized fluoride glass optical fibers.[13,14] Room-temperature, continuous-wave oscillation at various wavelengths covering the entire visible spectral region have been realized in fluoride fibers doped with Pr^{3+}, Tm^{3+}, or Er^{3+}.[31,32] Most of the reports on laser oscillation use the ESA pumping scheme. However, in some instances, Yb^{3+} is used for sensitization[33]; laser oscillations of Pr^{3+} have been realized at 521 and 635 nm pumped by the ETU scheme.

There are also reports of up-conversion lasers using single crystals instead of long fibers. Continuous-wave outputs of 40 mW at 551 nm have been reported at room temperature in $LiYF_4$:Er^{3+}; these crystals are pumped by the ESA scheme[15] using 810-nm excitation from a high-power Ti:saphire laser. Also, outputs have been obtained in BaY_2F_8:Ho^{3+},Yb^{3+} crystals using the ETU scheme.[16] Ongoing efforts are continuing toward the realization of up-conversion lasers that are small in size and pumped with diode lasers.

References

1. Bloembergen, N., *Phys. Rev. Lett.*, 2, 84, 1959.
2. Auzel, F., *Compt. Rend.*, 262, 1016, 1966.
3. General review: Auzel, F., *J. Lumines.*, 45, 341, 1990; Auzel, F., *Proc. IEEE*, 61, 758, 1973.
4. General review: Wright, J.C., Up-conversion and excited state energy transfer in rare-earth doped materials, in *Topics in Apllied Physics*, Vol. 4, Springer, 239.
5. Hewes, R.A. and Sarver, J.F., *Phys. Rev.*, 182, 427, 1969.
6. Galganaitis, S.V., *Met. Trans.*, 2, 757, 1971.
7. Johnson, L.F., Geusic, J.E., Guggenheim, H.J., Kushida, T., Singh, S., and Van Uitert, L.G., *Appl. Phys. Lett.*, 15, 48, 1969.
8. Ostermayer, F.W., van der Ziel, J.P., Marcos, H.M., Van Uitert, L.G., and Geusic, J.P., *Phys. Rev. B*, 3, 2698, 1971.
9. Mita, Y., *J. Appl. Phys.*, 43, 1772, 1972.
10. Mita, Y., *Appl. Phys. Lett.*, 39, 587, 1981.
11. Auzel, F., *Rev. Phys. Appl.*, 20, 273, 1985.
12. Johnson, L.F. and Guggenheim, H.J., *Appl. Phys. Lett.*, 19, 44, 1971.
13. Allain, J.Y., Monerie, M., and Poignant, H., *Electron. Lett.*, 28, 111, 1990.
14. Massicott, J.F., Briereley, M.C., Wyatt, R., Davey, S.T., and Szebesta, D., *Electron. Lett.*, 29, 2119, 1993.
15. Heine, F., Heumann, H., Danger, T., Scweizer, T., and Huber, G., *Appl. Phys. Lett.*, 65, 383, 1994.
16. Thrash, R.J. and Johnson, L.F., *J. Opt. Soc. Am. B*, 11, 881, 1994.
17. Jourbert, M.B., Guy, S., and Jacquier, B., *Phys. Rev. B*, 48, 10031, 1993.
18. Colling, B.C. and Silversmith, A.J., *J. Luminesc.*, 62, 271, 1994.
19. Riseberg, L.A. and Moos, H.W., *Phys. Rev.*, 174, 429, 1968.
20. Weber, M.J., *Phys. Rev.*, 157, 262, 1967.
21. Miyakawa, T. and Dexter, D.L., *Phys. Rev. B*, 1, 70, 1970.
22. Mita, Y., Hirama, K., Ando, N., Yamamoto, H., and Shionoya, S., *J. Appl. Phys.*, 74, 4703, 1993; Mita, Y., Wang, Y., and Shionoya, S., *Appl. Phys. Lett.*, 23, 173, 1973.
23. Ohwaki, J. and Wang, Y., *Jpn. J. Appl. Phys.*, 33, L334, 1994; Ohwaki, J. and Wang, Y., *Jpn. J. Appl. Phys.*, 31, L1481, 1992; Wang, Y. and Ohwaki, J., *J. Appl. Phys.*, 74, 1272, 1993.
24. Kishimoto, S. and Hirao, K., *J. Appl. Phys.*, 80, 1965, 1996.
25. Shikida, A., Yanagita, H., and Toratani, H., *J. Opt. Soc. Am. B*, 11, 928, 1994.
26. Auzel, F., Pecile, D., and Morin, D., *J. Electrochem. Soc.*, 112, 101, 1975.
27. DeLoach, L.D., Payne, S.A., Chase, L.L., Smith, L.K., Kway, W.L. and Krupke, W.F., *J. I.E.E.E. QE*, 29, 1179, 1993.
28. Ohwaki J. and Otsuka, M., *Electron. Lett.*, 31, 752, 1995; Ohwaki, J. and Wang, Y., *Appl. Phys. Lett.*, 65, 129, 1994.
29. Kodak IR Phosphor Plate, (Catalogue of Kodak Inc.).
30. Mita, Y., *Ext. Abstr. Int. Conf. Solid State Device Mater.*, 1992, 369.
31. Piehler, D., Craven, D., Kwong, N., and Zarem, H., *Electron. Lett.*, 29, 1857, 1993.
32. Zhao, Y., Fleming, S., and Poole, S., *Opt. Commun.*, 114, 285, 1995.
33. Piehler, D., Craven, D., Kwong, N., and Zarem, H., *Electron. Lett.*, 21, 1857, 1993.

Note: Recent advancement in the upconversion phenomena, including results on ions other than rare earth ions, are extensively reviewed by F. Auzel.(1) However, at least presently, upconversion efficiency obtained for such ions as transition metal ions and for uranium ion are much inferior to those observed in prevailing luminescent materials reported for rare earth ions, typically doped with Er^{3+} and Yb^{3+} ions.

In a recent article, a high conversion efficiency from infrared energy to visible energy near to 50% is reported in $NaY_{.88}Yb_{.20}Er_{.02}F4$ phosphors.(2) This experimental result was obtained under intense Ti:sapphire laser light excitation (up to 600mW) and by optimizing excitation wavelength. The conversion from infrared radiation to visible light is higher at 200 K than at lower temperatures. The effect is interpreted to be due to efficient energy transfer from Yb^{3+} ion to Er^{3+} ion due to thermal activation to higher multiplet of Yb^{3+} ions.

References:
(1) F. Auzel, Chem. Phys. 104, 139-173 (2004).
(2) J. F. Suyver, J. Grimm, K. W. Krämer and H. U. Güdel, J. Luminesc. 140, 53 (2005).

chapter twelve — section two

Other phosphors

Yoshihiko Murayama

Contents

12.2 Luminous paints 785
  12.2.1 Radioluminous paints 786
    12.2.1.1 Types and composition of radioluminous paints 786
    12.2.1.2 Brightness of radioluminous paints 786
    12.2.1.3 Emission colors of radioluminous paints 787
    12.2.1.4 Lifetime of radioluminous paints 788
    12.2.1.5 Radiation safety 788
  12.2.2 Phosphorescent paints 789
    12.2.2.1 Long phosphorescent phosphors 789
    12.2.2.2 Properties of phosphorescent paints 790
References 792

12.2 Luminous paints

There are two basic types of luminous paints: radioluminous paints and phosphorescent paints. Phosphorescent paints glow in the dark for a given duration after absorption of light, such as sunlight or electric lamp light. This absorption-emission cycle can be repeated many times. Consequently, it is only appropriate to use phosphorescent paints in locations where there is an excitation light source. However, radioluminous paints are capable of continuous light emission without an extraneous energy source because they contain radioisotopes that provide a constant source of energy to excite the phosphor continuously.

Surprisingly, ancient Chinese documents provide evidence that phosphorescent paints were produced in Japan approximately 1000 years ago.[1] This means that phosphorescent paints have been in existence since very early times. However, radioluminous paints have been utilized only since the beginning of the 20th century, following the development of industrial applications for radium (which was discovered by Pierre and Marie Curie).

Radium was mainly used in incipient radioluminous paints. However, man-made radioactive substances became available and promethium-luminous paints were developed in Japan in 1960. Because promethium-based paints have a bright after-glow and a lower unit price, and are very safe, the use of radium luminous paints in Japan was completely eliminated. During this same period, radium was replaced by tritium as the radioisotope of choice for radioluminous paints in other countries.

Table 2 Luminous Brightness and Radioactivity (phosphor; ZnS:Cu)

Radionuclide brightness[a] (mcd m–^{2})	^{3}H (GBq g^{-1})[b]	^{147}Pm (GBq g^{-1})	^{226}Ra (MBq g^{-1})
240	—	1.26	—
200	31.5	1.04	5.90
160	23.1	0.85	3.70
120	14.8	0.63	2.20
100	12.0	0.52	1.60
80	9.3	0.44	1.10
60	6.5	0.31	0.74
40	4.4	0.22	0.55
20	2.2	0.11	0.26
10	1.1	0.06	0.13

[a] Brightness = brightness of powder (JISK 5671).

[b] (Becquerel) = unit of activity of radionuclides; Bq = the number of nuclear disintegration per unit time (second).

12.2.1 *Radioluminous paints*

12.2.1.1 *Types and composition of radioluminous paints*

Radioluminous paints are categorized by the types of radionuclides employed in the paints. The main radionuclides for radioluminous paints are tritium (^{3}H), carbon-14 (^{14}C), promethium-147 (^{147}Pm), and radium-226 (^{226}Ra). Here, promethium and radium luminous paints are abbreviated as Pm and Ra luminous paint, respectively.

Radioluminous paints consist of radioluminous pigments and a varnish. The radioluminous pigments are produced by adding radioisotopes to a phosphor. Normally, zinc sulfide-type phosphors are used because of their high sensitivity to radiation. Specifically, ZnS:Cu is most widely used because of its highly visible yellow-green emission and bright after-glow. The concentration of the Cu dopant, added as the activator, influences the color of the products. When Cu is 10^{-2} wt%, the body color is pale yellow; and when Cu is reduced to between 10^{-3} and 10^{-4} wt%, it becomes white in color.[2] Both are used in radioluminous paints. Processes to produce luminous pigments are distinct for radioisotopes such as ^{3}H, ^{147}Pm, ^{14}C, and ^{226}Ra. In the case of ^{3}H, ^{3}H compounds are added to an organic polymer and stabilized, and then coated onto the surface of phosphor particles. For the others, ^{147}Pm, ^{14}C, and ^{226}Ra are chemically converted into oxide, insoluble carbonate, and sulfate, respectively. These are then fixed onto the phosphor surface using organic polymers such as a silicone resin.

On the other hand, varnishes are composed of synthetic resins and organic solvents. Any type of synthetic resin can be used as a varnish, provided it is transparent and highly resistant to radiation. Predominantly, acrylic-type resins are used. In addition, recent varnishes that are solventless and hardened by ultraviolet light are commonly used for radioluminous paints. Thus, radiation safety has improved remarkably.[3]

12.2.1.2 *Brightness of radioluminous paints*

The brightness of a radioluminous paint depends on the kinds and amount of radioisotopes included in the paint. As shown in Table 2, the brightness increases with increasing radioactivity. However, there is a large difference among radionuclides, which is caused by the specific radiation energy.

The brightness of a standard-thickness (50 mg cm^{-2}) layer of paint is less than that of the luminous pigments, that is, the luminance values of painted surfaces are approximately

Table 3 Brightness and Radioactivity of Tritium Luminous Paint

	Brightness		Radioactivity	
Grade (ISO)	Powder (mcd m^{-2})	Painted surface (ncd mm^{-2})	Powder (GBq g^{-1})	Painted surface (MBq mm^{-2})
8	135	31.5	17.2	8.6
7	90	20.0	10.5	5.3
6	58	12.5	6.7	3.3
5	35	8.0	4.1	2.0
4	25	5.0	2.8	1.4
3	15	3.2	1.7	0.8
2	10	2.0	1.0	0.5
1	6	1.3	0.6	0.3

Note: Painted thickness = 50 mg cm^{-2}.

Table 4 Brightness and Radioactivity of Pm Luminous Paint

	Brightness		Radioactivity	
Grade (JIS)	Powder (mcd m^{-2})	Painted surface (ncd mm^{-2})	Powder (MBq g^{-1})	Painted surface (kBq mm^{-2})
1	220	75	1110	550
2	150	50	740	370
3	90	30	440	220
4	60	20	300	150
5	30	10	150	75
6	15	5	75	40
	7.5	2.5	40	20

Note: Painted thickness = 50 mg cm^{-2}.

Table 5 Brightness of Painted Surface and Radioactivity

Brightness of painted surface (ncd mm^{-2})	Radioactivity (kBq mm^{-2})			
	^{3}H	^{14}C	^{147}Pm	^{226}Ra
30	8140	1480	220	1.10
15	3900	740	110	0.37
5	1300	370	37	0.11

Note: Painted thickness = 50 mg cm^{-2}.

25% of those of tritium and Ra pigments, and about 33% of the Pm luminous pigments. The relationship between the luminance and radioactivity is shown in Tables 3 through 5. Table 6 shows how the luminance of a layer of paint is affected by the color of the substrata.

12.2.1.3 Emission colors of radioluminous paints

Emission colors of radioluminous paints vary from blue to red-orange, depending on the kinds of phosphors used as luminous pigments. However, phosphors whose emission spectra are similar to the spectral response curve of the human eye, especially the dark-adapted human eye, are considered to be most effective. For this reason, green luminescence

Table 6 Reduction of Brightness (for painted surface among various substrata color)

Color	Reduction (%)
White	0
Silver	10–15
Yellow	20–25
Gold	25–30
Green	30–35
Red	35–40
Black	40–50

Note: Painted thickness = 50 mg cm^{-2}.

Table 7 Half-life (luminous brightness of painted surface)

Type	Half-life of brightness (year)	
	Low brightness (~5 ncd mm^{-2})	High brightness (20–30 ncd mm^{-2})
^{3}H	5–7	3–5
^{147}Pm	2.5	2.5
^{226}Ra	5–10	0.5–1

color, which is closest to the maximum sensitivity of the dark-adapted human eye still is commonly used.

12.2.1.4 *Lifetime of radioluminous paints*

The lifetime of a radioluminous paint is influenced by the type of paint, grade, kind of varnish, application of the paint, etc., and therefore is not always equivalent to the physical half-life of radioisotope in the radioluminous paint. Table 7 shows the half-life of luminance for luminous paints used in watches or indoor applications.

Discoloration is a serious problem for the longevity of luminescence in radioluminous paints because it causes a decrease in brightness, and consequently deterioration of the luminescence lifetime. There are two causes of discoloration.

One cause is poor radiation resistance of the constituent resins in the radioluminous paints. If resistance is poor, the radioactivity causes decomposition and the resin's color changes to yellowish-brown, resulting in a gradual darkening of the paint with age.

The other cause of discoloration is the use of radioluminous paints in outdoor applications. In the outdoors, the ZnS:Cu phosphors at the painted surface are exposed to ultraviolet light from sunlight and undergo photochemical decomposition. This process results in discoloration and darkening, or so-called blackening, of the painted surface with increased exposure.

12.2.1.5 *Radiation safety*

Whenever handling radioluminous paints, safety must be thoroughly considered because the paints contain radioisotopes. The degree of concern for radiation depends on the kind of radionuclides and radioactivity being used. However, it is primarily affected by the circumstances of the application of the radioluminous paint. The ideal condition is sealed containment of the radioisotope. The external exposure dose at a distance of 1 m from a 10-cm^2 area, with a luminance of 20 mcd m^{-2}, is 120 and 70 nSv h^{-1} for Ra and Pm, respectively, but almost zero for tritium luminous paints. However, tritium luminous paint

Table 8 Luminous Phosphors for Phosphorescent Paints

Composition	Luminescence color	Luminescence wavelength at peak (nm)	After-glow brightness (after 10 min) (mcd m^{-2})	After-glow persistence time (min)	
CaSrS:Bi^{3+} (Sr, 10–20%)	Blue	450	5	Semi-long	(about 90)
$CaAl_2O_4$:Eu^{2+},Nd^{3+}	Blue	440	35	Long	(over 1000)
ZnS:Cu	Yellow-green	530	45	Semi-long	(about 200)
ZnS:Cu,Co	Yellow-green	530	40	Long	(over 500)
$SrAl_2O_4$:Eu^{2+}	Green	520	30	Long	(over 2000)
$SrAl_2O_4$:Eu^{2+},Dy^{3+}	Green	520	400	Long	(over 2000)
CaS:Eu^{2+},Tm^{3+}	Red	650	1.2	Short	(about 45)
$Sr_4Al_{14}O_{25}$:Eu^{2+}, Dy^{3+}	Blue-green	490	400	Long	(over 2000)
$Sr_2MgSi_2O_7$:Eu^{2+}, Dy^{3+}	Blue	470	100	Long	(over 1000)
Y_2O_2S:Eu,Mg,Ti	Red	625	50	Long	(over 300)

Note: Light source: D_{65}, 1000 lx, 5 min.

decomposes and releases about 0.1 kBq MBq^{-1} day^{-1} of ^3H from the painted surface,[4,5] and users are subject to internal exposure from intake through respiration and dermal absorption. In spite of this, if luminous paints are used properly in common applications, there is virtually no possibility of users being exposed to hazardous radiation.

Sv (Sievert): Special unit of effective dose. *Effective dose* is the term currently used for the evaluation of the radiation exposure dose to humans. The effective dose is derived from the absorbed dose by weighting the quality factor of radiation and other modifying factors. The basic unit of the effective dose is Jkg^{-1}. The absorbed dose is the energy absorbed per unit mass of irradiated body. The dose limit for the public, as recommended by the ICRP, is 1 mSv per year.

12.2.2 Phosphorescent paints

12.2.2.1 Long phosphorescent phosphors

The presently known long phosphorescent phosphors are listed in Table 8. In this table, the luminance values of the phosphors with thickness of more than 200 mg cm^{-2}, measured 10 minutes after a 5-minute exposure to a 1000-lx (D_{65}) light source,[6] whose color temperature is 6500K, are shown. Persistent time refers to the time (minutes) that it takes for the after-glow to decrease to a luminance of 0.3 mcd m^{-2}, the lower limit of light perception of the human eye.

CaSrS:Bi^{3+} is produced by adding Bi^{3+} to a mixture of $CaCO_3$, $SrCO_3$, and S, and then heating to 1100°C in normal atmosphere for 1.5 hours. However, it is rarely used as a phosphorescent paint except in special applications, because this material readily decomposes when exposed to moisture.

The most widely used phosphors for phosphorescent paints are those that are most readily perceived by the human eye, such as ZnS:Cu, $SrAl_2O_4$:Eu^{2+}, and $SrAl_2O_4$:Eu^{2+},Dy^{3+}. After-glow characteristics of these three kinds of phosphors observed after a 4-minute exposure to a 200-lx (D_{65}) light source are shown in Figure 4.

ZnS:Cu, which has been in use for nearly 100 years, is produced by adding Cu, 10^{-2} wt% of the weight as the activator to ZnS, mixing with flux (NaCl, KCI, or NH_4Cl, etc.), and then heating to 1250°C for 2 hours in a normal atmosphere. If, in addition to Cu, several ppm of Co are added to ZnS, the after-glow persistence can be nearly doubled, but its initial brightness is decreased.

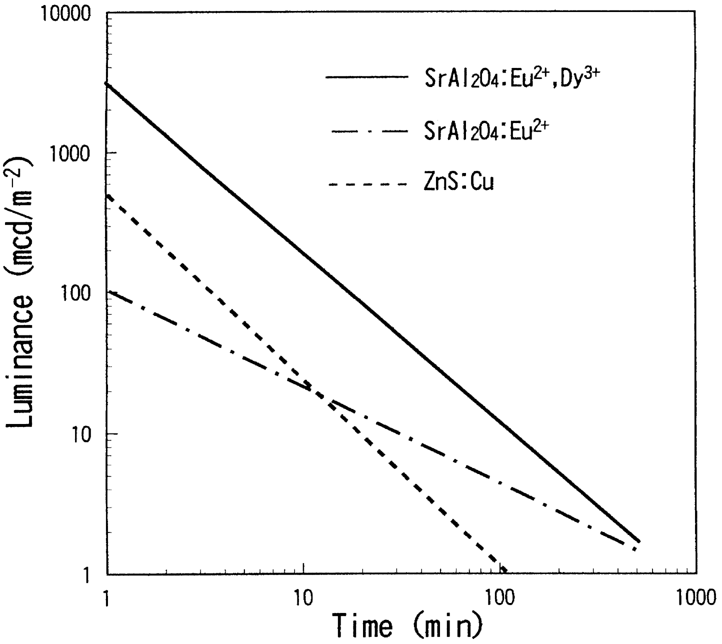

Figure 4 Afterglow characteristics of some phosphors[7] Excitation: D_{65} light, 200 Ix, 4 min Temp.: 22±1°C.

$SrAl_2O_4$:Eu^{2+},Dy^{3+} is a new phosphor invented by Nemoto & Co., Ltd. in 1993.[7,8] It is produced by mixing Al_2O_3 and $SrCO_3$, adding Eu^{2+} and Dy^{3+} as the activator and co-activator, respectively, and then heating in a reducing-atmosphere electric oven to 1300°C for 3 hours. $SrAl_2O_4$:Eu^{2+} emits a broad band green luminescence peaking at 520 nm due to the 4*f*-5*d* transition of Eu^{2+}, and has long after-glow persistence, as shown in Figure 4 and Table 8. Adding Dy^{3+} as the auxiliary activator dramatically increases the initial brightness, as shown in Figure 4.[7,8]

The invention of $SrA_{l2}O_4$:Eu^{2+}, Dy^{3+} phosphor has stimulated further research and development of new compositions of phosphorescent phosphors. In consequence, several practical phosphors, such as $Sr_4Al_{14}O_{25}$:Eu^{2+}, Dy^{3+}[9], $Sr_2MgSi_2O_7$:Eu^{2+},Dy^{3+} [10] and Y_2O_2S:Eu,Mg,Ti [11], have been newly developed, shown in Table 8.

12.2.2.2 Properties of phosphorescent paints

Phosphorescent paints are produced by mixing a phosphor (particle size is approximately 10–30 μm) with a transparent synthetic resinous varnish, which is easily penetrated by ultraviolet light, with a ratio of 50–100 wt%.

The excitation spectra for ZnS:Cu phosphor and $SrAl_2O_4$:Eu^{2+},Dy^{3+} phosphor both peak at 365 nm, so, as the intensity of 300- 400-nm light is raised, the after-glow brightness increases. Comparing the persistence brightness after the exposure to a white fluorescent lamp with that after the exposure under a tungsten lamp of equal intensity, it is observed that the persistence brightness of the latter is 40% lower because there is not much ultraviolet in the tungsten lamp light. Figure 4 shows the persistence decay curves for three kinds of phosphorescent paints at the saturation thickness, which refers to the maximum effective thickness. The saturation thickness for the ZnS:Cu phosphor is about 0.3 mm (75 mg cm^{-2}), while it is approximately 1 mm (150 mg cm^{-2}) for the $SrAl_2O_4$:Eu^{2+},Dy^{3+} phosphor.

The relationship between the after-glow luminance and the brightness of light source for $SrAl_2O_4$:Eu^{2+},Dy^{3+} and ZnS:Cu is shown in Figure 5. The relationships between the

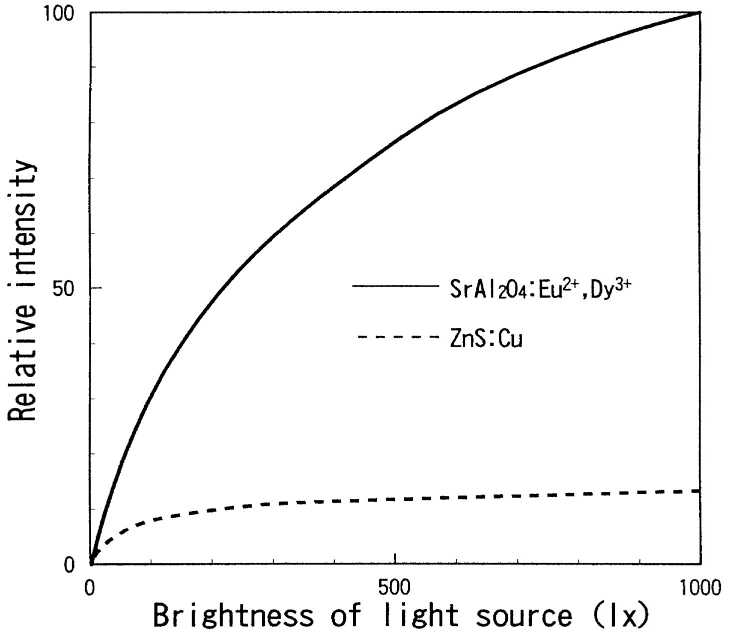

Figure 5 Relationship between afterglow intensity after 20 min and brightness of light source[7] Excitation: D_{65} light, 0~1000 Ix, 4 min Temp.: 22±1°C.

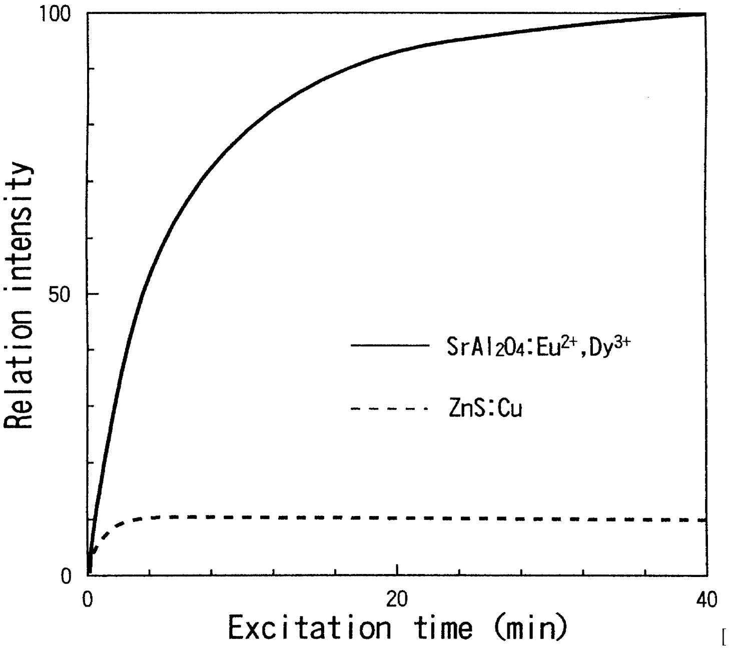

Figure 6 Relationship between afterglow intensity after 20 min and excitation time[7] Excitation: D_{65} light, 200 Ix, 0~40 min Temp.: 22±1°C.

after-glow luminance and the excitation time are shown in Figure 6. As shown in these figures, the after-glow characteristics of the new phosphor, $SrAl_2O_4$:Eu^{2+},Dy^{3+} are remarkably superior to the currently used ZnS:Cu. Also from a viewpoint of thermoluminescent characteristics, it can be proved that $SrAl_2O_4$:Eu^{2+},Dy^{3+} has much longer after-glow persistence than ZnS:Cu, because the peaks of the glow curve for these phosphors are about 50°C for ZnS:Cu and about 80°C for $SrAl_2O_4:Eu^{2+},Dy^{3+}$ was investigated and elucidated.[7] It was revealed that after excitation, holes are liberated from excited Eu^{2+} ions to the valence band, and that Dy^{3+} ions act as hole traps with a depth of 0.65 eV, which is very suitable in relation to the thermal release rate for holes at room temperature. Thus, the very bright and long phosphorescence is produced at room temperature.

When the phosphorescent paints produced from $SrAl_2O_4:Eu^{2+},Dy^{3+}$ are used in the manufacturing of luminous watches/clocks, even after 10 hours in absolute darkness, there is still sufficient after-glow brightness to read the watches. The reason is that it takes 2000 minutes for the brightness to decrease to the lower limit of light perception of the human eye (0.3 mcd m^{-2}). For these reasons, these phosphorescent paints can substitute for the previously mentioned radioluminous paints. This fact is a notable advancement because, through the use of $SrAl_2O_4:Eu^{2+},Dy^{3+}$, luminous watches/clocks do not require the use of radioactive materials.

Further, the $SrAl_2O_4:Eu^{2+},Dy^{3+}$ phosphor in these phosphorescent paints is very durable and does not deteriorate under strong ultraviolet light, so that its stability is far superior to paints containing ZnS:Cu. Therefore, these phosphorescent paints can be used in outdoor applications. It should be emphasized that the new phosphor $SrAl_2O_4:Eu^{2+},Dy^{3+}$ can be used in a broad range of phosphorescent paint applications for which ZnS:Cu could not be used.

References

1. Rump, H., *Die Leuchtmasse und ihre Verwendungen*, Berlin, 1937.
2. Nemoto & Co., Ltd., Japanese Patent, Radioluminescent Material, 751505, 1974.
3. Murayama, Y., *Technical Digest of Annual Meeting on Radioisotope in Physical Sciences and Industries*, 15th ed., Japan Isotope Association, 1978, 142.
4. Ikeda, M., *Tokyo Metropolitan Isotope Centre Annual Report*, 1965, 91.
5. Shell, W., *J. Appl. Radiat. Isot.*, 22, 653, 1971.
6. *Japanese Industrial Standard, JIS Z 8720*, Standard Illuminants and Source for Colorimetry.
7. Matsuzawa, T., Aoki, Y., Takeuchi, N., and Murayama, Y., *J. Electrochem. Soc.*, 143, 2670, 1996.
8. Nemoto & Co., Ltd., European Patent, Phosphorescent Phosphor, 0622440B1, 1996.
9. Tamaoki, H., Murasaki, Y., Ichinomiya, K., *1996 Annual Conf. IEI Jpn.*, No. 17 (in Japanese).
10. Kasei Optonix, Ltd., Japanese Patent Disclosure (kokai) H9-194833 (1997).
11. Murasaki, Y., Arai., K., Ichinomiya, K., *1998 Annual Conf. IEI Jpn.*, No. 11 (in Japanese).

chapter twelve — section three

Other phosphors

Xiaojun Wang and Dongdong Jia

Contents

12.3 Long persistent phosphors 793
  12.3.1 History of long persistent phosphors....794
  12.3.2 Electron and hole traps....795
    12.3.2.1 Defect and defect-related trapping centers....796
    12.3.2.2 Co-doped trapping centers....796
  12.3.3 Trapping and detrapping mechanisms....796
    12.3.3.1 Trapping mechanism....797
    12.3.3.2 Detrapping mechanism....800
  12.3.4 General methods to design long persistent phosphors....801
    12.3.4.1 Co-doping....801
    12.3.4.2 Persistent energy transfer....802
    12.3.4.3 Multiple center-doped materials....804
  12.3.5 Experimental techniques....804
    12.3.5.1 Excitation spectra of long persistent phosphors....804
    12.3.5.2 Thermoluminescence....805
    12.3.5.3 Photoconductivity....807
    12.3.5.4 Thermal conductivity....808
  12.3.6 Summary of long persistent phosphors....810
    12.3.6.1 Emission centers and their co-dopants....810
    12.3.6.2 Host materials....810
    12.3.6.3 The interests of color....814
References....814

12.3 Long persistent phosphors

Introduction

Long persistent phosphors are phosphors that have very long afterglow emission or phosphorescence. Afterglow is caused by trapped electrons produced by an excitation source. Long persistent phosphors are also called long lasting, long duration, long lived, or long afterglow phosphors.

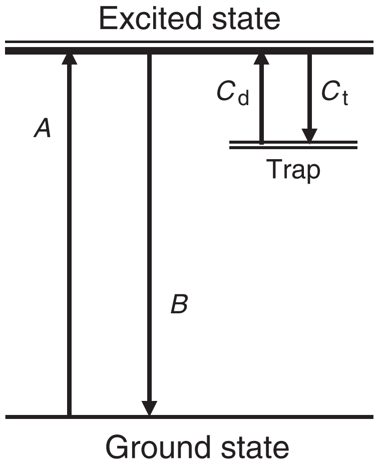

Figure 7 Three-level model showing the mechanism of long persistent materials. C_t and C_d are the trapping and detrapping rates, respectively, and A and B are the excitation and emission rates respectively.

The mechanism for long persistent phosphorescence can be explained in terms of a simplified three-level diagram including a ground state, an excited state, and a metastable trapping state for the active electron (Figure 7). Phosphorescence lifetimes are usually longer than the lifetime of the excited state and depend on the trap depth and trapping–detrapping mechanism. Fluorescence, on the other hand, is based on a two-level electron transition mechanism, which includes a ground state and an excited state only. The decay time of fluorescence depends on the transition strength between the two states.

Phosphorescence can be classified by its lifetime. Very short persistent phosphorescence has a lifetime of the same order of magnitude as the lifetime of the excited state. Normally, it is no longer than a few milliseconds and it is due to shallow traps. Short persistent phosphorescence lasts for seconds and it generally becomes noticeable to the human eye. Most common phosphors may show some short persistence especially after they have been exposed to UV, electron beam, plasma beam, X-rays, or to γ-rays. Persistent phosphorescence and long persistent phosphorescence have lifetimes in minutes or hours, respectively.

This review section concerns phosphors that have long or super long persistent phosphorescence. For practical visual applications, the persistence time is defined as the time for the afterglow emission intensity to decay to 0.032 mcd/m^2; this is approximately 100 times the limit of human perception with dark-adapted eyes.

12.3.1 History of long persistent phosphors

Long persistent phosphors discussed here are different from the radiation-stimulated phosphors that rely on nuclear decay as an excitation source. The first reported instances of light emission from materials entailed persistent phosphorescence similar to those discussed here, notably the so-called Bologna stone (BaS), and appeared in 1609.[1]

More recent research on long persistent phosphors dates to early years of the last century. ZnS-type phosphors, such as $ZnS{:}Cu^+$, were found to have persistent times as long as 40 min.[2] The mechanism for the phosphorescence was associated with electrons. The effects of co-doping were also investigated, for example, co-doping ZnS:Cu^+ with Co^{2+} doubled the persistence time of the Zn compound.[3] Many ZnS-based persistent phosphors have been developed which have found uses as night vision materials.[4,5] A number of mixed crystals such as $Cd(Zn_{1-x}Cd_xS)$ also exhibit long persistence but Cd-containing compounds are no longer in use because of environmental considerations.[6]

The next generation of long persistent phosphor compromised the alkali-earth sulfides, such as CaS and SrS. These phosphors are known as Lenard's phosphors.[7] They were rediscovered by Lehmann in the early 1970s.[8] Lehmann et al. activated these sulfides with various dopants such as Bi^{3+}, Eu^{2+}, and Ce^{3+}.[9–11] The main advantage of these phosphors is that they can be excited by sunlight. Their major disadvantage, however, is that they were chemically unstable and H_2S is released when they are exposed to moisture. During World War II, military applications shifted the focus to photostimulated phosphors with fast decays and research on phosphorescence materials largely ceased.[12]

In 1996, Matsuzawa et al. reported a new type of long persistent phosphor, $SrAl_2O_4$:Eu^{2+},Dy^{3+}, with a strong emission centered at 520 nm (green);[13] this phosphor is based on materials synthesized earlier by Abbruscato in 1971.[14] The persistence time of $SrAl_2O_4$:Eu^{2+},Dy^{3+} was found to be longer than 16 h with the introduction of a co-dopant, Dy^{3+}. A short time later, a similar long persistent phosphor, $CaAl_2O_4$:Eu^{2+},Nd^{3+}, was reported emitting at 450 nm.[15] These two phosphors drew considerable attention because of their ability to persist overnight, opening prospects of various applications.[16–19]

Recent long persistent phosphor research is concentrated in two directions. The first is in the identification of the trapping–detrapping mechanism leading to the long persistence.[20,21] Research on alkali-earth aluminates doped with Ce^{3+}, for example, have led to the conclusion that trapping–detrapping mechanisms are closely related to electron delocalization and localization processes.[22,23] Systematic study of the thermoluminescence (TL),[22] photoconductivity (PC),[23] and thermal conductivity (TC)[24] of these phosphors indicates that electron delocalization is closely associated with the overlap of impurity and host band energy levels.[25]

The second direction is in the development of new long persistent phosphors providing coverage through the visible spectrum; long persistent phosphors in the red are of particular interest. Many new long persistent phosphors have been found in past 10 years such as alkali-earth aluminates doped with Ce^{3+}, Mn^{2+}, and Tb^{3+};[24,26,27] alkali-earth silicates doped with Mn^{2+}, or Eu^{2+}/Dy^{3+};[27–29] alkali-earth oxide doped with Eu^{3+};[30] rare-earth oxides and oxysulfides doped with Er^{3+}, Eu^{3+}, Ti^{4+} and Mg^{2+};[31–34] and other systems such as Zn phosphate doped with Mn^{2+}.[35,36]

Although many new phosphors have been developed since 1996, only a few can be excited under natural light. The issue of a convenient excitation source is very important and actually limits the applications of long persistent phosphors.

Novel new methods in synthesis have been developed to produce persistent materials. These methods include preferential co-doping with ions to create electron or hole traps, co-doping ions to create defect-related electron traps, and introducing sensitizers for persistent energy transfer.

12.3.2 Electron and hole traps

It has been generally accepted that long persistent phosphorescence results from intrinsic traps or intentionally introduced traps or from both. Generally, traps can be divided into two groups, electron traps that capture electrons below the conduction band and hole traps that capture holes above the valence band.

12.3.2.1 *Defect and defect-related trapping centers*

Some traps appear as defects in the host material, F^- centers and V^+ centers in crystals are typical of this type of defect.[37,38] These centers are usually generated by charge compensation requirements to maintain neutrality in the host. For example, in CaS:Bi^{3+}, Bi^{3+} ions will occupy Ca^{2+} ion sites, and due to the necessity of charge compensation, two Bi^{3+} ions will replace three Ca^{2+} ions (Bi_2S_3–3CaS), resulting in a Ca^{2+} vacancy (V^{2+} center). The net negative environment at this site is capable of trapping a hole. If instead two Bi^{3+} ions simply replace two Ca^{2+} ions (Bi_2S_3–2CaS), then an interstitial S^- is needed to maintain neutrality. In this case, the resulting net positive charge environment will be able to trap electrons. Adding Na^+ ion as a co-dopant to Bi^{3+} can significantly reduce the number of defect centers. When a Na^+ ion and a Bi^{3+} ion replace two Ca^{2+} ions ($NaBiS_2$–2CaS), the likelihood of charge-related defect centers is reduced so that the persistence time is reduced significantly as shown in Figure 8.[39]

Another example of defect-trapping centers occurs in CaS:Eu^{2+}. Stoichiometrically grown CaS:Eu^{2+} (grown without fluxes such as NH_4Cl) does not evince any persistent afterglow. Eu^{2+} afterglow occurs only when ions such as Cl^- or Y^{3+} are present in CaS, as shown in Figure 9. The Eu^{2+} persistence is due to traps at defect centers when Cl^- ions replace S^{2-} ions or Y^{3+} ions replace Ca^{2+} ions.[39,40]

Traps may be created intrinsically or by introduction of specific dopants. Defect-related traps are easy to be produced in host materials that have complicated crystal structures. Ionic size differences can also produce traps by creating dislocation and other strain-related defects.

12.3.2.2 *Co-doped trapping centers*

With optical excitation, the dynamics of the excited ion can be such as to create metastable states which properly belong to dopant ions in modified valence states, for example, Tm^{2+} in CaS:Eu^{2+},Tm^{3+} and Dy^{4+} in $SrAl_2O_4$:Eu^{2+},Dy^{3+}. These metastable states can also act as traps since their electronic structure differs from that of the normal dopant ions.[13,41]

These processes are illustrated in Figure 10 and Figure 11. Because the excited electrons (or holes) do not modify the bonding situation of the dopants, they are labeled as Tm^{2+*} (or Dy^{4+*}), where $Tm^{2+*} = Tm^{3+} + e^-$ and $Dy^{4+*} = Dy^{3+} + h^+$ in the figures. The electron or hole created in such a way is loosely bound and can be easily detached thermally.

Even though the exact nature of the metastable ionic states of the co-dopants is not well understood, these states are not simply altered ionic states but are considered more complex entities. For example, to reduce Tb^{4+} to Tb^{3+} during the preparation of $CaAl_2O_4$:Tb^{3+}, the sample must be sintered at 1350°C for 2 h in a reducing environment.[22] Thermal activation of trapped electrons in the case cited above generally occurs in a temperature range from 50 to 300°C.[42–45]

The formation of an electron or a hole trap by a defect depends on the energy level position of these ions within the host band gap.[46] These positions may be determined experimentally.[15] As the nature of the traps of co-dopants is not clearly understood, it is difficult to determine the exact nature of the traps.[13,46]

12.3.3 *Trapping and detrapping mechanisms*

Trapping and detrapping of electrons or holes are understood to be the principal mechanisms responsible for long persistent phosphorescence, which have been discussed by many researchers.[47–54] For electrons, trapping can take place through electron tunneling

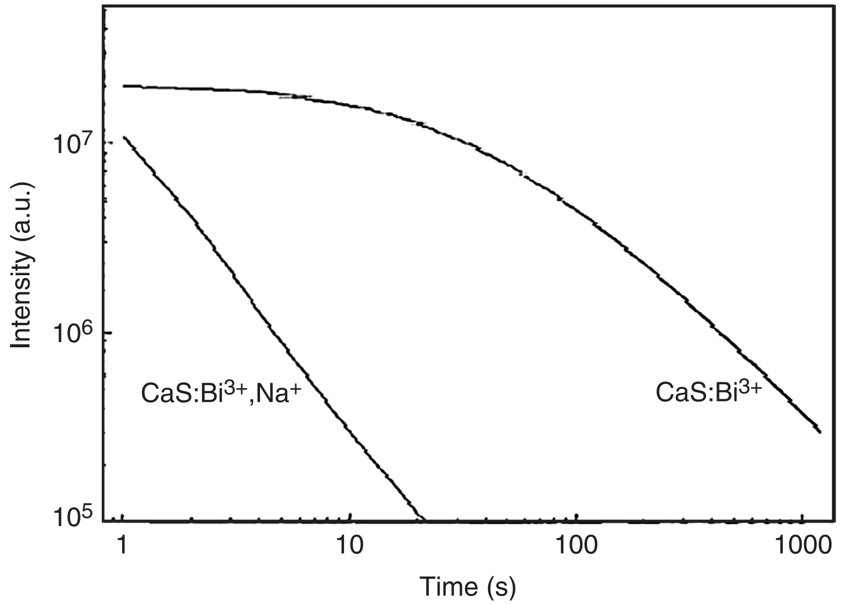

Figure 8 Afterglow decay curves of CaS:Bi^{3+} and CaS:Bi^{3+},Na$^+$ samples. (Jia, D., Zhu, J., and Wu, B., *J. Electrochem. Soc.*, 147, 386, 2000. With permission.)

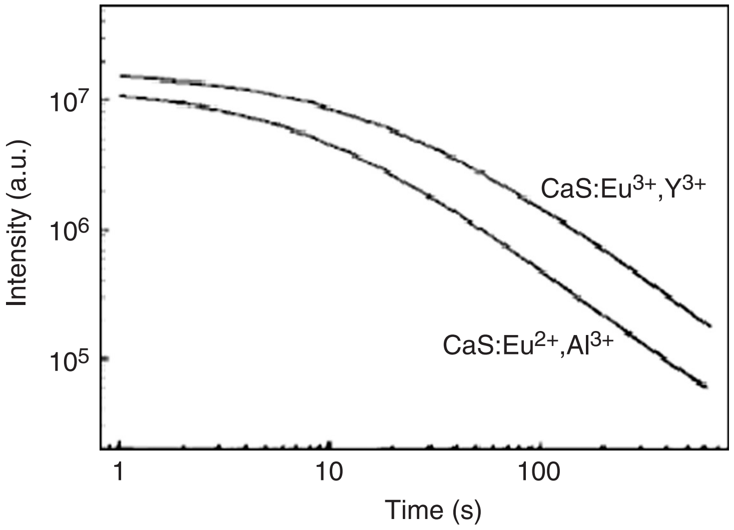

Figure 9 Afterglow decay curves of CaS:Eu^{2+},Y^{3+} and CaS:Eu^{2+},Al^{3+} samples. (Jia, D., Zhu, J., and Wu, B., *J. Electrochem. Soc.*, 147, 386, 2000. With permission.)

or through promotion to the conduction band. Recent work appears to support an electron-trapping model though a hole model has not been totally eliminated.[24,26]

12.3.3.1 *Trapping mechanism*

Electron trapping mechanisms are usually associated with electron excitation and delocalization. Following photoexcitation of an electron from the ground state to an excited state, the electron is delivered to a trap by some mechanism associated with electron delocalization.

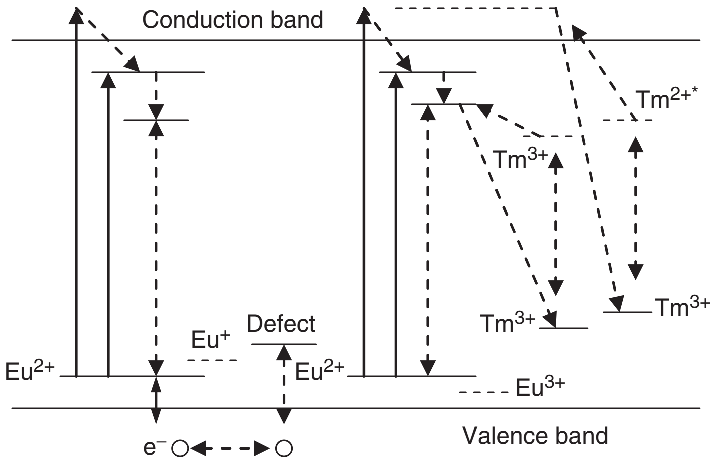

Figure 10 A schematic diagram of trapping processes in CaS:Eu^{2+},Tm^{3+}. (Jia, D., et al., *J. Appl. Phys.*, 88, 3402, 2000. With permission.)

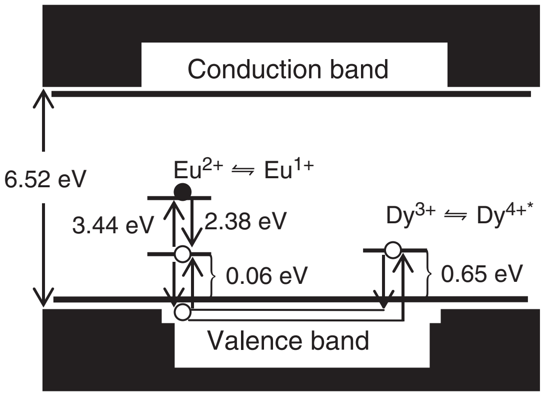

Figure 11 Energy level diagram for the $SrAl_2O_4$:Eu^{2+},Dy^{3+} phosphor. (From Matsuzawa, T., Aoki, Y., Takeuchi, N., and Murayama, Y., *J. Electrochem. Soc.*, 143, 2670, 1996. With permission.)

Under normal circumstances, in both the ground and excited states, electrons are localized around their parent ion. If sufficient photoenergy is provided to allow the electron to reach the conduction band of the host, it becomes mobile and delocalization of an electron can occur. This process is called photoionization and is illustrated for $SrAl_2O_4$:Ce^{3+} in Figure 12 and Figure 13.[25]

Phonon-assisted delocalization can also occur when the excited state to which an electron is promoted lies just below the host conduction band. At finite temperatures, electrons can be thermally excited to the conduction band where delocalization can occur. This mechanism is called thermal ionization and is much weaker than photoionization. Two-photon ionization process or excited state absorption (ESA)[55] is also observed at times. This process will not be strong enough to trap a large number of electrons to produce persistence.

It has been recently reported that the delocalization rate is in the same order of magnitude as the electron–phonon relaxation rate (of the order of 10^{13} s^{-1}) for a d electron in Ce^{3+}.[25] Delocalization of electrons generally happens in the p and d orbitals. Because of better shielding, delocalization from electrons on the f orbital does not generally occur even when the f orbital energies are larger than the d state energies. As a result of this,

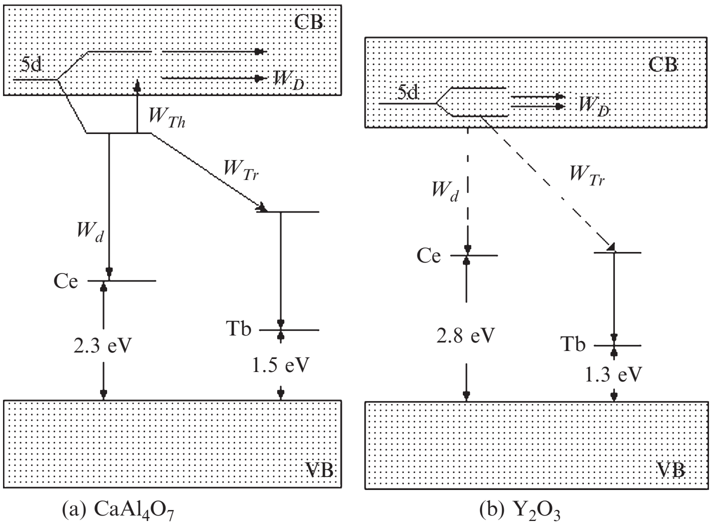

Figure 12 Energy diagram of (a) $CaAl_4O_7:Tb^{3+},Ce^{3+}$ and (b) $Y_2O_3:Tb^{3+},Ce^{3+}$. W_d is the decay rate of 355 nm 5*d* level of Ce^{3+}, W_{Tr} the energy transfer rate from Ce^{3+} to Tb^{3+}, W_{Th} the thermal ionization rate, and W_D the delocalization rate (solid lines: occurred; dashed lines: did not occur). (Jia, D., Wang, X.J., and Yen, W.M., *Phys. Rev. B*, 69, 235113, 2004. With permission.)

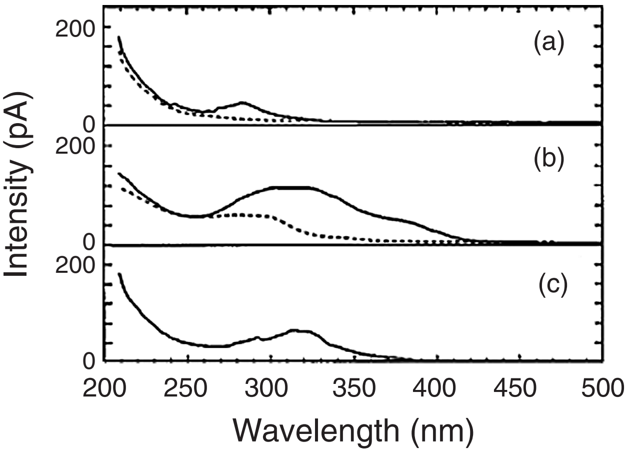

Figure 13 Photoconductivity spectra of the CaAl4O7 samples: (a) $CaAl_4O_7:Tb^{3+}$; (b) $CaAl_4O_7:Ce^{3+}$; (c) $CaAl_4O_7:Tb^{3+},Ce^{3+}$ (solid lines: 290 K; dashed lines: 140 K). (Jia, D., Wang, X.J., and Yen, W.M., *Phys. Rev. B*, 69, 235113, 2004. With permission.)

long persistence phosphorescence from rare-earth ions can be found only when the electrons are excited to the high lying 5d excited states. UV or VUV photons are needed for the ionization and delocalization. Long persistent phosphors that can be charged by natural light are rare as a consequence.

Although the delocalization of electrons is one of the major processes allowing trapping of carriers, there are other methods to produce this result. Electron tunneling[22,24,56] requires trap levels to be energetically close to the excited state. The tunneling traps are necessarily also physically close to the emission centers, and hence they are usually defects near the ions, or local traps.

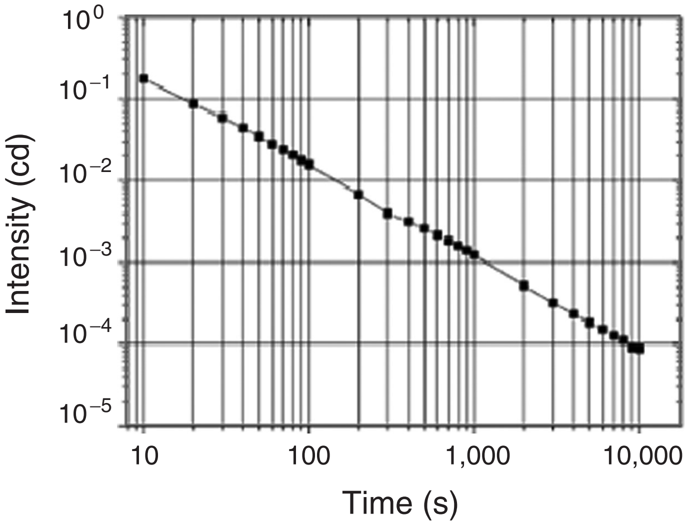

Figure 14 Long persistent phosphorescence decay curve of the 2 mol% Sm^{3+}-doped yttrium oxysulfide. (From Lei, B., et al., *Mater. Chem. Phys.*, 87, 227, 2004. With permission.)

12.3.3.2 Detrapping mechanism

The traps that give rise to persistence usually have depths ranging from a few tenths to several eVs. In the case of thermal activation, the detrapping rate A is associated with temperature and is given by

$$A = se^{-\Delta E/kT} \tag{1}$$

where s is the frequency factor for electron detrapping, ΔE the trap depth, and T the temperature.[57] Trap depths are measured from the bottom of the conduction band. The s factor is related to the electron–phonon interaction.[25] Excited electrons may at times return to the trap. This process is called retrapping.

Detrapping mechanisms become complicated if retrapping processes are included and taking this into account, higher order model of the processes has been developed.[58]

If the retrapping rate is very low or negligible, the decay of the afterglow intensity is exponential as shown in Figure 14 and the decay is given by

$$I = \sum_{i=1}^{n} I_i e^{-\Delta E_\mathrm{i}/kT} \tag{2}$$

where I is the intensity of the afterglow and i refers to the i^{th} trap with trap depth ΔE_i, and n to the number of different types of traps in the material.[59] This model is called the first order or monomolecular reaction mechanism.

If the retrapping rate is very high then a second-order mechanism applies. The decay of afterglow intensity is given by (Figure 15)

$$I = I_0/(1+\gamma t)^n \tag{3}$$

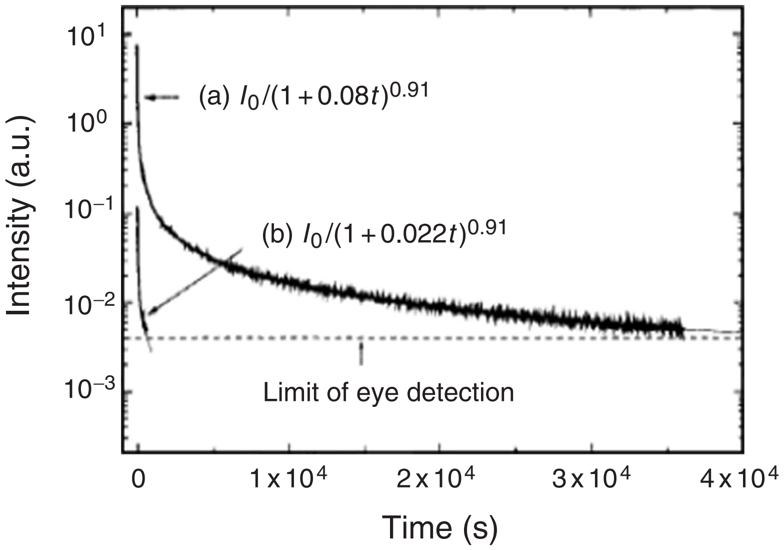

Figure 15 Afterglow decay curve at 413 nm after irradiation for 30 min (a) by unfiltered light from the Xe UV lamp. This curve is described by the formula $I(t) = I_0 / (1 + 0.08t)^{0.91}$ and (b) with filtered light (λ = 320 nm) from the Xe UV lamp. This curve is described by the formula $I(t) = I_0 / (1 + 0.22t)^{0.91}$. The horizontal dashed line shows the limit of eye detection in the dark. (Jia, D. and Yen, W.M., *J. Electrochem. Soc.*, 150, H61, 2003. With permission.)

where I_0 is the initial afterglow intensity and n is generally less than 2 and depends on the material. $\gamma = N/An_{t0}$, where N is the density of traps, n_{t0} the population of trapped electrons at $t = 0$, and A the detrapping rate as defined in Eq. 1. This model is also called the bimolecular reaction type.[59,60]

To study detrapping mechanisms, afterglow decay curves are usually measured. For systems that undergo first- or second-order mechanisms, the decay curves can be fitted using one of the equations given above. Usually, however, the system will fall between the two approximations, and so auxiliary measurements are required to characterize the system completely. TL measurements provide alternate and complementary results.

12.3.4 General methods to design long persistent phosphors

For the practical applications of long persistent phosphors, persistence time of their afterglow emission is always of most interest. Many methods have been used to increase the persistence time by producing more traps in the host and by increasing trapping efficiency.

In addition to the long persistence time, the emission color of the phosphor is also very important. The perceived color of the phosphor, for example, should remain stable throughout the decay time.

12.3.4.1 Co-doping

Co-doping ions into the host to serve as trapping centers or to produce defect-related trapping centers is one of the most commonly used methods to make long persistent phosphors. The persistent time can be substantially increased with the introduction of the proper co-dopants. Introduction of co-dopants with different valences produce defects because of charge compensation requirements. For example, Cl^- doped into CaS to replace

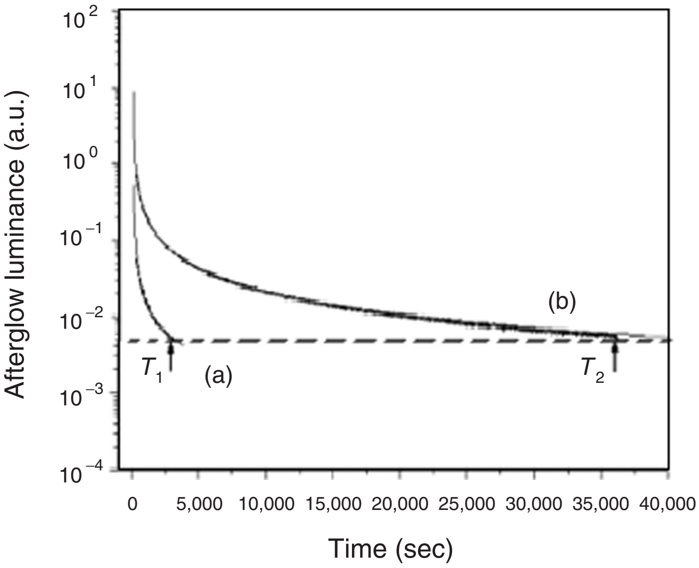

Figure 16 The afterglow decay curves monitored at 520 nm after the samples were irradiated with a mercury UV lamp for 10 min. (a) Undoped sample; (b) Ce^{3+}-doped sample. The horizontal dashed line indicates the limit of visual detection of the afterglow. T_1 and T_2 are the persistence times for undoped and Ce^{3+}-doped samples, respectively. (Jia, D. and Yen, W.M., *J. Lumin.*, 101, 115, 2003. With permission.)

S^{2-},Y^{3+} and Al^{3+} doped into CaS to replace Ca^{2+},[39,40] Mg^{2+} and Ti^{4+} doped into Y_2O_2S:Eu^{3+} to replace Y^{3+},[32] all produce additional defects which extend the persistence lifetimes.

Some ions themselves serve as trapping centers when they are co-doped into the host. These ions usually trap electrons or holes and produce different metastable ionic valence states, which can act as traps. Nd^{3+} in $CaAl_2O_4$:Eu^{2+},Nd^{3+} and Dy^{3+} in $SrAl_2O_4$:Eu^{2+},Dy^{3+},[15] are examples of this type of trap.

Ions co-doped into the host not only can create extra trapping centers but also enhance trapping efficiency. Ions that have stronger transition rates can pump electrons into the host conduction band more efficiently, resulting in larger trap populations. An example is Ce^{3+}-doped $MgAl_2O_4$ where electrons pumped into the traps through Ce^{3+} 4f–5d transitions populate 30 times more traps than those populated through host band gap absorptions (Figure 16).[61]

12.3.4.2 Persistent energy transfer

The majority of ions in the 4f and 3d series do not show persistence phosphorescence so that the color coverage of emissions presently available is limited and does not provide complete coverage of the spectrum. A method which exploits interionic interactions leading to optical energy transfer has been proposed to remedy this situation; this entails a process known as persistent energy transfer.

In persistent energy transfer, the emission center of a known long persistent phosphor is used as a donor, and the acceptor is chosen based on its color being pursued. The choice of the acceptor ion depends on the presence of absorptions at the donor emission frequency. The traps associated with the donors when charged will continuously transfer energy to support emission by the acceptors. The long persistence of the donor is converted into the long persistence of the acceptor at the required frequency. This novel method is effective in preparing long persistent phosphors particularly in the lower energetic regions of the visible spectrum. Examples for persistent energy transfer are $CaAl_2O_4$:Ce^{3+}, Tb^{3+}

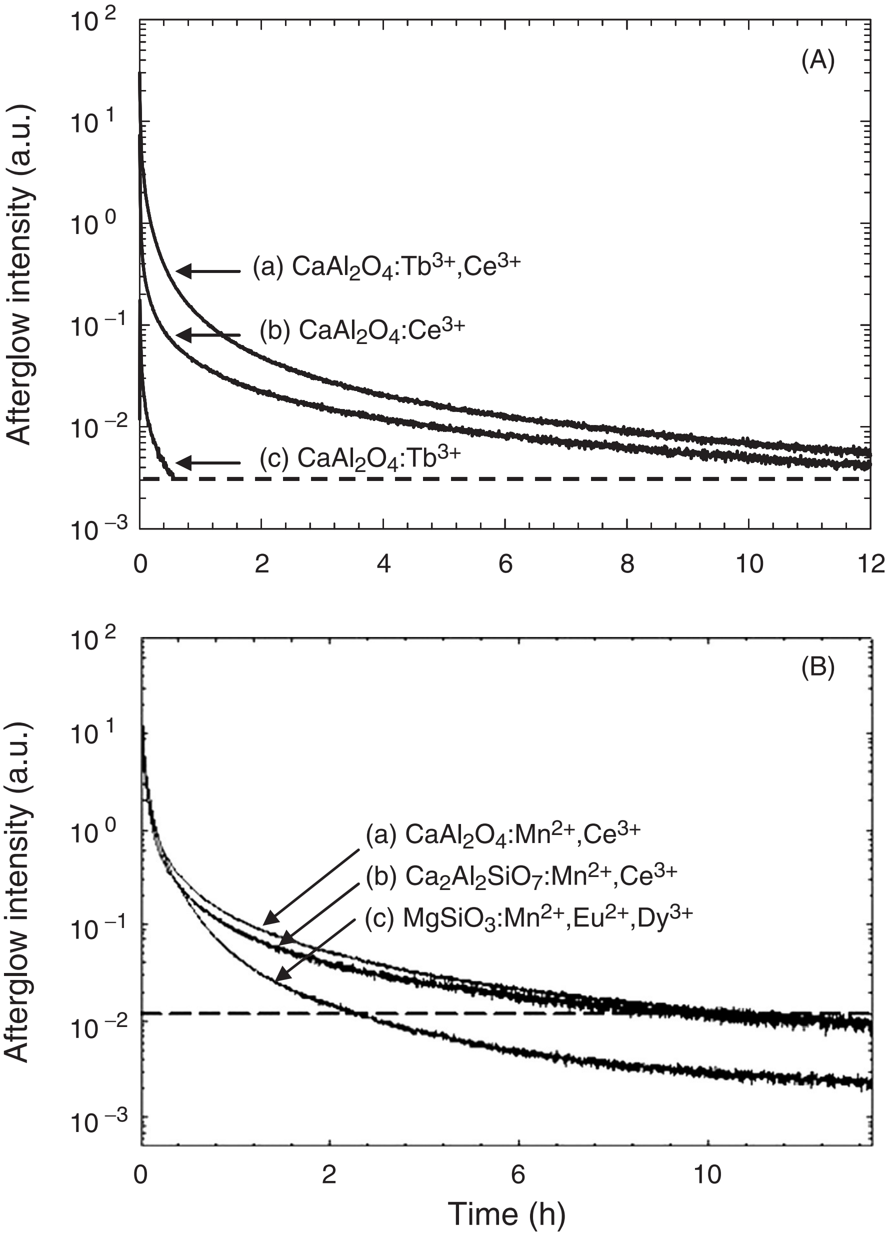

Figure 17 Afterglow decays due to persistent energy transfer for more than 10 h. (A): 1 at. % $CaAl_2O_4$ samples: (a) Tb^{3+} and Ce^{3+} co-doped sample, detected at 543 nm; (b) Ce^{3+} singly doped sample, detected at 400 nm; and (c) Tb^{3+} singly doped sample, detected at 543 nm (dashed line: limit of eye detection); (B): afterglow at different colors: (a) $CaAl_2O_4$:Mn^{2+},Ce^{3+} at 525 nm (green); (b) $Ca_2Al_2SiO_7$:Mn^{2+},Ce^{3+} at 550 nm (yellow), and (c) $MgSiO_3$:Mn^{2+},Eu^{2+},Dy^{3+} at 660 nm (red). (Jia, D., et al., *J. Appl. Phys.*, 93, 148, 2003; Wang, X.J., et al., *J. Lumin.*, 102/103, 34, 2003. With permission.)

and $CaAl_2O_4$:Ce^{3+},Mn^{2+}. The 10 h blue long persistent afterglow of Ce^{3+} ion has been successfully transferred to yield a 10 h green Tb^{3+} and yellow Mn^{2+} long afterglow emission (Figure 17).[27,62,63]

12.3.4.3 Multiple center-doped materials

Another way to obtain long persistent phosphors at different colors is to mix two types of long persistent phosphors similar to the so-called two- or three-band-type methods. Admixture of phosphors, however, can result in time-dependent emission color changes because of the difference of persistence times for each of the components. To overcome this difficulty, multiple emission centers can be doped into the same host in the hope that the decay times are equalized by the same detrapping mechanism. An example of a material produced by this method is Eu^{2+}- and Bi^{3+}-doped CaS. A purple color was obtained by mixing Eu^{2+} (red) and Bi^{3+} (blue) long persistent afterglow emissions. The afterglow coloration is very stable because they have the same afterglow decay mechanism.[64]

12.3.5 Experimental techniques

Techniques to study the persistence mechanism include TL, PC, TC, as well as standard spectroscopy techniques such as emission and excitation spectral measurements. Some of these methods have to be modified to address the long persistence character.

12.3.5.1 Excitation spectra of long persistent phosphors

Because phosphors, in many cases, are in powder and ceramic forms, absorption measurements are usually difficult to perform. Reflection or diffuse reflection spectra are usually not accurate enough to provide optical absorption directly. Measuring the excitation spectra of the emissions becomes the only reliable method to obtain energy structures of long persistent phosphors.

Excitation spectrum measurement for long persistent phosphors requires extra care because the trapping and detrapping processes are considerably longer than the excitation measurement time. When a large number of electrons are being trapped and detrapped during the excitation process, the excitation spectrum measured can be distorted and at times requires correction.

There were two ways to compensate for the trapping effect and to obtain the correct excitation spectra. One is to use a weak excitation source followed by deconvolution of the trapping effects. The other is to use a strong excitation source to saturate the trapping effect.

When excitation spectra are measured with a very weak excitation source then the number of trapped electrons, n, is much smaller than the total number of electrons in the ground state, N ($n << N$), therefore it can be neglected. In this case, the excitation intensity measured by the spectrometer is given by

$$I(\lambda) = A_0(\lambda) + \int_{\lambda_0}^{\lambda} A(\lambda_{\mathrm{x}}) D(\lambda_{\mathrm{x}})\, \mathrm{d}\lambda_{\mathrm{x}} \tag{4}$$

where $A_0(\lambda)$ is the true absorption, $D(\lambda)$ the decay function, and λ_0 the initial wavelength. Corrections can be done using the deconvolution as shown in Figure 18.[65]

In case of strong excitation, most of the traps are populated and the process can be saturated. Charging effects have been observed in many persistent systems in the early time behavior of the charging or population process.[66] Generally, for the simple three-level model (see Figure 7) the charging curves are given by

$$I = I_0 \left(1 - C_{\mathrm{t}}(C_{\mathrm{d}} - A)/(B + C_{\mathrm{t}}) C_{\mathrm{d}} N e^{-(AC_{\mathrm{t}} + BC_{\mathrm{d}})t/(B + C_{\mathrm{t}})}\right) \tag{5}$$

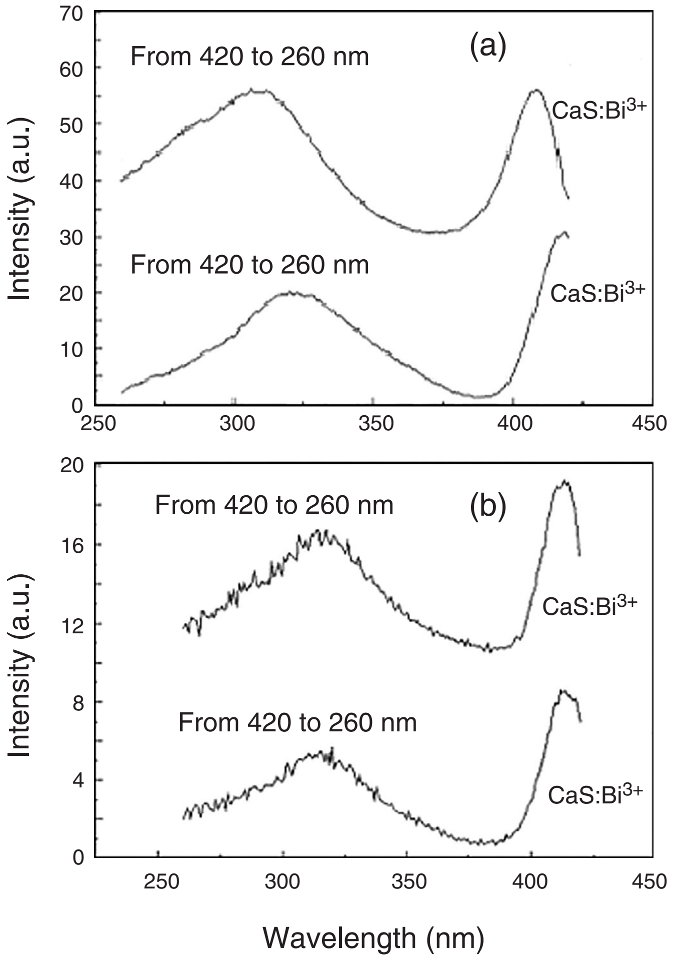

Figure 18 (a) Excitation spectra of CaS:Bi^{3+} for two scan directions between 420 and 260 nm, monitoring at 450 nm; (b) corrected excitation spectra of CaS:Bi^{3+} based on the equation in Ref. 65. (Jia, D., Zhu, J., and Wu, B., *J. Lumin.*, 90, 33, 2000. With permission.)

where C_t and C_d are the trapping and detrapping rates, respectively, A and B the excitation and emission rates, respectively, and I_0 the intensity without traps. It is found that, with strong excitation intensity, the emission intensity reaches equilibrium very quickly. The charging effect can be reduced using a strong excitation source with a slow scanning speed.

12.3.5.2 Thermoluminescence

TL measurements provide important information on the nature of the traps in long persistent phosphors. TL records glow intensity as a function of temperature, providing information regarding trapping energies and detrapping mechanisms.[59] Generally, the theoretical considerations are based on a single type of trap. The glow intensity $I(T)$ at temperature T is given by

$$I(T) \propto n_{t0} s e^{-\Delta E/kT} e^{-\int s e^{-\Delta E/kT} \mathrm{d}T/\beta} \qquad (6)$$

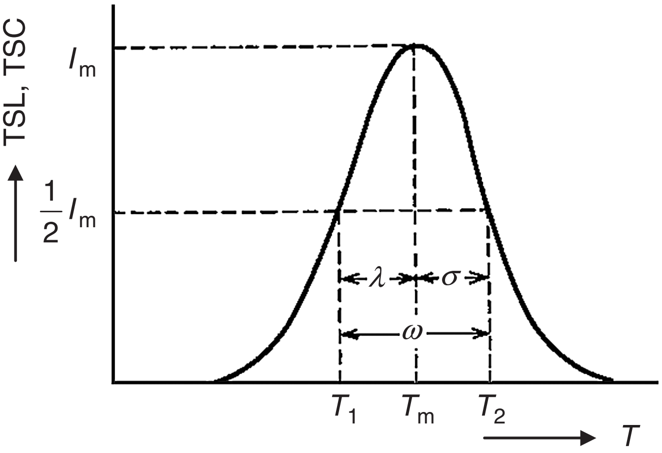

Figure 19 Predicted shape of a glow curve. (From McKeever, S.W.S., *Thermoluminescence of Solids*, Cambridge University Press, Cambridge, 1985. With permission.)

where n_{t0} is the number of electrons in the trap at beginning, β the heating rate, s the frequency factor, and ΔE the depth of the trap.

For the rising part of the TL curve at low temperatures, the number of electrons in the traps remain approximately constant, and hence the glow intensity can be given as

$$I(T) \propto se^{-\Delta E/kT} \tag{7}$$

The depth of electron trap can be determined by plotting $I(T)$ as a function of $1/T$ (log plot). In most of such cases, unfortunately, the trap depth calculated in this way is not accurate because determination of the rise time of the signal is difficult.

The electron trap depth can also be obtained using T_m, the peak position of a glow curve in TL, where one has the following expression:

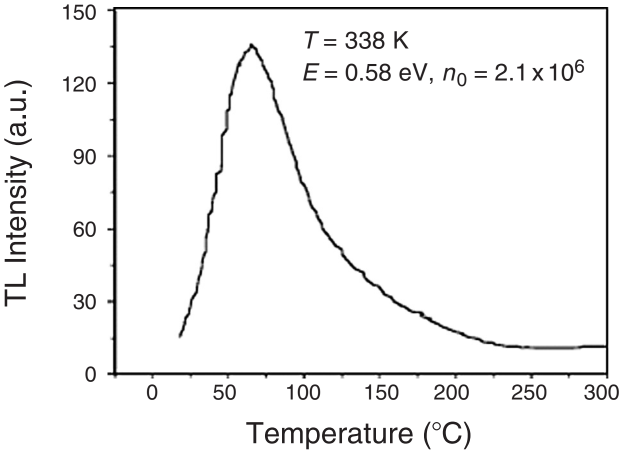

Figure 20 Thermoluminescence curve of $Sr_2ZnSi_2O_7$:Eu^{2+},Dy^{3+} phosphor (sol–gel) from 20 to 300°C. (Jiang, L., et al., *Mater. Lett.*, 58, 1825, 2004. With permission.)

$$\beta\Delta E / kT_{\mathrm{m}}^{2} = se^{-\Delta E / kT_{\mathrm{m}}} \tag{8}$$

In this case, if the frequency factor s is calculated by other methods, the electron trap depth can be estimated as:

$$\Delta E = \left(T_{\mathrm{m}} - T_{0}(\beta / s)\right) / K(\beta / s) \tag{9}$$

where $T_0(\beta/s)$ and $K(\beta/s)$ are parameters, given in Ref. 57, determined by the ratio (β/s).

More generally, trap depth can be evaluated from the TL curves. As shown in Figure 19, T_1 and T_2 are the temperatures at half maxima, the other parameters are defined as $\lambda = T_{\mathrm{m}} - T_1$, $\sigma = T_2 - T_{\mathrm{m}}$, and $\omega = T_2 - T_1$. On the basis of Chen and McKeever's theory,[60] the order of the detrapping mechanism can be found from the symmetry of the TL curves. The trap depth ΔE is given by

$$\Delta E = c_{\gamma}(kT_{\mathrm{m}}^{2} / \gamma) - b_{\gamma}(2kT_{\mathrm{m}}) \tag{10}$$

where c_γ, b_γ, and γ are the shape parameters and are given in Ref. [60]. According to McKeever, a second-order mechanism will yield a more symmetrical peak shape (Gaussian like) and a first-order mechanism will give a nonsymmetrical peak shape (Pekarian like) (Figure 20). By finding the trap depth from the curve, one can estimate the frequency factor s using the relationship

$$\beta\Delta E / kT_{\mathrm{m}}^{2} = s\left(1 + (b-1)2kT_{\mathrm{m}} / \Delta E\right)e^{-\Delta E / kT_{\mathrm{m}}} \tag{11}$$

where b refers to the general order of the detrapping mechanism between the first and second order. ($1 \leq b \leq 2$). The frequency factor is less important. Values of s were found ranging from 10^7 to 10^{16}.[57,59,60]

The estimate based on the theory above may not be accurate especially when traps are not of unique types. A very recent publication by Basun et al. provides a more detailed discussion of the effects of multiple types of traps. They found that when more than one type of trap is present in the system the TL curves may depend on electron sharing.[67]

Experimentally, the TL spectrum is obtained by first populating the traps at low temperatures. The temperature is then increased at a constant speed β, and the glow intensity is monitored at selected wavelengths using a filter or a monochromator. TL peaks in persistent phosphors are only observed when they are exposed to higher energy excitation. This is evidence that the trapping mechanism is related to the ionization process of the emission centers.

12.3.5.3 *Photoconductivity*

Electrons in the conduction band are free to move. By applying a voltage across a sample while exposing it to photons with the proper energy, an electric current can be collected from electrons excited to the conduction band. This is the source of PC.

The basic apparatus for PC experiments consists of a photon source, a crystalline (preferred) sample, a high voltage supply, and a current detector. The photon source should be tunable across the region of interest. The sample is mounted between two semitransparent electrodes; efforts should be made to avoid photoelectric effects between the two electrodes. Generally, the photocurrent is in the order of pA; the sample surfaces should be polished to improve the signal.

Temperature-dependent PC can provide the energy position of excited states relative to the host band gap. Electrons in an excited state, which is below the host band gap, can be thermally ionized into the conduction band, and hence generate photocurrent. The thermal ionization rate is give by

$$W = se^{-\Delta E/kT} \tag{12}$$

where s is the thermal ionization frequency factor and ΔE the energy difference between the excited state and the host conduction band. By measuring the onset of the PC signal at two different temperatures, the distance of the excited state to the conduction band can be determined. Because the thermal ionization rates are the same at the onset wavelengths at two temperatures (Figure 21), by taking the excitation intensity difference into account, we have

$$I_1 se^{-\Delta E_1/kT_1} = I_2 se^{-\Delta E_2/kT_2} \tag{13}$$

where I_1 and I_2 are the excitation intensities at the two onset positions. I_2/I_1 can be estimated from the excitation spectrum; ΔE_1 and ΔE_2 are the differences in energy from the onset wavelengths to the conduction band. ΔE_2 can be expressed by

$$\Delta E_2 = \left(T_2/(T_1 - T_2)\right)\left((\Delta E_1 - \Delta E_2) - T_1 T_2 k \ln(I_2/I_1)\right) \tag{14}$$

As T_1, T_2, I_2/I_1, and $\Delta E_1 - \Delta E_2$ are known, the energy position of the excited state can be calculated.[23]

12.3.5.4 Thermal conductivity

Yuan et al. observed a persistent current associated with the persistent emission of a single crystal phosphor.[68] The result suggested that thermally detrapped electrons, responsible for the long persistent afterglow, are promoted into the host conduction band from the traps.

TC is similar to TL. Instead of measuring glow intensity, TC measures the current generated in the conduction band due to thermal excitation from the electron traps. The current measured in TC is proportional to the number of electrons detrapped into the host conduction band. The conductivity is related to the lifetime of the conduction electron before it is recaptured by a trap.[15]

TC measurement apparatus is similar to that of PC measurement. The photon source is replaced by a thermal heater. The procedure for TC measurements is also similar to that of TL measurements. Samples are cooled down to a low temperature and are irradiated to trap electrons. The temperature is then scanned at a constant heating rate. Thermal current is then collected with a high field applied across the sample.

Differences between TL and TC results can reveal important information about the electron traps. In the $CaAl_2O_4$:Tb^{3+} system, for example, both TL and TC spectra show two peaks at the same temperatures, indicating the presence of two electron traps. One trap has a much greater TL peak, while the other has a larger thermal current peak. These facts provide information as to the position of these traps in relation to the emitting centers (Figure 22).[24]

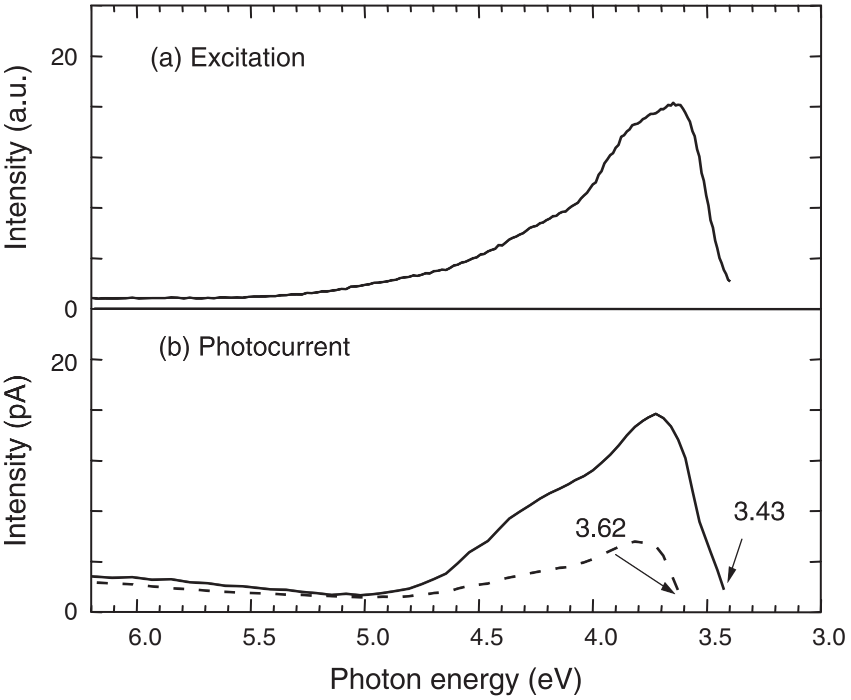

Figure 21 Photocurrent spectra. (a) The excitation spectrum recorded at 3.22 eV emission; (b) the photocurrent spectrum measured at room temperature 290 K (solid curve, onset at 3.43 eV); at 140 K (dashed curve, onset at 3.62 eV). 1 pA offset for plots of photocurrent. (Jia, D., et al., *J. Lumin.*, in press (2006). With permission.)

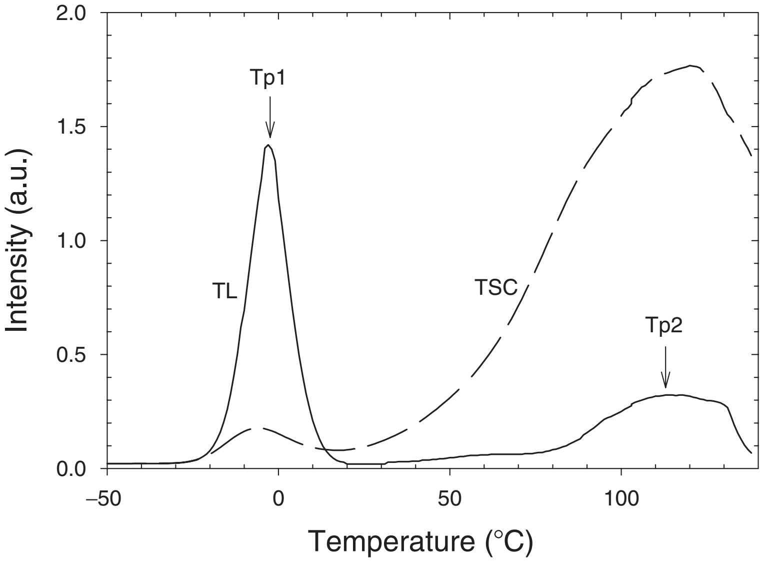

Figure 22 Thermoluminescence (solid line) and thermally stimulated current (dashed line) spectra. Sample was cooled down to −50°C, and irradiated with Xe lamp for 10 min. The heating rate is 0.04 °C/s. (Jia, D., Wang, X.J., and Yen, W.M., *Chem. Phys. Lett.*, 363, 241, 2002. With permission.)

In addition, electron paramagnetic resonance (EPR) spectroscopy is also employed to investigate the mechanism of long persistence phosphorescence.[69–71]

12.3.6 *Summary of long persistent phosphors*

12.3.6.1 *Emission centers and their co-dopants*

So far, about 100 long persistent phosphors have been found; most of the phosphors, listed in Table 9, were developed during the past decade.

Most of the ions where the 5d state can be populated are good candidates showing persistence, for example, Ce^{3+}, Tb^{3+}, and Eu^{2+}. Upon UV and VUV excitation, almost all the trivalent rare-earth ions exhibit persistent afterglow because the 5d electronic state of the trivalent rare-earth ions is energetically close to the conduction band of the host, making delocalization and trapping of electrons possible.

Eu^{2+} is a half shell-filled rare-earth ion, which is a common emission center in persistent materials. Its emission wavelength from $4f^65d^1$ to $4f^7$ varies from host to host and it can give good coverage of the spectrum. Phosphors containing Eu^{2+} can often be pumped by the sunlight. Typical systems include $CaAl_2O_4$:Eu^{2+},Nd^{3+} (>10 h blue), $SrAl_2O_4$:Eu^{2+},Dy^{3+} (>10 h green), and CaS:Eu^{2+},Tm^{3+} (>1 h red), as shown in Table 9.

Other long persistent phosphors used transition metal ions with 3d electrons, such as Cu^+, Mn^{2+}, and Ti^{4+}. Some ns^2-type centers such as Bi^{3+} can also generate persistent phosphorescence. Defect centers can yield long persistence; an example is the $V_k{}^{3+}$ centers in $MgAl_2O_4$.[72]

12.3.6.2 *Host materials*

Host materials are of critical importance for long persistent phosphors. Early host materials for long persistence were of the ZnS type. ZnS has a low band gap energy of 2.16 eV. The persistence time for ZnS-type of phosphors is usually less than an hour. It is difficult to have long persistent emission in these materials because the deep traps are hard to create in narrow band gaps.

During the 1970s, CaS and other alkali-earth sulfides were developed as long persistent phosphor host materials because Eu^{2+}- and Bi^{3+}-doped CaS exhibit strong afterglow emission under visible excitation. Host mixing of alkali-earth sulfides has been used to adjust emission color and has been found effective because of their simple cubic structure. Unfortunately these materials are chemically unstable, for example, $CaS + 2H_2O \rightarrow Ca(OH)_2 + H_2S$. Encapsulation is usually required in such applications.[73]

After sulfide materials, alkali-earth aluminate hosts became important and a large number of long persistent phosphors were developed using the aluminates. Aluminates are more chemically stable than CaS, but they are also sensitive to moisture. Many ions exhibit long persistence in aluminates even without co-doped trapping centers; this is because it is easy to create defects in aluminates due to charge compensation and cation disorder. The band gap energies of aluminates are usually above 6 eV, where deep traps can be created. On the other hand, because of the wide band gap, excitation energies for the long persistent phosphors using aluminates are usually in the UV or VUV regions, which is a disadvantage for some applications.

In the recent years, silicates have been shown to be promising candidates as host materials for long persistent phosphors. The Eu–Dy system worked almost in all alkali-earth silicates. Moreover, some blue silicate long persistent phosphors can be charged under natural light.[74]

Rare-earth oxides and oxysulfides are also important host materials for long persistent phosphors. But these long persistent phosphors cannot be charged by visible light, which limits their potential in applications. Other host materials such as phosphates also face the same problem.

Table 9 Long Persistent Phosphors Listed by Emission Centers

Emission center	Co-dopant	Host material	Emission wavelength (nm)	Persistence time (h)
Eu^{2+}	—	$SrAl_{1.7}B_{0.3}O_4$ [75]	520	2
—	—	$CaAl_2B_2O_7$ [76]	510	8
—	—	$SrAl_2SiO_6$ [77]	510	24
—	—	$CaMgSi_2O_6$ [45]	438	>4
—	Dy^{3+}	$SrAl_2O_4$ [13]	520	>10
—	Dy^{3+}	$BaAl_2O_4$ [18]	500	>10
—	Dy^{3+}	$SrAl_4O_7$ [78]	475	—
—	Dy^{3+}	$Sr_4Al_{14}O_{25}$ [79]	424, 486	15
—	Dy^{3+}	$Sr_4Al_{14}BO_{25}$ [80]	490	>1
—	Dy^{3+}	$Sr_2ZnSi_2O_7$ [81]	457	—
—	Dy^{3+}	$Sr_2MgSi_2O_7$ [28,82]	466	5
—	Dy^{3+}	$Ca_2MgSi_2O_7$	447, 516	5
—	Dy^{3+}	$Ba_2MgSi_2O_7$ [28,82]	505	5
—	Dy^{3+}	$CaMgSi_2O_6$ [45,83]	438	>4
—	Dy^{3+}	$Sr_2MgSi_2O_7$ [84]	469	10
—	Dy^{3+}	$Sr_3MgSi_2O_8$ [85]	475	5
—	Dy^{3+}	$(Sr,Ca)MgSi_2O_7$ [86]	490	20
—	Dy^{3+}	$CaAl_2Si_2O_8$ [87]	440	—
—	Dy^{3+}	$Ca_3MgSi_2O_8$ [88]	475	5
—	Ho^{3+}	$Sr_3Al_{10}SiO_{20}$ [89]	466	6
—	Ho^{3+}	$CaGaS_4$ [90]	560	0.5
—	Mn^{2+}	$BaMg_2Si_2O_7$ [91]	400, 660	—
—	Nd^{3+}	$CaMgSi_2O_6$ [45,83]	438, 447	>4
—	Nd^{3+}	$(Sr,Ca)Al_2O_4$ [13,15]	450	>10
—	Nd^{3+}	$Ca_{12}Al_{14}O_{33}$ [92]	440	1
—	Tm3+	CaS [41]	650	1
—	Y^{3+}	CaS [41]	650	1
—	Al^{3+}	CaS [41]	650	1
—	Cl^-	CaS [40]	670	0.8
Mn^{2+}	—	$CdSiO_3$ [93]	580	1
—	—	$Zn_{11}Si_4B_{10}O_{34}$ [94]	590	12

(*continued*)

Table 9 Long Persistent Phosphors Listed by Emission Centers

Emission center	Co-dopant	Host material	Emission wavelength (nm)	Persistence time (h)
—	—	Zn_2GeO_4 [95]		—
—	—	$ZnAl_2O_4$ [96]	512	2
—	—	$ZnGa_2O_4$ [97]	504	>2
—	—	Mg_2SnO_4 [98]	499	5
—	Eu^{2+},Dy^{3+}	$MgSiO_3$ [27]	660	4
—	Sm^{3+}	β-$Zn_3(PO_4)_2$ [36]	616	2
—	Zn^{2+}	β-$Zn_3(PO_4)_2$ [35]	616	2
—	Al^{3+}	β-$Zn_3(PO_4)_2$ [99]	616	2.5
—	Ga^{3+}	β-$Zn_3(PO_4)_2$ [99]	616	2.5
—	Zr^{4+}	β-$Zn_3(PO_4)_2$ [100]	616, 475	2.5
—	Gd^{3+}	$CdSiO_3$ [93]	580	2
—	Ce^{3+}	$Ca_2Al_2SiO_7$ [27]	550	10
—	Ce^{3+}	$CaAl_2O_4$ [27]	525	10
Tb^{3+}	—	$CaAl_2O_4$ [24]	543	1
—	—	CaO [101]	543	>1
—	—	SrO [101]	543	>1
—	—	$CaSnO_3$ [102]	543	4
—	—	$YTaO_4$ [103]	543	2
—	Ce^{3+}	$CaAl_2O_4$ [62]	543	10
—	Ce^{3+}	$CaAl_4O_7$ [104]	543	10
—	Ce^{3+}	$Ca_{0.5}Sr_{1.5}Al_2SiO_7$	542	—
—	Yb^{3+}	$Na_2CaGa_2SiO_7$	543	1
Ce^{3+}	—	$SrAl_2O_4$ [25]	385, 427	>12
—	—	$CaAl_2O_4$ [22]	413	>12
—	—	$BaAl_2O_4$ [26]	450, 412	>12
—	—	$Ca_2Al_2SiO_7$ [27]	417	>10
—	—	$CaYAl_2O_7$ [107]	425	>1
—	—	CaS [21]	507	0.2
Eu^{3+}	—	CaO [30]	626	1
—	—	SrO [30]	626	1

Table 9 Long Persistent Phosphors Listed by Emission Centers

Emission center	Co-dopant	Host material	Emission wavelength (nm)	Persistence time (h)
—	—	BaO [30]	626	1
—	Ti^{4+}, Mg^{2+}	Y_2O_3 [33]	612	1.5
—	Ti^{4+}, Mg^{2+}	Y_2O_2S [32]	627	1
Pr^{3+}	—	$CaTiO_3$ [108]	612	0.1
—	Al^{3+}	$CaTiO_3$ [108]	612	0.2
—	Li^{+}	$CaZrO_3$ [109]	494	3
Dy^{3+}	—	$CdSiO_3$ [44]	White	5
—	—	Sr_2SiO_4 [110]	White	1
—	—	$SrSiO_3$ [111]	White	1
Ti^{4+}	—	Y_2O_2S [31]	565	5
—	—	Gd_2O_2S [112]	590	1.5
—	Mg^{2+}	Y_2O_2S [113]	594	—
Bi^{3+}	—	CaS [114]	447	0.6
—	Tm^{3+}	CaS [114]	447	1
—	Tm^{3+}	$Ca_xSr_{1-x}S$ [39]	453	1
Cu^{+}		ZnS [115]	530	0.6
—	Co^{2+}	ZnS [115]	530	1.5
Pb^{2+}	—	$CdSiO_3$ [116]	498	2
—	—	SrO [117]	390	1
Sm^{3+}	—	$CdSiO_3$ [118]	400, 603	5
—	—	Y_2O_2S [34]	606	>1
V^{3+}	—	$MgAl_2O_4$ [61]	520	1
—	Ce^{3+}	$MgAl_2O_4$ [61]	520	10
Cu^{2+}	Sn^{2+}	$Na_4CaSi_7O_{17}$ [119]	510	>1
Er^{3+}	Ti^{4+}	Gd_2O_2S [112]	555, 675	1.2
Tm^{3+}	—	Y_2O_2S [120]	588, 626	1
In^{3+}	—	$CdSiO_3$ [121]	435	2

12.3.6.3 *The interests of color*

The emission colors of long persistent phosphors are always of importance and interest from the applications point of view. Many blue, green, yellow, orange, and red color long persistent phosphors have been developed so far. UV long persistent phosphors have been developed and have potential applications in some special areas.

References

1. Yen, W.M. and Weber, M.J., *Inorganic Phosphors: Compositions, Preparation, and Optical Properties*, CRC Press, Boca Raton, FL, 2004.
2. de Groot, W., Luminescence decay and related phenomena, *Physica*, 6, 275, 1939.
3. Gasting, N.L., The decay of the afterglow of ZnS–Cu and ZnS–Cu, Co phosphors in the region of temperature quenching and near it, *Optika i Spektroskopiya*, 3, 624, 1957.
4. Fonda, G.R., Preparation and characteristics of zinc sulfide phosphors sensitive to infrared, *J. Opt. Soc. Am.*, 36, 352, 1946.
5. Kroger, F.A., *Some Aspects of Luminescence of Solids*, Elsevier, Amsterdam, 1948.
6. Leverenz, H.W., *An Introduction to Luminescence of Solids*, John Wiley & Sons, New York, 1949.
7. Lenard, P.E.A., Schmidt, F., and Tomaschek, R., *Phosphoreszenz und Fluoreszenz*, in *Handbuch der Experimentalphysik*, Vol. 23, Akademie Verlagsgesellschaft, Leipzig, 1928.
8. Lehmann, W., Activators and coactivators in calcium sulfide phosphors, *J. Lumin.*, 5, 87, 1972.
9. Lehmann, W. and Ryan, F.M., Fast cathodoluminescent calcium sulfide phosphors, *J. Electrochem. Soc.*, 119, 275, 1972.
10. Lehmann, W. and Ryan, F.M., Cathodoluminescence of CaS–Ce^{3+} and CaS–Eu^{2+} phosphors, *J. Electrochem Soc.*, 118, 447, 1971.
11. Lehmann, W., Optimum efficiency of cathodoluminescence of inorganic phosphors, *J. Electrochem. Soc.*, 118, 1164, 1971.
12. Garlick, G.F.J. and Mason, D.E., Electron traps and infrared stimulation of phosphors, *J. Electrochem. Soc.*, 96, 90, 1949.
13. Matsuzawa, T., et al., A new long phosphorescent phosphor with high brightness, $SrAl_2O_4:Eu^{2+},Dy^{3+}$, *J. Electrochem. Soc.*, 143, 2670, 1996.
14. Abbruscato, V., Optical and electrical properties of $SrAl_2O_4:Eu^{2+}$, *J. Electrochem. Soc.*, 118, 930, 1971.
15. Yamamoto, H. and Matsuzawa, T., Mechanism of long phosphorescence of $SrAl_2O_4:Eu^{2+},Dy^{3+}$ and $CaAl_2O_4:Eu^{2+},Nd^{3+}$, *J. Lumin.*, 72, 287, 1997.
16. Nakazawa, E. and Mochida, T., Traps in $SrAl_2O_4:Eu^{2+}$ phosphor with rare-earth ion doping, *J. Lumin.*, 72–74, 236, 1997.
17. Katsumata, T., et al., Effects of composition on the long phosphorescent $SrAl_2O_4:Eu^{2+},Dy^{3+}$ phosphor crystals, *J. Electrochem. Soc.*, 144, L243, 1997.
18. Katsumata, T., et al., Growth and characteristics of long duration phosphor crystals, *J. Cryst. Growth.*, 198/199, 869, 1999.
19. Jia, W., et al., Phosphorescent dynamics in $SrAl_2O_4:Eu^{2+},Dy^{3+}$ single crystal fibers, *J. Lumin.*, 76/77, 424, 1998.
20. Thiel, C.W., et al., Systematic of 4f electron energies relative to host bands by resonant photoemission of rare-earth-doped optical materials, *J. Lumin.*, 94/95, 1, 2001.
21. Jia, D., Meltzer, R.S., and Yen, W.M., Ce^{3+} energy levels relative to the band structure in CaS: Evidence from photoionization and electron trapping, *J. Lumin.*, 99, 1, 2002.
22. Jia, D. and Yen, W.M., Trapping mechanism associated with electron delocalization and tunneling of $CaAl_2O_4$: Ce^{3+}, a persistent phosphor, *J. Electrochem. Soc.*, 150, H61, 2003.
23. Jia, D., et al., Temperature-dependent photoconductivity of Ce^{3+} doped $SrAl_2O_4$, *J. Lumin.*, 119/120, 55, 2006.
24. Jia, D., Wang, X.J., and Yen, W.M., Electron traps in Tb^{3+}-doped $CaAl_2O_4$, *Chem. Phys. Lett.*, 363, 241, 2002.
25. Jia, D., Wang, X.J., and Yen, W.M., Delocalization, thermal ionization, and energy transfer in singly doped and codoped $CaAl_4O_7$ and Y_2O_3, *Phys. Rev. B*, 69, 235113, 2004.

26. Jia, D., et al., Site-dependent thermoluminescence of long persistent phosphorescence of $BaAl_2O_4:Ce^{3+}$, *Opt. Commun.*, 204, 247, 2002.
27. Wang, X.J., et al., Mn^{2+}-activated green, yellow, and red long persistent phosphors, *J. Lumin.*, 102/103, 34, 2003.
28. Fei, Q., Chang, C., and Mao, D., Luminescence properties of $Sr_2MgSi_2O_7$ and $Ca_2MgSi_2O_7$ long lasting phosphors activated by Eu^{2+}, Dy^{3+}, *J. Alloy. Comp.*, 390, 133, 2005.
29. Zhang, G.B., et al., Photoluminescence of ($Eu^{2+}Dy^{3+}$) co-doped silicate long lasting phosphors, *J. Elec. Spec. Rel. Phen.*, 144–147, 861, 2005.
30. Fu, J., Orange- and red-emitting long-lasting phosphorescence $MO:Eu^{3+}$ (M = Ca,Sr,Ba), *Electrochem. Solid State Lett.*, 3, 350, 2000.
31. Zhang, P., et al., Luminescence characterization of a new long afterglow phosphor of single Ti-doped Y_2O_2S, *J. Lumin.*, 113, 89, 2005.
32. Wang, X., et al., Characterization and properties of a red and orange Y_2O_2S-based long afterglow phosphor, *Mater. Chem. Phys.*, 80, 1, 2003.
33. Lin, Y., et al., Anomalous afterglow from Y_2O_3-based phosphor, *J. Alloy. Comp.*, 361, 92, 2003.
34. Lei, B., et al., Spectra and long-lasting properties of Sm^{3+}-doped yttrium oxysulfide phosphor, *Mater. Chem. Phys.*, 87, 227, 2004.
35. Wang, J., Wang S., and Su, Q., The role of excess Zn^{2+} ions in improvement of red long lasting phosphorescence (LLP) performance of β-$Zn_3(PO_4)_2:Mn$ phosphor, *J. Solid State Chem.*, 177, 895, 2004.
36. Wang, J., Su, Q., and Wang, S., A novel red long lasting phosphorescent (LLP) material β-$Zn_3(PO_4)_2:Mn^{2+},Sm^{3+}$, *Mater. Res. Bull.*, 40, 590, 2005.
37. Hosono, H., et al., Long lasting phosphorescence properties of Tb^{3+}-activated reduced calcium aluminate glasses, *J. Phys.*, C10, 9541, 1998.
38. Jain, V.K., Charge carrier trapping and thermoluminescence in calcium fluoride-based phosphors, *Radiat. Phys. Chem.*, 36, 47, 1990.
39. Jia, D., Zhu, J., and Wu, B., Trapping centers in $CaS:Bi^{3+}$ and $CaS:Eu^{2+},Tm^{3+}$, *J. Electrochem. Soc.*, 147, 386, 2000.
40. Jia, D., Zhu, J., and Wu, B., Influence of co-doping with Cl^- on the luminescence of $CaS:Eu^{2+}$, *J. Electrochem. Soc.*, 147, 3948, 2000.
41. Jia, D., et al., Trapping processes in $CaS:Eu^{2+},Tm^{3+}$, *J. Appl. Phys.*, 88, 3402, 2000.
42. Aitasalo, T., et al., Low temperature thermoluminescence properties of Eu^{2+}- and R^{3+}-doped $CaAl_2O_4$, *J. Alloy. Comp.*, 380, 4, 2004.
43. Aitasalo, T., et al., Effect of temperature on the luminescence processes of $SrAl_2O_4:Eu^{2+}$, *Radiat. Meas.*, 38, 727, 2004.
44. Liu, Y., Lei, B., and Shi, C., Luminescent properties of a white afterglow phosphor $CdSiO_3:Dy^{3+}$, *Chem. Mater.*, 17, 2113, 2005.
45. Jiang, L., et al., Luminescent properties of $CaMgSi_2O_6$-based phosphors co-doped with different rare-earth ions, *J. Alloy. Comp.*, 377, 211, 2004.
46. Dorenbos, P., Mechanism of persistent luminescence in Eu^{2+} and Dy^{3+} co-doped aluminate and silicate compounds, *J. Electrochem. Soc.*, 152, H107, 2005.
47. Yamaga, M., et al., Radiative and nonradiative decay processes responsible for long-lasting phosphorescence of Eu^{2+}-doped barium silicates, *Phys. Rev. B*, 71, 205102, 2005.
48. Clabau, F., et al., Mechanism of phosphorescence appropriate for the long-lasting phosphors Eu^{2+}-doped $SrAl_2O_4$ with codopants Dy^{3+} and B^{3+}, *Chem. Mater.*, 17, 3904, 2005.
49. Li, C.Y. and Su, Q., Action of co-dopant in electron-trapping materials: The case of Sm^{3+} in Mn^{2+}-activated zinc borosilicate glasses, *Appl. Phys. Lett.*, 85, 2190, 2004.
50. Aitasalo, T., et al., Persistent luminescence phenomena in materials doped with rare-earth ions, *J. Solid State Chem.*, 171, 114, 2003.
51. Lin, Y.H., et al., Influence of co-doping different rare-earth ions on the luminescence of $CaAl_2O_4$-based phosphors, *J. Euro. Ceram. Soc.*, 23, 175, 2003.
52. Yamaga, M., et al., Mechanism of long-lasting phosphorescence process of Ce^{3+}-doped $Ca_2Al_2SiO_7$ melilite crystals, *Phys. Rev. B*, 65, 235108, 2002.
53. Lin, Y.H., et al., The characterization and mechanism of long afterglow in alkaline-earth aluminates phosphors co-doped by Eu_2O_3 and Dy_2O_3, *Mater. Chem. Phys.*, 70, 156, 2001.

54. Kamada, M., Murakami, J., and Ohno, N., Excitation spectra of a long-persistent phosphor $SrAl_2O_4$:Eu, Dy in vacuum ultraviolet region, *J. Lumin.*, 87–9, 1042, 2000.
55. Basun, S.A., et al., Optical and photoelectrical studies of charge-transfer processes in $YAlO_3$:Ti crystals, *Phys. Rev. B*, 54, 6141, 1996.
56. Peskin, U., Analysis of a dissipative resonant tunneling trap by temperature-dependent Langevin–Schrodinger equations, *J. Chem. Phys.*, 113, 1, 2000.
57. Nakazawa, E., *Fundamentals of Luminescence*, in *Phosphor Handbook*, Shionoya, S. and Yen, W.M., Eds., CRC Press, Boca Raton, FL, 1999, chap. 2, sec. 6.
58. Curie, D., *Luminescence in Crystals*, Methuen & Company Ltd., London, 1963, pp. 195.
59. McKeever, S.W.S., *Thermoluminescence of Solids*, Cambridge University Press, Cambridge, 1985.
60. Chen, R. and McKeever, S.W.S., *Theory of Thermoluminescence and Related Phenomena*, World Scientific, Singapore, 1997.
61. Jia, D. and Yen, W.M., Enhanced V^{3+} center afterglow in $MgAl_2O_4$ by doping with Ce^{3+}, *J. Lumin.*, 101, 115, 2003.
62. Jia, D., et al., Green phosphorescence of $CaAl_2O_4$:Tb^{3+},Ce^{3+} through persistent energy transfer, *Appl. Phys. Lett.*, 80, 1535, 2002.
63. Jia, D., et al., Persistent energy transfer from Ce^{3+} to Tb^{3+} in $CaAl_2O_4$, *J. Appl. Phys.*, 93, 148, 2003.
64. Jia, D., Wu, B., and Zhu, J., Luminescence of Bi^{3+} and Eu^{2+} double centers doped in CaS host, *Acta Phys. Sin.*, 8, 813, 1999.
65. Jia, D., Zhu, J., and Wu, B., Correction of excitation spectra of long persistent phosphors, *J. Lumin.*, 90, 33, 2000.
66. de Groot, W., Saturation effects in the short-duration photoluminescence of zinc sulfidephosphors, *Physica*, 6, 393, 1939.
67. Basun, S., et al., The analysis of thermoluminescence glow curves, *J. Lumin.*, 104, 283, 2003.
68. Yuan, H., et al., The long-persistent photoconductivity of $SrAl_2O_4$:Eu^{2+},Dy^{3+} single crystal, *J. Electrochem. Soc.*, 147, 3154, 2000.
69. Kumar, V.R., et al., EPR, luminescence, and IR studies of Mn-activated $ZnGa_2O_4$ phosphor, *J. Phys. Chem. Solids*, 65, 1367, 2004.
70. Nakamura, T., et al., High frequency EPR of Eu^{2+}-doped strontium aluminate phosphors, *J. Mater. Chem.*, 10, 2566, 2000.
71. Nakamura, T., et al., EPR investigations on Eu^{2+}-doped barium aluminate, *Phys. Chem. Chem. Phys.*, 1, 4011, 1999.
72. Xu, C., et al., Enhancement of adhesion and triboluminescence of ZnS:Mn films by annealing technique, *Thin Solid Films*, 352, 273, 1999.
73. Lü, X., Silica encapsulation study on $SrAl_2O_4$:Eu^{2+},Dy^{3+} phosphors, *Mater. Chem. Phys.*, 93, 526, 2005.
74. Xiao, Z. and Xiao, Z., Long afterglow silicate luminescent material and its manufacturing method, US Patent 6093346, 2000.
75. Sánchez-Benítez, J., et al., Optical study of $SrAl_{1.7}B_{0.3}O_4$:Eu, R (R = Nd, Dy) pigments with long-lasting phosphorescence for industrial uses, *J. Solid State Chem.*, 171, 273, 2003.
76. Qiu, J. and Hirao, K., Long lasting phosphorescence in Eu^{2+}-doped calcium aluminoborate glasses, *Solid State Commun.*, 106, 795, 1998.
77. Qiu, J., et al., Phenomenon and mechanism of long-lasting phosphorescence in Eu^{2+}-doped aluminosilicate glasses, *J. Phys. Chem. Solids*, 59, 1521, 1998.
78. Chang, C., et al., Preparation of long persistent $SrO_2Al_2O_3$ ceramics and their luminescent properties, *J. Alloy. Comp.*, 348, 224, 2003.
79. Lin, Y., Tang, Z., and Zhang, Z., Preparation of long-afterglow $Sr_4Al_{14}O_{25}$-based luminescent material and its optical properties, *Mater. Lett.* 51, 14, 2001.
80. Nag, A. and Kutty, T.R.N., The mechanism of long phosphorescence of $SrAl_{2-x}B_xO_4$ ($0 < x < 0.2$) and $Sr_4Al_{14-x}B_xO_{25}$ ($0.1 < x < 0.4$) co-doped with Eu^{2+} and Dy^{3+}, *Mater. Res. Bull.*, 39, 331, 2004.
81. Jiang, L., et al., A new long persistent blue-emitting $Sr_2ZnSi_2O_7$:Eu^{2+},Dy^{3+} prepared by sol–gel method, *Mater. Lett.*, 58, 1825, 2004.

82. Lin, Y., et al., Preparation and characterization of long afterglow $M_2MgSi_2O_7$-based (M:Ca, Sr, Ba) photoluminescent phosphors, *Mater. Chem. Phys.*, 82, 860, 2003.
83. Jiang, L., Chang, C., and Mao, D., Luminescent properties of $CaMgSi_2O_6$ and $Ca_2MgSi_2O_7$ phosphors activated by Eu^{2+},Dy^{3+} and Nd^{3+}, *J. Alloy. Comp.*, 360, 193, 2003.
84. Alvani, A.A.S., Moztarzadeh, F., and Sarabi, A.A., Preparation and properties of long afterglow in alkaline-earth silicate phosphors co-doped by Eu_2O_3 and Dy_2O_3, *J. Lumin.*, 115, 147, 2005.
85. Alvani, A.A.S., Moztarzadeh, F., and Sarabi, A.A., Effects of dopant concentrations on phosphorescence properties of Eu/Dy-doped $Sr_3MgSi_2O_8$, *J. Lumin.*, 114, 131, 2005.
86. Chen, Y., et al., Luminescent properties of blue-emitting long afterglow phosphors $Sr_{2-x}Ca_xMgSi_2O_7$: Eu^{2+},Dy^{3+} ($x = 0,1$), *J. Lumin.*, 118, 70, 2006.
87. Wang, Y.H., et al., Synthesis of long afterglow phosphor $CaAl_2Si_2O_8$:Eu^{2+}, Dy^{3+} via sol–gel technique and its optical properties, *J. Rare Earth*, 23, 625, 2005.
88. Lin, Y., et al., Luminescent properties of a new long afterglow Eu^{2+}- and Dy^{3+}-activated $Ca_3MgSi_2O_8$ phosphor, *J. Euro. Ceram. Soc.*, 21, 683, 2001.
89. Kuang, J.Y., et al., Blue-emitting long-lasting phosphor, $Sr_3Al_{10}SiO_{20}$:Eu^{2+},Ho^{3+}, *Solid State Commun.*, 136, 6, 2005.
90. Guo, C., et al., Luminescent properties of Eu^{2+} and Ho^{3+} co-doped $CaGa_2S_4$ phosphor, *Phys. State Sol.* (a), 201, 1588, 2004.
91. Yao, G.Q., et al., Luminescent properties of $BaMg_2Si_2O_7$:Eu^{2+},Mn^{2+}, *J. Mater. Chem.*, 8, 585, 1998.
92. Zhang, J., et al., Preparation and characterization of a new long afterglow indigo phosphor $Ca_{12}Al_{14}O_{33}$:Nd:Eu, *Mater. Lett.*, 57, 4315, 2003.
93. Lei, B., et al., Luminescence properties of $CdSiO_3$:Mn^{2+} phosphors, *J. Lumin.*, 109, 215, 2004.
94. Li, C., et al., Photostimulated long lasting phosphorescence in Mn^{2+}-doped zinc borosilicate glasses, *J. Non-Cryst. Solids*, 321, 191, 2003.
95. Qiu, J., Igarashi, H., and Makishima, A., Long-lasting phosphorescence in Mn^{2+}:Zn_2GeO_4 crystallites precipitated in transparent GeO_2–B_2O_3–ZnO glass ceramics, *Sci. Tech. Adv. Mater.*, 6, 431, 2005.
96. Matsui, H., et al., Origin of mechanoluminescence from Mn-activated $ZnAl_2O_4$: Triboelectricity-induced electroluminescence, *Phys. Rev. B*, 69, 235109, 2004.
97. Uheda, K., et al., Synthesis and long-period phosphorescence of $ZnGa_2O_4$:Mn^{2+} spinel, *J. Alloy. Comp.*, 262/263, 60, 1997.
98. Lei, B., et al., Green emitting long lasting phosphorescence (LLP) properties of Mg_2SnO_4:Mn^{2+} phosphor, *J. Lumin.*, 118, 173, 2006.
99. Wang, J., Wang, S., and Su, Q., Synthesis, photoluminescence, and thermostimulated-luminescence properties of novel red long-lasting phosphorescent materials β-$Zn_3(PO_4)_2$:Mn^{2+}, M^{3+} (M = Al and Ga), *J. Mater. Chem.*, 14, 2569, 2004.
100. Wang, J., Su, Q., and Wang, S., Blue and red long lasting phosphorescence (LLP) in β-$Zn_3(PO_4)_2$:Mn^{2+}, Zr^{4+}, *J. Phys. Chem. Solids*, 66, 1171, 2005.
101. Kuang, J.Y., et al., Long-lasting phosphorescence of Tb^{3+}-doped MO (M = Ca,Sr), *Chin. J. Inorg. Chem.*, 21, 1383, 2005.
102. Liu, Z. and Liu, Y., Synthesis and luminescent properties of a new green afterglow phosphor $CaSnO_3$:Tb^{3+}, *Mater. Chem. Phys.*, 93, 129, 2005.
103. Takayama, T., et al., Growth and characteristics of a new long afterglow phosphorescent yttrium tantalite crystal, *J. Cryst. Growth*, 275, e2013, 2005.
104. Jia, D., Zhu, J., and Wu, B.Q., Luminescence and energy transfer in $CaAl_4O_7$:Tb^{3+},Ce^{3+}, *J. Lumin.*, 93, 107, 2001.
105. Ito, Y., et al., Luminescence properties of long-persistence silicate phosphors, *J. Alloy. Comp.*, 408–412, 907, 2006.
106. Yamazaki, M. and Kojima, K., Long-lasting afterglow in Tb^{3+}-doped SiO_2–Ga_2O_3–CaO–Na_2O glasses and its sensitization by Yb^{3+}, *Solid State Commun.*, 130, 637, 2004.
107. Kodama, N., et al., Long-lasting phosphorescence in Ce^{3+}-doped $Ca_2Al_2SiO_7$ and $CaYAl_3O_7$ crystals, *Appl. Phys. Lett.*, 75, 1715, 1999.
108. Jia, W., et al., UV excitation and trapping centers in $CaTiO_3$:Pr^{3+}, *J. Lumin.*, 119/120, 13, 2006.
109. Liu, Z., et al., Long afterglow in Pr^{3+} and Li^+ co-doped $CaZrO_3$, *Opt. Commun.*, 251, 388, 2005.

110. Kuang, J. and Liu, Y., White-emitting long-lasting phosphor Sr_2SiO_4:Dy^{3+}, *Chem. Lett*., 34, 598, 2005.
111. Kuang, J., Liu, Y., and Zhang, J., White-light-emitting long-lasting phosphorescence in Dy^{3+}-doped $SrSiO_3$, *J. Solid State Chem*., 179, 266, 2006.
112. Zhang, J., Liu, Y., and Man, S., Afterglow phenomenon in erbium and titanium codoped Gd_2O_2S phosphors, *J. Lumin*., 117, 141, 2006.
113. Kang, C.C., et al., Synthesis and luminescent properties of a new yellowish-orange afterglow phosphor Y_2O_2S:Ti,Mg, *Chem. Mater*., 15, 3966, 2003.
114. Jia, D., Zhu, J., and Wu, B., Improvement of persistent phosphorescence of $Ca_{0.9}Sr_{0.1}S$:Bi^{3+} by codoping Tm^{3+}, *J. Lumin*., 91, 59, 2000.
115. Murayama, Y., *Other phosphors*, *Phosphor Handbook*, Shionoya, S. and Yen, W.M., Eds., CRC Press, Boca Raton, FL, 1999, chap. 12.
116. Kuang, J. and Liu, Y., Luminescence properties of a Pb^{2+}-activated long-afterglow phosphor, *J. Electrochem. Soc*., 153, G245, 2006.
117. Fu, J., Orange- and violet-emitting long-lasting phosphors, *J. Am. Ceram. Soc*., 85, 255, 2002.
118. Lei, B., et al., Pink light emitting long-lasting phosphorescence in Sm^{3+}-doped $CdSiO_3$, *J. Solid State Chem*., 177, 1333, 2004.
119. Qiu, J. and Makishima, A., Ultraviolet radiation-induced structure and long-lasting phosphorescence in Sn^{2+}–Cu^{2+} co-doped silicate glass, *Sci. Tech. Adv. Mater*., 4, 35, 2003.
120. Lei, B., Liu, Y., and Tang, G., Unusual afterglow properties of Tm^{3+}-doped yttrium oxysulfide, *Chem. J. Chin. Univ*., 24, 782, 2003.
121. Kuang, J. and Liu, Y., Trapping effects in $CdSiO_3$:In^{3+} long afterglow phosphor, *Chin. Phys. Lett*., 23, 204, 2006.

chapter twelve — sections four–six

Other phosphors

Atsushi Suzuki

Contents

12.4 Phosphors for marking 819
12.5 Stamps printed with phosphor-containing ink 819
12.6 Application of near-infrared phosphors for marking 820
References 822

12.4 Phosphors for marking

With the advent of more sophisticated computer and automation systems, advanced recording or labeling processes as well as the systems needed for decoding or reading these labels have been developed. Optically and magnetically recorded data are widely used in these systems. For the former, preprinted characters, symbols, or bar codes are read automatically by exploiting the differences in optical reflectivity between printed and blank sections of the material. These type of reading systems can yield inaccurate results due to imperfections in the recording media, such as creases or stains. In order to avoid this problem, a system in which data are recorded on a surface using fluorescent ink has been proposed. By using a fluorescent material whose emission is at a different wavelength than the reflected light, the deleterious effect of imperfections can be greatly reduced.

Figure 23 shows a schematic of the method used for reading data recorded with phosphor-containing ink. The system uses a light source with a wavelength suitable to excite the phosphor and an optical filter that blocks the excitation light and passes the emitted light. Phosphors used in the system should have characteristics such as high luminous efficiency, strong absorption at the excitation wavelength, and longevity under operating conditions.

Phosphors widely used at present are organic materials such as thioflavine (yellow luminescence), fluoreceine (yellow), eosine (red), and rhodamine 6G (red) (see Chapter 11). They all have strong ultraviolet absorption and high luminous efficiency. These phosphors are first dispersed in a polymer such as acryl, alkyd, or melamine resins, then crushed and 1 blended with compounds necessary to make an phosphor-containing ink.[1]

12.5 Stamps printed with phosphor-containing ink[2,3]

The state-of-the-art in the phosphor labeling systems presently used to imprint postage stamps is briefly reviewed; and in the next section, a new marking system that uses a recently invented inorganic phosphor is described.

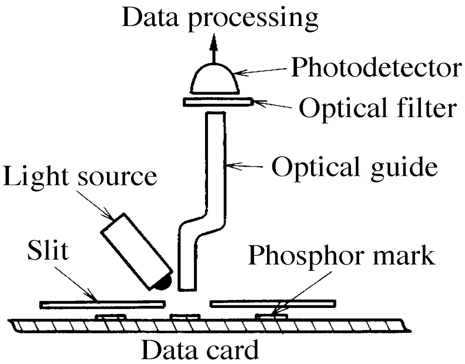

Figure 23 An apparatus for phosphor mark reading.

In countries such as the U.S., Great Britain, Germany, and Japan, phosphorescent inks have been used in printing of all kinds of postage stamps. By optically reading these phosphor data, high-speed automatic sorting and verification at a rate of 30,000 letters per hour has been achieved.

The first system was introduced in Great Britain in 1959. Multiple lines of 5- to 8-mm width of a blue-violet phosphor were imprinted in relief on the surface of the stamps. Information on the stamp was encoded in the number of lines that were printed. A short-wavelength (<300 nm) ultraviolet lamp is used as an excitation source. Persistent phosphors are used in the labeling as their long phosphorescent lifetime permits their discrimination from the fast emission associated with bleaching agents blended in the paper used for envelopes.

In the system developed in Germany in 1961, long-wavelength (365 nm) ultraviolet light is used as an excitation source for a yellow-emitting phosphorescent ink. This system was developed in order to spectrally discriminate between emission from the labeling ink and the bleaching dyes of the envelopes. The preparation method of the German stamps is different from that used in Great Britain; phosphorescent ink is printed on the entire stamp sheet prior to printing the stamp design. Since the ink used to print the stamp design is chosen so as to absorb the ultraviolet excitation light without luminescing in the visible, only the parts of the stamp not covered by the design will phosphoresce under 365-nm excitation.

In both of the examples cited above, the phosphor labels or prints are hardly distinguishable by the human eye. This is an additional function of phosphor mark, which makes it effective for the preservation of secrecy and the prevention of forgery.

12.6 *Application of near-infrared phosphors for marking*

As shown in the previous section, a phosphor mark reader usually makes use of phosphor excited by ultraviolet light. There are two weak points in these systems: (1) the relatively short life-time of the UV excitation lamp, and (2) ultraviolet light is easily absorbed by stains on the phosphor mark, which may lead to erroneous readings.

To overcome these problems, new systems that make use of phosphors excitable by near-infrared light in combination with long life-time, solid-state, near-infrared light sources have been proposed. This system is advantageous because near-infrared light is absorbed less by usual stains than ultraviolet light.

The application of infrared up-conversion phosphors activated with Yb^{3+} and Er^{3+} ions (see 12.1) was first proposed.[4] The Yb^{3+} ion has an excited state in the near-infrared region (~970 nm), and efficiently sensitizes the Er^{3+} ion, which emits red and green luminescence

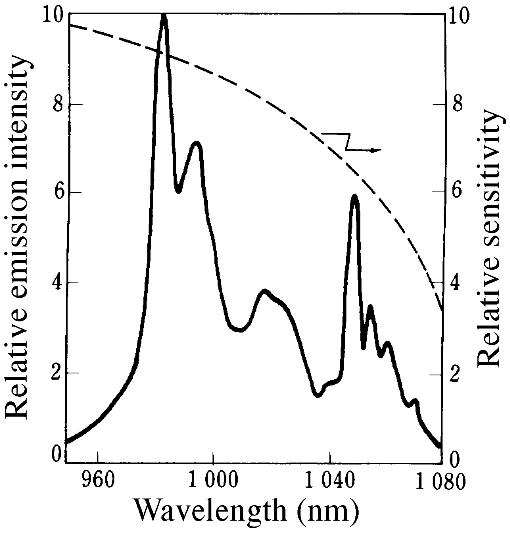

Figure 24 Emission spectrum (solid line) of $Li(Nd_{0.9}Yb_{0.1})P_4O_{12}$ excited by a GaAlAs 800-nm light-emitting diode and sensitivity spectrum (dotted line) of a silicone phototransistor in the near-infrared region. (Observed by the author.)

as a result of up-conversion processes. The Yb^{3+} ion is very suitable for this purpose since it has the strong infrared absorption band and exhibits little concentration quenching. A GaAs:Si infrared light (~970 nm)-emitting diode is used as the light source. Up-conversion phosphors need high-intensity excitation; this is a serious demerit for the use of marking. Therefore, this type of phosphor is not presently in practical use.

Thus, the use of phosphors excitable by near-infrared light and emitting near-infrared luminescence is surely desirable for marking. Based on this, a group of phosphors activated with Yb^{3+} and Nd^{3+} ions have been investigated and developed,[5,6] as described below.

As the solid-state detector of near-infrared light to be used for the present purpose, a Si phototransistor is most suitable; its sensitivity spectrum is shown in Figure 24. To fit this spectrum, the Yb^{3+} ion exhibiting ~980-nm luminescence is most suitable. It also has the advantage of minimal concentration quenching. It has only one excited state (see 3.3), so that the excitation and emission spectra overlap. A sensitizer that absorbs near-infrared light and transfers excitation energy to a Yb^{3+} ion is needed. The Nd^{3+} ion is appropriate for this kind of sensitizer, and a GaAlAs 800-nm light-emitting diode can be used as the light source.

As Nd^{3+} phosphors to be used, so-called stoichiometric type[7] phosphors were investigated. This group of phosphors was developed first in 1972 as miniature solid-state laser materials such as NdP_5O_{14}, in which the Nd^{3+} ion concentration is 60 times higher than that in typical solid-state laser materials such as $Y_3Al_5O_{12}$:Nd^{3+}. One reason for the minimal concentration quenching observed in this group of phosphors is thought to be that the distance between the nearest activator ions is much larger, 5.19 Å in NdP_5O_{14}, compared to typical phosphors, 3 to 4 Å.[8,9] Table 10 summarizes typical Nd^{3+}-activated phosphors in this group. These phosphors with high concentrations of activator ions have strong absorption for excitation light and are very suitable for marking, since printed phosphor marks are usually very thin.

Figure 24 depicts an emission spectrum of $Li(Nd_{0.9}Yb_{0.1})P_4O_{12}$, a typical phosphor developed for use in marking. It is believed that an excitation energy transfer assisted by phonons (see 2.8.1) takes place from the Nd^{3+} ion to the Yb^{3+} ion. Peaks around 980–1080 nm correspond to the emission of Yb^{3+} ions and those around 1060–1080 nm are the

Table 10 Stoichiometric Type Nd^{3+} Phosphors

Compound	The nearest Nd ion distance (Å)	Nd ion concentration (× 10^{21} cm^{-3})
NdP_5O_{14}	5.19	3.96
$LiNdP_4O_{12}$	5.62	4.42
$Na_5Nd(WO_4)_4$	6.45	2.61
$Al_3Nd(BO_3)_4$	5.91	5.43
$Cs_2NaNdCl_6$	7.7	3.2

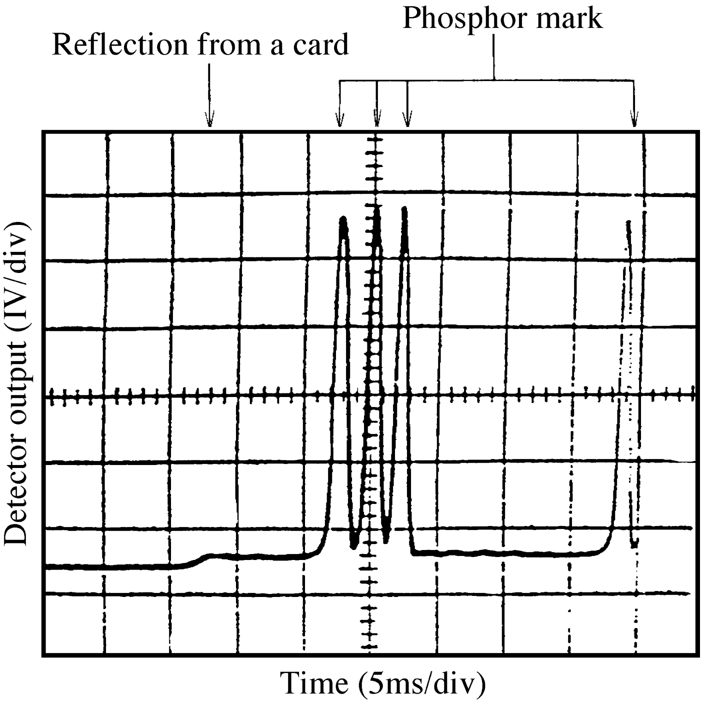

Figure 25 An example of detector output $Li(Nd_{0.9}Yb_{0.1})P_4O_{12}$ phosphor mark reader system. Reading speed is 2 m s^{-1}. (Observed by the author.)

emission of Nd^{3+} ions. It is observed that the emission from Yb^{3+} ions coincides well with the sensitivity spectrum of the Si phototransistor.

Figure 25 shows an example of the detector output of a phosphor mark reader system making use of the above-mentioned phosphors, a GaAlAs light source, and a detecting unit, which is composed of an InP polycrystaline filter and an Si phototransistor, together allowing for the detection of wavelengths greater than 950 nm. It is possible to obtain a signal-to-noise ratio greater than 20, although a small amount of the source light reflected at the surface of the phosphor mark sheet also is detected.

References

1. Sagara, J. et al. ed., *Printing Ink Technology*, 108, CMC Press, 1982.
2. Uemura, S., *Printing Technology of World Postage Stamps*, Insatsukyoku-Choyokai, 1979.
3. Printing Department, Ministry of Finance ed., *Production of Postage Stamps*, Insatsukyoku-Choyokai, 1969.
4. Malmberg, T.A.H. et al., *United States Patent* 4, 047, 03, 1979.

5. Suzuki, A., *FOP (Future Oriented Processes)*, 5, 16, 1980.
6. Suzuki, A., *United States Patent* 4, 202, 491, 1980.
7. Danielmeyer, H.G. and H.P. Weber, *IEEE J. Quantum Electronics*, QE-8, 805, 1972.
8. Quiesser, H.J. ed., *Festkörperproblem*, vol. 15, 253, 1975.
9. Lempicki, A., *Optics Communications*, 23, 376, 1977.

chapter thirteen — sections one–seven

Solid-state laser materials

William M. Yen

Contents

13.1 Introduction 825
13.2 Basic laser principles 826
13.3 Operational schemes 829
13.4 Materials requirements for solid-state lasers 830
13.5 Activator ions and centers 832
13.6 Host lattices 833
13.7 Conclusions 836
References 838

13.1 *Introduction*

In addition to applications in display and lighting, luminescent materials are also essential in our modern technologies that are based in the exploitation and manipulation of light for various purposes. Crucial to the evolution of these technologies has been the extension of quantum electronics into the infrared and optical frequencies spearheaded by the invention of the optical maser or laser.[1] Since the advent of the first laser,[2] laser action has been attained in luminescent materials in all its physical states, i.e., in solids, liquids, and gases, with output frequencies spanning the electromagnetic light spectrum. The focus of this brief chapter is on materials that can be employed as solid-state laser sources; these materials are generally crystals or glasses that are either intrinsic light emitters or that have been optically activated with ionic impurities or other defect centers. Indeed, many of the phosphors discussed elsewhere in this volume share common features and properties with the laser materials of interest in this chapter and are in some instances identical to each other. Thus, the task here is made easier since much of the descriptive material relevant to the properties of phosphors appearing in this Handbook is applicable to this discussion. In addition, this is a mature subject and there have been many excellent reviews and compendia on lasers and laser technology; for example, a comprehensive handbook edited by Weber on lasers and optical materials has appeared,[3] as has a very useful volume by Kaminskii that specifically addresses laser crystals.[4]

Historically, the stimulated emission of radiation was postulated by Einstein[5] in explaining thermal equilibrium between radiation and matter through the principle of detailed balance; however, no studies in this area were pursued until 1954 when the principle of the Maser (Microwave Amplification through the Stimulated Emission of Radiation) was advanced and demonstrated by Townes and others.[6,7] In 1958, Schawlow and Townes[1] proposed the extension of the maser principle to infrared and optical frequencies; in their paper, the authors discussed ways to excite the luminescence in the active medium and the means to feed back the radiation to produce stimulation. Prophetically, they suggested the possibility of employing rare-earth-activated solids as likely candidates for stimulation. Two years later, Maiman[2] succeeded in demonstrating pulsed laser action in a flashlamp-pumped ruby crystal; a transition metal ion, Cr^{3+}, was responsible for the laser action, which was shown to occur in the red or R-line region of the visible spectrum. Shortly thereafter, laser action was also achieved in crystals and glasses activated by lanthanide and actinide ions; for example, Sorokin and Stevenson[8] succeeded in stimulating U^{3+} and Sm^{2+} in CaF_2, while Snitzer[9] reported laser oscillations in Nd^{3+}-doped glasses. The first instance of a continuous-wave or cw solid-state laser was attained by Johnson and Nassau[10] using $CaWO_4$:Nd^{3+} and occurred at about the same time the He-Ne gas discharge laser was invented.[11] Coherent radiation was obtained in light-emitting semiconductors (GaAs) in 1962 by several groups.[12] Laser tunability over broad spectral regions was initially obtained in organic liquid dyes in the mid-1960s,[13] while tunable solid-state lasers appeared somewhat later and relied initially on defect centers of various types.[14] Presently, the most commonly used solid-state laser is the Nd^{3+}-doped yttrium aluminum garnet ($Y^3Al_5O_{12}$) or YAG laser due to Geusic and co-workers[15] and with an output at 1.06 μm in the near-infrared (NIR).

In the past 3 decades, a multitude of systems has been stimulated under an equally large variation of technical conditions. In the course of these developments, the desired properties of those solids that can be advantageously used as solid-state lasers have been established, and it is these properties that determine the nature of the discussion below. Below, the principles of the laser and an outline of the optical and physical properties required of a material for it to usable as a laser device will be discussed. The various classifications of solids that have been and are currently used in the construction of lasers will be enumerated, and some general comments on expected future developments will be given.

13.2 Basic laser principles[16]

A light beam passing through a medium that contains absorbing centers is attenuated according to:

$$I(l) = I_0 \exp\left[-\alpha(\nu) l\right] \tag{1}$$

where $\alpha(\nu)$ is the absorption coefficient, which is generally frequency dependent and given by:

$$\alpha(\nu) = \frac{\lambda^2}{8\pi n^2 \tau_R}\left[\left(g_b/g_a\right)N_a - N_b\right]\Gamma(\nu) \tag{2}$$

In Eq. 2, λ is the wavelength of the peak absorption, N_a and N_b are the populations of the ground and excited states, respectively, n is the index of refraction at λ, and $\Gamma(\nu)$ is the lineshape function of the absorption. The lifetime τ_R is determined by the so-called Einstein A coefficient, i.e.,

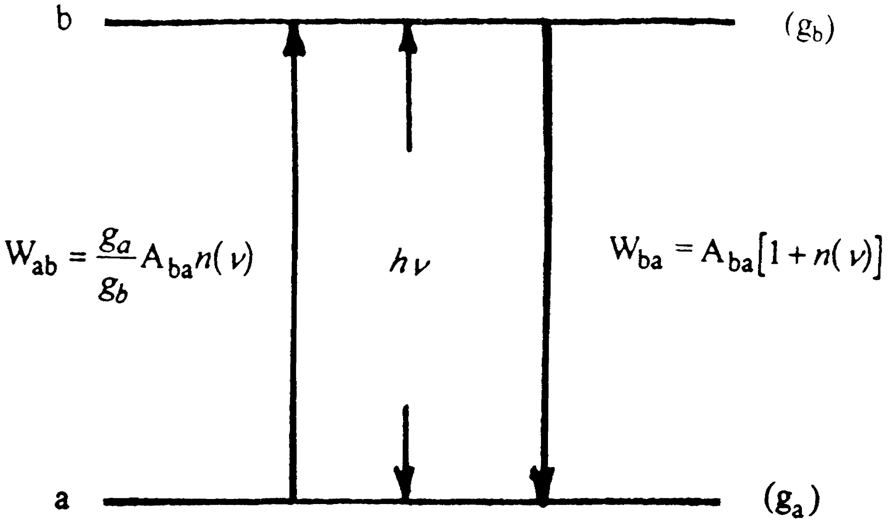
b
(g_b)
$W_{ab} = \frac{g_a}{g_b} A_{ba} n(\nu)$
$h\nu$
$W_{ba} = A_{ba}[1 + n(\nu)]$
a
(g_a)

Figure 1 Absorption and emission probabilities in a two-level system expressed in terms of the spontaneous transition probability A_{ba}. The radiation density at the resonance frequency ν is n(ν); the statistical weights of the ground and excited states are g_a and g_b, respectively.

$$A_{ba} = {}^{1}\!/_{\tau_R} \tag{3}$$

A_{ba} is a measure of the spontaneous transition probability from state *b* (excited) to the ground state *a*. The A coefficient is also related to the absorption probability from *a* and the stimulated radiative probability from state *b*; these latter two processes are only activated in the presence of radiation of density n(ν). For a two-level system, Figure 1 illustrates these radiative interactions.

With energy splittings in the NIR or optical range and at thermal equilibrium, the population in the ground state N_a will be much larger than that in the excited state N_b and α(ν) is positive, leading to attenuation of the beam. However, under conditions of population inversion, i.e., when

$$\Delta N = N_b - (g_b/g_a)N_a \geq 0 \tag{4}$$

the population in the excited state exceeds that in the ground state and α(ν) becomes negative. I(l) then becomes:

$$I(l) = I_0 \exp[\gamma(\nu)l] \tag{5}$$

where γ(ν) is the so-called small gain coefficient. Passage of a light beam through an inverted medium results in amplification of the beam; lasers operate on the basis of this condition.

Figure 2 is a schematic representation of an operational laser[16]; a simple laser consists of an active medium that can be brought to the condition of population inversion while being contained in a cavity consisting of a pair of parallel mirrors. In such a case, since spontaneous emission is isotropic, all the emitted photons can escape through the side

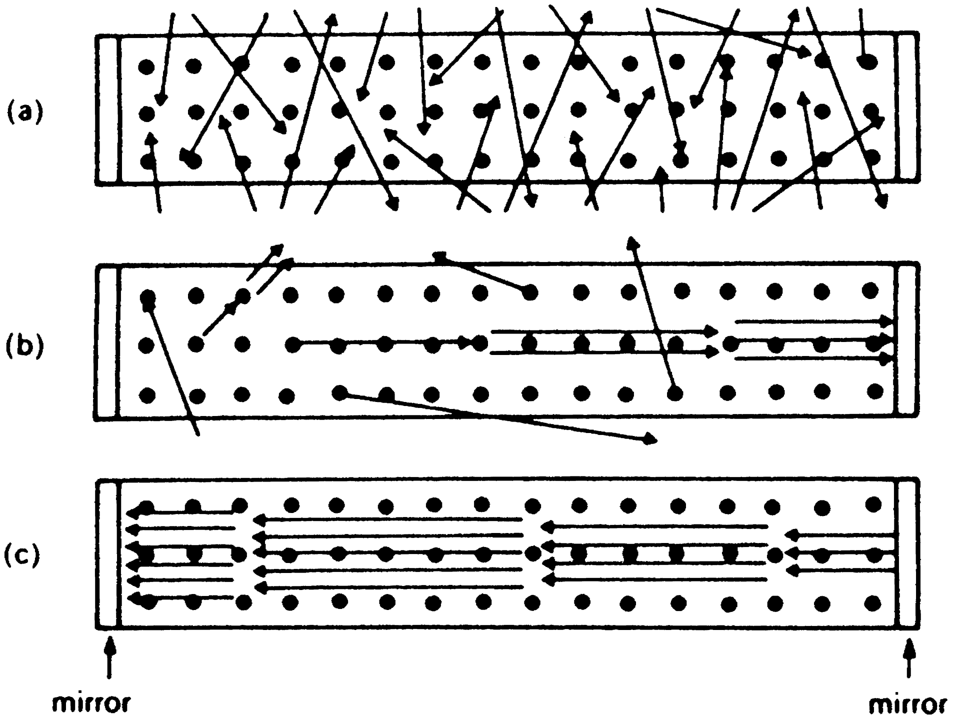

Figure 2 Schematic representation of the process leading to laser action in a simple resonant cavity. The end mirrors are flat and parallel to each other and form a Fabry-Perot interferometer; they need not be attached to the active medium. (a) Spontaneously emitted photons escape the cavity through the side walls, (b) photons emitted in a direction parallel to the cavity axis cannot escape and can instead stimulate others excited centers into emitting in the same direction, (c) photons traveling parallel to the cavity axis are reflected back and forth and produce the laser output. (Adapted from Henderson, B. and Imbusch, G.F., *Optical Spectroscopy of Inorganic Solids*, Oxford Science Publications, Oxford, 1989, chaps. 4 and 11. With permission.)

walls except those that travel parallel to the axis of the cavity. These photons can then be reflected back and forth between the mirrors, stimulating other excited atoms to emit colinearly; the gain per pass can be written as

$$G_M = \exp\left[\gamma(\nu)L\right] \tag{6}$$

where L is the length of the active medium. The magnitude of the gain needs to be compared to the losses incurred during transit of the photons in the laser medium in order to determine where laser action can be achieved; losses in the cavity can occur because of light scattering and/or absorption by the medium at the emission wavelength and by transmission and diffraction effects at the end mirrors. The losses may be expressed in terms of cavity decay time τ_c, i.e., the time required for a beam to decrease to 1/e of its original intensity,

$$\tau_c = \frac{nL}{c\Delta} \tag{7}$$

where Δ is the cavity loss coefficient, which includes all the photon loss sources. This decay time determines the quality or Q-factor of the cavity; for lasers, Q values run in the vicinity of 10^6.

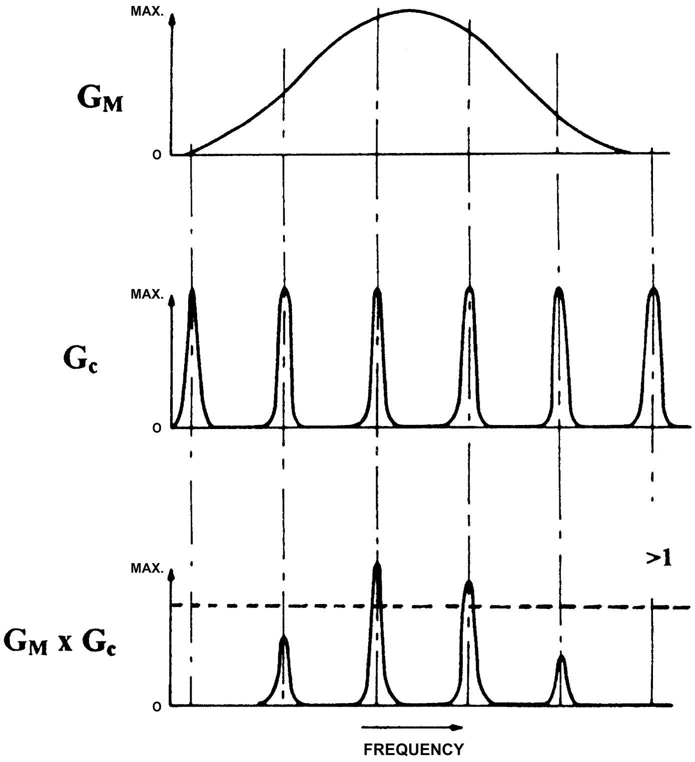

Figure 3 G_M and G_c are the gain/pass of the inverted material and of the Fabry-Perot interferometer, respectively. Laser oscillations occur when the product of these two gains exceeds 1.

Combining the above, one obtains the single pass gain G of the system:

$$G = G_M G_c = \exp\left[\gamma(\nu)L - \Delta\right] \tag{8}$$

In order to achieve laser action, G needs to be larger than 1 and this determines the threshold condition as:

$$\frac{\lambda^2 c \Delta N_t \tau_c}{8\pi n^3 \tau_R}\Gamma(\nu) \geq 1 \tag{9}$$

Eq. 9 is the necessary condition for obtaining laser action. The exact frequency position of the laser beam depends on the modal structure of the cavity as well as the lineshape of the emission g(ν); this is illustrated in Figure 3 for the Fabry-Perot cavity depicted in Figure 2. The lineshape of the transition may be intrinsic (homogeneous) or it may arise from random sources (inhomogeneous).[17]

13.3 Operational schemes

It should be clear from Figure 1 that in the presence of radiation at the resonant frequency, the stimulated emission will always be equal to or larger than the absorption probability so that inversion cannot be achieved by pumping directly into the two levels and other electronic states of the system need to be involved in the excitation process. Depending upon the manner in which the system is pumped, solid-state lasers may be classified into two categories, i.e., three- and four-level lasers. Figure 4 shows schematically the pumping cycle for a three- and a number of four-level laser systems. The properties and threshold conditions for pulsed and cw operation for three- and four-level lasers have been thoroughly analyzed and discussed in the literature.[18]

The ruby laser (Al_2O_3:Cr^{3+}) is prototypical of the three-level laser system; the energy levels and spectra of Cr^{3+} are discussed in Section II of this handbook. Laser action is achieved by broad-band excitation of the $^4T_1$ and $^4T_2$ bands in the blue-green (level 3); ions excited to these levels relax rapidly and nonradiatively to the metastable ^2E level (level 2). Laser action occurs in the $^2E \rightarrow {}^4A_1$ (R-line) transition, with the $^4A_1$ state (level 1) being the ground state; this transition is partially forbidden and thus has a long radiative lifetime; a metastable state such as the ^2E serves as a reservoir for the excited-state population needed to attain inversion, $N_2 > N_1$.[3,4]

Four-level lasers are exemplified by the Nd^{3+} ion in YAG; the relevant levels involved are shown in Figure 4. Again, the spectroscopic properties of the lanthanides have been discussed in detail in Section II. NIR laser action occurs between the metastable $^4F_{3/2}$ (level 3) and the $^4I_{11/2}$ (level 2), which is some 2000 cm^{-1} above the $^4I_{9/2}$ (level 1) ground state. Inversion between levels 2 and 3 is obtained by pumping the $^4F_{5/2}$ and higher Stark manifold (level 4); ions excited into these states decay rapidly to the lasering state through the emission of phonons. Similarly, ions in the terminal state of the laser return efficiently to the ground state via the same nonradiative process; because of this, the population of level 2 is small and the condition for laser action, $N_3 > N_2$, can be readily satisfied.[3,4]

The majority of lasers that have been operated, such as the two cited above, involve transitions between pure electronic states (zero-phonon lines) within the same atomic configuration. Although the output frequency can be tuned to some extent, these solid-state lasers are essentially monofrequency devices. Tunable output over a larger range is possible if vibronically assisted or sideband transitions are employed as the radiation source; the assisted transition reflects in some sense the density of states of the lattice excitations as well as the ion lattice coupling strength and can be quite broad. The so-called vibronic or phonon terminated lasers are a variant of the four-level system in which the terminal state of the laser is an unoccupied phonon rather than an electronic state. This concept was initially demonstrated in MgF_2:Ni^{2+} by Johnson and co-workers[19]; more recent examples of tunable solid-state lasers include various types of F centers in alkali halide host[14] and Cr^{3+}-activated alexandrite ($BeAl_2O_4$).[20]

13.4 *Materials requirements for solid-state lasers*

Though laser action has been reported in many activated solid-state systems, not all of these systems are viable in terms of practicality and usefulness; solid-state lasers are attractive because they can provide high power from compact spaces. In order to be fully competitive with other devices; solid-state lasers need to be efficient and easy to operate at room temperature. The desirable optical and physical properties of materials to be used in this context have been established from experience. First and most obvious, the host material should be readily available in a suitable and workable size and the costs of synthesis and growth need to be reasonable. The host material should be as optically inert as possible; for example, the crystal or glass containing the active ions or centers should be transparent to the radiation produced by the laser and should not be susceptible to optically induced color centers and defects. The host should also allow the incorporation of the activator ions at the proper site and with the necessary valence. In addition, the materials should possess sufficient physical strength to withstand

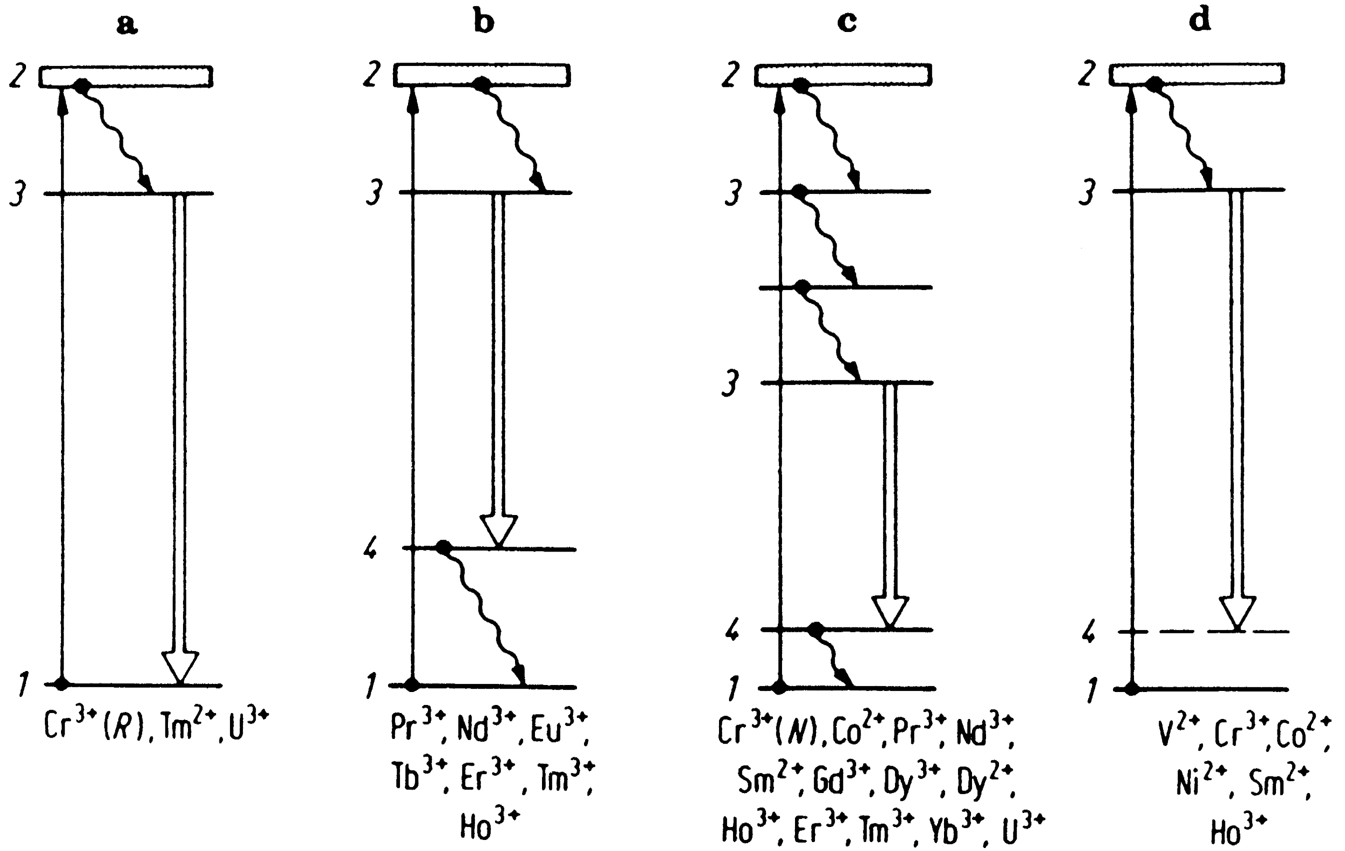
a
b
c
d
2
3
1
4
Cr3+(R), Tm2+, U3+
Pr3+, Nd3+, Eu3+, Tb3+, Er3+, Tm3+, Ho3+
Cr3+(N), Co2+, Pr3+, Nd3+, Sm2+, Gd3+, Dy3+, Dy2+, Ho3+, Er3+, Tm3+, Yb3+, U3+
V2+, Cr3+, Co2+, Ni2+, Sm2+, Ho3+

Figure 4 Three- and four-level laser operating schemes. Double arrows represent the stimulated transition, while wavy arrows indicate nonradiative relaxation processes. The dashed line indicates the presence of a phonon or vibrational level. Case (a) is for three-level systems exemplified by ions such as Cr^{3+}; ions operating in the different four-level schemes, (b) to (d), are noted at the bottom of figure.

mechanical shaping and optical polishing and be of sufficiently good optical quality that scattering and other loss mechanisms can be ignored. Though hygroscopic materials have been occasionally used as hosts, chemical inertness is obviously a desirable property that simplifies laser design considerations. Depending upon the requirements placed on the laser, additional factors such as the thermal conductivity and the nonlinear refractive index of the host material need to be considered to reduce higher order effects in the laser output.[3,4]

In addition, certain basic requirements can also be placed on the nature of the optical transitions to be stimulated. For the three- and four-level systems, the conditions for optimizing the efficiency of the laser have already been alluded to in the previous section.[18] Further, in order to minimize the threshold, the radiative lifetime of the transition needs to be as long as possible; this is equivalent to saying that the metastable state should be as stable as possible against nonradiative or other channels that dissipate the energy in the excited state. It is also desirable to have a transition that has a narrow intrinsic or homogenous width, and to have strong absorption bands that feed the metastable state. Some of the optical parameters of the activated materials can be improved by introducing other ions that can serve as sensitizers for the metastable state and as deactivators for the terminal state.[4,21]

13.5 Activator ions and centers

Invariably in the activated laser materials of interest here, the positive impurity ion replace the cation in the ionic host material. With the exception of U^{3+}, all of the ions used as activators in solid-state lasers belong to the transition metal $(3d)^n$ or to the lanthanide $(4f)^n$ series of elements.[4] However, a number of additional ions in solids have shown optical gain but not as laser sources; a summary of these ions and lattices appear in Table 1.

In the case of the transition metal series, divalent Co, Ni, and V, trivalent Cr and Ti, and tetravalent Cr in various lattices have been stimulated; these systems have been operated as single-frequency as well as broadly tunable devices. The laser transitions in this series are intraconfigurational, i.e., the excited and terminal states originate in the same $(3d)^n$ electronic configuration strongly modified by the crystal field. The spectral coverage of the 3*d* solid-state lasers reported to date is summarized in Figure 5.[4,22]

All thirteen lanthanide or rare-earth ions have been lasered in solids, mostly in their trivalent form. Because of better shielding the 4f states are only weakly affected by the crystal field and intraconfigurational transitions are generally weak because of parity considerations. Most of the laser transitions in the blue and near-UV entail the 5*d* configuration; the transition is then allowed and the resultant luminescence is broad and can be used as tunable source.[23] The same holds for Sm^{2+}.[8] A summary of the wavelengths that can be generated by lanthanide ions is shown in Figure 6.

When defects and vacancies are created in certain ionic solids, free electrons or holes can be trapped at these imperfections; these complexes can be optically active and are generically known as F-centers. Though a flashlamp-pumped F_A was first operated as early as 1965,[24] their potential as a solid-state tunable source was not realized until 1974.[25] The first tunable laser employed the F_A (II) in KCl and RbCl; since then, many other types of defect centers have been made into tunable lasers. Some of the F-centers tend to be unstable under various pumping conditions; in order to stabilize the centers, the lasers are either operated at cryogenic temperatures or additional ions are introduced into the lattice to act as electron donors or getters. The frequency coverage provided by F-center lasers is summarized in Figure 7.[14,26]

Table 1 Ions in Crystal Exhibiting Gain

Wavelength (μm)	Ion	Crystal	Temperature (K)	Ref.
0.219[a]	F(2*p*)–Ba(5*p*)	BaF_2	300	1,2
~0.337	Ag^+	RbBr, Kl	5	3,4
0.388–0.524	Ti^{4+}	Li_2GeO_3	300	5
0.392	Biexcition	CuCl:NaCl	77	6,7
0.407	Tl^+	CsI		8
0.420	Tl^+	KI		9
0.442	In^+	KCl		10
0.500–0.550	UO_2^{2+}	$Ca(UO_2)(PO_4)\cdot H_2O$		11
0.5145	Cu^+	Na–β″–alumina[b]	300	12
0.6328	Cu^+	Ag–β″–alumina	300	12
0.700–0.720	Rh^{2+}	$RbCaF_3$	300	13
1.064	V^{2+}	$KMgF_3$		14
~1.080[c]	Nd^{3+}	ZnS film	77	15
1.15	Mn^{5+}	Ca_2PO_4Cl	300	16
~1.2	Mn^{5+}	$Sr_5(PO_4)_3Cl$	300	16

Note: References for table:

1. Itoh, M. and Itoh, H., *Phys. Rev.*, B46, 15509, 1992.
2. Liang, J., Yin, D., Zhang, T. and Xue, H., *J. Lumin.*, 46, 55, 1990.
3. Schmitt, K., *Appl. Phys.*, A38, 61, 1985.
4. Boutinaud, P., Monnier, A., and Bill, H., *Rad. Eff. Def. Solids*, 136, 69, 1995.
5. Loiacono, G.M., Shone, M.F., Mizell, G., Powell, R.C., Quarles, G.J., and Elonadi, B., *Appl. Phys. Lett.*, 48, 622, 1986.
6. Masumoto, Y. and Kawamura, T., *Appl. Phys. Lett.*, 62, 225, 1993.
7. Masumoto, Y., *J. Lumin.*, 60/61, 256, 1994.
8. Pazzi, G.P., Baldecchi, M.G., Fabeni, P., Linari, R., Ranfagni, A., Agresti, A., Cetica, M., and Simpkin, D.J., *SPIE*, 369, 338, 1982.
9. Nagli, L.E. and Plovin, I.K., *Opt. Spectrosc. (USSR)*, 44, 79, 1978.
10. Shkadeverich, A.P., in *Tunable Solid State Lasers*, Shand, M.L. and Jenssen, H.P., Eds., Optical Society of America, Washington, D.C., 1989, 66.
11. Haley, L.V. and Koningstein, J.A., *J. Phys. Chem. Solids*, 44, 431, 1983.
12. Barrie, J., Dunn, B., Stafsudd, O.M., and Nelson, P., *J. Lumin.*, 37, 303, 1987.
13. Powell, R.C., Quarles, G.L., Martin, J.J., Hunt, C.A., and Sibley, W.A., *Opt. Lett.*, 10, 212, 1985.
14. Moulton, P.F., in *Materials Research Society Symposium Proceedings*, 24, 393, 1984.
15. Zhong, G.Z. and Bryant, F.J., *Solid State Commun.*, 39, 907, 1981.
16. Capobianco, J.A., Cormier, G., Moncourge, R., Manaa, H., and Bertinelli, M., *Appl. Phys. Lett.*, 60, 163, 1992.

[a] Core-valence cross-over transition: $F^-(2p) \rightarrow Ba^{2+}(5p)$.

[b] Typical composition: $Na_{1.67}Mg_{0.67}Al_{10.33}O_{19}$.

[c] Direct current electroluminescence (DCEL) and cathodoluminescence.

13.6 *Host lattices*

There are a multitude of solids, both crystalline and amorphous, that will accommodate the desired activator ions and in which the centers can emit light efficiently. As the host lattice determines the environs of the activator and hence the position of the luminescence and the radiative and nonradiative transition probabilities, the choice of the appropriate solid depends on the technical specifications placed on the laser.

Glasses have been used in large solid-state laser systems; this is because glassy materials may be formed in large sizes at not totally forbidden costs and can be engineered and tailored to meet technical requirements to a certain extent. The majority of the glasses used for laser purposes have been compounded materials consisting of so-called network

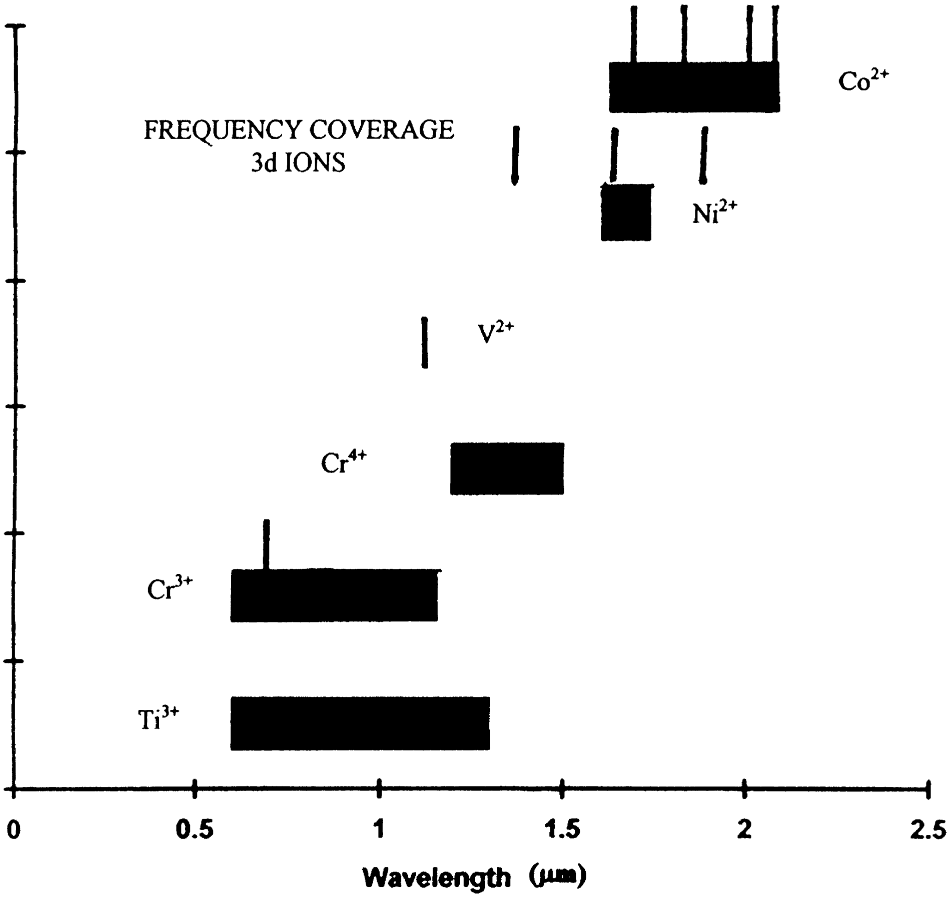

Figure 5 Summary of transition metal ions that have been lased to date and their frequency coverage. Each line indicates a sharp transition that may have been lased in several host materials. The broad bars represent ranges over which the ions have been tuned; again, this may have been done in several host lattices.

formers and network modifiers; ions entering glasses depending upon size and charge can enter network or modifier sites. For complex laser glasses that already contain modifiers such as alkali and alkaline earth ions, activator ions generally are incorporated as additional modifiers. Several categories of glasses have been employed in lasers; these include silicate, phosphate, and fluoride glasses and mixtures such as fluorophosphates, etc. A comprehensive description of laser glasses is to be found in Reference 3.

Crystals have overall better physical and optical properties from the viewpoint of laser performance, but they are more expensive and difficult to grow in large sizes. Again, many crystalline hosts have been used for laser systems incorporating both transition metal and rare-earth ions; these include oxides, chlorides, and fluorides, as well as mixed fluoride and oxide crystals. Some of the common laser host lattices are listed in Table 2.[3,4]

The alkali halides such as LiF, NaCl and KBr when properly treated (additive coloration) and/or exposed to high energy (X-ray, γ ray or high energy electron) radiation produce the required F centers. Again the materials in which laser action has been reported are illustrated in Figure 7.[14,26]

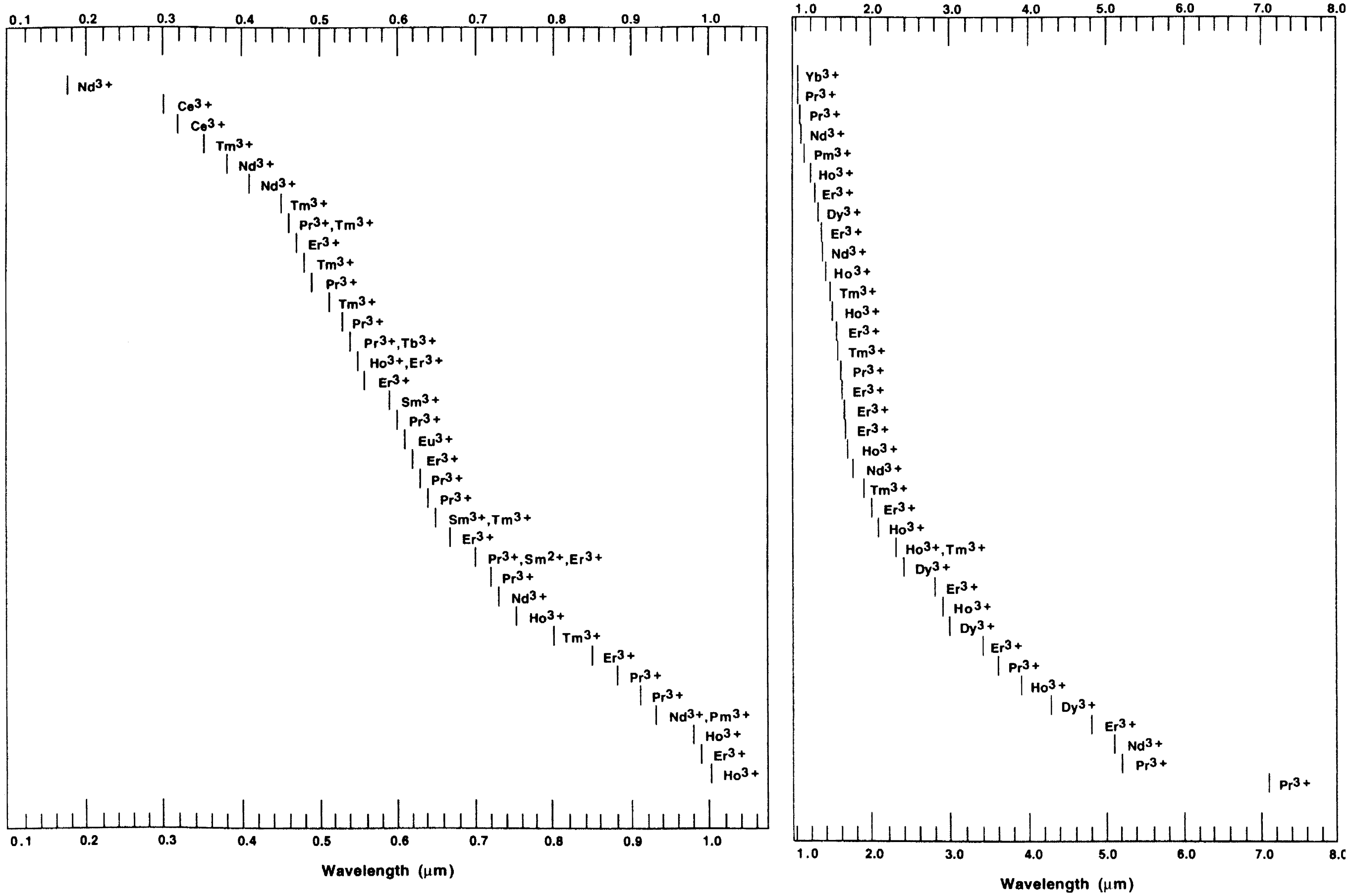

Figure 6 Summary of all laser wavelengths that have been generated by rare-earth ions. Each line indicates transitions for an ion that may have been lased in one or more host lattices. (Adapted from Payne, S.A. and Albrecht, G.F., Solid State Lasers, in *Encyclopedia of Lasers and Optical Technology*, R.A. Meyers, Ed., Academic Press, New York, 1991, 603; see also Weber, M.J., *Handbook of Laser Wavelengths*, CRC Press, Boca Raton, FL, to be published. With permission.)

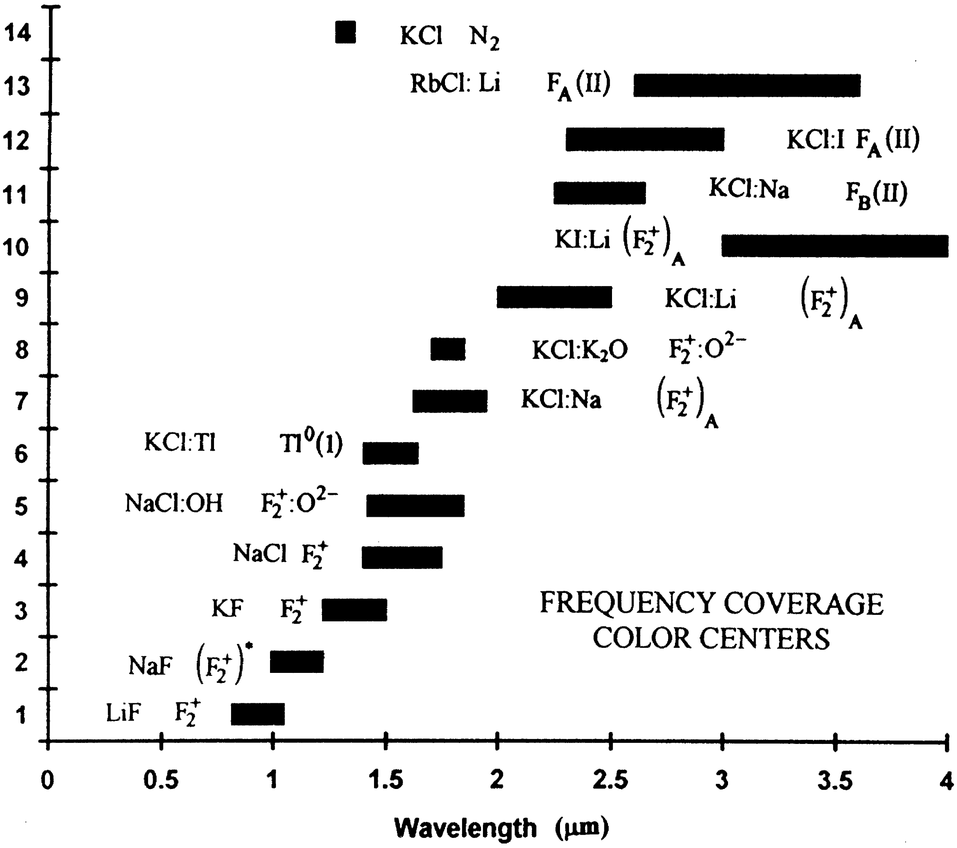

Figure 7 Summary of the wavelengths that have been generated and the frequency coverage provided by F-center lasers in various alkali halide hosts. Some of these lasers operate stably only at cryogenic temperatures. (From Pollack, C.R., Color Center Lasers, in *Encyclopedia of Lasers and Optical Technology*, R.A. Meyers, Ed., Academic Press, New York, 1991, 9. With permission.)

13.7 *Conclusions*

To date, nearly 500 combinations of host lattice and activator ion have shown laser action. Of course, only a small percentage of the large number of laser systems reported have been developed into viable practical or commercial systems.[3] A sampling of the solid-state lasers that are commercially available appears in Table 3.

Indeed, though solids were the first medium in which laser action was obtained, solid-state lasers were soon outperformed and superseded for a time by gas, ion, and liquid dye lasers. The only exceptions to this statement were ruby and Nd^{3+} in glass or in YAG, their principal disadvantage being their limited frequency coverage capabilities. Renewed interest arose in the solid-state system with the discovery and advent of various devices tunable over large spectral ranges. As mentioned earlier, tunability was first achieved in F-center systems; this was followed by Cr systems in so-called "weak field" lattices such as alexandrite and emerald and Ti^{3+} in Al$_2$O$_3$.[27] Tunable laser action has also been demonstrated in systems activated by transition metal ions in unusual valence states, such as Cr^{4+}.[28,29] More recently, new interest has been shown in the Ce^{3+} 5*d* states in fluoride crystals as a potential source of tunable UV. In all the above cases, invariably the broad-band luminescence required to obtain tunable action entails phonon-assisted transitions and it is indeed in this area that one looks for additional activities and developments.

Table 2 Abbreviated List of Laser Crystals

- Fluorides[a]
  - BaF_2
  - BaY_2F_8
  - CaF_2
  - $KMgF_3$
  - $LiYF_4$ (YLF)
  - $LiBaAlF_6$
  - $LiCaAlF_6$
  - $LiSrAlF_6$
  - MgF_2
  - SrF_2
- Oxides[a]
  - Al_2O_3
  - $BeAl_2O_4$
  - $Bi_4Ge_3O_{12}$
  - $CaAl_4O_7$
  - $Ca(NbO_4)_2$
  - $CaMoO_4$
  - $CaWO_4$
  - $GdAlO_3$
  - $Gd_3Sc_2Ga_3O_{12}$
  - $Gd_3Ga_5O_{12}$
  - $KY(WO_4)_2$
  - LaP_5O_{14}
  - $LiNbO_3$
  - $LuAlO_3$
  - $Lu_3Al_5O_{12}$
  - MgO
  - $YAlO_3$ (YALO)
  - $Y_3Al_5O_{12}$ (YAG)
  - $Y_3Ga_5O_{12}$
  - Y_2O_3
  - $Y_3Sc_2Al_3O_{12}$
  - $Y_3Sc_2Ga_3O_{12}$
  - YVO_4
- Miscellaneous
  - $Ca_5(PO_4)_3F$
  - $LaBr_3$
  - $LaCl_3$
  - La_2O_2S

Note: Two or more ions have been stimulated in the sample crystals listed above.

[a] Mixed fluoride and oxide crystals such as CaF_2:ErF_3, CaF_2:CeO_2, and $YScO_3$ have also been used as hosts.[4]

Semiconductor lasers constitute a large class of solid-state devices that continues to develop rapidly, but which are not discussed here; though initially this type of laser was made of stand-alone chips, the techniques employed now are identical to the technology used to manufacture large-scale integrated electronic devices. The optical properties of light-emitting semiconductors were discussed in Part II of this Handbook, and detailed discussion of semiconductor laser devices is to be found elsewhere. These lasers have found many practical applications and, as a consequence, they are very reliable and

Table 3 Brief Compendium of Commercial Solid State Laser*⁺

Material	Output (µm)	Mode	Outputs (in J or W)
Alexandrite (Cr^{3+} beryl)	0.72–0.79	Pulsed: 1–50 pps	0–2-1.0 J
	0.75	cw diode pumped	0.1–0.2 W
Er: YAG	1.560	Pulsed: 2–50 pps	1-3 J
	2.950	Pulsed: 1–15 pps	1.0 J
Ho: YAG	2.100	Pulsed: 1–20 pps	0.01-0.25 J
	2.123	Pulsed: 5–30 pps	30-50 J
Nd: YAG	1.054, 1.064	Pulsed: 0.1–1000 pps	0.1–300 J
	1.064	cw diode pumped	0.1–100 W
Nd: YLF	1.053	Pulsed, 1–5000 pps	0.02-0.20 J
	1.047, 1.053	cw diode pumped	0.15-10 W
Nd: YVO_4	0.355	Pulsed: 100,000 pps	1-30 µJ
	1.064	cw diode pumped	0.1-20 W
Ruby: Cr^{3+} sapphire	0.694	Pulsed, 1–5 pps	0.1–1.5 J
Ti^{3+}: Sapphire	0.723–0.990	Pulsed, $1–10^9$ pps	0.1-1.0 J
	0.70–1.10	cw diode pumped	0.3-5.0 W

*From *The Laser Focus World* Buyer's Guide 2003, vol. 38 (Penn Well Publications, Nashua, NH).

⁺Most of the lasers cited in table are available with built-in frequency multiplier crystals.

reasonable in cost. High-power semiconductor diode laser bars are attractive as pump sources for other solid-state lasers because of their compactness, efficiency, and ease of use; the incorporation of diode lasers as pumped sources has been commercialized.

In this brief review, the focus has been on inorganic systems only, leaving a large class of materials that can be made into solids uncovered. Tunable laser outputs were obtained early on in various organic laser dyes dissolved in an appropriate liquid; these dyes were also introduced into gellated sols and into plastics and then made to lase. Readers are referred to the literature for further reading.[13]

It is expected that the use of solid-state lasers will very likely continue to increase in the future. These applications continue to produce a demand for more efficient and more versatile materials that can be used as solid-state laser sources. This brief review hopefully serves as a useful starting point for fulfilling these technical demands.

References

1. Schawlow, A.L. and Townes, C.H., Infrared and optical maser, *Phys. Rev.*, 112, 1940, 1958.
2. Maiman, T.H., Stimulated optical radiation in ruby masers, *Nature*, 187, 493, 1960.
3. Weber, Marvin J., Ed., *CRC Handbook of Laser Science and Technology* (CRC Press, Boca Raton, FL); Vol. I. Lasers and Masers (1982), Vol. II. Gas Lasers (1982), Vol. III-V. Optical Materials: Parts 1-3 (1986-1987), Supplement 1. Lasers (1991), Supplement 2. Optical Materials (1995).
4. Kaminskii, A.A., *Laser Crystal*, Springer Series in Optical Sciences 14 (Springer Verlag, Berlin; 2nd Ed., 1989); *Crystalline Lasers: Physical Processes and Operating Schemes* (CRC Press, Boca Raton, FL, 1996).
5. Einstein, A., Strahlungs-Emissions und -Absorption nach der Quantentheorie, *Verh. Dtsch Phys. Ges.*, 18, 318, 1916.
6. Gordon, J.P., Zeiger, H.J., and Townes, C.H., Molecular microwave oscillator and new hyperfine structure in the microwave spectrum of NH_3, *Phys. Rev.*, 95, 282, 1954.
7. Basov, N.G. and Prokhorov, A.M., Molecular beams application for radiospectroscopic study of molecular spectra, *Zh. Eksp. Teor. Fiz.*, 27, 431, 1954.

8. Sorokin, P.P. and Stevenson, M.J., Stimulated infrared emission from trivalent uranium, *Phys. Rev. Lett.*, 5, 557, 1960; Solid-state optical maser using divalent samarium in calciumfluoride, *IBM J. Res. Dev.*, 5, 56, 1961.
9. Snitzer, E. and Young, C.G., Glass Lasers in *Lasers 2*, A.K. Levine, Ed., Marcel Dekker, New York, 1968, 191.
10. Johnson, L.F. and Nassau, K., Infrared fluorescence and stimulated emission of Nd^{3+} in $CaWO_4$, *Proc. IRE*, 48, 1704, 1961.
11. Javan, A., Bennett, Jr., W.R., and Herriot, D.R., Population inversion and continuous optical maser oscillations in a gas discharge containing a He-Ne mixture, *Phys. Rev. Lett.*, 6, 106, 1961.
12. Hall, R.N., Fenner, G.E., Kingsley, J.D., Soltys, T.J., and Carlson, R.O., Coherent light emission from GaAs junctions, *Phys. Rev. Lett.*, 9, 366, 1962.
13. Schafer, F.P., Ed., *Dye Lasers, Topics in Applied Physics 1*, Springer Verlag, Berlin, 1973.
14. Mollenauer, L.F., Color Center Lasers, in *Methods of Experimental Physics*, 15B, C.L. Tang, Ed., Academic Press, New York, 1979, chap. 6.
15. Geusic, J.E., Marcos, H.M., and Van Uitert, L.G., Laser oscillations in Nd-doped yttrium aluminum, yttrium gallium and gadolinium garnets, *Appl. Phys. Lett.*, 4, 182, 1964.
16. Henderson, B. and Imbusch, G.F., *Optical Spectroscopy of Inorganic Solids*, Oxford Science Publications, Oxford, 1989, chaps. 4 and 11.
17. Yen, W.M., Scott, W.C., and Schawlow, A.L., Phonon-induced relaxation in the excited states of trivalent praseodynium in LaF_3, *Phys. Rev.*, 136, A271, 1964.
18. Yariv, Amnon, *Quantum Electronics*, John Wiley, New York, 3rd ed., 1989.
19. Johnson, L.F., Dietz, R.E., and Guggenheim, H.J., Optical maser oscillations from Ni^{2+} in MnF_2 involving simultaneous emission of phonons, *Phys. Rev. Lett.*, 11, 318, 1963; see also: Phonon terminated optical masers, *Phys. Rev.*, 149, 179, 1966.
20. Walling, J.C., Heller, D.F., Samelson, H., Harter, D.J., Pete, J.A., and Morris, R.C., Tunable alexandrite lasers, Development and performance, *IEEE J. Quantum Electronics*, QE-21, 1568, 1985.
21. Auzel, F., Materials for Ionic Solid State Lasers, in *Spectroscopy of Solid State Laser-type Materials*, B. di Bartolo, Ed., Ettore Majorama International Science Series 30, Plenum Press, New York, 1987, 293.
22. Payne, S.A. and Albrecht, G.F., Solid State Lasers, in *Encyclopedia of Laser and Optical Technology,* R.A. Meyers, Ed., Academic Press, New York, 1991, 603; see also Weber, M.J., *Handbook of Laser Wavelengths*, CRC Press, Boca Raton, FL, to be published).
23. Ehrlich, D.J., Moulton, P.F., and Osgood, Jr., R.M., Optically pumped Ce:LaF_3 at 286 nm, *Opt. Lett.*, 5, 539, 1980.
24. Fritz, B. and Menke, E., Laser effect in KCl with F_A(Li) centers, *Solid State Commun.*, 3, 61, 1965.
25. Mollenauer, L.F. and Olson, D.H., Broadly tunable lasers using color centers, *J. Appl. Phys.*, 24, 386, 1974.
26. Pollock, C.R., Color Center Lasers, in *Encyclopedia of Lasers and Optical Technology,* R.A. Meyers, Ed., Academic Press, New York, 1991, 9.
27. Moulton, P.F., Spectroscoic and laser characteristics of Ti:Al_2O_3, *J. Opt. Soc. Am.*, B3, 4, 1986.
28. Petrocevic, V., Gayen, S.K., and Alfano, R.R., Continuous wave operation of chromium doped forsterite, *Opt. Lett.*, 14, 612, 1989.
29. Jia, W. Eilers, H., Dennis, W.M., Yen, W.M., and Shestakov, A.V., Performance of Cr^{4+}:YAG laser in the near infrared, *OSA Proceedings on Advanced Solid State Lasers*, L.L. Chase and A.A. Pinto, Eds., OSA, Washington, D.C., 1992, Vol. 3, 31.

part four

Measurements of phosphor properties

chapter fourteen — sections one–five

Measurements of luminescence properties of phosphors

Taisuke Yoshioka and Masataka Ogawa

Contents

14.1 Luminescence and excitation spectra 844
  14.1.1 Principles of measurement 844
  14.1.2 Measurement apparatus 845
    14.1.2.1 Monochromator 845
    14.1.2.2 Light detector 849
    14.1.2.3 Signal amplification and processing apparatus 856
  14.1.3 Excitation sources 858
    14.1.3.1 Ultraviolet and visible light source 859
    14.1.3.2 Electron-beam excitation 864
  14.1.4 Some practical suggestions on luminescence measurements 867
14.2 Reflection and absorption spectra 867
  14.2.1 Principles of measurement 867
  14.2.2 Measurement apparatus 869
14.3 Transient characteristics of luminescence 872
  14.3.1 Principles of measurement 872
  14.3.2 Experimental apparatus 873
    14.3.2.1 Detectors 873
    14.3.2.2 Signal amplification and processing 874
    14.3.2.3 Pulse excitation source 876
14.4 Luminescence efficiency 876
  14.4.1 Principles of measurement 876
  14.4.2 Measurement apparatus 877
    14.4.2.1 Ultraviolet excitation 877
    14.4.2.2 Electron-beam excitation 879
14.5 Data processing 880
  14.5.1 Spectral sensitivity correction 880
  14.5.2 Baseline correction 882
  14.5.3 Improvement of signal-to-noise ratio 882
Appendix 883
References 885

The luminescence properties of a phosphor can be characterized by its emission spectrum, brightness, and decay time. The absorption and reflectance spectra of phosphors provide additional information pertaining to both the basic luminescence mechanisms and their practical application.

This chapter describes how to measure the optical properties of a phosphor. The apparatus used and the method of measurement are introduced. The operating principles of each instrument employed are explained. Methods of obtaining meaningful data from raw experimental data are given.

14.1 Luminescence and excitation spectra

14.1.1 Principles of measurement

The luminescence spectrum is obtained by plotting the relationship between the wavelength and the intensity of the emitted light from a sample excited by an appropriate excitation source of constant energy. The excitation source can be light, an electron beam, heat, X-rays, or radiation from radioactive materials. The spectrum is obtained using a monochromator (see 14.1.2) equipped with an appropriate light detector.

In the case of an excitation spectrum, on the other hand, the relationship is obtained by observing changes in the emitted light intensity at a set wavelength while varying the excitation energy. When the excitation source is light, single-frequency light produced by a monochromator impinges on the sample and the emitted light intensity is recorded as the excitation wavelength is varied.

In a spectrum, light intensity at a given wavelength is expressed along the ordinate and the wavelength along the abscissa. The units of the ordinate are either irradiance E ($\mathrm{W \cdot m^{-2}}$) or number of photons E_p ($\mathrm{photons \cdot m^{-2}}$). The units of the abscissa are expressed in terms of wavelength λ (nm) or wave number $\tilde{\nu}$ ($\mathrm{cm^{-1}}$).

Using these units, the spectrum irradiance is expressed as:

$$E(\lambda) = \frac{dE}{d\lambda} \qquad \left(\mathrm{W \cdot m^{-2} \cdot nm^{-1}}\right) \tag{1}$$

or

$$E(\tilde{\nu}) = \frac{dE}{d\tilde{\nu}} \qquad \left(\mathrm{W \cdot m^{-2} \cdot \left(cm^{-1}\right)^{-1}}\right) \tag{2}$$

and the spectral photon irradiance is expressed as:

$$E_p(\lambda) = \frac{dE_p}{d\lambda} \qquad \left(\mathrm{photons \cdot m^{-2} \cdot nm^{-1}}\right) \tag{3}$$

or

$$E_p(\tilde{\nu}) = \frac{dE_p}{d\tilde{\nu}} \qquad \left(\mathrm{photons \cdot m^{-2} \cdot \left(cm^{-1}\right)^{-1}}\right) \tag{4}$$

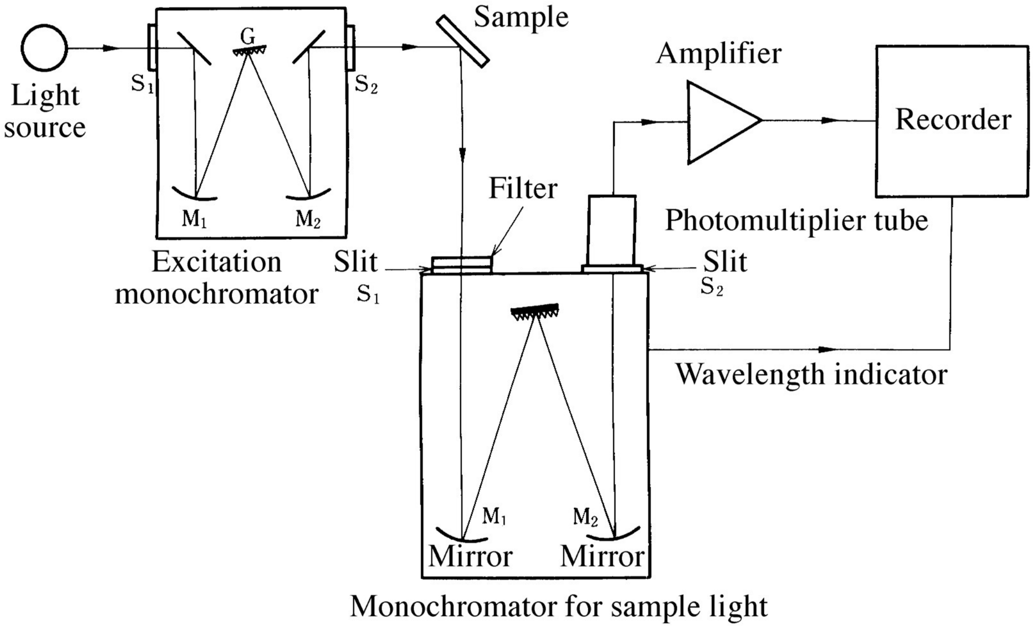
Sample
Amplifier
Recorder
Light source
S1
G
S2
M1
M2
Excitation monochromator
Slit S1
Filter
Photomultiplier tube
Slit S2
Wavelength indicator
M1
M2
Mirror
Mirror
Monochromator for sample light

Figure 1 Spectroscopic measurement apparatus.

The units used depend on the purpose of the experiment. For energy efficiency, irradiance is employed and for quantum efficiency, photon irradiance is employed. The luminosity of a phosphor is expressed in terms of irradiance, which is obtained by integrating the spectral data, $E(\lambda)$, multiplied by the relative photopic spectral luminous efficiency, $V(\lambda)$, divided by the light equivalence value,[1,2] $K_m = 673$ lm·Watt^{-1}; that is,

$$L = K_m \int_0^{\infty} V(\lambda)E(\lambda)d\lambda, \qquad \text{lm} \cdot \text{m}^{-2} \tag{5}$$

14.1.2 Measurement apparatus

The apparatus for measuring the spectral characteristics of phosphors is shown in Figure 1. The excitation source consists of the light source and a monochromator, which selects a specific wavelength range from the incoming light. (The monochromator can be replaced by a filter.) The light emitted from the sample is analyzed by a monochromator equipped with a light detector. The light detector transforms the photons into electrical signals. After the signals are amplified, they are recorded, typically on a strip chart recorder. It is often convenient to collect all spectral data in the form of digitized electrical signals and to use a computer for further processing the data.

The equipment used to measure the fluorescence characteristics of phosphors is as follows.

14.1.2.1 Monochromator

The monochromator is an apparatus used to select a particular wavelength of light. The monochromator consists of an entrance slit, an exit slit, a dispersing element for polychromatic light, and optics that focus the entrance slit image onto the exit slit. Monochromators can be classified by the dispersing element employed as either prism type, diffraction-

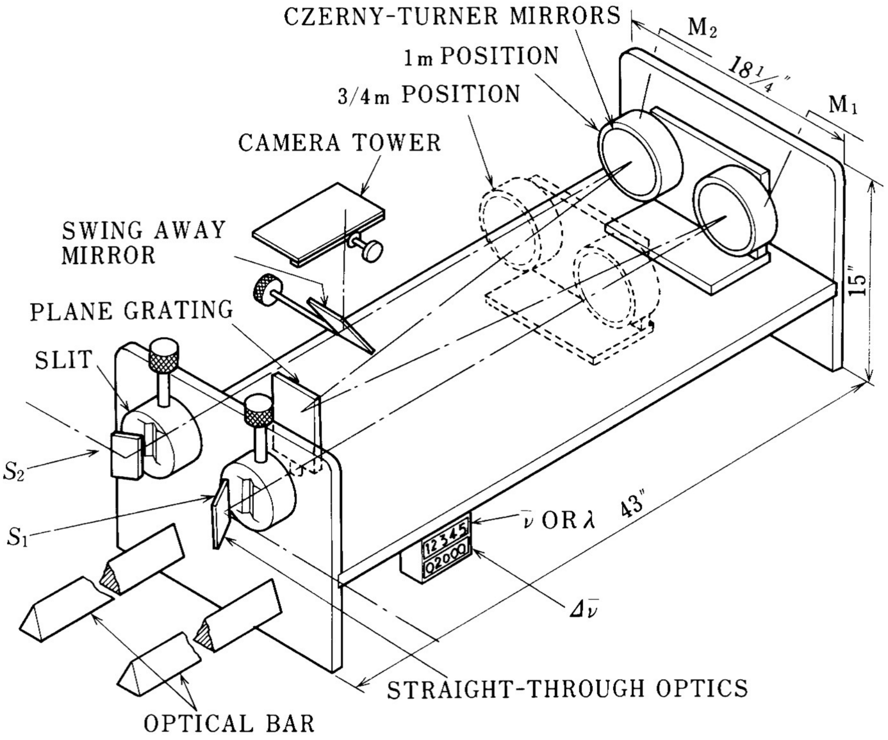

Figure 2 Interior of Czerny-Turner mount grating spectrometer. An illustration of Model 1702 of Jobin-Yvon-Spex is chosen because of its simplicity. This model has been replaced by Model 750M. (From *Model 1702 Instruction Manual*, Jobin Yvon-Spex, Edison, New Jersey. With permission.)

grating type, or interference type, the most popular being the latter two. The interference type is mainly used to measure light in the infrared region because these instruments are fast and have high sensitivity. The prism-type monochromator has the advantage of durability, and can be made very compact. The prism type, however, has lower resolution than the other two types, and is quite often employed as an optical filter for a diffraction-grating monochromator in high-resolution work.

The Czerny-Turner mount shown in Figure 1 is a typical diffraction-grating monochromator configuration.[3] The detailed internal structure can be seen in Figure 2.[4]

The optics of the Czerny-Turner instrument consist of two concave mirrors with equal focal length. The collimator mirror M_1 is positioned at a distance equal to its focal length from the entrance slit S_1. Light entering through the entrance slit is thus collimated and the parallel beam is diffracted by diffraction grating G. The diffracted beam is now monochromatic and is focused by the second concave mirror M_2 on the exit slit. The mirror M_2 is often called the camera mirror. By adjusting the angle of the diffraction grating with respect to the direction of the incident light, the wavelength of the diffracted monochromatic beam can be changed at the exit slit. One of the advantages of the Czerny-Turner mount is that the camera mirror cancels exactly the aberration generated by the collimator mirror, because the configuration is totally symmetric. Also, because the light is incident along the plane perpendicular to the grooves of the diffraction grating, the wavelength dependence on light polarization is small. Other than the Czerney-Turner mount, there are the Ebert-Fastie mount, which has a simpler optical configuration, and the double-grating mount for high-resolution studies.

The brightness of a monochromator is described by the aperture ratio *F*, defined as the focal length of the concave mirror, *f*, divided by its effective diameter *D*:

$$F = \frac{f}{D} \tag{6}$$

The ability to separate two closely spaced spectral lines is expressed in terms of a linear dispersion by:

$$\frac{dx}{d\lambda} = f\frac{d\theta}{d\lambda} \qquad \left(\mathrm{mm}\cdot\mathrm{nm}^{-1}\right) \tag{7}$$

where two spectral lines separated by $d\lambda$ in wavelength at the exit slit are separated by a spatial distance of dx. The reciprocal linear dispersion is more commonly used, however:

$$\frac{d\lambda}{dx} = \frac{1}{f}\frac{d\lambda}{d\theta} \qquad \left(\mathrm{nm}\cdot\mathrm{mm}^{-1}\right) \tag{8}$$

The product of the reciprocal linear dispersion and the slit width gives the separation of the two spectral lines (full width at half maximum) at a given wavelength. For observation of low light intensity, a monochromator having a small *F* number, i.e., having a short focal length, should be used. For high-resolution studies, on the other hand, a monochromator with a longer focal length is generally employed.

Figure 3 shows a microscopic cross-section of an echelette-type planar diffraction grating. As is seen in this figure, the grating has a saw-tooth shape. The angle between the grating plane and the saw-tooth plane is called the blaze angle θ. The grating constant *d* is defined as the pitch of the grooves. Light diffraction occurs when the following geometrical relation is satisfied:

$$m\lambda = d(\sin\alpha + \sin\beta), \qquad (m = 0, \pm 1, \pm 2, \ldots), \tag{9}$$

where α is the angle between the line perpendicular to the plane of the grating and the direction of the incident light, and β is the angle between the same normal and the direction of the diffracted light. Light from adjacent grooves interferes constructively when a multiple, *m*, of the diffracted light wavelength is equal to the difference in the incident and diffracted light path lengths. This integer *m* is called the spectral order.

Geometrical optics describe the reflection condition when the incident angle, the diffraction angle, and the blaze angle satisfy the following relation:

$$\theta = \frac{\alpha + \beta}{2} \tag{10}$$

Under this condition, Eq. 9 becomes:

$$m\lambda = 2d\sin\theta\cos\frac{\beta - \alpha}{2} \tag{11}$$

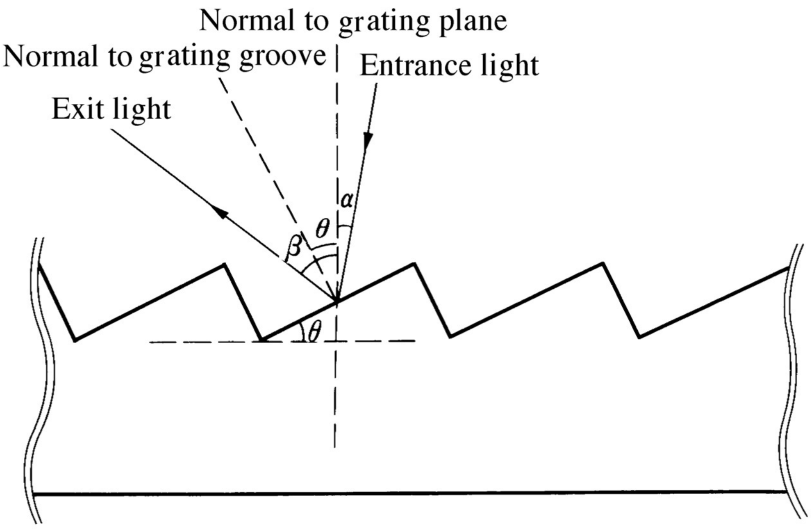

Figure 3 Cross-section of echelette plane grating.

When the incident light is perpendicular to the plane of the grating grooves, $\alpha = \beta = \theta$ holds and the following relation is obtained:

$$m\lambda = 2d \sin\theta \tag{12}$$

The first-order diffracted light is maximized at $\lambda = 2d \sin\theta$ and this λ is called the blaze wavelength.

The wavelength region where echelette gratings are most effectively utilized is defined by dividing the blaze wavelength by the grating order. For example, an echelette grating employed for the UV and visible regions has a 500-nm blaze wavelength; hence, it is useful between 250 and 750 nm in first order and between 125 and 375 nm in second order.

The term $\sin\alpha + \sin\beta$ in Eq. 9 expresses the degree of light dispersion, which can be seen to be proportional to m, λ, and d^{-1}. The resolution improves with longer wavelengths, with higher-order diffracted light, and with finer groove pitch of the grating.

The above situation applies for grating monochromators in general, but when dealing with the UV region, there is an additional consideration. Because air absorbs light of wavelengths below 200 nm, the optical path must be kept in vacuum. Since no materials with good reflectivity in this wavelength region are available, no reflecting mirrors are used. Because even window materials such as LiF do not transmit light below 105 nm, the light detector must also be placed in the vacuum. The vacuum of the sample chamber, which is located between the light source and the rest of the optical components, normally can be independently broken to change samples.

The optical configuration of a vacuum-UV spectrometer consists of a concave diffraction grating and entrance and exit slits. This configuration, proposed by Seya and Namioka,[5] is shown in Figure 4. The concave diffraction grating and the entrance and exit slits are placed on a Rowland circle. Only the grating rotates; the other components are fixed in position. The diameter of Rowland circle is defined by the center of the concave diffraction grating and its radius of curvature. When the entrance slit and exit slits are positioned so as to form an angle of 30°15' with a line from the center of the grating to the point immediately opposite on the Rowland circle, and the distance between the center

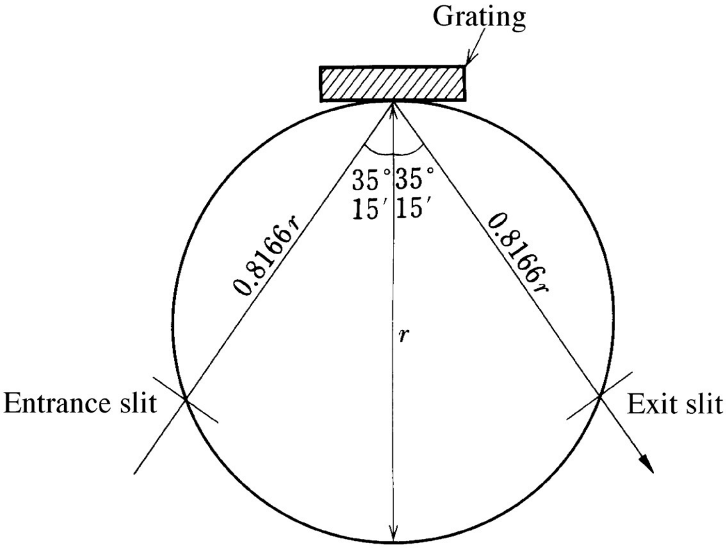

Figure 4 Configuration of optical components of Seya-Namioka vacuum ultraviolet spectrometer.

of the grating and the slits is 0.8166*r*, where *r* is the radius of curvature of the concave grating, as in Figure 4, the entrance slit focuses at the output with minimum distortion, which is caused by the rotation of the grating.[6]

In the wavelength region below 50 nm, light reflectivities become extremely small, and the total reflected light must be measured at a wide angle of incident light. In this optical configuration, since the two slits and the grating are on a Rowland circle, their geometrical relations become quite complex.

14.1.2.2 Light detector

Light is usually detected by converting its energy to electrical energy. The two light conversion elements most commonly used due to their reliability and ease of handling are photomultiplier tubes and solid-state detectors. There are a number of other methods of detecting light, for example, by using a thermoelectric element that measures the thermal energy generated by absorbed light energy or by observing the chemical products formed in a photochemical reaction.

Photomultiplier tube.[7] The photomultiplier tube is frequently used for detecting UV and visible light. Because the initial photoelectrons are multiplied many fold and because of their fast response time, photomultiplier tubes are employed for measuring very low-level light and fast transient phenomena. The inside structure of a side-on type photomultiplier tube is shown in Figure 5. As can be seen in this figure, the photomultiplier tube consists of a photoelectric surface (cathode) from which photoelectrons are generated by the incident photons. The photoelectrons then enter into a multistage dynode structure in which they are accelerated by the voltage applied to adjacent dynodes. Each dynode stage produces many secondary electrons so that the initial number of photoelectrons is multiplied many fold. All electrons generated in this way are collected by the anode. Anywhere from several tens to hundreds of volts are applied between the dynodes. Since the number of secondary electron emission surfaces in a photomultiplier tube K are commonly about ten and the electron multiplication factor δ, at each surface is a factor of 4 to 5, the overall multiplication δ^K is of the order of 10^6.

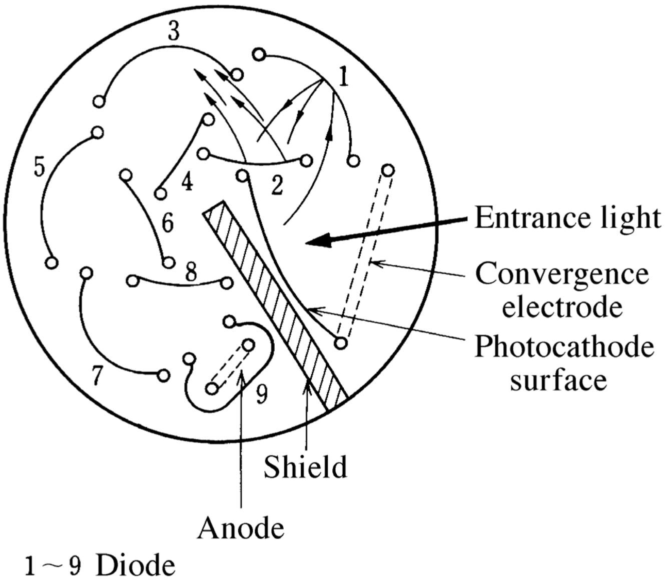

Figure 5 Side-on type photomultiplier tube.

A photomultiplier tube having the appropriate spectral sensitivity for the wavelength region of interest must be chosen. Figure 6 shows spectral sensitivity curves for different photoelectric surfaces.[6] For the UV and visible regions, the multi-alkaline metals (Na-K-Cs-Sb) exhibit the highest sensitivity. A Ga-As surface shows good sensitivity well into the near-infrared region. For studies in the longer wavelength region, an Ag-O-Cs surface is employed. For the vacuum-UV (VUV) region, a Cs-I and Cs-Te photoelectron surface is employed. Beyond this region, VUV light is converted into visible light by means of a phosphor screen using a phosphor such as sodium salicylate; the visible light is detected by a photomultiplier whose sensitivity is appropriate for the emitted light of the phosphor.

When an electric potential is applied to a photomultiplier tube, even in the absence of photons, a minute current flows through the tube. This current is called the dark current and is mainly due to thermal electron emission from the photoelectron surface. Besides this constant thermal emission, there is irregular shot noise caused by discharges in the residual gases and by light emission from the glass envelope caused by the bombardment of electrons. When measuring very low-level light, it is important to select an appropriate low dark-current photomultiplier tube and sometimes it is useful to cool the photomultiplier tube to minimize thermal noise.

One way to supply voltage to each dynode stage of a photomultiplier tube is shown in Figure 7. The value of the resistors R is set so that the maximum current at a given anode voltage is approximately ten times the anode current. When an AC signal is observed, the peak anode current can be unexpectedly large, so capacitors are provided in the later stages of dynodes to stabilize their voltage.

The following cautions must be taken when handling a photomultiplier tube:

1. Even when voltage is not applied to the tube, the tube should not be exposed to light.
2. A few hours prior to measurement, voltage should be applied to the tube in the dark to stabilize the output.

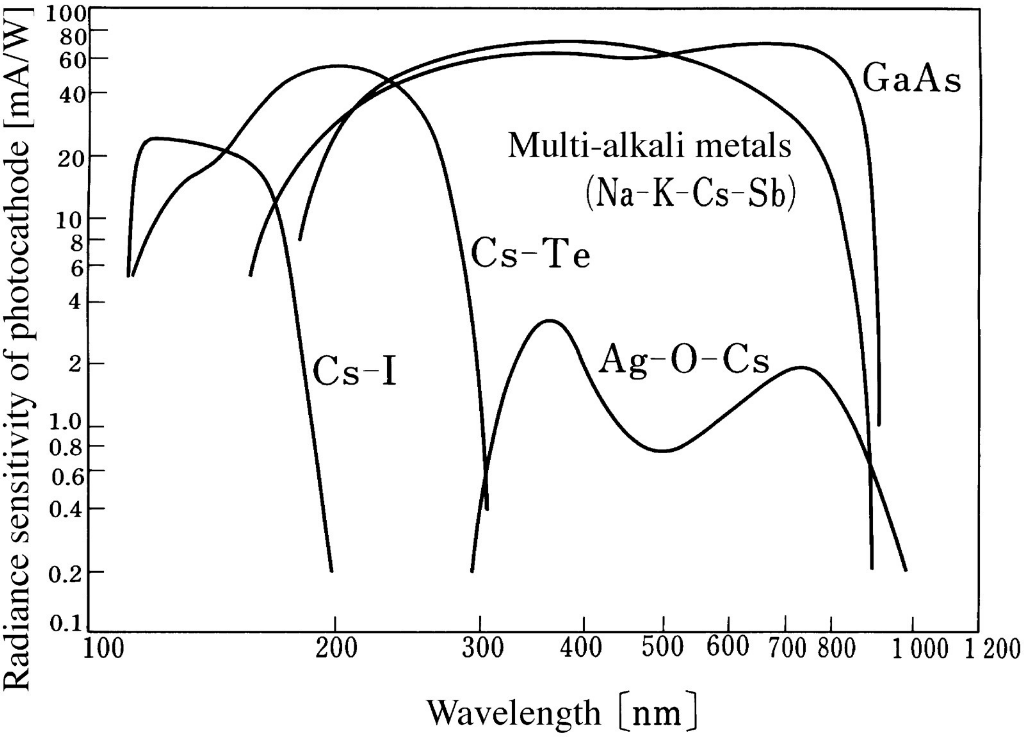

Figure 6 Spectral sensitivity curve of various photoelectic surfaces. (From *Photomultiplier Tubes Catalog*, Hamamatsu Photonics, Shizuoka, Japan, August 1995. With permission.)

3. Tubes must be operated under the manufacturer's specified conditions. Particularly, the anode current must not exceed one tenth of the maximum allowed anode current, except during transient peaks measurements.
4. Tubes are extremely delicate and great care must be taken in their handling.

Solid-state detectors. For *p*-*n* junctions in semiconductors, a region depleted of mobile charge carriers with a high internal electric field across it exists between the *p*- and *n*-type materials. This region is known as the depletion region. When light irradiates the depletion region, electron-hole pairs are generated through the absorption of photons and the internal field causes the electrons and holes to separate.

This accumulated charge can be detected by measuring the electric potential between the *p* and *n* regions while the device is open-circuit (the photovoltaic mode of operation). The charge can also be detected by measuring the current flow between the *p* and *n* regions by applying a reverse bias (the photoconductive mode of operation).

The most common semiconductor material used for photodiodes is silicon. A typical structure is shown in Figure 8.[8] It should be noted that electrical contact to the semiconductor material is always made via a metal-n^+ (or -p^+) junction. Silicon photodiodes have a bandgap of 1.14 eV, with quantum efficiencies up to 80% at wavelengths between 0.8 and 0.9 μm. Detection efficiency may be increased by providing antireflection coatings on the front surface of the detector consisting of a $\lambda/2$ coating of SiO_2.

The amount of dark current of solid-state detectors can be reduced by cooling the detectors, as is the case in photomultiplier tubes. For this reason, the signal-to-noise ratio of detectors can be improved by using thermoelectric devices to cool them.

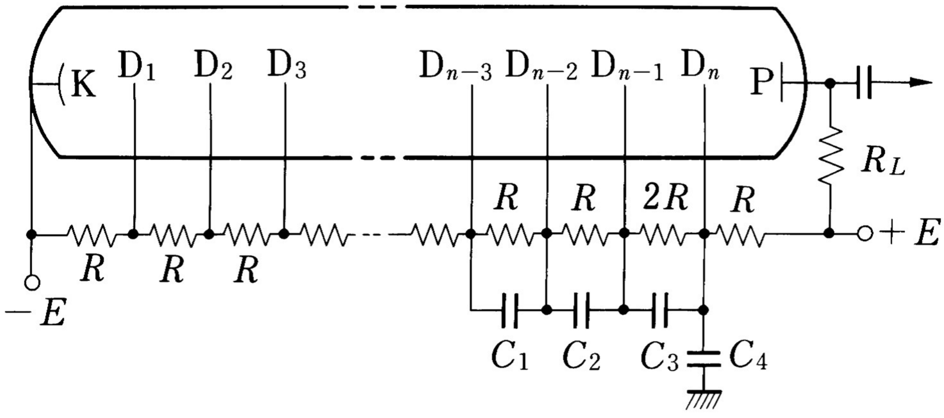
K
D1
D2
D3
Dn−3
Dn−2
Dn−1
Dn
P
RL
R
R
2R
R
+E
R
R
R
−E
C1
C2
C3
C4

(a) AC measurement

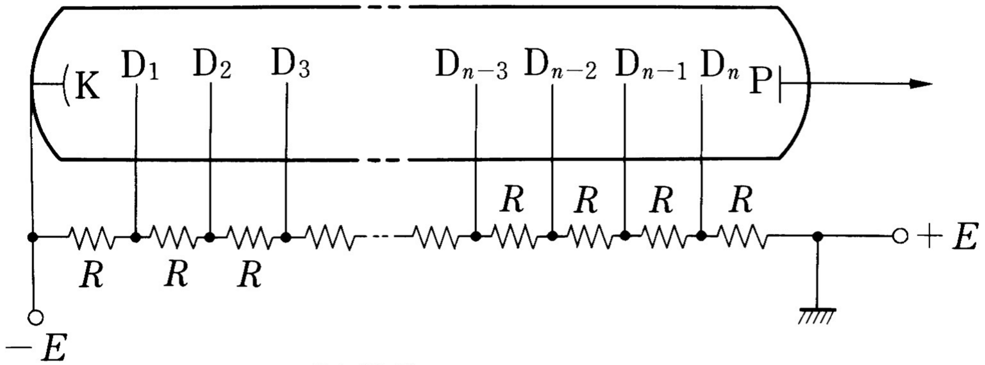
K
D1
D2
D3
Dn−3
Dn−2
Dn−1
Dn
P
R
R
R
R
+E
R
R
R
−E

(b) DC measurement

Figure 7 Method of supplying voltage to photomultiplier tube.

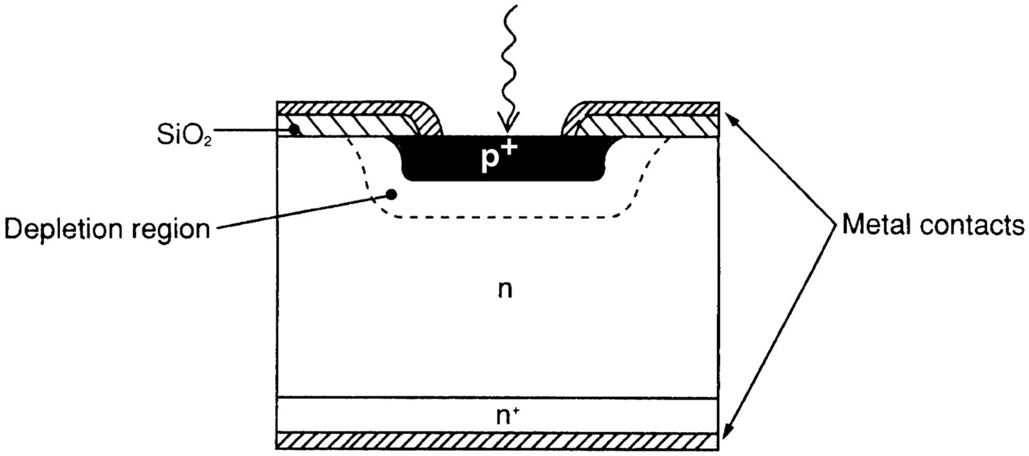
SiO2
p+
Depletion region
Metal contacts
n
n+

Figure 8 Silicon photodiode structure. (From Wilson, J. and Hawkes, J.F.B., *Optoelectronics, An Introduction*, Prentice-Hall, 1989, 284. With permission.)

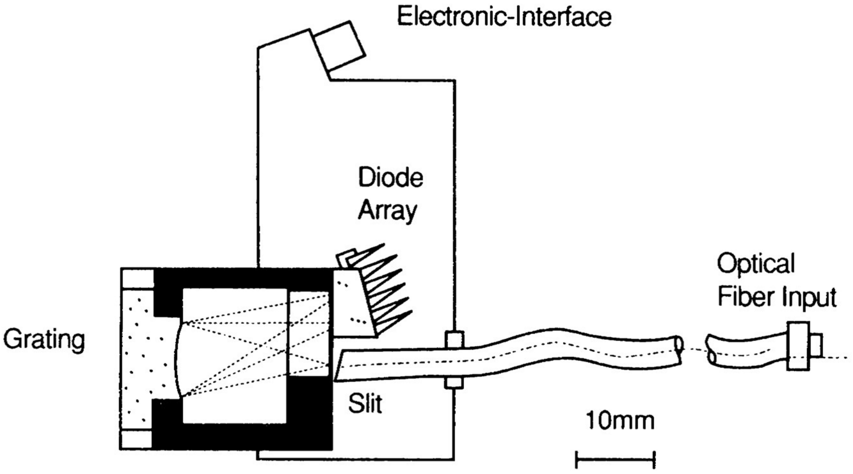

Figure 9 A compact spectrometer using a photodiode array. (From *Monolithic Miniature Spectrometer, Product Information*, Carl Zeiss, Germany. With permission.)

Single-channel and multichannel detectors. Light detectors employed for spectral studies can be classified as single-channel or multichannel detectors. The single-channel detector has a single light-detecting element. Typical examples of these detectors are the photomultiplier tube and the solid-state photodiode. The single-channel detector is placed in front of the exit slit of a monochromator. The detector measures light intensity at a given wavelength. A spectrum is obtained by scanning the wavelength range of interest, taking intensity data at each wavelength.

The multichannel detector has multiple light-detecting elements arranged linearly or in two dimensions, with each element operating individually. Examples of this type of detector are MOS-FET photodiode arrays and charge-coupled devices (CCDs). A classic example of a multichannel detector is a photographic plate used in conjunction with a spectrograph. The multichannel detector is positioned at the focal plane of the light exit of a monochromator with the exit slit removed. The detector can, therefore, cover a wide wavelength region. The width and height of each photodetecting element are equivalent to the width and height of the exit slit in a monochromator. When a multichannel detector is used, the monochromator does not have to scan the wavelength region of interest and it can measure the total spectrum within several to several hundreds of milliseconds. The other advantage of a multichannel-type detector is that since it accumulates the light energy, signal levels can be increased by extending the exposure time.

An efficient spectrum-measuring system can be built in this way, as the data can be read out electrically and digitized, then fed into a personal computer for further processing. Many such systems are commercially available, together with the appropriate software. An extremely compact spectrometer of this type is shown in Figure 9.[9]

Figure 10 shows an equivalent circuit for an all-solid-state one-dimensional array detector. The operating principle is that each MOS-FET photodiode is initially charged by an applied electric field. When light irradiates on the photodiode, electron-hole pairs are generated and the holes discharge the previously accumulated electric charge, so that the recharge of the diode is proportional to the light intensity. The solid-state detector feeds the recharging current by means of electronic switching. Namely, in order to scan the channel, a shift register provides gate signals to each FET in succession.

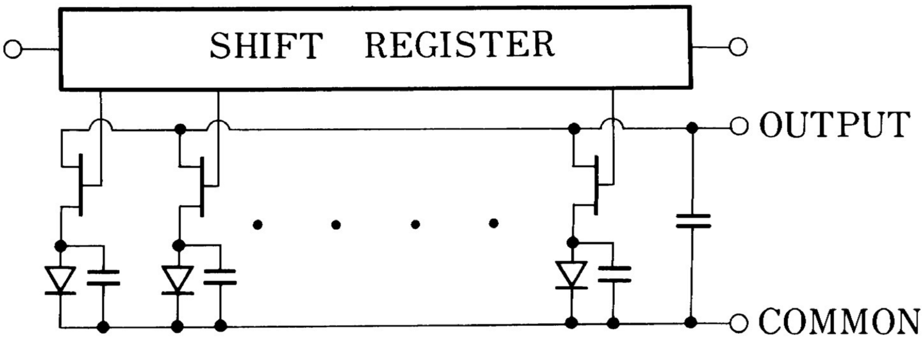

Figure 10 An equivalent circuit for an all solid-state one-dimensional array detector.

The standard photodiode array element is 25 µm wide and 2.5 mm high. The photodiode array itself is 25.6 mm wide and contains 1024 diodes.

Charge-coupled device (CCD). A spectral image formed on the array detector is converted into an electrical signal by each discrete element. If the detector elements are arranged in two dimensions and their number is typically 380,000, reading the electrical signal in each element requires a special technique. One method of obtaining the electrical signal sequentially is to use a charge-coupled device (CCD).

The upper portion of Figure 11 illustrates the basic configuration of the CCD consisting of a metal-oxide-semiconductor (MOS) capacitor.[10] A layer of silicon dioxide is grown on a *p*-type silicon substrate; a metal electrode is then evaporated on the oxide layer. The metal electrode acts as a gate and is biased positively with respect to the silicon. Electron-hole pairs are formed when the device is irradiated by light and electrons are attracted and held at the surface of the silicon under the gate when the voltage is positive. The electrons are effectively trapped within a potential well formed under the gate contact. The amount of charge trapped in the well is proportional to the total light flux falling onto the device during the measurement period.

The lower portion of Figure 11 illustrates how the trapped electrons are sequentially read out. The gate potentials are supplied by three voltage lines (L_1, L_2, L_3), which are connected to every third electrode (G_1, G_2, G_3) as shown. If the potential of L_1 is positive V_g, while L_2 and L_3 are at zero potential, a photogenerated charge proportional to the light falling on G_1 will be trapped under the electrode. (Figure 11(a)). After a suitable integration time, the charge can be removed by applying a voltage V_g to L_2 while maintaining L_1 at V_g; the charge initially under L_1 will now be shared between G_1 and G_2 (Figure 11(b)). If the potential of L_1 is then reduced to zero, all the charge that was initially under G_1 is moved to G_2 (Figure 11(c)). Repetition of this cycle will progressively move the charge along the MOS capacitors from left to right. At the end of the line, the amount of charge arriving as a function of time then provides a sequential scan of the "G_1" detector output.

In order to achieve a faster scanning rate, a second CCD array (the transport register) is provided. The transport register is shielded from the incident light and lies alongside the light-sensing array. Once a charge has built up in the sensing array, it is transferred "sideways" to the transport register and can be read out at the output of the transport register. This readout can take place at the same time as a new image is being built up in the sensing array.

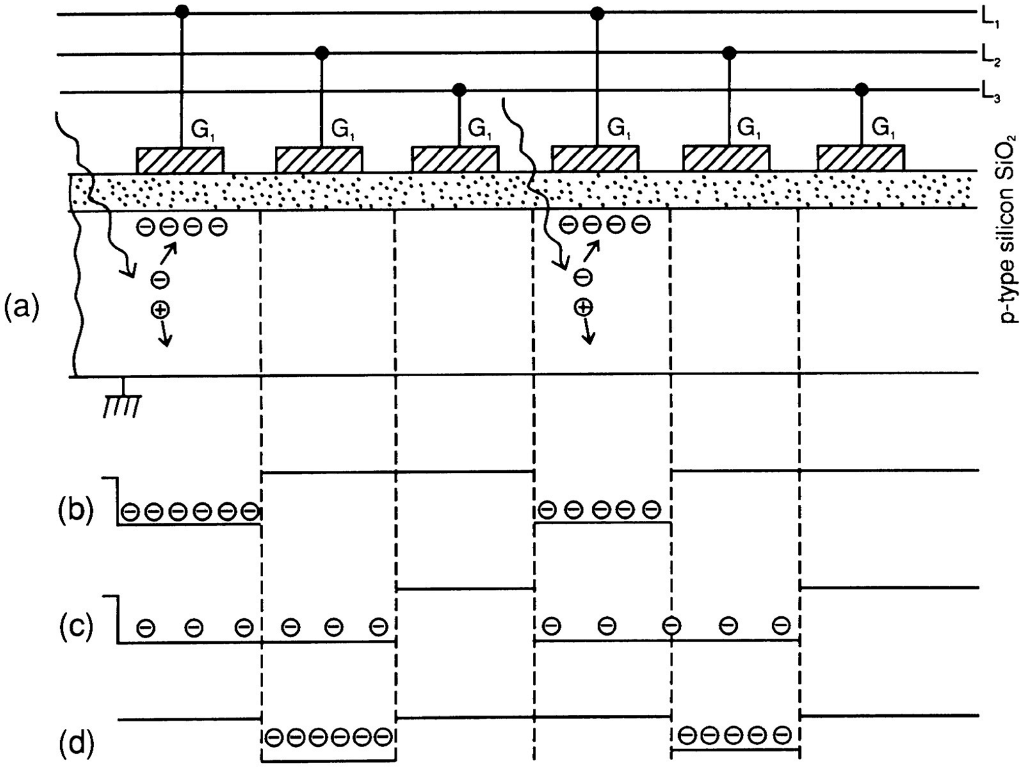

Figure 11 Basic CCD array composed of a line of MOS capacitors. (From Wilson, J. and Hawkes, J.F.B., *Optoelectronics, An Introduction*, Prentice-Hall, 1989, 296. With permission.)

Two-dimensional arrays based on the above one-dimensional designs are also possible and are known as frame-transfer devices. The transfer registers feed into a readout register running down the edge of the device. The contents of each line are read out in sequence into the readout register so that the signal appearing at the output of these registers represents a line-by-line scan of the image.

A great advantage of the two-dimensional CCD detector is that by introducing multiple images on different portions of the CCD, the upper, middle, and lower portions for example, separate spectra can be obtained simultaneously by reading out the sectional data separately.

The MOS-CCD has a quantum efficiency of about 45 to 50% at the peak of its sensitivity, 750 nm. The quantum efficiency can be improved at shorter wavelengths by coating the elements with a fluorescent dye that converts UV light to longer wavelengths to match the maximum quantum efficiency of the MOS photodetector. The efficiency of the detector in the longer wavelength region can be improved by making the potential well of the depletion region deeper than that of a standard chip. Another technique to improve the efficiency of the CCD device is to make the substrate very thin. In this back-thinned CCD, light is incident on the back rather than the front. This is because the gates are on the top, creating a thick layer for electrons to travel through and thus reducing their probability of reaching the depletion region. With the back-thinned chip, the chances for an electron to reach the depletion region are greater, and thus the quantum efficiency is higher. The spectral response curves of a variety of CCDs are shown in Figure 12.[11,12]

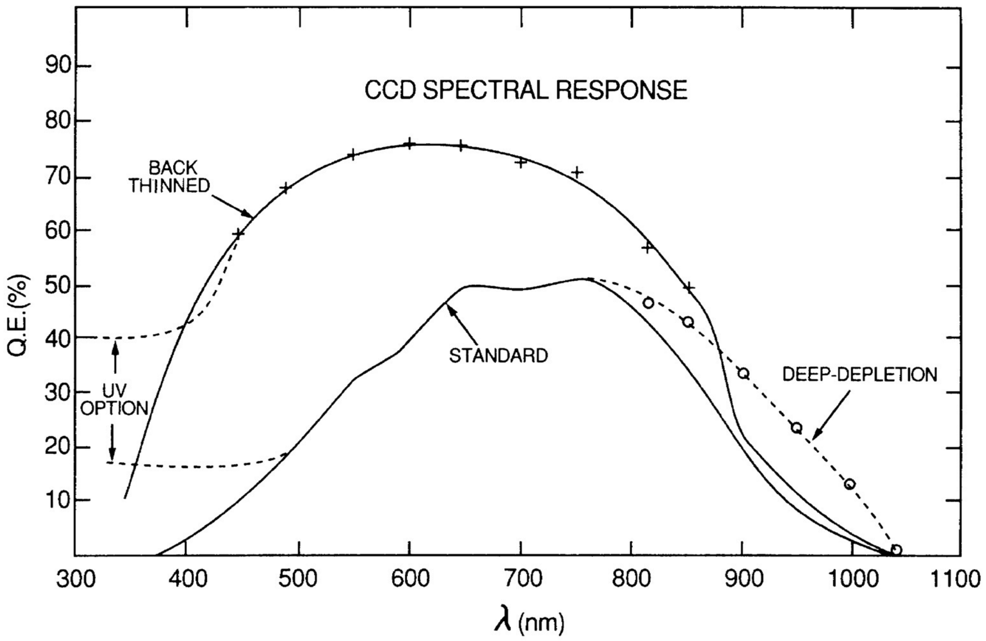

Figure 12 Spectral response curves of a variety of CCD detectors. (From *Guide for Spectroscopy,* Jobin Yvon-Spex, Edison, New Jersey, 1994, 217. With permission.)

The noise in a CCD is composed of shot noise, dark current, and read-out noise. CCDs can be cooled either thermoelectrically or with liquid nitrogen to reduce the dark current and associated thermal noise. The liquid nitrogen-cooled CCD is one of the most sensitive detectors available, having a dark signal of 1 electron per pixel per hour. The photodiode array device previously described cannot be cooled to liquid nitrogen temperature as it must have associated electronic circuits that cannot operate at low temperatures.

CCDs come in standard sizes of 1152 × 298, 512 × 512, and 578 × 385 pixels, with individual pixel sizes of 22 × 22 μm.

Image intensifier.[13,14] To measure extremely weak light, a detector with an image intensifier is used. Intensifiers are particularly useful when used in conjunction with solid-state detector arrays, as the latter are not very sensitive to low light levels, relative to photomultipliers. The operating principle of the image intensifier is shown in Figure 13 and is similar to that of a photomultiplier tube. When light is incident on the photocathode, photoelectrons are generated. The photoelectrons travel through a microchannel plate to the phosphor screen, being accelerated by a potential applied between the photocathode and the phosphor screen. The microchannel plate consists of thin metalized glass fibers. The electrons from the photocathode collide along the metalized walls, generating secondary electrons. Thus, multiplication by more than a factor of 1000 can be obtained. The photocathode material employed will vary depending on the wavelength sensitivity required, as in the case of a photomultiplier tube.

14.1.2.3 Signal amplification and processing apparatus

The signal from the photodetector must be further processed electrically to obtain meaningful data. In order to acquire data with a good signal-to-noise ratio, a variety of techniques are employed. In this section, some useful techniques are described.

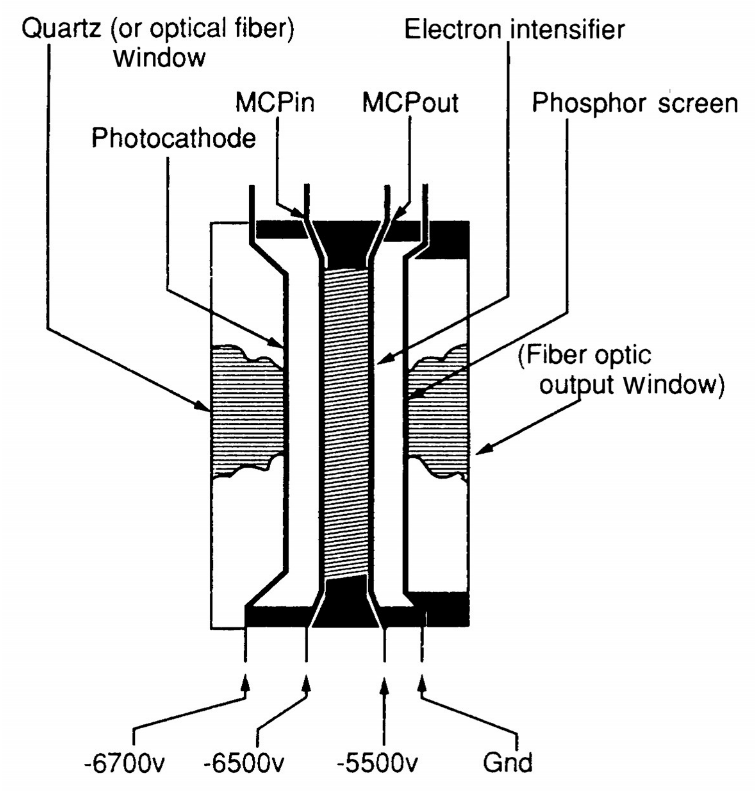

Figure 13 Inside structure of an image intensifier. (From *Applications of Multi-channel Detectors Highlighting CCSs*, Jobin Yvon-Spex, Edison, New Jersey. With permission.)

DC current-voltage converter. The output signal from photoelectric detectors such as a photomultiplier tube or a photodiode is in the form of a photocurrent. To display the signal on a strip-chart recorder, the photocurrent must be converted into a voltage. A current-voltage converter is used for this purpose. The simplest converter is a load resistor placed serially between the output, such as the photomultiplier anode plate, and the ground to allow observation of the output voltage. To observe this voltage directly by using a measuring apparatus (e.g., a strip-chart recorder), the instrument must have a higher input impedance than the load resistance. For DC measurements, an impedance conversion circuit as shown in Figure 14 is frequently used. An operational amplifier that requires an input off-set current much smaller than the photocurrent can be used as a DC amplifier with a V/A conversion ratio of up to 10^9.

Lock-in amplifier. The circuit diagram for this type of amplifier is shown in Figure 15. When the light signal is chopped at a certain frequency, the detector output consists of the signal and the non-signal component, alternately. The modified signal passes through a coupling capacitor and only the chopped frequency component is amplified by the synchronous amplifier. Using a reference signal generated by the chopper, the signal is phase-detected relative to the modulated signal. A phase shifter is adjusted to give a maximum output signal and a low-pass filter is adjusted for a time constant that optimizes the signal-to-noise ratio. Since only the input signal's phase is the same as that of the reference, the stray light that did not pass through the light chopper and other random electric noises are eliminated.

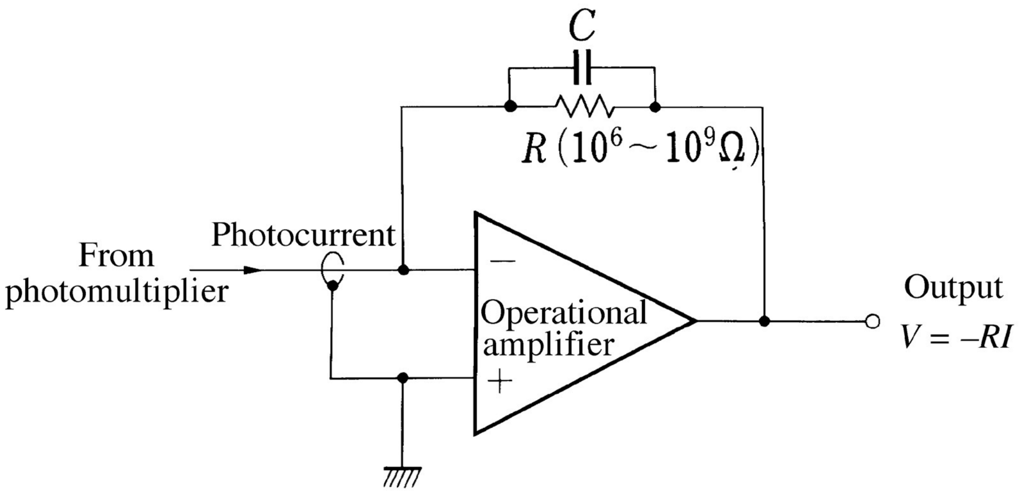
C
R (10⁶ ~ 10⁹Ω)
Photocurrent
From photomultiplier
−
Operational amplifier
+
Output
V = −RI

Figure 14 Current-voltage converter employing an operational amplifier.

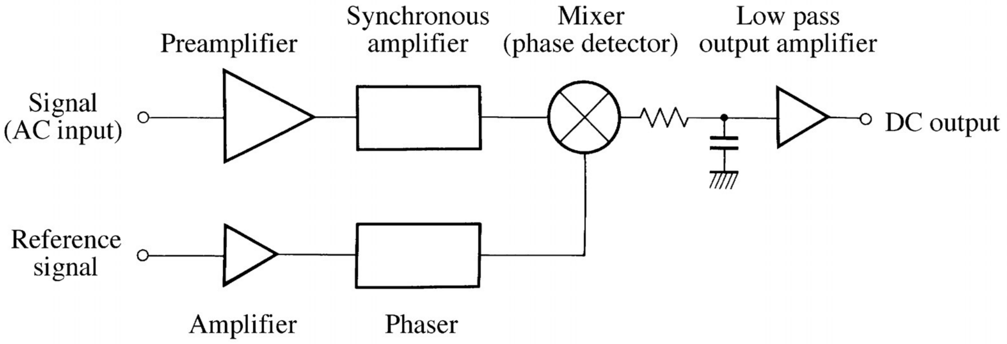
Preamplifier
Synchronous amplifier
Mixer (phase detector)
Low pass output amplifier
Signal (AC input)
DC output
Reference signal
Amplifier
Phaser

Figure 15 Block diagram of a lock-in amplifier.

Photon counter. A photon counting technique is employed when the light signal is extremely weak. The output from the photomultiplier can be observed as discrete photoelectron pulses. The intensity of the light signal is proportional to the number of photoelectron pulses per unit time. Pulses with a range of amplitude are input to a pulse-height discriminator circuit that distinguishes the signal from the dark current, as shown in Figure 16. In order to eliminate contributions from stray light and other noise sources from the signal, a light chopper is employed, as in the case of the lock-in amplification technique. The output signal from the detector contains [signal + stray light + noise] and [stray light + noise] on alternate half cycles so the difference yields the signal only. This technique is particularly useful to reduce shot-type noise because its occurrence is random, it contributes to both cases.

14.1.3 Excitation source

In order to observe fluorescence from a sample, some form of energy must be supplied to the sample. In this section, a variety of excitation sources for the investigation of fluorescence properties of material is described.

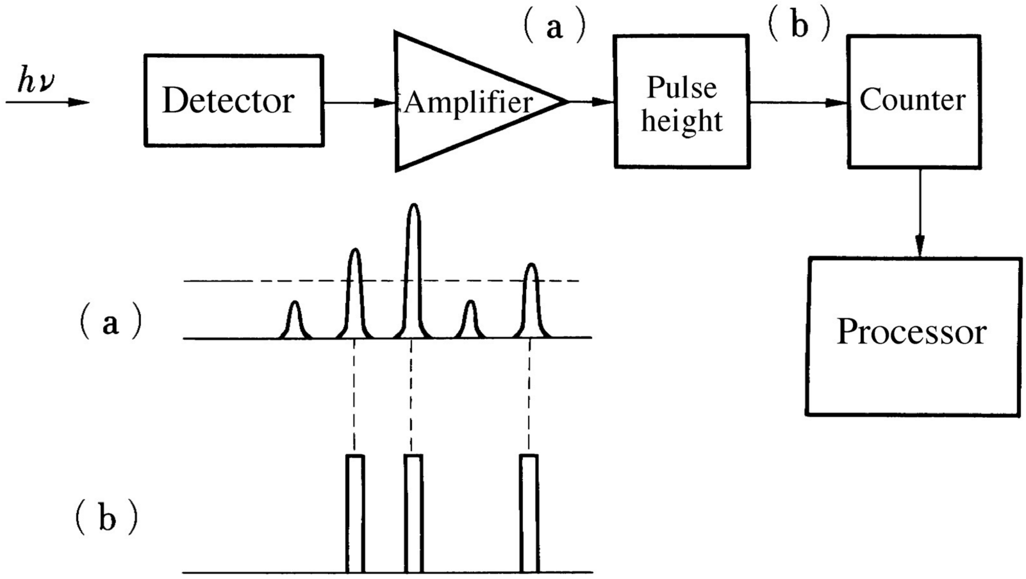

Figure 16 Block diagram and operational principle of photon counter. (a) Relation between input photoelectron pulse to the pulse-height discriminator and the discriminator voltage. (b) Output pulse to be counted from the pulse-height discriminator corresponding to the input signal.

14.1.3.1 Ultraviolet and visible light sources

The photo-excited fluorescent spectrum of material is most commonly studied in the ultraviolet to visible region. An appropriate light source is selected for experimental purposes in combination with a suitable filter and/or monochromator. The usual sources are discussed below.

Tungsten lamp. A tungsten lamp is easy to handle, is economical, has a relatively long life, and exhibits radiation characteristics similar to those of black-body radiation. As the temperature of the filament is raised, the radiation intensity in the short-wavelength region increases. Using a quartz or borosilicate glass envelope, which has good transmittance in the short-wavelength region, this lamp is useful for a variety of optical measurements from the near-UV to the near-IR. One disadvantage of tungsten lamps is that during operation, tungsten evaporates from the filament and is gradually deposited on the inside wall; this causes blackening of the surface of the envelope and absorption of light at shorter wavelength. In order to avoid the deposition of tungsten, either a sufficiently large envelope is used or Ar gas is introduced into the envelope.

To increase the life and improve the stability of the lamp, a metal halogen lamp has been developed. The metal halogen lamp contains small amounts of halogen gases such as bromine or iodine. Tungsten vapor from the high-temperature filament reacts with halogen in the vicinity of the lower-temperature wall and becomes a volatile tungsten halogenide. The tungsten halogenide is carried to the high-temperature filament by convection and decomposes into tungsten and halogen. The tungsten is redeposited on the filament. Wall blackening and tungsten loss from the filament can be avoided by this process. Metal halogen lamps can thus be operated at higher temperatures than conventional tungsten lamps, resulting in increases in radiation intensity in the short-wavelength region, in a doubling of lamp life, and in a higher lamp efficiency.

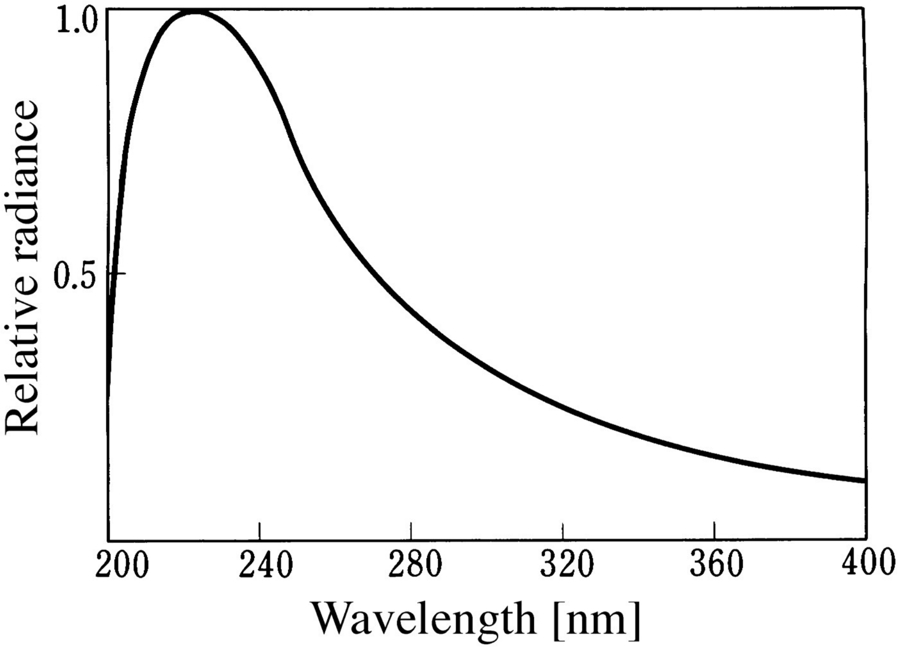

Figure 17 Spectral intensity distribution of hydrogen discharge lamp.

Discharge lamp. Discharge lamps most often used as excitation sources are hydrogen (deuterium), xenon, and mercury lamps.

Hydrogen discharge lamp. The hydrogen discharge lamp contains several torr pressure of either hydrogen or deuterium gas. The lamp is operated with a DC discharge between the hot electrodes. As is shown in Figure 17, the emission spectrum of the lamp is continuous in the ultraviolet region. High-intensity lamps are equipped with a glass jacket in which cooling water is circulated. The jacket encloses the entire lamp except around the window area. The window is made of quartz, which has high UV transmission.

Xenon discharge lamp. This lamp emits high-intensity light from the ultraviolet through the visible and infrared regions. Its relatively continuous spectrum is shown in Figure 18. Two types of this lamp are available: one in which the electrode gap is short (2 to 10 mm) with the gas at high pressure (several tens of atmospheric pressure), and one in which the electrode gap is long (several tens of cm) with low gas pressure. The light-emitting portion in the short-gap lamp is concentrated in the vicinity of the cathode area, so that this lamp can be regarded as a point source. The position of this bright discharge point tends to fluctuate, however, so caution must be taken when the source is focused on a sample. The long-arc lamp emits lower intensity light than the short-arc lamp. It emits a stable light output and is used as a standard in the UV region.

Mercury discharge lamp. The light emitted from a mercury discharge lamp spans the wavelength region from 185 to 365 nm. This lamp is the most common light source in the ultraviolet region. The mercury vapor pressure in the lamp is anywhere from below 1 mmHg to 50–200 atm, depending on the operating temperature. The spectrum of the output changes as the mercury pressure changes. At higher mercury pressures, the main line emissions broaden and their wavelength shifts toward longer wavelength; a continuous emission component also appears. At high mercury vapor pressures, the radiation

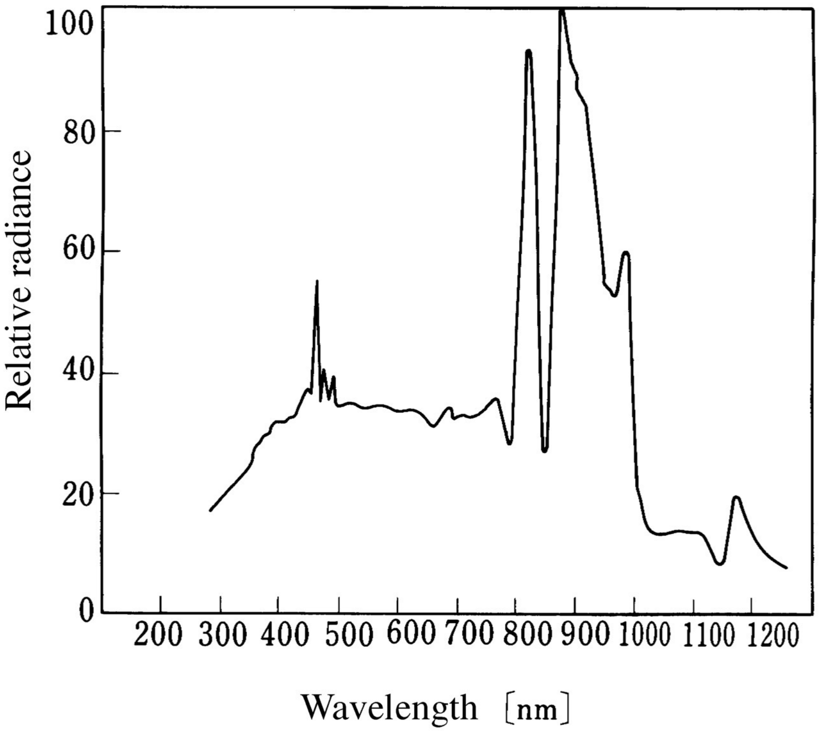

Figure 18 Emission spectrum of xenon short-arc lamp.

at 253.7 nm disappears due to self-absorption; the 365-nm line then becomes the main contributor to the UV region. A typical emission spectrum of the lamp is shown in Figure 19. As can be seen from the spectrum, the emissions are concentrated at particular wavelengths. Taking advantage of the nature of the spectrum, a strong monochromatic light source can be obtained by choosing particular wavelengths.

In order to eliminate the visible output of the mercury emission, a colored glass filter is employed such as the Toshiba UV-D33S or Corning 7-37 filters. For further absorption of visible light, a saturated aqueous solution of nickel sulfate is used for isolating 254-nm light and copper sulfate for isolating 365-nm light.

There are three kinds of commercially available mercury discharge lamps:

- A low-pressure mercury lamp in which the temperature of the lamp wall is relatively low and the main emission is at 254 nm. The typical input power of the lamp is anywhere from 5 to 20 W. There are two kinds of luminescence-detection (black light) lamps, which combine a glass filter with a low-pressure mercury lamp: one is for short (254 nm) and the other is for longer wavelengths (365 nm). The latter uses a filter containing a UV-emitting phosphor.
- A medium-pressure mercury lamp. By raising the wall temperature, the intensity of the longer wavelength components can be increased. The lamp has intermediate characteristics between the low- and the high-pressure lamps and is operated at 100 to 200 W input power. The main emission wavelengths are 254, 313, and 365 nm.
- A high-pressure mercury lamp. The lamp wall temperature is more than 200°C and this lamp can be used as a high-intensity point source. The lamp is operated at 150 to 2000 W input power. Recently, a stable and high-intensity UV source for appli-

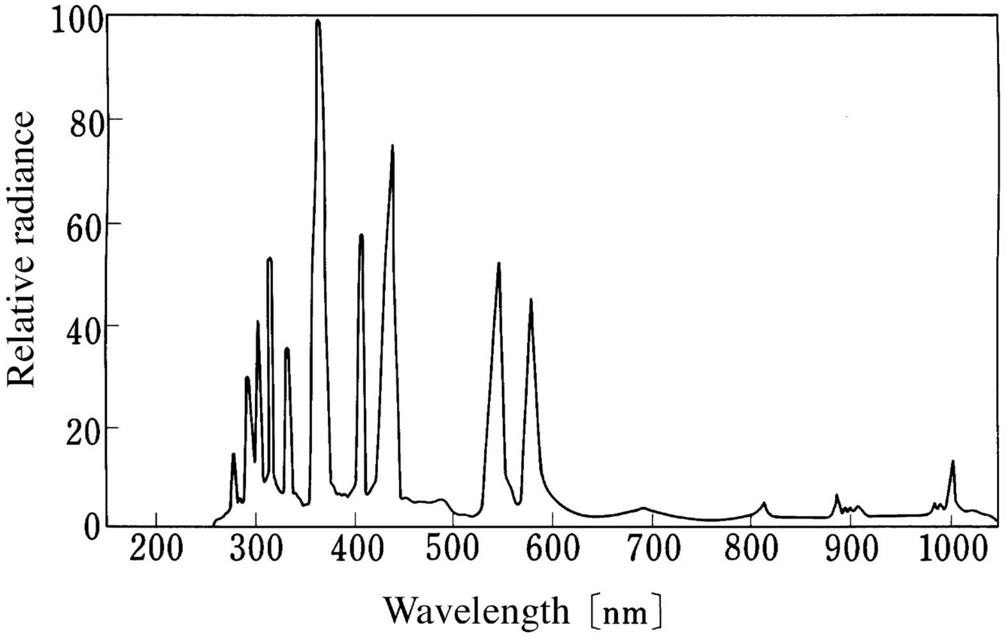

Figure 19 Emission spectrum of an ultra-high-pressure mercury lamp.

cation in photolithography has been developed; it contains a mixture of rare gas and mercury vapor.[15]

Laser.[16,17] A laser is an excellent monochromatic light source and has a radiative power at a given frequency several orders of magnitude greater than that of other light sources. Some lasers can operate in a pulsed mode and produce extremely short pulses. An appropriate gas, solid-state, liquid or dye laser, or semiconductor laser can be chosen depending on the experimental requirements. According to the mode of operation, lasers are either operated in continuous wave (cw) mode or in a pulsed mode. In some lasers, the output wavelength is tunable in a limited range. In the following, lasers useful for measuring luminescence properties are described.

Typical gas lasers used for the study of luminescence are the He-Ne, Ar^+ ion, Kr^+ ion, He-Cd, N_2, and excimer lasers.

- The He-Ne laser produces lasing line emission at 632.8 nm with high coherence, directionality, and wavelength stability. The output power can reach 35 mW. This laser is most frequently employed to align optical instruments.
- The Ar^+ ion laser has a total of ten lasing lines in the visible region 454 to 529 nm operating in cw mode. The most prominent line is at 514.5 nm, with an output power of up to 10 W. The total output power in the entire visible region can reach 25 W. This laser generates three lasing lines in the ultraviolet (wavelengths are 351.1, 351.4, and 363.8 nm), each with output powers of up to 1.5 W.
- The Kr^+ ion laser has a total of 15 lasing lines in the ultraviolet to visible region (350–676 nm) operating in cw mode. Unlike the Ar^+ laser, the Kr^+ laser has its strongest line in the red at 647.1 nm, with output powers up to 3.5 W.
- The He-Cd laser uses a mixture of He gas and Cd metal vapor, and has emission peaks in the ultraviolet and visible region. When it is operated in the cw mode, the

325-nm peak is most prominent, with output powers of 100 mW. This laser is very useful as an ultraviolet excitation source for measuring luminescence spectra.

- The N_2 laser is pulse-mode operated. There are high- and low-pressure types of N_2 lasers, differing in pulse width. The high-pressure N_2 laser has a pulse width of 0.1 to 1 ns, whereas the low-pressure N_2 laser has one of 5 to 10 ns. The N_2 laser has output peak power of as much as 200 kW and can be operated at a repetition rate of 100 Hz. The lasing wavelength of an N_2 laser is 337.1 nm. The laser is utilized as a high output power laser in the ultraviolet region, useful for high-intensity excitation of luminescence and for pumping dye lasers.
- The excimer laser. A series of excimer lasers is available. When the laser is operated in the pulse mode, all the excimer gases produce strong ultraviolet outputs: ArF excimer lases at 193 nm, KrF at 248 nm, XeCl at 308 nm, and XeF at 351 nm. The peak power of these laser is typically 20 MW (pulse energy of 200 mJ) but can produce 100 MW (1J) with pulse widths of 10 ns and repetition rates of 100 to 200 Hz. The lasers are useful for high-intensity excitation of luminescence and for pumping dye lasers.

The solid-state lasers employed for luminescence study are:

- The Nd^{3+}:YAG (yttrium aluminum garnet, $Y_3Al_5O_{12}$) laser is pumped by a xenon flash lamp, the most efficient lasing line being at 1.064 μm. Both continuous-mode lasing, which is now seldom used, and pulse-mode lasing can be obtained. The pulse-mode operation by Q-switching generates peak powers up to 110 MW (pulse energy of 1J) with a pulse width of 8 to 9 ns and repetition rates of 10 to 100 Hz. Since an extremely high output power can be achieved by this class of lasers, light can be generated at other frequencies using nonlinear processes. For example, the Nd^{3+}-YAG laser can generate (using the proper anharmonic crystal) light in the second order of 532 nm, in third order of 355 nm, and in fourth order of 266 nm, with conversion efficiencies of 30 to 40, 20, and 10%, respectively. Both the fundamental laser and its harmonics can be used to excite luminescence or to pump dye lasers. The laser can be mode-locked by acousto-optical modulation to yield extremely short pulse widths of 90 to 100 ps, with repetition rate of 100 MHz. The time-averaged power of these lasers can be as high as 7 W. This laser is useful for observing high-speed transient phenomena.
- The Nd^{3+}:YVO_4 laser has the same lasing line as Nd^{3+}:YAG at 1.064 μm. The crystal can be pumped by a laser diode (semiconductor laser) and can be operated in cw mode. Output power of the second harmonic (532 nm) has reached 5 W and this output is used to pump Ti^{3+}:sapphire lasers. A compact laser device can be constructed using laser diodes as a pumping source.
- The Ti^{3+}:sapphire (Al_2O_3) laser output is tunable and can be continuously varied from 670 to 1100 nm, in both cw-mode and pulse-mode operation. An 18% pumping power efficiency in cw-mode operation can be obtained when the crystal is pumped by the 532-nm laser output of a diode-pumped Nd^{3+}:YVO_4 laser, as noted above. The same pumping method is employed to attain mode-locked pulse operation. The mode-locking is carried out utilizing the Kerr effect.

  The Ti^{3+}:sapphire laser gives very stable and extremely short pulses of 20 fs to 60 ps, tunable within the wavelength range of 680 to 1100 nm. The time- averaged output power of a commercially available laser is of the order of 2 W at 790 nm. Utilizing the second harmonic, light pulses at 395 nm with 150-mW power output have been obtained. By combining the fundamental and the second harmonics of

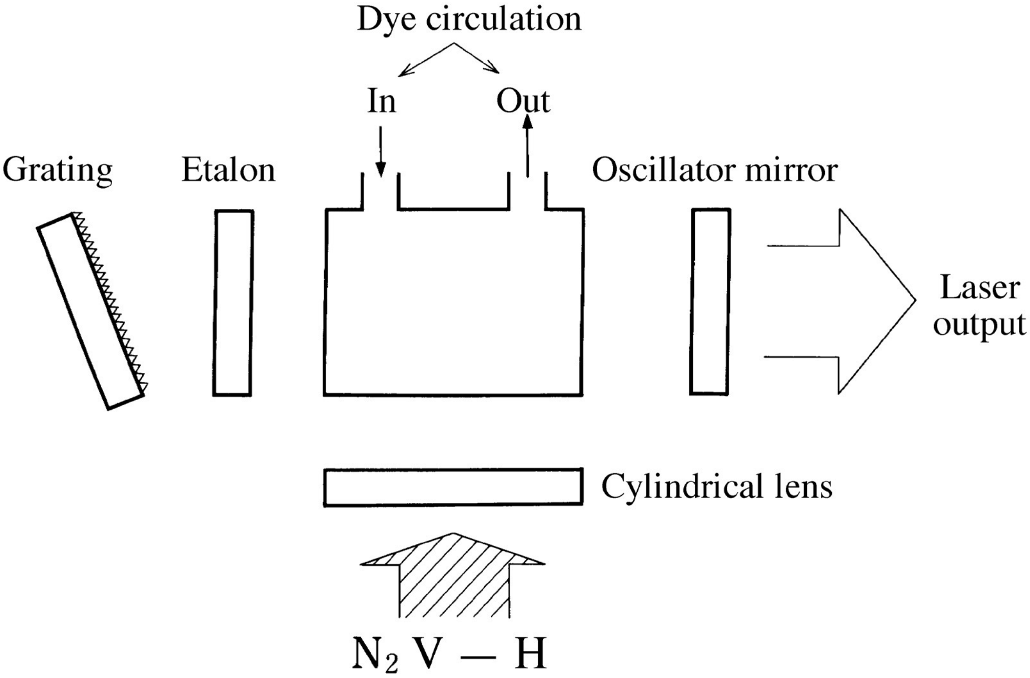

Figure 20 Configuration of a dye laser.

this laser, very useful femtosecond and picosecond laser pulses, tunable from the near-ultraviolet to near-infrared, can be obtained with a window around 600 nm.

- Dye laser. The lasing wavelength of a dye laser can be varied continuously from 370 to 1036 nm, depending on the dye employed.[11] As the fluorescence spectrum of a dye is, in general, a broad band, narrow-band lasing can be achieved using a diffraction grating or other wavelength-tuning element. By scanning the grating, the lasing wavelength can be changed. In order to obtain a higher output power, amplification stages can be used. The typical optical arrangement of a dye laser is shown in Figure 20.

Pulsed lasers can be used to pump dye lasers. Two approaches are available for obtaining output at a particular UV wavelength using dye lasers. One is to use an appropriate ultraviolet dye, and the other is to use the second or third harmonics of a visible dye laser. For example, the third harmonic of a visible dye laser pumped with a mode-locked Ti:sapphire laser can cover the wavelength region 273 to 322 nm with output powers of 10 to 120 mW.[18]

Other pumping sources include the N_2 laser, the XeCl excimer laser, and the Q-switched Nd^{3+}:YAG laser. Among dyes, the Rhodamine 6G laser covering a wavelength range of 565 to 620 nm is most efficient.

Excimer lamp. An excimer lamp containing a mixture of rare gas and halogen gas has been recently developed and commercialized by Ushio Co. The main output wavelengths are 172, 222, and 308 nm.[19]

14.1.3.2 Electron-beam excitation

Electron-beam energies used to excite phosphors range from several electron-Volts to several tens of keV. An electron beam of up to several hundred electron-Volts is called a

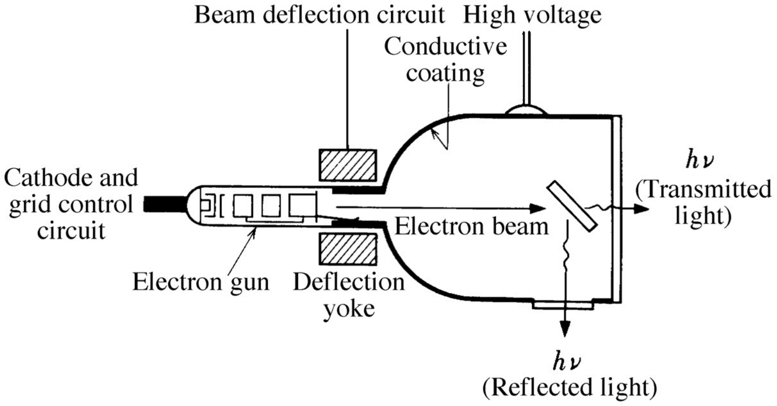

Figure 21 Structure of an electron-beam excitation apparatus.

low-energy beam, while beams of several kiloelectron-Volts energy are called high-energy beams. A low-energy electron beam penetrates into a phosphor particle a distance of only a few atomic layers, whereas a high-energy electron beam can excite the entire phosphor crystal.

Electron-beam excitation utilizes energy almost four times higher than optical excitation, which is several electron-Volts at most. In a cathode-ray tube, an electron beam of several tens of kiloVolts energy is converted to visible light by phosphor particles. The phosphor must be placed in a vacuum to allow excitation by the high-voltage electron beam. An example of the apparatus used for electron beam excitation is shown in Figure 21.

In order to observe reflected luminescence from a powder phosphor, the phosphor powder is tightly packed into the cavity in a metal sample holder. This cavity-filling technique is a simple and convenient way to test phosphors. The reflected luminescence is observed on the same side as the electron excitation; this method is different from that of the conventional cathode-ray tube and yields slightly different results. To simulate the configuration used to observe transmitted luminescence, a slide glass is coated with the sample phosphor by either sedimentation or slurry coating. Since phosphors are generally good insulators, the sample charges up as the electron beam is turned on; because of this space charge, the beam is deflected to areas where the electrical potential is highest and optical measurements can be disturbed. To avoid space charges, a tin-oxide-coated glass is employed, making the holder conductive. Another way to make a sample conductive is to evaporate aluminum onto the sedimented phosphor layer.

To prepare a sample for transmission luminescence measurements, the thickness of the phosphor layer is critical. If the phosphor layer is too thin, some of the electrons pass through the layer without colliding with the particles and thus do not fully excite the phosphor. On the other hand, if the phosphor layer is too thick, and since the accelerated electrons have a certain penetration depth, layers below this depth are not excited and a portion of the resulting luminescence can be self-absorbed. The luminescence spectrum therefore changes, depending on the sample thickness, and this thickness must be optimized to obtain the greatest possible light output. The optimum thickness depends on the particle size distribution and the excitation conditions, so the optimum layer thickness is best determined empirically. In the case of the measurement of reflected luminescence, the thickness is adjusted so that the sample does not charge up; hence, the place being irradiated does not change. Optically, this case can be regarded as being equivalent to measuring a sample with infinite thickness.

There are two ways to apply high voltages to phosphor samples: the sample can be anode-grounded or cathode-grounded. The appropriate grounding depends on the purpose of the experiment. When the sample is anode-grounded, it is at the same potential as the ground and it is relatively safe to experiment near the sample. On the other hand, as all the circuits that control the electron beam are at high negative voltages, operations are generally hazardous. When the sample is cathode-grounded, the control circuits are on the ground-potential side and there is less danger to the operator. For direct measurement of the magnitude of the current of the electron beam irradiating the phosphor sample, for example by employing anode-grounding, a measuring device can be readily placed on the sample side. For modulating the beam current or applying a pulsed beam to the sample, it is advisable to use cathode-grounding.

The grounding of a vacuum envelope that contains a sample and an electron source differs, depending on which high-voltage grounding method is employed. With anode-grounding, as the sample side is earth-grounded, metal can be used for the sample holder and jigs with exception of a window observation. These metal parts and the vacuum envelope are isolated by an insulator (usually glass) from each other. As the vacuum envelope is at a negative high voltage, it is generally covered by an insulating material. A glass vacuum envelope is employed in cathode-grounding as the sample is at high voltage; the inside of the envelope is coated with conductive carbon or evaporated aluminum in order not to disturb the electron trajectories. At the same time, the outside wall of the glass envelope is coated in a similar way and is earth-grounded.

When electrons are accelerated by more than several kiloelectron-Volts, an electron gun is used as an electron-beam source. The structure of an electron gun is described in 6.1. It is convenient to use a commercially available monochrome electron gun for this purpose. An oxide-coated cathode in an electron gun can generate sufficient current and the gun can modulate the current quite readily. A mixture of alkaline-earth metal (Ca, Sr, Ba) carbonates is initially coated on the cathode metal cap. By heating the carbonates under vacuum pumping, they become oxides. These oxides are activated by further heating to temperatures higher than the operating temperature. The activation process is further carried out by applying high voltage to the anode and by adjusting current flowing through the filament in a preprogrammed way while the entire system is kept under vacuum.

To evaluate a phosphor under electron-beam excitation, the beam is usually scanned over the sample. If the beam stays at the same position, the sample either becomes electrically charged or is damaged by the heat generated by electron impact. In order to avoid these undesirable effects and to simulate the conditions in a cathode-ray tube, beam scanning is recommended. The scanning is conveniently achieved using a deflection yoke placed near the top of the electron gun. In some instances, a pair of deflection plates is provided, with electron guns allowing the beam to be scanned electrostatically, but deflection sensitivity is usually low. If beam deflection or scanning is not practical in a given measurement system, the sample can be excited using DC with very low current or using a pulsed beam to achieve excitation conditions similar to those of beam scanning.

The basic principle of measurement of a phosphor by low-energy electron-beam excitation is similar to the high-energy system described above. Since measurements are done at a low voltage and the beam is irradiated evenly over the surface of the sample, the procedures are much simpler. As an example, the structure of a test tube having the same configuration as that of a triode tube is shown in Figure 22. The filament is oxide-coated, as in small vacuum tubes, and the magnitude of the current irradiating the anode sample is controlled by the grid.

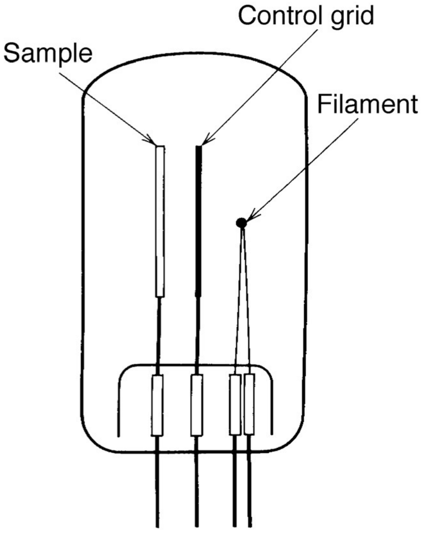

Figure 22 Structure of a low-voltage electron beam excitation test tube.

Since electron-beam excitation is carried out in vacuum, the degree of vacuum greatly affects the measured characteristics of the sample and the cathode. The vacuum must always be maintained higher than 10^{-4} Pa. When it is necessary to break the vacuum, the cathode and the heating filament should be cooled to room temperature. Care must be taken to keep the electron gun clean (i.e., free from dust in the air and other contaminants) in order to avoid high-voltage discharges.

14.1.4 Some practical suggestions on luminescence measurements

1. The environment surrounding a monochromator must be kept at a constant temperature and as low a humidity as possible. Attention must be paid to keeping mechanical shocks from the monochromator.
2. All optical paths must be vibration- and shock-free.
3. The spectral sensitivity of the photodetector must reflect the spectral range of interest.
4. A diffraction-grating monochromator is sensitive to the direction of light polarization, so light from the sample should be either unpolarized or polarized to match the polarization due to the grating.
5. A light source, photodetector, and amplifier subject to temperature drift must be warmed to attain stability before making measurements.
6. By selecting a proper filter, higher-order spectral components from the excitation source and from the monochromator should be eliminated.
7. The system must be light tight to stray light.

14.2 Reflection and absorption spectra

14.2.1 Principles of measurement

Reflection and absorption spectra measure the wavelength dependence of the intensity of light absorbed near the sample surface and in the bulk of the sample, respectively. By measuring the reflection and the absorption spectra, the absorbance of light energy by the

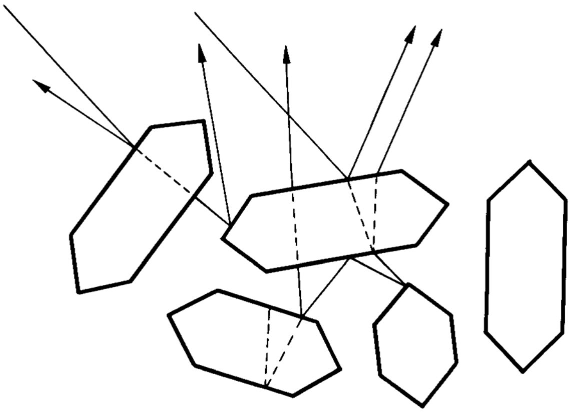

Figure 23 Light scattering by powder layers.

sample can be obtained. From the absorbance data, the energy bands of the material and the impurity levels within the material can be determined. The luminescence spectrum reveals only energy levels related to light emission. The absorption spectrum, on the other hand, gives energy levels that may or may not be involved in light-emitting transitions. In a practical sense, light absorption by a phosphor is important because the phosphor's body color greatly influences the picture contrast in a color cathode-ray tube.

When the absorption and reflection spectra of a powder phosphor sample—as opposed to a transparent solution or solid—are measured, a special experimental technique must be applied to collect the light since the powders scatter the light. A detailed theoretical discussion of the optical properties of a powder sample is given in 16.

In this section, methods to measure the absorption and reflection spectra of a sample that does not luminesce are described. There are three components in the reflected and transmitted light from a powder sample: (1) light that is deflected or scattered after being partially absorbed by the sample; (2) light that is totally reflected by the surface of the sample (specular reflection); and (3) light that passes through the gaps of the sample (see Figure 23). The first light component is what must be measured. As this light component is diffuse due to scattering, the detector only detects light within the spatial angle subtended by its aperture, and its signal decreases as the distance between the detector and the sample is increased. The intensity of the unscattered light, on the other hand, is independent of this distance if the light is collimated.

The reflectance R and/or transmittance T of a powder sample can be expressed as:

$$R \text{ or } T = \frac{I}{I_0} \tag{13}$$

where I is the intensity of the reflected or transmitted light, while I_0 is the intensity of the light source. I is the sum of intensities of the direct light I_s and the scattered light I_d, or

$$I = I_d + \alpha I_s \tag{14}$$

where α is the damping factor of the scattered light whose intensity is reduced. For the reason discussed above, generally $\alpha \ll 1$. In order to obtain good experimental results, it is desirable to have α as close to unity as possible and/or to minimize I_s. An experimental system with α is close to unity can be achieved when I_d and I_s are scattered to the same degree. Alternatively, the ratio of the intensity of scattered light between the sample and a standard material that does not absorb light at the wavelength of interest is:

$$\begin{aligned} R \text{ or } I &= \frac{\alpha\left(I_d + I_s\right)}{\alpha I_0} \\ &= \frac{I_d + I_s}{I_0} \quad (\alpha\text{: damping coefficient}) \end{aligned} \tag{15}$$

The scattered light includes both the specularly reflected and absorbed light components. The specular reflected light can be described by Snell's law. If the complex reflective index and Fresnel's formula are applied to Snell's law, the reflection index approaches unity as the absorption coefficient and reflective index increase. The larger the reflection index, the larger the specular component becomes and the less light absorbed by the sample. As the average particle diameter of the powder sample becomes smaller, the number of reflective surfaces increases, resulting in less penetration of light into the sample layer. This is why the body color of a sample fades when the sample is ground down to smaller particle size. When the sizes of the powder particles become as small as the wavelength of light, the intensity of scattered light has a wavelength dependence like that observed in Rayleigh scattering by gaseous molecules.

The case described above applies to a sample that does not luminesce or only luminesces weakly under excitation. The following is the experimental procedure when luminescent light from the sample is significant.

When the excitation wavelength region and luminescence wavelength region are well separated, the scattered light is observed through a filter that absorbs light in the excitation wavelength region. When the wavelength regions of excitation and luminescence overlap, special techniques must be employed. Generally, excitation light absorbed by a sample is more energetic than the emitted light. This decrease in light energy is called the Stokes' shift[20] and must be considered in most measurements. Light from the excitation source is passed through a monochromator to reduce it to a sufficiently narrow bandwidth. The scattered light is analyzed through another monochromator set at a wavelength similar to that of the first monochromator. The bandwidth of the latter monochromator should be narrow enough as to be within the range of the Stokes' shift. Thus, absorption and reflection spectra without the luminescent light component are obtained.

14.2.2 *Measurement apparatus*

A spectrophotometer is employed to obtain the absorption and reflection spectra of samples. The configuration of the spectrophotometer is shown in Figure 24. The spectrophotometer shown is a double-beam type and the intensity of the monochromatized sample beam is compared to a reference beam as the wavelength is scanned. An automatic spectrophotometer generates a spectrum on a recorder or has the ability to output spectral data after appropriate computation.

Generally speaking, a DC measurement of the photocurrent is susceptible to the influence of stray light and to the drift of electronic circuits. It is therefore advantageous to use an AC measurement method, as described in 14.1.2.3 utilizing a lock-in amplifier. In the AC method, the light beam is passed through a light chopper; the chopped beam is used alternately as the sample beam and the reference beam, respectively. The beam is

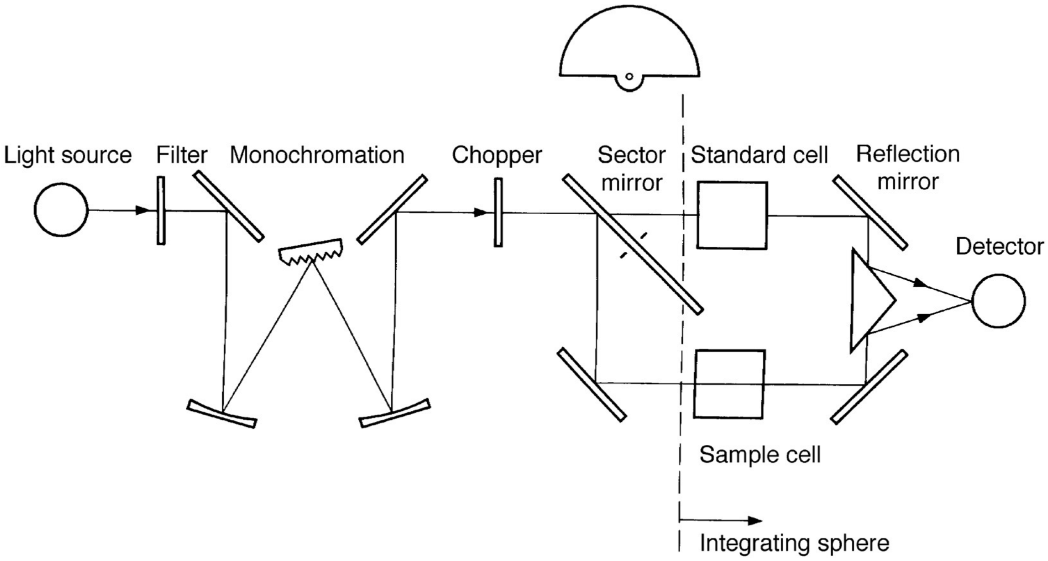

Figure 24 Optical arrangement of a double-beam spectrophotometer.

switched by a sector mirror. The two alternate beams are then detected by a photodetector. The electric signals are separated by a phase separator and then compared to each other.

There are many ways to compare the sample signal and the reference signal. When a photomultiplier is employed as the detector, comparison is achieved by adjusting the photomultiplier gain by changing the applied anode voltage. In other words, when the radiance of the reference beam at a given wavelength λ is $E_0(\lambda)$ and the detector gain is $A(\lambda)$, satisfying Eq. 16.

$$A(\lambda)\cdot E_0(\lambda)=V_c \tag{16}$$

Since $A(\lambda) = V_c/E_0(\lambda)$ and if the sample beam $E(\lambda)$ is detected at this gain, the output signal becomes:

$$V_0=A(\lambda)\cdot E(\lambda)=\frac{E(\lambda)}{E_0(\lambda)}V_c \tag{17}$$

Consequently, the ratio of the sample beam to the reference beam is obtained. The above method of obtaining the ratio of the sample beam to the reference beam is useful in the wavelength range where photomultiplier tubes can be employed. For photodetectors of the thermoelectric type (thermopile) or photoconductive type (PbS and others) used in the infrared to far-infrared region, this method of comparison is difficult to apply.

As an alternate way to controlling the detector gain electrically, an optical wedge or an optical comb can be used to reduce the intensity of the reference beam. The system is designed so that the magnitude of the optical-wedge movement is proportional to the amount of light intensity reduction. When the optical wedge moves to make the intensity of the reference beam equal to that of the sample beam, the magnitude of the movement represents the light absorbance. An absorption spectrum is obtained by plotting the optical-wedge movement in the wavelength being scanned on a strip-chart recorder.

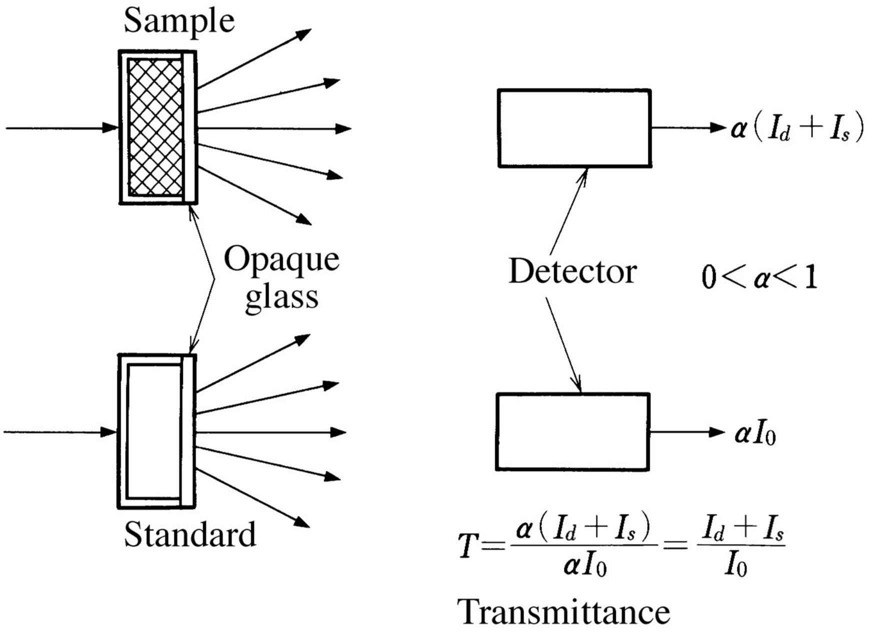

Figure 25 Absorption spectrum measurement of a powder sample by means of sample holder with opaque glass.

When the absorption spectrum of a powder sample is measured, it is important to correct for the effects of light scattering by the sample. As is expressed in Eq. 15, in order to make the direct light I_d scattered equal to the scattered light I_s, an opaque glass is employed, as shown in Figure 25.[21] When the absorption spectrum is measured, light exiting through the sample is completely scattered by an opaque glass plate placed on the sample holder. With this arrangement and since the light I_d has already been scattered by the sample layer, the degree of scattering is not changed significantly by the opaque glass plate. By comparing I_s and the light directly from the source I_0 scattered by the opaque glass, the condition required for Eq. 15 is satisfied. This technique makes the signal intensity low, so special attention must be paid to increasing the signal-to-noise ratio. As the opaque glass absorbs the infrared and the ultraviolet, this technique is not applicable to measurement in these regions.

An integrating sphere shown in Figure 26 is often employed for high-precision measurement of absorption and reflection spectra of powder samples.[22] The entire inner wall of the integrating sphere is coated with MgO or $BaSO_4$ powder. These powders have highly uniform reflectivity over a wide wavelength region, so incident light is evenly diffused. If the area of the entrance window is smaller than that of the inner wall, the light intensity anywhere on the wall can be regarded as constant.

When an integrating sphere is employed for absorption or reflection spectral measurements, the sphere is located in front of a spectrophotometer and the sample is attached to the interior wall with the excitation light shining directly on it. If a double-beam measurement is carried out, a standard white reflectance plate is provided on the sphere wall, together with an entrance window for the reference light beam. Although the inner wall of the sphere can be regarded as a perfectly diffusing surface, the resultant light may still contain a minute contribution from the direct excitation and reference beams. In order to reduce these stray components, the detector is placed perpendicular to the line between the window and the sample. To further reduce the direct beam

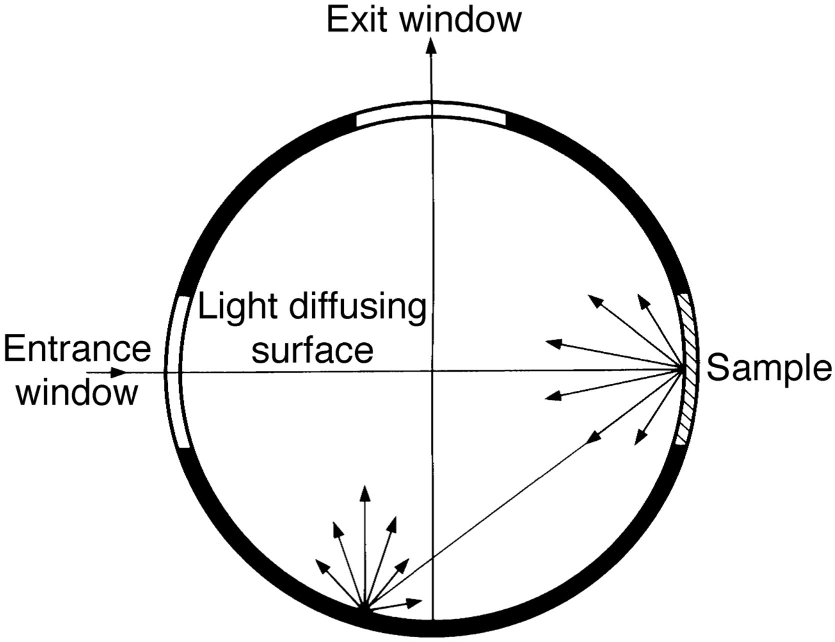

Figure 26 Integrating sphere.

contributions, the place where the direct reflecting beam shines is painted black or a black hole is positioned there.

14.3 *Transient characteristics of luminescence*

14.3.1 *Principles of measurement*

Transient properties of the luminescence of a phosphor are as important as the spectra in elucidating luminescence mechanisms. By measuring transient properties, information about the lifetimes of luminescence levels and the effective nonradiative relaxation processes can be obtained. For practical applications, these measurements yield the decay time of luminescence of the phosphor and changes in emission color with time. To obtain information about the transient properties, two types of measurements should be conducted: fluorescence lifetime and time-resolved spectroscopy.

Assuming the radiative transition rate from a fluorescent level to the ground state is R_r, and the nonradiative transition rate between the same levels is R_n, the fluorescence intensity at time t, $I(t)$, is given by:

$$\frac{d(I)}{dt} = -(R_r + R_n) \cdot I(t) \tag{18}$$

Assuming the initial condition to be $I(0) = I_0$, the above equation becomes:

$$I(t) = I_0 \exp[-(R_r + R_n) \cdot t] \tag{19}$$

The average lifetime τ measurable at this energy level can then be expressed as:

$$\tau = \frac{\int_0^\infty t \cdot I(t)dt}{\int_0^\infty I(t)dt} \tag{20}$$

By substituting the above equation into Eq. 19, one obtains:

$$\tau = \frac{1}{R_r + R_n} \tag{21}$$

From the above equation, in the ideal case where no nonradiative relaxation exists, $\tau_r = 1/R_r > 1/(R_r + R_n)$, then the experimental τ value becomes shorter than τ_r. The luminescence intensity can then be written, taking into account the time dependence of the excitation energy change $E(t)$, as follows:

$$I(t) = \eta \int_0^\infty E(t - t') \cdot D(t')dt' \tag{22}$$

where η is a constant and $D(t)$ is the decay function. For experimental purposes, the condition $E(t) = \delta(t)$ should be adhered to as close as possible, but the resulting waveform may be affected if the sample has a very short lifetime.

Measurement of a time-resolved spectrum is similar to conventional spectrum measurements. However, the time-resolved spectrum is observed instantaneously at a given time right after the excitation source is turned off. The relation between instantaneous luminescence intensity $I(\lambda,t)$ at given time t and wavelength λ can be written as:

$$I(\lambda) = \int_0^\infty I(\lambda, t)dt \tag{23}$$

14.3.2 *Experimental apparatus*

All the components in a system for measuring transient luminescence phenomena—that is, the light detector, the amplifier, and the analyzer—must have fast response times. When high-speed phenomena of less than a few microseconds are being measured, the response time of the entire circuit becomes critical. The signal-transmission impedance, the signal-line impedance, and the terminating impedance in the circuit must match or the signal waveform will be distorted. The pulse duration of the excitation source must also be very short.

14.3.2.1 *Detector*

A typical photomultiplier tube with high gain and fast response time (a rise time of a few nanoseconds) is suitable for experimental purposes. When a photodetector such as a photomultiplier tube is connected to an oscilloscope or to an amplifier, the tube's load resistance must be 50 Ω, which is the impedance of most high-frequency measuring devices. On the other hand, the maximum current that can be drawn from a photomultiplier tube is typically of the order of several hundred microamperes, so that the output voltage generated in the 50-Ω load resistance is only a few millivolts.

A convenient method of obtaining a larger output voltage from a photomultiplier tube is to connect a high-speed IC amplifier as close as possible to the tube, converting the output impedance of the tube to 50 Ω. With this technique, it is difficult to reduce the stray capacity between the photomultiplier tube anode and the amplifier to a level below several pF. The response time of the detection circuit is of the order of a few nanoseconds when the input impedance of the IC is set to exceed 1 kΩ. This is the reason a photomultiplier tube cannot monitor changes in signal waveform that are faster than a few nanoseconds, even if a high-speed IC amplifier or an oscilloscope is employed. Another disadvantage of using a photomultiplier tube to observe high-speed phenomena is that around 10 nanoseconds of delay time is required for electrons to travel between the dynodes.

As is stated in 14.1.2.2, the maximum current that can be drawn from the photomultiplier tube in the region of linear response (the region where the photocurrent is proportional to incident light intensity) is several 100 μ*A* for usual DC light measurements. For observation of high-speed light pulses, care still must be taken not to exceed these photocurrent limits. If the photocurrent exceeds the maximum current value, there will not only be a nonlinear relationship between the light intensity and the photocurrent, but also random multiple output pulses will be generated by a single light pulse. Generally, side-on type photomultiplier tubes draw more current than head-on types.

For use when subnanosecond response time is required, a photomultiplier tube equipped with a microchannel plate and/or a biplanar phototube is available (although the biplanar phototube's sensitivity is less than that of the photomultiplier).

Linear optical detectors described in detail in the 14.1.2.2 are quite useful for measuring fast transient phenomena. The linear detector is mounted on the exit focal plane of the monochromator. The output of individual photocells are stored in the corresponding CCD memory; the data are then transferred in serial form to a personal computer or to an oscilloscope through an A/D converter.

Using a combination of a two-dimensional CCD photodetector array and an image intensifier equipped with vertical deflection electrode, a streak camera type detector can be constructed.[23,24] By choosing the proper photocathode, these devices can cover a very wide spectral range, from X-rays to the near-infrared at 1.6 μm. Streak cameras are now commercially available with time resolutions of 2 ps for synchro-scan and 200 fs for single-sweep type units. The image intensifier is particularly suited for observation of high-speed transient phenomena, as it has an inherent built-in light shutter. The sensitivity of this arrangement is comparable to that of a photomultiplier tube. A multichannel type detector in combination with a monochromator is convenient for time-resolved spectroscopy, as spectroscopic data can be obtained even with single-pulse excitation. Presently, time-resolved spectra can be obtained with ~15-ps resolution.

14.3.2.2 *Signal amplification and processing*

To measure an analog signal, a boxcar integrator can be used. To measure a digital signal, on the other hand, a photon counter is employed in the boxcar integrator mode. A transient recorder holds transient data after the signal is digitized and this technique can be used to record single-shot phenomena. A transient recorder stores light intensity data as a function of time, whereas a multichannel detector stores light intensity changes as a function of wavelength.

Boxcar integrator. The basic circuit of this apparatus is a sample-and-hold circuit, which is shown in Figure 27. Signals are accumulated in the capacitor *C* with time constant $\tau = RC$ by opening and closing switch S synchronized to a repetitive signal. The output signal $V(t)$ can be expressed by the following equation:

$$V(t) = V_0\left[1 - \exp\frac{-t}{\tau}\right] \qquad (24)$$

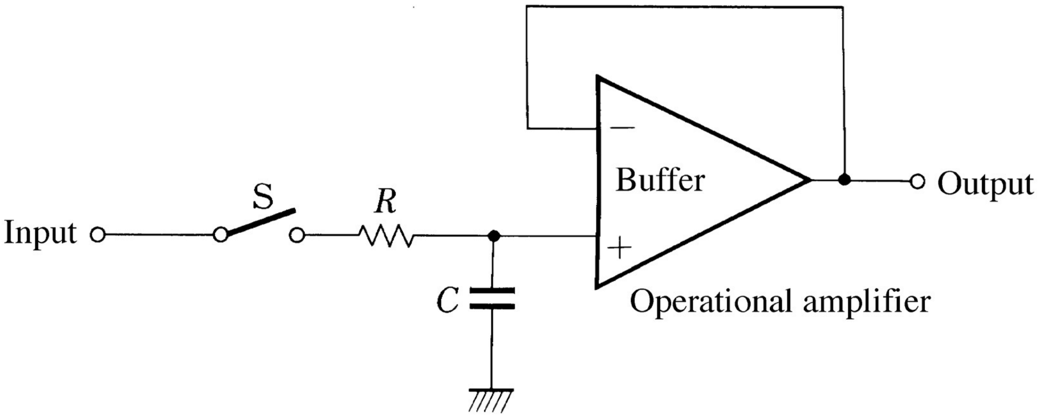

Figure 27 Sample-hold circuit diagram.

where V_0 is the final achievable value. With the time the switch is open as t_s and number of samplings per unit time as N, then $t = N \cdot t_s$. When $N \approx \tau/t_s (t = \tau)$, the output signal is about 63% of the input signal. For the output signal to be more than 99% of the input signal, the time required to accumulate the signal in the capacitor is $t \geq 5\tau$ and the number of samplings is $N \geq 5\tau/t_s$. Since the signal-to-noise ratio is defined as $\sqrt{\tau/t_s}$, the noise can be reduced by taking a smaller t_s and a longer τ. In order to obtain a good signal-to-noise ratio, therefore, the measuring time must be extended.

To measure the entire signal waveform, the timing for the opening of the gate is delayed and the delay time is stepped to cover the temporal extent of the signal. When the delay time is kept constant while the spectrometer wavelength is being scanned, a time-resolved spectrum is obtained. An electronic switching device such as an FET is often employed. Taking advantage of the fact that a photomultiplier tube is a high-gain and high-impedance current source, sampling can be done only when a high voltage is applied to the photomultiplier tube. The output current from the photomultiplier tube is then accumulated in the capacitor.

Photon-counting apparatus. When measuring light of extremely weak intensity, the analog technique described above requires long measuring times. To overcome this disadvantage, a photon-counting technique using the boxcar mode is employed. As with a boxcar integrator, intensity changes as a function of time can be obtained by varying the delay time of the photon-counting gate. The measured value can be stored in a digital memory device. Digital storage, unlike analog signals stored in boxcar integrators, is not subject to current leakage. The digital data thus obtained are convenient for further data processing.

Transient recorders. This device stores the waveform as digital data, from analog signals that are converted by a high-speed analog-to-digital converter. As this device can store data produced by a single-shot transient phenomenon, it is particularly useful for measuring chemically unstable samples. The device is normally equipped with a microprocessor that can process and manipulate the stored data; these functions include smoothing. The digital signals can be redisplayed on an oscilloscope after they have been converted back to analog by a digital-to-analog converter. Some recent commercial oscilloscopes have these capabilities built in and are convenient for optical measurements.

A transient recorder device in conjunction with a multichannel detector is useful for measuring the time-resolved spectrum of the sample, since the multichannel detector can monitor the intensity data as a function of the wavelength. A multichannel detector equipped with an image intensifier, which functions as light shutter and signal amplifier, is often employed in these cases. (See 14.1.2.)

14.3.2.3 Pulse excitation source

A conventional discharge lamp containing a rare gas such as Xe and pulsed lasers usually are employed as the excitation source. A rare-gas discharge lamp is convenient to use, as its emission light has a wide wavelength range but its power output is much lower than that of a laser. A discharge lamp with a rare gas can generate pulses of a few microseconds. When hydrogen or deuterium gas is introduced, the pulse width can be reduced to several nanoseconds. The pulse width of the discharge lamp can be further reduced to a single nanosecond by changing its electrode configuration.[25]

A pulsed laser generates a high-intensity, short pulse-width light. Detailed description of lasers is given in 14.1.3.3.

For electron beam excitation, an electron beam pulse can be obtained by applying a pulsed voltage to the control grid of the electron gun. With a conventional electron gun, it is necessary to apply 100 to 200 V to the grid. Pulse generators having rise times of several tens of nanoseconds are readily available commercially. If a shorter pulse width or rise time is required, a pulse generator equipped with a thyratron is necessary.

When using the equipment described above, the following should be noted. The discharge lamp, laser, and electron beam all generate radio-frequency noise when they are activated by high-speed, high electric-power switching. Since a small signal is commonly measured by a high-impedance detector in optical studies, the system tends to pick up radio-frequency noise readily. Noise of electromagnetic origin can be picked up by signal cables, which act as an antenna. It is necessary, therefore, to have a large grounding area so that the signal cables do not form closed loops. The noise source and the detector system must also be spatially separated from each other and each individual system must be electromagnetically shielded. When a trigger signal from the excitation source to the detector system is required, either light from the excitation source is used or the trigger signal is transmitted through an optical-fiber line.

14.4 Luminescence efficiency

14.4.1 Principles of measurement

The luminescence efficiency of a phosphor concerns the radiation from the sample in the ultraviolet, visible, and infrared regions and excludes heat or X-ray radiation. Luminescence efficiency is defined as the ratio of the energy (quanta) required to excite a phosphor to the energy (quanta) emitted from the sample. Luminescence efficiency is expressed in terms of either energy efficiency (watts/watts) or quantum efficiency (photons/photons), depending on the application.

Since the radiation emitted from the phosphor sample must be measured over the entire range of its emitted wavelengths, a detector whose sensitivity is independent of wavelength should be chosen, except when only a limited wavelength range is of interest or when the luminescence efficiency between samples having the same spectral distribution is compared. A thermopile, whose spectral sensitivity is independent of the wavelength over a wide range, is normally employed to measured energy efficiency. For quantum efficiency measurements, Rhodamine B, whose excitation wavelength dependence on the quantum efficiency is known to be constant when it is excited by a shorter-

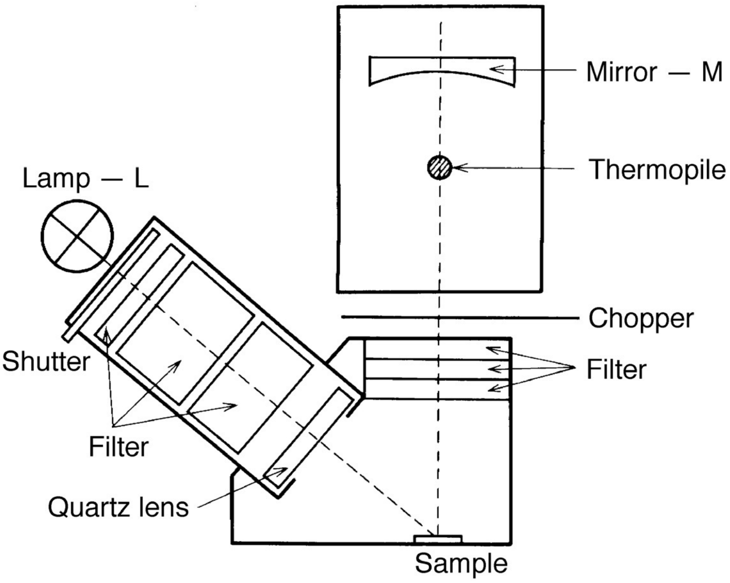

Figure 28 Luminescence efficiency measurement apparatus. (From Bril, A. and de Jager-Veenis, A.W., *J. Res. Natl. Bur. Stand., A*, 80A, 401, 1976. With permission.)

wavelength light than its emission wavelength, is often used.[26] A photon quanta-meter measures the light emitted from a phosphor sample irradiated on wavelength conversion materials such as Rhodamine B. When emitted light from a phosphor is expressed as spectral radiance distribution, the spectral distribution of photons and the total number of photons are obtained.

14.4.2 Measurement apparatus

14.4.2.1 Ultraviolet excitation

A typical apparatus for measuring the luminescence efficiency of a phosphor is shown in Figure 28.[27] The optical filters located in front of the excitation source transmit light between 250 and 270 nm, so they can isolate the 254-nm line from a high-pressure mercury lamp. A combination of a chlorine gas filter (4 atm and 4 mm thick), a nickel sulfate aqueous solution (500 g l^{-1} of $NiSO_4 \cdot 6H_2O$ in a cell 1 cm thick), and a Schott UG5 glass filter are used.[28] The output filter is a combination of glass filters that transmit the emission light but absorb the excitation light.

In the conventional method of measuring the luminescence-energy efficiency, a standard material of known energy efficiency is compared with the sample whose energy efficiency is to be measured. The energy efficiency can readily be obtained by comparing the luminescence intensity of the phosphor with that of the standard material. Standard materials are supplied by NIST (The National Institute of Standards & Technology, U.S.)[28,29]; sodium salicylate (for the far-ultraviolet and ultraviolet regions),[30] Ekta S10,[31] and Lumogen T red GC[32] are also available.

In order to measure absolute energy efficiency, the following procedure is employed using the apparatus shown in Figure 28.

Step 1. The diffuse reflectance intensity of excitation light is measured using a material such as $BaSO_4$. The wavelength dependence of the reflectance is known and is almost constant over a broad range of wavelengths.

Step 2. Without the filters, the sum of the intensities of luminescent light from the phosphor sample and the excitation light reflected by the sample is measured.

Step 3. Using filters, the intensity of luminescent light from the sample is measured.

The desired energy efficiency η_p and the reflectance of the sample r_p can be obtained from the output values of the thermopile at each step of the above measurement procedure. The reflectance of the standard material, the intensity of the excitation light, and the intensity of the reflected excitation light are denoted as R, I, and V_r, respectively. Designating the luminescence intensity as L, the thermoelectric power generated by both the luminescence from the sample and the excitation light reflected by the sample as V_p and the thermoelectric power generated by the luminescence light after passing through the filters as $V_{p,f}$, the following relations are obtained.

$$\begin{aligned} C \cdot V_r &= I \cdot R \\ C \cdot V_p &= I \cdot r_p + L \\ C \cdot V_{p,F} &= \tau \cdot L \end{aligned} \tag{25}$$

where C is the ratio of light energy to thermoelectric power and τ is the transmittance of the filters. From the above relations, the following equations can be derived.

$$\begin{aligned} \eta_p &= \frac{L}{I\left(1-r_p\right)} = \frac{R \cdot V_{p,F}}{\tau\left(1-r_p\right)V_R} \\ r_p &= \frac{R\left(V_p - V_{p,F}/\tau\right)}{V_R} \end{aligned} \tag{26}$$

Thus, from the three measurement steps described above, the luminescence energy efficiency and reflectance of a phosphor sample can be obtained. From the measured energy efficiency, the quantum efficiency q_p can be expressed in terms of the luminescence intensity of a sample $p(\lambda)$ at a given excitation wavelength λ_{exc}

$$q_p = \frac{\eta_p \int \lambda p(\lambda) d\lambda}{\lambda_{exc} \int p(\lambda) d\lambda} \tag{27}$$

If the luminescence intensity distribution over the wavelength range $p(\lambda)$ is known, the quantum efficiency can be calculated using the above relation.

To obtain energy efficiency even more precisely, the amount of luminescence light absorbed by the sample itself must be taken into account. Suppose the reflectance of a sufficiently thick sample is R_∞; then the true energy efficiency η_i becomes:

$$\eta_i = \frac{2\eta_p}{1+R_\infty} \tag{28}$$

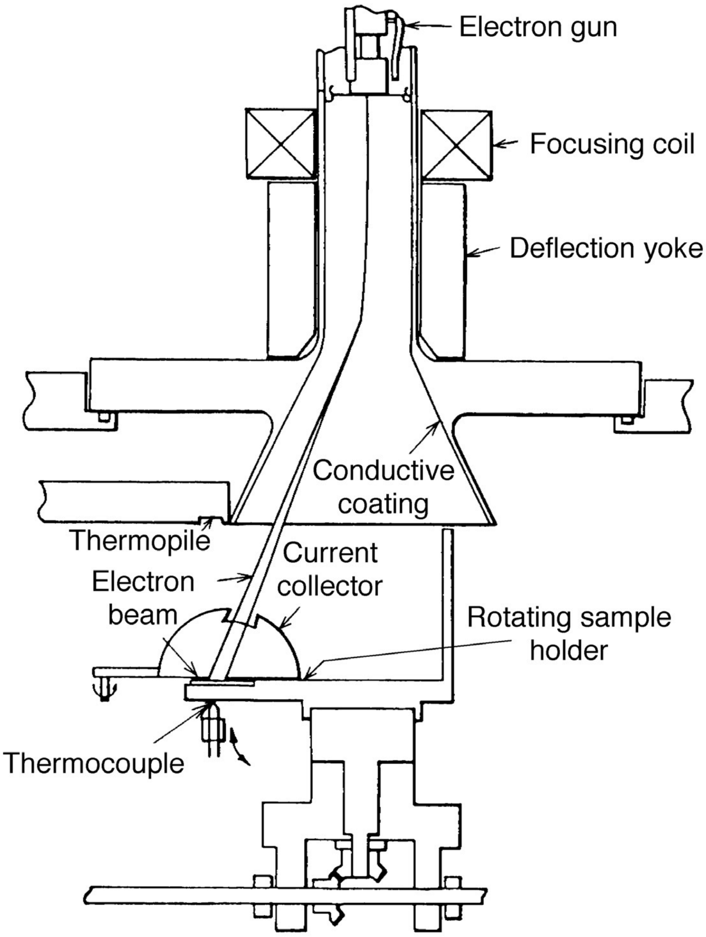
Electron gun
Focusing coil
Deflection yoke
Conductive coating
Thermopile
Current collector
Electron beam
Rotating sample holder
Thermocouple

Figure 29 Luminescence efficiency measurement by electron-beam excitation. (From Meyer, V.D., *J. Electrochem. Soc.*, 119, 920, 1972. With permission.)

In the above expression, it is assumed that half of the luminescence is emitted from the phosphor surface, the other half goes into the phosphor layers, and a portion of this is reflected out in turn. The excitation light is assumed not to penetrate inside the phosphor.

14.4.2.2 Electron-beam excitation[33]

An apparatus measuring the energy efficiency of a phosphor excited by an electron beam is shown in Figure 29.[33] To measure excitation energy, one must determine not only the beam current flowing into the sample, but also the secondary electrons emitted from the sample. To measure these quantities, a semispherical current collector (Faraday cage), which has a small window to allow passage of the electron beam, is employed. When energy of the emitted luminescence from the sample is measured using a thermopile, the Faraday cage is removed.

Luminescence efficiency for electron beam excitation η can be written as:

$$\eta = \frac{2\pi \cdot r^2 \cdot C \cdot V_p}{I_0 \cdot V_0 \left(1 + R_\infty\right)} \tag{29}$$

where r is the distance between the sample and the detector, C is the sensitivity of the detector ($W/W\cdot\mathrm{cm}^2$), V_p is the thermoelectric power, I_0 is the incident electron beam current, V_0 is the electron acceleration voltage, and R_∞ is the reflectance of a thick sample. The electron beam is scanned over the sample, as in TV raster scanning. Eq. 29 is satisfied when the diagonal distance of the raster scanning area is less than one-fifth of r.

14.5 Data processing

14.5.1 Spectral sensitivity correction

Since optical components such as spectrometers and light detectors used to measure the optical properties of phosphors do not have uniform sensitivity over the entire spectral range, the raw data must be corrected. The correction coefficients at each wavelength are obtained by measuring the intensity of a standard lamp with known radiation power at a given wavelength. A tungsten lamp calibrated by NIST or a halogen lamp manufactured by Ushio (JPD 100V500WCS) is available for these purposes. The correction coefficients should be obtained by measuring the standard under the same operating conditions used to measure the spectrum of a phosphor sample. These factors include parameters such as voltage applied to the photomultiplier and slit width and height of the spectrometer.

A sensitivity-corrected spectrum is generated as the product of the correction coefficients and raw spectral data. Because the correction coefficients of each optical component can vary, the entire system as a combination of components must be calibrated as a whole using a standard lamp. As the spectral sensitivity of the system also changes over time, periodic calibration of the system is recommended. When a rigorous measurement is required, corrections are made by comparing the sample's light with light from the standard lamp, point for point at each wavelength.

An example of spectral correction is shown in Figure 30. The arrow in Figure 30(b) shows Wood's anomaly, which is the non-monotonic rise of the transmission of light from a grating spectrometer as function of wavelength. This phenomenon is due to irregularities in the grating pitch. When spectra (a) and (c) in the same figure are compared, the sensitivity distortion of the spectrum becomes quite obvious.

Wavelength values as read from the counter of a scanning spectrometer are not always true values. The difference between the observed wavelength values and the true values fluctuates as the spectrometer is scanned. The wavelengths, therefore, need to be adjusted with correction coefficients, particularly when high-resolution work is being conducted. Normally, a linear approximation is used for the corrections using a few spectral lines of a mercury discharge lamp as a reference. For more precise work, a polynomial approximation is made, using as many lines as possible from several gas discharge lamps. The values for the characteristic spectral lines from the discharge lamps of various elements are tabulated in the reference books.[34]

Assuming the correction coefficients thus obtained for spectral sensitivity is $f(\lambda)$ and that of for the wavelength is $C(\lambda_0)$, the true spectrum can be written as:

$$\begin{aligned} I(\lambda) &= f(\lambda)\cdot I_0(\lambda) \\ \lambda &= C(\lambda_0)\cdot\lambda_0\lambda = C(\lambda_0)\cdot\lambda_0 \end{aligned} \tag{30}$$

where $I_0(\lambda)$ is measured luminescence intensity at a given wavelength and λ_0 is the value read from the spectrometer.

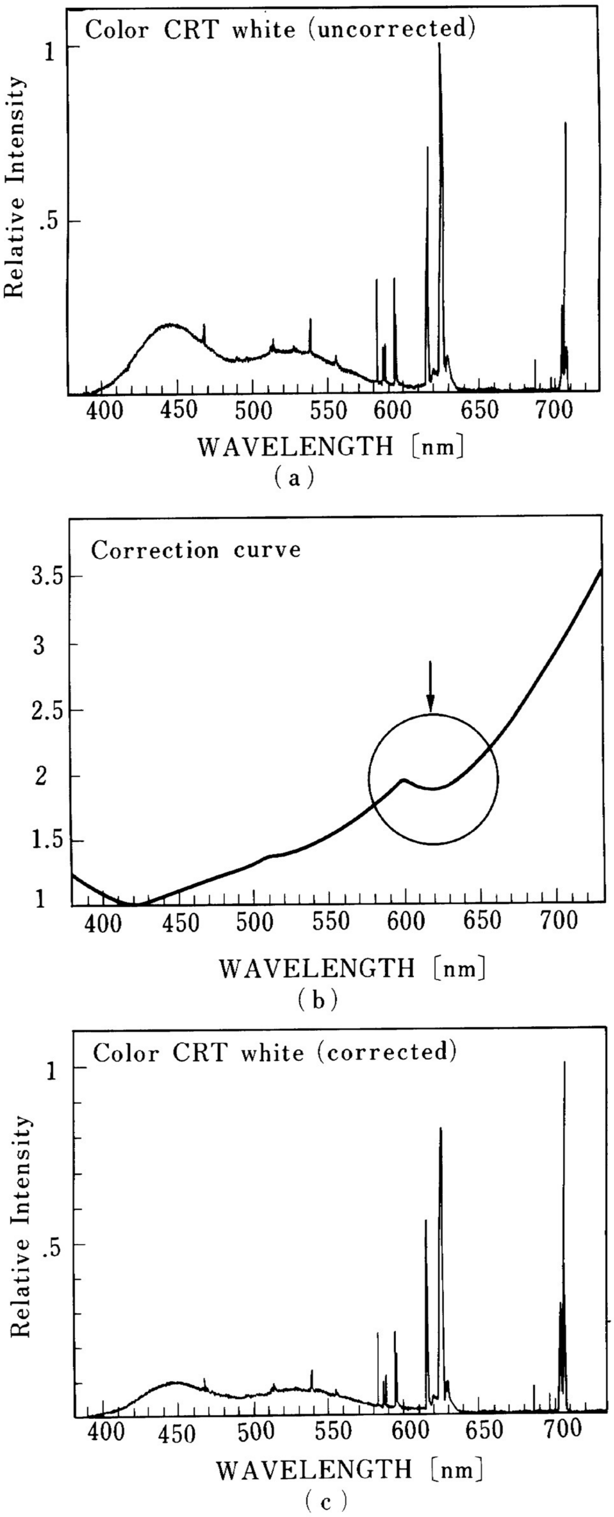

Figure 30 (a) Spectral sensitivity uncorrected spectrum. (b) Correction curve. (c) Spectral sensitivity corrected spectrum.

14.5.2 *Baseline correction*

Spectral data obtained from a measurement are usually superimposed on a baseline. The baseline is due to the total DC signal originating from various optical and electrical components of the system. The dark current of photomultiplier tube, stray light, and the DC bias of electronic components all contribute to the baseline value. True spectral data can be obtained by subtracting or adding the baseline to the observed spectral data. Using AC measurements described above, most of the baseline corrections can be eliminated.

The dark current value can be estimated by measuring the current at the photodetector while the optical shutter is closed. The value is recorded and used to correct the spectral data. Correction for stray light can be achieved by measuring the photocurrent for the entire wavelength region of interest without a sample and then subtracting this signal from the spectral data. This method of correcting the baseline is not applicable when the stray light intensity fluctuates. In this case, an improved measuring environment is recommended. Stray light generated within a spectrometer due to multiple reflections within the spectrometer is difficult to measure quantitatively. A spectrometer with low stray light should be selected for use.

The conventional method of correcting the baseline is to subtract the lowest signal data from the complete data. Care must be taken, however, to find the true minimum by observing the entire spectral distribution. Otherwise, small data peaks could be erroneously eliminated by this correction.

14.5.3 *Improvement of signal-to-noise ratio*

The shape of the spectrum and/or the decay curve can be distorted if random noise is superimposed on the data. In this case, smoothing of experimental data becomes necessary. There are two ways of smoothing the data: one is to acquire data repeatedly and then obtain the arithmetic mean of the total signal (the averaging method); another technique is to estimate the value at a point by taking the average of adjacent data points (the moving average method).

When the averaging method is applied to spectral data, the data must be reproducible as a function of wavelength. Likewise, when the averaging method is applied to decay curves, the time coordinates must be perfectly synchronized. If a simple arithmetic mean is computed for the accumulated values for each data point, the standard deviation of random noise decreases in proportion to $1/\sqrt{N}$, where N is the number of scans. (See Appendix.) The signal-to-noise ratio, therefore, can be improved to a certain extent by increasing the number of measurements. The degree of improvement brought about by this averaging, however, becomes smaller as the contribution per measurement becomes smaller and the total measuring time becomes longer.

The moving average method has an advantage over the averaging method in that it has a shorter measuring time and uses a numerical filter to smooth the experimental data. A simple moving average, $\bar{x}$, for equally spaced data x_i is defined as:

$$\bar{x} = \frac{1}{N}\sum_{i=-m}^{m} x_i, \qquad N = 2m+1 \tag{31}$$

where m is an integer. The standard deviation of noise in a random noise environment is therefore proportional to $1/\sqrt{N}$, as in the averaging method. If the number of data points increases while the interval between data points is kept constant, the region over which the

Table 1 Weighted Smoothing Coefficients for 2nd- and 3rd-Order Polynomial Fits

	Number of points			
Position	5	7	9	11
–5				–36
–4			–21	9
–3		–2	14	44
–2	–3	3	39	69
–1	12	6	54	84
0	17	7	59	89
1	12	6	54	84
2	–3	3	39	69
3		–2	14	44
4			–21	9
5				–36
Normalization coefficients	35	21	231	429

average is computed is broadened and, consequently, the shape of the spectrum or decay curve is distorted. On the other hand, if one simply increases the number of data points by narrowing the data interval, the low-frequency noise component is not eliminated.

For the purpose of smoothing experimental data while minimizing the distortion of spectral data or signal-shape data, the weighted moving average method is sometimes used. Using weighting coefficients w_i, the average value can be written in analogy to Eq. 31.

$$\bar{x} = \frac{\sum_{i=-m}^{m} w_i x_i}{\sum_{i=-m}^{m} w_i} \tag{32}$$

Distortion of data can be avoided if the weighting coefficients are adjusted to yield the same result as provided by a least-squares polynomial fit. The weighting coefficients obtained in the case of second- and third-order polynomial fits are tabulated in Table 1.[35]

An example of smoothing spectral data using a combination of the averaging method and the moving average method is shown in Figure 31. In this instance, to make the signal-to-noise ratio be 10/1 using the averaging method only, the number of measurements required is 100. A similar result can be obtained using a combination of the moving average method with 9 accumulations of data (1/3) and averaging 11 data points (1/3.3).

Optimization of data processing is required even for the weighted moving average method, as unnecessary increases in the number of data points results in a distortion of the spectral-shape data.

Appendix
Standard deviation of random noise with averaging

Data sampling is used to extract multiple samples from a parent population having an average value μ, and a dispersion σ^2 defined by probability theory. If the number of samples to be extracted is N and the sample varieties are $X_i (i = 1, \ldots, N)$, then the sample mean $\overline{X}$ can be written as:

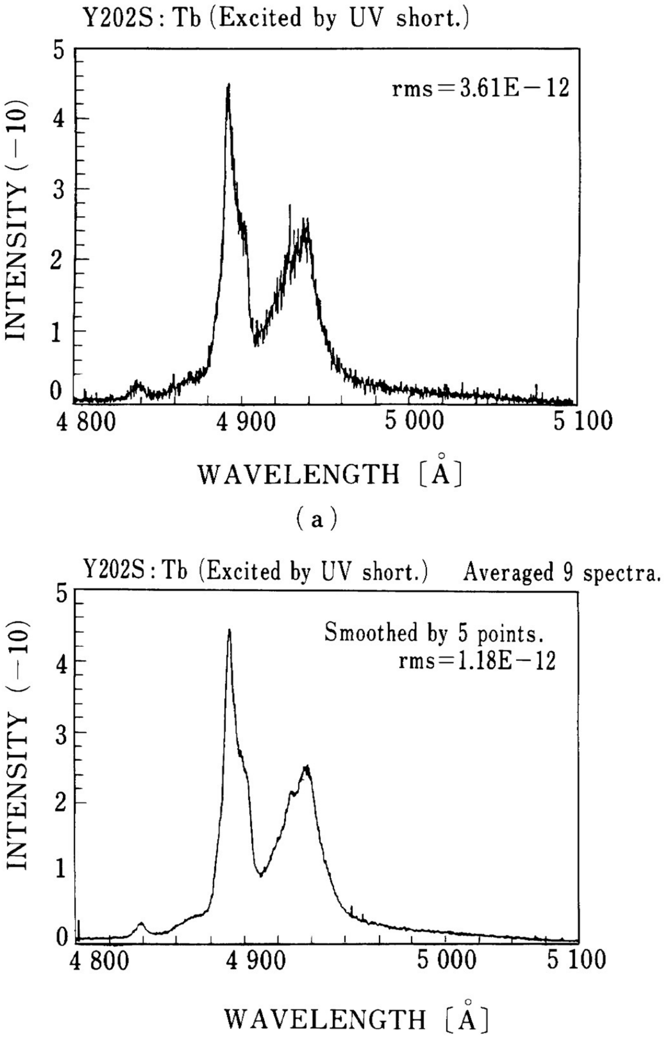

(a)

(b)

Figure 31 (a) Spectral data obtained by single measurement. (b) Smoothed spectrum after 9-times data accumulation.

$$\overline{X} = \frac{1}{N}\sum_{i=1}^{N} X_i \tag{33}$$

In this case, the expectation value μ_N of $\overline{X}$ is given as:

$$\begin{aligned} \mu_N &= E(\overline{X}) = \frac{1}{N}\sum_{i=1}^{N} E(X_i) \\ &= \frac{1}{N}\sum_{i=1}^{N} \mu_i = \mu \end{aligned} \tag{34}$$

where μ_i is the expectation value of X_i. The dispersion $\sigma_N{}^2$ of the $\overline{X}$ is expressed as:

$$\begin{aligned}\sigma_N^2 &= E\left\{\left(\overline{X} - E\left(\overline{X}\right)\right)^2\right\} \\ &= E\left\{\left[\frac{1}{N}\sum_{i=1}^{N}\left(X_i - \mu_i\right)\right]^2\right\} \\ &= \frac{1}{N^2}\left\{\sum_{i=1}^{N} E\left(X_i - \mu_i\right)^2 + \sum_{i\neq j}^{N} E\left[\left(X_i - \mu_i\right)\left(X_j - \mu_j\right)\right]\right\}\end{aligned} \tag{35}$$

If X_i and X_j are mutually independent, the second term of the left-hand side of the above equation becomes 0 and the following equation is obtained.

$$\sigma_N^2 = \frac{1}{N}\sum_{i=1}^{N} E\left\{\left(X_i - \mu_i\right)^2\right\} = \frac{\sigma^2}{N} \tag{36}$$

This means that the standard deviation σ_N of sample varieties is equal to $1/\sqrt{N}$ of the standard deviation of population σ. Consequently, the expectation value of averaging N sample data thus obtained is the true value and the component of superimposed random noise on the true value is $1/\sqrt{N}$.

References

1. Driscoll, W.G., *Handbook of Optics*, Section 1, MacGraw-Hill, New York, 1978.
2. Bass, M., Van Stryland, E.W., Williams, D.R., and Wolfe, W.L., Eds., sponsored by the Optical Society of America, *Handbook of Optics*, I & II, McGraw-Hill, New York, 1995.
3. Czerny, M. and Turner, A.F., *Z. Phys.*, 61, 792, 1930.
4. *Model 1702 Instruction Manual*, Jobin Yvon-Spex, Edison, New Jersey.
5. Seya, M., *Sci. Light*, 2, 8, 1952 Namioka, T., *Sci. Light*, 3, 15, 1954; Namioka, T., *J. Opt. Soc. Am.*, 49, 951, 1959.
6. Chemical Society of Japan, Ed., *New Experimental Chemistry Series, Fundamental Technique 3, Light [1]*, Maruzen, 1976, 165 (in Japanese).
7. *Photomultiplier Tubes Catalog*, Hamamatsu Photonics, Shizuoka, Japan, August 1995.
8. Wilson, J. and Hawkes, J.F.B., *Optoelectronics, An Introduction*, Prentice-Hall, 1989, 284.
9. *Monolithic Miniature Spectrometer, Product Information*, Carl Zeiss, Germany.
10. Wilson, J. and Hawkes, J.F.B., Reference 8, p. 296.
11. *Guide for Spectroscopy*, Jobin Yvon-Spex, Edison, New Jersey, 1994, 217.
12. Bilhorn, R.B., Sweedler, J.V., Epperson, P.M., and Denton, M.B., *Appl. Spectrosc.*, 41, 1114, 1987.
13. *Applications of Multi-channel Detectors Highlighting CCDs*, Jobin Yvon-Spex, Edison, New Jersey.
14. Nagamura, A., Mugishima, T., and Sakimukai, S., *Rev. Sci. Instrum.*, 60, 617, 1989.
15. *Discharge Lamps, Technical Brochure*, Ushio, Tokyo, Japan.
16. *CRC Handbook of Laser Science and Technology, Supplement 1: Lasers*, Weber, M.J., Ed., CRC Press, Boca Raton, FL.
17. Maeda, M. and Miyazoe, Y., *J. Appl. Phys.*, 41, 818, 1972; *Laser Handbook*, Ohm Sha, 1982 Tokyo, Japan (in Japanese).
18. Spinelli, L., Couillaud, B., Goldblatt, N., and Negus, D. K., *CLEO'91*, post deadline submission, 1991.
19. Sugahara, H., Ohnishi, Y., Matsuno, H., Igarashi, T., and Hiramoto, T., *Proc. 7th Int. Symp. the Science & Technology of Light Sources*, Kyoto, Japan, 1995.

20. Pankove, J.I., *Optical Process in Semiconductors*, Dover Publication, New York, 1975, 113.
21. *Applied Optics Handbook*, Yoshinaga, H., Ed., Asakura Shoten, Tokyo, 1973, 605 (in Japanese).
22. Chemical Society of Japan, *ibid., light[II]*, pp. 401.
23. Bradley, D.J., Liddy, B., Sibbett, W., and Sleat, W.E., *Appl. Phys. Lett.*, 20, 219, 1972.
24. Wang, X.F., Uchida, T., Coleman, D.M., and Minami, S., *Appl. Spectrosc.*, 45, 360, 1991.
25. Hundley, L., Coburn, T., Garwin, E., and Stryer, L., *Rev. Sci. Instrum.*, 38, 488, 1967.
26. Velapoldi, R.A., *Accuracy in Spectrophotometry and Luminescence Measurements*, U.S. Dept. of Commerce, Washington, D.C., 1973.
27. Bril, A. and de Jager-Veenis, A.W., *J. Res. Natl. Bur. Stand., A*, 80A, 401, 1976.
28. Bril, A. and Hoekstra, W., *Philips Res. Repts.*, 16, 356, 1961.
29. Ludwig, G.W. and Kingsley, J.D., *J. Electrochem. Soc.*, 117, 348 & 353, 1970.
30. Samson, J.A.R., *Techniques of Vacuum Ultraviolet Spectroscopy*, John Wiley & Sons, New York, 1967.
31. Grum, F., *C. I. E. Report of Subcommittee on Luminescence*, 18th Session, London, 1975.
32. Bril, A. and de Jager-Veenis, A.W., *J. Electrochem. Soc.*, 123, 396, 1976.
33. Meyer, V.D., *J. Electrochem. Soc.*, 119, 920, 1972.
34. Harrison, G.R., *MIT Wavelength Table*, The MIT Press, 1969.
35. Savitzky, A. and Golay, M.J.E., *Anal. Chem.*, 36, 1627, 1964.

chapter fourteen — section six

Measurement of luminescence properties of phosphors

Shinkichi Tanimizu

14.6 Measurements in vacuum-ultraviolet region 887
  14.6.1 Light sources 888
  14.6.2 Monochromators 889
  14.6.3 Sample chambers 890
  14.6.4 Measurements of excitation spectra 891
References 892

14.6 Measurements in the vacuum-ultraviolet region

The wavelength region between about 0.2 and 200 nm is called the vacuum-ultraviolet (abbreviated to VUV) region; most of the VUV spectrometers need to be evacuated in this region because of the opacity of oxygen in air to this radiation. Following Samson's definition,[1] the region between 100 and 200 nm is called the Schumann UV region; here, the H_2 discharge lamp can provide useful radiation as an excitation light source. The wavelength region between 100 and 0.2 nm is known as the extreme UV (EUV) region, and it includes the region of 0.2 to 30 nm, called the soft X-ray region.

The absorption spectra of O_2 at a pressure of 10^4 Pa in the Schumann UV region, known as the Schumann-Runge bands and continuum, are shown in Figure 32.[2,3] This figure shows that the absorption coefficients of O_2 at 121.6 nm (the position of the Lyman α emission line of hydrogen atoms), and also at 184.9 nm (one of the resonance emission lines of mercury atoms) are 1 cm^{-1} or less at this O_2 pressure. These two emission lines can be used as light sources by merely flowing transparent N_2 gas along the optical path instead of evacuating the spectrometer.

The above-referenced book by Samson (1967)[1], despite its age, is still an excellent textbook for beginners of spectroscopy in the VUV region. The book describes details of concave gratings, their mountings, light sources, window materials, detectors, polarizers, and absolute intensity measurements in the VUV region.

Spectroscopic measurements of powder phosphors can be carried out conveniently in the Schumann UV region using LiF crystal windows, which have the shortest wavelength transmittance limit (105 nm) among any known windows. Hydrogen discharge lamps can be used as excitation light sources.

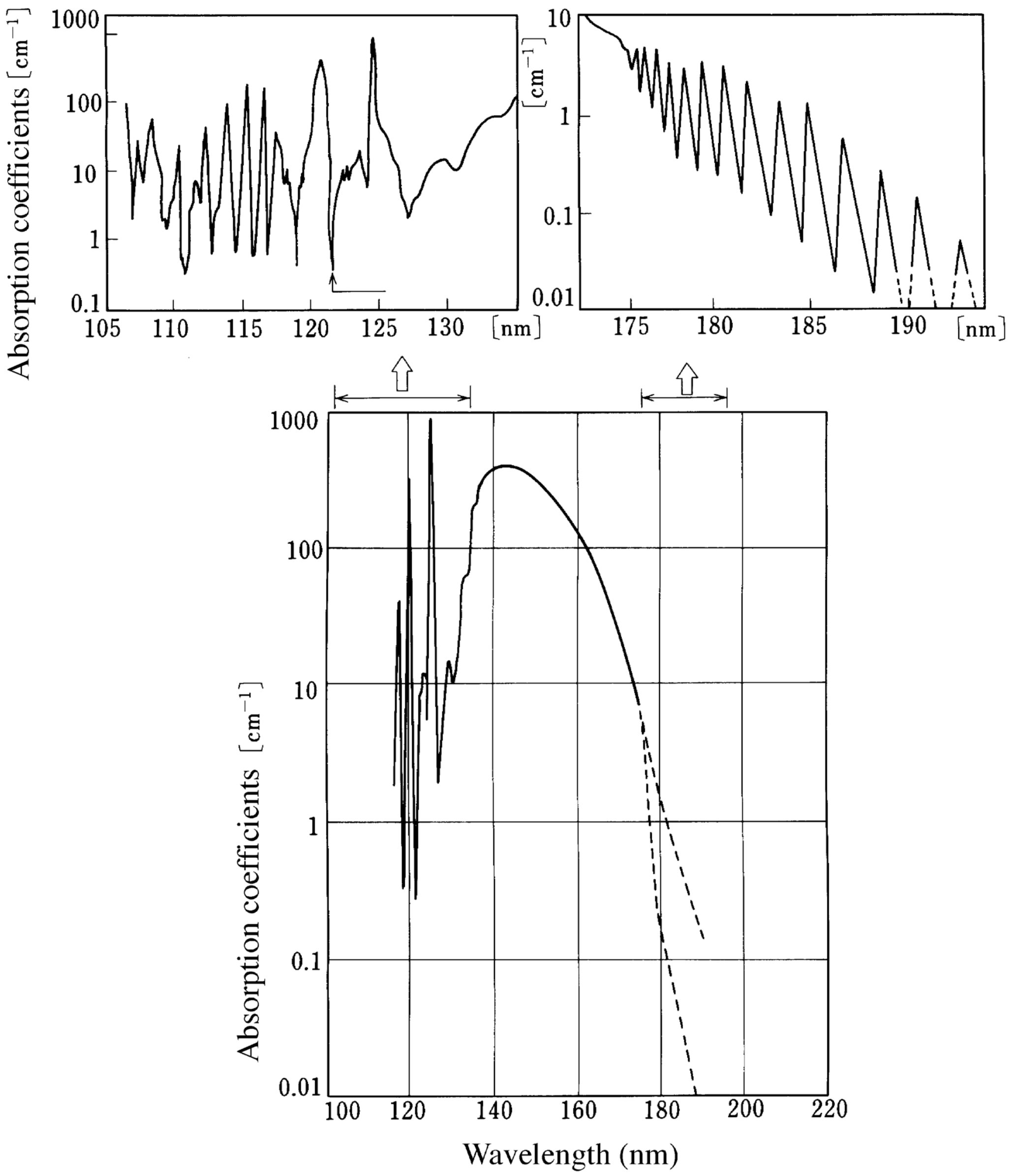

Figure 32 Absorption spectra of O_2 at a pressure of 10^4 Pa in the Schumann UV region. (From Watanabe, K., Inn, E.C.Y., and Zelikoff, M., *J. Chem. Phys.*, 21, 1026, 1953; Tanaka, Y., Inn, E.C.Y., and Watanabe, K., *J. Chem. Phys.*, 21, 1651, 1953. With permission.)

Some spectroscopic instruments and their applications in the Schumann UV region will be described.

14.6.1 Light sources

Conventional hydrogen or deuterium discharge lamps of 30 to 150 W[4] are normally used in conjunction with 0.2 to 0.4 m (focal length) VUV monochromators. Figure 33 shows the spectral output of a 30-W D_2 lamp with a MgF_2 window.[5] Emission between 165 and 370 nm

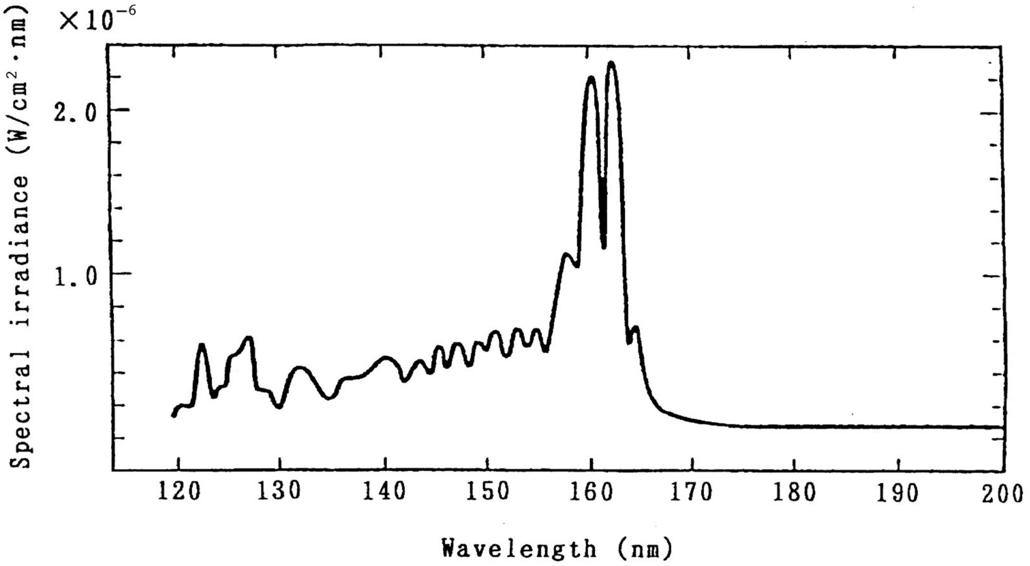

Figure 33 Spectral output of a deuterium lamp with a MgF_2 window in the Schumann UV region. (From Oyama, K.-I., Suzuki, K., Kawashima, M., Zalpuri, K.S., Teii, S., and Nakamura, Y., *Rev. Sci. Instrum.*, 62, 1721, 1991. With permission.)

is continuous, while below 165 nm, molecular lines predominate. The transmittance limit of polished MgF_2 lies at 115 nm. In these low-power lamps, the cathode (filament) and anode structures are supported in a quartz tube with dimensions of 30 to 50 mm in diameter and 70 to 190 mm in length. Starting voltages are 350 V for 30 W and 500 V for 150 W lamps, respectively. Operating currents and voltages are 0.3 A at 80 V for a 30-W lamp and 1.2 A at 120 V for a water-cooled 150-W lamp. For hot cathode lamps, the life is determined by the loss of H_2 or D_2 gas caused by a reaction with the qualtz wall. This loss is lower for D_2 than for H_2; thus, the D_2 lamp is widely used as an excitation light source. However, the continuous gas diffusion of D_2 or H_2 through the quartz envelopes[6] is the primary cause of the decrease in light output of the hot cathode lamps. It should be noted that the output of the D_2 lamp is lower than that of H_2 lamps below 170 nm.[7]

For 0.5 to 1 m VUV monochromators, the use of much stronger gas flow type H_2 lamp of 0.3 to 1 KW is recommended. Both McPherson Co. and Acton Research Co. have developed various types of VUV light sources of this type.[8] Typical parameters for cold cathode discharge lamps are: starting voltage 1.5–2 KV; operating voltage 0.5–0.8 KV, discharging current ~0.5 A, and H_2 gas pressure 150–300 Pa.

14.6.2 Monochromators

Seya-Namioka mount monochromators[1,9–11] are recommended for laboratory use because of the simplicity of the focusing mechanism and the possibility of using a sine drive to obtain a linear wavelength scale. As shown in Figure 34,[12] the entrance slit S_1, the exit slit S_2, and the concave grating G are placed on a Rowland circle. The grating G rotates around the vertical axis fixed at the center of G. The angle $\angle S_1GS_2$ is set at 70°15' for an equally spaced concave grating; this configuration has the advantage of having enough space to allow the excitation light source to be set in front of S_1 and the sample chamber to be placed at the rear of S_2. The astigmatic and comatic errors of this mounting arising from large incidence angles can be greatly reduced by using a mechanically ruled aberration-corrected concave

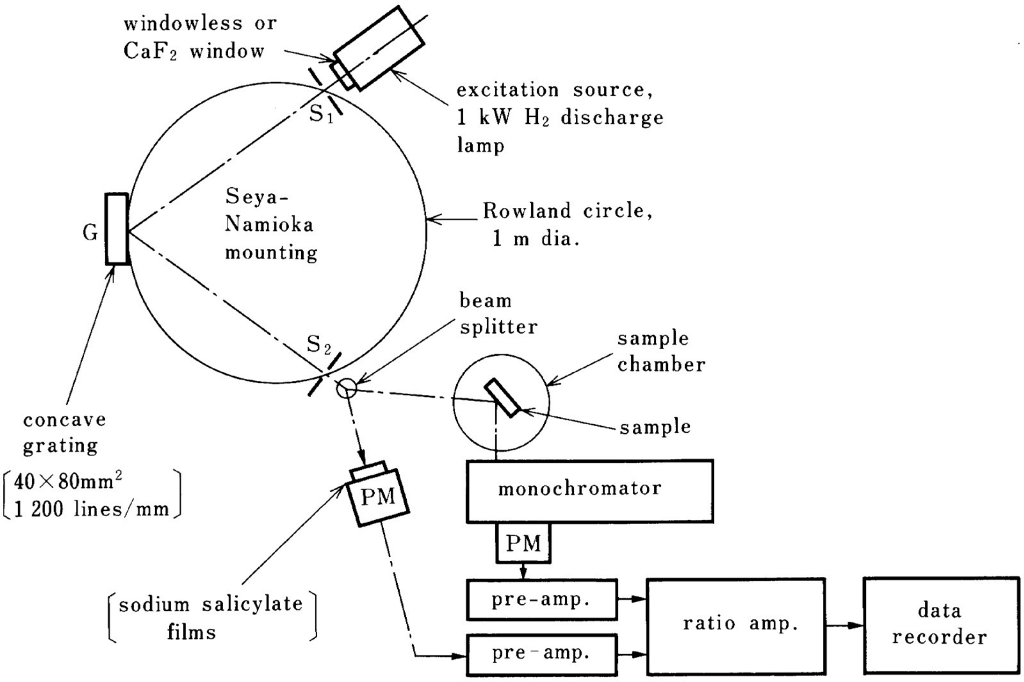
windowless or
CaF₂ window
excitation source,
1 kW H₂ discharge
lamp
S₁
G
Seya-
Namioka
mounting
Rowland circle,
1 m dia.
beam
splitter
S₂
sample
chamber
sample
concave
grating
40×80mm²
1 200 lines/mm
PM
monochromator
PM
sodium salicylate
films
pre-amp.
pre-amp.
ratio amp.
data
recorder

Figure 34 Schematic diagram of equipment used to measure excitation spectra of powder phosphor samples. (From Tanimizu, S., unpublished results. With permission.)

grating[13] or a specially designed holographic grating. Holographic gratings are interference gratings recorded with the use of wavefronts; in particular, the use of aspheric wavefronts reduces coma aberration in the Seya-Namioka mounting.[14]

Apart from the Seya-Namioka mount, the Johnson-Onaka mount,[15,16] which is of the normal incidence type, has been widely used for measurements of optical constants, *n* and *k*, in semiconductors.[17] High resolution can be achieved by this mount. However, it is necessary to design both the excitation source and sample chamber as compact as possible, inasmuch as they are located on the same side of the monochromator tank.

14.6.3 Sample chambers

The monochromatic light beam is divided into two beams at the rear of S_2 by a beam splitter consisting of a reflecting toroidal mirror pile; one beam excites the sodium salycilate film and the other enters into a sample chamber. Sodium salycilate is used to convert VUV light to visible light. It emits blue luminescence peaking at 420 nm with about a 10-ns decay time, and has a nearly constant quantum efficiencies of ~60% for wavelengths between 90 and 350 nm.[1,18–20] Its luminescence peak coincides with the maximum sensitivity of common photomultipliers so that the VUV radiation from the H_2 discharge lamp can be detected efficiently. Sodium salycilate films can be easily prepared by spraying a saturated methyl alcohol solution of sodium salicylate on a glass substrate kept at a temperature of 90 to 110°C. The optimum surface density of a film is about 1 mg cm^{-2}.

The chamber (inner size; 190 mmϕ × 160 mm) is equipped with a vertically rotatable turret located near the center, a small goniometric stand for mounting a detector and filters, and vacuum-sealed windows for detecting the emission, transmission, and reflection

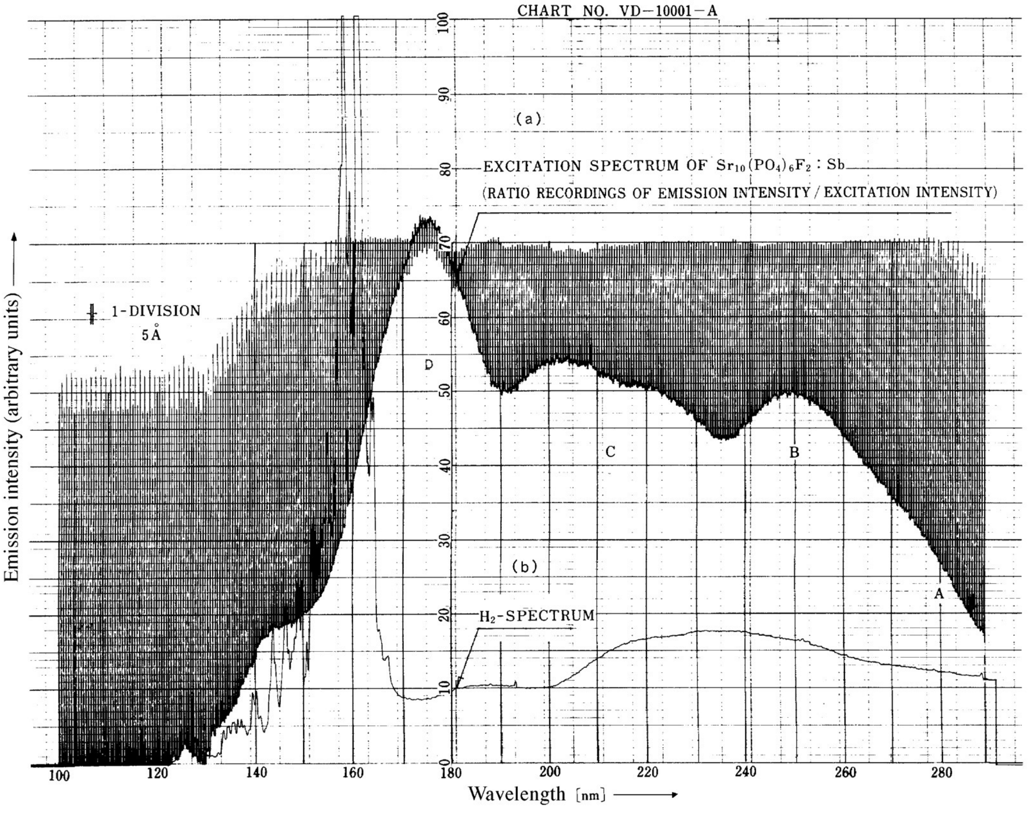

Figure 35 Recordings of an excitation spectrum for $Sr_5(PO_4)_3F:Sb^{3+}$ and the H_2 spectrum. (From Tanimizu, S., unpublished results. With permission.)

beams. A powder sample is packed into a hole of about 10 × 10 × 1 mm^3 drilled at the center of a stainless steel sample holder of dimensions of the order of 25 × 35 × 2 mm^3; the sample is then made flat by a glass plate. It is convenient to mount four sample holders at a time on the turret before evacuating the vacuum system. By opening or closing a gate valve located between the grating and the exit slit, one can change samples in about 10 minutes.

14.6.4 Measurements of excitation spectra

The excitation of powder phosphor samples is made at 45° incidence, and the relative output from the samples as a function of wavelength is determined in comparison with the output from the sodium salycilate screen.

Figure 35[21] shows an example of an excitation spectrum with subnanometer resolution for the 500 nm emission of $3Sr_3(PO_4)_2{\cdot}SrF_2:Sb^{3+}$ [= $Sr_5(PO_4)_3F:Sb^{3+}$]. Here, the signals from the sodium salycilate screen and the powder sample are detected by a pair of EMI 9789QB (bialkali) photomultipliers[22] of the head-on type. The normal A, B, C, and D excitation bands of Sb^{3+}, an s^2-type ion, are observed (see 3.1). Scanning from longer wavelengths to shorter wavelengths was found to be effective in the prevention of color center formation in the sample. In order to determine the quantum efficiency from Figure 35, it is necessary to measure a reflection spectrum of the sample in order to calculate the rate of photon absorbtion. The combination of a side-view photomultiplier coated with sodium salicylate and optical filters, both of which are mounted on the above-mentioned goniometric stand, are useful for angular-dependent reflection measurements on the sample.

In the EUV region below 100 nm, synchrotron radiation spectroscopy is very useful; this type of spectroscopy is now entering the third-generation development phase.[23] The instrumentation used in this spectroscopy (such as optical systems, detectors, electronics, and data acquisition) has been extensively reviewed. Readers are referred to References 24 through 28. Reference 27 presents quantum efficiency spectra in the 5- to 25-eV region for well-known powder phosphors excited by synchrotron radiation.

References

1. Samson, J.A.R., *Techniques of Vacuum Ultraviolet Spectroscopy,* John Wiley & Sons, New York, 1967; Samson, J.A.R.,Ederer, D.L.(Eds), *Vacuum Ultraviolet Spectroscopy, I, II,* Academic Press, San Diego, 1998.
2. Watanabe, K., Inn, E.C.Y., and Zelikoff, M., *J. Chem. Phys.*, 21, 1026, 1953.
3. Tanaka, Y., Inn, E.C.Y., and Watanabe, K., *J. Chem. Phys.*, 21, 1651, 1953.
4. See the following technical data sheets (1996). Hamamatsu Photonics K.K. (Shizuoka Pref., Japan), Models L879 & L1835. Nisseisangyo Co. (Tokyo, Japan), Model H4141SV. McPherson Co. (MA, U.S.), Model 632. Carl Zeiss Jena GmbH. (Jena, Germany), Model CLD 500.
5. Oyama, K.-I., Suzuki, K., Kawashima, M., Zalpuri, K.S., Teii, S., and Nakamura, Y., *Rev. Sci. Instrum.*, 62, 1721, 1991.
6. Lee, R.W., Frank, R.C., and Swets, D.E., *J. Chem. Phys.*, 36, 1062, 1962.
7. Levikov, S.I. and Shishatskaya, L.P., *Opt. Spectrosc.*, 11, 371, 1961.
8. See the following technical data sheets (1996). McPherson Co. (MA, U.S.), Models 630 & 631. Acton Research Co. (MA, U.S.), Model CSW-772-W.
9. Seya, M., *Science of Light (Tokyo)*, 2, 31, 1952.
10. Namioka, T., *Science of Light (Tokyo)*, 3, 15, 1954; and *J. Opt. Soc. Am.*, 49, 951, 1959.
11. Pouey, M., Principles of vacuum ultraviolet instrumental optics, in *Some Aspects of Vacuum Ultraviolet Radiation Physics*, Damany, N., Romand, J., and Vodar, B., Eds., Pergamon Press, New York, 1974, Part IV.
12. Tanimizu, S., unpublished results.
13. Harada, T. and Kita, T., *Appl. Opt.*, 19, 3987, 1980.
14. Noda, H., Harada, Y., and Koike, M., *Appl. Opt.*, 28, 4375, 1989.
15. Johnson, P.D., *Rev. Sci. Instrum.*, 28, 833, 1957.
16. Onaka, R., *Science of Light (Tokyo)*, 7, 23, 1958.
17. Philipp, H.R. and Ehrenreich, H., *Phys. Rev.*, 129, 1550, 1963.
18. Allison, R., Burns, J., and Tuzzplino, A.J., *J. Opt. Soc. Am.*, 54, 747, 1964.
19. Nygaard, K.J., *Br. J. Appl. Phys.*, 15, 597, 1964.
20. Seedorf, R., Eicheler, H.J., and Kock, H., *Appl. Opt.*, 24, 1335, 1985.
21. Tanimizu, S., unpublished results.
22. See the technical data sheets of Thorn EMI Electron Tube Ltd. (Middlesex, U.K.), 1993.
23. Ishii, T., *J. Synchrotron Rad.*, Inaugural Issue, 1, Part 1, 95, 1994.
24. Koch, E., Haensel, R., and Kunz, C., Eds., *Vacuum Ultraviolet Radiation Physics*, Pergamon-Vieweig, Braunschuweig, 1974.
25. Kunz, C., Ed., *Synchrotron Radiation—Techniques and Application*, Springer-Verlag, 1979.
26. Hafmann, H., *The Physics of Synchrotron Radiation*, Cambridge University Press, UK, 2004.
27. Berkowitz, J.K. and Olsen, J.A., *J. Luminesc.*, 50, 111, 1991.
28. J-stel., T., Krupa, J-C., Wiechert, D. U., *J. Luminesc.*, 93, 179, 2001.

chapter fifteen — sections one–three

Measurements of powder characteristics

Sohachiro Hayakawa

Contents

15.1 Particle size and its measurement 894
  15.1.1 Shape and size of particles 894
    15.1.1.1 Circularity and sphericity 895
    15.1.1.2 Shape factor and effective and equivalent diameters 895
  15.1.2 Particle size distribution 896
    15.1.2.1 Types of particle size distribution 896
    15.1.2.2 Mean diameter of particles 896
    15.1.2.3 Particle-size distribution function 896
  15.1.3 Classification and selection of the method for measuring particle size 899
15.2 Methods for measuring particle size 899
  15.2.1 Image analysis of particles 899
    15.2.1.1 Preparation of microsection 899
    15.2.1.2 Image analysis 899
  15.2.2 Volume analysis of particles 902
    15.2.2.1 Sieving 902
    15.2.2.2 Coulter counter 902
  15.2.3 Analysis of particle motion 904
    15.2.3.1 Sedimentation method 904
    15.2.3.2 Centrifugal sedimentation method 907
    15.2.3.3 Inertia force method 907
    15.2.3.4 Laser doppler method 908
  15.2.4 Analysis of the surface area of particles 909
    15.2.4.1 Adsorption method 909
    15.2.4.2 Transmission method 911
  15.2.5 Scattering of electromagnetic waves caused by particles 912
    15.2.5.1 Light scattering method 912
    15.2.5.2 Diffraction method 914
    15.2.5.3 X-ray diffraction and X-ray scattering 914
15.3 Measurements of packing and flow 916
  15.3.1 Definition of packing 916

15.3.2 Measurements of apparent density 917
15.3.3 Measurements of fluidity 918
15.3.3.1 Rest angle 918
15.3.3.2 Motion angle 918
15.3.3.3 Powder orifice 918
References 919

Powder characteristics of powders depend on their state, whether dry or wet, compressed in mold, sintered, or dispersed as slurry. Devices and methods for measurement also depend on the state of the powders. The physical properties are determined by some basic characteristics of the powders, as follows:

1. Size and shape of powder particles.
2. The packing and flow properties are partially dependent on the particle size and shape, whereas the aggregation and flow properties depend on their kinematic or dynamic behavior. These properties are called powder characteristics in the narrow sense of the word.
3. Electrical, magnetic, optical, and acoustical properties of the powder. These characteristics are determined by the intrinsic conductivity, the light scattering behavior, the surface properties, etc. of the powder. Powder characteristics in the broad sense of the word include these properties.

Each of the physical properties of the powder can be measured experimentally using methods developed for that specific purpose. As powders are found in the different states mentioned above, different techniques are employed, as will be described below.

Powder characteristics treated in this chapter are limited to topics 1 and 2 above. Optical properties are described in Chapter 16.

15.1 *Particle size and its measurement*

15.1.1 *Shape and size of particles*

If all particles are spherical or cubic in shape, one can express their size by measuring the diameter or the length of sides, but such a case is extremely rare with fluorescent powders. For irregular-shaped particles, when they are statistically almost similar in shape, one can

Table 1 Mean and Equivalent Diameter of One Particle

Term	Definition
Two axes mean diameter (m.d.)	$(1 + b)/2$
Three axes m.d.	$(1 + b + h)/3$
Harmonic m.d.	$3(l/l + l/b + l/h)^{-1}$
Enveloping rectangular equivalent diameter (e.d.)	$(bl)^{1/2}$
Square e.d.	$(f)^{1/2}$
Circle e.d.	$(f/\pi)^{1/2}$
Cuboid e.d.	$(lbh)^{1/3}$
Cylinder e.d.	$(fh)^{1/3}$
Cube e.d.	$(V)^{1/3}$
Sphere e.d.	$(6V/\pi)^{1/3}$

Note: l: length, b: breadth, h: height, f: projected area, V: volume.

compare their size by length (l), breadth (b), and height (h), or use either a mean or equivalent diameter, as shown in Table 1.

15.1.1.1 *Circularity and sphericity*

Generally, the shape is described by the ideal shape closest to the actual shape of the particles, i.e., sphere, cube, cylinder, needle, flake, lump, etc. It is necessary, however, to describe the shape of the particles quantitatively or with numbers, since the shape is very important in determining other physical properties. Quantities such as circularity and sphericity are therefore defined to quantify the degree of difference in shape between an ideal sphere and the actual particles, as follows:

$$\text{Circularity} = \frac{\begin{array}{c}\text{Circumference of a circle whose area equals}\\ \text{the projection area of a typical particle}\end{array}}{\text{Circumference of the projection of a typical particle}}$$

and

$$\text{Sphericity} = \frac{\begin{array}{c}\text{Surface area of a sphere whose volume}\\ \text{equals the volume of a typical particle}\end{array}}{\text{Surface area of a typical particle}}$$

For irregular-shaped particles for which measurements of circumference and surface area are difficult, one uses:

$$\text{Practical sphericity} = \left(\text{Volume of a typical particle}/\text{Volume of circumscribing sphere}\right)^{1/3}$$

15.1.1.2 *Shape factor and effective and equivalent diameters*

Various methods for measuring the particle size use the applicable law of physics, assuming that the shape of particles is spherical or of a simple shape. In this case, the shape factors are defined in terms of the relation between the representative diameter (e.g., diameter of a sphere) D_p and the particle size for the particles of interest. Generally, the mean volume and mean surface area per particle are measured, and the volume factor ϕ_v and area shape factor ϕ_s are calculated by the following equations.

$$V = \phi_v D_p{}^3 \tag{1}$$

and

$$S = \phi_s D_p{}^2 \tag{2}$$

For spherical particles, $\phi_v = \pi/6$ and $\phi_s = \pi$.

It should be noted that the numerical values of the shape factors depend on the physics laws applicable to the measurements. For example, consider the determination of the effective diameter of a powder using their sedimentation in a solution. The measured sedimentation rate is compared with the rate for ideal spherical particles of equivalent density as determined by the Stokes equation (see 15.2.3.1). The diameter of the sphere thus determined is called the Stokes diameter, and is adopted as the effective diameter of the powder particles.

Another definition of the diameter of particles that does not use the shape factor is equivalent diameter. This diameter is that of an ideally shaped particle that is comparable in size to the particle to be measured. Typical equivalent diameters are shown in Table 1.

15.1.2 *Particle size and distribution*

The diameter of each particle in a powder is defined in Table 1. In general, the particles forming a powder can be described in terms of a mean or average diameter. However, actual powders are made up of particles having a statistical size distribution.

15.1.2.1 *Types of particle size distribution*

There are two types of distribution: frequency and accumulative distributions. Besides these two, one can define the following frequency distributions for particles ranging in diameter from D_n to D_{n+1}.

1. *Number-based distribution:* the number of particles ranging from D_n to D_{n+1} within the total number of particles, Σn.
2. *Length-based distribution:* the length of the diameter of particles ranging from D_n to D_{n+1} in the total length of diameter, ΣnD.
3. *Area-base distribution:* the surface area covered by particles from D_n to D_{n+1} in the total surface area, ΣnD^2.
4. *Weight-base distribution:* the weight of the particles ranging from D_n to D_{n+1} in total weight, ΣnD^3.

Even in the same sample, the mean of the distribution (i.e., the particle size) depends on what kind of base distribution is used. Theoretically, distribution 1 above is easy to use, but distributions 3 and 4 are frequently adopted to express that characteristics of actual powders.

15.1.2.2 *Mean diameter of particles*

When the properties of some powders are expressed by those of a group with a diameter $\overline{D}$ representing the particle size distribution, $\overline{D}$ is called the mean diameter. Among various D values calculated from the distribution, the one most suitable for this definition is used as the mean diameter. Various expressions for mean diameters are listed in Table 2, where L is nD, S is nD^2, and W is nD^3. As an example, the length-, area-, and weight-base distributions derived on the basis of a given number-base distribution and the mean diameters of particles, D_1 to D_4, are shown in Figure 1.

For phenomena and processes that occur on the surface of particles, such as adsorption, the total surface area of particles per unit weight of powder, i.e., the specific surface area S_w, can be defined. For spherical particles in a powder with density ρ, the specific surface area S_w can be written as follows:

$$\begin{aligned} S_w &= \sum\left(n\pi D^2\right)\Big/\sum\left(n\rho\pi D^3/6\right) = (6/\rho)\sum\left(nD^2\right)\Big/\sum\left(nD^3\right) \\ &= 6\big/\rho\overline{D} \end{aligned} \tag{3}$$

where the mean diameter $\overline{D}$ is given by the volume-area mean diameter D_3; D_3 is also called the specific surface area diameter. Eq. 3 can be rewritten as $(6/\rho)(\Sigma n/\Sigma(n/D))$, if the harmonic mean diameter D_h (see Table 2) is used instead of $\overline{D}$.

15.1.2.3 *Particle-size distribution function*

Attempts have been made to describe the particle-size distribution by using comparatively simple analytic functions. No set of equations can describe all the distributions. For the distribution used or encountered most frequently, some approximations can be made.

Table 2 Mean Particle Diameter Based on Various Standard Distributions

Mean particle diameter based on the number-base distribution			Definition formulae for mean particle diameter based on another base		
Term	Symbol	Calculation formula	Length s.d.	Area s.d.	Weight s.d.
Length m.p.d.	D_1	$\frac{\Sigma nD}{\Sigma n}$	$\frac{\Sigma L}{\Sigma(L/D)}$	$\frac{\Sigma(S/D)}{\Sigma(S/D^2)}$	$\frac{\Sigma(W/D^2)}{\Sigma(W/D^3)}$
Area-length m.p.d.	D_2	$\frac{\Sigma(nD^2)}{\Sigma(nD)}$	$\frac{\Sigma(LD)}{\Sigma L}$	$\frac{\Sigma S}{\Sigma(S/D)}$	$\frac{\Sigma(W/D)}{\Sigma(W/D^2)}$
Volume-area m.p.d.	D_3	$\frac{\Sigma(nD^3)}{\Sigma(nD^2)}$	$\frac{\Sigma(LD^2)}{\Sigma(LD)}$	$\frac{\Sigma(SD)}{\Sigma S}$	$\frac{\Sigma W}{\Sigma(W/D)}$
Weight m.p.d.	D_4	$\frac{\Sigma(nD^4)}{\Sigma(nD^3)}$	$\frac{\Sigma(LD^3)}{\Sigma(LD^2)}$	$\frac{\Sigma(SD^2)}{\Sigma(SD)}$	$\frac{\Sigma(WD)}{\Sigma W}$
Area m.p.d.	D_5	$\sqrt{\frac{\Sigma(nD^2)}{\Sigma n}}$	$\sqrt{\frac{\Sigma(LD)}{\Sigma(L/D)}}$	$\sqrt{\frac{\Sigma S}{\Sigma(S/D^2)}}$	$\sqrt{\frac{\Sigma(W/D)}{\Sigma(W/D^3)}}$
Volume m.p.d.	D_v	$\sqrt[3]{\frac{\Sigma(nD^3)}{\Sigma n}}$	$\sqrt[3]{\frac{\Sigma(LD^2)}{\Sigma(L/D)}}$	$\sqrt[3]{\frac{\Sigma(SD)}{\Sigma(S/D^2)}}$	$\sqrt[3]{\frac{\Sigma W}{\Sigma(W/D^3)}}$
Volume-length m.p.d.	D_{vL}	$\sqrt{\frac{\Sigma(nD^3)}{\Sigma(nD)}}$	$\sqrt{\frac{\Sigma(LD^2)}{\Sigma L}}$	$\sqrt{\frac{\Sigma(SD)}{\Sigma(S/D)}}$	$\sqrt{\frac{\Sigma W}{\Sigma(W/D^2)}}$
Harmonic m.p.d.	D_h	$\frac{\Sigma n}{\Sigma(n/D)}$	$\frac{\Sigma(L/D)}{\Sigma(L/D^2)}$	$\frac{\Sigma(S/D^2)}{\Sigma(S/D^3)}$	$\frac{\Sigma(W/D^3)}{\Sigma(W/D^4)}$
Geometrical m.p.d.	D_g	$\frac{\Sigma(n \cdot \log D)}{\Sigma n}$	$\frac{\Sigma\{(L/D)\log D\}}{\Sigma(L/D)}$	$\frac{\Sigma\{(S/D^2)\log D\}}{\Sigma(S/D^2)}$	$\frac{\Sigma\{(W/D^3)\log D\}}{\Sigma(W/D^3)}$

Note: m.p.d.: mean particle diameter. s.d.: standard deviation.

Normal distribution. The relationship between the size of particles D and the integrated number n(D) from 0 to D for a normal distribution is expressed by the following equation:

$$\begin{gathered} dn(D)/dD = \left\{\sum n/\sigma\,(2\pi)^{1/2}\right\}\exp\left[-\left(D-\overline{D}\right)^2/\sigma^2\right] \\ \sigma = \left\{\sum\left(D-\overline{D}\right)^2/(n-1)\right\}^{1/2} \end{gathered} \tag{4}$$

where Σn is the total number of particles and σ is the standard deviation of the distribution.

Logarithmic normal distribution. This is the distribution obtained by substituting log D and log σ for D and σ in Eq. 4, respectively. In this case, the relationship between D and n(D) is expressed by:

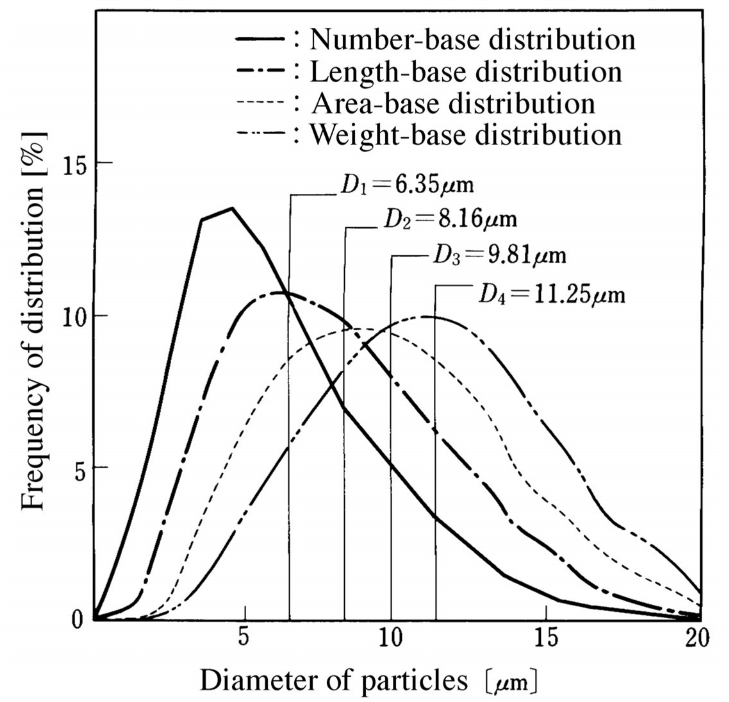

Figure 1 Example of various base distributions and the mean diameter of particles.

$$
\begin{aligned}
&dn(D)/d\log D = \left\{\sum n/\log\sigma_g(2\pi)^{1/2}\right\}\exp\left[-\left(\log D - \log\overline{D}_g\right)^2 / 2\log^2\sigma_g\right]\\
&\log\overline{D}_g = \left(\sum n\log D\right)/\left(\sum n\right)\\
&\log\sigma_g = \left\{\sum\left[n\left(\log D - \log\overline{D}_g\right)^2\right]/\sum n\right\}^{1/2}
\end{aligned}
\tag{5}
$$

Rosin-Ramler's equation. Rosin and Ramler proposed the following equation for the particle-size distribution of crushed coal. The percentage of particles with diameter R, larger than D, is expressed as:

$$R = 100\exp\left(-bD^n\right) \tag{6}$$

With the substitution $b = 1/D_e^n$, this equation is rewritten as:

$$R = 100\exp\left\{-\left(D/D_e\right)^n\right\} \tag{7}$$

n and b(or D_e) are characteristic parameters of the distribution to be determined by measurement. The parameter n is called the R-R distribution constant and has a value of 0.5 to 1.5.

15.1.3 Classification and selection of the method for measuring particle size

Measurements of the particle size commonly used at present can be classified according to the technique employed and depending on the range of particle sizes to be measured. These methods are summarized in Table 3. Various common methods for these measurements are described in the next section.

In selecting the method for measuring particle size, careful consideration must be given to the properties of the sample, the purpose of the measurement, the required measuring accuracy, etc. In general, the measuring methods are classified according to powder conditions for the ranges of particle sizes to be measured, and are shown in Table 4. In selecting the appropriate method, one needs to be aware of an approximate particle size in addition to the general physical properties of powder samples.

15.2 Methods for measuring particle size

15.2.1 Image analysis of particles

15.2.1.1 Preparation of microsection

Measurements of particle size conducted using an optical microscope require special care to insure that the particles are homogeneously dispersed in a medium and no aggregation occurs to affect the distribution in a microsection; this care is required so that the particle distribution in the sample can be considered to be representative of the whole powder. The particles may be homogeneously dispersed by sprinkling a small amount of the powder on a glass plate; but more commonly, a small amount of the powder is dissolved in a suitable dispersion medium, coated on a glass plate, and then dried. Particles can also be dispersed homogeneously by admixing the powder into a viscous resin and then thinly coating the resin on a glass plate.

For electron microscope inspections, special care is required so that the supporting lamella does not affect the distribution. As in the case above, powders may be sprinkled over the supporting film with a writing brush. Otherwise, samples dispersed in a mixture of water and linseed oil can be deposited on a supporting film; the dispersion medium is then removed by a suitable solvent, leaving a well dispersed specimen. In addition to direct observation of samples using TEM (transmission electron microscopy), observation of the morphology of particles by the shadowing method and SEM (scanning electron microscopy) observation by the metal replica method can also be used.

15.2.1.2 Image analysis

The measurement of particle size may be made directly using the visual image produced by an optical microscope; in most cases, however, sizes are measured using photographs of particles. The size of particles on the photograph is determined using an appropriate scale once the magnification factors have been established. At present, uses aided by computer systems for semiautomatic or fully automatic analysis are being developed for these measurements.

The number-base distribution, and various representative diameters, shape factors, etc. can now be determined by a semiautomatic digitizer, which measures the x and y coordinates of each particle image and analyzes these coordinates with a computer. A fully automatic image analysis apparatus are used predominantly at present. The three-dimensional analysis using shadowing and holography and the study of the morphology analysis of particles also can be conducted with these instruments.[1]

The image treatment method above can cover the broadest range of particle sizes in principle, and it is capable of determining the sizes ranging from ultrafine to coarse. The

Table 3 Classification and Characteristics of the Methods for Measuring Particle Size

Principle of measurement	Measuring method	Measurable range of size mm µm nm	Measured particle size	Distribution base	Sample condition
Image analysis	Optical microscope		Length	Number	Wet, dry
	Electron microscope		Area	Number	Dry
Volume analysis	Sieving		Sieve opening	Weight	Wet, dry
	Coulter counter		Equivalent diameter	Number	Wet
Analysis of particle motion	Gravity sedimentation		Stokes diameter	Weight	Wet, dry
	Centrifugal sedimentation			Weight	Wet, dry
(Sedimentation)	Light transmission			Area	Wet
	Air sieving			Weight	Wet, dry
	Elutriation				
(Inertia force method)	Cascade impactor		Stokes diameter	Weight	Dry
	Cyclone			Weight	Wet, dry
Surface area analysis	Kozeny-Carman method		Specific area diameter		Wet, dry
(Permeability method)	Knudsen method				Dry
(Adsorption method)	BET method		Specific area diameter		Dry
	Fluxion method				Wet, dry
	Heat of wetting				Dry
Electromagnetic wave scattering	Light diffraction		Reduced diameter of sphere	Weight	Wet, dry
	Light scattering (angle distribution)		Mean effective diameter		Wet, dry
	(Doppler width)				Wet, dry
	X-ray diffraction (Sherrer width)				Wet, dry
	X-ray small angle scatter				Wet, dry

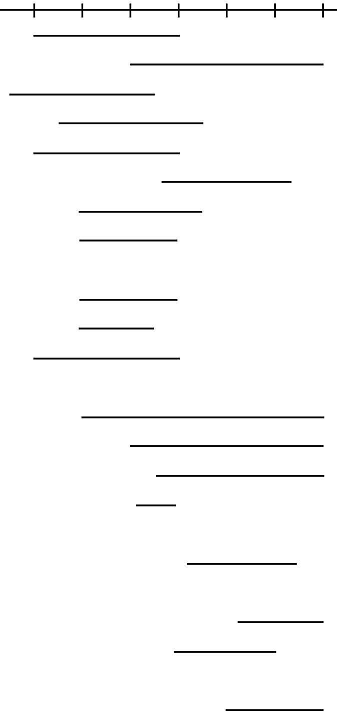

Table 4 Powder Conditions and Methods of Measurement to be Applied

Condition	Purpose of measurement		Coarse powder / Fine powder / Super fine powder: cm, mm, 100 µm, 10 µm, µm, 100 nm, 10 nm, nm	Diameter	Time required
Powder	Approximate	Distribution	Sieve	E	L
↓			Micros. (Opt.)	S	Sh
↓			Touching	—	Sh
↓		Mean	Bulk density	—	Sh
↓			Transmission	E	Sh
↓			Sieve	E	L
Wet method	Detail	Dis.	Air sieve	E	L
↓			Micros. (Opt. and Electron.)	S	L
↓			Transmission	Sp	Sh
↓		Mean	Adsorption	Sp	L
↓			Sieve	E	L
Suspension	Approximate	Dis.	Grinding	—	Sh
			Micros.	S	Sh
			Sedi.	E	L
			Sedi. (volume)	—	L
		Mean	Wet trans.	Sp	Sh
			Sieve	E	L
			Micros. (Opt.)	S	L
			Micros. (Electron)	S	L
	Detail	Dis.	Sedi.	E	L
			Centrifugal sedi.	E	L
			Coulter counter	E	Sh
			Light scatter.	Sp	Sh
		Mean	Adsorb. (Liquid)	Sp	L
			Permeability (Wet)	Sp	L

Note: E: Effective diameter, S: Statistical diameter (particle size depends on the treatment of results obtained), Sp: Specific area diameter, L: Long, Sh: Short, Dis.: Distribution, Sedi.: Sedimentation.

relative errors of the mean particle diameter ε, however, increase with a decrease in the number of particles N being measured. In general, the relation between ε and N may be expressed by:

$$\log[\varepsilon] = -(1/2)\log N + \log K \tag{8}$$

where K is a constant determined by the degree of dispersion, the shapes, the definition of representative diameters, and the size distribution.[2]

Recent measurements on some common samples conducted by a group sponsor by the Society of Powder Technology shows that these errors are influenced by the personal skills of the experimentalist. For a broad particle-size distribution, even when the particles are of ideal shape, more than 1000—preferably several thousand—particles need to be measured to reduce errors to a range of 2 to 3%. Highly accurate determinations require that the particle analysis be totally automated after good-quality microscope images have been obtained.

15.2.2 Volume analysis of particles

This analysis is based on the measurement of particle size using the volume of particles of some phenomenon proportional to this volume. Techniques often used are sieving and the coulter counter. Both techniques can be regarded as measurements of cross-sectional areas of particles, which can then be readily converted to a volume.

15.2.2.1 Sieving

Measurement of particle size by sieving is effective for powders composed of relatively coarse particles. In sieving, special attention should be given to the accuracy of the sizes of the sieve and also to the motion of the sieve. Methods need to be developed to estimate particle diameters, especially those of particles with shapes far from spherical. Standard sieves are produced by JIS, Tyler Co. (U.S.), ASTM, and others. JIS and Tyler Co. sieves are most widely used in Japan. Both types have sieve openings that vary in a $2^{1/4}$ geometric series. For the JIS sieves, 30 stages cover the range from 37 µm to 5.660 mm. Particles larger than 100 µm in diameter are rarely used in practical fluorescent materials. Special microsieves are manufactured for fine-grained samples down to few micrometers in size, as shown in Table 5; often, wet sieving is employed to avoid aggregation of powders.

15.2.2.2 Coulter counter

This method determines the size of particles in a suspension by measuring changes in the electrical resistance and the number of particles by counting electrical current pulses. This method is widely applied in fields such as medicine and the food and ceramics industries; for example, the size and number of blood corpuscles and bacteria are determined in this way. The measuring range of the particle sizes is between 0.25 and 500 µm.

A diagram of the apparatus used in this method is shown in Figure 2; the principle of measurement for particle sizes is described below. An electrolytic solution fills a vessel with a wall having a capillary hole that divides the solution into two parts. The electrodes are put in both sides of the divider. When a voltage is applied through the electrodes, the flow of electric current is controlled predominantly by the electrical resistance of the capillary hole. When the capillary is filled with a suspension, fine particles in the capillary region change the electrical resistance, depending on their size and resistivity. The capillary is assumed to be a cylinder with a cross-sectional area of A and a length of l. The change in electrical resistance ΔR, when a particle of volume V and cross-sectional area *a* enters the capillary, is given by:

Table 5 The Standard Specification of Microsieves

1. Sieve opening:

Normal Opening (µm)		63	53	45	32	25	20	16	12.5	10	8	5
Allowance (µm)	Max.	65	55	47	34	27	22	18	13.5	11	9	6
	Min.	64	51	43	30	23	8	14	11.5	9	7	4
Porosity (%)		40	40	40	40	40	40	40	39	25	12	10

2. Material of sieves:
   Precision sieves: silver alloy plated with nickel

3. Size of screen frame:

Class	*D*	*d*	*H*	*h*
L	90	75	38	20
S	52	38	56	19

4. Material of screen frame:
   Aluminum and transparent acrylate resin

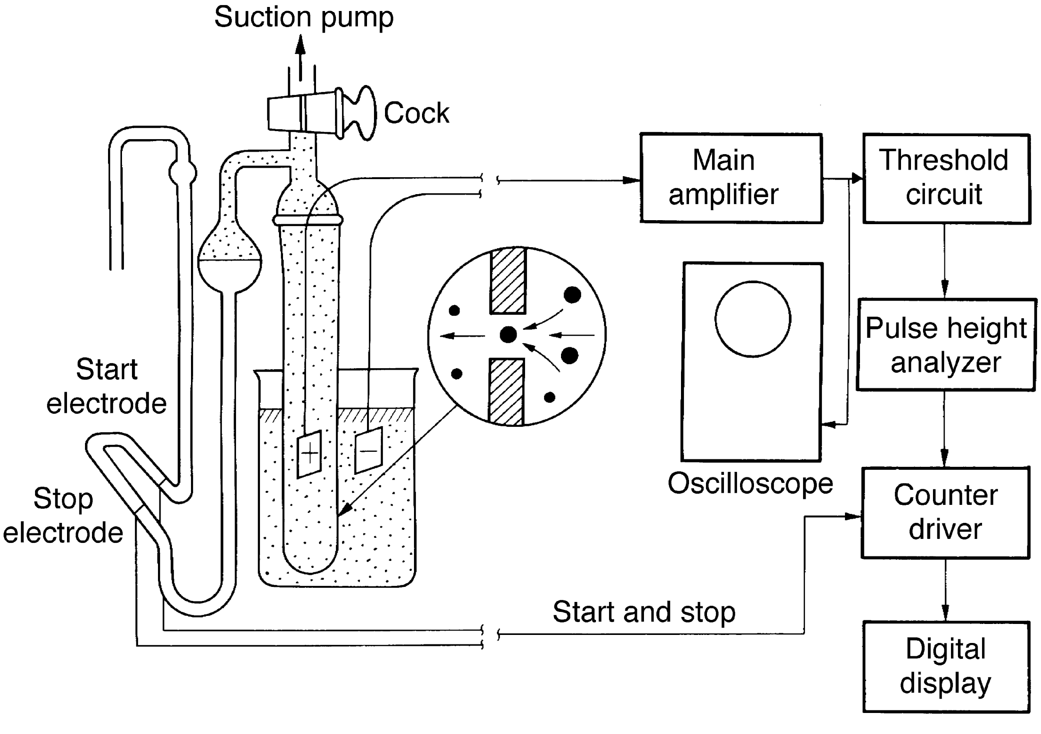
Suction pump
Cock
Main amplifier
Threshold circuit
Start electrode
Stop electrode
+
−
Pulse height analyzer
Oscilloscope
Counter driver
Start and stop
Digital display

Figure 2 Coulter counter.

$$\Delta R = \left(\rho_0 V/A^2\right)\left\{1/\left(1-\rho_0/\rho\right)-\left(aD/1A\right)\right\} \qquad (9)$$

where ρ_0 and ρ are the specific resistivity of the electrolytic solution and the particle, respectively. D is the reduced diameter of the sphere approximating the irregular-shaped particle. The change ΔR is approximately proportional to V for $\rho \gg \rho_0$. The accuracy of the detector and the counter used in this apparatus for measuring the diameter of particles is ±0.01 µm.

The procedure for measurement is as follows. A particle suspension is placed in a beaker (50–400 ml in volume). The suspension is then introduced into the tube through the capillary (30–560 μm in pore diameter and 0.10–1 mm in length). Each time a particle passes through the capillary, the electrical resistance changes an amount ΔR given by Eq. 9. The pulses generated by the changes, ΔR, are amplified and the height and number of pulses are analyzed to give the particle-size distribution.[3,4]

This method is suitable for samples that are difficult to analyze using the sedimentation techniques (see 15.2.3.1); this method is suitable for samples of lower relative density or for samples containing trace amounts of powder. This method, however, is unsuitable for a sample having a fairly broad particle-size distribution, and cannot be used for powders soluble in the electrolytic solution. Particle sizes obtained in this method are not absolute, but relative; results need be compared with standard samples of known size and distribution in order to obtain absolute values.

15.2.3 *Analysis of particle motion*

A particle moving in a field of force such as gravity, centrifugal force, etc. experiences a retarding force when moving through a viscous medium and eventually reaches a constant velocity, i.e., the terminal velocity. Measurements of the terminal velocity provide a method for determining the size of the particle.

15.2.3.1 *Sedimentation method*

The sedimentation method has traditionally been used to determine the diameter by measuring the sedimentation terminal velocity v of the particles. The method for size determination depends on Stokes' law; namely, the terminal velocity of a spherical particle in a viscous liquid is given by:

$$v = (1/18)(\rho_p - \rho) g D_p^{\,2} / \eta \qquad (10)$$

where ρ_p and ρ are the density of the particle and the medium, respectively, η is the viscosity of the medium, D_p is the diameter of the particle, and g is the acceleration due to gravity.

The sedimentation rate depends upon the particle-size distribution. This distribution is determined by measuring the weight distribution as a function of depth in the vessel and the sedimentation time. The weight distribution is generally determined by the number of particles passing through a fixed depth; in some methods, such as the specific gravity balance and the light transmission methods, the variation of the distribution with depth is determined instantaneously. The method at fixed depth is classified into two types, as follows:

1. *Increment type:* the variation of particle concentration at a certain depth h (the pipette method, the light transmission method, and the specific gravity balance method) is measured.
2. *Accumulation type:* at a depth h, the variation in a quantity related to the total concentration above h or below h is determined (the hydrometer method and the sedimentation balance method).

The difference between these two techniques and an outline of analyzing procedures are shown schematically in Figure 3.

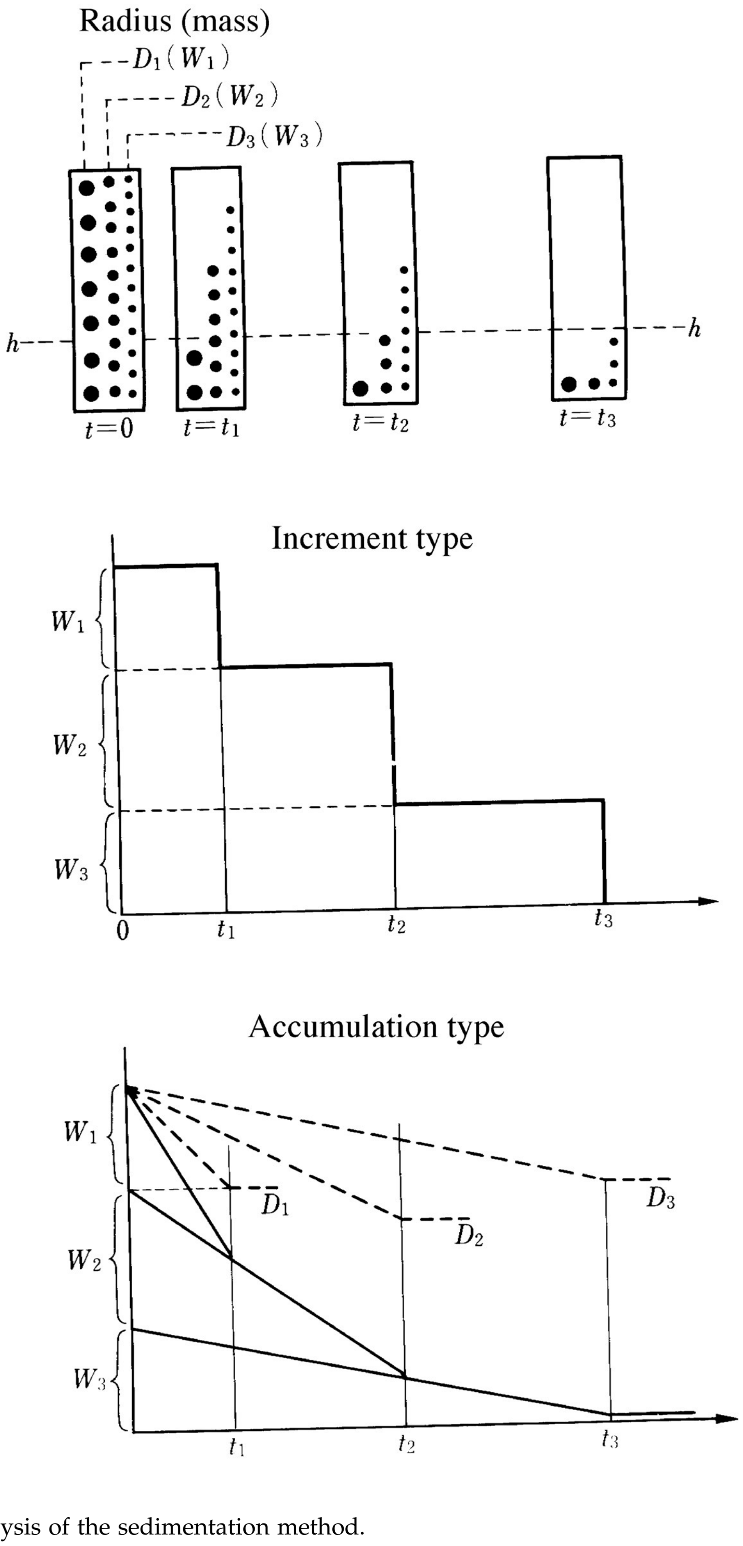
Radius (mass)
$D_1(W_1)$
$D_2(W_2)$
$D_3(W_3)$
h
h
$t=0$
$t=t_1$
$t=t_2$
$t=t_3$
Increment type
W_1
W_2
W_3
0
t_1
t_2
t_3
Accumulation type
W_1
W_2
W_3
D_1
D_2
D_3
t_1
t_2
t_3

Figure 3 Analysis of the sedimentation method.

The outlines of various measuring methods are as follows:

Pipette method. A small amount of the suspension is drawn into a pipette inserted to a fixed depth h; the particle concentration of the suspension is obtained by measuring the density of the liquid. The measurement is repeated at fixed time intervals so that the variation of the particle concentration with time can be obtained. The particle diameter D_p can be derived using the Stokes equation (Eq. 10) with the substitution v = h/t where t is the time when the pipette is filled. Using the particle concentration as measured above, the corresponding particle diameter gives the cumulative distribution curve. The Andreasen pipette is often used in this method because of its simplicity.

Light transmission method. This method determines the particle concentration by estimating the decay of a narrow beam of collimated light incident into the suspension. Let the intensity of incident light be I_0, the intensity of transmitted light I, and the length of the optical path in the liquid L. The logarithm of the ratio of the intensity of incident light to that of transmitted light is given by:

$$\log(I_0/I) = kcL\sum_{i}^{D_{\max}} K_R n_i D_i^{\,2} \tag{11}$$

where c is the concentration of suspension, n_i the number of particles with the particle diameter D_i in a sample of 1 gram, and k an experimental constant that depends on the equipment and the operating conditions. The constant K_R is called the Rose's extinction coefficient due to the optical properties of particles and is usually assumed to be unity. The limit of summation is to the highest value $D_{\max}$ of D calculated by Eq. 10 using a velocity v = h/t for the depth h and time t. Application of Eq. 11 is limited to the range of conditions for which geometrical optics is applicable; the minimum particle diameter measurable must be two or three times larger than the wavelength used.

While the sedimentation method provides the weight-base distribution, the light transmission method provides the area-base distribution of particles as understood from Eq. 11. Also, the relation between $D_{\max}$ and the concentration distribution can be derived by scanning the light at various depths h at a fixed time t. This method can be used to obtain the particle-size distribution very quickly.

Specific gravity balance method. If the powder suspension is allowed to settle, a concentration gradient is caused by the particle-size distribution. The particle concentration can be determined by measuring the buoyancy experience by a small sinker hung on a thin string, while changing the depth of the sinker h without disturbing the suspension. This method provides the cumulative distribution because the depth h gives the particle diameter D.

Hydrometer method. Instead of a sinker, a hydrometer (liquid densitometer) can be dipped into the suspension. The mean specific weight of the part of the suspension where the hydrometer is submerged, determines the particle concentration in that region. Changes in the concentration with time provide the particle-size distribution. This method is used to determine particle-size distribution for soils and similar substances (*JIS A 1204*).

Sedimentation balance method. This method is applicable both in the liquid and gaseous phases. The balance pan is placed at a level near the bottom of the sedimentation tube and measures the weight of all particles being deposited in time. An increase in the

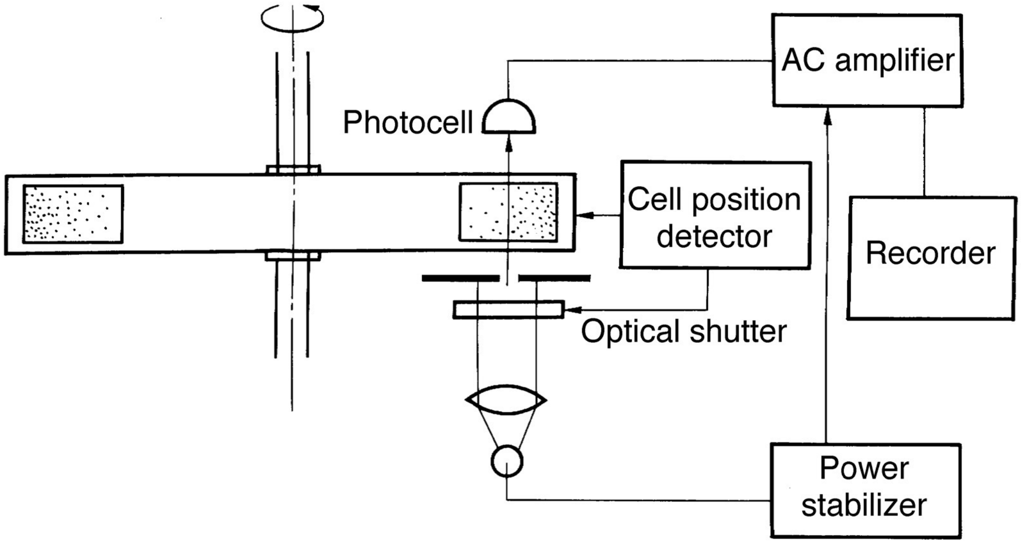

Figure 4 Equipment for measuring particle size by centrifugal sedimentation method of light transmission type.

weight of the sediments with time provides a sedimentation curve and the differentiation of the curve can provide the particle-size distribution. This method is generally used in apparatuses for particle-size measurement in which the results are automatically recorded and processed by computers.

15.2.3.2 Centrifugal sedimentation method

Fine particles that precipitate very slowly through gravitation may do so quickly under the action of a centrifugal force; as in the previous case, the terminal velocity v (=dr/dt, r is the radial position from the axis of rotation) can be written as:

$$v = (1/18)(\rho_p - \rho)\omega r D_p^2/\eta \tag{12}$$

where ω is the angular velocity of rotation. In this equation ωr replaces g in Stokes equation (Eq. 10).

As the relative change of the distance due to the movement of the particles is small for large r, the value of r is assumed to be a constant and results obtained can be analyzed by the same methods as in sedimentation discussed above. The suspension is disturbed, when the system starts or stops the rotation. Consequently it is desirable to measure the terminal velocity of particles while the suspension is rotating at a constant rate. Figure 4 shows the equipment used in light transmission measurements of centrifugal sedimentation. Many kinds of commercial equipment are available, and this is by far the most common method used for these measurements.

15.2.3.3 Inertia force method

The above two methods use the principle that the masses of particles control the terminal velocities in their movements. A second method uses the difference in momentum caused by the difference in the mass, although the particles might have the same velocity.

Cascade Impactor: An air current containing particles is passed through a series of nozzles; the direction of the air flow is changed by impact plates. Larger particles are

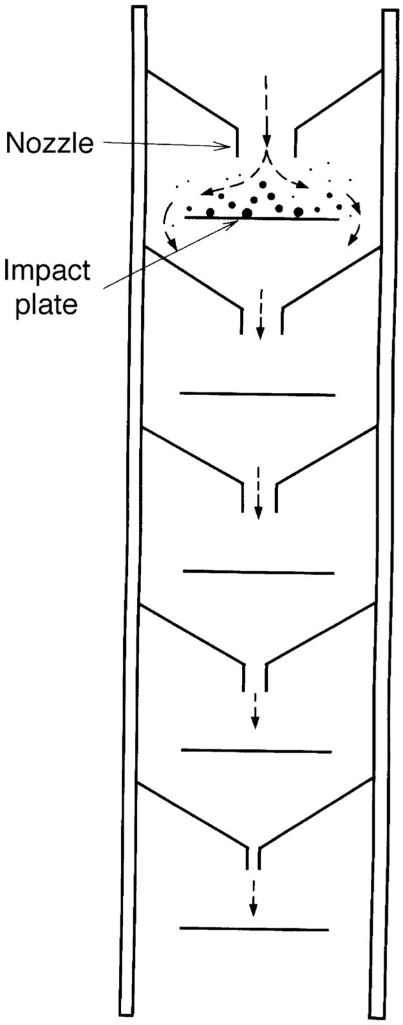

Figure 5 Cascade impactor.

collected on the plates but smaller particles are deflected sufficiently to pass through into the successive regions. By stacking the impact plates with decreasing diameters of the nozzles, as shown in Figure 5, the particles are sorted on each impactor according to their sizes. The results yield the weight-base distribution. This method is, however, purely empirical because there is no formal theory that allows the calculation of the diameter of particles; use of so-called small multistage cyclones suffers from the same problem.

15.2.3.4 Laser doppler method

The methods above analyze the movement of groups of particles from which the weight-base distribution can be deduced. The number-base distribution can also be derived by analyzing the velocity of each particle and calculating the particle mass. There is another method for counting the number of particles possessing a given sedimentation rate, i.e., using the principle of the laser velocity meter. This method can be applied to a broad range of sedimentation rates for fine particles, both in air and in fluids.

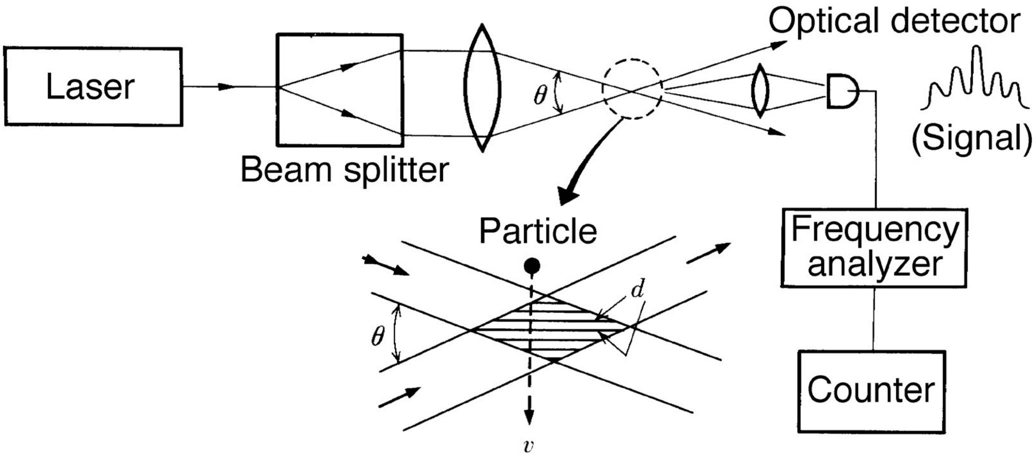

Figure 6 Laser Doppler method.

Figure 6 shows the schematic of this method. A laser beam is split into two beams that are then made to cross each other to produce an interference pattern. The width of an interference d is given by:

$$d = \lambda/2\sin(\theta/2) \tag{13}$$

where λ is the wavelength of the laser and θ is the crossing angle. When the particles enter the interference region, they scatter light. The scattered light produces a so-called Doppler beat as shown in the right portion of Figure 6. The frequency of the beat, f_{LD}, is given by the following equation with v the velocity of particles:

$$f_{LD} = (v/d)\{2\sin(\theta/2)/\lambda\}v \tag{14}$$

By analyzing the frequency of the beat, a signal at the frequency f_{LD} corresponds to a particle having a velocity v. This velocity v can be reduced to D_p using Eq. 10 as in the case of the sedimentation, or Eq. 12 as in the case of measurements in a centrifugal force field. A number-base distribution is obtained in this way. This method has been applied for the observation of Brownian motion of fine particles.

15.2.4 Analysis of the surface area of particles

The basis for measuring surface reactions and reactivity of particles is the determination of their surface area. Measurements give the surface area per weight from which the mean particle diameter can be calculated when the solid density of particles is known and the shape of particles is assumed to be spherical or granular. Common methods for these measurements are the adsorption and the wetting heat method, both of which rely on surface reaction of the solids; the transmission method is based on another principle, which will be described in 15.2.4.2.

15.2.4.1 Adsorption method

This method uses a solute molecular compound in liquid or a low molecular weight compound in gaseous phase as an adsorption substance. In the former, the colorimetric method, which is simple and convenient, is used to determine the amount of dye molecules adsorbed from the dye solution onto the powders; its accuracy, however, is poor. In most cases, gaseous adsorption is used. Measurements for this method are divided into two categories: the volumetric and gravimetric methods.

Volumetric method (BET method). This method measures the amount of adsorbed substance on the basis of the change is pressure or volume due to adsorption of a gas on the particles; this process is named the BET method after its three co-founders: Brunauer, Emmett, and Teller. A known amount of powder in a sample container is heated and evacuated to remove adsorbed gases; the container is then removed from the vacuum pump system. A volume of gas, measured beforehand, is transferred into the sample container at low temperature; the amount of gas in the container can be calculated by measuring the pressure. A sample of 10 to 15 ml is generally sufficient for these measurements; this is not difficult for samples having total surface areas of more than several square meters (m^2). This method, however, is unsuitable for volatile samples or for powders with low melting points, from which it is generally difficult to remove absorbed gases. The adsorption isotherm obtained by determining the relation between the equilibrium pressure and the amount of adsorption gives the surface area of the sample through the analysis described for the adsorption isotherm below.

Gravimetric method. In this method, the amount of adsorption is determined by measuring the increment in the weight of sample. For example, the increment due to the adsorption of N_2 gas molecules on a 100-m^2 surface is 28.6 mg. The adsorption balance method gives the highest accuracy, but the spring balance method and the cantilever method can also be used.

In order to determine the adsorption isotherm as a function of gas pressure, it is necessary to calculate the true amount of adsorption W_a using the following equation.

$$W_a = W_{as} + \rho V_s + \rho V_a - W_s \tag{15}$$

where W_{as} is the apparent weight of the powder after adsorption has taken place, W_s the weight of sample in a vacuum, V_s and V_a the volumes of sample and the absorbed gas, respectively, and ρ the density of the gas at equilibrium. For pressures not exceeding 1 atm, ρV_a is negligible.

Adsorption isotherm. In addition to N_2, Ar, H_2O, etc., various gases are used as adsorption media; N_2 is the most suitable because of its inertness and ease of use. Typical isotherms, shown as types I and II, are illustrated in Figure 7, though adsorption isotherms take various forms depending on the method of measurement. In the figure, P is the equilibrium pressure, P_0 is the saturated vapor pressure, and V is the amount of gas adsorbed. Usually, a type I isotherm indicates monolayer adsorption, whereas multilayer adsorption yields type II isotherms. Adsorption isotherms are usually reversible, but hysteresis occurs in samples with particularly strong adsorption and/or in porous samples. Equations representing adsorption isotherms for these two types, I and II, have been derived. Representative equations corresponding to type I and II in Figure 7 are as follows.

$$\text{The Langmuir equation: } P/V = 1/(V_m b) + P/V_m \tag{16}$$

$$\text{The BET equation: } V = \mathrm{V_m} C_p/(P_0 - P)\{1 + (C-1)P/P_0\} \tag{17}$$

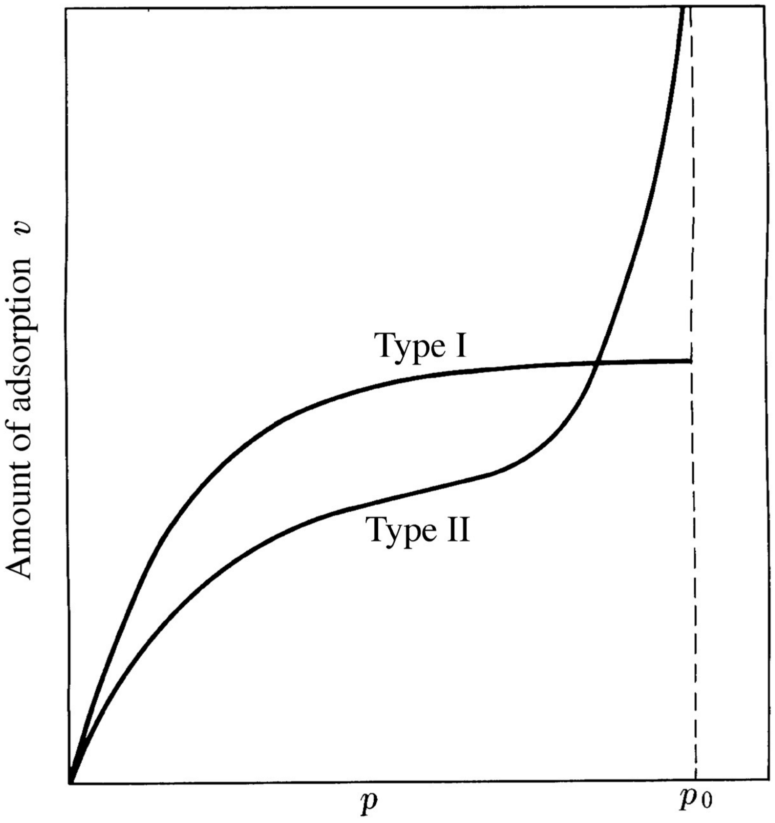

Figure 7 Types of adsorption isotherms.

where b, C, and V_m are constants determined experimentally. The constant V_m in the BET equation represents the volume of adsorption molecules necessary to form a monolayer. The BET equation can be rewritten as:

$$P/V(P_0 - P) = 1/V_mC + \{(C-1)/V_mC\}(P/P_0) \tag{18}$$

Plotting $P/V(P_0 - P)$ vs. P/P_0, the slope and the intercept give V_m if the plots are linear. The weight-specific surface area S_w ($m^2\ kg^{-1}$) is given by the product of the number of gaseous molecules, calculated from V_m, and the molecular cross-section σ as:

$$S_w = V_m \sigma N \tag{19}$$

where N is Avogadro's number. The standard values of σ are listed for each gaseous molecule in Reference 5; for N_2, $\sigma = 0.162\ nm^2$.

15.2.4.2 Transmission method

In this method, the specific surface area is determined by measuring the transmission of fluid through a packed bed of powder. When high accuracy is not required, this method is frequently employed in industry because the apparatus is simple to operate and allows for quick measurement. The basis of this method is described by the Kozeney-Carman equation (Eq. 20). Letting U be the amount of fluid per unit time passing through the powder of cross-sectional area A and thickness L over which there exists a pressure difference ΔP, the weight-specific surface area S_w is given by:

$$S_w = (1/\rho)\left[g\Delta P \cdot A\,\varepsilon^3 / k\eta LU(1-\varepsilon)^2\right]^{1/2} \tag{20}$$

where ρ is the specific gravity of the powder, η the viscosity of fluid, ε the porosity of powder bed (i.e., 1 – (W/ρLA)), g is the acceleration of gravity, and k is a constant, called the Kozeney's constant is related to the porosity of the powder bed. The value of k is determined experimentally and is usually taken as 0.5.

The fluids used in the transmission method are liquid (such as water for powders consisting of large particles) or gaseous (mostly dried air, for powders of small particle size). In using this method, the amount of transmission U is measured at a constant pressure difference ΔP. The Blaine method is the simplest way for these measurements and instruments are commercially available. For these purposes, it is used generally for cement and other industrial powders according to JIS and ASTM.[6] The pressure difference ΔP, however, changes during measurement in this method. An apparatus for the transmission method using air and operating under constant pressure is shown in Figure 8 as an example. The principle and operation of the apparatus can be understood from the figure. The pressure difference ΔP is given by ρgh (ρ is the density of the liquid that produces the pressure difference) and can be varied over a range of 10 to 100 g cm^{-2} in an apparatus using water.

The most important factor in the transmission method is the packing of the powder. Eq. 20 takes into account the porosity of samples ε, but the dependence of the weight-specific surface area S_w on the porosity is, in fact, very complicated. Measurement of porosities will be described later (see 15.3.1).

15.2.5 Scattering of electromagnetic waves caused by particles

The optical properties of a particle depend on the state of assemblage of particles; a dilute dispersion of particles has different properties from thick powder aggregates such as those encountered in powder beds or in paints.[7] In the former state, the optical character of individual particles dominates, whereas in the latter, complicated multiple scattering occur. Multiple scattering is discussed elsewhere (see Chapter 16). On the other hand, X-ray scattering from particles is not affected by the assemblage of particles, but does depend on other properties such as the size and structure of particles.

15.2.5.1 Light scattering method

Light scattering depends largely on physical properties such as the shape of the particles, their mean diameter, and their physical state (i.e., liquid or solid). Typical changes in the scattering due to a change in the particle diameter are summarized in Table 6.[8] Theoretically, there are the Rayleigh scattering and the Mie equations; the latter equation extends Rayleigh scattering to larger particles. The Mie equation was obtained by solving electromagnetically the interaction between particles and light and is applicable to dispersed systems of powders. The scattered light intensity I(θ) in the direction θ to the incident light is given by:

$$I(\theta) = \lambda^2\{i_1 + i_2(\theta)\}/8\pi^2 R^2 \tag{21}$$

where λ is the wavelength, R is the distance between particle and observation point, i_1 is the light component having its electric vector perpendicular to the plane of observation

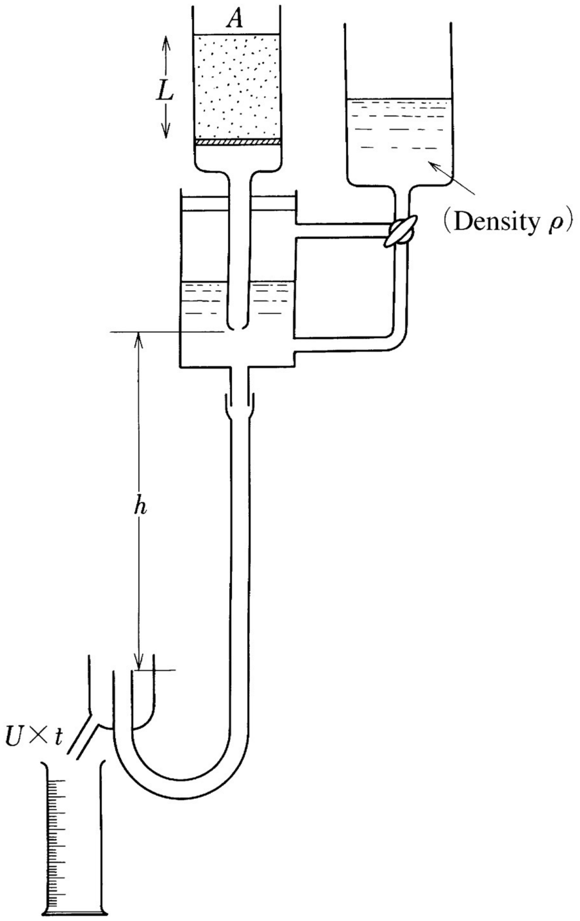

Figure 8 Apparatus for air transmission method, operating under constant pressure.

Table 6 Characteristics of Light Scattering Phenomena Depending on Particle Diameter

Particle diameter	x	Character of light scattering used for measurement	Characteristics
0–0.1 µm	0–0.5	Proportional to the square of volume and inversely proportional to wavelength to the 4th power	Rayleigh scattering
0.1–0.2 µm	0.5–1	1. Scattering angle for maximum polarization 2. Ratio of polarization in the direction of 90° 3. Color of scattering light in the direction of observation 4. Intensity ratio of scattering light at 45° and 135°	Mie scattering (3-term approximation)
0.2–2.0 µm	1–10	1. Change of absorption coefficient by wavelength 2. Maximum and minimum angles in scattering pattern 3. Tyndall spectrum of high order	Complicated diffraction and scattering regions
2–10 µm	10–50	1. Maximum and minimum sites in diffraction pattern 2. Diameter of diffraction ring and angle between rings	Fraunhofer diffraction
>10 µm	>50	1. Maximum site of rainbow 2. Color of shining ring 3. Shadowing by cross-section of particle	Geometrical optics region

Note: $x = \pi dm/\lambda$ (d: particle diameter, m: relative diffractive index of particle to medium, λ: wavelength).

and is independent of θ, and $i_2(\theta)$ is the light component parallel to the plane and is dependent on θ. The total amount of scattered light S is given by:

$$S = \left(\lambda^2/2\pi\right)\sum_{n=1}^{\infty}(2n+1)\left(\left|a_n\right|^2+\left|b_n\right|^2\right) \tag{22}$$

where $|a_n|$ and $|b_n|$ are complicated functions that include Ricatti-Bessel functions and their derivatives. Both functions depend on θ and a parameter x (= 2π rm/λ, where r is the radius of spherical particle and m the refractive index) and have been tabulated.[9,10] The radial distribution of the scattered light is also complicated, as is its wavelength dependence; interference occurs when the particle diameter approaches the wavelength of light. In actual measurements, one obtains the ratio of the scattered light at two different angles (0° and 90°, or 45° and 135°), and compares these with the calculated values through Eq. 22.

In practice, there are two methods that use light scattering. Light scattering photometers determine the mean particle diameter and the degree of dispersion by measuring the angular distribution of the scattered light from a large number of particles. In the other method, the particle-size distribution is obtained by measuring the scattered light intensity of individual particles.

15.2.5.2 Diffraction method

Measurements with this method are performed using Fraunhofer diffraction and are effective for particles having diameters around 1 to 10 µm. The intensity of the diffracted light due to a disk as a function of the angle θ is given as:

$$S(\theta) = x^2(1+\cos\theta)J_1(x\sin\theta)/2x\sin\theta \tag{23}$$

where x is 2π rm/λ (r: the radius of particle, m: the relative refractive index) as mentioned above, and J_1 is a Bessel function. When x sinθ is larger than 10, $J_1(x \sin\theta)/\sin\theta$ is negligible. Normalized values of S(θ) are shown in Figure 9.

In this method, an intense collimated light beam is made incident on a system of particles dispersed in a liquid or gaseous phase; the angular distribution of the scattered light intensity is measured. The particle-size distribution is determined computationally using the angular distribution as a function of x (Figure 9) in conjunction with Eq. 23. Several kinds of instruments for these measurements are commercially available; some commercial equipment is capable of yielding accuracies down to ±0.1 µm.

15.2.5.3 X-ray diffraction and X-ray scattering

The Debye-Scherrer method is used to obtain X-ray diffraction measurements in powders. It is well known that broadening occurs in the diffraction rings as the particle size of the powders decreases. The width at half height of the diffracted ray, as shown in Figure 10, is related to the particle diameter of the crystallite D by the Scherrer equation:

$$D = K\lambda/(B-b)\cos\theta \tag{24}$$

where λ is the wavelength of monochromatic X-ray, θ is the Bragg angle (the diffracted ray appears at angle 2θ). b and B are the peak widths at half height for small and large (larger than ~10 µm) crystallites, respectively, as shown in the figure. This method is applicable to crystallites ranging from 1.0 to 0.01 µm in diameter, but the grains must have good crystallinity.

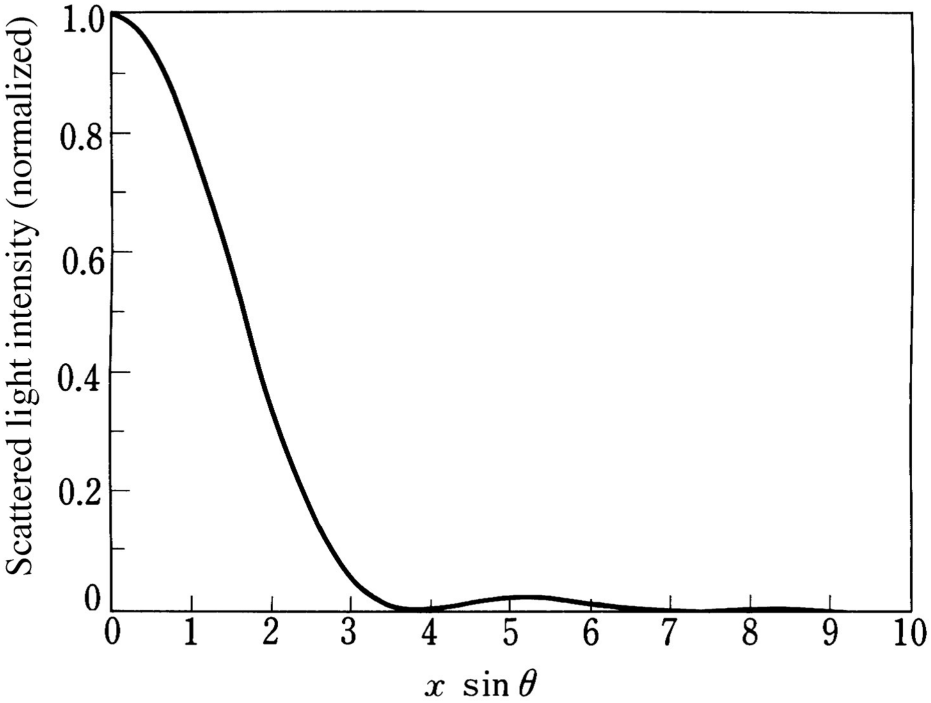

Figure 9 Intensity distribution of Fraunhofer diffraction.

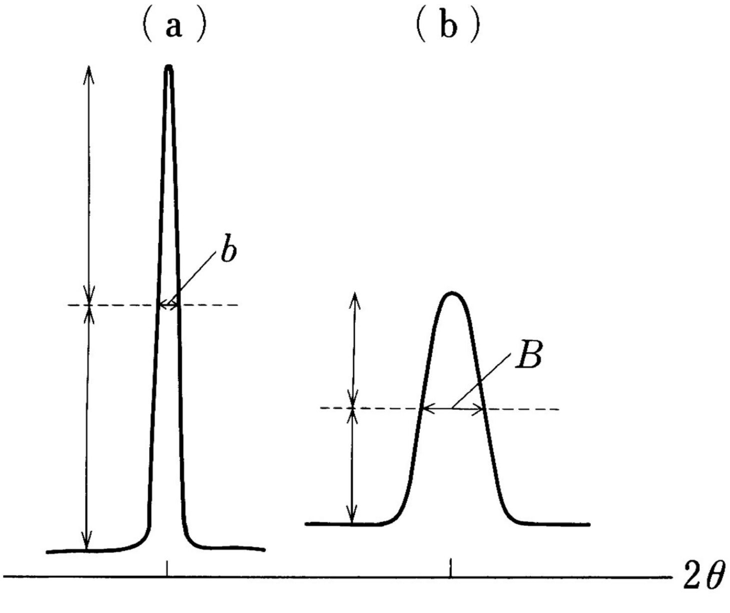

Figure 10 Intensity curves of X-ray diffraction profiles for large (a) and small particles (b).

The method for measuring the angular distribution of the intensity of the scattered X-ray is called the small angle method because only small incident angles are involved. The intensity of the scattered radiation is given approximately by:

$$\begin{aligned} \log I(\theta) &= \log I_0 - \pi^2 D^2 s^2 / 3\lambda^2 \\ s &= (4\pi/\lambda)\sin(\theta/2) \sim 2\pi\theta/\lambda \end{aligned} \tag{25}$$

A plot of log I(θ) vs. s^2 is linear and its slope gives the particle diameter. This method is applicable to particles ranging in size from 1 to 200 nm. Recently, instruments for measuring small angle scattering as well as line broadening have become commercially available as attachments to analytic X-ray equipment.

15.3 *Measurements of packing and flow*

The properties of each powder particle appear fairly distinctly when the powder is dispersed in a medium. Usually, however, aggregations of dried particles are found in a container or in a pile. One of the characteristics of dried powders is that they behave like a fluid, even though they are solid particles. The static and dynamic properties characteristic of powders depends on the mechanical interactions between individual particles.[10,11]

15.3.1 *Definition of packing*

The following quantities are used for describing the packing pattern of powder particles, i.e., the degree of packing, (See Figure 11):

1. *Apparent specific volume:* the volume that a powder of unit weight occupies when packed:

$$V_a = V/W \tag{26}$$

2. *Apparent density, bulk density:* the reciprocal of the apparent specific volume:

$$\rho_a = W/V \tag{27}$$

3. *Porosity, void ratio:* the ratio of the volume of void to the total volume of packed powder:

$$\varepsilon = V_v/V = 1 - V_s/V \tag{28}$$

4. *Packing ratio:* the ratio of the volume of the substantial solid part to the total volume of packed powder:

$$\phi = V_s/V = 1 - \varepsilon \tag{29}$$

Among the quantities above, the apparent specific volume, porosity, and void ratio are used frequently; the conversion between each quantity is simple. For powders with

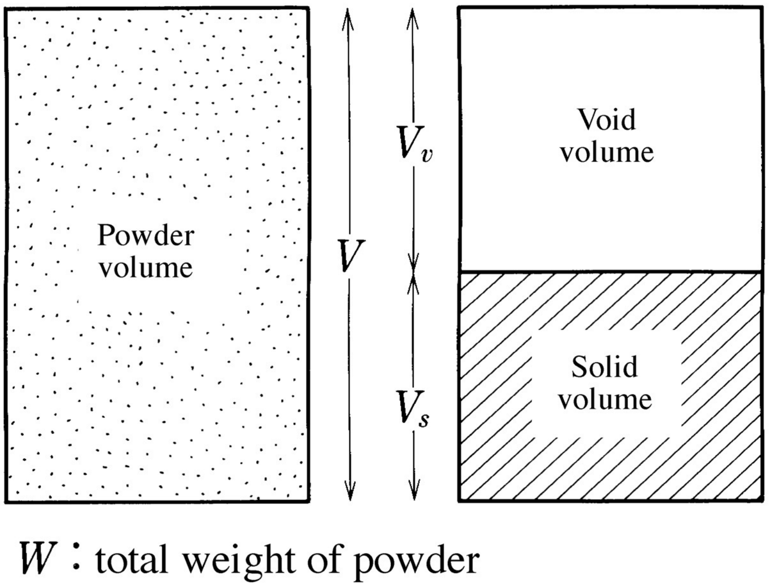

Figure 11 Expression for packing of powder (the weight of void is neglected).

secondary structures like porous powders, granules, and crushed powders of sintered materials, V_v is divided into a void volume inside the particles, V_1 and the void volume between particles, V_2. Then, $V = V_s + V_1 + V_2$. The solid density ρ_s and the grain density ρ_g (also called the green density) are defined as follows:

$$\rho_s = W/V_s, \qquad \rho_g = W/(V_s + V_1) \tag{30}$$

For a powder dispersed in water or a liquid medium, the apparent specific volume of the powder sedimented by gravity, called the sedimentation volume, sometimes also is used.

15.3.2 Measurements of apparent density

Methods for measuring the apparent density shown in JIS, etc. are described below. This density is usually measured using home-made apparatuses. According to the measuring methods, the following names are used.

1. *Static bulk density:* A powder sample is sieved, piled into a vessel, and its density is measured. This method gives the bulk density in the loosest packing state of the powder.
2. *Funnel-damper bulk density:* A powder sample is placed in a funnel and is transferred into a vessel by opening the funnel aperture quickly; the bulk density of the material in the vessel is then measured. This density is the loosely packed bulk density. This method is used frequently in JIS, but to make this method a standard, it is necessary to specify the shape and size of the funnel, the size of the aperture, and the position, shape, and size of the vessel.
3. *Lateral vibration bulk density:* This method packs the sample by producing lateral vibrations in a side of the vessel. Again, the bulk density measured is for a relatively loosely packed sample.

4. *Vertical vibration bulk density:* This method packs the sample by giving vertical vibrations to the vessel; this measurement gives a denser bulk density because it is a more efficient compaction method than the lateral vibration procedure.
5. *Tap-bulk density:* This is the bulk density after the sample is packed into a constant volume by tapping; tapping heights of powders are usually 1 or 2 cm. The powders in this case are considerably denser.
6. *Compression bulk density:* This is the bulk density of a cake-like powder obtained by compressing with a piston after the powder sample is placed in a cylindrical vessel. This method is similar to cold casting.

The bulk density of relatively large spherical particles (larger than about 100 μm) is not very dependent on the measurement method used; however, it is not unusual that for some powders, the ratio of the static bulk density (1) to the tap-bulk density (2) is used when the difference in packing states between samples is sought; the tap-bulk density (5) is suitable for discussing the relation between the bulk density and other physical properties of the compacted material.

15.3.3 *Measurements of fluidity*

The following experiments are carried out to measure the fluidity of powders through measurements of the tap-packing process, determination of the shearing stress inside a powder cake, rest angle, compressibility, and efflux rate from a hopper. These measurements, however, only look at one of the characters of the flow phenomena of powders. They are essentially all related to each other.

15.3.3.1 *Rest angle*

The measurement of the rest angle is widely used as a method to determine the fluidity of powder. This was one of the earliest measurements and continues to be used because it is a simple and convenient method; it is still widely accepted as a method for giving basic data. The rest angle is defined by ϕ in Figure 12; the mechanical meaning of the angle differs slightly, depending on the method of measurement.

In Figure 12, (a) and (b) give ϕ directly. In (c), the powder is placed into a horizontal cylinder and then the cylinder is slowly rotated. When the surface of the powder bed starts to slip, the inclination of the surface of the powder bed to a horizontal plane is measured, defining ϕ. (d) is much the same as (c), and only the vessel is different. The results obtained from all these methods depend on the shape and size of the apparatus; thus, the measurement is generally considered to be a relative one.

15.3.3.2 *Motion angle*

In determining the rest angle, the internal friction must be taken into consideration when the powder starts to slip; for the powder in motion, the dynamical friction of particles must also be considered. This friction is also important in determining the fluidity of powders. In the apparatus shown in Figure 12(c), the motion angle is given by the inclination angle Θ (different from ϕ) of the surface of the powder bed when the cylinder is rotating at a constant angular velocity ω. The viscosity coefficient of a fluid is proportional to $\sin \Theta/\omega$. By applying this relation to powders, it is possible to define a quantity corresponding to the viscosity coefficient.

15.3.3.3 *Powder orifice*

The efflux rate of powders from an orifice opened at the bottom of a vessel is a measure of the fluidity of powders and is also widely used. The difference from fluid flow is that the powder efflux rate does not depend significantly on the height of the powder. Various

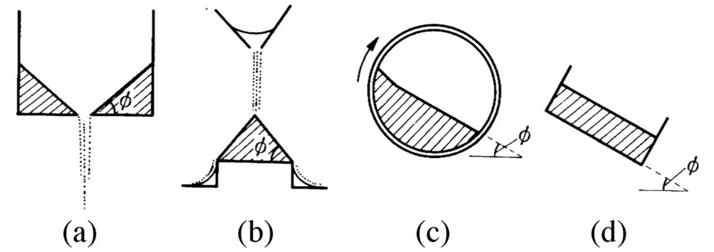

Figure 12 Measurement of the rest angle.

experimental relations between the weight efflux rate Q (kg/min) and the orifice diameter D_0 have been reported. The following equation, as an example, is applicable to the fluid orifice efflux rate:

$$Q = C(\pi/4)(g/2\mu)^{1/2} D_0^{5/2} \tag{31}$$

where g is the acceleration of gravity, μ the frictional coefficient of the wall surface, and C the efflux coefficient to be experimentally determined.

References

1. Jimbo, G., *J. Soc. Powder Technology, Japan*, 17, 307, 1980 (in Japanese).
2. Masuda, M. and Iinoya, K., *J. Chem. Eng. Japan*, 4, 60, 1971.
3. Mullin, J.W. and Ang, H.M., *Powder Technol.*, 10, 153, 1974.
4. Alliet, D.F., *Powder Technol.*, 3, 3, 1976.
5. McClellan, A.L. and Harnsberger, H.F., *J. Colloid Interface Sci.*, 23, 577, 1967.
6. Homma, E. and Isono, N., *Annu. Rep. Cement Eng.*, XX, 135, 1966 (in Japanese).
7. Bohren, C.F. and Huffman, D.R., *Absorption and Scattering of Light by Small Particles*, Wiley-Interscience, 1983.
8. Hayakawa, S., *Surface and Fine Particles*, Kinoshita, K., Ed., Kyoritsu Publ. Co., 1986, 284 (in Japanese).
9. Kerker, M., *Scattering of Light and Other Electromagnetic Radiations*, Academic Press, 1963.
10. Hayakawa, S., *J. Japan Soc. Color Material*, 52, 515, 1979 (in Japanese).
11. Miwa, S., *Powder Science and Engineering*, 11(5), 44, 1979 (in Japanese).

part five

Related important items

chapter sixteen — section one

Optical properties of powder layers

Kazuo Narita

Contents

16.1 Kubelka-Munk's theory....923
  16.1.1 Introduction....923
  16.1.2 Basic equations and their general solutions....924
  16.1.3 Light reflection and transmission of powder layers....926
  16.1.4 Optical properties of phosphor layers....928
    16.1.4.1 Cathode-ray excitation....928
    16.1.4.2 X-ray excitation....931
    16.1.4.3 Ultraviolet excitation....932
    16.1.4.4 Light output of fluorescent lamps....933
  16.1.5 Measurement of the scattering coefficient....935
References....936

16.1 Kubelka-Munk's theory

16.1.1 Introduction

Within a phosphor coating, excitation energy is absorbed after multiple scattering by individual particles.* The generated luminescent light also comes out of the coating after scattering. Hence, it is impossible to describe the total optical processes of absorption, excitation, and emission in a phosphor layer in a rigorously analytical manner, and some approximations must be introduced.

Three different approaches have been employed to calculate the optical properties of the phosphor layer. They are:

1. A method based on the solution of a set of simultaneous differential equations known as the Schuster-Kubelka-Munk equations, in which it is assumed that the phosphor layer is a continuous optical medium, and its optical properties are determined by two phenomenological constants, the absorption and scattering coefficients.

---

* In cases of excitation by X- and γ-rays, scattering can be neglected.

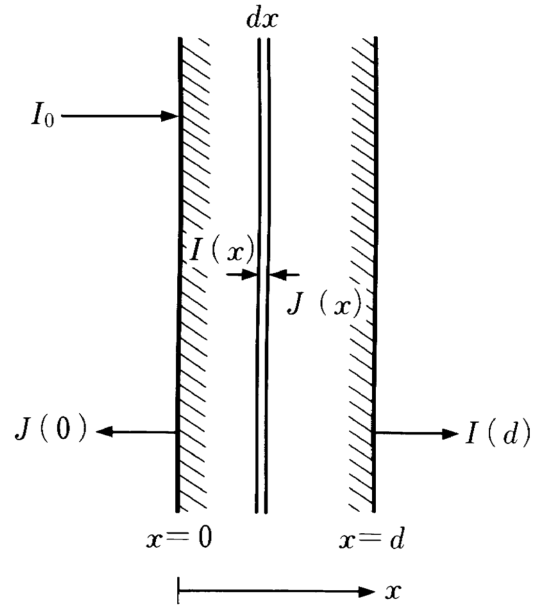

Figure 1 Absorption and scattering of light by a particle layer.

2. The Johnson method, in which the phosphor layer is regarded as a stack of thin layers, each layer having a thickness equal to the particle diameter of the phosphor; the optical properties of the entire layer is determined by an iterative calculation.
3. The Monte Carlo method, in which the path of the scattered light is determined in a stochastic manner using random numbers.

Each method has both advantages and disadvantages, and the most suitable method must be selected for each case. In this chapter, the details of these calculational methods and their applications to several kinds of phosphor coatings are presented.

16.1.2 *Basic equations and their general solutions*

Consider a layer consisting of a large number of particles and having a thickness d. It is assumed that light travels only in $\pm x$ directions in the layer, as shown in Figure 1.[1,2] Light with intensity I_0 falls on the layer, and is scattered in $+x$ and $-x$ directions with intensities $I(x)$ and $J(x)$, respectively. Let the absorption coefficient of the layer be k and the scattering coefficient be s. In the $+x$ direction, then, the light absorbed in an infinitesimal layer of thickness dx is $kI(x)dx$, and the light scattered is $sI(x)dx$. Further, a part of $J(x)$ (i.e., $sJ(x)dx$) is scattered back and has to be added to $I(x)$. Thus, one obtains:

$$\frac{dI(x)}{dx} = -(k+s)I(x) + sJ(x) \tag{1}$$

By considering the change of $J(x)$, one can write a similar equation:

$$\frac{dJ(x)}{dx} = (k+s)J(x) - sI(x) \tag{2}$$

The general solutions to this set of equations are:

$$I(x) = A(1-\beta_0)e^{\alpha_0 x} + B(1+\beta_0)e^{-\alpha_0 x} \tag{3}$$

$$J(x) = A(1+\beta_0)e^{\alpha_0 x} + B(1-\beta_0)e^{-\alpha_0 x} \tag{4}$$

Here, A and B are constants whose values are determined by boundary conditions, and α_0 and β_0 are defined by:

$$\alpha_0 = \sqrt{k(k+2s)} \tag{5}$$

$$\beta_0 = \sqrt{k/(k+2s)} \tag{6}$$

Kubelka[3] generalized this one-dimensional formulation and showed that the same kind of equations can be derived even when the incident light is diffuse and scattering inside the particle layer takes place in all directions. In this case, the light is not always falling on the layer perpendicularly. Hence, the length of the light path in the layer is longer than dx. It can be verified that the mean path $d\xi$ is expressed as:

$$d\xi = 2dx \tag{7}$$

Therefore, Eq. 1 can be written as:

$$dI(x) = -(k+s)I(x)\cdot 2dx + sJ(x)\cdot 2dx \tag{8}$$

If one defines the new coefficients K and S by:

$$2k \equiv K, \qquad 2s \equiv S \tag{9}$$

then, equations similar to Eqs. 1 and 2 are obtained:

$$\frac{dI(x)}{dx} = -(K+S)I(x) + SJ(x) \tag{10}$$

$$\frac{dJ(x)}{dx} = (K+S)J(x) - SI(x) \tag{11}$$

The solutions can be written down simply by replacing α_0 and β_0 in Eqs. 3 and 4 by α and β, where

$$\alpha = \sqrt{K(K+2S)} \tag{12}$$

$$\beta = \sqrt{K/(K+2S)} \tag{13}$$

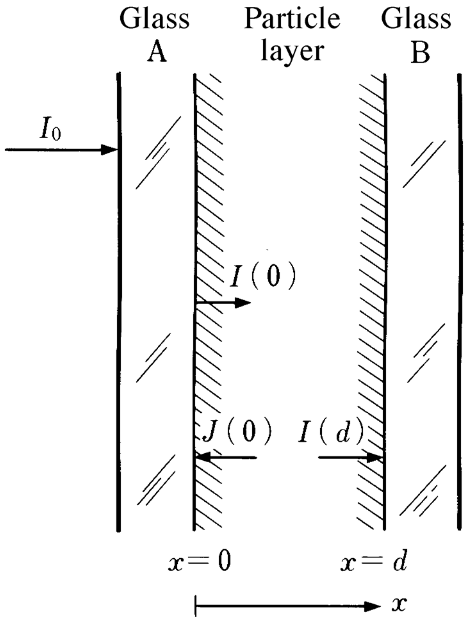

Figure 2 Particle layer between two glass plates.

The results are:

$$I(x) = A(1-\beta)e^{\alpha x} + B(1+\beta)e^{-\alpha x} \tag{14}$$

$$J(x) = A(1+\beta)e^{\alpha x} + B(1-\beta)e^{-\alpha x} \tag{15}$$

16.1.3 *Light reflection and transmission of powder layers*[4]

Consider a particle layer placed between glass plates A with reflectance r_a and transmittance t_a, and B with r_b and t_b, respectively (Figure 2). If the layer thickness is d, the boundary conditions are:

$$I(0) = t_a I_0 + r_a J(0) \tag{16}$$

$$J(d) = r_b I(d) \tag{17}$$

By introducing ρ_a and ρ_b defined by:

$$\rho_a = (1-r_a)/(1+r_a) \tag{18}$$

$$\rho_b = (1-r_b)/(1+r_b) \tag{19}$$

Eqs. 16 and 17 can then be written as:

$$(1+\rho_a)I(0) = t_a(1+\rho_a)I_0 + (1-\rho_a)J(0) \tag{20}$$

$$(1+\rho_b)J(d) = (1-\rho_b)I(d) \tag{21}$$

From the general solutions in Eq. 14, Eq. 15, and the above boundary conditions, the constants *A* and *B* are found to be:

$$A = -t_a I_0 \frac{(\rho_b - \beta)(1+\rho_a)e^{-\alpha d}}{2(\rho_a+\beta)(\rho_b+\beta)e^{\alpha d} - 2(\rho_a-\beta)(\rho_b-\beta)e^{-\alpha d}} \tag{22}$$

$$B = t_a I_0 \frac{(\rho_b + \beta)(1+\rho_a)e^{\alpha d}}{2(\rho_a+\beta)(\rho_b+\beta)e^{\alpha d} - 2(\rho_a-\beta)(\rho_b-\beta)e^{-\alpha d}} \tag{23}$$

If a glass plate exists only on one side (for example only glass B), then $t_a = 1$ *and* $r_a = 0$ ($\rho_a = 1$). In this case, transmittance *T* and reflectance *R* of the particle layer are given by Eqs. 24 and 25, respectively.

$$T = \frac{I(d)}{I_0}t_b = t_b \frac{(1+\beta)(\rho_b+\beta) - (1-\beta)(\rho_b-\beta)}{(1+\beta)(\rho_b+\beta)e^{\alpha d} - (1-\beta)(\rho_b-\beta)e^{-\alpha d}} \tag{24}$$

$$R = \frac{J(0)}{I_0} = \frac{(1-\beta)(\rho_b+\beta)e^{\alpha d} - (1+\beta)(\rho_b-\beta)e^{-\alpha d}}{(1+\beta)(\rho_b+\beta)e^{\alpha d} - (1-\beta)(\rho_b-\beta)e^{-\alpha d}} \tag{25}$$

Reflectance of a powder layer having a semi-infinite thickness, R_∞, is of practical importance, as reflection spectra of phosphors are measured in this manner. By extrapolating $d \rightarrow \infty$ in Eq. 25, one obtains:

$$R_\infty = \frac{1-\beta}{1+\beta} \tag{26}$$

Using Eq. 13, this can be rewritten as:

$$\frac{K}{S} = \frac{(1-R_\infty)^2}{2R_\infty} \equiv F(R_\infty) \tag{27}$$

The resultant function $F(R_\infty)$ is called the remission or Kubelka-Munk function. If *S* is independent of wavelength, $F(R_\infty)$ is proportional to the absorption coefficient *K*.

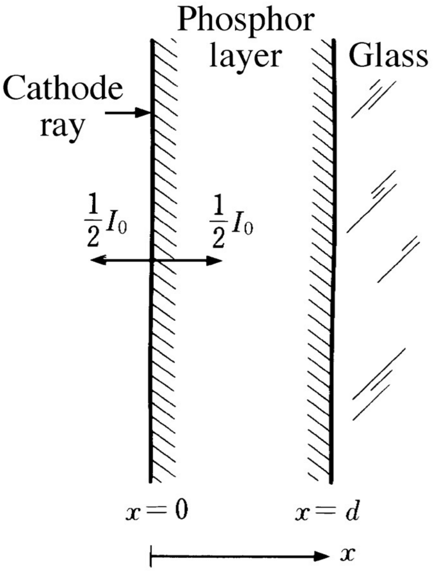

Figure 3 Generation of cathodoluminescence in the phosphor screen of a cathode-ray tube.

16.1.4 *Optical properties of phosphor layers*

The excitation energy given to a phosphor layer penetrates to the interior of the layer, with the intensity becoming gradually smaller because of absorption and scattering by the phosphor particles. Luminescence light arises approximately in proportion to the absorbed excitation energy, and emerges out of the layer after multiple scattering and some absorption. The entire process of excitation and luminescence emission by phosphor layers is described in the following.

16.1.4.1 *Cathode-ray excitation*

Bril et al.[5] calculated the intensity of cathodoluminescence emission on the assumption that the energy of incident electrons is completely absorbed at the surface of the phosphor layer.*

Figure 3 illustrates the face plate of a cathode-ray tube. If emission with intensity I_0 is generated at the surface of the phosphor coating, $I_0/2$ of it is emitted into space and another $I_0/2$ is directed into the inside of the layer. The boundary conditions for the emission of intensity $I(x)$ and $J(x)$ are:

$$I(0) = I_0/2 \qquad (x = 0) \tag{28}$$

$$J(d) = r_g I(d) \qquad (x = d) \tag{29}$$

where r_g is the reflectance of the glass.

When ρ_g is defined by:

$$\rho_g = \frac{1 - r_g}{1 + r_g} \tag{30}$$

---

* This approximation can be applied to all cases in which the penetration depth of the incident energy is much smaller than the thickness of the layer.

one can calculate the absorption and scattering of the emitted light using Eqs. 14 and 15. The result is:

$$\begin{aligned} I(d) &= I_0 \frac{\beta(1+\rho_g)}{(1+\beta)(\rho_g+\beta)e^{\alpha d} - (1-\beta)(\rho_g-\beta)e^{-\alpha d}} \\ &= \frac{1}{2} I_0 \frac{1}{\dfrac{K+(1-r_g)S}{\alpha}\sinh \alpha d + \cosh \alpha d} \end{aligned} \tag{31}$$

$$\begin{aligned} J(0) &= \frac{1}{2} I_0 \frac{(1-\beta)(\rho_g+\beta)e^{\alpha d} - (1+\beta)(\rho_g-\beta)e^{-\alpha d}}{(1+\beta)(\rho_g+\beta)e^{\alpha d} - (1-\beta)(\rho_g-\beta)e^{-\alpha d}} \\ &= \frac{1}{2} I_0 \frac{r_g \cosh \alpha d + \dfrac{-Kr_g + (1-r_g)S}{\alpha}\sinh \alpha d}{\dfrac{K+(1-r_g)S}{\alpha}\sinh \alpha d + \cosh \alpha d} \end{aligned} \tag{32}$$

The emission intensity observed at the excitation side, I_R, is given by:

$$I_R = J(0) + \frac{1}{2} I_0 \tag{33}$$

while the emission intensity at the glass side, I_T, is:

$$I_T = t_g I(d) \tag{34}$$

where t_g is transmittance of the glass. If a metallic reflecting film of reflectance r_a is deposited on the phosphor layer, as is the practice for the commercial cathode-ray tube, the boundary condition

$$I(0) = \frac{I_0}{2} + \left(\frac{I_0}{2} + J(0)\right) r_a \tag{35}$$

is used in place of Eq. 28. In this case, the solution is given by Eq. 36 instead of Eq. 31,

$$I(d) = I_0 \frac{\beta(1+\rho_g)}{(\rho_a+\beta)(\rho_g+\beta)e^{\alpha d} - (\rho_a-\beta)(\rho_g-\beta)e^{-\alpha d}} \tag{36}$$

where ρ_a is defined as:

$$\rho_a = \frac{1-r_a}{1+r_a} \tag{37}$$

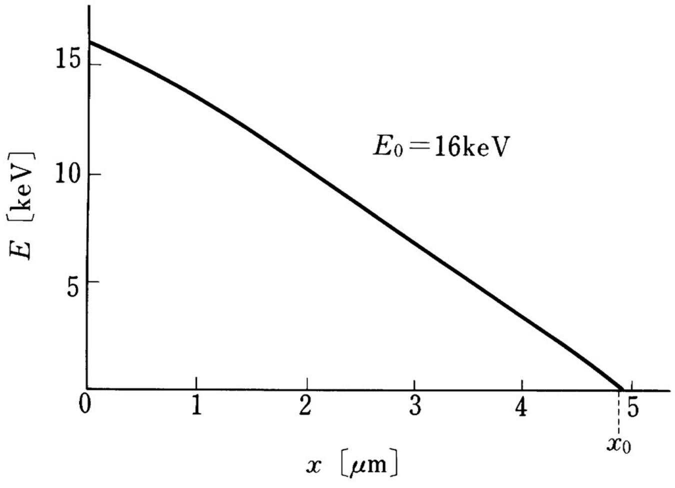

Figure 4 Relation between electron energy and penetration depth. (Phosphor: ZnCdS (60:40), acceleration voltage = 16 kV). (From Giakoumakis, G.E., Nomicos, C.D., and Euthymiou, P.C., *Can. J. Phys.*, 59, 88, 1981. With permission.)

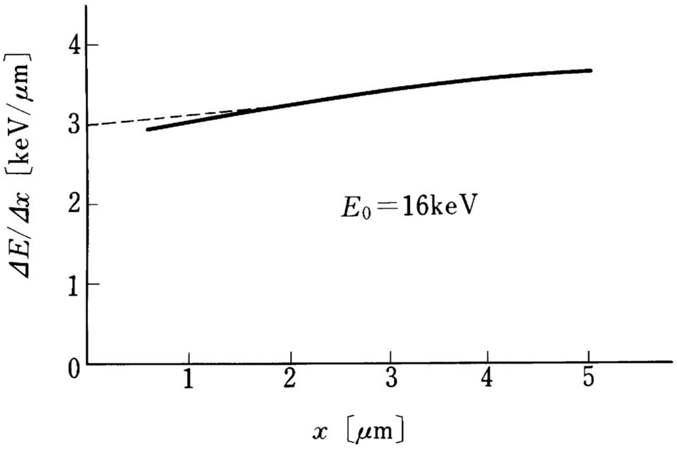

Figure 5 Relation between electron energy loss per unit length and penetration depth (Phosphor: ZnCdS (60:40), acceleration voltage = 16 kV). (From Giakoumakis, G.E., Nomicos, C.D., and Euthymiou, P.C., *Can. J. Phys.*, 59, 88, 1981. With permission.)

If the acceleration voltage is below 10 kV, the penetration depth of electrons into the phosphor layer, which is usually 20 to 30 μm thick, is estimated to be less than 2 μm. Hence, the above approximation is justified. When the acceleration voltage is greater, however, a more sophisticated treatment is necessary. Work by Giakoumakis[6] is described below.

A calculation based on Landau's theory on the energy loss of electrons in matter shows that an electron loses its energy in a phosphor layer [in this case, (Zn,Cd)S:Ag] in a manner shown in Figure 4. Differentiation of this curve yields the energy loss per unit thickness, $\Delta E/\Delta x$, which is shown in Figure 5. If the energy loss can be expressed by:

$$\frac{\Delta E}{\Delta x} = u + nx \qquad (u,\ n\text{: constants}) \tag{38}$$

and if the luminescence intensity is proportional to $\Delta E/\Delta x$, one obtains a pair of equations (Eqs. 39 and 40) on emission with intensities $I(x)$ and $J(x)$:

$$\frac{dI(x)}{dx} = -(K+S)I(x) + SJ(x) + \frac{1}{2}C_e(u+nx) \tag{39}$$

$$\frac{dJ(x)}{dx} = (K+S)J(x) - SI(x) - \frac{1}{2}C_e(u+nx) \tag{40}$$

where C_e = factor of proportionality between energy loss and emission intensity.

As Figure 4 shows, however, an electron penetrates only to a depth x_0, and Eqs. 39 and 40 are valid only for $0 \le x \le x_0$. When $x_0 \le x \le d$ (d = phosphor layer thickness), Eqs. 10 and 11 must be used.

By solving these four equations, the luminescence intensity radiated to the outside through the glass, I_T, is found to be:

$$I_T = t_g C_e\left(\rho_g + 1\right)\frac{(\rho_a - \beta)(P+n)e^{-\alpha x_0} + (\rho_a + \beta)(P-n)e^{\alpha x_0} + 2\beta\{n - u\rho_a(K+2S)\}}{2K(K+2S)\left\{(\rho_a+\beta)\left(\rho_g+\beta\right)e^{\alpha d} - (\rho_a-\beta)\left(\rho_g-\beta\right)e^{-\alpha d}\right\}} \tag{41}$$

where P is defined by:

$$P = \beta(K+2S)\left(u+nx_0\right) \tag{42}$$

16.1.4.2 X-ray excitation[4]

X-ray radiation penetrates the phosphor layer without being scattered, and its intensity decreases exponentially in accordance with Lambert's law. Luminescence of intensity $c_x e^{-\mu x}dx$ is generated in the layer of thickness dx, where c_x is constant and μ is the X-ray absorption coefficient of the phosphor. The following equations describe the emission intensity changes in the $+x$ and $-x$ directions.

$$\frac{dI(x)}{dx} = -(K+S)I(x) + SJ(x) + \frac{1}{2}c_x e^{-\mu x} \tag{43}$$

$$\frac{dJ(x)}{dx} = (K+S)J(x) - SI(x) - \frac{1}{2}c_x e^{-\mu x} \tag{44}$$

The general solutions of these equations are

$$I(x) = A(1-\beta)e^{\alpha x} + B(1+\beta)e^{-\alpha x} - \frac{1}{2}c_x\frac{\mu + \alpha/\beta}{\mu^2 - \alpha^2}e^{-\mu x} \tag{45}$$

$$J(x) = A(1+\beta)e^{\alpha x} + B(1-\beta)e^{-\alpha x} + \frac{1}{2}c_x\frac{\mu - \alpha/\beta}{\mu^2 - \alpha^2}e^{-\mu x} \tag{46}$$

For X-ray intensifying screens, the phosphor layer of the screen is placed between a photographic film and a plastic base, as shown in Figure 6. It is assumed that the photo-

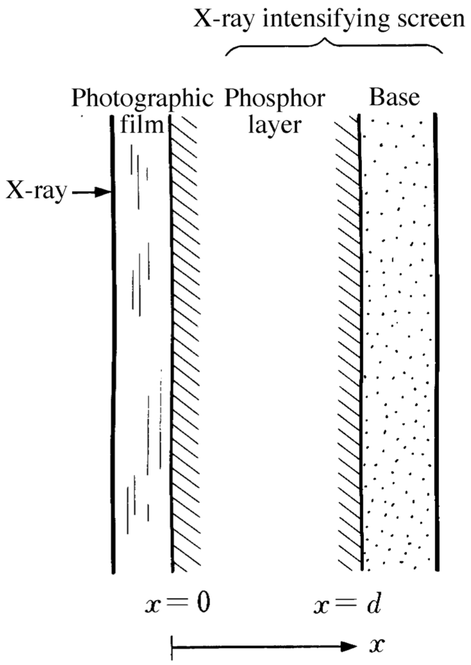

Figure 6 X-ray photography using an intensifying screen.

graphic film and the base have reflectances for the emitted light, r_f and r_c, respectively. Then, the boundary conditions are as follows:

$$I(0) = r_f J(0) \quad \text{or} \quad (1+\rho_f)I(0) = (1-\rho_f)J(0) \tag{47}$$

$$J(d) = r_c I(d) \quad \text{or} \quad (1+\rho_c)J(d) = (1-\rho_c)I(d) \tag{48}$$

The luminescence intensity at the photographic plate, $J(0)$, is given by Eq. 49.

$$J(0) = \frac{1}{2}c_x(1+\rho_f)\frac{(\rho_c+\beta)(\mu-\alpha)e^{\alpha d} - (\rho_c-\beta)(\mu+\alpha)e^{-\alpha d} + 2(\alpha\rho_c - \mu\beta)e^{-\mu d}}{\left\{(\rho_f+\beta)(\rho_c+\beta)e^{\alpha d} - (\rho_f-\beta)(\rho_c-\beta)e^{-\alpha d}\right\}(\mu^2-\alpha^2)} \tag{49}$$

16.1.4.3 *Ultraviolet excitation*[7–9]

The total process of photoluminescence is now described. Suppose a phosphor is coated on a glass plate, which is excited with ultraviolet radiation incident on the phosphor side. Absorption and scattering of the incident light can be described in the same manner as discussed in 16.1.3. The intensity of the light emitted by the phosphor layer of thickness dx is $qK(I(x) + J(x))dx$, where $I(x)$ and $J(x)$ are the intensity of ultraviolet radiation in the $+x$ and $-x$ directions, respectively, q is the energy efficiency of luminescence of the phosphor, and K is the absorption coefficient of the phosphor for ultraviolet radiation. Using Eqs. 14 and 15, the above intensity of light is found to be $2qK(Ae^{\alpha x} + Be^{-\alpha x})dx$. If the emitted light is directed equally to the $+x$ and $-x$ directions, the equations to describe its behavior are:

$$\frac{dI'(x)}{dx} = -(K'+S')I'(x) + S'J'(x) + qK\left(Ae^{\alpha x} + Be^{-\alpha x}\right) \tag{50}$$

$$\frac{dJ'(x)}{dx} = (K'+S')J'(x) - S'I'(x) - qK\left(Ae^{\alpha x} + Be^{-\alpha x}\right) \tag{51}$$

To distinguish between exciting radiation and emitted light, symbols with a prime are used for the latter.

The general solutions to these equations are:

$$I'(x) = \frac{qKA}{\beta'} \cdot \frac{\alpha\beta' - \alpha'}{\alpha^2 - \alpha'^2} e^{\alpha x} - \frac{qKB}{\beta'} \cdot \frac{\alpha\beta' + \alpha'}{\alpha^2 - \alpha'^2} e^{-\alpha x} + A'(I - \beta')e^{\alpha' x} + B'(I + \beta')e^{-\alpha' x} \tag{52}$$

$$J'(x) = -\frac{qKA}{\beta'} \cdot \frac{\alpha\beta' + \alpha'}{\alpha^2 - \alpha'^2} e^{\alpha x} + \frac{qKB}{\beta'} \cdot \frac{\alpha\beta' - \alpha'}{\alpha^2 - \alpha'^2} e^{-\alpha x} + A'(I + \beta')e^{\alpha' x} + B'(I - \beta')e^{-\alpha' x} \tag{53}$$

Here α' and β' are defined by:

$$\alpha' = \sqrt{K'(K'+2S')} \tag{54}$$

$$\beta' = \sqrt{K'/(K'+2S')} \tag{55}$$

The values of A' and B' are calculated by the boundary conditions:

$$\begin{aligned} &I'(0) = 0 \\ &J'(d) = r'I'(d) \quad \text{or} \quad (1+\rho')J'(d) - (1-\rho')I'(d) = 0 \end{aligned} \tag{56}$$

with r′ = reflectance of glass at the luminescence frequency

and are given by Eqs. 57 and 58.

$$A' = qK\frac{(1+\beta')\left\{A(\alpha\beta' + \alpha'\rho')e^{\alpha d} - B(\alpha\beta' - \alpha'\rho')e^{-\alpha d}\right\} + (\rho' - \beta')\left\{A(\alpha\beta' - \alpha') - B(\alpha\beta' + \alpha')\right\}e^{-\alpha' d}}{\beta'\left(\alpha^2 - \alpha'^2\right)\left\{(1+\beta')(\rho' + \beta')e^{\alpha' d} - (1-\beta')(\rho' - \beta')e^{-\alpha' d}\right\}} \tag{57}$$

$$B' = -qK\frac{(1-\beta')\left\{A(\alpha\beta' + \alpha'\rho')e^{\alpha d} - B(\alpha\beta' - \alpha'\rho')e^{-\alpha d}\right\} + (\rho' + \beta')\left\{A(\alpha\beta' - \alpha') - B(\alpha\beta' + \alpha')\right\}e^{\alpha' d}}{\beta'\left(\alpha^2 - \alpha'^2\right)\left\{(1+\beta')(\rho' + \beta')e^{\alpha' d} - (1-\beta')(\rho' - \beta')e^{-\alpha' d}\right\}} \tag{58}$$

16.1.4.4 Light output of fluorescent lamps

As shown in Figure 7(a), the ultraviolet radiation generated by the discharge in a fluorescent lamp is absorbed in the phosphor coating after multiple reflection. The total intensity of the ultraviolet radiation incident on the phosphor is:

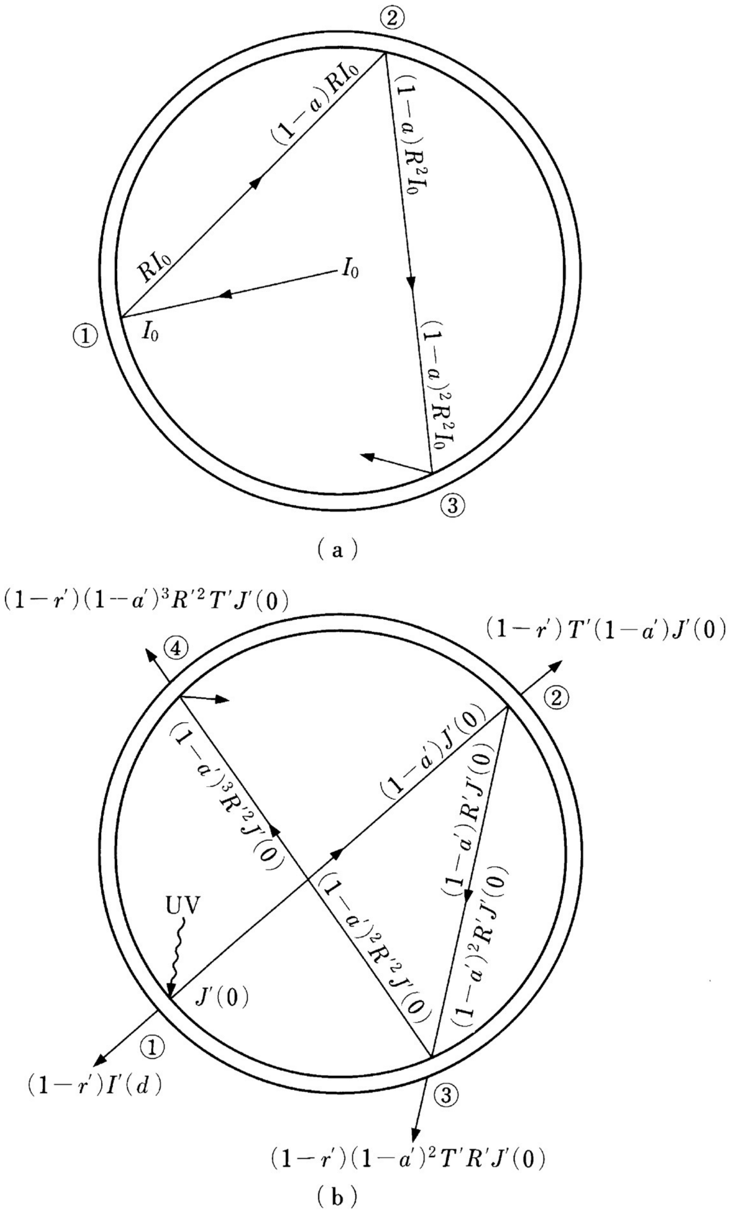
②
$(1-a)RI_0$
$(1-a)R^2I_0$
RI_0
I_0
①
I_0
$(1-a)^2R^2I_0$
③
(a)
$(1-r')(1-a')^3R'^2T'J'(0)$
④
$(1-r')T'(1-a')J'(0)$
②
$(1-a')^3R'^2J'(0)$
$(1-a')J'(0)$
$(1-a')R'J'(0)$
UV
$(1-a')^2R'^2J'(0)$
$(1-a')^2R'J'(0)$
$J'(0)$
①
$(1-r')I'(d)$
③
$(1-r')(1-a')^2T'R'J'(0)$
(b)

Figure 7 Multiple scattering of light inside a fluorescent lamp: (a) ultraviolet radiation; (b) luminescent light.

$$I_0+(1-a)RI_0+(1-a)^2R^2I_0+\ldots=\frac{I_0}{1-(1-a)R} \tag{59}$$

where I_0 = intensity of ultraviolet radiation created by the discharge
a = proportion of ultraviolet radiation lost by absorption in the discharge space
R = reflectance of phosphor coating for ultraviolet radiation

Let the intensity of fluorescent light emitted to the excitation side be $J'(0)$, and that to the outer side be $I'(d)$. The emitted light is transmitted or reflected as shown in Figure 7(b), and leaves the lamp with intensity F given by:

$$\begin{aligned} F &= \frac{1}{1-(1-a)R}\left\{(1-r')I'(d)+(1-r')(1-a')T'J'(0)+(1-r')(1-a')^2T'R'J'(0)+\ldots\right\} \\ &= \frac{1-r'}{1-(1-a)R}\left\{I'(d)+\frac{(1-a')T'}{1-(1-a')R'}J'(0)\right\} \end{aligned} \tag{60}$$

where r' = reflectance of glass for the fluorescent light
a' = proportion of fluorescent light lost by absorption in the discharge space and lamp ends
R' = reflectance of phosphor layer for the fluorescent light
T' = transmittance of phosphor layer for the fluorescent light

The values of $J'(0)$ and $I'(d)$ are calculated from Eqs. 52 and 53, and R, R', and T' from Eqs. 24 and 25.

16.1.5 *Measurement of the scattering coefficient*

To carry out the calculations mentioned above, a measured value of either the absorption or scattering coefficient must be known. If one of them is available, the other can be derived from Eq. 27 using the readily measurable reflectance of a thick layer. The easier way is to find the value of the scattering coefficient S by the reflectance measurements, described below, and then to calculate the absorption coefficient.

If one measures the reflectance of a sample layer R_0 coated on a black plate for which the reflectance can be neglected, the scattering coefficient S is given by[10–12]:

$$S = \frac{R_\infty}{d\left(1-R_\infty^{\,2}\right)}\ln\frac{R_\infty\left(1-R_0R_\infty\right)}{R_\infty-R_0} \equiv \frac{1}{d}F\left(R_0, R_\infty\right) \tag{61}$$

where d is the thickness of the sample layer.

If Eq. 61 is valid, a d vs. $F(R_0, R_\infty)$ plot will yield a straight line, and its gradient gives the value of S. Figure 8 shows an experimental result on a calcium halophosphate phosphor.[13] It is seen that S is certainly a constant for this wavelength.

In general, the value of the scattering coefficient does not depend on wavelength when the particle size is sufficiently greater than the wavelength, typically >2 μ, while it is reciprocally proportional to particle sizes between 1 and 10 μ.[14–15] Further, in the case where absorption is not strong (i.e., $R_\infty \geq 0.50$), the scattering coefficient can be regarded as being independent of the absorption coefficient.[14]

In the ultraviolet region, where phosphors have strong absorption, it is impossible to use the above-mentioned method to determine S. The Kubelka-Munk theory itself does not predict the interdependence of S and K either. ter Vrugt[16] compared the Kubelka-Munk theory with Bodo's noncontinuous body approximation,[17] and concluded that the scattering coefficient is proportional to the absorption coefficient as far as $R_\infty \leq 0.30$. However, no experimental confirmation has been made. Therefore, application of the Kubelka-Munk theory to the ultraviolet region must be made carefully.

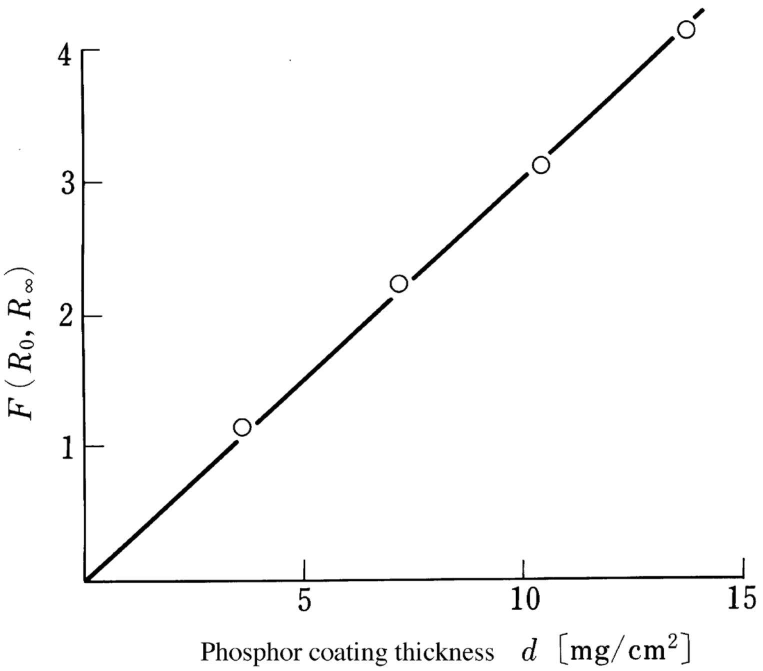

Figure 8 Relation between the coating thickness of phosphor and $F(R_0, R_\infty)$, measured at 500 nm. (From Narita, K., unpublished results, 1981. With permission.)

References

1. Schuster, A., *Astrophys. J.*, 21, 1, 1905.
2. Kubelka, P. and Munk, F., *Z. f. tech. Physik*, 12, 593, 1931.
3. Kubelka, P., *J. Opt. Soc. Am.*, 38, 448, 1948.
4. Hamaker, H.C., *Philips Res. Rep.*, 2, 55, 1947.
5. Bril, A. and Klasens, A., *Philips Tech. Rev.*, 15, 63, 1953.
6. Giakoumakis, G.E., Nomicos, C.D., and Euthymiou, P.C., *Can. J. Phys.*, 59, 88, 1981.
7. Ivanov, A.P., *Zhurnal eksper. teor. Fiz.*, 26, 275, 1954.
8. ter Vrugt, J.W., Manders, L.W.J., and Wanmaker, W.L., *Lighting Res. Technol.*, 7, 23, 1975.
9. Fonger, W.H., *Appl. Opt.*, 21, 1219, 1982.
10. Kortüm, G., *Reflectance Spectroscopy*, Springer, 1969, 112.
11. Gillespie, J.B., Lindberg, J.D., and Laude, L.S., *Appl. Opt.*, 14, 807, 1975.
12. Patterson, E.M., Shelden, C.E., and Stockton, B.H., *Appl. Opt.*, 16, 729, 1977.
13. Narita, K., unpublished data, 1981. Refer also to Reference 15.
14. Kortüm, G., Braun, W., and Herzog, G., *Angew. Chem.*, 75, 653, 1963.
15. Narita, K., *Electrochem. Soc. Spring Meeting Abstr.*, 1981, 177.
16. ter Vrugt, J.W., *Philips Res. Rep.*, 20, 23, 1965.
17. Bodo, Z., *Acta Physica Hungarica*, 1, 135, 1951.

chapter sixteen — section two

Optical properties of powder layers

Akira Tomonaga* and Yoshiharu Komine

Contents

16.2 Johnson's theory 937
  16.2.1 Reflection, absorption, and transmission in a single layer 937
  16.2.2 Reflection, absorption, transmission and emission in a single layer within multiple layers 938
  16.2.3 Light flux of a fluorescent lamp 942
  16.2.4 Application to the white fluorescent lamp 943
References 947

16.2 Johnson's theory

As an application of Johnson's theory, this section presents an analysis of the relationship between the light flux of a fluorescent lamp and the thickness of its phosphor coating.

16.2.1 Reflection, absorption, and transmission in a single layer

First, assume that the thickness of a single phosphor layer is the same as the volume surface diameter d. The reflection, absorption, and transmission of incident light with an intensity I_0 are shown in Figure 9. In the figure, m indicates the ratio of the light reflected on the layer interface, and γ is the absorption coefficient (cm^{-1}) of the phosphor.

As shown in Figure 9, the incident light I_0 repeats the reflection, absorption, and transmission processes within the layer, and therefore, the final total reflection is:

$$\begin{aligned} & I_0 m + I_0 m(1-m)^2 e^{-2\gamma d} + I_0 m^3 (1-m)^2 e^{-4\gamma d} + \ldots \\ & = I_0 m\left\{1 + \frac{(1-m)^2 e^{-2\gamma d}}{1 - m^2 e^{-2\gamma d}}\right\} \\ & = I_0 \cdot t \end{aligned} \tag{62}$$

---

* Akira Tomonaga is deceased.

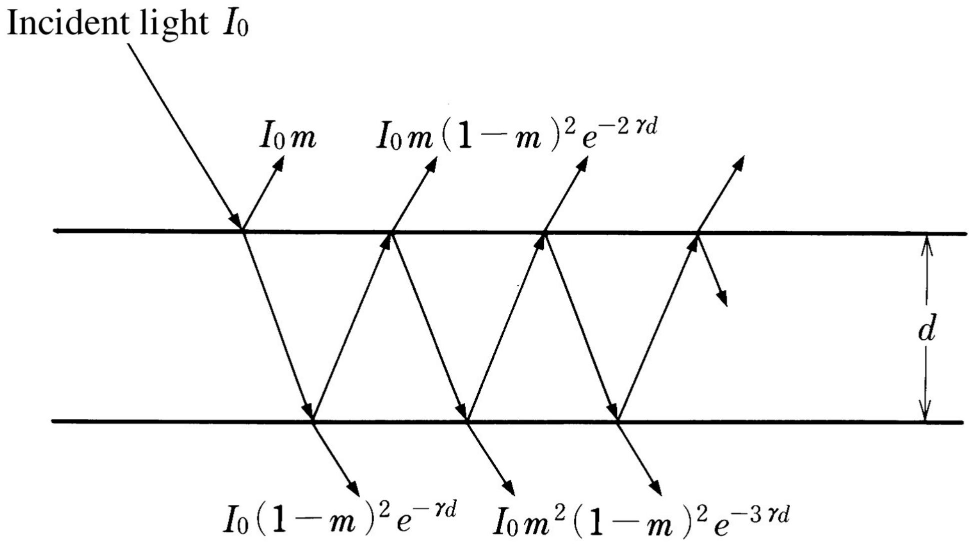
Incident light I_0
$I_0 m$
$I_0 m(1-m)^2 e^{-2\gamma d}$
d
$I_0(1-m)^2 e^{-\gamma d}$
$I_0 m^2(1-m)^2 e^{-3\gamma d}$

Figure 9 Reflectance, absorption, and transmission in a single phosphor layer.

The total transmission is:

$$\begin{aligned} & I_0(1-m)^2 e^{-\gamma d} + I_0 m^2 (1-m)^2 e^{-3\gamma d} + \ldots \\ & = I_0 \cdot \frac{(1-m)^2 e^{-\gamma d}}{1-m^2 e^{-2\gamma d}} \\ & = I_0 \cdot s \end{aligned} \tag{63}$$

Here, t and s are given by

$$\begin{aligned} t &= m\left\{1 + \frac{(1-m)^2 e^{-2\gamma d}}{1-m^2 e^{-2\gamma d}}\right\} \\ s &= \frac{(1-m)^2 e^{-\gamma d}}{1-m^2 e^{-2\gamma d}} \end{aligned} \tag{64}$$

Then, the absorbed light A_b is:

$$A_b = I_0 \cdot (1 - s - t) \tag{65}$$

16.2.2 Reflection, absorption, transmission and emission in a single layer within multiple layers

Figure 10(a) shows a configuration of layers, and Figure 10(b) shows the reflection, absorption, and transmission that takes place in the i^{th} layer. In figure 10(b), if the light traveling down (to the glass) and up (to the positive column) from the i^{th} layer are denoted by I_i and J_i, respectively, the following equations hold:

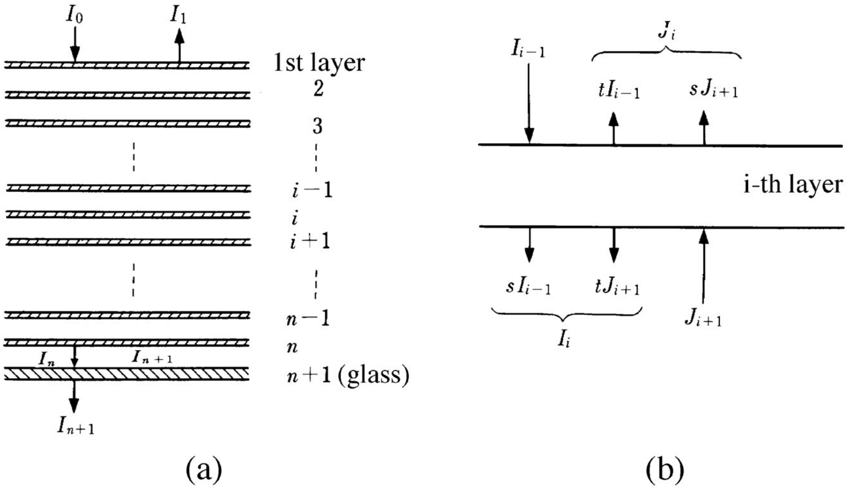
I_0
I_1
1st layer
2
3
$i-1$
i
$i+1$
$n-1$
n
$n+1$ (glass)
I_n
I_{n+1}
I_{n+1}
(a)
I_{i-1}
J_i
tI_{i-1}
sJ_{i+1}
i-th layer
sI_{i-1}
tJ_{i+1}
J_{i+1}
I_i
(b)

Figure 10 Layer configuration.

$$
\begin{aligned}
I_i &= sI_{i-1} + tJ_{i+1} \\
J_i &= sJ_{i+1} + tJ_{i-1}
\end{aligned}
\tag{66}
$$

In Figure 10(a), if the (n + 1)th layer represents the glass, and *s* and *t* for the glass is denoted by s_g and t_g, respectively, then Eq. 67 gives the boundary conditions:

$$
\begin{aligned}
I_{n+1} &= s_g I_n \\
J_{n+1} &= t_g I_n
\end{aligned}
\tag{67}
$$

From these equations and those in Eq. 66, one obtains:

$$
\begin{aligned}
I_{n-i} &= A_i I_n \\
J_{n-i+1} &= B_i J_{n+1}
\end{aligned}
\tag{68}
$$

$$
\begin{aligned}
A_i &= \frac{1}{s} A_{i-1} - \frac{t \cdot t_g}{s} B_{i-1} \\
B_i &= \frac{t}{s \cdot t_g} A_{i-1} + \frac{s^2 - t^2}{s} B_{i-1} \\
A_0 &= B_0 = 1
\end{aligned}
\tag{69}
$$

If it is assumed that:

$$
\frac{1}{s} = \alpha
$$

$$
\frac{-t \cdot t_g}{s} = \beta
$$

$$\begin{aligned} \frac{t}{s \cdot t_g} &= \eta \\ \frac{s^2 - t^2}{s} &= \delta \end{aligned} \tag{70}$$

then A_i and B_i can be represented using the matrix representation as follows:

$$\begin{aligned} \begin{pmatrix} A_i \\ B_i \end{pmatrix} &= \begin{pmatrix} \alpha & \beta \\ \eta & \delta \end{pmatrix} \begin{pmatrix} A_{i-1} \\ B_{i-1} \end{pmatrix} \\ &= \begin{pmatrix} \alpha & \beta \\ \eta & \delta \end{pmatrix}^i \begin{pmatrix} A_0 \\ B_0 \end{pmatrix} \\ &= \begin{pmatrix} \alpha_i & \beta_i \\ \eta_i & \delta_i \end{pmatrix} \begin{pmatrix} 1 \\ 1 \end{pmatrix} \end{aligned} \tag{71}$$

Since $\alpha\delta - \beta\eta = 1$, α_i, β_i, η_i, and δ_i are expressed as follows:

$$\begin{aligned} \alpha_i &= T_i(\theta) + \xi U_i(\theta) \\ \beta_i &= BU_i(\theta) \\ \eta_i &= \eta U_i(\theta) \\ \delta_i &= T_i(\theta) - \xi U_i(\theta) \end{aligned} \tag{72}$$

$T_i(\theta)$ and $U_i(\theta)$ are *Chebyshev polynomials* expressed by Eq. 73.[1]

$$\begin{aligned} T_i(\theta) &= \frac{1}{2}\left\{\left(\theta + \sqrt{\theta^2 - 1}\right)^i + \left(\theta - \sqrt{\theta^2 - 1}\right)^i\right\} \\ U_i(\theta) &= \frac{1}{2} \cdot \frac{\left(\theta + \sqrt{\theta^2 - 1}\right)^i - \left(\theta - \sqrt{\theta^2 - 1}\right)^i}{\sqrt{\theta^2 - 1}} \\ \theta &= \frac{\alpha + \beta}{2}, \quad \xi = \frac{\alpha - \beta}{2} \end{aligned} \tag{73}$$

From Eqs. 71, 72, and 73, one obtains Eq. 74.

$$\begin{aligned} A_i &= \frac{1}{2}\left\{\left(1 + \frac{\beta + \xi}{\sqrt{\theta^2 - 1}}\right)\left(\theta + \sqrt{\theta^2 - 1}\right)^i + \left(1 - \frac{\beta + \xi}{\sqrt{\theta^2 - 1}}\right)\left(\theta - \sqrt{\theta^2 - 1}\right)^i\right\} \\ B_i &= \frac{1}{2}\left\{\left(1 + \frac{\eta - \xi}{\sqrt{\theta^2 - 1}}\right)\left(\theta + \sqrt{\theta^2 - 1}\right)^i + \left(1 - \frac{\eta - \xi}{\sqrt{\theta^2 - 1}}\right)\left(\theta - \sqrt{\theta^2 - 1}\right)^i\right\} \end{aligned} \tag{74}$$

Therefore, if s, t, s_g, and t_g are given, Eq. 68 can be used to obtain the relationship between the incident light and emitted light, in which the reflection between the layers is taken into account.

In Figure 10(b) the amount of light absorbed by the i^{th} layer, A_{bi} is:

$$\begin{aligned} A_{bi} &= I_{i-1} + J_{i+1} - I_i - J_i \\ &= \frac{1-s-t}{s+t}\left(I_i + J_i\right) \\ &= \frac{1-s-t}{s+t}\cdot\frac{1}{A_n}\left(A_{n-i} + t_g \cdot B_{n-i+1}\right) I_0 \end{aligned} \tag{75}$$

To obtain Eq. 75, I_i can be expressed by substituting $(n - i)$ into Eq. 68 for i as follows:

$$I_i = A_{n-i} I_n \tag{76}$$

Similarly, J_i can be expressed by substituting $(n - i + 1)$ for i in Eq. 68:

$$\begin{aligned} J_i &= B_{n-i+1} J_{n+1} \\ &= t_g B_{n-i+1} I_n \end{aligned} \tag{77}$$

Using Eqs. 76 and 77, one has:

$$I_i + J_i = \left(A_{n-i} + t_g B_{n-i+1}\right) I_n \tag{78}$$

By substituting n for i in Eq. 68,

$$I_0 = A_n I_n \tag{79}$$

Combining Eqs. 78 and 79, one obtains Eq. 75.

In the following, the ultraviolet and visible regions (fluorescence) are treated separately, so that these regions are indicated by adding the superscripts uv and v to the characters. Under this nomenclature, A_{bi}^{uv} stands for the ultraviolet rays absorbed by the i^{th} layer. If the conversion efficiency to visible light is μ, then the visible light emitted from the i^{th} layer is $2P = 1/2\cdot\mu A_{bi}^{uv}$. One half, $P = 1/2\cdot\mu\, A_{bi}^{uv}$, travels into the fluorescent lamp. The other half, $P = 1/2\cdot\mu_{bi}^{uv}$, escapes to the glass. As for the light traveling outward from the i^{th} layer, P:

$$I_{n-i+1} = \frac{s_g^v}{A_{n-i}^v}\cdot P \tag{80}$$

is emitted through the glass to the outside. Some of the light P is reflected on the glass surface (reflection: $J_{n-i+1} = \left(t_g^v \big/ A_{n-i}^v\right)\cdot P$) and

$$\frac{J_{n-i+1}}{A_n^v} = \frac{t_g^v}{A_n^v \cdot A_{n-i}^v} \tag{81}$$

is returned to the positive ion discharge column within the lamp structure. On the other hand, of the light P traveling inward from the i^{th} layer, P/A_{i-1}^{v} is emitted to the positive ion discharge column. Therefore, the light E_i emitted from the i^{th} layer to the outside of the lamp is:

$$E_i = \frac{s_g^v}{A_{n-i}^v} \cdot P \tag{82}$$

and the light F_i emitted from the same layer to the positive ion discharge column is:

$$F_i = \left(\frac{1}{A_{i-1}^v} + \frac{t_g^v}{A_n^v \cdot A_{n-i}^v} \right) \cdot P \tag{83}$$

Some of F_i is absorbed by the positive ion discharge column, and a fraction, ρ_v ($\rho^v \leqq 1$), reenters the phosphor layer. Some of this light is again emitted to the outside of the lamp, and some is returned to positive ion discharge and partly absorbed by the column. This process is repeated several times so that the final emitted light to the outside of the lamp is:

$$G_i = \frac{s_g^v \cdot \rho^v}{A_n^v - B_n^v \cdot t_g^v \cdot \rho^v} \cdot F_i \tag{84}$$

Therefore, the total visible light emitted from the i^{th} layer to the outside of the lamp is expressed by the sum ($E_i + G_i$).

16.2.3 Light flux of a fluorescent lamp

As shown in the previous section, the visible light emitted from the i^{th} layer to the outside of the lamp is expressed by ($E_i + G_i$). Therefore, the light emitted from the entire phosphor layer is $\Sigma(E_i + G_i)$. Here, it should be noted, however, that, just like the visible light, the incident ultraviolet light I_0 undergoes multiple reflection in the lamp, a part of it being absorbed by the positive column. For this reason, the effective incident ultraviolet light becomes:

$$\frac{I_0}{1 - \dfrac{B_n^{uv}}{A_n^{uv}} \cdot t_g^{uv} \cdot \rho^{uv}} \tag{85}$$

Therefore, the visible light L_{pn} emitted from the phosphor multilayers to the outside of the lamp is:

$$L_{pn} = \frac{\sum_{i=1}^{n} \left(E_i + G_i \right)}{1 - \dfrac{B_n^{uv}}{A_n^{uv}} \cdot t_g^{uv} \cdot \rho^{uv}} \tag{86}$$

Furthermore, the visible light from the lamp contains mercury resonance lines which are transmitted:

$$L_{hn} = k \cdot \frac{s_g^v}{A_n^v - B_n^v \cdot t_g^v \cdot \rho^v} \cdot I_0 \qquad (k = \text{constant}) \tag{87}$$

and the total light flux L_n from the fluorescent lamp is:

$$L_n = L_{pn} + L_{hn} \tag{88}$$

16.2.4 Application to the white fluorescent lamp

How well Eq. 88 agrees with measurements for a white fluorescent lamp using a white-light-emitting calcium halophosphate phosphor (volume surface diameter d = 6.7 μm)[2] is examined here.

According to Johnson,[3] the ratio m of reflection by one layer is $m = 1.5(n-1)^2/(n+1)^2$, where n is the refractive index and depends on the wavelength. The refractive indices for the visible and ultraviolet regions are represented by those of the Na D line and the Hg 254-nm-wavelength light. The refractive indices are 1.648 and 1.71 for the halophosphate phosphor, and 1.5 and 1.55 for glass.[2] Since the ratio m for the glass can be assumed to be $m = (n-1)^2/(n+1)^2$, the values of m for the phosphor and glass are as follows:

Halophosphate phosphor : $m^v = 0.090,\ m^{uv} = 0.103$

Glass : $m^v = 0.04,\ m^{uv} = 0.05$

The absorption coefficient γ of the halophosphate phosphor can be obtained by measuring the diffuse reflectance R of the phosphor with a large thickness. If the number of layers is increased to infinity in Figure 10, the diffuse reflectance is given by:

$$\begin{aligned} R &= \lim_{n-\infty} \frac{J_1}{I_0} \\ &= t_g \lim_{n-\infty} \frac{B_n}{A_n} \\ &= t_g \cdot \frac{1 + \dfrac{\eta - \xi}{\sqrt{\theta^2 - 1}}}{1 + \dfrac{\beta + \xi}{\sqrt{\theta^2 - 1}}} \end{aligned} \tag{89}$$

By substituting s, t, s_g, and t_g for β, η, θ, and ξ, Eq. 89 becomes:

$$R + \frac{1}{R} = \frac{1 - s^2 + t^2}{t} \tag{90}$$

Since $e^{-\gamma d}$ is obtained from Eqs. 90 and 64, and d is known, the coefficient γ can be determined. For practical purposes, however, Eq. 64 can be simplified by neglecting m^2, since m is much smaller than 1, as stated above.

$$\begin{aligned} s &\simeq (1-2m)e^{-\gamma d} \\ t &\simeq m\left\{1+(1-2m)e^{-2\gamma d}\right\} \end{aligned} \tag{91}$$

In Eq. 90, by neglecting t^2 ($\ll 1$) and using Eq. 91, one obtains Eq. 92.

$$e^{-2\gamma d} = \frac{1-m\left(R+\frac{1}{R}\right)}{(1-2m)\left\{(1-2m)+m\left(R+\frac{1}{R}\right)\right\}} \tag{92}$$

This indicates that the absorption coefficient γ can be obtained by measuring the diffuse reflectance R. Since measurements of R give $R^{uv} = 0.18$ and $R^{v} = 0.86$, the absorption coefficient of the phosphor is $\gamma^{uv} = 750\ \text{cm}^{-1}$ and $\gamma^{v} = 3.6\ \text{cm}^{-1}$. Therefore, the values of s and t for the phosphor can be obtained using Eq. 91.

Consider the values of s and t for the glass. By substituting measured values of $s_g^v = 0.92$–0.94 and $s_g^{uv} = 0$ into Eq. 91, one obtains $\gamma_g^v = 0$ and $\gamma_g^{uv} \simeq \infty$. These results can be used to obtain the values of t for the glass. Values of s and t for the phosphor and glass are listed in Table 1.

When the values of s and t are given the values of α, β, η, θ, and ξ in Eqs. 70 and 73 can be obtained; in turn, one can calculate the values of A_i and B_i in Eq. 74. The results are listed in Table 2.

With A_i and B_i, $(E_i + G_i)$ in Eq. 86 can be expressed by Eq. 93, and Eq. 86 becomes Eq. 94.

$$E_i + G_i = \frac{s_g^v}{2}\cdot \mu I_0 \cdot \frac{s^{uv}+t^{uv}}{1-s^{uv}-t^{uv}}\cdot \frac{A_{n-i}^{uv}+t_g^{uv}B_{n-i+1}^{uv}}{A_n^{uv}}\cdot\left\{\frac{1}{A_{n-i}^{v}}+\frac{\rho^v}{A_n^v-B_n^v\cdot t_g^v\cdot\rho^v}\left(\frac{1}{A_{i-1}^v}+\frac{t_g^v}{A_n^v\cdot A_{n-i}^v}\right)\right\} \tag{93}$$

$$\begin{aligned} L_{pn} = {} & \frac{s_g^v}{2}\cdot\mu I_0\cdot\frac{s^{uv}+t^{uv}}{1-s^{uv}-t^{uv}}\cdot\frac{1}{A_n^{uv}-B_n^{uv}\cdot t_g^{uv}\cdot\rho^{uv}}\cdot\left[\left\{1+\frac{\rho^v\cdot t_g^v}{A_n^v\left(A_n^v-B_n^v\cdot t_g^v\cdot\rho^v\right)}\right\}\sum_{i=1}^{n}\left(\frac{A_{n-i}^{uv}}{A_{n-i}^{v}}\right)\right. \\ & +t_g^{uv}\left\{1+\frac{\rho^v\cdot t_g^v}{A_n^v\left(A_n^v-B_n^v\cdot t_g^v\cdot\rho^v\right)}\right\}\sum_{i=1}^{n}\left(\frac{B_{n-i+1}^{uv}}{A_{n-i}^{v}}\right)+\frac{\rho^v}{A_n^v-B_n^v\cdot t_g^v\cdot\rho^v}\sum_{i=1}^{n}\left(\frac{B_{n-1}^{uv}}{A_{i-1}^{v}}\right) \\ & \left.+\frac{\rho^v\cdot t_g^{uv}}{A_n^v-B_n^v\cdot t_g^v\cdot\rho^v}\sum_{i=1}^{n}\left(\frac{B_{n-i+1}^{uv}}{A_{i-1}^{v}}\right)\right] \end{aligned} \tag{94}$$

The results of calculations for $n = 1$ to 10 are shown in Table 3. The calculations are based on the values $\rho^v = 1.0$ and $\rho^{uv} = 0.65$.[4,5]

Next, using the same phosphor, prototypical 40-W fluorescent lamps are fabricated with varying coating weights of the phosphor to examine the relationship between the coating weight of the phosphor, w (g cm^{-2}), and the light flux (relative value). The results are shown in Table 4. In the table, the number of layers n was obtained using a halophosphate phosphor density of 3.2 g cm^{-3} and particle diameter (layer thickness) of 6.7×10^{-4} cm from Eq. 95.

Table 1 Values of *s* and *t* for the Ultraviolet and Visible Regions

	Calcium halophosphate phosphor		Glass	
	s	t	s_g	t_g
Ultraviolet region	0.483	0.133	0	0.05
Visible region	0.818	0.164	0.92	0.08

Table 2 Values of A_i and B_i for the Ultraviolet and Visible Regions

	A_i	B_i
Ultraviolet region	$1.0245 \cdot 2.019^{i} - 0.0245 \cdot 0.495^{i}$	$3.58 \cdot 2.019^{i} - 12.25 \cdot 0.9145^{i}$
Visible region	$1.635 \cdot 1.0935^{i} - 0.635 \cdot 0.9145^{i}$	$13.25 \cdot 1.0935^{i} - 12.25 \cdot 0.9145^{i}$

Table 3 Calculated Results

n	A_n^{uv}	B_n^{uv}	A_n^{v}	B_n^{v}	$\sum_{i=1}^{n} \frac{A_{n-i}^{uv}}{A_{n-1}^{v}}$	$\sum_{i=1}^{n} \frac{B_{n-i+1}^{uv}}{A_{n-1}^{v}}$	$\sum_{i=1}^{n} \frac{A_{n-i}^{uv}}{A_{i-1}^{v}}$	$\sum_{i=1}^{n} \frac{B_{n-i+1}^{uv}}{A_{i-1}^{v}}$
1	2.056	5.951	1.207	3.286	1	5.951	1	5.951
2	4.170	13.96	1.424	5.598	2.703	17.51	2.542	18.88
3	8.429	29.15	1.652	7.955	5.632	37.98	6.575	44.89
4	17.02	59.33	1.894	10.38	10.73	73.89	13.93	96.88
5	34.37	120.0	2.150	12.88	19.72	137.3	28.71	201.2
6	69.40	242.5	2.424	15.49	35.71	250.0	58.47	411.3
7	140.1	489.6	2.717	18.22	64.34	452.0	118.5	835.0
8	282.9	988.5	3.032	21.09	115.9	815.8	239.6	1690
9	571.1	1996	3.371	24.14	20.92	1474	484.1	3415
10	1153	4030	3.737	27.38	378.6	2670	977.9	6899

n	$1+\frac{\rho^{v} \cdot t_g^{v}}{A_n^{v}\left(A_n^{v} - B_n^{v} \cdot t_g^{v} \cdot \rho^{v}\right)}$	$\frac{\rho^{v}}{A_n^{v} - B_n^{v} \cdot t_g^{v} \cdot \rho^{v}}$	$\frac{1}{A_n^{uv} - B_n^{uv} \cdot t_g^{uv} \cdot \rho^{uv}}$	$\frac{L_{pn}}{\mu I_0}$
1	1.0701	1.0583	5.368×10^{-1}	1.094
2	1.0576	1.0245	2.691×10^{-1}	1.461
3	1.0477	0.9844	1.337×10^{-1}	1.635
4	1.0397	0.9404	6.625×10^{-2}	1.597
5	1.0332	0.8931	3.282×10^{-2}	1.504
6	1.0279	0.8445	1.625×10^{-2}	1.395
7	1.0234	0.7940	8.052×10^{-3}	1.285
8	1.0196	0.7439	3.988×10^{-3}	1.180
9	1.0165	0.6945	1.975×10^{-3}	1.082
10	1.0138	0.6465	9.784×10^{-4}	0.993

$$\begin{aligned} n &= \frac{w}{3.2 \times 6.7 \times 10^{-4}} \\ &= 4.7 \times 10^{2} \cdot w \end{aligned} \tag{95}$$

In Table 4, the light flux for $w = 0$ represents the light flux in the visible region of the mercury arc. Therefore, since Eq. 87 with $n = 0$ is:

Table 4 Light Flux Measurements (Relative Values) for Varying Coating Weights of Phosphor

Measurement		
w × 10^3	Light flux (relative value)	Number of layers (n)
0	0.091	0
0.66	0.305	0.31
1.32	0.495	0.62
1.98	0.817	0.92
3.43	0.958	1.6
5.85	0.998	2.7
10.3	0.916	4.8
16.7	0.776	7.8

Table 5 L_n and the Number of Layers (Calculated Values)

n	L_{hn}	L_{pn}	L_n
0	0.091	0	0.091
1	0.089	0.614	0.703
2	0.086	0.820	0.906
3	0.083	0.917	1.000
4	0.079	0.896	0.975
5	0.075	0.834	0.909
6	0.071	0.783	0.854
7	0.067	0.721	0.788
8	0.062	0.662	0.724
9	0.058	0.607	0.665
10	0.054	0.557	0.611

$$\begin{aligned} L_{ho} &= k\frac{0.92}{1-0.08}I_0 \\ &= kI_0 \\ &= 0.091 \end{aligned} \tag{96}$$

one obtains:

$$L_{hn} = \frac{0.084}{A_n^v - 0.08B_n^v} \tag{97}$$

Table 5 shows the calculated dependence of L_{hn} on the number of layers n. In Table 3, $L_{pn}/\mu I_0$ reaches a maximum at n = 3. Thus, if one assumes that:

$$\begin{aligned} L_{p3} + L_{h3} &= L_{p3} + 0.083 \\ &= 1 \end{aligned} \tag{98}$$

then, L_{p3} = 0.917. Therefore, from:

$$\frac{L_{p3}}{\mu I_0} = \frac{0.917}{\mu I_0} = 1.635 \tag{99}$$

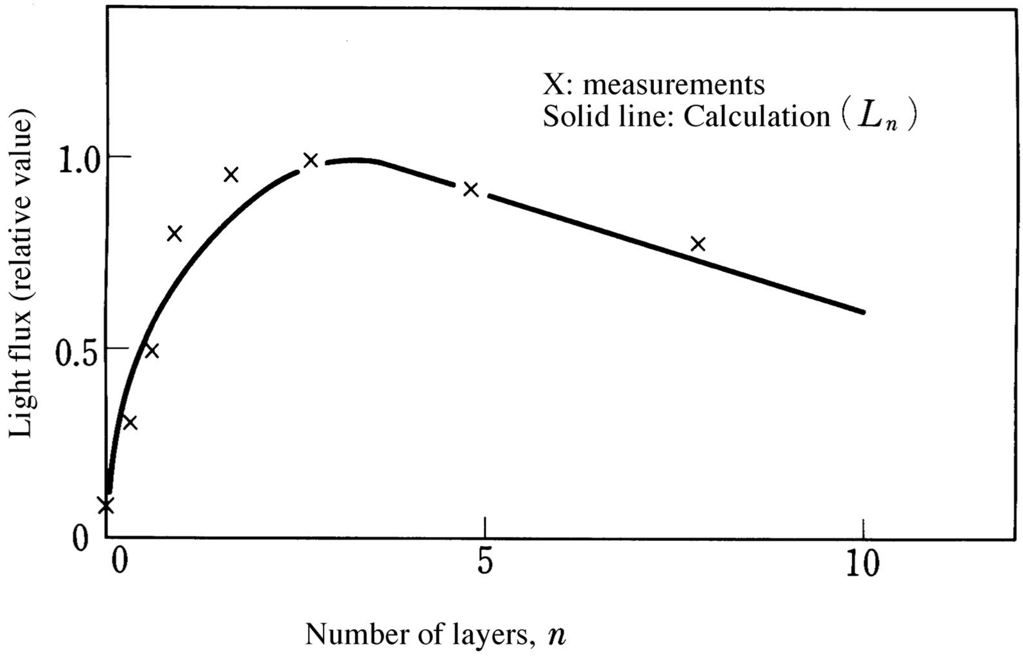

Figure 11 Relation between the number of layers and light flux. (From Tomonaga, A., Sueyasu, T., and Komine, Y., *Mitsubishi Denki Giho*, 46, 416, 1972 (in Japanese). With permission.)

$\mu l_0 = 0.561$; values of L_{pn} are shown in Table 5 as well as those for the light flux, L_n $(= L_{pn} + L_{hn})$, plotted in Figure 11. Figure 11 shows measured values for comparison. The figure reveals that the measurement and calculation agree almost completely for $n \geqq 3$, whereas they do not agree very well for $n \leqq 2$. Particularly for $1 \leqq n \leqq 2$, the measurements are larger than the calculated values. The numbers of layers giving the maximum light flux are 2.2 for the experimental and 3.0 for the calculated values. The most probable reasons for these discrepancies are:

1. The values of the absorption coefficient, s, and t were calculated using approximate equations.
2. There may be a difference in the thickness of the phosphor layer within the lamp.
3. Pores within the phosphor layer composed of phosphor particles were disregarded.
4. Real phosphor powder does not have a uniform particle size. However, the theory omits the distribution of particle sizes.

Despite these problems, Johnson's theory, which employs easily conceivable parameters such as particle diameter, number of layers, and absorption coefficient, is an effective method for analyzing the phosphor thickness of fluorescent lamps.

References

1. Kawakami, M., *Kisodenkikairo (Basic Electrical Circuit)*, Koronasha, 1960 (in Japanese).
2. Tomonaga, A., Sueyasu, T., and Komine, Y., *Mitsubishi Denki Giho*, 46, 416, 1972 (in Japanese).
3. Johnson, P.D., *J. Opt. Soc. Am.*, 42, 978, 1952.
4. Bo, H. and Takeyama, S., *J. Illum. Eng. Inst. Japan*, 44, 227, 1960 (in Japanese).
5. Ouweltjes, J.L., *Electrizitas Verwertung*, 11, 12, 1958.

chapter sixteen — section three

Optical properties of powder layers

Koichi Urabe

Contents

16.3 Monte Carlo method....949
  16.3.1 Features of the Monte Carlo method 949
  16.3.2 Monte Carlo simulations for phosphor screens 949
    16.3.2.1 Particle layer model....950
    16.3.2.2 Continuum model....954
  16.3.3 Further problems 957
References....957

16.3 Monte Carlo method

16.3.1 Features of the Monte Carlo method

Problems of light scattering and absorption in powder layers are easily handled by two-flux methods based on Kubelka-Munk's theory or Johnson's theory when the path of light can be reduced to one dimension. Calculations for powder screens with a complicated structure, however, or those for the resolution of simple and uniform screens require a method that explicitly uses tilted light rays. For example, it is difficult to use a two-flux method to find out how much emitted light is absorbed by each component in the phosphor screen of a color picture tube like that shown in Figure 12. A six-flux method[1–4] or a many-flux method[5] is expected to give better results in some cases, but such methods are still not adequate for these types of practical problems.

Several authors have used Monte Carlo methods to represent the angular dependence of light intensities.[6–9] A Monte Carlo method is a mathematical method explicitly utilizing random numbers and is applicable to any problems that can be formulated probabilistically. This method is also compatible with various boundary conditions, and it seems that there is no simpler method meeting the above requirement.

16.3.2 Monte Carlo simulations for phosphor screens

Soules[6] studied the light scattering of powder layers composed of spherical or randomly shaped particles. By using a Monte Carlo method, scattering parameters to simulate the angular distribution of reflected and transmitted light were obtained. This seems to be

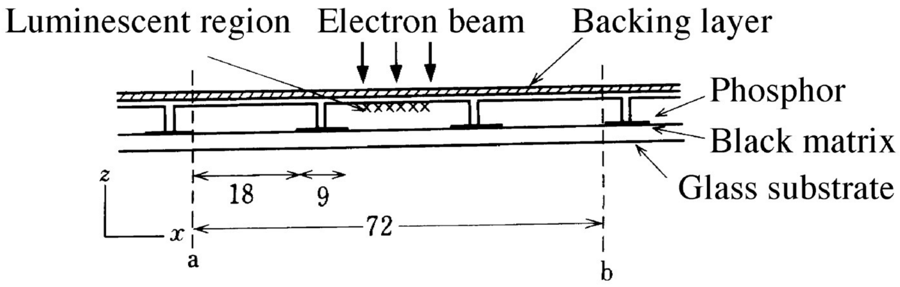

Figure 12 Cross-section of the phosphor screen of a color picture tube. Calculations were carried out for the region between a and b. (From Urabe, K., *Jpn. J. Appl. Phys.*, 19, 885, 1980. With permission.)

the first application of a Monte Carlo method to powder screens, although such methods had been used previously to evaluate light scattering in clouds,[10] oceans,[11] and emulsion films.[12]

Here, the phosphor screen model shown in Figure 12 provides an example. Various quantities, from excitation to final light output, that are suitable for analysis by the Monte Carlo technique are as follows:

- Incident point of an excitation beam at the screen surface, that is, selection of the excitation beam.
- Direction of a beam scattered at a screen component (backing layer, particle, black matrix, or glass substrate).
- Energy absorbed by a small part of a particle: its location in the particle.
- Energy absorbed at the surfaces of glass substrate, black matrix, and backing layer.
- Direction, polarization, and intensity of a light ray emitted from a small portion of a particle.
- Fraction of the emission that is absorbed in the particle.
- Direction and intensity of a ray scattered at the inner surface of the particle: location of scattering site.
- Absorption at various components on which the emitted ray falls.
- Intensity and angle of light scattered at the surface of each component.

As the result of the calculation, the intensities and directions of light emitted outward from the screen can be obtained as functions of position on the screen surface.

Two types of screen models are considered here. One, the particle layer model, uses a screen composed of individual particles and other entities. This model is suitable for thin screens and screens with complicated structures. The other, the continuum model, uses as a screen a three-dimensional continuum with absorption and scattering parameters characterizing constituent particles. This is a statistical approach and is used to model thick layers.

16.3.2.1 *Particle layer model*

Model of a phosphor screen. Urabe[7] used a phosphor screen model like that shown in Figure 12. The screen consists of spherical phosphor particles arranged in stripe patterns. Two types of particle arrangements (Figure 13(a) and (b)) were studied: (a) a regular arrangement of particles of the same size, and (b) an irregular arrangement of particles of three sizes. These arrangements are repeated in the *y*-direction, and the unit of length is the diameter of the sphere in Figure 13(a).

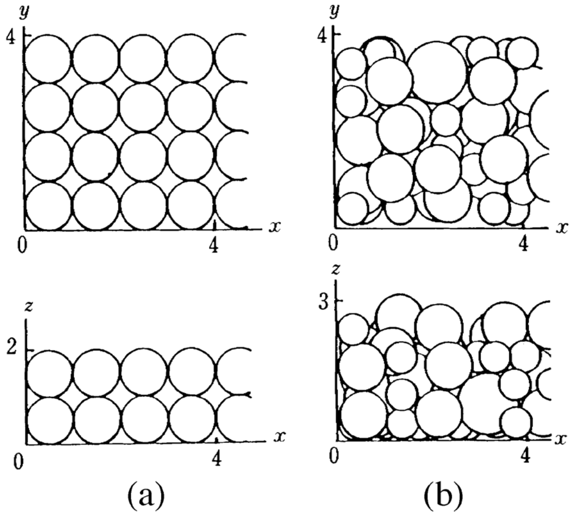

Figure 13 Packing of particles in the screen: (a) Regular packing of spheres with the same diameter: 1. (b) Irregular packing of spheres with three different diameters: 0.7, 1.0, and 1.3. Screen weights are the same in (a) and (b). (From Urabe, K., *Jpn. J. Appl. Phys.*, 19, 885, 1980. With permission.)

Principles of calculation. Rays from excited phosphor particles are traced by geometrical optics until they are absorbed in the screen or escape from the screen. It is assumed that when a ray hits a surface, only one event—reflection, refraction, or absorption—occurs. The intensity of a ray remains constant unless it is absorbed. The flow chart of the calculation is shown in Figure 14. Other assumptions simplifying the calculation are as follows:

- The electron beam passing through the backing layer irradiates the particles, the substrate glass, or the black matrix. The beam power is completely absorbed there; scattering and penetration of the beam are not considered.
- The luminescence intensity of each particle is proportional to the power it absorbs. Emitted light is unpolarized and is normal to the surface of the excited particle. The angular distribution of its intensity is uniform.
- Reflection of light at the surfaces of the backing layer, glass substrate, and black matrix is specular, and reflectivities are independent of the incident angle of the light. Absorption in the glass is not considered.
- A constant fraction of the light incident on a particle is absorbed at the surface but is not absorbed inside the particle. The reflection and refraction of the residual light at the particle surface are given by Fresnel's law. Four internal reflections are taken into account in the calculation.

Application of the Monte Carlo method. Random numbers R_i (i = 1, 2, …) uniformly distributed between 0 and 1 determine the following items:

1. Direction of rays emitted with a uniform angular distribution: the direction (θ,ϕ) of a ray is calculated from two random numbers R_1 and R_2 as:

$$\theta = \cos^{-1}\left(1-2R_1\right) \tag{100}$$

$$\phi = 2\pi R_2 \tag{101}$$

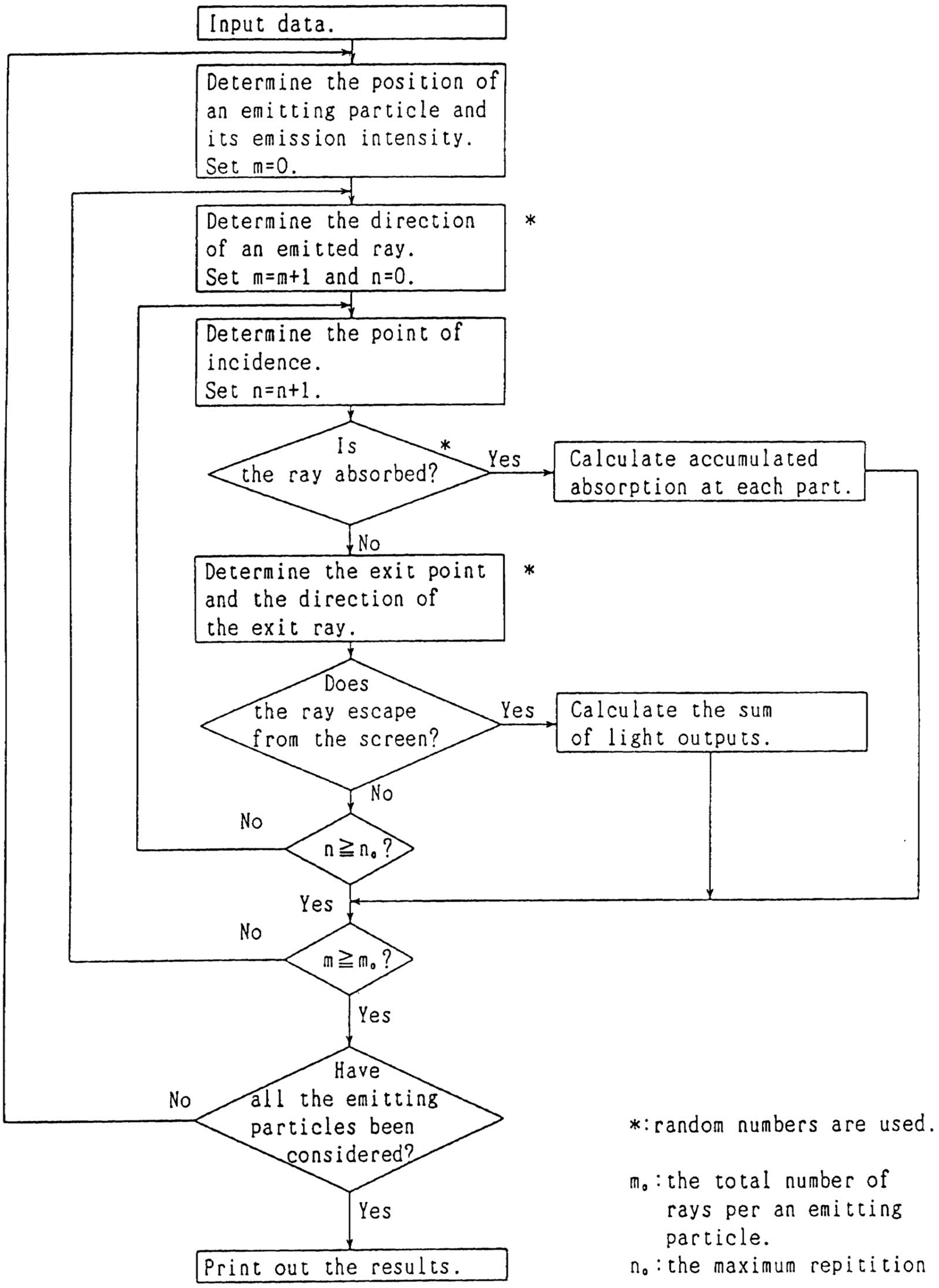
Input data.
Determine the position of an emitting particle and its emission intensity. Set m=0.
Determine the direction of an emitted ray. Set m=m+1 and n=0.
*
Determine the point of incidence. Set n=n+1.
Is the ray absorbed?
*
Yes
Calculate accumulated absorption at each part.
No
Determine the exit point and the direction of the exit ray.
*
Does the ray escape from the screen?
Yes
Calculate the sum of light outputs.
No
No
n≧n₀?
Yes
No
m≧m₀?
Yes
No
Have all the emitting particles been considered?
Yes
Print out the results.
*:random numbers are used.
m₀:the total number of rays per an emitting particle.
n₀:the maximum repitition

Figure 14 Flow chart of the calculations. (From Urabe, K., *Jpn. J. Appl. Phys.*, 19, 885, 1980. With permission.)

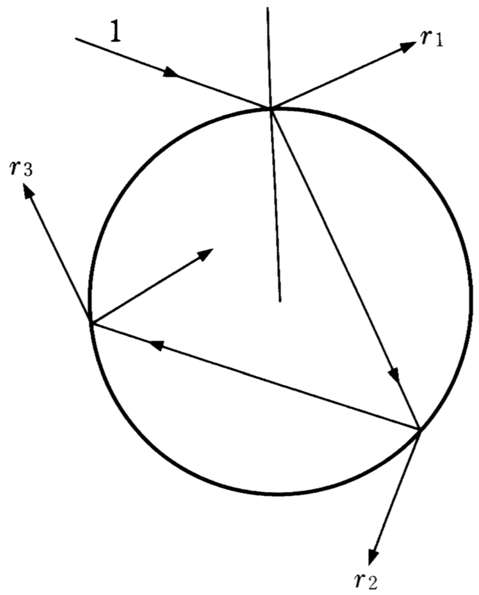

Figure 15 Light reflection and refraction at a particle surface. (From Urabe, K., *Jpn. J. Appl. Phys.*, 19, 885, 1980. With permission.)

2. Selection of events: which process, i.e., absorption, reflection, or refraction, occurs when a ray falls on a surface is also determined by random numbers.

A ray is completely absorbed at the incident point if a random number R_3 is smaller than the absorption ratio k. For the backing layer and black matrix, k = (1 – reflectivity) and a nonabsorbed ray is reflected. At the glass substrate, a ray is reflected when R_4 ð reflectivity; otherwise, it is transmitted. A ray that hits a particle surface and is not absorbed at the incident point suffers an i number (i = 1, …, m; here, m is taken to be 6) of reflections and/or refractions at the outer or inner surface before leaving the particle (Figure 15). The intensity r_i of this departing ray, with initial intensity 1, is calculated by Fresnel's formula and is interpreted as the escape probability. The point on the surface and the direction of the escaping beam are obtained geometrically. The number i is determined by a random number R_5 as:

$$\sum_{j=0}^{i-1} r_j/R < R_5 \le \sum_{j=0}^{i} r_j/R \tag{102}$$

where

$$r_0 = 0, \qquad R = r_1 + r_2 + \ldots + r_m$$

Results of calculation. The luminescent light output from the screen and the quantities absorbed by various components are obtained in relation to the position of the emitting particle. Figures 16 and 17 show the fractions of light emitted to the outside or absorbed by various screen components when the phosphor particles are packed regularly.

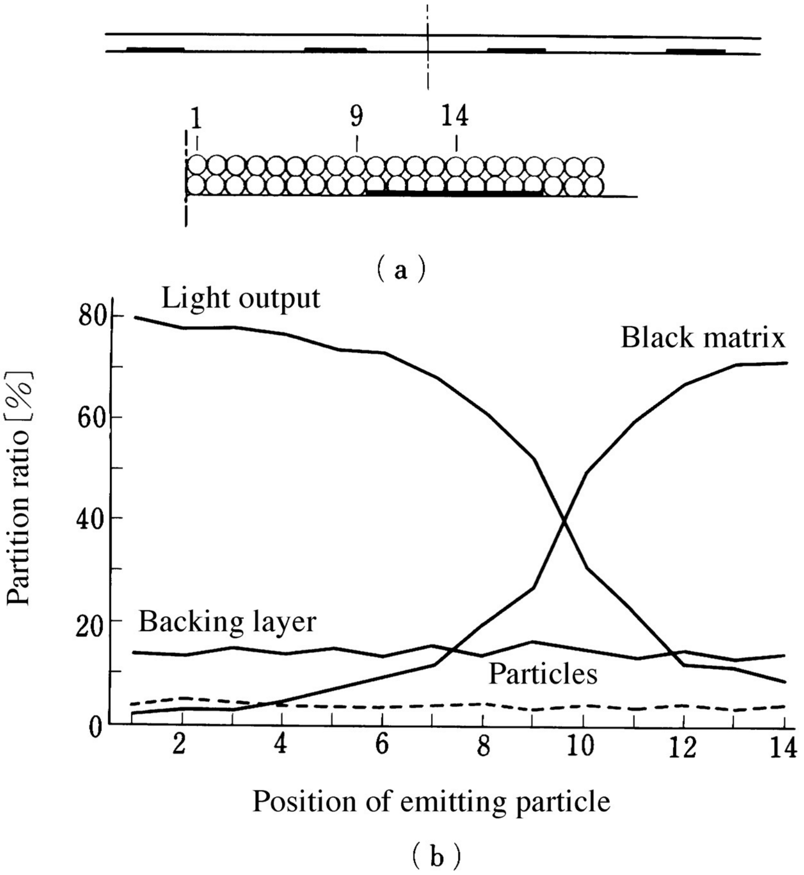

Figure 16 (a) Crosssection of fully coated phosphor screen. (b) Partition ratios of luminescent emission from a phosphor particle in model (a). (From Urabe, K., *Jpn. J. Appl. Phys.*, 19, 885, 1980. With permission.)

Any required information can be obtained by these types of calculations using the appropriate parametric values. Figure 18, for example, shows the partitioning of the total emission and the relative brightness as functions of the width of the emitting region, and Table 6 lists the partition ratios of the total emission for regular and irregular packing arrangements.

16.3.2.2 Continuum model

Soules and Klatt[8] studied the optical properties of powder coatings with spherical particles and of those with polyhedral particles. The former case is described here to show how the Monte Carlo method is applied. For a sphere of diameter d and a relative index of refraction $n = n_r - n_i i$, the scattering intensities for parallel and perpendicular polarization, $I_p(\theta)$ and $I_s(\theta)$, are calculated by the Mie theory for 181 values of the angle θ. The scattering cross-section efficiency Q_{sca} and extinction cross-section efficiency Q_{ext} are also calculated. The distance to the first scattering event is chosen as:

$$s = -\left(Q_{sca}/N\right)\ln\left(R_1\right) \tag{103}$$

where N is the average number of particle layers and R_i is a random number between 0 and 1. The angles θ and ω of the scattered ray are determined by two other random numbers:

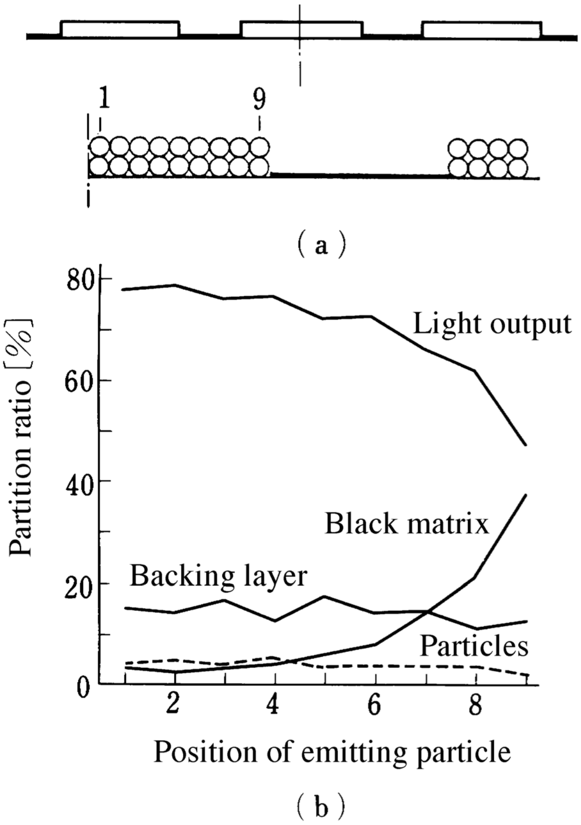

Figure 17 (a) Cross-section of a partially coated phosphor screen. (b) Partition ratios of luminescent emission from a phosphor particle in model (a). (From Urabe, K., *Jpn. J. Appl. Phys.*, 19, 885, 1980. With permission.)

$$\omega = 2\pi\left(R_2\right) \tag{104}$$

$$R_3 = \sum_{0}^{\theta}\left(f_p I_p(\theta) + f_s I_s(\theta)\right) \Big/ \sum_{0}^{180}\left(f_p I_p(\theta) + f_s I_s(\theta)\right) \tag{105}$$

The intensity of the scattered ray is attenuated by Q_{sca}/Q_{ext}, and the polarization of the scattered radiation in the plane of scattering is determined by the ratio I_p/I_s times the fraction of the incident polarization intensities f_p and f_s. The distance to the next scattering event is determined by another random number, and the ray is followed until it leaves the boundary of the coating or is attenuated to 0.0001 of its original intensity. The light absorption of various phosphor coatings is obtained in this way. Soules and Klatt[8] proposed a relation between the absorption coefficient of ultraviolet light and the optimum particle size of phosphors for a fluorescent lamp; they also used the Monte Carlo technique for particles with size distributions.

Busselt and Raue[9] used a continuum model for a uniform phosphor screen of a cathode-ray tube. The electron beam generates photons in the powder layer near the Al film and electron scattering in the powder is ignored. A generated photon is deemed to be a particle and to make a random walk (i.e., to move in steps whose lengths and

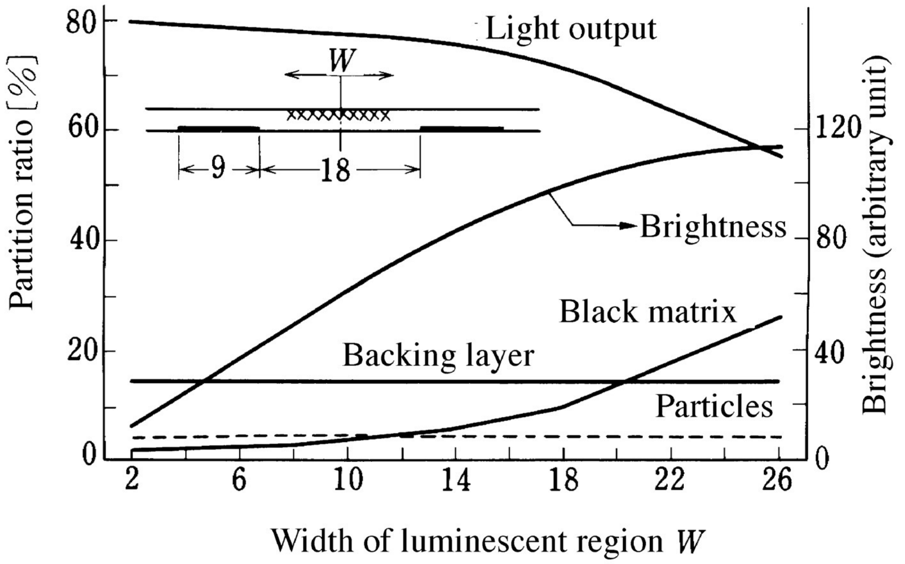

Figure 18 Dependence of partition ratios of total luminescent emission and of brightness on the width of the luminescence region. The unit of the abscissa is particle diameter and the packing of the phosphor screen is as in Figure 16. (From Urabe, K., *Jpn. J. Appl. Phys.*, 19, 885, 1980. With permission.)

Table 6 Partition Ratios for Two Packing Modes

	Partition ratio (%)			
Packing of particles	Light output	Backing layer	Black matrix	Particles
(a)	69.9	14.5	11.4	3.8
(b)	70.1	13.2	13.7	3.0

From Urabe, K., *Jpn. J. Appl. Phys.*, 19, 885, 1980. With permission.

directions are random). A Monte Carlo technique is used in the ray tracing to determine an absorption length, x, according to the probability distribution $p(x) = A^{-1}\exp(-x/A)$, where A is the absorption coefficient. A scattering length, y, is similarly determined according to the probability distribution $p(y) = S^{-1}\exp(-y/S)$, where S is the scattering coefficient. The absorption and the total scattering lengths (i.e., the sum of all previous scattering lengths) are compared after each scattering event, and the photon is assumed to be absorbed if the total scattering length is greater than or equal to the absorption length. A photon hitting the Al film is reflected or absorbed according to the reflectance of the Al film. A new scattering length and a new direction of the photon are chosen subsequent to each scattering event, and the angular distribution is assumed to be isotropic. This procedure is repeated until the photon is absorbed or escapes from the phosphor layer. An escaped photon is classified according to its position and angle of emergence. The screen efficiency, the angular distribution of photons leaving the screen, and the line spread function are obtained from these calculations. On the basis of these calculations and the results of measuring brightness and resolution of the screen experimentally, Busselt and Raue proposed a relation between the optimum screen weight and the brightness and a relation between the maximum layer thickness and the resolution.

16.3.3 Further problems

The following problems are left to be studied using Monte Carlo methods:

1. Calculation of scattering and absorption of excitation beams in a phosphor particle.
2. Calculation of the position on a spherical particle surface from which luminescent light is emitted and of the direction and intensity of the emitted light.

Several parameters need to be introduced to represent shapes other than spheres and to represent irregular or rough surface conditions.

Some additional work has been carried in this area. A Monte Carlo based simulation of the effects of coating on phosphor particles showed, for example, that thick coatings could increase the absorptivity of the phosphors. Comparison of this modeling to reflectance data on Eu^{3+}-activated yttria allowed the extraction of an absorption coefficient and allowed the simulations to make contact with a simplified Kebulka–Munk relationship.[13]

References

1. Chu, C.M. and Churchill, S.W., *J. Phys. Chem.*, 59, 855, 1955.
2. Emslie, A.G. and Aronson, J.R., *Appl. Opt.*, 12, 2563, 1973.
3. Meador, W.E. and Weaver, W.R., *Appl. Opt.*, 15, 3155, 1976.
4. Egan, W.G. and Hilgeman, T., *Appl. Opt.*, 17, 245, 1978.
5. Mudgett, P.S. and Richard, L.W., *Appl. Opt.*, 10, 1485, 1971.
6. Soules, T.F., *Electrochem. Soc. Extended Abstracts*, 74-1, 311, 1974.
7. Urabe, K., *Jpn. J. Appl. Phys.*, 19, 885, 1980.
8. Soules, T.F. and Klatt, W.A., *J. Illum. Eng. Soc.*, 17, 92, 1988.
9. Busselt, W. and Raue, R., *J. Electrochem. Soc.*, 135, 764, 1988.
10. Plass, G.N. and Kattawar, G.W., *Appl. Opt.*, 7, 415, 1968.
11. Gordon, H.R. and Brown, O.B., *Appl. Opt.*, 12, 1549, 1973.
12. DePalma, J.J. and Gasper, J., *Photgr. Sci. Eng.*, 16, 181, 1972.
13. Ling, M. and Soules, T.F., *Electrochem. Soc. Extended Abstracts*, 86, 1038, 1988.

chapter seventeen — section one–seven

Color vision

Kohei Narisada and Sueko Kanaya

Contents

17.1 Color vision and the eye 960
  17.1.1 Retina 960
  17.1.2 Spectral sensitivity of the eye 961
17.2 Light and color 962
  17.2.1 Psychophysical colors 962
  17.2.2 Perceived colors....963
17.3 Models of color vision 963
17.4 Specification of colors and the color systems....965
  17.4.1 Specification of the psychophysical colors 965
    17.4.1.1 CIE colorimetric system 966
    17.4.1.2 CIE UCS colorimetric system....969
    17.4.1.3 ULCS colorimetric system 970
  17.4.2 Specification of perceived colors....972
    17.4.2.1 Munsell color system 972
    17.4.2.2 NCS 972
17.5 The color of light and color temperature....972
  17.5.1 Chromatic adaptation and colors of light sources 972
  17.5.2 Color temperature....973
  17.5.3 Mired (micro-reciprocal degree)....973
17.6 Color rendering 974
  17.6.1 Methods of measurement....974
  17.6.2 Color rendering index....975
    17.6.2.1 General color rendering index (R_a)....975
    17.6.2.2 Special color rendering indices....975
  17.6.3 General color rendering index and perceived colors 975
  17.6.4 Color appearance of light sources and perceived colors 976
  17.6.5 Color rendering and brightness 976
17.7 Other chromatic phenomena....976
  17.7.1 Purkinje phenomenon....976
  17.7.2 Metamerism 977
  17.7.3 Bezold-Brucke effect 977
  17.7.4 Helmholz-Kouroshe effect....977
References....977

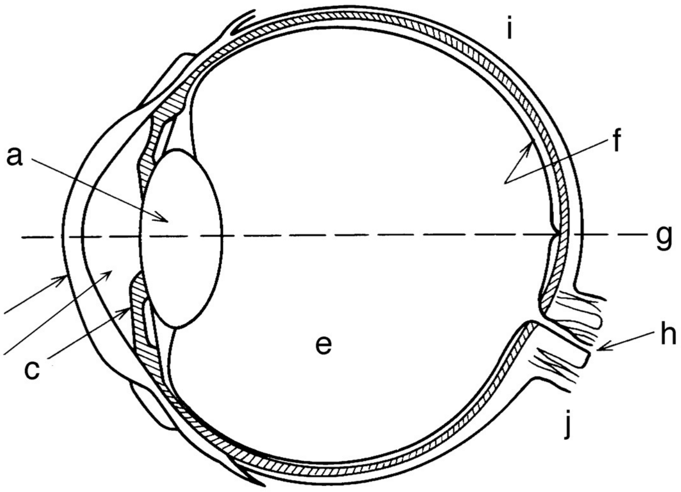

Figure 1 Schematic of the horizontal cross-section of the human eye. a: lens, b: cornea, c: iris, d: aqueous humor, e: vitreous humor, f: retina, g: visual axis, h: optic nerve, i: ear side, j: nose side.

Human eyes have two fundamental visual functions: to perceive brightness and to detect color.[1] In this chapter, the physiological mechanism of color vision and the basis for the specification of colors will be outlined. Some associated psychological phenomena will also be briefly described.

17.1 Color vision and the eye

The organ of human vision consists of the eyeball, the visual center of the brain, and the optic nerves connecting the two. As schematically shown in Figure 1, the eyeball is an optical system consisting of the cornea, aqueous humor, iris, crystalline lens, vitreous humor, and the retina. By means of refraction, the cornea and the crystalline lens focus an upside-down optical image of the outer world within the field of vision on the retina. Optical signals corresponding to the optical image on the retina are transformed into neural signals and sent through the optic nerves to the visual center of the brain.

17.1.1 Retina

The retina is a light-sensitive organ made up of an extremely large number of optic receptors connected to each other by a sophisticated neural network. There are two types of the receptors having different shapes and physiological functions. The light-sensitive portion of the first receptor has a relatively short and thick shape (Figure 2(a)), while the other type has a slender and thin shape (Figure 2(b)). From these shapes, the former are called cones and the latter rods. There are three kinds of cones, each of which is sensitive to the optical radiation in different wavelength ranges, i.e., red (R), green (G), and blue (B) ranges. These three kinds of cones are distributed over the entire retina, except in the fovea where almost no blue- sensitive cones exist with an angular extent of about 2°. The fovea, on the other hand, has rods that are all the same and are not sensitive to different colors; consequently, rods have no function in perceiving colors.

The sensitivity of the cones to optical radiation is relatively low in comparison with that of the rods. The cones are fully active when there is a field of view with a

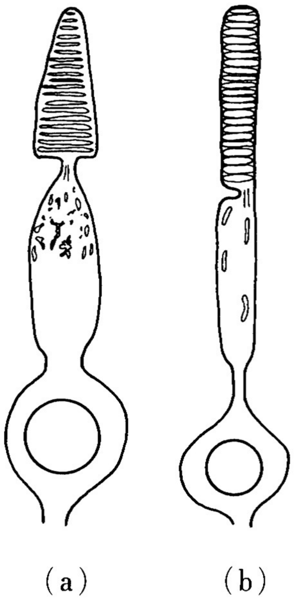

Figure 2 Sketch of two types of visual receptor cells: (a) cone receptor; (b) rod receptor.

luminance higher than about 1 cd m^{-2}. The rods, on the other hand, have a higher sensitivity and are fully active in dark environments, having luminance of less than ~0.01 cd m^{-2}. The visual condition in bright environments with luminances of about 1 cd m^{-2}, under which only the cones are active, is called *photopic vision*. The opposite condition in dark environments with luminance less than 0.01 cd m^{-2}, where only the rods are active, is called *scotopic vision*. Intermediate conditions, where the luminance range in the field of view is between 0.01 and 1 cd m^{-2}, and where the cones as well as the rods are partially active, is called *mesopic vision*. The roles of the two types of receptors—the cones and the rods—vary gradually as the luminance level in the field of view changes.

17.1.2 Spectral sensitivity of the eye

The spectral sensitivity of the eye is not solely determined by that of the retina. The spectral transmission characteristics of the optical components of the eye (i.e., cornea, crystalline lens, and humors) also play some role. As a whole, the eye is sensitive to optical radiation with a wavelength between 380 and 760 nm when it is incident on the eyeball through the cornea. The sensitivity over this wavelength range, however, is not constant and has specific spectral characteristics. This spectral dependence is called the spectral luminous efficiency function of the eye.

The eye has two different spectral luminous efficiency functions corresponding to the cones or the rods. These two sensitivity curves are shown in Figure 3 as a function of the wavelength, and are similar in shape but have different peak wavelengths. Strictly speaking, the eye of each individual has a different spectral luminous efficiency function depending on such factors as age, etc. To deal with the light quantitatively, however, the international standard visual spectral efficiency curves were established by the CIE (Commission Internationale de l'Eclairage) and the ISO (International Standardization Organization) and are used for photopic vision $V(\lambda)$ and scotopic vision $V'(\lambda)$, respectively,[1] as

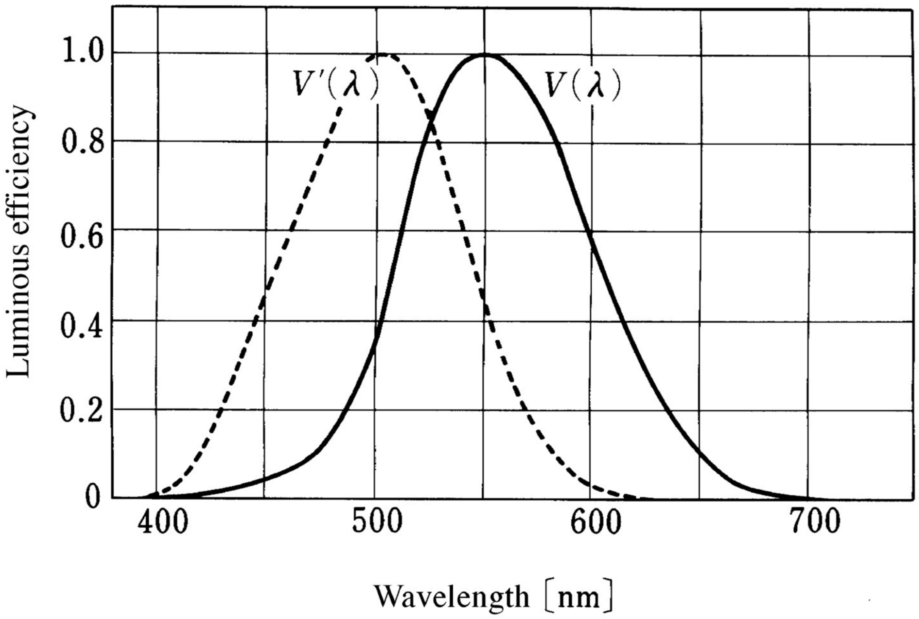

Figure 3 Standard visual spectral efficiency curves, photopic vision V(λ), and scotopic vision V′(λ). From CIE, *The Basis of Physical Photometry,* CIE Publication No. 18.2, 1983. With permission.)

shown in Figure 3. The two standard visual spectral efficiency curves in the figure are given relative to the maximum value of 1 at the wavelength of peak sensitivity. The absolute maximum value of the luminous efficiency at the peak wavelength of 555 nm is 683 lm W^{-1} for photopic vision V(λ) and 1700 lm W^{-1} at 507 nm for scotopic vision V′(λ). The mesopic vision is thought to have intermediate spectral sensitivity characteristics. Presently, no definite standard has been established for mesopic vision, since, as mentioned previously, it varies gradually as the luminance changes.

Photometric quantities such as the luminous intensity (cd), the luminous flux (lm), the illuminance (lx), and the luminance (cd m^{-2}), etc. are derived after integrating the energy of the optical radiation at different wavelengths over the standard spectral efficiency function for photopic vision.

17.2 Light and color

As previously stated, the eye is sensitive to optical radiation with a wavelength range between 380 and 760 nm. Optical radiation within this wavelength range is called visible light. The eye perceives different colors for different wavelengths. Colors with a single wavelength or those with a narrow range of different wavelengths are called pure colors or monochromatic. The visual sensation for perceived colors is a composite of the sensations for the different pure colors that make up the color. Colors are divided into two categories: phychophysical and perceived colors.

17.2.1 Psychophysical colors

The psychophysical colors are those that can be treated and measured in terms of the chromatic response of the eye to pure colors of different wavelengths. The response is derived by psychophysical color matching experiments to be described below.

17.2.2 Perceived colors

The perceived colors are those subjectively perceived by the eye. These colors cannot be measured quantitatively. To specify a perceived color, visual comparisons are made to find a match to the color among a series of specific color samples arranged visually in a graded scale. The perceived colors are divided further into three subcategories: object, luminous, and aperture colors.

The object colors are those belonging to the object. They are classified by the principal hue, the lightness, and the chroma of the colors. The light source or luminous colors are those of produced by light emitting-objects. Finally, the aperture colors are those of a lighted surface as seen through a small aperture. The human eye perceives the same colors differently according to various environmental, physiological, and psychological conditions.

17.3 Models of color vision

It is thought that human beings have had the same color vision for thousands of years. It is found that primitive pictures of natural objects discovered in a number of archaeological ruins, some tens of thousand years old, were painted in colors somewhat similar to those observed at present. In the earlier stages of human history, such as the periods of ancient Egypt or Sumer, people already were interested in colors and color perception. Since then, various ideas on color and color perception have been advanced; among these are works by Leonardo da Vinci[2] in 1651 and Newton[3] in 1704.

The first theory directly connected to modern theories on color perception or color vision was presented by Young in 1802.[4] This theory was extended by Helmholtz[5] in 1852. Today, their theories have been combined and are jointly called the Young-Helmholtz's trichromatic theory. This theory gave an explanation for the perception of mixed colors. It could not explain, however, some phenomena concerning the perception of colors and chromatic functions of defective color vision. One of the problems that could not be explained was why yellow appears as one of the primary colors among various perceptible colors, and why the four primary colors are made up of two sets of opposite colors, red-green and blue-yellow. For this reason, a number of ideas opposing the trichromatic theory were proposed. These opposite colors are called opponent colors. Hering[6] addressed the phenomenon concerning the opponent colors in 1875. He pointed out that colors were perceived as a mixture of each of the opponent colors of these two sets. On the basis of this idea, a model for color vision called the opponent color theory was proposed.

The trichromatic theory and the opponent color theory contain sharply contrasting ideas on this matter. Later in 1896, Müller et al.[7] assumed that the three kinds of receptors, each responding to one of the three primary colors, act in the way the trichromatic theory predicts. In the neural network of the retina, however, three different neural signals are activated by the three types of optic receptors, but are processed and transformed as two sets of opponent color signals, consistent with the opponent color theory. This was the beginning of the zone theory.

From the model by Müller, Walraven, and Bouman[8] proposed in 1966, a schematic model explaining the zone theory for color vision. Later, in 1980, the model was slightly modified by Ikeda,[9] as shown in Figure 4. Though the theory has not yet been proven conclusively, in the following with reference to the figure, the likely process for color vision is explained in a simplified way (for further details, the original publications should be referred to). In Figure 4, boxes represent hypothetical components of the neural system, which can add or subtract input signals and send their outcomes to the next stages. Lines

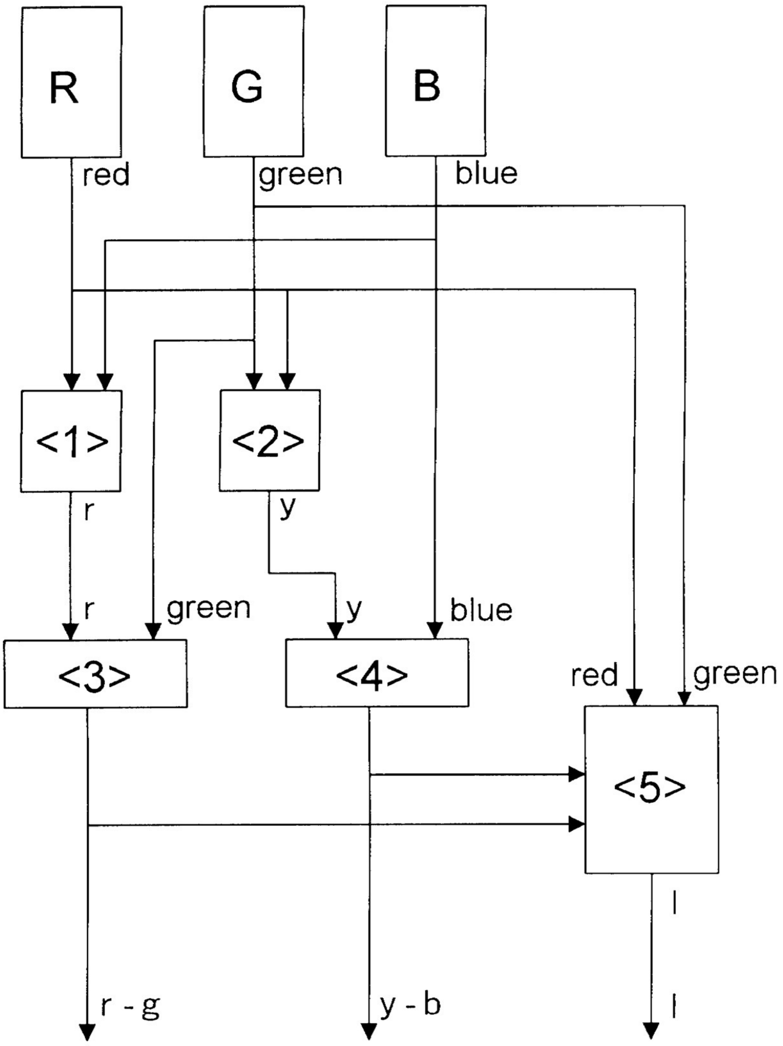

Figure 4 A model for color vision. (From Ikeda, M., *Fundamentals of Colour Engineering*, Asakura Bookstore, 1980, 244-245. With permission.)

with arrows show the direction of flow of the neural signals. Three boxes, R, G, and B on top of the diagram, represent three types of cones, each sensitive to one of the three primary colors—red, green, and blue, respectively. If the cones, as a group, are stimulated by a color, each of the three cones generates a neural signal proportional to the primary colors contained in the color stimulus.

Among the three neural signals, the red and green signals are sent to <5> and added to each other. The signal I is sent to the brain. Precisely speaking, signals from rods under mesopic or scotopic conditions are also sent to <5> to register as the brightness signal I. At this stage, the blue signal from cone B is not sent to this channel, since it contains only a color signal, but no brightness signal.

The signals red and blue from R and B, respectively, are added in <1> and a signal r, corresponding to real red (a temporary expression), is created. Similarly, in <2>, the signals green and blue from G and B, respectively, are mixed and a signal y, corresponding to yellow, is formed. The intensity of the two signals green and r from <1> are compared in <3> and only the stronger signal is sent to the brain. Such a comparison of the two signals produces the so-called opponent signal expressed as r-g. In this case, either the r (real red) or the green signal only is sent to the brain.

In the same way, the intensities of the two signals y (yellow) from <2> and blue from B are compared to form the opponent signal y-b. Again, the stronger of the two will be sent to the brain. Consequently, the eye sends to the brain a brightness signal and two color signals composed of one of the components of the opponent colors.

It is interesting to note (see the figure) that the two opponent signals r-g and y-b flow into <5> and contribute to the brightness channel. Since no opponent signal concerning color will be sent to the brain when the eye sees a white object, the brightness detected is influenced by the color of the object.

In the experimental process through which the standard luminous efficiency functions shown in Figure 3 were derived, however, the contribution of chromatic signals to the brightness has not been incorporated. For this reason, even if the same luminance value is obtained through the function for a colored and a non-colored object, the perceived brightness of the two objects is not necessarily the same. The matter is still the subject of active discussion among color scientists.[10]

17.4 *Specification of colors and the color systems*

Color is quantitatively specified by color systems. Color systems are divided into two categories. The first specifies psychophysical colors while the second deals with perceived colors.

Psychophysical colors are specified by the principle of additive mixture of stimuli of the three primary colors. As mentioned previously, colors are composed of primary colors, and their mixing ratios determine the colors. This means that a color can be specified with a mixing ratio of two of the three primary colors; since the sum of the primary color must always be 100%, the specification of the mixing ratio of two automatically determines the remaining primary color. A representative system is the CIE color system, which specifies colors by two coordinates (equivalent to the designation of the mixing ratio of two primary colors) on a chromaticity diagram. This is discussed 17.4.1.1. The position of a color in the diagram is called the chromaticity point of the color.

Systems that specify the perceived colors, on the other hand, classify and scale many colors systematically according to their sensual attributes, such as hue, lightness, and chroma. Two color systems, the Munsell Color System and the NCS (Natural Color System), are in current use.

17.4.1 *Specification of the psychophysical colors*

Psychophysical colors are specified by three systems: the CIE, the CIE UCS (Uniform Chromaticity Scale), and the CIE ULCS (Uniform Lightness Chromaticness Scale) colorimetric systems. Each system specifies colors using the coordinates of a chromaticity diagram to be described later. The UCS colorimetric system evolved from the CIE system. In the UCS, the distance between two chromaticity points on the chromaticity diagram corresponds to the sensation of perceived color difference. The color difference on the UCS colorimetric coordinates, however, does not correspond to the difference in perceived colors if the lightness of the two colors differs. The ULCS colorimetric system was then introduced to compensate for the difference in the lightness of the colors. A number of programs to be used in personal computers have been developed for calculations associated with the use of these color systems.

17.4.1.1 CIE colorimetric system

The CIE colorimetric system was established by the CIE in 1931. This system consists of the RGB and the XYZ colorimetric systems. The XYZ system, which will also be explained below, was laid down as an extension of the RGB system for practical applications.

The RGB system was derived from results of psychophysical experiments. In the experiments, the observers viewed a circular field with an angular diameter of 2°. (The angular diameter is the angle of arc subtended by the circular field at the eye.) The circular field consisted of two identical half circles adjacently located on the right and left. The color of the two half circles was independently variable. One of the two half circles was used as the reference field and another was used as the test field.

Colors of the reference field were called the reference colors and those of the test field were called the test colors. The reference colors were expressed by monochromatic light of the same intensity at various wavelengths over the entire visible range. The test colors, on the other hand, were composed with a mixture of the three primary colors, red (700 nm), green (546.1 nm), and blue (453.8 nm). The numbers in parentheses show the wavelengths of the respective primary colors.

By varying the mixing ratio of the three primary colors, the observers varied the colors of the test field. In this way, the color of the test field was made to match that of the adjacent reference field. During the observations, it was found that in some wavelength ranges mixtures of the three primary colors could not match the reference colors. In these wavelength ranges, matches were established if an amount of one of the three primary colors was added to the monochromatic reference colors.

This implies that matches can be established by subtracting one of the primary colors from the mixtures. In other words, there are some wavelength ranges where the stimulus of the primary colors is negative. In this way, the mixture ratio of the primary colors to match all the spectral colors over the entire visible range were obtained.

It was assumed, when a match was established, that the reciprocals of the energy ratio of each primary color of the test field corresponded to the relative strength of the stimuli of the respective primary colors at the wavelength of the reference with which the color was matched. Based on the above assumption, three spectral distribution curves of the relative strength of the stimulus for each of the three primary colors (red, green, and blue) over the entire visible range were obtained. The curves are called the spectral tristimulus values or the color matching coefficients. They are $r(\lambda)$, $g(\lambda)$, and $b(\lambda)$, respectively. λ in the parentheses is the wavelength.

Since, the sum of the three tristimulus values at each wavelength is always 100%, the mixture ratio of the three primary colors can be determined by any two of the three tristimulus values. The RGB colormetric system is based on this and all colors are indicated on the $r(\lambda)$ and $g(\lambda)$ coordinates.

To overcome difficulties associated with the negative stimulus of the primary colors, based on the above mentioned color matching experiments, three imaginary reference color stimuli [X], [Y], and [Z] were introduced. By employing the imaginary reference color stimuli, the original tristimulus values were converted mathematically into positive values and all colors could be composed by mixing (not subtracting) these three stimuli. This is the basis of the XYZ colorimetric system. Y has been chosen to correspond with the lightness stimulus. Based on the similar idea with that of the RGB colorimetric system, all colors are indicated by these coordinates.

More recently, similar color matching observations have been conducted for a larger circular field with an angular diameter of 10°. From the results obtained, a colorimetric

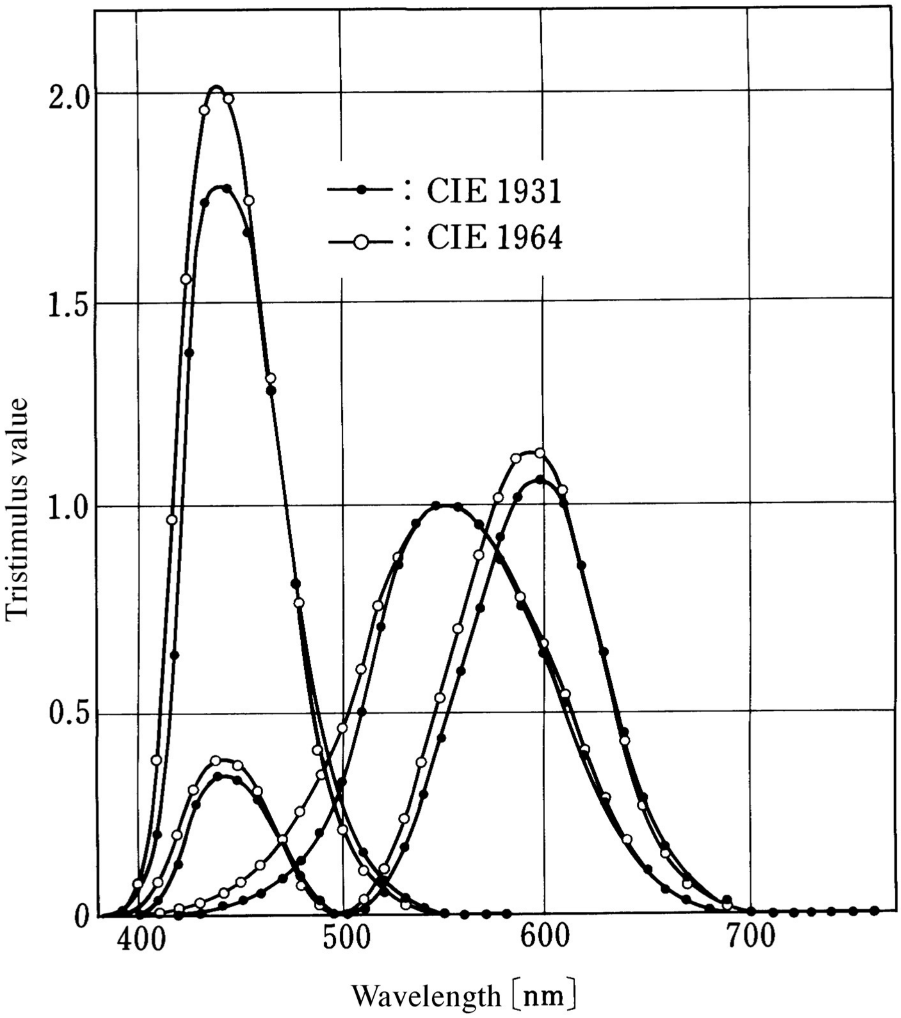

Figure 5 Curves of spectral tristimulus values. ○: CIE 1964 supplementary standard colorimetric observer; ●: CIE 1931 standard colorimetric observer. (From CIE, *Testing of Supplementary Systems of Photometry,* TC1-21, in preparation. With permission.)

system was established by the CIE in 1964. The results of these experiments are shown in Figure 5. In the figure, the curves marked with black dots show the spectral tristimulus values for the circular field of 2° established in 1931, which can be used for a field smaller than about 4°; and the curves marked with white circles are those for 10° established in 1964, which can be used for a field greater than about 4°. Each curve is used according to the size of the object field in which the color is to be specified.

Specification of light source colors. Test light source colors are specified below: the tristimulus values (X, Y, and Z) for a test light source, which has a spectral energy distribution P(λ), are calculated with the following formulae.

$$X = K\int_{380}^{780} P(\lambda)\bar{x}(\lambda)d\lambda \tag{1a}$$

$$Y = KP(\lambda)\bar{y}(\lambda)d\lambda \tag{1b}$$

$$Z = K\int_{380}^{780} P(\lambda)\bar{z}(\lambda)d\lambda \tag{1c}$$

where $$K = \frac{1}{P(\lambda)Y(\lambda)d\lambda}$$

and x(λ), y(λ), and z(λ) are the spectral stimulus values for 2°. These quantities are written as $x_{10}(\lambda)$, $y_{10}(\lambda)$, $z_{10}(\lambda)$ for 10.

The chromaticity coordinates of the color of the light sources x and y are calculated with the following formulae.

$$x = \frac{X}{X + Y + Z} \tag{2a}$$

$$y = \frac{Y}{X + Y + Z} \tag{2b}$$

The colors of light sources on the XYZ colorimetric system are specified with Y calculated with Eq. 1b and with x and y calculated with Eq. 2a, b.

Figure 6 shows the CIE chromaticity diagram in which the ISCC-NBS (Intersociety Color Council–National Bureau of Standard) color designation for every color[11] is indicated. The number beside the spectrum locus shows the wavelength of the monochromatic light. Points labeled Illuminant A and Illuminant C corresponding to color temperature of 2854K and 6774K, respectively, are shown in the central white region.

Specification of the nonluminous object colors. The tristimulus values (X, Y, and Z) of the object for which the spectral reflectance (or spectral transmittance) is ρ(λ) and τ(λ) are given by:

$$X = \frac{1}{K}\int_{380}^{780} P(\lambda)\rho(\lambda)\bar{x}(\lambda)d\lambda \tag{3a}$$

$$Y = \frac{1}{K}\int_{380}^{780} P(\lambda)\rho(\lambda)\bar{y}(\lambda)d\lambda \tag{3b}$$

$$Z = \frac{1}{K}\int_{380}^{780} P(\lambda)\rho(\lambda)\bar{z}(\lambda)d\lambda \tag{3c}$$

where $$K = \int_{380}^{780} P(\lambda)\bar{y}(\lambda)d\lambda \tag{3d}$$

P(λ) is the spectral power distribution of the light source which illuminates the object, and x(λ), y(λ), and z(λ) are the CIE spectral trichromatic stimuli for fields of 2° or 10°. The chromaticity coordinates of the color of the objects can then be calculated, as with the light sources, using Eq. 2.

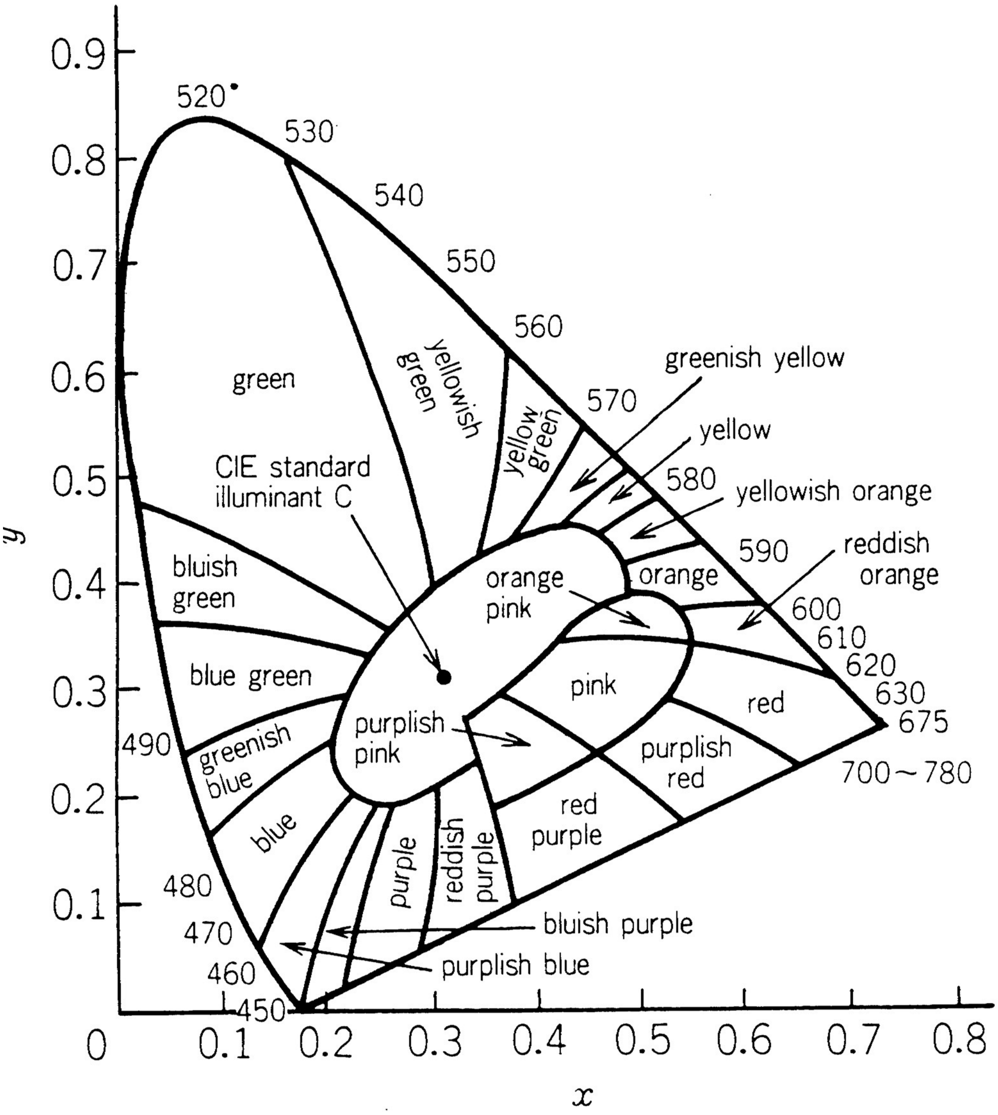

0.9
0.8
0.7
0.6
0.5
0.4
0.3
0.2
0.1
0
0.1
0.2
0.3
0.4
0.5
0.6
0.7
0.8
y
x
520
530
540
550
560
570
580
590
600
610
620
630
675
700~780
490
480
470
460
450
green
yellowish green
yellow green
greenish yellow
yellow
yellowish orange
reddish orange
orange
orange pink
CIE standard illuminant C
bluish green
blue green
greenish blue
blue
purplish pink
pink
red
purplish red
red purple
purple
reddish purple
bluish purple
purplish blue

Figure 6 CIE Chromaticity diagram. (From Kelly, K.L., *J. Opt. Soc. Am.*, 33, 627, 1943. With permission.)

17.4.1.2 CIE UCS colorimetric system

The distance between two chromaticity points on the chromaticity diagram gives the color difference. The extent of the color difference on the CIE chromaticity diagram shown in Figure 6, however, does not correspond to the actual perceived color difference. This means that for two pairs of colors with the same distance between their chromatic points but in different areas of the diagram are not perceived to have the same color difference.

The UCS chromaticity diagram was developed to overcome this problem by modifying the chromaticity coordinates to make the distance between any two color points correspond to the perceived color difference. In 1960, based on the assumption that the standard deviation of the data on the matching observations corresponded to the color discrimination threshold, the CIE established a modified chromaticity diagram. This is the UCS diagram shown in Figure 7.

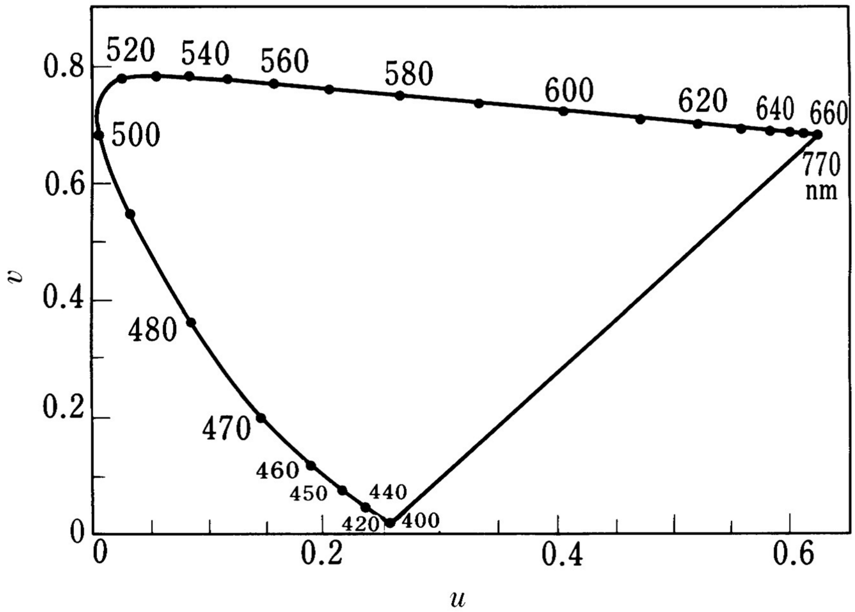

Figure 7 CIE UCS 1960 chromaticity diagram. (From CIE, *Testing of Supplementary Systems of Photometry,* TC1-21, in preparation. With permission.)

The chromaticity coordinates of the UCS chromaticity diagram (u, v) can be obtained by transformation of the x, y, and z coordinates for the XYZ chromaticity diagram into new coordinates, u and v, using the transformations in Eqs. 4a and 4b.

$$u = \frac{4x}{-2x + 12y + 3} \tag{4a}$$

$$v = \frac{6y}{-2x + 12y + 3} \tag{4a}$$

The coordinates u and v can also be obtained from X, Y, and Z from the XYZ chromaticity diagram using the following formulae.

$$u = \frac{4X}{X + 15Y + 3Z} \tag{5a}$$

$$v = \frac{6Y}{X + 15Y + 3Z} \tag{5b}$$

In 1976, the CIE established the u′, v′ color system as an improvement to the UCS system. The new coordinates u′ and v′ can be obtained simply by u′ = u and v′ = 1.5v.

17.4.1.3 ULCS colorimetric system

As explained above, the UCS colorimetric system was developed to make the distance between the two color points on the chromaticity diagram correspond to actual perceived color differences. The system is valid, however, only when the lightness of the colors is the same.

The ULCS colorimetric system was introduced to improve the UCS system. At present, the CIE recommends two ULCS colorimetric systems. They are the CIE 1976 $L^*u^*v^*$ Color Space and the CIE 1976 $L^*a^*b^*$ color space.

X, Y, and Z in the XYZ colorimetric system can be transformed into the coordinates in the $L^*u^*v^*$ color space using Eqs. 6a, b, and c, or into the $L^*a^*b^*$ color space using Eqs. 8a, b, c. The $L^*u^*v^*$ colorimetric system is plotted on an orthogonal coordinate system with axes given by:

$$L^* = 116\left[\frac{Y}{Y_0}\right]^{1/3} - 16 \tag{6a}$$

$$u^* = 13L^*\left(u' - u'_0\right) \tag{6b}$$

$$v^* = 13L^*\left(v' - v'_0\right) \tag{6c}$$

where

$$u' = \frac{4X}{X + 15Y + 3Z} \tag{7a}$$

$$v' = \frac{9Y}{X + 15Y + 3Z} \tag{7b}$$

$$u'_0 = \frac{4X_0}{X_0 + 15Y_0 + 3Z_0} \tag{7c}$$

$$v'_0 = \frac{9Y_0}{X_0 + 15Y_0 + 3Z_0} \tag{7d}$$

X, Y, and Z refer to the trichromatic stimulus of the object, while X_0, Y_0, and Z_0 refer to the light source that illuminates the object. The value of Y_0 is normalized to 100. The value of L^* corresponds to the psychometric lightness and is 10 times Munsell's value (V). As will be described below, the value V in the Munsell color system indicates the lightness of the colors. The values of u^* and v^* relate to the hue and the chroma in the Munsell color system, respectively, and are called the chromaticness index.

The $L^*a^*b^*$ colorimetric system gives the L^*, a^*, and b^* values on the right-angle coordinates by the following formula.

$$L^* = 116\left[\frac{Y}{Y_0}\right]^{1/3} - 16 \tag{8a}$$

$$a^* = 500\left[\left(\frac{X}{X_0}\right)^{1/3} - \left(\frac{Y}{Y_0}\right)^{1/3}\right] \tag{8b}$$

$$b^* = 200\left[\left(\frac{Y}{Y_0}\right)^{1/3} - \left(\frac{Z}{Z_0}\right)^{1/3}\right] \tag{8c}$$

The value of L^* corresponds to the psychometric lightness, and the values of a^* and b^* correspond to the hue and chroma in the Munsell color system, respectively. X, Y, and Z are the trichromatic stimulus of the object and X_0,Y_0, and Z_0 are the trichromatic stimulus of the light source that illuminates the object. The normal value of Y_0 is 100.

17.4.2 Specification of perceived colors

There are two systems that specify the perceived colors: the Munsell color system and the NCS (Natural Color System).

17.4.2.1 Munsell color system

The Munsell color system is based on the color chart in which the many colors are arranged systematically in equally perceived difference intervals for each of the three attributes of colors: hue (H), value (V), and chromaticness (C). The system was invented by Munsell in 1905 and formalized with some corrections in 1943 by the Optical Society of America. The colors are specified by a combination of quantities in the form HV/C (specifying the color properties quantitatively).

17.4.2.2 NCS

The NCS was proposed by Hard et al.[12] and initially specified as the Swedish National Standard by the Swedish Standards Institution (SIS). In this system, the colors are specified with the three attributes of whiteness (w), blackness (s), and chromaticness (c). The hues of the colors are indicated by the mixing ratios of the opponent colors red-green and yellow-blue. For example, a reddish-yellow that contains 70% yellow and 30% red is specified as Y_{30R}. The NCS system is based on the opponent color theory; thus, colors with a hue are specified by a mixing ratio of the three attributes whose sum is equal to 100. A pure color with a red hue, for example, is indicated as c = 100. Achromatic colors contain no chromaticness and are specified only by the ratio of the blackness (s) and the whiteness (w).

17.5 The color of light and color temperature

17.5.1 Chromatic adaptation and colors of light sources

Photometric measurements show that the color of natural daylight varies as the day progresses. Immediately after sunrise, it is very reddish. Under a very clear blue sky in the daytime, in the northern hemisphere, at the north side of buildings with no direct sunlight, daylight colors are bluish. Just before sunset, it again turns to a very reddish color. Nevertheless, human eyes are able to perceive colors in daylight hours with relative stability and accuracy, irrespective of the location. The reason is that the spectral sensitivity of the retina automatically compensates for changes in the color of the light illuminating an object. This physiological function of vision is called chromatic adaptation.

Chromatic adaptation is a function of vision that minimizes the influence of the color of illumination on the perception of colors of the object. Consequently, human eyes perceive the color of the light sources as being much more whitish than they actually are, depending on the chromatic environment or the state of the chromatic adaptation of the eye. This means that the chromaticity coordinates of colors of lights illuminating the object do not always correspond to the perceived colors. A number of methods to correct for the influence of the chromatic adaptation have been proposed by the CIE. It is important that chromatic adaptation does not compensate for the colors of light sources if lamps with different color temperatures are mixed in the field of view. Under such conditions, the lamps are seen in contrasting colors to one another; a bluish lamp is seen as more bluish, and a reddish lamp is seen as more reddish.

17.5.2 *Color temperature*

For the reasons mentioned above, it is necessary to define the color of the light in an objective way or by physical measurements. To define the color of light, the concept of the color temperature has been introduced. The color temperature is defined by the absolute temperature of a Planckian radiator (black body) that has the same color or the same colorimetric coordinates as that of the light source. Figure 8 shows the locus of the colorimetric coordinates of the color of the Planckian radiator in the CIE chromaticity diagram for a wide range of color temperatures. Further explanation of the locus will be given later. As seen in the figure, the color of the light sources changes from reddish to bluish color as the color temperature increases. When the chromaticity coordinates of a light source are not exactly on the locus of the Planckian radiator, the absolute temperature of the Planckian radiator closest to the light source is taken, and that temperature is called the correlated color temperature. A number of straight lines with designated temperatures are shown in the figure, each line being drawn perpendicular to the Planckian locus, and they show the closest line to the relevant temperature. Some examples of approximate figures of the color and the correlated color temperatures of natural and artificial light sources are shown in the table below.

Light source	Color temperature (K)
Blue sky	15000–20000
Cloudy sky	6500
Fluorescent lamps	
Daylight color	6500
Cool white color	4200
Halogen incandescent lamps	3000
Ordinary incandescent lamps	2800
High-pressure sodium lamps	2000
Candle flame	2000

17.5.3 *Mired (micro-reciprocal degree)*

The difference in the colors of lights with different color temperatures is indicated as the distance between their chromaticity points on the chromaticity diagram in Figure 8. As before, the difference in the perceived colors in different areas of the diagram is not the same, even if the distance on the chromaticity diagram is the same. To make the difference closer to the perceived color difference, a value of mired (micro-reciprocal degree) is used. Mired is defined as one million (10^6) times the reciprocal of the color temperature of the light source. If the difference in mired is the same, the difference in the perceived colors between the two light sources is roughly the same.

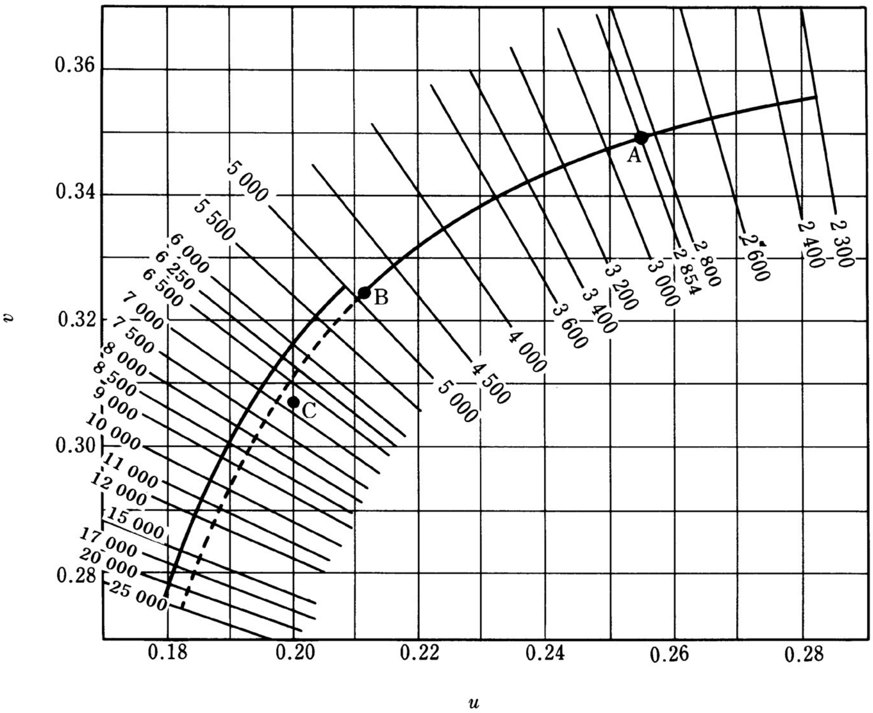

Figure 8 Locus of the color of the Planckian radiator in CIE 1964 chromaticity diagram for a wide range of color temperatures. (From CIE, *Testing of Supplementary Systems of Photometry*, TC1-21, in preparation. With permission.)

17.6 Color rendering

17.6.1 Methods of measurement

Color rendering is the property of the light source that changes the colors of the object illuminated by that light source. To deal with the color rendering, the following two methods are normally employed.

The first method is psychophysical. The basic approach of this method is to examine how the color of an object illuminated by a sample light source compares with the color observed under illumination with a reference light source having an ideal color rendering.

The second method, on the other hand, is psychological. The approach of this method is to examine by visual observation whether the color of an object under a sample light source is preferred by the observer or not. To conduct these observations, a careful selection of the colors to be examined is essential. Since this method is subjective, no definite method to determine this kind of color rendering has been developed. However, in some cases, the results derived by this method are practically more relevant and important than the results obtained through the psychophysical method.

To examine the color rendering properties of a sample light source based on the psychophysical method, colors of a number of objects illuminated by a sample light source are compared psychophysically with the colors obtained when the objects are illuminated by a reference light source. For this purpose, the chromaticity points of object colors are calculated with the CIE colorimetric system already described. Before the chromaticity points can be calculated for the reference light source, the spectral energy distributions and the color temperature of the reference light must be specified.

The CIE specifies two series of Reference Light Sources to be used for these calculations. The first is a Planckian radiator and the second is the CIE "daylight" standard. To examine the color rendering of a sample light source, it is recommended that a reference light source with a color temperature lying within a range of 5 mireds of the correlated color temperature of the sample light source be used. For color temperatures lower than 5000K, it is recommended that the Planckian radiator be used. As a standard for temperatures higher than 5000K, on the other hand, the CIE daylight standard is recommended.

The two curved lines in Figure 8 show the loci of the chromaticity points of the Planckian radiator and the CIE daylight reference light sources, respectively. The color temperature is taken as a parameter. The dotted curve shows the overlap zone of the locus of the Planckian radiator with that of the CIE "daylight" standard.

17.6.2 Color rendering index

17.6.2.1 General color rendering index (R_a)

The color rendering index (R_a) indicates the extent of the color rendering properties of a light source. The basis of the calculation of the general color rendering index (R_a) of a sample light source is the use of color differences. This difference is the distance between the chromaticity points of the sample and the reference light source, and is obtained for each of eight selected object colors. R_a is calculated by taking the average of these differences. If no color difference is found for all eight object colors, then the general color rendering index (R_a) is the maximum, 100; it is observed that the larger the averaged difference is, the lower the R_a figure. To use these estimates, however, care must be taken as to the limits of applicability and the meanings of the indices. Careful interpretation of the indices is always necessary. Some of the pitfalls encountered are discussed below.

17.6.2.2 Special color rendering indices

Special color rendering indices are calculated for one of six test colors specified by the CIE. The special color rendering index of a sample light source for one of the test colors shows the closeness of that test color to that under a reference source having the same color temperature.

The special color rendering indices of a sample light source are calculated in a similar way to the general color rendering indexes. However, the special color rendering index is calculated individually for each of the following six selected colors. The six colors are selected to represent the colors of normal objects. They are red, yellow, green, blue, each with a high chroma, and the colors of a Caucasian complexion and a green leaf. The indices are expressed according to the selected colors as R_9, R_{10}, R_{11}, R_{12}, R_{13}, and R_{14}. In the Japanese standard, the color of an Oriental complexion is added as R_{15}.

17.6.3 General color rendering index and perceived colors

To use the general color rendering index R_a, some caution is necessary, since there is some limitation of its applicability. Some of these limitations are summarized below.

1. No valid comparisons can be made using only the general color rendering index R_a between lights with different color temperatures. A difference in R_a is valid only for light sources with similar color temperatures. If the color temperatures of the two light sources to be compared are considerably different, then the difference has no actual meaning. This is because the perceived colors under reference light sources vary for different color temperatures.

2. Judgment of the perceived colors cannot always be made between light sources with low R_a values. As described, the R_a value is calculated using an average of the color differences for the eight specified test colors. As can be easily seen, this average can be obtained with many different combinations of the color differences.

   This implies that the color rendering properties can be considerably different, even if the R_a value is the same. For example, one lamp may have color rendering properties that cause a color difference for all eight test colors nearly to the same extent. Another lamp, on the other hand, may have other color rendering properties that cause considerable color differences for some of the test colors, whereas there is almost no color difference for the remaining test colors. If the latter lamp is used in an application where only some colors are to be perceived correctly and the lamp causes no big color difference in these colors, then the color rendering properties of the lamp are effectively comparable to another lamp with a very good R_a value.
3. Another aspect of importance is that a very high R_a value for a lamp only means that the colors perceived under its illumination are similar to the colors under the reference light source. Sometimes, however, colors that are slightly different from the reference colors are preferred. As the above examples show, the color rendering properties of such lamps cannot be judged correctly solely by the Ra value.

17.6.4 Color appearance of light sources and perceived colors

As described, the influence of the difference in the color temperature of the light sources on the perceived color is compensated, at least partly, by chromatic adaptation. Lamps of the same color temperature, however, can be made with many different spectral energy distributions. For this reason, the color rendering properties of lamps with the same color temperature can differ considerably because their spectral energy distribution is different.

17.6.5 Color rendering and brightness

The stimulus that yields the brightness sensation is the luminance. However, if one observes an object carefully, the perceived brightness of the object can be different, depending on its colors, even if they have the same luminance. Experimental observations revealed that the sensation of illuminated objects being lighter or darker in a room depends very much on the color rendering properties of the light source employed.[13] These comparisons were made in a room illuminated with fluorescent lamps of different R_a values and with an incandescent lamp with an R_a value of 100. The results are shown in Figure 9, in which the ratio of the illuminance under the incandescent lamp to that under the test fluorescent lamps to obtain the equivalent subjective brightness is plotted as a function of the R_a value of the test lamps. It is observed that, with decreasing R_a of the test lamps, the illuminance under those lamps necessary to obtain the equivalent subjective brightness increases remarkably.

17.7 Other chromatic phenomena

17.7.1 Purkinje phenomenon

This phenomenon was named after the Czech psychologist Purkinje, who discovered it in the early 19th century. The phenomenon concerns variation in the relative lightness of perceived colors between red and blue with changes in the luminance of the field of view. As the field becomes darker, the perceived red colors become relatively darker than the blue colors.

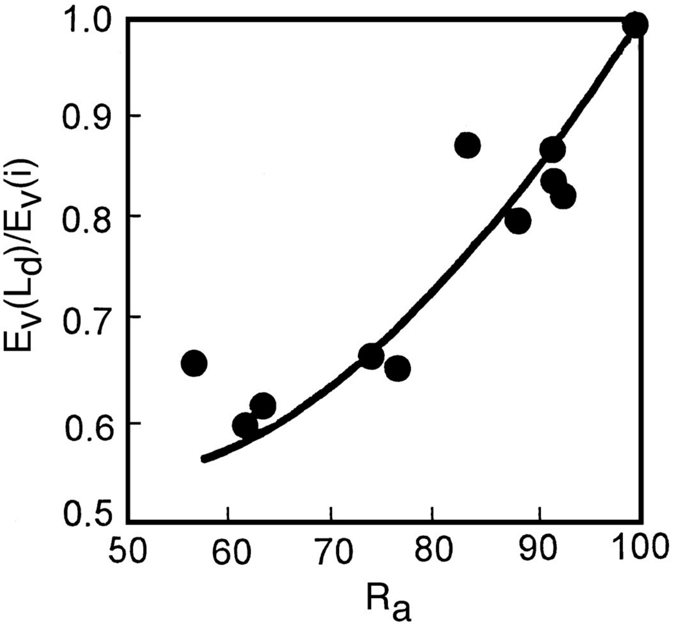

Figure 9 Relationship between the illuminance ratio to obtain equivalent subjective brightness ($E_v(L_d)/E_v(i)$) and the R_a of a test light source. $E_v(L_d)$: Vertical illuminance under an incandescent lamp with R_a of 100; $E_v(i)$: Vertical illuminance under a test light source. (From Kanaya, S., Hashimoto, K., and Kichizpe, E., *CIE Kyoto, 19th Session*, 1979, 274-278. With permission.)

17.7.2 Metamerism

Metamerism is a visual phenomenon in which two different colors (with different spectral reflection factors) are seen as the same color under a specific set of conditions. The condition requires a proper combination of spectral reflection factors of the object, of the spectral energy distribution of the lamps, and of the spectral sensitivity of the observer's eyes.

17.7.3 Bezold-Brucke effect

The Bezold-Brucke effect is a chromatic phenomenon in which the color of a light with constant spectral characteristics is perceived as a different color as the lamp's luminance is varied. A definite relationship between the perceived colors and the luminance has not yet been established.

17.7.4 Helmholz-Kouroshe effect

The Helmholz-Kouroshe effect is a visual effect in which a colored object is perceived to be lighter than an achromatic object with the same reflectance factor or the same luminance.

References

1. CIE, *The Basis of Physical Photometry,* CIE Publication No. 18.2, 1983.
2. Leonardo da Vinci, *Trattato della Pittura*, Langlois, Paris, 1651.
3. Newton, Sir Isaac, *Opticks*, Sam. Smith & Benj. Watford, London, 1704.
4. Young, Thomas, On the theory of light and colours, *Phil. Trans.*, 1802, 12-48.

5. von Helmholtz, H., Uber die Theorie der zusammengesetzten Farben, *Ann. Phys. Lpz.*, 87, 45-66, 1852.
6. Hering, E., Zur Lehre vom Lichtsinne Grundzug einer theorie des Farben sinnes, SB K, *Akad. Wiss Wien. Math. naturwise.*, K70, 169-204, 1875.
7. Muller, G.E., Zur Psychophysik der Gesichtsempfindungen, *Z. Psy. Physiol., Sinnesorg.*, 10, 1-82 and 321-413, 1896.
8. Walraven, P.L. and Bouman, M.A., Fluctuation theory of colour discrimination of normal trichromats., *Vision Res.*, 6, 567-586, 1966.
9. Ikeda, M., *Fundamentals of Colour Engineering*, Asakura Bookstore, 1980, 244-245.
10. CIE Publication in preparation, *Testing of Supplementary Systems of Photometry,* TC1-21.
11. Kelly, K.L., *J. Opt. Soc. Am.*, 33, 627, 1943.
12. Hard, A. and Sivik, L., NCS—Natural Color System: A Swedish standard for color notation, *Color Res. Appl.*, 6, 129-138, 1981.
13. Kanaya, S., Hashimoto, K., and Kichizpe, E., Subjective balance between general colour rendering index, colour temperature, and illuminance of interior lighting, *CIE Kyoto, 19th Session*, 1979, 274-278.

part six

History

chapter eighteen — sections one–twelve

History of phosphor technology and industry

Shigeharu Nakajima* and Masaaki Tamatani

Contents

18.1 Introduction 982
18.2 Phosphors for fluorescent lamps 982
  18.2.1 Early history (till 1955) 982
  18.2.2 Halophosphate phosphors for general purpose lamps and blended phosphors for deluxe lamps (1955–1980) 993
  18.2.3 Rare-earth phosphors for three-band type lamps and widespread applications (1980–) 994
18.3 Phosphors for high-pressure mercury vapor lamps 997
18.4 Photoluminescent devices from 1995 to 2005 998
  18.4.1 Fluorescent lamps 998
  18.4.2 White light-emitting diodes 1000
  18.4.3 Plasma display panels 1002
18.5 Phosphors for black-and-white picture tubes 1003
  18.5.1 Early history (till 1955) 1003
  18.5.2 TV and other applications (1955–) 1004
18.6 Phosphors for color picture tubes 1005
  18.6.1 Early history (till 1965) 1005
  18.6.2 Rare-earth phosphors and screen improvement (1965–) 1006
18.7 Cathodoluminescent displays from 1995 to 2005 1009
  18.7.1 Cathode-ray tubes 1009
  18.7.2 Field emission displays 1010
18.8 Phosphors for X-ray 1011
  18.8.1 Fluoroscopic screen 1011
  18.8.2 Intensifying screens 1012
  18.8.3 X-ray computed tomography and imaging systems 1014
18.9 Medical devices using radioluminescence from 1995 to 2005 1015
  18.9.1 X-ray computed tomography 1015
  18.9.2 Positron emission tomography 1016
  18.9.3 X-ray flat panel detector (X-FPD) 1017
18.10 A short note on the history of phosphors 1017

---

*Deceased.

18.11 Production of luminescent devices utilizing phosphors 1019
18.12 Production of phosphors 1021
References 1022

18.1 Introduction

Materials that absorb light and emit it at other wavelengths in the visible region (i.e., phosphors) have been known in Europe since the age of alchemy,* but it was not until the end of the 19th century and particularly after the end of World War II that equipments for producing electron beams, X-rays, and UV rays were combined with phosphors to create luminescent devices. In recent years, fields of application have expanded greatly, to include lighting, display, and medicine (see Chapter 1, Table 1). For these diverse purposes, thousands of different phosphors have been synthesized. However, approximately 50 of them have properties (luminescence efficiency, emitted light color, chemical and physical stability, etc.) satisfactory for practical use. In this chapter, the history of phosphors used in mass-produced fluorescent lamps, mercury lamps, and cathode ray tubes (CRTs), as well as in X-ray screens are reviewed. For descriptions of phosphors used in luminous paints, electroluminescent materials, vacuum fluorescent tubes, and plasma displays, see other sections in this handbook.

Before World War II, Western Europe was at the forefront of phosphor technology and industry. After the war, the United States occupied this position. During this period, Japan was not engaged substantially in phosphor development. However, even in those days, Japan mass produced phosphors for domestic devices. Japan has a unique, long history as far as the technology of phosphors is concerned. On the basis of the technological developments and applications, Japan has emerged as the preeminent player in this field in recent years. The focus here will be on the early developments in Japan and their relationship to technical activities worldwide. Table 1 and Table 2 show the years when various luminescent devices and representative phosphors used in them first appeared in Japan.

Various new light-emitting devices developed recently have demanded good phosphors as key materials for them. Items studied have become almost common to phosphor engineers worldwide. Brief descriptions concerning trends seen in the development of each device from 1995 to 2005 are added to the previous version of this handbook.

18.2 Phosphors for fluorescent lamps

18.2.1 Early history (till 1955)

First luminescent device in which phosphors were used was the Geissler tube. In *La Lumière* (France, 1859), Becquerel describes how he succeeded in making a phosphor to fluoresce in an electric-discharge tube with gas pressures of 1–2 mm Hg.[1]

In 1896, Edison applied for a patent for a lamp made by introducing a $CaWO_4$ phosphor into a glass tube as it was being blown, thus causing the phosphor to fuse with the inner glass wall, and then using two electrodes to produce a discharge in the residual gas. Edison called this a fluorescent electric lamp.[2] The 1904 edition of the *Encyclopaedia Britannica* credits the invention of the fluorescent lamp, which does not have an incandescent filament, to Edison.[3] At the start of the 20th century, it became possible to produce rare gases industrially, and the development of electric-discharge tubes progressed rapidly. In 1916, Claude (France)[3] developed an electric-discharge lamp using neon, and exhibited

---

* There is a Chinese record that the Japanese knew phosphors in far earlier times than the age of alchemy in Europe. See Section 18.10 for a short note on the history.

Table 1 Development of Luminescent Devices in Japan

Year	Lamp	X-ray	CRT	Others	Ref.
World					
1859	Becquerel; fluorescent lamp				[1]
1896		Pupin; intensifying screen			[217]
1897			Braun; CRT		[129]
1933	GEC; mercury lamp production				[3]
1938	GE; fluorescent lamp production				[10–12]
Japan					
1921		Fluoroscopic screen commercialized			[219]
1925			CRT trial production		[133]
1926			Takayanagi TV image		[133]
1934	Mercury lamp production				[3]
1934				Luminous paint using Ra	[276]
1934		Intensifying screen production			[224]
1940	Fluorescent lamp production				[3]
1941–1945			Radar	IR-stimulable phosphors	[277]
				Long persistent phosphors	[278]
1946	Insect trapping lamps				[1]
1951	Rapid expansion of production (Ca-halophosphate)				
1952				Tuning indicator	[279]
1953			B&W TV broadcast		
1955–1965				Intensive study of EL lamp	
1953				Scintillation counter	[280]
1954	Color-corrected mercury lamp				[84]
1956		Image intensifier (II) trial production			[227]

continued

Table 1 Development of Luminescent Devices in Japan

Year	Lamp	X-ray	CRT	Others	Ref.
1956			Metallizing		[281]
1960			Color TV broadcast		
1958–1965			Transparent thin-film phosphors		[282]
~1961				Inversion viewer	[283]
1960–1975				Study of laser materials	[284]
1965			Eu^{3+} red color CRT		[170]
1967				Vacuum fluorescent tubes	[285]
1965–				TLs for atomic reactor	[286]
1968–1973				IR–visible conversion phosphors	[287]
1969			Black matrix		[178,179]
1972		X-ray CT			[239]
1972–				Study of thin film EL	[288]
1973				Plasma display	[289]
1974		II with evaporation deposited phosphor			[229]
1976		First commercial PET			[262]
1977	Three-band fluorescent lamp				[36,39,44]
1978	Ball-type fluorescent lamp				[65]
1981		Digital radiography using stimulation phosphors			[240]
			Outdoor large screen display		[290]

1982–			Improvement in projection CRT		[291]
1985–	Compact lamp				[292]
			Invar shadow-mask		[293]
				Flat panel displays	[294]
	LCD backlight				[66,75]
1989		X-ray CT helical (spiral) scanning			[255]
		X-ray CT using ceramic scintillator			[245]
1990				Commercial color plasma display	[295]
1993				Long persistence oxide phosphors	[61]
1994	Long-life fluorescent lamp				[74]
			Micro-filter CRT		[188]
1996				Field emission display	[296]
1996	White-LED				[108]
1997, 1998		Flat panel detectors			[272–274]
2001				First year of PDP-TV	[123]
2003		Rapid spread of PET			

Table 2 Timeline for the First Use of Representative Phosphors in Japan
(a) For Fluorescent Lamps and Other UV- to Visible-Light Excited Devices

Year	Composition	Emitted color	Application[a]	Notes[b]	Ref.[c]
1940	$Zn_2SiO_4:Mn^{2+}$	Green	FL	GEC	[297]
	$MgWO_4$	Blue-white	FL	GEC	[298]
	$(Zn,Be)_2SiO_4:Mn^{2+}$	Yellow to orange	FL	GEC, RCA, Telefunken	[9]
	$Cd_2B_2O_5:Mn^{2+}$	Orange	FL	Electric & Musical Ind	[299]
1942	$CaWO_4$	Blue	For lure	Thomson-Houston	[300]
1947	$3Cd_3(PO_4)_2 \cdot CdCl_2:Mn^{2+}$	Orange	FL	GEC	[301]
1950	$CaSiO_3:Pb^{2+},Mn^{2+}$	Orange	FL	Sylvania	[15,16,302]
1951	$3Ca_3(PO_4)_2 \cdot Ca(F,Cl)_2:Sb^{3+},Mn^{2+}$	White	FL	GEC	[18,20]
1952	$6MgO \cdot As_2O_5:Mn^{4+}$	Red	HCR, later HF		[26,80]
1952	$(Ca,Zn)_3(PO_4)_2:Tl^{+}$	UV		Westinghouse	[303]
1953	$Ba_2P_2O_7:Ti$	Blue-white		Thorn	[27,304]
1954	$3.5MgO \cdot 0.5MgF_2 \cdot GeO_2:Mn^{4+}$	Red	HCR, HF, later FL	Westinghouse	[79]
1955	$(Sr,Ca)_3(PO_4)_2:Sn^{2+}$	Red	HCR, later HF	Sylvania	[28,93]
1957	$(Sr,Mg)_3(PO_4)_2:Sn^{2+}$	Red	HCR, HF		[88,305]
1958	NBS standard phosphors			Table 2(d)	[306]
1960	$BaSi_2O_5:Pb^{2+}$	UV	Black light	Sylvania	[307]
	$3Sr_3(PO_4)_2 \cdot SrF_2:Sn^{2+},Mn^{2+}$	Yellow	FL	GEC	[308]
1964	$Sr_2P_2O_7:Sn^{2+}$	Blue	For plant growth	GEC, Thorn, Sylvania	[83,309]
1967	$YVO_4:Eu^{3+}$	Red	HF	GTE Labs	[89]
1968	$MgGa_2O_4:Mn^{2+}$	Green	For copying	Sylvania	[310]
	$Sr_3(PO_4)_2:Eu^{2+}$	Blue	For copying		[41,175]
	$Sr_2P_2O_7:Eu^{2+}$	Blue	For copying, medical use		[41,174,175]
	$SrMgP_2O_7:Eu^{2+}$	Blue	For copying		[42,174,175]
1970	$SrFB_2O_{3.5}:Eu^{2+}$	UV	Black light	Sylvania	[43]
	$Y(P,V)O_4:Eu^{3+}$	Red	HF	Philips	[311]
1976	$Y_3Al_5O_{12}:Tb^{3+}$	Green	HF		[312]
1977	$BaMg_2Al_{16}O_{27}:Eu^{2+}$	Blue	Three-band	Philips	[44]
	$(Ce^{3+},Tb^{3+})MgAl_{11}O_{19}$	Green	Three-band	Philips	[44]
	$Y_2O_3:Eu^{3+}$	Red	Three-band		[44]
1978	$3Sr_3(PO_4)_2 \cdot CaCl_2:Eu^{2+}$	Blue	Three-band	Sony, Toshiba	[49]
	$Y_2SiO_5:Ce^{3+},Tb^{3+}$	Green	Three-band	Toshiba	[45]
	$2SrO \cdot 0.84P_2O_5 \cdot 0.16B_2O_3:Eu^{2+}$	Blue-green	HCR	Mitsubishi	[52]
1981	$LaPO_4:Ce^{3+},Tb^{3+}$	Green	Three-band	Nichia	[46]
1982	$(Ba,Ca,Mg)_5(PO_4)_3Cl:Eu^{2+}$	Blue-green	HCR	Toshiba	[53]
1983	$Sr_{0.96}Mg_{0.81}Al_{5.44}B_{0.02}O_{10}:Eu^{2+}$	Blue-green	HCR	Matsushita	[54]
	$(Ce,Gd,Tb)MgB_5O_{10}$	Green	Three-band	Philips	[47]

Table 2 Timeline for the First Use of Representative Phosphors in Japan
(a) For Fluorescent Lamps and Other UV- to Visible-Light Excited Devices

Year	Composition	Emitted color	Application[a]	Notes[b]	Ref.[c]
1990	$(Y,Gd)BO_3:Eu^{3+}$	Red	PDP	Fujitsu, Kasei-Optonix	[125]
	$Zn_2SiO_4:Mn^{2+}$	Green	PDP		
	$BaMgAl_{10}O_{17}:Eu^{2+}$(BAM:Eu)	Blue	PDP		
1993	$SrAl_2O_4:Eu^{2+},Dy^{3+}$	Green	Long persistent	Nemoto	[61]
1996	$(Y,Gd)_3(Al,Ga)_5O_{12}:Ce^{3+}$	Yellow	White-LED	Nichia	[108]
	BAM:Eu^{2+},Mn^{2+} (G), $La_2O_2S:Eu^{3+}$(R), BAM:Eu^{2+} (B), $(Sr,Ca)_5(PO_4)_3Cl:Eu^{2+}$ (B)		White-LED	Toshiba, Toyoda-Gosei	[109,110]
2002	$(Sr,Ba,Ca)_2SiO_4:Eu^{2+}$	Yellow	White-LED	Leuchtstoffwerk, Toyoda-Gosei	[313]
2003	$Sr_2Si_5N_8:Eu^{2+}$	Red	White-LED	Osram, Nichia	[113,117]
2006	$CaAlSiN_3:Eu^{2+}$	Red	White-LED	Tokyo University of Technology, NIMS[d]	[119]
	α-SiAlON:Eu^{2+}	Yellow	White-LED	Osram, NIMS	[120]
	$SrSi_2O_2N_2:Eu^{2+}$	Yellow-green	White-LED	Lumileds	[118]

[a] FL: fluorescent lamp for general illumination; HF: high-pressure mercury lamp; HCR: high color-rendering fluorescent lamp.

[b] Company name means the company that invented the phosphor or the company that used the phosphor first.

[c] Patent application is shown specially in the references in the early history.

[d] NIMS: National Institute for Materials Science.

the first neon sign in Paris. In 1923, Risler (France)[4] demonstrated a lamp in which the outer surface (later the inner surface) was coated with zinc sulfide phosphors. It was in 1935 that the phosphors $Zn_2SiO_4:Mn^{2+}$ and $CaWO_4$ were first used in neon signs.[5]

In 1937, Claude-General Neon Lights[6] (France) created a cold-cathode, low-pressure vapor-discharge lamp (Ne, Ne+Ar+Hg) and a variety of colored lamps (Zeon tubes) consisting of combinations of colored glasses with phosphors that emitted blue and green light. These were displayed at expositions in Paris (1937) and New York (1939).

In 1938, General Electric Company (GEC, Britain)[7] announced that it had developed phosphors of the type listed in Table 3, and used them to coat lamps (Osira tubes) 8 ft 6 in. in length (Ar+Ne+Hg). Table 3 shows the emitted light colors and efficacies of these lamps. GEC selected three of these lamps and combined them to synthesize white light for illumination. The patents for the above classical phosphors are shown in the references cited in Table 2. Most of these patents were applied for by GEC in 1936 and 1937. Britain was several steps ahead of the rest of the world in those days. The most important phosphor for practical use at the time,[8] $(Zn,Be)_2SiO_4:Mn^{2+}$, was invented independently[9] in Germany, the United States, and Britain. The electric-discharge lamps mentioned above, however, required a high-voltage leakage transformer to operate as well as long lengths to obtain high efficiencies. Hence, these lamps were mainly used for stationary colored advertising displays, rather than for illumination.

Encouraged by these activities in Europe, General Electric (United States) in 1934 formed a team to develop a lamp for the purpose of illumination. On April 1, 1938, they

Table 2 (b) For CRT Use

Year	Composition	Emitted color	Application	Notes	Ref.
1925	$CaWO_4$	Blue		Trial	[130,133, 314]
1930	$Zn_2SiO_4:Mn^{2+}$	Green			[130,133, 314]
1939	(Zn,Cd)S:Ag + ZnS:Ag	White	TV		[135]
1943	ZnS:Cu,Ag		Radar		[279]
1951 to 1959	JEDEC; P1–P29 (ZnS:Cu, ZnS:Ag, $MgSiO_3:Mn^{2+}$,$MgF_2:Mn^{2+}$, $(Ca,Mg)SiO_3:Ti$, ZnO:Zn, $Ca_2MgSi_2O_7:Ce^{3+}$,		Radar, Oscillograph, Storage tube, Flying spot scanner (FSS)		[143]
1958	NBS standard phosphors			Table 2(d)	[306]
1959	$Zn_3(PO_4)_2:Mn^{2+}$	Red	Color TV		[166]
	$Zn_2SiO_4:Mn^{2+}$	Green	Color TV		[166]
	ZnS:Ag	Blue	Color TV		[166]
1962	(Cd,Zn)S:Ag	Red	Color TV	All sulfide	[167]
	(Zn,Cd)S:Ag	Green	Color TV		[167]
1965	$YVO_4:Eu^{3+}$	Red	Color TV	First rare-earth phosphor	[170]
1967	ZnO:Zn	Green-white	Vacuum fluorescent tube (VFT)		[285]
1967	$Y_2O_2S:Eu^{3+}$	Red	Color TV		[172]
	P36–P40 (ZnS:Ag,Ni, (Zn,Cd)S:Ag,Ni,		FSS, Display		[143]
1969	(Zn,Cd)S:Cu,Al	Green	Color TV	Later B&W TV	[142]
1971	P42–P45 ($Ln_2O_2S:Tb^{3+}$, etc.)		Display		[143]
1972	P46–P48 ($Y_3Al_5O_{12}:Ce^{3+}$, $Y_2SiO_5:Ce^{3+}$, etc.)		FSS		[143]
1973	cub-ZnS:Cu,Al	Green	Color TV		[180]
1975	P49–P52 ($Zn_2SiO_4:Mn^{2+}/YVO_4:Eu^{3+}$ $Zn_2SiO_4:Ti$, etc.)		Penetration CRT, Photography, Recording		[143]
1977	ZnS:Cu,Au,Al	Green	Color TV		[180]
1978	In_2O_3-blended phosphors	Blue, Green, Red	VFT	Electro-conductive	[315]
	$SnO_2:Eu^{3+}$	Red	VFT		[316,317]
	Pigmented phosphors	Red, Blue	Color TV		[184]
1980	P53–P57 ($Y_3Al_5O_{12}:Tb^{3+}$,$Y_2O_3:Eu^{3+}$, $Zn_2SiO_4:Mn^{2+}+MgF_2:Mn^{2+}$, etc.)		Head-up display, Color display, Projector, radar		[143]
1982 to 1985	$CaS:Ce^{3+}$, $Y_2SiO_5:Tb^{3+}$, P53+P1, $LaOCl:Tb^{3+}$, $Y_3(Al,Ga)_5O_{12}:Tb^{3+}$	Green	Projector		[154] [147,318] [319]

Table 2 (b) For CRT Use

Year	Composition	Emitted color	Application	Notes	Ref.
1982	$Cd_5(PO_4)_3Cl:Mn^{2+}$	Orange	Display	Monochrome, Long persistence	[145]
1985	ZnS:Ag,Ga	Blue	Display (white)	Long persistence	[320]
	$InBO_3:Eu^{3+},Tb^{3+}$	Orange	Display (white)	Medium persistence	[148]
1995	Spherical phosphors	Green, Red	Projector		[195]

Table 2 (c) For X-ray Use

Year	Composition	Emitted color	Application	Notes	Ref.
1918	$BaPt(CN)_4{\cdot}4H_2O$	Green	Fluoroscopic screen	Giba green	[219]
to 1921	Tungstate phosphors	Blue-white	Fluoroscopic screen	Giba white	[219]
1925	$Zn_2SiO_4:Mn^{2+}$	Green	Fluoroscopic screen		[217]
1933	$CdWO_4$	White	Fluoroscopic screen		[221]
	(Zn,Cd)S:Ag	Green	Fluoroscopic screen	Production in 1939	[222]
1934	$CaWO_4$	Blue	Intensifying screen		[224]
1956	ZnS:Ag	Blue	II		[227]
1967	(Zn,Cd)S:Ag	Green	II		[228]
1971	$Gd_2O_2S:Tb^{3+}$	Green	II, Fluoroscopic screen		[176]
1972	$Ba_3(PO_4)_2:Eu^{2+}$	Blue	Intensifying screen		[234]
1974	$(Y,Gd)_2O_2S:Tb^{3+}$	White	Intensifying screen		[235]
	$Gd_2O_2S:Tb^{3+}$	Green-white	Intensifying screen		[321]
	CsI/Na	Blue	II	Evaporated layer	[229]
1977	$BaFX:Eu^{2+}$	Blue	Intensifying screen		[236]
	$LaOBr:Tm^{3+}$	UV-blue	Intensifying screen		[232]
1978	$Bi_4Ge_3O_{12}$ (BGO)	Blue-white	Scintillator for PET	Single crystal	[262,265]
1981	$BaFX:Eu^{2+}$	UV-blue	Radiography	Photo-stimulation	[240]
1984	$YTaO_4:Nb$	UV-blue	Intensifying screen		[236]
	$YTaO_4:Tm^{3+}$	Blue	Intensifying screen		[236]
1985	$Gd_2SiO_5:Ce^{3+}$	Blue	Scintillator for PET	Single crystal	[263,266]
1988	RbBr:Tl	UV	Radiography	Photo-stimulation, Evaporated layer	[251]
1989	$(Y,Gd)_2O_3:Eu^{3+}$	Red	Scintillator for X-ray CT	Ceramic phosphor	[245]
1995	$Gd_2O_2S:Pr^{3+}(Ce^{3+})$	Green	Scintillator for X-ray CT	Ceramic phosphor	[243,244]
1998	CsI:Tl	Green	Flat panel detectors	Evaporated layer	[272]
	$Gd_2O_2S:Tb^{3+}$	Green	Flat panel detectors		[273]
2000	$Lu_2SiO_5:Ce^{3+}$	Blue	Scintillator for PET	Single crystal	[262,267]

Note: II = image intensifier; CT= computed tomography; PET= positron emission tomography.

announced that they had succeeded in producing a fluorescent lamp, which they touted as the new light source of the century.[10–12] This lamp was composed of hot cathodes that could be switched on even using low household voltages, and the tube sizes were short enough for easy handling. The characteristics of the phosphors used in this lamp are listed in Table 4. Note that, prior to these developments, in 1926 Meyer's group (Germany) had applied for a patent for a fluorescent lamp basically identical to the structure just described

Table 2 (d) NBS Standard Phosphors

Sample number	Phosphor	Sample number	Phosphor
For CRT use		For FL	
1020	ZnS:Ag	1028	$Zn_2SiO_4:Mn^{2+}$
1021	$Zn_2SiO_4:Mn^{2+}$	1029	$CaSiO_3:Pb,Mn^{2+}$
1022	ZnS:Cu	1030	$(MgO)_x(As_2O_5)_y:Mn^{4+}$
1023	ZnCdS:Ag	1031	$3Ca_3(PO_4)_2 \cdot Ca(F,Cl)_2:Sb^{3+},Mn^{2+}$
1024	ZnCdS:Cu	1032	$BaSi_2O_5:Pb^{2+}$
1025	$Zn_3(PO_4)_2:Mn^{2+}$	1033	$Ca_3(PO_4)_2:Tl^{+}$
For CRT, X-ray, FL			
1026	$CaWO_4:Pb$		
1027	$MgWO_4$		

Note: 1. FL: fluorescent lamps.

2. These phosphors became available from NBS at $3 per sample (14 or 28 g) since 1958, and had been used as standards at phosphor manufacturers worldwide. Stocks exhausted in 1979, however, and the standards were abolished in 1981.

Table 3 Cold Cathode Fluorescent Lamps of GEC (1938)

Phosphor	Light color	Efficacy (lm/W)
$Zn_2SiO_4:Mn^{2+}$	Bright green	55
$(Zn,Be)_2SiO_4:M^{2+}$	Off-white	25
$CaWO_4$	Deep blue	15
$3Cd_3(PO_4)_2 \cdot CdCl_2:Mn^{2+}$	Apricot	30
$MgWO_4$	Sky blue	30
$CaWO_4$	Pink (Neon)	15
$Zn_2SiO_4:Mn^{2+}$	Gold (Neon)	22

(GE type).[13] Due to unknown reasons, Meyer's lamp did not attract much attention and the patent rights were transferred to General Electric.

In Japan, at the time when General Electric announced its fluorescent lamp, some electric companies were also researching electric-discharge lamps and phosphors. However, since the performance of the General Electric lamp was outstanding, engineers from Toshiba were sent to GE to learn the technology, including the use of phosphors (April 1939). In 1940, a lamp using a phosphor mixture of $MgWO_4$, $(Zn,Be)_2SiO_4:Mn^{2+}$, and $Cd_2B_2O_5:Mn^{2+}$, which emitted daylight color, was produced by Toshiba. In the same year, 136 lamps using these phosphors were used to illuminate the world's most ancient Buddhist mural paintings at the Horyuji temple to facilitate their reproduction.[1] The artist, who sketched the murals, was said to have become almost "intoxicated with aesthetic delight" as the full beauty of the murals was revealed in the soft, bright light produced by the lamps.[3] Thus, the practical use of fluorescent lamps got off to a brilliant start, so as to speak. However, this was a false beginning as Japan, in 1941, entered World War II and blackouts were imposed. Fluorescent lamps were mainly used in submarines and aircraft carriers during the war.[1]

Table 4 Fluorescent Lamps of GE (1938)

Phosphor	Peak wavelength (nm)	Quantum efficiency	Light color	Luminous flux 20 W (lm)	Luminous flux 40 W (lm)	Flicker (%)
$CaWO_4$:Pb	440	0.70	Blue	460		95
Zn_2SiO_4:Mn^{2+}	525	0.74	Green	1300		15–20
$Cd_2B_2O_5$:Mn^{2+}	615	0.66	Pink	440		20
$(Zn,Be)_2SiO_4$:Mn^{2+}	595	0.53	Gold[a]	540		30
$CdSiO_3$:Mn	595	0.55	Red	60		10
$MgWO_4$	480	0.70				
			Daylight	660	1600	70
			White[b] (3500K)	760	1880	35

[a] The phosphor was coated on the pigment layer.

[b] Three specifically selected phosphors in proper proportion were used.

Table 5 Early Fluorescent Lamps in Japan

	Toshiba Rev. (April 1950)				Toshiba catalogue (1951)	
Light color	Phosphor	Blend ratio (%)	Input (W)	Luminous flux (lm)	Phosphor	Luminous flux (lm)
Daylight	$MgWO_4$	46	10	250	$Ca_5(PO_4)_3(F,Cl)$:Sb,Mn	350
	$CaSiO_3$:Pb,Mn	54	17	450		610
			20	555		750
			40	1340		1850
White	$MgWO_4$	17	10	280	$Ca_5(PO_4)_3(F,Cl)$:Sb,Mn	380
	$CaSiO_3$:Pb,Mn	75	17	490		680
	Zn_2SiO_4:Mn	8	20	600		840
			40	1440		2100
Blue	$CaWO_4$		17	175	$CaWO_4$	175
			20	230		230
Blue-white	$MgWO_4$		17	450	$MgWO_4$	450
			20	555		555
Pink	$Cd_2B_2O_5$:Mn		17	250	$Cd_2B_2O_5$:Mn	250
			20	325		320
Green	Zn_2SiO_4:Mn		17	—	Zn_2SiO_4:Mn	850
			20	—		1050

After the war, lamp production restarted in April 1946, mainly for use as lures in moth and insect traps; this development occurred because of the urgent need to increase the country's food supply. During the war, researchers had discovered that blue-emitting lamps coated with the $CaWO_4$ phosphor were the most effective bug lures. Lamp production increased from 2400 pieces in 1947 to 140,000 in 1949 (corresponding to the use of 500 kg of phosphors).[1] In that year, however, a new pesticide (BHC) became available and the occupation authorities promoted its use; consequently, production of lamps for use as bug lures plummeted.

Production of daylight-color fluorescent lamps restarted in 1947, but since ethyl silicate and BeO, two of the raw materials of $(Zn,Be)_2SiO_4:Mn^{2+}$, were hard to obtain in Japan, $3Cd_3(PO_4)_2\cdot CdCl_2:Mn^{2+}$ was produced as a substitute. To synthesize daylight-color light, $MgWO_4$ and $Cd_2B_2O_5:Mn^{2+}$ were blended with the chlorophosphate. Later, these materials became available and test production of $(Ze,Be)_2SiO_4:Mn^{2+}$ began. It was discovered, however, that BeO brought with it a risk of skin ulceration,[14] and its use in fluorescent lamps was therefore stopped in the United States in 1949. Reflecting this move, Japanese companies also gave up plans to use BeO, and no such lamps reached the market. As a replacement phosphor, $CaSiO_3:Pb^{2+},Mn^{2+}$ (610 nm) was produced,[15,16] in 1950. At that point, 40 W lamps were added to the lineup for the first time, and a 4500 K white light was also produced (Table 5).[17] The fact that a 17 W version for home use, which could be operated at low voltage, was also included in the lineup, indicated the country's poor power generation situation at the time.

18.2.2 Halophosphate phosphors for general purpose lamps and blended phosphors for deluxe lamps (1955–1980)

In 1942, a group led by McKeag, the inventor of $3Cd_3(PO_4)_2 \cdot CdCl_2{:}Mn^{2+}$, discovered[18] that when Cd was replaced by Ca and Sb^{3+} was incorporated in the phosphor, the phosphor absorbed UV rays sufficiently thereby emitting white light, the blue component due to Sb^{3+} and the orange component due to Mn^{2+}. They applied for a patent in 1942 (Brit. Pat. 578192) for the calcium halophosphate phosphor ($3(Ca,Sr,Ba)_3(PO_4)_2 \cdot (Ca,Sr,Ba)X_2{:}Sb^{3+},Mn^{2+}$). In Japan, this information was not known until Jenkins et al.[18] published a paper in 1949. It happened that a Japanese patent[19] specifying incorporation of Cd into the calcium halophosphate phosphor had appeared before the original patent for this phosphor was published in Japan[20] in 1954. In this phosphor, it was possible to control the intensity ratio of the blue and orange components, and to produce white lights with a wide range of color temperatures. Moreover, it was chemically stable and had good lumen maintenance properties. Furthermore, this phosphor was cheap and produced light with high efficiency. Even though strict control of the firing process during the manufacture of the phosphor was necessary to obtain a stable light color, due to the raw materials that contained volatile halogen and Sb_2O_3, the phosphor constituted a truly epoch-making development. Nonetheless, production started in 1951 at a rate of 200 kg per month. As given in Table 5, the luminous flux of lamps using this phosphor was 40% higher than those using the previous multicomponent-blended phosphor. At this point, fluorescent lamps entered the age of calcium halophosphate phosphors, leaving the poor color-rendering problems unresolved (insufficient intensity in the red region). Over the many years since then, a great deal of research has been done on improving the material's luminous efficacy and lumen maintenance. The most important developments have been controlling particle size within the 3–30 μm range (1960),[21] incorporating small amounts of Cd (1963),[22] using $CaHPO_4$ with a plate-like particle shape as raw material (1964),[23] and making the chemical composition stoichiometric (1965).[24] The successive adoption of these techniques into the production process resulted in progressive increases in luminous efficacy, as shown in Figure 1. Note that although products containing Cd were available on the market in 1965, their use ceased in 1971 in Japan because of problems associated with cadmium pollution.

While these calcium halophosphate lamps were produced in increasing numbers, conventional lamps using the classical three-color phosphor mixture ($MgWO_4$ + $Zn_2SiO_4{:}Mn^{2+}$ + $CaSiO_3{:}Pb^{2+},Mn^{2+}$) remained as deluxe (DL) lamps, the lamps of choice for high color-rendering properties. At the time, $Ca_3(PO_4)_2{:}Ce^{3+},Mn^{2+}$ was known as a phosphor that emitted intense red light,[25] but it was not put to practical use because of severe deterioration in the lamp-making process. Around 1952, a so-called European-type DL lamp appeared on the market, which used the calcium halophosphate phosphor together with the magnesium arsenate phosphor, giving enough intensity of red light to compensate halophosphate's shortcomings.[26] In the above-mentioned three-color phosphor mixture (the so-called U.S. type), the green-emitting $Zn_2SiO_4{:}Mn^{2+}$ showed poorer lumen maintenance than the other two components. Consequently, the light produced gradually became red in the course of long-term use. To counter this, in 1953 a new blue-emitting $Ba_2P_2O_7{:}Ti$ phosphor, which had a more intense green component than $MgWO_4$, was introduced, reducing the proportion of $Zn_2SiO_4{:}Mn^{2+}$ in the mixture.[27] In 1957 and 1958, the main components ($Ba_2P_2O_7{:}Ti$ and $Zn_2SiO_4{:}Mn^{2+}$) were replaced by calcium halophosphate mixed with red-emitting $CaSiO_3{:}Pb^{2+},Mn^{2+}$ or $(Ca,Sr)_3(PO_4)_2{:}Sn^{2+}$.[28] The new mixture brought the luminous flux (of a 40 W DL lamp) up from 2000 to 2350. In 1956, a super deluxe (SDL) lamp was put on the market,[29] in which deep-blue-emitting $CaWO_4$ and deep-red-emitting $6MgO{\cdot}As_2O_5{:}Mn^{4+}$ were added to the DL phosphor to broaden the luminescence spectral region.

It should also be mentioned that the color-rendering properties of these lamps were evaluated using a color solid (an improved Munsell system) that could also express brightness. Deviations in the color stimuli produced when the lamps are used to illuminate pieces of reference colored paper were expressed as vectors in the color solid.[30]

In this way, a variety of DL and SDL lamps were commercialized in the 1950s. However, since these lamps were 20–30% less luminous than those that could be produced using calcium halophosphate, and since the color-rendering concept was not accepted widely by the public, sales were generally poor. For this reason, there were no major developments in this area in the first half of the 1960s. In 1966, the luminous flux of a 40 W DL lamp reached 2500 lm[31] by the addition of red-emitting $(Sr,Mg)_3(PO_4)_2{:}Sn^{2+}$ [32,33] to the calcium halophosphate phosphor. The poor sales situation, however, did not change.

In 1965, a method for evaluating color-rendering properties was established by the *Commission Internationale de l'Eclairage* (CIE).[34] To the special color-rendering indices (R_9–R_{14}), Japan added its own index (R_{15}), appropriate to the facial skin color of Japanese women. With the establishment of this method for the evaluation of color rendering, it became much easier to tailor the lamp spectrum to specific purposes, and it became possible to compare the rendering of different lamps using a common measure.

In 1965, the Japanese Society of Printing Science and Technology announced that a lamp with color temperature of 5000 K, $R_a \geq 95$, and energy of mercury lines less than 15% of the total output was desirable as a light source for evaluating color.[35] This 5000 K temperature had a good balance of energies in the blue and red regions, producing a "natural" light. Thereafter, the color temperature of DL lamps constructed changed throughout the early 1970s, from 4300 K (previously popular whites) and 6500 K (daylight colors) to 5000 K. Nonetheless, sales still did not grow appreciably, due to the low luminous flux of these lamps. It was at the end of 1977 that a sufficiently high luminous flux fluorescent lamp with good rendering properties (the modern three-band type using rare-earth phosphors) was brought onto the market by Matsushita Electric.[36] The lamp at last broke through the DL barrier. As people realized that this type of lamp was suitable for household lighting, sales have increased steadily despite the higher price. Today, products with the three-band phosphor represent a far larger business of the market than those with calcium halophosphate.

18.2.3 *Rare-earth phosphors for three-band type lamps and widespread applications (1980–)*

Koedam (Philips) and Thornton (Westinghouse) had already pointed out in 1971 that combining three spectral bands having narrow half-widths of the primary colors (blue, green, and red) could produce high luminance and high color-rendering properties simultaneously.[37,38] A paper[39] on a lamp that combined the phosphors known at the time to have narrow luminescence bands (blue: $Sr_5(PO_4)_3Cl{:}Eu^{2+}$,[40] green: $Zn_2SiO_4{:}Mn^{2+}$, red: $Y_2O_3{:}Eu^{3+}$) appeared the next year (1972). Of these, blue- and red-emitting phosphors contain the rare earth element europium. These phosphors could also be called rare-earth phosphors, as it would be reasonable to say that, following the color picture tubes (1967), fluorescent lamps for general lighting purposes also entered the age of rare-earth phosphors with the appearance of the three-band lamps. Note that for special purposes, Eu^{2+}-doped phosphors had been in use ($SrFB_2O_{3.5}{:}Eu^{2+}$ for black light and $Sr_2P_2O_7{:}Eu^{2+}$ as a light source in diazo-type copying machines) since 1968.[41–43]

In 1974, Philips developed two new phosphors;[44] green-emitting $(Ce,Tb)MgAl_{11}O_{19}$, in which Tb^{3+} emits light with narrower lines (peak wavelength at 544 nm) than Mn^{2+}, and blue-emitting $BaMg_2Al_{16}O_{27}:Eu^{2+}$. These phosphors, combined with $Y_2O_3:Eu^{3+}$, made it possible for lamps to have both a higher luminous flux, above 80–82 lm/W, and a higher color-rendering index, $R_a = 85$, than those using calcium halophosphate (80 lm/W, $R_a = 65$). Three-band type fluorescent lamps in Japan originated from this combination. Subsequent efforts to improve the green- and blue-emitting phosphors were made mostly by Japanese manufacturers and by Philips; a new green-emitting $Y_2SiO_5:Ce^{3+},Tb^{3+}$ was commercialized in 1977,[45] followed by others, $LaPO_4:Ce^{3+},Tb^{3+}$ (1981)[46] and $(Ce,Gd,Tb)MgB_5O_{10}$.[47] Three-band type lamps utilizing a Eu^{2+}-activated alkaline-earth chlorophosphate (1978, 1980) as a blue component also appeared.[48] Since these phosphors are expensive, double-layer coating of the three-band phosphor and calcium halophosphate was also contrived at that time to reduce cost.[49]

In 1978, an energy-saving lamp was commercialized with a power consumption 6–10% less than that of previous lamps by using narrower diameter tubes and increasing the number of discharge gas species.[50] Subsequently, this technology was applied to three-band fluorescent lamps. Thereafter, manufacturers made efforts to improve phosphors and coating technology, resulting in, for example, a 30% increase in luminous flux from 1670 lm (1978), through 1950 lm (1983), to 2200 lm (1985) for the 30 W 5000 K circular lamp. In 1981, lamps with color temperatures of 6700 and 4200 K were added to the lineup (see Figure 1 for the luminous flux improvement for the straight-type 40 W lamp).

In addition to the DL and the three-band type lamps described above, the excellent deluxe (EDL) lamp series was available to meet demands in special fields such as color printing, where light sources are required to have as high a color rendering as possible.[51] For these lamps, a Mn^{4+}-activated phosphor layer having a yellow body color was formed between the other phosphor layers and the tube glass in order to reduce the mercury line intensity in the blue region. This phosphor layer structure required, however, troublesome procedures for color adjustment in mass production. In 1978, a new blue-green-emitting phosphor, $2SrO\cdot 0.84P_2O_5\cdot 0.16B_2O_3:Eu^{2+}$, with peak wavelength at 480 nm was developed.[52] It was then demonstrated that even a single layer consisting of this phosphor blended with the $(Sr,Mg)_3(PO_4)_2:Sn^{2+}$ phosphor could give the lamp R_a of 99, with a 20% increase in luminous flux. Similar blue-green-emitting phosphors, $(Ba,Ca,Mg)_5(PO_4)_3Cl:Eu^{2+}$ (1982),[53] $Sr_{0.96}Mg_{0.81}Al_{5.44}B_{0.02}O_{10}:Eu^{2+}$ (1983),[54] and $BaMgAl_{10}O_{17}:Eu^{2+},Mn^{2+}$,[55] were developed and commercialized later.

These blue-green-emitting phosphors were added to the three- (blue-, green- and red-emitting) phosphor blend to create the 6700 K color temperature with improved color rendering.[56] Further, a 5000 K lamp for general illumination purpose with a blend of five phosphors, (i.e., the blue-green-emitting and the deep-red-emitting magnesium fluorogermanate phosphors added to the three primary-color-emitting phosphors), appeared on the market[57] in 1990.

The phosphors for the three-band type are sometimes known by their abbreviated names as the number of phosphors has increased dramatically. The abbreviated names are: BAL ($1.29(Ba,Ca)O\cdot 6Al_2O_3:Eu^{2+}$, 440 nm); BAM ($BaMgAl_{10}O_{17}:Eu^{2+}$, 450 nm); SAL ($2SrO\cdot 3Al_2O_3:Eu^{2+}$, 460 nm); BAE ($BaO\cdot 4Al_2O_3:Eu^{2+}$, 480 nm); SAE ($4SrO\cdot 7Al_2O_3:Eu^{2+}$, 490 nm); CBT ($(Ce,Gd,Tb)MgB_5O_{10}$, 545 nm); LAP ($(Ce,La,Tb)PO_4$, 545 nm); SCAP ($Sr_5(PO_4)_3Cl:Eu^{2+}$, 445 nm); CAT ($(Ce,Tb)MgAl_{11}O_{19}$, 545 nm); and YOX ($Y_2O_3:Eu^{3+}$, 611 nm). Among them, the various aluminate phosphors were mainly developed by researchers at Philips following detailed crystallographic and spectroscopic studies,[58] though several preliminary studies were performed earlier in the United States and Japan.[59] The chemical composition of BAM was originally proposed to be $BaMg_2Al_{16}O_{27}$, but a true single phase was later found to take the form $BaMgAl_{10}O_{17}$.[55] The latter showed better performances, both in the lamp manufacturing process and in lamp operation.[60] Other than the fluorescent lamps, some of the aluminate family phosphors have also been used in plasma display

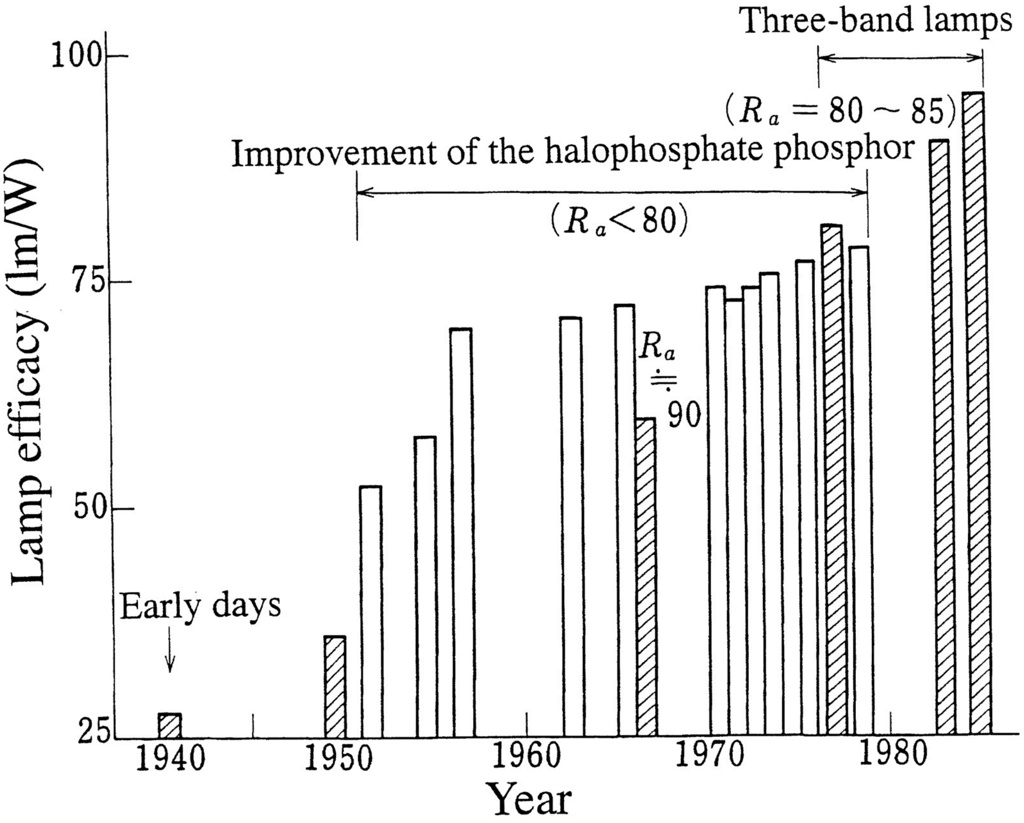

Figure 1 Increase in lumen efficacy of fluorescent lamps (40 W). Shadowed bars show the values for high color-rendering lamps with blended phosphors.

panels. The long-persistent oxide phosphor $SrAl_2O_4$:Eu^{2+},Dy^{3+}(Nd^{3+}) was also developed using an aluminate host;[61] it was utilized by a Japanese company to serve as a component of a lamp capable of illumination even during power outages.[62]

After the oil crisis in 1973, fluorescent lamps with a light color approximating that of energy-consuming incandescent lamps (color temperature 2800–2900 K) were developed using Mn^{4+}- and Sn^{2+}-doped phosphors.[63,64] Their R_a and efficiency were low, however, and the light color was still quite different from that of the incandescent lamps; therefore, they were not widely used. On the other hand, a ball-shaped fluorescent lamp was put on the market[65] in Japan in 1980. This lamp used three-band phosphors, and could produce a light color close to that of the incandescent lamp. In addition, the durability of the rare-earth phosphors under high load conditions made possible the miniaturization of the lamp. A ballast, a starter, and a folded saddle-shaped fluorescent tube were integrated in a single unit covered with a glass or plastic outer globe. The lamp socket was the same as that used in conventional incandescent lamps, so that the same fitting is used. This type of lamp was made possible by the advent of rare-earth phosphors.

Various types of the miniaturized fluorescent lamp have been developed since then.[66] They differ in lamp structure (with or without the outer globe; combination of one, two, or three U-type tubes; short straight tubes bridged like a H; and helicals), input power (13–55 W), and light color. In Japan, lamps that require separate operating circuit units are called compact lamps in the narrow definition. In addition to the conventional hot-cathode type, with or without ballasts, the electrode-less type lamp in which the discharge plasma is produced by inductively coupled radio frequency power was also introduced in the market. They are now recognized as a new type of light source rather than mere substitutes for incandescent lamps.

For the development of small lamps, decrease in luminous efficacy caused by high-power density loading on the tube wall and higher temperature operation had to be avoided. In particular, the degradation caused by the interactions of mercury with glass and phosphors have been investigated in detail, in addition to the degradation of phosphors themselves. For high-load lamps, blackening of the glass due to mercury penetration is considerable.[67] A thin powder layer (or continuous film) consisting of alumina or rare-earth oxides is generally deposited between the phosphor layer and the glass wall to reduce or prevent such interactions.[68] The extent of mercury oxide deposition on phosphor particle surfaces leading to the blackening of the phosphor layer was found to be dependent on the type of phosphors being employed.[69] The reason for the dependence was attributed to the difference in the contact charging tendency, defined by Oguchi and Tamatani between the phosphor particle surface and mercury oxide.[70] Appropriate colloidal oxide deposition on phosphor surfaces has been shown to be effective in preventing the blackening.[71] Lamp lives have increased markedly in the past few years; for example, the life of an 85 W electrode-less compact fluorescent lamp has increased to 60,000 h.[72]

Recently, studies of efficiencies, discussed above, were deemed important from the global environmental viewpoint as the total mercury consumption needs to be reduced.[73] Electric power production, when obtained from fossil fuels, affects the environment by generating unwanted emissions (e.g., NO_x, SO_2, and CO_2). Further, fossil fuels release other toxic materials, such as mercury. The mercury emitted by these sources in producing power to operate a fluorescent lamp has been calculated to exceed the mercury dose in the lamp itself. From such calculations it can be concluded that less mercury is released into the environment per lumen-hour of use of a fluorescent lamp compared with similar use of an incandescent lamp. Therefore, the increase in the lamp life and lumen efficacy, as well as the reduction in mercury dose in the lamp, contributes significantly to the improvement of this environmental problem. The techniques developed for increasing the life of a compact fluorescent lamp can also be applied to conventional lamps. Lifetimes of 30,000 h and mercury dose reduction to 3 mg have been achieved in improved lamps used for general illumination use; in contrast, the numbers are 6,000 h and more than 10 mg for conventional lamps.[74]

Other than conventional and miniaturized compact lamps, a variety of lamps have been developed and their production is increasing.[75] For backlighting the liquid crystal displays (LCDs), narrow-tube fluorescent lamps with diameter as small as 2.6 mm are being produced; though their electron emission efficiency is low, these lamps generally use cold cathodes because of their reliability throughout the lifetime of the tube. Low-pressure xenon discharge lamps are used for indicators in automobiles and in office automation equipment because this type of lamp maintains its efficacy, even at low ambient temperatures.

18.3 Phosphors for high-pressure mercury vapor lamps

A lamp similar in structure to the modern high-pressure mercury vapor lamps used for such purposes as illuminating streets was developed in 1933 by Ryde of the General Electric Company (Britain)[3]; soon thereafter, their commercial production began in Japan (1934–1935)[76] and elsewhere. These lamps did not use phosphors; but later, proposals were advanced in Britain and Germany[5,77] to coat the outer tubes of the mercury lamps with sulfide phosphors to compensate for their poor spectral intensity in the red region. According to Riehl,[77] $ZnS{\cdot}CdS(30\%){:}Cu$ (620 nm) suited this purpose. Sulfides, however, have poor temperature characteristics and deteriorate easily; further, because of their strong body color, they absorb the visible mercury emissions, resulting in an overall decrease in lamp luminous efficacy.

Meaningful progress in color-corrected mercury vapor lamps took place after the end of World War II. Several deep-red-emitting phosphors were already known at that time, including $Mg_2TiO_4:Mn^{4+}$,[78] $3.5MgO{\cdot}0.5MgF_{2{\cdot}}GeO_2:Mn^{4+}$,[79] $6MgO{\cdot}As_2O_5:Mn^{4+}$,[80,81] $(MgO{\cdot}Li_2O){\cdot}0.1Sb_20_3:Mn^{4+}$,[82] and $2(Ba,Sr)O{\cdot}Li_2O{\cdot}SiO_2:Ce^{3+},Mn^{2+}$.[83] Among them, arsenate and fluorogermanate phosphors were used in commercial lamps. In Japan, nontoxic fluorogermanates were used primarily, and fluorescent mercury lamps employing this phosphor appeared on the market in 1954 and 1955.[84] The original form of the phosphor was $2MgO{\cdot}GeO_2:Mn^{4+}$ (1936).[85] A modified composition, $4MgO{\cdot}GeO_2:Mn^{4+}$ (1944),[86] showed a five fold improvement in brightness under 365 nm excitation. Further modification of the phosphor by introducing a small amount of fluorine, $3.5MgO{\cdot}0.5MgF_2{\cdot}GeO_2:Mn^{4+}$ (1950),[79] improved its temperature characteristics; the fluorinated material exhibited 1.5 times higher brightness at the high temperatures inside the lamp (about 350°C) than at room temperature.

In 1953, Butler[28] developed the alkaline-earth orthophosphate phosphors activated with Sn^{2+}. This family of phosphors had high luminescence efficiency and good temperature characteristics for a wide range of practical uses. The orthophosphates showed polymorphism, and in most cases there are luminescence bands from both α- (495 nm) and β-forms (630 nm). It was found for these Sr salts that partial replacement of Sr with Zn or Mg suppressed the formation of the α-form, resulting in a red-emission only suitable for mercury lamp use.[87,88] In 1956 and 1957, $(Ca,Zn)_3(PO_4)_2:Sn^{2+}$,[89,90] $(Sr,Zn)_3(PO_4)_2:Sn^{2+}$,[88,91] and $(Sr,Mg)_3(PO_4)_2:Sn^{2+}$ [87,88,92] were brought into use in the United States. In Japan, a lamp coated with $(Ca,Sr)_3(PO_4)_2:Sn^{2+}$ was commercialized in 1957, and named "silver white."[93] This phosphor was replaced in the next several years by $(Sr,Zn)_3(PO_4)_2:Sn^{2+}$, and then by $(Sr,Mg)_3(PO_4)_2:Sn^{2+}$. In a 1959 mercury lamp catalog,[94] several color types of fluorescent mercury lamps are listed, depending on their field of application, as shown in Table 6. At that time, some of the lamps were coated with color pigment filters on the outer face of the bulb to reduce the intensity of blue or yellow emission from the discharge.

In 1966, Pallila's group showed that the rare-earth phosphor $YVO_4:Eu^{3+}$ was useful not only in CRTs, but also in mercury-lamp downconversion.[89] The vanadate used had the advantage of not absorbing the mercury emissions in the blue region, and it came to replace $3.5MgO{\cdot}0.5MgF_2{\cdot}GeO_2:Mn^{4+}$. Since then, it has been replaced by the solid solution phosphor, $Y(V,P)O_4:Eu^{3+}$, currently in use, which has better luminous flux maintenance properties.

18.4 Photoluminescent devices from 1995 to 2005

18.4.1 Fluorescent lamps

In manufacturing general purpose illumination fluorescent lamps, energy-saving and environmental issues have been the major driving forces for the technological improvements in the last decade. Technologies have been developed to achieve mercury reduction in lamps[95] and recycling of used lamps,[96] as well as reduction in bulb diameter, high-frequency operation, and further miniaturization. Electrode-less lamps are now widely available in the market. Mercury-less discharge has been studied intensively. For self-ballasted compact fluorescent lamps, run-up speed has been increased greatly by applying appropriate mercury amalgam and by improving the lamp structure, including electric circuits.[97] Helical and spiral tubes have been adopted in addition to those based on the U-shaped tubes.[98] Spherical and thermally durable $BAM:Eu^{2+}$ phosphor was used by a company for a certain period.[99] Blue-green-emitting $(Ba,Sr)MgAl_{10}O_{17}:Eu^{2+},Mn^{2+}$ was optimized for use as a component of the three-band phosphor in high color-rendering fluorescent lamps.[100] However, generally, change concerning phosphors was not significant during this period.

Table 6 Examples of High Pressure Mercury Vapor Lamps

	Mercury lamp	Fluorescent mercury lamp			
Lamp type	H	HF	HF-SW (Silver-white)	HF-Y (Yellow)	HF-DL (Natural color)
Phosphor	—	$3.5MgO \cdot 0.5MgF_2 \cdot GeO_2:Mn^{4+}$	$(Ca,Sr)_3(PO_4)_2:Sn^{2+}$	$(Ca,Sr)_3(PO_4)_2:Sn^{2+}$	$3.5MgO \cdot 0.5MgF_2 \cdot GeO_2:Mn^{4+}$
Filter	—	—	—	Yellow pigment	Red-violet pigment
Luminous flux (lm)	20,000	18,000	22,000	15,000	14,000
Application	Garden lighting	General lighting	Factory lighting	Parking space lighting	Shopping street lighting

Production scale of cold-cathode fluorescent lamps (CCFL) has grown very rapidly in the last decade as they emerged as the dominant light sources for backlighting LCDs (see Section 18.11). As one of the means of elongating operation life,[101] a protecting layer made of alumina or rare-earth oxide between the inner bulb wall and a phosphor layer has become necessary.[102] Continuing efforts have been made to improve the life performance of three-band phosphors, which have been used throughout the last decade. Interest in phosphors has increased for enlarging the color gamut area in LCD-TVs. Two types of CCFLs were developed and introduced into the market in 2005: one has a deep-red emission added to the conventional red, green, and blue emissions,[103] and the other has adopted new green- and red-emitting phosphors with suitable color filters.[104] Using the "spectrum" sequential LCD combined with two different types of CCFLs, a six-primary-color LCD display was also demonstrated.[105] Prompted by the evolution of LCDs with faster response properties, phosphors with a shorter luminescence decay time have been proposed.[106] Competition from CCFLs to other light sources that do not use mercury will be severe in the near future; intensive studies have been done on light sources such as rare-gas discharge lamps and LEDs for backlighting.

18.4.2 *White light-emitting diodes*

Recently developed white light-emitting diodes (white-LEDs), which combine a blue- or a near-UV-LED with phosphors, paved the way for new mercury-less solid-state light sources. Only a brief description on their progress is given here, since their advent is too recent for a detailed development history. Readers should refer to Sections 3.14 and 5.9.

Phosphors have been used as wavelength converters for several centuries. Almost all the light-emitting devices described in this book utilize phosphors that convert the absorbed energy of gamma rays, UV rays, and visible light to visible light. The idea of converting the wavelength of light emitted from LED to a different wavelength is also old (see Section 12.1). Two years before commercializing the modern GaN-type blue-LED in 1993, the inventor, Nakamura of Nichia, filed an application for a patent for a wavelength-converted diode, for which his blue-emitting diode was combined with fluorescent dyes and pigments capable of absorbing the blue light and emitting light at a longer wavelength than the blue.[107] In 1996, Nichia filed an application for a patent for white-LEDs combining the blue-LED with complementarily yellow-emitting YAG:Ce-type phosphors.[108] In the same year they were commercialized to be used mainly for backlighting in cellular phones.

Soon after the appearance of the blue-LED-based white-LED, near-UV-LED-based white-LED was proposed and commercialized[109] using white-emitting phosphor blends. In 1998, a 5-year national project called "The Light for the 21st Century" was launched in Japan with the aim of developing a highly efficient light source based on near-UV-LED and the phosphor system (60 to 80 lm/W by 2003, and 120 lm/W by 2010), in order to reduce the amount of energy used for lighting. It was considered that the efficiency of electricity-to-light conversion in GaN-type LEDs could be made higher in near-UV than in blue-spectral region. In 2003, the project achieved the external quantum efficiency surpassing the goal (40%) set for an LED for emission centered at 400 nm. The luminous efficacy of the white-LED was, however, 20–30 lm/W using blue-$(Sr,Ca,Ba,Mg)_5(PO_4)_3Cl:Eu$, green-ZnS:Cu,Al, and red-$La_2O_2S:Eu$ phosphors.[110]

Meetings in Japan and overseas concerning the white-LEDs have attracted many researchers. Worldwide development efforts have focused on LED chips, phosphors, and packages. The luminous efficacy of the blue-LED-based white-LED has increased rapidly from 5 lm/W at an early stage of development, mainly due to the increase in the external efficiency of the blue-LEDs; it reached 50–70 lm/W in a commercially available product and 80–113 lm/W in a laboratory prototype in 2005,[111,112] which is larger than that of a typical fluorescent lamp. New red-emitting phosphors capable of absorbing blue light were developed, which overcame the shortcoming of low color-rendering properties of the blue-LED-based white.[113] Power LEDs that can be operated under high input power of more than 1 W have been commercialized (conventional LEDs are operated at 0.07 W input). The price of the blue-LED-based white-LED has been lowered. At present, most white-LED commercial products are based on blue-LED. By using a diode laser to excite phosphors, very high brightness comparable to that of HID lamps has also been obtained.[111] These advances have widened the application fields to include display, optical communication, etc., in addition to illumination.

Phosphors have to meet the excitation of near-UV or blue lights from LEDs, which have wavelength longer than 254 nm in fluorescent lamps. Conventional phosphors including those used for fluorescent lamps and CRTs and those reported in the literature have been extensively reexamined with respect to luminous efficacy, color rendering, and durability in LEDs[114] (see Section 5.9). For this application, Eu^{2+}- and Ce^{3+}-doped phosphors are promising candidates,[115] since their 5d level energies (and excitation bands) are known to move depending on their surroundings in crystal lattices. For combination with blue-LED and YAG:Ce-type phosphors, $(Y,Gd)_3(Al,Ga)_5O_{12}:Ce^{3+}$, which was first proposed by Nichia for the LED, and whose photoluminescence properties had been well known because they had been used as lamp and CRT phosphors since the 1970s,[116] is still widely used. For near-UV excitation, other phosphors are being applied, because YAG:Ce phosphors absorb little light in this wavelength region. Several proposed oxide phosphors,[114] such as alkali-earth orthosilicate activated with Eu ($Me_2SiO_4:Eu^{2+}$), Mg-fluorogermanate activated with Mn^{4+}, BAM:Eu^{2+}, and BAM:Eu^{2+},Mn^{2+}, have sufficiently high quantum efficiencies for practical use. ZnS-type sulfides were found to have some deterioration problems under intense light irradiation, though they do offer the advantage of excitation bands with wavelength longer than those of oxides.

Newly developed nitride and oxynitride phosphors such as Eu^{2+}- or Ce^{3+}-activated Me-Si-N,[117] Me-Si-O-N,[118] Me-Al-Si-N,[119] and Me-Si-Al-O-N[120] compounds, are promising for this purpose (see Section 3.14). They are mechanically and chemically more stable than sulfides, in addition to offering the advantage of an excitation band with a wavelength as long as that for sulfides through strong covalent bonding. At present, the red, yellow, green, and blue emission colors can be obtained by using nitride phosphors.[121] Based on the increased scientific interest in nitride compounds in the 1990s, several groups in Europe and Japan developed these new phosphors from the late 1990s to early 2000s.[122] The manufacturing techniques for nitride ceramics, which were intensively studied in the 1980s, such as synthesizing nitride powders, and sintering at a high temperature under pressurized atmosphere, as well as the accumulated knowledge concerning nitride compounds, were utilized effectively for phosphor development. Further findings can be expected, because the study of nitride compounds for application as phosphors is still in its infancy compared with oxide and sulfide phosphors.

The history of phosphor development includes several instances of the birth of important new phosphor families addressing the requirements of new light-emitting devices. An example is a rare-earth oxysulfide family originating from a red-emitting $Y_2O_2S:Eu^{3+}$ for color CRTs. Phosphors from $Y_2O_2S:Eu^{3+}$, modified by different rare earth elements (Ln) such as $Ln_2O_2S:Tb^{3+}$ and $Ln_2O_2S:Pr^{3+}$, constitute a family of oxysulfide phosphors, several of which were in turn applied to other new devices (ceramic scintillators) or to improve old devices (intensifying screens). Likewise, the nitride phosphors developed for white-LEDs will form a new family of phosphors, which will be important to industry as well as to science.

18.4.3 Plasma display panels

The history of commercial plasma display panels (PDPs)[123] started with the introduction of Nixie tubes developed by Burroughs in the early 1950s, which utilized direct current (DC) discharge of Ne gas. The Japan Broadcasting Corporation (NHK) started development of a color DC-PDP in 1972, with the hope of realizing a wall-hanging high definition (HD) TV. Intensive efforts devoted to developing color DC-PDPs over a long period, however, did not result in the commercialization of such a TV, because brightness and operating life did not reach practical levels. Alternative current (AC) PDP was invented by a team at the University of Illinois in 1964, which subsequently investigated a color PDP using phosphors in 1967. The present-day PDP TV is based, however, on the 21-in. diagonal full-color AC-PDP commercialized in 1993 by Fujitsu, which had begun studying the subject in the late 1970s. Important technological breakthroughs for realizing the panel were the development of the surface discharge structure (in the late 1970s; greatly reduced phosphor degradation), the three electrode structure (in 1983; simplified driving circuits and display control), the reflection structure (in 1989; greatly increased brightness), the stripe rib structure (in 1992; realized high resolution), and the address display period separation (ADS) method (in 1992; realized high speed and stable addressing). Shinoda of Fujitsu has named 2001 as the first year of the plasma television, since it was the year in which the number of plasma TVs sold for home use first surpassed the number sold for business use.[123] In 2005, mainly larger than 37-in. diagonal PDP TVs including HD TVs were being sold in Japan. Even a 102-in. diagonal TV was demonstrated in 2004. The luminous efficacy is expected to grow rapidly from about 1.5 lm/W for the presently commercialized PDPs, since values of 3.7–5.7 lm/W have already been realized in small-sized laboratory PDPs by optimizing the panel structure, the Xe gas density, and the operating method.

At an early stage of PDP development at NHK, elementary selection of phosphors was already done, by evaluating the excitation spectra in the vacuum-UV region including the wavelength of Xe gas discharge (see Sections 10.1–10.5). During the past decade, investigation has focused once again on modifying the existing phosphors for PDPs, for example, by means of activator doping quantity (reducing luminescence decay time in Zn_2SiO_4:Mn^{2+}), particle surface treatment (improving electric properties of Zn_2SiO_4:Mn^{2+} particle surface), and fabrication process (reducing the deterioration in BAM:Eu during panel fabrication and operation). In particular, several groups have studied the reasons for the deterioration of the blue-emitting BAM phosphor independently or in collaboration.[124] Oxide phosphors other than the conventional BAM:Eu (blue), Zn_2SiO_4:Mn^{2+} (green), and (Y,Gd)BO_3:Eu^{3+} (red) phosphors have also been proposed[125] for a blue component with less deterioration, for a green component with surface electric properties similar to those of the blue and red, and for a red component with more saturated color. Several of these phosphors are being used to a certain extent by some companies.

Studies on PDP phosphors have enriched scientific knowledge in the field of phosphors. Analytical tools such as transmission electron microscopy, X-ray absorption fine structure analysis using synchrotron radiation, and theoretical molecular orbital calculation[126] have been applied effectively to improve phosphors. Increased interest in the vacuum-UV region has lead to accurate experiments on optical spectra using synchrotron radiation. A diagram containing energy levels in the higher energy region than that addressed by the Dieke diagram, which has been a useful standard for understanding optical properties of trivalent rare-earth ions for almost half a century, is now available.[127,128]

18.5 *Phosphors for black-and-white picture tubes*

18.5.1 *Early history (till 1955)*

Cathode ray tubes (CRTs), in which a cathode ray beam (electron beam) is scanned over the inside of the tube to excite a phosphor layer, were first described in 1897 by Braun.[129,130] It was already known at that time that a large number of ores, glass, gemstones, rare earth compounds, alkali-earth sulfides, etc. emitted light under cathode ray irradiation.[131] Thereafter, CRTs were used in measuring instruments. It was not until the beginning of research on televisions that CRT structures and phosphors used in them were greatly improved. Soon after J. L. Baird succeeded in performing the first wire-linked television experiments (1925), Takayanagi (1927) reproduced on a CRT screen the Japanese "katakana" character for "i" written on a mica wafer. This was the first demonstration[132] of an electronically scanned video image in the world.* The tube was filled with argon gas and operated at an anode voltage of 400 V. As the screen brightness was very low, the CRT was placed in a black box and was observed by "peeking in" on the inside surface of the fluorescent screen. The screen was composed of a thick coating of the blue-emitting $CaWO_4$ phosphor.[133] In 1930, Asao made a high-vacuum CRT with an anode voltage of 2 kV. The screen was thinly coated with the green-emitting Zn_2SiO_4:Mn^{2+} phosphor and showed a brightness about 100 times that of Takayanagi's tube; it could be viewed from the outer surface of the screen. In May of the same year, this rudimentary TV was demonstrated before the Emperor. Since tubes in those days had face plates only 2–3 mm thick, one of those involved in the presentation commented later[133] that the tube did not explode "thanks to the grace of God and the help of divine Providence".

In the United States too, green-emitting Zn_2SiO_4:Mn^{2+} or ZnS:Cu was used for the early black-and-white picture tubes.[134] The white-emitting phosphor consisting of blue-emitting ZnS:Ag and yellow-emitting (Zn,Cd)S:Ag was invented[135] in 1931. In Japan, development of the sulfide phosphors for CRT use began around 1938.[136]

Worldwide research on television became active in the later half of the 1930s, led mainly by RCA. In Japan, plans were made for the TV broadcast of the Tokyo Olympic Games scheduled to be held in 1940. In 1939, various television broadcasts were exhibited in some Japanese department stores.[133] In addition to white-emitting screens, green-emitting screens were also displayed, and a survey was conducted to determine which color people preferred.[137] However, with the start of World War II, television research stopped completely.

Before the war, efforts were made to develop a large-sized screen that could be seen by many people at the same time. A TV screen as big as 160×200 cm^2 was obtained with a projection system employing a CRT with an acceleration voltage of 50 kV and a magnifying lens and assorted optics to enlarge the CRT screen image. For such a CRT, the Zn_2SiO_4:Mn^{2+} phosphor was used because of its low brightness saturation even under high current density excitation; an electrically conductive graphite screen was installed on the screen to prevent electrical charging.[133] Around 1950, there was an attempt to redevelop this projection-type television, but since the screen brightness was low at that time, the image was too dim to be of much use. In the United States and Europe, projection televisions were developed for theaters, and white-emitting phosphor screens of $(Zn,Be)_2SiO_4$:Mn^{2+} + ZnS:Ag and $(Zn,Be)_2SiO_4$:Mn^{2+} + $CaMg(SiO_3)_2$:Ti^{3+} were put to practical use.[138]

During the war, CRTs for radar systems were produced using ZnS:Ag,Cu. For the phosphor coating, sulfur vapor was introduced into the tube first, and when the vapor condensed on the tube wall, phosphor powder was let in the tube and allowed to adhere to the inner surface of the face plate.[133] This method, as well as the sedimentation in water-glass solution and the spray methods, which had been used before the sulfur method, were not suitable for mass production. Since 1951, the sedimentation method in an electrolyte solution that contains water–glass has been adopted most widely.[139]

---

* Baird applied the rotating Nipkow disks both for video pickup and picture reproduction. Takayanagi used mechanical scanning for the video pickup, but used a CRT for picture reproduction. In 1929, Zworykin realized a television system using electronic scanning for both image pickup and reproduction.

18.5.2 TV and other applications (1955–)

In the United States, commercial TV broadcasting using 525 scanning lines started in 1941, and the numbers of the broadcasting stations and domestic picture tubes reached 109 and 15 million, respectively, by the end of 1951. In Europe, TV broadcasting restarted in 1946–1948. In Japan, regular black-and-white TV broadcasting started in 1953. CRT development had restarted 1 to 2 years before this. In the beginning, the imported phosphor ZnS:Ag + (Zn,Cd)S:Ag was used in round face plate tubes. These tubes sometimes suffered from a problem called "high-voltage rash," i.e., the appearance of black spots on the fluorescent screen.[140] In 1954, the face plate became rectangular, but a new problem of "X-burn" appeared instead; in "X-burn," black X-shaped patterns were formed due to ion bombardment of the screen. These problems were caused by the uneven distribution of electrical charge over the phosphor screen.[141] Countermeasures such as changing flux materials during phosphor manufacturing, and depositing silica colloids on the phosphor particles were taken.[140]

In 1956, it became possible to deposit a metallic film on the phosphor screen, though the technology had been developed at RCA in 1946. This film is electrically conductive and could protect the screen from all the effects of ion bombardment, resulting in a remedy for the ion-burn problem. Furthermore, since the metal film reflects the emitted light from the phosphor layer toward the observers, it was expected to make the screen brightness twice as before. In fact, the resulting improvement in brightness was even greater. This was because an anode voltage could be applied to the screen without reductions due to space charge effects. However, since the blue-component light reflected by the metal film is absorbed by the phosphor that has a yellow body-color, uneven discoloration (called yellow center) occurs in the center of the screen, where the coating thickness is different from that in the fringe areas. To counteract this, the amounts of Cd and Ag in the phosphor were decreased to reduce the body color and to optimize the emitted color.

At this stage, the performance of made-in-Japan phosphors caught up with that of phosphors produced by DuPont and Sylvania. Afterward, during the golden age of black-and-white television lasting until 1969, ZnS·CdS(56%):Ag continued to be used as the yellow-component phosphor. In 1970, this was replaced by ZnS·CdS(14%):Cu,Al which has a modified composition of a green-emitting phosphor, developed originally for use in color television.[142] With this phosphor, the degradation that had occurred during the CRT manufacturing process was reduced, the screen brightness was improved by 10–15%, and the yellow-center problem was almost eliminated because smaller amounts of CdS in the composition made the body color paler.

The technology embodied in black-and-white television phosphors has been extended to numerous other applications such as radars, oscilloscopes, flying-spot scanners, storage tubes, computer terminal displays, projectors, etc. All these CRTs (including tricolor tubes) were usually registered with the Electronic Industries Association (EIA) in the United States. Pertinent information about the tube characteristics were publicized and a type number was assigned to the phosphor screen; phosphors commonly used in the tube were designated by the letter P followed by a number. P numbers started with P1 in 1945 and reached P57 in 1982.[143] The year of registration and the chemical compositions of some of these phosphors are shown in Table 2(b). Japan (EIAJ) followed the U.S. system and most phosphor screens were given[144] the same number with the letter B instead of P. In Europe there was another registration system.[145] In 1982, a worldwide system was proposed,[146] mainly following the European system, and is now being used instead of the P or B numbers (see Section 6.6).

The black-and-white CRTs for TV use were almost completely replaced by color picture tubes in the early 1980s. However, even after the 1980s, new phosphors were developed to meet specific needs of monochrome CRTs (Table 2(b)).[147] For example, a direct-view screen for word processors required a "paper white" color with medium decay time of around 20 ms; these characteristics are needed to image documents on the screen with a color comfortable to the eye and with reduced flicker. A blended phosphor composed of $InBO_3:Eu^{3+}$, $InBO_3:Tb^{3+}$, and ZnS:Ag was found to be suitable for this purpose,[148] replacing the green-($Zn_2SiO_4:Mn^{2+}$,(As)) and orange-($Cd_5(PO_4)_3Cl:Mn^{2+}$) monochrome screens. For screen coating, in addition to the conventional sedimentation method in an aqueous solution, silk-screening[149] and centrifugal sedimentation[150] methods have also come into practical use.

For projection systems, directionally reflective screens brought about large increases in projected screen brightness.[151] Particularly in the United States, there has been considerable demand for color TV projectors that comprise a row of three monochrome (red-, green-, and blue-emitting) CRTs, mirrors, and magnifying lenses. Japanese CRT manufacturers entered the market to fulfill this demand. From 1982 to 1988, Japan switched from the previously used green-emitting $Gd_2O_2S:Tb^{3+}$ to new phosphors such as $Y_3Al_5O_{12}:Tb^{3+}$,[152] $Y_2SiO_5:Tb^{3+}$,[153] $LaOCl:Tb^{3+}$,[154] and $Y_3(Al,Ga)_5O_{12}:Tb^{3+}$,[155] which have high luminescence efficiency at high operating temperature and under high current density. This resulted in a doubling of the luminous efficacy.[147]

In the course of applying these phosphors to the projection CRT, phosphor degradation under intense electron bombardment (electron burning) was studied extensively. This is because electron current density used for projection CRTs are more than 100 times larger than those in the direct-view CRTs. Various factors affecting the degradation were analyzed,[156] and countermeasures were taken. In addition to surface treatment of the phosphor particles, co-doping with a small amount of impurities other than the activator ions has been found to be effective in improving the lifetime of these Tb^{3+} phosphors, for example, using Yb and Si for $Y_3(Al,Ga)_5O_{12}:Tb^{3+}$,[157] Sc for $Y_2SiO_5:Tb^{3+}$,[158] and Ti for $LaOCl:Tb^{3+}$.[159] Although each of these phosphors has merits and demerits in fluorescence color, efficiency, and degradation properties, all of them are presently being used. A manufacturer has added $InBO_3:Tb^{3+}$ and $Zn_2SiO_4:Mn^{2+}$ to $Y_3(Al,Ga)_5O_{12}:Tb^{3+}$ to improve green color purity.[160] Phosphor screens, together with water-cooled CRTs and improved optics, have made it possible for an over 40-in. TV screen projected from behind to have sufficient brightness to be watched by an observer, even in a room with normal illumination. The production of this rear-type projector was accelerated in the 1990s with increasing demand for home use as well as for display uses, for example, in public spaces and arenas (and for computer game displays in so-called "game centers" in Japan).[161]

18.6 *Phosphors for color picture tubes*

18.6.1 *Early history (till 1965)*

In 1954, 12 years after the beginning of black-and-white TV broadcasting, color TV broadcasting was inaugurated in the United States, using the National Television System Committee (NTSC) color system that remained compatible with the black-and-white system (525 scanning lines, 30 frames per second, and frequency band region of 6 MHz). The original idea for a color tube had been proposed in 1938 by Flechsig;[162] the design remains in current use. RCA commercialized it in 1950 as a color picture tube comprising three electron guns, a shadow mask having 117,000 holes, and 351,000 phosphor dots.[163] Although there are variations today in the shape and number of the holes, (and correspondingly, the shape and number of the phosphor picture elements), the basic structure of a color picture tube has not changed since then, even for tubes designed for use with different broadcasting systems. PAL (phase alternation by line) is used in Britain and Germany (625 lines, 25 frames, and 7 MHz) and SECAM (*séquentiel couleur à mémoire*) in France and Russia (625 lines, 25 frames, and 8 MHz).

In Japan, regular color television broadcasting started in 1960 using the NTSC system. In 1957, test broadcasts began, and a shadow-mask type color picture tube with a round faceplate was assembled at NHK using device components imported from a U.S. company, CBS.[164] A committee was organized to promote the domestic production of color picture tubes. It was centered on NHK and its members were drawn from related government agencies, seven CRT manufacturers, four parts and materials manufacturers, and two other companies (1957–1960).[165] The committee conducted the development of a small-sized (17 in.) CRT with a rectangular face plate and with a deflection angle of 70°. In 1958, the world's first rectangular 17-in. picture tube made entirely of Japanese parts was manufactured. The fluorescent screen at the time consisted of the blue-emitting ZnS:Ag (peak wavelength of 450 nm), the green-emitting $Zn_2SiO_4:Mn^{2+}$ (525 nm), and the red-emitting $Zn_3(PO_4)_2:Mn^{2+}$ (638 nm) phosphors.[166] Following this development, color picture tube production in Japan reached a level of several hundred 14-in. tubes per month by the end of 1962. These tubes, however, suffered from a number of problems, including low brightness, long persistence of the image, an imbalance in the beam currents when producing a white screen, and chemical instability of the red-component phosphor.

In 1962 "all sulfide" phosphors appeared on the scene, and greatly reduced the shortcomings of the screens described above. These phosphors were the blue-emitting ZnS:Ag (450 nm), the green-emitting ZnS(65%)·CdS(35%):Ag (512 nm), and the red-emitting CdS(82.5%)·ZnS(17.5%):Ag (680 nm).[167] However, the problems of insufficient brightness and difficulty in photoprinting due to intense body color in the red component remained.

18.6.2 Rare-earth phosphors and screen improvement (1965–)

The concept that the ideal red-component phosphor for color televisions should have a luminescence spectrum consisting of a "sharp peak in the area of 610 nm" had already been proposed[168] in 1955. In other words, phosphors like $Zn_3(PO_4)_2:Mn^{2+}$ and (Zn,Cd)S:Ag had a disadvantage in luminous brightness as perceived by the human eye because their broad luminescence band spread well into the deep-red region where the eye is least sensitive. At the time, however, no phosphors having the ideal spectral properties were known. Extensive study of luminescence due to rare-earth ions in various oxides began subsequent to the advent of the laser in 1960; a luminescence spectrum close to the ideal was discovered[169] in $YVO_4:Eu^{3+}$ in 1962. In 1964, GTE Labs proposed that this substance would be suitable for use as the red-component phosphor for color televisions.[170] This was the first practical use of a rare-earth phosphor, and its historical significance was immense. At the time, rare-earth elements were extremely expensive, and their use in large quantities in industry was out of the question. The need for these phosphors necessitated the establishment of a rare-earth refinery industry. With the increasing popularity of color televisions, this industry grew explosively, making it possible to supply high-purity rare earths on a large scale.[171]

Despite the fact that the energy efficiency of $YVO_4:Eu^{3+}$ is less than half that of the red-emitting (Cd,Zn)S:Ag, its luminous efficacy is about 10% higher; the brightness of white produced by CRTs that combined this phosphor with blue- and green-emitting phosphors was improved by several percent. Since it had a white body color, its use shortened the UV exposure time required to prepare phosphor patterns on the face plate by photolithography, thereby increasing efficiency in the manufacturing process. Furthermore, $YVO_4:Eu^{3+}$ did not show color shift problems during the baking process and under high current density operation of the CRT. This phosphor was used only for a short time, being replaced in 1967 by the yttrium oxysulfide, $Y_2O_2S:Eu^{3+}$ (626 nm),[172] developed by RCA. Although the latter emits a more orange-hued light than $YVO_4:Eu^{3+}$, its luminous efficacy is 80% higher, resulting in a 30% increase in white brightness. The beam currents in all the guns are balanced for producing the standard white color. This phosphor has a further merit in that it is resistant to burning, even under intense electron beam irradiation. $Y_2O_3:Eu^{3+}$ (611 nm), which emits an even more orange-hued light but has a slightly higher luminous efficacy, was also used as the red component by some CRT manufacturers at that time.[173] However, the oxide was eventually replaced by $Y_2O_2S:Eu^{3+}$, since the latter had better chemical stability in the slurry and could be recycled more easily from the coating process.

Oxysulfide phosphors have high luminescence efficiency not only when activated with Eu^{3+} (red) but also with Tb^{3+} (blue-white to green), Pr^{3+} (green), and other rare earths. This family of phosphors plays an important role comparable to that of the zinc sulfide family in electron- and X-ray-excited applications.

After 1965, encouraged by the success achieved with the rare-earth red, extensive research and development were conducted on various phosphor hosts activated with rare-earth ions such as Eu^{3+} (red), Tb^{3+} (green), Eu^{2+} (violet to blue), and Ce^{3+} (UV to blue). The advantages these materials present are wide variety of luminescence colors to select from, narrow spectral band outputs, high luminescence efficiency, durability under high excitation load, and large atomic numbers for stopping power. Utilizing these advantages, they were put to use in mercury-vapor lamps (1966),[89] special-purpose fluorescent lamps (1967),[42,43,174,175] X-ray image intensifiers (1970),[176] display CRTs (1971),[177] and general purpose fluorescent lamps (1974),[36,39,44] leading to what is now known as "the age of rare-earth phosphors".

As for green-emitting phosphors in color CRTs, RCA synthesized and deployed $ZnS \cdot CdS(7.2\%):Cu,Al$ (538 nm) in 1968[142] in place of $(Zn,Cd)S:Ag$. Its use began in Japan the following year. This phosphor reduced the deterioration that takes place during the tube-baking process, and eliminated fluorescence color shifts caused by copper contamination during the phosphor-coating process.

While these improvements were being made in phosphor technology, a milestone improvement known as the "black matrix method" was introduced to CRT screens (1969).[178] Until then reduction in picture contrast due to ambient light reflection from the face plate was prevented by lowering the light transmittance of the face plate glass. In the new method, areas surrounding the phosphor dots were blackened instead. This allowed the use of glass with high transmittance as face plates; the light emitted from the phosphors could then come out through the glass without attenuation. Another innovation entailed an in-line electron-gun/slit-mask system in CRTs,[179] which is being used worldwide for TV use, replacing the combination of triangularly arrayed electron guns and round-holed shadow masks. In-line electron guns were first proposed by GE and adopted by Sony (1968, Trinitron), Toshiba (1971, slit-mask tube), and RCA (1972 precision in-line tube). These guns make color adjustments much easier. Striped phosphor pattern screens were initially introduced in Trinitron, followed by their use in slit-mask tubes and black stripe tubes (1972, Toshiba). The striped pattern allowed increased transmission of electron beams through the shadow mask (or aperture grill in the case of Trinitron), as well as increasing the ease in adjusting color. CRT screen brightness has doubled as a result of these improvements.

As can be seen from Figure 2, improvements in color picture tube brightness reached a zenith during the late 1960s. Thereafter the focus shifted to other issues. Around 1970, the cadmium pollution problem attracted much attention in Japan, and the green-emitting phosphor (Zn,Cd)S:Cu,Al was replaced by cub-ZnS:Cu,Al (530 nm) (1973).[180] The latter produces a purer green-hued light well suited to the high color temperature white (9300 K) used in Japanese color televisions. A good current balance among the three electron guns is obtained in producing this white. For the 6500 K white preferred in the United States and Europe, this phosphor led to a notable imbalance. As the proportion of made-in-Japan CRTs destined for export approached 50%, the current imbalance became an issue. To deal with the problem, a phosphor emitting a yellow color ZnS:Cu,Au,Al (535 nm) was developed.[180] It was used by about half of the country's manufacturers from 1977 onward. In the late 1980s, use of the phosphor was replaced again by that of cub-ZnS:Cu,Al in such CRTs where purer green and red colors were required for broadening the color reproduction area.

In 1982, a new screen fabricating method using photoadhesive resists was developed, and put to use for small-sized tubes[181] (see Section 4.5). This method was designed to replace the polyvinyl alcohol/dichromate/phosphor slurry method, which had been developed by RCA and used throughout the world. Although the new technique produces high-quality phosphor patterns and simplifies the production process, it has not been widely adopted for mass production.

During 1980–1990s, phosphor powder properties such as particle size distributions, particle surface treatments, and particle shapes have been improved constantly to obtain better coating properties in high-resolution (fine pitch) screens of high-definition color picture tubes and computer terminal color display tubes. In order to reduce eye fatigue due to flicker in color display tubes, increased frame frequency and sometimes long-persistence phosphors have been used.[182,183]

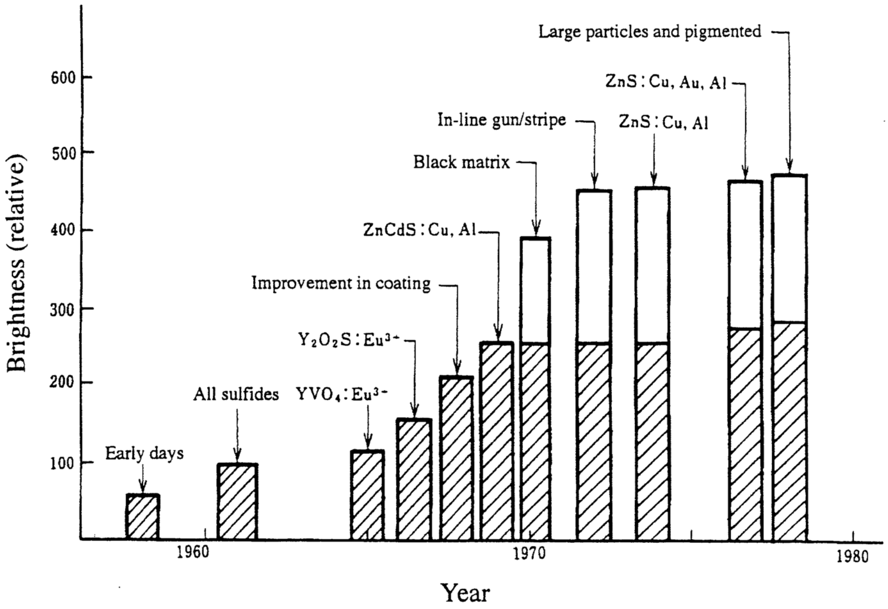

Figure 2 Increase in brightness of color picture tubes. Shadowed areas in the bars show the contribution from phosphors.

Among all the picture qualities of importance—such as color purity, contrast, resolution, and brightness—contrast and related properties have experienced most improvements due to the modification of face plates and to the phosphors themselves. Since 1978, blue and red pigments have been deposited on the blue- and red-emitting phosphor particle surfaces, respectively.[184] The blue (red) pigment absorbs the green and red (blue and green) components of ambient light without strongly absorbing the blue (red) light emitted from the phosphor, and thus enhancing the screen contrast. For the same reason,a manufacturer has tried the use of neodymium-doped glasses as the face plate,[185] to take advantage of the absorption spectrum of Nd^{3+} ions. Meanwhile, to improve contrast under weak ambient light, addition of a rare-earth green-emitting phosphor to zinc sulfide was attempted.[186] The rare-earth phosphor has linear, while the zinc sulfide has sublinear current–brightness properties. Therefore, the background light emission caused by scattered electrons in the CRT was reduced, resulting in a darker black level when rare earths were used.

In 1989, a CRT having a lavender-colored thin film coated on the outer surface of the face plate was launched in the market.[187] The film was fabricated using sol–gel film technology; the films consisted of organic pigments embedded in inorganic silica. It selectively absorbed 570 nm light to increase the contrast by 35% and the color purity by 14%. It could also be made to contain electrically conductive materials in order to reduce the electrostatic charge on the surface of the face plate. In 1994, an epoch-making technique was developed independently by Sony and Toshiba to form blue, green, and red transparent filters between the inner surface of the face plate and the respective color-emitting phosphor stripes (dots).[188] This idea was proposed long ago,[189] but remained impractical until transparent color filters could be prepared using commercial ultrafine inorganic pigments. As expected, the screen brightness was increased by 35% compared with the conventional CRT with tinted glass face plates while maintaining the same contrast value. A number of other techniques have been applied to color CRTs; for example, the use of antireflection layer coatings on the outer surface of the face plate[190] and the introduction of Invar shadow masks,[191] which have a low thermal expansion coefficient against thermal deformation (antidoming) even under high current density irradiation. These improvements are especially relevant to large-sized picture and display tubes.

18.7 *Cathodoluminescent displays from 1995 to 2005*

18.7.1 *Cathode-ray tubes*

Although no new phosphors have been adopted for direct-view CRTs in recent years, their screen-forming techniques have been improved. For example, in 2003, Sony announced an advanced phosphor screen process using a new exposure and color filter technology;[192] it applied thermal transfer film technology for coating phosphors, instead of the conventional slurry-spinning method that has been used worldwide since the early stages of CRT development. One of the other important progresses is a study on a system having more than four primary colors for widening color gamut area,[193] showing a possibility to change the design of not only CRTs but also of all the other color display devices. Although efforts such as developing thinner CRTs with an astonishingly large deflection angle,[194] have been undertaken to battle against flat panel display devices, a recent market analysis predicts that CRTs will be outdated by 2015 and subsequently phased out (the end of the CRT-life cycle).

The projection TV market has grown rapidly in the United States, Europe, and China since the mid-1990s: production surpassed 4 million units in 2002. Most of them were CRT projectors. $Y_2SiO_5:Tb^{3+}$ has survived as a dominant green-emitting phosphor since the late 1990s, although various phosphors were used previously (see Section 18.6). Spherical red-emitting $Y_2O_3:Eu^{3+}$ and green-emitting $Y_2SiO_5:Tb^{3+}$ phosphors were adopted in 2000 by a company for projection CRTs.[195] A new technique, the thermal plasma method, realized the spherical shape, which brought high resolution in a phosphor screen through close particle packing. Since 2003, projectors with liquid crystal (LC) devices or digital micromirror devices (DMD) (or digital light processing (DLP)) used in digital display engines have increased their shares in the market. Bulky and heavy CRT projectors, which previously were cheaper than other types of projectors, have fallen from favor due to, in particular, the falling prices of DLP projectors. In addition, flat panel displays such as LCD and PDP have recently made inroads in the market for TVs of 40 in. or more, which was previously dominated by projectors.

18.7.2 Field emission displays

LETI, a French government laboratory, presented a new principle in 1986[196] and demonstrated a prototype[197] of a flat panel display in 1990, which combined two techniques already developed independently: electric field emission of microtips fabricated with advanced microelectronic technology (Spindt-type field emission cathode)[198] and low-voltage cathodoluminescent phosphor layers. This was called a field emission display (FED), and showed the possibility of realizing a high-definition vacuum fluorescent display tube (VFD) that overcomes difficulties mainly attributable to the filaments used for thermoelectronic emission in previous VFDs.

Worldwide display makers and laboratories started the studies in the early 1990s. Various field emission cathodes have been proposed for FEDs in addition to the Spindt emitter:[199] carbon emitters including carbon nanotubes (CNT) and new electron sources other than carbon, such as surface conduction electron (SCE) emitter, Pt/SiO_x/Si/Al structure emitter, ballistic electron surface emitter, and metal-insulator-metal (MIM) emitter. Of these, carbon nanotube devices have been most intensively studied in the hope of improving field emission characteristics by utilizing their extremely sharp needle shape and, at the same time, reducing the manufacturing cost of the cathode.[200]

Futaba, a major manufacturer of VFDs, presented an FED monochrome panel[201] in 1995 and started supplying it commercially in 1999 as audio–visual equipment (accelerating voltage of 200 V) for professional use. For color FEDs, the voltage was lower than 1 kV at an early stage of the development, but it shifted to higher voltage (3, 5, and 10 kV) at a later stage. This shift occurred due to the low phosphor luminescence efficiencies and the requirement of electroconductivity for the phosphor layer at lower accelerating voltages, whereas the high-voltage FED can utilize the high-efficiency phosphor screen combined with an electroconductive and light-reflective metal film. When compared with other flat panel displays such as LCD and PDP, it has the advantages CRTs and VFDs, and above all, has lower power consumption. Several companies have demonstrated full color FED TV panels at international meetings and exhibitions, for example, LETI (Spindt; 6 in.; 400 V; 1991),[202] Motorola (Spindt; 5.6 in.; 5 kV; 1998),[203] Candescent-Sony (Spindt; 13.2 in.; 7 kV; 2000),[204] Samsung SDI (CNT; 32 in.; 1 kV; 2002),[205] Futaba (Spindt, 11.3 in.; 3 kV; 2004),[206] and SED (a joint venture of Canon and Toshiba) (SED; 36 in.; 10 kV; 2005).[207] In 2003, a 3-year national project for realizing FED operable with carbon nanotubes, discovered by a Japanese,[208] started in Japan.[209] Although no full-color FED had been commercialized by 2005, Futaba and SED announced that they would mass produce FEDs within a few years. The rapidly falling prices of competitors, namely LCD TVs and PDP TVs, at present are considered to be the most important factor determining the fate of FED TVs in the near future.

Compared with conventional CRTs, the accelerating voltage of FEDs is lower and the electron beam current is higher. Deterioration and brightness saturation under high excitation densities have posed problems in the development of FEDs. Experience and improvements concerning projection CRTs and VFDs,[210] which are also operated under high-density electrons, have been utilized for FED phosphors. For the monochrome FED, electroconductive ZnO:Zn was used, For low- to mid-voltage color FEDs, Y_2O_3:Eu^{3+}, Y_2SiO_5:Tb^{3+}, and Y_2SiO_5:Ce^{3+} phosphors are applied as red, green, and blue primaries, respectively;[206] they show less brightness saturation under high excitation density than conventional P22 phosphors for CRTs. Reasons for the deterioration and brightness saturation[211] have been studied. For blue-emitting ZnS:Ag phosphors, morphology changes on particle surface layers under electron irradiation have been clarified by the TEM technique[212] and by the various Ag site distributions elucidated by the MAS-NMR technique.[213] A nitride phosphor, blue-emitting GaN:Zn, has been developed, and shows higher durability than sulfides, though luminescence efficiency has not reached the level of ZnS:Ag.[214] In a new phosphor for low-voltage FED, red-emitting $SrTiO_3$:Pr^{3+}, prominent enhancement of the emission was observed when it was highly co-doped with Al_2O_3. The enhancement was correlated with the disappearance of defect layers that existed without Al_2O_3 doping.[215] This finding may help to clarify the longstanding unsolved problem that a considerable number of phosphors show the best luminescence performance at compositions deviating from their stoichiometric ones.

18.8 Phosphors for X-ray

It is well known that Roentgen discovered X-rays in 1895 by noticing the induced fluorescence from a barium platinum cyanide phosphor lying near a vacuum tube with which he was working. This discovery induced a sensation worldwide. In the following years, a large number of compounds were tested for induced fluorescence with X-ray irradiation by many researchers including Edison, who developed the fluoroscopic screen made of barium platinum cyanide.[216] According to Harvey,[217] the principle of X-ray intensifying screens is found in a work by Pupin, carried out as early as 1896. He showed a photograph of a human hand injured by buckshot that was taken by combining a fluorescent screen with a photographic plate to shorten the X-ray exposure. In 1897, the bright radiofluorescence of sheelite ($CaWO_4$) was discovered by Arnold and Precht[217]; this mineral is a representative X-ray phosphor and is still in use today. X-ray applications to medicine have evolved in parallel with phosphor developments.[218] This section describes the developmental history of these applications limited to Japan especially in the early stages, since much information regarding worldwide developments was not available for various reasons.

18.8.1 Fluoroscopic screen

The history of fluoroscopic screens in Japan, which were used to downconvert X-ray images to the visible, started (see Table 2(c)) when Toshiba began research into green-emitting $BaPt(CN)_4 \cdot 4H_2O$ and white-emitting tungstate phosphors, because World War I (1914) interrupted the availability of imported screens. It was not until 1921, however, that products for research use actually appeared on the Japanese market.[219] The green-emitting screen was found to be chemically unstable due to the water of hydration it contained; hence, it was replaced by Zn_2SiO_4:Mn^{2+} around 1925. In 1929, the importation of white-emitting fluoroscopic screens composed of $CdWO_4$ phosphors from Patterson, a U.S. company, was restarted. In 1933, however, the production of domestic screens having good contrast was initiated, following intense research into the relationship among brightness, particle size, coating weight, etc. of the $CdWO_4$ screen.[220,221]

Around 1935, fluoroscopic screens named Patterson B, Liossal (green-yellow) and Neossal (green) were imported from Patterson and from Heyden, a German company. These screens were composed of ZnCdS:Ag phosphors which had the advantage of high brightness.[222] The first Japanese product to use phosphors of this type was the "Giba" fluoroscopic screen produced by Toshiba in 1939.

In those days, three companies (Toshiba, Dai Nippon Toryou, and Shimadzu) were engaged in the development of fluoroscopic screens in Japan.[223,224] As the need for indirect X-ray photography suitable for the chest diagnosis of large groups of people in the military increased, all three companies began mass production of the screens in 1943.

There were no major developments for some time after the end of World War II. In the latter half of the 1960s digestive tract disease diagnosis using X-rays became a central procedure in medical checkups; the indirect photography method using mirror cameras with Schmidt optics was widely adopted since it could reduce the radiation dose. The ZnCdS:Ag phosphor remained in use until it was replaced in 1977 by $Gd_2O_2S:Tb^{3+}$. Later, however, X-ray image intensifiers became popular, and except for special purposes, fluoroscopic screens are seldom used anymore.

18.8.2 Intensifying screens

Whereas the phosphors used for the fluoroscopic screens underwent various transitions in the early days described above, the $CaWO_4$ phosphor has been used for X-ray intensifying screens ever since the screen first appeared on the market in Japan. (In the United States, $BaSO_4:Pb^{2+}$ (380 nm) and other materials have also been tested and used). During 1929–1931, imported photographic films with both sides coated with photosensitive emulsion came into use; the film was sandwiched between two intensifying screens to enhance the exposure light produced by the screens on the film.[222] Intensifying screens made by Patterson and by Heyden controlled the market at the time. Japanese products by two manufacturers (Hayano Chemical Laboratory (a subsidiary of Shimadzu) and Toshiba) appeared in 1934 and 1935. In 1937, intensifying screens with higher sensitivities than the imported ones were reported,[225] following the development of evaluation methods for screen resolution. The quality of Japanese products was thus gradually improved. In 1945, however, production stopped because of severe damage inflicted on the production facilities by the war.

In the postwar recovery period, production of the fluoroscopic screens and intensifying screens was restarted only after several years. In the early 1950s, the product variety became larger than it had been before the war. Table 7 shows the types of the products available at that time. Increases in phosphor particle size, in total coating percentage of the phosphors, and in reflectance of the base paper resulted in higher sensitivity; decreases in these parameters, on the other hand, led to higher resolution.

Until 1955, the main application of the intensifying screen in Japan was for chest disease diagnosis, but in the late 1950s it was expanded to the inspection of the digestive tract and other organs. To meet the resulting need for higher energy X-ray, (i.e., from 80 keV to 120–140 keV), intensifying screens with an increased coating of small particle

Table 7 Types of Fluoroscopic Screens and Intensifying Screens (~1955)

Fluoroscopic screen ((Zn,Cd)S:Ag)		
For indirect photograph	High sensitivity	High resolution
For direct view	High brightness	High resolution
Intensifying screen ($CaWO_4$)		
High sensitivity	Medium	High resolution

phosphors were commercialized in 1954 and 1955. These screens were used together with rotating-anode small-focus X-ray tubes, and reduced the radiation dose necessary while improving image resolution. Between 1956 and 1958, multilayer intensifying screens for cross-sectional images (two types for 80 and 120 kVp) were developed and commercialized.[226]

An X-ray image intensifier (II) was produced for tests[227] in 1956, and mass-produced in the late 1960s. Phosphors used in the X-ray input screen evolved from ZnS:Ag (1956)[227] through ZnCdS:Ag (1967)[228] to $Gd_2O_2S:Tb^{3+}$ (1969). In 1974, these were followed by a $CsI:Na^+$ crystal layer deposited through evaporation into a pillar structure.[229] This brought about marked improvements in brightness and resolution, which have been of great benefit in reducing exposure.

The X-ray intensifying screen can also be used in the nondestructive examination of materials. These devices were already on the market as early as in 1952/1953, and sold as "intensifying screens for industrial use." In 1961, a screen was developed that consisted of a thin lead foil placed between phosphor layers and the base paper. In this screen, the scattered X-ray contribution was reduced, resulting in high-resolution photographs.[230] This idea was also applied in medicine for the imaging of high-energy radiation such as ^{60}Co γ-rays. Intensifying screens for head and blood vessel tissue images that use contrast-enhancing agents have a similar layer structure.

In 1969, a cassette system was developed that allowed a single set of intensifying screens to be used successively in conjunction with a number of film sheets. Barite paper, which had been used as the base, was replaced with a plastic sheet. Further, the mechanical strength of the protective film on the phosphor layer was increased. These techniques improved resistance to abrasion and moisture and enhanced elasticity.

In the first half of the 1970s, the phosphors used in intensifying screens were further improved. First, for $CaWO_4$, the impurity content was reduced to trace amounts, the particle shape was improved, and the particle-size distribution in the phosphor coating layer was optimized. In 1973, the use of these measures helped reduce the afterglow and increased both the sensitivity and the resolution of the screen. Second, the introduction of rare-earth phosphors to be used in intensifying screens was initiated in this time period.

During this period, $Gd_2O_2S:Tb^{3+}$, $Y_2O_2S:Tb^{3+}$, $(Gd,Y)_2O_2S:Tb^{3+}$, $La_2O_2S:Tb^{3+}$, $BaSO_4:Eu^{2+}$, $BaFCl:Eu^{2+}$, $LaOBr:Tb^{3+}$, and $LaOBr:Tm^{3+}$ were all considered good candidates for intensifying screen applications. Among these, oxysulfide phosphors had been proposed by Tecotzky et al.[231] (US Radium) as early as in 1968. LaOBr phosphors had been developed and extensively studied by Rabatin[232] (GE) since 1969. Several investigations were conducted to find which of the above phosphors could be best adopted for practical use.[233] One factor that determines the total sensitivity of the screen and film system to X-rays is the energy conversion efficiency of the phosphor itself. For X-ray excitation, the material density should be high to obtain high stopping powers and efficiencies. Rare earth elements have large atomic numbers and the phosphors using them meet this condition. Another factor is the extent of overlap between the luminescence spectrum and sensitivity curve of the film. There are two types of X-ray film; the "regular type" has a sensitivity peak in the blue spectral region and the "ortho type" has a peak in the green region. Blue-emitting phosphors doped with Eu^{2+} are suitable for the former, while green-emitting ones doped with Tb^{3+} for the latter. For practical screens, however, properties other than sensitivity—such as particle morphology, chemical stability, and cost—are also very important. For example, BaFCl and LaOBr phosphors have a plate-like particle shape when produced by conventional methods, and they have a tendency to emit light from the sides of the plate rather than frontally, resulting in spatial noise due to screen graininess. Efforts were made to obtain a spherical particle shape by contriving phosphor preparation, and $BaFCl:Eu^{2+}$ (Du Pont) and $LaOBr:Tm^{3+}$ (Agfa-Gevaert) were introduced into the market.[218]

Use of rare-earth phosphors has gradually increased and has resulted in the improvement of screen characteristics; these phosphors now coexist with $CaWO_4$.

In Japan, an intensifying screen with $Ba_3(PO_4)_2:Eu^{2+}$, a phosphor with a higher sensitivity than $CaWO_4$, was commercialized in 1972 for digestive tract disease diagnosis.[234] This was replaced in 1974, however, by screens with phosphors such as $Gd_2O_2S:Tb^{3+}$ and $(Gd,Y)_2O_2S:Tb^{3+}$, which had still higher sensitivity.[235] In the late 1970s, the availability of a variety of both rare-earth intensifying screens and X-ray films expanded considerably.

In addition to these rare-earth-activated phosphors, a new phosphor family M′-$YTaO_4$(:Nb) with a Fergusonite-M′ structure was developed by Brixner[236] in 1983 (Du Pont), and commercialized shortly thereafter. M′-$YTaO_4$ is essentially an UV emitter. Partial substitution of Nb for Ta shifts the emission to longer wavelength. The X-ray-to-light conversion efficiency of $YTaO_4$:Nb (density d = 7.55 g cm^{-3}) is 1.5 times higher than that of $CaWO_4$ (d = 6.06 g cm^{-3}). $LuTaO_4$:Nb (d = 9.75 g cm^{-3}) is expected to have a still higher efficiency, although Lu_2O_3 is much more expensive for general applications. The modification of this family of phosphors has been actively investigated. For example, doping Sr into $YTaO_4$ simultaneously increases the luminescence efficiency and decreases the afterglow.[237] According to Blasse and Grabmaier (1994),[238] the best X-ray phosphors, at the moment, for conventional X-ray intensifying screens are $LaOBr:Tm^{3+}$, $Gd_2O_2S:Tb^{3+}$, and M′-$YTaO_4$(:Nb).

In the late 1970s, Japanese X-ray film makers (Fuji Photo Film and Konica) began to sell intensifying screens with their own brand names. Imported screens from the United States (Kodak and Du Pont) and European companies (Agfa-Gevaert) still enjoy a considerable share of the market. In 1980–1990s, rare-earth phosphors have gradually replaced $CaWO_4$ in these applications, and the ortho-type system using $Gd_2O_2S:Tb^{3+}$ is being produced in larger quantities than the regular type.

18.8.3 X-ray computed tomography and imaging systems

In the late 1970s, computer image-processing techniques were applied to the analysis of conventional X-ray images. New technologies of X-ray computed tomography (CT)[239] and radiography[240] also evolved and were developed for medical use, all exploiting the availability of computers.

In CT, X-rays are detected by converting them to electric signals, indirectly using photomultipliers to detect scintillation, or directly using xenon ionization chambers. In the late 1980s, a solid-state detector consisting of an array of several hundred silicon photodiodes, each having an attached scintillator chip, was adopted by some CT manufacturers. Single crystals of bismuth germanate, cadmium tungstate, and cesium iodide have been tested and put to practical use as scintillators.[241] In terms of luminescence efficiency and chemical stability, X-ray phosphors have better intrinsic properties for scintillator purposes than the crystals. From this point of view, a powder phosphor of $Gd_2O_2S:Pr^{3+},Ce^{3+}$ was proposed for scintillator use.[242] It was not widely adopted, however, because it required a complex device structure due to light scattering. Instead, translucent ceramic phosphors composed of $Gd_2O_2S:Pr^{3+},(Ce^{3+})$[243,244] and $(Y,Gd)_2O_3:Eu^{3+}$[245] have been developed and have been put into practical use as replacements for the single crystals. $Gd_3Ga_5O_{12}:Cr^{3+},Ce^{3+}$ also has been proposed[246] for this purpose. These translucent phosphor ceramics were realized by utilizing newly developed ceramic technologies such as hot isostatic pressing (HIP). Along with the higher luminescence efficiency, ceramic scintillators have additional advantages over single crystals; ceramics can be prepared with uniform chemical composition within the whole ingot, and cleavages and rupture do not occur during cutting or shaping processes. In the future, ceramic scintillators may find wider application as the technology continues to improve.

In 1981, Fuji Photo Film announced the success of an X-ray imaging system that they called Fuji Computed Radiography[240] (see Section 7.5). In this system, an imaging plate coated with a BaFX:Eu^{2+} (X = halogen) phosphor plays a major role.[247] After a latent image is produced by X-ray exposure on the plate, a He–Ne laser at 628 nm scans over it and reproduces the X-ray image as a blue-violet luminescence image (photo-stimulated luminescence). The emitted light is then submitted to computer image processing. This system has the advantages of higher sensitivity, larger dynamic range, and, in particular, easier computer processing than the conventional combination of the intensifying screens with photographic films. The stimulation phenomenon was found long ago in classical sulfide and oxysulfide phosphors, but has been little utilized in practical applications. By combining it with modern digital technologies, as well as developing high-efficiency phosphors, this significant advance in technology was realized.

Patent disclosures by Fuji Photo Film and Kasei Optonix describe a number of photostimulable phosphors, including oxides, sulfides, and halides.[248] Among them the BaFBr:Eu^{2+} phosphor was found best suited for the imaging system using a He–Ne laser. Its photostimulated luminescence efficiency was further improved by modifying the halide composition with iodine.[249] In addition to powder phosphors, evaporated crystal plates such as CsI:Na^{+} [250] and RbBr:Tl^{+} [251] with pillar-like morphology were also proposed for obtaining high resolution. The former was photostimulable by infrared light from laser diodes. Even thermoluminescence, instead of photostimulated luminescence, has been shown to be capable of producing two-dimensional images.[252] Screen properties and luminescence mechanisms of photostimulation have become the focus of much research and are being actively studied.[253]

Other than X-rays, latent images can be produced by irradiation with γ-, α-, β-rays, neutrons, or UV light. This technology can be expanded to numerous other applied fields.[254] They include crystallography, quality control, dosimetry, and data storage.

18.9 Medical devices using radioluminescence from 1995 to 2005

Medical diagnostic equipments have evolved greatly in the last decade, supported by developments in peripheral technologies such as digital imaging, cyclotron, and thin-film transistor (TFT). These equipments have been brought rapidly into clinical service since the early 2000s.

18.9.1 X-ray computed tomography

In the late 1980s, a new technique called helical or spiral[255] continuous scanning was proposed. It was realized in the early 1990s, endowing CT with a substantially faster scanning procedure (see Sections 7.3 and 18.8.3). Since the late 1990s, the speed of scanning has been further increased by the development of multislice CTs.[256] In a multislice CT, multiple transaxial images are simultaneously obtained by each rotation of an X-ray source combined with a detector around an object. In the detector, multiple arrays, each array transversely (around a body) consisting of about 1000 scintillator photodiode segments, are arranged longitudinally (along a body axis). Although the “second generation” CT scanners[257] in the 1970s also employed a split detector, the dual or split detector systems were not used until the early 1990s in the “third generation” CT, increasing the number of segments by two orders compared with the second generation.[256] Several companies, including GE, Toshiba, Siemens, Philips, and Hitachi have successively commercialized 4-, 8-, 10-, 16-, 32-, 40-, and 64-slice CTs since 1998.[258] Even a 256-slice CT has been announced.[259] With the increase in the number of slices, a three-dimensional volume image (and a two-dimensional image along an arbitrary direction of the object) can be obtained more easily. Along with further reduction in scanning time due to short rotation time below 0.5 s, medical diagnosis in the near future is expected to utilize real-time volume images of organs such as a breathing lung or a beating heart.

In the case of 256 slices, a detector has about 230,000 scintillator elements, each about 1 × 1 × 1 mm, separated optically from one another. For reconstructing a good image without artifacts, high accuracy with respect to size of scintillator elements, when formed from an ingot and also while assembling the elements into a detector, is required along with high uniformity in optical properties among the elements. Ceramic scintillators of $Gd_2O_2S:Pr^{3+},(Ce^{3+})$ and $(Y,Gd)_2O_3:Eu^{3+}$ meet these requirements, in addition to having superior optical properties as described in the previous Section 18.8.3. Since the late 1990s, they have almost completely superseded the xenon detectors and $CdWO_4$ single-crystal scintillators. Optical properties of the ceramic scintillators, such as luminescence efficiency, light translucency, and afterglow, have improved by using material fabricating techniques, such as doping trace amounts of foreign impurities, selecting proper particle sizes of raw phosphor powders for hot pressing, and controlling anneal conditions.[260]

18.9.2 Positron emission tomography

In a positron emission tomography (PET) scanner, a circular array of scintillator–photomultiplier combined elements detects two high-energy (511 keV) coincident γ photons emitted 180° apart from each other, following a positron–electron annihilation reaction caused by a short-lived positron-emitting radiopharmaceutical injected into a patient. The distribution of the pharmaceutical obtained by mapping of the emitted radiation gives functional information such as brain oxygen metabolism and positions of cancers in whole-body oncology. In combination with X-ray CT and MRI, which give morphological information, medical usefulness of PET is further enhanced.[261]

As a result of intensive study since the 1970s, PET has advanced greatly and its usefulness in medical diagnosis has gained wide acceptance among medical professionals. During past 5 years, it has spread rapidly in clinics in the United States, Europe, and Japan. According to Nutt,[262] the most important events that shaped modern PET include the discovery of $Bi_4Ge_3O_{12}$ (BGO; 1977–1978) and $Lu_2SiO_5:Ce$ (LSO; 1989–1992) scintillator materials, in addition to items such as the synthesis of the radiopharmaceutical ^{18}F-FDG (2-fluoro-2-deoxy-D-glucose; 1978–1980), the development of the medical cyclotron (1984–1986), the entry of major medical imaging companies (GE and Siemens) to the field (1987–1990), and government approval (Food and Drug Administration (FDA) drug approval and Health Care Financing Administration (HCFA) reimbursement (in the United States during 1997–1998)). In Japan, the National Institute of Radiological Sciences (NIRS) and Akita Research Institute for Brain and Blood Vessels initiated the development of PET scanners, independently in the late 1970s[263] with the cooperation of manufacturers (including Hitachi group of companies and Hamamatsu Photonics). Following adoption of government health insurance system for PET examinations using $^{15}O_2$ (1996) and for ^{18}F-FDG studies (2002), PET scanners have been rapidly introduced in medical clinics. (As of January 2004, the total number of PET facilities in Japan having their own cyclotrons reached 58.)[263]

Scintillators for this purpose are required to have a luminescence decay time in the nanosecond range. In an early study, NaI(Tl) single crystal was used.[264] For 20 years following commercialization of the first CT in 1978, however, BGO single crystal was dominant because of its high chemical stability, high density, and high effective atomic number.[265] During 1984–1985, $Gd_2SiO_5:Ce^{3+}$ was developed by Hitachi Chemical[266] and partly introduced, triggering further study of orthosilicates (see Section 7.3). LSO was discovered and the first crystals were grown in the period from 1989 to 1992. It has five times more light output and 7.5 times faster decay time than BGO.[267] It was used in 1995, however, only for a special small-sized CT, because the raw material, lutetium oxide, was very expensive. This problem was resolved by the work done by chemists on Lu refinement[262] and the first LSO tomograph for human medical applications was achieved in 1999. Today, PET scanners using BGO, LSO, and $(Lu,Gd)_2SiO_5:Ce^{3+}$ (LGSO) are being commercialized in parallel. Improvements in the detector structure have also contributed to high speed and high resolution of recent PET scanners. The first PET scanner for medical applications (1974) used 48 NaI(Tl) circular detectors, each with a diameter of 50 mm. The number of individual crystals in a PET has doubled approximately every 2 years for the past 25 years. A recent PET scanner is equipped with 120,000 scintillator elements, each 2 × 2 mm.

18.9.3 X-ray flat panel detector (X-FPD)[268]

There have been various attempts to replace the combination of X-ray fluorescent screens and photographic films (see Sections 7.1, 18.8.1, and 18.8.2). Successful examples are an II tube (see Sections 7.4 and 18.8.2) and Fuji Computed Radiography (Sections 7.5 and 18.8.3). Other proposals were methods such as a combination of a charge-coupled device (CCD), in place of the photographic film, with an X-ray phosphor screen, and zero radiography, in which a photoconducting layer of amorphous-selenium (a-Se) converts the X-ray signal into electric charge and displays the X-ray image using a toner.[269] These methods, however, have not gained widespread acceptance due to their small image size and low conversion efficiency. In order to obtain large two-dimensional X-ray images with high resolution, intensive studies on X-ray flat panel detectors (X-FPD) started in the late 1980s with a view of applying active matrix TFT panels, which made great progresses in the 1990s. The TFT panels detect electric charges generated "indirectly"[270] through a combination of X-ray phosphor layer and a-Si photodiodes or "directly"[271] through an a-Se photoconductor layer upon X-ray irradiation.

In the late 1990s, indirect-type X-ray FPDs using a CsI(Tl) evaporated layer[270,272] and a Gd_2O_2S:Tb phosphor layer[270,273] were developed and commercialized. The CsI(Tl) layer offers the advantage of high resolution over the Gd_2O_2S:Tb phosphor layer as it has the same pillar structure like CsI(Na) in the II tube, In addition, it has longer emission wavelength for better matching to photodiode sensitivity and higher chemical stability than CsI(Na). These indirect FPDs are replacing the conventional screen–film combination and are competing with the computed radiography system. On the other hand, a direct FPD, which has higher resolution than indirect FPDs, was commercialized in the late 1990s and early 2000 using a -Se film.[274] For the direct FPD, photoconductive layers of PbI_2, HgI_2, CdTe, etc. have also been proposed for realizing higher sensitivity.[275] FPDs are being improved to obtain real-time moving images. They will replace bulky II tubes and also the screen–film systems in the near future.

18.10 A short note on the history of phosphors

Harvey describes the following story concerning a painting of the Emperor Tai Zong (976-998), of the Song dynasty.* Here the story is cited from his book.(Chinese character representations are changed to the modern system from the older one in Harvey's book)

First, in the miscellaneous notes by a Song monk, titled *Xiang-Shan Ye-Lu* (11th century A.D.), there is a story concerning an interesting painting that was presented to the second emperor of the Song dynasty. The painting showed a cow that appeared during the day as eating grass outside a pen, but at night as resting within the pen. When it was shown

---

* Harvey, E. N., *A History of Luminescence*, American Philosophical Society, 1957, 18.

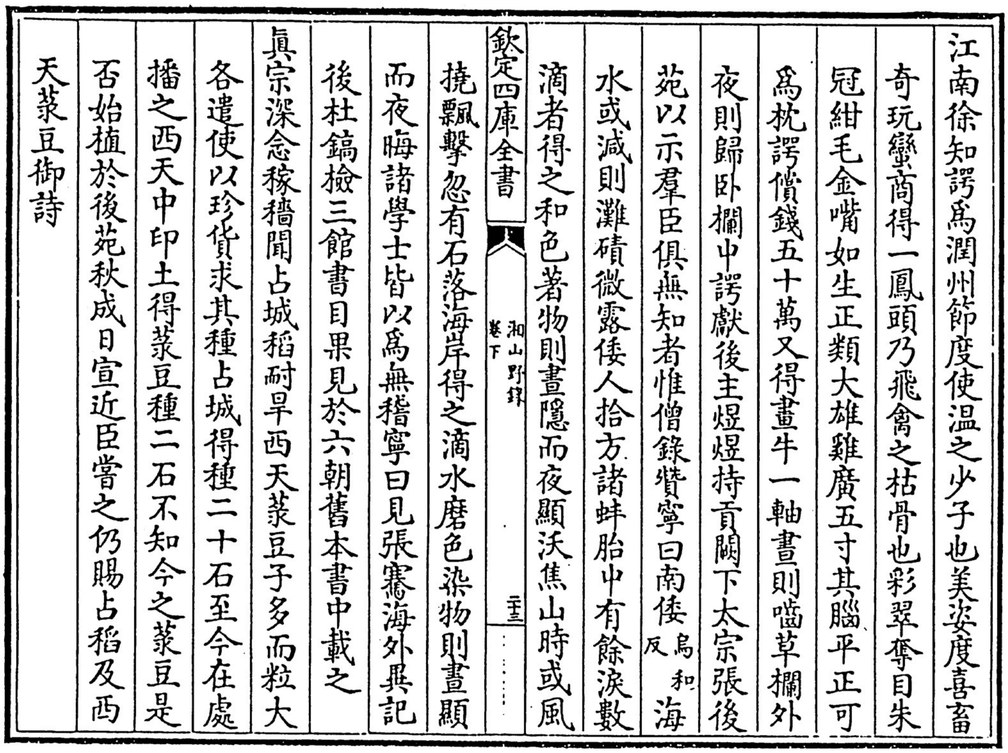

江南徐知諤爲潤州節度使温之少子也美姿度喜畜
奇玩蠻商得一鳳頭乃飛禽之枯骨也彩翠奪目朱
冠紺毛金嘴如生正類大雄雞廣五寸其腦平正可
爲枕諤償錢五十萬又得畫牛一軸晝則嚙草欄外
夜則歸卧欄中諤獻後主煜煜持貢闕下太宗張後
苑以示羣臣俱無知者惟僧錄贊寧曰南倭（烏和反）海
水或減則灘磧微露倭人拾方諸蚌胎中有餘淚數
滴者得之和色著物則晝隱而夜顯沃焦山時或風
欽定四庫全書　湘山野錄　卷下　二十三
撓飄擊忽有石落海岸得之滴水磨色染物則晝顯
而夜晦諸學士皆以爲無稽寧曰見張騫海外異記
後杜鎬檢三館書目果見於六朝舊本書中載之
眞宗深念稼穡聞占城稻耐旱西天菉豆子多而粒大
各遣使以珍貨求其種占城得種二十石至今在處
播之西天中印土得菉豆種二石不知今之菉豆是
否始植於後苑秋成日宣近臣嘗之仍賜占稻及西
天菉豆御詩

Figure 3 A note concerning a luminous paint in the Chinese book *Xiang-Shan Ye-Lu*.

to the court, none of the officials could offer an interpretation for the phenomenon. The monk Zan Ning, however, said that the ink (or color) that appeared only at night was mixed with drops from a (special kind of) pearl shell and the ink (or color) that appeared only during the day was made by grinding a rock that had fallen from a volcano to the seashore. The monk claimed that the information came from a book by Zhang Xian, the famous envoy sent to the Western Regions by Han Wu Di (reigned 140-88 B.C.). A scholar who consulted the imperial collections found the reference in a work dated from the Six Dynasties.

The authors of this chapter found the original Chinese book *Xiang-Shan Ye-lu* describing the story.* Figure 3 shows the record of the cow's painting. Further informtion can be obtained from the text. For example, the painting was bought by an officer Xu Zhi E at a price of 500 thousands taels. It was gifted to the Song court. The pearl shells were gathered by Japanese (the 7th column from right) at a seashore in southern Japan (small characters in the 6th column shows the place name). The rock was carried to the seashore from a volcano in the course of a whirlwind.

Harvey gives comments that the story of the luminous cow should be given little serious consideration because nothing is known of any book left by the explorer Zhang Xian, and because Wen Ying, the author of the *Xiang-Shan Ye-Lu*, who lived in the 11th century, was not noted for his veracity. However, it seems certain that the Japanese (and

---

* Wen Ying (a monk in the Song dynasty), *Xiang-Shan Ye-Lu*, Vol 3, 23 collected in *Wen-Yuan-Ge Si-Ku-Quan-Shu*, Vol. 1037, p. 265, Taiwan Shang-Wu Yin-Shu-Guan (Taiwan Commercial Press) 1983-1986 (in Chinese). We are indebted to Mr. K. Hunakoshi of Uchiyama Bookstore and Ms. I. Kasai of Tokyo University for finding the literature.

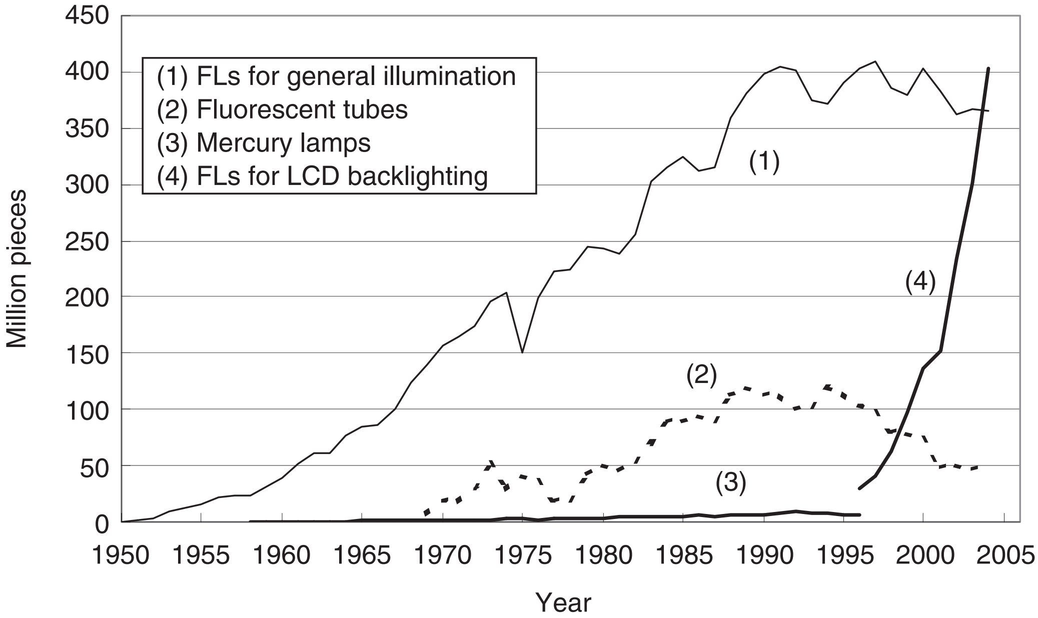

Figure 4 Production of lamps in Japan: (1) Fluorescent lamps (FLs) for general illumination, (2) Fluorescent tubes, (3) Mercury lamps, and (4) Fluorescent lamps for backlighting. (Source: *Yearbook of Machinery Statistics 1955 to 2005*, Ministry of Economy, Trade and Industry). (For mercury lamps, the classification was changed to HID lamps from 1984, adding high pressure Na-lamps. Fluorescent lamps for backlighting have been counted since 1996.)

Chinese) knew of luminous paint more than 1000 years ago, and that the paint had some relationship with seashells and materials from a volcano. It is well known that sulfur obtained from a volcano was one of representative exports from Japan to China at that time. In Europe, a phosphor was prepared from oyster shells reacted with sulfur in 1768 by John Canton.

18.11 Production of luminescent devices utilizing phosphors

Figure 4 shows the number of fluorescent lamps for general illumination, vacuum fluorescent tubes, mercury lamps, and fluorescent lamps for LCD backlighting, produced in Japan. Figure 5 shows the production quantities of black-and-white picture tubes, color picture tubes, and CRTs for industrial use (CRTs for computers since 1984).There are no statistics for X-ray fluoroscopic screens and intensifying screens.

The number of fluorescent lamps produced in Japan for general-purpose illumination had increased steadily for more than 40 years, reaching 390 million pieces (Mp) in 1990. Since 1990, however, it has remained at a level of 360 to 400 Mp annually. This reflects an increased production overseas by Japanese companies: the number of fluorescent lamps imported grew year by year and exceeded that exported from Japan in 2004. Worldwide production has increased steadily and Japan is estimated to account for 10% to 15% of it. On the other hand, production in Japan of cold-cathode fluorescent lamps (CCFLs) for LCD backlighting has been increasing rapidly at an annual rate of more than 30%; it reached the same level, ~400 Mp*, as that of conventional lamps in 2004, reflecting Japan's

---

* The symbol "~" means "approximately".

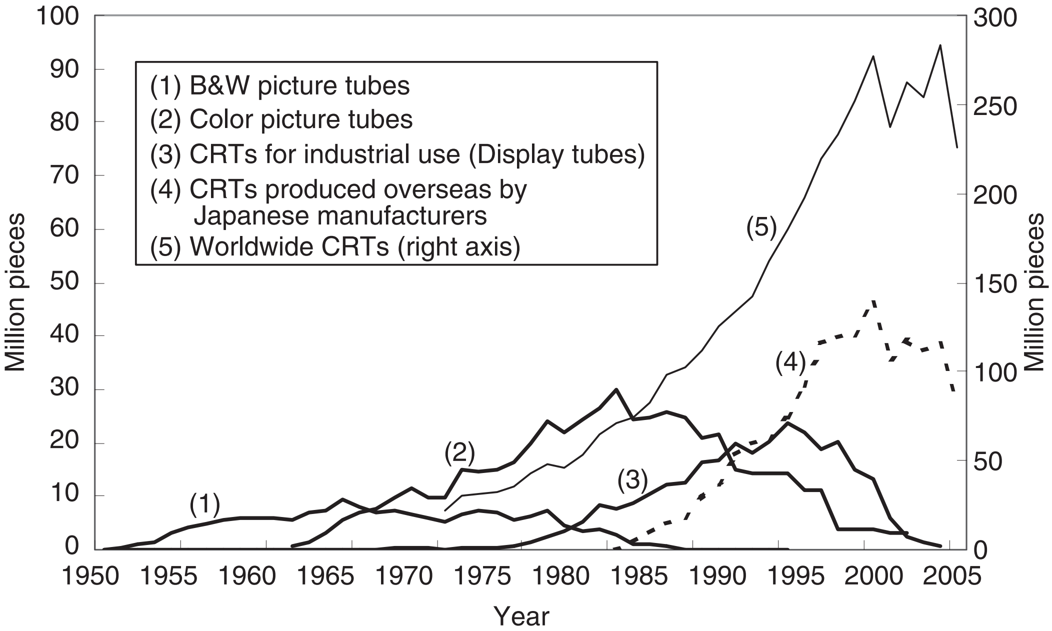

Figure 5 Production of CRTs: (1) B&W picture tubes in Japan, (2) Color picture tubes in Japan, (3) Display tubes in Japan, (4) CRTs produced overseas by Japanese manufacturers, and (5) CRTs produced worldwide (right axis). (Source: For (1), (2), and (3), *Yearbook of Machinery Statistics 1955 to 2005*, Ministry of Economy, Trade and Industry. For (4) and (5), estimation by Nippon Electric Glass Co., Ltd.)

large share of worldwide CCFL production. Note that only ~1/3 of LCD panel production is for television use.

Production of black-and-white tubes in Japan peaked in 1965. Following the peak, they were superseded by color picture tubes. The peaks in 1985 and 1996 for color picture tubes (CPTs) and color display tubes (CDTs), respectively, occurred for a reason different from that for the peak in black-and-white tubes: Japan shifted production of both CPTs and CDTs overseas, in order to compete with manufacturers based elsewhere in Asia The number of CRTs produced overseas by Japanese manufacturers greatly surpassed domestic production during the last decade (curve (4) in Figure 5). Worldwide CRTs production increased from 1985 to 2000 at an average annual rate of 10% (~5% for CPTs and ~25% for CDTs), reaching ~280 Mp in 2000 (~160 Mp for CPTs and ~120 Mp for CDTs).

The situation has changed dramatically since the late 1990s, a transition from bulky CRTs to flat panels has occurred. For computer use, CDTs have been rapidly superseded by liquid crystal displays (LCDs). The decrease in worldwide CDT production from 2000 to 2005 (at a rate of ~-15%, ~30 Mp in 2005) has cancelled out the increase in CPT production (at a rate of 3%, 180 Mp in 2005), resulting in saturation of the worldwide CRT market. In regard to TV use, there has also been rapid change. Figure 6 shows worldwide TV demand predicted in 1996 and 2005 for CRT, LCD, plasma display panel (PDP), and projection devices. Predictions made for CRT-TV in 1996 have been in good agreement with the results until 2005. Production has increased in the last decade, reaching 130 Mp in 2005, and CRT-TV is still dominant in terms of the production quantity among the various types of TV sets: production was 14 Mp for LCD (over 10 inch), 4 Mp for PDP, and 6 Mp for projectors in 2005. Flat-panel TV demand is predicted to increase steeply in the near future. Huge investments planned by Japanese, Taiwanese, and Korean manufacturers in 2005 and 2006 will realize a far steeper increase than the trend in Figure 6. In

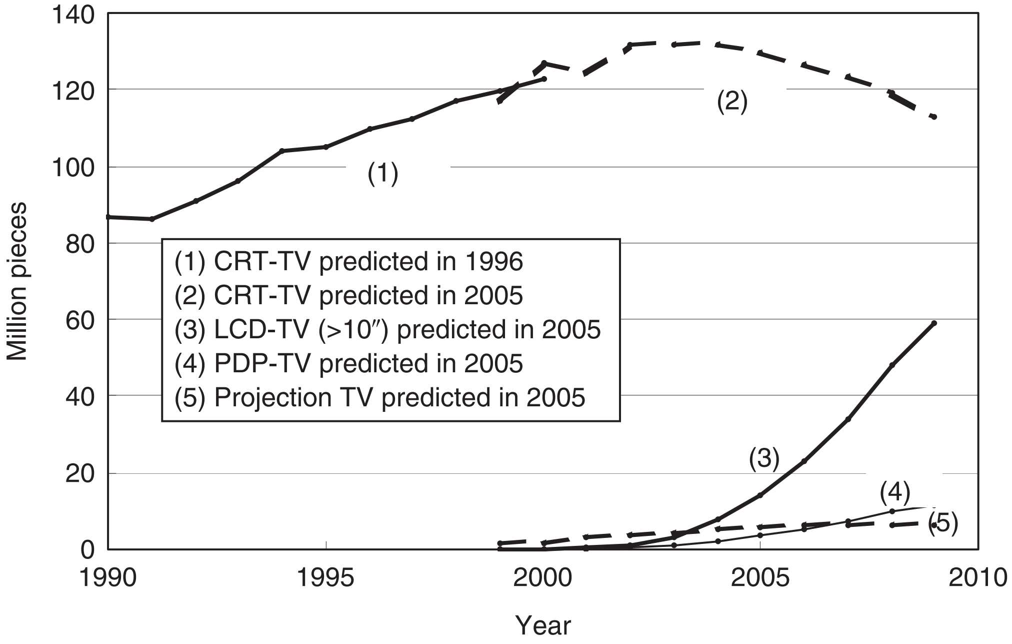

Figure 6 Worldwide demand for TV sets. (Source: *Worldwide demand prediction for AV7 devices 1996 and 2005*, Japan Electronics and Information Technology Association (JEITA).)

the Japanese market in 2005, flat-panel TV sets were already far outselling CRT-TV sets (i.e., 4.210 thousand pieces (kp), 468 kp, and 3,980 kp for LCD-, PDP-, and CRT-TV sets, respectively). Japan has experienced this change in advance of the rest of the world. CRT production in Japan ceased in 2005. Japan's share of worldwide CRT production decreased from 40% in 1990 to 10% in 2004.

It is estimated that about 3 billion white light-emitting diodes (LEDs) were produced worldwide in 2004, of which ~70% were produced in Japan. Production is expected to increase at an annual rate of ~20%. The rate will vary, however, depending on whether LEDs replace fluorescent lamps for general-purpose illumination by 2010. In this regard, reduction in the cost per luminous flux emitted (yen/lm) will have a decisive influence.

18.12 Production of phosphors

Commercial production of luminescent devices utilizing phosphors was established around 1960. Since 1965, the scale of phosphor production on a monetary basis has increased because expensive rare-earth phosphors have been widely used, and moreover, the variety and number of luminescent devices has increased.

There are no statistics available for phosphor production. On the basis of several different estimates of rare-earth consumption and the production of light-emitting devices, it is reasonable to suppose that worldwide phosphor production for conventional devices in 2004 was as follows: 9,000-10,000 tons of halo-phosphate for fluorescent lamps, 3,000-4,000 tons of rare-earth phosphors for three-band fluorescent lamps, 7,000-8,000 tons for CRTs, and 100-150 tons for X-ray applications. When compared with quantities in 1995, the amounts of rare-earth phosphors for lamps and phosphors for CRTs have both doubled, although halo-phosphate and phosphors for X-ray applications have remained at the same level. Production is concentrated in Japan, Korea, China, the United States, and Western Europe.

For newly developed devices, on the other hand, the scale of worldwide production of novel phosphors in 2004 was as follows: 300-500 tons for PDPs, 600-800 tons for LCD backlight lamps (cold-cathode fluorescent lamps), and ~1 ton for white LEDs. Demand for each of these phosphors is increasing by more than 20% annually. Reflecting Japan's high shares in the worldwide production of the new devices, the share of phosphor production in the world is quite high, while competing with up-and-coming Korea and China also in this field.

Author's notes:

Production volumes are estimated on the basis of the following references in addition to the author's estimates. He thanks Nippon Electric Glass Co., Ltd. for permitting disclosure of the CRT production data estimation.

1. *Yearbook of Machinery Statistics 1955 to 2005*, Ministry of Economy, Trade and Industry.
2. *Worldwide demand prediction for AV7 devices 1996 and 2005*, Japan Electronics and Information Technology Association (JEITA) and other JEITA Publications.
3. Private communication, Nippon Electric Glass Co., Ltd.

References

1. Itoh, T., *Keikoutou shoumei nyuumon* (*Introduction to Fluorescent Lamp Illumination*), Denkishoin, Tokyo, 1954 (in Japanese).
2. Edison, T.A., U.S. Patent 865367 (Appl. 1896).
3. Harada, T., *Houdentou* (*Discharge Lamps*) OHM, 1950 (in Japanese).
4. Honjou, I., *J. Illum. Engng. Jpn.*, 40, 40, 1956 (in Japanese).
5. McKeag, A.H. and Ranby, P.W., *Ind. Chem.*, 23, 513 and 597, 1947.
6. McDermott, J.A., *Elec. Eng.*, 57, 286, 1938.
7. Jenkins, H.G. and Bowtell, J.N., *Trans. Illum. Eng. Soc.* (London), 13, 61, 1948.
8. Jenkins, H.G., *GEC Journal*, 13, No. 4, 1945.
9. McKeag, A.H. and Randall, J.T., Brit. Pat. 480356 (Appl. 1936-7-23); Leverenz, H.W., U.S. Patent 2118091 (Appl. 1936-2-29); (Telefunken), Brit. Pat. 478302 (Appl. 1935-7-11).
10. Inman, G.E. and Amick, C.L., *J. Illum. Engng. Jpn.*, 72, 232, 1988 (translated into Japanese by Kohmoto, K.); Fujita, B., *J. Illum. Eng. Jpn.*, 24, 159, 1940 (in Japanese).
11. Inman, G.E., *Trans. Illum. Eng. Soc.*, 34, 65, 1939.
12. Thayer, R.N. and Barnes, B.T., *J. Opt. Soc. Am.*, 29, 131, 1939.
13. Meyer, F., Spanner, H., and Germer, E., U.S. Patent 2182732, 1939.
14. Sakabe, H., *J. Illum. Engng. Jpn.*, 35, 168, 1951 (in Japanese).
15. Merril, J.B. and Schulman, J.H., *J. Opt. Soc. Am.*, 38, 471, 1948.
16. Froelich, H.C., *Trans. Electrochem. Soc.*, 93, 101, 1948.
17. Fujita, B. and Itou, T., *Toshiba Rev.*, 4, 147, 1950 (in Japanese).
18. Jenkins, H.G., McKeag, H.G., and Ranby, P.W., *J. Electrochem. Soc.*, 96, 1, 1949.
19. Aoki, Y., Japanese Patent Publication (Kokoku) 29-967 (1954).
20. McKeag, A.H. and Ranby, P.W., U.S. Patent 2488733; Japanese Patent Publication (Kokoku) 29-1268 (1954) (Appl. in Britain 1942-6-17).
21. Butler, K.H. and Homer, H.H., *Illum. Eng.*, 55, 396, 1960.
22. Aia, M.A. and Poss, S.M., Japanese Patent Publication (Kokoku) 38-4325 (1963).
23. Aia, M.A., Japanese Patent Publication (Kokoku) 39-1211 (1964).
24. Gillooly, G.R., and Rabatin, J.G., Japanese Patent Publication (Kokoku) 40-6843 (1965); Rabatin, J.G., Gillooly, G.R. and Hunter, J.W., *J. Electrochem. Soc.*, 114, 956, 1967.
25. Froelich, H.C. and Margolis, J.M., *J. Electrochem. Soc.*, 98, 400, 1951.
26. Ide, H., Japanese Patent Publication (Kokoku) 28-6270 (1953)

27. Henderson, S.T. and Ranby, P.W., *J. Electrochem. Soc.*, 98, 479, 1951.
28. Butler, K.H., *J. Electrochem. Soc.,* 100, 250, 1953.
29. Nakajima, S. and Honda, Y., *J. Illum. Engng. Jpn.*, 40, 305, 1956 (in Japanese).
30. Azuma, T. and Mori, L., *J. Illum. Engng. Jpn.*, 38, 187, 1954 (in Japanese).
31. Hashimoto, K., Someya, A., and Hanada, T., *Toshiba Rev.*, 21, 909, 1966 (in Japanese).
32. Koelmans, H. and Cox, A.P.M., *J. Electrochem. Soc.*, 104, 442, 1957.
33. Sarver, J.F., Hoffman, M.V., and Hummel, F.A., *J. Electrochem. Soc.*, 108, 1103, 1961.
34. CIE Publication No. 13, Method of Measuring and Specifying Color Rendering Properties of Light Sources, 1st Edition (1965); 2nd Edition (1974).
35. The Color Science Association of Japan, *Shikisai Kagaku* (*Color Science) Handbook,* University of Tokyo Press, Tokyo, p. 1006, 1980 (in Japanese).
36. Kamiya, S., Shibata, H., Watarai, Y., and Kanaya, S., *Tech. Digest, Phosphor Res. Soc. 173rd Meeting*, 1978 (in Japanese); *National Tech. Rept.*, 27, 11, 1981 (in Japanese).
37. Koedam, M. and Opstelten, J.J., *Lighting Research and Technology,* 3, 205, 1971.
38. Thornton, W.A., *J. Opt. Soc. Am.*, 61, 1155, 1971.
39. Haft, H.H. and Thornton, W.A., *J. IES*, 2, 29, 1972; Doi, S., Magome, K., and Ohtani, M., *Mitsubishi Denki Giho*, 48, 1059, 1974 (in Japanese).
40. Pallila, F.C. and O'Reilly, B.E., *J. Electrochem. Soc.*, 115, 1076, 1968.
41. Nazarova, V.P., *Bull. Acad. Sci. USSR Phys. Ser.*, 25, 322, 1961.
42. Blasse, G., Wanmaker, W.L., and ter Vrugt, J.W., *J. Electrochem. Soc.*, 115, 673, 1968.
43. Chenot, C.F., Japanese Patent Publication (Kokoku) 45-2293 (1970); U.S. Patent 3431215 (1969).
44. Verstegen, J.M.P.J., *J. Electrochem. Soc.*, 121, 1623, 1974; Verstegen, J.M.P.J., Radielovic, D., and Vrenken, L.E., *ibid*, 121, 1627, 1974; *J. IES*, 4, 90, 1975.
45. Watanabe, M., Nishimura, T., Kohmoto, K., Shimizu, K., and Narita, K., *Tech. Digest, Phosphor Res. Soc. 167th Meeting*, 1977 (in Japanese).
46. Nakajima, S., Ichinomiya, K., Okada, K., Tsuchikura, K., and Kashiwagi, M., *Tech. Digest, Phosphor Res. Soc. 186th Meeting*, 1981 (in Japanese); Royce, M.R., Nakajima, S., and Sumoto, H., *Electrochem. Soc. Fall Meeting*, Abstr. 631, 1990.
47. Saubat, B., Fouassier, C., Hagenmuller, P., and Bourcet, J.C., *Mater. Res. Bull.,* 16, 193, 1981; de Hair, J.Th.W. and van Kemenade, J.T.C., *Proc. 3rd Inter. Symposium on the Science & Technology of Light Sources (LS-3),* Toulouse, Paper 54, 1983.
48. Taya, A., Nakamoto, M., Akiyama, J., and Narita, K., *Tech. Digest, Phosphor Res. Soc. 180th Meeting*, 1980 (in Japanese); Tsuda, T., Sugiyama, H., Nishimura, T., and Narita, K, *Toshiba Rev.*, 34, 578, 1979 (in Japanese).
49. Mituma, T. and Ishikawa, R., Japanese Patent Publication (Kokoku) 46-40604 (1971).
50. Ikeda, S., Ehara, H., and Komiya, A., *Toshiba Rev.*, 33, 312, 1978 (in Japanese); Ohno, H., *J. Illum. Engng. Jpn.*, 63, 442, 1979 (in Japanese); Peters, R.C. and Tak, M.G.A., *Electrochem. Soc. Spring meeting,* Abstr. 129, 1977; GTE Sylvania Catalogue ES180 Series; Philips Catalogue TL-D Super 80 Series.
51. Hanada, T., Sugiyama, H., and Kobuya, A., *Toshiba Rev.*, 23, 513, 1968 (in Japanese); Ohta, J., Asanaga, H., and Yamazaki, S., *Mitsubishi Denki Gihou*, 42, 1076, 1968 (in Japanese); Kruithof, A.A. and Ouweltjes, J.L., *Philips Tech. Rev.*, 18, 249, 1956/1957.
52. Murakami, K., Anzai, Y., Itoh, H., Doi, S., and Awazu, K., *Tech. Digest, Phosphor Res. Soc. 173rd Meeting*, 1978 (in Japanese); *Mitsubishi Denki Gihou*, 52, 701, 1978 (in Japanese).
53. Taya, A., Narita, K., Akiyama, J., Asada, M., and Nira, H., *Tech. Digest, Phosphor Res. Soc. 192nd Meeting*, 1982 (in Japanese).
54. Yamamoto, T., Iwama, K., Shibata, H., and Kamiya, S., *Tech. Digest, Phosphor Res. Soc. 197th Meeting*, 1983 (in Japanese).
55. Smets, B.M.J. and Verlijsdonk, J.G., *Mater. Res. Bull.*, 21, 1305, 1986.
56. Shibata, H., Otaka, Y., and Inukai, Y., *Tech. Digest, Phosphor Res. Soc. 212th Meeting*, 21, 1986 (in Japanese).
57. Sakakibara, Y., Tominaga, M., and Terashima, K., *Toshiba Rev.*, 45, 808, 1990 (in Japanese).
58. Ronda, C.R. and Smets, B.M.J., *J. Electrochem. Soc.*, 136, 570, 1989; Smets, B., Rutten, J., Hoeks, G., and Verlijsdonk, J., *J. Electrochem. Soc.*, 136, 2119, 1989; Stevels, A.L.N., *J. Lumin.*, 17, 121, 1978.

59. Amster, R.L., *7th Rare Earth Res. Conf.*, San Diego, 1968.; Tamatani, M., *Jpn. J. Appl. Phys.*, 13, 950, 1974.
60. Kijima, N., Hisamune, T., Fujino, S., and Oguri, Y., *Electrochem. Soc. Fall Meeting*, Abstr. 766, 1995; Oshio, S. and Matsuoka, T., *Proc. 7th Inter. Symposium on the Science & Technology of Light Sources* (*LS-7*), Kyoto, 313, 1995.
61. Matsuzawa, T., *Proc. Int. Display Workshop (IDW '95)*, Vol. 1, 85, 1995; Matsuzawa, T., Aoki, Y., Takeuchi, N., and Murayama, Y., *Electrochem. Soc. Fall Meeting*, Abstr. 160, 1995.
62. Nagashima, Y. and Nomura, K., *Tech. Digest, Phosphor Res. Soc. 262nd Meeting*, 1996 (in Japanese).
63. Hanada, T., Kobuya, A., Sugiyama, H., and Akiyama, J., *Toshiba Rev.*, 30, 722, 1975 (in Japanese).
64. Murakami, K., Ohtani, M., Anzai, Y., Itoh, H., and Awazu, K., *Mitsubishi Denki Gihou*, 50, 573, 1976 (in Japanese).
65. Kamei, T., Hayashi, G., Nagata, K., Ikeda, S., and Takano, M., *Toshiba Rev.*, 35, 679, 1980 (in Japanese).
66. Yagi, T., *J. Illum. Engng. Inst. Jpn.*, 79, 730, 1995 (in Japanese); Jack, A.G. and Vrenken, Q.H.F., *Philips Tech. Rev.*, 42, 342, 1986.
67. Mulder, B.J. and van Heusen, S., *J. Electrochem. Soc.*, 130, 440, 1983; Doughty, D.A., Wilson, R.H., and Thaler, E.G., *J. Electrochem. Soc.*, 142, 3542, 1995.
68. Tomioka, H., Higashi, T., and Iwama, K., *Proc. 7th Inter. Symposium on the Science & Technology of Light Sources* (*LS-7*), Kyoto, 323, 1995.
69. Verhees, P.W.C., *Proc. 5th Inter. Symposium on the Science & Technology of Light Sources* (*LS-5*), York, Abstr. 105:L, 1989.
70. Oguchi, T., and Tamatani, M., *J. Electrochem. Soc.*, 133, 841, 1986; Ito, H., Yuge, Y., Taya, A., Tamatani, M., and Terashima, K., *J. Light & Vis. Env.*, 17, 41, 1993 (English version of *J. Illum. Engng. Inst. Jpn.*, 76, 536, 1992 (in Japanese)).
71. Ronda, C.R., *Proc. Int. Display Workshop* (*IDW '95*), Vol. 1, 69, 1995.
72. Vegter, K., de Bijl, A., Kemenade, J.V., and Schlejen, J., *1993 IESNA Annual Conference Technical Papers,* Houston, 641, 1993.
73. Stormberg, H.P., *Proc. 7th Inter. Symposium on the Science & Technology of Light Sources* (*LS-7*), Kyoto, 327, 1995.
74. de Backer, J. and van Disseldorp, B., *Int. Lighting Rev.*, 28, 1995.
75. Kamiya, S., *Proc. 6th Inter. Symposium on the Science & Technology of Light Sources* (*LS-6*), Budapest, 37, 1995; Hanada, T., *Proc. 7th Inter. Symposium on the Science & Technology of Light Sources* (*LS-7*), Kyoto, 17, 1995.
76. Tokyo Denki, Tokyo, 50 years of Tokyo Denki, p. 350, 1940 (in Japanese).
77. Riehl, N., *Physik und technische Anwendungen der Lumineszenz*, Berlin, 1941.
78. Kröger, F.A., *Some Aspects of the Luminescence of Solids*, p. 64 Elsevier, Amsterdam, 1948.
79. Thorington, L., *J. Opt. Soc. Am.*, 40, 579, 1950; U.S. Patent 2748303 (1956).
80. Ouweltjes, J.L., Elenbaas, W., and Labberte, K.R., *Philips Tech. Rev.*, 13, 109, 1951.
81. Travnicek, M., Kroeger, F.A. Botden, Th.P.J., and Zalm, P., *Physica,* 18, 33, 1952.
82. Ranby, P.W., Brit. Patent 707101 (1954).
83. McKeag, A.H. and Steward, E.G., *Br. J. Appl. Phys.*, Suppl. No. 4, S26, 1955.
84. Ohsuka, T., *Toshiba Rev.*, 10, 1087, 1955 (in Japanese).
85. Leverenz, H.W., U.S. Patent 2066044 (1936).
86. Patten, S.H. and Williams, F.E., *J. Opt. Soc. Am.*, 39, 702, 1949.
87. Koelmans, H. and Cox, A.P.M., *J. Electrochem. Soc.*, 104, 442, 1957.
88. Sarver, J.F., Hoffman, M.V., and Hummel, F.A., *J. Electrochem. Soc.*, 108, 1103, 1961.
89. Pallila, F.C. and Levin, A.K., *Appl. Optics,* 5, 1467, 1966.
90. Thomas, M.J.B. and Butler, K.H., U.S. Patent 2901647 (1959).
91. Thomas, M.J.B., Butler, K.H., and Harris, J.M., *Illum. Eng.*, 52, 279, 1957.
92. GE, Advertisement in *Illum. Eng.*, 60, 5, 1957.
93. Nomura, M., Tanibayashi, M., and Inoue, H., *Toshiba Rev.*, 12, 1143, 1957 (in Japanese).
94. Toshiba, Catalogue for Mazda Mercury Lamps.

95. Hayama, N., *J. Illum. Engng. Inst. Jpn.*, 89, 192, 2005 (in Japanese); Oomen, M., *Proc. 8th Inter. Symposium on the Science & Technology of Light Sources* (*LS-8*), 24, 1998.
96. Oshima, T., *J. Illum. Engng. Inst. Jpn.*, 89, 195, 2005 (in Japanese).
97. Takahara, Y., *J. Illum. Engng. Inst. Jpn.*, 87, 974, 2003 (in Japanese).
98. Ikeda, T. and Urataki, E., *J. Illum. Engng. Inst. Jpn.*, 87, 967, (in Japanese); Soules, T.F., Barry, J.I., Steinbrenner, E.G., and Kicher, L., *Proc. 7th Inter. Symposium on the Science & Technology of Light Sources* (*LS-7*), 59, 1995.
99. Oshio, S., Kitamura, K., Shigeta, T., Horii, S., Matsuoka, T., Tanaka, S., and Kobayashi, H., *J. Electrochem. Soc.*, 146, 392, 1999.
100. Hisamune, T., Fujino, S., Oguri, Y., and Endo, T., *J. Illum. Engng. Inst. Jpn.*, 82(8A), 573, 1998 (in Japanese).
101. Manabe, N., *J. Illum. Engng. Inst. Jpn.*, 87, 15, 2003 (in Japanese).
102. Nishihara, T. and Takeda, Y., *Proc. IDW '00*, 379, 2000.
103. Nihon Keizai Shinbun (Nikkei), 2005-6-4 (in Japanese).
104. Igarashi, T., Kusunoki, T., and Ohno, K., *Tech. Digest, Phosphor Res. Soc. 310th Meeting*, 3, 2005 (in Japanese); *Proc. 25th Int. Display Research Conference* (*Eurodisplay 2005*), 233, 2005.
105. Jak, M.J.J., Hekstra, G.J., Hoppenbrouwers, J.J.L., Vossen, F.J., Raman, N., and Belik, O., *SID '05 Digest*, 1120, 2005.
106. Fukuzawa, T., Toyooka, T., Sakaguchi, Y., Takeda, K., and Yamada, F., *SID '98 Digest*, 247, 1998; Yoshimatsu, R., Yoshida, H., and Minamoto, M., *Abstr. 37th Annual Meeting Illum. Engng. Inst. Jpn.*, 86, 2004 (in Japanese).
107. Japanese Patent Disclosure (Kokai) PH05-152609 (1993) (Appl. 1991-11-25).
108. Bando, K., Noguchi, Y., Sakano, K., and Shimizu, Y., *Tech. Digest*, *Phosphor Res. Soc. 264th Meeting*, 5, 1996 (in Japanese); Japanese Patent Disclosure (Kokai) PH10-242513 (1998) (Appl. 1996-07-29), Note that similar white-LEDs were proposed only 3 months later in the same year by Kasei Optonics. Japanese Patent Disclosure (Kokai) PH10-163535 (1998) (Appl. 1996-11-27).
109. For example, *Electronic Products*, June 2001, p. 61; *Nikkei Techno-Frontier*, 01-9-24, 2, 2001.
110. Taguchi, T., *Proc. IDW'03*, 653, 2003; Taguchi, T., *Ext. Abstr. Int. Symp. on the Light for the 21st Century*, 2, Tokyo, 2002.
111. Tamaki, H., Takashima, Y., Kameshima, M., and Murazaki, Y., *Proc. 122nd Crystal Engineering Meeting*, 29, 2005 (in Japanese).
112. Narukawa, Y., Nagahama, S., Tamaki, H., and Mukai, T., *Oyo Buturi*, 74, 1423, 2005 (in Japanese).
113. Yamada, M., Naitou, T., Izuno, K., Tamaki, H., Murazaki, Y., Kameshima, M., Mukai, T., *Jpn. J. Appl. Phys.*, 42, L20, 2003.
114. Yoshino, M., Suzuki, H., and Miwa, T., *Ext. Abstr. Int. Symp. on the Light for the 21st Century*, Tokyo, Tokyo, 66, 2002; a number of papers presented at *The Phosphor Global Summit 2003* (Scottsdale, March 19–21), *2004* (Miami, March 16–18), *2005* (San Diego, February 28–March 2); See also Section 3.14 and 5.9 in this book.
115. van Uitert, L.G., *J. Lumin*, 29, 1, 1984.
116. For example, Section 5.7.6 and 6.5.3 in this book; Watanabe, M. and Sumita, T., *Tech. Rpt., the Institute of Electronics and Communication Engineers* (*IECE*) *of Jpn.*, ED 72–67, 1973.
117. van Krevel, J.W.H., Thesis, *On new rare-earth doped M-Si-Al-O-N materials*, Technische Universiteit Eindhoven, 2000, ISBN 90-386-2711-4; Höppe, H.A., Lutz, H., Morys, P., Schnick, W., and Seilmeier, A., *J. Phys. Chem. Solids*, 61, 2001, 2000.
118. Höppe, H.A., Stadler, F., Oeckler, O., and Schnick, W., *Angew. Chem. Int. Ed.*, 43, 5540, 2004; Mueller-Mach, R., Mueller, G., Krames, M.R., Höppe, H.A., Stadler, F., Schnick, W., Juestel, T., and Schmidt, P., *Phys. Stat. Sol.* (*A*), 202(9), 1727, 2005.
119. Uheda, K., Hirosaki, N., Yamamoto, H., and Xie, R.-J., *Tech. Digest*, *Phosphor Res. Soc. 305th Meeting*, 37, 2004 (in Japanese); Uheda, K., Hirosaki, N., Yamamoto, H., Yamane, H., Yamamoto, Y., Inami, W., and Tsuda, K., *206th Electrochem. Soc. Meeting*, Honolulu, Abstr. No. 2073, 2004; Uheda, K., Hirosaki, N., Yamamoto, Y., Naito, A., Nakajima, T., and Yamamoto, H., *Electrochem. and Solid State Letters*, 9, H22, 2006.

120. Hirosaki, N., Uheda, K., Xie, R.-J., and Yamamoto, H., *Tech. Digest, Phosphor Res. Soc. 305th Meeting*, 27, 2004 (in Japanese); Xie, R.-J., Mitomo, M., Uheda, K., Xu, F.-F., and Akimune, Y., *J. Am. Ceram. Soc.*, 85(5), 1229, 2002; van Krevel, J.W.H., van Rutten, J.W.T., Mandal, H., Hintzen, H.T., and Metselaar, R., *J. Solid State Chem.*, 165, 19, 2002.
121. Sakuma, K., Hirosaki, N., Kimura, N., Xie, R.-J., Hirafune, S., Yamamoto, Y., and Suehiro, T., *Proc. IDW/AD '05*, 1589, 2005; Hirosaki, N., Xie, R.-J., Yamamoto, Y., and Suehiro, T., *Ext. Abstr. 66th Autumn Meeting Jpn. Soc. Appl. Phys.*, Abstr. 7a-K-7, 1266, 2005; Fiedler, T., Jermann, F., and Zachau, M., *201st Electrochem. Soc. Meeting, Philadelphia*, Abstr. 1191, 2002.
122. Uheda, K., *Kagaku to Kogyou* (*Chemistry and Industry*), 57(11), 1187, 2004.
123. Shinoda, T. and Awamoto, K., *Oyo Buturi*, 75, 5, 2006 (in Japanese); Shinoda, T., *Proc. 8th Asian Symposium on Information Display* (*ASID '04*), Nanjing, 1, 2004.
124. Onimaru, T., Fukuta, S., Misawa, T., Sakita, K., and Betsui, K., *J. SID*, 13(1), 45, 2005; Diaz, A.L. and Dawson, B., *Proc. IDW/AD '05*, 509, 2005.
125. Hisamune, T., *Proc. IDW '02*, 685, 2002.
126. Ogasawara, K., Watanabe, S., Sakai, Y., Toyoshima, H., Ishii, T., Brik, M.G., and Tanaka, I., *Jpn. J. Appl. Phys.*, 43, L611, 2004.
127. Wegh, R.T., Meijerink, A., Lamminmäki, R-J., and Hölsa, J., *J. Lumin.*, 87/89, 1002, 2000.
128. Jüstel, T., Krupa J.C., and Wiechert, D.U., *J. Lumin.*, 93, 179, 2001.
129. Braun, F., *Wied. Ann.*, 60, 552, 1897.
130. Alberti, E., *Braunische Kathodenstrahlroerhen und ihre Anwendung*, Julius Springer, p. 2 and p. 55, 1932.
131. Harvey, E.N., *A History of Luminescence*, American Philosophical Society, p. 345 and p. 410, 1957.
132. Sagara, I., *Nikkei Electronics* No. 660, 135 (1996.4.22) (in Japanese).
133. Institute of Television Engineers of Japan, *History of Television Technology*, pp. 25–26, p. 109, p. 152 and p. 106 (in Japanese).
134. Leverenz, H.W., *RCA Rev.*, 5, 131, 1940.
135. Michelssen, F., German Patent 640929; U.S. Patent 1988605 (Appl. 1931).
136. Izawa, S. and Ishizu, Y., *Mazda Kenkyu Gihou,* 16, 37, 1941 (in Japanese).
137. A report of a talk meeting report, *Toshiba Rev.*, 8, 89, 1953 (in Japanese).
138. Zworykin, V.K. and Morton, G.A., *Television*, 2nd Ed., John-Wiley & Sons, West Sussex, U.K., p. 433, 1954.
139. Bracco, D.J. and Watson, W.R., Sylvania Technical Article (Oct. 1951); de Boer, F. and Emmens, H., *Philips Tech. Rev.*, 16, 232, 1955.
140. Kobayashi, D., Private communication.
141. Laponsky, A.B., Ozeroff, M.J., Thornton, W.A., and Young, J.R., *J. Electrochem. Soc.*, 103, 498, 1956.
142. Larach, S. and Hardy, E., *Proc. IEEE*, 61, 915, 1973.
143. Electronic Industries Association, *Optical Characteristics of Cathode Ray Tube Screens*, The Tube Engineering Advisory Council (TEPAC) Publication No. 116, 1980.
144. Japanese Industrial Standard JIS C-7003, Type Designation System for Cathode Ray Tubes (1982).
145. Pro Electron, Phosphor Screen Characteristics, Doc. ET 55A (1981).
146. EIA TEPAC, Worldwide Type Designation System for TV Picture Tubes and Monitor Tubes, *Proc. SID,* 24, 301, 1983.
147. Tamatani, M., *J. Inst. TV. Engnr. Jpn.,* 39, 150,1985 (in Japanese); Uehara, Y., Morita, Y., Watanabe, H., and Yamamoto, H., *Tech. Report Inst. TV Engnr. Jpn.*, IPD66-3, 1982 (in Japanese).
148. Matsuda, N., Tamatani, M., Tetuishi, Y., and Higuchi, K., *Proc. Japan Display '86* 152, 1986.
149. Ohno, K, Kusunoki, T., and Itoh, T., *Tech. Digest, Phosphor Res. Soc. 217th Meeting*, 1987 (in Japanese).
150. Uehara, Y., Morita, Y., Asano, T., Nakayama, T., Nakai, H., and Fujimaki, K., *Tech. Digest, Phosphor Res. Soc. 243rd Meeting*, 1992 (in Japanese).
151. Chander, J.S. and de Palma, J.J., *J. SMPTE*, 77, 1012, 1968.
152. Ohno, K. and Abe, T., *Electrochem. Soc. Fall Meeting,* Abstr. 611, 1983; Ohno, K., Abe, T., Kuboniwa, S., and Katoh, H., *Tech. Digest, Phosphor Res. Soc. 195th Meeting*, 1983 (in Japanese).
153. Denpa Shinbun, 1983.8.19 (in Japanese).

154. Tsuda, N., Tamatani, M., and Satoh, T., *Tech. Digest, Phosphor Res. Soc. 199th Meeting* 1984 (in Japanese).
155. Ohno, K. and Abe, T., *Electrochem. Soc. Fall Meeting,* Abstr. No. 593A, 1984.
156. Yamamoto, H. and Matsukiyo, H., *J. Lumin.*, 48 & 49, 43, 1991.
157. Ohno, K., Abe, T., and Kusunoki, *Jpn. J. Appl. Phys.*, 29, 103, 1990.
158. Awazu, K. and Matsunaga, K., Jpn. Patent Publ. (Kokoku) 61-21505 (1986).
159. Tamatani, M., Matsuda, N., Hattori, H., and Tsuda, N., *Electrochem. Soc. Fall Meeting,* Abstr. 594, 1984.
160. Uehara, Y., Morita, Y., Watanabe, H., and Yamamoto, H., *Tech. Digest, Phosphor Res. Soc. 226th Meeting*, 1989 (in Japanese).
161. Nikkei Shinbun, 1986-12-3 (in Japanese).
162. Flechsig, W, Germ. Pat. 736,575 (1938).
163. Law, H.B., *RCA Rev.*, 12, 466, 1951.
164. Yamada, M., *J. Inst. TV Engnr. Jpn.*, 12, 58 and 106, 1958 (in Japanese).
165. Committee for trial preparation of a color picture tube, *A report on a study of 17-inch color picture tubes,* 609 pp., 1961 (in Japanese).
166. Nakajima, S., Kobayashi, D., Yasuoka, S., and Ogihara, Y., *Toshiba Rev.,* 16, 865, 1961 (in Japanese).
167. Kobayashi, D., Ichise, W., and Matsuura, S., *J. Inst. TV Engnr. Jpn.*, 16, 642, 1962 (in Japanese).
168. Bril, A. and Klasens, H.A., *Philips Res. Repts.*, 10, 305, 1955.
169. Van Uitert, L.G., Linares, R.C., Soden, R.R., and Ballman, A.A., *J. Chem. Phys.*, 36, 702, 1962.
170. Levine, A.K. and Pallila, R.C., *Appl. Phys. Lett.*, 5, 118, 1964.
171. Kano, T., *Kagaku to Kogyou*, 33, 106, 1980 (in Japanese).
172. Royce, M.R. and Smith, A.L., *Electrochem. Soc. Spring Meeting,* Abstr. 34, 1968.
173. Awazu, K., *J. Inst. TV Engnr. Jpn.,* 22, 179, 1968 (in Japanese).
174. Wanmaker, W.L. and ter Vrugt, J.W., *Philips Res. Repts.*, 22, 355, 1967.
175. Hoffman, M.V., U.S. Patent 3484383 (Appl. 1967); *J. Electrochem. Soc.*, 115, 560, 1968.
176. Nishimura, T., *Tech. Digest, Phosphor Res. Soc. 139th Meeting*, 1971 (in Japanese).
177. The Joint Electron Device Engineering Council (JEDEC, TEPAC later), Registration of P43–P45 Phosphors (Thomas Electronics 1971-6-28).
178. Fiore, J.P. and Kaplan, S.H., *IEEE Trans.,* BTR-15, 267, 1969; U.S. Patent 3146368 (Appl. 1961).
179. Tsuneta, T and Takenaka, S, *Denshi-gijutu*, 16, No. 2, 8, 1975; Tsuneta, T., Ohta, Y., and Suzuki, K., *Toshiba Rev.*, 29, 894, 1974 (in Japanese).
180. Matsuura, S., Itou, T., Koga, Y., and Tamatani, M., *Tech. Digest, Phosphor Res. Soc. 166th Meeting,* 1977 (in Japanese); Matsuura, S. and Tamatani, M., *Electrochem. Soc. Spring Meeting,* Abstr. 334, 1978; Itou, T., *ibid*, 333 1978.
181. Nonogaki, S. and Tomita, Y, *Electrochem. Soc. Spring Meeting,* Abstr. 497, 1982.
182. Ishii, T. and Awazu, K., *Tech. Digest, Phosphor Res. Soc. 204th Meeting,* 1985 (in Japanese).
183. Ikegaki, N., *Tech. Digest, Phosphor Res. Soc. 213rd Meeting*, 1986 (in Japanese).
184. Kaplan, S.H. and Longe, H., *SID Digest of Tech. Papers,* 70, 1975; RCA Technology Documents for Y-tube, 1975.
185. Ishii, T. and Ueba, Y., *Electrochem. Soc. Spring Meeting,* Abstr. 493, 1982.
186. Inoue, K., Watanabe, M., Takahara, T., Wakatsuki, T., and Nishimura, T., *Electrochem. Soc. Spring Meeting,* Abstr. 180, 1981; Itou, T., Watanabe, S., Tsukagoshi, H., and Koike, N., *Tech. Digest, Phosphor Res. Soc. 184th Meeting,* 1981 (in Japanese).
187. Itou, T., Matsuda, H., and Shimizu, K., *Toshiba Rev.*, 45, 831, 1990 (in Japanese).
188. Itou, T,. Matsuda, H., and Onodera, M., *SID '95 Digest,* 25, 1995; Ohno, K. and Kusunoki, T., *J. Electrochem. Soc.*, 143, 1063, 1996.
189. Kaplan, S.H., U.S. Patent 2959483 (Appl. 1960).
190. Itou, T., *Tech. Digest, Phosphor Res. Soc. 252nd Meeting*, 1994 (in Japanese).
191. Inaba, M., Teshima, K., Higashinakagawa, E., and Ohtake, Y., *IEEE Trans. Electron Devices*, 35, 1721, 1988.
192. Ohno, K. and Kusunoki, T., *Proc. IDW '03*, 751, 2003; *Tech. Digest of SID'04*, 1048, 2004.
193. den Engelsen, D., Heynderickx, I., and Shuyterman, S., *J. SID*, 12(3), 241, 2004; Tu, Y., Heynderickx, I., and Li, X., *Tech. Digest of SID '04*, 322, 2004.

194. den Engelsen, D. and Brouwer, W., *Proc. IDW '03*, 1695, 2003.
195. Albessard, A.K., Matsuda, N., Tamatani, M., Yokota, S., Inoue, Y., Terajima, A., Hattori, H., Akitsuki, A., and Suzuki, T., *Proc. IDW '00*, 877, 2000.
196. Labrunie G. and Meyer, R., *Disp. Technol. Appl.* (UK), 8(1), 37–40, 1987; Meyer, R., Ghis, A., Rambaud, P., and Muller, F., *Proc. Japan Display '86*, 512, 1986.
197. Meyer, R., *Proc. Eurodisplay '90*, Amsterdam, 374, 1990.
198. Spindt, C.A., Brodie, I., Humphrey, L., and Westerberg, E.R., *J. Appl. Phys.*, 47(12), 5248, 1976.
199. Itoh, S. and Tanaka, M., *Proc. IEEE*, 90(4), 514, 2002.
200. Itoh, S., Tanaka, M., and Tonegawa, T., *J. Vac. Sci. Technol*. B22(3), 1362, 2004.
201. Itoh, S., Watanabe, T., Yamaura, T., and Yano, K., *Tech. Digest*, *Asia Display '86*, 617 1995.
202. Vaudaine, P. and Meyer, R., *Technical Digest Int. Electron Devices Meeting* (*IEDM*), 197, 1991; Levy, F. and Meyer, R. *Conference Record of the 1991 International Display Research Conference*, 20, 1991.
203. Newman, S.J., Smith, R.T., and Penn, C., *Tech. Digest of SID* '98, 95, 1998.
204. Curtin, C.J. and Iguchi, Y., *Tech. Digest of SID'00*, 1263, 2000.
205. Lee, C.G., Lee, S.J., Whang, S.Y., Chi, E.J., Yun, T.I., Lee, J.S., Kim, J.W., Jang, J.E., Cho, S.H., Lee, B.G., Lee, S.J., Han, H.S., Ahn, S.H., Ryu, K.S., Jung, K.W., Kang, J.H., Jin, S.H., Jo, S.K., Jung, J.E., Choi, J.S., Oh, T.S., Kang, S.K., and Kim, J.M., *Proc. IDW '02*, 1021, 2002.
206. Tanaka, M., Obara, Y., Naito, Y., Kobayashi, H., Toriumi, M., Niiyama, T., Sato, Y., Itoh, S., and Kawasaki, H., *Tech. Digest SID '04*, 832, 2004.
207. Ishizuka, Y., Oyaizu, T., Oguchi, T., Hoshi, H., and Yamaguchi, E., *Proc. IDW/AD'05*, 1655, 2005; Oguchi, T., Yamaguchi, K., Sasaki, K., Suzuki, K., Uzawa, S., and Hatanaka, K., *Tech. Digest of SID'05*, 1929, 2005; Yamaguchi, E., Sakai, E., Nomura, I., Ono, M., etc., *Tech. Digest of SID '97*, 52, 1997.
208. Iijima, S., *Nature*, 354, 56, 1991.
209. Okuda, S., Nakata, S., Shiroishi, T., Nishimura, K., Takai, M., Uemura, S., Yotani, J., Kurachi, H., Hayashi, N., Okai, M., Sugawara, T., Murakami, T., and Kuroki, Y., *Tech. Digest of SID '05*, 1712, 2005.
210. Itoh, S., Kimizuka, T., and Tonegawa, T., *J. Electrochem. Soc.*, 136, 1819, 1989.
211. Bechtel, H. and Nikol, H., *Electrochem. Soc. Proceedings*, Volume 97/29, 256, 1998.
212. Kajiwara, K., *J. Vac. Sci. Technol.* A19, 1083, 2001.
213. Hanazono, T. and Tokunaga, Y., *Tech. Digest*, *Phosphor Research Society 297th Meetin*g, 2, 2003 (in Japanese).
214. Sato, Y., Takahashi, H., Tamaki, H., and Kameshima, M., *Proc. IDW '02*, 951,2002.
215. Okamoto, S., Kobayashi, H., and Yamamoto, H., *J. Appl. Phys*., 86, 5594, 1999.
216. Pupin, M., *Radiologic Science for Technologists*, p. 8, C. V. Mosby, St. Louis, 1975; Izawa, S., *J. Illum. Engng. Jpn.*, 24, 178, 1940.
217. Harvey, E.N., *A History of Luminescence*, pp. 416–417. The American Philosophical Society, Philadelphia, 1957.
218. Brixner, L.H., *Mater. Chem. Phys*. 16, 253, 1987.
219. Tokyo Denki, Tokyo, *Fifty years of Tokyo Denki*, p. 573, 1940 (in Japanese).
220. Tanaka, M. and Harada, O., *Mazda Res. Rpt*, 8, 167, 1933 (in Japanese).
221. Izawa, S., *Mazda Res. Rpt*., 9, 1, 1934 (in Japanese).
222. Katoh, Y. and Iizuka, Y., *Nippon Houshasen Gijutu Gakkai-shi*, 38, 633, 1982 (in Japanese).
223. Dainippon Toryou, Osaka, *Dainippon Toryou no 40nen*, 1969 (in Japanese).
224. Shimadzu Seisakusho, Kyoto, *Shimadzu Seisakusho-shi*, 1967 (in Japanese).
225. Izawa, S., *Mazda Res. Rpt*., 12, 178, 1937 (in Japanese).
226. Takizawa, T., *Kagaku to Kogyou*, 22, 1003, 1969 (in Japanese).
227. Coltman, J.W., *Radiology*, 51, 359, 1948; Ogawa, I., Uchida, Y., Ono, N., and Maejima, T., *Toshiba Rev*., 12, 1363, 1957.
228. Stevels, A.L.N. and Kuhl, W., *Medica Mundi*, 19, 3, 1974.
229. Stevels, A.L.N. and Schrama-de Pauw, A.D.M., *Philips Res. Repts.*, 29, 340, 353, 1974.
230. Takizawa, T. Shimiya, K., and Kaji, A., U.S. Patent 3389255 (1968).
231. Tecotzky, M., Rings, S.A., Wickersheim, K.A., and Buchanan, R.A., *Electrochem Soc. Spring Meeting* RNP-335, 1968.

232. Rabatin, J.G., *J. Electrochem. Soc.*, 129, 1552, 1982.
233. Stevels, A.L.N., *Medica Mundi*, 20, 12, 1975.
234. Toma, S.Z. and Shaffer, F.N., U.S. Patent 3527710 (1970).
235. Yokota, K., Nishimura, T., Takeuchi, T., and Tuchiya, J., *Toshiba Rev.*, 30, 353, 1975 (in Japanese).
236. Brixner, L.H. and Chen, H.-Y., *J. Electrochem. Soc.*, 130, 2435, 1983.
237. Royce, M.R., Nakamura, S., Shinomiya, G., Chikutei, S., and Kondo, T., *Electrochem. Soc. Fall Meeting,* Abstr. 637, 1988; Minamidani, T., Royce, M.R., Chikutei, S., Kondo, T., Shinomiya, G., Murata, Y., Sakata, T., Mori, H., Imanaka, N., and Adachi, G., *Electrochem. Soc. Fall Meeting*, Abstr. 644, 1991.
238. Blasse, G. and Grabmaier, B.C., *Luminescent Materials*, p. 162, Springer-Verlag, Berlin, 1994.
239. Hounsfield, G., *Br. J. Radiol.*, 46, 1016, 1973.
240. Sonoda, M., Takano, M., Miyahara, M., and Shibahara, Y., *Radiography,* 148, 833, 1983.
241. Furukhi, M.R., *IEEE Trans. Nucl. Sci.*, NS-31, 372, 1984; Grabmaier, B.C., *J. Lumin.* 60/61, 967, 1994.
242. Suzuki, A., Yamada, H., Uchida, Y., Kawano, H., and Yoshida, M., *Tech. Digest, Phosphor Res. Soc. 197th Meeting*, 1983 (in Japanese).
243. Yokota, K., Matsuda, N., and Tamatani, M., *Electrochem. Soc. Fall Meeting* RNP-1870, 1987; *ibid*, Abstr. 633, 1988.
244. Yamada, H., Suzuki, A., Uchida, Y., Yoshida, M., and Yamamoto, H., *J. Electrochem. Soc.*, 136, 2713, 1989.
245. Cusano, D.A., Hoffman, D., and Riedner, R.J., *Am. Ceram. Soc. Bull.*, 71, 1120, 1992.
246. Greskovich, C.D., Cusano, D.A., and DiBianca, F.A., U.S. Patent 4 518 546 (1985).
247. Takahashi, K., Shibahara, S., and Miyahara, J., *J. Electrochem. Soc.*, 132, 1492, 1985.
248. Japanese Patent Disclosure (Kokai) 55-163472, 55-12142, 55-12143, 55-12144, 55-12145 and others.
249. Umemoto, C., Kitada, A., Takahashi, K., and Matsuda, T., *Electrochem. Soc. Fall Meeting,* Abstr. 640, 1988.
250. Kano, T., Takahashi, T., Okajima, K., Umetani, K., Ataka, S., Yokouchi, H., and Suzuki, R., *Appl. Phys. Lett*., 48, 1117, 1986.
251. Amitani, K. and Honda, S., *Electrochem. Soc. Fall Meeting,* Abstr. 641, 1988.
252. Matsuzawa, T. and Murayama, Y., *Tech. Digest, Phosphor Res. Soc. 245th Meeting,* 1993 (in Japanese).
253. For example, the number of talks on the photostimulable phosphors presented at Electrochem. Soc. Meeting is seven at 1988 Fall, six at 1990 Fall, and six at 1992 Fall. These high numbers show that the imaging plate created a new scientific era.
254. Amemiya, Y. and Miyahara, J., *Nature*, 336, 89, 1988; von Seggern, H., *Nucl. Instrum. Methods A*, 322, 467, 1992; Takebe, M., *Oyo Buturi*, 65, 601, 1996.
255. Mori, I., U.S. Patent 4630202 (1986); Kalender, W.A., *Radiology,* 177(3) Supplement SS108, 1990; Kalender, W.A., Seissler, W., Klotz, E., and Vock, P., *Radiology,* 176, 181, 1990.
256. Prokop, M., *Principles of CT, Spiral CT, and Multislice CT* in *Spiral and Multislice Computed Tomography of the Body,* Prokop, M., Galanski, M., van der Molen, A.J., and Schaefer- Prokop, C., Eds., 2, Thieme, 2003; Taguchi, K. and Aradate, H., *Med. Phys.*, 25(4), 550, 1998.
257. Boyd, D.P., *Transmission Computed Tomography,* in *Radiology of the Skull and Brain, Technical Aspects of Computed Tomography,* Newton, T.H. and Potts, D.G., Eds., 4357, The C. V. Mosby Company, St. Louis, 1981.
258. *Multislice CT 2005*, *Eizo Joho* (*Image Information*), 37(7) (an extra issue), 2005 (in Japanese).
259. Saito, Y., Aradate, H., Miyazaki, H., Kudo, Y., Tsujita, K., Shimadu, N., Sawanaga, Y., *Proc. SPIE*, Vol. 4682, 801, 2002.
260. Okumura, M, Tamatani, M, and Igarashi, K., *Proc. SPIE*, Vol. 4682, 1, 2002; Fukuta, Y., Tamatani, M., Matsuda, N., and Okumura, M., *Tech. Digest, 296th Phosphor. Res. Society*, 1, 2003 (in Japanese); Greskovich, C. and Duclos, S., *Annu. Rev. Mater. Sci.*, 27, 69, 1997; Rossner, W. and Ostertag, M., *Electrochem. Soc. Fall Meeting*, Boston, Abstr. 879, 1998.

261. Beyer, T., Townsend, D.W., Brun, T., Kinahan, P.E., Charron, M., Roddy, R., Jerin, J., Young, J. Byars, L., and Nutt, R.J., *Nucl. Med.*, 41(8), 1369, 2000; Townsend, D.W., Beyer, T., Kinahan, P.E., Brun, T., Roddy, R., Nutt, R., and Byars, L.G., *IEEE Nuclear Science Symposium and Medical Imaging Conference*, Vol. 2, 1170, 1998.
262. Nutt, R., *History of PET*, https://www.cpspet.com/our_company/history_o_pet.shtml; Eriksson, L., Townsend, D., Eriksson, M., Melcher, C., Schmand, M., Bendriem, B., Nutt, R., *Nucl. Instrum.* Methods, A525, 242, 2004.
263. Tanaka, E. and Kanno, I., *Development of Positron Emission Tomography* (*PET*) *in Japan—Commemorating the Silver Anniversary since the First PET Image*, http://www.ricoh.co.jp/net-messena/ACADEMIA/JAMIT/MITVM/PET/TANAKA04/index.html. (in Japanese)
264. See section 7.3.; Blasse, G., and Grabmaier, B.C., *Luminescent Materials*, Springer-Verlag, Berlin, 1994, 170.
265. Weber, M.J. and Monchamp, R., *J. Appl. Phys.*, 44, 5495, 1973.
266. Takagi, K. and Fukazawa, T., *Appl. Phys. Lett.*, 42(1), 43, 1983.
267. Melcher, C.L. and Schweitzer, J.S., *IEEE. Trans. Nucl. Sci.*, 39(4), 502, 1992.
268. Rowlands, J.A. and Yorkston, J., Flat Panel Detectors for Digital Radiography, in *Handbook of Medical Imaging*, Beutel, J., Kundel, H.L., and Van Metter, R.L., Eds., Vol. 1, 223, SPIE Press, 2000.
269. Mcmaster, R.C. and Hoyt, H.L., *Mater. Eval.*, 29(12), 265, 1971; Boag, J.W., *Phys. Med. Biol.*, 18, 3, 1972.
270. Antonuk, L.E., Bourdry, J., Huang, W., McShan, D.L., Morton, E.J., Yorkston, J., Longo, M.J., and Street, R.A., *Med. Phys.*, 19, 1455, 1992; Nishiki, M. and Iinuma, K., U.S. Patent 4689487 (1987).
271. Lee, D.L., Cheung, L.K., and Jeromin, L.S., *Proc. SPIE*, Vol. 2432, 237, 1995; Zhao, W. and Rawlands, J.A., *Med. Phys.*, 22, 1595, 1995.
272. Hamers, S. and Freyschmidt, J., *Medica Mundi* 42(3), 1, 1998; Granfors, P.R. and Aufrichtig, R., *Med. Phys.*, 27, 1324, 2000; Reiff, K.J., *Eur. J. Radiol*, 31, 125, 1997; Antonuk, L.E., El-Mohri, Y., Hall, A., Jee, K-W., Maolinbay, M., Nassif, S.C., Rong, X., Siewerdsen, J.H., Zhao, Q., and Weisfield, R.L., *Proc. SPIE*, Vol. 3336, 2, 1998; Schiebel, U., Conrads, N., Jung, N., Weibrecht, H., Wieczorek, H., Zaengel, T., Powell, M.J., French, I.D., and Glasse, C., Proc. SPIE, vol. 2163, 129, 1994.
273. Yamazaki, T., Morishita, M., Kaifu, N., and Endo, Y., *Proc. 12th International Symposium and Exhibition CAR'98* (Elsevier Int. Congress Series 1165), 536 1998.
274. Lee, D.L., Cheung, L.K., Jeromin, L.S., Palecki, E.F., Rodricks, B., *Proc. SPIE*, Vol. 3032, 88, 1997; Tsukamoto, A., Yamada, S., Tomisaki, T., Tanaka, M., Sakaguchi, T., Asahina, H., and Nishiki, M., *Proc. SPIE*, Vol. 3336, 388, 1998; Sato, T., Koyama, H., Izumi, Y., Yamane, Y., Shimura, Y., and Tsuruta, H., *Oyo Buturi*, 73(7), 931, 2004 (in Japanese).
275. Antonuk, L.E., Jee, K.-W., El-Mohri, Y., Maolinbay, M., Nassif, S., Rong, X., Zhao, Q., Siewerdsen, J.H., Street, R.A., and Shah, K.S., *Med. Phys.*, 27(2), 289, 2000.
276. Murayama, Y, *Isotope News*, 12, 1971-4; 5, 1980-11 (in Japanese).
277. Kameyama, N., *Theory and Application of Fluorescence and Phosphors*, Maruzen, Tokyo, 1960 (in Japanese).
278. Hakomori, S., *Synthesized Phosphors*, Kyouritsu, p. 134, 1938 (in Japanese).
279. Toshiba, Kawasaki, *Eighty five years of Tokyo Shibaura Denki*, p. 512, p. 746, 1975 (in Japanese).
280. Nishikawa, K. and Kawai, K., *Shimadzu Hyouron*, 14, 223, 1957 (in Japanese).
281. Higashide, H., *Toshiba Rev.*, 15, 1371, 1960 (in Japanese).
282. Kojima, T. and Yoshikawa, S., *Tech. Digest, Phosphor Res. Soc. 132nd Meeting*, 1970; Sakamoto, H. and Tanaka, S., *Oyo Buturi*, 29, 413, 1960; Yamada, M. and Kojima, T., *J. Inst. TV Engnr. Jpn.*, 12, 547, 1958 (in Japanese).
283. Tatsuoka, S., *Shashin Kogyo* (*Photography Industry*), 19, 12,1961; Suzuki, T., *ibid*, 15; Kato, K., *ibid*, 19 (in Japanese).
284. Kiss, Z.J. and Pressley, R.J., *Appl. Optics.*, 5, 1474, 1966.
285. Masuda, M. and Kiyozumi, K., *Tech. Digest, Phosphor Res. Soc. 150th Meeting*, 1973 (in Japanese).
286. Yamashita, T., *Tech. Digest, Phosphor Res. Soc. 179th Meeting*, 1980 (in Japanese).

287. Maeda, K. and Tamatani, M., *Gazou Gijutsu*, 3, 35, 1972 (in Japanese).
288. Inoguchi, T., Takeda, M., Kakihara, Y., Nakata, Y., and Yoshida, M., *SID '74 Digest*, 84, 1974.
289. Koike, S., Toyonaga, T., Kojima, T., Takahashi, K., Hase, T., and Kagami, A., *Tech. Digest, Phosphor Res. Soc. 161st Meeting*, 1976 (in Japanese).
290. Kurahashi, K., Yagishita, K., Fukushima, N., and Kobayashi, H., *SID '81 Digest*, p. 132, 1981.
291. Denpa Shinbun, 1986-8-11; Nikkei Shinbun, 1986-12-3 (in Japanese).
292. Denpa Shinbun, 1986-5-16; Nakano, S., Ishii, K., Takeda, T., Gannen, K., and Tanaka, N., *Mitsubishi Denki Gihou* 60, 357, 1986 (in Japanese).
293. Ikegaki, N., *Tech. Digest, Phosphor Res. Soc. 213th Meeting*, 1986 (in Japanese).
294. Denpa Shinbun, 1986-11-25 (an extra issue) (in Japanese).
295. Shinoda, T., Wakitani, M., Nanto, T., Kurai, T., Awaji, N., and Suzuki, M., *SID '91 Digest*, p. 724, 1991.
296. Nikkei Sangyou Shinbun, 1996.8.23. (Futaba Electronics).
297. Randall, J.T., Brit. Patent 457126 (Appl. 1935-5-22) (Device application).
298. Randall, J.T., Brit. Patent 469732 (Appl. 1936-1-27).
299. Strange, J.W., Brit. Patent 410159 (Appl. 1932-12-13) (For white-emitting CRTs).
300. British Thomson-Houston, Brit. Patent 494299 (Appl. 1936-4-22) (Device application).
301. McKeag, A.H. and Randall, J.T., Brit. Patent 495706 (Appl. 1937-4-16).
302. Merril, J.B. and Stewart, W.E., Brit. Patent 581951 (Appl. 1946-10-30).
303. Nagy, R., Wollentin, R.W., and Lui, C.K., *J. Electrochem. Soc.*, 97, 29, 1950.
304. Ranby, P.W., U.S. Patent 2596509 (1952).
305. Koelmans, H., Wanmaker, W.L., Cox, A.P.M., and Emmens, A.S., U.S. Patent 3110680 (1963).
306. News, *J. Electrochem. Soc.*, 105, 194C, 1958; NBS Standard Reference Materials Catalogue—Special Publication 260 (1979, 1981–1983).
307. Ginther, R.J., U.S. Patent 2499307 (1950).
308. Hunt, B.E. and McKeag, A.H., *J. Electrochem. Soc.*, 106, 1032, 1959.
309. Butler, K.H., U.S. Patent 2826553 (1958); Ranby, P.W., Mash, D.H., and Henderson, S.T., *Brit. J. Appl. Phys. Suppl.*, 4, 518, 1955.
310. Brown, J.J., U.S. Patent 3407325 (1968).
311. Wanmaker, W.L. and Verlijsdonk, U.S. Patent 3417027 (1968).
312. Ijima, S., Matsuoka, M., and Ide, S., *Tech. Digest, Phosphor Res. Soc. 162nd Meeting*, 1976 (in Japanese).
313. Starick, D., *Phosphors Global Summit 2003*, Scottsdale, Arizona, Speaker 19, March 19–21, (2003); Yajima, T., *Phosphors Global Summit 2005*, San Diego, Speaker 16, Feb. 28–March 2, (2005); U.S. Pat. 6809347 (Toyoda Gosei, Tridonic Optoelectronics, Litec, Leuchtstoffwerk Breitungen, 2004).
314. Leverenz,H.W., *An Introduction to Luminescence of Solids*, John-Wiley & Sons Inc., West Sussex, p. 399, 1950.
315. Kagami, A., Hase, T., Narita, K., and Mimura, Y., *Tech. Digest, Phosphor Res. Soc. 158th Meeting*, 1975 (in Japanese); *J. Lumin.*, 12/13, 941, 1976.
316. Morimoto, K., *Electronic Ceramics*, 11, Winter, 42, 1980 (in Japanese).
317. Matsuoka, T., *Tech. Digest, Phosphor Res. Soc. 169th Meeting*, 1978 (in Japanese).
318. Yamazaki, E., Asano, T., Morita, Y., Yamauchi, M., and Ueyama, T., *Proc. Annual Meeting Inst. TV Engnr. Jpn.*, pp. 99–100, 1984 (in Japanese).
319. Ohno, K. and Abe, M., *Tech. Digest, Phosphor Res. Soc. 204th Meeting*, 1985 (in Japanese).
320. Hase, T., Yoshida, H., and Mikami, T., *Tech. Digest, Phosphor Res. Soc. 205th Meeting*, 1985 (in Japanese).
321. Wickersheim, K.A., Alves, R.V., and Buchanan, R.A., *IEEE Trans. Nucl. Sci.*, 17, 57, 1970.